A NEW METHOD FOR THE IN-SITU DIFFUSE REFLECTANCE FTIR ANALYSIS OF COALS

Dongtao Li, Wen Li, Haokan Chen and Baoqing Li

State Key Laboratory of Coal Conversion,
Institute of Coal Chemistry, Chinese Academy of Sciences,
030001, Taiyuan, P.R.China

Introduction

Since the first application of infrared spectroscopy in coal science made by Cannon et al.[1], it has been being used as the main characteristic method for coal. However, when the conventional transparent IR spectroscopy was used, KBr must be used to dilute the coal samples, which can result in many problems such as the adsorbing of moisture and catalyzing the pyrolysis of coal etc. Hence Fuller et al.[2] proposed to use the diffuse reflectance infra red spectroscopy (DRIFT) for the analysis of coal, and the disturbance from KBr was eliminated consequently. Moreover, it was proved to be possible to use neat coal samples for DRIFT, and since then this method has been used more and more widely in coal science. Moreover, because of the use of isolated reactor chamber this technique is very likely to be used for the in-situ analysis of coal. However, because of condensation of the volatiles produced by coals during pyrolysis, its application has been limited. In this paper, a new method that mainly deals with this problem is proposed, and it implied that this method could also be used for other samples that can produce volatiles when heated.

Experimental

Samples. The dimineralized (with HF/HCl) Huolinhe lignite was used. Sample of –100 mesh was further ground under argon for 30 min in a glove box with an agate mortar. Both proximate and ultimate analysis of the parent Huolinhe lignite (abbreviated as HLH) are given in **Table 1**.

Table 1 Analysis of samples

Sample	Proximate analysis (%)			Ultimate analysis (%, daf)				
	V (daf)	M (ad.)	A (ad.)	C	H	N	S	O (diff.)
HLH	48.42	17.38	25.56	73. 11	4. 70	1. 22	0.44	20.53

Apparatus and procedure. The diffuse reflectance spectra were measured on EQUINOX 55 FTIR spectrometer (BRUKER) with the 0030-102 high temperature/high pressure accessory of Thermo Spectra-Tech using ZnSe windows. The detector was liquid nitrogen cooled MCT (mercury cadmium telluride). A mirror that is believed not to absorb water was used as the background[3]. The DRIFT spectra were collected with the co-additions of 100 scans and resolution of 8 cm^{-1}. The resultant spectra were converted to Kubelka-Munk function.

Because of the condensation of volatiles produced from heated coal samples, a piece of porcelain was used. About 0.2~0.3mg coal samples was placed onto it and was pressed with a spatula, then the porcelain was placed into the center of the original reactor (**Figure 1**) and the dome was fixed. Before IR measurement, about 260ml/min argon was introduced for about 90 minutes for the stabilization of moisture adsorbed by sample. After that, the flow rate of argon was adjusted to 400 ml/min and the spectra of sample were collected from room temperature (26 ^oC) to 620 ^oC at every 30^oC when the sample was heated at a rate of 6 ^oC/min. The heating was manually controlled and the plot of temperature versus time is given in **Figure 2**. The accuracy of the temperature controlling is about ±1^oC, and the coefficient of fit linear result (Temperature [^oC]= 5.99835 ^oC/min)*Time[min.]+26.14465[^oC]) in **Figure 2** is >99.99%, hence this manually temperature-controlled heating is as good as automatically temperature-programmed-heating when the sample is heated slowly.

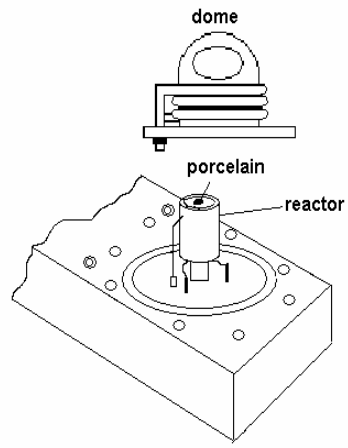

Figure 1 The schematic of the high temperature/high pressure reactor of Spectra-Tech[4].

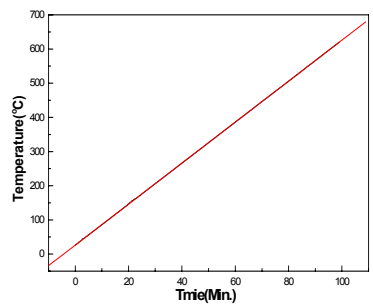

Figure 2 The manually temperature-controlled curve at a heating rate of 6^oC/min

Results and Discussion

The reliability of this method. For many researchers, the in-situ DRIFT analysis of coals from room temperature to high temperature is limited by the condensation of volatile produced by coal heated, and we also encountered this difficulty when we applied the commercial DRIFT accessory for our experiments. With the original commercial accessory, about 20 mg coal is needed, and even the argon was introduced at the rate of about 600ml/min, the condensation of volatile produced by coal could not be eliminated.

Fraser[5] and Iwanski[6] had proved that, for the DRIFT analysis, only the sample on the top 10 microns can contribute to the diffuse reflectance spectra of coal. When the reactor of the commercial accessory (with a depth of 2 mm and a diameter of 6 mm) were used, the amount of sample loaded into the reactor is too large, which is not necessarily needed for IR measurement. Volatile will condense on the windows and disturb the spectra of the solids consequently. Therefore, reducing and/or removing the amount of volatiles produced is probably the key to solve this problem.

In order to achieve this, two measures were taken. One is to reduce the amount of samples used so that the volatile matter produced is ignored. Obviously, it is impossible to reduce the amount

of sample loaded into the original reactor shown in **Figure 1**, because on the one hand it is required to press the samples in it so that the sample surface is smooth, which means that the reactor must be cramed; and on the other hand, the tip of thermocouple is just in the middle of the reactor, and it is not convenient to press the sample with a smaller spatula when only a thin layer of sample is loaded (in fact, this operation is not permitted, because the infrared light will be shut out by the wall of the reactor). To solve this difficulty, a piece of porcelain with a height of 2 mm (which is just the depth of the original reactor) and a diameter of 3 mm (which is the diameter of the section area of the infrared light) was used. About 0.2~0.3mg coal was placed on the top of it and pressed with a spatula. Finally the porcelain was placed into the center of the reactor provided by Spectra-Tech company (**Figure 1**). The subsequent experimental procedures are the same as those of using the original reactor. Another measure taken by us was increasing the flow rate of carrier gas so that the small amount of volatiles produced is purged out as soon as possible, and 400ml/min was set as the common flow rate used after optimization.

As for the amount of sample used, through calculating, it was proved that 0.2~0.3 mg coal is enough for the requirement on the height of sample in DRIFT analysis. In fact, only a layer of coal was needed if the diameter of coal particle were supposed to be 10 microns. So it is clearly that the amount of sample used is enough, while the amount of volatiles produced can been greatly reduced.

The spectrum of demineralized HLH (abbr. as HHD) measured at 620 ^{o}C with the original reactor, named A, and that with the porcelain, named C, are both shown in Figure 3. Unexpected absorbance was observed in spectrum A, particularly at the wavenumber of 2930cm^{-1} and 3560cm^{-1}, which is believed to be due to the tar and water condensed in ZnSe window respectively. We try to modify the spectrum A with abstraction of the effect of tar and water, the resultant spectrum named B showed that only the effect of tar could be partly eliminated, but the water disturbance still existed due to its strong absorption by tar. This suggested that only using the porcelain as the reactor, the true in-situ spectrum of the coal at high temperature could be obtained.

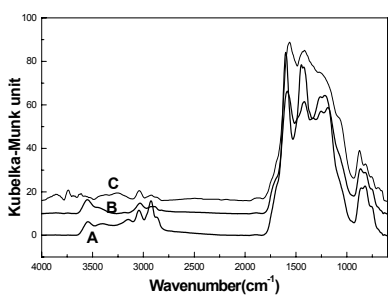

Figure 3 The spectra of HHD (A, measured with original reactor;
B, the spectrum after the subtraction of the contribution of tars condensed on windows; C, the spectrum measured with porcelain reactor.)

The spectra shown in **Figure 4** are measured directly by the spectrometer during the in-situ analysis of the same coal without any modifications, and the quality of them was found very good. When the variation trend of the spectra is compared with that in a reference [(7)], it was found almost the same as that proved by other researchers. Therefore, we think the method can be used for the in-situ analysis of coal with high reliability.

The keys of using this method. We have used this method successfully for the in-situ analysis of coal macerals and the kinetics of the decomposition of hydrogen bonds in coal. However, to get proper and reliable spectra, some cares should be taken. First, to press the coal sample placed on the top of porcelain, the surface of the sample pressed cannot reflect light when it is seen under light. Second, the porcelain should be placed just in the center of the reactor. Third, the flow rate of carrier gas should be as large as 400ml/min so that the small amount of volatiles produced was purged out as quickly as possible.

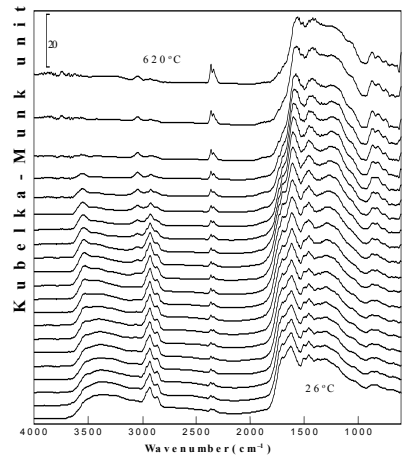

Figure 4 The in-situ DRIFT spectra of HHD from 26°C to 620 ^{o}C measured at every 30°C

Conclusions

Using a small porcelain (with a height of 2mm and a diameter of 3mm) to support coal, combined with increasing the flow rate of carrier gas, it is possible to get high quality spectra for in-situ DRIFT analysis of coal samples. With this method, the samples can be analyzed at as high as 620 ^{o}C or higher. We suggest this method is also useful for the in-situ analysis of other samples producing volatiles when heated.

Acknowledgement

This work was supported by the Natural Science Foundation of China, under contract No. 29906012. The authors gratefully acknowledge many valuable discussions with Prof. Dong Q in our institute.

References

(1) Cannon, C. G.; Sutherland G. B. M. *Transaction of Faraday Society*, **1945**, *41*, 279~288.
(2) Fuller M. P.; Griffiths, P. R. *Analytical Chemistry*, **1978**, 50(13), 1906~1910.
(3) Miura, K.; Mae, K.; Li W. et al.. Energy & Fuels, 2001,15(3), 599~610.
(4) *High temperature/High Pressure chamber (P/N 0030-102) User's Manual(Version 2.1)*, Spectra-Tech(USA), p. 3.
(5) Iwanski P. *Energy &Fuel*s, **1990**, 4, 589.
(6) Fraser, D. J. J.; Groffiths, P. R. *Applied Spectroscopy*, **1990**, 44 (2), 193.
(7) Solomon, P. R. Relation between coal structure and thermal decomposition products. In *Coal Structure: Advances in Chemistry Series, Vol. 192* (Edited by Gorbaty, M. L. and Ouchim, K.), American Chemical Society: Washington D. C., 1981, 95~112.

POTENTIAL OF STABLE NITROGEN ISOTOPE RATIO MEASUREMENTS TO RESOLVE FUEL AND THERMAL NO_x IN COAL COMBUSTION

Colin E. Snape[1], Chenggong Sun[1], Anthony E Fallick[2], Robin Irons[3], and John Haskell[3]

[1]Nottingham Fuel &Energy Centre, School of Chemical, Environmental & Mining Engineering, University of Nottingham, University Park, Nottingham NG7 2RD, UK

[2]Scottish Universities Research & Reactor Centre (SURRC), Rankine Avenue, East Kilbride Glasgow, G75 0QF, UK

[3]Power Technology Centre, Powergen, Ratcliffe-on-Soar, Nottingham, NG11 0EE, UK

Introduction

Atmospheric stable nitrogen isotope ($\delta^{15}N$) measurements on NO_2 suggest that significant differences may exist between NO_x derived from coal and that from transport fuel sources [(1)], which predominantely is formed from air nitrogen via thermal and prompt meachanistic pathways. However, thus far, no nitrogen isotopic data have been reported directly for NO from coal combustion due to the problems of first adsorbing the NO and then determining the $\delta^{15}N$ of the NO which, in terms of minimizing sample size and maximizing throughput is best achieved using an elemental analyzer linked to an isotope ratio mass spectrometer (EA-IRMS). If fuel and thermal NO_x can be quantified, this will be an important development to help guarantee combustor performance and aid combustion modeling.

To address the issue of whether a significant isotopic difference exist between prompt/thermal and fuel NO_x in PF combustion of coal, we describe the development of a nitrogen-free active carbon for adsorbing NO. The preparation is based on previous work that has indicated promising substrates that can adsorb sufficiently large quantities of NO_x to meet the requirements for subsequent isotope analysis include zirconia supported manganese (MnO_y-ZrO_2) [(2)], and active carbon supported iron oxide (Fe/AC)[(3,4)] promoted by other metals including cerium. The nitrogen free Fe/AC sorbent prepared here is used to determine, for the first time, the $\delta^{15}N$ values for thermal and actual NO from PF coal combustion. In addition, we report the stable isotope values for a number of combustion chars to help explain the isotopic fractionation that occurs during PF combustion.

Experimental

Preparation of the N-free sorbent Granulated white sugar purchased from a local supermarket was used. About 200 g of this sugar was first dehydrated in ~ 250 ml concentrated sulfuric acid to produce a char-like porous solid. This solid material was then washed using excess distilled water and dried in an air-blown oven at 60°C. The dried solid material was then carbonised at 650°C for about 3 hours in a fixed-bed reactor to yield the sugar-based char, which was subsequently activated at 1000 °C in a flow of CO_2 (~90 min.) in order to obtain the final sugar-based activated carbon product. For 100 g of sugar, about 15~20 g of activated carbon can be obtained from this procedure.

In order to prevent any nitrogen incorporation during the sorbent preparation, the use of nitrogen-bearing chemicals was avoided. The sugar-based AC material was first treated in 0.2 N $KMnO_4$/0.5 N KOH solution for about 5 hrs and, subsequently, the same volume of 0.5M N $Fe_2(SO_4)_3$ solution was poured into the mixture. The pH of the new mixture was controlled at 12 and the mixture was then stirred for 5 hrs before it was filtrated, washed with distilled water and dried at 120°C. The dried raw sorbent material was then calcined at 500°C for 10 hrs to obtain the final Fe-Mn/AC sorbent.

Laboratory measurements indicated that, with a typical flue gas composition, the breakthrough for NO corresponds to a nitrogen uptake of over 0.5 % w/w.

NO_x sampling and analysis A thermal/prompt and an actual PF NO_x sample have been collected in duplicate from a 1 MW test facility at Powergen. The sampling time available enabled nitrogen uptakes as NO of approximately 0.1-0.2% to be achieved without any NO breaking through the adsorbent bed (*ca*. 2 g). The thermal NO sample was collected when the PF facility was starting up with a fuel oil containing litttle nitrogen (0.1% cf. 1-2% for coals). The NO samples and the blank sorbent have been analysed using a Europa EA-IRMS instrument with 4 determinations being carried out for each of the NO_x samples. System blanks were measured before and after each set of replicates for the five samples. Seven determinations were also carried out on the sorbent blank. In addition to the NO_x samples, a number of coals and a series of char samples has also been analysed using the same instrument.

Results and Discussion

Coals The nitrogen stable isotope values for a number of coals using the standard permil notation references to atmospheric nitrogen are listed in Table 1. The $\delta^{15}N$ values all occur over the relatively narrow range of + 1-4 ‰ with the range being even smaller for the UK coals with all the values being close to +2 ‰.

Table 1 A summary of stable nitrogen isotope ratios for a selection of coals.

Coal	$\delta^{15}N$, ‰
Blair Athol, Australia	1.6
Ensham, Australia	1.5
Gedehoop, South Africa	1.4
Irui, Brazil (high ash, high vol.)	3.8
Polish coal	2.6
Prodeco, Colombia (high vol.)	0.6
N. Dakota lignite, USA	2.2
Marrowbone, (USA, high vol.)	2.5
Walter, USA (low vol., Alabama)	1.4
Daw Mill, UK	2.6
Harworth, UK	1.8
Gascoigne Wood, UK	2.6

Table 2. Interferences (m/z of 28) in EA-IRMS for determination of nitrogen stable isotope ratios

	Total ion beam, A	% N (20 mg)
1. System background	2-3 x 10^{-10}	0.002
2. Sample		
(a) inherent N content (AC)	0.5-3 x 10^{-8}	0.05-0.2
(b) comb. catalyst, V_2O_5	1.5-3 x 10^{-9}	0.01-0.02

Thermal/prompt and actual PF NO_x samples Before discussing the $\delta^{15}N$ values for the NO samples, it is important to assess the interferences that can arise in the EA-IRMS. Table 2 lists the interferences in terms of current observed which is translated into a nitrogen content for a 20 mg samples size which was largely used throughout this study. The system background (empty sample capsule) corresponds to 10% of the count obtained with the combustion catalyst in the sample capsules. However, the ion

currents obtained with active carbons containing appreciable nitrogen contents are an order of magnitude greater still. This summary indicates the necessity to work with adsorbents containing extremely low nitrogen contents.

The results for the NO_x samples and the sorbent blank (no NO adsorbed) are presented in Table 3. The total beam intensity for these analyses did not vary systematically with sample weight but averaged 3.1 x 10^{-9} A; this compares to an average system blank of (1.9 x 10^{-10} A over the course of the entire experiment. For a 20 mg sample size, this corresponds to a nitrogen content of *ca*. 0.01%.

For the four replicates of the first thermal NO (1A) sample, the mean %N was (0.125 ± 0.006) and the mean $\delta^{15}N$ was -6.2 ± 1.3‰ (Table 3). The average total beam was 1.96 x 10^{-8}A meaning that the sorbent blank represents 16% of the sample total beam. No correction was made here. For the four replicates of the second thermal NO sample (1B), the mean %N was 0.09 ± 0.00 and the total beam of 1.44 x 10^{-8}A meant that the sorbent blank represents 21.5% with a mean $\delta^{15}N$ = -6.1 ± 0.5 ‰. The two mean values for thermal samples 1A and 1B are indistinguishable, supporting the decision not to correct for the blank. For the 8 replicates of the thermal NO_x samples, the mean $\delta^{15}N$ was -6.2 ± 0.9 ‰.

Table 3 Thermal/prompt and actual PF NO_x samples collected with the nitrogen-free Fe/AC adsorbent

Sample/ Determin. no.	Weight mg	Total Beam A	% N	$\delta^{15}N$ ‰ air
1. sorbent blank	10.8	3.87 10^{-9}	0.02	37.1
2. sorbent blank	16.0	3.13 10^{-9}	0.01	-0.7
3. sorbent blank	20.9	2.73 10^{-9}	0.01	-4.1
4. sorbent blank	24.9	3.16 10^{-9}	0.01	-12.0
5. sorbent blank	20.4	3.18 10^{-9}	0.01	13.2
6. sorbent blank	15.7	2.98 10^{-9}	0.01	28.0
7. sorbent blank	10.4	2.68 10^{-9}	0.02	7.1
1. Thermal 1A	20.7	1.95 10^{-8}	0.12	-4.7
2. Thermal 1A	19.5	1.94 10^{-8}	0.13	-5.6
3. Thermal 1A	19.5	1.93 10^{-8}	0.13	-7.5
4. Thermal 1A	20.9	2.02 10^{-8}	0.12	-7.0
1. Thermal 1B	19.6	1.42 10^{-8}	0.09	-6.7
2. Thermal 1B	20.1	1.49 10^{-8}	0.09	-5.6
3. Thermal 1B	21.1	1.43 10^{-8}	0.09	-6.1
4. Thermal 1B	19.3	1.41 10^{-8}	0.09	-6.1
1. PF 2A	19.1	3.52 10^{-8}	0.23	15.1
2. PF 2A	21.2	3.90 10^{-8}	0.23	14.5
3. PF 2A	20.8	3.89 10^{-8}	0.24	13.8
4. PF 2A	20.5	3.82 10^{-8}	0.23	14.4
1. PF 2B	20.8	3.41 10^{-8}	0.21	18.1
2. PF 2B	19.9	3.06 10^{-8}	0.19	14.4
3. PF 2B	20.0	3.06 10^{-8}	0.19	14.8
4. PF 2B	20.5	3.04 10^{-8}	0.19	13.2

For four replicates of the actual PF sample (1B), the mean %N was 0.23 (± 0.00) and mean $\delta^{15}N$ was 14.5 ± 0.5 ‰ (Table 3). The mean total beam intensity was 3.78 ± 0.18 10^{-8} A so the sorbent blank represents 8 %. For the second sample, the mean %N was 0.19 ± 0.01 with $\delta^{15}N$ of 15.1 ± 2.1‰. The mean total beam intensity was 3.14 x 10^{-8} A so the sorbent blank represents 10%. Again, no correction has been made here and again the means for the PF samples 2A and 2B are isotopically indistinguishable, with the overall average from the eight measurements being 14.8 ± 1.5 ‰. These measurements indicate that differences of up to *ca*. 20 ‰ can exist between thermal and PF fuel (char) NO_x isotopic values.

Table 4 Nitrogen stable isotope ratios for combustion chars prepared in a drop tube reactor from 3 coals

Sample/drop tube resience time		% N w/w	$\delta^{15}N$ ‰ air
1. Oreganal (Colombia)	200 ms a	1.92	4.2
	200 ms a	2.28	3.9
	200 ms b	2.15	3.3
	200 ms b	1.82	4.3
Mean $\delta^{15}N$ ‰			*3.9*
	400 ms a	1.24	4.8
	400 ms a	1.13	4.2
	400 ms b	1.37	5.7
	400 ms b	1.83	5.4
Mean $\delta^{15}N$ ‰			*5.0*
	600 ms a	0.37	5.9
	600 ms a	0.29	6.4
	600 ms a	0.54	5.5
	600 ms b	0.82	5.3
	600 ms b	0.93	5.5
Mean $\delta^{15}N$ ‰			*5.7*
2. Kaltima Pr.	200 ms a	2.02	3.9
	200 ms a	2.28	2.6
	200 ms b	1.72	3.9
	200 ms b	2.24	2.1
Mean $\delta^{15}N$ ‰			*3.1*
	400 ms a	2.19	4.1
	400 ms b	2.28	4.6
	400 ms b	1.74	3.3
Mean $\delta^{15}N$ ‰			*4.0*
	600 ms a	0.80	4.2
	600 ms a	0.63	2.4
	600 ms b	1.40	4.1
	600 ms b	1.30	2.8
Mean $\delta^{15}N$ ‰			*3.3*
3. Pocahontas	200 ms a	1.38	5.3
	200 ms a	1.40	6.0
	200 ms b	1.28	6.1
	200 ms b	0.92	5.7
Mean $\delta^{15}N$ ‰			*5.8*
	400 ms a	0.65	6.5
	400 ms a	0.76	6.5
	400 ms b	1.17	6.9
	400 ms b	1.38	6.4
Mean $\delta^{15}N$ ‰			*6.6*
	600 ms a	0.76	6.3
	600 ms a	0.85	6.4
	600 ms b	0.73	5.9
	600 ms b	0.95	7.2
Mean $\delta^{15}N$ ‰			*6.5*

Char analysis Table 4 lists the nitrogen stable isotope ratios for a series of partially combusted chars prepared at different residence times (200, 400 and 600 ms) in a drop-tube reactor from

three different coals. Pyrolysis chars from each coal were prepared in the drop tube reactor and these were then fed back into the reactor using an atmosphere containing 5 % oxygen. Two separate char samples were analysed for each residence time. Of the 3 coals investigated, the Indonesian coal (Kaltima Prima) is the most reactive and Pocahontas (USA) the least.

In all cases, the nitrogen stable isotope ratios of the chars are heavier than than those of coals and range from 3 to 7 ‰. However, Table 4 indicates that the isotopic fractionation is roughly in the order Pocahontas > Oreganal > Kaltima Prima, which is the opposite trend to that in reactivity. For the two least reactive coals, the extent of isotopic fractionation increases with burnout (cf. 600 with 400 and 200 ms chars in Table 3 for Pocahontas and Oreganal). Table 5 lists the stable nitrogen isotopic ratios for a Spanish coal, a pyrolysis char and four combustion chars obtained at high levels of burnout. The data for the Spanish coal reveal that the nitrogen stable isotope ratios of combustion chars obtained at high levels of burnout do not change markedly (Table 5).

In conclusion, it would appear that much of the isotopic fractionation that occurs between coal nitrogen and fuel NO occurs in the formation of char, although further fractionation can be inferred to occur during char combustion. In contrast, a lesser degree of isotopic fractionation is associated with the formation of thermal NO (*ca*. –6 ‰), atmospheric nitrogen having a value of 0 ‰.

Table 5 Nitrogen stable isotope ratios of a Spanish coal, a pyrolysis char and three combustion chars prepared in a drop tube reactor

Sample	% N	$\delta^{15}N$	
1. Coal	2.27	2.5	Mean 2.5
	2.12	2.5	
2. Pyrolysis char	1.51	4.7	Mean 4.5
	2.28	4.3	
3. Combustion char,.	N.D.	5.7	Mean 6.0
86 % burnout	1.98	6.3	
4. Combustion char,	1.54	5.7	Mean 5.6
93 % burnout.	1.44	5.4	
5. Combustion char,.	4.9	5.1	Mean 5.3
95 % burnout	5.6	5.4	
6. Combustion char,	5.1	5.2	Mean 5.5
97 % burnout.	6.0	5.7	

Conclusions

The fact that differences of up to *ca*. 20 ‰ can exist between thermal and PF fuel (char) NO_x isotopic values augurs well for the further development of the approach to help quantify the extent of thermal/prompt NOx formation in PF combustion. However, measurements on char have indicated that the extent of isotopic fraction that occurs between coal-N and NO_x from char is related to the reactivity of coals. We will report shortly the stable isotope ratios of NO_x samples collected under a variety of PF combustion conditions.

Acknowledgement. The authors thank the UK Department of Trade and Industry (DTI) for financial support (coal programme, contract no. 231). We thank Dr. Ana Arenillas (INCAR) and Dr. E. Lester (Univ. of Nottingham) for supplying the char samples and Mitsui Babcock (Dr S.C. Mitchell) for technical assistance.

References

(1) Heaton,. T. H. E.: *Atmospheric Environm*., **1987**, *21*, 843.
(2) Eguchi, K. and Hayashi T. *Catalyst Today,* **1998**, *45*, 109.
(3) Kaneko, K. and Inoyue, K. *Carbon*, **1986**, *24*, 772.
(4) Kaneko, K., Ozeki, S. and Inouyue: K., *Atmospheric Environm*, **1987**, *21*, 2053.

FOLLOWING COKE FORMATION BY CARBON-13 SOLID-STATE NMR

1. *Menezes, Sonia M.C.*
2. *Sugaya, Marcos F.*
3. *Silva, Naira M.*
4. *Emmerich, Francisco G.*
5. *Girelli, Carlos M.A.*
6. *Rajakopal, Krisnaswamy*

1,2. PETROBRAS/CENPES, Ilha do Fundão – Quadra 7, Cidade Universitária, 21949-900 – Rio de Janeiro, RJ, Brazil, sonia@cenpes.petrobras.com.br
3. PUC –Departamento de Química, Rio de Janeiro, RJ - Brazil
4,5. UFES, Lab. de Materiais Carbonosos, Vitória, ES - Brazil
6. UFRJ, Escola de Química, Rio de Janeiro,RJ - Brazil

Introduction

Coke is produced in petroleum refineries mostly by the delayed coking process. One of the difficulties in studying the chemical reactions involved in this process lies in the fact that the composition of petroleum distillation residues is largely unknown. The available analytical methods are very limited because of the large number of complex molecules involved. Only average properties can be obtained, making the attainable description of the system very poor. This contribution explores the coking process of a vacuum distillation residue using solid state nuclear magnetic ressonance (NMR) to characterize the thermal craking and condensation reactions taking place.

The reactions were followed mostly by cross polarization and magic angle spinning (CP/MAS) ^{13}C NMR. Non-quaternary supreesion (NQS) and a quantitative MAS experiments were also used. With those techniques it was possible to distinguish bridged aromatic carbons from protonated ones and also aliphatic carbons.

Experimental

SAMPLES. Vacuum destillation residue from the refining of a brazilian petroleum was processed on a laboratory furnace (Figure1) simulating the conditions in industrial delayed coking drums. The samples were treated at different temperatures varying from 440°C to 500°C. For each temperature the residence time at the furnace was varied from 0 to 4h.

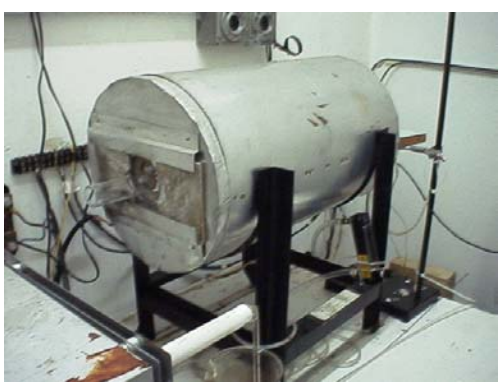

Figure 1. Laboratory furnace used for the coking studies

NMR. The experiments were conducted at room temperature using a Varian INOVA-300 (7.1T) NMR spectrometer operating at 75.4 MHz for ^{13}C. For the CP/MAS experiments a pulse width of 5.5 µs was applied with a delay time of 3s and 8000 transients were accumulated. A spectral width of 50 kHz and an acquisition time of 0.05s were used for data collection. The contact time was 4000 µs. The spectra were referenced to the hexamethylbenzene (methyl peak at 17.3 ppm from TMS). The pulse power was calibrated to achieve Hartmann-Hahn conditions. The samples were spun at 4.5KHz at MAS (54.7°) in a 7mm zirconia rotor. The NQS experiments used the same conditions of the CP/MAS and a decoupling window of 60µs. The MAS experiments were acquired using a 100s pulse delay and a 1000 transients. All spectra were processed using a 70Hz line broadening and a 0.004s gaussian function.

Spectra were integrated for the following resonance intervals: 100 to 165ppm (aromatic carbons) and 0 to 80ppm (aliphatic carbons). Corrections for sidebands contributions were considered for spectra calculations.

Results and Discussion

CP/MAS and NQS are faster but non-quantitative experiments. For one sample a variable contact time experiment was acquired in order to choose the contact time that mostly reproduces a quantitative MAS analysis. This condition was achieved at 4000µs. The CP/MAS and MAS experiments provided the total distribution of carbons present in a sample. The NQS experiment distinguishes quaternary carbons and also the methys when they are present.

Figure 1 shows typical ^{13}C MAS, CP/MAS and NQS spectra for one of the coke samples. The MAS and CP/MAS spectra, regions from 0 to 80 ppm and 100 to 165ppm are attributed to the aliphatic and to total aromatic (quaternary plus protonated) carbons, respectively. On the NQS spectra the signals from 100 to 165 ppm are due to quaternary carbons.

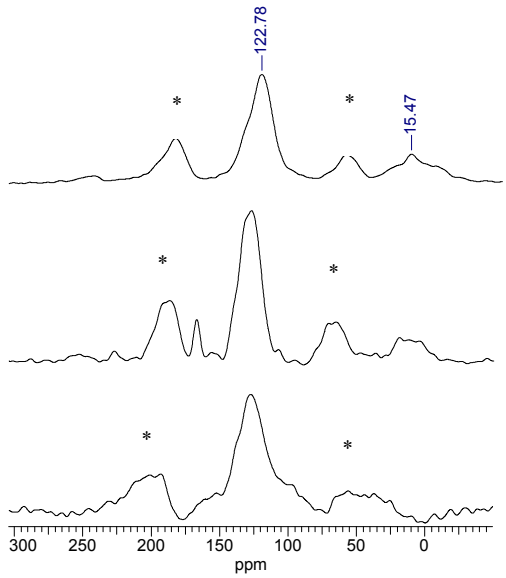

Figure 1. Coke sample treated at 440°C for 2 hours (TT 440-2H): ^{13}C MAS (top), CP/MAS with 4000µs contact time (midle) and NQS with a 60µs of decoupling window (bottom).
* spinning sidebands

In order to get the total distribution of carbons in the samples the quaternary aromatic carbons obtained by the NQS spectra were related to the total aromatic carbons from the CP/MAS spectra. The protonated carbons were obtained subtracting the total aromatic and

quaternary aromatic carbons. Aliphatic carbons were calculated from MAS spectra. Table 1 sumarizes the results.

Table 1. Carbon distribution of coke samples

SAMPLES	AROMATIC CARBONS (%)			ALIPHATIC (%) (0 - 80ppm)
	Total (100 - 165ppm)	Quaternary	Protonated	
Vacuum residuel	48,0	36,2	11,8	52,0
TT440 –0H	62,6	27,7	34,9	37,4
TT440 – 30min	79,7	39,5	40,2	20,3
TT440 –1H	85,0	35,0	50,0	15,0
TT440 –2H	85,5	41,8	43,7	14,5
TT440 –4H	86,0	66,4	19,6	14,0
TT460 –0H	70,7	26,5	44,2	29,3
TT460 – 30min	87,9	45,3	42,6	12,1
TT460 –1H	87,2	53,4	33,8	12,8
TT460 –2H	86,3	43,2	43,1	13,7
TT460 –4H	93,2	79,3	13,9	6,8
TT480 –0H	83,7	44,5	39,2	16,3
TT480 – 30min	88,6	51,3	37,3	11,4
TT480 –1H	87,9	42,7	45,2	12,1
TT480 –2H	88,4	47,4	41,0	11,6
TT480 –4H	93,9	54,0	39,9	6,1
TT500 –0H	80,9	23,6	57,3	19,1
TT500 – 30min	89,0	31,6	57,4	11,0
TT500 –1H	86,8	37,3	49,5	13,2
TT500 –2H	92,8	48,0	44,8	7,2
TT500 –4H	89,2	32,4	56,8	10,8

The results indicated well the increase of the percentage of total aromatic carbons as the temperature and residence time increase. It was also observed that quaternary aromatic carbons has raised with residence time for a given temperature. These were somehow expected although at 500°C the aromatic quaternary carbons surprinsingly presented lower values.

At industrial delayed coking units the temperature of the coking drums usually stays between 490°C (bottom) and 440°C (top). The data showed at Table 1 indicated that the thermal cracking and condensation reactions leading to the final composition (high aromatic carbon content) of the coke was completed in less than 2 hours in the drum.

Conclusions

The results indicated that the solid state ^{13}C NMR data were efective to evaluate the progress of the the coking process for the series of samples analysed. In all samples, the NMR data revealed an increase of aromaticity with the temperature and also an increase of the quaternary carbons. These results showed that the coking process was already completed in less than two hours of total residence time.

Acknowledgement. The authors acknowlwdge Dr. Luís Fernando Leite (PETROBRAS/CENPES/PROTER).

References

(1) Callejas, M.A.; Martínez, M. T.; Blasco, T.; and Sastre, E. P. - *Appl. Caalysis A*, **2001**, *218*, 181-188.
(2) Schabron, J. F.; Pauli, A. T.; Rovani, J.F.; Miknis, F. P.; *Fuel,* **2001**, 114.
(3) Saito, K. , Hatakeyama, M., Komaki, I., and Katoh, K.. *Journal Of Molecular Structure*; **2002**, 9, 602-603.

On-line determination of total sulfur in fuels

Rodney W. Spitler, Patrick J. Moore, and Rodney Friudenberg

Thermo ONIX
A Thermo Electron Business
9303 W. Sam Houston Parkway S.
Houston, TX 77099

Introduction

Environmental regulatory agencies, such as the U.S. E.P.A., are promulgating dramatic motor fuel sulfur level reductions. By 2006 the U.S. E.P.A requires the sulfur content of highway diesel to be reduced from 500 ppm S (w/w) to 15 ppm S (w/w).[1] The reduction of gasoline sulfur content is equally dramatic with the sulfur cap moving from 300 ppm S (w/w) to 80 ppm S (w/w) by 2006.[2] Reduction of motor fuel sulfur content is not isolated to the US. Sweden and Finland have had 10 ppm S (w/w) diesel for several years. Japan will require 50 ppm S (w/w) diesel by 2005 and Australia by 2006. Proposals being considered by the European Union may require < 10 ppm S (w/w) gasoline and diesel to be available by January 2005.[3] Latin American countries are also considering significant reductions in gasoline and diesel sulfur content. The challenge of meeting low sulfur fuel specifications is having a worldwide impact.

Low sulfur fuel specifications are presenting challenges to both refining and distribution. In the U.S., the low sulfur gasoline specifications, together with the expected elimination of MTBE, poses a new and potentially expensive challenge to gasoline blending operations. Should MTBE be eliminated as a gasoline additive the refiner will lose the use of a valuable gasoline diluent. Elimination of MTBE will increase the value of low sulfur gasoline blend components, such as, alkylate.[4] Distribution of refined motor fuels by pipelines presents yet another set of challenges. It is expected that 15 ppm S (w/w) diesel will necessarily be transported in a common pipeline system with 1,000 to 3,000 ppm S (w/w) distillates, such as, jet fuel. The opportunity for sulfur contamination of the 15 ppm S (w/w) diesel is enormous.[5] Rapid, precise and on-line determination of total sulfur will enable the economic operation of fuel blenders and provide a means for sulfur contamination detection in the fuel distribution system.

To meet these challenges, we have developed and validated a fully automated method for the on-line determination of total sulfur in diesel and gasoline. The method is similar to the well-accepted ASTM method D5453-00, "Determination of Total Sulfur in Light Hydrocarbons, Motor Fuels and Oils by Ultraviolet Fluorescence".[6] In our on-line method the sample is oxidized in an air atmosphere at 1100 °C. The oxidation process converts organic sulfur compounds and hydrogen sulfide to CO_2, H_2O and SO_2. The concentration of SO_2 in the oxidized sample is proportional to the total sulfur content of the fuel. Quantification of the SO_2 is accomplished with a pulsed ultra violet fluorescence, PUVF, spectrometer. Dominate applications for the on-line determination of total sulfur include: 1) detection of sulfur contamination in pipelines (pipeline transmix) and 2) fuel blending operations. In order to address these applications, particular attention was paid to response time and measurement precision during the development of our on-line method.

Experimental

Instrumentation. **Figure 1** is a simplified diagram of the instrumentation developed in this study. An automated liquid sample valve is used to pulse sample into the air bath oven at a typical rate of 2 µl/min. Air was selected as the carrier gas/oxidant over oxygen to ensure safe operation in potentially explosive atmospheres (the common installation environment for on-line analyzers). The air bath oven is typically held at 190 °C to ensure the complete vaporization of the sample. A mixing chamber is used to create a near constant flow of vaporized fuel and air to the combustion furnace. The combustion furnace is held at 1100 °C to ensure the complete oxidation of all sample components. Following oxidation a constant flow of analyte is presented to the PUVF spectrometer. The PUVF is selected for its superior sensitivity over ultraviolet fluorescence spectrometers with continuous UV light sources.

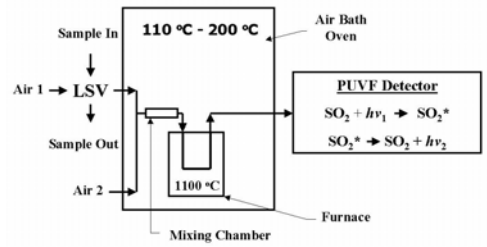

Figure 1. Simplified block diagram of instrumentation used for on-line determination of total sulfur in fuels.

Results and Discussion

Validation of Total Sulfur Measurement. Gasoline and diesel contain a wide variety of organic sulfur compounds plus potentially some hydrogen sulfide. Since approximately 90% of the gasoline pool sulfur comes from fluid catalytic cracked, FCC, gasoline, we examined its sulfur compound distribution.[7] FCC gasoline can contain thiophene, C_1-C_4 alkyl substituted thiophenes, benzothiophenes, tetrahydrothiophene, sulfides, disulfides and thiols.[8,9] To ensure that our on-line method fully accounts for all gasoline sulfur species a series of various sulfur compounds dissolved in iso-octane, toluene, hexane and benzene were analyzed as unknown samples. The instrument was calibrated with a thiophene in iso-octane standard prior to beginning these analyses. The purpose of these tests was to determine the conversion efficiency of the various sulfur compounds to SO_2 and to quantify errors, if any, resulting from dissimilar matrices. Results of this series of tests are presented in **Figure 2.** Examination of **Figure 2** indicates an ideal linear relationship between the reported and calculated total sulfur values, demonstrating a full accounting for the organic sulfur compounds tested. Additionally, one can conclude there is no aromatic matrix measurement error.

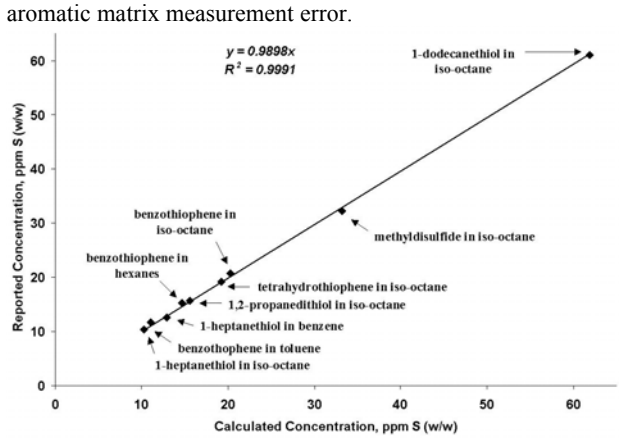

Figure 2. Reported vs. calculated values for gasoline range organic sulfur compounds in paraffinic and aromatic solvents.

Diesel fuel contains the same classes of sulfur compounds as gasoline, however, the sulfur compounds found in diesel will necessarily have higher boiling points than those found in gasoline.

Unlike gasoline, low sulfur diesel (≤ 15 ppm S (w/w)) can contain significant concentrations of refractory sulfur compounds, such as, dibenzothiophenes with alkyl substitutions at the 4 and 6 positions. Refractory sulfur compounds are difficult to remove by hydrotreating because steric hinderance prevents the sulfur atom from interacting with the catalytic site.[10,11] The response to various diesel range sulfur compounds were measured as described previously for gasoline range sulfur compounds, however, sulfur free (≤ 1 ppm S (w/w)) # 2 diesel fuel was used as the solvent. The results of this study are presented in **Figure 3**. **Figure 3** indicates an ideal linear relationship between the reported and calculated total sulfur values, demonstrating all sulfur compounds tested are fully converted to SO_2, including, the common refractory sulfur compound, 4,6-dimethyldibenzothiophene.

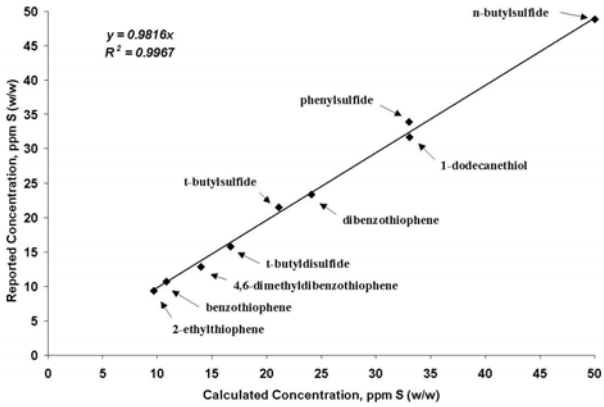

Figure 3. Reported vs. calculated values for diesel range organic sulfur compounds.

Measurement Linearity. Measurement linearity was evaluated for gasoline and diesel applications by preparing successive dilutions of thiophene in iso-octane and thiophene in # 2 diesel, respectively. **Figure 4** indicates excellent measurement linearity for thiophene in iso-octane from 4.98-99.60 ppm S (w/w) and thiophene in #2 diesel from 2.24-99.60 ppm S (w/w).

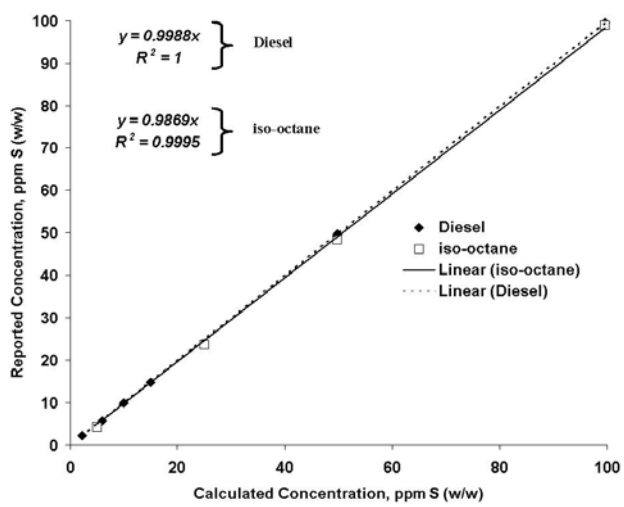

Figure 4. Thiophene in iso-octane and thiophene in #2 diesel measurement linearity.

Measurement Precision. Table 1 shows key statistics for a 14 hour run of a California gasoline and a 16 hour run of a Japanese diesel with mean sulfur concentrations of 4.01 ppm S (w/w) and 21.59 ppm S (w/w), respectively. More than 800 data points were collected for each measurement precision study. Excellent measurement precision is indicated for each fuel.

Table 1. Measurement Precision

Statistic	Gasoline 14 hr Run	Diesel 16 hr Run
Mean	4.01	21.59
Median	4.01	21.59
Mode	4.02	21.58
Standard Deviation	0.12	0.10
Range	0.79	0.66
Minimum	3.60	21.28
Maximum	4.38	21.93

Response Time. Response time was evaluated by switching between #2 diesel samples containing 22 ppm S (w/w) and 66 ppm S (w/w). The results of this test are summarized in **Figure 5**. As shown in **Figure 5** when switching from 22 ppm S (w/w) to 66 ppm S (w/w) approximately 1.0 minute is required to begin detecting the change in sulfur concentration. When switching from 66 ppm S (w/w) to 22 ppm S (w/w) approximately 1.5 minutes are required to begin detecting the change in sulfur concentration.

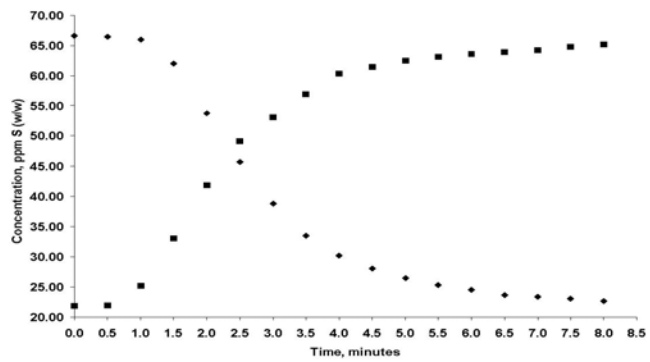

Figure 5. Response Time Measurements.

Conclusions

An on-line method for determination of total sulfur in gasoline and diesel was shown to provide an excellent linear accounting for gasoline and diesel range organic sulfur compounds at the lower expected future concentration requirements. The demonstrated response time of 1.0-1.5 minutes may be useful for detection of pipeline transmix, however, it is likely that improved response time would be valuable. The demonstrated measurement precision will allow this on-line method to be a valuable fuel blending control tool.

References

(1) *Federal Register,* **2000**, *66* (12), 5064.
(2) *Federal Register,* **2000**, *65* (28), 6754.
(3) Huss, A. In *Production of Low Sulfur Gasoline and Diesel Fuels*, Oral Presentation August **2002**.
(4) Barsamian, A. *World Refining* September **2001**, 30.
(5) Higgins, T. *World Refining* January/February **2002**, 4.
(6) *Annual Book of ASTM Standards* **2002**, Vol. 05.03, 446.
(7) Golden, S.; Fulton. S. *World Refining* July/August **2000**, 20.
(8) Shiraishi, Y.; Tachibana, K.; Taki, Y.; Hirai, T.; Komasawa, I. *Ind. Eng. Chem. Res.* **2001**, *40* (4), 1225.
(9) Albro, T.; Dreifuss, P.; Wormsbecher, R. *J. High Res. Chrom.* **1993**, *16*, 13.
(10) Rodgers, R.; White, F.; Hendrickson, C.; Marshall, A; Andersen, K. *Anal. Chem.* **1998**, *70* (22), 4743.
(11) Isoda, T.; Nagao, S.; Ma, X.; Korai, Y; Mochida, I.; *Energy Fuels* **1996**, *10* (2), 482.

Petroleomics: Electrospray ionization FT-ICR mass analysis of NSO compounds for correlation between total acid number, corrosivity, and elemental composition

Geoffrey C. Klein[a], Ryan P. Rodgers[b], Marco A.G. Teixeira[c], Ana Maria R. F. Teixeira[d], and Alan G. Marshall[b]

[a]Department of Chemistry and Biochemistry, Florida State University, Tallahassee, FL 32306
[b]Ion Cyclotron Resonance Program, Florida State University, National High Magnetic Field Laboratory,1800 East Paul Dirac Drive, Tallahassee, FL 32310-3706
[c]Petrobras R&D Center/Chemistry, Cidade Universitaria, Rio de Janeiro, Brazil EEP 21949-900
[d]Fluminense Federal University-GQA, Outeiro do Valonguinho, s/n, Niteroi, RJ, Brazil

Introduction

Hughey et. al. recently reported the assignment of elemental composition of NSO compounds by microelectrospray Fourier transform ion cyclotron resonance (FT-ICR) mass spectrometry.[1] Electrospray selectively ionizes the polar compounds and FT-ICR MS provides the high resolution (> 100,000) and high mass accuracy (< 1 ppm) needed to resolve and identify thousands of components in a complex mixture. Polar compounds, containing N-, S-, and O- (<15% of crude composition), are critically important in refining.[2] For example, heteroatom-containing hydrocarbons, particularly those containing nitrogen, are known to play a key role in catalyst deactivation through coke formation on the catalyst surface. Similarly, naphthenic acids are known to cause process corrosion in refining equipment. Here, we try to correlate total acid number (TAN), corrosivity, and elemental composition within crude oils.

Experimental

Oil samples. Ten crude oils exhibiting different total acid number (TAN) and corrosivity, provided by Petrobras, are shown in Table 1. TAN was determined by the amount of KOH needed to neutralize one gram of crude oil. A wire probe composed of the same material as refining equipment is placed in the stream of the crude oil. Decay (and therefore a measure of process corrosion) of the wire is detected by changes in wire resistance. Corrosive character was assigned by a team of specialists based on this wire test, field data, and their expertise.

Table 1. Crude oils analyzed

Crude Oil	TAN	Corrosivity
A1	4.0	High
A2	2.3	High
A3	1.8	High
A4	1.5	High
A5	0.3	High
B1	1.0	Medium
B2	0.5	Medium
B3	0.5	Medium
C1	0.8	Negligible
C2	0.3	Negligible

Sample Preparation. 20 mg of the crude was dissolved in 3 mL of toluene, and then diluted to 20 mL with methanol. 1 mL of the final solution was spiked with either 3 µL of acetic acid or 10 µL of ammonium hydroxide to facilitate protonation (+ ion ESI) or deprotonation (- ion ESI). All mass spectra were collected by both positive- and/or negative-ion electrospray (ESI) with a homebuilt 9.4 T FT-ICR mass spectrometer.[3] Spectra were externally calibrated from #G2421A electrospray "tuning mix" from Agilent, and then recalibrated from a homologous series within each crude oil.

Data analysis. Analysis was performed by convertion of IUPAC measured mass to the Kendrick mass scale (CH_2 = 14.00000 instead of 14.01565 Da) to facilitate identification of homologous series. Kendrick mass is obtained by multiplying the IUPAC mass with 14/14.0156. The advantage to the Kendrick mass scale is that the members of a single homologous series (compounds with the same heteroatomic composition and number of rings and double bonds, but differ by a CH_2 group) have identical Kendrick mass defect (KMD), seen in Eq. (1),

$$\text{KMD} = (\text{Nominal Kendrick Mass} - \text{Kendrick Mass}) \qquad (1)$$

where nominal Kendrick mass is determined by rounding up the Kendrick mass to the nearest whole number. Series are then separated based on even and odd nominal Kendrick mass and KMD as described elsewhere.[4]

Results and Discussion

Figure 1 shows compositional data and O_2/N ratio for all ten crude oils. This ratio was determined by summing the relative abundance of all compounds that contain O_2 (representing a carboxylic acid) divided by the sum of relative abundances for neutral nitrogen compounds. A higher ratio may indicate a higher abundance of carboxylic acids that are known to contribute to the corrosion of refining equipment. Some of the carboxylic acids contained more than one heteroatomic atom, such as in crude oil A2 and C2, which contains a high abundance of NO_2-species. This ratio is not the only clue to the corrosivity, as evident by A3, which contains high corrosivity (by wire measure) contains a low O_2/N ratio.

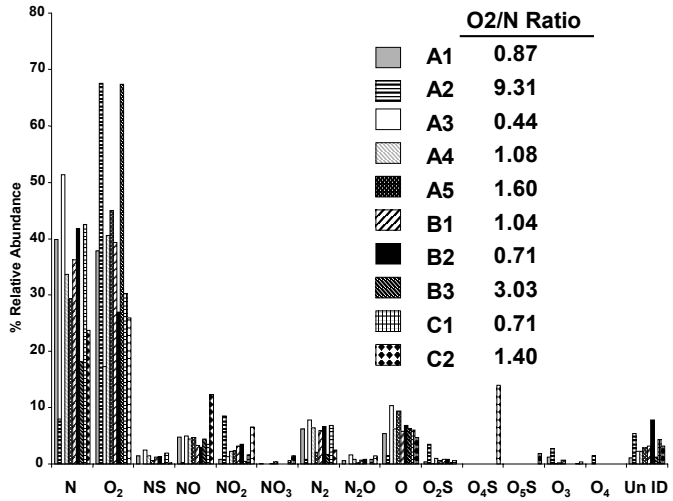

Figure 1. Comparison of compound classes in negative-ion mode microelectrospray FT-ICR MS for each crude oil. Only those classes with relative abundance > 1% are shown.

Carboxylic acids found in the ten crude oils are composed of naphthenic acids (containing 1-3 rings and double bonds) and a variety of aromatic acids, from mono-aromatic to hexa-aromatic. **Figure 2** shows the distribution of rings and double bonds found in the O_2- species in the crude oils. The composition of the carboxylic acids was determined by summing the relative abundance of each

acid and dividing by the total relative abundance of all compounds present in the crude oil. For 9 out of 10 crude oils (all except B2), the relative abundance of the naphthenic acids is higher than all other components found in the O_2-species. The relative abundance of naphthenic acids tends to be higher for crude oils exhibiting high corrosive character. This is not true for all oils. B3 has the highest naphthenic relative abundance but only exhibits medium corrosivity; however, it contains a TAN value of 0.5, which is still considered acidic. Surprisingly, A3 has the second lowest naphthenic acid relative abundance but exhibits high corrosivity and a TAN value of 1.8. This suggests that NSO polar compounds may not be the only components of crude oils that contribute to process corrosivity.

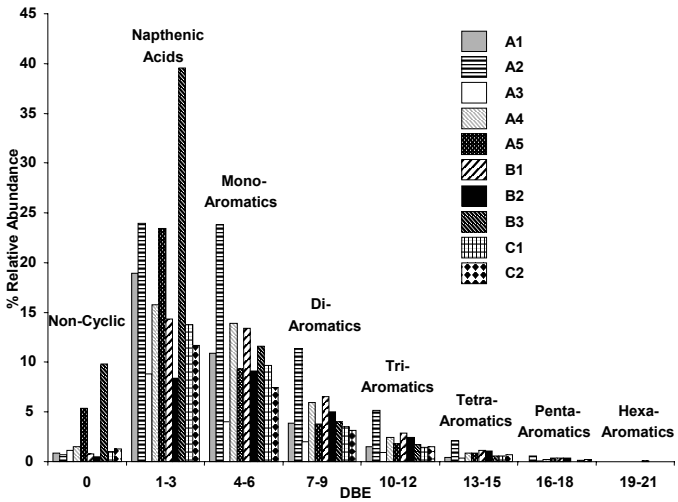

Figure 2. Comparison of the distribution of double bond equivalence (DBE) in O_2-species, where DBE is the number of rings and double bonds.

Petroleum acids are found in predominantly immature, biodegraded, and heavy crudes.[5] Higher corrosive crudes should exhibit a smaller carbon number distribution than lower corrosive crudes. **Figure** 3 shows the carbon distribution of 4 DBE O-series for 4 crude oils with different corrosive character. The two oils

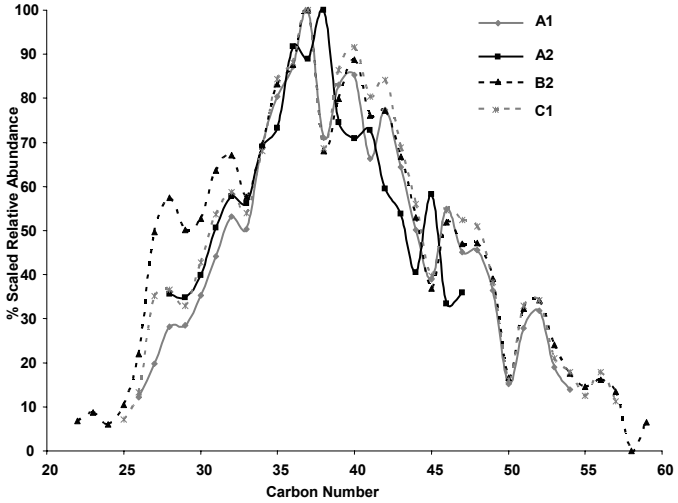

Figure 3. Distribution of Carbon in O-series (Phenol) with 4 rings or double bonds.

with high corrosivity have a carbon number distribution of 26-54 and 28-47, while the less corrosive crudes have distributions from 22-59 and 25-57 carbons. The slightly smaller carbon distribution of the high corrosive crudes suggests that the compounds have undergone a higher degree of biodegradation.

Positive-ion spectra were collected for three of the crude oils to determine the effect of the basic compounds on corrosivity and TAN. **Figure 4** clearly illustrates that the basic nitrogen compounds do not affect the components found in negative-ion mode. All three crude oils are composed of ~ 83% basic nitrogen species, with comparable carbon number distributions and rings and double bonds.

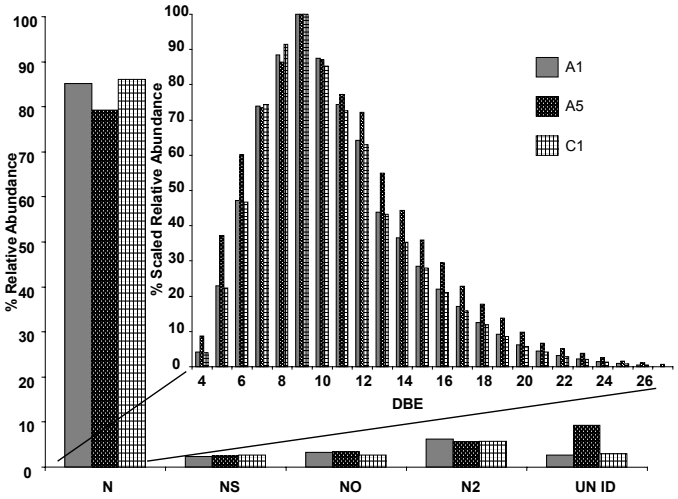

Figure 4. Comparison of compounds classes and double bond equivalence for N-series identified in positive-ion mode for 3 crude oils.

Conclusions

FT-ICR MS provides the necessary mass resolving power and mass accuracy (<1ppm) to assign elemental composition to the NSO compounds found by negative-ion microelectrospray. Our results suggest that these polar compounds are not the only components contributing to the process corrosivity of crude oils, but can provide helpful clues. A higher ratio of O_2/N species, a higher relative abundance of naphthenic acids and a smaller distribution of carbon number may indicate that a crude oil exhibits higher corrosive character. Positive spectra were also collected and determined that the basic components identified do not play a role in the correlation of TAN, corrosivity and elemental composition.

Acknowledgement. The authors would like to thank Daniel MacIntosh for machining all of the custom parts required for the 9.4T instrument construction. This work was supported by NSF (CHE-99-09502), Florida State University, Petrobras, and the National High Magnetic Field Laboratory.

References

(1) Hughey, H. A.; Rodgers, R. P.; Marshall, A. G.; Qian, K.; and Winston, K. R. *Org. Geochem.*, **2002**, 33 (7), 743.
(2) Altgelt, K. H., Boduszynski, M.M. In *Composition and Analysis of Heavy Petroleum Fractions*; Marcel Dekker: New York, 1994; pp 393-484.
(3) Senko, M.W.; Hendrickson, C. L.; Pasa-Tolic, L.; Marto, J. A.; White, f. M.; Guan, S.; Marshall, A. G. *Rapid Commun. Mass Spectrom.* **1996**, 10, 1824.
(4) Hsu, C.S.; Qian, K.; Chen, Y.C. *Anal. Chim. Act.* **1992**, *264*, 79.
(5) Ahsan, A.; Karlsen, D. A.; Patience, R. L. *Mar. Pet. Geol.* **1997**, 14, 55.

THE POTENTIAL OF HYPY-GC-MS FOR FINGERPRINTING PETROLEUM SOURCE ROCKS AND COALS

Colin E. Snape[1]*, William Meredith*[1]*, Christopher A Russell*[1]*, Mick Cooper*[1]*, Gordon D. Love*[2] *and Daniele Fabbri*[3]

[1]Nottingham Fuel and Energy Centre, School of Chemical, Environmental and Mining Engineering, University of Nottingham, University Park, Nottingham NG7 2RD, UK
[2]School of Civil Engineering and Geosciences, Drummond Building, The University, Newcastle upon Tyne NE1 7RU, UK
[3]Laboratorio di Chimica Ambientale, Università di Bologna, via Marconi 2, 48100 Ravenna, Italy

Introduction

The use of hydropyrolysis (commonly abbreviated to *hypy*), which refers to pyrolysis assisted by high hydrogen gas pressures (>10 MPa) in the presence of a dispersed catalyst, as an analytical pyrolysis method for liberating covalently-bound biomarker hydrocarbon structures from kerogen was first reported by Love *et al.*[(1)]. This and other subsequent studies have demonstrated the unique capability of the fixed-bed catalytic hydropyrolysis procedure to release much higher yields of aliphatic biomarker hydrocarbons (including *n*-hydrocarbons, hopanes, steranes and methyl steranes) from immature kerogens compared to mild catalytic hydrogenation and traditional pyrolysis methods[(1-5)]. These characteristics allow for the bound biomarkers released by hydropyrolysis to offer potential solutions to tackling many problems in oil exploration, especially where the conventional geochemical approach using the free (extractable) hydrocarbon biomarkers cannot be employed, such as for severely biodegraded oils and samples contaminated with oil based drilling muds.

Although pyrolysis-GC-MS is widely used as a fingerprinting technique for sedimentary organic matter[(6-9)] and also for other materials, notably polymers, the inherent low yields limit the application of the technique to the more thermally labile moieties in kerogens. Thus, if hydropyrolysis can be interfaced with GC-MS (hypy-thermal desorption-GC-MS), this new development should have considerable commercial potential as a superior technique for rapid characterisation of all macromolecular substances. This study describes the development of an experimental procedure in which product oils are trapped on silica to facilitate analysis by thermal desorption GC-MS without any prior work-up.

Experimental

Samples Göynük oil shale (GOS) was used to assess the capability of the silica-filled trap for recovering hydropyrolysis product oil. This lacustrine oil shale of Tertiary age has been classified as a type I kerogen, and characterised previously (Love et al., 1997). It was pre-extracted with DCM/methanol (93:7 v/v), washed with dilute HCl (2M) at 50ºC for 3 hours and re-extracted with DCM/methanol (93:7 v/v), so any products generated will be predominantly released from the kerogen phase.

Hydropyrolysis Fixed bed hydropyrolysis was conducted using the apparatus and procedure that have been described in detail elsewhere (Snape et al., 1989; Lafferty et al., 1993; Love et al., 1995). Briefly, the samples were pyrolysed with resistive heating from 50°C to 250°C at 300°C min^{-1}, and then from 250°C to 500°C at 8°C min^{-1}, under a hydrogen pressure of 15 MPa. A hydrogen sweep gas flow of 10 dm^3 min^{-1}, measured at ambient temperature and pressure ensured that the products were quickly removed from the reactor vessel. As in previous studies, the hydropyrolysates were recovered with multiple washes of DCM from the dry ice cooled trap, which consisted of coils of ⅜" stainless steel. These results could then be compared to those obtained with the hydropyrolysates collected in the silica filled trap constructed from ¼" stainless steel (0.180" i.d.), and designed to hold approximately 0.75 g of silica. To ensure that there was no contamination of the products, the silica used for trapping (35-70 mesh) was pre-extracted in a soxhlet with *n*-hexane for 24 hours and DCM/methanol (93:7 v/v) for 48 hours, and dried in a baffle furnace at 600°C for 4 hours.

In order to quantitatively assess the recoveries of hydrocarbons by hydropyrolysis, aliquots (~50 mg) of a light crude oil were adsorbed to a small amount of silica and pyrolysed. The desorbed oils were recovered from each of the two designs of trap, cooled by both dry ice and with liquid nitrogen. The temperature within the silica trap was measured by inserting a thermocouple into the trap at the base of the silica column during a blank run with each of the two coolants. Quantification of the recovered hydrocarbons (DCM soluble fraction) was achieved by the addition of squalane, with analysis by gas chromatography-flame ionisation detection (GC-FID).

The aliphatic hydrocarbon, aromatic hydrocarbon and polar (NSO) fractions of the oil shale and asphaltene hydropyrolysates were separated by silica gel adsorption chromatography with successive elutions of *n*-hexane, *n*-hexane/DCM (4:1 v/v) and DCM/methanol (1:1 v/v). The yields of each fraction were determined by evaporation under a stream of dry nitrogen in pre-weighed vials. In order to assess the degree of carbon conversion during hydropyrolysis, and the yield of carbon recovered, the carbon content of the samples, pyrolysis residues, hydropyrolysates and desorption residues were determined with a UCI Coulometrics CO_2 coulometer.

Thermal desorption of hypy oils The off-line thermal desorption of the silica trapped hydropyrolysis products of the GOS were performed in the hydropyrolysis reactor under an atmospheric pressure of hydrogen with a sweep gas flow of 100 cm^3 min^{-1}, measured at ambient temperature. The samples were desorbed with a heating rate of 50°C to 300°C at 300°C min^{-1}, with the final temperature held for 2 mins. The desorbed products were then trapped on silica as for the hydropyrolysis experiments. Further tests were carried out to a maximum temperature of 350, 400, 450 and 500°C, at the same heating rate, with the final temperature again held for 2 mins. The on-line thermal desorption-GC-MS of the silica trapped hydropyrolysis oils were performed Pyrolysis experiments were performed using a CDS 1000 pyroprobe platinum heated filament pyrolyser (Chemical Data System, Oxford, USA) directly connected to a Varian 3400 gas chromatograph coupled to a Varian Saturn II ion trap mass spectrometer. The Py/GC interface and the split/splitless Varian 1077 injector (at split ratio 30:1) were kept at 280°C. Silica trapped sample (about 5 mg) and Göynük oil (about 0.2 mg) were pyrolysed at 700°C (set temperature) for 10 sec at the maximum heating rate. The solution containing aliphatic fraction was analysed by direct injection into the GC-MS apparatus using the above described conditions.

Results and Discussion

Comparison of coiled trap and silica The recovery of the light crude oil desorbed by hydropyrolysis is illustrated in Fig. 1. The whole oil gas chromatogram (Fig. 1A) is dominated by a homologous series of *n*-alkanes (nC_7 to nC_{32}), and low molecular weight aromatic compounds such as benzene and toluene. Table 1 summarises information on the recovery of the light oil for the two

types of trap, using the different coolants. It can be seen that for the relatively high molecular mass alkanes (>nC_{10}), both the normal coiled trap and silica are very efficient (generally >80% w/w), with no significant differences between the two coolants. Major differences in recovery are only apparent for the relatively low molecular weight compounds (<nC_{10}), and so the trapping efficiency of biomarker hydrocarbons (>nC_{20}) should be equally as good for the silica trap as for the coiled steel design. Therefore, the recovered DCM soluble oil fractions (Figs. 1B & 1C) are illustrated as partial gas chromatograms showing only the distribution of the low molecular weight compounds.

Table 1. Recovery (% w/w) of selected hydrocarbons desorbed from a light crude oil under hydropyrolysis conditions.

Compound	Coiled trap		Silica trap	
	Liquid N_2	Dry ice	Liquid N_2	Dry ice
Benzene	58	0	43	0
nC_7	58	0	46	0
Toluene	83	52	83	37
nC_8	79	51	77	4
nC_9	83	75	85	84
nC_{10}	87	83	97	88
nC_{11}	89	87	96	89
nC_{12}	89	88	91	91
nC_{13}	91	90	87	94
nC_{14}	97	95	99	98
nC_{15}	96	93	102	96
nC_{20}	86	88	92	92
nC_{25}	81	85	78	89
nC_{30}	77	94	81	88

The use of liquid nitrogen as the coolant in place of dry ice resulted in a significantly enhanced recovery of low molecular weight compounds such as the nC_7 and nC_8 alkanes, benzene and toluene. The recovery of these compounds was slightly greater from the coiled steel trap cooled with liquid nitrogen than from the silica filled trap. The higher recovery from the coiled steel trap was more significant with dry ice as the coolant, with just 4% w/w of the nC_8 alkane and 37% w/w of the toluene recovered from silica trap, compared to 51% and 52% w/w respectively recovered from the coiled steel trap.

Due to its much lower temperature (-196ºC), the liquid nitrogen should be a much more efficient coolant than the solid dry ice (-78ºC). However, the liquid nitrogen tended to quickly evaporate during the course of the run as the hot sweep gas warmed the trap. Therefore, the temperature at the base of the trap rose steadily from -130ºC when the reactor was at 300ºC, to 85ºC at the end of the test. This was similar to the final temperature observed when dry ice was used as the coolant (65ºC), and might have caused some of the low molecular weight compounds to evaporate and be swept out of the trap.

Information on the efficiency of the different designs of trap in recovering the hydropyrolysate generated by the hydropyrolysis of GOS is presented in Table 2. As in previous studies on this shale, hydropyrolysis resulted in carbon conversions of >90%, with relatively high yields of the GC amenable aliphatic and aromatic hydrocarbons generated. The errors of these analyses are estimated at ±5% based on previous described repeat analyses (Love et al., 1995). The efficiencies of the traps are expressed as the % of the converted carbon, and the wt. % of the total products recovered in each type, and show that the silica-filled and coiled steel traps recover a very similar proportion of the converted organic carbon, principally as DCM-soluble products. These recovery figures may be a slight underestimation of the true values, due to evaporative losses, inevitable while removing the excess DCM to obtain the total hydropyrolysate yield.

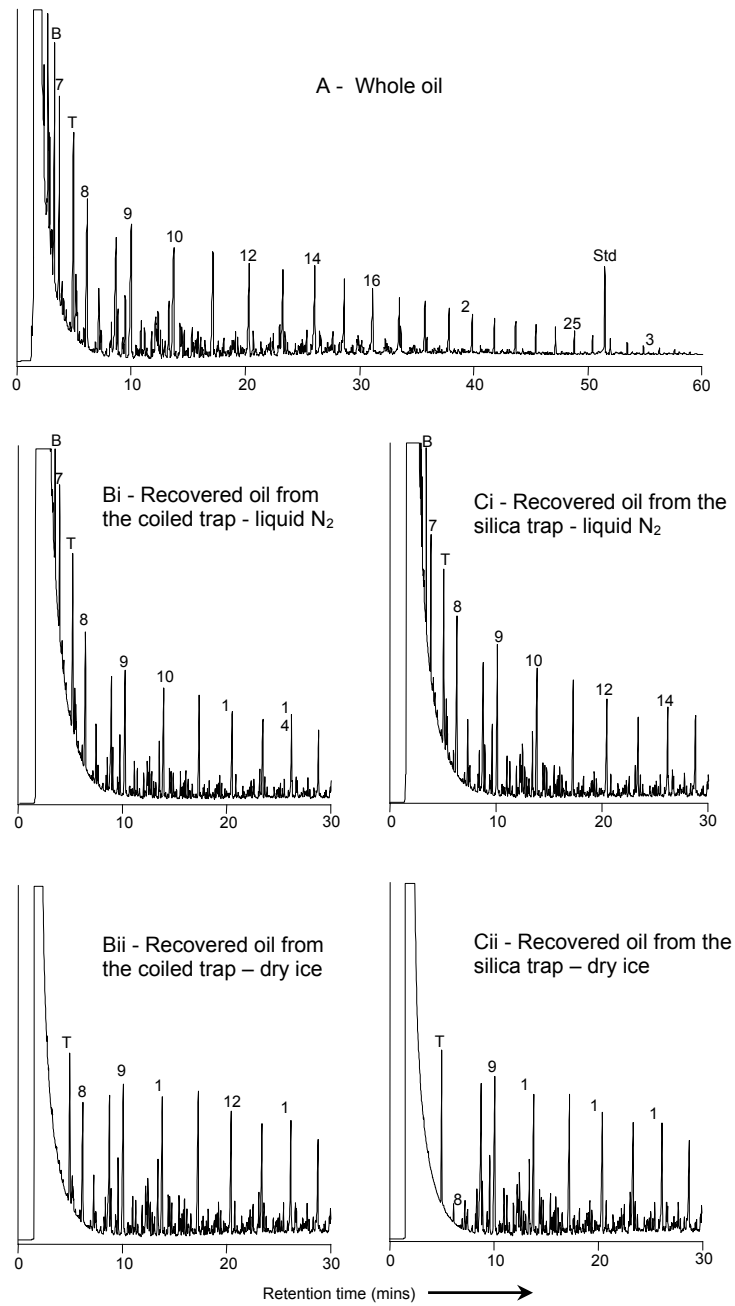

Figure 1. Comparison of the whole oil gas chromatogram (A), and the partial gas chromatograms of the DCM-soluble fraction desorbed by the hydropyrolysis of a light crude oil, with trapping by the coiled steel (B) and silica filled trap (C), cooled by liquid nitrogen (i) and dry ice (ii). Numbers refer to the carbon number of the *n*-alkanes; B - Benzene; T - toluene; Std - squalane.

The distribution of the GOS hydropyrolysate throughout the trap silica column is presented in Table 3. The results for each section are expressed as the wt. % of each fraction present, together

with the proportion of carbon recovered. The vast majority of the hydropyrolysate is adsorbed to the upper quarter section, with >70% w/w of each fraction, and of the total carbon in this section. There is then a rapid decrease in the proportion of hydropyrolysate adsorbed to the middle sections, with <5% w/w present in the lower silica section. These results indicate that providing sufficient silica is present in the trap for the mass of carbon generated from the sample, no significant quantities of the product, other than highly volatile compounds, should pass through the trap without adsorbing to the silica.

Table 2. Comparison of the results obtained from the hydropyrolysis of the Göynük oil shale with the different trapping methods.

	Coiled trap	Silica trap
Sample weight (mg)	100	50
Trap silica weight (g)	-	1.0
Carbon conversion (% initial TOC)[a]	91.2	93.0
Trapping efficiency (% TOC generated)[b]	91.5	94.5
Trapping efficiency (wt. % of products)[c]	80.0	80.9
Yield of aliphatics (mg/g initial TOC)[d]	159	175
Yield of aromatics (mg/g initial TOC)[e]	89	101
Yield of total oil (mg/g initial TOC)[f]	1110	1200

[a] % TOC removed from sample by hydropyrolysis. [b] % of generated TOC recovered. [c] % of sample weight loss recovered as DCM soluble product oil. [d] Weight of recovered aliphatic fraction (mg) / weight of initial TOC (g). [e] Weight of recovered aromatic fraction (mg) / weight of initial TOC (g). [f] Total weight of recovered DCM soluble product oil (mg) / weight of initial TOC (g).

Table 3. Distribution of the hydropyrolysate fractions (wt. %) and TOC (%) throughout the silica column containing the hydropyrolysate of the Göynük oil shale.

Silica section	% Aliphatic	% Aromatic	% Polar	% TOC
Upper	80	71	70	73
Upper middle	13	16	18	15
Lower middle	5	8	7	8
Lower	2	5	5	4

Table 4. Selected aliphatic biomarker maturity parameters from the hydropyrolysate of the Göynük oil shale.

Ratio	Coiled trap	Silica trap	
		All silica	Top section
C31αβ(22S/S+R)[a]	0.21	0.18	0.18
C32αβ(22S/S+R)[b]	0.14	0.12	0.14
C30βα/αβ[c]	1.97	2.03	2.02
Ts/Tm[d]	0.29	0.29	0.32
C29ααα(20S/S+R)[e]	0.05	0.05	0.05
C29αββ/ααα+αββ[f]	0.27	0.25	0.27

[a] αβ-homohopane 22S / S + R - starting value 0, ratios reach end point at 0.6 before the onset of intense oil generation. [b] C_{32} αβ-dihomohopane 22S / S + R - as ratio [a]. [c] C_{30} βα-moretane / C_{30} αβ-hopane - ratio decreases with increasing maturity. [d] 18α,21β(H)-22,29,30-trisnorneohopane / 17α,21β(H)-22,29,30-trisnorhopane - ratio increases with increasing maturity. [e] C_{29} ααα-ethylcholestane 20S / S + R - increases to 0.5 with increasing maturity. [f] C_{29} ethylcholestane αββ / ααα + αββ – increases to 0.8 with increasing maturity.

In addition to the total yield of hydropyrolysate recovered, it is also important that the silica-filled trap produces biomarker hydrocarbon profiles similar to those obtained from the coiled steel trap. A number of maturity dependant biomarker ratios based on the abundance of individual isomers are listed in Table 4, and indicate that the composition of the hydropyrolysates recovered from the silica-filled traps are very similar to those from the coiled steel trap. In addition, it can be seen that the top section of the silica column, which as described contains the highest concentration of hydropyrolysate is representative of the silica column as a whole. This has implications for the on-line thermal desorption py-GC-MS of the silica trapped hydropyrolysis oil described below as only a small amount of the total silica recovered from the trap can be introduced to the pyroprobe at any one time.

Off-line thermal desorption of silica trapped hypy oils The yields recovered from the off-line thermal desorption pyrolysis of the silica trapped hydropyrolysis oils are presented in Fig. 2. Although the total yield of products desorbed at all temperatures is significantly lower than that of the starting hydropyrolysis oil, the effect of temperature is apparent with a steady increase in the recovery of the aliphatic, aromatic and polar fractions from a final temperature of 300ºC through to 500ºC. The yield of aliphatic components at 500ºC is similar to that in the original hydropyrolysis oil, with the reduction in overall yield due to the poor recovery of the aromatic and polar fractions.

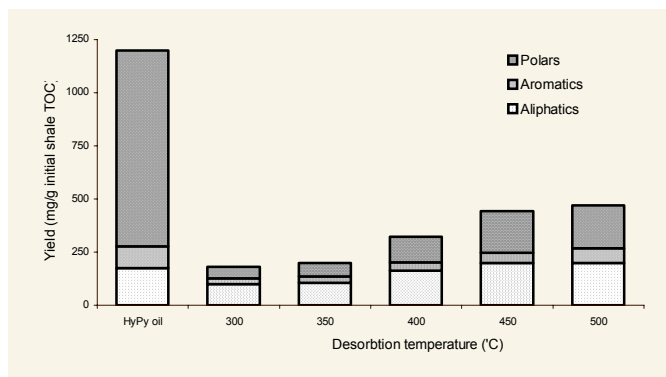

Figure 2. Yield (mg/g initial shale TOC) of aliphatic, aromatic and polar fractions in the thermally desorbed (off-line) Göynük oil shale hydropyrolysates compared to the original hydropyrolysate.

A significant proportion of the carbon in the hydropyrolysate was not desorbed from the trapping silica (131 mg/g initial shale TOC at 300ºC; 33 mg/g initial shale TOC at 500ºC). As noted for reduced yields of asphaltenes adsorbed on silica during hydropyrolysis, interactions between silica and polar functional groups in the sample my result in the reduced desorption of this fraction relative to the non-polar aliphatic and aromatic compounds.

The distribution of aliphatic hydrocarbons in the hydropyrolysate of GOS (Fig. 3A) is dominated a bimodal distribution of *n*-alkane /*n*-alk-1-ene doublets (maximum at C_{30} and submaximum at C_{21}), with the homologous series extending up to C_{40}.[1]. The *n*-alkanes are the more abundant, with an even-over-odd predominance (EOP) apparent among the longer chained homologues, and the distribution of *n*-alk-1-enes mirroring that of their saturated analogues. Such doublets are ubiquitous components of kerogen pyrolysates[7], although as noted earlier[1], the survival of *n*-alkanes heavier than ~C_{35} are not often observed in on-line pyrolysis experiments (e.g. Derenne *et al.*,[10]). Changes in the profiles with increasing desorption temperature can be assessed by measuring the ratio in abundance between a long chain alkane e.g. *n*-C_{30} and a relatively short chain one not subject to evaporative losses e.g. *n*-C_{18}.

This parameter may also vary as a result of cracking of the longer chained *n*-alkanes, which could potentially arise at higher desorption temperatures resulting in a concurrent increase in the abundance of the shorter chained homologues[11]. As indicated in Table 2, for desorption at 300ºC the higher molecular mass *n*-alkanes are clearly not desorbed efficiently as the doublet envelope has a different shape with a maximum abundance at C_{16}. However, desorption at 500ºC gives a profile is very similar to that of the original hydropyrolysate oil (Fig. 3B).

Table 5. Molecular abundance ratios to monitor secondary cracking during the thermal desorption of the silica trapped hypy oil. CPI after Philippi, 1965 = $2*C_{29}/(C_{28}+C_{30})$.

Desorption T/ºC	n-C_{18} / n-C_{30} alkane	CPI[a]	Total alkanes / alk-1-enes
300	1.21	0.71	0.36
350	0.50	0.83	0.33
400	0.50	0.83	0.33
450	0.50	0.83	0.34
500	0.50	0.82	0.37
HyPy oil	0.33	0.79	0.30

Secondary cracking during both the hydropyrolysis and desorption phases would also result in a decrease in the magnitude of the EOP amongst the longer chained *n*-alkanes[3], which can be assessed by the carbon preference index (CPI), and lead to an increase in the abundance of the unsaturated *n*-alk-1-enes in these samples relative to the *n*-alkanes[12, 13]. These ratios for each desorption temperature are presented in Table 5, and suggest that with the exception of the poorly desorbed 300ºC sample, and some evidence of minor cracking at higher temperature, the distribution of these compounds in the desorbed oils are not that dissimilar to that of the original hydropyrolysis oil. Indeed, high recoveries of individual hopanes and steranes with no evidence of isomerisation and cracking were also achieved at 500°C.

On-line thermal desorption of silica trapped hypy oils The on-line thermal desorption pyrolysis of the silica trapped GOS hydropyrolysate (Fig. 3C) resulted in greater evidence of secondary cracking than was apparent in the off-line studies. In addition to the generation of a higher proportion of shorter chain *n*-alkenes (n-C_{12} - n-C_{16}), the envelope of *n*-alkanes also shows a different pattern, with, in addition to the higher relative abundance of shorter chain *n*-alkenes, a maximum at n-C_{28} instead of n-C_{30} and fewer of the very long chain *n*-alkanes apparent. However, as with the off-line studies the recovery of high molecular mass extended hopanes and steranes with the biologically inherited and thermodynamically unstable stereochemistry, which would be the most susceptible to isomerisation and/or cracking of the alkyl side chain [3], suggests that the extent of cracking is not extensive. Thus, with scope for further optimization of the pyrolysis conditions, on-line thermal desorption shows considerably potential in retaining considerable more structural integrity than py-GC-MS for fingerprinting petroleum source rocks and coals.

Conclusions

It has been demonstrated that hypy oils can be recovered on silica and the quantitative recovery of hydrocarbons from a light crude oil desorbed from silica under hydropyrolysis conditions demonstrates no significant loss of the high molecular mass *n*-alkanes (>$n$$C_{10}$). The use of liquid nitrogen as the trap coolant results in significantly improved recovery of the lower molecular mass constituents. The silica-adsorbed oils undergo relatively little cracking during thermal

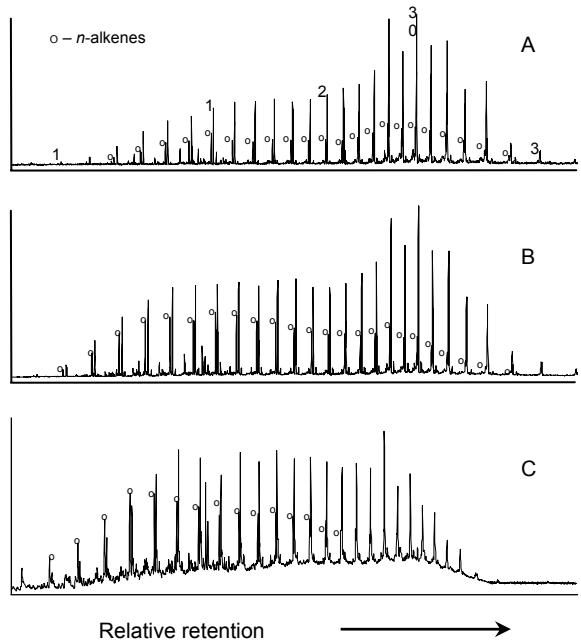

Figure 3. TIC of: A - the aliphatic hydrocarbon fraction of the GOS hydropyrolysate; B - the aliphatic hydrocarbon fraction of the oil recovered from the off-line thermal desorption at 500ºC of the silica trapped GOS hydropyrolysate; C - the on-line pyrolysis (700ºC) of the silica trapped GOS hydropyrolysate.

desorption, with similar *n*-alkane and biomarker profiles being obtained as with normal work-up and GC-MS analysis. Thus, in terms of fingerprinting hydrocarbon moieties in geomacromolecules, hypy-GC-MS, in terms of retaining a high level of structural integrity is potentially an attractive alternative to traditional py-GC-MS.

Acknowledgement. The authors thank the Natural Environment Research Council (NERC) for financial support (Ocean Margins LINK grants, nos. NER/T/S/2000/01366 and 2001/01153).

References

(1) Love, G.D., Snape, C.E., Carr, A.D., Houghton, R.C., 1995. *Organic Geochemistry,* **1995**, *23*, 981.
(2) Love, G.D., Snape, C.E., Carr, A.D., Houghton, R.C., *Energy & Fuels*, **1996**, *10*, 149.
(3) Love, G.D., McAulay, A., Snape, C.E., Bishop, A.N., *Energy & Fuels,* **1997**, *11*, 522.
(4) Bishop, A.N., Love, G.D., Snape, C.E., Farrimond, P., Organic Geochemistry, **1998**, *29*, 989.
(5) Murray, I.P., Love, G.D., Snape, C.E., Bailey, N.J.L., *Organic Geochemistry,* **1998**, *29*, 1487.
(6) Gallegos, E.J., 1975. Analytical Chemistry, **1975**, *47*, 1524.
(7) Larter, S.R., Horsfield, B., In Engel, M.H., Macko, S.A. (Eds.) *Organic Geochemistry*, **1993**, Plenum Press, New York. pp. 271.
(8) Philip, R.P., Gilbert, T.D., *Geochimica et Cosmochimica Acta*, **1985**, *49*, 1421.
(9) van Graas, G., *Organic Geochemistry*, **1986**, *10*, 1127.
(10) Derenne, S., Largeau, C., Casadevall. E., Tegelaar, E., de Leeuw, J.W., *Fuel Processing Technology*, **1988**, *20*, 93.
(11) Kissin, Y.V., *Geochimica et Cosmochimica Acta*, **1987**, *51*, 2445.
(12) Behar, F., Pelet, R., Roucache, J., *Organic Geochemistry*, **1984**, 6, 587.
(13) van Lieshout, M.P.M., Janssen, H-G., Cramers, C.A., van den Bos, G.A., J. of Chromatography A, **1997**, *764*, 73-84.

STUDY ON THE STRUCTURE OF ANTHRACITE BY ANALYZING ITS HYDROGEN CONTENT

Hiromi Aso, Koichi Matsuoka and Akira Tomita
(Institute of Multidisciplinary Research for Advanced Materials, Tohoku University, Sendai 980-8577, Japan)
e-mail: tomita@tagen.tohoku.ac.jp

Introduction

There have been many attempts to elucidate the chemical structure of heavy hydrocarbons using various techniques [1-3]. The data of elemental analysis are the most important information among all [4]. However, the materials with more carbon and less hydrogen are quite difficult to analyze. In fact, little attention has been paid on the elemental analysis of carbonaceous materials. This is partly because the carbon content is overwhelmingly high and the contents of minor elements are too small to accurately analyze. The present paper attempts to make every effort to determine hydrogen content of carbonaceous materials as accurately as possible. After temperature-programmed oxidation (TPO) of hydrogen to water, careful analysis of water was made with gas chromatography and mass spectroscopy. It is definitely necessary to have reliable elemental analysis data for deeper understanding on the structure. For example, the accurate H/C atomic ratio can be used to directly speculate the size of aromatic ring system.

Experimental

Samples. In this study, three Chinese anthracites (<150 μm) were used as examples of carbonaceous materials. The ultimate analysis of the raw anthracites determined by a conventional method is presented in Table 1. These anthracites were demineralized by washing with HF and HCl solutions, and the effect of mineral matter removal on the hydrogen content was examined by comparing two sets of anthracites.

Table 1. Ultimate Analysis of Raw Anthracites

sample	code	ultimate analysis [wt %, daf[a]]			
		C	H	N	S+O[b]
Si Wang Zhang	SWZ	93.96	1.18	0.61	4.25
Men Tou Gou	MTG	95.69	1.16	0.25	2.90
Guo Er Zhuang	GEZ	96.27	1.32	0.66	1.75

[a]dry ash free [b]by difference

Apparatus. The reactor for TPO was a fixed bed reactor, which was made of quartz tube with an inner diameter of 7 mm. The gas analyses were made with a gas chromatograph and a quadrupole mass spectrometer. In order to remove H_2O in the carrier gas, a drying tube was installed before the reactor.

Procedure. About 200 mg of sample was fixed in the center of reactor using quartz wool. The reactor was purged with He gas flow until O_2, N_2, CO_2 and H_2O disappeared in GC signals. TPO was carried out by heating the sample under 5% O_2 in He (200 ml/min) at a rate of 2 °C/min up to 1000 °C and the temperature was kept at 1000 °C for 60 min. The gas products during TPO were continuously analyzed with GC and MS. Temperature programmed desorption, TPD, was carried out under a similar condition as TPO, except that pure He flow was used instead of O_2/He flow. We measured the amount of H_2O evolved during TPO and TPD mainly by GC. The GC response was calibrated using calcium oxalate monohydrate.

Results and Discussion

Gas Evolution during TPO and TPD. TPO patterns of raw anthracite are shown in Figure 1. H_2O evolution rate is shown in the upper panel, and CO/CO_2 evolution rate together with O_2 consumption rate are shown in the lower panel. Roughly speaking, two H_2O evolution peaks were observed for SWZ and MTG, and most of these peaks are composed of several sub-peaks. In the first H_2O-evolution range from 50 to 500 °C, no O_2 was consumed and no CO and CO_2 were formed. On the other hand, the H_2O evolution peak from 500 to 800 °C was accompanied by O_2 consumption and CO/CO_2 formation. It should be noted that GEZ gives no H_2O evolution peak at the low temperature region.

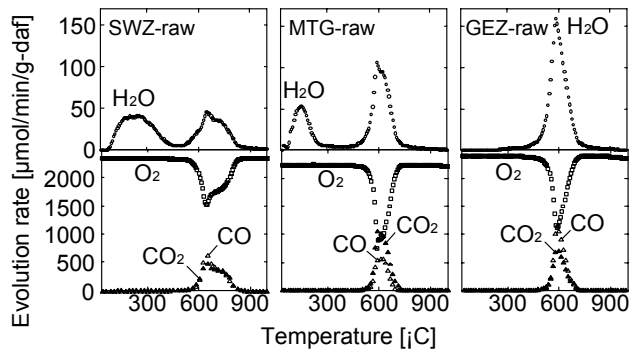

Figure 1. CO, CO_2 and H_2O evolution pattern and O_2 consumption pattern for raw anthracites during TPO.

The H_2O evolution pattern in the low temperature range between 50 – 500 °C was almost the same between TPO and TPD and also between raw and demineralized samples. In the higher temperatures, however, a very small amount of H_2O was evolved between 500 - 700 °C upon TPD of raw anthracite, and it disappeared if the demineralized sample was used.

H_2O Evolution in the Low Temperature Region. The lower temperature peak in Figure 1 can be due either to adsorbed water, dehydration of mineral matter or decomposition of hydroxyl group. Since the amount of H_2O evolved from raw anthracite in the low temperature region was almost the same as that for demineralized anthracite, dehydration of mineral matter would not be the main reason for the H_2O evolution in this region. Furthermore, the content of hydroxyl group in anthracite is very low [5]. The decomposition of surface functional groups, if any, can account only for a slight portion of H_2O evolution. Contrary to the above possibilities, H_2O desorption from anthracite would be more plausible explanation.

Careful examination on the H_2O adsorption and desorption behavior with these anthracites revealed that a considerable amount of H_2O was kept in MTG and SWZ anthracite even after He purge prior to TPO and TPD experiments. This adsorbed H_2O evolved in the region between 50 and 500 °C in both TPO and TPD. The adsorption rate as well as desorption rate with GEZ was much faster than the others. Thus, H_2O in GEZ was almost completely removed during He purge, and therefore no H_2O evolution was observed with GEZ in the low temperature region.

Small H_2O Evolution Peak at 500 - 600 °C. SWZ and MTG raw anthracites evolved a small amount of H_2O at around 600 and 530 °C, respectively, under TPD condition. It is likely that the origin of these small peaks were the dehydration of mineral matter, since these peaks were not seen in TPD of demineralized anthracites. Furthermore, the temperature range reported for the dehydration of

kaolinite is close to the small H_2O evolution observed at 500 - 700 °C.

H_2O Evolution in the High Temperature Region during TPO. Now we are in a position to discuss on the major part of H_2O evolution at high temperatures. These H_2O come from inherent hydrogen in anthracite, and thus the H_2O evolution should be closely related to the structure of anthracite. The H_2O formation pattern in the high temperature region during TPO is different in shape, temperature and quantity between three anthracites (Figure 1). This is undoubted indication of the different structure of these anthracites.

More detailed analysis of high temperature peak will be of great interest. A closer look at the H_2O evolution peak reveals that the peak in the high temperature region is composed of multiple peaks. This suggests that anthracite have several different types of hydrogen. The separation of these peaks was not attempted in the present study because of rather poor peak resolution. The quantification of well-resolved peak components will provide much more useful information on the structure of anthracite.

Implication of hydrogen content to the structure of anthracite. In TPO, hydrogen in anthracite was converted to H_2O, and carbon was converted to CO and CO_2. The atomic ratio of H/C in the evolved gas corresponds to the ratio of H/C in the anthracite molecule. To eliminate the contribution from mineral matter in the following discussion, the data on demineralized anthracites are used (Table 2).

Table 2. Gas Evolved from Dem-Anthracite in the High Temperature Range during TPO.

sample	gas	gas evolved [mmol/g-daf]	atomic ratio, H/C [-]
SWZ-dem	CO	28.0	0.08
	CO_2	47.8	
	H_2O	3.0	
MTG-dem	CO	33.9	0.13
	CO_2	44.1	
	H_2O	5.0	
GEZ-dem	CO	40.4	0.18
	CO_2	33.7	
	H_2O	6.8	

These values give straightforward information on the chemical structure of anthracites. The structure was speculated under the following assumptions: (1) anthracite molecule consists only of carbon and hydrogen, (2) the molecule has graphene-type hexagon, and (3) all peripheral carbon atoms are occupied with hydrogen. Under these assumptions, the H/C ratio of 0.08 for SWZ-dem corresponds to a hexagon of 469 rings and with an edge of 3.2 nm long, whereas that of 0.2 for GEZ-dem to a hexagon of 61 rings and with an edge of 1.2 nm long. Even though this is only average value and this was deduced from audacious assumptions, such calculation made it possible to visualize a remarkable difference between SWZ-dem and GEZ-dem. It is almost impossible to imagine this difference only from the elemental analysis data.

Another important message from this study is that the present result suggests the inadequacy of using ultimate analysis data to speculate the chemical structure of hydrocarbon sample. This becomes obvious if the H/C ratio from TPO result is compared with that calculated from the ultimate analysis (Table 1). The H/C ratio determined from the yield of H_2O, CO and CO_2 in the higher temperature region during TPO was 0.09, 0.14 and 0.20 for SWZ-raw, MTG-raw and GEZ-raw, whereas the H/C ratio calculated from ultimate analysis is 0.151, 0.145 and 0.165, respectively. The difference is incredible. The former value faithfully reflects the aromatic hydrocarbon structure of anthracite, but the latter does not. Hydrogen in ultimate analysis contains not only hydrogen in organic moiety but also hydrogen in adsorbed water and mineral matter.

Further comment should be made on the so-called coal rank. It is generally thought that the extent of coalification is higher for coals with higher carbon contents. In this sense, the rank among three anthracites should be SWZ < MYG < GEZ. However, the carbon content only in the organic portion of anthracite is 96, 97 and 98 wt % for GEZ, MTG and SWZ, respectively. From this viewpoint, the order of rank becomes GEZ < MTG < SWZ, which is opposite to the above order. Of course, the latter order is more meaningful. In this way, careful quantification of hydrogen content in carbonaceous materials provides various information of great value.

Conclusions

The hydrogen content in anthracite was carefully determined by TPO and TPD techniques. H_2O evolved from adsorbed water, dehydration of mineral matter, and decomposition of hydroxyl group was quantitatively evaluated, and the rest of H_2O evolution was attributed to that from organic portion in anthracite. This H_2O evolution constitutes the major portion of the TPO peak in the range of 500 - 800 °C. The yield of this H_2O together with those of CO and CO_2 gives an H/C atomic ratio of the anthracite molecule. Three anthracites used in this study gave the H/C ratio ranging from 0.08 to 0.18. The former value corresponds to a hexagon molecule with a size of 3.2 nm on average, while the latter corresponds to 1.2 nm. Ultimate analysis data cannot provide such essential information.

Acknowledgement. The anthracite samples used in this work were kindly supplied by Professor Peng Chen of Beijing Research Institute of Coal Chemistry.

(1) Hirsch, P. B. *Proc. Roy. Soc. A* **1954**, *226*, 143.
(2) Shinn, J. H. *Fuel* **1984**, *63*, 1187.
(3) Sharma, A.; Kyotani, T.; Tomita, A. *Energy Fuels* **2000**, *14*, 1219.
(4) Brown, J. K.; Ladner, W. R. *Fuel* **1960**, *39*, 87-96.
(5) Hatami, M.; Osawa, Y.; Sugimura, H. *J. Fuel Soc. Jpn* **1967**, 46, 819.

PROBING COAL HETEROGENITY ON THE NANOSCALE BY NMR

Robert E. Botto and David L. VanderHart^*

*Chemistry Division, Argonne National Laboratory, 9700 S. Cass Ave., Argonne, IL 60439 and Polymer Division, National Institute for Standards and Technology, Gaithersburg, MD

Introduction

Exploring chemical and materials' properties on the nanometer scale presents significant challenges. Characterization methods such as neutron and x-ray scattering, diffuse-reflectance infrared spectroscopy and nuclear magnetic resonance (NMR) spectroscopy are being applied to probe variations in chemistry on the nanoscale. However, many challenges remain when studying extremely complex, heterogeneous substances. Several obstacles are not easily overcome, particularly when applying NMR techniques to structurally complex fossil resources.[1]

Work carried out during the past decade in our laboratory has focused on identifying the variation in chemistry of complex carbonaceous solids. One particular focal point of our work has been on a study of coals from the Argonne Premium Coal Sample Program. Coal has been described as being an "organic rock" comprised of different plant remains that have been geologically altered over time, and as such, are considered to be extremely heterogeneous in nature. We have tried to address the following question: "On what length scale does the chemical heterogeneity in coal end?"

Earlier experiments have provided some insight into this question. Magnetic resonance imaging (MRI), [2,3] and more recently, synchrotron-based scanning transmission x-ray microscopy (STXM)[4,5] have provided detailed, two- and three-dimensional pictographs showing the chemical variation of the organic phases of coal. As an example, a carbon STXM micrograph highlighting microspores (magenta colored regions) within a thin section of Pittsburgh No. 8 coal (APCS 4) is shown in Figure 1 below. While the images obtained show a definitive, sharp separation in chemistry along maceral (metamorphosed plant organic matter) boundaries, the maximum image resolution that could be achieved was 50-100 nm at best, which lies on the upper limit of the nanoscale.

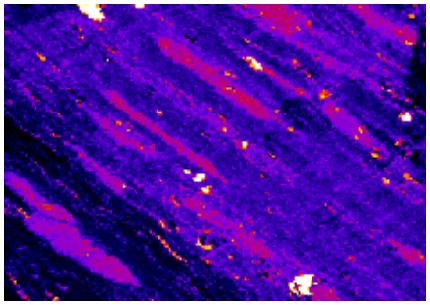

Figure 1. STXM micrograph of a thin section of Pittsburgh No. 8 Bituminous coal (APCS 4) recorded at an absorption energy of 285.5 eV (carbon π^*-aromatic absorption); clear white features in the image are holes.

In principle, spin-diffusion NMR techniques are capable of probing chemical heterogeneity on a scale of a few nanometers. These methods have been applied successfully to the study of phase-separated polymer blends whose components have sufficient chemical distinction.[6-8] The concept behind the experiment is to establish a magnetization gradient, or non-equilibrium magnetization condition, between the chemically different protons that reside in different domains, and then to allow the magnetization to equilibrate, or to 'diffuse' through domains. From the time dependence of the diffusion process, one can estimate the size of the domains. The challenge has been to apply the method to a substance as complex as coal, whose CRAMPS spectra seldom display more than two broad resonance bands associated with aromatic and aliphatic protons.

In this paper, we demonstrate the utility of proton spin diffusion methods for determining the size of submicroscopic resinite domains in Utah Blind Canyon coal (APCS 6) on a length scale down to a few nanometers.

Experimental Section.

Sample Preparation. A solid block of Utah Blind Canyon coal (APCS 6), which is a predominantly bimaceral coal comprised of resinite and vitrinite, was machined into a cylinder to match the exact internal dimensions of Bruker 7-mm diameter MAS rotors. The sample remained intact throughout the entire study.

Solid-State NMR Spectroscopy and Spin Diffusion. Solid-state proton NMR experiments were recorded on a Bruker Instruments spectrometer, model CXP-200, in the pulsed Fourier-transform mode. Combined rotation and multipulse spectroscopy (CRAMPS)[9] was used both to narrow the proton resonance lines and to establish a chemical-shift based polarization gradient for implementation of the proton spin diffusion experiment designed to probe domain size.[10] The polarization gradient was established by varying the duty cycle between pulses in the CRAMPS experiment to give a negative aromatic proton polarization and a positive aliphatic proton polarization. Proton signal was recorded after a variable delay period to allow for spin diffusion. Proton spin-lattice relaxation times were measured by using the standard inversion recovery method followed by CRAMPS readout of the proton magnetization.

Results and Discussion

Proton NMR experiments, both inversion-recovery and spin-diffusion types, employing CRAMPS (combined rotation and multiple pulse spectroscopy) methods were performed on a sample of Utah Blind Canyon coal (Argonne Premium Coal Sample No. 6), which is largely a bimaceral coal composed of vitrinite with about 7% resinite. Pure maceral fractions were obtained by physical separation methods in order to measure proton NMR spectra and proton relaxation times on the pure macerals, information that is needed to perform the analyses. Inversion-recovery data for measuring the longitudinal proton relaxation time, T_{1H}, is shown in Figure 2. The T_{1H} relaxation time decays of the resinite and vitrinite polarizations are distinct and the resinite line shape is extracted from this data based on two characteristics, namely, a) that line width for resinite is significantly narrower than for vitrinite and b) that T_{1H}'s of the vitrinite and resinite are distinct and quantifiable. Thus, knowing the general aliphatic line shape from the CRAMPS spectrum of each maceral, one can separate the resinite spectrum appropriate to this mixed sample from the inversion recovery data. The resinite spectrum is isolated when the broader aliphatic vitrinite component passes through the null condition. Note in Figure 2 that the resinite polarization does not decay exponentially for all time. Nevertheless, the fact that the T_{1H} decays are separable and, in particular, that the resinite component, representing about 20% of the total protons, has an upward rather than a downward deviation from exponential behavior, implies that most of the resinite domains exceed 100 nm in size.

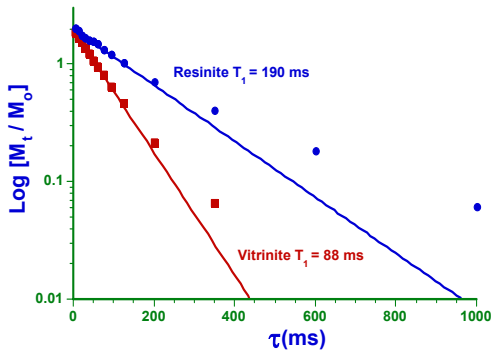

Figure 2. Proton magnetization decay curves and estimated spin-lattice relaxation times (T_1^H) for Utah Blind canyon coal (APCS 6).

We were also interested in the possibility that there might be some resinite domains, which were significantly smaller and within spin diffusion (SD) distances. The CRAMPS preparation chosen produces a modestly negative aromatic and a more strongly positive aliphatic proton polarization. An initial gradient of proton polarization is established between the two maceral phases, thereby allowing the use of the CRAMPS line shape to monitor any subsequent SD between those components. Changes in relative polarization levels of resinite and vitrinite domains with diffusion time are shown in Figure 3 with P_o representing the polarization at Boltzmann equilibrium. Only data for > 4 ms are included, because intra-phase equilibration dominates at earlier times. There is a reproducible, slightly accelerated rate of decay for the resinite polarization (see results in Figure 4), and a correspondingly, hardly perceptible rise in the vitrinite polarization in the 4 ms to 12 ms range. The deduction from Figure 4 in terms of mixing is that a maximum of 20% of the resinite protons are in domains small enough (< 6 nm) to undergo SD on the timescale of 12 ms or less. However, the majority of the protons of resinite are isolated from those of the vitrinite so that the resinite decay rate seen is indistinguishable from the resinite T_{1H} observed in the inversion-recovery experiment. From the similarity of slope for the SD and inversion recovery data for resinite, it is clear that most of the resinite is found in domains large enough (> 100 nm) so that SD on a time scale of 250 to 1000 ms has an insignificant effect on the rate of decay.

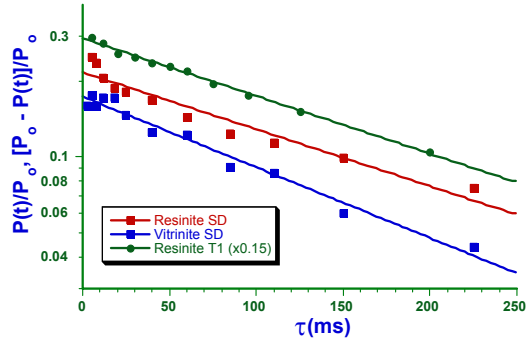

Figure 3. Proton magnetization decay curves for spin-lattice relaxation in resinite and spin diffusion in resinite and vitrinite.

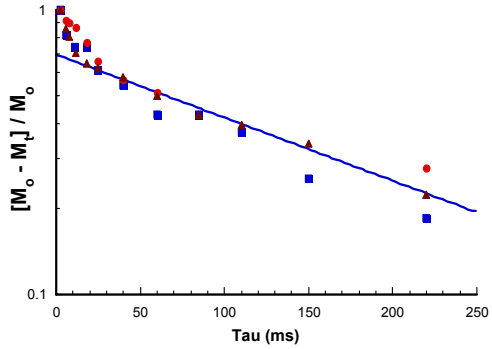

Figure 4. Summary of proton magnetization decay curves of spin diffusion for resinite domains in Utah coal.

Conclusions

The findings suggest that while most of the resinite inclusions found in the Utah coal are relatively large in size, consistent with the previous images obtained by STXM, there is a significant fraction of resinite material that is submicroscopic in size. These submicroscopic inclusions are about 6 nm or less, and represent about 20% of the resinite in the Utah coal. They have not been identified previously. Their existence can be explained by a geological process whereby small molecular weight resins produced in the plant epithelial cells were preserved throughout the woody micro-pores, and subsequent burial and diagenesis led to their ultimate polymerization to form small resinite inclusions intimate with the vitrinite matrix. These findings are entirely in accord with the known paleobotany and geochemistry of resins in coal bearing formations, and explain some of the unusual properties (reflectance, fluorescence, H/C ratio, and f_a) of the vitrinite in the Utah coal.

Acknowledgement. This work was performed under the auspices of the Office of Basic Energy Sciences, Division of Chemical Sciences, Biosciences and Geosciences, U. S. Department of Energy, under contract number W-31-109-ENG-38.

References

(1) Cheung, T. T. P.; Gerstein, B. C. *J. Appl. Phys.*, **1981**, *52* (9), 5517.
(2) Dieckman, S. L.; Gopalsami, N.; Botto, R. E. *Energy Fuels,* **1990**, *4* (4), 417.
(3) French, D. C.; Dieckman, S. L.; Botto, R. E. *Energy Fuels,* **1993**, *7*, 90.
(4) Botto, R. E.; Cody, G. D.; Kirz, J.; Ade, H.; Behal, S.; Disko, M. *Energy Fuels,* **1994**, *8*, 151.
(5) Cody, G. D.; Botto, R. E.; Kirz, J.; Ade, H.; Behal, S.; Disko, M.; Warick, S. *Energy Fuels,* **1995**, *9*, 525.
(6) Havens, J. R. ; VanderHart, D. L. *Macromolecules*, **1985**, *18* (9), 1663.
(7) Vanderhart, D. L.; McFadden, G. B. *Solid State Nucl. Magn. Reson.*, **1996**, *7*, 45.
(8) Neagu, C.; Puskas, J. E.; Singh, M. A.; Natansohn, A. *Macromolecules*, **2000**, *33*, 5976.
(9) Gerstein, B. C. *Philos. Trans. R. Soc. London*, **1981**, *A299*, 521.
(10) Campbell, G.C.; VanderHart, D. L. *J. Magn. Reson.,* **1992,** *96* (1), 69.

Solvent and Matrix Effects in the Mass Spectrometric Analysis of Polyaromatic Sulfur Compounds in the Presence of Palladium (II)

Walter E. Rudzinski, Xuemei Luo

Department of Chemistry
Southwest Texas State University
San Marcos Tx, 78666

Introduction

The nucleophilic interaction of sulfur compounds with $PdCl_2$ to form complexes has been well documented in the literature,[1-6] and the interaction has been exploited for the ligand exchange chromatography (LEC) of polyaromatic sulfur heterocycles (PASH). There are however some deficiencies in the LEC method: organosulfur compounds elute as $PdCl_2$ complexes, benzothiophenes are not completely recovered, and constituents with a terminal (as opposed to an internal) thiophene ring elute early.[7] In addition, the affinity of the $PdCl_2$ varies with the organosulfur ring size and decreases in the order 3-ring> 2-ring> 1-ring PASH. [3,7] The results seem to indicate that the goal of a general chromatographic method for the separation of polyaromatic sulfur heterocycles (PASH) remains elusive.

An alternative approach for the separation of PASH compounds involves mass spectrometry. As recently reported, a redox reaction can occur between Pd(II) and PASH compounds in the electrospray ionization source of a mass spectrometer.[8] The reaction yields PASH radical cations which are easily identified and quantified. We now report significant improvements to the sensitivity, and limit of detection for the method when using a (50:50) methanol: dichloromethane solvent mix, as well as the selectivity of the method when detecting PASH compounds in a hydrogenated oil matrix. The applications of chromatography and mass spectrometry to petroleum analysis have recently been reviewed.[9-11]

Experimental

Reagents and Chemicals. Methanol (CH_3OH), acetonitrile (CH_3CN), dichloromethane (CH_2Cl_2), and hexane were all chromatographic grade and obtained from EM Science (Gibbstown, NJ); $PdCl_2$ and the organosulfur compounds: dibenzothiophene (DBT), thianthrene (TAN), benzonaphthothiophene (BNTP), 4,6-dimethyl-dibenzothiophene (4,6-DBT) and 2-methyl dibenzothiophene (2-DBT) were obtained from Sigma-Aldrich (Milwaukee, WI). Hydrogenated oil was obtained from Exxon-Mobil.

Preparation of Samples. PASH stock solutions were prepared as either 10mM or 1 mM (TAN) solutions in either (50:50) CH_3OH: CH_3CN or CH_2Cl_2. A 20 mM $PdCl_2$ stock solution was prepared either in (50:50) CH_3OH: CH_3CN or CH_3CN. The hydrogenated oil was dissolved in hexane to a final concentration of 100 mg/mL.

PASH mixture #1 was prepared by taking a 1-20 µl aliquot of the appropriate compound in (50:50) CH_3OH: CH_3CN then diluting to 1 mL in (50:50) CH_3OH: CH_3CN to the following concentrations: $1.5x10^{-4}$ M TAN, $1x10^{-3}$M DBT, $1x10^{-3}$M 2-DBT, $1x10^{-3}$M 4,6-DBT, $2x10^{-3}$M BNTP and 2 - 4 mM $PdCl_2$.

PASH mixture #2 was prepared by taking the appropriate PASH in CH_2Cl_2 then diluting to 1 mL in (50:50) CH_3OH: CH_2Cl_2 to the following concentrations: $1x10^{-6}$M TAN, $5x10^{-4}$M DBT, $1x10^{-4}$ M 2-DBT, $2x10^{-5}$M 4,6-DBT, $5x10^{-5}$M BNTP and 0.5 - 1 mM $PdCl_2$.

PASH mixture #3 in hydrogenated oil was prepared by taking an appropriate aliquot of PASH in CH_2Cl_2, $PdCl_2$ in CH_3CN, and hydrogenated oil in hexane then diluting to 1 mL in (50:50) CH_3OH: CH_2Cl_2: to the following concentrations: $1x10^{-6}$M TAN, $5x10^{-4}$M DBT, $1x10^{-4}$ M 2-DBT, $2x10^{-5}$M 4,6-DBT, $5x10^{-5}$M BNTP, 0.5 - 1 mM $PdCl_2$ and 10mg/mL hydrogenated oil.

Instrumentation. Mass spectra were obtained on a Finnigan LCQ ion trap mass spectrometer (MS) equipped with an electrospray ionization (ESI) source. Excalibur software, version 1.2 (Finnigan Corp., 2000) was used for data acquisition and plotting.

Instrumental parameters used with the ESI ionization source and Finnigan LCQ were as follows: nitrogen sheath gas pressure, 80psi; nitrogen sheath gas flow rate, 60 (arbitrary units); positive ion mode; ion spray voltage, 3.5kV; capillary temperature, 200°C; capillary voltage, 60V; tube lens offset voltage, 40V. Each MS scan was based on the average of 5 microscans and MS spectra were averaged based on at least 25 scans.

The samples were introduced by direct infusion at a flow rate of 2µl/min.

Results and Discussion.

The limit of detection (LOD) was determined both in the (50:50) CH_3OH: CH_3CN and (50:50) CH_3OH: CH_2Cl_2 binary solvent mixtures using the formula, LOD = 3s/m where s is the average background noise and m is the response/ molar concentration. The results are presented in Table 1 which clearly show a lowering of the LOD in (50:50) CH_3OH: CH_2Cl_2 by a factor of 150 or more for TAN, 4,6-DBT and BNTP, 18 for 2-DBT and 5 for DBT. As previously intimated by Van Berkel and coworkers, this result is probably due to the increased stabilization of radical cations in CH_2Cl_2.[12]

Table 1. Limit of Detection for PASH Compounds

Compounds	LOD in CH_3OH: CH_2Cl_2 (50:50)	LOD in CH_3OH: CH_3CN (50:50)
TAN	3.0×10^{-7}M	4.5×10^{-5}M
DBT	1.8×10^{-4}M	9.0×10^{-4}M
2-DBT	5.0×10^{-5}M	9.0×10^{-4}M
4,6-DBT	7.5×10^{-6}M	4.5×10^{-3}M
BNTP	1.8×10^{-5}M	4.5×10^{-3}M

Figure 1 shows the mass spectrometric results obtained for several samples in the (50:50) CH_3OH: CH_2Cl_2 binary solvent mixture.

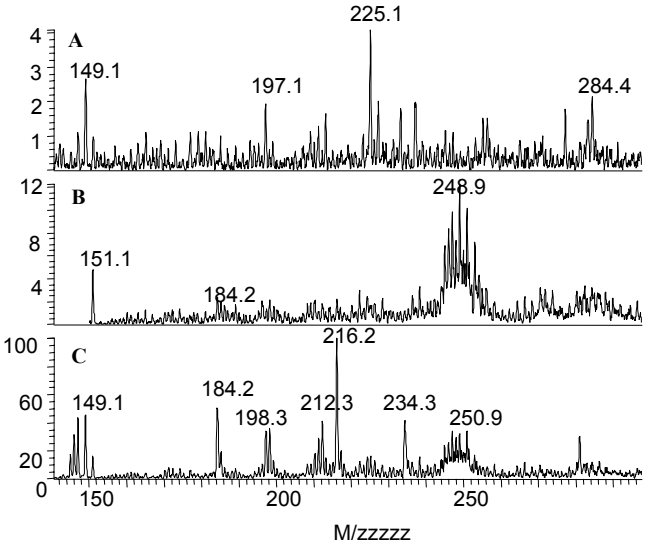

Figure 1. Mass Spectrometric response for: (A) 10 mM hydrogenated oil; (B) 10 mM hydrogenated oil and 0.5 mM $PdCl_2$; (C) mixture #3 which consists of TAN, DBT, 2-DBT, 4,6-DBT, BNTP, $PdCl_2$ and hydrogenated oil.

Figure 1 (A) clearly illustrates that the matrix, the hydrogenated oil, does not generate many peaks and those which are present generate minimal response (less than 4). Figure 1B illustrates the response for a mixture of the hydrogenated oil and $PdCl_2$. A broad envelope is centered about an m/z of 249 which is attributed to a palladium cluster. Figure 1C illustrates the response of the hydrogenated oil, $PdCl_2$ and PASH mixture that clearly shows peaks which can be attributed to DBT (184), 2-DBT (198), 4,6-DBT (212), TAN (216), and BNTP (234). The m/z ratio of the radical cation is in parentheses following the acronym of the PASH.

Conclusions

The mass spectrometric results clearly indicate that PASH compounds in the presence of $PdCl_2$ in (50:50) CH_3OH: CH_2Cl_2 give an enhanced response even in the presence of a hydrogenated oil. Further work is now in progress to extend the approach to complicated crude oils.

Acknowledgement. WER would like to thank the Environmental Protection Agency (Grant No.R825503) and the Texas Higher Education Coordinating Board through the Advanced Technology Program (ATP) for support of this project. WER would also like to thank the Institute for Industrial and Environmental Science of Southwest Texas State University and Exxon Mobil for donation of the hydrogenated oil.

References

1. Nishioka, M. *Energy Fuels,* **1988**, *2,* 214-219.
2. Later, D.W.; Lee, M.L.; Bartle, K.D.; Kong, R.C.; Vassilaros, D.L., *Anal. Chem*., **1981**, *53*, 1612-1620.
3. Milenkovic, A.; Schultz, E.; Meille, V.; Loffreda, D.; Forissier, M.; Vrinat, M.; Sautet, P.; Lemaire, M., *Energy Fuels*, **1999**, *13,* 881-887.
4. Wright, B.W.; Peaden, P.A.; Lee, M.L.; Stark, T., *J. Chromatogr*., **1982**, *248,* 17-34.
5. Grang, B.Y., *Anal. Lett.* **1985**, *18,* 193-202.
6. Nishioka, M.; Campbell, R.M.; Lee, M.L.; Castle, R.N., *Fuel* **1986**, *65*, 270 - 273.
7. Rudzinski, W.E.; Sassman, S.; Watkins, L.M., *Prepr.- Am. Chem. Soc. , Div. Petr. Chem.,* **2000**, *45(4)*, 564-566.
8. Rudzinski, W.E.; Zhang, Y.; Luo X., *J. Mass Spec.*, **2003**, in press.
9. Mansfield, C.T.; Barman, B.N.; Thomas, J.V.; Mehrotra, A.K.; McCann, J.M., *Anal. Chem.*, **1999**, *71*, 81R-107R.
10. Barman, B.N., Cebolla, V.L., Membrado, L., *Crit. Rev. Anal. Chem.,* **2000**, *30*, 75-120
11. Rudzinski, W.E., In *Analytical Advances in Hydrocarbon Research*, C. Hsu ed, Kluwer Academic: New York, N.Y., **2003** in press.
12. Van Berkel G.J.; Kertesz, V., *J. Mass Spectrom*., **2001**, 36, 1125-1132.

TRANSFORMING COAL INTO PREMIUM CARBON PRODUCTS: AN OUTLOOK

John M. Andresen[1], Joel L. Morrison[1], Frank Rusinko Jr.[1], John W. Zondlo[2], John Stipanovich[3], John C. Winslow[3] and Harold H. Schobert[1]

[1]The Energy Institute, The Pennsylvania State University, 209 Academic Projects Bldg., University Park, PA 16802
[2] Department of Chemical Engineering, College of Engineering and Mineral Resources, P.O. Box 6102, Morgantown, WV 26506-6102
[3]National Energy Technology Laboratory, U.S. Department of Energy, P. O. Box 10940, Pittsburgh, PA 15236-0940

Introduction

The great abundance of coal in the U.S. carries an inherent potential of introducing benign and affordable premium carbon products to the general public (1). Low cost carbon fibers from coal could ensure lighter vehicles and result in a tremendous rise in energy efficiency for the traffic sector. Large production of inexpensive activated carbon could significantly increase the use of activated carbon in water treatment facilities thus vastly improve water quality throughout US. Further, high quality binder pitches and cokes for anodes in the aluminum industry and electrodes for the steel industry can be derived from coal. An industry driven consortium, Consortium for Premium Carbon Products from Coal, has for the last four years strived for the recognition of coal as a valuable resource for producing premium carbon products and some of its recent advances are discussed.

Carbon fibers from coal

Carbon fibers carry a great potential for providing several markets with a high strength and light-weight alternative material (2). The automobile industry is highly interested in using carbon fibers to replace heavier materials used throughout various vehicles (3). The reduced weight of the vehicles could significantly improve their fuel efficiency. Further, the inherent inertness and stiffness of carbon fibers lends them to be used for construction purposes, such as bridges and reinforcement materials in concrete. Currently, carbon fibers are mainly obtained from polyacrylnitrile (PAN), a chemical commodity, which has kept the cost of carbon fibers high (4). Therefore, carbon fibers have traditionally been used for applications where price is not prohibitive of introducing superior materials, such as for sports gear and space exploration. However, for the automobile industry the high cost has been a limiting factor. Consequently, fibers from heavy petroleum streams and coal tar pitches have been proposed but are still battling with high costs (5).

The introduction of coal-based carbon fibers has been pursued through various projects funded by CPCPC to reduce costs to a very competitive level. Several technological improvements involving removal of mineral matter by solvent extraction, adjustment of the viscosity, optimization of spinning properties and shortening of the stabilization time needed during carbonization have significantly strengthen the possibility of using coal as feedstock for carbon fibers. Preliminary results indicate that coal-derived carbon fibers can be very cost-effective with competitive fiber properties.

Activated carbon from coal and its combustion by-products

With the ever-expanding market for activated carbons (AC) due to their widespread number of environmental applications, manufacturers of AC are constantly seeking for cost effective and abundant feedstocks. Such feedstocks include coal as well as industrial byproducts (6-8). Traditionally coal is the main precursor for activated carbons produced in U.S. However, carbon from combustion byproducts can also be competitive precursors for AC manufacturers, and simultaneously, reduce waste disposal costs for other industries. One industrial by-product of particular interest is fly ashes of high unburned carbon content from coal-fired combustors. In 2000, about 57 million tons of fly ash was generated by the electric utilities in the U.S. Only about 32% was used mainly for applications in the cement and concrete industries as well as structural fills and waste stabilization applications (9, 10). Unburned carbon has so far hindered the use of most of the remaining fly ash. An increasing role of coal as a source of energy in the 21st century will demand environmental and cost-effective strategies for the use of these carbonaceous waste products from coal combustion. There are already various commercial technologies to separate the unburned carbon from the ash (11, 12). These separation techniques can generate ashes with carbon contents below 6% that are suitable for use in the cement industry, as well as concentrate the unburned carbon that could subsequently be used as feedstock for the production of ACs (13).

Extensive research through CPCPC funded activities has shown that activated carbons with specific surface area up to 1270m^2/g could be produced from the unburned carbon where the porosity of the resultant activated carbons can be related to the properties of the unburned carbon feedstock as well as the activation conditions used. However, not all unburned carbon samples are equally suited for activation since their potential as AC precursors could be inferred from their physical and chemical properties. The developed porosity of the activated carbon also appears to be a function of the oxygen content, porosity and H/C ratio of the parent unburned carbon feedstock. It was further established that extended activation times and high activation temperatures increased the porosity of the produced activated carbon at the expense of the solid yield.

Binders and fillers for carbon products from coal

Many items that we take for granted have some relation to carbon, including aluminum based products where anode carbon is used to reduce the aluminum ore, steel from arc-furnaces using graphite electrodes, and even electric contacts on the key-boards (14). However, the carbon we use is increasingly dependent on the availability of petroleum-derived streams or other foreign sources (15). The decrease in domestic produced oil and the subsequent reliance on imported crude oil may have a serious impact on the future of carbon products and related materials in the US, since most carbon products are typically based on petroleum coke (16). Further, petroleum-derived carbon is also marred by increasing hetero-atom, especially sulfur, and heavy-metal content, and a paradigm shift in the petroleum industry of moving away from producing coke by increasing the use of hydro-cracking and hydro-treatment (17).

The demand for coal tar pitch as a binder for carbon materials is expected to increase with around 3% annually in the coming years (18). A strong driving force for this increase is the Chinese pre-baked anode market that is likely to change from a net exporter in 2002 to a net importer in 2003 as well as a tight coal tar market in Europe. Simultaneously, there is a sharp decrease in coal tar production in US due to the continuous decrease in the production of metallurgic coke caused by environmental and economical reasons. It is also likely that these pressures will decrease the coal tar production in regions such as East Europe and Russia that will further put a pressure on the availability of coal tar binder pitch. Already, synthetic pitches are available that are derived from aromatic monomers. One such example is the AR pitch produced

from naphthalene (19). Naphthalene is reacted at fairly low temperatures (<200°C) at the present of HF and BF_3 to form a oligomeric structure by creating -bonds between the naphthenic monomers as well as leading to some degree of condensation. However, this pitch prohibitive expensive to be used as a binder for anodes and electrodes. Another solution has been to mix petroleum pitch with coal tar pitch but has received mixed results.

Several projects funded through CPCPC have targeted the reduction in dependence of petroleum coke as filler for carbon materials and import of coal tar pitch for binder purposes by investigating the production of both materials directly from coal. Several advances have been made where solvent extracted material from coal has functioned as a binder as well as a coke precursor (20, 21) and anthracite derived carbon has produced promising candidates for graphite (22, 23).

Future outlook

Emerging markets for carbon products involve energy storage and nano-technology. A great drive towards storage of environmental friendly fuels, such as hydrogen, is taking place in US. Safe storage of hydrogen is of great concern towards the general public. Carbon materials can satisfy this public demand. A vast amount of carbon would be needed to supply every vehicle on the road with adequate storage capacity for hydrogen. Carbon materials derived from coal could easily supply this in an inexpensive and effective manner. Further, the great potential of nano-technology may not be fully achieved if cost-barriers hinder its introduction into the society. Again using coal as a low-cost and abundant starting material may revolutionize the nano-technology era.

Acknowledgement

The Consortium for Premium Carbon Products from Coal (CPCPC) is supported by the U.S. Department of Energy, National Energy Technology Laboratory under the Cooperative Agreement No. DE-FC26-98FT40350.

References

1. Krevelen, D.W. van. *Coal--typology, physics, chemistry, constitution* Elsevier, New York, 1993.
2. Burchell, T. D *Carbon materials for advanced technologies* Pergamon, New York, 1999
3. Chand, S *J. Materials Science* **2000**, *35*, 1303-1313.
4. Marsh, H., Heinz, E.A. and Rodriguez-Reinoso, F. (Eds.) Introduction to Carbon Technologies, Publicaciones Universidad de Alicante, Spain, 1998.
5. Donnet, J.-B. *Carbon fibers* Marcel Dekker, New York, 1998.
6. Patrick, J. W. *Porosity in carbons : characterization and applications* Halsted Press, New York, 1995
7. Haghseresht, F. and Lu, G.Q. *Energy & Fuels* **1998**, *12*, 1100-1107.
8. You, S.Y.; Park, Y.H. and Park, C.R. *Carbon* **2000**, *38*, 1453-1460.
9. Sloss, L.L. *Trends in the use of coal ash* IEA coal research, CCC/22, 1999.
10. Kalyoncu, R.S. *Coal combustion products* US Geological Survery Mineral Yearbook, 2000
11. Ban, H.; Li, T.X.; Hower, J.C.; Schaefer, J.L. and Stencel, J.M. *Fuel* **1997,** 76(8), 801-805
12. Groppo, J.G.; Robl, T.L.; Lewis, W.M.; McCormick, C.J. *Minerals and Metallurgical Processing* **1999**, *16(3),* 34-36.
13. Zhang, Y.; Lu, Z.; Maroto-Valer, M. M.; Andrésen, J. M.; and Schobert, H. H. *Energy & Fuels*, **2002**, submitted.
14. Delhaes, P. *Graphite and Precursors*, Gordon and Breach Sci. Pub., Amsterdam, 2001
15. Farzin, Y.H. *Resource and Energy Economics* **2001**, *23*, 271-291.
16. Marsh, H. *Introduction to Carbon Science* Butterworth & Co Ltd., London, 1989.
17. Speight, J. G.; and Özüm, B. *Petroleum refining processes* Marcel Dekker, New York, 2002.
18. Gipson, J.D., Great Lakes Carbon Corp. 6th Carbon Conf., Sept. 26-28, 2000, Houston, USA, Ch. 9.
19. Korai, Y.; Yoon, S.H.; Oka, H.; Mochida, I.; Nakamura, T.; Kato, I.; and Sakai, Y. *Carbon* **1998**, 36, 369-375.
20. Yang JL; Stansberry PG; Zondlo JW; and Stiller AH, *Fuel Processing Technology* **2002**, *79*, 207-215.
21. Stansberry, P.G.; and Zondlo, J.W. *Prepr. Am. Chem. Soc. Div. Fuel Chem.* **2001**, *46(3)*, 555-556.
22. Andrésen, J.M.; Zhang, Y.; Burgess, C.E.; and Schobert, H.H. *Fuel Processing Technology* **2002**, submitted.
23. Schobert, H.H.; Andresen, J.M.; Pappano, P.J.; Burgess, C.E.; and Zengel, J.J. Pacifichem 2000, Honolulu, Hawaii, USA, December 14-19, 2000, IORG 6, 555.

CARBON AS CATALYST FOR ORGANIC ELECTRON-TRANSFER REACTIONS

Francelys A.Medina, John W. Larsen and Harold H. Schobert

The Energy Institute, The Pennsylvania State University, University Park PA 16802

Introduction

Carbons catalyze a variety of reactions.[1,2] Because of their low cost and wide variety of reasonably well-defined physicochemical properties and morphologies, carbons are desirable catalytic materials. However, little systematic attention has been given to their use and behavior as catalysts and we have initiated a research program to understand the fundamentals of carbons as catalysts. We address here two carbon catalyzed reactions (Eq. 1 and 2 below) for which there exists some mechanistic information: the reduction of nitrobenzene to aniline by hydrazine[3] and the decomposition of hydrazine.[4] These reactions are thermodynamically highly favorable, but do not readily proceed at a measurable rate in homogeneous solution due to kinetic barriers.[5] The nitrobenzene reduction follows the overall equation,

$$2PhNO_2 + 3N_2H_4 \xrightarrow{C} PhNH_2 + 4H_2O + 3N_2. \qquad (1)$$

The decomposition of hydrazine also yields gas products,

$$N_2H_4 \xrightarrow{C} 4/3\ NH_3 + 1/3\ N_2 \qquad (2)$$

Thus, the kinetics can easily be followed by measuring gas production as a function of time.

Experimental

Carbon Samples. The carbon samples that were examined in this study include carbon blacks (Cabot Corp.), activated carbons (MeadWestvaco Corp.), non-activated charcoals and graphite (Fisher Scientific). They were used as received. The BET surface area was determined by N_2 physisorption at 77 K using a Quantachrome Autosorb 1 analyzer. Elemental analysis of the carbon samples was carried out with a LECO CHN-600 elemental analyzer, a LECO SC-132 sulfur determinator and a LECO MAC-400 proximate analyzer.

Kinetic measurements. All compounds were obtained from Fisher Scientific and were used without purification. Reactions were carried out by adding hydrazine to a refluxing solution of nitrobenzene and carbon in *iso*propanol under a N_2 atmosphere. In the decomposition of hydrazine reaction, nitrobenzene was not added to the reaction mixture. The reactions were followed by measuring gas volumes as a function of time using a gas burette.

Results and Discussion

Typical results for nitrobenzene reduction using different carbons as catalysts are shown in **Figure 1**, plotted as gas volume evolution vs. time. The production of gases upon addition of carbons to otherwise stable solutions of the reactants demonstrates that the carbons tested catalyze the nitrobenzene reduction by hydrazine, although with different activities. For each carbon, the gas evolution plots show simple time dependence. The kinetics are complex as evidenced by deviations from first-order reactions for higher activity carbons and from second-order reactions for lower activity carbons. This is not surprising for a heterogeneous bimolecular reaction

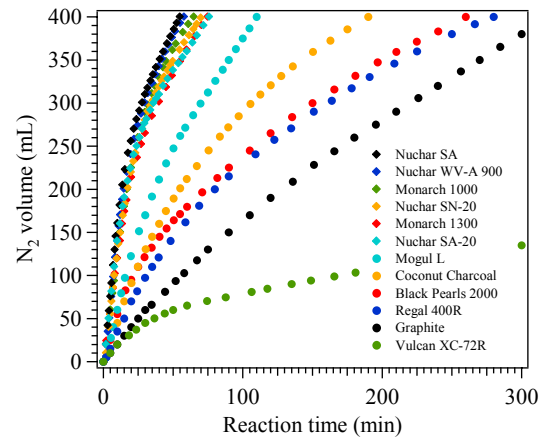

Figure 1. Gas evolution from carbon-catalyzed nitrobenzene reduction in the presence of hydrazine. Legend shows the approximate plot order from top to bottom.

The observed activity (activated carbons > carbon blacks > natural charcoals > graphite), determined by the initial rate, generally parallels the BET surface area of the carbon catalysts as shown in **Figure 2**. In general, the initial rate increases with the surface area of the carbon catalyst. However, there is not a straightforward relationship between the BET surface areas of the carbons in **Figure 2** and the rates of nitrobenzene reduction. This indicates that other factors are important for catalysis on these carbons. The best candidates for these factors are the amount and the type of surface groups. It is well known that different carbons have different surface functionality depending on the nature and the mode of formation of the carbon samples.

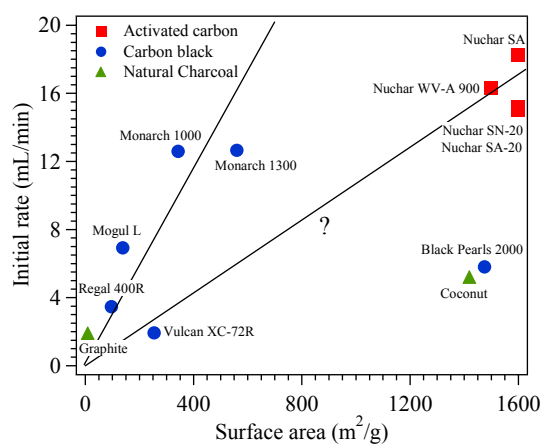

Figure 2. Influence of surface area on the rate of nitrobenzene reduction by hydrazine on various carbons.

The results in **Figure 3** demonstrate that the rate of nitrobenzene reduction increases with increasing total oxygen content of the catalyzing carbon. Because the total oxygen content is plotted, no information is available about the relative importance of different oxygen functional groups. The fact that the reaction rate differs considerably for activated carbons with similar oxygen contents indicates that not all of the oxygen functional groups are equally important to this reaction. Infrared analysis can be used to provide additional information on the types of oxygen functional groups that are present on the carbon samples.

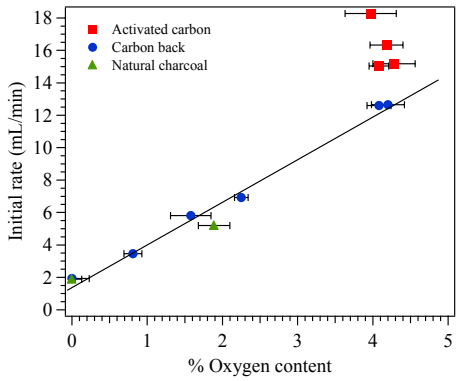

Figure 3. Influence of oxygen content of the rate of nitrobenzene reduction by hydrazine on various carbons. Oxygen concentration was obtained from elemental analysis. Solid line indicates the trend of the data.

As shown in **Figure 4**, the reaction rate initially increases with nitrobenzene concentration and goes through a maximum before falling off at the higher concentrations, in agreement with a Langmuir-Hinshelwood surface-controlled reaction model.[6] According to this model, the rate of nitrobenzene reduction is limited by the degree of adsorption of both nitrobenzene and hydrazine on the carbon catalysts. This observation supports the idea that carbon serves as an adsorbent.[3]

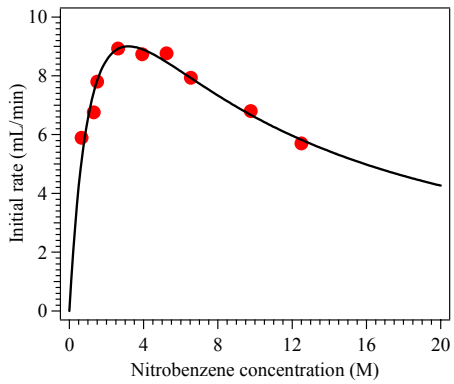

Figure 4. Variation of nitrobenzene reduction rate with nitrobenzene concentration. Black Pearls 2000 was used as catalyst. Solid line indicates the trend of the data

Figure 5 shows the gas volume evolved vs. time for solutions of hydrazine in refluxing *iso*propanol with different carbons added. As in the case of the nitrobenzene reduction, we found that all of the carbons catalyze the reaction to different extents. The reaction rate for the nitrobenzene reduction is directly proportional to the rate of the hydrazine decomposition and faster by a factor of ten or more. When both reactions proceed simultaneously, the contribution to the gases evolved from hydrazine decomposition does not affect significantly the nitrobenzene reduction kinetics. Under the reaction conditions used in this experiment, the decomposition of hydrazine on carbons was found to be a third-order reaction, as shown in **Figure 6**. The mechanism is not known yet, however, the existence of third order kinetics for hydrazine decomposition on carbons is similar to electrochemical results on glassy carbon electrodes showing that three molecules of hydrazine are involved in hydrazine decomposition.[7]

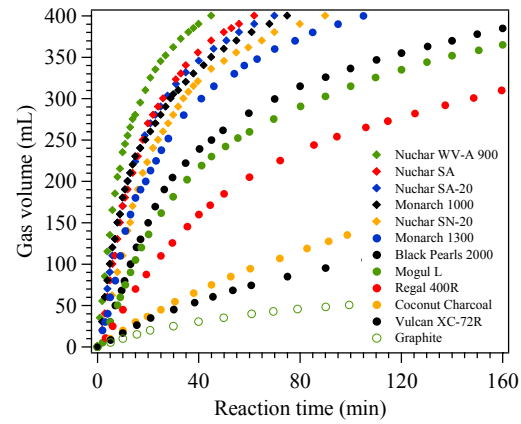

Figure 5. Gas evolution from carbon-catalyzed decomposition of hydrazine. Legend shows the approximate plot order from top to bottom.

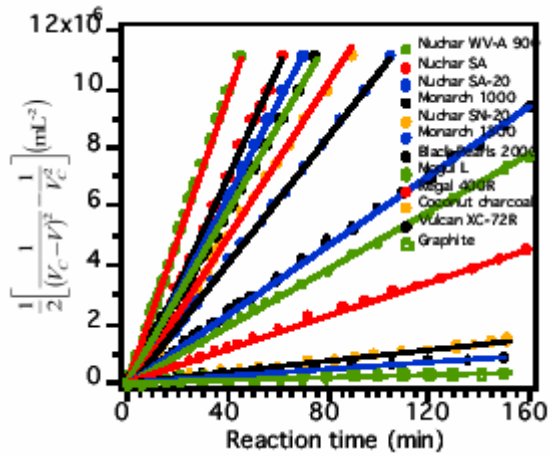

Figure 6. Kinetics of the carbon catalyzed decomposition of hydrazine plotted as a third order reaction (V, gas volume at time t; V_C, calculated final gas volume using the stoichiometric of Eq. 2).

Conclusions

The results obtained in this study demonstrate a correlation between the reaction rate and the physicochemical properties of the carbon catalyst. In particular, the oxygen groups that are present on the carbons surface are believed to participate in the nitrobenzene reduction by hydrazine, and their presence may enhance the reaction rate.

The physical chemistry of carbon materials may indeed make a decisive contribution to their catalytic properties by the determination of the quantitative and qualitative features of active sites. Thus, by changing these parameters in a wide range it is possible to vary the catalytic properties of carbon materials.

References

(1) Spiro, M. *Catal. Today* **1990**, *7*, 167-178.
(2) Radovic, L. R.; Rodriguez-Reinoso, F. In *Chemistry and Physics of Carbon*; Thrower, P. A., Ed., 1997; Vol. 25, pp 243-358.
(3) Larsen, J. W.; Freund, M.; Kim, K. Y.; Sidovar, M.; Stuart, J. L. *Carbon* **2000**, *38*, 655-661.
(4) Larsen, J. W.; Jandzinski, J.; Sidovar, M.; Stuart, J. L. *Carbon* **2001**, *39*, 473-476.
(5) Furst, A.; Berlo, R. C.; Hooton, S. *Chem. Rev.* **1965**, *65*, 51.
(6) Laidler, K. J. *Chemical kinetics*; 3rd ed.; Harper & Row: New York, 1987.
(7) Cao, X.; Wang, B.; Su, Q. *J. Electroanal. Chem.* **1993**, *361*, 211-214.

ACTIVATED CARBONS PRODUCED FROM UNBURNED CARBON IN FLY ASH AND THEIR APPLICATION FOR MERCURY CAPTURE

Yinzhi Zhang[1], Evan J. Granite[2], M. Mercedes Maroto-Valer[1], and Zhong Tang[1]

[1]The Energy Institute and Department of Energy and Geo-Environmental Engineering, The Pennsylvania State Univrstiy, 405 Academic Acativities, University Park, PA 16802
[2]National Energy Technology Laboratory, United States Department of Energy, P.O. Box 10940, Pittsburgh, PA 15236-0940

Introduction

Following the current demand to develop technologies to utilize high carbon content fly ash from coal-fired utility combustors or gasifiers, a one-step activation protocol has been developed by the authors to produce activated carbons from unburned carbon in fly ash[1-3]. Compared to the conventional two-step process that includes a devolatilization of the raw materials, followed by an activation step, unburned carbon only requires a one-step activation process, since it has already gone through a devolatilization process while in the combustor or gasifier. The produced activated carbons with a fine particle size are not only rich in micropores, but they also present a high content of mesopores, which leads to good mass transfer properties during the adsorption process.

Mercury has been identified as a hazardous air pollutant of greatest potential public health concern by the Environmental Protection Agency (EPA), with coal-fired utility boilers being the largest source of anthropogenic mercury emissions[4,5]. Based upon the EPA report, in 1997 it was estimated that 48 tons of mercury were emitted into atmosphere from coal-fired utilities, including 26 tons of elemental mercury and 20.5 tons of oxidized mercury, and where the state of Pennsylvania emitted around 5 tons[6]. The injection of carbon adsorbent upstream of the electrostatic precipitator (ESP) or baghouse particulate collection devices is a promising technology to control mercury emissions from coal-fired combustion systems[7]. A large excess of carbon adsorbent is normally required for injection upstream of the ESP or baghouse in order to obtain a high level of mercury capture. This is because the concentration of mercury in the flue gas is extremely low, (on the order of 1 ppb by volume[8]), as well as the complexity of the flue gas composition and the poor selectivity of the carbon sorbent towards mercury. The typical carbon-to-mercury mass ratios used in recent pilot-scale studies of mercury capture in power plant systems were between 1000:1 to 100,000:1[7,8]. Therefore, the cost of the carbon sorbent plays an important role in the feasibility of the proposed technologies. Based on the low cost of fly ash carbon, its inherent porosity together with its fine particle size, the unburned carbon has been tested as a potential mercury sorbent candidate[8,9]. However, its mercury capacity is lower than that of commercial carbons, probably due to its high ash content and low surface area. Accordingly, the present paper focuses on the activation of the unburned carbon after conventional demineralization process in order to increase the porosity of the unburned carbon. In addition, the prepared activated unburned carbon samples were tested for mercury adsorption using a fixed-bed with a simulated flue gas at 280°F.

Experimental

Six unburned carbon samples, named DA, FA1, PO, SH, WE and CFA were collected from different combustors, including pulverized coal units and cyclone units.

Beneficiation of fly ash carbons. The unburned carbon content of fly ash samples SH were enriched by using conventional froth flotation methods and reagents. A 2.5-liter WEMCO laboratory froth flotation cell and coal froth flotation reagents were used, including several scavenger stages to remove additional carbon from the ash product and various cleaning stages to reduce the ash content in the carbon product. A sink/float test was also conducted with fly ash sample FA1 in order to determine the feasibility of using sink/flotation techniques to separate the unburned carbon from the fly ash. In addition, an acid digestion step was also conducted by following conventional $HCl/HNO_3/HF$ treatment to further reduce the ash content in the carbon concentrate.

Characterization of the samples. The loss–on-ignition (LOI) contents of the fly ash samples were determined according to the ASTM C311 procedure. The porosity of the samples was characterized by conducting N_2 adsorption isotherms at 77K using a Quantachrome adsorption apparatus, Autosorb-1 Model ASIT. The pore volume was calculated from the volume measured in the nitrogen adsorption isotherm at a relative pressure of 0.95 ($V_{0.95}$). The total specific surface area, S_t, was calculated using the multi-point BET equation in the relative pressure range 0.05-0.35, as described previously[10,11].

Production of activated carbon by one-step activation. The activation of the samples was carried out in an activation furnace consisting of a stainless steel tube reactor inside a vertical tube furnace, as previously described[2]. The sample was heated under nitrogen flow to the desired temperature, and then steam was introduced in the reactor, while the reactor was kept under isothermal conditions for 1-3 hours.

Mercury adsorption tests. A detailed description of the assembly and instruments used for testing the mercury capacity of unburned carbon samples and their activated counterpart can be found elsewhere[8]. The system features an elemental mercury permeation tube, a flue gas blending system, an elemental mercury detector (atomic fluorescence spectrophotometer), and digestion of used sorbents by cold vapor atomic absorption spectrophotometry.

Results and Discussion

Cleanability of fly ash carbons. The feedstock used for the froth flotation test was sample SH, which was collected from a cold-side hopper in a pulverized coal combustion unit, and had an initial LOI content of around 44%. As expected, the scavenger tailings had the lowest level of carbon at 23% and a yield of 48%; while the products from the final recleaner stage contained about 75-76% carbon and have a yield of 21%. Therefore, froth flotation can be used for the separation of fly ash into a carbon and an ash stream. The feedstock used for the sink/float test was sample FA1 with an initial LOI of around 59% and the separation results are listed in Table 1.

Table 1. Sink/float separation results for sample FA1.

Sample	LOI, %	Yield, %
1.6 float	84.9	1.8
1.6 sink	64.7	98.2
1.7 float	83.7	1.6
1.7 sink	64.8	98.4
1.8 float	86.5	6.5
1.8 sink	63.3	93.5
1.9 float	86.6	31.3
1.9 sink	53.4	68.7
2.2 float	72.7	86.0
2.2 sink	20.3	14.0
2.5 float	67.2	96.1
2.5 sink	31.2	3.7

The data in Table 1 shows that using a conventional density liquid medium, unburned carbon can be separated from ash at different purity levels. For example, using the medium with density of 2.2 g/ml, an ash stream with the lowest carbon content (20.3%) can be obtained. On the other hand, a carbon stream with a low ash content (around 13-14%) can be obtained by using a wide range of media (density 1.6-1.9 g/ml), where using the 1.9g/ml medium the carbon stream has highest LOI (86.6%) together with the highest yield (31.3%). Chemical digestion was also conducted on fly ash sample FA1 using $HCl/HNO_3/HF$ treatment, and the resultant fly ash carbon stream has an ash content of only ~1%.

Porosity of the fly ash samples. The LOI values and the total surface area and pore volume of the six fly ash carbon calculated from 77K nitrogen isotherm are presented in Table 2. For the purpose of comparison, all the data have been converted into dry ash-free basis. The LOI values range from 46-87wt%. The LOI values reported here are higher than those reported in previous studies that are typically around 15wt%. However, this work focuses on the characterization of high carbon fly ashes for their subsequent use as feedstock for activated carbons, and therefore, samples with high LOI contents were intentionally selected.

Table 2. LOI and porosity of the fly ash samples.

Sample	LOI %	S_t m^2/g	$V_{0.95}$ ml/g	D_{av}, nm
DA	50.0	35	0.032	3.69
WE	32.0	48	0.040	3.35
PO	50.8	51	0.046	3.60
SH	45.8	39	0.036	3.76
FA1	58.9	125	0.077	2.45
CFA	86.6	18	0.019	4.31

The specific surface areas for unburned carbon samples collected from different units range from 18 to 125 m^2/g. The sample FA1, one of the samples from pulverized coal unit, has the highest surface area and pore volume of 125 m^2/g and 0.077 ml/g, respectively. This suggests that the sample FA1 has already generated certain porosity while in the combustor prior to the activation process. On the other hand, the sample from cyclone combustor has the smallest surface area and pore volume of 18 m^2/g and 0.019 ml/g, respectively. This could be due to the higher temperature experienced in the cyclone[13] for CFA compared to the other samples from PC units. Microporosity in carbons is well known to be dependent on the heat treatment temperature and the heating rate experienced by the coal particles in the different furnace[14, 15]. In addition to temperature and heating rate, another factor that could influence the porosity development in the unburned carbons is the mineral composition, which may have a catalytic effect on carbon gasification reactions[16].

One-step activation. Table 3 shows the surface area and pore volume for the activated carbon from the six samples investigated here. As described for the data presented in Table 2, the data have been corrected into dry ash-free basis. The samples were steam activated at 850°C for different periods of time until the burn-off was around 70%, except for CFA, whose burn-off is only around 37% even after 3 hours activation, probably due to its low reactivity.

Compared to the porosity data in Table 2 for the parent unburned carbon, for all the samples the one-step steam activation process has successfully increased the surface area and pore volume. For example, the unburned carbon sample WE has a surface area of only 48 m^2/g, while its activated counterpart has a surface area of approximately 800m^2/g. The activated carbon from sample FA1 has the highest surface area of ~1200 m^2/g, which is comparable to typical commercial activated carbons like F-400 with a surface area of around 1200 m^2/g[11]. Mercury adsorption tests will be conducted and their adsorption capacities will be compared to those obtained for conventional activated carbons.

Table 3. Surface area and pore volume of activated unburned carbons.

Sample	S_t m^2/g	$V_{0.95}$ ml/g	D_{av}, nm
AC-DA	540	0.556	4.05
AC-WE	803	0.647	3.22
AC-PO	499	0.514	4.12
AC-SH	242	0.221	3.64
AC-FA1	1273	0.815	2.56
AC-CFA	157	0.153	3.88

Conclusions

The unburned carbon collected from coal-fired combustors can be separated from the ash by conventional froth/flotation and sink/float methods. By applying acid digestion, a high purity unburned carbon with an ash content less than 1% can be obtained. The one-step activation process can dramatically increase the surface area and pore volume of the carbon. The resulting activated carbons possess surface areas greater than 1200 m^2/g, which is comparable to many commercially available activated carbons.

Acknowledgements

The authors wish to thank the Consortium for Premium Carbon Products from Coal (CPCPC) at The Pennsylvania State University for financial support, and to Dr. Mark Klima (Penn State University) and Dr. Barbara Arnold (Prep Tech) for their help with the cleanability studies.

References

(1) Maroto-Valer, M.M.; Taulbee, D.N. and Hower, J.C. *Energy & Fuel*, **1999**, *13,* 947.
(2) Maroto-Valer, M.M.; Taulbee, D.N. and Schobert, H.H. Prepr. Pap. - *Am. Chem. Soc., Div. Fuel Chem.*, **1999**, *44* (1), 101.
(3) Maroto-Valer, M.M.; Taulbee, D.N. and Schobert, H.H. *Proceedings of the 24th Biennial Conf. On Carbon,* **1999**, *1,* 588
(4) DOE fossil energy – mercury control technologies – fact sheet: http://fossil.energy.gov/coal_poer/existingplants/mercurycontrol_fs.shtml, Sept. 6, **2002**
(5) U.S. EPA mercury web site: general information, http:// www.epa.gov/mercury /information.htm#fact_sheets, May 17, 2002
(6) EPA report: Emission of mercury by state, **1999**.
(7) Activated carbon injection for mercury control in coal-fired boilers, Newsletter of center for air toxic metals, Energy and environmental research center in University of North Dakota, 6(1), May **2000**.
(8) Granite, E.J.; Pennline, H.W. and Hargis, R. A. *Ind. Eng. Chem. Res.* **2000**, *39*, 1020-1029
(9) Hwang, J.; Li, Z. U.S. Patent 6027551, **2000**
(10) Zhang, Y.; Wang, M.; He, F. and Zhang, B. *J. Mater. Sci.* ***1997,*** *32*,6009
(11) Zhang, Y.; Maroto-Valer, M.M.; Tang, Z.; Lu, Z.; Andrésen, J.M. and Schobert, H.H. *Proceedings of 19th annual international Pittsburgh coal conference,* paper 126.pdf, **2002**
(12) Zhang, Y.; Lu, Z.; Maroto-Valer, M.M.; Andrésen, J.M. and Schobert, H.H., Energy & Fuel, in press.
(13) Boram, G.L.and Ragland, K.W. *Combustion Engineering,* WCB McGraw-Hill, **1998**
(14) Marsh, H. and Wynne-Jones, W.F.K. *Carbon,***1964**, *1*, 269
(15) Marcilla, A.; Asensio, M. and Martin-Gullon, I. *Carbon* **1996**, *34,* 449
(16) McEnaney, B. Active sites in relation to gasification of coal chars, *Fundamental issue in control of carbon gasification reactivity,* Edited by Lahaye, J. and Enrburger, P., Kluwer Academic Publishers, **1991**, 175

SIMULTANEOUS HYDRODENITROGENATION AND DEEP HYDRODESULFURIZATION

M. Egorova and R. Prins

Laboratory for Technical Chemistry, Federal Institute of Technology (ETH), Zurich, Switzerland

The hydrodenitrogenation (HDN) of 2-methylpyridine and 2-methylpiperidine and the hydrodesulfurization (HDS) of dibenzothiophene (DBT) and 4,6-dimethyl-dibenzothiophene (4,6-DMDBT) were studied separately and simultaneously over a sulfided $NiMo/Al_2O_3$ catalyst. Reaction conditions were 5 MPa total pressure, 300-340°C, and 35 kPa H_2S to minimize the influence of the H_2S formed during HDS. The first product in the HDN of 2-methylpyridine is 2-methylpiperidine, which reacts by ring opening to 2-aminohexane rather than hexylamine.

The same ring-opening pattern was observed for 2-ethylpiperidine, which demonstrates that the piperidine ring opens on the sterically less hindered side of the molecule and not on the side with the most H atoms. This, and the small number of olefins formed, suggests that elimination does not play an important role in the HDN of piperidine. In accordance with our HDN studies of dihexylamine, we therefore assume that piperidine mainly undergoes HDN by nucleophilic substitution by H_2S, followed by elimination and hydrogenolysis of the resulting alkanethiol.

2-Methylpyridine and 2-methylpiperidine completely blocked the hydrogenation pathway of the HDS of DBT (leading to cyclohexylbenzene) and inhibited the direct desulfurization route (leading to biphenyl). The inhibitory effect of 2-methylpyridine on the direct desulfurization was stronger than that of 2-methylpiperidine.

The main route in the HDS of 4,6-DMDBT was hydrogenation to tetrahydro-4,6-DMDBT followed by desulfurization, whereas in the HDS of DBT the selectivity towards hydrogenation was only 15%. Both the direct desulfurization and the hydrogenation pathway in the HDS of 4,6-DMDBT were strongly inhibited by 2-methylpyridine and 2-methylpiperidine. The hydrogenation to tetrahydro-4,6-DMDBT was slow and further hydrogenation and HDS were blocked.

The only remaining HDS pathway, direct desulfurization to 3,3'-dimethylbiphenyl, was very slow. The inhibitory effect of 2-methylpyridine on the HDS of 4,6-DMDBT was equal to that of 2-methylpiperidine. Thus, the HDS of di-alkyldibenzothiophenes in the presence of nitrogen-containing molecules is extremely difficult.

H_2S promoted the hydrogenation of 2-methylpyridine up to 10 kPa and inhibited it at higher H_2S partial pressures. H_2S, however, had a positive influence on the HDN of 2-methylpiperidine at all pressures. DBT and 4,6-DMDBT had a negative effect on the hydrogenation of 2-methylpyridine but did not influence the C-N bond cleavage in the HDN of 2-methylpiperidine. Therefore, C-N and C-S bond breaking take place at different active sites, whereas the hydrogenation sites for N- and S-containing molecules may be the same.

INFLUENCES OF NITROGEN SPECIES ON THE HYDRODESULFURIZATION REACTIVITY OF A GAS OIL OVER SULFIDE SPENT CATALYSTS.

SRI DJANGKUNG SUMBOGO MURTI, KI-HYOUK CHOI, YOZO KORAI and ISAO MOCHIDA
Institute of Advanced Material Study, Kyushu University, Kasuga, Fukuoka 816-8580, Japan

INTRODUCTION

The recent trend to tighten the regulation very rapidly to 10ppm S in gas oil requires better ways to achieve such a very low level of sulfur content at the least increase of cost. The major task is to hydrodesulfurize effectively and deeply the refractory sulfur species, which have been identified to be 4-methyl (4M), 4,6-dimethyl (4,6-DM), and 4,6,x-trimethyl (4,6,x-TM) dibenzothiophenes (DBTs). Such species are of very low reactivity apparently because of their methyl groups located to the neighbor of sulfur atoms in the center ring. In addition, they suffer marked inhibition by H_2S and NH_3 produced from the reactive sulfur species, nitrogen and aromatic species especially at their very low concentration below 500ppm, which makes further difficult their deep desulfurization. Hence removal of nitrogen species before the HDS is very effective [1].

Catalyst deactivation is an important fact in petroleum industries, from both economic and technological points of view. Coke deposition on the catalyst is generally believed to be the primary cause of catalyst deactivation in hydrotreating petroleum [2]. The loss of catalyst activity makes necessary to terminate the operation to regenerate the catalyst. Sintering during coke oxidation complicates regeneration of the supported catalyst.

In the present study, spent NiMo and CoMo alumina catalysts were evaluated in the hydrodesulfurization (HDS) reactivities of gas oil and its nitrogen species-free oil, in term of gross and molecular based desulfurization behaviors. The effects of nitrogen species removal and roles of the catalysts in the deep HDS of the gas oils and their respective sulfur species were discussed. Additionally, the reactivity of nitrogen species briefly discussed over the spent catalyst in HDS.

EXPERIMENTAL

I. Gas Oil sample and catalysts.

Some representative properties of gas oil and its nitrogen free one are summarized in Table 1. Spent $NiMo/Al_2O_3$ and $CoMo/Al_2O_3$ catalysts were provided in the test runs of a catalyst vendor. The catalyst was presulfided before reaction by H_2S (5vol%)/H_2 flow at 360 ^oC for 2 hours.

Table 1. Composition of original and N-free GOs

	Gas Oil (GO)	N free Gas Oil (NF-GO)
Carbon (wt%)	85.95	86.08
Hydrogen (wt%)	12.30	12.30
Sulfur (wt%)	1.64	1.60
Nitrogen (ppm)	300	0

II. Hydrotreatment

HDS was performed in a 100 ml autoclave-type reactor. Gas oil (10 g) was hydrotreated at 340 ^oC under 50 kg/m^2 H_2 (initial H_2 pressure at room temperature) over 1 g of pre-sulfided catalyst by single and two-stage reaction configurations. The reaction times for the single stage were 30 and 60 min, while the two-stage reaction was consisted of two 30 min reactions. The second stage was operated after refreshing the reaction atmosphere with fresh H_2 at room temperature. The hydrotreated product was analyzed by GC-AED (Atomic Emission Detector, HP5890P, G2350A).

RESULTS AND DISCUSSION

1) Molecular composition of gas oils

Figure 1 illustrates carbon, sulfur and nitrogen chromatograms of feed gas oil (GO). GO consisted basically of paraffinic hydrocarbons as shown by spike peaks. Sulfur species found in GO were alkylbenzothiophenes (BTs), dibenzothiophene (DBT), and alkylated-dibenzothiophenes. Considerable amounts of 4-DBT, 4,6-DMDBT and 4,6,X-TMDBT were found in the oil. Most of the nitrogen species in the oil were non-basic species as carbazole and alkylated carbazoles.

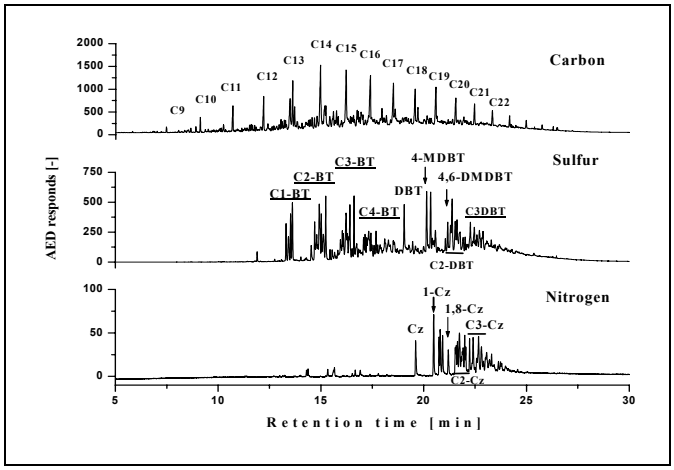

Figure 1. Carbon, sulfur and nitrogen chromatograms of gas oil.

2) HDS of total sulfur

HDS of GO and NF-GO over virgin and spent NiMoS and CoMoS catalysts is showed in Table 2. Relatively reactive sulfur species (benzothiophenes) were easily removed by 30 min HDS, however, refractory sulfur species still remained after 60 min of reaction. HDS activity of spent NiMo and CoMo catalysts decreased compare to the virgin ones. HDS over spent NiMo and CoMo left 1440 and 940ppmS, respectively, which are lower than both the virgin one 900 and 420ppmS, respectively. Nitrogen removal and two-stage reaction enhanced the HDS over spent NiMo and CoMo to 550 and 310ppmS, respectively, less than that of over virgin ones to be 130 and 160ppmS, respectively. It can be noted that nitrogen inhibition over spent catalysts is smaller than that of over virgin ones.

Table 2 HDS activity for total sulfur removal

Catalysts	GO			NF-GO		
	30	60	2st	30	60	2st
NiMo Virgin	2245	901	349	1079	260	129
Spent	5733	1439	1090	5244	958	594
CoMoVirgin	1177	421	333	686	194	161
Spent	3525	943	493	2810	689	310

3) HDS of refractory sulfur species

HDS activity of spent catalysts decreased more against refractory sulfur species (DBTs) as listed in Table 3. These catalysts suffer to much inhibition product gases such H_2S and NH3 especially spent NiMo one. HDS of refractory species in the first 30 min of reaction over spent NiMo and CoMo achieved 2300 (29%) and 1430 (56%) much lower than that over virgin one. Nitrogen removal and two-stage reaction enhanced the HDS over spent NiMo and CoMo catalysts up to 94 and 95% conversion, respectively.

Table 3 HDS activity for refractory sulfur removal

Catalysts	GO			NF-GO		
	30	60	2st	30	60	2st
NiMo Virgin	2116	885	194	605	161	139
Spent	2303	798	692	2150	576	195
CoMo Virgin	691	264	229	384	120	93
Spent	1432	455	270	1284	207	161

Among refractory sulfur species, 46DMDBT and 4E6MDBT were the most refractory ones. 46DMDBT over spent NiMo catalysts exhibited nuch the same reactivity than that over virgin one by single reaction, while that over spent CoMo was certainly lower than that over virgin one. Two stage reaction enhanced HDS over virgin NiMo to be much more active than the spent one. The same trend was observed in the HDS of 4E6MDBT as summarized in Table 4.

Table 4 HDS activity for 46DMDBT and 4E6MDBT removal

	46DMDBT			4E6MDBT		
Catalysts	30	60	2st	30	60	2st
NiMo Virgin	123	77	33	59	39	16
Spent	121	76	71	59	33	32
CoMo Virgin	69	48	45	28	20	20
Spent	113	80	52	49	33	24
NiMo Virgin	63	25	24	29	12	11
Spent	114	58	19	57	28	10
CoMo Virgin	56	28	24	24	13	12
Spent	98	62	41	42	29	19

Nitrogen free oil enhanced the HDS of 46DMDBT over spent NiMo and CoMo, although the extent was smaller.

Carbon deposited on the spent catalysts was detected by RAMAN. The carbonization extent of carbon on the NiMo and CoMo catalysts was indicated by relative intensity of 1580 and 1360 cm^{-1} peaks. NH3 desorption measured by TPD suggested the spent NiMo lost the acidity while spent CoMo maintained acidity.

4) HDN over spent catalysts

HDN conversion of GO over virgin and spent NiMoS, CoMoS catalysts is illustrated in Figure 2. HDN activity of spent NiMo and CoMo catalysts was much decreased compared to that of the virgin ones, although the reactivity of nitrogen species was much the same.

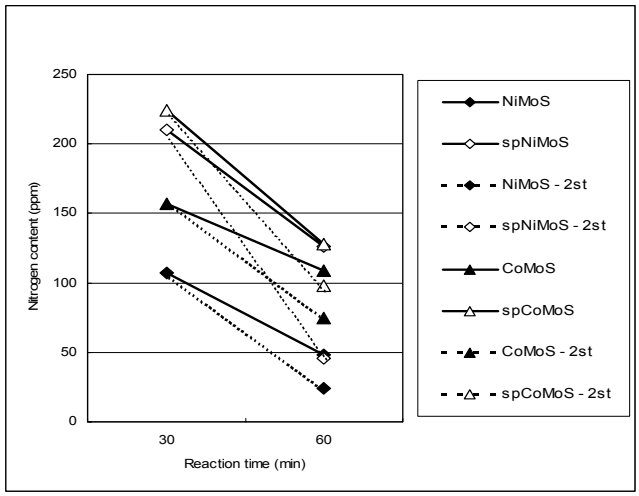

Figure 2. HDN conversion of GO over virgin and spent NiMoS, CoMoS alumina catalysts

Discussion

Spent catalysts lost their activity apparently due to the carbon deposition, which covered the active sites. Such carbon deposition reduced the acidity of NiMo catalyst while activity of CoMo can survive. Such carbon deposition changed the catalyst performances for the HDS against reactive and refractory sulfur species of original and NF oil in single and two-stage reaction.

The activity for refractory sulfur species is reduced more than that for the reactive species. The effect of two-stage and n-removal were markedly reduced over spent NiMo while rather limited over spent CoMo. Loss of activity by carbon deposition may be related with such changes in catalytic selectivity.

References

1. D. D. Whitehurst, T. Isoda, and I. Mochida, *Adv. Catal*. **42** (1998)345.
2. E. Furimsky, F.E. Massoth, *Catal. Today* **17** (1993) 537

MECHANICAL PROPERTIES OF CARBON FOAMS DERIVED FROM SOLVENT EXTRACTED CARBON ORE

Elliot B. Kennel
Chong Chen
Peter G. Stansberry
Alfred H. Stiller
John W. Zondlo

West Virginia University
Department of Chemical Engineering
PO Box 6102
Morgantown WV 26506-6102

Introduction

Coal derived feedstocks are economical precursors for fabricating carbon foam.[1,2] Solvent Extracted Carbon Ore (SECO) is produced by first dissolving coal in a dipolar aprotic solvent such as N-methyl pyrrolidone.[3] Insoluble coal solids including the ash are removed by filtration and centrifugation. When the solvent is removed either by evaporation or some other means, the result is an solid organic material. The foam is produced through a controlled coking process. Foaming occurs in a nitrogen or inert gas pressurized autoclave. Because the solvent extracted coal pitch is based on complex, aromatic hydrocarbons, it is expected to form strong bonds upon carbonization and heat treatment, thus making it especially suitable for carbon foam applications.

Experimental

The baseline protocol is to first grind SECO to a mesh size of -50 to -100. The ground SECO is then placed in a non-reactive container, which may be manufactured from ceramic or aluminum. The diameter of the container is limited by the size of the enclave to about 20 cm. The container is placed in a autoclave pressurized to 3.4 MPa with nitrogen. The temperature is ramped at about 2 ^{o}C/min to a peak temperature of 400 ^{o}C to 500 ^{o}C. Outgassing volatiles result in creation of porous foam. The foam is rigidized as the outgassing proceeds. Subsequently, the samples are calcined at 1100 ^{o}C to 1200 ^{o}C at ambient pressure.

Optionally, SECO can be blended with a reinforcement material, which may include, for example, carbon nanofibers, conventional carbon or other fibers.

The samples are recovered and then calcined at 1000 ^{o}C to 1200 ^{o}C in ambient pressure nitrogen or inert gas. This completes the devolatilization as well as cross-linking processes, resulting in improved mechanical properties.

A higher density foam can be created by interrupting the devolatilization process and returning the sample to ambient conditions. The partially foamed SECO is then re-compacted and re-heated. This results in a higher density material with better mechanical properties.

Nanofiber reinforcement was added using carbon nanofibers supplied by Applied Sciences Inc.[4] Nanofibers are carbon filaments with diameters ranging from 50-200 nm and lengths about 100 microns. Sample 8 was wet mixed by incorporating SECO in NMP solvent. All other samples were dry mixed.

Since carbon is exceptionally strong, a network of microspherical carbon structures might also be expected to demonstrate robust mechanical properties.

Results and Discussion

Compression tests were conducted with the use of an Instron device in accordance with ASTM standards, and the results of these tests are shown in Table I. The results indicate that nanofibers act to reinforce carbon foam. However, since the density of the samples also increased as a consequence of nanofiber addition, it is possible that the property improvements were due to increased density rather than contributions from the nanofibers. However, the wet-processed foam (Sample 8) produced superior strength than the dry-processed counterpart (Sample 4). Thus it can be confidently asserted that wet-processed nanofibers, at least, produce enhanced strength in carbon foam over and above any density effects.

Table I. Summary of Compression Results.

Sample Number	Fiber Content	Density, g/cc	Modulus, MPa	Strength, MPa
				MPa
1	0.00	0.491	361	19.8
2	0.697	0.499	481	23.8
3	1.327	0.497	487	23.5
4	2.599	0.509	321	21.8
5	3.862	0.523	501	26.4
6	6.212	0.551	426	25.4
7	7.406	0.577	487	23.2
8	3.829	0.507	448	34.7

Crush Resistance. During compression testing, the sample continues to resist compression after the initial rupture strength S of the sample is reached, though with a lower resistance. The total energy required to crush the sample is taken as the area under the curve, that is,

$$E = \int SALd\varepsilon \quad ,$$

where A is the unit normal area, L is the original thickness of the sample, and ε is the normalized strain. Assuming that the rupture strength is invariant with respect to strain, the rupture energy is simply

$$E = SAL\varepsilon \quad ,$$

the crush energy per unit volume is

$$E_V \equiv \frac{dE}{dV} = S\varepsilon \quad ,$$

and the crush strength per unit mass is

$$E_m \equiv \frac{dE}{\rho dV} = \frac{S\varepsilon}{\rho} \quad .$$

Here ρ is the apparent density.

Assuming a foam with apparent density of 500 kg/m^3, and compressive strength of 3.5 x 10^7 Pa and maximum achievable compressive strain of 0.7, the approximate specific crush energy is 50 kJ/kg. The actual specific crush energy will likely depend upon the energy delivery rate, as well as geometry.

Conclusions

Carbon foams can be created using coal derived feedstocks. Nanofiber reinforcement can be of value in increasing the compressive strength and probably the compressive modulus. Wet mixing of the nanofibers appears to have been more effective than dry mixing. However, the related effect of density increase due to nanofiber addition may also have contributed to the observed improvement in strength.

Acknowledgement. This work was sponsored by the Department of Energy, Contract DE-FC26-01NT41359. Also cited were data from the Office of Naval Research, No.N00014-97-C-0374. Applied Sciences Inc., Cedarville OH, was the source of the nanomaterials for these experiments.

References

(1) Stiller, A. H.; Stansberry; P. G.; and Zondlo; J. W.; US Patent 6,346,226, February 12, 2002.
(2) Stiller, A. H.; Stansberry; P. G.; and Zondlo; J. W.; US Patent 6,183,854, February 6, 2001.
(3) Zondlo, J. W.; Stansberry; P. G.; and Stiller, A. H.; US Patent 5,955,375, September 21, 1999.
(4) Alig R. L.; Kennel, E. B.; Stiller, A. H.; and Zondlo, J. W., Office of Naval Research Contract No.N00014-97-C-0374 Final Report.

COAL AND PETROLEUM BLENDS AS FEEDSTOCK IN THE DELAYED COKING PROCESS TO OBTAIN HIGH VALUE CARBONACEOUS MATERIALS

María M. Escallón, Gareth D. Mitchell, Harold H. Schobert and Mark W. Badger

The Energy Institute, The Pennsylvania State University, University Park, PA 16802

KEYWORDS: Co-coking, delayed coking, mesophase.

Introduction

The delayed coking process has been widely used for the conversion of heavy distillates into lighter ones. Besides obtaining lighter distillates, this process can produce needle coke, a high-value carbonaceous material.

The addition of coal to the decant oil provides more aromatic units to the system; coal components bring both more stability to the distillates [1], and provide to the end coke a better-organized structure. Therefore, the feedstock is converted into a coke via a mechanism involving the formation of mesophase [2].

It is known that the mesophase development plays an important role on the quality of the end-coke. With increasing temperature and, to certain extent, with time at a fixed temperature, the mesophase spheres grow larger [3], leading to the formation of coalesced mosaics with different orientations. This generates more mesophase that leads to anisotropy. The anisotropy is measured by optical microscopy and is the most important parameter to determine the end-use of the coke; the higher anisotropy, the higher is the potential value of the coke.

This work shows the different properties of the coke formed in the delayed coking process at constant temperature and decant oil/coal ratio to determine the best reaction time to obtain a high-value carbonaceous product.

Experimental

The experimental procedure has been previously described [1]. The reactor has three sections, bomb, transfer pipe and catchpot. Approximately 20 g of the mixture decant oil / coal (2:1) was added to the bomb of the reactor. A blank with 20g of pure decant oil was run at six hours to compare the coke obtained with those of co-coking.

The reactor was assembled, purged with N_2 and heated in a sand bath at a constant temperature of 465°C. Reaction times were varied from 2 to 12 hours. At the completion of each timed reaction sequence, the system was cooled at room temperature. The three sections were disconnected. Solids were collected for further evaluation.

The solid product remaining in the bomb was subjected to soxhlet extraction with THF and dried for 1 hour at 100°C in an oven. The characterization of the coke was carried out using a Zeiss Universal Microscope; proximate analyzer, LECO MAC-400; CHN elemental analyzer and total sulfur in a LECO SC-132.

Samples:

Decant oil: Obtained from Seadrift Coke in Texas. This feed is used for making the premium needle coke.

Coal: A number of compatible coals with regard to thermoplastic properties, ash and sulfur values were evaluated in past investigations [1, 4]; it has led to the selection of the Powellton Coal. This coal as was received, was previously cleaned by mechanical processing; this coal is called hereafter as "whole clean Powellton". Another sample of the Powellton coal was obtained from the froth flotation cells at the cleaning plant and subjected to further flotation procedures to reduce the ash yield and sulfur content and maximize the concentration of those components of coal that possess thermoplastic properties. After the cleaning of the "whole Powellton", the sample was stored suspended in water [4]. Sub-samples were removed as slurry and dried at room temperature under a fume hood over a period of four days. Then, it was homogenized and packaged under argon atmosphere. This coal is named hereafter "re-cleaned Powellton froth". Tables 1 and 2 compare some of the properties of the whole clean Powellton coal and the sample taken as slurry, dried and homogenized (re-cleaned Powellton froth).

Table 1. Comparison of Powellton Seam Product with Re-cleaned froth. Proximate and Ultimate Analysis

	Proximate Analysis %			Ultimate Analysis, %			
Analytical Procedure	Fixed carbon	Volatile Matter	Ash	Carbon	Hydrogen	Nitrogen	Total Sulfur
Coal A	65.1	29.9	5.0	87.6	5.8	1.6	0.9
Coal B	68.7	29.4	1.9	86.3	5.2	1.5	0.9

Table 2. Comparison of Powellton Seam Product with Re-cleaned froth. Plasticity and Maceral Content.

	Gieseler Plastometer		Organic Petrography, vol.%		
Analytical Procedure	T. at maximum fluidity (°C)	ddpm	Vitrinite	Liptinite	Inertinite
Coal A	448	30,000	68.0	8.6	23.4
Coal B	448	23,619	88.1	2.0	9.9

A: Whole clean Powellton
B: Re-cleaned Powellton Froth

It is important to notice from the tables that the whole clean Powellton showed a higher fluidity compared to the Re-cleaned Powellton, even though both samples are derived from the same coal and cleaning facility. The lower fluidity can be attributed to the finer particle size of the Re-cleaned Powellton Froth as well as to oxidation during storage.

Results and Discussion

Volatile Matter. This is a good parameter to compare the product coke quality, especially for metallurgical coke. As reaction time increased, volatile matter decreased (figure 1). The volatile matter of the coke derived from the decant oil (100%) at a reaction time of 6 hours has the higher volatile matter of the entire samples tested (56% volatile matter).

THF Solubles. The soxhlet-extracted cokes have been analyzed by microscopy and ultimate/proximate. It is noteworthy that the amount of THF solubles in the coke is reduced as reaction time is increased. This indicates that at higher reaction times, coal is giving more volatile compounds to the liquids, making of the solid at

higher reaction times a better coke, visibly darker and more difficult to be broken.

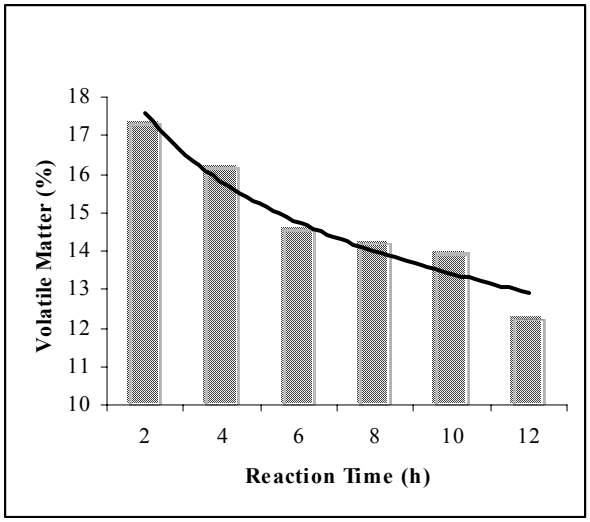

Figure 1. Volatile Matter vs. Reaction Time. Decant oil/coal 2:1 ratio.

Comparison Whole clean Powellton with Re-cleaned Powellton Froth. Both samples expose the same behavior for volatile matter and liquid and solid yields but microscopically, whole clean powellton shows a better interaction with the decant oil.

Acknowledgement. The authors are pleased to acknowledge the financial support for this work provided by the Air Force Office of Scientific Research. We thank Seadrift Coke for the sample of decant oil used in this work. We also thank Dr. Barbara J. Arnold, PrepTech, Inc., for technical advice and the froth flotation separation.

References

(1) Fickinger A. M.S. Thesis, the Pennsylvania State University, **2000**.
(2) Martinez-Escandell M., et. al., *Carbon*, **1999**, 37, 1567-1582
(3) Chemistry and Physics of Carbon; P L. Walker Jr. Ed. Marcel Dekker, Inc, N.Y., 1968, vol. 4. "The formation of some graphitizing carbons" by Brooks JD and Taylor GH. **1968**. 243-286.
(4) Badger, M., Mitchell G., Final Report **2001** – Co-coking of Coal/Decant Oil Blends. The Pennsylvania State University – The Energy Institute.

THE MUTIPLE SITE MODEL FOR FLUE GAS–MERCURY INTERACTIONS ON ACTIVATED CARBONS: THE BASIC SITE

Edwin S. Olson, Jason D. Laumb, Steven A. Benson, Grant E. Dunham, Ramesh K. Sharma, Stanley J. Miller, and John H. Pavlish

Energy & Environmental Research Center
University of North Dakota
Box 9018
Grand Forks, ND 58202

Introduction

The control of mercury emissions in flue gas from coal-burning utilities continues to be an important issue. Powdered activated carbons (ACs) prepared from coal precursors are effective sorbents under these flue gas conditions, but further advances in understanding the chemisorption mechanisms are needed to better design carbons with faster kinetics and greater capacities. The commercial powdered carbon Norit FGD sorbent has been thoroughly investigated at the Energy & Environmental Research Center (EERC) as a sorbent for elemental mercury (Hg^0) in flue gas streams (1, 2). Extensive factorial evaluations of powdered sorbents were conducted in a bench-scale system consisting of a thin fixed-bed reactor in gas streams containing 15 $\mu g/m^3$ of Hg^0 in various simulated flue gas compositions consisting of acidic SO_2, NO_2, and HCl gases plus a base mixture of N_2, O_2, NO, CO_2, and H_2O (1). In an atmosphere containing HCl or NO_2, the Norit FGD, which is a Texas lignite-derived AC, was effective for capture of Hg^0 from the gas phase at temperatures of 100° to 150°C. Without either HCl or NO_2 in the gas stream, the carbon sorbents are ineffective, and immediate breakthrough occurred.

In tests conducted with the FGD sorbent in the simulated flue gas containing NO_2 but not SO_2, very little breakthrough was observed over an extended time period, indicating that the bound mercury form is quite stable. The capture is attributed to oxidation of the Hg^0 and concomitant reduction of NO_2 with formation of a low-volatile oxidized mercury species that remains bonded to the sorbent (3). Reactions of Hg^0 with NO and NO_2 in a glass container were previously reported to form mercuric oxide and mercuric nitrate–nitrite mixtures (4). When SO_2 was added to the gas mixture containing the NO_2, the mercury sorption rate was initially high (98% of inlet Hg^0 was sorbed); however, breakthrough occurred at times inversely proportional to the concentration of SO_2; that is, the higher the concentration of SO_2 is, the shorter the breakthrough time. With typical flue gas SO_2 concentrations (1500 ppm), the breakthrough occurs after 1 hour at the 107°C conditions. The breakthrough curve was relatively steep, increasing to 100% or greater emission after about 2 hours. Thus, not only is mercury no longer sorbed, but mercury sorbed earlier in the experiment is released. Similar interactions were observed for ACs produced from Fort Union lignites under certain similar conditions (5). These breakthrough capacity results are consistent with the hypothesis that SO_2 poisons the binding site for Hg(II) on the sorbent surface.

The Dual-Site Model for Mercury–Flue Gas Interactions with FGD Sorbent

An important fact leading to the development of a model for the interactions occurring on the carbon surface is that the mercury that is emitted from the sorbent after breakthrough is entirely an oxidized mercury species. This was noted when the converter on the continuous emission monitor was taken off after breakthrough and the Hg signal dropped from 100+% emission to close to 0%. Furthermore, in reactions conducted with NO_2 and SO_2 and no HCl, this emitted volatile oxidized mercury product was actually trapped and identified as mercuric nitrate (6, 7).

We, therefore, postulated that the carbon sorbents have two or more independent reaction sites comprising at least an oxidation site and a binding site for the oxidized Hg (8). By definition, the oxidation site is an electron-accepting Lewis acid site, and the Hg (II) binding site is an electron-donating basic site. Poisoning of the binding site by acid components from the flue gas at breakthrough does not affect the functioning of the oxidation site. Thus the mechanistic multiple site model shown in Figure 1 is proposed (5). It should be noted that there could be additional separate sites for NO_2 reduction, SO_2 oxidation, and oxygen reduction (the latter two are omitted from the diagram for simplicity).

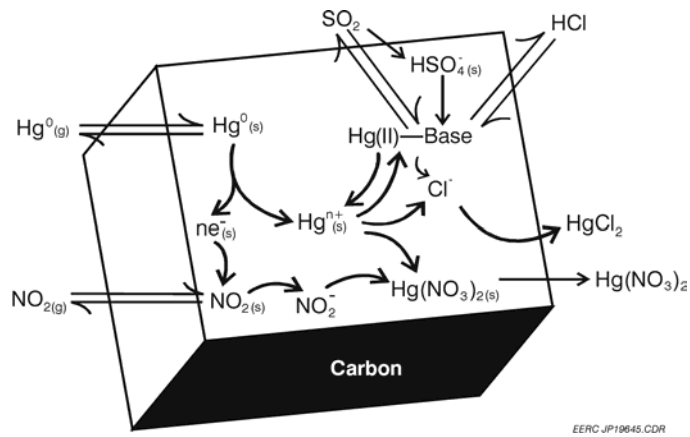

Figure 1. Mechanism for mercury capture on FGD sorbent.

The location, structure, and mechanistic functioning of the oxidation and binding sites are of great importance in understanding the mercury–flue gas interactions. Of interest is the question of whether the extensive mineral matter (35%) of the FGD sorbent contributed to the Hg binding. Recent EERC data show that sequential removal of the inorganic matter from the FGD sorbent did not significantly affect the breakthrough behavior (8); thus the basic groups, such as calcium oxide present in the FGD sorbent, played no role in the mercury–flue gas interactions that determine the breakthrough capacity. Thus the binding site was postulated to be a Lewis basic site residing on the carbon surface. The nature of this binding site is the subject of this paper.

Summary of X-Ray Photoelectron Spectroscopy Analysis of Flue Gas-Exposed Sorbents

Further insights into the mechanisms of the mercury–flue gas–sorbent interactions were derived from the x-ray photoelectron spectroscopy (XPS) data obtained from two AC sorbents, Norit FGD and the EERC lignite-derived AC, exposed to various simulated flue gas compositions containing Hg^0 with various levels of SO_2, NO_2, HCl, and H_2O for time periods before and after breakthrough of mercury (9). Because of the interference caused by silicon, XPS data could not be obtained for the mercury species present in the exposed sorbents. However, information on the forms of sulfur and chlorine was especially important in understanding the interactions. The conclusions from the detailed, high-resolution XPS scan spectroscopic study are summarized here.

The XPS analysis indicated that sulfur(VI) (sulfate or bisulfate) is the major sulfur species on all the sorbent samples exposed to flue gas compositions. The longer the exposure to SO_2, the more sulfate is found in the sample. When NO_2 was omitted from the flue gas, less sulfate was accumulated. A decrease in sulfate was also observed

when H_2O was omitted from the gas composition. The presence or absence of HCl had no effect on the sulfate formed. Based on these analyses, several adsorption as well as chemisorption events must occur during the exposure of carbon sorbents to flue gas components. The adsorbed SO_2 is clearly oxidized on the sorbent surface, resulting in bound bisulfate. The continued accumulation observed for sulfate or bisulfate should occur at basic sites, including basic sites on carbon that are responsible for binding the Lewis acid Hg(II). This is consistent with the large sensitivity of Hg breakthrough observed for SO_2 concentrations. Physical pore blockage by sulfate cannot explain the poisoning, because that would also block the oxidation sites. The oxidation of SO_2 is influenced strongly by the availability of NO_2, a good oxidizing agent. Although O_2 may also serve as the electron sink, the reaction in the absence of NO_2 gives much less sulfate. These data also indicate that the SO_2 oxidation reaction involves water.

The XPS data showed that chlorine is present as both chloride ion and covalent (organic) chlorine. If mercuric chloride were present on the surface, the very small amount could not be seen owing to the interference of these forms. More chlorine was present on the exposed sorbent when no SO_2 was used in the gas composition. Importantly, the chlorine forms disappear from the carbon surface when breakthrough occurs. Thus the HCl in the flue gas can donate a hydrogen ion to a basic site, as well as add both hydrogen and chlorine to a basic site to form the organochlorine product. This addition is well-known in olefin chemistry where alkyl halides are formed. The accumulation of chlorine in the absence of SO_2 as well as the disappearance of chlorine after continued exposure in SO_2 is explained by competition of HCl with bisulfate. As more bisulfate is generated from SO_2 at the carbon surface, it displaces the HCl, owing to the high volatility of HCl.

Model for the Lewis Basic Binding Site for Hg(II)

A refinement of the Lewis acid basic binding site model is now proposed that offers more detail on the nature of the carbon site and its interaction with flue gases and Hg. This model uses the concept of zig-zag carbene structures recently proposed for electronic states at the edges of the carbon graphene layers (10). An alternative, plausible mechanism can be proposed for the armchair sites, but is not presented here.

In the carbene model, the zig-zag carbon atom positioned between aromatic rings is assumed to be the Lewis base site. Aliphatic and haloaliphatic carbenes are always highly electrophilic as exhibited by rapid addition reactions to alkenes and sigma bonds. In contrast, heteroatom and aromatic substituted carbenes are in fact nucleophilic, exhibiting no reactivity to alkenes or reactivity to alkenes with electron-withdrawing groups, respectively.

The interactions that appear to be adequate for explaining the behavior of the FGD sorbent are summarized in more detail in the scheme shown in Figure 2. Thus, in the proposed model for the basic site, the zig-zag Lewis basic carbene reacts with the oxidized Hg species (postulated as a mobile "spill-over" species like mobile hydrogen). But the basic carbene also reacts with HCl, H_2SO_4, and SO_2 to form the bound chlorine, sulfate, and sulfinate as demanded in the XPS results. The reaction is thus a reversible addition of hydrogen ion from the acid to the carbene to form carbenium ion intermediates, which subsequently bond to the anion. Flue gas interactions occurring at the Lewis acid oxidation site on the carbon are currently under investigation.

Acknowledgments

Support is gratefully acknowledged from the EERC Center for Air Toxic Metals[K] Industrial Affiliates Program.

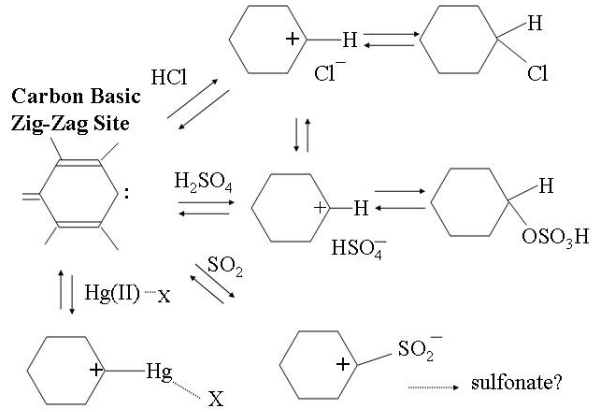

Figure 2. Basic site model.

References

(1) Miller, S.J.; Dunham, G.E.; Olson, E.S.; Brown, T.D. Flue Gas Effects on a Carbon-Based Mercury Sorbent. In *Air Quality: Mercury, Trace Elements, and Particulate Matter*, Special Issue of *Fuel Process. Technol.* **2000**, *65–66*, 343–363.
(2) Miller, S.J.; Dunham, G.E.; Olson, E.S.; Miller, S.J. Impact of Flue Gas Constituents on Carbon Sorbents. In *Proceedings of the Air Quality II: Mercury, Trace Elements, and Particulate Matter Conference*; McLean, VA, Sept 19–21, 2000; Paper A4-3.
(3) Olson, E.S.; Miller, S.J.; Sharma, R.K.; Dunham, G.E.; Benson, S.A. *J. Hazard. Mater.* **2000**, *74*, 61–79.
(4) Freeman, E.S.; Gordon, S. *J. Amer. Chem. Soc*. **1956**, *78*, 1813.
(5) Olson, E.S.; Sharma, R.K.; Eylands, K.E.; Stepan, D.J. Fuel Chem. Div. Prepr. 2002, 47(2), 472.
(6) Olson, E.S.; Sharma, R.K.; Miller, S.J. Dunham, G.E. Mercury in the Environment. In *Proceedings of a Specialty Conference*; VIP-91, Air & Waste Manag. Assoc., Minneapolis, MN, Sept 15, 1999; p 121.
(7) Olson, E.S.; Thompson, J.S. Cryogenic and Solvent Trapping of Oxidized Mercury Species in Flue Gas. In *Proceedings of the EPA–DOE–EPRI Combined Power Plant Air Pollutant Control Symposium: "The Mega" Symposium*; Chicago, IL, Aug 21–23, 2001; Session 16, No. 212.
(8) Olson, E.S.; Dunham, G.E.; Sharma, R.K.; Miller, S.J. *Prepr. Pap.—Am. Chem. Soc., Div. Fuel Chem.* **2000**, *45* (4), 886.
(9) Laumb, J.D.; Benson, S.A.; Olson, E.S.; Dunham, G.E. Characterization of Coal-Derived Mercury Sorbents. Presented at the 26th International Clearwater, FL, March 5–8, 2001.
(10) Radovic, L.R.; Bockrath, B. *Fuel Chem. Div. Prepr.* **2002**, *47* (2), 428.

Hydrodesulfurization of DBT over a NiMo catalyst: Inhibition by sulfur and aromatic compounds

Edd A. Blekkan[1], Anastasia Virnovskaia[1], Håkon Bergem[2], Petr Steiner[1]

1. Department of Chemical Engineering, The Norwegian University of Science and Technology (NTNU), N-7491 Trondheim, Norway
2. SINTEF Applied Chemistry, N-7465 Trondheim, Norway

Introduction

The key to achieving deep hydrodesulfurization (HDS) is the removal of complex sulfur molecules like dibenzothiophene (DBT) and the alkyl-substituted analogues of DBT, compounds that have a very low reactivity in catalytic HDS. In this paper we describe experimental work aimed at understanding the influence of sulfur and aromatic compounds in the oil on the activity of a Ni-Mo catalyst. DBT was used as a model compound for the HDS reaction.

Experimental

The experimental work was done in a fixed-bed microreactor using a model feed consisting of DBT in a hydrocarbon solvent (n-heptane). The feed was spiked with sulfur as dimethyldisulfide (DMDS) or thiophene or with aromatics (toluene or naphtalene) in varying concentrations. The hydrodesulfurisation of DBT was investigated, especially with respect to the products of the desulfurization. The catalyst used was a commercial Ni-Mo sample, which was crushed and sieved to 75-125 µm and presulfided according to the instructions from the manufacturer prior to the experiments.

Results and Discussion

After an initial period of stabilization in DBT/n-heptane, the catalytic activity for HDS of DBT was investigated as a function of the composition of the solvent. Fig. 1 shows the conversion of DBT as a function of the sulfur concentration in the feed. Added sulfur

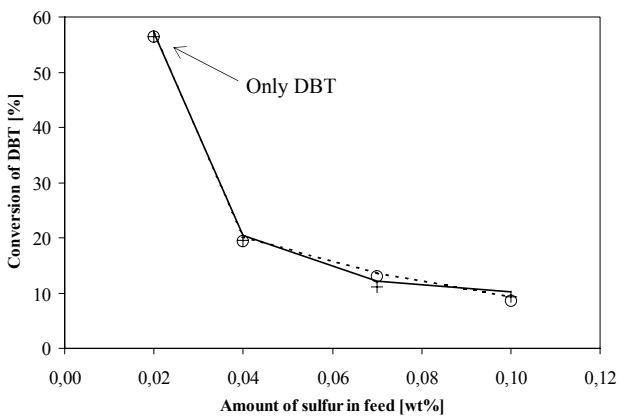

Figure 1. Effect of total sulfur concentration on catalytic conversion of DBT. Conditions: 2 MPa, 200 °C, LHSV=21.4 hr^{-1}, 0.1 wt% DBT in n-heptane. Extra sulfur added as DMDS (solid line) or thiophene (dashed line)

clearly inhibits the HDS, and there is no difference between the sulfur compounds added. This probably indicates that both compounds are rapidly converted to H_2S, and that the inhibition in this case is due to a competitive effect of H_2S. The order with respect to sulfur was determined, and found to be –0.6, a value that corresponds well with widely used LHHW-type rate expressions for HDS of DBT, where the H_2S-concentration appears in the denominator of the expression.

Fig. 2 shows the effect of added aromatics in the feed, keeping

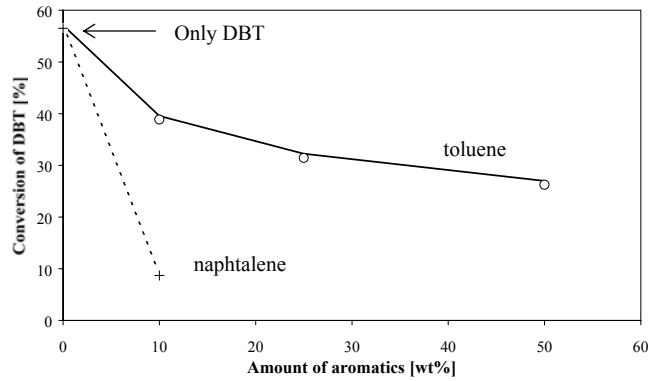

Figure 2. Effect of added aromatics on the catalytic conversion of DBT. Conditions: 2 MPa, 200 °C, LHSV=21,4 hr^{-1}, 0,1 wt% DBT in n-heptane or n-heptane/aromatic solvent.

DBT concentration constant. The order with respect to toluene was estimated to be approximately –0.2, again a value that can be rationalized in terms of a classical LHHW rate-equation with the aromatic compound as an inhibitor in the denominator. A stronger inhibition by naphtalene was observed, but further experiments were not performed due to a strong, irreversible deactivation, probably due to coking. The same effect, though even more pronounced, was observed for 1-methyl-naphtalene.

The products of the DBT reaction were identified to be cyclohexylbenzene (CHB), biphenyl (BP) and partially hydrogenated DBT (TetrahydroDBT, THDBT and hexahydroDBT, HHDBT). All these products were observed in all experiments, but their concentrations varied according to conversion and the use of the added components. These products are usually ascribed to a direct desulfurization of DBT, giving BP as the product, or a route involving hydrogenation of the aromatic ring to THDBT/HHDBT as intermediates followed by desulfurization to CHB. BP can also be hydrogenated to CHB, but this is reported to be a slow process (1). The final hydrogenation product, bicyclohexyl (BCH) was not observed here.

BP was the main product in all cases, indicating that the direct desulfurization route is the most important also over NiMo, as has been concluded earlier for CoMo catalysts (1). In general, the ratio between CHB and BP increased with increasing DBT conversion. However, the influence of the inhibitors on the overall activity was different. Even though the effect of DMDS and thiophene on the overall DBT conversion was similar there were subtle differences in the selectivities. Small amounts of thiophene seemed to favour the direct desulfurization, seen as an increased selectivity to BP. With DMDS as the source of the added sulfur the opposite effect was observed, at least at low conversions. Addition of toluene led to a higher selectivity to BP at the expense of CHB, apparently inhibiting the hydrogenation stronger than the hydrogenolysis sites on the catalyst.

(1) H. Topsøe, B.S. Clausen, F.E. Massoth, Hydrotreating Catalysis, Springer-Verlag, Berlin Heidelberg, 1996, and references cited therein.

HYDRODESULFURIZATION OF LIGHT CYCLE OIL

*Ki-Hyouk Choi, Yosuke Kinoshita, Yozo Korai, and Isao Mochida**

Institute of Advanced Material Study, Kyushu University
Kasuga-Koen, Kasuga, Fukuoka 816-8580 JAPAN
*e-mail : mochida@cm.kyushu-u.ac.jp

INTRODUCTION

Light cycle oil from fluid catalytic cracker(FCC) is one of the main streams for diesel oil pool. About one-third of the total diesel product was reported to be from cracked feedstocks in America[1]. As the regulations on the sulfur content of diesel fuel become stricter, hydrotreating of LCO to meet forecasted specifications has been urgent issue in refinery industry. It has been well-known that hydrodesulfurization of LCO is much more difficult than that of straight run gas oil due to its large content of aromatic components[2]. Nitrogen species is also strong inhibitor for HDS reaction. Fundamental properties of LCO strongly depend on the feed and operating conditions of FCC.

In this study, LCO having different aromatic contents, distillation ranges and nitrogen contents were hydrodesulfurized by using sulfide catalysts supported on alumina and silica-alumina-zeolite as an effort to find a better way to hydrodesulfurize LCO to meet the future regulations on sulfur content of diesel fuel.

EXPERIMENTS

ALCO, BLCO and CLCO were provided from refiners. Their basic properties were summarized in Table 1. Hydrodesulfurization experiments were conducted by using autoclave-type reactor(100 ml internal volume) at 340 ^{o}C and 360 ^{o}C. Initial hydrogen pressure was adjusted to 50 kg/cm^2. The catalysts, which were obtained from commercial catalyst vendors, were CoMo and NiMo supported on alumina(-A) and silica-alumina-zeolite(-SAZ). Pre-sulfidation was performed at 360 ^{o}C for 2 hours under 5% H_2S/H_2 stream

Reaction products were analyzed by GC-AED(HP5890P and G2350A).

Table 1. Basic Properties of LCO.

Property	ALCO	BLCO	CLCO
Total Sulfur Content	9,070 ppmS	9,156 ppmS	8,928 ppmS
Total Nitrogen Content	230 ppmN	1,322 ppmN	825 ppmN
Non-aromatics*1	22.2 wt%	12.6 wt%	13.1 wt%
Aromatics*1	77.8 wt%	87.4 wt%	86.9 wt%
IBP(^{o}C)	173.0	227.5	
T50(^{o}C)	270.0	323.5	
T90(^{o}C)	358.0	345.5	
FBP(^{o}C)	-	374.5	

*1: ASTM D2549-91

RESULTS AND DISCUSSIONS

Although total sulfur contents were almost same for each other, BLCO and CLCO had much higher nitrogen content as shown in Table 1. BLCO and CLCO contained more aromatic fraction and high boiling-point species than ALCO. Fig. 1 showed carbon, sulfur, nitrogen chromatograms of ALCO and BLCO. Although total nitrogen content of CLCO was 62% of that of BLCO, carbon and sulfur chromatograms of CLCO were not different from those of BLCO. Most of sulfur species present in LCO samples were analyzed to be aromatic. Alkylated benzothiophenes were found in BLCO and CLCO as in trace level while ALCO contained small amount of them. BLCO and CLCO showed dominant presence of alkylated DBT such as 4-MDBT, 4,6-DMDBT, 4,6,X-TMDBT. Broad peaks on sulfur chromatograms of BLCO seems to be from the non-aromatic sulfur species. Most of nitrogen species found in LCO samples were Carbazoles.

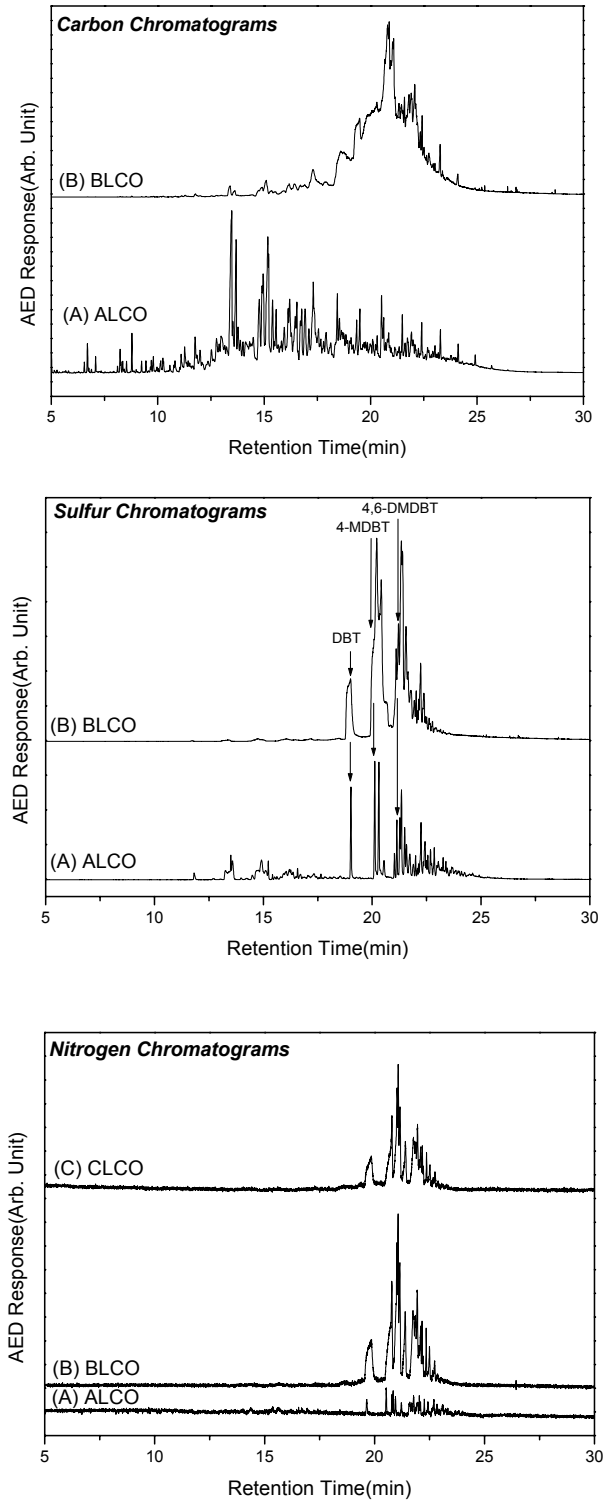

Figure 1. Carbon, sulfur, and nitrogen chromatograms of (A) ALCO, (B) BLCO, (C) CLCO.

Table 2 is the total sulfur, total nitrogen, DBT, 4-MDBT, and 4,6-DMDBT contents remained after 2 hours hydrodesulfurization. The HDS of SRGO having total sulfur and nitrogen contents of 14,354 ppmS and 250 ppmN, respectively, by the same conditions(340°C and CoMo-A catalyst for 2 hours) resulted in 95% conversion(661 ppmS) of total sulfur content. As can be seen in Table 2, the reactivity order of HDS is ALCO >> CLCO > BLCO for all catalysts. Remained sulfur content in ALCO was around 14 - 25%. However, BLCO and CLCO resulted in the total sulfur content of 26 - 47% after reaction at 340 ^{o}C. While the reaction at higher temperature of 360 ^{o}C gave less sulfur contents, the lowest sulfur content was 953 ppmS by NiMo-A from CLCO. Remained sulfur species from ALCO were 4-MDBT, 4,6-DMDBT, 4,6,X-TMDBT and DBT was less than detectable level as in Table 2 in the case of NiMo-A and CoMo-A. Although quantification of each sulfur species in HDS products of BLCO and CLCO had some uncertainty due to broad peaks as in Fig. 1, HDS conversion of DBT was much higher than those of 4-MDBT and 4,6-DMDBT. Furthermore, remained content of 4-MDBT and 4,6-DMDBT was not much different in the case of 340 ^{o}C reactions of BLCO and CLCO although HDS at 360 ^{o}C resulted in lower content of 4-MDBT than that of 4,6-DMDBT.

HDN activity also depended on the LCO type. ALCO showed much lower nitrogen content of HDS products than BLCO and CLCO. The difference in HDN activity between BLCO and CLCO was small except for CoMo-SAZ. HDS activity was higher over CoMo catalyst for all cases irregardless of support type except for BLCO HDS at 360°C. HDS of 4-MDBT and 4,6-DMDBT in ALCO were more active over CoMo and NiMo catalyst respectively. However, NiMo catalyst showed higher activity for HDS of 4-MDBT and 4,6-DMDBT in BLCO and CLCO except for CLCO at 360 ^{o}C over -SAZ catalyst. HDS of DBT was faster over NiMo catalyst than CoMo catalyst in the case of BLCO and CLCO. HDN Activity was higher over NiMo catalyst in all reactions. -SAZ catalysts, which are more acidic than -A catalyst, were inferior to those supported on alumina in HDS reaction. HDN activity order was NiMo-A>NiMo-SAZ>CoMo-SAZ>CoMo-A for BLCO and CLCO. HDS and HDN of gas oil was reported to be strongly inhibited by the aromatic species[3, 4]. In this study, LCO having larger content of aromatic fraction showed much lower HDS and HDN activity.

CoMo catalyst, which has been reported to have higher activity for direct desulfurization than NiMo catalyst, showed higher activity in the HDS of all LCO samples. In contrast, HDS of 4,6-DMDBT was higher over NiMo catalyst than CoMo catalyst. This observation could be rationalized by higher activity of NiMo catalyst toward hydrogenative route in the HDS of hindered DBT[4]. Zeolite has been known to be active for hydrogenation, hence could enhance HDS by partial hydrogenating aromatic partner of dibenzothiophene. However, catalytic function of zeolite components for the HDS of LCO was blocked by large content of aromatic species. Although nitrogen species was also inhibitor for HDS, their effects was not distinct in this study when compared to aromatic content. In spite nitrogen species was reported to have more inhibiting effect than aromatic species in HDS of model gas oil[5], much higher aromatic content of LCO might hinder the observation of the effect of nitrogen content. Nevertheless, CLCO showed slightly higher HDS activity than BLCO. This different activity became more definite at the HDS of 360 ^{o}C. HDN of carbazoles was believed to proceed via hydrogenative ways. Hence, NiMo catalyst showed higher activity to HDN of LCO samples.

CONCLUSIONS

LCO showed very limited activity for HDS when compared to that of SRGO. LCO having larger aromatic content showed much lower activity. Nitrogen content in LCO had relatively small effects on HDS. CoMo and alumina showed better performance than NiMo silica-alumina-zeolite for HDS.

Acknowledgement. Partial funding for this work has been provided by SK Corp. of KOREA.

REFERENCES

(1) U. S. E.P.A. IN *Regulatory Impact Analysis: Heavy-Duty Engine and Vehicle Standards and Highway Diesel Fuel Sulfur requirements*, EPA 420-R-00-026, Washington DC., **2000**.
(2) Turaga, U and Song, C. Prepr. Pap. -*Am. Chem. Soc., Div. Petrol. Chem*., **2002**, *47(1)*, 97.
(3) Ma, X; Sakanishi, K; Isoda, T.; Mochida, I. *Ind. Eng. Chem. Res*. **1995**, *34*, 748.
(4) Whitehurst, D. D; Isoda, T.; Mochida, I. *Adv. Catal*. **1998,** *42*, 345.
(5) Koltai, T; Macaud, M; Guevara, A; Schulz, E; Lemaire, M; Bacaud, R; Vrinat, M. *Appl. Catal. A*. **2002**, *231*, 253.

Table 2. Remained total sulfur content of hydrodesulfurized LCO samples after 2 hours reaction at 340°C and 360°C.

Catalyst	Temp. (°C)	ALCO					BLCO					CLCO				
		S (%)	N (%)	DBT	4-MDBT	4,6-DMDBT	S (%)	N (%)	DBT	4-MDBT	4,6-DMDBT	S (%)	N (%)	DBT	4-MDBT	4,6-DMDBT
NiMo-A	340	16%	6%	N.D.	26%	56%	35%	7%	6%	44%	58%	28%	7%	3%	36%	47%
CoMo-A	340	14%	8%	N.D.	20%	71%	30%	41%	2%	46%	64%	26%	35%	2%	39%	51%
NiMo-SAZ	340	25%	4%	2%	48%	69%	47%	17%	17%	50%	49%	43%	15%	16%	48%	48%
CoMo-SAZ	340	20%	5%	1%	39%	76%	40%	32%	16%	52%	53%	34%	16%	10%	47%	51%
NiMo-A	360	-	-		-	-	14%	5%	0%	18%	47%	11%	10%	0%	13%	36%
CoMo-A	360	-	-		-	-	16%	24%	0%	21%	61%	11%	28%	0%	14%	44%
NiMo-SAZ	360	-	-		-	-	28%	18%	4%	37%	60%	23%	18%	2%	30%	43%
CoMo-SAZ	360	-	-		-	-	27%	23%	4%	41%	65%	17%	18%	1%	26%	49%

Kinetic Study of 4,6-Dimethyldibenzothiophene Hydrodesulfurization over Ni Phosphide, NiMo and CoMo Sulfide Catalysts

Jae Hyung Kim[1], Xiaoliang Ma[1], Chunshan Song[1*]
S. Ted Oyama[2] and Yong-Kul Lee[2]

[1] Clean Fuels and Catalysis Program, The Energy Institute and Department of Energy & Geo-Environmental Engineering, Pennsylvania State University, University Park, PA 16802

[2] Environmental Catalysis and Materials Laboratory, Department of Chemical Engineering, Virginia Polytechnic Institute and State University, Blacksburg, VA 24061

Introduction

Ultra-deep hydrodesulfurization (HDS) of diesel fuel is an important research area due to increasingly stringent environmental regulations for fuel sulfur content (1). Alkyl dibenzothiophenes, especially, those with two alkyl groups at the 4- and/or 6-positions of dibenzothiophene (DBT) are still remained in the current commercial diesel fuel, such as 4,6-dimethyldibenzothiophene (4,6-DMDBT), which has been reported as one of the most refractory sulfur compounds in diesel fuel (2,3). HDS of dibenzothiophenes general proceed through two pathways, hydrogenation and hydrogenolysis pathways (4,5). Kinetic data of 4,6- DMDBT HDS for individual reaction pathways are necessary for evaluating new catalysts and for designing new ultra-deep HDS processes. However, such kinetic data are very limited in the literature. In the present study, HDS of 4,6-DMDBT HDS over a Ni_2P/USY phosphide catalyst and two commercial sulfide catalysts was conducted and the rate constants of the three catalysts for the two pathways were measured.

Experimental

4,6-DMDBT was used as the model sulfur compounds in the present study, and decalin was used as solvent. The reactions were carried out in 25-mL, horizontal micro-reactor agitated at 200 strokes/min in a fluidized sand bath within reaction time of 20 min. Reaction temperature was varied from 275˚C to 325˚C under 300 psi H_2 pressure, and H_2 pressure was also varied from 200 psi to 600 psi at 300˚C. In order to examine the effect of aromatic or nitrogen compound on HDS of 4,6-DMDBT, 1-methylnaph-thalene with the same mole as 4,6-DMDBT was added into the feed, and about 800 ppmw quinoline was added. Gas chromatography with a FID detector was used for quantitative analysis of products. GC-MS was used for identification of products.

Two commercial catalysts from Criterion, Cr344 ($CoMo/Al_2O_3$) and Cr424 ($NiMo/Al_2O_3$), were used after presulfidation at 350˚C for 4 h with 10 vol % H_2S in H_2 at a flow rate of 200 mL/min. After presulfidation, the catalysts were stored in decalin before use in order to minimize oxidation. Ni_2P/USY catalyst, which was provided by Virginia Tech, was treated in a H_2 flow at 420˚C for 4 h because it has been reduced at 580˚C in H_2 and passivated in 0.5%O_2/Ar flow. After treatment, the reduced Ni phosphide catalyst was also stored in decalin before use.

Results and Discussion

In order to get better kinetic data, the conversion of 4,6-DMDBT was kept below 15%. The main products were tetrahydro-dibenzothiphene (4HDMDBT), dimethlybipheny (DMBP) and meth-ylcyclohexyl-toluene (MCHT). Dimethyldicyclohexane (DMDCH) was also detected when the reaction time was more than 7 min. Hexa-hydrodibenzothiophene (6HDMDBT) was also detected in the HDS reaction over sulfided NiMo and reduced Ni_2P catalysts even under low hydrogen pressure. 6HDMDBT was observed in the HDS over sulfided CoMo catalyst under high hydrogen pressure. The schematic diagram of 4,6-DMDBT HDS is shown below;

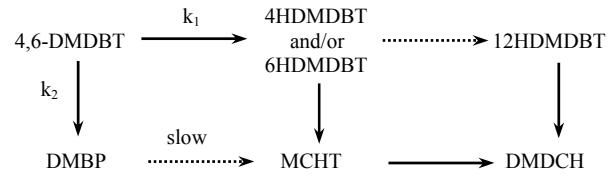

In general, HDS of individual sulfur compound follows the pseudo-first-order kinetics, thus: $\ln(C_{DMDBT}/C_{DMDBT0}) = -(k_1+k_2)\cdot t$, where k_1 is the pseudo first-order rate constant for the hydrogenation pathway, and k_2 is the pseudo first-order rate constant for the hydrogenolysis pathway. The value of (k_1+k_2), overall rate constant, can be calculated from experimental data. **Figure 1** shows the pseudo first order kinetic profile and **Table 1** lists the overall rate constants of 4,6-DMDBT HDS over the NiMo, CoMo and Ni_2P catalysts.

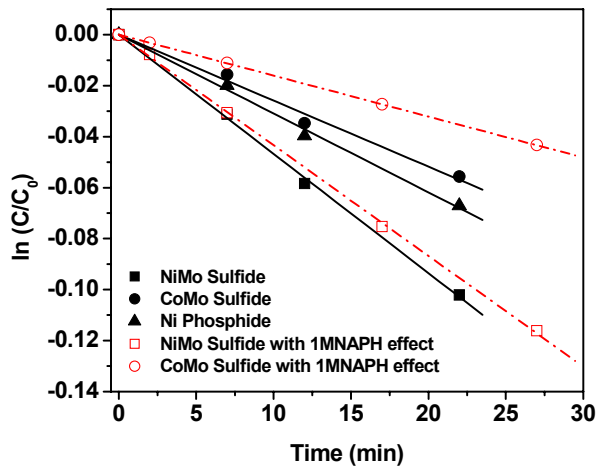

Figure 1. Pseudo first-order kinetics of 4,6-DMDBT HDS over the NiMo, CoMo and Ni_2P catalysts. (Reaction temp. = 300 °C and H_2 pressure = 300 psi).

As shown in **Figure 1,** the NiMo catalyst is more active than the CoMo catalyst in HDS of 4,6-DMDBT. 4HDMDBT and 6HDMDBT, which are the hydrogenated products of 4,6-DMDBT, were found to be dominant over the three catalysts, especially, over the NiMo catalyst and Ni phosphide. It was reported that NiMo catalysts favor HDS of 4,6-DMDBT because Ni catalysts have excellent activity for hydrogenation. After hydrogenation of 4,6-DMDBT, elimination of the sulfur atom becomes easy because hydrogenation reduces the methyl steric hindrance through molecular puckering and increases the electron density on the S atom (6). In general, HDS reaction is inhibited by coexisting aromatics and nitrogen compounds. However, in the present study, 1-methylnaphthalene was found to have only slightly inhibiting effect toward HDS of 4,6-DMDBT as the rate constants and product distributions in the presence of 1-methylnaphthalene and in the absence of 1-methylnaphthalene were similar. Quinoline was found to be a strong inhibitor toward the reaction. The conversion of 4,6-DMDBT was below 5% over both the NiMo and the CoMo catalysts even for the reaction at 300 ˚C over 60 min.

In order to measure the individual value of k_1 and k_2, we tried to measure k_1/k_2 ratio, as k_1 and k_2 values can be calculated by combination of (k_1+k_2) and k_1/k_2 values. We explored three methods to determine k_1/k_2 ratio. In Method 1, k_1/k_2 ratio is considered to be equal to $[C_{HDMDBT}+C_{MCHT}+C_{DMDCH}]/C_{DMBP}$ ratio, assuming that the conversion of DMBP to MCHT is negligible. In Method 2, k_1/k_2 ratio is considered to be equal to the initial selectivity ratio of hydrogenation products to hydrogenolysis products. Initial selectivity of each compound is obtained by extrapolating the selectivity curve to zero conversion as shown in **Figure 2**. **Table 1** lists the kinetic data at different temperatures and pressures, obtained by Method 2.

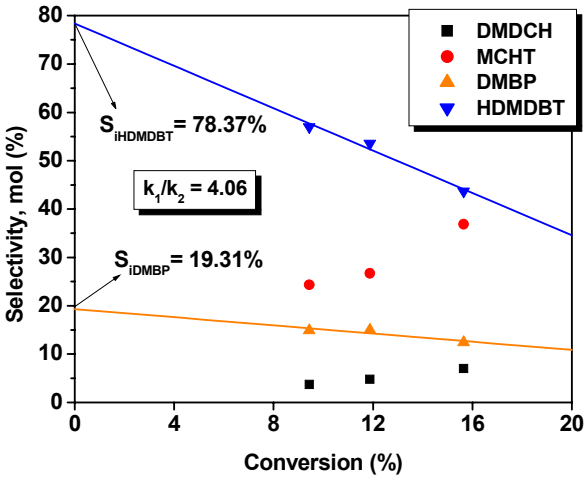

Figure 2. First order fitting of HDMDBT and DMBP products on NiMo sulfide for estimating initial selectivity (Reaction Temp.= 300°C, H_2 Pressure = 300 psi).

In Method 3 (computational simulation method), the formation rate constant of hydrogenation products and hydrogenolysis products can be described respectively as: $C_{HDMMDBT}+C_{MCHT}+C_{DMDCH} = C_o \cdot e^{-k1} \cdot t$, $C_{DMBP} = C_o \cdot e^{-k2} \cdot t$. The optimum k_1/k_2 value was determined by comparing the error between the actual product concentration and the product concentration calculated on the basis of different given k_1/k_2 values. **Table 1** compares rate constants, k_1 and k_2 from three different methods over CoMo, NiMo sulfides and Ni phosphide catalysts. The kinetic data from the three methods are similar in general. Based on overall rate constants estimated, the total activity of the three catalysts for HDS of 4,6-DMDBT decreases in the order of NiMo > Ni_2P > CoMo. The hydrogenation activity of the catalysts decreases in the order of NiMo > Ni_2P > CoMo, while the hydrogenolysis activity decreases in the order of CoMo ≥ NiMo > Ni_2P. It is clear that the NiMo catalyst is better than CoMo for HDS of 4,6-DMDBT because of its higher hydrogenation activity. However, if ranked based on active sites, then the catalytic activity would appear to be Ni_2P > NiMo > CoMo. This trend also reveals that transition metal phosphides might be more promising catalysts for ultra-deep HDS.

Conclusions

In this study, overall rate constant and individual rate constants of each pathway for HDS of 4,6-DMDBT over the NiMo, CoMo and Ni_2P catalysts were determined by three different methods. The Method 2, which is based on the initial selectivity, appears to be the most reasonable for estimating k_1 and k_2 value among the three methods.

It is clear that NiMo catalyst is better than CoMo for deep HDS of 4,6-DMDBT because of its higher hydrogenation activity. However, if ranked based on active sites, then the catalytic activity would appear to be Ni phosphide > NiMo sulfide > CoMo sulfide.

As shown by the resuts with Ni phosphide, transition metal phosphide can have good activity for HDS of 4,6-DMDBT and may become promising catalyst for deep HDS with some further improvement.

Acknowledgement. This work was supported in part by the New Energy and Industrial Technology Development Organization (NEDO), Japan, US Department of Energy-National Energy Technology Laboratory, The Pennsylvania State University, and the Post-doctoral Fellowship Program of Korea Science & Engineering Foundation (KOSEF, to JHK).

References

(1) C. Song and X. Ma, *Appl. Catal. B*, **2002** in press; C. Song. *Am. Chem. Soc. Div. Fuel Chem. Prepr.*, **2002**, 47 (2), 438.
(2) X. Ma, K, Sakanishi, I. Mochida, *Ind. Eng. Chem, Res.*, **1994**, 33, 218.
(3) B.C. Gates, H. Topsoe, *Polyhedron* **1997**, 16, 3213.
(4) D.H. Broderick and B.C. Gates, *AIChE J.,* **1981**, 27, 663.
(5) K. Sakanishi, T. Nagamatsu, I. Mochida, and D. Whitehurst, *J. Mol. Cat. A* , **2000**, 155, 101.
(6) X. Ma, K, Sakanishi, T. Isoda, I. Mochida, *Energy Fuels.*, **1995**, 9, 33.

Table 1. HDS Rate Constants of 4,6-DMDBT over the NiMo, CoMo and Ni_2P by Method 2

Catalyst	Rate constant 10^5 (s^{-1} g cat^{-1})	300 psi			200 psi	600 psi
		275°C	300°C	325°C	300°C	300°C
NiMo sulfide	k_1+k_2	60.0	78.0 (72.3[2])	159.3	55.2	133.5
	k_1/k_2[1]	4.3	4.1	2.7	4.2	5.1
	k_1	48.6	62.6	115.8	44.6	111.6
	k_2	11.4	15.4	43.5	10.6	21.9
CoMo sulfide	k_1+k_2	14.5	43.2 (26.8[2])	66.5	-	43.8
	k_1/k_2[1]	5.8	1.2	1.6	-	2.7
	k_1	12.4	23.1	35.8	-	31.9
	k_2	2.1	20.1	30.8	-	12.0

[1] $k1/k_2$ = [Initial selectivity of HDMDBT]/[Initial selectivity of DMBP] [2] Overall rate constant of 4,6-DMDBT HDS with 1-methylnaphthalene

New starting CoMo heteropolyoxomolybdates for the preparation of HDS catalysts

C. Martin[1], C. Lamonier[1], E. Payen[1], V. Harlé[2]

[1]Laboratoire de Catalyse de Lille, UMR C.N.R.S N° 8010, Université des Sciences et Technologies de Lille, Bâtiment C3, 59655 Villeneuve d'Ascq, France.
[2]Institut Français du Pétrole, 1-4 av de Bois-Préau, 92852 Rueil-Malmaison, France.

Introduction

Hydrodesulfurization (HDS) of petroleum feedstocks is a catalytic process that is based on the use of $CoMo/Al_2O_3$ catalysts. It is now well recognized that the active phases are the CoMoS phases [1] that consist of well dispersed MoS_2 nanocrystallites decorated with the Co or Ni promotor atoms. These phases are obtained through the sulfidation of an oxidic precursor that is generally prepared by incipient wetness impregnation of an alumina support with ammonium heptamolybdate (AHM) and cobalt (nickel) nitrate. Unfortunately a part of this Co penetrates inside the alumina support, a location considered as detrimental for the activity. That is one of the reasons why the use of complexing agents have been proposed [2]. Direct complexation of the Co or Ni atoms by the molybdenum is also possible to form the 6molybdo-cobaltate anion ($H_6CoMo_6O_{24}^{3-}$), an Anderson type heteropolyanion (HPA). Nevertheless the Co/Mo atomic ratio (1/6) is not sufficient to provide very efficient catalysts. Moreover its solubility limits the total amount of Mo that can be deposited by the incipient wetness impregnation method. The ammonium salt of the decamolybdocobaltate $(H_4Co_2Mo_{10}O_{38})^{6-}$, which is the dimeric form of this Anderson HPA, has a higher solubility and allows us to increase the Mo loading. It appears also very interesting to synthesize Co or Ni salts of these HPA, in order to increase the Co (or Ni)/Mo atomic ratio to the optimum ratio defined for the classical preparation. In the present work we focused on the preparation and characterization of the aforementionned HPA and their use as starting materials for the preparation of new HDS oxidic precursors [3].

Experimental

The synthesis of the ammonium salts, $(NH_4)_3CoMo_6O_{24}H_6,7H_2O$ and $(NH_4)_6Co_2Mo_{10}O_{38}H_4,7H_2O$, were respectively adapted from the method employed by Nomiya et al.[4] and Tsigdinos [5] and the products were checked by XRD, EXAFS, FTIR and Raman spectroscopies. These ammonia salts were dissolved in water and the Ni and Co salts were obtained by cationic exchanges at 50 °C of the ammonium entities using a solution of cobalt or nickel phosphomolybdates. The impregnating solution is directly obtained and contains only Co (and/or Ni) ions and the HPA as shown in the following example where X is the Co or the Ni:

$$2(3/2X^{2+},PMo_{12}O_{40}^{3-})+(NH_4)_6Co_2Mo_{10}O_{38}H_4 \rightarrow$$

$$\downarrow$$

$$2(NH_4)_3PMo_{12}O_{40}+(3X^{2+},Co_2Mo_{10}O_{38}H_4^{6-})$$

The catalysts were prepared by incipient wetness impregnation of a alumina with these solutions. Reference CoMo solids having the same metal loadings were also prepared for comparison purposes by using the conventional impregnating solutions made of AHM and cobalt (nickel) nitrate. The solids were dried overnight at 100°C and then calcined at 500°C under oxygen. These oxidic precursors are designated with the formula of the starting material preceded by the Mo loading expressed as MoO_3 wt%. These oxidic precursors were then sulfided and their activities were evaluated in HDS of thiophene.

Results and discussion

Raman, UV-visible and EXAFS analysis have been performed on the ammonium and cobalt salts of the HPA. In particular, Raman spectroscopy allowed us to distinguish between $CoMo_6$ and Co_2Mo_{10} HPA. Indeed, the Raman spectra differ by a shift of the two most intense lines, corresponding to the symmetric and antisymmetric stretching modes of the $Mo\text{-}O_{terminal}$ groups, respectively at 952 and 903 cm^{-1} for $CoMo_6C_{3/2}$, and 960 and 917 cm^{-1} for $Co_2Mo_{10}Co_3$ as shown in figure 1. Characterization of the catalysts at each step of the preparation by various physical techniques (UV-visible, Raman, XPS, EXAFS) allowed us to follow the evolution of the starting materials upon impregnation, drying, and calcination. As an example we focussed here on the $Co_2Mo_{10}Co_3$ based catalyst. The Raman spectrum of the dried $Co_2Mo_{10}Co_3$ based catalyst presents a line at 957 cm^{-1} (figure 1). However, its broadness prevents us from concluding unambiguously on the conservation of the HPA structure. Figure 1 also shows the Raman spectrum of $16Co_2Mo_{10}Co_3$ catalyst after calcination at 773 K under oxygen. Whatever the atmosphere of calcination the HPA entities are transformed into the classical surface polymolybdate as shown in Raman spectroscopy by a broad line around 950 cm^{-1}.

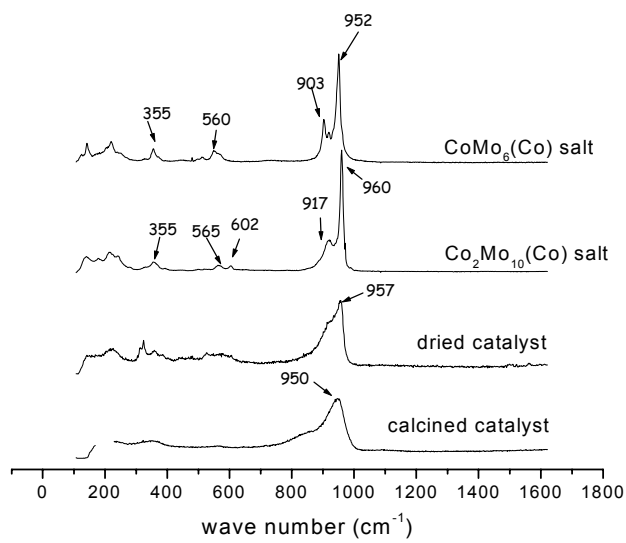

Figure 1. Raman spectra of $Co_2Mo_{10}(Co)$ and $CoMo_6(Co)$ salts and $16Co_2Mo_{10}(Co)$ catalyst after drying at 373 K and calcination at 773 K.

In figure 2 are shown the diffuse reflectance spectra (DRS) of the ammonium and cobalt salts of the dimeric HPA, $Co_2Mo_{10}Co_3$ based dried catalyst and the dried reference one. According to literature data, the absorption feature around 510 nm clearly indicates that the cobalt counter-ion presents an oxidation state of 2+ [6]. The cobalt species in the HPA structure are characterized by the feature around 615 nm, corresponding to the low spin Co^{3+} ion in octahedral coordination. Thus, the DRS spectrum of the dried $Co_2Mo_{10}Co_3$ catalyst indicates that at least a part of Co^{3+} species are preserved on the support at this stage of the preparation, whereas the conventional catalyst only contains Co^{2+} species.

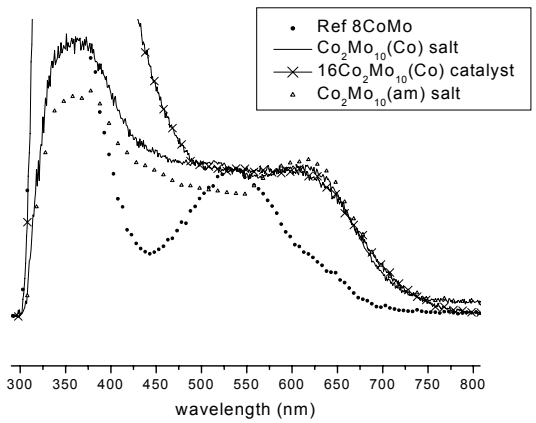

Figure 2. DRS spectra of $Co_2Mo_{10}(Co)$ and $Co_2Mo_{10}(am)$ salts, $16Co_2Mo_{10}(Co)$ catalyst and a conventionnal catalyst after drying at 373 K.

Complementary results were obtained through XAS experiments. Figure 3 shows the comparison between the experimental EXAFS signal of the dried 16 $Co_2Mo_{10}Co_3$ catalyst and the simulation obtained using the FEFF calculated contributions. These contributions were calculated using the crystallographic data derived from the structure resolution of the monocrystal HPA salt. The simulation is in good agreement with the experience. Thus, analysis of the EXAFS data showed that the dimeric HPA structure is maintained upon impregnation and after drying.

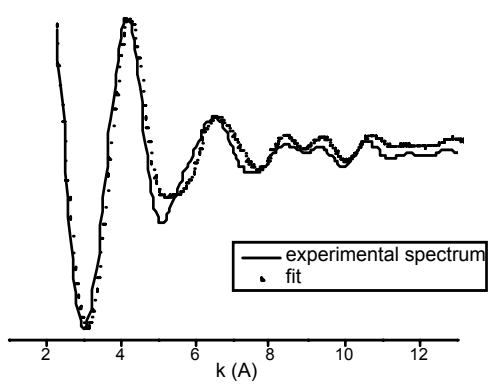

Figure 3. Comparison between the experimental EXAFS of $16Co_2Mo_{10}(Co)$ catalyst and its fit.

These solids were characterized after sulfidation. XPS results confirmed that, after treatment at 673 K under H_2S/H_2, this polymolybdate phase is well sulfided. Moreover, HREM micrographs of the solids showed the presence of well-dispersed MoS_2 crystallites. The comparison between HPA based catalysts and reference solids showed that these crystallites were more stacked and had a shorter size on the first ones.

Table 1 shows the thiophene conversion of these HPA-based catalysts, compared with those of the reference solids.

Table1: metal loading and HDS conversion of typical $CoMo/Al_2O_3$ catalysts

Catalysts Nomenclature	Precursor	MoO_3 loading (wt %)	CoO loading (wt %)	Conversion (%)
8 $CoMo_6C_{3/2}$	$Co_{32}CoMo_6O_{24}H_6$	8.0	1.7	20.0
Ref8CoMo	AHM, Co nitrate	8.0	1.5	15.0
8 $Co_2Mo_{10}Co_3$	$Co_5Co_2Mo_{10}O_{38}H_4$	8.0	2.1	27
16 $Co_2Mo_{10}Co_3$	$Co_5Co_2Mo_{10}O_{38}H_4$	16.0	4.2	38.0
Ref16CoMo	AHM, Co nitrate	16.0	4.2	22.0

The results show unambiguously that the solids 8 $CoMo_6C_{3/2}$ and $16Co_2Mo_{10}(Co)$ are more active than the reference ones. Moreover, the improvement is more important with the use as starting material of the dimeric HPA, which has a higher Co/Mo ratio.

Thus, the use of such compounds as starting materials appears very promising for the preparation of HDS oxidic precursors. The physical characterisations allowed us to conclude that the catalytic improvement is due to a better interaction between the promoter and the molybdenum atoms in their oxidic state. The optimisation of the interaction is assigned to the complexation of the Co atoms in the HPA structure.

Conclusion

This study confirms that the use of Co (or Ni) salts of heteropolyoxomolybdates is a promising way to improve the efficiency of HDS catalysts. The use of these complexes allows to impregnate alumina with stable anions in which Co is included. This permits to improve the interaction between the Co or Ni counterions with the HPA. Both lead to an improvement of the promoting effect of the Co or Ni as shown by the catalytic performances.

Références

[1]N.-Y. Topsoe and H. Topsoe, *J. Catal.*, 75 (1982) 354-374.
[2]P. Blanchard et al., *Studies in Surf. Sc. and Catal.*, 106 (1995) 211-223.
[3]V. Harle et al., *Patent n°02/09 840*, France (2002).
[4]K. Nomiya, T. Takahashi, T. Shirai and M. Miwa, *Polyhedron*, 6 (1987) 213-218.
[5]G. Tsigdinos, *Thesis*, Boston university graduate school (1961).
[6]N. V. Kosova et al., *J. Solid State Chem.*, 165 (2002), 56-64.

CATALYTIC DEEP HDS OF MODEL FCC FEED OVER A $CoMo/Al_2O_3$ CATALYST MODIFIED BY POTASSIUM

D. MEY[1], S. BRUNET[1], G. PEROT[1], F. DIEHL[2]

1) UMR CNRS 6503, Catalyse en Chimie Organique, Université de Poitiers, 40 avenue du Recteur Pineau, 86022 Poitiers Cedex, France
Email : sylvette.brunet@univ-poitiers.fr
2) IFP, 1 et 4 avenue de Bois Préau, BP 311, 92850 Rueil Malmaison Cedex, France

Introduction

It is well known that the gas emission (NO_x and SO_x) from motor vehicles contribute widely to air pollution. To address this environmental problem, new restrictive regulations were adopted by the European Community (Directive 98/70/EC). For instance, the sulfur level in Diesel fuel and gasoline will have to be lowered down to 50 ppm [1] by 2005.

Consequently, it is essential to modify conventionnal hydrotreating catalysts in order to achieve deep HDS with a minimum of alkene saturation. Several catalytic processes are commercialized by licensors to help the refiners to meet the future stringent regulations on FCC gasoline (Scan-fining® from ExxonMobil, Prime® G+ from Axens-IFP). Moreover, several authors have proposed new catalysts with reduced acidity of the alumina carrier [2-6] or the use of less acidic or basic supports such as TiO_2, SiO_2 or MgO. It was also reported recently that the selectivity for HDS could be increased with CoMo catalysts supported on Mg-Al oxide supports [7-10]. For the HDS of gasoline, hydrotalcite supported catalysts showed a decrease in the total activity (HDS and hydrogenation) but an increase in the HDS selectivity.

In this paper we report the activity of a $CoMo/Al_2O_3$ commercial catalyst modified by potassium, for the transformation of a model feed made of compounds (2-methylthiophene –2MT-, 2,3-dimethylbut-2-ene –23DMB2N and orthoxylene in n-heptane) which are considered as representative of the sulfur containing molecules and olefins found in FCC gasoline [11].

Experimental

Catalyst. The reference hydrotreating catalyst was a commercial $CoMo/Al_2O_3$ catalyst, containing 3 wt% CoO, and 14 wt% MoO_3. The catalyst modified by potassium ($CoMoK/Al_2O_3$) was prepared by incipient wetness impregnation of the reference catalyst with an aqueous solution of potassium carbonate (3 wt. %). The impregnated catalyst was dried at 100 °C and calcined at 500°C under air flow during 10 hours. The catalyst samples were presulfided at 400°C for 10 hours with a mixture of 10 mol% H_2S in H_2 under atmospheric pressure and then cooled down to 200°C.

Activity measurements. Catalytic activity measurements were carried out in a dynamic fixed-bed reactor at 200°C under a total pressure of 20 bar. The model feed made of 2-methylthiophene (10000ppm S), 2,3-dimethylbut-2-ene (20 wt. %) and orthoxylene (30 wt. %) in n-heptane was injected into the reactor with a syringe pump and the reaction products were analyzed on-line by means of a Varian gas chromatograph equipped with an automatic sampling valve, a PONA capillary column, a flame ionization detector and a cryogenic system. The identification of the products was made possible by GC-MS coupling (Table 1).

No significant transformation of orthoxylene was observed, whatever the experimental conditions.

Table 1. Products resulting from the transformation of model compounds

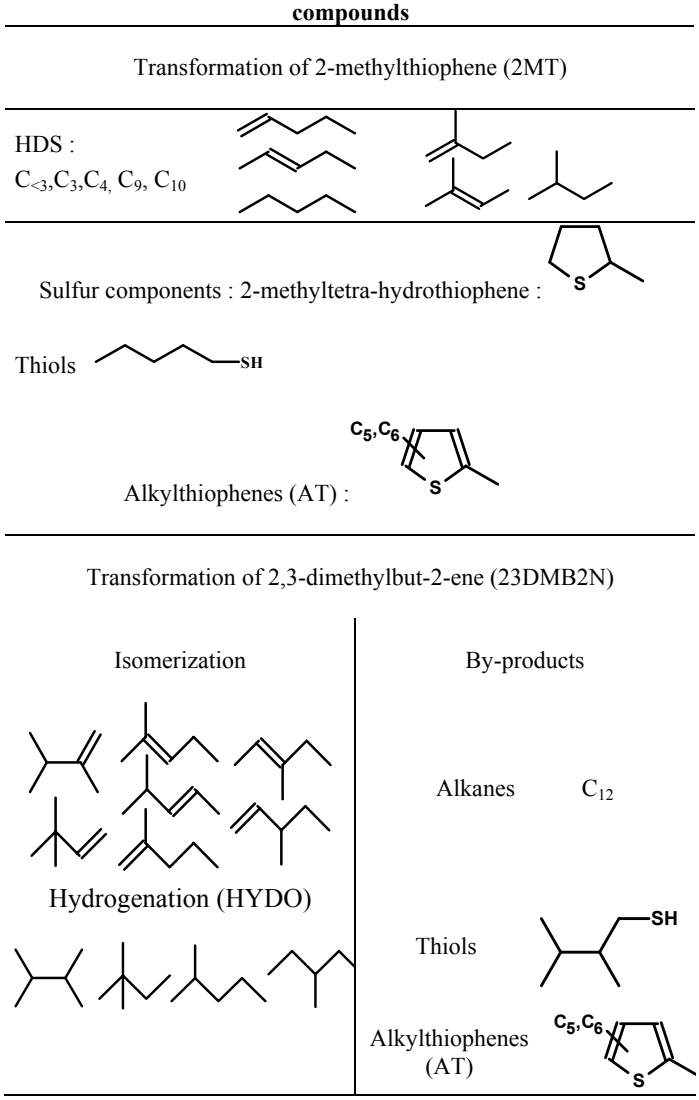

The major products of 2-methylthiophene (2MT) transformation were pentane and pentenes. The main by-products were alkylthiophenes obtained through the alkylation by alkenes (2,3-dimethylbut-2-ene and pentenes) of 2-methylthiophene. Thiols were also observed in small amounts.

The transformation of the 2,3-dimethylbut-2-ene (23DMB2N) led to the formation of hydrogenation products (mainly 2,3-dimethylbutane) and isomerization products (mainly 2,3-dimethylbut-1-ene).

Desulfurized products resulting from the transformation of 2-methylthiophene were designated as HDS products. The selectivity of the reaction was given by the ratio "hydrodesulfurization conversion of 2MT/hydrogenation conversion of 23DMB2N" (HDS/HYDO).

Results and Discussion

The transformation of the model FCC gasoline was carried out over the reference $CoMo/Al_2O_3$ and over the same catalyst modified by 3 wt.% of potassuim ($CoMoK/Al_2O_3$).

First of all we could notice a decrease in the total activity for the transformation of both molecules corresponding mainly to a lower conversion of 2MT into of alkylthiophenes and of 23DMB2N into 2,3-dimethylbutane. However, the decrease in hydrogenation conversion was more significant than the decrease in the HDS of 2MT (figure 1).

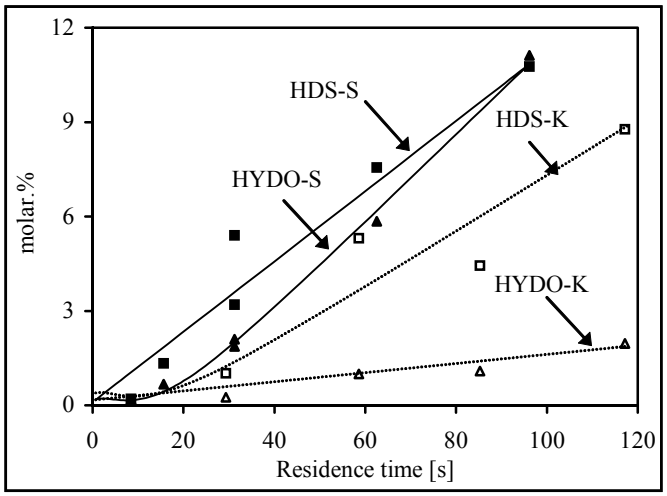

Figure 1. Transformation of the synthetic model gasoline over $CoMo/Al_2O_3$ (S) and $CoMoK/Al_2O_3$ (K). 20 bar; H_2/Feed = 200 l/l; 200°C; 500 mg. Hydrodesulfurization (HDS) of 2MT and hydrogenation (HYDO) of 23DMB2N.

The transformation of the pentenes resulting of the HDS of 2MT into pentane was also less significant with the potassium-modified catalyst, which was also a consequence of the decrease in its hydrogenation activity.

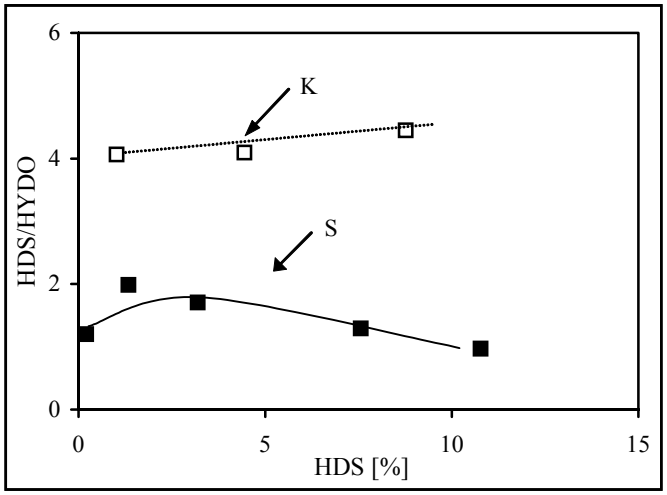

Figure 2. Transformation of the synthetic model gasoline.over $CoMo/Al_2O_3$ (S) and $CoMoK/Al_2O_3$ (K). 20 bar; H_2/Feed = 200 l/l; 200°C; 500 mg. Effect of the presence of potassium on the selectivity HDS/HYDO.

The selectivity HDS/HYDO measured by the ratio of the HDS reactivity of 2MT to the hydrogenation reactivity of 23DMB2N was improved by the presence of potassuim (figure 2). It was multiplied by 2 and was nearly constant in the range of HDS conversion which was obtained. These results can be explained both by a modification of the electronic properties of the catalyst because of the presence of potassium and by a decrease of the activity of the potassium-modified catalyst in the isomerization of 23DMB2N into 2,3-dimethylbut-1-ene. Actually it was found that on the unmodified catalyst, this reaction was very fast [11] and that the hydrogenation of 2,3-dimethylbut-1-ene was much faster than the hydrogenation of 23DMB2N. Consequently any inhibition of the isomerization activity is likely to decrease the hydrogenation activity of the catalyst.

The characterization of these materials (by the adsorption of probe molecules followed by infra-red and by electron microscopy) showed that the presence of potassium decreased the number and the strength of the acid sites without modification of the promoted active phase. The formation of the by-products (isomerization and alkylation) which involves the acid properties of the catalyst is therefore inhibited in the presence of potassium.

Conclusions

The modification by potassium of a commercial catalyst makes it possible to improve its selectivity in HDS of a synthetic FCC gasoline with respect to the hydrogenation of the olefins. In fact, the addition of potassium decreases the hydrogenation activity more than the HDS activity. This is considered to be the consequence of both a modification of the electronic properties of the sulfide phase and of the isomerization properties of the support.

References

(1) *Off. J. Eur. Commun*. L350 (28 december 1998) 58.
(2) Hatanaka, S.; Yamada, M.; Sadakane, O. *Ind. Eng. Chem. Res* **1997**, 36, 1519-1523.
(3) Hatanaka, S.; Yamada, M.; Sadakane, O. *Ind. Eng. Chem. Res* **1997**, 36, 5110-5117.
(4) Hatanaka, S.; Yamada, M.; Sadakane, O. *Ind. Eng. Chem. Res* **1998**, 37, 1519-1523.
(5) Hillerova, E.; Vir, Z.; Zdrazil, M. *Appl. Catal*. **1994**, 118, 111.
(6) Bertolacini, R.J.; Sue-A-Quan, T.A. U.S. Patent 4,140,626.
(7) Sherwood, D.E. Jr; Dai, E.P.; **1995** AIChE Spring National Meeting.
(8) Klimova, T. Casados, D.S., Ramirez, J. *Catalysis Today*, **1998**, 43, 135.
(9) Zhao, R.; Yin, C.; Liu, C. *Prepr. Pap.- Am.Chem.Soc., Div. Pet.Chem.* **2001**, 46 (1), 30-32.
(10) Zhao, R.; Yin, C.; Liu, C. *Prepr. Pap.- Am.Chem.Soc., Div. Pet.Chem.* **2002**, 47 (3), 309-311
(11) Mey, D., Brunet, S., Perot, G., Diehl, F., Kasztelan, S. *Prepr. Pap.- Am.Chem.Soc., Div. Pet.Chem.* **2002**, 47, 69-72

CONSIDERATION ON THE DENSITY EVALUATION OF THE MODEL OF HEAVY HYDROCARBONS BY COMPUTER SIMULATION

Masakatsu NOMURA, Satoru MURATA, Koh KIDENA, Takenao OOKAWA and Hisanori KOMODA**

Department of Molecular Chemistry, Graduate School of Engineering, Osaka University; *Department of Information Systems Engineering, Graduate School of Information Science and Technology, Osaka University
2-1 Yamada-oka, Suita, Osaka 565-0871 Japan

Introduction

The authors have been studying the modeling of molecular structure of heavy hydrocarbons such as coal and petroleum derived asphaltene because these heavy hydrocarbons have a very complicated mixture of relatively higher molecular weight hydrocarbons. In order to convert these materials into more useful smaller molecular weight fractions it is believed indispensable to know the chemical structures of these materials at molecular level. For this purposed measurements of molecular weight of original substances, identification of the bridge bonds of aromatic clusters and quantitative analysis of carbon functionalities of heavy hydrocarbons are considered indispensable. Molecular weight distribution of a complicated mixture of hydrocarbons is now determined by the use of MALDI although the more heavy portions due to association structure can not be detected even by this method. As for the bridge bonds connecting aromatic nuclei which are thought to govern the reactivity of heavy hydrocarbons has been studied by many researchers, however, for coal Stock[1] applied ruthenium ion catalyzed oxidation reaction to clarify these chemical structures and Strausz[2] undertook the same reaction for asphaltene derived from oil sand bitumen. Both groups published the model structures based on these results in 1993 and 1992, respectively. As for the quantitative analysis of carbon functionalities, Snape[3] published the successful application of ^{13}C NMR spectroscopy with single pulse excitation MAS method. Using these data available so far the authors published the model structures of Zao Zhuang coal[4] and Arabian light/medium vacuum residue derived asphaltene[5] in 1998 and 1999, respectively.

However, in spite of these continuing efforts of many researchers, there are few means to examine the comprehensiveness of the model structures. One seems to be the estimation of density of proposed model structures using computer simulation method, however, which needed an expensive software and high-performance calculator at the beginning of 1990's. Right now such calculation can be easily attained due to the rapid growth of computer science. Recently several researchers still are proposing model structures of these heavy hydrocarbons without knowing the spacious arrangement of these chemical structures.[6] This is the reason why the authors are going to present this article.

Experimental

Estimation of the physical density of model molecule was performed with CAMD (computer-aided molecular design) software, which is running on Polygraf (ver.3.0, Molecular simulations Inc.). Detail of the procedure was shown elsewhere[7], but it would be shown here briefly. At first, the model molecule was input, and its potential energy was then optimized. The conformation having the lowest potential energy was extracted as a best conformer. This model molecule was enclosed in cell, periodic boundary condition. For this PBC calculation, hydrogen atoms attached to carbon or oxygen atoms were treated as included in each carbon or oxygen group such as methane, methylene, methyl or hydroxyl group according to DREIDING's method. Molecular mechanics calculation was then carried out in order to reduce the potential energy of the system up to its minimum value, by using a cell volume of which the true density can be calculated.

Results and Discussion

Calculation of density of the model structure of oil sand bitumen derived asphaltene by Strausz *et al*.[2] Figure 1 shows the structure of asphaltene proposed by Strausz *et al*. This structure has the molecular formula of $C_{410}H_{817}N_5O_2S_{13}$ with molecular weight of 5950.1. The structural features of this model are the presence of porphyrine moiety and a relatively large loop structure with two small loop structures. The authors have applied their own method to calculate the density to get the value of 0.98 g/cm^3. According to the reported value of this asphaltene's density, 1.2 g/cm^3 the loose packing due to the presence of above mentioned structural portions is considered as the reason for such a very low density value. The authors have succeeded in getting reasonable value of density such as 1.17 g/cm^3 by rearranging two molecules from the original structure by cutting two bridge bonds shown in Figure 1. The resulting structure has still small loop structures in it, however, the presence of these loops shows little effect for the reasonable value of the density. This consideration should be examined. Incidentally, in the previous paper about coal structure that was published in 1992 by one of the author, the model structure had loop structure. It was considered to represent the average size of the void that could be measured experimentally for the sample. The asphaltene structure by Strausz *et al*. had several loop structures which probably were assumed to represent the presence of void structures in the asphaltene sample.

Calculation of the density of Arabian light/medium vacuum residue derived asphaltene model structure by Nomura *et al*.[5] The model structure is shown in Figure 2 where the model has molecular formula of $C_{490}H_{528}N_4O_5S_{15}$ with molecular weight 7034.5. This model is constructed based on the results from RICO reaction results and measurements of ^{13}C NMR spectrum and solid proton NMR spectroscopy. According to the measurement of molecular weight of this fraction using gel permeation chromatography the use of chloroform eluent gave relatively higher molecular weight while the use of more polar tetrahydrofuran eluent made the maximum peak of the molecular weight of the fraction to the relatively lower molecular weight. From the Figure 2, this asphaltene fraction consists of four portions and each portion can associate each other. This feature seems to be natural according to the current studies on these heavy hydrocarbons. The calculation was conducted to give 1.06 g/cm^3 of its density, this value being close to the observed value of 1.16 g/cm^3. In fact the real structure has more than thousand compounds in it so that the authors are thinking to take two phase models into consideration because in this asphaltene the relatively smaller fraction can be contained to exert a little effect on the calculation of the density of this fraction.

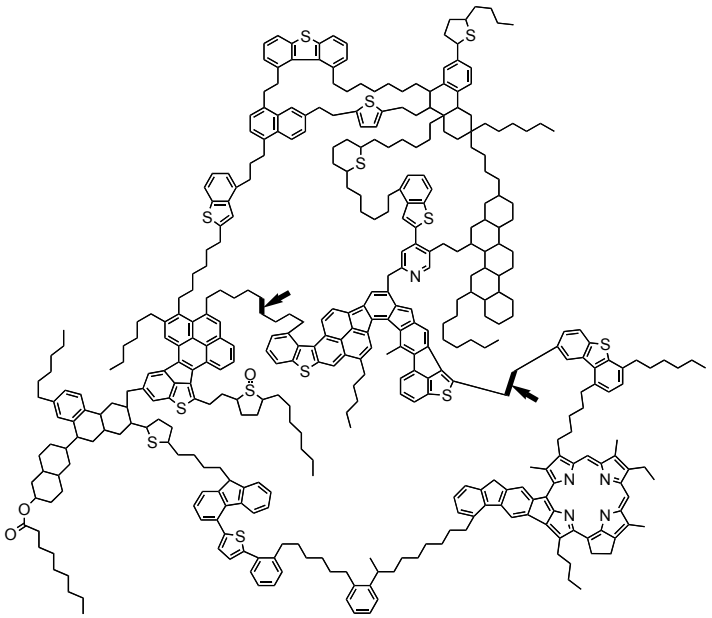

Figure 1. Hypothetical asphaltene molecule proposed by Strausz *et al*. (reference 2) Bold line and arrows in the figure indicate the position of cutting bridges in order to rearrange the three-dimensional structure of the molecule.

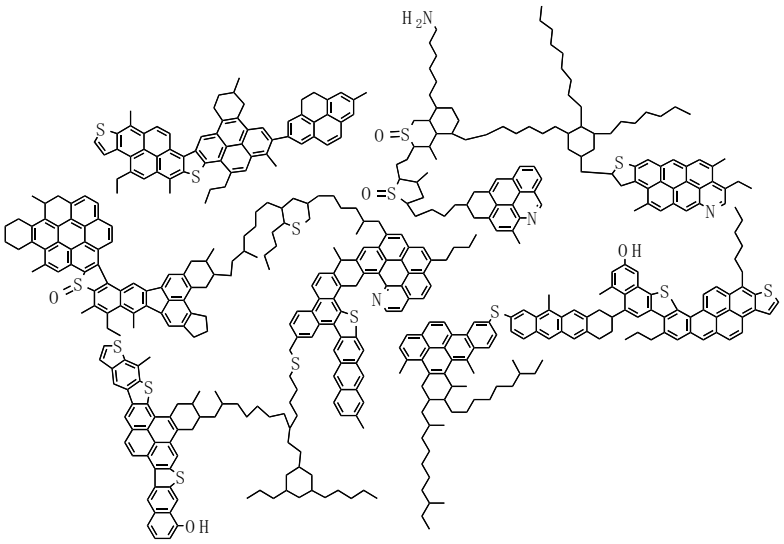

Figure 2. A model molecule for Arabian light/medium vacuum residue derived asphaltene proposed by Nomura *et al*. (reference 5)

Summary

This paper considers over again about the density evaluation with computer simulation method. One model structure was proposed by Strausz *et al.* that had a moiety of porphyrin and several loops. The other model was ours.

Acknowledgement. This work has been carried out as a research project of The Japan Petroleum Institute commissioned by The Petroleum Energy Center with the subsidy of The Ministry of International Trade and Industry.

References

(1) Stock, L. M.; Muntean J. V. *Energy Fuels*, **1993**, *7*, 704.
(2) Strausz, O. P.; Mojelsky, T. W.; Lown, E. M. *Fuel*, **1992**, *71*, 1355.
(3) Franz, J. A.; Garcia, R.; Linehan, J. C.; Love, G D.; Snape, C. E. *Energy Fuels*, **1992**, *6*, 598.
(4) Nomura, M.; Artok, L.; Murata, S.; Yamamoto, A.; Hama, H.; Gao, H.; Kidena K. *Energy Fuels*, **1998**, *12*, 512.
(5) Artok, L.; Su, Y.; Hirose, Y.; Hosokawa, M.; Murata, S.; Nomura, M. *Energy Fuels*, **1999**, *13*, 287.
(6) Mathews, J. P.; Hatcher, P. G.; Scaroni, A. W. *Energy Fuels*, **2001**, *15*, 863.
(7) Nakamura, K.; Murata, S.; Nomura, M *Energy Fuels*, **1993**, *7*, 347.

VAPOR LIQUID EQUILIBRIUM IN POLYCYCLIC AROMATIC COMPOUND MIXTURES AND IN COAL TARS

Vahur Oja and Eric M. Suuberg

Division of Engineering, Brown University, Providence, RI 02912, USA (Eric_Suuberg@brown.edu)

Introduction

There exist very few data in the literature concerning the vapor-liquid equilibrium (VLE) behavior of mixtures of high molecular weight organics. This is because it is difficult to measure the vapor pressures of high molecular weight organics without their undergoing thermal degradation during measurement. The present study addresses the problem, by presenting some new data on mixtures of polycyclic aromatic compounds (PAC) and mixtures of PAC with coal tar. The data were obtained by using the Knudsen effusion method, which avoids the degradation problem. The main focus of the present study is the question of whether high molecular weight PAC mixtures can be regarded as "ideal", and therefore, whether Raoult's law can describe their VLE behavior.

Experimental

Vapor pressures were indirectly determined, using the implementation of the Knudsen effusion method published earlier [1]. Briefly, this method involves the measurement of the rate of effusion of a compound (or mixture components) through a pinhole leak in a capsule that is suspended from one arm of a continuously recording microbalance. These results are readily related to vapor pressures. The measurements were conducted in a high vacuum ($<10^{-7}$ torr), which permitted measurements of vapor pressure to as low as 10^{-6} torr. Because of the low vapor pressures that can be measured, the temperatures of measurement can be kept sufficiently low so as to prevent significant thermal degradation of the sample during the measurement.

The PAC materials examined here were pure (reagent grade or best available purity) materials, and were used as received with no further purification. The materials were in all cases of 98+% purity. Preparation of mixtures of PAC was accomplished using the so-called "quenching" method. This method involved measuring the desired amounts of two PAC compounds into a stainless steel capsule, under inert gas. After closing, the capsule was shaken, while the contents were heated to melting. "Instant" cooling was achieved by plunging the capsule into liquid nitrogen. It was assumed that this method provided "perfect" mixing of the components. No visible phase separation was observed in the samples prepared in this manner. It is fair to note that questions have been raised regarding the efficacy of this method, for preparing truly homogeneous crystalline mixtures [3]. This will be considered further below.

The coal tar was prepared from a sample of Illinois No. 6 coal, obtained from the Argonne Premium Coal Sample Program [2]. The tar was prepared by pyrolysis of the coal in a tube furnace, in inert gas at 700°C, and collected by washing the cold end of the reactor (at which the tars condensed) using tetrahydrofuran (THF). The THF solvent was fully removed from the tar sample by vacuum drying at 45°C. This procedure allowed capture of the tars with molecular weight greater than 150 daltons. Following preparation, the tar was separated on a preparative-scale gel permeation chromatography (GPC) column, using two styrene-divinylbenzene GPC columns in series. The separation solvent was THF. The separation was not a pure size separation, but depended somewhat on molecular properties. This is not important in the present work. The number average molecular weight of the tar was determined by vapor phase osmometry (VPO), in pyridine. The separated tar fraction was dried in vacuum at 50°C, to fully remove the THF solvent.

Results and Discussion

Figure 1 shows results typical of those obtained in this study. The results are for an equimolar mixture of anthracene (MP=491 K) and perylene (MP=551 K). As might be concluded from the above melting points, results in Figure 1 are, strictly speaking, for sublimation of the compounds. The predicted behavior, assuming that Raoult's Law is followed, is also shown in Figure 1. The calculation of the mixture vapor pressure in this case is assumed to follow:

$$P = x_1 P_1^0 + x_2 P_2^0$$

In which the x_i represent the component mole fractions and the P_i^0 represent the respective pure component vapor pressures. These pure component vapor pressures were determined as part of this study, and were generally in excellent agreement with values found in the literature [4].

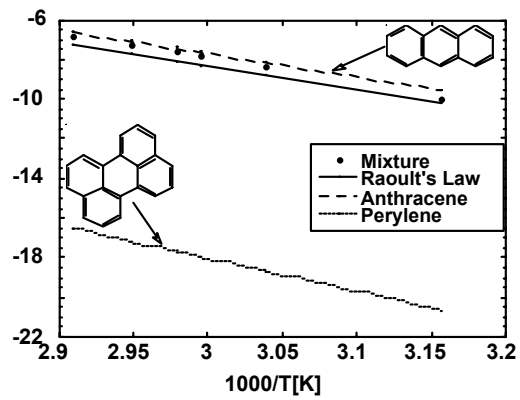

Figure 1. Vapor pressures of an equimolar mixture of anthracene and perylene.

While these data seem to suggest that Raoult's Law behavior might represent a fair approximation of the behavior, it is difficult to make a firm judgment of this, insofar as the disparity in pure component vapor pressures is so large that the lower molecular weight component (anthracene) dominates the behavior. On the other hand, Figure 2 shows that in a mixture of anthracene and benzofluorene, Raoult's Law is clearly not followed. This figure presents clear evidence of mixture non-ideality. The result might have been anticipated, since the mixture was below the melting point. Even though to the eye, the mixture appeared homogeneous, it could well have been phase separated. In such a case, the two solid phases behave as thermodynamically separate entities, as far as the vapor pressures they exert. The tendency to approach Raoult's Law behavior at higher temperatures was observed here and in several other cases. This suggests that as the systems approach melting they begin to behave as more nearly ideal single phases.

What is important to note from Figure 2 is the direction of deviations from Raoult's Law. If two phases behave independently of one another, their combined vapor pressure is

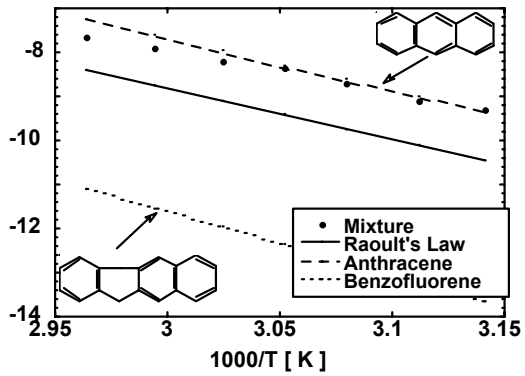

Figure 2. Vapor pressure behavior of a mixture of 25 mol % anthracene and 75mol % bezofluorene.

essentially the summation of the individual vapor pressures. Keeping this in mind, the contrasting results of Figure 3, for a mixture of 1-hydroxypyrene and phenanthridine are considered. In this instance, the mixture deviates in a direction of lower vapor pressure than the Raoult's Law prediction. This behavior cannot be explained by the possibility of phase separation. Rather, there is here strong evidence of a molecular interaction between the mixture partners. This could have perhaps been anticipated in light of the nitrogen base character of the phenanthridine and the acid (phenolic) nature of the 1-hydroxypyrene.

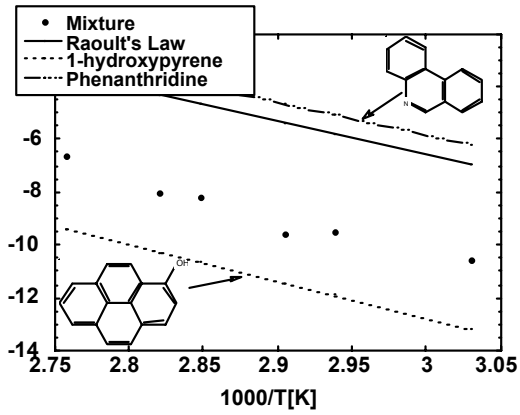

Figure 3. Vapor pressure behavior of a mixture of 54 mol% 1-hydroxypyrene and 46 mol% phenanthridine.

With these pure component and mixture results as a guide, the phase behavior of mixtures of PAC with coal tars was examined. A fraction of Illinois coal tar with a number average molecular weight of 270 daltons was mixed with pure compounds of similar molecular weight. It was estimated from elemental analysis that each "average" molecule of the tar contained about two hydroxyl groups, and the hydroxyl-rich character of this fraction was supported by its elution behavior in the GPC (its elution time was consistent with that of OH-rich species). The elemental analysis of this fraction showed that, by comparison, only every fifth tar molecule could contain nitrogen.

Figure 4 displays the VLE behavior of a mixture of the Illinois coal tar and 1-hydroxypyrene.

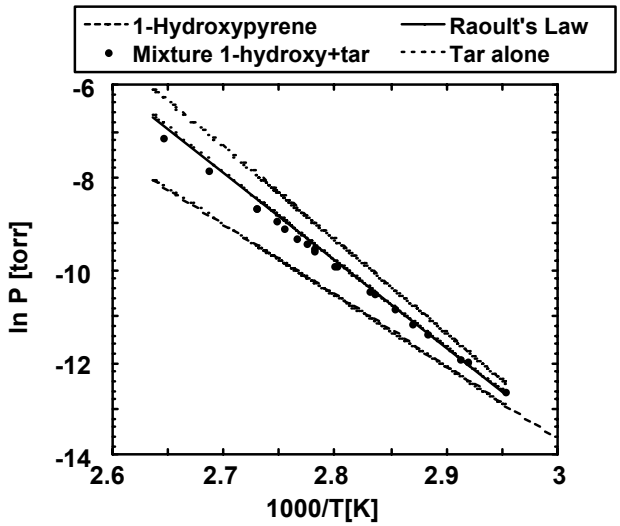

Figure 4. Vapor pressure behavior of 50 mol% 1-hydroxypyrene with 50 mol% Illinois No. 6 coal tar.

It is observed that the mixture of a phenolic compound with the coal tar produces what is very close to ideal mixture behavior. This is because the chemical nature of both components of the mixture is quite similar. On the other hand, addition of phenanthridine to the coal tar produces a mixture (Figure 5) that shows a significantly lower vapor pressure than predicted by Raoult's Law, and consistent with the behavior observed in Figure 3. This shows that the behavior of nitrogen compounds in the coal tar mixtures cannot be assumed to necessarily follow ideal mixture rules.

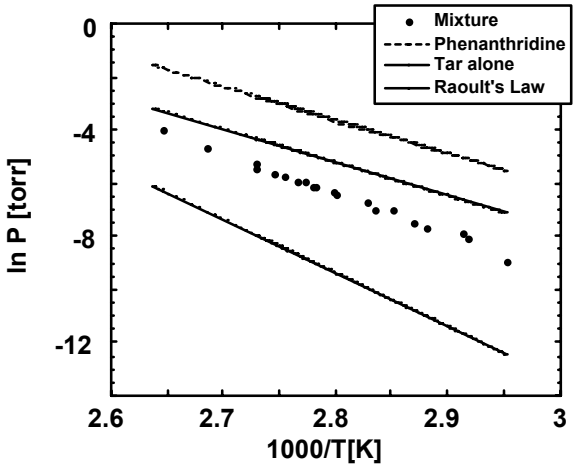

Figure 5. Vapor pressure behavior of phenanthridine (35 mol %), and Illinois coal tar (65 mol%).

Reference:

(1) Oja, V.; Suuberg, E.M. *Anal. Chem.*. **1997**, *69* 4619.
(2) Vorres, K. *Energy and Fuels*, **1990**, *4*, 420.
(3) DeKruif, C.G.; van Genderen, C.G.; Bink, J.C.W.; Oonk, H.A. J., *J. Chem. Thermodyn.*, **1981**, *13*, 1081.
(4) Oja, V.; Suuberg, E.M. *Jl of Chem. Eng. Data*, **1998**, *43*, 486.

UPGRADING OF HAMACA CRUDE OIL USING FORMIC ACID AS HYDROGEN PRECURSOR UNDER STEAM INJECTION CONDITIONS.

[1,3]*Scott C. E,* [1]*Delgado O.,* [1]*Bolívar C., and.* [2]*Ovalles C.*

[1] Centro de Catálisis Petróleo y Petroquímica, Facultad de Ciencias, Universidad Central de Venezuela, Apartado Postal 47102, Los Chaguaramos, Caracas 1042A, Venezuela.
[2] PDVSA Intevep, Departamento de Exploración y Producción, Sector El Tambor, Los Teques, Estado Miranda, Venezuela.
[3] Corresponding author: cscott@strix.ciens.ucv.ve

Introduction

Heavy and extra-heavy crude are found in vast abundance in different places, thus, for instance the heavy oil and tar sands bitumen in Alberta Providence of Canada and in the Orinoco Belt of Venezuela are each as large as the oil deposits in Saudi Arabia[1]. However, there are tremendous disadvantages in the recovery, transportation and refining of heavy crude oils because their densities and viscosities are much higher than the conventional ones. The use of downhole upgrading has been proposed in order to enhance heavy crude oil recovery. Several methods, as deasphalting[2-5], visbreaking[6-9] underground hydrogen[10-17] or ***in situ*** combustion[18-20], as well as hydrogen donor solvents[21-23] have been proposed as possible enhanced recovery technologies. Also, the injection of hydrogen precursors downhole has been reported as a way of ***in situ*** partially upgrading heavy crude oils. In fact, a 1992 patent[24] claims that ***in situ*** hydrogenation in a subterranean formation is readily performed by introducing a non gaseous hydrogen precursor into the oil bearing subterranean formation to enhance oil recovery. Formic acid and its organic and inorganic salts are among the hydrogen precursors proposed in the patent. It is reported that after treating a crude oil in a batch reactor with formic acid and MoS_2 (as catalysts), at 573 K and 1600 psig, API gravity of the upgraded oil is increased and asphaltene content is reduced, however, a detailed characterization of the upgraded product is not given.

In this work, a detailed study of the effect of formic acid in the upgrading of Hamaca extra-heavy oil, under steam injection conditions, was carried out. Laboratory physical simulations, using a batch reactor, at 553 K and 1500-1600 psig will be presented. The reactor was fed with a mixture of crude oil and sand (99 w % SiO_2) having 10 wt % crude oil, together with formic acid, and water. We believe that this conditions more closely represent the actual situation found during crude oil recovery by steam stimulation processes.

Experimental

Upgrading reactions were performed in a stainless-steel 300 cm^3 batch reactor (Parr), without stirring. In a typical test, the reactor was fed with 55 g. of Hamaca crude oil and sand (silboca, 99 w% SiO_2, specific area < 1 $m^2\ g^{-1}$) containing 10 % by weight of oil, 5 g. of formic acid and 5g. of distilled water. Experiments with no water added were also carried out. The reactor was heated at 4.2 K min^{-1}, to 553 K. Prior to heating the system was purged with nitrogen and pressurized up to 500 psig. Final pressure, after heating, was around 1300 psig (for experiments without Formic Acid) and 1600 psig (for experiments with Formic Acid). All the reactions were carried out for 24 hours. The reactor was then allowed to cool down to room temperature and the upgraded oil was removed from sand by solvent extraction with dichloromethane.

Original Hamaca and Extracted oils were analyzed for sulfur, using an ANTEK sulpfur analyzer**.** Saturated, Aromatics Resins and Asphaltene (SARA) separation and quantification were done in a Iatroscan MK-5 on samples separated on thin layer chromatography and detected by a hydrogen flame ionization system**.**

Results and Discussion

SARA analysis are presented in Table 1. It is found that treating the Hamaca crude oil in presence of water (W) produces a decrease in the Asphalthene and Resins (13.9 and 35.5 % conversions respectively), with the corresponding increase in the Aromatics and Saturates fractions. This is in agreement with previous reports[25] in which a reduction of the Asphaltenes and Resins fractions, and the corresponding increase of Aromatics and Saturates ones is found after treating heavy crude oils in the presence of steam.

When the crude oil is treated in presence of formic acid (FA), a slightly higher degree of Asphaltene conversion is obtained (23.1 %), while resins are converted to a lesser extend (22.2%). Again Aromatics increase, but in this case, Saturates are close to its content in the original oil. When formic acid was used in conjunction with water (FA+W) best results are obtained. Thus, Asphaltenes are reduced in 29.2 % and Resins in 44.5 %. Obviously, formic acid is more efficient in upgrading the oil when used together with water.

Table 1. SARA Fractions for Untreated and Upgraded Hamaca Crude Oil.[a]

	Saturates/ wt %	Aromatics/ wt %	Resins/ wt %	Asphaltenes/ wt %
HAMACA	(8.0 ± 0,8)	(34 ± 4)	(45 ± 2)	(13 ± 1)
W	(11.9 ± 0,6)	(48 ±2)	(29 ± 1)	(11.2 ± 0.6)
FA	(7 ± 1)	(51 ± 1)	(32 ± 1)	(10 ± 1)
FA+W	(10.4 ± 0,5)	(55 ± 3)	(25 ± 1)	(9.2 ± 0.5)

[a] Reactions carried bachwise, no stirring, at 1600 psi and 553 K for 24 h. Ratio solid: crude oil: formic acid: water = 10:1:1:1.

Sulfur content on the Hamaca crude oil, before a after upgrading was also measured, and the results are presented in Table 2. For the crude oil treated in presence of water a sulfur reduction of 20 %, is observed, which is due to thermal desulfurization[25]. When formic acid alone is used, the percentage of desulfurization is less (only 12%), but when formic acid and water are used together, the desulfurization is increased to 38 %, which is an important amount if we take into account that this is intended to be a downhole process.

All the results (SARA and sulfur content) presented show that an important degree of upgrading is obtained when Hamaca crude oil is treated in very mild conditions, i.e. conditions that are normally used in the reservoir during steam injection, using formic acid to generate hydrogen in the reaction media. The upgrading is more important when formic acid is used together with water.

Formic acid thermal decomposition have been proposed to proceed by two different basic mechanisms [26,27]

$$HCOOH \longrightarrow CO + H_2O \qquad (1)$$
$$HCOOH \longrightarrow CO_2 + H_2 \qquad (2)$$

It has been found that major products are CO_2 and H_2, for conversions between 38 to 100 %, temperatures of 593-773 K and pressures in the range of 2600-4500 psia. These conditions are similar to the ones used in this work, so it can be assumed that in the upgrading reactions conditions used in this work the main decomposition path way is the decarboxilation (reaction 2). In fact, molecular H_2 an CO_2 were observed in high proportions in the gaseous products, with only small amounts of CO. On the other hand, thermodynamic calculations[23] have shown that during the

hydrothermal decomposition of formic acid water acts as a catalyst, by forming an intermediate between a water dimmer and formic acid. It is suggested that Formic Acid and the water dimmer are bound with two hydrogen bodings and that the water dimmer acts simultaneously as a proton donor and acceptor. This configuration greatly reduces activation energy of the decomposition process.

Table 2. Sulfur content for original and upgraded oil. [a]

	(S ± 0.06)/ %	Desulfurization/ %
HAMACA	3.79	-
W	3.02	20
FA	3.34	12
FA+W	2.36	38

[a] Same conditions as for Table 1.

The results here presented show the potential of formic acid when used together with water, for giving up H_2 in steam injection conditions. H_2 produced in this way is effectively used for upgrading Hamaca crude oil disperse in sand. In the process water acts as a catalysts for the thermal decomposition of the formic acid.

Conclusions

H_2 produced by decomposition of formic acid can be effectively used for upgrading Hamaca crude oil disperse in sand at mild conditions (553 K, 1500 to 1600 psig of N_2). When formic acid is used in conjunction with water, water acts as a catalysts for the thermal decomposition of the formic acid, and the oil is upgraded to a higher extend. Thus, for Hamaca oil upgraded in the presence of formic acid and water, a 29 % conversion of asphaltene, and 38 % of desulfurization are obtained.

Acknowledgement. The authors are grateful to FONACYT (CONICIT-CONIPET 97003783) for financial support. Also the assistance from Laboratorio de Fisicoquímica de Hidrocarburos of the UCV in the SARA analyses is gratefully acknowledged.

References

(1) Wiehe, I. A., *Am. Chem. Soc*., *Div. Pet. Chem*. *Prepr*. **2001,** 46 (1), 60.
(2) US Patent 3 608 638, **1971**.
(3) US Patent 4 753 293, **1988**.
(4) Butler, R. M. and Mokry, I. J. SPE 25425, presented in Productions Operations Symposium, Oklahoma City, USA, March 21-23, **1993**.
(5) Duerksen, J. H. and Eloyan, A. M. Proceeding 6th UNITAR Int. Conf. On Heavy Crude and Tar Sands, Houston, Texas, USA, Feb 12-17, 1995, 353.
(6) Henderson, J. H. and Weber, L. *J. Can. Pet. Tech*., Oct-Dec, **1965**, 206.
(7) Kasrale, M. and Faroug, A. SPE 18784 presented in SPE California Regional Meeting, Bakersfield, USA, April 5-7, **1989**, 389.
(8) Shu, W. R. and Hartman, K.J. SPE *Reserv. Eng*. **1986** (September), 474.
(9) Monin, J. C. and Audibert, A. SPE *Reserv. Eng*. **1988** (Nov), 1243.
(10) US Patent 3 208 514, **1965**.
(11) US Patent 4 050 515, **1977**.
(12) US Patent 4 444 257, **1984**.
(13) US Patent 4 597 441, **1986**.
(14) Stapp, P. R. Report NIPER-434, Bartleswille, OK, December, **1989**.
(15) Weisman, J. G. and Kessler, R. V., *Appl. Catal*. **1996**, 140, 1.
(16) US Patent 5 105 877, **1992**.
(17) US Patent 4 505 808, **1985**.
(18) Roychaudhury, S., Rao, N. S., Sinha, S. K., Gupta, K. K., Sapkal, A. V., Jain, A. K., Saluja, J. S. SPE Nº 37547, presented in Int. Thermal Oper. Heavy Oil Symp. Bakersfield, CA, Feb. 10-12, **1997**.
(19) Wichert, G. C., Okazawa, N. E., Moore, R. G., Belgrave, J. D. M. SPE Nº 30299, presented in Inter. Heavy Oil Symp., Calgary, Alberta, Canada, June 19-21, **1995**, 529.
(20) Weissman, J. G., Kessler, R. V., Sawicki, R. A., Belgrave, J. D. M., Laureshen, C. J., Metha, S. A., Moore, R. G., Ursenbach, M. G. *Ener. & Fuel* **1996**, 10, 883.
(21) US Patent 5891829, **1999**.
(22) Vallejos C., Vasquez T. and Ovalles C. *Am. Chem. Soc., Div. Petrol Chem*. *Prepr*. **2000**, 45 (49), 591.
(23) Scott C., Alfonso H., Delgado O., Pérez-Zurita M. J., Bolívar C. and Ovalles C. *Am. Chem. Soc., Div. Petrol Chem Prepr*. **2000**, 45 (49), 588.
(24) US Patent 5 105 887, **1992**.
(25) Burger, J., Sourieau, P., Combarnous, M. 'Thermal Methods of Oil Recovery', Techni, Paris, **1985**, p. 81.
(26) Yu, J. and Savage, P. *Ind. Eng. Chem. Res.* **1998**, 37, 2
(27) Wang, B., Hou, H., Gu, Y. *J. Phys. Chem. A*, **2000**, 104, 10526.

THERMAL PROPERTIES AND DISSOLUTION BEHAVIOR OF ASPHALTENES

Yan Zhang[1], Toshimasa Takanohashi[1], Sinya Sato[1], Ikuo Saito[1] and Ryuzo Tanaka[2]*

[1]Institute for Energy Utilization,
National Institute of Advanced Industrial
Science and Technology,
16-1 Onogawa, Tsukuba 305-8569, Japan
[2]Central Research Laboratories,
Idemitsu Kosan Co., Ltd.
Kamiizumi1280, Sodegaura, Chiba 299-0293, Japan

Introduction

Asphaltenes are very complex mixtures containing more than tens of thousands of compounds with different functionalities and a wide molecular weight distribution. To date, characterization for asphaltenes was almost focused on the chemical structural parameters, compositions, or aggregates sizes[1-2]. For some processes, however, in addition to such knowledge of the chemical structure and composition, information of thermal properties can be needed. The latter may be more helpful for understanding the thermodynamic behavior of asphaltenes in various reactions.

Asphaltene molecules are known to form aggregates through various nonconvalent interactions in crude oils or vacuum residues (VR), which can be responsible for the formation of coke-precursor as well as the deactivation to catalytic reactions in upgrading and refining processes. Our recent results suggested that coke formation can be decreased by dissociation of asphaltene aggregates in organic solvents.[3] In order to control the relaxation of the aggregated structure in solvents more effectively, it is important to acquire the knowledge about the thermal properties of asphaltenes, and the interactions between asphaltene and solvent molecules.

In the present study, the thermal properties of asphaltenes, and their heats of solution in organic solvents were measured using differential scanning calorimetry (DSC) and microcalorimetry, respectively. By combination of the two techniques, the contribution of the thermal properties to the heat of solution, and the interaction between asphaltene and solvent molecules were investigated.

Experimental

Samples. Asphaltenes (AS) fractionated from Iranian Light (IL) and Maya (MY) vacuum residues (VR, after 500 °C vacuum distillation of the crude oils). A resin fraction (Re) from Maya VR was also used for comparison. Both asphaltenes and resin are solid powders at room temperature.

Differential scanning calorimetry measurements. Thermal properties of the samples were measured with a Seiko DSC 120 calorimeter. Temperature and enthalpy were calibrated with high purity indium, tin, lead and zinc, and the heat capacity was calibrated with synthetic saphhire. In a typical run, 6-10 mg of sample was heated at a heating rate of 10 °C/min from 8 to 300 °C under 50 mL/min nitrogen flow. For a repeated scan, after the first scan the sample was quickly quenched to 8 °C and heated again in the same way.

Microcalorimetry measurements. Heats of solution of the samples were measured by using a micro-twin-calorimeter (MPC-11, Tokyo Riko Co., Ltd.). Quinoline was used as a solvent. The detailed procedures have been reported in a previous paper[4].

Results and Discussion

It is known that the enthalpy change during mixing of a nonpolar liquid solute with a nonpolar solvent arises from interactions between the solute and solvent. If the mixing process is assumed to occur at a constant volume, the heat of mixing follows Van Laar-Hildebrand equation[5]:

$$\Delta H_{mix} = kT\chi_h n_1 \phi_2 \qquad (1)$$

where n_1 is the mole of solvent; ϕ_2 is the volume fraction of solute; χ_h is the interaction parameter between the solute and solvent. However, when a solid-state solute dissolves in a solvent, there will be an exothermic effect due to the dissolution of the glass[6,7], and/or an endothermic effect due to the fusion of crystalline structure[8]. In this case, the heat of solution (ΔH^M) should be the sum of the heat of mixing and the enthalpy change due to the phase transition (ΔH_{tran}) :

$$\Delta H^M = \Delta H_{tran} + \Delta H_{mix} \qquad (2)$$

where

$$\Delta H_{tran} = \lambda + \Delta Cp\,(T - T_m) \qquad (3)$$

here λ is the heat of fusion; ΔCp is the difference of heat capacity between solid and liquid states, and T_m is the melting temperature. The ΔH^M can be directly determined by the microcalorimeter, and ΔH_{tran} can be estimated by using DSC. Thus, the heat of mixing ΔH_{mix} can be estimated based on the values of ΔH^M and ΔH_{tran}, which reflects the essential interactions when mixing a liquid solute with a solvent.

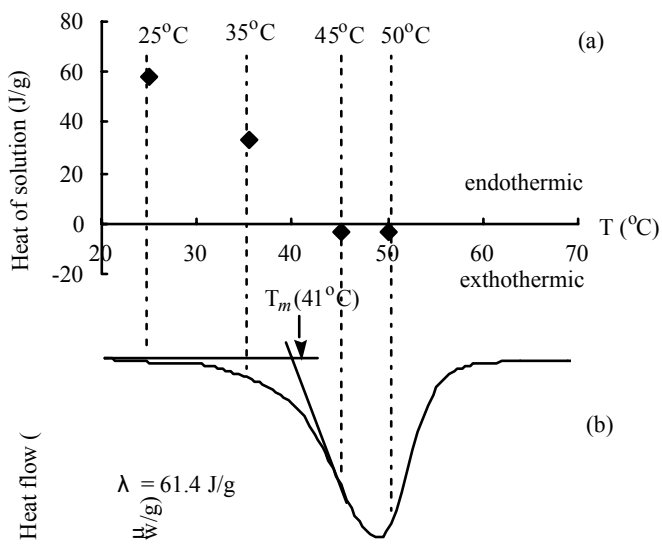

Figure 1. Heat of solution of N,N-dimethylnaphthylamine in quinoline (a) and its DSC thermogram(b).

As an example, Figure 1 shows the heat of solution of *N,N*-dimethylnaphthylamine (DMNA) in quinoline (Figure 1a) and its DSC thermogram (Figure 1b). According to DSC thermogram, the melting point and heat of fusion (λ) are determined as 41 °C and 61.4 J/g, respectively. Because no baseline shift was observed on the DSC diagram before and after melting ($\Delta Cp \approx 0$ J/g °C), the second term in equation (3) could be neglected. Thus, the enthalpy change (ΔH_{tran}) during the phase transition was approximately equal to the heat of fusion (λ). On the other hand, as shown in Figure 1a, in quinoline the

heat of solution below the melting temperature T_m was endothermic, while that above T_m was exothermic. At 25 °C, DMNA was completely solid, and the heat of solution was 58 J/g. Based on equation (2) and (3), the ΔH_{mix} can be calculated as – 3.4 J/g (exothermic). This value was nearly the same to the measured ΔH_{mix} above T_m, -3.7 J/g at 45 °C and –2.9 J/g at 50 °C (Figure 1a). Thus, ΔH_{mix} can be directly measured above the melting point of solute by using the microcalorimetry. However, for other solutes having their melting temperatures beyond the limit of operating temperature of the microcalorimeter, the value of ΔH_{mix} can not be measured. Thus, by the combination of DSC and microcalorimetry, for various kinds of solutes ΔH_{mix} can be estimated.

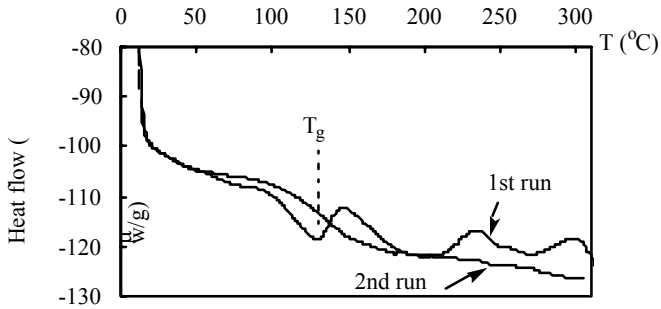

Figure 2. DSC thermogram of ASMY.

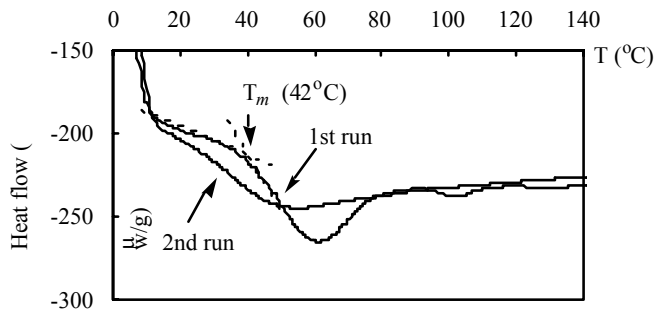

Figure3. DSC thermogram of ReMY .

Figure 2 shows the DSC thermogram of ASMY. Three endothermic peaks were observed on the 1st scan. While on the 2nd scan, all the peaks disappeared and only baseline shift was observed in the temperature range from 100 to 180 °C. The similar behaviors were also observed for ASIL. The disappearance of three peaks on the 2nd scan indicates that all changes occurring during the first heating run were irreversible. On the other hand, the reversible baseline shift on the 2nd scan may provide evidence that asphaltenes have glass transition property.

Figure 3 shows the DSC thermogram of ReMY. Different from the thermal behavior of asphaltenes, the changes started from very low temperature near 42 °C (the 1st scan), and ReMY didn't seem to show such a glass transition in the temperature range studied as shown on the 2nd scan.

Table 1. Thermal Properties and Heats of Solution for Asphaltenes and Resin.

	ΔH^M	T_g	λ	ΔCp	ΔH_{tran}	ΔH_{mix}
	J/g	°C	J/g	J/g°C	J/g	J/g
ASIL	-20.2[a]	136	9.1	0.127	-14.1	-15.2
ASMY	-22.1[a]	139	7.8	0.115	-13.3	-16.2
ReMY	6.1[a]	-	4.6	0.129	-1.8	3.3 (4.4[b])

[a]Measured at 25°C in quinoline. [b]Measured at 50°C in quinoline.

Table 1 summarizes the thermal properties of asphaltenes and resin determined by DSC, and their heats of solution in quinoline measured by microcalorimeter. It should be noted that heat of fusion (4.6 J/g) for ReMY determined by DSC, was close to the heat of solution in quinoline at 25 °C (6.1 J/g). By considering the difference of heat capacity (ΔCp=0.129 J/g °C) between solid and liquid ReMY, the calculated ΔH_{mix} (3.3 J/g) is nearly in accordance with the measured one (4.4 J/g at 50 °C). The endothermic nature of ΔH_{mix} for ReMY suggests that resin molecules are solvophobic to quinoline.

Table 1 also shows that for asphaltenes their glass transition energy (ΔH_{tran}) makes a large contribution to the heat of solution. According to other thermal properties determined by DSC and the heat of solution in quinoline at 25 °C, ΔH_{mix} were estimated as –15.2 and -16.2 J/g for ASIL and ASMY, respectively. These values reflect the enthalpy change due to the favorable interaction between asphaltenes and quinoline. Thus, the exothermic nature of ΔH_{mix} suggests that asphaltenes are strongly solvophilic to quinoline.

References

(1) Su, Y.; Artok, L.; Murata, S.; Nomura, M. *Energy Fuels*, **1998**, *16*, 1265.
(2) Sheu, E. Y.; Ling, K. S.; Sinha, S. K.; Overfield, R. E. *J. Colloid Interface Sci.* **1992**, *153*, 399.
(3) Takanohashi, T.; Sato, S.; Tanaka, R. *Petr. Sic. Technol.,* in press.
(4) Zhang, Y.; Takanohashi, T.; Sato, S.; Saito, I. Tanaka, R. *Energy Fuels*, **2003**, *18*, in press.
(5) Hidebrand, J. H., Scott, R. L. *The solubility of Non-electrolytes,* Reinhold, New York, 1950, Chapter 20.
(6) Bianchi, U.; Pedemonte, E.; Rossi, C. *Markromol. Chem.,* **1966**, *92*, 114.
(7) Cottam, B. J.; Cowie, J. M. G.; Bywater, S. *Makromol Chem.,* **1965**, *86*, 116.
(8) Schreiber, H. P.; Waldman, M. H. *J. Polymer Sci.* **1967**, *A2, 5*, 555.

CHARACTERIZATION OF CONSTITUENTS OF ARABIAN VACUUM RESIDUES BY FT-ICR MS COUPLED WITH VARIOUS IONIZATION TECHNIQUES

Keiko Miyabayashi, Yasuhide Naito, Kazuo Tsujimoto, Mikio Miyake

School of Materials Science,
Japan Advanced Institute of Science and Technology (JAIST)
1-1 Asahidai, Tatsunokuchi,
Ishikawa 923-1292 Japan

Introduction

Fourier transform ion cyclotron resonance (FT-ICR) mass spectrometry provides ultrahigh resolution spectra with exact mass of more than 6 orders magnitudes. Such novel performance causes us to investigate potential application of FT-ICR mass spectrometry to determine molecular formula of constituents in vacuum residues directly without any pre-separation procedures. Electrospray ionization (ESI) is promising technique to ionize non-volatile compounds without fragmentation. In our previous report, we have demonstrated effectiveness of ESI FT-ICR mass spectrometry to estimate molecular formulas of constituents in Arabian vacuum residues.[1] Recent our results suggest that aromatic compounds with more than 4 condensed rings are ionized under adopted ESI conditions. On the other hand, electro ionization (EI) proved to ionize aliphatic compounds in vacuum residues.[2] Therefore, selection of ionization is very important to analyze specific types as well as variety of compounds in vacuum residues.

In the present study, liquid secondary ionization (LSI) is applied to analyze vacuum residues, which is known to have extensive ionization ability irrespective of polar and apolar compounds. The results obtained by three different ionization systems are discussed to characterize features of respective ionization methods.

Experimental

Vacuum Residue Samples. The sample used in this study is Arabian vacuum residue with elemental composition (wt%) of C 84.3, H 9.9, S 5.2, N 0.4, and O 0.2 (diff.) . The ESI and LSI were applied to whole the sample without any separation procedures, while the fraction eluted by *n*-heptane was used for EI.[1,2] HPLC grade methanol and chloroform were used without further purification. All the other solvents and reagents were at least guaranteed reagent grade obtained from Wako Pure Chemical Industries, Ltd.

Ionization Conditions. For LSIMS measurement, the vacuum residue sample was mixed with 3-nitrobenzylalchol used as a liquid matrix. Approximately 1 µl of the liquid slurry was directly loaded on the probe tip. The primary ion (Cs^+) gun was operated at anode potential of 10 kV. The extraction voltage in the source was 10 V and the ionization pulse length was set to 600 ms.

For EI measurement, the sample dissolved in methylene chloride was loaded on the In-beam EI probe tip. The optimum conditions of probe temperature and ionization energy were estimated to be 300 °C and 30 eV, respectively in a previous study[2] and adopted in the present study.

The sample dissolved in methanol/chloroform (0.8/0.2, v/v) were infused into the ESI source in a positive ion mode and were desolvated by countercurrent nitrogen gas heated at 250˚C. Nitrogen needle-gas was flowed from the grounded needle to metal-capped glass capillary (~ −3.5 kV). Ions were accumulated in the hexapole for 3s before transporting to the FT-ICR cell. Detailed procedures were described previously.[1]

Mass Spectrometry. All spectra were accumulated by BioAPEX 70e with an external ion source. A broad band chirp excitation was used for all the experiments. Molecular formulas (possible combination of atomic masses which give the least deviation from the measured mass) were obtained by using *mass analysis* module. ESI and SIMS FT-ICR mass spectra were internally calibrated by using (poly)-ethylene glycol with the average molecular weight of 300 and/or 600. EI FT-ICR mass spectra were internally calibrated by using perfluorotributhylamine. Detailed conditions are similar to those reported previously.[1,2]

Results and Discussion

FT-ICR mass spectra obtained by using LSI (a), EI (b), and ESI (c) are shown in **Figure 1**. Over 500 distinguishable peaks originating from components of Arabian vacuum residues were observed for every spectrum. An order of ionization methods to detect higher masses were as follows: ESI (~800 Da) > EI (~600 Da) > LSI (~450 Da). It should be mentioned that heavier fraction in vacuum residue is eliminated for EI sample. The low acceleration voltage of primary ion (10 kV) adopted for LSI may be responsible for the low upper mass limit. The peaks with small masses detected by LSI should originate from molecular ions because LSI is known to be one of the soft ionization techniques by the aid of matrix and the low acceleration voltage was adopted in the present study. On the other hand, such peaks with low molecules are mostly olefins, resulting from fragmented ions of alkyl side-chains.[2] Adoption of the higher acceleration voltage is expected to detect molecules with the higher masses by LSI.

The expanded mass spectra show significant difference in peak positions and patterns depending on ionization methods (**Figure 1** insets). The difference in peak positions should be caused by the detection of compounds with different kinds of hetero-atoms, number of double bonds, or number of rings. When focused on patterns of a sequence of adjacent peaks appeared in ESI spectrum, abundance of peaks with even masses was observed compared to those with odd masses, compatible with the detection of compounds with monoisotopic and ^{13}C isotopic ions, respectively. On the other hand,

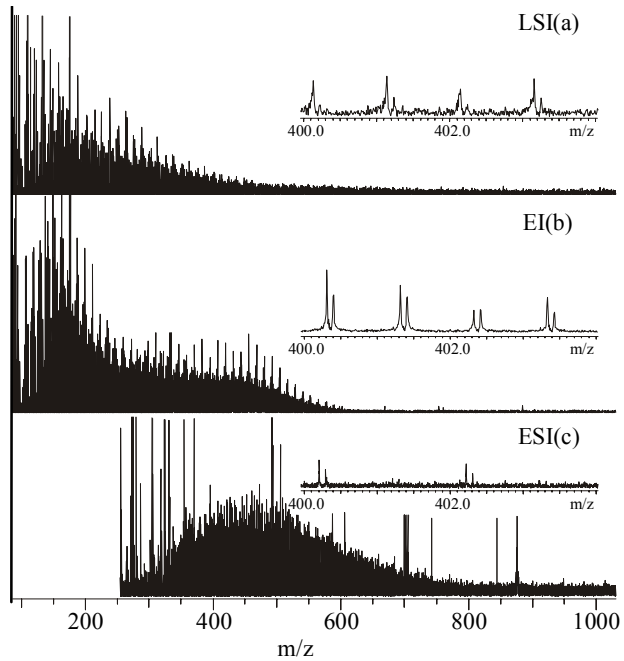

Figure 1. FT-ICR mass spectra of Arabian vacuum residue in each ionization technique; LSI(a), EI(b), and ESI(c). Insets show mass scale expansion from 400 to 404 Da.

Table 1. Estimated Molecular Formulas for the Peaks m/z 271.1503, 272.1426, 274.1588, 275.0900 and 275.1796 in Fig. 1(a)

Measd. mass / Da	Molecular formula	Formula mass / Da (Difference / mDa)	Z*
271.1503	$[C_{18}H_{22}S+H]^+$	271.1515 (0.8)	-14
272.1426	$[C_{20}H_{17}N+H]^+$	272.1434 (-0.8)	-23
274.1588	$[C_{20}H_{19}N+H]^+$	274.1590 (0.2)	-21
275.0900	$[C_{19}H_{15}S+H]^+$	275.0889 (1.1)	-23
275.1796	$[C_{21}H_{22}+H]^+$	275.1794 (0.2)	-20

*Hydrogen deficiency index: $[C_nH_{2n+Z}N_mS_s+H]^+$

adjacent peak intensities were random for EI spectrum, due to existence of the molecular ions (even mass) and fragment ions (odd mass) simultaneously.[2] LSI showed similar peak patterns to those of EI. Odd-mass ions detected in LSI may correspond to the compounds with zero or even-numbers of nitrogens based on soft ionization conditions. In every mass spectrum, a clear periodicity appears with similar peak intensities repeating at every 14 nominal mass unit. This periodicity predicts the presence of a series of compounds with different methylene chains. These homologues were detected irrespective of compound species, since the detected components changed by ionization. The chemical formulas of compounds detected by LSI were characterized on the basis of accurate mass measurements. The most plausible molecular formulas estimated for the measured peaks of 271 < *m/z* < 275 are shown in **Table 1**, together with hydrogen deficiency index denoted by $C_nH_{2n+Z}X$. The deviation between measured and calculated masses is very small; less than 1.1 mDa. Hydrocarbons, S-containing compounds, and N-containing compounds ($[C_nH_{2n+Z}+H]^+$, $[C_nH_{2n+Z}S+H]^+$, and $[C_nH_{2n+Z}N+H]^+$, respectively) are detected as major peaks in the LSI mass spectrum (230 < *m/z* < 330), whose distributions are summarized in **Figure 2**.

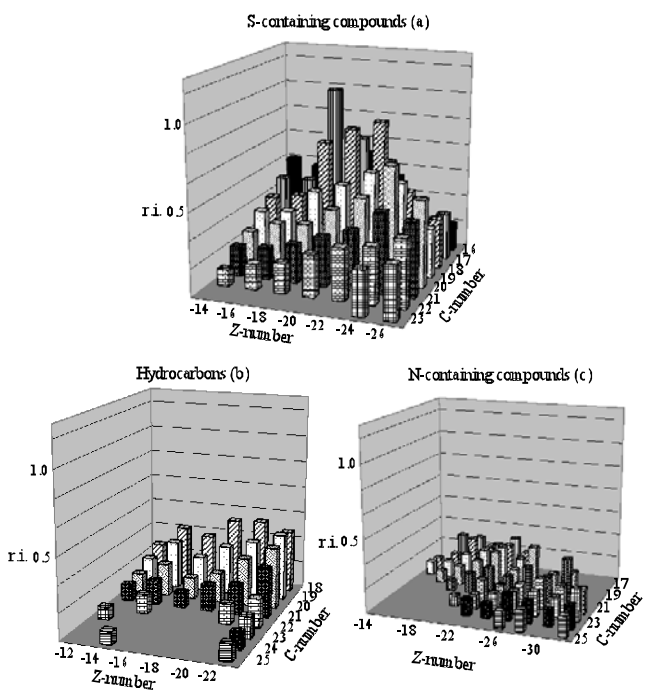

Figure 2. The Compounds distribution detected in LSI mass spectrum; (a) S-containing compounds, (b) Hydrocarbons, and N-containing compounds(c).

The most abundant constituents were S-containing compounds with carbon and Z number of 17~18 and −18~−22, respectively. Considerable difference in compound type distribution was observed for hydrocarbons, S-containing and N-containing compounds. Furthermore, we observe significant difference in peak intensities for kinds and types of compounds among three ionization techniques. For example, hydrocarbons and S-containing compounds were detected in similar intensities by EI, whereas N-containing compounds were detected preferentially by ESI.

The ranges of detected carbon numbers and hydrogen deficiency indexes for each ionization technique were summarized for comparison in **Table 2**. Hydrocarbons and S-containing compounds with similar carbon numbers are detected by EI and LSI, while whose hydrogen deficiency indexes by LSI is smaller than those by EI. Thus, it is anticipated that paraffinic and highly aromatic compounds are preferentially ionized by EI and LSI, respectively. N-containing compounds were detected both by ESI and LSI. Therefore, it is demonstrated that the detectable compounds vary depending on an ionization technique; each of them complements the analysis of complex mixture.

Table 2. Detectable Constituents of Arabian Vacuum Residue in EI, ESI, and LSI Mass Spectrometry.

	EI	ESI	LSIMS
C-number	7 ~ 30 (C_nH_{2n+Z})		12 ~ 22 (C_nH_{2n+Z})
	8 ~ 27 ($C_nH_{2n+Z}S$)		11 ~ 30 ($C_nH2_{n+Z}S$)
		27 ~ 59 ($C_nH_{2n+Z}N$)	12 ~ 33 ($C_nH_{2n+Z}N$)
Z-number	-16 ~ 2 (C_nH_{2n+Z})		-24 ~ -12 (C_nH_{2n+Z})
	-14 ~ -4 ($C_nH_{2n+Z}S$)		-26 ~ -14 ($C_nH_{2n+Z}S$)
		-46 ~ -8 ($C_nH_{2n+Z}N$)	-32 ~ -14 ($C_nH_{2n+Z}N$)

References

(1) Miyabayashi, K.; Suzuki, K.; Teranishi, T.; Naito, Y.; Tsujimoto, K.; and Miyake, M. *Chem. Lett.*, **2000**,172.

(2) Miyabayashi, K.; Naito, Y.; Tsujimoto, K.; and Miyake, M. *Int. J. Mass. Spectrom*. **2002**, *221*, 93.

ESTIMATION OF THE STRUCTURAL PARAMETER DISTRIBUTION OF ASPHALTENE USING PREPARATIVE GPC TECHNIQUE

Shinya Sato and Toshimasa Takanohashi

Institute for Energy Utilization
National Institute of Advanced Industrial
Science and Technology
16-1 Onogawa, Tsukuba,
Ibaraki, 305-8569, JAPAN

Ryuzo Tanaka

Central Research Laboratory
Idemitsu Kosan Co. Ltd.
1280 Kami-izumi, Sodegaura
Chiba, 299-0393, JAPAN

Introduction

In the investigation of the reactivity of heavy hydrocarbons, the structure of asphaltene is an important factor. Although asphaltene shows a wide variety of properties because it is a complex mixture of molecules with a wide range of molecular weights, most of the discussions have conventionally been based on the average molecular structure. Even though some researchers have been trying to reflect structural distributions into structural parameters, most of them are expressions of parameters such as molecular weight with an assumption of a mathematical distribution function1) and not an expression of distribution based on the results of analyses.

In a previous study, we found a tendency of the asphaltene properties to be that the aromaticity is high when the average molecular weight is low, whereas the aromaticity is low when the average molecular weight is high. Thus, in the present study, asphaltene was fractionated according to the molecular weight using Gel Permeation Chromatography (GPC), average structural analyses were carried out on each fraction, and the molecular weight dependency of the structural parameters was investigated.

Experimental

The asphaltenes used in this study were recovered from the vacuum residue distillation of Maya crude oil (AS-MY) from Mexico (Table 1). Two series of runs were carried out for AS-MY. In the first run, AS-MY was separated into 50 GPC fractions around the peak area through a Shodex KF-2003 GPC column using chloroform as solvent. This process was repeated 50 times and 500 mg of asphaltene was separated. Then the collected fractions were put together into 5 consolidated fractions so that the recovery rate of each fraction was about the same. Subsequently, average structure analyses[3)] were carried out using the results from the GPC molecular weight measurement using Shodex K403F column, elemental analysis, and ^{1}H- and ^{13}C-NMR analysis[2)] in order to investigate the molecular weight dependency of the representative parameters of the average structure.

Table 1 Properties of Asphaltene

Content in VR %	24.9
Elemental analysis, wt%	
C	82.0
H	7.5
N	1.3
S	7.1
Ni, ppm	390
V, ppm	1800
H/C	1.11
Carbon aromaticity	0.50
Molecular weight	
Number averaged	873
Weight averaged	2148
by LD/MS	1221

VR : Vaccuum residue

In the second run, AS-MY was separated into 50 fractions by GPC. Then the 50 fractions were analysed as the same manner as those in the first experiment except ^{13}C-NMR. The results were compared with those for the consolidated fractions.

Results and Discussion

GPC separation The recovery rate of asphaltene was calculated using the sum of the recovery amounts in the 30 fractions and the residual amount in the waste as 100 wt% value. The recovery rate from AS-MY in the 30 fractions was 69 wt%. For the second experiments, similar results were observed indicating a good reproducibility in the GPC separations.

Based on this value, the fractions were put together into 5 consolidated aliquot of the fractions so that each fraction consists of approximately 14 wt%. The physical properties of each fraction for AS-MY, summarized in Table 2, show that the properties were constant in fractions 1 to 3, but in fractions 4 and 5, the H/C values seem to be decreasing and the fa value increasing.

Table 2. Properties of fractionated asphaltenes for AS-M

Fraction	1	2	3	4	5
Recovery, wt%					
	18	13	13	16	10
Elemental analysis, wt%					
C	79.4	81.5	81.6	83.2	81.6
H	7.88	7.91	7.67	7.47	6.98
N	1.18	1.20	1.39	1.63	1.60
S	7.17	7.52	6.90	5.34	6.70
H/C	1.18	1.16	1.12	1.07	1.02
^{1}H-NMR					
Ha	7.5	8.7	7.2	10.0	11.7
H_{α}	13.6	14.7	20.5	18.0	23.8
H_{β}	59.3	57.3	56.3	54.4	50.7
H_{γ}	19.7	19.3	15.9	17.6	13.8
fa	0.42	0.47	0.45	0.46	0.55
MW	6984	3318	1677	674	145

MW: number averaged molecular weight by GPC

Structural parameter distribution Average structural analysis utilizes a number of structural parameters for the consolidated 5 fractions. Among them, we have especially focused on H/C, N/C, S/C, terminal methyl group carbon (Cγ/C), fa (Ca/C), total ring numbers (Rt), and aromatic ring numbers (Ra) that are closely related to the structure of condensed rings which contain aromatic ring(s). However, there is no established consensus on the significance of molecular weight in GPC, so the average structural parameters obtained from the molecular weight in GPC were converted into values for a single carbon atom for this study. The parameters including H/C, N/C, S/C, and fa values were calculated directly from the analytical values. Cγ/C was calculated using H/C and the results of ^{1}H-NMR. Since Rt itself is dependent on the number of carbons, the Rt′ value obtained by the equation 1 was used in the evaluation as the parameter of the total ring number.

$$Rt' = (Rt - 1)/C = 1 - (H/C + fa)/2 \quad (1)$$

The structural parameters obtained in the above-mentioned way are summarised in Table 3.

Table 3. Structural parameters of fractions from AS-

Fractions	1	2	3	4	5
MW	6984	3318	1677	674	145
H/C	1.18	1.16	1.18	1.12	1.02
N/C	0.013	0.013	0.012	0.015	0.017
S/C	0.034	0.035	0.033	0.032	0.031
fa	0.45	0.46	0.46	0.48	0.58
Cr/C	0.077	0.074	0.058	0.062	0.046
Rt'/C	0.186	0.190	0.175	0.198	0.202
Ra/C	0.124	0.136	0.126	0.143	0.143

Among these parameters, H/C and fa varied through fractions 3 to 5, whereas other parameters did not vary as much. Indeed, Rt´/C values, which are a function of H/C+fa, showed as almost constant; the results suggest that the variations of H/C and fa were complementary.

When asphaltene is fractionated, H/C values can readily be obtained by elemental analysis, while the actual measurement of the fa value is relatively difficult due to the sample amount. Therefore, the relationship between them is thought to be very useful. Fig.1 shows that on the low molecular weight side with the boundary at around MW 1000 to 1500, the aromaticity decreases as molecular weight increases, whereas on the high molecular weight side, the parameters become constant.

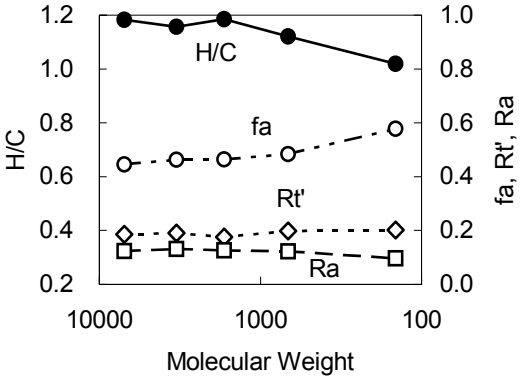

Fig. 1 Correlations of H/C and fa on MW determined by GPC

From the observed parameter variations, the following assumptions on the condensed rings of AS-MY were obtained: As molecular weight increases, (1) the lower the molecular weight is, the higher the aromaticity is; (2) up to MW 1000 to 1500, the molecular unit grows and the rate of having a side chain increases, therefore H/C increases and the fa value decreases; (3) over MW 1500, condensation or agglomeration of the fused ringsystem becomes predominant instead of the growth of the fused ring system.

For the fractions in the second experiments, the only the No.10-24 fractions can be analysed. The others were recovered too small amounts for the analyses. The trends for H/C and O/C, the content of O was the differential, are shown in Fig. 2. N/C and S/C are not varied. H/C curve had two boundaries. The higher boundary is around MW 1500, wich is almost the same as MW in the first experiment. Fig. 2 also shows that low MW molecule contains more oxygen, indicating that small asphaltene molecule is significantly polar. The average molecular structurer would be analysed from

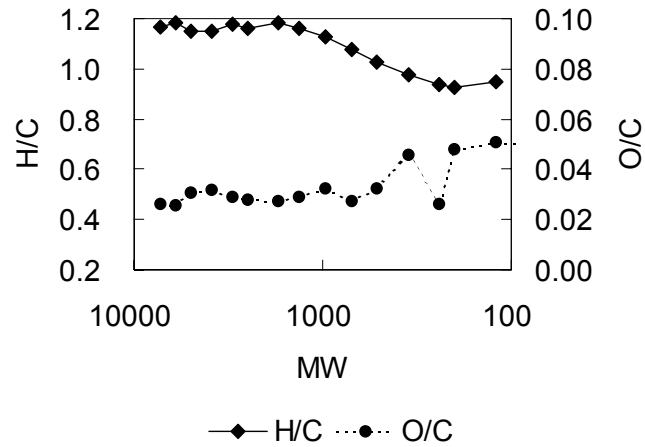

Fig. 2 H/C and O/C for 30 fractions separated by GPC

those data by estimating the fa using the correation H/C + fa is constant.

Conclusion

AS-MY was separated into 5 and 30 fractions by two runs of preparative GPC, respectively. Average structural parameters were estimated by structure analyses for those fractions, and the trends of structural parameters per carbon were discussed.

H/C for both runs increased with increase in the molecular weight up to the molecular weight of 1000-1500, while fa was decreased with increase in the molecular weight in the same range. For the higher molecular weight, all parameters mentioned above, including H/C and fa, are almost constant. In the case of the first run, the sum of H/C and fa, which is related to the number of total rings, was almost constant in a wide range of molecular weight observed as well as the parameter for the number of aromatic rings. N/C and S/C were also constant for both runs.

It is thought that asphaltene molecule was monomer and the growth of core structure mainly occurred up to the molecular weight of 1000 - 1500, and the polymerisation or agglomeration of monomer was predominant for the higher molecular weight.

Acknowledgment

This study was supported by an International Joint Research Grant Program from New Energy and Industrial Technology Development Organization (NEDO) and carried out in collaboration between the National Institute of Advanced Industrial Science and Technology (AIST), the Central Research Laboratory, Idemitsu Kosan Co., Ltd., and the Argonne National Laboratory, USA.

References

1. Neurock M., Nigam A., Trauth D., Klein M. T., *Chem. Eng. Sci.,* .49, 4153 (1994).
2. Sato S., Takanohashi T., Tanaka R., *Prepr. Am. Chem. Soc., Div. Fuel Chem.,* 46-2, 353 (2001).
3. Sato S., *J. Jpn Petrol. Inst.,* 40, 46 (1997).

EFFECTS OF ACTIVATION CONDITIONS ON THE ACTIVITY OF CARBONS FROM FORT UNION LIGNITES

Ramesh K. Sharma and Edwin S. Olson

Energy & Environmental Research Center
University of North Dakota
PO Box 9018
Grand Forks, ND 58202

Introduction

Activated carbon has been prepared from coals of various ranks and types, but the highly reactive Fort Union lignites have not been utilized commercially for preparing adsorbent carbons or other useful carbons. We recently reported that the high-sodium Fort Union lignites can be utilized as the precursor for preparing superior powdered activated carbon (PAC) adsorbents for removal of very-high-molecular-weight-humate molecules from water (1). Activation conditions were relatively mild (750°C, 30 min) in order to limit excessive burnout during steam activation; consequently, the surface areas obtained for these carbons were relatively low (240 m^2/g for the Freedom lignite) and varied considerably depending on the lignite seam. Yet the intercept of the modified Freundlich plot (1) representing the K value for sorption of humate on the high-sodium carbon was much larger than that for the Calgon F400 carbon. The success in removing macromolecules was attributed to the larger pore structure in these carbons. Because of the high activity and low production and transportation cost, there is considerable potential for application of these low-area PACs to water treatment in the northern tier states with surface waters draining peatlands. Tests with actual surface waters from this region showed improved removal with the high-sodium carbons. Removal of these humate precursors of the disinfection by-products will enable water treatment facilities to meet newly promulgated federal drinking water regulations.

The Fort Union activated carbons were less effective, however, for adsorption of small molecules, such as hydrocarbons or chlorinated hydrocarbons, owing to the low surface areas or low number of micropores (1). Thus methods for achieving activation to larger micropore dimensions were desired to expand the potential market for the Fort Union carbons as granulated carbon. The effects of demineralizing coals on the resulting carbon properties were reported by several investigators (2–5). Since the inorganic cations in chars catalyze the gasification reaction, removal of the inorganic species resulted in slower rates and development of higher microporosity during activation. Consistent with this deactivation behavior, exchange of ammonium for sodium in the Freedom lignite prior to carbonization (under identical conditions) resulted in activated carbons with somewhat higher surface areas (BET = 350–370 m^2/g) compared to the low values of the carbon from the as-received lignite. Humate removal was less effective than with the high-sodium carbons. Toluene isotherms showed improved adsorption but were not as effective as Calgon F400.

The objective of these studies was to determine if low-cost cation removal methods evaluated earlier by Baria (6) could give lower-activity chars from the Fort Union lignites and whether more severe activation conditions could then be applied to the exchanged lignites without excessive loss of mass and loss of microporosity. The demineralization method chosen was a sulfurous acid wash that would be the most cost-effective with these lignites in removing cations.

Experimental

Preparation of Activated Carbons. Activated carbons were prepared from a high-sodium Dakota Gasification Company Freedom mine coal, ground, and sieved to 8 × 20-mesh particle size. Ion exchange was carried out by stirring the coal in 6% sulfurous acid solution overnight. The ion-exchanged coal was filtered, washed with deionized water, and air dried at 110°C. For carbonization, 50 g of the granular coal was placed in a stainless steel tube reactor and heated to 400°C in a gentle flow of nitrogen. The reactor was held at this temperature until tarry material ceased to evolve. The carbonization yield for the exchanged coal at 400°C (30 min) was 65%. For steam activation, the char was added to a quartz reactor, which was heated to the desired activation temperature in a gentle flow of nitrogen. A steam–nitrogen mixture was passed through the reactor for the desired time at the reaction temperature. The activated carbon was cooled under nitrogen and removed from the reactor, weighed, and stored under nitrogen for further use.

Carbon Properties. The steam-activated carbon was ground to −200-mesh size prior to using for water treatment. Iodine numbers were determined to investigate the effect of conditions used for generating the activated carbons on the surface area of the carbons. Isotherms were determined for solutions of trichloroethylene (TCE) (10.2 μg/mL) and toluene (10.2 μg/mL) in water by adding known weights of the carbons (1.00 to 20.00 mg) to 50 mL of the solution and stirring for 2 hr. Concentrations were determined in the equilibrated solution supernatants by extraction into minimal dichloromethane containing the internal standard fluorobenzene and gas chromatography analysis on a 3-μ DB5 phase column.

Results

Cation Removal. Lignites typically have a large content of inorganic cations (especially sodium) associated with the weak acid carboxylate groups of the organic structure. The sodium content of the Fort Union lignite ash amounts to 4%–12% as Na_2O where the ash represents 10% of the as-received weight. These cations are responsible for ash fouling during combustion and, as mentioned above, have a large effect on the gasification rate and consequently on the development of the metaplast and subsequent formation of the micropore structure. Thus dramatic effects on carbon properties and behavior are obtained by removal of these ions. The ions are removed by an exchange process, with sodium being the most easily exchanged ion. Although ammonium exchange is effective and used in analytical procedures, the use of acid is less expensive (Baria). Impure dilute sulfurous acid potentially available from flue gas represents the least costly alternative.

Washing the 16% ash (mf basis) Freedom lignite with sulfurous acid gave an ash content of 8.57% (mf basis) after drying. Thus, not only sodium, but other cations and minerals such as carbonate were removed.

Activation at Various Temperatures. The 400°C char was activated using a matrix of temperatures and activation times. The carbon yields are given in Table 1. The longer reaction times and higher temperatures gave lower carbon yields, as expected.

Activated Carbon Properties. Surface areas of the activated carbons from the exchanged lignite char are reported in Table 1. Increasing the activation temperature from 650° to 750°C resulted in increases in surface area, but further increase to 800°C gave a lower iodine number. This temperature behavior parallels that of the as-received coal, but at higher values. At 750°C, the surface areas decreased dramatically with increasing activation time. Thus optimum surface areas are obtained at 750°C for 30 min, the same conditions as with the as-received coal.

Adsorption Isotherms. To evaluate the potential for the exchanged lignite-activated carbons in PAC applications in treating

Table 1. Effect of Reaction Temperature and Time on the Carbon Yield and Surface Area (exchanged lignite char = 50 g)

Activation Conditions	Carbon Yield, %	Iodine #
Char Carbonized @400°C		179
Steam Activation @ 650°C/90 min	87	310
Steam Activation @ 700°C/90 min	83	330
Steam Activation @ 750°C/90 min	60	439
Steam Activation @ 750°C/30 min	68	483
Steam Activation @ 800°C/30 min	60	467
Steam Activation @ 750°C/60 min	64	448
Steam Activation @ 750°C/120 min	40	350
Steam Activation @ 750°C/90 min*	30	368

* = volume of steam was doubled.

halocarbon- or hydrocarbon-contaminated water, adsorption isotherms were determined for the 750° and 800°C activated carbons from the sulfurous acid-exchanged lignite in solutions of toluene and TCE in water. The isotherm data were plotted using the conventional Freundlich method (log µg removed/g sorbent versus log C_{eq} in µg/mL). The results of these plots are given in Table 2. Results from earlier tests performed with the carbons from as-received lignite and ammonium acetate-exchanged lignite (1) are also shown in Table 2. The intercepts for the isotherms of the carbons from the exchanged lignite show significant increases over those obtained for the carbon from the as-received lignite. The lower-surface-area 800°C carbon exhibits lower intercept values for toluene and TCE. Thus these intercepts, which represent the log K values for the systems, are consistent with the surface areas determined for the carbons. The 750°C conditions optimize both the surface area and adsorption potential. The intercept for the 750°C carbon from sulfurous acid-washed lignite was also improved over that observed earlier for the 750°C carbon from ammonium acetate-exchanged lignite.

Table 2. Isotherm Data for Activated Carbons from Lignite

Activated Carbon		Toluene		TCE	
Lignite	Act. Temp.	Intercept	Slope	Intercept	Slope
Freedom – H_2SO_3	750°C	4.69	0.25	4.66	0.29
Freedom – H_2SO_3	800°C	4.09	0.48	3.27	1.47
Freedom – NH_4^+ Ac	750°C	4.30	0.59		
Freedom – a.r.	750°C	3.00	1.17		

Conclusions

The sulfurous acid wash appears to be more effective than the ammonium exchange in removing organically associated cations that can catalyze excessive burnout during activation and perhaps other minerals, such as calcium carbonate, that may plug pores. Activation of the sulfurous acid-exchanged lignite resulted in higher surface areas, owing to development of microporosity in the carbon. Higher activation temperatures resulted in lower surface area, which may be attributed to the very high reactivity of the char, even in the absence of the cations. Thus surface areas are lower than those attainable from bituminous coals. Removal of toluene and TCE representing small hydrocarbon and halocarbon molecules was improved by the exchange procedure.

Acknowledgment. This research was done with the support of the U.S. Department of Energy (DOE) National Energy Technology Laboratory Cooperative Agreement No. DE-FC26-98FT40320. However, any opinions, findings, conclusions, or recommendations expressed herein are those of the authors and do not necessarily reflect the views of DOE.

References

(1) Olson, E.S.; Sharma, R.K.; Eylands, K.E.; Stepan, D.J. *Fuel Chem. Div. Preprints* **2002**, *47(2)*, 472.
(2) Samaras, P.; Diamadopoulas, E.; Sakellaropoulos, G.P *Carbon* **1994**, *32*, 771.
(3) Mahajan, O.M.; Walker, P.L., Jr. *Fuel* **1979**, *58*, 333.
(4) Calahorro, C.V.; Cano, T.C.; Serrano, V.G. *Fuel* **1987**, *66*, 479.
(5) Serio, M.A.; Solomon, P.R.; Bassilakis, R. *Proceedings of International Conference on Coal Science* 1989, 341.
(6) Baria, D.N. *Proceedings of the Third Annual Pittsburgh Coal Conf.* Pittsburgh, PA, 1986, 71.

DEVELOPMENT OF MICROPOROUS ACTIVATED CARBONS FROM UNBURNED CARBON IN FLY ASH

Yinzhi Zhang, Zhong Tang, M. Mercedes Maroto-Valer and John M. Andrésen

The Energy Institute and the Department of Energy and Geo-Environmental Engineering,
The Pennsylvania State University,
405 Academic Activities, University Park, PA 16802, USA

1. Introduction

Due to the widely application of low-NO_x burner technologies, fly ashes of high unburned carbon content derived from coal-fired combustors are an increasing problem for the utility industry [1]. High carbon content fly ashes cannot be marketed as a cement extender[2], and therefore, have to be disposed. In 1999, over 60 million tons of fly ash and around 6 million tons of fly ash carbon were generated by the utility coal industry [3]. The authors have previously conducted extensive studies on the characterization of unburned carbon and showed the potential to produce activated carbons from unburned carbon by a one-step steam activation process [4,5]. However, the unburned carbon in fly ash has gone through a devolatilization process while in the combustor at temperatures above 1200°C that are much higher than those conventionally used for devolatilization or carbonization of precursors of activated carbons. Therefore, the reactivity of fly ash carbons during the activation process is relatively low and the activated carbons produced from fly ash carbon by one-step activation have a high content of mesopores[6]. Accordingly, the present study focuses on the modification of the one-step activation process in order to promote the development of microporosity, which is highly desired in commercial activated carbon. Nitric acid and hot air are widely used to modify the surface of carbon solids[7-9]. Accordingly, in this study nitric acid and hot air were selected to pre-oxidize the fly ash carbon prior to activation in order to produce activated carbon with comparable properties to those reported for commercial activated carbons.

2. Experimental

2.1 Samples. The parent study sample, FA-1, was collected at Penn State University from a 2 MM Btu/hour pulverized coal-fired suspension firing research boiler that uses a high volatile bituminous coal from the Middle Kittanning seam. Two pretreatment methods were developed, where the first one involves oxidizing the fly ash carbon in boiling nitric acid. Prior to the nitric treatment, the unburned carbon was enriched by flotation/sink and acid ($HCl/HNO_3/HF$) digestion at 65°C. The carbon content of the sample after demineralization is higher than 97%. The resulting samples after nitric acid oxidation were named as FA1-NX, with X representing the nitric acid oxidation time (in hours). The activation of the pretreated samples was carried out in a fixed bed reactor that was placed inside a horizontal furnace. The resulting activated carbons were designated as FA1-NX-851, with X representing the hours of nitric acid pretreatment and 851 representing activation at 850°C for 1 hour. For the second pretreatment method, the fly ash sample was oxidized in air for different time periods. The resultant activated carbons were designated as FA1-GPX-851, with X representing the number of hours pretreated in air. The activation experiments for the air pretreated samples were carried out in a fluidized bed reactor that was placed inside a vertical furnace, as previously described [5]. For the purpose of comparison, the untreated samples were also activated under the same conditions.

2.2 Characterization. A Kratos Analytical Axis Ultra XPS was used to study the surface chemistry of the samples. XPS quantification was performed by applying the appropriate relative sensitivity factors (RSFs) for the Kratos instrument to the integrated peak areas. The approximate sampling depth under these conditions is 25Å. The porosity of the samples was characterized by conducting standard N_2 adsorption isotherms at 77K using a Quantachrome adsorption apparatus, Autosorb-1 Model ASIT. The pore sizes 2nm and 50nm were taken as the limits between micro- and mesopores, and meso- and macropores, respectively, following the IUPAC nomenclature [10].

3. Results and Discussion

3.1 Nitric acid pretreatment. As expected, nitric acid pretreatment successfully introduced oxygen surface groups on the fly ash carbon, as showed by the XPS data presented in Table 1. The sample FA1 prior to nitric acid treatment already contains 10.5% oxygen on the surface, probably due to oxygen introduced by the acid digestion process ($HCl/HNO_3/HF$). With increasing oxidation time, the oxygen content on the surface of the fly ash carbon increases, and when the pretreatment time is extended to 5 hours, the surface oxygen content of the fly ash carbon is as high as 16.7%. Species observed on the surface of the samples include C-C, C-(O, N) and COO^-. All the pretreated samples contain distinct COO^- bands at 288.5eV. A smaller, unresolved C-(O, N) peak might also have been present. A curve fit to the experimental carbon 1s spectra showed that the nitric acid pretreatment created a large amount of carboxylic COO- groups on the surface of the fly ash carbon, as previously reported for oxidation of anthracites [9].

Table 1. Summary of Elements Detected by XPS (Rel. Atom %)

Sample	C	O	Others*
FA1	81.3	10.5	8.2
FA1-N1	84.8	14.6	0.6
FA1-N3	84.5	14.0	1.5
FA1-N5	82.5	16.7	0.8

* Includes halogen, nitrogen, and earth mineral elements.

The porous texture properties, as determined from the 77K N_2-isotherms, of the parent sample and its counterparts oxidized with nitric acid are presented in Table 2. It can be seen that the nitric acid pretreatment increased the porosity of the fly ash carbon. For example, the surface area of the fly ash carbon increases to 278m^2/g for 5 hours pretreatment compared to 125m^2/g for the parent sample. The average pore size decreases to 2.21 nm from 2.46 nm, which indicates that the pores developed during pretreatment are mainly micropores.

Table 2. Porous texture characteristics of the parent sample and its counterparts oxidized with nitric acid.

Sample	BET surface area, m^2/g	Pore volume, ml/g	Average pore diameter, nm
FA1	125	0.077	2.46
FA1-N3	179	0.104	2.34
FA1-N5	278	0.153	2.21

3.2 Activation of nitric acid pretreated samples. The samples pretreated with nitric acid were then activated by steam at 850°C for 1 hour. The N_2-77K isotherms of the resultant activated samples (FA1-N1-851, FA1-N3-851, and FA1-N5-851) are shown in Figure 1, and Table 3 lists the surface area and pore volumes calculated from the isotherms. For the purpose of comparison, the sample without pretreatment (FA1-851B) is also included in Figure 1 and

Table 3. The isotherms of all the pretreated samples have higher adsorbed volumes than the sample without pretreatment (Figure 1). For the 1 hour pretreatment sample (FA1-N1-851), the isotherm has similar shape to the sample without pretreatment, but it has a larger adsorbed volume for the micropore filling. For the 3 and 5 hours pretreatment samples (FA1-N3-851 and FA1-N5-851), the micropore filling at low relative pressure has not changed significantly, except than the isotherms present a more open knee, indicating a wider micropore size distribution.

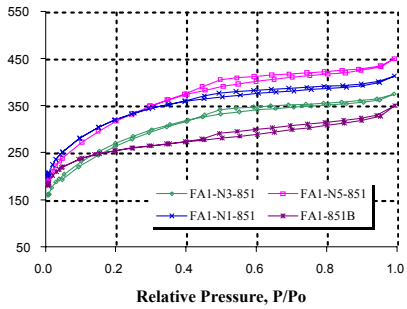

Figure 1. N_2-77K isotherms of the activated parent sample and the samples activated after nitric acid pretreatment.

Table 3 shows that after 1 hour pretreatment, the surface area of the resultant activated carbon is as high as 1139m^2/g, compared to 890m^2/g for the sample without pretreatment. Similarly, the pretreated sample has a smaller average pore size, 2.16nm, compared to 2.27nm for the sample without pretreatment. This activated sample also has a micropore surface area of 1053m^2/g. With longer pretreatment time, the surface area decreases together with a larger average pore size. Therefore, for the nitric pretreatment, the optimal pretreatment time is 1 hour.

Table 3. Porous Texture Characteristics of the Activated Parent Sample and the Samples Activated after Nitric Acid pretreatment.

Sample	BET surface area, m^2/g	Pore volume, ml/g	Average pore diameter, nm
FA1-851B	890	0.505	2.27
FA1-N1-851	1139	0.615	2.16
FA1-N3-851	1131	0.666	2.36
FA1-N5-851	969	0.558	2.30

3.3 Activation of air treated samples. The samples were pretreated for 1-3 hours in hot air and then steam activated at 850°C for 1 hour. Table 4 presents the porous texture characteristics of the samples activated after air pretreatment (FA1-GP-1, FA1-GP-2, and FA1-GP-3) and the parent sample (FA1-851).

Table 4. Porous Texture Characteristics of the Parent Sample (FA1-851) and Samples Activated After Air Pretreatment (FA1-GP-1, FA1-GP-2, and FA1-GP-3).

Sample	BET surface area, m^2/g	Pore volume, ml/g	Average pore diameter, nm
FA1-851	585	0.326	2.23
FA1-GP-1	732	0.434	2.37
FA1-GP-2	931	0.526	2.26
FA1-GP-3	892	0.546	2.45

When comparing the two samples activated without pretreatment (FA1-851 and FA1-851B), FA1-851 has a much smaller surface area, 585m^2/g (Table 4) than that reported for FA1-851B, 890m^2/g (Table 3). Although both samples were activated at the same temperature and for the same period of time, FA1-851B was obtained from the FA1 fly ash carbon after acid digestion under 65°C, while FA1-851 was obtained directly from FA1 without the acid digestion step. As discussed in Section 3.1, the acid digestion process introduced some oxygen, which will probably improve the reactivity of the sample during activation. Furthermore, for FA1-851 and FA1-851B different reactor designs and operation conditions were used, where FA1-851 was activated under fixed bed conditions, while FA1-851B was activated in a fluidized bed. The data in Table 4 show that the pretreated samples present surface areas up to 59% larger than their untreated counterpart (931 m^2/g with 2 hour pretreatment compared to 585m^2/g without pretreatment). When extending the pretreatment time to 2 hours, the surface area and pore volume for the resultant activated carbon increase to 931m^2/g and 0.526ml/g, respectively, together with an average pore size of 2.26nm. However, extending the pretreatment time to 3 hours resulted in a decrease of the surface area and pore volume.

4. CONCLUSIONS

The two pretreatment methods used here have increased the surface area and pore volume compared to the samples without pretreatment. The results reported here show that both methods are effective to increase the surface area of the resultant activated carbon, especially the micropore volume. The resultant activated carbons have a surface area up to 1139m^2/g (including micropore surface area 1053m^2/g), and pore volume 0.615ml/g (including micropore volume 0.518ml/g). The properties of the produced activated samples will be compared to commercial activated carbons.

ACKNOWLEDGEMENTS

The authors wish to thank the Consortium for Premium Carbon Products from Coal (CPCPC) at The Pennsylvania State University for financial support.

REFERENCES

(1) Tyson, S. S. Unintended effects of NOx emissions control strategies on unburned carbon and CCP marketability, Proceedings of 3rd annual conference on unburned carbon on utility fly ash, 1997, Pittsburgh, 3-5

(2) Hill, R. L.; Sarkar, S. L.; Rathbone, R. F. and Hower J.C. Cement and Concrete Research, 1997, 27(2), 193-204

(3) Zhang, Y.; Maroto-Valer, M.M; Lu, Z.; Andresen, J.M. and Schobert, H.H. Potential non-fuel uses of unburned carbon from fly ash for value added carbon products. Proceedings of 18th annual international Pittsburgh coal conference, 2001, New South Wales, Australia.

(4) Maroto-Valer, M.M.; Taulbee, D.N. and Hower, J.C. Novel separation of the differing forms of unburned carbon present in fly ash using density gradient centrifugation, Energy & Fuels, 1999, 13, 947-953

(5) Zhang, Y.; Maroto-Valer, M.M.; Lu Z.; Andrésen, J.M. and Schobert, H.H. One step activation of coal combustion waste, Proceedings of American carbon society Carbon'01 conference, 2001, CD-ROM Zhang38.1.pdf.

(6) Zhang, Y.; Lu, Z.; Maroto-Valer, M.M.; Andrésen, J.M. and Schobert, H.H. Comparison of high unburned carbon fly ashes from different combustor types and their steam activated products, submitted to Energy & Fuel.

(7) Stoekli, F. and Huguenin, D, Pretreatment and physical activation of acetylene cokes, Fuel, 1994, 73, 1929-1930

(8) Lee. S. H. and Lee, C.D., Influence of pretreatment and activation conditions in the preparation of activated carbons from anthracite, Korean J. Chem. Eng., 2001, 18(1), 26-32.

(9) Serrano-Talavera, B.; Muñoz-Guillena, M.J.; Linares-Solano, A.L. and Salinas-Martînez de Lecea, C. Activated carbons from Spanish coals. 3. Preoxidation effect on anthracite activation, Energy & Fuels, 1997, 11, 785-791

(10) Sing, K.S.W.; Everett, D.H.; Haul, R.A.W. and et al, Reporting physisorption data for gas/solid systems with special reference to the determination of surface area and porosity, Pure & Appl. Chem., 1985, 57(4), 603-609

FORMATION OF CRYSTAL STRUCTURES DURING ACTIVATED CARBON PRODUCTION FROM TURKISH ELBISTAN LIGNITE

Sevil Çetinkaya[1], Billur Sakintuna[2] and Yuda Yürüm[2]

[1]Department of Chemistry,
Hacettepe University,
Beytepe, Ankara 06532, Turkey
[2]Facuty of Engineering and Natural Sciences, Sabanci University,
Tuzla, Istanbul 34956, Turkey

Abstract

In this study, activated carbons were produced from raw, HCl treated and HCl/HF treated (demineralized) Elbistan lignites under various experimental conditions. In carbonization experiments, coals were heated to four different temperatures 700°C, 800°C, 900°C, and 1000°C with a heating rate of 10°C/min, under a nitrogen flow of 100 ml/min for two hours. In activation experiments, coals were first carbonized as described and then activated in carbon dioxide atmosphere at the final carbonization temperature for an additional two hour. The flow rate of pure carbon dioxide was held at 100 ml/min. The BET surface area of the lignite was measured as 3.7 m^2. The highest surface area was measured for the HCl-HF treated sample activated at 1000°C as 1177.6 m^2. Scanning tunnelling microscopy was used to analyze surfaces of carbonized and activated coal samples. X-ray diffractograms indicated the presence of some crystalline carbon structures in the products of carbonization and activation reactions.

Introduction

The problem of environmental protection is continually increasing the importance of treatment of wastewater and gas emissions in order to remove toxic substances. This has renewed interest in the production of activated carbons. Continous increase in demand makes it necessary to make use of different basic materials. Among these, coal is the most widely used so that about 60% of the activated carbon production is obtained from this source [1]. Both high and low rank coals are used for the production of activated carbons [2]. At the same time, activated carbon is manufactured from various raw materials such as peat, polymeric resins, wood and coconut shells [3-6]. The effecting factors for the production of activated carbons are: initial material (used for manufacturing), the heat treatment conditions, reagent gas, residence time, inorganic impurities [7-9].

The total porous structure of an activated carbon is formed by a wide range of pore sizes. The macropores of an activated carbon act as transport pores, enabling the molecules of the adsorptive to reach the smaller pores situated in the interior of the carbon particle. Thus, the macropores are not important from the point of view of the amount adsorbed in them, since their surface area is very low, but they affect the rate of diffusion into the meso and micropores. The micropores constitue the largest part of the internal surface and consequently, most of the adsorption takes places within them; at least 90% of the total surface area of an activated carbon corresponds to the micropores. The mesopores, which branch off from the macropores, serve as passages to the micropores for the adsorptive besides acting as pores where capillary condensation can take place.

The two main steps in the production of the activated carbon are carbonization and activation. The first step is carbonization and is usually performed in an inert atmosphere to remove volatile matter. The coal structure decomposes by the breakage of the least stable bonds within the structure which are methylene , oxygen, and sulfur-bridges between the aromatic building blocks [10]. The char is enriched in carbon and more aromatic in comparison with the raw coal particle. The latter step of activation consist of mild oxidation with such oxidizing gases as steam, CO_2 and air to develop an appropriate pore structure [11].

The aim of this study was the preparation of activated carbons from a low rank lignite. Effect of carbonization and activation temperatures, influence of the mineral matter content of the coal used on the properties os carbons produced were investigated. Changes in surface area, surface structures and crystal structures developed during carbonization and activation were also investigated.

Experimental

Materials

Elbistan lignite was used in this study. Lignite samples were ground and sieved to a particle size less than 100 μm. Proximate and ultimate analyses of the materials are shown in Table1. There are three main steps as demineralization, carbonization and activation of samples at different temperatures during production of activated carbons from materials. To compare the effect of mineral matter on carbonization and activation experiments, the acid treatment was carried out by washing the coal with HCl followed by HF. 18.0 g coal sample was mixtured for 1 hour in 120 ml 5 N HCl solution. Then the treated coal washed in water with warm distilled water. Washed coal was mixtured with 120 ml 22 N HF for 1 hour. The coal was filtered off and washed. Treated (HCl and HF) coals dried at 100°C in an inert atmosphere.

Carbonization Experiments

Raw, HCl and HCl-HF treated coal samples were dried at 100°C an inert atmosphere. 8.00 g sample was placed into a porcelain crucible and then dropped into a furnace purged with ultra high pure nitrogen. Coal samples were heated to four different temperatures 700, 800, 900 and 1000°C with a heating rate of 10°C/min, under a nitrogen flow of 100 ml/min for two hours. After the carbonization experiments, system was cooled to room temperature under the nitrogen flow. Chars were taken out from the system.

Activation Experiments

Carbonized coals were activated under a CO_2 flow of 100 ml/min at the final carbonization temperature for an additional two hours. System was cooled to room temperature under the nitrogen flow. After that, chars were taken out from the system. Chars obtained from carbonization and activation experiments stored for physical characterization tests.

Surface Analysis

Surface areas of activated carbons were determined by ASAP2000 Accelerated Surface Area and Porosimetry system manufactured by Micromeritics Co., USA. Surface area of the samples were determined by using BET equation in the relative pressure range of between 0.05 to 0.25, over five adsorption points.

Scanning Tunnelling Microscopy Studies

A scanning tunnelling microscope which was designed and constructed in our laboratories was used to obtain the images of the coal surfaces. All STM measurements were performed in air at room temperature. The STM was operated at a variable current mode with Pt/Ir sharp tip, with an average tunneling current of 0.5 nA and with a bias voltage in the range of 250-500 mV. Median and Lowpass Filters were used to reduce the noise from the environment and recover the background.

X-Ray Diffraction Measurements

X-ray diffractograms of the samples of carbonized and activated products were measured with a Bruker axs advance powder

diffractometer fitted with a Siemens X-ray gun and equipped with Bruker axs Diffrac PLUS software. The sample was rotated (15 rpm) and swept from 2q = 10º through to 90º using default parameters of the program. The X-ray generator was set to 40kV at 40 mA.

Results and Discussion

The aim of this study was to investigate the effects of acid treatments and temperature on the pore structure of the coal char after the carbonization and activation processes. Nitrogen gas adsorption measurements of raw Elbistan lignite, carbonized and activated lignite were given in Table 2. The BET surface area for raw Elbistan lignite was found as 3.7 m^2/g. Surface areas of HCl and HCl-HF treated lignite samples were measured as 3.8 m^2/g and 2.5 m^2/g, respectively. Treatment with HCl dissolved minerals which were soluble in HCl such as carbonates, silicates, etc. and treatment with HCl-HF eliminated all mineral matters except pyrite. The changes in BET surface areas were due to the removal of inorganic matter which generated high surface area and developed micropores. When the raw and demineralized lignites were carbonized at 700°C, surface areas of chars obtained from carbonization processes increased enormously. The rapid increase in the surface area was attributed to the widening of existing pores or the creation of new pores. As shown in Table 2, surface area of carbonized char (340.4 m^2/g) produced from HCl-HF demineralized lignite greater than those produced from raw and HCl treated lignite (147.6 m^2/g and 243.6 m^2/g). The char obtained from HCl-HF treated lignite at 700°C possessed the higher adsorption capacity than raw and HCl treated chars. It showed that more micro or macropores developed in this sample at 700°C than for the raw and HCl treated lignite and HCl-HF treatment increased the accessible micropores. The similar trends were found at 800°C, 900°C and 1000°C. Surface areas of carbonized chars obtained from HCl-HF treated samples were found to be much higher than those obtained from untreated and HCl treated lignite samples. Surface areas of chars prepared under carbonization at 800°C for raw, HCl and HCl-HF treated samples were 170.8 m^2/g, 254.0 m^2/g and 395.9 m^2/g. The further activation with CO_2, after carbonization, increased the surface area of these samples and changed the surface area of activated chars to 201.3 m^2/g, 283.5 m^2/g and 494.0 m^2/g, respectively.

The variation of carbonization and activation temperature affected the surface area of chars obtained after these processes. Surface areas of carbonized samples obtained at 800°C were greater than that of at 700°C. The increase of the surface areas from 147.6 to 170.8, from 243.6 m^2/g to 254.0 m^2/g, from 340.4 m^2/g to 395.9 m^2/g by increasing the temperature of carbonization from 700°C to 800°C was explained with the loss of volatile matter which leads to development of porosity. So surface areas of chars increased as the carbonization temperature increased. Similar trends were determined in the activated chars. The surface characteristics of the activated carbons were influenced by the activation temperature. The char obtained from activation at 1000°C from HCl-HF treated lignites has the biggest area.

X-ray diffractograms indicated the presence of crystalline carbon structures in the products of carbonization and activation reactions.

Table 1. Proximate and Ultimate Analysis of Elbistan Lignite

Proximate analysis	**%, dry**
Volatiles	44.8
Fixed Carbon	20.9
Ash	34.3
Ultimate Analysis	**%, dmmf**
C	53.0
H	5.8
N	1.8
S	3.6
O (by difference)	35.8

Table 2. BET Surface Areas of Carbonized and Activated Lignite Samples

Sample	**BET Area (m^2/g)**
Raw	3.7
HCl treated	3.8
HCl-HF treated	2.5
Raw- 700°C carbonized	147.6
HCl treated- 700°C carbonized	243.6
HCl-HF treated- 700°C carbonized	340.4
Raw- 700°C activated	213.8
HCl treated- 700°C activated	257.2
HCl-HF treated- 700°C activated	440.5
Raw- 800°C carbonized	170.8
HCl treated- 800°C carbonized	254.0
HCl-HF treated- 800°C carbonized	395.9
Raw- 800°C activated	201.3
HCl treated- 800°C activated	283.5
HCl-HF treated- 800°C activated	494.0
Raw- 900°C carbonized	182.5
HCl treated- 900°C carbonized	328.8
HCl-HF treated- 900°C carbonized	527.9
Raw- 900°C activated	71.5
HCl treated- 900°C activated	377.7
HCl-HF treated- 900°C activated	675.0
Raw- 1000°C carbonized	135.0
HCl treated- 1000°C carbonized	413.9
HCl-HF treated- 1000°C carbonized	562.4
Raw- 1000°C activated	20.9
HCl treated- 1000°C activated	437.2
HCl-HF treated- 1000°C activated	1177.6

References

(1) Wilson J.; *Fuel* **1981,** *60*, 823.
(2) Samaras P.; Diamadopoulos E.; Sakellaropoulas P.; *Carbon* **1991**, *29*, 1181.
(3) Hashimoto K.; Miura K.; Yashikawa F.; Pajares J.A.; *Fuel Process. Tech.* **1993**, *33*, 333.
(4) Rodriguez-Reinoso F.; Lopez-Gonzalez J.; Berenguer C.; *Carbon* **1982**, *20*, 513.
(5) Derbyshire, F.; McEnaney, B.; *Energia* **1991**, *2*, 1.
(6) Clements, A.H.; Matheson, T.W.; Rogers, D.E.; *Fuel* **1991**, *70*, 215.
(7) Wiagmans T.; *Carbon* **1989**, *27*, 13.
(8) Gomez M.J.I.; Garcia A.G.; Martinez de Lecea C.S.; Solano A.L.; *Energy and Fuels* **1996**, *10*, 1108.
(9) Vyaz S.N.; Patwardhan S.R.; Vijayalaksmi S.; Gangadhar B.; *Fuel* **1993**, *72*, 551.
(10) Tromp, J.J.P; Moulijn J.; in New Trends in Coal Science; Yürüm Y., Ed.; NATO ASI Series, 1988, *244*, pp. 305-331.
(11) Rist L.P.; Harrison D.P.; *Fuel* **1985**, *64*, 291.

EFFECT OF OXIDATIVE RESISTANT HYDROGEN DONORS FROM AROMATIC LIQUIDS TOWARDS REDUCED AUTOXIDATIVE AND PYROLYTIC DEPOSITIONS IN THERMALLY STRESSED JET FUEL

John M. Andresen, James J. Strohm and Chunshan Song

The Energy Institute, The Pennsylvania State University,
209 Academic Projects Bldg., University Park, PA 16802, USA

Introduction

In future high-Mach jet aircraft the jet fuel is expected to experience temperatures as high as 480°C (900°F) or above due to its dual role as a coolant for the mechanical and electrical parts of the aircraft (1). Coal-based liquids that are rich in naphthalenes have shown great potential to be transferred into additives for advanced jet fuels that meet the more stringent thermal stability requirements under pyrolytic conditions (2). An additional problem with jet fuels is the presence of dissolved oxygen (from air), which reacts with the fuel in the autoxidative regime (150-250°C) before the fuel and its oxygenated reaction products enter the pyrolytic regime (400-500°C) (3, 4). Oxygen substituted antioxidants are added to the fuel to prevent gum formations in the autoxidative regime while hydrogen donors can be used to prevent thermal degradation of the jet fuel by capturing free radicals generated by pyrolytic cracking of the paraffinic compounds (5, 6). However, traditional antioxidants may not prevent hydrogen donors from interacting with oxygen in the pyrolytic regime thus reducing the thermal stability of the jet fuel by prohibiting the hydrogen donors from stopping the free radical propagation reactions leading to solid deposits (7).

Oxygen substituted hydrogen donors that can be derived from coal liquids, including α-tetralone and α-tetralol, could increased thermal performance of jet fuels both in the pyrolytic and oxidative regime. Scheme 1 outlines one such route and suggests that the utilization of coal derived chemicals can be the key in reaching the thermal stability requirements for future high-Mach jet aircrafts.

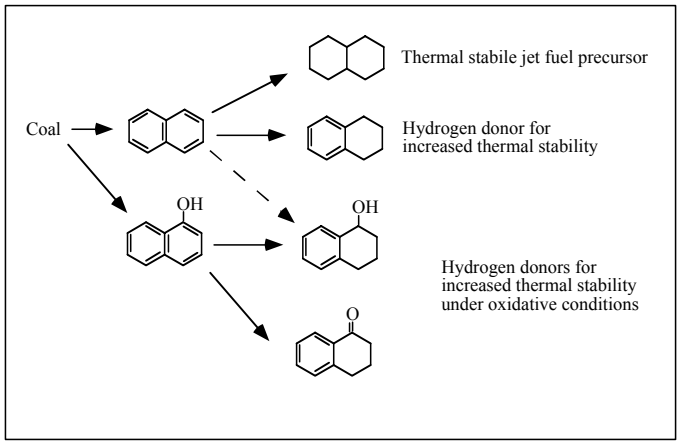

Scheme 1. Possible utilization of coal derived chemicals as a key element in reaching the thermal stability requirements for future high-Mach jet aircrafts.

Firstly, naphthalene is readily obtained from coal. It can then either be fully hydro-treated to decahydronaphthalene and serve as a precursor for thermal stabile jet fuel in itself, or be partially hydro-treated over to hydrogen donors, i.e. tetralin. Further, coal-derived naphthols can be partially hydrogenated to α-tetralone or α-tetralol (8), which may improve the oxidation-resistance both of the fuels and the hydrogen donors derived from coal. Accordingly, this study has investigated the above coal-derived chemicals as benign thermal stabilizers for jet fuels using flow-reactor tests, where the thermal stressing of the high performance liquids was closely related to the actual operational conditions under both non-oxidative and oxidative conditions. Significant improvements in the ability of these modified hydrogen donors to withstand interaction with oxygen dissolved in the jet fuel were observed.

Experimental

The jet fuel studied was JP-8 that is similar to the commercial jet fuel Jet-A. The hydrogen donors tested were α-tetralone (Aldrich, 98%) and α-tetralol (Acros, 97%). For the flow reactor studies the charge tank was purged with high purity O_2 (99.5%) for the autoxidative studies and high purity N_2 (99.995) for the pyrolytic experiments. A liquid hourly space velocity (LHSV) of 450 was used. A silcosteel tubing was used to avoid secondary surface reactions and the maximum bulk liquid fuel temperature at the exit of the furnace was measured by a stripped thermocouple inserted into the tube. The GC/MS traces were reported according to this exit temperature. The GC/MS analysis was conducted on the liquid products using a Shimadzu GC-174 coupled with a Shimadzu QP-5000 MS detector. The column used was a Restek XTI5 column with a coating phase of 5% diphenyl / 95% dimethyl polysiloxane and was heated from 40 to 290°C with a heating rate of 6°C min^{-1}. The carbon deposit analyses were carried out using a LECO RC 142 multiphase carbon analyzer on 2 cm pieces of the flow reactor tubing.

Results and Discussion

Figure 1 shows the GC/MS traces of JP-8 prior to stressing (bottom), stressed under O_2 at 772°C for 3 hr without addition of hydrogen donors (middle), and with addition of candidates for coal-derived hydrogen donors (top). When stressed without hydrogen donors there is a significant production of aromatic compounds and a tremendous reduction in the paraffinic content for the JP-8. Accordingly there is a significant boost in the thermal stability of the jet fuel JP-8 when a mixture of the hydrogen donors α-tetralone and tetralin was added to the jet fuel as shown from the GC/MS traces in Figure 1. The addition of α-tetralone seems to reduce the impact of oxygen on the JP-8 and also to enhance the overall performance of the tetralin added.

Further, the hydrogen donors inhibit the formation of 3 and 4 ring aromatic compounds that are clearly present for the JP-8 stressed alone (Figure 1). These compounds are mainly associated with the formation of solid deposit (3). This is also illustrated in Figure 2 where the solid deposit along the fuel line is compared. The initial length at 8 cm corresponds to the inlet temperature around 25°C. The first peak at 25 cm indicates autoxidative deposition while the deposit above 50 cm derives from pyrolytic deposit. Clearly for the JP-8 stressed alone there is a significant formation of deposit in both the autoxidative and pyrolytic regimes. The combination of α-tetralone and tetralin clearly helped preventing both deposition of oxygenated compounds as well as solid deposit at higher temperatures.

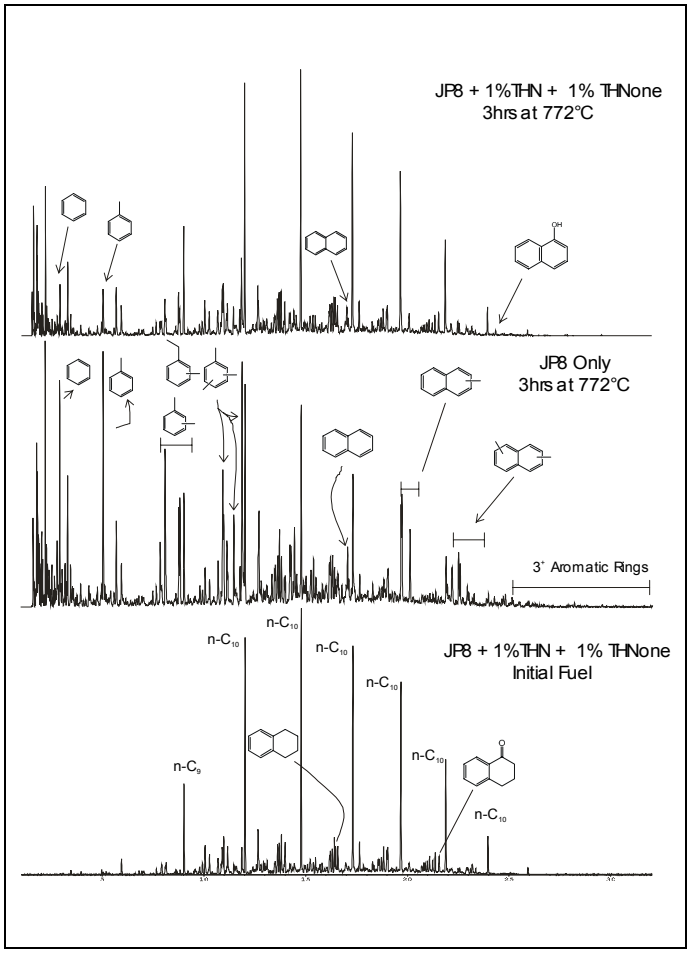

Figure 1. Comparison of GC/MS traces for JP-8 prior to stressing (bottom), stressed under O_2 at 772°C for 3 hr without addition of hydrogen donors (middle), and with addition of candidates for coal-derived hydrogen donors (top).

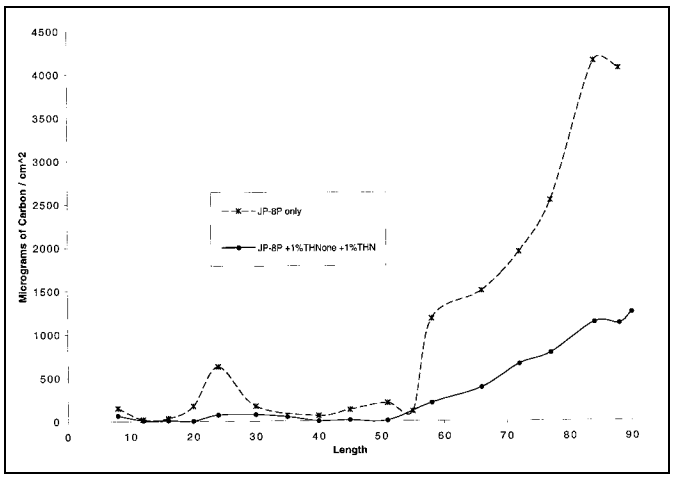

Figure 2. Comparison of the solid deposit along the fuel line for JP8 with and without hybrid donor stressed at 772C for 3 hrs in a flow reactor under oxygen.

Conclusions

The use of oxygenated hydrogen donors, such as α-tetralone, significantly increased the thermal stability of the jet fuel JP-8 under oxidative conditions. Further, the mixture of the hydrogen donors α-tetralone and tetralin suppressed the formation of aromatic compounds during stressing of the jet fuel JP-8, especially 3 and 4 ring aromatics. In addition, the use of α-tetralone and tetralin reduced both the autoxidative and pyrolytic solid deposition from the JP-8 jet fuel in the fuel lines studied.

Acknowledgement. The authors wish to thank the U.S. Air Force Office of Scientific Research for financial support. We are grateful to Prof. Harold H. Schobert form Penn State and to Mr. William Harrison, Dr. Cindy Obringer and Dr. Tim Edwards of the U.S. Air Force Wright Laboratory for helpful discussions.

References

(1) Edwards, T., Prepr. - Am. Chem. Soc. Div. Petrol. Chem. 1996, 41(2), 481.
(2) Song, C.; Eser, S.; Schobert, H.H.; Hatcher, P.G., Energy & Fuels 1993, 7, 234.
(3) Andresen, J.M.; Strohm, J.J.; Sun, L.; Song, C., Energy & Fuels 2001, 15, 714.
(4) Song, C.; Eser, S.; Schobert, H.H.; Hatcher, P.G., Energy & Fuels 1993, 7, 234.
(5) Hazlett, R.N., Thermal Oxidative Stability of Aviation Turbine Fuels, ASTM, Philadelphia, PA; 1991.
(6) Andresen, J.M.; Strohm, J.J.; Coleman, M.M.; Song, C. Prepr. - Am. Chem. Soc., Div. Fuel Chem. 2000, 45(3), 454.
(7) Strohm, J.J.; Andresen, J.M.; Song, C., Prepr. - Am. Chem. Soc., Div. Fuel Chem. 2001, 46(2), 487.
(8) Shao, J.; Holtzer, G.; Song, C., Prepr. - Am. Chem. Soc. Div. Petr. Chem. 2000, 45(1), 18.

OXIDATION OF BITUMINOUS COAL IN ALKALINE SOLUTION WITH FATTY ACID AS PROMOTER

Zhang Qiu-min Guan Jun Zhao Shu-chang Guo Shu-cai

Coal chemical institute of Dalian University
of Technology, Dalian 116012 China

Introduction

Coal has several positive attributes when considered as a feedstock for aromatic chemicals, specialty chemicals, and carbon-based materials. Substantial progress in advanced polymer materials, incorporating aromatic and polyaromatic units in their main chains, has created new opportunities for developing value-added or specialty organic chemicals from coal.

Coal oxidation in alkaline solution can directly obtain a mixture so-called coal acid (CA), aromatic carboxylic acid are mainly contained. Among them the major part is benzene ploycarboxylic acids, which are quite useful. But the mixtures are too complex to be completely separated. The recent researches indicated that selective decarboxylation and isomerization can extend the utilization of coal acid by converting them into value-added chemicals such as terephthalic acid, benzene tetracarboxylic acid and simple mixture of benzene dicarboxylic acid ect.

Based on this point of view a new method including oxidation of bituminous coal followed by coal acids isomerization to producing Terephthalic acid. The work was focused on the influence of fatty acid on coal oxidation by oxygen and alkaline solution. Based on it, other reaction conditions are also investigated.

Experimental

Two coals (DT coal and CT coal), which have great different in coalification, had been used in this work. Table 1 shows the analysis result.

Table 1. Analysis of Samples

	Proximate analytical %			Ultimate analytical % (daf)			
Sample	Mad	Aad	Vdaf	C	H	N	S
DT COAL	3.52	3.29	30.61	84.06	4.65	0.78	0.41
CT COAL	1.72	10.65	13.09	90.56	3.99	1.39	1.37

Coal is oxidized by oxygen and alkaline solution in an autoclave by adding fatty acid as promoter. Discharge materiel after cooling, separate coal cinder (unreacted coal and mineral matter) by filtration. Filter liquor is acidized to PH=3 by concentrated sulphuric acid, separate deposition (humic acids) by another filtration. Then the filter liquor is acidized to PH=1.5, thus water soluble acids dissociated. Coal acid can be obtained after except the solution by butanone and desiccate butanone by vacuum drying. The colors of coal acids are from yellow to brown.

Coal acids were analyzed both qualitatively and quantificationally by gas chromatograph after esterification by diazomethane.

Results and discussion

Promoter. The activity of acetic acid and propanoic acid are appraised under fixed oxidation conditions of temperature 270 °C, reaction time 2h, ratio of alkali to coal 3 to 1, CO_2 initial pressure 6.0Mpa, water to coal ratio 6 to 1, in K_2CO_3 solution, aiming at the yield of CA. Results are shown in **Figure 1.**

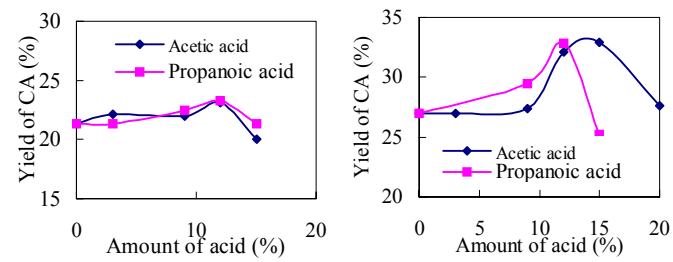

A---DT COAL B---CT COAL

Figure 1. Yield of CA from different amount of promoter by coal oxidation in K_2CO_3 solution

The result indicates that both acetic acid and propanoic acid can promote coal oxidation a lot but the activities of the two promoter and the influences on different coal are a little difference. The optimum amount of the is about 12%, and the yield of CA for DT coal increased from 21.3% to 23.1% with acetic acid, and to 23.3% with propanoic acid, compared to that without promoter.

For CT coal, the yield of CA increased from 27.0% to 32.95% by adding acetic acid, and to 32.8% by propanoic acid, which is a 22% increase relatively.

For compare the activities in different alkaline solution, an oxidation experiment has done with DT coal and CT coal adding acetic acid as promoter in KOH solution. The conditions are similar except for ratio of alkali to coal (2 to 1) and ratio of water to coal (5 to 1). Figure 2 shows the results.

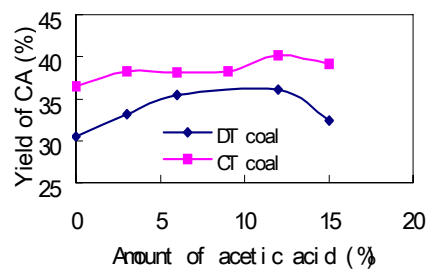

Figure 2. Yield of CA from different amount of acetic acid by coal oxidation in KOH solution

As shown in **Figure 2**,the influences of amount of acetic acid to the yield of CA are similar to those in K_2CO_3. The optimum amounts of the promoter for two coals are also about 12%. For DT coal oxidation under optimum conditions, the yield of CA grew from 30.5% (daf) to 36.1% (daf), which is a 18.5% increase relatively. For CT coal oxidation, the yield of CA grew from 36.5% (daf) to 40.0% (daf) , which is a 9.9% increase relatively.

Reaction temperature. Since the activities of the two promoters are about the same, only acetic acid used as the promoter here.

Figure 3 shows the influences of reaction temperature to the yield of CA under the conditions motioned above, except that the ratio of alkali to coal is 4 to 1 and the amount of acetic acid is 12%.

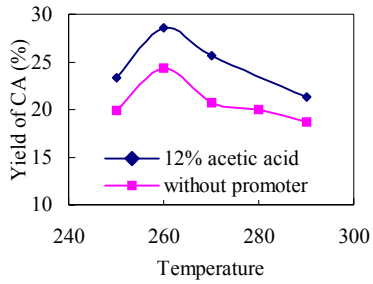

Figure 3 Change in yield of CA through the temperature

The yield of CA rose sharply with temperature grew from 250℃ to 260℃, and then declined. The optimum temperatures are 260℃. Under optimum temperatures, the yield of CA grew from 23.33% (daf) without acetic acid to 28.6% (daf) with 12% acetic acid as promoter, which is an 18% increase relatively. The yields of CA with promoter are higher in the range 250～290 °C.

Ratio of alkali to coal .Figure 4 shows the influences of ratio of alkali to coal to the yield of CA under the conditions motioned above, in K_2CO_3 solution.

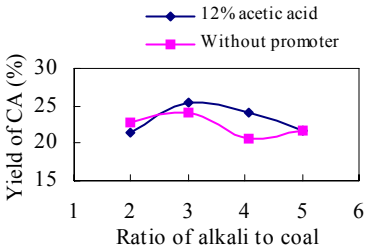

Figure 4. Change in yield of CA through the ratio of alkali to coal

Yield of CA through the ratio of alkali to coal first rose, via maximum, and then declined. With or without promoter, the optimum ratios of alkali to coal are 3～4. The yields of CA with promoter added are higher than those blank one in the whole range.

Reaction time. Figure 5 shows the influences of reaction time to the yield of CA under the conditions motioned above, except that the ratio of alkali to coal is 4 to 1 and the amount of acetic acid is 12%.

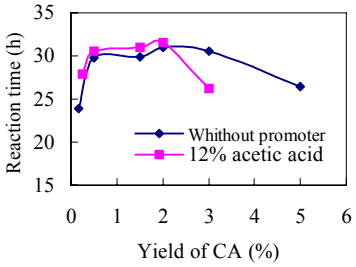

Figure 5. Change in yield of CA through the reaction time

The yield of CA grew sharply before half an hour, and then fixed as time goes through. With or without promoter the maximum yield of CA are similar. The yield of CA declined after 5h without promoter and declined after 3h with promoter, this shows promoter can promote the oxidation.

Composition of coal acids. This paper merely analyzed composition of coal acids with chromatogram under optimum amount of acetic acid as promoter. BPCA in coal acids are qualitatively and quantitatively analyzed, which are the calculations of composition of coal acids and yields of BPCA based on, as shown in table 2.

Table 2. Composition of Coal Acids

compositition		DT COAL (added in acetic acid)		CT COAL(added in acetic acid)	
		0%	12%	0%	12%
Yield of CA %(daf)		24.33	28.67	36.54	40.14
Benzoic acid		0.48	0.73	0.14	1.16
Benzene dicarboxylic acid	1,2	5.79	9.44	11.93	17.34
	1,4	—	—	1.32	1.81
	1,3	—	—	0.38	2.11
Benzene tricarboxylic acid	1,2,3	4.56	6.79	6.13	10.96
	1,2,4	6.28	8.71	10.56	12.66
	1,3,5	0.69	5.28	0.30	0.26
Benzene tetracarboxylic acid	1,2,3,4	8.03	14.23	11.09	17.85
	1,2,4,5	4.77	6.52	6.18	7.42
	1,2,3,5	3.10	4.63	3.67	4.40
Benzene pentacarboxylic acid		—	—	7.39	9.93
Benzene hexacarboxylic acid		—	—	1.54	1.53
Total		33.7	56.89	60.62	87.68
Yield of BPCA % (daf)		8.20	16.31	22.13	35.18

* in K_2CO_3 medium **in KOH medium

Table 2 shows composition of coal acids and yields of BPCA from DT COAL oxidation in K_2CO_3 medium and CT COAL oxidation in KOH medium. DT COAL oxidation compared with no promoter, the BPCA content of CA increased enormously by adding 12% acetic acid in rose from 33.7% to 56.89%, which is a 68.8% increase relatively. The yields of BPCA to coals grew from 8.2% to 16.31%, which is a 98.8% increase relatively. CT COAL oxidation compared with no promoter, the BPCA content of CA increased also enormously by adding 12% acetic acid in rose from 60.6% to 87.8%, which is a 44.7% increase relatively. The yields of BPCA to coals grew from 22.1% to 35.2%, which is about 60% increase relatively.

The effect of adding acetic acid at the amount of 12% on coal oxidation is not only it can improve the yield of CA but also it can improve the content of BPCA in CA sharply, which lead to the yields of BPCA to coal increased. This further evidenced that the promoter has directional function to coal oxidation.

Acknowledgment

This work was supported by National Natural Science Foundation of China (29806003)

Reference

1. Song, C.S.; Schobert, H.H., *Fuel Proc. Technol.,* 1993. 34: P. 157-196.
2. Schobert, H.H., Song, C.S., *Fuel*, 2002. 81(1): P 15-32.
3. Salbut,P.D., Mozliwosci, *Przem. Chem.,* 1986. 65(1): P 23-35
4. Zhao shu-chang, Deng Yizhao, *Journal of Dalian University of Technology,* 1994. 34(6): P 682

PREPARATION OF TEREPHTHALIC ACID BY COAL ACIDS ISOMERIZATION

Zhang Qiu-min Guan Jun Zhao Shu-chang Guo Shu-cai

Coal chemical institute of Dalian University of Technology, Dalian 116012 China

Introduction

Coal may become more important both as an energy source and as the source of organic chemical feedstock in the 21st century. Coal has several positive attributes when considered as a feedstock for aromatic chemicals, specialty chemicals, and carbon-based materials. Substantial progress in advanced polymer materials, incorporating aromatic and polyaromatic units in their main chains, has created new opportunities for developing value-added or specialty organic chemicals from coal.

Coal oxidation in alkaline solution can directly obtain a mixture so-called coal acid (CA), aromatic carboxylic acid are mainly contained. Among them the major part is benzene ploycarboxylic acids, which are quite useful. But the mixtures are too complex to be completely separated. The recent researches indicated that selective decarboxylation and isomerization can extend the utilization of coal acid by converting them into value-added chemicals such as terephthalic acid, benzene tetracarboxylic acid and simple mixture of benzene dicarboxylic acid ect.

Based on this point of view this paper provides a new method of non-fuel uses of coal that is Oxidation of Bituminous Coal and Preparation of Terephthalic Acid by Coal Acids Isomerization. Based on it, other reaction conditions are also investigated. The influences of temperature, initial pressure of CO_2, reaction time and amount of catalyst to the yield of TPA are mainly investigated in iosmerization. And the optimum conditions are found out. High-activated cadmium salt is used as catalyst. Coal acids are prepared into kali salt before isomerization.

Experimental

Coal acids for isomerization were the mixture of oxidation product obtained. Using KOH to prepare kali salt of CA and using $CdCO_3$ as catalyst. **Table 1** shows the analyses of mixed coal acids by chromatogram.

Table 1. Analyses of Mixed Coal acids by Chromatogram

Composition		
Benzoic acid		-
Benzene dicarboxylic acid	1,2	9.11
	1,4	-
	1,3	0.8
Benzene tricarboxylic acid	1,2,3	0.98
	1,2,4	7.16
	1,3,5	9.45
Benzene tetracarboxylic acid	1,2,3,4	13.00
	1,2,4,5	6.75
	1,2,3,5	3.98
Benzene pentacarboxylic acid		1.64
Benzene hexacarboxylic acid		10.86
Total		63.73

Use a micro reactor (25ml) isomerizate kali salt of CA, with $CdCO_3$ as catalyst and in CO_2. The product is so-called black powder. Crude TPA can be obtained after dissolve by water, filtration and acidification.

Put the micro reactor in after sand bath stove was adjusted into an appropriate temperature. The temperature of reactor would reach the reaction temperature with in 10 min.

Figure 1 shows the equipment.

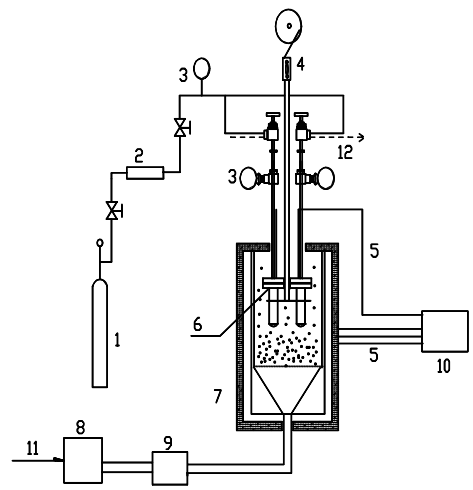

1. CO_2 cylinder 2. Drying tube 3. Pressure gage
4. Bracket 5. Thermoelement 6. Reactor
7. Sand bath stove 8. Air compressor 9.Preheater
10. Control system 11. Air 12. CO_2

Figure 1. The equipment for isomerizatiom

Coal acids and TPA were analyzed by gas chromatogram after esterification by diazomethane. The purity of TPA was analyses by titration at same time.

Results and discussion

Catalyst. The results obtained with fiffrent amount of catalyst ($CdCO_3$) are shown in Figure 2, 470℃, 2h, and CO_2 initial pressure 1Mpa，has investigated.

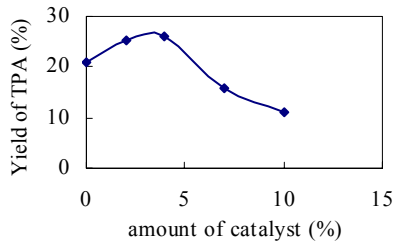

Figure 2. Influence of amount of catalyst to the yield of TPA

As shown in **Figure 2**, the yield of TPA is 20.79% without catalyst $CdCO_3$ at 470℃. As the amount of $CdCO_3$ grows, the yields of TPA grew and reached the maximum yield at 4%. This expresses the beneficial function of isomerization with catalyst. The yield of TPA declined when the amount of catalyst exceeded 4%, which indicates large amount of catalyst would restrain isomerization. Therefore the optimum amount of catalyst is 4%, the optimum yield of TPA is 23.5%.

Initial pressure of CO_2. Figure 3 shows the influence of initial pressure of CO_2 to the yield of TPA with $CdCO_3$ as catalyst(7%), 470 ℃, 2h .

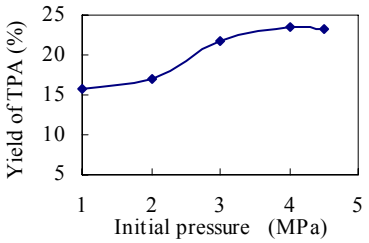

Figure 3. Influence of initial pressure of CO_2 to the yield of TPA

As shown in **Figure 3**, the yield of TPA grew sharply before 3.0MPa,then grew slowly during 3.0-4.0MPa, and then fixed after 4.0MPa. Increase of initial pressure of CO_2 not only added the opportunities of CO_2 molecule impact, but also benefit to carboxylation reaction. Therefore the appropriate pressure of CO_2 is necessary, 4.0MPa is properly.

Temperature. Temperature is the most important factor. Isomerizations proceeded within the scope 410-470℃. To compare the experiment, isomerizations with benzoic acid adding in proceeded at the same time. Figure 4 shows the result.

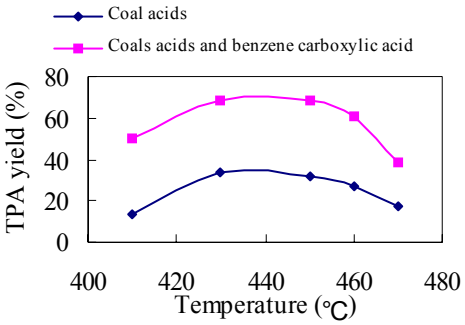

Figure 4 Influence of temperature to the yield of TPA

Figure 4 shows that without adding benzoic acid the yield of TPA grew as temperature rose, maximum yield of TPA occurs at 430℃ -450℃, and then declined. Isomerization is incomplete at low temperature. When temperature is higher than 450℃, polymerization and carbonization occur seriously, the color of production darken, then led to the declination of yield. The optimum temperature(about 450℃) of isomerizating by kali salt of coal acid and kali salt of benzoic acid are similar to that of kali salt of coal acid isomerization only, except that the yield of TPA is much higher. The yield of crude TPA rose from 34.10% to 68.58% by adding kali salt of benzoic acid. The yield of TPA to CA is up to 70% deducting the theoretical yield of BA dispropornation, which is two times of CA isomerization only. It is advisable to add benzoic acid in when the coal acid contains too much high-level benzene polycarboxylic acids.

Reaction time. Figure 4 shows the influence of reaction time to the yield of TPA with $CdCO_3$ as catalyst(7%), 470℃, 2h .

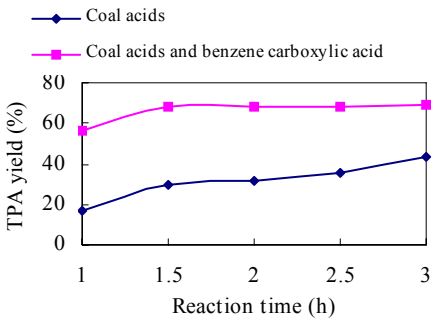

Figure 5 Influence of reaction time to the yield of TPA

The yield of TPA grew as reaction time less than 1.5h and increased a little after 1.5h, as **Figure 5** shows. Isomerizitions of kali salt CA are fundamentally completed therefore the yield of TPA no longer increased. It is confirmed that 2h is the optimum reaction time. The yield of crude TPA also rose more than 100% by adding kali salt of benzoic acid.

Product purification

Crude TPA which purity is about 90% can be obtained after dissolve by water, filtration and acidification. The purity can be further improved by hot water scrubbing and activated carbon discoloring, reaching 99.37% after once and 99.71 after twice.

Conclusion

1.The better conditions of kali salt of coal acid isomerizating are temperature 430-450℃, initial pressure of CO_2, 4.0Mpa, content of catalyst 4%, reaction time 2h. The optimum conditions of isomerizating by kali salt of coal acid and kali salt of benzoic acid are similar to that of kali salt of coal acid isomerization only.

2.The yield of crude TPA to CA is about 34% in case of coal acid isomerizating. It equals to 75% of the theoretical yield to BPCA.

3.The yield of crude TPA is up to 68% when kali salt of coal acid and salt of benzoic acid isomerizating under the best conditions. The yield of TPA to CA is up to 70% deducting the theoretical yield of BA dispropornation, which is two times of CA isomerization only. It is advisable to add benzoic acid in when the coal acid contains too much high-level benzene polycarboxylic acids.

4.The TPA purity can be further improved by refining crude TPA, reaching 99%.

Acknowledgment

This work was supported by National Natural Science Foundation of China (29806003)

Reference

1. Song, C.S.; Schobert, H.H., *Fuel Proc. Technol.,* 1993. 34: P. 157-196.
2. Schobert, H.H., Song, C.S., *Fuel*, 2002. 81(1): P 15-32.
3. Salbut,P.D., Mozliwosci, *Przem. Chem.,* 1986. 65(1): P 23-35
4. Zhao shu-chang, Deng Yizhao, *Journal of Dalian University of Technology,* 1994. 34(6): P 682

New Methods for Characterization of Products from Micro-activity Testing (MAT) of Residue from Estonian Shale Oil

Yevgenia Briker, Zbigniew Ring, and Angelo Iacchelli

National Centre for Upgrading Technology, 1 Oil Patch Drive, Devon, Alberta T9G 1A8, Canada

Abstract

The utilization of fossil fuels is going through drastic changes due to growing transportation fuel consumption and stricter environmental regulations. Both will result in an increase in the proportion of diesel fuel produced from synthetic crude oils, which in turn will lead to the expanding of existing and the development of new processing technologies. Most of the crude oils used for fuel production consist predominantly of hydrocarbons and contain only relatively small amounts of sulphur, oxygen, and nitrogen. Shale oils, in contrast, can contain large amounts of organic sulphur and /or oxygen compounds. Therefore, during processing of shale oils, in addition to making fuels, there may be an opportunity to extract valuable chemicals. Knowledge of the physical and chemical properties of these hydrocarbon materials is very important for the development of technologies necessary to fully utilize these materials.

In this paper we discuss the possibility of increasing the utilization of Estonian shale oil by application of the fluid catalytic cracking (FCC) process to the atmospheric residue fraction boiling between 320 and 750°C. FCC, being the most common conversion process in the oil refining industry, uses micro-activity testing (MAT) as its research tool to test various feedstocks and catalysts. The main emphasis in this paper is on the development of characterization methodology to analyze mono- and di-hydric phenols in MAT products that are inherently produced in very small amounts (<2mL) and have a wide boiling range.

Introduction

Over the past 50 years, fluid catalytic cracking (FCC) has been the most important heavy gas oil conversion process. FCC generates products ranging from gases and light olefins, through naphtha to light cycle oil, and heavy cycle oil. In this paper we discuss the possibility of applying the FCC process (through the micro activity test - MAT) to the atmospheric residue derived from an Estonian shale oil. This oil is the source of fuel oils and synthetic gas, but it could also be a source of a number of chemicals such as antiseptic oil for wood impregnation, electrode coke, rubber softeners, casting binders, etc. The shale oil phenols are used as feedstocks for epoxy and other resins, and as glueing compounds, rubber modifiers, synthetic tanning agents, etc. The most valuable phenols are in the 200-360°C boiling range. Therefore, there is an interest in exploring the behavior of heavy residue in the cracking environment, particularly in terms of the production of phenols in the useful boiling range.

A characterization procedure described by Čherný et al. (1) was adopted as the basis of the new separation procedure developed here for quantification and identification of various fractions from the total liquid product from catalytic cracking of residue from an Estonian shale oil. The extrography procedure was replaced with open column chromatography, and the elution solvents were used in the order reported earlier (2). A different way of calculating the material balance was proposed for the full boiling-range material.

Experimental

The residual material derived from an Estonian shale oil was used as the feed for the macro-activity testing. Some properties of the feed and the total liquid product (TLP) are presented in Table 1. Simulated distillation curves are shown in Figure 1.

Table 1. Properties of feed and TLP from MAT testing of residue from Estonian shale oil

Feed		**Product**	
BP, ^{o}C	**%OFF**	**BP, ^{o}C**	**%OFF**
IBP (301.2^{o}C)	0.5	IBP (84.5^{o}C)	0.5
FBP (750.0^{o}C)	99.5	FBP (587.5^{o}C)	99.5
IBP-360°C	4.16	IBP-200°C	13.81
360-525°C	60.91	200-360°C	36.69
Density, g/mL	1.0660	Density, g/mL	1.0106

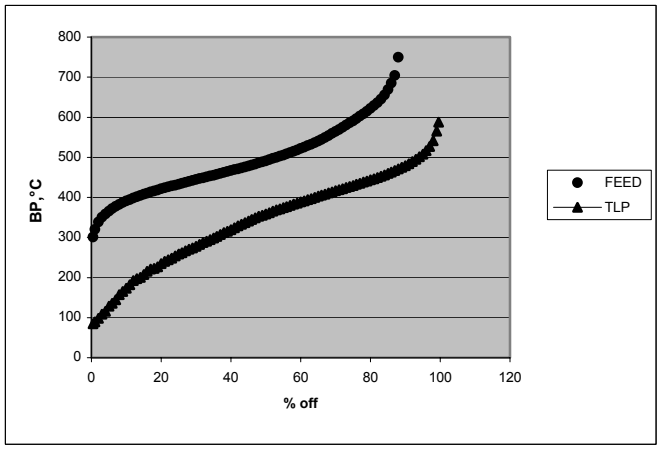

Figure 1. Simulated distillation of feed and TLP

The total liquid product (TLP) from the MAT was separated using the modified liquid chromatography method. This method was based on the extrography method described in the literature (1). The extrography column that was equipped with plunger pump and filled with basic alumina and silica in the original method was replaced with an open glass column (13.5-mm I.D. and a 450-mm length) filled with silica gel. Silica gel from Fisher Scientific (28-200 mesh) was activated for 12 h at 140°C. Its activity was adjusted by the addition of 4wt% water.

While in the original method, the analyzed sample was evenly distributed throughout the whole surface of the silica gel prior to extraction; in our modified method the total amount of TLP (0.7286 g) was applied on top of the column. The elution solvents were used in order of increasing polarity (2). Since TLP contained some of the material boiling below 200°C (13.81wt%), the calculation of material balance using gravimetric determination would not be suitable. Removal of solvents on vacuum rotary evaporator and vacuum dryer would result in the loss of light ends. In our case, the solution of each fraction was reduced to a known volume by using a mild rotary evaporation and a nitrogen gas sweep. The fractions were further analyzed by gas chromatograph-flame ionization detector (GC-FID). Quantification of fractions in the specified temperature intervals was performed by using the calibration standards prepared from previously separated fractions. All fractions were quantified only from 200°C, therefore the slight loss of the light ends encountered

during the nitrogen purge did not affect the results. The retention time calibration was performed by analyzing the normal paraffin standards at the identical conditions.

Results and Discussion

Micro activity testing of the material derived from an Estonian shale oil with IBP 301.2°C and FBP 750.0°C, yielded a product with IBP 84.5°C and FBP 587.5°C. From the simulated distillation data it was calculated that 13.81wt% of the material boiled below 200°C in the product. The yield of the material boiling between 200-360°C was 36.69wt%, while there was only 4.1wt% below 360°C in the feed. This temperature interval was important since it represented the fraction that might contain the phenolic compounds of interest, produced by cracking of heavy material.

The results of LC separation of TLP are presented in Table 2. The retention times for 200°C and 360°C were 5.727 min and 17.482 min respectively. The chromatograms of each fraction were integrated between these two points and the results were balanced with the results from the simulated distillation data.

According to the original method, the phenolic fractions are represented by fraction 4 (monohydric phenols) and fraction 5 (dihydric phenols). The GC-FID chromatograms of these fractions are shown in Figures 2 and 3.

Table 2. Results of LC separation of TLP from MAT testing of residue from Estonian shale oil

			200 - 360°C	200 - 360°C	IBP - 200°C	360°C - FBP	IBP - FBP
			GC-FID	SimDist	SimDist	Sum	Sum
Fr. No	Solvent	Designation	Recovery, wt%	wt%	wt%	wt%	wt%
Fr.1	Hexane	Saturates	2.3				
Fr.2	Toluene	Aromatics	24.6				
Fr.3	Chloroform	Esters+	0.6				
Fr.4	Chlor./Dieth.Ether	Monophenols	5.2				
Fr.5	THF/Methanol	Diphenols	3.3				
Fr.6	Methanol	Polars	0.7				
Total			36.7	36.7	13.8	49.5	100.0

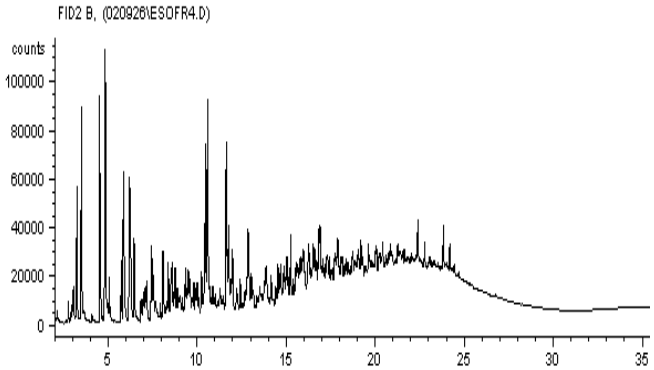

Figure2. GC-FID chromatogram of Fraction 4

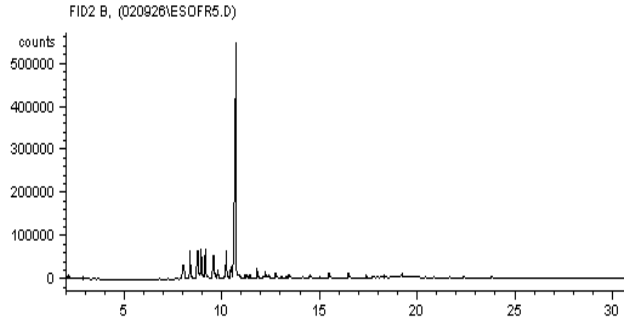

Figure 3. GC-FID chromatogram of Fraction 5

The combined phenolic fraction was the second largest (8.5wt%) after the aromatic fraction (24.6wt%). Both were analyzed by gas chromatography-mass spectrometry (GC-MS-equipped with mass selective detector from HP) with the library search option. Most of the peaks in Fraction 4 were designated as phenols with the largest peaks being cresols and 2,5-dimethyl phenol at 6.78 min, 6.86,min, 7.10,min, and 7.57, min. The rest of the chromatogram represents the variety of di- and tri-methyl phenols. There were no acids found in this fraction. Apparently, they decomposed during cracking. No clear assignments for peaks were given by the GC-MS in Fraction 5 due to a very low concentration of individual compounds. The largest outstanding peak was designated as phenol, 2,5-bis(1,1-dimethyl)-4-methyl.

Conclusions

Cracking of the residual material derived from an Estonian shale oil with a density 1.066 g/mL resulted in the production of a lighter liquid product with the density 1.0106 g/mL, and also resulted in quite a significant shift in the boiling point range. The starting material boiling between 301.2oC and 750oC was converted to a lighter material boiling between 84.5oC and 587.5oC.

The usefulness of this material in terms of the presence of phenolic compounds was verified by applying the separation technique, which was adapted from the original extrography method and modified into a simplified open column chromatography procedure. The new procedure was developed for analyzing the samples having a full boiling range.

The results of separation showed that useful phenols were produced as the result of catalytic cracking.

The project is ongoing and the full extend of catalytic cracking on the production of phenols and other streams at different conditions will be investigated, and the results will be published in future publications

Acknowledgment.
Partial funding for NCUT has been provided by the Canadian Program for Energy Research and Development (PERD), the Alberta Research Council (ARC) and the Alberta Energy Research Institute (AERI). This paper was partially funded by VKG of Estonia.

References

(1) J. Čherný, H. Pavlicová and V. Machovič, "Compound-class fractionation of coal-derived liquids by extrography", FUEL, 1990,Vol 69, 966-971.

(2) M.M. Boduszynski, R.J. Hurtubise and H.F. Silver, Anal. Chem., 1982, 54, 375.

Table 3. Peak assignments for Fraction 4 of TLP from MAT of Estonian shale oil

Peak RT,min	Assignation
5.70	phenol
6.78	phenol,2-methyl
6.86	phenol,2-methyl
7.10	phenol,3-methyl
7.57	phenol,2,5-dimethyl
8.03	phenol,2-ethyl
8.18	phenol,3,5-dimethyl
8.47	phenol,3-ethyl
8.60	phenol,2,3-dimethyl
8.84	phenol,2,4-dimethyl
8.99	phenol,2,3,6-trimethyl
9.32	phenol,2-ethyl-5-methyl
9.39	phenol,2-ethyl-6-methyl
9.47	phenol,3-(1-methylethyl)-
9.53	phenol,3-ethyl-5-methyl
9.77	phenol,2-(1-methylethyl)-
9.88	phenol,3,4,5-trimethyl
9.94	phenol,2,4,6-trimethyl
10.58	4-allylphenol
10.95	phenol, 3,5-diethyl
11.90	6-methyl-4-indanol
12.44	phenol, 4-(3-methyl-2-butenyl)-
13.06	1-naphthalenol
13.18	2-naphthalenol
14.33	1-naphthalenol,2-methyl
14.39	1-naphthalenol,3-methyl
14.64	1-naphthalenol,4-methyl
15.30	benzaldahyde, 2-chloro-6-fluoro-
15.48	1-naphthol, 5,7-dimethyl
16.37	2-hydroxy-1-naphthalenepropanol

.

Upgrading of Extra-Heavy Crude Using Hydrogen Donor under Steam Injection Conditions. Characterization by Pyrolysis GC-MS of the Asphaltenes and Effects of a Radical Initiator

Cesar Ovalles, Pablo Rengel-Unda, Jenny Bruzual and Arelys Salazar

PDVSA-Intevep
P.O. Box 76343, Caracas
Venezuela, 1070A
Email: ovallesc@pdvsa.com

Introduction

The development of a downhole upgrading process has always attracted the attention of the oil industry, mainly because of its advantages compared with aboveground counterparts. Lower lifting and transportation costs from the reservoir to the refining centers could be achieved. A volumetric well production increase can easily be achieved. A decrease in the consumption of costly light and medium petroleum oils used as diluents for heavy and extra-heavy crude oil production could be also obtained. Finally, higher value products (reduced viscosity and asphaltene, sulfur and heavy-metal content), with the concomitant reduction of refining severity would generate additional benefits.[1-5]

However, technical challenges involve in the developing of an underground upgrading process are enormous. First at all, downhole processes are difficult to control and monitor under reservoir conditions. This is probably the main reason why these technologies are not widely used at the present time. Also, each well and reservoir requires individual treatment. This will increase the complexity of the field operations.[5]

Recently, a new concept was developed involving the underground addition of a hydrogen donor additive (tetralin), which in the presence of steam, natural formation (catalyst) and methane (natural gas) leads to extra-heavy crude oil upgrading.[5,6] This process can be coupled to a steam stimulation process with 70-80% hydrogen donor recycling.[5,6] In this work, the characterization of the asphaltenes by pyrolisis GC/MS is presented in order to gain insight into the mechanisms occurring during the extra heavy crude oil upgrading process. Also, the effect of a radical initiator on the properties of the upgraded products is also studied.

Experimental

The extra-heavy crude oil from the Orinoco Belt (Hamaca) used has the following properties: 9.1°API Gravity, 22.0% asphaltenes (heptane), 14.2% Carbon Conradson, viscosity (80°C) = 1810 ± 150 cP, 500°C$^+$ residue = 71%, 7500 ppm nitrogen, 3.75% sulfur, 450 ppm of vanadium and 102 ppm of nickel. All percentages are reported by weight. A mixture of 1:1.7 tert-amyl-methyl ether (TAME) and methyl-tert-butyl ether (MTBE) was evaluated as radical initiator. The above mixture was used in a 1:1 ratio with hydrogen donor (tetralin).

Upgrading reactions were carried out in a stainless-steel 300-ml batch Parr reactor equipped with a heating mantle and a temperature controller. In a typical experiment, the reactor was loaded with sand (containing 10% of crude oil), water, and tetralin at a weight ratio of 10:1:1, respectively. The reactor was heated at 5°C/min to 315°C, generating a final pressure of approximately 1600 psi for 24 h (850 psi initial CH_4 pressure). After completing the experiment, water and tetralin were separated from the oil sand by vacuum distillation at 280°C. The residual tetralin was less than 0.05%, as revealed by H^1 NMR of the distillated fraction. The reactor was then cooled to room temperature, and the remained oil was removed from the sand by solvent extraction with dichloromethane.

Crude oil mass balances were in the 93-99% w/w range. Percentages of recovery of tetralin were in the 92-105% range due to distillation of light fractions from the upgraded crude oils. Each experiment was repeated at least three times, the results presented herein correspond to an average of at least two different reactions with 90% confident using t-Student's value.

The asphaltene samples were isolated by precipitation with 50:1 v/v heptane:crude ratio followed by drying at 80°C for 1 h. The Py-GC/MS analyses were carried out in a RUSKA analyzer, model Thermachrom, coupled to a mass selective detector Hewlet-Packard, model HP5971B. Weighed samples were heated in a porous fused quartz crucible with continuous gas (helium) flowing through it. The asphaltene samples were heated from 70 to 600°C. Species evolved during the heating process were entrained in the flow and delivered to cryogenically cooled gas chromatograph (GC). Once sample heating is complete, the capillary column (DB-5, 30 m x 0,25 mm, 0,25 μm film thickness) is heated and trapped species were eluted into the mass analyser. The temperature program was 11 min at -35 °C, followed by a 10°C /min ramp rate to a final temperature of 300°C, the column was held at this temperature for 30 min. The mass spectrometer was operated at 70 eV in the electron impact mode. The mass range was from 50 to 650 amu. The pyrograms were analyzed by using the algorithms reported by Robinson[7] and Piemonti.[8]

Results and Discussion

Table 1 shows the effect that radical initiator has on the extra-heavy crude oil upgrading process. A mixture of 1:1.7 TAME/MTBE was chosen because of its low cost (being refining stream) and the known ability to generate free radicals under low severity conditions.[9] These additives were evaluated in conjunction with tetralin or by themselves.

Table 1. Effects of a Radical Initiator on the Upgrading of Extra-Heavy Crude Oil in the presence of tetralin under Steam Injection Conditions (315°C)[a]

Additive (Reaction time)	°API (±0.5°)	% Asphalt.[b] (±0.3%)	Visc.[c] (cP) at 80°C
Hamaca Crude Oil	9.1	22.0	1810 ± 50
Tetralin-Control Exp. (0 h)	10.2	20.7 (6%)	1770 ± 160
Tetralin (24 h)	14.7	18.0 (18%)	110 ± 40
Tetralin + TAME/MTBE[d] (24 h)	15.0	18.2 (17%)	800 ± 140
TAME/MTBE[e] (24 h)	11.8	19.5 (11%)	1100 ± 300

[a]Experiments were carried out under batchwise conditions, no stirring, at different reaction times. See experimental for details. Results are the average of at least two different reactions. [b]Weight percentages of asphaltenes. Numbers in brackets indicate conversions with respect to the original crude oil. [c]Viscosity of the upgraded crude oil in cP measured at 80°C. Results presented with 90% confident using Student's value. [d]Mixture of 1:1.7 tert-amyl-methyl ether (TAME) and methyl-tert-butyl ether (MTBE) was used in a 1:1 ratio with respect to tetralin. [e]Same radical initiator as before but no tetralin was used.

Firstly, control experiment (0 h) was carried in order to determine the effects of sample handling procedure (Table 1). The results showed an increase of only 1°API, 6% reduction of

asphaltenes, and slight decrease on viscosity (measured at 80°C). This is mainly due to the time needed to reach the distillation temperature (280°C). This time was approximately 30-45 min.

As observed in Table 1, the upgraded crude oil obtained from a mixture of hydrogen donor/TAME/MTBE has similar API gravities (ca. 15°) and asphaltene conversion (17-18%) and somehow a higher viscosity (800 vs 110 cP) than the one from the experiment with tetralin. In contrast, the upgraded crude oil generated by the use of the radical initiator alone present lower API gravity (12°API) and percentage of asphaltenes conversion (11%) with the concomitant higher viscosity (1100 cP) than the previous experiments. The latter experiment indicates that the presence of a hydrogen donor is necessary in order to maximize the properties of the upgraded crude oils, as reported in the literature.[4-5]

The best results were obtained when tetralin was used, as seen on Table 1. These indicate a general trend, i.e. effective crude oil upgrading can be achieved downhole at steam injection conditions, despite the intrinsic experimental error.

Table 2. Characterization by Pyrolysis GC-MS of the Asphaltenes Isolated from the Upgrading of Extra-Heavy Crude Using Hydrogen Donor under Steam Injection Conditions (315°C)[a]

Types of Hydrocarbons[b]	Control Exp.[c]	Tetralin[d]	Tetralin + TAME/MTBE[e]	TAME / MTBE[f]
Total Saturates	**46.9**	**47.2**	**48.9**	**47.8**
Paraffins	9.0	9.8	10.6	9.9
Monocycloparaffins	9.1	9.7	10.3	9.8
Dicycloparaffins	8.1	9.1	9.3	9.4
Tricycloparaffins	20.6	18.6	18.6	18.7
Total Aromatics	**53.1**	**52.8**	**51.1**	**52.2**
Monoaromatics	21.5	20.8	20.6	21.3
Benzenes	6.8	6.7	7.0	6.8
Naphtenebenzenes	6.1	5.9	5.6	5.9
Dinaphtenebenzenes	8.6	8.2	8.0	8.6
Diaromatics	11.2	10.7	10.2	10.5
Naphtalenes	3.0	3.1	3.0	3.4
Acenaphtenes /Dibenzofuranes	3.0	2.7	2.4	2.5
Fluorenes	5.3	4.9	4.8	4.7
Triaromatics	2.6	3.2	3.0	3.3
Phenantrenes	1.0	1.4	1.5	1.5
Napthenephenantrenes	1.6	1.8	1.5	1.8
Tetraromatics	4.2	4.4	4.2	4.2
Pyrene	2.9	2.9	2.9	2.9
Crysene	1.3	1.5	1.3	1.2
Pentaromatics	0.3	0.3	0.1	0.2
Aromatic tiophenes	12.0	12.0	11.6	11.5
Non identified	1.3	1.4	1.3	1.2

[a]Same experimental conditions as Table 1. [b]Weight percentage as determined by INT101 algorithm. [c]Control experiment with 0 h at 315°C. [d]Exp. were carried out using tetralin as hydrogen donor at 315°C for 24h. [e]Exp. were carried out using a 1:1 tetralin:TAME/MTBE as hydrogen donors at 315°C for 24 h. [f]Exp. were carried out using TAME/MTBE as hydrogen donors at 315°C for 24 h.

In order to get more detailed information about the composition of asphaltenes, the samples were further investigated by Py-GC/MS technique. In all cases, GC/MS analysis of pyrolisates yielded a complex trace containing an unresolved hump that was more or less pronounced depending on the asphaltene samples. Due to their complexities, the INT101 norm algorithm was applied.[7,8] This norm is useful to check the quality of feeding streams and petroleum products. INT101 gives the hydrocarbon distribution in terms of weight and/or volume percentage of aliphatic and aromatic compounds. The results of this characterization are shown in Table 2. For the case of tetralin, the results show that the percentage of total saturates increase slightly and the aromatics decrease when compared with the control experiment. A more complete analysis of the hydrocarbons detected in the control experiment and the one with tetralin indicates that the total aromatic fraction, mono- and di-aromatics decrease whereas mono- and dicycloparaffins increase. After hydrogen donor removal by vacuum distillation, naphthalene was detected in the distillated residue by gas chromatography. These results are consistent with a hydrogen transfer mechanism from the tetralin to the asphaltenes (eq. 1) at the low severity conditions (315°C).[10,11]

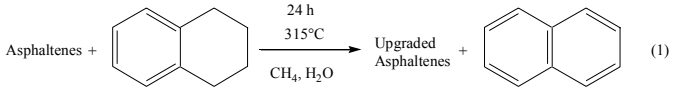

In the case of the asphaltenes isolated from the crude oil treated with mixture tetralin/TAME:MTBE, there is an agreement with above results (Table 2). It was observed an increase in the total percentage of saturates with a decrease in the total percentage of aromatics in comparison with the control experiment. Also, lower percentages of mono- and diaromatics were found in the upgraded asphaltenes. These data are also similar to the experiment with tetralin. This result gives evidences to a hydrogen transfer mechanism (eq. 1) from the tetralin to the asphaltenes.[10,11]

Using TAME/MTBE mixture alone, a slight reduction of the percentages of aromatic compound with the concomitant increase in the total saturates was observed (see Table 2). Therefore, the relative order of hydrogen transfer from donor to the extra heavy crude oil can be inferred as shown in eq. 2:

$$\text{Tetralin/TAME:MTBE} \geq \text{Tetralin} > \text{TAME:MTBE} \qquad (2)$$

Conclusions

The characterization by pyrolysis GC-MS of the asphaltenes isolated from the upgraded crude oil under steam injection conditions gives evidence of a hydrogen transfer mechanism from the hydrogen donor (tetralin) to the hydrocarbon fractions.

The presence of a radical initiator (TAME:MTBE) has little effect on the properties of the upgraded crude oil steam injection conditions.

Acknowledgement. The authors would like to thank PDVSA-INTEVEP for permission to publish this manuscript.

References

(1) Weisman, J. G., Kessler, R. V., *Appl. Catal.*, **1996**, *140*, 1 and references therein.
(2) Weissman, J. G., Kessler, R. V., Sawicki, R. A., Belgrave, J. D. M., Laureshen, C. J., Metha, S. A., Moore, R. G., Ursenbach, M. G., *Energy & Fuels*, **1996**, *10*, 883 and references therin.
(3) Vallejos, C.; Vasquez, T.; Ovalles, C. Amer. Chem. Soc., Div. Petrol. Chem. Prep., **2000**, *45*, 591.
(4) Ovalles, C., Vallejos, C., Vásquez, T., Martinis, J., Peréz-Peréz, A., Cotte, E., Castellanos, L., Rodríguez, H., SPE Paper No. 69692, Proc. SPE Inter. Thermal Oper. Heavy Oil Symp. held in Margarita, Venezuela, March 12-14th (**2001**).
(5) Ovalles, C, Vallejos, C., Vasquez, T., Rojas, I., Ehrman, U., Benitez, J. L., Martinez, R., accepted for publication in *J. Pet. Sci. Tech*. **2003**
(6) Vallejos, C.; Vasquez, T.; Ovalles, C., US Patent No. 5,891,829; **1999**.
(7) Robinson, C., J., *Anal. Chem*., **1971**, *43*, 1425.
(8) Piemonti, C., Amer. Chem. Soc., Div. Petrol. Chem. Prep., **1992**, *37*, 1521.
(9) Urbano, N., Machin, I., Jamal, A., Golindano, T., Cotte, E., Abstract Amer. Chem. Soc., **2002**, *224*, 277
(10) Tagaya, H., Sugai, J., Onuki, M., Chibsa, K., *Energy & Fuels*, **1987**, *1*, 397.
(11) Iino, M., Shen, J., *Energy & Fuels*, **1994**, 8, 978.

EFFICACY OF COAL-BASED ACID ON THE BIOACTIVITY OF TRIBENURON-METHYL

Caifeng Zhang[1,2], Shanxiang Li[1], Baoqing Li[1] and Wen Li[1]

1 State Key Lab of Coal Conversion, Institute of Coal Chemistry, Chinese Academy of Sciences, P. O. B. 165, Taiyuan, 030001, P.R. China
2 Department of Chemistry, Taiyuan Normal College, Houjiaxiang, Taiyuan, 030001, P.R. China

Introduction

Pesticide plays an important role in agriculture. It was reported that the loss made by insect, plant disease and weed occupied 10% ~ 15% of the total agricultural product but the pesticide can save 15%~30% of the loss. However, the application of the pesticide brought about many serious side effects such as environmental pollution and harmfulness to human and animal. Nowadays, research on the pesticide is focused on exploring the method decreasing the usage and harm of pesticide.

Many studies have proved that the pesticides in soil and water may interact with humic substances (HS), the most widespread and ubiquitous natural non-living organic materials occurring in all terrestrial and aquatic environments from the end products of chemical and biological degradation of plant residues[1,2]. The interaction affected degradation and detoxication of the pesticides, residue persistence and monitoring, mobilization and transport, bioavailability and phytotoxicity, and bioaccumulation[3,4,5,6]. In general, the modes of interaction include adsorption, partitioning and solubilization, catalysis and dealkylation, and photosensitization[7]. HS is well recognized and widely applied as fertilizer and growth plant regulator. Patents reported that humic acid was used as adjuvants for slow-release pesticide compositions when pesticides were added into fertilizer with humic substances[8,9]. Our patents showed that coal-based acid enhanced the bioactivity of fungicide and insecticide[10,11].

Tribenuron-methyl is Sulfonylurea herbicide against two-leaf weed with the advantage of the best bioactivity as yet. But it is clear that the Sulfonylurea led to resistance to pesticide when the herbicide was used continuously. The surface adjuvant can improve the bioactivity of tribenuron-methyl.

Coal-based acid (CA) is the humic substance resulted from coal. There are two kinds of water-soluble coal-based acid (WSCA): (1) originally existed in coal, and (2) newly formed through oxidation-degradation of coal. This work studied the adjuvant effect of the two kinds of WSCA on the bioactivity of tribenuron-methyl.

Experimental

Preparation of WSCA. W-WSCA was prepared by the following procedures. Wuchuan weathered lignite was oxidized and dissociated by HNO_3 with Zn as catalyst for 2h, in which the ratio of solid and liquid was adjusted to 1:2~1:4 by water. After the first product was alkalized by NaOH for 2h at 80~100°C, the degradation was performed using H_2SO_4, and pH value of the product was further adjusted to 4~6 by HNO_3. Finally, the liquid of the product was separated by precipitation and dried with infrared lamp at 70°C to get W-WSCA. H-WSCA was prepared using Huolinhe lignite by the same procedure as that of W-WSCA. Jincheng weathered coal mixed with 10 times water was stirred and the mud was poured, the residue was precipitated for 0.5~1 h. The residue was added with 10 times water again and its pH value was adjusted to 1.2~1.5 by H_2SO_4, and then extracted for 1~2 h in water bath at 60~70°C. Finally, the liquid was separated and dried with infrared lamp at 70°C. The product was purified further with acetone to get J-WSCA.

The content and functional groups of WSCA were determined with the method described by Schnitzer and Khan[12].

Tribenuron-methyl. The commercial formulation of tribenuron-methyl (content: 75% DF) produced by E. I. du Pont de Nemours and Company.

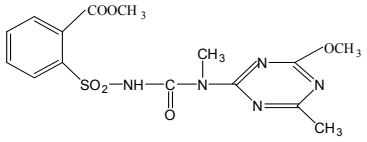

Figure 1 The chemical structure of tribenuron-methyl (T)

Instrumentation. An EA1108 elemental analyzer (Carlo Erba) was used for determining elemental composition.

Bioassay of tribenuron-methyl against.eed. Firstly, maize plumule was used for comparing the effect of W-WSCA, H-WSCA and J-WSCA on bioactivity of tribenuron-methyl (T). Maize seeds were sown in agriperlite, watered and allowed to germinate in the dark at 26 ℃ for 2 days. The germinated seeds were laid in glass beaker with sterilized sand in 3cm high and covered by the sand in 3cm high again. Then the beakers were saturated with 1 μ g/ml of T without or with 5 μ g/ml of W-WSCA, H-WSCA and J-WSCA. Each treatment was repeated for three beakers. The weeds were grown in a greenhouse with a photoperiod of 16 h (22-25 ℃ in the light, 16-18 ℃ in the dark). After a week, the length of plumules was measure. Secondly, *Brassia campestri* was planted with pot culture in greenhouse in order to dose-response assays and index of relative toxicity. When the weed developed one leaf, herbicides were applied with spraying. Based on the prepared test, the tribenuron-methyl concentrations of 0.30, 0.90, 2.70, 8.40, 24.30, 72.90 g a.i./hm^2 were used. The concentrations of W-WSCA and J-WSCA were 10 g/h hm^2. The fresh weight of plant above land was measured at 14 days after herbicides were applied three replications. The fresh weight loss ratio indicated the activity of T, T-W-WSCA and T-J-WSCA.

Field trials of T against weed in field of wheat. The field trials of T, T-W-WSCA and T-J-WSCA against weed in field of wheat were carried out in Taiyuan, Shanxi province on Apr. 23, 2000. The concentration of T was 2 g/hm^2 in all tests. The concentration of WSCA were 18.7 and 187g/hm^2, and the The test area was 30 m^2 in replication for 4 times with random arrangement. The fresh weight of weed was surveyed after 20th day. Duncan's test was used for statistical analysis.

Results and discussion

The elemental analysis and properties of WSCA were listed in Table 1 and Table 2. The highest content of phenolic hydroxyl was found in W-WSCA among the three kinds of WSCA, while the most carboxyl and HA in J-WSCA. WSCA can bond with Fe^{3+}, Ca^{2+} and Mg^{2+} because of its good metal complexer and prevent coagulation emerged. Coag. value means the capacity of WSCA against electrolyte. The capacity of WSCA obtained by oxidized degradation (W- and H-WSCA) is about 60 times as large as that existing in coal (J-WSCA).

Maize plumule was used for comparing the adjuvant effect of W-WSCA, H-WSCA and J-WSCA on bioactivity of tribenuron-methyl (T). The shorter the length of plumule was, the stronger the bioactivity of herbicide was. The result was shown in Fig 2. WSCA

can enhance the bioactivity of T. And WSCAs newly formed through oxidation-degradation of coal were better than that existed in coal. W-WSCA was the best.

Table 3 listed the parameter of dose-response assays of T, T-W-WSCA and T-J-WSCA. The results of bioassay on *Brassia campestri* showed that W-WSCA and J-WSCA can enhance the inhibitory action of T on plant growth. ED_{50} (the concentration of herbicide when the death ratio of weed is 50%) of T, T-W-WSCA and T-J-WSCA was 1.20, 0.90 and 1.05 g a.i./hm^2. Using T as standard, index of relative toxicity of T-W-WSCA and T-J-WSCA was 133.3 and 115.4, respectively. From Table 4 it was seen that the index of relative toxicity was increased with increasing effective dose of T in the mixtures. The index of relative toxicity of the mixture of WSCA with T is more remarkable at ED_{70} than that ED_{50}, which further indicates the adjuvant effect of WSCA on T.

The field trials of T, T-W-WSCA and T-J-WSCA against weed in field wheat also proved the adjuvant effect of WSCA on T. The results were listed in Table 5. The effectiveness differed with different weeds. For *Lepiaium* and *Amaranthus retroflexus L*, the effectiveness of T with WSCAs were 2 times than that of T without WSCA. For other weed, WSCAs can raise 20% of T effectiveness.

Table1 Elemental analysis of W-WSCA and J-WSCA

Samples	Elemental analysis /W % daf					Functional Group$_{daf}$	
	C	H	O	N	S	OH_{ph}	COOH
W-WSCA	60.15	3.65	28.52	2.38	3.38	2.96	3.46
H-WSCA	60.91	3.62	29.87	3.04	0.59	1.92	4.25
J-WSCA	50.01	3.14	44.57	0.91	0.87	1.52	8.96

Table2 Properties of W-WSCA and J-WSCA

Samples	M_{ad} %	A_d %	HA_{daf} %	pH	Coag. value mmoll$^-$
W-WSCA	8.71	33.33	58.12	4.0	<36
H-WSCA	9.56	41.26	39.25	3.5	<36
J-WSCA	13.2	5.50	94.50	1.0	0.6

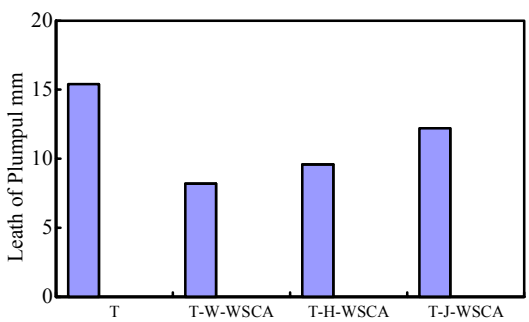

Figure 2 Effect of WSCA on the restraint of T on maize plumule

Table 3 Parameters of T, T—W-WSCA and T—J-WSCA

herbicide	Regression line y=a+bx	ED_{50} g/h hm^2	r	Index of relative toxicity
T	y=5.61+0.56x	1.2	0.9958	100
T—W-WSCA	y=5.88+0.72x	0.9	0.9942	133.3
T—J-WSCA	y=5.77+0.65x	1.05	0.9975	115.4

Table 4 Effective dose of T, T—W-WSCA and T—J-WSCA in dose-response assays

ED_p	Effective dose g/hm^2		
	T	T—W-WSCA	T—J-WSCA
ED_{30}	0.15	0.15	0.15
ED_{50}	1.20	0.90	1.05
ED_{70}	10.20	4.82	6.30

Conclusion

WSCA can enhance the biological activity of glyphosate, and the adjuvant effect was significant. The action of newly formed W- and H-WSCA was better than that of J-WSCA originally existed in coal. Moreover, the cost was reduced because W-WSCA and H-WSCA were the raw product, while J-WSCA was the purified product.

Table 5 Adjuvant effect of WSCA on G against weed in orchard with class

herbicide	Effectiveness at 20th day after herbicide applied					
	Aretisia	Chenopoaium Serotinium	Bothirospeimum chinense bge	Lepiaium	Amaranthus retroflexus L.	Convolvulus arvensis
T	69.7 b B	54.7 a AB	68.4 b B	44.9 b B	43.0 b B	73.9 c B
T—W-WSCA$_1$	86.4 a A	71.7 a A	82.0 a A	88.9 a A	83.3 a b A	92.2 ab A
T—W-WSCA$_2$	94.6 a A	87.9 a A	85.7 a A	95.8 a A	92.7 a A	96.9 a A
T—J-WSCA$_1$	88.2 a A	68.8 a A	80.8 a A	91.8 a A	87.9 a A	89.5 b A
T—J-WSCA$_2$	95.4 a A	80.6 a A	88.9 a A	95.3 a A	95.3 a A	98.4 a A

W-WSCA$_1$ and W-WSCA$_2$ means the content of WSCA were 18.7, 187 g/hm^2, J-WSCA$_1$and J-WSCA$_2$ 18.7 and 187 g/hm^2.

Reference

1. Tang, C.C., Pesticide Chemistry, Nankai University Press, Tianjing, China, 1998.
2. Kuckuk, R., Hill, W., Nolte, J., Pestic. Sci., 1997, 51, p450-454.
3. Almendros, G. European Journal of Soil Science, 1995, 46, p287-301.
4. Chlou, C.T., Malcolm, R.L., Brlnton, T.I. Environ. Scl. Technol. 1986, 20, p502~508.
5. Cary, G.A., Mcmahon, J.A., Kuc, W.J., Environmental Toxicology and Chemistry, 1987, 6, p469~474.
6. Day, K.E ., Environmental Toxicology and Chemistry, 1987, 10, p91-101.
7. Senesi, N., The Science of the Total Environment, 1992, 123/124: 63~67.
8. Graham, A.G., Amar, Nath N.S., United States Patent 4062855, 1977.
9. Rehberg, B.E., Hall, W.L., United States Patent 5174804, 1992.
10. Li, S.X., Zhang, C.F., Li, B.Q., China States 99117700.2, 1999.
11. Li, S.X., Zhang, C.F., Li, B.Q., China States 99124922.4, 1999.
12. Schnitzer, M., Khan, S.U., Humic Substances in the Environment, MARCEL DEKKER. INC. press, New York, US, 1972.

VERSATILES CLUES FROM *AB INITIO* MODELING TO IMPROVED METAL SULFIDES CATALYSTS

P. Raybaud and H. Toulhoat

Institut Français du Pétrole
1&4 avenue de Bois-Preau
92852 Rueil-Malmaison Cedex, FRANCE

Introduction

The production of ever cleaner fuels by hydrotreating processes can vastly be improved if a rational understanding of the nano-structure of γ-alumina supported Co(Ni)MoS catalysts is established. Modern density functional simulation techniques have been proven to be well suited for providing new clues to challenging issues such as active sites characterization, role of promoters, morphology effects, influence of sulfo-reductive conditions, poisoning effects of inhibitors, role of the support. The goal of the present paper is to give an overview of recent IFP's achievements obtained through *ab initio* molecular modeling: we show that it provided rational interpretations for many experimental results. Moreover, we outline how molecular modeling may open exploratory routes for the pre-screening of new potential active phases.

Methods

The results presented here are the outcome of simulations based on density functional theory (DFT) within the generalized gradient approximation, and employing a plane wave basis set together with periodic boundary conditions. To solve the Kohn-Sham equations, we used the Vienna *Ab initio* Simulation Package (VASP) (1). For all details on calculation hypothesis (electronic convergence criteria, energy cut-off...), the reader may refer to the papers cited herein.

Results and Discussion

Nano-structures of Co(Ni)MoS. As well-established by TEM and XPS, the active phase of HDT catalysts consists of nano-sized MoS_2 layers promoted by Co or Ni. Under HDT conditions, this highly active mixed phase exhibits two competing edges : the (10-10) metal edge and the (-1010) sulfur edge. DFT simulations revealed the electronic and structural properties of these edges in *vacuum* (2), and in typical sulfo-reductive conditions (3,4,5). Using a simple thermodynamic model to describe the equilibrium state of the Co(Ni)MoS nano-phase in contact with the gas phase, the edge energy, σ_{edge}, can be expressed as a function of the H_2S and H_2 partial pressures, and temperature:

$$\sigma_{edge} = \sigma_0 - \alpha\mu_S \quad [1]$$

$$\text{where } S\sigma_0 = E_{cluster} - E_{bulk} \quad [2]$$

$$\text{and } \mu_S = g_{H_2S}(T) - g_{H_2}(T) + RT\ln\left(p_{H_2S}/p_{H_2}\right) \quad [3]$$

μ_S stands for the chemical potential of sulfur and α for a constant depending on the cluster's stoichiometry. σ_0 is calculated using the size dependent energies of model triangular clusters, $E_{cluster}$, per surface unit, S.

By injecting the σ_{edge} values in the Gibbs-Curie-Wulff law, the morphologies of nano-particles were deduced, as depicted in **Figure 1.** The calculated morphology varies from a triangle to an hexagon via a deformed hexagon, which is compatible with the geometrical model of Kasztelan (6). At the same time, the edge structures (**Figure 2a**) were consistent with EXAFS distances ($d_{Co(Ni)-Mo}$=2.75-2.90 Å and $d_{Co(Ni)-S}$ =2.10-2.20 Å), and revealed typical electronic properties (**Figures 2b and c**). Thus, total energy calculations demonstrated unambiguously the stable localization of Co and Ni in substitution for Mo at the edges.

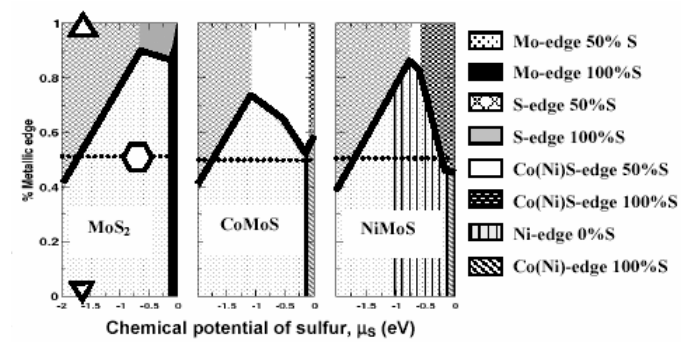

Figure 1. Equilibrium morphologies (thick broken lines) and edge compositions of the nano-particles as a function of μ_S. The ordinate represents the percentage of (10-10) metal edge exposed for the corresponding equilibrium morphology.

Moreover, as shown by the thick lines in **Figure 1**, and according to the preferential affinity of Co or Ni for one type of edge, the promoter acts as a morphology modifier (5). The sulfiding conditions have an impact on the stable shape of the nano-particles (4,5), whereas for very high reductive conditions (μ_S < -1.1 eV), the mixed phase becomes unstable, leading to the catalyst's deactivation.

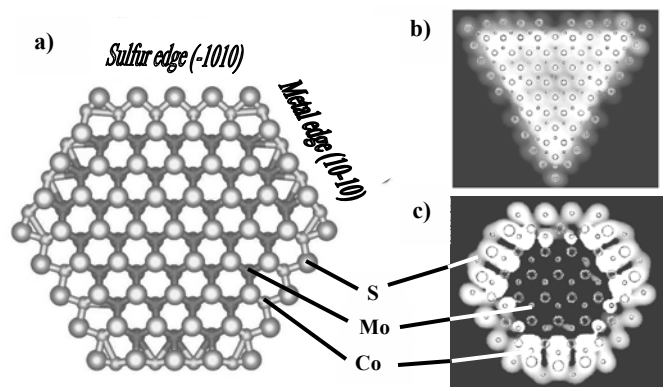

Figure 2. a) Ball and stick representations of the local structures of a Co(Ni)MoS cluster and simulated STM images of **b)** a MoS_x triangle (4) and **c)** a CoMoS cluster with Co on the sulfur edge (5).

Prediction of new active phases. The former modeling aims at two main objectives: improving industrially used active phases, and establishing robust basis for exploring new phases. Indeed, DFT calculations of relevant energy descriptors are well suited for providing a predictive approach. For HDT reactions, it was shown that the sulfur-metal bond energy, E_{MS}, as defined in (7,8,9), correlates well with the activity via a volcano master curve.

Actually, combining adapted Bronsted-Evans-Polanyi relationships with fitted Langmuir-Hinshelwood rate expressions, allows to recover HDS activity pattern exhibiting a volcano, when plotted against the E_{MS} descriptor (**Figure 3**). Since this approach also correctly predicted HDS activity of mixed sulfides, we are convinced that micro-kinetic modeling is improved when integrating *ab initio* descriptors. This approach, has been recently extended to various reactions by calculating carbon-metal bond energy descriptors in carbides (11).

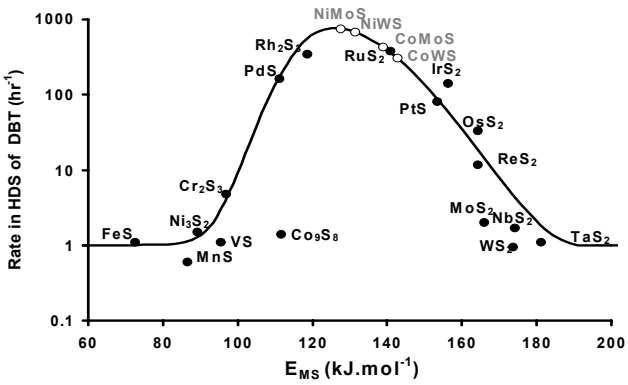

Figure 3. Pattern of experimental activity (particle size corrected) for the HDS of DBT ((10) •) plotted against the computed E_{MS}. ▬ : theoretical relationship that best fits the data. Predictions for mixed M'Mo(W)S sulfides (o) are superimposed. The "bulk" averages of E_{MS} computed for binaries are used to locate mixed sulfides.

Inhibitors effects. HDT feedstocks contain nitrogen compounds, that may compete with sulfur or aromatic compounds for the active sites. Using a similar approach as for the thiophene adsorption on MoS_2 (12,13), we calculated adsorption energies of various nitrogen compounds on the (10-10) edge of a NiMoS model catalyst, supposed to contain 50% of Ni atoms in substitution for Mo at the edge. The adsorption energy is defined as:

$$E_{ads} = E(catalyst + molecule) - E(catalyst) - E(molecule) \quad [4]$$

For a given species, we first observe a clear dependency of the adsorption energy with the type of adsorption site. Almost all compounds exhibit higher adsorption energies on Mo-CUS sites than on Ni-CUS, due to the stronger Lewis acidity of the Mo-CUS. Azaarenes are also adsorbed on Mo-SH sites with an intermediate adsorption level. Furthermore, as shown in **Figure 4**, nitrogen compounds (including ammonia) are more strongly bonded than sulfur compounds and aromatics. Thus, by displacing sulfur and aromatic compounds on the CUS, and by poisoning SH groups required for HDS reaction, nitrogen compounds inhibit HDS and HYD reactions. Moreover, our simulations reveal that azaarenes are more strongly adsorbed on CUS than pyrrole and derivatives, pointing out crucial differences between the two nitrogen compound families regarding the NiMo active site.

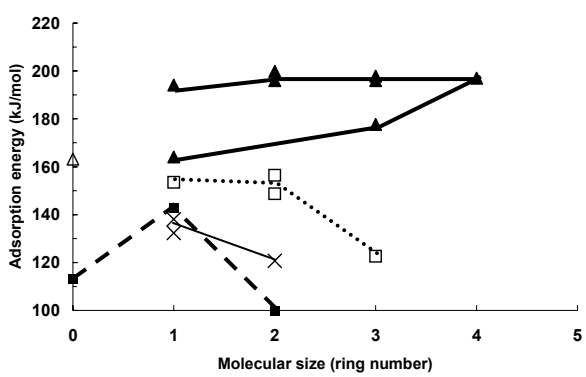

Figure 4. Adsorption energies as a function of the molecular size: azaarenes (▲), pyrrole derivatives (□), sulfur compounds (■), aromatics (x), ammonia (Δ).

Role of the support. DFT simulations on the active phase cannot overlook support effects. Significant progresses have been made in the description of relevant aluminum oxide surfaces (14,15,16). In particular, a recent work on γ-alumina models (16) investigated the variations of surface hydroxylation rate as a function of temperature and a subsequent vibrational analysis led to a precise assignment of bands in the high frequency IR spectrum to surface hydroxyl groups (**Table 1**). This revisited interpretation of Knözinger's assignments establishes a fresh and robust basis for further DFT investigations on active phase-support interactions.

Table 1. Calculated Vibrational Stretching Frequencies of γ-Alumina Surface Hydroxyl Groups

Site	Surface	ω_{calc} (cm^{-1})	ω_{exp} (cm^{-1})
HO-μ_1-Al_{IV}	(110)	3842	3785-3800
HO-μ_1-Al_{VI}	(100)	3777	3760-3780
HO-μ_1-Al_V	(110)	3736	3730-3735
HO-μ_2-Al_V	(110)	3707	3690-3710
HO-μ_3-Al_{VI}	(100)	3589	3590-3650

Conclusions

Ab initio modeling asserted itself as a versatile tool to investigate complex issues raised by HDT catalysis. In line with the long story of experimentation on sulfides, it may go beyond when traditional techniques are reaching their limits. Finally, in the spirit of high throughput screening, *ab initio* bond energy activity descriptors such as volcano curves are very promising as a first screening tool.

Acknowledgement. The authors are grateful to S. Kasztelan, V. Harlé and IFP's colleagues, to Profs. J. Hafner and G. Kresse from Universität Wien (Austria), to Prof. P. Sautet from Ecole Normale Supérieure de Lyon (France), and to Dr. H. Schweiger, M. Digne and G. Izzet for their fruitful collaboration.

References

(1) Kresse, G.; and Hafner, J., *Phys. Rev B.*, **1993**, *47 (588)*, 14251. Kresse, G.; and Furthmüller, J., *Comput. Mat. Sci.*, **1996**, *15*, 6.
(2) Raybaud, P.; Hafner, J.; Kresse, G.; and Kasztelan, S; and Toulhoat, H., *Surf. Sci.*, **1998**, *407 (1-3)*, 237.
(3) Raybaud, P.; Hafner, J.; Kresse, G.; Kasztelan, S; and Toulhoat, H., *J. Catal.*, **2000**, *189*, 129; ibid. **2000**, *190*, 128.
(4) Schweiger, H.; Raybaud, P.; Kresse, G.; and Toulhoat, H., *J. Catal.*, **2002**, *207*, 76.
(5) Schweiger, H.; Raybaud, P.; and Toulhoat, H., *J. Catal.*, **2002**, *212*, 33.
(6) Kasztelan, S.; Grimblot, J.; Bonelle, J.P.; Payen, E.; Toulhoat, H.; and Jaquin, Y., *Appl. Catal.*, **1983**, *7*, 91.
(7) Raybaud, P.; Hafner, J.; Kresse, G.; and Toulhoat, H., *J. Phys.: Condens. Matt.*, **1997**, *9*, 11085; ibid. **1997**, *9*, 11107.
(8) Toulhoat, H.; Raybaud, P.; Kasztelan, S.; and Hafner, J., *Catal. Today*, **1999**, *50*, 629.
(9) Chianelli, R.R.; Berhault, G.; Raybaud, P.; Kasztelan, S.; Hafner, J.; and Toulhoat, H., *Appl. Catal. A : General*, **2002**, *227*, 83.
(10) Pecoraro, T.A.; and Chianelli, R.R., *J. Catal.*, **1981**, *67*, 430.
(11) Toulhoat, H.; and Raybaud, P., *J. Catal.* (in press).
(12) Raybaud, P.; Hafner, J.; Kresse, G.; Kasztelan, S.; and Toulhoat, H., *Phys. Rev. Lett.*, **1998**, *80*, 1481.
(13) Raybaud, P.; Hafner, J.; Kresse, G.; Kasztelan, S.; and Toulhoat, H., *Stud. Surf. Sci. Catal.*, **1999**, *127*, 309.
(14) Raybaud, P.; Digne, M.; Iftimie, R.; Wellens, W.; Euzen, P.; and Toulhoat, H., *J. Catal.*, **2001**, *201*, 236.
(15) Krokidis, X.; Raybaud, P.; Gobichon, A-E.; Rebours, B.; Euzen, P.; and Toulhoat, H., *J. Phys. Chem. B*, **2001**, *105*, 5121.
(16) Digne, M.; Sautet, P.; Raybaud, P.; Euzen, P.; and Toulhoat, H., *J. Catal.*, **2002**, *211*, 1.

AN APPROACH TO DESIGN THE CATALYST FOR DEEP HYDRODESULFURIZATION TO ACHIEVE 10PPM SULFUR LEVEL

Naoyuki Kunisada, Ki-Hyouk Choi, Yozo Korai, Isao Mochida, and K. Nakano*+*

*Institute of Advanced Material Study, Kyushu University, Kasuga-Koen, Kasuga Fukuoka 816-8580, JAPAN
+Catalysts & Chemicals Ind. Co. Ltd, JAPAN

*e-mail: mochida@cm.kyushu-u.ac.jp

INTRODUCTION

NOx, SOx and particulate matters exhausted from diesel engine which combusts gas oil as fuel has provided a sincere social problem all over the world. The drastic reduction of sulfur in gas oil is expected to reduce those environmental pollutants and burden for diesel engines. Removing sulfur species deeply from gas oil has two difficulties; the first one is very low reactivity of some refractory sulfur species in gas oil such as 4,6-dimethyldibenzothiophene (4,6-DMDBT), 4,6,x-trimethyldibenzothiophene (4,6,x-TMDBT) having methyl group at 4 and 6 positions, the second is the strong inhibitors in feed oil and the products such as H_2S, NH_3, nitrogen species and aromatic compounds[1,2]. Hence deep HDS of these refractory sulfur species in gas oil can be achieved rather easily by the first and second stages of the catalysts when H_2S removal is performed between stages. Another approach is to develop catalysts of higher activity. Larger amount or better dispersion of sulfides have potential possibility for higher activity. Nevertheless severe condition appeared necessary.

In this present study, several NiMo and CoMo sulfide catalysts were examined in first and second layers with or without H_2S and NH_3 reduction between the layers. The functions of the catalysts in the two layers are defined as follows. 1st layer : complete removal of reactive sulfur species and 95% removal of refractory sulfur species. 2nd layers : remaining refractory sulfur species (around 400-500ppm) must be removed to less than 10ppm in the presence of H_2S and NH_3.

EXPERIMENTALS

a, Gas oil samples

Straight Run Gas Oil (SRGO) and Hydrodesulfurized Straight Run Gas Oil (HSRGO) were used as typical feedstocks for the first and second layer catalysts, respectively in this study. The SRGO contains 11780ppm while the HSRGO contains 340ppm of sulfur. Furthermore, the SRGO contains 155ppm while the HSRGO contains 20ppm of nitrogen.

b, Catalysts

The catalysts used in this study were CoMo and NiMo supported on alumina(-A), silica-alumina(-SA) and alumina-zeolite composite(-AZ), which were manufactured by a commercial catalyst vendor. **Table 1** shows their surface area, average pore size measured by BET and NH_3 desorbed amount measured by NH_3-TPD. **Figure 1** shows the pore size distribution of the several catalysts.

c, Hydrotreatment

SRGO and HSRGO were hydrotreated over the catalyst at 340°C under 50kg/cm^2 of H_2 for first layer, 50 kg/cm^2 H_2 with H_2S (1.67%) and 50 kg/cm^2 H_2 with H_2S (1.67%) added ethylenediamine (15ul) for second layer in a 100ml autoclave.

The ratio of catalyst to feed was 1g/10g. Catalyst was presulfided at 360°C under the stream of H_2S(5%)/H_2 mixture for 2hr before the catalytic reaction.

Table 1. Catalysts properties

	Surface area (m^2/g)	Pore volume (cm^3/g)	NH_3-Desorbed area (Arb. Unit)
CoMoA	191	0.41	0.48
NiMoA	175	0.34	0.62
CoMoSA	221	0.41	0.56
NiMoSA	242	0.39	0.49
CoMoAZ	265	0.34	0.81
NiMoAZ	262	0.30	0.66

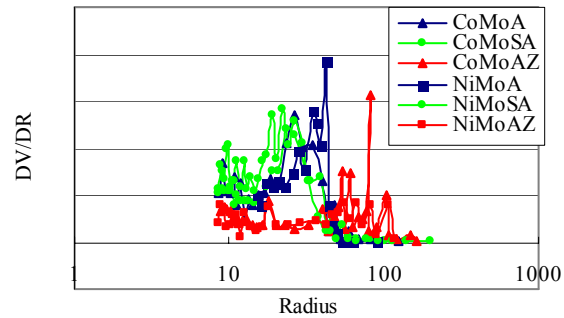

Figure 1. pore size distribution of several catalysts

RESULTS

a, HDS of SRGO

Figure 2 shows remaining sulfur chromatograms of SRGO after HDS over NiMo- and CoMo-A, NiMo- and CoMo-SA NiMo- and CoMo-AZ catalysts at 340°C under 50 kg/cm^2 H_2. NiMo-AZ shows the highest activity among six catalysts, and its remaining sulfur content is less than 300ppmS. Zeolite containing catalysts tend to show higher activity than SA- and A-series catalysts for HDS of SRGO that contained major reactive sulfur species. The HDS at this stage removed all reactive sulfur species and about 95% of refractory sulfur species to achieve sulfur level of 500ppm.

Remaining nitrogen compounds of SRGO after HDS over six catalysts were as follows. Three of NiMo catalysts showed higher activity than themselves couples of CoMo. NiMo-A, NiMo-SA, NiMo-AZ and CoMo-AZ achieved less than 20ppm of nitrogen content. From this result and the last time, NiMo-SA, NiMo-AZ and CoMo-AZ catalyst were the suitable catalyst for the first layer.

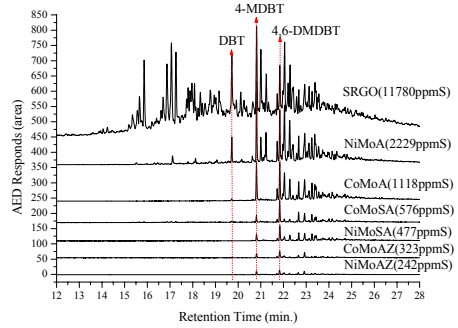

Figure 2. HDS of SRGO over several NiMo and CoMo catalysts

b, HDS of HSRGO without H_2S and NH_3

Hydrodesulfurization of H-SRGO without H_2S or NH_3 over several NiMo or CoMo catalysts was assumed to simulate the two stage with separation of produced inhibitors (see **Figure 5**). Many of the catalysts achieved sulfur level less than 10ppm.

c, HDS of HSRGO in the presence of H_2S

Figure 3 shows GC-AED sulfur chromatograms on HDS of H-SRGO with H_2S. For HDS of refractory species, H_2S has been believed as the major inhibitor[3]. In directly connected two layer HDS, the second layer catalyst must stand with H_2S.

CoMo-AZ, NiMo-AZ, and NiMo-A of more acidic sites showed higher activity than any other catalysts. In contrast, CoMo-A or NiMo-SA which was less acidic showed lower activity. The acidity of the catalyst provides the tolerance to H_2S to show high HDS activity. HDS product oil over CoMo-AZ contains not 4,6-DMDBT but unidentifical peak was observed near 4,6-DMDBT.

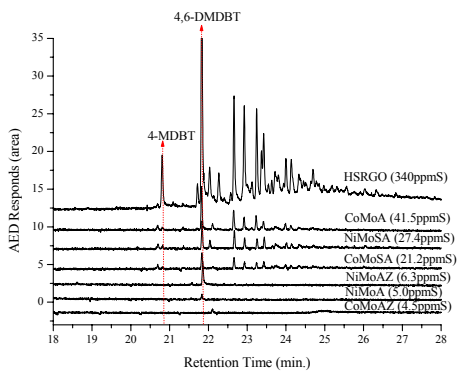

Figure 3. GC-AED sulfur chromatograms on HDS of H-SRGO in the presence of H_2S

d, HDS of HSRGO in the presence of H_2S and NH_3

Figure 4 shows HDS of H-SRGO in the presence of both H_2S and NH_3. **Figure 5** summarizes the inhibition effects of H_2S and NH_3 on the HDS of H-SRGO. NiMo-A of large pore was found very active for HDS of refractory sulfur species in the presence of H_2S and NH_3 to achieve less than 6ppmS. In contrast, CoMo-A, NiMo-SA and CoMoSA were less active. NiMo-AZ and CoMo-AZ were much inhibited by addition NH_3.

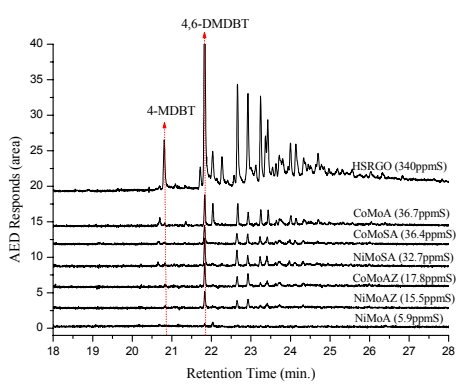

Figure 4. GC-AED sulfur chromatograms on HDS of H-SRGO in the presence of H_2S and NH_3

AZ and NiMo-A with a number of acidic sites received little inhibition of H_2S. In contrast, SA and CoMo-A with less acidity received much inhibition of H_2S. NiMo-A and CoMo-A suffers little inhibition effects of NH_3 while NiMo-AZ and CoMo-AZ suffers marked inhibitions of both inhibitors.

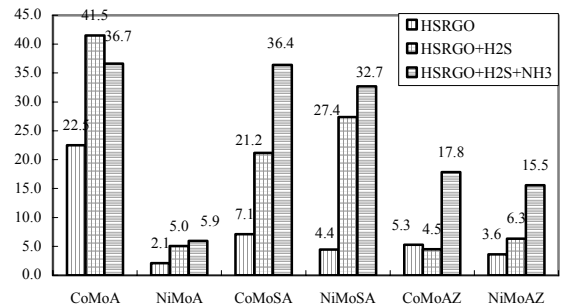

Figure 5. Inhibition effect of H_2S and NH_3 on HDS of HSRGO

DISCUSSIONS

The present study revealed that the two layers of the best HDS catalysts with appropriate activity under respective conditions can be a logical approach to achieve deep HDS of gas oil.

The first layer catalyst must eliminate 100% of reactive sulfur species, first of all. Hence, the catalyst must have larger surface area, slightly smaller pore being allowed for the larger surface area. Acidity helps higher activity. 95% of refractory sulfur species must be also eliminated. Its content is still in relatively large range, being less influenced by inhibitors. Moderate acidity is helpful for the hydrogenative HDS. Another important function of the first layer catalyst appears the activity for HDN to send less nitrogen inhibitor for the second layer.

The second layer catalyst eliminates the refractory sulfur species of 100-500ppm to less than 10ppm in the presence of H_2S and NH_3. Least nitrogen species is required. The present HSRGO contains 20ppmN. The catalyst must have larger pores to accept the refractory sulfur species of tri aromatic rings with methyl groups more than di aromatic rings. Acidity is important to enhance HDS of the refractory sulfur species in the hydrogenation route by moderate H_2S inhibition. However too strong acid may suffer inhibition of NH_3 which is more basic than carbazoles. Zeolite containing CoMo and NiMo showed higher activity in SRGO, HSRGO and HSRGO+H_2S. On the other hand, as you know, zeolite having strong acidity is easily deactivated. Hence, AZ catalyst need larger the life time. Appropriate sets of two catalysts with successive layers are very active to achieve regulated Sulfur level of gas oil. It is always discussed whether CoMo or NiMo is better catalyst for the first and second layers. The support and supporting procedure appear very influential and hence we can not tell which is better at this stage. Nevertheless high dispersion in designed shape of the sulfides must be practiced in any supports.

Acknolwedement This work has been entrusted by the New Energy and Industrial Technology Development Organization under a subsidy of the Ministry of Economy, Trade and Industry of Japan.

REFERENCES

1. Isoda, T.; Ma, X.; Mochida, I. *Sekiyu Gakkaishi*, **1994**, *37*, 506.
2. Whitehurst, D. D.; Isoda, T.; Mochida. I, *Adv. Catal*., **1998**, *42*, 345.
3. Isoda, T.; Ma, X.; Mochida, I. *Sekiyu Gakkaishi*, **1995**, *25*, 38.

QUANTUM CHEMICAL MOLECULAR DYNAMICS SIMULATION ON CATALYTIC REACTION DYNAMICS OF METHANOL SYNTHESIS PROCESS

Momoji Kubo[1], Minako Ando[1], Satoshi Sakahara[1], Changho Jung[1], Kotaro Seki[1], Tomonori Kusagaya[1], Akira Endou[1], Seiichi Takami[1], Akira Imamura[2], and Akira Miyamoto[1,3]

[1] Department of Materials Chemistry,
Graduate School of Engineering, Tohoku University,
Aoba-yama 07, Sendai 980-8579, Japan.
[2] Department of Mathematics,
Faculty of Engineering, Hiroshima Kokusai Gakuin University,
6-20-1, Nakano, Aki-ku, Hiroshima 739-0312, Japan.
[3] New Industry Creation Hatchery Center, Tohoku University,
Aoba-yama 04, Sendai 980-8579, Japan.

Introduction

Recently, computational chemistry made great impacts on catalysts design. First-principles method is mainly employed in order to elucidate the catalytic reaction mechanism, catalyst activity, catalyst selectivity, and other important information. However, since the first-principles calculation can investigate only the static states at 0 K, this approach is not enough for theoretical catalyst design and research. For example, catalytic reaction dynamics depending on temperatures cannot be investigated by the first-principles calculation. Moreover, many reaction paths should be assumed in order to clarify the catalytic reaction mechanism and a lot of experimental information is essential to assume the reaction paths. Since a lot of experimental information is essential before the first-principles calculation, the present first-principles approach cannot contribute to the proposal of completely new catalysts. In addition to the understanding of the well-known catalytic properties at atomic and electronic levels, computational chemistry is expected to have an important role to predict new catalysts, which have high activity, selectivity, and tolerance to poisons.

In order to solve the above problem, the simulation on the catalytic reaction dynamics at reaction temperatures is strongly demanded. The products can be proposed directory from the reactants and catalysts by the reaction dynamics simulation, and any assumption of the reaction paths is not needed. Moreover, by-products and selectivity depending on the temperature can be clarified. First-principles molecular dynamics method is one of the most promising methodologies to realize the reaction dynamics simulation. However, it requests large computational costs, and then only a small model can be employed by the first-principles molecular dynamics method. Hence, the realistic catalysts model including active metals, supports and additives cannot be simulated by the first-principles molecular dynamics method.

Recently, we have succeeded in the development of an accelerated quantum chemical molecular dynamics program "Colors", which is more than 5,000 times faster than the regular first-principles molecular dynamics method [1,2]. This program was developed based on our original tight-binding theory, which enables us to simulate the catalytic reaction dynamics on large catalyst model at reaction temperatures. We have already applied the above tight-binding quantum chemical molecular dynamics simulator to various systems, such as Si semiconductor, GaN light emitting materials, ionics materials, and so on [1-5]. We have confirmed that the above tight-binding quantum chemical molecular dynamics simulator is very effective to simulate the chemical reactions and electron transfer dynamics at finite temperatures.

On the other hand, recently the synthesis of the high-quality transportation fuels is strongly demanded in terms of high-efficient utilization of energy and low environmental impact. In order to advance the synthesis of high-quality transportation fuels, the development of highly active and highly selective methanol synthesis catalysts with high-tolerance to the sulfur is essential and expected. Cu/ZnO is a most famous catalyst for the methanol synthesis reaction, and a large amount of experimental results for the Cu/ZnO catalyst were accumulated [6-8]. Moreover, recently Pd/SiO_2 gained much attention as a new methanol synthesis catalyst.

Hence, in the present study, we applied our original tight-binding quantum chemical molecular dynamics program to the methanol synthesis reaction on various catalysts and the applicability of our new simulator was demonstrated.

Methods

Our accelerated quantum chemical molecular dynamics program was based on our original tight-binding theory. The equations to be solved in this simulator are shown in Eqs. (1) and (2).

$$HC = SC\varepsilon \quad (1)$$

$$C^T SC = I \quad (2)$$

where, H is the Hamiltonian matrix, S is the overlap matrix, C is the eigenvector matrix, ε is the eigenvalue matrix, and C^T is the transformation matrix of C. The total energy in the system is calculated employing Eqs. (3) and (4).

$$E = \sum_{i=1}^{n} \frac{1}{2} m_i v_i^2 + \sum_{k}^{occ} \varepsilon_k + \sum_{i=1}^{n} \sum_{j=i+1}^{n} \frac{Z_i Z_j e^2}{R_{ij}} + \sum_{i=1}^{n} \sum_{j=i+1}^{n} E_{ij}^{repul}\left(R_{ij}\right) \quad (3)$$

$$E_{ij}^{repul}(R_{ij}) = b_{ij} \times \exp\left(-\frac{R_{ij} - a_{ij}}{b_{ij}}\right) \quad (4)$$

In this formula, m_i is the atomic weight, v_i is the atomic velocity, e is the elementary electric charge, and R_{ij} is the interatomic distance. The parameters a_{ij} and b_{ij} represent the size and stiffness of each atom, respectively. Z_i is the atomic charge obtained by the tight-binding electronic states calculation. Here, Mulliken analysis is employed to evaluate the above atomic charge. The first term refers to the kinetic energy of the atoms, the second term is the summation of the eigenvalues of all the occupied orbitals calculated by the tight-binding electronic states calculation, and the third term represents the Coulombic interaction. The last term corresponds to the short-range exchange repulsion energy.

Results and Discussion

In addition to the acceleration of the calculation speed, the realization of high accuracy, similarly to the first-principles molecular dynamics method, is essential. In order to accelerate the calculation speed, we employed some parameters in the Hamiltonian. If the parameters are determined as to fit the experimental results, our simulator will be lack of the predictability. Hence, in our program all the parameters were determined by the first-principles calculation results. In order to realize it, we developed a new parameter-fitting program. Here, we demonstrate the applicability and effectiveness of our new parameterization procedure.

Fig. 1 shows the CO adsorption structure on the Pd_3 cluster. Some distances and atomic charges calculated by our new simulator were compared with those obtained by the static first-principles calculation (Table 1). Our simulator results are in good agreement with the first-principles results. It indicates that our simulator has high accuracy, similarly to the first-principles calculation. After the validity of our parameterization procedure was

confirmed, we performed a quantum chemical molecular dynamics simulation of the CO adsorption on Pd surface model (Fig.2). Here, Pd(111) surface was employed as the catalyst, and the calculation was performed under three-dimensional periodic boundary condition. Vibrational frequency of CO molecule adsorbed on the Pd surface was calculated (Table 2). Here, we compared the simulation results with the experimental results. As shown in Table 2, our simulation results are in significantly good agreement with the experimental results. Moreover, we applied our quantum chemical molecular dynamics simulation to the H_2 adsorption and the methanol synthesis reaction dynamics on the large Pd catalyst model.

We also applied our tight-binding quantum chemical molecular dynamics simulator to the Cu/ZnO methanol synthesis catalyst. We constructed a significantly large Cu/ZnO catalyst model for the reaction dynamics simulation as shown in Fig. 3. Fig. 3 includes more than 1,000 atoms and some Al additives are incorporated in the ZnO support in order to clarify the effect of the additives. Moreover, formate intermediate is also placed on the Cu particle. Calculation results show that the average charge of the Cu atoms on the ZnO support is +0.1, which indicates that the ZnO support strongly influences the electronic states of the Cu ultrafine particle. The regular first-principles molecular dynamics simulator cannot obtain the above information, since it requests large computational costs and cannot be applied to the huge catalyst model as shown in Fig. 3. After we constructed an appropriate model for Cu/ZnO catalyst, we simulated a catalytic reaction dynamics of the methanol synthesis process on the above huge Cu/ZnO model.

Conclusions

In the present study, we confirmed that our tight-binding quantum chemical molecular dynamics simulator is very effective to simulate the catalytic reaction dynamics on large catalyst model at reaction temperatures, which cannot be performed by the regular first-principles molecular dynamics.

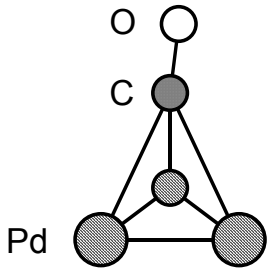

Fig. 1 CO adsorption structure on Pd_3 cluster

Table 1 Bond distances and atomic charges of Pd_3 cluster with CO molecule

Bond Distances [Å]

	C-O	Pd-Pd	Pd-C
First-principles	1.19	2.64	2.01
Our program	1.20	2.67	2.00

Atomic Charges

	Pd	C	O
First-principles	0.11	-0.01	-0.32
Our program	0.11	-0.02	-0.31

References

(1) Yamada, A.; Endou, A.; Takaba, H.; Teraishi, K.; Ammal, S. S. C.; Kubo, M.; Nakamura, K. G.; Kitajima, M.; Miyamoto, A. *Jpn. J. Appl. Phys.* **1999**, *38*, 2434.

(2) Takaba, H.; Endou, A.; Yamada, A.; Kubo, M.; Teraishi, K.; Nakamura, K. G.; Ishioka, K.; Kitajima, M.; Miyamoto, A. *Jpn. J. Appl. Phys.* **2000**, *39*, 2744.

(3) Inaba, Y.; Onozu, T.; Takami, S.; Kubo, M.; Miyamoto, A.; Imamura, A. *Jpn. J. Appl. Phys.* **2001**, *40*, 2991.

(4) Yokosuka, T.; Kurokawa, H.; Takami, S.; Kubo, M.; Miyamoto, A.; Imamura, A. *Jpn. J. Appl. Phys.* **2002**, *41*, 2410.

(5) Suzuki, K.; Kuroiwa, Y.; Takami, S.; Kubo, M.; Miyamoto, A.; Imamura, A. *Solid State Ionics*, in press.

(6) Sun, Q.; Liu., C.-W.; Pan, W.; Zhu, Q.-M.; Deng, J.-F. *Appl. Catal. A* **1998**, *171*, 301.

(7) Peppley, B. A.; Amphlett, J. C.; Kearns, L. M.; Mann, R. F. *Appl. Catal. A* **1998**, *179*, 31.

(8) Fujita, S.; Kanamori, Y.; Satriyo, A. M.; Takezawa, N. *Catal. Today*, **1998**, *45*, 241.

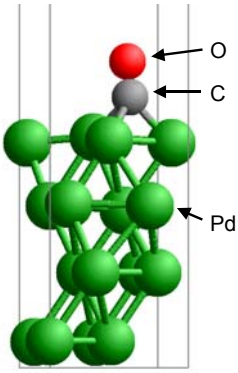

Figure 2 Adsorption structure of CO molecule on Pd(111) surface

Table 2 Vibrational frequency of CO molecule on Pd(111) surface

CO Molecule in Vapor Phase

	Frequency [cm^{-1}]	Bond Distance [Å]
Experiments	2143	1.13
Our Program	2163	1.13

CO Molecule on Pd (111) Surface

	Frequency [cm^{-1}]	Bond Distance [Å]
Experiments	1825	1.15
Our Program	1836	1.15

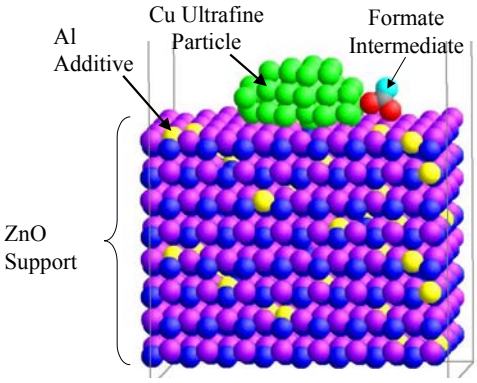

Figure 3 Structure of huge Cu/ZnO catalyst model including Al additives and formate intermediate

Atomic-scale study of hydrodesulfurization model catalysts

Jeppe V. Lauritsen [1], Bjerne S. Clausen [2], Henrik Topsøe [2], Jens K. Nørskov [3], Flemming Besenbacher [1,].*

[1]Center for Atomic-Scale Materials Physics (CAMP) and Interdisciplinary Nanoscience Center (iNANO)
Department of Physics and Astronomy, University of Aarhus,
Ny Munkegade
DK-8000 Aarhus C
Denmark.

[2]Haldor Topsøe A/S,
Nymøllevej 55
DK-2800 Lyngby
Denmark.

[3]Center for Atomic-Scale Materials Physics (CAMP),
Department of Physics
Technical University of Denmark
DK-2800 Lyngby
Denmark.

Introduction

The production of clean transport fuels by hydrotreating and especially hydrodesulfurization (HDS) has recently attracted increased attention due to the introduction of new environmental legislation regarding fuel specifications and technological requirements of high-purity fuels . In order to meet the new stringent demands there is a need to understand and improve HDS catalysts. It is generally accepted, that the HDS activity is related to the presence of so-called Co-Mo-S structures which consist of small MoS_2 nanoclusters with promoter atoms located near the edges[1]. Controversy prevails, however, since the traditional spectroscopy-based techniques for catalyst characterization provide no conclusive information regarding the cluster morphology, catalytically relevant edge structures, active sites or the promotional effect of Co.

To aid the understanding of the industrial catalyst, new insight has been gained from studies of catalyst model systems by applying surface science techniques. In a series of studies, we have successfully used high-resolution Scanning Tunneling Microscopy (STM) to study the real space atomic structure of single-layer MoS_2 nanoclusters synthesized on an inert Au(111) substrate as a model system for the HDS catalysts. The insight gained from the STM studies gives a hitherto unprecedented view of the atomic details of the MoS_2 nanoclusters[1].

Experimental

The experiments are performed in an ultra-high vacuum chamber equipped with the unique home-built high-resolution Aarhus STM, which has demonstrated the capability of providing atom-resolved images of a large variety of systems on a routine basis[2]. The Au(111) surface is chosen as a model substrate for two reasons. Gold is chemically rather inert, and furthermore gold belongs to the class of metal the surface of which reconstructs in its clean state. Specifically the Au(111) has a characteristic "herringbone" reconstruction pattern, which is ideal for providing nucleation sites for the deposited metal atoms and thereby dispersing submonolayer amounts of material into Mo or Co nanoclusters[3,6]. En ensemble of ~30 Å wide crystalline MoS_2 nanoclusters were formed by initially depositing Mo (10% coverage) in an background H_2S (10^{-6} mbar) followed by high-temperature annealing (673K) for 15 min while maintaining the sulfiding atmosphere.

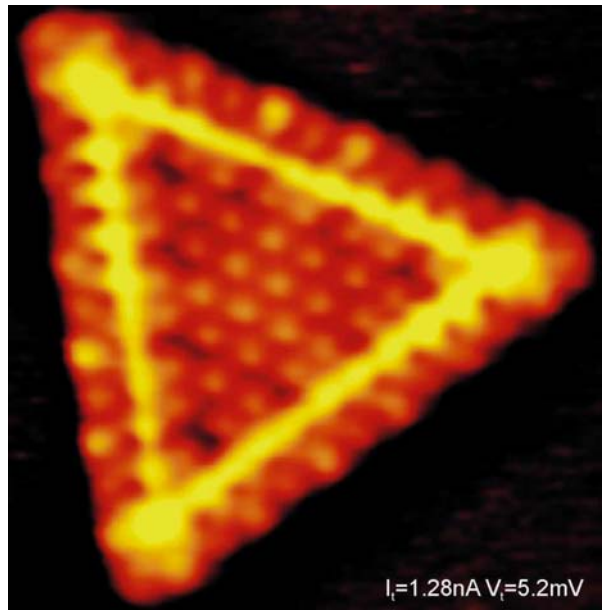

Figure 1: Atom-resolved (41x42Å^2) STM image of an unpromoted single-layer MoS_2 nanocluster synthesized on a Au(111) template[3].

Results and Discussion

High resolution STM images reveal new insight into the atomic details of the MoS_2 nanostructures (**Figure 1**). Contrary to our expectations based on the structure of bulk MoS_2, the majority of the nanoclusters are found to exhibit a pronounced triangular morphology. The shape of a single-layer MoS_2 cluster is in principle governed by the relative stability of two low-index types of edge terminations, an S-edge and a Mo-edge. Equal stability between these would produce a perfectly hexagonal cluster. The observed triangular morphology implies, however, that one type of edge termination is considerably more stable than the other.

It is important to point out that STM to a first approximation measures contours of constant local density of states (LDOS) in the surface projected onto the apex of the STM tip, and that STM images therefore reflect a rather complicated convolution of both geometric and electronic structure. This is especially true for adsorbates on surfaces, oxide or sulfide materials and in the STM images of the MoS_2 nanoclusters we indeed observe two examples of this. First of all, we observed the protrusions at the edge of the MoS_2 triangle to be out of registry with the basal plane S atoms. Second, a pronounced bright brim extending all the way around the perimeter of the triangular MoS_2 nanoclusters is identified in the STM image. Rather than geometrical effects pertaining to the triangular MoS_2 cluster (Figure 1), these features reflect subtle electronic changes at the edges, and are therefore attributed to distinct electronic features existing only near the edges, i.e. one-dimensional electronic edge states. The brim is seen in the STM image to be highly localized in the direction perpendicular to the edge and furthermore exhibits a very high electronic conductivity. It can thus be associated with a one-dimensional nanosized, metallic wire[2].

In density functional theory (DFT) calculations of the band structure of the MoS_2 edges we indeed find the existence of several

localized electronic edge states pertaining to the Mo edge. By comparing the detailed atomic-scale structure observed in the experimental images with STM simulations resulting from the DFT calculations (**Figure 2**) we have confirmed that electronic edge states are responsible for the features observed at the edges of the MoS_2 triangles and we have identified the edge termination as the Mo edge fully saturated with S dimers[3,4].

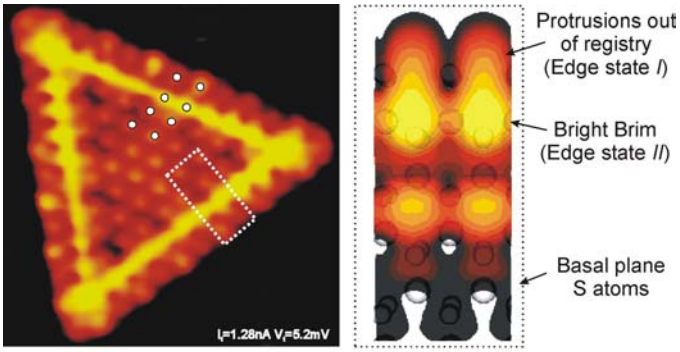

Figure 2: Left: Experimental STM image. White dots denote the position of protrusions on the MoS_2 nanocluster. Right: STM simulation (Tersoff-Hamann) of part of the Mo edge fully saturated with S dimers.

By means of the STM we have recently investigated the interaction of the MoS_2 clusters with thiophene (C_4H_4S) - a typical sulfur containing molecule widely used to test HDS reactivity. Upon adsorption of thiophene molecules we find in STM images that relatively inert molecules like thiophene preferentially interact with unusual sites located near the edges. Interestingly, we find that this interaction is modified by the presence of hydrogen species, and that the adsorption serves as an initial activation of thiophene molecules during catalytic hydrotreating reactions. This is followed by extrusion of sulfur at, for instance, edge vacancies, provided by reaction with gaseous hydrogen. We have exploited the capability of the STM to image in real-space these active sites on the atomic-scale with STM and investigated the energetics of the reaction with DFT calculations. The results thus provide new detailed insight into the reaction mechanism resulting in the extrusion of sulfur in the HDS process[5].

The industrial MoS_2-based HDS catalysts are typically promoted with Co which enhances the catalytic activity by more than an order of magnitude. By applying an approach similar to the unpromoted MoS_2 experiments described above we have also obtained the first atomic-scale images of the structure of Co-Mo-S nanocrystals[6]. The idea behind our synthesis of Co-Mo-S is first to form MoS_2 embryos on the Au(111) surface followed by capping of these nanoclusters to facilitate the addition of Co to the edges of MoS_2 nanocrystals.

High resolution STM images of the resulting CoMoS structures reveal that the presence of the Co atoms has a dramatic influence on the morphology of the single-layer MoS_2 clusters (**Figure 3**). This surprising morphological transition, from triangular to hexagonally truncated, appears to be driven by a preference for Co to be located at only one type of MoS_2 edges - the S edge. The STM results also provide direct information on changes in the local electronic environment neighboring the Co edge atoms. This novel insight into the atomic and electronic structure may be important for understanding the promoting role of Co.

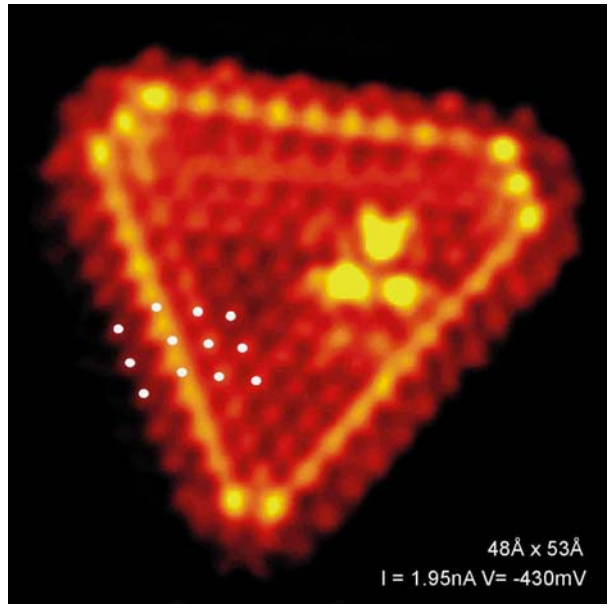

Figure 3: Atom-resolved STM image (48x53Å^2) of a promoted Co-Mo-S nanocluster[6] supported on Au(111).

Acknowledgements. The Center for Atomic-scale Materials Physics is sponsored by the Danish National Research Foundation. J.V.L acknowledges support from the Danish National Research Academy and the Interdisciplinary Center for Catalysis (ICAT).

References

(1) Topsøe, H., Clausen, B. S. & Massoth, F. E. *Hydrotreating Catalysis, Science and Technology* (ed. M. Boudart, J. R. Anderson.) (Springer Verlag, Berlin, 1996).
(2) Besenbacher, F., Reports on Progress in Physics **59**, 1737-1802 (1996).
(3) S. Helveg, J. V. Lauritsen, E. Lægsgaard, I. Stensgaard, J. K. Nørskov, B. S. Clausen, H. Topsøe, F. Besenbacher, Phys. Rev. Lett. **84**, 951 (2000).
(4) M. Bollinger, J. V. Lauritsen**,** K. W. Jakobsen, J. K. Nørskov, F. Besenbacher, Phys. Rev. Lett. **87**, 196803 (2001).
(5) J. V. Lauritsen, R. T. Vang, M. Nyberg, M. Bollinger, K.W. Jacobsen, B. S. Clausen, H. Topsøe, J. K. Nørskov, E. Lægsgaard, F. Besenbacher, Submitted (2002).
(6) J. V. Lauritsen, S. Helveg, E. Lægsgaard, I. Stensgaard, B. S. Clausen, H. Topsøe, F. Besenbacher, Journal of Catalysis **197**, 1-5 (2001).

Development of highly active hydrodesulfurization catalysts - Effect of the Addition of CyDTA and Boria -

Hideyuki Itou, Masahiro Shingu, Yosuke Kikuchi, Naoto Koizumi, and Muneyoshi Yamada

Department of Applied Chemistry, Graduate School of Engineering, Tohoku University
07 Aoba, Aramaki, Aoba-ku, Sendai 980-8579, JAPAN

Introduction

To meet the severe regulation for reductions of SOx, NOx, and SPM contained in the exhaust gases from diesel vehicles, the improvement of catalyst performances especially for hydro-desulfurization (HDS) is one of the most important subjects. van Veen *et al.*[1] reported that CoMo catalysts modified with nitric tri-acetic acid (NTA) show higher activities for HDS of thiophene at atmospheric pressure. We have investigated effects of other chelating reagents such as ethylenediamine-N, N, N', N'-tetra-acetic acid (EDTA) and *trans*-1, 2-Cyclohexanediamine-N, N, N', N'-tetraacetic acid (CyDTA) and found that CyDTA improves the activity of $CoMo/Al_2O_3$ catalyst for HDS of dibenzothiophene (DBT) at high pressure more more effectively than NTA.[2] Besides, CyDTA is found to be effective for hydrogenation of *o*-xylene[3] and tetralin over NiW/Al_2O_3 catalyst. Since CyDTA forms stable complexes with Co or Ni in the impregnating solution, it is suggested that CyDTA retards the sulfidation of Ni species, leading to the effective formation of active phases, namely Co(Ni)-Mo-S or Ni-W-S phases.

On the other hand, the addition of boric acid to $NiMo/Al_2O_3$ catalyst has been reported to improve the activities for HDS of DBT[4]. From EXAFS analysis of $NiMo/B_2O_3/Al_2O_3$ catalyst, the addition of boric acid improves the sulfidation degree of Mo sulfide species. Since Decanio *et al.*[5] showed that the addition of boric acid to γ-Al_2O_3 affects the distribution of hydroxyl groups on γ-Al_2O_3 surface by means of IR spectroscopy, it is suggested that boria weakens the interaction between Mo sulfide species and γ-Al_2O_3.

Since the additions of CyDTA and boric acid affects the structure of sulfide phases in different ways, it is expected that the simultaneous addition of both CyDTA and boric acid improves the HDS activities of hydrotreating catalysts than CyDTA and boric acid alone. Thus, in the present study, we have prepared the catalysts modified with both CyDTA and boric acid and investigated their activities for HDS of 4, 6-dimethyldibenzothiophene (4,6-DMDBT) and their surface fine structures.

Experimental

Catalyst Preparation. Catalysts were prepared by an incipient wetness method. γ-Al_2O_3 was impregnated with an aqueous H_3BO_3 solutions followed by drying and calcination. B_2O_3/Al_2O_3 thus prepared was then impregnated with an aqueous solution containing ammonium heptamolybdate (or ammonium metatungstate), cobalt nitrate (or nickel nitrate) and CyDTA followed by the drying at 393 K. MoO_3 (WO_3) loading of the prepared catalyst was 10 (or 14) mass% with Co(Ni)/Mo(W) molar ratio of 0.32.

Activity Measurement. The catalyst was packed in a fixed bed flow reactor and sulfided *in-situ* in a stream of 5% H_2S/H_2 at 673 K and 1.1 MPa. After the sulfidation, the catalyst was cooled down to 573 K and the feed composed of 0.3 mass% 4, 6-DMDBT and decalin. was flown into the catalyst bed under the flow of H_2 at 5.1 MPa.

Characterization. SO_2 Uptake Measurement. The catalyst was pretreated in a stream of He 673 K and 0.1 MPa. Then, SO_2 was introduced into the catalyst bed by pulse method. SO_2 uptake was determined with GC-TCD. NO Uptake Measurement. The catalyst was sulfided in the same manner as employed for the activity measurements, and then NO was introduced into the catalyst bed by pulse method. NO uptake was detected with GC-TCD. EXAFS Measurement. The catalyst was pressed into a self-supporting wafer and set in the high-pressure EXAFS cell. The catalyst wafer was sulfided in the same manner as employed for the activity measurements. X-ray absorption spectra near W L_{III} edge were measured in a transmittance mode at room temperature using EXAFS 2000 spectrometer (RIGAKU).

Results and Discussion

The effect of CyDTA and boria on HDS activities for 4,6-DMDBT. In HDS of 4,6-DMDBT, dimethylbicyclohexane (DMBiCH) , bimethylcyclohexylbenzene (DMCHB) and dimethyl-biphenyl (DMBiPh) and their isomers were observed to be produced. We have investigated the effects of CyDTA and boria on HDS activity for 4,6-DMDBT. Here, HDS activity is defined by the sum of product yields per the loading amount of Co(Ni) and Mo(W).

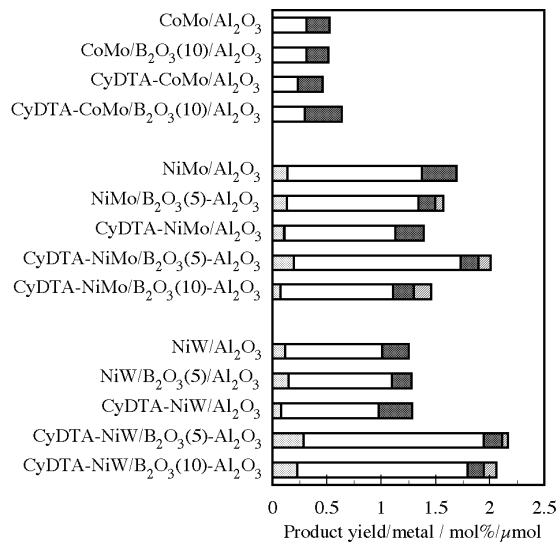

Figure 1. Effect of CyDTA and boria on HDS activities of $Co(Ni)Mo/Al_2O_3$ and NiW/Al_2O_3 for 4,6-DMDBT. ( ); DMBiCH, ( ); DMCHB, ( ); DMBiPh, ( ); iso-DMBiCH or iso-DMCHB. Numbers in parentheses indicate boria loading.

Figure 1 shows HDS activities of $Co(Ni)Mo/Al_2O_3$ and NiW/Al_2O_3. The main product is DMCHB over every catalysts. Comparing HDS activities of the catalysts without additives, the order of HDS activity is as follows: $CoMo/Al_2O_3 < NiW/Al_2O_3 < NiMo/Al_2O_3$. By the addition of CyDTA, no positive effects appears on HDS activities for 4,6-DMDBT while HDS activity of CyDTA-NiW/Al_2O_3 for DBT was about 1.6 times higher than NiW/Al_2O_3 [2]. From this result, it is suggested that the active phase which is selectively formed by CyDTA isn't efficient for HDS of 4,6-DMDBT. As with CyDTA, HDS activities were not improved by the addition of boria. Contrary to these results, catalysts modified with both CyDTA and boria shows much higher HDS activity than non-modified catalysts. In other word, we found the synergetic effect between CyDTA and boria on HDS activity of 4,6-DMDBT. The effect of both CyDTA and boria on HDS activity of NiW catalyst is more remarkable than those of $Co(Ni)Mo/Al_2O_3$. Perhaps, it is related to the fact that sulfidation of W species is more difficult than that of Mo species.

The effect of CyDTA and boria on the surface structure of NiW/Al_2O_3. Sulfur dioxide (SO_2) is known to adsorb on the basic

OH groups on Al_2O_3 surface. Therefore it is expected to investigate the effect of boria on Al_2O_3 surface by using SO_2 as probe molecules. **Figure 2** shows SO_2 uptake on B_2O_3/Al_2O_3. As B_2O_3 loading increases, SO_2 uptake sharply decreases and it reaches almost zero at above 60 * 10^{13} B atoms/cm^2-Al_2O_3 (10 mass% B_2O_3). This indicates that boria interacts with basic OH groups of Al_2O_3. Considering the fact that WO_3 species interact with basic OH groups of Al_2O_3, it is expected that boria induces the change of the structure of WS_2 after sulfidation.

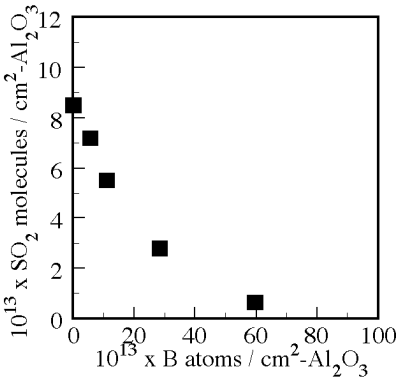

Figure 2. SO_2 uptake on B_2O_3/Al_2O_3.

It is well-known that nitric oxide (NO) adsorbs on the coordinatively unsaturated sites (CUS) on active metals, where the reaction is considered to take place. We have measured NO uptake on (CyDTA-)NiW/B_2O_3/Al_2O_3 (**Figure 3**). Regardless of whether CyDTA is present or not, NO uptake decreases with the increase in boria loading. This is due to the relaxation of the interaction between W and Al_2O_3. The change of NO uptake on CyDTA-NiW/B_2O_3/Al_2O_3 is more notable rather than that on NiW/B_2O_3/Al_2O_3. This result indicates that the number of CUS decreases while HDS activity is improved by the addition of CyDTA and boria. Therefore, the effect of CyDTA and boria can't be explained in terms of the number of CUS. Therefore, it is assumed that boria improves the HDS activity of CUS and it causes the higher HDS activity for 4,6-DMDBT.

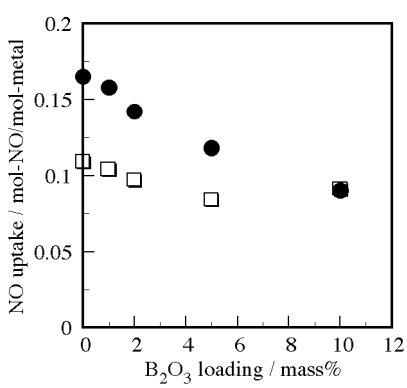

Figure 3. Effect of CyDTA and boria on NO uptake on NiW catalysts. ( ); NiW/B_2O_3/Al_2O_3, ( ); CyDTA-NiW/B_2O_3/Al_2O_3.

We have investigated that the effect of CyDTA and boria on the structure of WS_2 on CyDTA-NiW/B_2O_3/Al_2O_3 by EXAFS analysis (**Table 1**). Table 1 presents W-W and W-S coordination numbers of CyDTA-NiW/B_2O_3/Al_2O_3 which contained different amount of boria. It is found that the W-W coordination number hardly changes by the addition of boria to CyDTA-NiW/Al_2O_3. The dispersion of WS_2 is considered to be almost constant on each catalyst. This is the opposite result to that obtained from NO uptake measurements (see **Figure 3**). In contrast to this, W-S coordination number increases with the increase in boria loading. This result suggests that the sulfidation degree of WS_2 is improved by the addition of boria. Therefore, the decrease of the number of CUS by the addition of boria is due to the increase in the crystallinity of WS_2. Since there is a good correlation between HDS activity and the sulfidation degree of WS_2, the improvement of HDS activity by the addition of boria to CyDTA-NiW/Al_2O_3 is explained in terms of the sulfidation degree of WS_2. This means that boria induces the improvement of the quality of CUS. To sum up, the addition of boria causes the opposite effects on the surface structure of CyDTA-NiW/Al_2O_3, in other words, the improvement of the HDS activity of CUS and the decrease in the number of CUS.

Table 1. Structural Parameter of W-S, W-W Coordination

sample[a)]	W-S		W-W	
	N[b)]	R (nm)[c)]	N	R (nm)
WS_2 powder	6.0[d)]	0.24	6.0[d)]	0.32
CyDTA-NiW/Al_2O_3	4.9	0.24	3.5	0.32
CyDTA-NiW/B_2O_3(1)/Al_2O_3	5.0	0.24	2.9	0.32
CyDTA-NiW/B_2O_3(2)/Al_2O_3	5.3	0.24	3.0	0.32
CyDTA-NiW/B_2O_3(5)/Al_2O_3	5.7	0.24	3.0	0.32
CyDTA-NiW/B_2O_3(10)/Al_2O_3	5.7	0.24	2.9	0.32

a) Numbers in parentheses indicate boria loading.
b) Coordination number. c) Interatmic distance.
d) Both coordination numbers are fixed for 6.

Conclusion

It is considered that the addition of boria enhances the formation of highly sulfided and highly crystallized WS_2. It causes the two opposite effects, in other words, the improvement of the HDS activity of CUS and the decrease in the number of CUS. Moreover, it is considered that CyDTA enhances the coordination of Ni to the edge sites of the WS_2 and it promotes the positive effect of boria. Consequently, it is suggested that highly active site is selectively formed by the simultaneous addition of both CyDTA and boria, and it leads to the improvement of HDS activity for 4,6-DMDBT.

Acknowledgement. This work has been entrusted by the New Energy and Industrial Technology Development Organization under a subsidy of the Ministry of Economy, Trade and Industry.

References

(1) van Veen, J. A. R.; Gerkema, E.; van der Kraan, A. M.; and Knoester, A., *J. Chem. Soc. Chem. Commun.*, **1987**, 1684.
(2) Shimizu, T.; Hiroshima, K.; Honma, T.; Mochizuki, T.; Yamada, M., *Catal. Today*, **1998**, *45*, 271.
(3) Ohta, Y.; Shimizu T.; Honma, T.; Yamada, M., *Hydrotreatment and Hydrocracking of Oil Fractions*, **1999**, 161.
(4) Li, D.; Sato, T.; Imamura, M.; Shimada, H.; Nishijima. A., J. Catal., **1997**, *170*, 357.
(5) DeCanio, E. C.; Weissman, J. G., *Colloids and Surface A*, **1995**, *105*, 123.

NOVEL PREPARATION OF TITANIA (TiO_2) CATALYST SUPPORT BY APPLYING THE MULTI-GELATION METHOD FOR ULTRA-DEEP HDS OF DIESEL OIL

Shinichi Inoue[*1], *Hidehiko Kudou*[*1], *Akihiro Muto*[*1], *Takeo Ono*[*2]

*1: Research & Development Center, Chiyoda Corporation, 1-1 Minamiwatarida-cho, Kawasaki-ku, Kawasaki, 221-0022, Japan
E-mail : sinoue@ykh.chiyoda.co.jp
*2 : Ono Professional Engineer Office
1-38 Furuichiba, Saiwai-ku, Kawasaki 211-0952, Japan

Introduction

It is widely accepted that specific activity of titania (TiO_2) catalyst is superior to alumina catalyst. But, TiO_2 supported metal catalyst has not been employed, so far, for industrial use in hydrodesulfurization (HDS) or hydrotreating processes, because TiO_2 is regarded having a small specific surface area less than 50-60m^2/g and poor thermal stability.

In this study, a novel synthesis method of multi-gelation of TiO_2 as catalyst carriers or catalysts has been proposed [1]. The physical properties of TiO_2 can be controlled to enhance some catalytic activity. Since the physical properties of well controlled TiO_2 have superior characteristics to the conventional TiO_2, we tried to apply TiO_2 as the catalytic materials to the fields of petroleum refining for ultra-deep HDS of diesel oil.

Multi-Gelation Method

Multi-gelation method, originally developed for Alumina [2], is the procedure to produce the inorganic oxides gel by swinging of pH of solution dexterously several times. This method can be employed in preparation of hydrous titanium. It can control a particle size of TiO_2 uniformly with a designed pore size.

Experimental

Preparation Method of TiO_2 Support

Figure 1 shows the principle of the multi-gelation method to synthesize TiO_2. The raw materials are acidic $TiCl_4$ and basic ammonia solutions. Hydroxyl gel of TiO_2 was synthesized by swinging pH from $TiCl_4$ and ammonia solutions. $TiCl_4$ and ammonia solutions were supplied to the gelation vessel alternately, and hydrous titanium was synthesized. Particles of hydrous titanium were controlled in desirable particle size by alternately supplying $TiCl_4$ or ammonia solution. And hydrous titanium was washed by water to remove ammonium chloride. After filtration, TiO_2 as a catalyst or a catalyst carrier was molded to cylindrical shapes by the extruder, for example. And it was dried at 120 °C and is calcined at 500 °C in the standard procedure.

Catalyst

TiO_2 supports properties used in this study are as follows: Specific surface area is 162m^2/g, average pore diameter is 9nm whose pH swing number is 3 times. The CoMo/TiO_2 catalysts were prepared by gel impregnation method: TiO_2 gel was impregnated with ammonium heptamolybdate and Cobalt nitride as required. This was followed by drying at 120°C for 3h and calcination in air at 500°C for 3h.

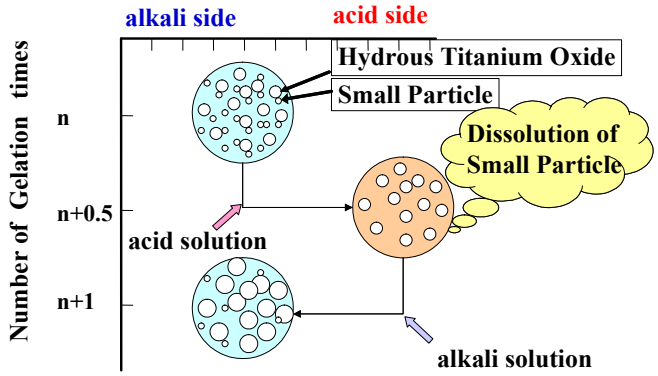

Figure 1 Principle of Multi-Gelation Method

Measurement of HDS activity

The HDS experiments were carried out with a fixed-bed reactor. The cata1yst was presulfided with the feed oil spiked by DMDS. Typical reaction conditions were as follows: H_2/Oil ratio 250, LHSV 2 h^{-1}, reaction pressure 5 MPa, Reaction temperature 330 - 350°C. The Middle-East straight run gas oil with 1.3wt% sulfur was used as feed stock.

Results and Discussion

Specific surface area, particle size and crystal form are summarized in Table 1.

Table 1 Properties of TiO_2

Preparation Method	No. of Geration (-)	Surface Area (m2/g) by BET	Crystallite Size (nm) by XRD	Crystalline Form by XRD
Multi-geration	1	175	5.9	anatase
	2	170	6.3	anatase
	3	162	6.7	anatase
	4	151	7.1	anatase
	5	138	8.5	anatase
	6	133	9	anatase
Convensional(CS-300)	-	61	19	anatase

Particle Size, Pore Distributions and Crystal Structures

Photo 1 shows TEM image of the primary particles of TiO_2 obtained by multi-gelation method. It was found that the particle size varies according to the number of gelation times. Namely as shown in Table 1, for example, two times of gelation gives ca. 6.3 nm, while five times of gelation gives ca.8.5 nm size of the particle. In addition, it was observed that each particle size becomes more uniform with times of gelation.

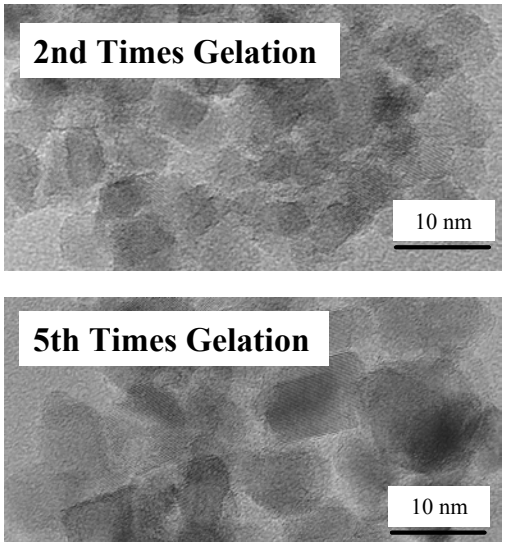

Photo 1 TEM Image of Multi-gelation TiO_2

The multi-gelation method has a good performance for controlling pore structures, i.e., pore size distributions as shown in Figure 2. The figure shows the pore diameter versus differential value of pore volume on various numbers of gelation times. This method gives well controlled nano-porous structures of TiO_2. The pore size distribution, which can be controlled sharply in accordance with numbers of gelation times, reflects that of particle size. In other words, it shows that this synthesis method can materialize the TiO_2 of arbitrary and uniform particles. This is an important point to evaluate the catalytic performance in relation to the physical properties, especially the particle size, of TiO_2.

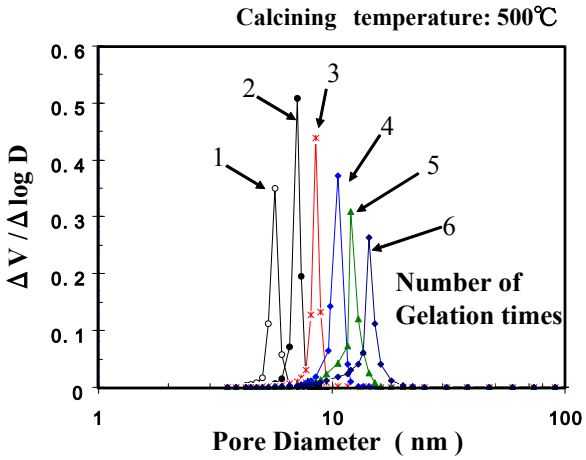

Figure 2 Pore Distributions of TiO_2 Controlled by Multi-gelation Method

Specific Surface Area

TiO_2 obtained by this method has higher specific surface area even after the calcinations at 500 °C than the conventional TiO_2, shown in Table 1. It decreases from 175m^2/g to 133m^2/g by increasing gelation times from one to six times. This may be due to the growth of crystal particle with gelation times.

Hydrodesulfurization Activity

The activity of the proprietary TiO_2 catalyst compared with the conventional CoMo/alumina catalyst for 500 ppm HDS are shown in Figure 3. This Figure also shows the reactivity of CoMo/TiO_2 catalyst prepared using conventional TiO_2 carrier with 60 m^2/g of surface area. It is important to mention that the catalytic activity of the TiO_2 supported prepared by multi-gelation method with high surface area and good pore distribution is much higher than that of the catalyst using conventional TiO_2 support with low surface area. Furthermore, it also shows that the new TiO_2 catalyst has 2 times higher hydrodesulfurization activity than that of the commercial alumina catalyst.

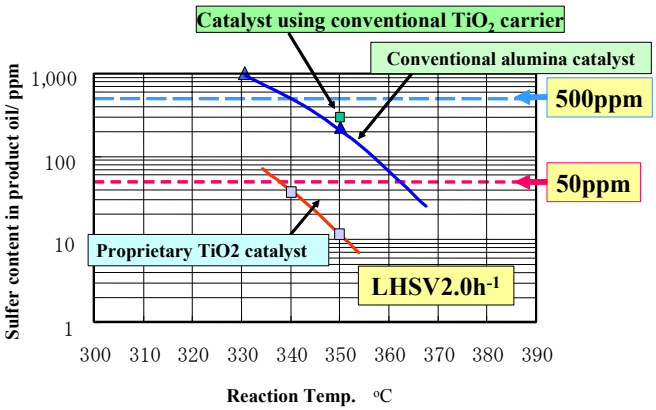

Figure 3 HDS Performance of Proprietary TiO_2 Catalyst

Conclusions

It was confirmed that TiO_2 with high specific surface area by the novel multi-gelation method showed good performance of catalytic activity in ultra-deep HDS reaction. Since the multi-gelation method can control the physical properties of TiO_2, it expected to be widely employed in various application fields. The proprietary TiO_2 catalyst prepared by the multi-gelation method is good candidates for the hydrodesulfurization or hydrotreating processes.

Acknowledgement

This work has been entrusted by the New Energy and Industrial Technology Development Organization under a subsidy of the Ministry of Economy, Trade and Industry of Japan.

References

[1] Kudou, H., Inoue, S., Takatsuka, T., Ono, T., Nakata, S., Kato, S., The 6th International Conference on TiO_2 Photocatalytic Purification and Treatment of Water and Air, Abstracts, p.63, Ontario, Canada, June25-29, 2001.

[2] Shiroto, Y., Ono, T., Asaoka, S., Nakamura, M., USP:4,422.960

ULTRASOUND ASSITED SYNTHESIS AND HYDRODESULPHURIZATION ACTIVITY OF Ru-Al-PILLARED CLAYS

M. Josefina Pérez-Zurita, Gabriela Pérez Quintana, José Gregorio Biomorgi and Carlos Eduardo Scott*

Universidad Central de Venezuela, Facultad de Ciencias, Escuela de Química, Centro de Catálisis, Petróleo y Petroquímica.
Apartado Postal 47102, Caracas, Venezuela

Introduction

The need for more active catalysts for hydrotreatment reactions has lead researchers to work on non conventional systems capable of meet the continuously increasing demands of the environmental national agencies for cleaner fuels. An alternative for the afore mentioned non conventional systems could well be Pillared Interlayer Clays (PILC) as catalysts, supports or precursors of highly disperse catalysts. The synthesis of PILC has been carried out for many research groups and many applications have been found for these type of materials. However, their use in a commercial scale is not yet a reality mainly because, on their synthesis, a great amount of water has to be used. In the past five years some efforts has been done to overcome this problem and good advances has been achieved (1-4). Besides, Chianelli et al. (5) reported on the hydrodesulphurization of dibenzotiophene (DBT) on a series of transition metal sulfide catalysts and found that ruthenium shows the best catalytic performance, even better than Ni, Mo or Co sulfides. The synthesis of a ruthenium based PILC was reported by Lenarda et al.(6) who used two different preparation procedures and tested the resulting catalysts in the hydrogenation and isomerization of 1-butene. The aim of the present work was to synthesize and study the behavior of the Ru-Al-PILC system in the hydrodesulphurization of tiophene.

Experimental

Ru-Al-PILC catalyst was prepared following the method reported by Lenarda et al.(6) but using ultrasound radiation on the exchange step in order to diminish exchange time. A Ru/Al-PILC catalyst was also prepared as a reference by conventional wet impregnation of an aqueous solution of $RuCl_3.xH_2O$ (Aldrich) on an Al-PILC. The preparation method of the Al-PILC was reported elsewhere (3).

Ru-Al-PILC Synthesis. A commercial montmorillonite, KWK-200 from American Colloid Company, without further purification, was used during the study. The precursor solution of aluminium and ruthenium was prepared by adding, under continuous stirring, NaOH drop wise to a mix solution of $AlCl_3.6H_2O$ (Riedel-DeHaën) and $RuCl_3.xH_2O$ (Al/Ru ratio of 20). The resultant solution had a OH / (Al+Ru) ratio of 2.4 and was left to stand for 24 hours at room temperature. After this time, the solution was added to a 50% suspension of clay in acetone and the mixture was divided in 3 portions and placed immediately into the ultrasonic bath which was kept at 44 ºC. The portions were retired from the bath at various times (60, 75, 90 min). Once the exchange process was completed, the solids were centrifuged, washed 5 times with double distillated water and dried at 60 ºC overnight. This series of catalysts was named Al-Ru-$PILC_x$ where x represent the time of exchange. In some cases the samples were calcined in flowing air at 400 ºC for 4 hours. The catalysts were characterized by XRD (Philips, PW1830), Textural properties (MICROMERITICS, ASAP-2400) and Chemical analyses (GBC AVANTA).

HDS reaction. Prior to reaction, the catalysts were suphided with a 5:1 mixture of H_2/H_2S or N_2/H_2S at 400 ºC for 4 hours in an atmospheric flow system and using a specially designed reactor able to be transported sealed. The sample was then transferred to the catalytic system were the reaction was conducted at 280 ºC and atmospheric pressure. The flow of hydrogen was 0.1 cc/s and a solution of 10% tiophene in hexane was fed to the system through a syringe pump at a rate of 1 cc/h.

Results and Discussion

Synthesis results. Table 1 shows the Chemical Analyses, Specific Surface Area and the Basal Spacing of the studied samples.

Table 1. Chemical Analyses, Specific Surface Area and Basal Spacing results

Solid	% Ru	SSA (m^2/g)	d (001)
Original clay	-----	33	13
Al-Ru-$PILC_{60}$	-----	207	18
Al-Ru-$PILC_{75}$	1.02	229	18
Al-Ru-$PILC_{90}$	-----	228	18
Ru/Al-PILC	3.00*	175	-----

* Nominal

The pillaring process on the mix pillared clay was evidenced as the specific surface area and basal space increased substantially. The use of ultrasonic radiation resulted in an excellent tool to reduce time of exchange, as the optimal time of exchange was 75 minutes which represent a decrease of ≈ 90% in time, as compared with the conventional synthesis reported by Lenarda et al. (6). As reported by these authors, only around 1% ruthenium was incorporated on the Ru-Al-PILC.

A complete textural characterization was conducted on the Ru-Al-PILC catalysts and on the Al-PILC support. Both solids shown a type II isotherm (following BET classification) with a type B hysteresis, characteristic of laminar solids. Detailed results are shown in table 2.

Figure 1 shows the pore distribution plot.

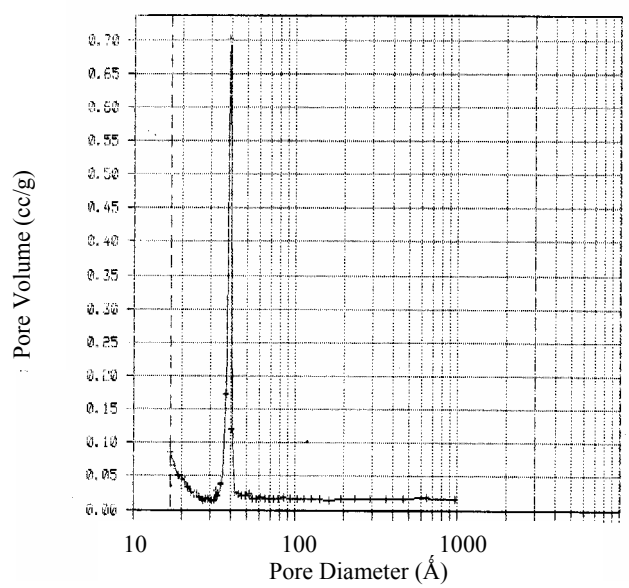

Figure 1. BJH average pore diameter of Ru-Al-PILC

A narrow pore distribution at around 40 Å is observed providing evidence of a great homogeneity of the Ru-Al-PILC sample

Table 2. Textural properties

Solid	SSA (m^2/g)	D_p (Å)	Vp (cc/g)	Vμ (cc/g)	SSAμ (m^2/g)
Al-Ru-$PILC_{75}$	229	46	0.123	0.077	195
Al-PILC	300	50	0.180	0.097	255

As expected, ruthenium impregnation leads to a decrease on surface area, porous volume and pore diameter.

Catalytic results. The catalytic results are shown in table 3.

Table 3. Catalytic results on the HDS of tiophene

Catalyst	Sulphiding mixture	Conv. (%)	Activity * 10^7 (mol/s*g)
Ru/Al-PILC	H_2/H_2S	4	0.42
Ru-Al-PILC	H_2/H_2S	14	1.42
Ru-Al-PILC	N_2/H_2S	21	2.10
Ru-Al-PILC*	N_2/H_2S	3	0.33

* Calcined

It is expected that ruthenium on a PILC structure could be better dispersed as it would take defined positions in the pillar. Our results show that the Ru-Al-PILC catalyst is almost three times more active than the impregnated catalyst. This result seems to indicate that indeed the PILC structure lead to a better disperse ruthenium catalyst which in turn is more active. Further measurements are in progress in order to confirm this statement.

When the sulphiding mixture was changed from H_2/H_2S to N_2/H_2S, an increase in activity was observed. This result seems to point out that a high hydrogen concentration could lead to a loss of S atoms from the RuS_2 formed and, as a consequence, the active phase would be replaced by ruthenium completely reduced. A similar result was reported by De los Reyes et al.(7) and more recently by Castillo and Ramirez(8) in a 7% Ru/Al_2O_3 catalyst. These authors attributed the lost of activity to the fact that a high concentration of hydrogen in the sulphiding mixture, do not allow ruthenium atoms to complete its coordination sphere with S atoms but rather favors that part of ruthenium reduces completely to Ruº possibly segregated. These ruthenium atoms do not participate in the active phase RuS_2. Castillo and Ramirez(8) also reported that when the catalysts was pretreated with the H_2/H_2S mixture, the stability of the catalysts was very poor as compare with that of the N_2/H_2S pretreated catalysts. In their case, however, the lost of activity was more important. While their result show a lost of activity of up to 80% when the suphiding mixture was H_2/H_2S, we only observe a 33% lost of activity. This result seems to give evidence that ruthenium in our catalyst is more stable probably because it is in the PILC structure and as a consequence, its reduction is more difficult.

When the catalyst is calcined before sulphurization, the activity is lost probably because ruthenium is stabilized on the PILC structure hindering the formation of RuS_2 at the activation conditions.

Conclusions

By using ultrasonic radiation in the synthesis of a ruthenium based PILC, the time of exchange can be reduced in more than 90%.

The Ru-Al-PILC was a good precursor of a highly dispersed catalyst which showed higher hydrodesulphurization activity than ruthenium impregnated on Al-PILC.

The sulphiding mixture showed to have an important effect on the catalytic performance of the Ru-Al-PILC studied, the stability of the ruthenium species generated by the PILC structure minimized the reducibility of ruthenium when the sulphiding mixture was H_2/H_2S.

Acknowledgement. The author would like to recognize the financial support of FONACIT through Project G-97000658

References

(1) Katdare S., Ramaswamy V. and Ramaswamy A. *Catal. Today*, **1999**, 49, 313.
(2) Katdare S., Ramaswamy V. and Ramaswamy A *Micro & Meso Porous Mat.* **2000**, 37, 329
(3) Pérez Zurita M.J., Pérez Quintana G., Maldonado A., Biomorgi J.G. and Scott C.E., *Prepr. Pap TOCAT IV*, **2001**, 279
(4) Pérez Zurita M.J., Pérez Quintana G., Maldonado A., Biomorgi J.G. and Scott C.E.*, to be published*
(5) Chianelli R.R, **1984,** Catal. Rev- Sci. Eng., 26, 361
(6) Lenarda M., Storaro l., Ganzerla R., Rinaldi A., *J. Mol. Catal. A* **1999**, 144, 151.
(7) De los Reyes A., Vrinat M., Geantet C., Breysse M., Catal. Today, **1991,** 10, 645
(8) Castillo Villalón P. and Ramírez Solis J., Prepr. Pap. – *XVIII Simposio Iberoamericano de Catálisis* **2002***, 1068*.

Characterization of refractory sulfur compounds in residua: help for deep residue hydrodesulfurization

I.Guibard[1], F.X. Haulle[1], S.Kressmann[1], I. Merdrignac[2]

1-Institut Français du Pétrole, CEDI "René Navarre", BP3, 69390 Vernaison, France
2-Institut Français du Pétrole, 1-4 av de Bois Préau, 92852 Rueil Malmaison cedex, France

Introduction

The refinery of petroleum residues is more and more focussed on the removal of sulfur compounds from fuel oils. This low sulfur fuel oil (LSFO) is essentially used in power plant for electricity production that enables to reduce SOx emissions. Moreover desulfurized fuel oil is necessary to have a suitable feed for Resid Catalytic Cracking (RCC) unit. Atmospheric residues (AR) and above all vacuum residues (VR) are the most difficult feeds to process catalytically as they contain and concentrate most of the crude impurities. Among them, asphaltenes, metals and heavy sulfur compounds affect the process performances.

These residues are generally hydrotreated in a fixed bed unit using high pressure of hydrogen and specific catalysts. The process consists of two complementary sections installed in series: the demetallization (HDM) section and the refining section (HDS). The main objective of the HDM section is to disaggregate asphaltenes and to remove most of the metals. However in this section a partial hydrodesulfurization (HDS) also occurs. In the HDS section the deeply transformed feed is refined to remove most of the sulfur content from the effluent and to reduce Conradson Carbon to product a RCC feed. Depending on case, an intermediate section could be included with a specific catalyst, which is able to continue the demetallization and to begin the desulfurization step (1,2). For each section, specific catalysts were developed in order to achieve high severity levels and high duration cycle lengths. The IFP Hyvahl residue upgrading process developed in 1982 (1) has a well adapted graded catalyst system that is able to cope with a wide range of feeds and to associate high severity levels together with constant product quality and increased cycle lengths. Since a few years, the demand for very low sulfur fuel oil (until 0.5 - 0.3 weight %) during long cycle has been increased on the worldwide market. This objective is difficult to achieve and requires increasing knowledge of heavy refractory sulfur compounds and kinetic information on the sulfur compound reactivity. But the characterization of sulfur compounds in fuel oil is complex due to the high boiling range of these products and the unavailability of detailed analytical technique as sulfur speciation for diesel.

The main purpose of this work is to characterize the refractory sulfur compounds in heavy oils using standard analyses in order to have a first approach of their location. In this study, the evolution of heavy sulfur compounds during hydrotreating process was followed along reactors.

Experimental

Feed and hydrotreatment experiments. A first set of experiments was performed on Middle East resid in order to locate sulfur compounds. Several feedstocks (AR, VR) were hydrotreated in a fixed bed reactor unit under the same standard operating conditions to achieve the target of 0.3%wt sulfur. Experiments were conducted using industrial residue hydrotreatment catalysts (HDM and HDS sections). The characteristics of these feedstocks are given in Table 1.

A second set of experiments was carried out only on HDM catalyst with varying residence time in order to study precisely the HDS performance.

Analytical techniques. Liquid products were distillated in three cuts (PI-375, 375-520°C and 520°C+). The heaviest cut is subjected for separation to asphaltenes (Asph) and maltenes fractions using n-heptane. The maltenes fraction and 375-520°C cut were further fractionated by liquid column chromatography into saturates (Sat), aromatics (Aro) and resins (Res). On each SARA fractions, elemental analysis (Carbon, Hydrogen, Nitrogen, Sulfur, Oxygen) was performed. Metal (Nickel and Vanadium) concentrations in asphaltenes and resins were measured by ICP method.

Size exclusion chromatography (SEC) was performed on the different fractions using a refractive index detector. Calibration was carried out using polystyrene standards (3).

Table 1. Main characteristics of Middle East feedstocks

	Arabian Medium AR	Arabian Light VR	Arabian Heavy VR
Total S (%wt)	**3.7**	**4.5**	**5.3**
Total Ni+V (ppm)	80	125	218
Asph (% wt)	**6.3**	**9.9**	**16.2**
S (%wt)	7.16	6.76	7.6
Res 520°C+	**20**	**34.8**	**34.3**
S (%wt)	5.66	5.4	6.4
Aro 520°C+	**20**	**44.5**	**40.7**
S(%wt)	3.82	4.0	4.5
Sat 520°C+	**4.3**	**8.0**	**4.2**
S(%wt)	0.1	0.9	-
520°C- cut	**49.4**	**2.8**	**4.6**
S(%wt)	2.6	3.5	3.9

Results and Discussion

Sulfur evolution during hydrotreatment. In atmospheric or vacuum residua, sulfur is initially concentrated in the heaviest fraction (cut 520°C+) and specifically in asphaltenes, which are described as the most refractory class to hydrodesulfurization (4). During hydrotreatment, the total sulfur content decreases all along reactors and can reach 0.3%wt at the outlet of the unit using appropriate operating conditions (temperature, residence time). In the same time, residue conversion occurs and heavy fraction as asphaltenes, resins and aromatics decrease to product lighter fractions. **Figure 1** shows the evolution of the sulfur content inside the SARAs fraction versus residence time for the HDM and HDS section, in the case of arabian medium AR hydrotreatment. All fractions are continuously desulfurized along reactors but at different rate. Thus for HDM section, we observe an important decrease of sulfur content for all the fractions. The HDM catalyst is able not only to disaggregate the asphaltenes but also to eliminate a great part of sulfur compounds.

In the HDS section, the desulfurization rate seems lower for each fraction but the removal of ultimate sulfur is much more difficult. The sulfur content in resins and aromatics fractions reach a low level due to the use of a specific catalyst whereas it still remains at a high level in asphaltenes. This indicates that the sulfur is located in high molecular weight and doesn't access to the active site in the porosity of the HDS catalyst. However, this specific porosity is necessary for efficient removal of sulfur in lower molecular weight fractions.

After HDM and HDS section, the residual sulfur (0.3%wt) is still concentrated in 520°C+ fraction. The sulfur distribution is about 15% in asphaltenes, 40% in resins and aromatics fraction, 5% in light

compounds (520°C-). Therefore the sulfur is concentrated in heavy aromatics and resins fractions. The sulfur compounds in the asphaltenes fraction cannot be eliminated even at high residence time in HDS section. Consequently the desulfurization of asphaltenes is essentially done in the HDM section. The same observation has been done for VR hydrotreatment.

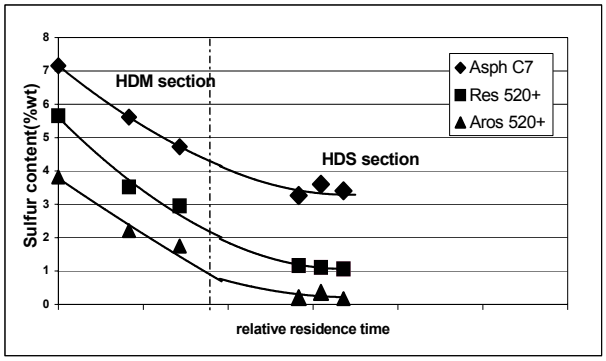

Figure 1. Arabian Medium AR hydrotreatment
Sulfur content evolution in 520°C+ cut

In fact, it seems very important to study the evolution of sulfur compounds in the HDM section for different relative residence time. Experiments are carried out on Arabian heavy VR for the HDM section. We can observe an apparent slowing down of resin and aromatics desulfurization (see **figure 2**). The same experiments were conducted with desasphalted oil (DAO/C7) obtained from n-heptane precipitation of the same vacuum residue. The decrease of sulfur content in resins and aromatics fractions after DAO/C7 hydrotreatment is more important than for vacuum residue (see Figure 2). This shows the inhibitor effect of asphaltenes for HDS reaction. However aromatics and resins produced by hydrocracking of the asphaltenes may be also more refractory than the initial fractions that could explain the difference between DAO and VR (5).

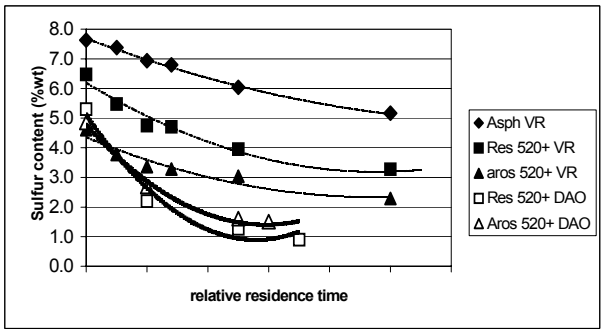

Figure 2. Arabian Heavy VR and DAO hydrotreatment in HDM section. Evolution of sulfur content in 520°C+ fractions

In conclusion, asphaltenes appear like the most difficult class to desulfurize and also have strong inhibitor effect on desulfurization reactions. Moreover, the presence of asphaltenes on the catalytic surface probably slowdown the desulfurization rate of resins and aromatics fractions.

SEC analyses. In order to obtain more information about evolution of heavy compounds, Size Exclusion Chromatography (SEC) has been performed on asphaltenes fraction in Arabian medium AR before and after hydrotreatment. Profiles of relative distribution size are reported in **Figure 3.**

Results show that the structure of high molecular weight molecules is not affected in the HDM section, but an increase of the low to high molecular weight peaks ratio is observed. During this step smaller molecules can be formed. After the second step of the process (HDS), chromatogram profiles show however a significant decrease of the low molecular weight peak. Interpretations of such results may be a preferential conversion of small asphaltene molecules into resins and aromatics due the high level of hydrogenation of HDS catalyst. Besides, high molecular weight population seems to be equivalent after the first and the second step of the process. In conclusion, the highest molecular weight asphaltenes that are not eliminated on HDM catalyst are still remaining at the outlet process after HDS. This confirms the kinetic evolution of asphaltenes sulfur.

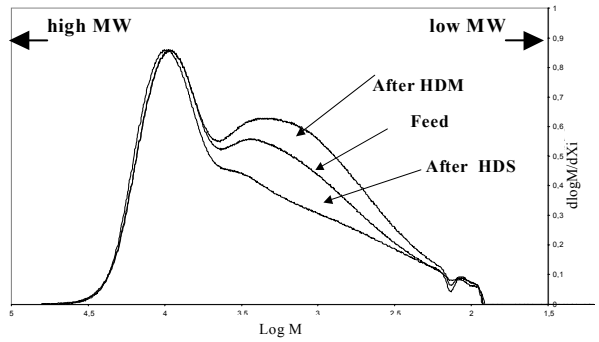

Figure 3. Arabian medium AR hydrotreatment
SEC chromatograms of non converted and converted asphaltenes after HDM and HDS section of the Hyvahl process.

Conclusion

The increasing severity of sulfur specifications for fuel oil involves the need of more knowledge about the heaviest sulfur compounds. Deep desulfurization can be achieved with appropriate catalytic system and operating conditions. Usual analyses like liquid chromatography separation and elemental analysis give a first approach of the location of refractory compounds and can be a help to well-understand the specific role of each catalyst for HDS reactions. So, this study demonstrates that after deep hydrotreatment sulfur is essentially concentrated in heavy aromatics and resins fractions (cut 520°C+). The desulfurization of asphaltenes is difficult and occurs mainly in the HDM section. Moreover the presence of asphaltens on the catalytic surface slowdowns the desulfurization rate of others fractions.

The development of new appropriate analytical method seems to be required to isolate and characterize heavy sulfur compounds. This analysis should involve a better understanding of kinetic HDS reactions and should be a real help to define the best catalyst layout depending on the feed composition and origin.

References

(1) Billon, A.; Peries, J.P.; Espeillac,M.; Des Courrières,T. NPRA 89th Annual Meeting, San Antonio, **1991**
(2) Kressmann, S.; Harlé, V; Kasztelan, S.; Guibard, I.; Tromeur, P.; Morel, F. Prepr. Pap - Am chem Soc., Div Fuel chem, **1999**
(3) Merdrignac, I.; Truchy, C.; Robert, E.; Desmazieres, B.; Guibard, I.; Haulle, F.X.; Kressmann, S. Heavy Organics Deposition Conference (HOD), Puerta Vallarta, **2002**
(4) Speight, J.G. In *The Desulfurization of heavy oils and residua 2nd edition*; Dekker, M.,Inc : New York, 2000; pp. 127-167.
(5) Haulle, F.X; Kressmann, S. AICHE Spring Meeting, New Orleans, **2002**

CHARACTERIZATION OF SOLUBLE Mo COMPLEX DURING TRANSFORMATION TO Mo SULFIDE

Izumi Watanabe[1], Kinya Sakanishi[2], Isao Mochida[1], and Masao Yoshimoto[3]*

1) Institute of Advanced Material Study, Kyushu University, Kasuga, Fukuoka 816-8580, Japan
2) National Institute of Advanced Industrial Science and Technology (AIST), Tsukuba West, Ibaraki 305-8569, Japan
3) Japan Cooperation Center, Petroleum(JCCP), 3-2-1 Sakado, Takatsu-ku, Kawasaki, Kanagawa 213-0012, Japan

Introduction

Highly dispersed Mo sulfide catalysts with fine particles have been reported very active for the hydrotreatment of heavy hydrocarbons such as vacuum residue(VR) and coal.[1-6] Several oil-soluble Mo complexes can be one of the most promising candidates for the application to slurry phase catalytic upgrading of vacuum residues, because they form very fine MoS_2 particles during their heating upto around 350 ºC.[7] It is reported that the difference in the catalytic activities of Mo-DTC(dithiocarbamate) and Mo-DTP(dithio-phosphate) can be ascribed to the different extent of MoS_2 formation from the complexes under the hydrotreatment conditions. It is also noted that MoS_2 or solid Mo compounds derived from the two complexes are fine particles of very low crystallinity that can be highly dispersed in vacuum residue or asphaltene, because such solid particles are allowed to stay in asphaltene micelle which is dissolved or dispersed in toluene or maltene during the heating. Thermal decomposition of Mo-DTC stoichiometrically gave MoS_2, whereas Mo-DTP appears to provide MoS species in the presence of remaining phosphorous ligands. It seems that the remaining phosphorous ligands may retard the conversion of MoS to MoS_2 in VR, however, no clear evidence is not found by XRD, TGA, far-IR or TEM measurements.

In the present study, Raman spectroscopy is applied to the identification of MoS species formed from the soluble Mo complexes, since it can distinguish the layered graphite and amorphous-like carbon species. Because of the similarity in the layered structure of MoS_2 and graphite-like carbon, Raman spectroscopy is expected to give a clue to the difference in the structures of MoS species produced from the two Mo complexes.

Experimental

Materials. Mo-DTC and Mo-DTP used as MoS catalyst precursors in the present study are commercially available in the forms of crystal and solution, respectively. Their structures are illustrated in Fig.1. Commercially available MoS_2 powder is used as a reference compound. An Arabian heavy vacuum residue(AH-VR) is used for the hydrotreatment with Mo-complexes.

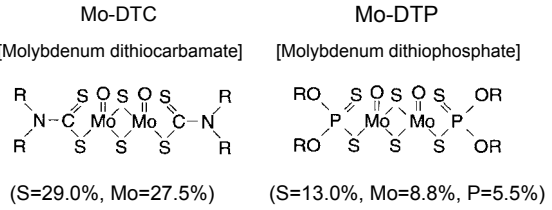

Fig.1 Structures of Mo-DTC and Mo-DTP

Heat-treatment. The mixture of Mo complex with VR was heated at 110 ºC for 1 h for well dispersion, and then hydrotreated at 380 ºC over the decomposition temperature of the complexes in a mini-autoclave under 10 MPa H_2. The heated mixture was extracted with n-hexane to separate the maltene and asphaltene fractions.

Analysses. The thermal behavior of the Mo complexes was examined using TGA(Seiko, SSC/5200) by their weight changes. The complexes and their decomposed products in the residue were analyzed by FT-Far IR(Jasco-620), XRD, and Raman spectroscopy.

Results and Discussion

According to TG/DTA profiles of Mo-DTC, three endothermic peaks were observed, and the first two of them were derived from the structural change in the ligands with a small weight change. The last peak around 300 ºC was ascribed to the formation of MoS_2 with a large weight loss. This was in good agreement with the formation of Mo-S bond observed by far IR spectroscopy in Fig.2.

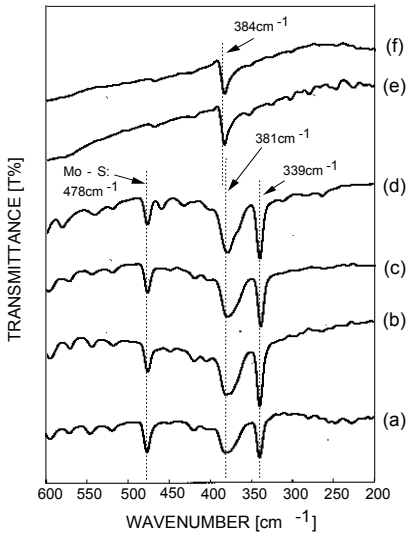

Fig.2 Far IR spectra of Mo-DTC before and after heat-treatment (a: non-treated, b: 200ºC, c: 250ºC, d: 260ºC, e: 300ºC, f: 400ºC)

The decomposition of Mo-DTP was started from 200 ºC based on the TG/DTA, reaching to 26 wt% at around 300ºC, however, no clear peak of Mo-S was observed in the far IR as shown in Fig.3.

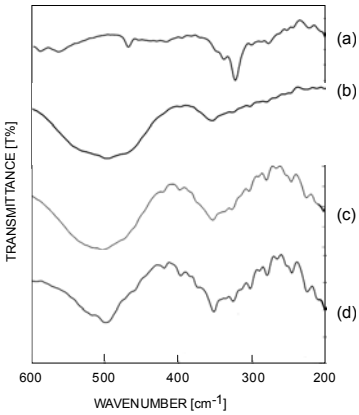

Fig.3 Far IR spectra of Mo-DTP before and after the heat-treatment (a:non-treated, b:350ºC, c:400ºC, d:500ºC)

When Mo-DTP was heat-treated under the atmosphere of 10% H_2S in H_2, the formation of Mo-S species was observed by Raman spectroscopy as shown in Fig.4.

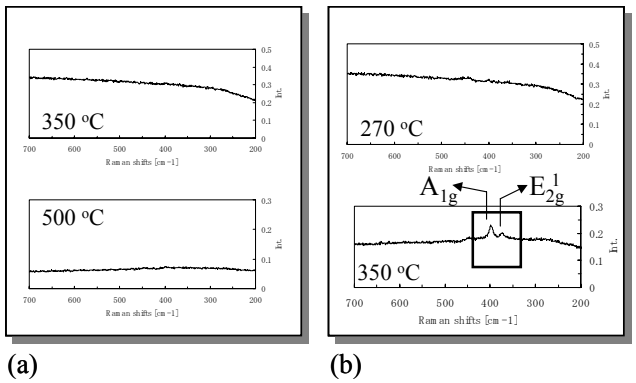

Fig.4 Raman spectra of Mo-DTP before and after the heat-treatment (a: under N_2, 1h; b: 10%H_2S/H_2, 1h)

It is revealed that MoS_2 should be produced from Mo-DTP over its decomposition temperature under the sufficient sulfiding conditions. It is pointed out that Mo-DTC produced MoS_2 at around 300ºC even under the N_2 atmosphere as illustrated in Fig.5.

The difference in the properties and crystallinity of MoS2 between Mo-DTC and Mo-DTP may reflect in the Raman spectroscopy. Further details on the transformation of MoS2 morphology and crystallinity during the hydrotreatment are now on investigation

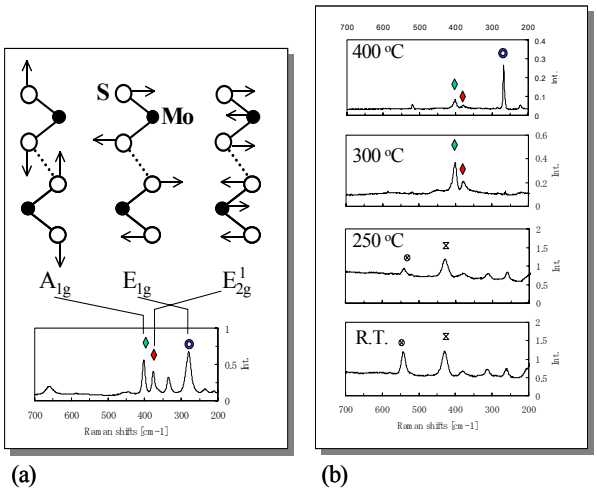

Fig.5 Raman spectra of Mo-DTC before and after the heat-treatment
(a: MoS_2; b: heat-treated Mo-DTC under N_2)

Fig. 6 shows TEM micrograph of Mo-DTC heat-treated with asphaltene at 370ºC. A clear formation of lamella-like MoS_2 crystalline structure was observed on the asphaltene matrix.

Fig.7 illustrates TOF-MAS spectra of asphaltene after the hydrotreatment with or without Mo-DTC or Mo-DTP. Compared to the spectra without catalyst, both of the Mo complexes hydrocracked the asphaltene farction significantly, the cracking extent being a little higher with Mo-DTP. The yield of the asphaltene was lower with Mo-DTC than that with Mo-DTP, reflecting the higher hydrogenation activity of Mo-DTC.

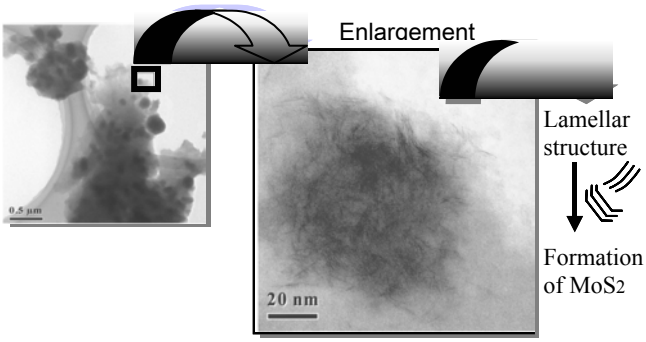

Fig.6 TEM of Mo-DTC treated at 370ºC with asphaltene

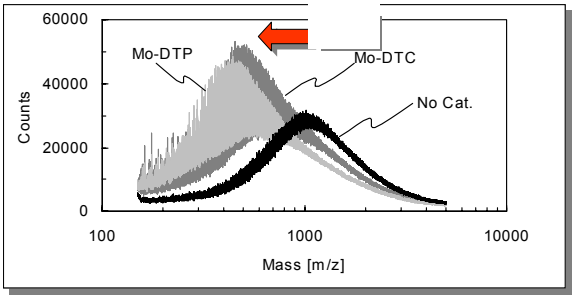

Fig.7 TOF-MAS of asphaltene after the hydrotreatment with or without Mo complex catalysts

References

1. Strausz, O.P., Lown, E.M., Mojelsky, T.W., *Prepr.ACS Div. Petrol. Chem.*, 1995, 40(2), 741.
2. Del Bianco, A., Panarti, N., Marchionna, M., *Prepr.ACS Div. Petrol. Chem.*, 1995, 40(2), 743.
3. Fixari, B., Peureux, S., Elmouchnino, J., Le Perchec, P., *Energy Fuels*, 1994, 8, 588.
4. Del Bianco, A., Panariti, N., Di Carlo, S., Beltram, P.L., Carniti, P., *Energy Fuels*, 1994, 8, 593.
5. Panariti, N., Del Bianco, A., Del Piero, G., Marchionna, M., Carniti, P., *Appl.Catal. A: Gen.,* 2000, 204, 203.
6. Panariti, N., Del Bianco, A., Del Piero, G., Marchionna, M., Carniti, P., *Appl.Catal. A: Gen.,* 2000, 204, 215.
7. Watanabe, I., Otake, M., Yoshimoto, M., Sakanishi, K., Korai, , Y., Mochida, I., *Fuel,* 2002, 81, 1515.

THE EFFECT OF ANTI FOULING ADDITIVES ON HEAT-INDUCED DEPOSITION

John F. Schabron and Joseph F. Rovani, Jr.
Western Research Institute
365 North 9th Street
Laramie, WY 82072

Introduction

Heat-Induced Deposition The problem of fouling due to deposition occurs when heavy oil materials are heated, blended, or pyrolyzed in visbreaking or vacuum distillation processes. This type of deposition can result from the formation of asphaltene flocs when a residuum is heated above a temperature at which the intermediate polarity material no longer protects the polar asphaltene cores[1,2], but below temperatures at which pyrolysis occurs (340 °C, 644 °F). This flocculation is not the same as asphaltene precipitation due to weak solvent addition. The temperature-induced asphaltene flocculation appears to be reversible when the material is cooled, as long as the material has not been heated to temperatures above which pyrolytic reactions occur. The polar asphaltene flocs can result in deposition and fouling problems in both upstream and downstream operations.

Residua are considered to be suspensions of polar asphaltene materials dispersed in a solvent phase.[3] Pal and Rhodes developed a model for emulsions that has been applied to petroleum residua.[3] The model features resins and solvent layers around an asphaltene core and solvated cores interacting with one another in an ordered system. Additional solvent is trapped between the asphaltene structures. Pal and Rhodes[4] considered a solvation shell magnitude term K (K=KS•KF), representing the amount of solvent adsorbed around a particle (KS) and the solvent trapped in a group of particles in the ordered system (KF). When a residuum is heated, the value for K decreases with increasing temperature, and less material is associated with the asphaltene structures, resulting in a flocculation of the polar asphaltenic-type core material.[1,2,5]

Using an apparatus constructed to quantify relative heat-induced deposition tendencies for petroleum residua, deposition density measurements were made for five residua materials.[5] The results suggested that the heat-induced deposition process is not significant at 100 °C (212 °F). It begins at 175 °C (347 °F), and is very evident at 250 °C (482 °F). At the latter temperature, the deposition density correlates with the free solvent volume, which is calculated from weight percent heptane asphaltenes and the Heithaus p_a parameter. The deposits were found to be enriched in porphyrins, and in nickel and vanadium. Activation energies of the reversible removal of the protective shell surrounding asphaltene cores were calculated from relative viscosity measurements at several temperatures. The energies were 470, 750, 940, 1,100, and 1,600 cal/mol for Vistar, CA Coastal, Boscan, MaxCL, and Redwater, B.C. residua, respectively.

Experimental

Additive Spiking Two commercially available anti-fouling additives designated A and B were added to a Lloydminster vacuum residuum at a level of 0.20 wt.% (2,000 ppm). Portions of 150g residua heated to 100 °C were poured into four round bottom flasks. A fifth round bottom flask for the control Lloydminster residuum with no additive was similarly prepared. A volume of 225 mL of cyclohexane was added to the residua in the round bottom flasks. The flasks containing the residua and solvent were attached to a rotary evaporator, which was used as a mixing device to spin the contents in a warm water bath at 65°C for about 30 minutes until the residuum was completely dissolved. The round bottom flask was removed and the contents were charged with a precise weight of additive. The flask was placed back on the rotary evaporator, and the cyclohexane was removed.

Heat-Induced Deposition Heat-induced deposition studies were conducted for the control Lloydminster residuum, the 0.2% A sample, and the 0.2% B sample using an apparatus described previously.5 This apparatus consists of a pivoting aluminum chamber that is continuously purged with flowing argon (Figure 1). A 1.75" diameter pre-washed aluminum pan containing 5 g of sample was

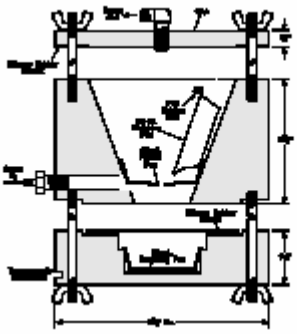

Figure 1. Heat-Induced Deposition Apparatus

placed inside the chamber in horizontal configuration. The chamber containing the sample was heated to 250 °C (482 °F) inside a convection oven, and at a predetermined timeframe, a trigger was released and the apparatus was rotated to position the sample pan in a vertical configuration (Figure 2). After a suitable timeframe to allow for the complete pouring of the sample from the sample pan into a collection pan, the oven was cooled, the chamber disassembled, and the sample pan examined for deposition phenomena. Deposition profiles were obtained at using a Kodak DC 265 zoom digital camera with a 37mm +10 macro lens.

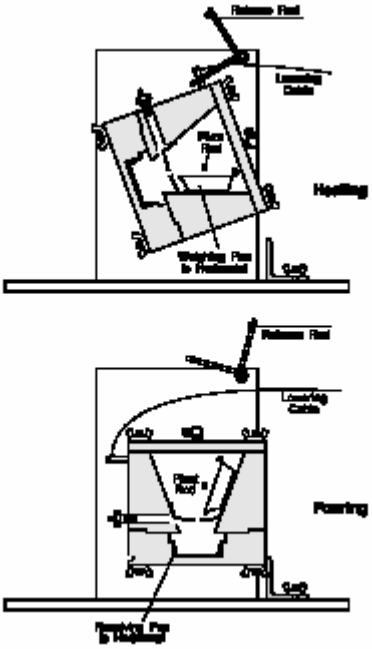

Figure 2. Use of the Deposition Apparatus

Results and Discussion

Deposition experiments were performed with three portions of whole Lloydminster residuum at 250 °/C with no additives. Single runs were made with the residuum containing 0.2 wt.% of each of the two additives A and B. The deposition patterns showed the presence of agglomerated deposition spots from the residuum without additive. The materials with the additives showed some spots, but overall smoother deposition profiles were evident. This effect was difficult to visualize, but it appears to be real. Close-up images of the deposition patterns with and without additives are presented in Figure 3.

Figure 3. Heat-Induced Deposition Patterns

These show exaggerated detail of the deposition spots. The additives appear to suppress agglomerization and cause a smoother dispersion of the deposition pattern than when they are not present.

Conclusions

Non-pyrolytic heat-induced deposition experiments were performed at 250 "C with Lloydminster vacuum residuum with and without the presence of anti fouling additives. The results showed that both of the additives appear to cause a smoother, more well dispersed deposition pattern than was observed with the residuum without additives. The effect was somewhat difficult to visualize but it appears to be real. Thus, the additives could be causing an enhanced dispersion of the asphaltene cores which are exposed when the residuum is heated, depressing association and agglomerization of the polar cores.

Acknowledgments Funding for this study was provided by the U.S. Department of Energy cooperative agreement DE-FC26-98FT40322 and co-sponsors BetzDearborn, ChevronLummus, ConocoPhillips, and ExxonMobil. The authors would like to thank Tony Munari for preparing the figures.

Disclaimer This report was prepared as an account of work sponsored by an agency of the United States Government. Neither the United States Government nor any agency thereof, nor any of their employees, makes any warranty, express or implied, or assumes any legal liability or responsibility for the accuracy, completeness, or usefulness of any information, apparatus, product, or process disclosed, or represents that its use would not infringe privately owned rights. Reference herein to any specific commercial product, process, or service by trade name, trademark, manufacturer, or otherwise does not necessarily constitute or imply its endorsement, recommendation, or favoring by the United States Government or any agency thereof. The views and opinions of authors expressed herein do not necessarily state or reflect those of the United States Government or any agency thereof.

References

1. Storm, D.A., Barresi, R.J., Sheu, E.Y. *Energy and Fuels*, 1995, **9** 168–176.
2. Storm, D.A., Barresi, R.J., Sheu, E.Y. *Fuel Science and Technology International*, 1996, **14** (1&2) 243–260.
3. Pauli, A.T., Branthaver, J.F., *Preprints, Division of Petroleum Chemistry, American Chemical Society*, 1999, **44** (2) 190-193.
4. Pal, R., Rhodes, E., 1989, *Journal of Rheology*, 1989, **33** (7) 1021–1045.
5. Schabron, J.F., A.T. Pauli, A.T., Rovani, J.F.,Jr., *Fuel*, 2001, **80** (7) 919–928.

CRACKING REACTIVITIES OF PETROLEM ASPHALTENES

Ryuzo Tanaka[1], Shinya Sato[2], Toshimasa Takanohashi[2], Satoru Sugita[3]*

[1] Central Research Laboratories, Idemitsu Kosan Co., Ltd.
Sodegaura, 299-0293, JAPAN
[2] Institute for Energy Utilization
National Institute of Advanced Industrial Science and Technology
Tsukuba, 305-8569, JAPAN
[3] Coal and Energy Project Department
Technical Development Group, Kobe Steel, Ltd.
Takasago, 676-8670, JAPAN

Introduction

Petroleum asphaltene is the heaviest portion of the oil fractions and may cause coking or plugging troubles in the refinery or in the transportation lines. Asphaltene is defined operationally by its solvent solubility, and it is an extremely complex organic mixture.

It is supposed that the cracking and coke formation reactivities of asphaltenes are dominated not only by their molecular structure but also by their aggregation tendency, because the size of asphaltene molecule is large and asphaltenes have various functional groups. The driving forces or the kinds of interaction contributing to the asphaltene aggregations have not yet completely clarified, because of the complexity of the phenomenon. Although, there must be some rigorously chemical relationships among the molecular structure, the aggregating tendency, and the coke making reactivity of asphaltenes.

Recently, some fundamental studies about molecular structure and aggregation phenomena of three petroleum asphaltenes, Maya, Khafji, and Iranian Light, with 13C-NMR[1)], Molecular dynamics simulation[2)], SANS[3)], and SAXS[4)] were carried out. In this paper, coke-making reactivities of those asphaltenes on thermal cracking were investigated with some set of autoclave experiments. The main concern of the paper is whether the braking up of the asphaltene aggregates contribute to the coke suppression of the reactions.

Experimental

Sample Preparation. The residua (> 500 °C) was obtained by vacuum distillation of three crude oils. Asphaltenes were isolated by addition of a 20:1 excess of *n*-heptane to each of the residua at 25 °C. The suspension was stirred 1 h at 100 °C in the autoclave. After cooling down and leaving at 25 °C overnight, the suspension was filterated. The precipitate was washed with *n*-heptane twice and dried. The yields of asphaltenes (precipitates) of Maya, Khafji, and Iranian Light are 24.9, 14.2, and 6.3wt%, respectively. **Table 1** shows the elemental analysis data of the asphaltenes.

Table 1. Elemental analysis data of asphaltenes.

	Maya	Khafji	Iranian Light
elemental, wt %			
carbon	82.0	82.2	83.2
hydrogen	7.5	7.6	6.8
sulfur	7.1	7.6	5.9
nitrogen	1.3	0.9	1.4
oxygen	1.2	1.1	1.5
H/C	1.10	1.11	0.98
metals, wtppm			
Ni	390	200	390
V	1800	550	1200
density, g/cm^3	1.1767	1.1683	1.1669

Asphaltene of Maya (As-MY) is the heaviest and contains the most amount of metals among the three asphaltenes. As-KF is medium heavy and contains the least amount of metals. H/C atomic ratio of As-KF is the highest, and this could be interpreted as the lowest aromaticity. As-IL is the lightest, but contains much nitrogen and metals. It has the lowest H/C atomic ratio, meaning the highest aromaticity. These properties are considered to affect aggregation phenomena and coking reactivities of asphaltene molecules much.

Asphaltene cracking. All reaction experiments were carried out batch wise in a 30 mL micro reactor. In a typical experiment, 2g of asphaltene and 8 g of solvent were loaded into the reactor. A stainless ball was also loaded for stirring. The reactor was then pressurized with nitrogen of 5 MPa at room temperature and was immersed in a preheated tin bath at 300 °C. In the case with the relaxation of asphaltene aggregates, tin bath temperature was hold at the temperature for 60 min. Then the temperature of tin bath was rose with the heating rate of 2 °C/min until the temperature reached 440 °C, the nitrogen pressure becomes ca. 8 MPa at the temperature. The reactor was oscillated all the time in tin bath. After the reaction was completed, the reactor was cooled in air. In the case without the relaxation of asphaltene aggregates, the temperature of tin bath start rising just after the reactor was immersed in it. 1-methylnaphthalene (1MN), quinoline (Qui), decalin (Dec), and the mixture of Qui and Dec (50/50) were used as the solvent.

Separation. Gas yields were calculated from the weight decrease of the reactor with releasing gas pressure after reaction. Liquid product and coke were washed out of the reactor with tetrahydrofuran (THF), then THF was evaporated. The product were separated with n-heptane and toluene into three fractions, heptane-soluble (HS), heptane-insolubleand toluene-soluble (HI-TS), and toluene-insoluble (TI).

Results and Discussion

The yields of the asphaltene cracking without solvent are shown in **Figure 2** (NS: No Solvent, /R: with relaxation of aggregates). TI (Coke) yields are around 50% in these experiments. The order of the TI yields of three asphaltenes is MY > IL > KF. In the case of As-KF, the relaxation of asphaltene aggregates by stirring for one hour shows no effect for coke suppression.

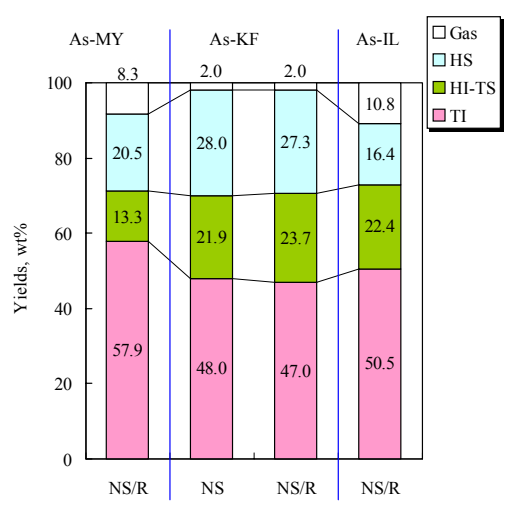

Figure 2. Yields of asphaltene cracking without solvent.

Figure 3 shows the yields of the asphaltene cracking with quinoline. The yields of TI from the asphaltene cracking decrease about 10 wt% and the order of TI yields from three asphaltene is the same with the case of without solvent (MY > IL > KF). With quinoline, the relaxation of asphaltene aggregates by stirring at 300 °C for one hour suppress the TI yields with ca. 5 wt% of all asphaltenes cracking.

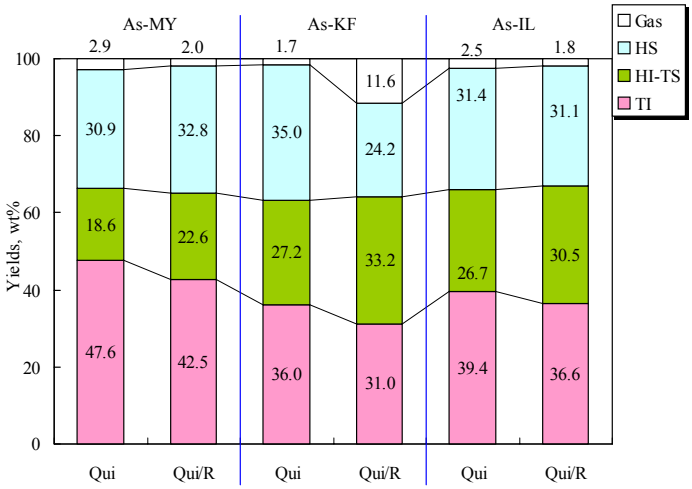

Figure 3. Yields of asphaltene cracking with quinoline.

Figure 4 shows the yields from As-KF. The order of TI yields with three solvents are 1MN > Qui > Q+D (quinoline and decalin mixture) >> Dec. Decalin shows the largest effect to suppress the coking and the TI yields of Q + D is almost average of Qui and Dec. In some literature, Dec is not a hydrogen donor at all. Although in this case, Dec seems to show the hydrogen donor ability. Indeed, the recovered solvent after reaction experiments contained the tetralin (tetralin content is 1.1 mol% of feed dcalin).

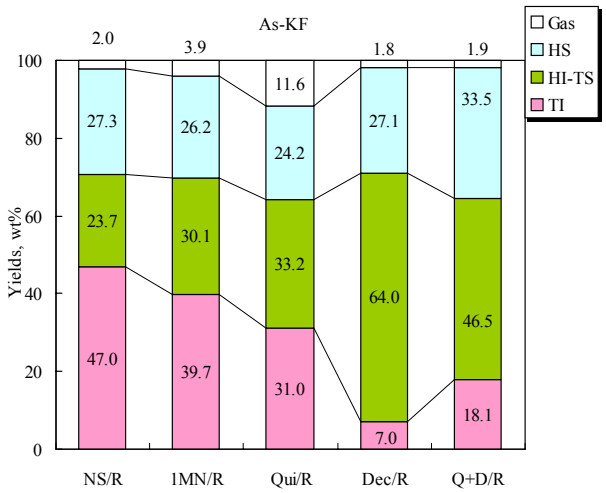

Figure 4. Yields of As-KF cracking without and with some solvents.

The yields of As-IL cracking have higher TI yields with each solvent than As-KF and show the same tendency depending on the solvent with As-KF. On the other hand, As-MY shows the different TI yields order with the solvents. The yields of As-MY craking is shown in **Figure 5**. Different from As-KF or As-IL, As-MY is converted into the least amount of TI with decalin and quinoline mixture solvent among four solvents.

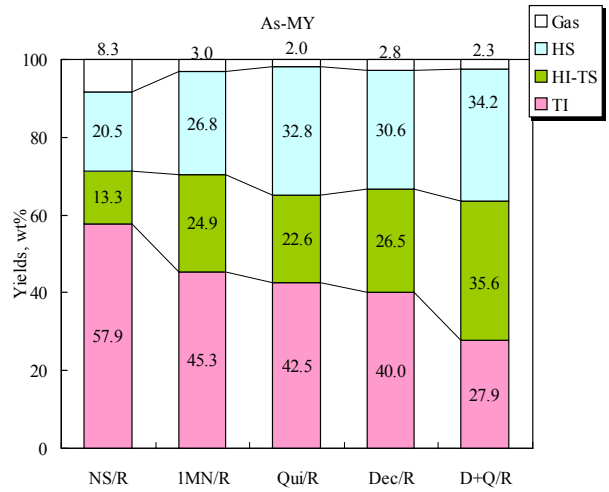

Figure 5. Yields of As-MY cracking without and with some solvents.

It may be interpreted that both aggregates of As-KF and As-IL brake up even in decalin at around reaction temperature and hydrogen is easily donated to the asphaltenes, but As-MY remains some aggregates in the decalin at around reaction temperature. In other word, quinoline assists the braking up of As-MY aggregates in the decalin and hydrogen donation to the asphaltene become easier. Results of SANS experiment indicate the large aggregates (fractal network) of Maya asphaltene exist in decalin solvent up to 350 °C. The feature of As-MY thermal cracking that higher coke yields than As-KF or As-IL and a multiplier effect to suppress the coke yields with Dec and Qui could be attributed to the fractal network.

Acknowledgment

This work was supported by the Proposal-Based International Joint Research Program, New Energy and Industrial Technology Development Organization (NEDO).

References

1. Sato, S.; Takanohashi, T.; Tanaka, R. *Prepr. Pap. Am. Chem. Soc. Div. Fuel Chem.* **2001**, *46 (2),* 353.
2. Takanohashi, T.; Sato, S.; Tanaka, R. *Prepr. Pap. Am. Chem. Soc. Div. Fuel Chem.* **2001**, *46 (2),* 357.
3. Tanaka, R.; Winans, R.E.; Hunt, J.E.; Thiyagarajan, P.: Sato, S.; Takanohashi, T. *Prepr. Pap. Am. Chem. Soc. Div. Fuel Chem.* **2001**, *46 (2),* 359.
4. Tanaka, R.; Seifert, S.; Winans, R.E.; Hunt, J.E.; Thiyagarajan, P.: Sato, S.; Takanohashi, T. *Proceedings of 3rd International Conference on Petroleum Phase Behavior & Fouling;* AIChE, 2002; pp 20-23.

A PROCEDURE FOR ASPHALTENE ISOLATION AIMING CORRELATION WITH CARBON RESIDUE

Marco Antonio G. Teixeira

Petrobras R&D Center/Chemistry
Av. Um, Q. 7, Cidade Universitaria, 21949-900, Rio de Janeiro, Brazil, Fax: 55-21-3865-6296, marcoa@cenpes.petrobras.com.br

Abstract

The use of atmospheric resids as feedstocks for FCC units allows profitable conversion of heavy fractions. PETROBRAS has developed its own RFCC technology after a complete study of properties of the possible feedstocks for the 2 industrial units that are now operating in Brazil. A very important point in this characterization is the Ramsbottom carbon residue (RCR). Asphaltenes are well-known to be the main carbon residue percursors. However, no correlation could be found with the regular IP-143 asphaltene content. This paper describes considerations on the precipitation procedure and the necessity to eliminate aliphatic long-chained hydrocarbons (paraffin waxes) that co-precipitate with asphaltenes. This elimination had to be done by supercritical extraction, the only way found to achieve selectivity. The work yielded a linear correlation between asphaltene contents and RCR.

Introduction

It has been mentioned in literature[1] that, though heavy petroleum fractions were limited to less economically attractive destinations, the increase in information about their constituents had been propitiating novel uses. About one of the most attractive ones, the conversion to light fuels, it has been recognized[2] that the key to improvement of conversion is the development of better understanding of coke formation (normally referred to by carbon residue) chemistry mainly through the main precursors, asphaltenes. Carbon residue is one of the most important variables to be controlled in catalytical cracking and hydroprocessing[3], and it limits the feedstock to be processed. Good predictions of carbon residua from asphaltene contents are not reached, however. This paper shows some reasons for that by the evaluation of asphaltene precipitation experiments and their products, and proposes a novel and efficient correlation.

Challenges in Correlation of Asphaltene Contents and Carbon Residue Values

There are clear descriptions in literature about asphaltenes of the chemical structure expected for these heavy petroleum fractions: large-sized aromatic nuclei, with aliphatic and naphthenic branches[4]. However, it is not possible to reach an analytical method for selective separation of such materials. So, operational definitions are employed in this case. The most accepted one is the fact that asphaltenes are n-heptane insoluble, toluene soluble constituents of petroleum, which is the basis of the well-known IP-143 method[5]. This definition has proved to be useful in many situations; literature cites for instance that a vaccum residue freed of n-heptane insoluble components does not show sludge in hydroprocessing, while the same residue does when it is integrally processed[6].

Nevertheless, this criterium has shown to fail in being useful by itself in several situations. Sometimes this is not related to the precipitation approach employed, but to the very complex chemistry involved in conversion[2]. But in the development of PETROBRAS's technologies for catalytical cracking of atmospheric residua(ARs)[7], some of the inconsistencies of the criterium were made clear, and those were basically related to prediction of carbon residua. So, efforts were developed to understand the reasons for that. Since asphaltenes are coke precursors, asphaltene contents should be strongly correlated to amounts of carbon residue. However, the first results of correlation obtained by the author, seen in figure 1, show that less than 50% of carbon residue formation is explained by the amounts of asphaltenes.

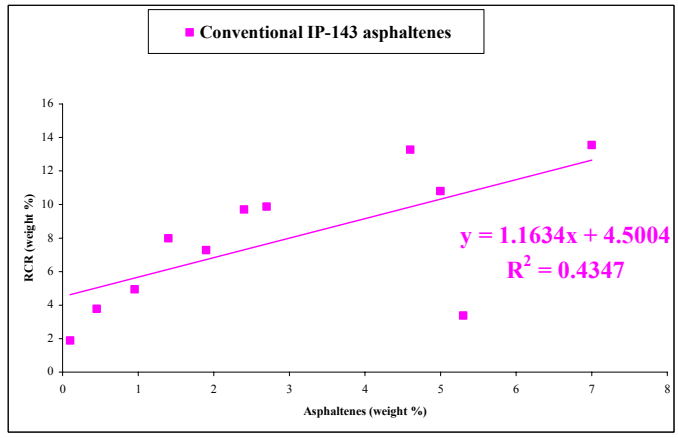

Figure 1. Plot of initial set of data for Ramsbottom carbon residue and conventional IP-143 asphaltene contents for various ARs, with very poor correlation

The reason to seek this understanding was not only the exact quantitative determination of carbon residue values from given characterizations of feedstocks, since Ramsbottom carbon residue values can be easily measured in refinery labs. The most important aim considered was the possibility to make clear this aspect related to the chemistry of carbon residue generation and its precursors, in such a way that information brought by this study could be useful for description of the phenomena involved and allow novel developments in conversion chemistry.

Asphaltene Precipitation

Investigation of asphaltene precipitation was the first step. Literature recommendations were developed for petroleum[5], and that is an initial medium for asphaltene precipitation very distinct from ARs. The basis is that asphaltenes are not supposed to be dissolved in petroleum or its fractions; it has been assumed for a long time[8,9] that they constitute micelles of aromatic materials maintained in suspension by other components, generically called resins, with similar characteristics but smaller molecular weights. Precipitation of asphaltenes depends on the ability of the precipitant to remove these resins around the asphaltenes and on the conditions it has to. That is why, in the comparison of 8 standardized methods for asphaltene precipitation from petroleum, different amounts of asphaltenes and *kinds of materials* can be found depending on the extraction procedure[10], since the precipitation efficiency is not a process dictated by equilibrium. In the case of ARs, the action of the precipitant, due to the differences in diffusivities and viscosities, very important parameters for the precipitation mechanism described, is much more difficult than it is in precipitation from petroleum.

So, a novel procedure was proposed with increased contact times of precipitant with the ARs. Due to the possibility of oxidation in the long precipitation periods studied, experiments were not performed under reflux; room temperature was preferred. The ratio of precipitant (n-heptane) to oil was 40:1, according to limiting values from the literature[11].Table 1 shows selected results.

Table 1. Results for asphaltene contents of a AR from a mixture of the petroleum productions of Brazilian fields with varied contact time with precipitant

Precipitation time (h)	Asphaltenes precipitated (weight %)
2	4.20
60	5.57
240	5.81

Contact times of sixty hours were chosen, because after that the amount of further precipitated material is negligible. It can be seen that 2 hours, as recommended by IP-143 (though conditions mentioned there employ reflux), are not enough for precipitation of all of the asphaltene content by this novel approach. The correlation with carbon residue values was sought again. Figure 2 shows that correlation for the same set of data in figure 1. It can be seen that better explanation of RCR is obtained, and that supports very much the hypothesis of being asphaltenes important coke precursors.

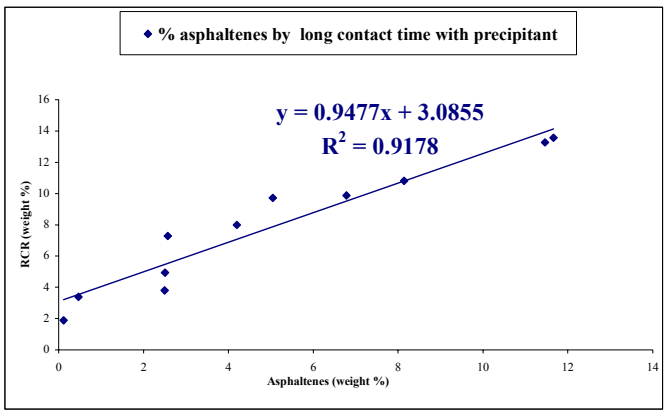

Figure 2. Plot of initial set of data of various ARs for RCR and asphaltene contents by the proposed method, considering only long contact time with precipitant, with very good correlation

The long contact time with precipitant could bring to the asphaltenes precipitated the possibility to explain more than 90% of the variations of carbon residue formation. The correlation indicates that about 3.1% of carbon residue would be expected if no asphaltene were present. The correlation is poor at low RCR values, but those are not the most worrisome cases. So, these first results were considered very promising ones.

The conditions of this precipitation method are not to be employed in refinery labs, of course, because precipitation times are prohibitive for operational needs. However, a databank could be made with this methodology for the most representative oils processed at PETROBRAS, since the approach showed to be useful. That was the next step in this research; about 20 ARs were chosen to compose that databank.

However, when twice as many ARs as we had in the initial set of data were analyzed, a new correlation showed that something had been missed when only the first set was considered, since the correlation was not as good as it was. That can be seen in figure 3. So, another aspect to explain these results was sought. Due to previous experiences with co-precipitation of asphaltenes and paraffin waxes in production facilities[12], the possibility of interference by co-precipitation was studied.

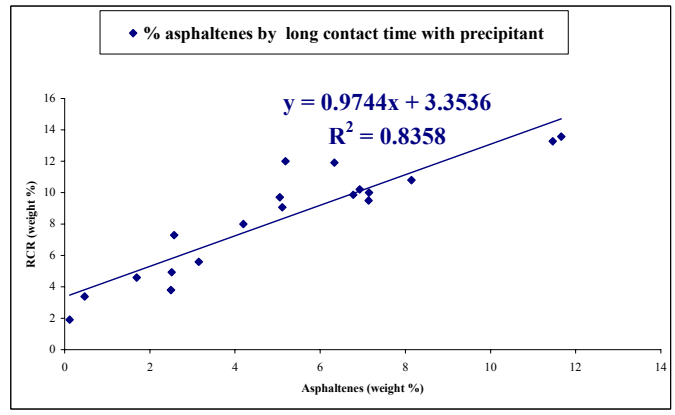

Figure 3. Plot of complete set of data of various ARs for RCR and asphaltene contents by the proposed method, considering only long contact time with precipitant

Correlation with Asphaltenes Precipitated by the Proposed Method after Extraction of Paraffinic Material

The possibility of co-precipitation had been considered since the first precipitation experiments, because the washing under reflux (that does not happen in this case, because of the preference for manipulation at room temperature) proposed by the conventional method should have as a major role the elimination of co-precipitated material. However, since good correlations were achieved, this problem was firstly assumed to be a minor one, if it existed. With the results in figure, they had to be considered.

The first approach was the comparison by the use of differential scanning calorimetry (DSC) measurements as it had been done in a previous work[12]. Paraffinic materials show melting transitions upon heating. If they are co-precipitated with asphaltenes, DSC analysis data can identify their presence. That was detected in several samples.

Quantitative results from these data are possible if an average heat of fusion is known. If the values were consistent, the subtraction of the total amount of paraffins from the asphaltene contents measured by the proposed procedure should improve the correlation. That was tried with a value from literature[13], but the correlation was even worst. Measurements for conventionally precipitated asphaltenes showed results in a similar order of magnitude as the ones found for the asphaltenes precipitated by the proposed method, indicating that co-precipitation does not happen only in the procedure discussed in the present work. This fact also indicates that even hot n-heptane is unable to dissolve these very long-chained aliphatic hydrocarbons.

For really quantitative results, a recently developed procedure[14] for selective extraction of paraffins by supercritical fluid extraction with pure CO_2 was employed. This technique allows selective extractions and improved solvation capacity. The selectivity is necessary since asphaltenes are constituted by thousands, maybe millions of components, and some of them could be inadequately extracted if selective extractions were not achieved. Solvation capacity is necessary because heavy paraffins have insolubility as their most remarkable characteristic, as it is well known from oil transportation pipeline plugging problems, for example.

Asphaltenes precipitated by the method proposed here were extracted. Absence of paraffins in the final material was checked by DSC. The selectivity of the extraction was proved by analysis of the extracts by a recently proposed thermogravimetric approach[15], in

which the distinct thermal behaviors of asphaltenes and paraffinic materials in coke generation are employed for characterization. Since the extracts can be weighed, gravimetric evaluation of paraffin-free asphaltenes was possible. Figure 4 shows the correlation obtained with this procedure. More than 90% of the variation in RCR is now explained by the amounts of asphaltenes. The slope is practically the unit, as expected. The linear coefficient shows that in the absence of asphaltenes, about 3.7% of carbon residue would be formed.

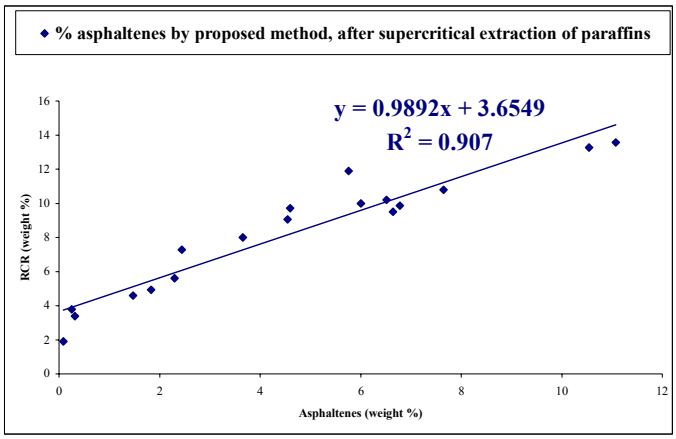

Figure 4. Plot of complete set of data of various ARs for RCR and asphaltene contents by the proposed method, considering long contact time with precipitant and supercritical extraction of paraffinic materials, with very good correlation

Conclusions

The work showed that asphaltenes yield amounts of coke equivalent to their contents in petroleum fractions. Those amounts can be predicted if paraffin-free asphaltenes are analysed after complete precipitation of asphaltenes. The precipitation is more difficult from heavy fractions, and long cantact time with the precipitant should be employed. Selective and quantitative extraction of heavy paraffins can be achieved with supercritical extraction with pure CO_2. However, RCR values are not completely explained by asphaltenes by themselves; other components also yield carbon residua. Though these coke precursors were not identified in this work, the conclusion by the analysis of a universe of 20 atmospheric residua of several different origins is that a fixed contribution of 3.7% can account for that.

References

(1) Yen, T. F. & Chilingarian, G. V., *18th AIChE et al Intersoc. Energy Convers. Eng. Conf. Proceedings 2*, pp.523-6 (**1983**)

(2) Speight, J. G. *Kentucky University & U. S. DOE EAST. Oil Shale Symposium Proceedings*, pp. 17-27 (**1992**)

(3) Sanford, E. C. *Energy & fuels*, 9(3), 549(**1995**)

(4) Bestougeff, M. A. & Byramjee, R. J. "Chemical Constitution of Asphaltenes" *in* Yen, T. F. & Chilingarian, G.V. (Editors), *Asphaltenes and Asphalts, 1. Developments in Petroleum Science, 40*, pp. 67-93

(5) IP Standars Methods for Petroleum and its Products, The Institute of Petroleum, London (**1965**), Part I, Section 2, p. 596

(6) Storm, D. A. et al., *Energy and Fuels*, 8, pp. 561-6 (**1994**)

(7) Baptista, C. M. A.; Bonfadini, P. R. G.; Gilbert, W. R.; Teixeira, M. A. G. In. 2000 NPRA Annual Meeting , **2000** , San Antonio Proceedings of the 2000 NPRA Annual Meeting, Washington D. C., EUA National Petrochemical & Refiners Association , 2000 , #AM - 00-23

(8) Mack, C. (**1932**), *Journal of Physical Chemistry*, 44, p. 2902

(9) Sachanen, A. N. (1945)"The Chemical Constituents of Petroleum", Chapter 9, Reinhold Publishing Corporation, N. York

(10) Speight, J. G. et al., *Fuel*, 63, pp.616-20 (**1984**)

(11) Speight, J. G. & Long, R. B. "The Concept of Asphaltenes Revisited", *AIChE Spring National Meeting Preprint* 78a, 7 pp. (**1995**)

(12) Teixeira, M. A. G.; Gonçalves, M. L. A. *Petroleum Science and Technology* , v. 18 , n. 3-4 , p. 273 -286 , **2000**

(13) Burlé, B. et al., "Relationships Between Characterization of Asphalt Cements by Differential Scanning Calorimetry and Their Physical Properties", *Symposium on chemistry and Characterization of Asphalts Proceedings*, 330-7 (**1990**)

(14) Teixeira, M. A. G.; Gonçalves, M. L. A. In. *219TH American Chemical Society Meeting* , **2000** , *San Francisco, American Chemical Society, Division of Petroleum Chemistry Preprints* , p. #34

(15) Teixeira, M. A. G.; Gonçalves, M. L. A. *Petroleum Science and Technology* , v. 17 , n. 1&2 , p. 1 -13 , **1999**

DETERMINATION OF COKING ONSET OF PETROLEUM FEEDSTOCKS USING SOLUBILITY PARAMETERS

Parviz M. Rahimi[1], Alem Teclemariam[1], Ed Taylor[1], Theo deBruijn[1] and Irwin A Wiehe[2]

[1]National Centre for Upgrading Technology (NCUT), 1 Oil Patch Drive, Suite A202, Devon, Alberta T9G 1A8 Canada
[2]Soluble Solutions, 3 Louise Lane, Gladstone, NJ 07934 USA

Abstract

Petroleum feedstocks are stable in nature, but if the fine balance in their chemical composition changes because of physical or thermal treatment, there is a possibility of solid formation due to asphaltenes precipitation. Formation of asphaltenes and high molecular weight components usually lead to coke and this has severe implications for refinery processing. For instance, significant coke formation can occur in heat exchangers, furnaces and fractionators during petroleum processing. It is important, then, to be able to predict the coking onset of different process streams and advise the operators to avoid process conditions (temperatures and space velocity) resulting in coke formation.

In the present work the coking onset of Athabasca bitumen was determined using a batch autoclave. Using the solubility parameters of the total liquid products, the onset of coke formation was determined. It was shown that coke formation was negligible up to a pitch conversion (conversion of resid to distillate) of 34wt%. Properties of the total liquid products as a function of severity are discussed.

Introduction

In refineries, in order to convert heavy oils and bitumen, it is necessary to subject these materials to thermal treatment to various degrees. In processes where relatively high temperatures are required, solid deposits may be formed as coke that significantly reduces the efficiency of the processing unit. For instance, in the delayed coking operation for processing Athabasca bitumen, the material is heated to temperatures in the range of 350-500°C (1). At these temperatures and in the absence of hydrogen, significant coke deposits can be formed on the walls of furnaces. These deposits currently can be removed by a pigging technique (1). It is believed that petroleum is a colloidal system consisting of asphaltenes cores dispersed in solution by a polar fraction, namely resins. During thermal reaction this protective resin layer is destroyed and the asphaltenes become exposed. They are no longer soluble in the media, resulting in precipitation and, finally, coke is formed. There are a number of methods and techniques that have been used to measure the stability and fouling tendency of petroleum feedstocks and products:

1. spot test (ASTM-D-4740-95);
2. total sediment (ASTM-4870-96);
3. solubility parameters, optical microscope (2);
4. light scattering (PORLA) (3)
5. peptization value (P-value) (4)
6. colloidal instability index (CII) (5-6);
7. coking index (7).

If the coking onset of petroleum materials can be predicted during thermal processing, it would then be possible to avoid processing severities at which coke formation occurs. Data on the coking onset are also necessary for the design of different processing units. In the present work we adapted solubility parameters, through an optical microscopy method that was developed by Wiehe (2) to determine the coking onset of Athabasca bitumen.

Experimental

Thermal reactions were performed using a 300 mL autoclave equipped with an insert (sleeve) for ease of removal and transfer of the products after the reaction. Feedstock used in this work was Athabasca bitumen obtained from Newalta, and originating from "Dover SAGD project" (previously UTF) operated by Devon Canada. To perform thermal cracking, about 100 grams of the bitumen was warmed to 40°C and transferred to the autoclave sleeve. The sleeve was inserted into the 300 mL autoclave and the head tightened down using a torque wrench. The autoclave was then purged with nitrogen three times and pressure tested to 550 psi.

The excess pressure was reduced down to 100 psi. The autoclave was then insulated and its content was soaked to 150°C for one hour while stirring. The reactor was heated at 2.5-5°C/min to the final reaction temperature of 370-430°C. The severity index (SI) of the reaction was calculated according to the following equation:

$$SI = t*\exp(-(Ea/R)*(1/T-1/700))$$

[where t = reaction time, seconds; Ea = activation energy, taken as 50.1 kcal/mole; R = gas constant, 0.001987 kcal/(mole °K); and T = reaction temperature, °K]

Upon achieving the pre-determined severity, the furnace was shut down and the insulation was removed. A cooling purge was directed to the head of the autoclave. The maximum internal temperature, the maximum pressure and the final severity index were recorded.

The autoclave was allowed to cool to room temperature and the gaseous products were collected into a gasbag (Calibrated Instruments Inc.) through a condenser. The condenser was cooled using dry ice to collect the light ends. The volume of the gas in the gasbag was determined by a gasometer with the barometric pressure and temperature recorded at that time. The contents of the gasbag was then analyzed for its components using a gas chromatograph (MTI Quad-series refinery gas analyzer).

The liquid products in the sleeve as well as the small amount of liquid collected in the reactor (as a result of overflow or condensation) were mixed. The light ends that were collected in the condenser were added to this mixture to produce total liquid products (TLP). The material balance (gas and TLP) and pitch conversion are shown in Table 1. The properties of TLP, including solubility numbers and stability index as defined by P-values, are shown in Table 2.

Results and discussion

During thermal treatment of petroleum in the refinery units, a solid deposit or coke is often formed. It has been shown that the coking onset coincides with the insolubility of converted asphaltenes (8) due in part to the conversion of resins that protect the asphaltenes (7). There is also an induction period for coke formation, which depends on the feedstock and the severity of the process (9). In order to determine the coking onset of Athabasca bitumen, this material was subjected to different severities shown in Table 1. Using high temperature simulated distillation, conversion of +524°C to distillate (pitch conversion) was calculated (Table 1). Up to a severity of almost 5000 seconds, there was no coke (toluene insolubles) formed. At this severity, the pitch conversion was about 34wt%. These results are consistent with our previous data on the visbreaking of Athabasca

bitumen in a continuous bench-scale unit where no coke was formed at a pitch conversion of around 33wt% (10).

The properties of the TLP are shown in Table 2. Although there is some scatter in the data, in general, as the severity of the process increased the heptane asphaltenes (not corrected for the small amount of toluene insolubles) increased. Toluene insolubles (coke) did not increase with severity up to 5000 seconds and examination of TLP under a microscope showed the presence of no solid particles or coke. Again, as expected and accepting the scatter in the data, both MCR and aromaticity increased with severity. A significant reduction in viscosity was observed as the severity increased. The solubility numbers including S_{BN} (solubility blending number) and I_N (insolubility number) as determined by Wiehe's method are shown in Table 2. The P-values, which are indicative of the stability of total liquid products, are calculated from the ratio of S_{BN}/ I_N and are also shown in Table 2. As the severity of the process increased the stability of products decreased because the converted asphaltenes became less soluble (higher I_N) and because the solvent quality became slightly poorer (lower S_{BN}). In a previous study (11) it was suggested that by using solubility numbers, it might be possible to predict the onset of coke formation for petroleum feedstocks. In Figure 1, S_{BN} and I_N are plotted against the severity of the process. From the least square straight-line equations obtained for S_{BN} and I_N, it is possible to predict that at a severity index of 7576 seconds asphaltenes will become insoluble ($S_{BN} = I_N$) and start forming coke. To verify, a series of autoclave runs were performed at a relatively high severity, as shown at the bottom of Table 2. Unfortunately, the data from experiments at 6000 and 7000 seconds are not available and will be carried out shortly to better define the coke induction period. Nevertheless, as predicted, all runs of severities higher than 7576 seconds did produce coke. For example, thermal cracking of Athabasca bitumen at a severity of about 8500 produced 4.5wt% coke, and the C7 asphaltenes (not corrected) also increased significantly. It is expected that at the end of the coke induction period (i.e., at the severity where coke starts forming) the asphaltenes concentration will be reduced (8). For this reason the percentage of C7 asphaltenes, after correcting for toluene insolubles, should have been lower than what is reported in Table 2. For the last three runs, at high severities beyond the coke induction period, it was necessary to filter out the solid particles (coke) in order to determine the solubility numbers (S_{BN} and I_N). These solubility numbers do not follow the linear behavior of those within the coke induction period because the least soluble asphaltenes precipitated to form coke.

Conclusions

Thermal reaction of Athabasca bitumen was carried out in a batch autoclave at SI ranging from approximately 500-9500 seconds. It was shown that up to a severity index of around 5000 seconds there was no solid or coke formed. At this severity, pitch conversion was estimated to be about 34wt%. From the solubility numbers of the total liquid products versus the severity, it was possible to predict the onset of coke formation for Athabasca bitumen.

Acknowledgements

Partial funding for NCUT has been provided by the Canadian Program for Energy Research and Development (PERD), the Alberta Research Council (ARC) and the Alberta Energy Research Institute (AERI).

References

(1) Parker, R. J., and McFarlane, R.A., " Mitigation of fouling in bitumen furnaces by pigging", Proceedings of International conference on petroleum phase behavior and fouling, AIChE Spring National Meeting, Houston, Texas, March 14-18, 1999.
(2) Wiehe, I.A. and Kennedy, R.I. "The oil compatibility model and crude oil incompatibility", *Energy & Fuels*, 14, 56, 2000.
(3) Vilhunen J, Alain Quignard, Pilvi► O, and Waldvogel, J. "Experience in use of automatic heavy fuel oil stability analyzer", Proceedings of the 7th international conference of stability and handling of liquid fuels, October 13-17, Vancouver, BC., 985-987, 1997.
(4) Rahimi, P.M., Parker, R.J. and Wiehe, I,A. "Stability of visbroken products obtained from Athabasca bitumen for pipeline transportation", Symposium on heavy oil resid compatibility and stability, 221st ACS National Meeting, San Diego, CA, USA, April 1-5, 2001.
(5) Gaestel, C., Smadja, R. and Lamminan, K.A. "Contribution a la Connaissance des proprietes des bitumen routiers". Rev Gen Routes Aerodromes, 85, 466, 1971
(6) Asomaning, S.A. and Watkinson, A.P. "Petroleum stability and heteroatoms species effects on fouling heat exchangers by asphaltenes. *Heat Transfer Engng*, 12, 10-16, 2000.
(7) Schabron, J.F., Pauli, A.T., Rovani Jr., J.F. and Miknis, F.P. "Predicting coke formation tendencies," *Fuel*, 80, 1435-1446, 2001.
(8) Wiehe, I.A. "A Phase-Separation Kinetic Model for Coke Formation", I&EC Research, 32, 2447-2454 (1993).
(9) Wiehe, I.A. "A Series Reaction, Phase-Separation Kinetic Model for Coke Formation from the Thermolysis of Petroleum Resid, presented at the AIChE Spring Meeting, New Orleans (1996).
(10) Parker, R. J., Lefebvre, B. and Pipke, A. "Visbreaking of heavy oils for pipeline transportation – quality and stability", presented at the 2nd Internation conference on petroleum and gas phase behavior and fouling, Auguat 27-31, 2000, Copenhagen, Denmark
(11) Rahimi, P.M., Parker, R.J., Knoblauch, R. and Wiehe, I.A., "Stability and compatibility of partially upgraded bitumen for pipeline transportation", Proceedings of the 7th International conference on stability and handling fuels, September 22-26, 2000, Graz, Austria, 177-192.

Table 1. Products yields as function of severity

SI, second	Liquid	Gas	Pitch Conv *
	wt%	wt%	wt%
591.97	98.1	0.20	5.4
599.86	98.9	0.04	5.4
708.28	99.2	0.26	5.4
795.31	99.2	0.31	ND
897.92	99.0	0.31	7.3
986.82	99.7	0.3	ND
1095.60	99.1	0.10	9.1
1163.00	98.0	0.3	ND
1445.25	98.1	0.43	14.5
1652.64	98.1	0.47	16.3
1740.50	99.2	0.5	ND
1858.48	99.6	0.51	15.4
2240.71	98.0	0.7	ND
2406.15	98.3	0.52	18.2
2999.42	99.2	0.87	24.5
4319.59	97.4	1.37	32.7
4602.50	98.4	1.29	34.5
5037.33	97.4	1.53	34.5

* Conversion of +524°C to distillate determined by GC simulated distillation

ND = not determined

Table 2. Properties of total liquid products

Severity Index, s	Heptane* Insol	Toluene Insol	MCRT	Aromaticity	Viscosity			
	wt%	wt%	wt%	f_a	cP @ 25°C	I_N	S_{BN}	P-value
Bitumen	**11.3**	**0.03**	**13.7**	**0.33**	**174000**	**33.2**	**101.5**	**3.1**
592	12.4	0.06	13.4	0.43	54800	37.3	111.0	3.0
600	12.4	0.07	13.0	0.41	57100	37.3	111.0	3.0
708	12.6	0.04	13.2	0.40	46300	38.2	101.5	2.7
795	ND	ND	ND	ND	ND	38.6	104.3	2.7
898	12.4	0.04	12.3	0.38	22000	40.7	106.6	2.6
987	ND	ND	ND	ND	ND	40.7	106.6	2.6
1096	12.7	0.02	13.1	0.39	19700	40.7	106.6	2.6
1163	ND	ND	ND	ND	ND	41.2	104.6	2.5
1445	11.5	0.03	14.2	0.40	11566	41.4	108.5	2.6
1653	12.4	0.11	14.0	0.42	9713	42.1	105.4	2.5
1741	ND	ND	ND	ND	ND	45.3	104.1	2.3
1858	12.5	0.00	13.2	0.45	5810	47.1	102.7	2.2
2241	ND	ND	ND	ND	ND	49.4	103.7	2.1
2406	11.6	0.04	13.9	0.38	3540	51.3	102.5	2.0
2999	12.9	0.04	14.9	0.39	2860	56.8	103.4	1.8
4320	13.6	0.04	15.1	0.40	984	69.4	101.3	1.5
4603	14.0	0.10	15.1	0.42	1686	72.1	102.3	1.4
5037	13.5	0.13	15.4	0.46	750	75.6	101.4	1.3
8564	**18.95**	**4.55**				**102.5**	**114.8**	**1.12**
9454	**16.42**	**4.58**				**89.4**	**109.1**	**1.22**
9692	**17.61**	**5.94**				**102.2**	**112.2**	**1.1**

* Including Toluene insolubles

ND = not determined

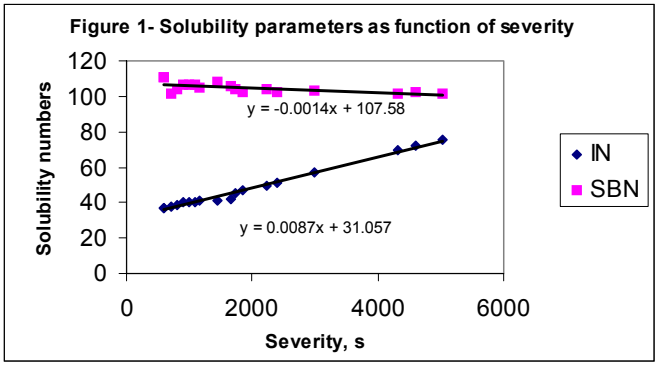

MOLECULAR CONSTITUTION, CARBONIZATION REACTIVITY, AND MESOPHASE DEVELOPMENT FROM FCC DECANT OILS

Jennifer Clemons, Guohua Wang and Semih Eser

Dept of Energy and Geo-Environmental Engineering/
Energy Institute
The Pennsylvania State University, 101 Hosler Building, PA 16802

Introduction

FCC (Fluidized Catalytic Cracking) decant oils are the primary feedstock to the delayed coker to produce highly graphitizable precursor—the needle coke. The quality of needle coke is determined, in essence, by the development of mesophase formation in the early stages of liquid-phase carbonization that, in turn, closely relates to the chemical composition, carbonization reactivity of coker feedstock, sulfur content and coking conditions [1,2,3].

The objective of this study was to investigate the effects of molecular composition and the reactivity of blending streams in coker feedstock on the mesophase development and needle coke texture.

Experimental

Coker Feedstocks. The samples used in this study come from a commercial needle coke plant. They include virgin decant oil, gas oils, hydrotreated decant oil stream and coker charge.

Carbonization Experiment. Carbonization experiments were conducted in tubing bomb reactors (15 mL) at 500°C for 3 hours under autogenous pressure. The reactors were heated in a fluidized-sand bath. After reaction, the reactors were quenched in cold water. The semi-coke product was recovered as whole piece for microscopic examination. For the study of reactivity of sample effects on the mesophase development, the sample was heated at 450°C from 20 minutes up to 5 hours in the same isothermal sand bath. The yields of semi-coke (defined as dichloromethane insoluble) and asphaltene (pentane soluble and dichloromethane insoluble) were determined by sequential solvent extraction.

Coker feedstock molecular analyses. Gas Chromatography with Mass Spectrometer (GC/MS, Shimadzu GC-17A, MS-OP-5000), High Performance Liquid Chromatography with Photodiode Array detector (HPLC/PDA), Laser Desorption with Mass Spectrometer (MALDI-TOF-MS) and Liquid Chromatography with dual mass spectrometers (LC/MS/MS) were used to characterize the samples.

Semi-coke optical texture. The extent of mesophase development in the liquid-phase carbonization of samples was measured quantitatively in terms of Optical Texture Index (OTI). Each semi-coke sample was mounted in a pellet of epoxy resin, then cut into two sections. The polished pellets were examined under a polarized light microscope (Nikon-Microphoto_FXAII). We used a 1.1 mm X 1.1 mm mask and 10X object lens to acquire the surface images. At least 250 images were examined for a pellet. The OTI of semi-coke was determined according to following equation [4]:

$\mathbf{OTI=\sum f_i * OTI_i}$ where f_i is the numerical fraction of individual texture types from microscopic analysis and $\mathbf{OTI_i}$ is the index value assigned to each texture type, as defined in Table 1.

Table 1. Index Assignments for OTI definition to characterize optical textures of semi-coke samples.

Type	Size/Shape	Index (OTI)
Mosaic	<10 µm	1
Small Domain	10-60 µm	5
Domain	>60 µm	50
Flow Domain	>60 µm long,>10 µm wide	100

Results and Discussion

OTIs of semi-coke samples produced at 500°C for 3 hours are listed in Table 2. We see a significant variation among the degree of mesophase development in the sets of coker feedstock samples. DO02-1 produced a semi-coke with much lower extent of mesophase development while DO02-4 produced more anisotropic coke with high proportion of flow domain texture. Coker charges of both decant oils give a better mesophase development than their parent decant oils, the heavy stream (VTB) of DO02-4 produced even more anisotropic coke (88 of OTI).

Table 2. OTI of semi-coke samples from coker feedstocks.

	Flow Domain	Domain	Small Domain	OTI
CF02-1	54	58	5	71
CF02-4	74	31	0	85
DO02-1	68	89	7	69
DO02-4	77	38	0	83
VTB 02-4	105	35	0	88

Decant oil 02-1 and 02-4 have different major hydrocarbon distributions: as GC/MS quantitative results show (Figure1 and Figure 2), there is much less pyrene and alkylated pyrenes present in DO02-1 than in DO02-4; normal alkanes concentration in DO02-1 is about two times higher than in DO02-4. Both Coker feeds have higher concentration of phenanthrenes and pyrenes, and lower concentration of normal alkanes than their parent decant oils. The variations in hydrocarbon compositions show similar trends as those noted for the corresponding decant oil samples.

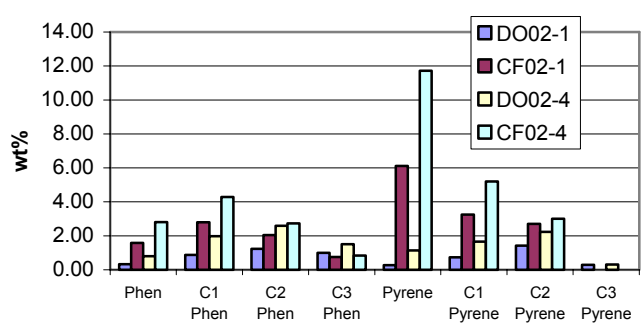

Figure 1. Aromatic compound distribution in feedstock samples.

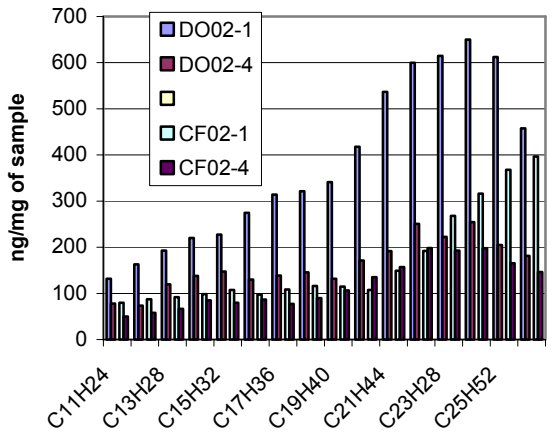

Figure 2. Aliphatic compound distribution in feedstocks.

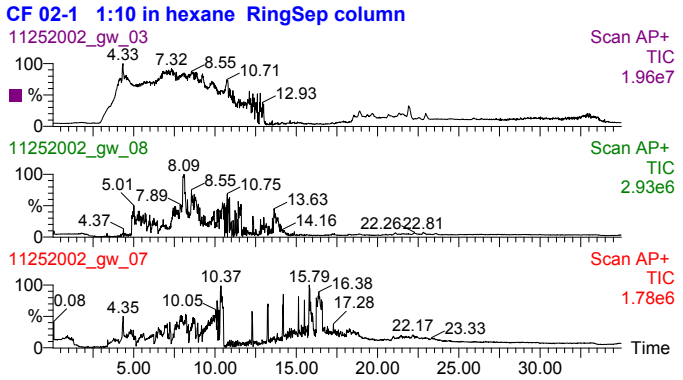

Figure 3. LC/MS/MS chromatograms of CF02-1 (Top), CF02-4 (Middle) and VTB02-4 (Bottom).

Differences in heavier hydrocarbon compound constitution are clearly seen on the TIC of LC/MS/MS chromatograms. We see the higher aliphatic contribution to the TIC in the initial region (retention time from 3 to 8 minutes) in sample CF02-1. In the five- to six- ring aromatic region (about 13min to 17min), the molecular constitution in CF02-4 is much simpler than in CF02-1. Major aromatic compounds include the trimethyl-, tetramethyl and pentamethyl-benzopyrene and benzoperylenes. Note the relatively high intensity peaks in the longer retention time region (20min to 25min) in CF02-1. These are the alkylated (up to C3) benzocarbazoles. In VTB sample, the heavy aromatic compounds almost exclusively consist of C1 to C4 benzopyrene and benzoperylenes (Figure 3, bottom).

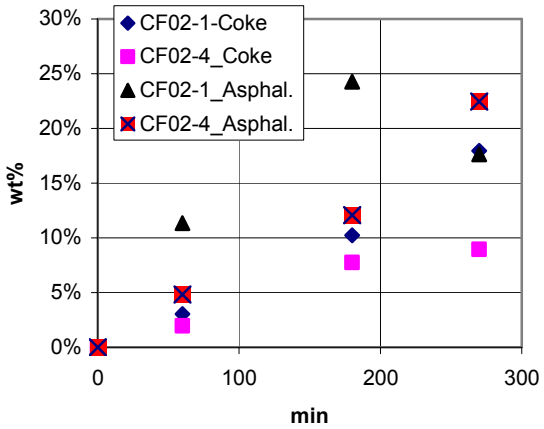

Figure 4. Coke and asphaltene yields of coker feeds

Intermediate (asphaltenes) and solid coke product yields from coking experiments (450°C) are presented in Figure 4. By comparing sample CF02-1 with CF02-4, the rapid build-up (within 180 minutes) in asphaltenes in CF02-1 indicated the high reactivity of compounds in this coker feed. The short time window in the case of CF02-1 for the mesogens to stack and grow into large mesophase sphere and form elongated flow domain may explain the lower anisotropy of the semi-coke produced. The difference of reactivity between these two samples is consistent with their molecular composition difference: CF02-1 contains a higher concentration of normal-alkanes than CF02-4. Alkanes are the least thermally stable compounds in the carbonization environment that easily crack to form free radicals to serve as polymerization initiators. Higher concentration of alkanes in coker feed would result in a higher rate of carbonization that would lead to a lower degree of anisotropy in the semi-coke texture.

Conclusions

Differences in molecular composition of FCC decant oils and coker feeds derived from decant oils can be related to the differences obtained in the degree of mesophase development obtained upon carbonization of these materials. Concentration of n-alkanes, ad the distribution of PAH in the coker feeds affect the rate of coke formation and, thus, the extent mesophase development.

Acknowledgement. Financial support from Chicago Carbon Company and many helpful discussions with Robert Miller of Chicago Carbon Company are gratefully acknowledged.

References

(1) Eser, S. in Suppercarbon: Synthesis, Properties and Applications, ed. By Yoshimura, S. and Chang, R.P.H., Springer-Verlag, Berlin, 1998, p147.
(2) Mochida, I. , Fujimoto, K. and Oyama, T. in Chemistry and Physics of Carbon, Vol 24, ed. By Thrower, P. A., Marcel Dekker Inc., New York, 1994, p111.
(3) Filley , R.M. and Eser, S. ,Energy & Fuels,1997,11, 623.
(4) Yang, M-G , Wang, G. and Eser, S., Eurocarbon 2000, International Conference on Carbon, pp. 163-164.

BIOCONVERSION OF AROMATICS IN LIGHT GAS OIL (LGO) IN A CONTINUOUS BIOREACTOR SYSTEM

Hans Kr. Kotlar[1], Kjetil Rasmussen [2], Knut Grande[1], Marit Ramstad [2], Sidsel Markussen [2] , Asgeir Winnberg [2], Sergey Zotchev [3] and Martin Gimmestad [3]

[1] Statoil R&D, Trondheim
[2] SINTEF Applied Chemistry, Trondheim
[3] Department of Biotechnology, NTNU

Introduction

The content of polyaromatic hydrocarbons (PAH's) in the diesel fuels contribute to low cetane numbers and particle emissions from combustion.

The present paper focuses on the use of a continuous bioreactor system for upgrading of the LGO as a potential industrial process. This is done by biocatalytic ring opening of the PAH's to generate a more paraffinnic diesel fuel.

Two different bacterial strains, Sphingomonas yanoikuyae DSMZ 6900 N2 and Pseudomonas. fluorescence LP6a 21-41(donated by Dr. Julia Foght, University of Edmonton Canada), were compared for biocatalysis of the PAH's in the LGO feed stock from the refinery.

S. yanoikuyae was found to have the all the enzymes necessary for the desired bioconversion. The PAH degradation pathway was genetically engineered in order to obtain a recombinant strain accumulating one of the precursors, 2-hydroxychromene-2-carboxylate. This could be achieved by eliminating the enzyme activity for the specific hydratase-aldolase (NahE) responsible for further degradation of 2-hydroxychromene-2-carboxylate. Thus, the degradation of PAH would terminate after the ring opening, which is important for keeping the octane number of the hydrocarbon fraction. The strategy chosen was to inactivate the gene encoding NahE by gene disruption. Five mutants with an inactive nahE gene have been constructed, and the N2 mutant was chosen for further investigation.

P. fluorescence LP6a has been obtained by transposon mutagenesis, and its genetic background remained unknown.

Results & Discussion

A toxicity test of LGO on both N2 and LP6a 21-41 was performed. Figure 1 shows the growth curves of both strains in a yeast extract (YE) based medium and medium with 50 % LGO. No inhibitory effects were observed. However, color change of the suspensions containing LGO strongly indicated conversion of LGO components. In addition, the color of the N2 suspension turned red while the LP6a developed a yellow color indicating a difference in the composition of converted LGO-components. These observations suggested that the two strains had different affinities for different hydrocarbons and that there may be a substrate competition for the active sites of the enzyme systems.

Since the LGO did not inhibit growth of either of the strains, a continuous feed of 20 vol % was used in the experiments on bioconversion. However, LP6a and N2 cells clearly differed in their ability to degrade PAH, since different colored intermediates were produced upon incubation of their suspensions with LGO.

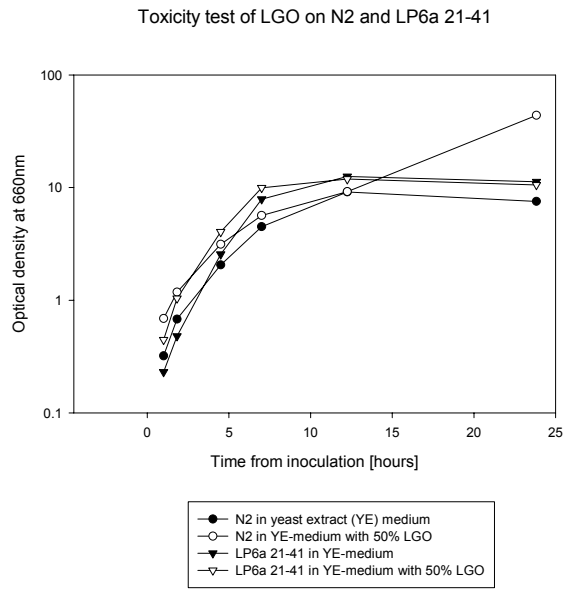

Figure 1. Toxicity testing of LGO on the N2 and LP6a strains

LP6a and N2 were also compared in a PAH degradation assay utilizing dibenzothiophene (DBT) as a main substrate with selective addition of naphthalene, benzene and toluene. Both strains were grown in YE-medium and induced with salicylic acid before harvesting. Equal amount of cells were then transferred to shaker flasks containing 100 ml mineral medium and 0.05 dibenzothiophene (DBT) dissolved in 10 ml hexadecane. The end product of DBT creates a red color absorbing at 475 nm. After two hours benzene, toluene, and naphthalene was added to separate flasks. Figure 2 shows the bioconversion of DBT by the two strains and the effect of adding different aromates. All the added aromates seemed to compete with DBT for the enzyme system of LP6a 21-41. The N2 strain had evidently a higher affinity for naphthalene than DBT, whilst benzene and toluene seemed less attractive.

The results of these experiments confirmed that substrate competition observed for the two cell suspension differed significantly, suggesting different preferences of the two strains for certain PAHs.

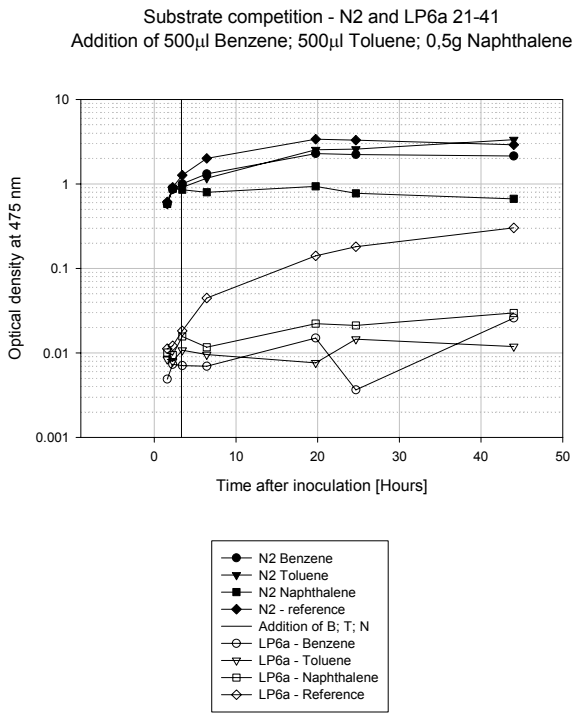

Figure 2. Substrate competition differences between the N2 and LP6a strains

Figure 3 shows the degree of bioconversion of LGO components from a bioreactor run in batch mode with N2. Cells were grown in YE-medium and induced with salicylic acid. Harvested cells were transferred to the bioreactor containing mineral medium and 20% LGO. The results shown in figure 3 indicate that the N2 strain has the highest bioconversion of the least substituted aromates and optimal residence time for the cells in the bioreactor at around 8 hours.

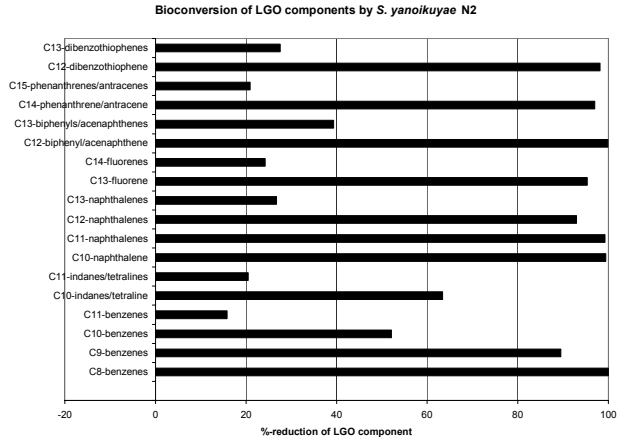

Figure 3. Bioconversion of light gas oil components

In an expanded reactor system the N2 strain will also be grown in a continuous feed bioreactor on oil. Our data suggest, that instead of energy-expensive distillation processes, bioreactor systems have the potential for upgrading of hydrocarbon refinery fractions.

SORPTION OF CARBON DIOXIDE BY COALS

John W. Larsen

The Energy Institute
Coal Utilization Laboratory
The Pennsylvania State University
University Park, PA 16802

Introduction.

When CO_2 is adsorbed on the surface of a coal, two equilibria are established. One is between adsorbed CO_2 and gas phase CO_2. The other is between adsorbed CO_2 and CO_2 dissolved in the coal. Pressure has a significant effect on both equilibria. In this paper, the sorption of CO_2 by coals will be considered in the light of these simultaneous equilibria. When the coal-CO_2 system is at equilibrium, CO_2 in the gas phase, on the coal surface, and dissolved in the coal will all have the same activity. The time required to dissolve CO_2 in coals and establish equilibrium may be long.

Results and Discussion.

Adsorption thermodynamics. It is difficult to measure the thermodynamics of adsorption of CO_2 on a coal. The problem is separating the two equilibria. Static techniques, such as those routinely used for BET surface area measurements, measure total CO_2 uptake by the coal, both surface CO_2 and dissolved CO_2. The resulting thermodynamic quantities are for some mixture of the two equilibria, the mixture depending on the pressure and the diffusion rate of the CO_2 into the coal.

Gas chromatography using coal packed columns (inverse GC) has been used to measure the isosteric heads of adsorption of CO_2 and other gasses on Illinois No. 6 coal.[1,2] This is a transient technique that does not allow time for the CO_2 to diffuse into the coal so only one equilibrium is established.[1] The isosteric enthalpy of CO_2 adsorption on Illinois No. 6 coal is –6.6 kcal/mole. Of this, London dispersion interactions are responsible for -2.5 kcal/mole and polar interactions are responsible for the rest. This enthalpy is greater than the corresponding value for methane (-3.1 kcal/mole) and about the same as for ethane (-6.4 kcal/mole)[2].

Coal surface areas measured by CO_2 adsorption. With two equilibria involved in static measurements, are the numerous coal surface areas that have been measured using CO_2 adsorption correct? I believe that they are approximately correct and still very useful. This belief is based in part on the agreement between surface areas measured by CO_2 adsorption and other techniques, such as X-Ray scattering.[3] Also, as pointed out by Walker and Mahajan, surface areas are measured by using very low CO_2 pressures and the amount of CO_2 dissolved under these conditions is usually too small to vitiate the surface area measurements.[4] As will be seen, the results for bituminous coals are more reliable than those for low rank coals.

Table 1 contains the surface areas of the Argonne Premium Coals measured by CO_2 and ethane (C_2H_6) using the standard static BET technique at –78 ˚C[5]. Ethane and CO_2 have similar cross sectional areas, 25.3 Å^2 and 25.1 Å^2 respectively. The surface areas measured using CO_2 are much larger, as much as 25 times larger, despite the gasses being of similar size and shape and the measurements being made at the same temperature. There are three possible explanations. 1) The pore structure of all of these coals is so finely tuned that it allows passage of CO_2 while not allowing ethane to pass. 2) The CO_2 is dissolving in the coals while ethane is not. 3) CO_2 diffuses rapidly through the coals while ethane diffusion is slow.

Explanation 1 is not reasonable. The molecules are of such similar size and shape that the necessary level of discrimination by a rigid pore system is most unlikely. That 8 pore systems should be so finely discriminatory is unreasonable. The only problem with explanation two is that CO_2 adsorption does give coal surface areas in agreement with other techniques. If this is generally correct (and it deserves more testing), then the CO_2 is not dissolving in the coal in large amounts. Explanation three is preferred. Stated again in more detail: CO_2 , because it interacts with coals in ways that ethane cannot, has some solubility in coals and diffuses rapidly through them to reach all of the pore surfaces where it is adsorbed. If this is the correct explanation, then ethane diffusivity through coals must be slow. It has been measured only for Illinois No. 6 coal. Ethane uptake was not complete in 131 hr. While I prefer explanation 3, uncertainty remains. The diffusivities of gasses through coals and diffusion mechanisms deserve more study.

Table 1. BET Surface Areas (m^2/g) of the Argonne Coals Measured at –78 ˚C Using CO_2 or Ethane (data from ref. 5)

Coal (%C, dmmf)	CO_2	Ethane
Pocahontas (92)	202	69
Upper Freeport (88)	166	72
Stockton (85)	175	34
Pittsburgh No. 8 (85)	177	37
Blind Canyon (81)	239	122
Illinois No. 6 (81)	132	38
Wyodak (76)	330	106
Beulah Zap (74)	274	11

Dissolution of CO_2 in coals. In order to understand the dissolution of CO_2 in coals, some background on the physical structure of coals is needed. Coals are strained glassy materials prevented from rearranging into their most stable physical structure by non-covalent interactions too strong to be overcome by thermal energy.[6] When substances dissolve in coals, the glass to rubber transition temperature (Tg) is lowered. Even small amounts of material, for example toluene adsorbed from the vapor state, suffice to enable the coal structure rearrangment.[7] The rearrangement has been characterized and proceeds to a more highly associated structure in which fluids are significantly less soluble.[6] Organic molecules dissolved in coals can be efficient plasticizers that enable physical structure rearrangements. They also lower the softening temperature of coals and can lead to flexible rubbery systems.[8]

It was known as early as the 1930s that CO_2 dissolved in coals, swelling them.[9] But it was not until 50 years later that it was suggested that CO_2 dissolution had an invidious effect on surface areas measured by CO_2 adsorption.[10,11] The pressure of CO_2 used, the volumetric swelling of the coal, and the % of the CO_2 that is dissolved are given in Table 2.

Table 2. Carbon Dioxide Adsorption and Dissolution (data from ref. 11)

Coal (% C, daf)	Pressure (atm)	Swellling Vol. %	% CO_2 Dissolved
KCER 7259 (84)	5	0.75	14
	10	0.85	16
	15	1.33	24
KCER 7122 (78)	5	1.24	23
	10	2.23	41
	15	3.11	58
KCER 7463 (66)	5	2.16	24
	10	3.00	33
	15	4.18	47

As expected, the amount of CO_2 absorbed by the coals increases with pressure as does the % of CO_2 that is dissolved. This is the expected effect of increases in CO_2 fugacity and further pressure increases will lead to greater CO_2 dissolution and increased swelling. The amount of CO_2 dissolved increases with decreasing coal rank as expected if polar interactions are important. With increasing pressure, the rates of coal swelling increase. For example, the time to reach half of the maximum swelling of the 84% C coal decreases from about 40 hr at 1 atm to about 10 hr at 15 atm. It is clear from these data that CO_2 readily dissolves in coals, swelling them. The initial swelling by CO_2 is anisotropic, just as it is with organic liquids.[12, 6] It is expected to act as a plasticizer enabling the coals to rearrange at some (probably slow) rate and lowering their softening temperatures. A crucial question for CO_2 sequestration in coals is "how good a plasticizer is CO_2 ?".

There are very few data that bear on this question. Figure 1 shows the effects of CO_2 and He at elevated pressures on the softening temperature of a high rank Lower Kitanning coal (PSOC 1197, 91 %C, dmmf).[13, 14] As expected, He has no effect on the coal's softening temperature. The data for CO_2 are stunning. The coal softening temperature begins to drop sharply at a CO_2 pressure of 30 atm and has dropped to about 300 ˚K at 55 atm CO_2 pressure. This is a 373˚C decrease in softening temperature. In this coal, CO_2 is a very effective plasticizer. It will efficiently enable coal structure rearrangements; these rearrangements are known to decrease the solubility of organic liquids in coals and I expect the rearrangement will have the same effect on CO_2 solubility and strongly decrease it. If these results are general, pumping high pressure CO_2 into coal seams will readily dissolve the CO_2 in the coals. This may enable structure rearrangements that will decrease CO_2 solubility forcing some of the dissolved CO_2 back out of the coal. Pressure will increase Tg and tend to keep the coal from rearranging. The rates of the possible coal rearrangement as a function of CO_2 pressure, temperature, and lithostatic pressure on the coal are not known. The effect of structure rearrangements on CO_2 solubility in coals is not known. This information is crucial to understanding and evaluating the possibility of sequestering CO_2 in coal seams for geological time periods.

Acknowledgement. My work in this area over the years has been supported by the U. S. Department of Energy to whom I am grateful.

References

(1) Glass, A. S.; Larsen, J. W. *Energy Fuels* **1994**, *8*, 629-636.
(2) Glass, A. S,; Larsen, J. W. *Energy Fuels* **1993**, *7*, 994-1000.
(3) Spitzer, Z.; Ulicky, L.*Fuel* **1977**, *55*, 212-224. Gethner, J. S. *J. Appl. Phys.* **1986**, *59*, 1068-1085.
(4) Walker, P. L. Jr.; Verma, S. K.; Rivera-Utrilla, J.; Khan, M. R. *Fuel* **1988**, *67*, 719-726.
(5) Larsen, J. W.; Hall, P.; Wernett, P. C. *Energy Fuels* **1995**, *9*, 324-330.
(6) Larsen, J. W.; Flowers, R. A. II; Hall, P.; Carlson, G. *Energy Fuels* **1997**, *11*, 998-1002.
(7) Hsieh, S. T.; Duda, J. L. *Fuel* **1987**, *66*, 170-178.
(8) Yang, X.; Silbernagel, B. G.; Larsen, J. W. *Energy Fuels* **1994**, *8*, 266-275.
(9) Briggs, H.; Sinha, R. P. *Proc. Roy. Soc. Edinburgh* **1933**, *53*, 48
(10) Reucroft, P.J.; Patel, K. B. *Fuel* **1983**, *62*, 279.
(11) Reucroft, P. J.; Sethuraman A. R. *Energy Fuels* **1987**, *1*, 72-75.
(12) Ceglarska-Stefanska, G; Czaplinski, A. *Fuel* **1993**, *72*, 413-417.
(13) Khan, M. R.; Jenkins, R. G. *Proc. Int. Conf. Coal Sci.* **1995**,
(14) Khan, M. R. Ph.D. Thesis, The Pennsylvania State Univ.**1985.**

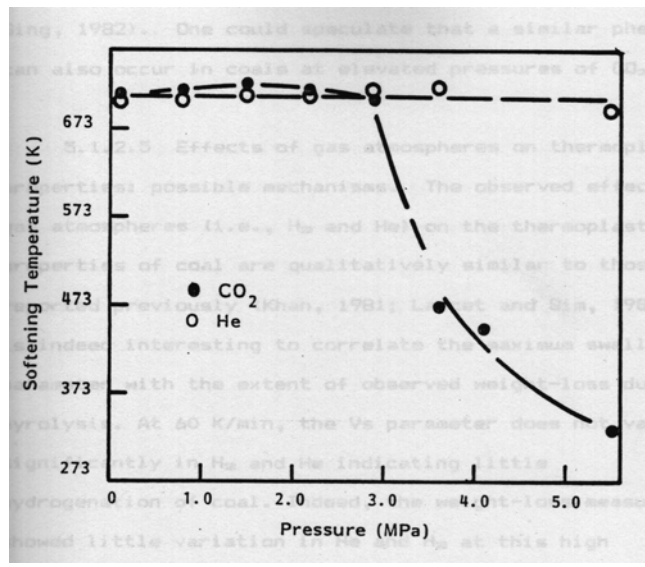

Figure 1. The Effect of He and CO_2 on the Softening Temperature of a Lower Kitanning (91% C, dmmf) Coal (from ref. 13)

AN INITIAL SET OF WORKING HYPOTHESES CONCERNING SOME CHEMICAL AND PHYSICAL EVENTS WHEN CO_2 IS INJECTED INTO A COALBED

CURT M. WHITE
National Energy Technology Laboratory
P. O. Box 10940
Pittsburgh, PA 15236

In any new area of science it is often beneficial to formulate hypotheses and then work toward proving, disproving and refining them. Such is the case with sequestration of CO_2 in coal seams with concomitant recovery of methane. This is a new technology that has been practiced in a few places but is not well developed. Off-the-shelf technology is available to perform CO_2-enhanced coalbed methane recovery/sequestration (CO_2-ECBM/sequestration). Burlington Resources performed CO_2-ECBM in deep unmineable coal seams in the San Juan Basin in New Mexico in 1996.[1] Very little information has entered the public domain from this or similar projects. There is a very incomplete understanding of what happens when CO_2 is injected into a coal seam. During the preparation of a review article on CO_2-ECBM/sequestration we formulated a number of hypotheses concerning the chemical and physical phenomena that occur when CO_2 is injected into a coal seam. Information gathered from the literature was combined with our knowledge of both the chemical and physical properties of coal and supercritical CO_2 to yield a set of working hypotheses that begin to describe the process.

Hypotheses

1) The glass-to-rubber transition temperature (T_g) of the coal will be dramatically reduced by imbibition of CO_2. The coal will become plasticized. [2]
2) The cleat system within the coalbed will begin to close and become restricted, slowing Darcy flow within that area of the seam due to swelling.
3) There will be a substantial increase in the self diffusivity of CO_2 in coal once it has become plasticized and is above its T_g.[2]
4) The diffusivity of CO_2 in coal swollen by high pressure CO_2 can be described by free volume theory.
5) Both liquid and supercritical CO_2 will extract small molecules trapped within the coal macromolecular network. As the network relaxes, these molecules will be released and move with the CO_2 as long as the pressure is above their threshold pressure.
6) Some of the minerals commonly found in coal will dissolve in the acidic, carbonated water during those times when both water and CO_2 are present together in the coal.
7) The Ca and Mg content of the coal will decrease due to dissolution of carbonate minerals by carbonic acid and to due Ca and Mg being displaced from carboxylic acids in low rank coal.
8) Injection of CO_2 will dry the coal, particularly in those areas where the flow rate of CO_2 is highest.
9) There will be a CO_2 pressure gradient across the coalbed. When dissolved minerals and organics reach areas of the seam with lower pressure they will precipitate causing the seam to begin to clog the coal's pores.

Discussion

Effect on Diffusivity The plasticization effects of CO_2 on coal (hypotheses 1 and 4) are discussed elsewhere.[2] Hypothesis 4 is an extension of one proposed by Larsen to include the self diffusion of CO_2 in plasticized coal. Mass transport through coal is a controlling function in the sequestration of CO_2 in coal. If the cleat fracture system in a coal becomes restricted due to swelling, then Darcy flow will be restricted and transport through the coal will be primarily Fickian and possibly Knudsen.

A substantial increase in molecular diffusivity of guest molecules in macromolecular systems in contact with supercritical CO_2 has been documented recently. For example, the diffusivity of ethylbenzene in CO_2 swollen polystyrene shows a 10^6 fold increase when supercritical CO_2 is present.[3] Experimental information that defines factors that impact and control transport properties in CO_2 swollen macromolecular systems is limited for polymeric systems and to our knowledge, unknown for coals. The transport properties of Co(II) complexes in polymeric systems in contact with supercritical CO_2 are dependent upon the degree of CO_2 swelling and the degree of plasticization.[4] These are plasticization induced changes in the transport properties of guest molecules in the swollen macromolecular network. We hypothesize that the substantial increases in diffusivity of guest molecules in polymeric systems applies to the self diffusion of CO_2 in CO_2 swollen macromolecular systems such as coal. As such, we expect diffusion of CO_2 in coal swollen by high pressure supercritical CO_2 will be much more rapid than in the same coal before plasticization.

What is the diffusivity of CO_2 in coal swollen by high pressure supercritical CO_2? Lee *et al.*[4] recently showed that in a polymeric system swollen by CO_2, the effect of CO_2 swelling on mass transport is related to free volume theory. They estimated the fractional free volume (FFV) of swollen polymeric system from the following relationship:

$$FFV = \frac{Vm - Vw}{Vm}$$

where Vm=M/d is the molar volume of the swollen polymer, M and d are the molecular weight and density of the swollen polymer, and Vw is the estimated van der Waals volume. CO_2 diffusivity should decrease exponentially with the reciprocal free volume, 1/FFV. As swelling increases, free volume increases and diffusivity increases. We strongly suspect that the same theoretical approach will explain CO_2 diffusion in supercritical CO_2 swollen coals, and allow estimation of the CO_2 diffusivity under a variety of conditions in swollen coal matrices.

Effect Of CO_2 Adsorption On Organic Matter When CO_2 interacts with coal, multiple processes occur. CH_4 sorbed onto coal is displaced by CO_2. CH_4 desorption occurs simultaneously with CO_2 adsorption. CH_4 is displaced into the cleat system of the coal where it begins to move toward an area of lower pressure, the production well. CH_4 desorption causes coal to shrink, whereas CO_2 adsorption causes the coal to swell. In general, coal swelling due to CO_2 sorption is greater than shrinkage caused by CH_4 desorption. The net effect is coal swelling. As CO_2 is imbibed by coal, the coal swells causing the

macromolecular structure to relax.[2] Weak intermolecular interactions such as van der Waals interactions, hydrogen bonds and charge transfer interactions between one part of the macromolecule and another or between two macromolecules are broken and replaced by interactions between the macromolecule and CO_2 molecules. This allows the small molecules trapped within the interwoven macromolecular network to be released, so that they are free to move. Liquid and dense gaseous CO_2 are excellent solvents. As the trapped molecules are released, they become solvated and extracted by the CO_2, and migrate with CO_2 throughout the coalbed. The extraction process and movement of formerly trapped molecules begins with the lower molecular weight compounds first. Movement of compounds is a function of each compound's threshold pressure. The threshold pressure of a substance was originally defined by Giddings as the lowest supercritical pressure that will cause a substance to just begin migrating in a flowing stream of supercritical fluid.[5] Among hydrocarbons the threshold pressure is an approximate function of their molecular weight. Generally, the amount extracted from coal is quite small, about 2.5 weight percent or less.

Effect Of CO_2 Adsorption On Mineral Matter The presence of high pressure CO_2 and water can also have a profound effect on the mineral matter present in coal. Many minerals present in coal are soluble in acidic aqueous solutions. The solubility of CO_2 in water is substantial at high pressures. According to simulations we performed, the pH of aqueous CO_2 solutions at 300 atm and 45°C is less than 3.0. The alkaline earth metals are removed from coal by treatment with acidic aqueous solutions. Calcite, dolomite, and other carbonate minerals are removed from coal at room temperature by extraction under acidic conditions with aqueous CO_2 solutions. Hayashi *et al.* studied the removal of Ca and Mg from several low rank coals by batch extraction with CO_2 dissolved in water at 600 kPa and 25°C at various extraction times.[6] They showed that the Ca removal yield is affected by the total Ca content of the coal and the total carboxyl content. Ca removal is also affected by the coal:water ratio in that Ca removal decreases as the amount of water decreases. During CO_2 sequestration in coal, it is expected that the water content of the coal will initially decrease with time. The coal will most probably be dewatered before CO_2 injection begins. This process will remove some of the bulk water in the cleat system. When CO_2 injection begins, we expect that the remaining water in the cleat system will be reduced further and the water present in the pores will also be reduced. The rate and extent of these processes are unknown. Thus, we expect that initially the Ca and Mg content of the coal will be reduced when both water and CO_2 are present. The dissolved minerals will be transported through the coal seam and eventually recovered in the produced water when the process is taken to completion. As the water content decreases, the amount of Ca and Mg removed will decrease. If water migrates back into the seam, then Ca and Mg removal could increase. The solubility of carbonate minerals in acidic aqueous solutions is dependent upon both H_2O and CO_2 being present.

Drying of Coal by Flowing CO_2 Iwai *et al.* report the use of supercritical CO_2 to dry coal.[7] Water could be removed by either becoming solubilized by the CO_2 or by being displced by it. Water is only sparingly soluble in supercritical CO_2. Under some conditions water is almost quantitatively removed from low rank coals. They showed that drying of ground and sieved coal (8 grams, 18-30 mesh) with CO_2 (1.5 moles/hour for 20 hours) at either 9.8 or 14.7 MPa and 40°C resulted in removal of water and increased both the surface area and the pore volume of the coal. The degree of coal drying that will occur during CO_2-ECBM/sequestration is unknown, but will probably not be quantitative except near the injection well. Water that is removed during the dewatering process and that removed by CO_2 can be continually replaced by recharge of water from the aquifers.

Precipitation Due to the Pressure Drop There will be both a pressure drop and a CO_2 partial pressure drop from the point of injection to the production well. The injected CO_2 follows the path of least resistance, moving from areas of high pressure near the injection well to those of lower pressure (toward the production well) through the areas of the coalbed that have the highest permeability. As injection continues, the areas of highest permeability become less permeable with time because the swelling process begins to close the cleat system which initially controls gas transport within the coalbed. The extracted compounds that are moving with the flowing CO_2 will begin to clog or plug the coal's pores.[8] The effect of this pore clogging on permeability is unknown. The back pressure increases due to closing of the cleat system caused by swelling. The CO_2 begins to flow into other areas of the coalbed that now represent areas of higher permeability. Eventually, many areas of the cleat system begin to swell. When this happens, the pressure across the coalbed begins to rise, increasing the density and solvating power of the CO_2. The precipitated components then begin to redissolve according to their threshold pressure. As the redissolution process occurs, flow begins again from areas of high pressure toward the production well. The CO_2 will move through the coal as a front, similar to frontal chromatography. The partial pressure of CO_2 will be high in areas behind the front and at the front, but low ahead of the moving CO_2 front. When dissolved carbonate minerals migrate to areas of lower CO_2 partial pressure and/or decreased amounts of water they will precipitate out of solution.

Eventually, the flowing CO_2 finds its way to the area of lowest pressure at the production well. The pressure decreases as CO_2 nears the production well, causing the CO_2 density and solvent strength to decrease. This in turn will cause the organic molecules extracted by the CO_2 and the dissolved minerals to precipitate again when the pressure becomes less than their threshold pressure, clogging the coal matrix adjacent to the production well. Eventually, these molecules will be re-extracted as the CO_2 pressure builds up behind them, redissolving them and moving them into the production well. These are only initial hypotheses that await additional experimental confirmation from the lab and field.

References

(1) Stevens, S. H.; Kuuskraa, V. A.; Spector, D.; Riemer, P. *CO_2 Sequestration in Deep Coal Seams: Pilot Results and Worldwide Potential*, IEA Greenhouse Gas R&D Programme 1999.

(2) Larsen, J. W. *Polymeric Nature of Coals: Some Consequences and Some Unknowns*, ICCS, San Francisco, 2001.

(3) Dooley, K. M.; Launey, D.; Becnel, J. M.; Caines, T. L. Measurement and Modeling of Supercritical Fluid Extraction from

Polymeric Matrices, 1995, *ACS Symp. Series 608*, Chapter 18, 269.
(4) Lee, D.; Hutchison, J. C.; Leone, A. M.; DeSimone, J. M.; Murray, R. W. *J. Am. Chem. Soc.* **2002**, *124*, 9310.
(5) Giddings, J. C.; Myers, M. N.; King, J. W. *J. Chromatographic Sci* **1969**, *7*, 276.
(6) Hayashi, J.; Hayashi, K.; Takeuchi, K.; Kusakabe, S. Morooka, *Fuel* **1991**, *70*, 1181.
(7) Iwai, Y.; Murozono, T.; Koujina, Y.; Arai, Y.; Sakanishi, K. *J. Supercritical Fluid* **2000**, *18*, 73.
(8) Levine, J. R. *Proceedings of the 1991 Coalbed Methane Symposium*, 307.

HYDROCRACKING OF ASPHALTENES WITH METAL CATALYSTS SUPPORTED ON MESOPOROUS SILICA

Enkhsaruul Byambajav, Ryozo Tanaka,[1)] Yasuo Ohtsuka

Institute of Multidisciplinary Research for Advanced Materials, Tohoku University, Katahira, Aoba-ku, Sendai 980-8577, Japan
[1)]Central Research Laboratories, Idemitsu Kosan Co., Ltd., Kamiizumi, Sodegaura, Chiba 299-0293, Japan

Introduction

Heavy oils contain significant amounts of asphaltenes, which are frequently responsible for catalyst deactivation in the upgrading processes. To produce lighter distillates efficiently from heavy oils, it may be necessary to better understand the chemistry of asphaltene cracking in the reaction space suitable for the molecules.

Since the molecular size of asphaltene aggregates is known to range more than 2 nm[1)], the present authors have been working on the utilization of mesoporous silica materials with pore diameters of 2 – 30 nm as catalyst supports for asphaltene cracking. When iron catalysts are loaded on mesoporous silica (SBA-15[2)]) supports with different pore diameters, asphaltene conversion during cracking at 573 K increases with increasing average pore diameter up to 12 nm but levels off beyond this value, regardless of the absence and presence of pressurized H_2[3)]. In this work, therefore, SBA-15 support with the pore diameter of 12 nm is used as a catalyst support, and the effects of metal type, loading and kind of asphaltene on the cracking performance in pressurized H_2 are examined.

Experimental

SBA-15 was synthesized by heating an acidic aqueous mixture of triblock copolymer ($EO_{20}PO_{70}EO_{20}$), trimethylbenzene, and TEOS at 308 K for 24 h, followed by post-synthesis heat treatment at 370 K[2), 4)]. The material recovered after filtration and subsequent dryness at room temperature was calcined in air at 773 K for 6 h. Fe or Ni catalyst was loaded on SBA-15 support by the impregnation method using an ethanol solution of $Fe(NO_3)_3$ or $Ni(NO_3)_2$, respectively, and the resulting sample was again air-calcined at 773 K, metal loading being 10 wt%, unless otherwise stated. All of catalysts were subjected to N_2 adsorption and X-ray diffraction (XRD) measurements. The pore size distribution and specific surface area were determined by the BJH and BET methods, respectively.

Asphaltene (soluble in toluene but insoluble in n-heptane), separated from vacuum residue of crude oil from the Middle East, was mainly used in this study. The elemental analysis is: C, 84.0; H, 7.8; N 0.9; S, 5.3, O (by difference) 2.0 wt%. Other asphaltenes from difference sources were also used. A toluene solution of asphaltene with a concentration of 100 mg/l was mixed with catalyst under ultrasonic irradiation, weight ratio of asphaltene and catalyst being 1.0. The resulting mixture was then evacuated at room temperature with a rotary evaporator to remove toluene, followed by dryness at 363 K under vacuum.

Cracking runs in pressurized H_2 at 5.0 MPa were carried out at 573 K for 1 h with a stirred autoclave. Solid products were separated by the Soxhlet method using n-heptane and toluene into maltene (heptane-soluble), recovered asphaltene (toluene-soluble), and coke plus catalyst (toluene-insoluble). The temperature programmed oxidation (TPO) of the latter mixture recovered was performed, and SO_2 evolved was on line determined.

Results and Discussion

Catalyst Properties and Structures. Figure 1 shows typical examples for the pore size distribution of SBA-15 support and fresh Fe/SBA-15 catalysts after air calcination. All of the materials used provided the narrow distribution with a sharp peak at pore diameter of about 10 nm. When the Fe was added to the support, the peak height decreased with increasing Fe loading, which means that Fe oxide particles are held inside the mesopores. Pore properties and XRD results are summarized in Table 1. The SBA-15 support had the average pore diameter of 12 nm, pore volume of 2.6 cm^3/g and BET surface area of 790 m^2/g. Catalyst addition did not change the pore diameter, irrespective of metal type and loading, but lowered the pore volume and surface area, as is expectable. The extent of the lowering was larger at a higher loading.

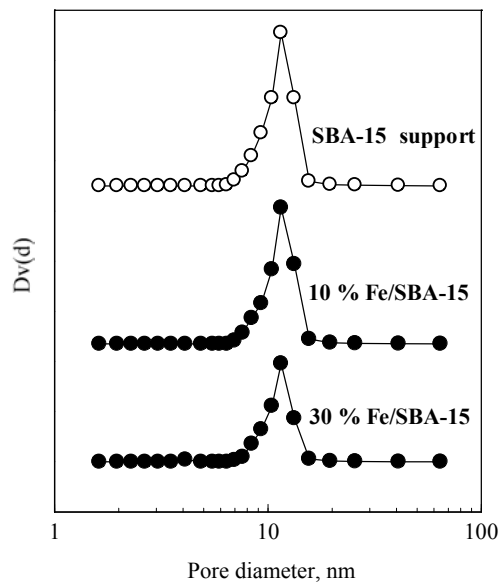

Figure 1. Pore size distribution of SBA-15 support and Fe/SBA-15 catalysts after air calcination.

Table 1. Properties of Metal Catalysts Supported on SBA-15

Metal	D_p[1)] (nm)	V_p[1)] (cm^3/g)	S_{BET}[2)] (m^2/g)	XRD species
None	12	2.6	790	-
10 wt% Fe	12	2.3	680	n.d.[3)]
30 wt% Fe	12	1.5	520	n.d.[3)]
10 wt% Ni	12	2.1	620	NiO

[1)]Average pore diameter (D_p) and pore volume (V_p).

[2)]BET surface area.

[3)]No species detectable.

As is seen in Table 1, the XRD measurements of the fresh catalysts revealed that no significant diffraction lines of Fe oxides were detectable, independently of Fe loading, whereas NiO peaks appeared with 10 % Ni/SBA-15. The average crystalline size of NiO determined by the Debye-Scherrer method was estimated to 8.0 nm, which was smaller than the average pore diameter (12 nm) of the Ni/SBA-15. These observations suggest that Fe species are more finely dispersed inside the mesopores than Ni species.

Hydrocracking Performances and Catalyst Forms. The results for hydrocracking at 573 K are shown in Figure 2, where asphaltene conversion and maltene yield are calculated by using the amounts of asphaltene and maltene recovered, respectively. With Fe catalysts, interestingly, the conversion was the highest at 4 % Fe and

decreased with increasing Fe loading, whereas maltene yield was the largest at 10 % Fe. It is evident that the optimum Fe loading exists for maltene formation. The 10 % Ni catalyst showed the lower conversion but the higher yield than the 10 % Fe catalyst. The latter may originate from higher hydrogenation ability of the Ni.

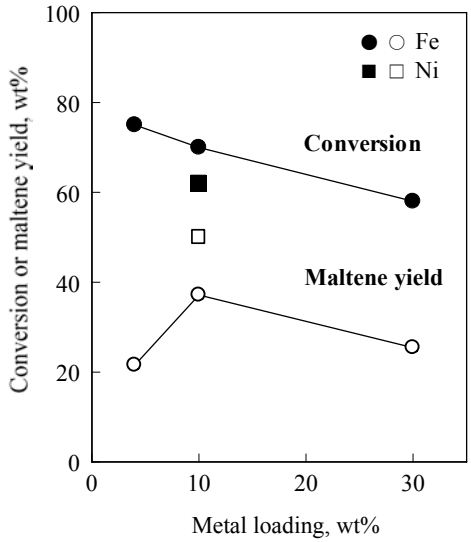

Figure 2. Asphaltene conversion and maltene yield in hydrocracking with Fe/SBA-15 and Ni/SBA-15 catalysts.

The XRD profiles after reaction showed that any Fe species could not be detected with 4 – 10 % Fe catalysts, but very small peaks of Fe_3O_4 were observed at 30 % Fe. The NiO observed with the fresh Ni/SBA-15 was reduced partly to metallic Ni after reaction.

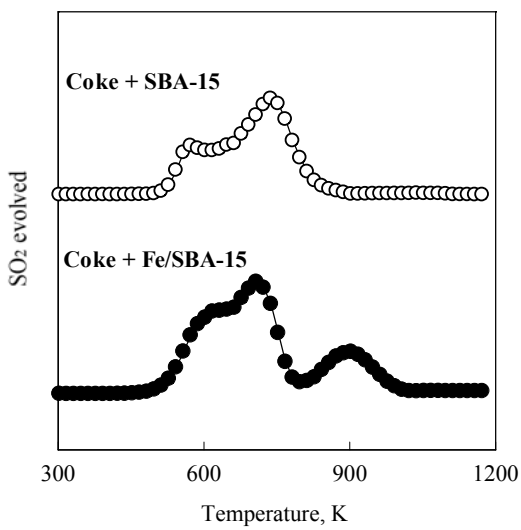

Figure 3. TPO profiles for the mixture of coke and SBA-15 support or 10 % Fe/SBA-15 catalyst recovered after reaction.

To examine the surface state of the 10 % Fe catalyst used, the TPO runs were carried out. The results are shown in Figure 3. When the profiles without and with the Fe catalyst were compared, SO_2 evolved newly at 900 K in the presence of the Fe. The SO_2 can be ascribed to the decomposition of $FeSO_4$[5], which arises probably from the oxidation of surface iron sulfides during the TPO. The elemental analysis revealed that most of the sulfur evolved during asphaltene cracking was retained in the mixture of coke and Fe/SBA-15 or Ni/SBA-15 catalyst. It is likely that Fe and Ni catalysts are present in the sulfided forms at the outermost layers.

From these observations, following speculations are possible for the optimum Fe loading for maltene formation observed in Figure 2. The sulfide species at 4 % Fe are the most highly dispersed and thus show the largest catalytic activity, which results in the highest coke yield. At 10 % Fe, on the other hand, fine particles with the larger size than that at 4 % Fe exist and show the medium activity and largest hydrogenation ability for maltene formation.

When two kinds of asphaltenes derived from different vacuum residues from the above-mentioned were cracked with the 10 % Fe/SBA-15, asphaltene conversion and maltene yield depended on its type, and the highest conversion reached about 80 %, which was larger than the value in Figure 2. Although atomic H/C ratios in all of feed asphaltenes used were almost the same, the XRD measurements revealed the different compositions of aliphatic and aromatic fractions observed at 2θ(Cu Kα) of 20 – 22 and 25 degrees[6], respectively. The proportion of the latter fraction seems to relate with the extent of coke formation.

Conclusions

Mesoporous silica (SBA-15) with narrow pore size distribution and average pore diameter of 12 nm is synthesized and used as a support of Fe or Ni catalyst in hydrocracking of asphaltenes at 573 K and under 5.0 MPa H_2. When Fe loading is changed in the range of 4 – 30 wt%, asphaltene conversion is higher at a smaller loading, and maltene yield is the largest at 10 % Fe. The 10 % Ni/SBA-15 shows the lower conversion but the higher yield than the 10 % Fe catalyst. The elemental analysis and temperature programmed oxidation show that most of sulfur evolved during hydrocracking is retained in the mixture of coke and catalyst, and the catalyst surface exists in the sulfided species, which are probably active for asphaltene cracking.

Acknowledgement. This work was carried out in part as a research project of the Japan Petroleum Institute commissioned by the Japan Cooperation Center, Petroleum, with the subsidy of the Ministry of Economy, Trade and Industry.

References

(1) Yen, T. F. In *Encyclopedia of Polymer Science and Engineering*; Grayson, M.; Krochwitz, J.L., Eds.; Wiley: New York, 1988; p.1.
(2) Zhao, E.; Feng, J.; Huo, Q.; Melosh, N.; Fredrickson, G.; Chmelka, B.; Stucky, G. *Science* **1998**, *279*, 548.
(3) Byambajav E.; Ohtsuka, Y. Proc., 52nd Canadian Chemical Engineering Conference, No. 405 (2002).
(4) Wang, Y.; Noguchi, M.; Takahashi, Y.; Ohtsuka, Y. *Catal. Today* **2001**, *68*, 3.
(5) LaCount, R. B.; Anderson, R. R.; Friedman, S.; Blaustein, B. D. *Fuel* **1987**, *66*, 909.
(6) Scotti, R.; Montanari, L. In *Structure and Dynamics of Asphaltenes*; Mullins O.C.; Sheu, E.Y., Eds.; Plenum Press: New York, 1998; p.79.

MECHANISM OF CARBON DIOXIDE (CO_2) ADSORPTION ON MOIST COALS

Ekrem Ozdemir,[1,2] Karl Schroeder,[1] Badie I. Morsi[1,2] and Curt M. White[1]

[1] U.S. Department of Energy - National Energy Technology Laboratory (NETL), P.O.Box 10940, Pittsburgh, PA 15236
[2] Chemical and Petroleum Engineering Department, University of Pittsburgh, 1249 Benedum Hall, Pittsburgh, PA 15261

Introduction

Sequestration of carbon dioxide (CO_2) in coal seams is being considered as a strategy for mitigating green house gas emissions. The adsorption of CO_2 onto a solid, immobile matrix that will be stable over geologic times is considered an important advantage of coal seam sequestration. However, the adsorption capacity and the stability of the adsorbed CO_2 are affected by the nature of the coal and the environment in which it is placed. Pressure, temperature, coal rank, coal moisture content, and changes in the pH of the coalbed water are factors that may limit the extent of adsorption.[1] Because it is well recognized that the methane adsorption capacity of coal decreases with increasing moisture content, the effect of moisture on the CO_2 adsorption capacity is of special interest.[2,3] To our knowledge, there is no systematic study of the effect of moisture on the adsorption isotherm and adsorption capacity of CO_2 on coals.

The adsorption mechanism in microporous adsorbents has been interpreted in terms of both a pore filling process, using the Dubinin pore filling equation, and a surface adsorption, using the Langmuir or BET equation.[4] Martinez *et al*.[5] studied the mechanism of adsorption of CO_2 on activated anthracite and concluded that the adsorption mechanism was dependent on the shape and size of the pores. They suggested that the adsorption was a pore filling process in narrow micropores of molecular dimensions and gave rise to the curvature seen at lower pressures in the adsorption isotherm. Adsorption in wider pores was dominated by surface adsorption that produced an isotherm with a rectilinear shape. Levy *et al*.[6] showed that the adsorption capacity of CH_4 on coals increased linearly from 12 ml/g to 26 ml/g as moisture decreased from 4% to 0.5%. While it is tempting to interpret some of the isotherm data as a simple competition between moisture and adsorbing gas (CH_4 or CO_2), it is recognized that moisture can play a role in the 3-dimensional structure of the organic coal matrix. Suuberg *et al*.[7] showed that coals shrink when dried. A plot comparing the volumetric shrinkage to the percent moisture loss was linear for a dozen coals of different ranks. For the lower rank coals, the volumetric shrinkage amounted to 25-30%. They pointed out that the measurement of the surface areas of dried coals might provide an erroneous estimate of the true accessibility of the coal structure.

Experimental

Moisture content. In order to obtain coal samples with various moisture contents, as-received samples of Argonne coals[8] were dried *in-situ* in the adsorption apparatus. Each of the samples was vacuum-dried individually at 22, 22, 45, 80, or 97°C for 4, 20, 10, 16, or 5 hrs, respectively. After drying, the coals were allowed to equilibrate at the temperature and pressure of the initial isotherm experiment for 2-3 hrs before beginning the adsorption isotherm measurements. After the adsorption experiments, the moisture content of each of the samples was determined using Thermal Gravimetric Analysis (TGA). TGA drying experiments were conducted on 23 mg samples, at 105 °C for 60 min.

Evaluation of adsorption isotherm data. Gaseous CO_2 adsorption isotherms were obtained by the volumetric method using a low-sample-volume apparatus described elsewhere.[9] The isotherms were evaluated using an equation derived previously (Eq.1) that attempts to account for the volumetric swelling of the coal.[9]

$$n^{ex} = n^{abs} + \left(\frac{\Delta V}{RT}\right)\left(\frac{P}{z}\right) \qquad (1)$$

The absolute amount adsorbed, n^{abs}, can be represented by the Langmuir or Dubinin-Astakhov equations which assume surface coverage or pore filling mechanisms, respectively. In the case of the pore filling mechanism, Eq.1 becomes Eq.2, which accounts for the volume of the adsorbed phase:

$$n^{ex} = \left(1 - \rho/\rho^{a}\right) n_0 e^{-D\left[\ln\left(P_S/P\right)\right]^{j}} - \rho\Delta V_c \qquad (2)$$

where n^{ex} is the experimentally determined adsorption (Gibbs adsorption), ρ is the density of the adsorbing gas, ρ^a is the density of the adsorbed phase, n_o is the adsorption capacity, P_s is the saturation pressure, ΔV_c is the change in the accessible pore volume, j is the Dubinin exponent related to the pore size distribution, and D is Dubinin constant defined as

$$D = \frac{RT}{\beta E_0} \qquad (3)$$

where R is the universal gas constant, T is temperature, β is the affinity coefficient, and E_o is the characteristic heat of adsorption.

Results and Discussion

Figure 1 shows the adsorption isotherms of CO_2 on four of the eight Argonne Premium coals. These are representative of the different ranks and moisture contents of the coals. Pocahontas No.3 was the highest rank coal and contained the least moisture (0.63%). Pittsburgh No.8, Blind Canyon, and Wyodak coals decrease in rank and increase in moisture content, successively. Drying the coals at 80 °C for 20 hrs under vacuum removed a smaller fraction of the total moisture content for the higher rank coals and a progressively larger fraction for the lower rank coals. For instance, the moisture content decreased from 0.63% to 0.54% (14% of the initial moisture was removed) for Pocahontas No.3, a high rank coal, but decreased from 20.72% to 3.40% (84% removed) for the low rank Wyodak coal.

The effect of moisture removal was smaller for the higher rank coals than for the lower rank coals. The CO_2 adsorption isotherm for the high rank Pocahontas No.3 changed little, but the original moisture content was small. On the other hand, significant increases in adsorption were seen for the dried low-rank coals.

The amount of CO_2 adsorbed on a particular coal was determined from the adsorption isotherm and was found to be directly related to the moisture content of the coal. **Figure 2** shows the adsorption isotherms of CO_2 on the Argonne Premium Illinois No.6 coal dried to different moisture contents. The apparent amount of CO_2 adsorbed (n^{ex}) increased as more and more moisture was removed from the as-received coal. The shapes of the adsorption isotherms for the as-received (moist) coals were Langmuir-like whereas the adsorption isotherms for the dried coals were more rectilinear.

Figure 3 shows the adsorption capacity of the eight Argonne Premium coals dried to different moisture contents. The adsorption capacity is linearly related to the moisture content of each coal, regardless of rank. This trend is similar to that observed by Suuberg[7] for volumetric shrinkage (*vide supra*) and we believe the two are related. The adsorption capacities of the dried coals calculated from the intercepts in Figure 3 were found to be rank dependent. Thus, the

extent of adsorption of CO_2 on a given coal is dependent on its rank and moisture content.

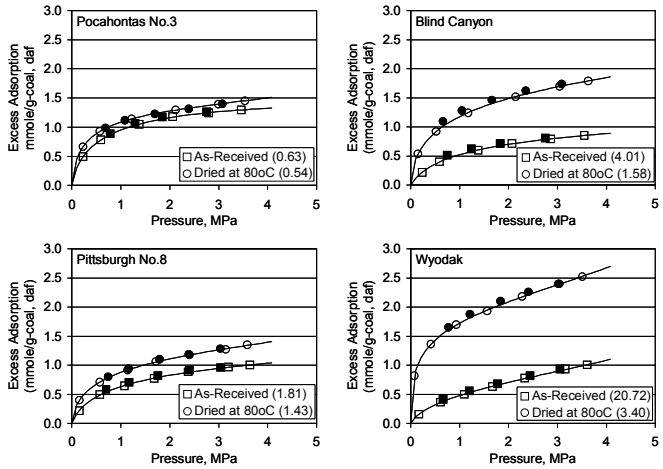

Figure 1. Excess adsorption of CO_2 on as-received and dried (at 80°C under vacuum for 20 hrs) Argonne coals. Open symbols: Adsorption, closed symbols: Desorption

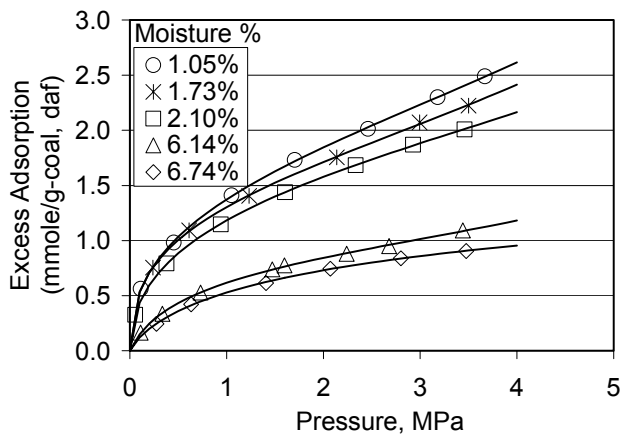

Figure 2. Adsorption isotherms of CO_2 on Argonne Premium Illinois No.6 coals having different moisture content

Discussion

The adsorption capacities of the wet coals are lower than the dried coals and display an isotherm that becomes almost linear for low-rank coals. Using the modified adsorption equation (Eq.1) to interpret this data leads to the conclusion that the nearly linear portion of the isotherm results from a volumetric change that may be related to the swelling properties of the coals. The surface (or pore-filling) adsorption is reflected in the curved, Langmuir-like portion of the isotherm which is more pronounced for higher rank coals and lower pressures.

If the CO_2 adsorption capacities are calculated by substituting an appropriate adsorption expression for the n^{ads} into Eq.1, e.g. as n^{ex} in Eq.2, the dependence of the adsorption on the moisture content appears to be linear as seen in Figure 3. The slopes of the lines are indicative of the importance of water to the adsorption of CO_2. Conversion of g water per 100 g coal (% moisture) to millimoles of water lost gives a slope of 1.1 moles of water lost per mole of CO_2 adsorbed for the higher rank coals. Thus, for the higher rank coals, it appears that the effect of moisture on the adsorption may be simply one of competition of H_2O and CO_2 for the same binding sites. However, the slopes become progressively smaller as one moves through the mid-rank to the low-rank coals. The slopes of the Wyodak and Beulah Zap coals are closer to 8 moles of water lost per mole of CO_2 adsorbed. Thus, in the case of low-rank coals, either many adsorption sites that are active for H_2O adsorption are unfavorable for CO_2 adsorption, perhaps because they are too polar, or, possibly, clusters of water molecules block each CO_2 binding site.

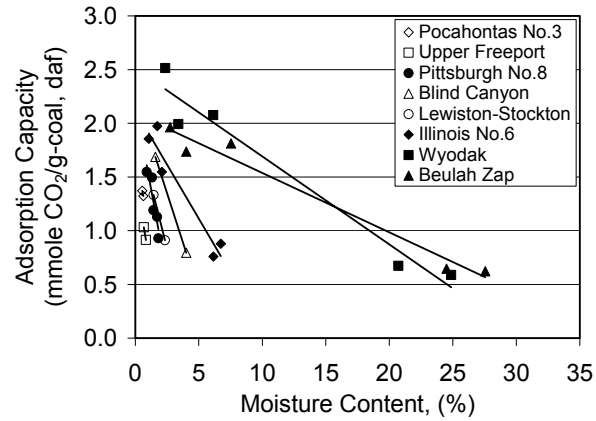

Figure 3. Adsorption of CO_2 on Argonne Premium coals as a function of moisture content.

Conclusions

The presence of moisture significantly decreases the CO_2 adsorption capacities of coals, regardless of rank. Therefore, CO_2 adsorption isotherms of dried coals may not provide the information needed to interpret or model CO_2.

References

[1] Shroeder,K., Ozdemir, E., and Morsi, B.I., *First National Conference on Carbon Sequestration*, **2001**, May 14-17, 2001, Washington D.C.

[2] Joubert, J., I., Grein, C., T., and Bienstock, D., *Fuel*, **1973**, 52, 181-185

[3] Joubert, J., I., Grein, C., T., and Bienstock, D., *Fuel*, **1974**, 53, 186-191

[4] Gregg, S., J., and Sing, K., S., W., Adsorption, Surface Area and Porosity, Academic Press, New York, 1982

[5] Martinez, J.M.M., Marcia, R.T., and Hazeleger, M.C.M., *Fuel*, **1995**, 74, 111-114

[6] Levy, J., H., Day, S., J., and Kilingley, J., S., *Fuel*, **1997**, 76, 813-819

[7] Suuberg, E.M., Otake, Y., Yun, Y., and Deevi, S.C., *Energy&Fuels*, **1993**, 7, 384-392

[8] Vorres, K, S., Users Handbook for the Argonne Premium Coal Sample Program, (ANL/PCSP-93/1), Argonne National Laboratory, Argonne, Illinois1993

[9] Ozdemir, E., Schroeder, K., and Morsi, B.I., *Am. Chem. Soc., Div. Fuel Chem. Prepr.*, *47 (1)*, 12-13, **2002**

CO_2 Sequestration with Oriskany Brine

Y. Soong, J. R. Jones, D. K. Harrison, A. L. Goodman, J. P. Baltrus, S. W. Hedges and G. F. Walbert [1]

U.S. Department of Energy, National Energy Technology Laboratory,
P.O. Box 10940, Pittsburgh, PA 15236
[1]Parsons Project Services, Inc. P.O. Box 618, South Park, PA 15129

Introduction

CO_2 is the major gas contributor to global warming [1]. Many techniques to capture and store CO_2 are currently being investigated. CO_2 injection into saline aquifer formations is one of the promising geologic CO_2 sequestration options. It is attractive, because there are regionally extensive aquifers capable of accepting large volumes of CO_2 (500 Gt. of CO_2) from power plants without the need for long transport pipelines. Upon injection of CO_2 into saline aquifers, CO_2 may be stored by hydrodynamic and/or mineral trapping. The most critical concern of hydrodynamic trapping is the potential for CO_2 leakage through imperfect confinement. In mineral trapping, CO_2 is converted into carbonate minerals by a series of reactions with aqueous ions found in the saline aquifer. Various carbonates such as calcite, magnesite, dolomite, and siderite can be formed in the brine aquifer by mineral trapping [1,2]. However, conversion of CO_2 to stable carbonate minerals is expected to be slow. Researchers from the Alberta Research Council in Canada [2] calculated times for precipitation of the various carbonates to occur on the order of hundreds of years. These results suggest that mineral trapping may contribute significantly to CO_2 sequestration within saline aquifers but only in the long term.

Sass et al., [3] studied CO_2 and brine reactions with mineral rocks for 7 days at a pressure of 5.44 MPa and 110 °C. They found increased levels of Ca, Mg, and carbonate in solution, which were due to the dissolution of dolomite. Lebro'n and Suarez [4] reported the precipitation rate of calcite increased as the partial pressure of CO_2 increased (0.035 to 10 kPa). However, no extensive laboratory studies directed at the sequestration of CO_2 in brine aquifers have been conducted. As such, brine from the Oriskany Sandstone aquifer of the Appalachian Basin is examined to assess its ability to sequester CO_2 in the near term via the mineral trapping pathway upon reaction with CO_2. This study attempts to evaluate the ability of such brines alone to serve as a mineral trapping medium. It is prudent to investigate the variables that effect mineral carbonates formation in brines in the absence of complication factors introduced by the presence of formation rocks. Specifically the effects of pH, CO_2 pressure, and temperature on the reaction between CO_2 and brine samples to form carbonate minerals were investigated. The optimum reaction conditions that favor the formation of mineral carbonates were investigated with autoclave experiments and geochemical modeling.

Experimental

To examine the mineral trapping under controlled temperature and pressure conditions in an autoclave reactor, brine samples were collected from the Oriskany Sandstone in Indiana County, PA., at a depth of 2,550 m. No effort was made to prevent oxygen from contacting the brine. The brine was tested as received without further filtration. Brine carbonation experiments were carried out in a ½ liter autoclave. The details of the experimental setup are shown elsewhere [5]. The brine was used either as received, or the pH was adjusted before reaction by adding KOH. The effects of pH (3.6 to 11), reaction time (1 to 6 hours), CO_2 pressure (0.34 to 7.63 MPa), and temperature (50 to 170°C) on brine carbonation were investigated. The brine carbonation reactions were also modeled with the computer program PHREEQC version 2. The simulation results were used as a guide in determining specific experimental conditions to investigate with the autoclave reactor.

Results and Discussion

The mineral dolomite was not allowed to precipitate in the simulation even though the saturation index for it was positive. The kinetics for dolomite precipitation is relatively slow and it is likely that this mineral may not precipitate out of solution [6]. In addition, XRD analysis of the solid precipitate from the autoclave reactions did not detect dolomite.

The autoclave experiments and simulations were conducted to study the reaction of CO_2 with brine samples as a function of pH at constant temperature (155°C) and CO_2 pressure (6.87 MPa) (Fig. 1). After reaction, the pH of the solution was measured and found to be lower than the starting pH (Fig.1a – solid circles). A similar trend between the pH before reaction and the pH after reaction with CO_2 is observed in the simulation results (Fig. 1a – dashed line). The pH of the brine decreases following reaction with CO_2 because CO_2 dissolves in solution to form carbonic acid, H_2CO_3, thus decreasing the pH. In addition, CO_2 not present after reaction due to the reactor was depressurized. As Ca and other metals are removed from solution by precipitation, the remaining solution become more acidic.

As the initial pH of the raw aqueous brine was increased from 3.6 to 11 by adding KOH, the concentration of the aqueous ion Ca in the reacted brine decreased by 25 %. The total grams of precipitate increased from 0.08 to 7.5 g/L (Fig. 1b – solid circles). The simulation results indicate a similar trend as pH increases, the total grams of solid precipitate increases from 0.1 grams at pH 2.7 to 30.5 grams at pH 11 (Fig. 1b – dashed line). However, the total grams of precipitate predicted by the model deviates significantly from experimental observations in that the model predicts almost four times as much solid precipitate than what is observed experimentally. This may be due to the fact the simulation is predicting total grams of precipitate under equilibrium conditions, while the total grams of solid precipitate from the autoclave experiments is measured after six hours of reaction followed by degasing CO_2 and cooling down to 25 °C. Although the experimental and model results differ on the amount of solid precipitate formed as pH is increased, both results follow the same general trend in that the total mass of solid precipitate increases as the pH increases (Fig. 1b). Only 0.09 g of Ca per gram of precipitate was observed at the initial brine pH of 7.2. Significantly more Ca precipitate was observed after the initial brine pH was increased to 9 and higher. The concentration of solid Ca precipitate increased by one order of magnitude (Fig. 1c). Both XRD analyses of the solid precipitate from the autoclave reactions and simulation results identified $CaCO_3$ and Fe_2O_3 to be the main components of the solid samples at pH values greater than 9. Thus, as the pH is increased from 9 to 11, the grams of $CaCO_3$ per total grams of precipitate (g Ca/g ppt) (Fig. 1c).

Next, a series of autoclave experiments and simulations were conducted to study the reaction of CO_2 with brine samples as a function of pressure at constant pH (pH = 11.0) and temperature (155 ^{o}C). The CO_2 pressure was varied from 0.34 to 7.64 MPa. The pH after reaction, concentration of the aqueous components, total grams of precipitate, and grams of Ca per total grams of precipitate versus pressure did not change significantly as pressure was increased. From these results, pressure does not seem to play a large role in the formation of carbonate minerals as long as a minimum CO_2 pressure is maintained in the reactor. Therefore, high CO_2 pressures are not required for the precipitation of carbonate minerals.

Finally, a series of autoclave experiments and simulations were conducted to study the reaction of CO_2 with brine samples as a

function of temperature at constant pH (pH = 11.0) and CO_2 (0.34 MPa) pressure (Fig. 2a-c). The temperature was varied from 50 to 170 ^oC. The pH after reaction, concentration of the aqueous components, total grams of precipitate, and grams of Ca per total grams of precipitate versus temperature changed very little for the autoclave experiments (Fig.2a-c). However, the simulation results predict a general increase in total grams of precipitate and grams of Ca per total grams of precipitate versus temperature. This may be due to the fact the simulation is predicting total grams of precipitate under equilibrium conditions, while the total grams of solid precipitate from the autoclave experiments is measured after six hours of reaction followed by degasing CO_2 and cooling down from reaction temperature to ambient condition. From these results, the experimental data suggest that temperatures above 50°C do not play a large role in the formation of carbonate minerals.

Mineral trapping occurs via reactions (1-5) shown below. CO_2 gas dissolves into solution (1). Carbonic acid is formed (2), which then dissociates into bicarbonate (3) and carbonate ions (4). Thus, pH of an aqueous solution decreases with the addition of CO_2 [4,7]. Then ions such as Ca, Mg, and Fe react with the carbonate ions to form minerals such as calcite, dolomite, siderite, and magnesite (5a-5d), respectively. 1) CO_2 (gas) -> CO_2 (aq);2) CO_2 (aq) + H_2O -> H_2CO_3 ;3) H_2CO_3 -> H^+ + HCO_3^- ; 4) HCO_3- -> H+ + CO_3^{2-} ;5a)Ca^{++} + CO_3^{2-} <--> $CaCO_3$ (calcite) ;5b)Ca^{++} + Mg^{++} + CO_3^{2-} <--> $CaMg(CO_3)_2$ (dolomite) ;5c)Fe^{++} + CO_3^{2-} <--> $FeCO_3$ (siderite) ;5d)Mg^{++} + CO_3^{2-} <--> $MgCO_3$ (magnesite)

The pH of the brine affects the reaction rate and species precipitated. In a closed system dissolved carbon dioxide, CO_2(aq) and H_2CO_3 (carbonic acid) predominate at low pH, HCO_3^- (bicarbonate) dominates at mid pH, and CO_3^{2-} (carbonate) rules at high pH. The solubility of carbonate also increases as the pH decreases. Thus, aqueous-phase equilibrium with CO_2(g) promotes carbonate precipitation under basic conditions, while acidic conditions favor carbonate dissolution. Therefore, to favor the precipitation of mineral carbonates, the pH must be basic. As demonstrated here, brine pH affects whether carbonate minerals will precipitate from solution (Fig. 1c).

Mineral trapping is also controlled by CO_2 pressure and temperature but by a lesser extent when compared to pH. Temperature and pressure also play an important role in determining the solubility of CO_2 in solution [8]. However, experimental results suggest that temperature does not play a major role in brine carbonation above 50°C (Fig. 2). The CO_2 pressure affects the CO_2-brine reaction, but it is very dependent upon pH. Dreybodt et al [9] conducted the study of the precipitation kinetics of calcite in the system $CaCO_3$-H_2O-CO_2. They concluded that the rate limiting step is equation 3. If the same rate-limiting step applied to the CO_2-brine system, then the pH of the system is dominated. Basic environments ,pH=11, favors the formation of HCO^-_3 and CO^{2-}_3 and finally the formation of $CaCO_3$. The formation of calcite would ease, once the basic conditions changed. Therefore, pH as more impact on the carbonation reaction than temperature and pressure. The overall equilibrium equation for calcite formation can be described by equations 6 and 7:

6) $$Ca^{2+} + CO_2(g) + H_2O \leftrightarrow CaCO_3(s) + 2H^+$$

7) $$K = \frac{[H^+]^2}{[Ca^{2+}]P_{CO2}}$$

According to equation 7, the calcite formation is dependent upon the hydrogen ion concentration, CO_2 pressure, and Ca ion concentration. When the CO_2 pressure increases at the constant initial pH, the amount of calcite precipitate remains the same. As the CO_2 pressure is increased, the pH decreases because carbonic acid is formed. As CO_2 pressure continues to increase, the pH drops from 11 to 4.5. At low pH values, calcite not longer precipitates from solution. As discussed earlier, calcite precipitation is favored at high pH, while calcite dissolution is favored at low pH. Thus the amount of Ca precipitate is limited by the pH not the CO_2 pressure as long as a minimum pressure is maintained. In order to increase the amount of $CaCO_3$ precipitation with increasing CO_2 pressure, the pH will need to be buffered at values higher than 9.0.

Conclusions

The reactions between CO_2 and brine samples collected from the Oriskany Formation in Indiana County, PA were investigated experimentally using a ½ liter autoclave under various conditions and theoretically using the geochemical code PHREEQC. The results indicate that the amount of calcite precipitate depends primarily on the pH of the brine. The CO_2 pressure and temperature have lesser impact on the formation of carbonates.

References

1. DOE report, DOE/SC/FE-1, Carbon Sequestration Research and Development, December 1999.
2. Hitchon, B. Gunter, W. D. Gentzis, T. and Bailey, R. T., *Ener. Conv. & Man.* 40 (1999) 825.
3. Sass, B. N., Gupta, J. Ickes, J.,Eagelhard, M., Bergman, P.D. and Byaer, C; Conference CD, 1st National Conference on Carbon Sequestration, Washington, D.C., May 15-17,2001.
4. Lebro'n, I and Suarez, D. L., *Geochim. Cosmochim. Acta* 62 (1998) 405.
5. Soong, Y., Jones, J. R., Hedges, S. W., Harrison, D. K., Knoer, J. P., Baltrus, J. P., and Thompson, R. L, *Am. Chem. Soc. Div. Fuel Chem.* 2002, 47 (1) 43
6. Lasaga A. C. (1998) "Kinetic Theory in the Earth Science," Princeton University Press, 811.
7. Krauskopf K. B., (1979) "Introduction to Geochemistry", McGraw-Hill, New York, 43.
8. Enick, B. M. Klara, S. M., *Chem. Eng. Comm.* 90 (1990) 23.
9. Dreybodt, W., Eisenlohr, L., Madry, B., and Ringer, S., (1997) *Geochim. Cosmo. Acta*, **61**, 3987.

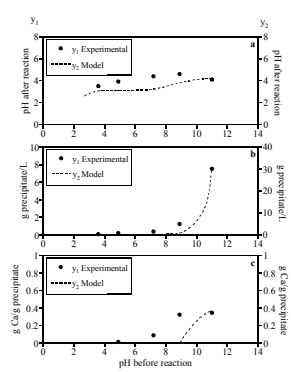

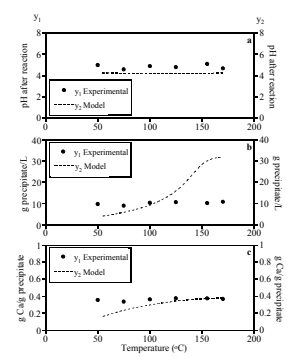

Fig 1. Brine carbonation as function of pH at 6.87 MPa CO_2 and 155 °C (left).

Fig 2. Brine carbonation as function of temperature at 0.343 MPa CO_2 and pH 11 (right).

UTILIZATION OF STATIC MIXER ON THE INJECTION OF LIQUID CO_2 INTO WATER FOR THE OCEAN DISPOSAL

Hideo Tajima, Akihiro Yamasaki, and Fumio Kiyono

National Institute of Advanced Industrial Science and Technology
16-1 Onogawa, Tsukuba, Ibaraki 305-8569, Japan

Introduction

Several scenarios of CO_2 disposal into the ocean have been proposed for a long-term sequestration as a counteraction measure for global warming. In the disposal process of liquid CO_2, especially, liquid CO_2 would be released from a pipeline through a nozzle to the ocean at the depth deeper than 500 m[1]. Since the density of liquid CO_2 is smaller than that of seawater at the depth shallower than 3000 m, the released CO_2 droplets would ascend to the ocean surface. During the droplet ascending process, the CO_2 would be dissolved into the seawater from the droplets, and the ascending speed would decrease by the reducing size of the droplets. The dissolution process should be completed before reaching the sea surface. Since the ascending and dissolution behavior depends on the size of the released CO_2 droplets, the releasing size of the droplet should carefully designed and controlled on the injection. On the other hand, the effect of CO_2 hydrate should be considered in the disposal process of liquid CO_2, because the thermodynamic condition of CO_2 hydrate formation would normally be satisfied in the ocean at depths greater than 500 m (T < 283 K and p > 44.5 bar[2]). The nozzle of the CO_2 pipeline could be blocked by the formation of solid CO_2 hydrate upon injection and sequent the agglomeration of the hydrates, and the blockage should be prevented for a continuous and stable injection process.

In this research, a novel injection process of liquid CO_2 into the ocean by utilization a static mixer was proposed as a possible solution for the above difficulties, and the hydrodynamic behavior of the liquid CO_2 in water was studied through laboratory-scale experiments for obtaining basic knowledge for the disposal process design.

Outline of utilization of static mixer on CO_2 disposal process

Figure 1 shows a conceptual drawing for the outline of the new disposal of CO_2 in the ocean. Liquid CO_2 is sent to the depths about 500m in the ocean through a pipeline, then disposed of through a static mixer in which liquid CO_2 was mixed with the ambient seawater.

The structure of a typical static mixer is shown in **Figure 2**. In the static mixer, elements are arranged and fixed inside a straight tube. The element could make the incoming fluid to be turbulent. The flow in the static mixer is close to a piston flow, and uniform radial mixing could be realized. The energy consumption for the mixing is only pressure droplet consumed by flowing through the static mixer, which is much lower than the power consumption by the stirring process with a stirred-tank type mixer.

The advantages of utilizing a static mixer in the disposal process of liquid CO_2 in the ocean would be the following: (1) droplet size control, (2) blockage control, and (3) energy saving process. With a proper design of the static mixer, continuous formation and disposal process of CO_2 hydrate could be realized as an extended version of the present process. Since no literature data are found for the behavior of liquid CO_2 in the static mixer, the hydrodynamic behavior of liquid CO_2 and water in a static mixer was examined in a laboratory scale experimental apparatus in this study.

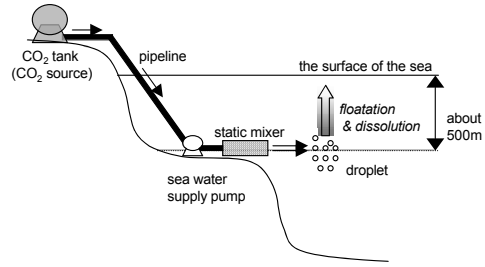

Figure 1. Concept drawing for utilization of static mixer on CO_2 injection into the ocean

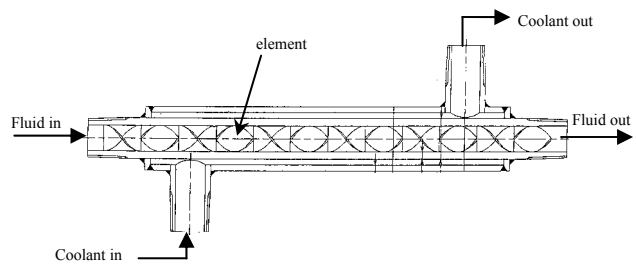

Figure 2. Noritake static mixer (Type: 3/8-N10-522-N)

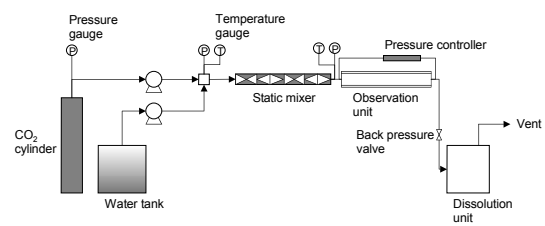

Figure 3. Schematic drawing of the apparatus of hydrate

Experimental

The schematic flow diagram for the experimental apparatus is shown in **Figure 3**. Liquid CO_2 with the highest purity (> 99.90%) and deionized water were introduced to the static mixer by a high-pressure pump (Nippon Seimitsu Co., Ltd., NP-AX-70, Fuji Pump Co., Ltd., 2JN224-10V) after pre-cooling to a desired temperature. The static mixer was specially designed and made for high-pressure and low temperature conditions by Noritake Co., Ltd., Japan based on the style: 3/8-N10-522-N. The behavior of the mixture was observed in a transparent observation unit made of polycarbonate tube (inner diameter 10.6 mm, length 300 mm) which was connected downstream side of the static mixer. The temperature of the system was controlled by the fluid flow in the jacket on the flow lines where temperature-controlled coolant of a mixture of water and ethylene glycol was circulated from a cooling unit. The behavior of the fluid mixing was recorded through the observation part with a high-speed video camera (Photron Ltd.; maximum 500 frame per second). Then, the video data was captured and analyzed by a Power Macintosh G4 computer using the public domain ImageJ (ver.1.27) program (developed at the U.S. National Institute of Health and available from the Internet, http//rsb. info. nih. gov/nih-image/).

Results and Discussion

Injection of CO_2 into Water Using Static Mixer. Figure 4 shows the CO_2 droplet formed in the static mixer. The pressure was 7.0 MPa, Note A) is out of hydrate formation condition and B) is within it. For the higher temperature conditions without hydrate formation, the CO_2 droplets could be formed in the static mixer, but would be merged to form a larger droplet. On the other hand, the merge of droplets would be prevented by the surface hydrate film for the lower temperature conditions; instead, sometimes grape-like agglomerates were formed through the contact of droplets.

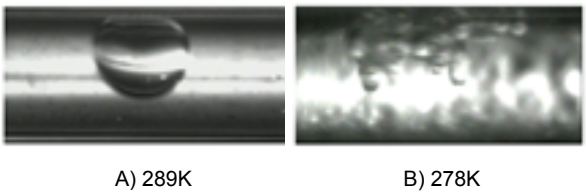

Figure 4. Effect of hydrate formation on CO_2 droplet

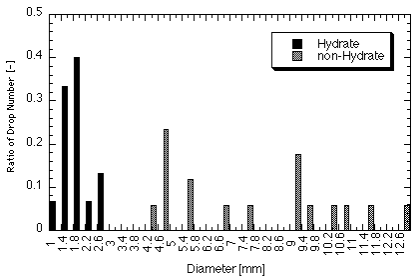

Figure 5. Distribution of CO_2 droplet diameter

Figure 5 shows the measured size distribution of CO_2 droplets. The droplet size for the lower temperature condition, the distribution of the diameter was limited in a narrow range of 1 to 2.6 mm. Thus, CO_2 droplets with relatively uniform size could be obtained for the condition with hydrate formation. This would express significantly the uniform distribution in an essential property of a static mixer.

Effect of water and CO_2 flow rate on droplet diameter. Figure 6 shows the effect of the water flow rate on the liquid CO_2 droplets formation in the static mixer with a constant CO_2 flow rate. The temperature was 276 K, and the pressure was 7.0 MPa for all the cases, which is in the hydrate formation region. The flow rate was denoted by the Reynolds number based on the diameter of the static mixer, and the viscosity and flow rate of pure water. For all the cases, the hydrate formation on the surface was noticed. With an increase in the flow rate, the average diameter decreased and the distribution became narrower. The average diameter decreased rapidly under lower Reynolds number conditions of laminar flow region. At higher flow conditions, the average diameter change was less sensitive to the flow conditions. Note the agglomeration of the droplets was scarcely observed for the higher Reynolds number (> 3000). The above results indicate that the mixing by the static mixer becomes more vigorously and more uniformly under higher flow conditions.

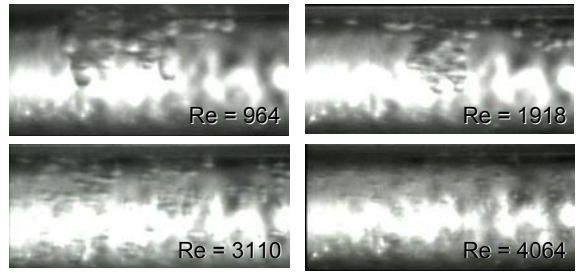

Figure 6. Effect of Reynolds number on droplet diameter

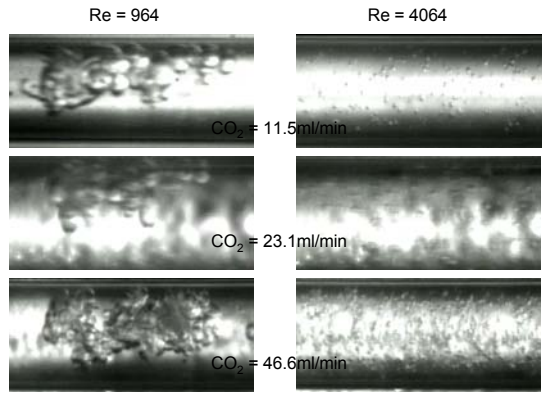

Figure 7. Effect of CO_2 flow rate on droplet diameter

Figure 7 shows the effect of CO_2 flow rate with a constant water flow rate and temperature (276 K), pressure (7.0 MPa). At the lower flow rate of water (Re=964), which is in the laminar flow region, larger droplets of liquid CO_2 were observed, and the droplet size decreased remarkably with an increase in the CO_2 flow rate. On the other hand, smaller droplets were observed at higher Reynolds number of 4064, and the size of the droplets seems independent of the CO_2 flow rate. The above results indicate that the droplet size of liquid CO_2 could be significantly affected by the flow condition of liquid CO_2 as well as that of water.

Fate of the CO_2 disposal through the static mixer. Assuming the releasing depth of liquid CO_2 500 m, the calculation showed the initial diameter should be smaller than 9.1 mm to be dissolved completely before reaching the sea surface. To avoid the vaporization, the initial diameter of the droplet should be smaller than 4.0 mm. When injected through the static mixer, the droplet size is under the above critical value for the conditions studied in this research. As the droplets with the average diameter 0.4 mm are formed through the static mixer, the energy consumption per 1g of CO_2 is estimated to be about 0.35 MJ/t-CO_2. This vale is negligible when compared with the energy consumption for the separation or liquefaction energy form the flue gas (48.0 J/g-CO_2 for separation, 336.2 J/t-CO_2 for liquefaction[1)]). Thus, utilization of static mixer would be very suitable for the liquid CO_2 injection disposal in the ocean.

References

(1) Halmann, M. M.; Steinberg, M. In *Greenhouse Gas Carbon Dioxide Mitigation: Science and Technology*; Lewis Publishers: Boca Raton, 1999

(2) Sloan E. D., In *Clathrate Hydrates of Natural Gases*, 2 Ed, Dekker: New York, 1998

FORMATION AND GROWTH OF CO_2 HYDRATE PARTICLES IN A FLUIDIZED BED REACTOR

Akihiro Yamasaki, Satoko Takano, Minoru Fujii, Yukio Yanagisawa, Hideo Tajima, Fumio Kiyono*

School of Frontier Sciences, The University of Tokyo
7-3-1 Hongo, Bunkyo-ku, Tokyo, JAPAN
*Institute for Environmental Management Technology
National Institute of Advance Industrial Science and Technology
16-1 Onogawa, Tsukuba, JAPAN

Introduction

Several carbon sequestration scenarios have been proposed as counteraction measures to the global warming issue including ocean sequestration and underground sequestration. In the sequestration scenarios, CO_2 captured and separated from the flue gas of the concentrated emission sources of anthropogenic CO_2 such as thermal power plants and steel industries is targeted. The ocean sequestration scenarios may have advantages over other scenarios from the viewpoints of the capacity and the sequestration term. The forms of CO_2 upon discharge for the ocean sequestration scenarios could be gaseous, liquid, and clathrate hydrate. Albeit the difference in the form of CO_2 upon disposal in the oceans, the discharged CO_2 will eventually be dissolved into the ambient seawater, and sequestered there for a certain period before releasing to the atmosphere. The dissolution of CO_2 would cause a pH change of the ambient seawater and consequently cause an impact to the marine ecosystem. In order to obtain the public acceptance for the sequestration practice, such environmental impact should be controlled and minimized. From the viewpoint of the environmental impact, the disposal scenario of CO_2 hydrate would be most appropriate because of the following reasons.

1. Since the density of CO_2 hydrate is greater than the seawater at any depth of the ocean, the disposed hydrate particles should descend toward the ocean bottom. This is in contrast with the cases of disposal of liquid or gaseous CO_2: liquid CO_2 is less dense than the seawater unless the depth is greater than 3000 m, and gaseous CO_2 is much less dense, the disposed CO_2 in such fluid phases will ascend to the sea surface. Thus, to avoid the risk of reemission of CO_2 to the atmosphere, the dissolution should be completed before reaching the surface.
2. The CO_2 hydrate particles would release CO_2 into the seawater due to its instability caused by the difference in the chemical potential of CO_2 between in the seawater and the hydrate. However, the releasing rate is known to be much smaller for CO_2 hydrate than that for liquid CO_2 from laboratory experiments simulating the deep ocean conditions.

The above-mentioned natures of CO_2 hydrate would lead us that the environmental impact caused by the released CO_2 could be more controllable for the CO_2 hydrate disposal by choosing a proper initial diameter and the disposal depth of the hydrate particles.

Disadvantage of the hydrate disposal process might be its energy consumption in the hydrate formation process because it requires high pressure (> 4.5 MPa) and low temperature (< 283 K) conditions. This difficulty by the thermodynamic constraint could be resolved by the submerged reactor at the depth greater than 450 m. However, to form hydrate particles with proper density, substantial energy consumption might be necessary to realize the highly turbulent condition to enhance the interfacial mass transfer in a stirred tank type reactor, which is commonly used for the hydrate formation process in a laboratory scale. Moreover, it is difficult to control the particle size of the hydrate in such a reactor.

Although intensive studies have been conducted for the formation process of CO_2 hydrate, no contribution could be found in the literature from the viewpoint of effective formation process of CO_2 hydrate particles with controlling the size. The authors have proposed here a concept of a novel process of CO_2 hydrate formation in a fluidized-bed type reactor. In this paper, the concept of the proposed process has been examined by a laboratory scale experiments.

Concept of hydrate formation process in a fluidized bed type reactor

The conceptual drawing for the proposed process of hydrate formation was shown in Fig. 1. The reactor is a three-phase fluidized bed type reactor where a mixture of CO_2 hydrate particles (solid), liquid CO_2 (liquid 1) and water (liquid 2) are in a circulated fluidization. Initially seed crystals of CO_2 hydrate would be supplied to the reactor with water saturated with CO_2 and liquid CO_2. The hydrate formation would be induced by the flow at the interface of CO_2 hydrate particles and water. Due to the difference in the solubility of CO_2 in water and the molar fraction of CO_2 in the hydrate crystals, the hydrate formation would result in a decrease in the concentration of CO_2 in water, which could be compensated from the accompanied liquid CO_2 phase. The hydrate particles of which the diameter is larger than the fluidization region would cease the fluidization, and be taken out from the reactor. On the other hand, the small particles that are too small to be fluidized would be released off from the top of the reactor, and could be circulated to become seed crystals after separation. The fluidization conditions would be so designed that hydrate particles with a proper size for the disposal process could be obtained at the bottom of the reactor. The main target in this study is to investigate the growth process and hydrodynamic behavior of CO_2 hydrate particles in the fluidized bed reactor under various flow conditions.

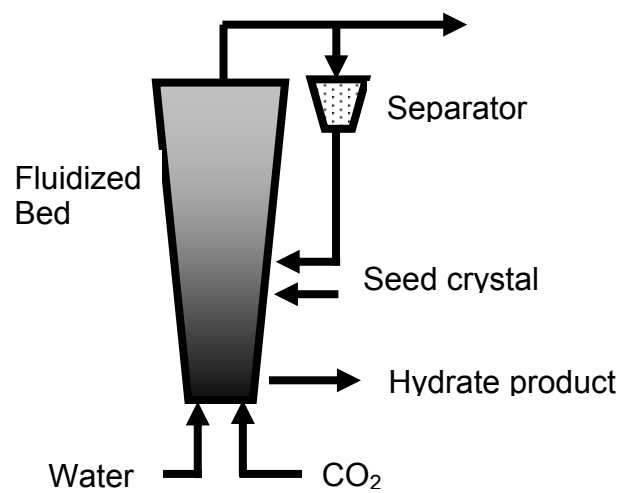

Fig. 1 Conceptual drawing for hydrate formation process in a fluidized bed type reactor

Experimental

Figure 2 shows a schematic drawing for the experimental apparatus. The main fluidization part of the apparatus is a cylindrical

tube of polycarbonate of which the inner diameter is 47 mm, and the length is 470 mm. The tube is connected with the stirred tank type reactor with a ball-valve, which could be utilized for the seed crystal formation. The inner diameter of the stirred tank type reactor is 43 mm and the length is 150 mm. The stirring could be conducted by 3-propeller stirrer at the rate of 0 ~ 760 rpm. The circulation of the fluid could be carried out by a high-pressure pump of which the maximum flow rate is 10 L/min, which corresponds to the liner fluid velocity to be about 10 cm/s in the fluidization part. The temperature of the experimental system was controlled by the circulation of water/ethylene glycol mixture in the jacket. The temperature of the coolant was controlled by the cooling unit and the system temperature could be controlled within 0.5 °C of the fluctuations. The pressure of the system was controlled via cylinder-type pressure controller within ±0.2 bar driven by nitrogen.

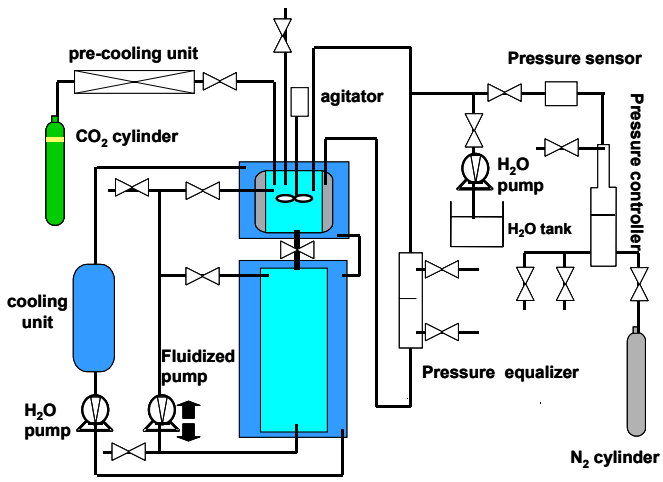

Fig.2 Schematic drawing for the experimental apparatus

Results and Discussions

Experimental procedure and preliminary results of hydrate formation

All the system (both the stirring vessel and the fluidization part) was first filled with deionized water under the atmospheric pressure and room temperature. Then a given amount of water was removed from the system to make room for the CO_2 insert. Liquid CO_2 was introduced to fill the system from the cylinder under stirring and flow condition. The system was cooled down gradually to the temperature for hydrate formation. At the same time, liquid CO_2 was added gradually to the system to compensate the increase in the solubility of CO_2 with decreasing temperature. Finally, the system was filled with water saturated with CO_2. Since the CO_2 solubility is much smaller than the molar fraction of CO_2 in CO_2 hydrate, all the CO_2 supplied should be dissolved in water at the beginning. Then, supply of excess liquid CO_2 was started to realize a super saturation state. Under such conditions, the excess amount of CO_2 should eventually be converted to CO_2 hydrate via fluidization process. The conversion rate should depend on the hydrodynamic conditions in the system, *i.e.*, flow rate.

Due to the non-uniform temperature and concentration profiles in the system, crystals of CO_2 hydrate emerged even under the conditions below the solubility of CO_2 as shown in Figure 3 (a). The CO_2 hydrate crystal so formed had negative buoyancy in the water. This is in contrast to the CO_2 hydrate crystals formed by the agitation of 2-phase fluid of liquid CO_2 and water, which had negative buoyancy at the initial stage of agitation (Fig.3 (b)). The difference in the apparent density would be due to liquid CO_2 drops might be remained in the hydrate particles for the case of agitation process. These hydrate particles were used as seed crystals for the further formation and growth of the CO_2 hydrate under the fluidization conditions.

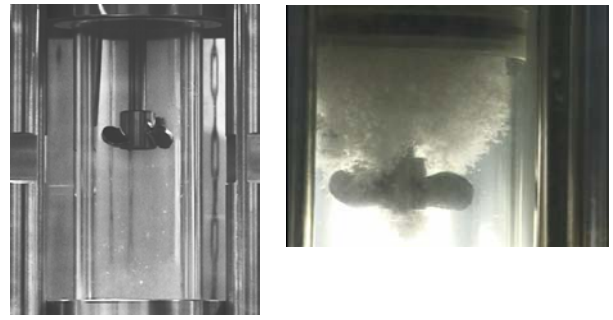

(a) (b)

Fig.3 Hydrate crystals formed (a) without stirring, (b)with stirring

Effect of the flow rate

The CO_2 hydrate particles were fluidized in water as shown in Figure 4 (time course, from left to right, about 10 s). The water flow rate was 5 L/min from the bottom to top, and the temperature was 275 K, the pressure was 6.4 MPa. During the fluidization, the increase of the average particle size was observed with time. The average size of the hydrate particles seemed smaller under higher flow rate conditions.

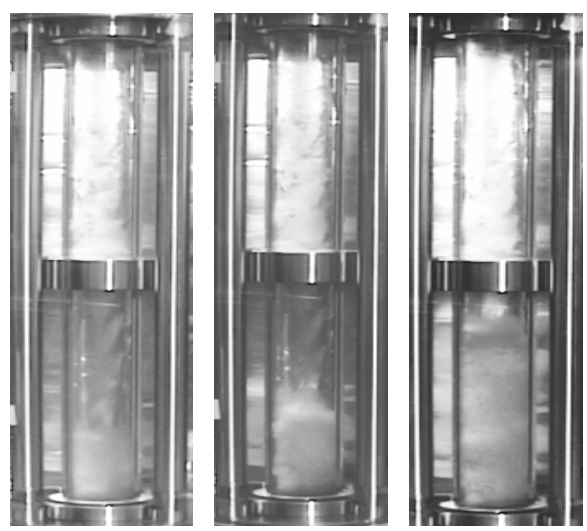

Figure 4 Fluidization of hydrate particles

Conclusions

A new process of CO_2 hydrate formation was proposed by using a fluidized bed reactor was proposed. The laboratory experimental study indicated that CO_2 hydrate particles could be formed and grow in fluidized bed under proper flow conditions.

Acknowledgement This work is financially supported by RITE (Research Institute of Innovative Technology for the Earth Research) and The Japan Gas Association.

PROPERTIES OF CARBON DIOXIDE HYDRATES CONCERNING THE SEQUESTRATION OF GLOBAL WARMING GASES

Fumio Kiyono, Hideo Tajima and Akihiro Yamasaki

Institute for Environmental Management Technology
National Institute of Advanced Industrial Science and Technology
16-1, Onogawa, Tsukuba, Ibaraki, 305-8569 Japan

Introduction

Hydrates may play an important role in future carbon dioxide sequestration systems because hydrates can be used for both purpose of separation and sequestration. Sequestration of carbon dioxide in the hydrates form has many merits like long term storage and less environmental impact. In addition to that, if the hydrates technology were adopted in the separation process of carbon dioxide from flue gases, the total cast for the separation and the sequestration could be dramatically decreased.

According to the purpose, whether the separation or the sequestration, a coexisting phase with a hydrate phase is different. In case of the separation, the hydrate phase mainly coexists with a gas phase, but in the sequestration the hydrates phase is accompanied by a liquid phase. Thus, to build the total system which can separate carbon dioxide from flue gases by forming the carbon dioxide hydrates and then send them to the deep sea floor it is necessary to clarify behaviors of the hydrate phase in the whole phase space, especially when the hydrate phase only coexists with the vapor phase or the liquid phase.

In this paper, properties of carbon dioxide hydrates when coexisting with the vapor phase or the liquid phase are studied.

Relationship between density, occupancy and mole fraction

One of the most important properties of hydrates relating to the sequestration may be the density of carbon dioxide hydrates. It determines whether hydrates can go downwards or upwards from the releasing point. The density of hydrates alters in accordance with the occupancy of carbon dioxide molecules in hydrate cages.

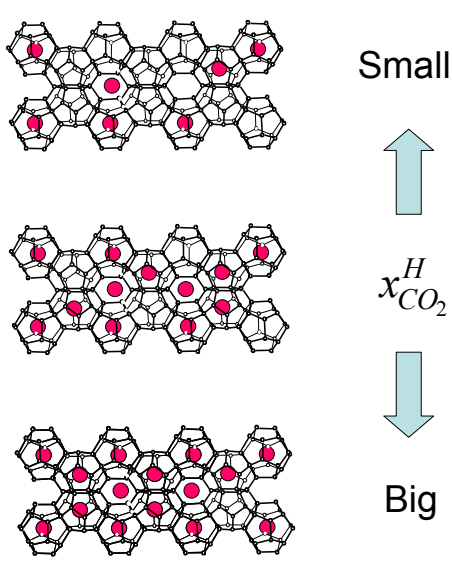

Figure 1. Mole fraction of guest component in hydrate phase

Figure 1 explains this relationship. The larger the occupancy is, the higher the density of hydrates and the mole fraction of carbon dioxide in the hydrates phase become. If we know the mass of a water molecule and a carbon dioxide molecule, we can calculate the density from the occupancy or the mole fraction.

Behaviors of the hydrate phase on a phase diagram

To clarify the behaviors of a hydrates phase when coexisting with a vapor phase or a liquid phase the location of the hydrate phase on a phase diagram should be specified. **Figure 2** illustrates possible arrangements of hydrates phases on the phase diagrams. In Fig.2 (a) the hydrates phase is represented by a line. If hydrates were the stoichiometric compound the hydrates phase would be designated by the line. In Fig.2 (b), (c) and (d) the hydrates phases are denoted by areas, but the inclination of each line which forms the boundary between other phases is different. In fig.2 (b) the hydrate line opposed to the liquid line, which express the equilibrium properties of hydrates coexisting with a liquid, has negative inclination, but the hydrate line opposed to the vapor line, which express the equilibrium properties of hydrates coexisting with a vapor, has positive inclination. In Fig.2 (c) the inclination of the both lines is positive and in Fig.2 (d) the inclination of the both lines is negative.

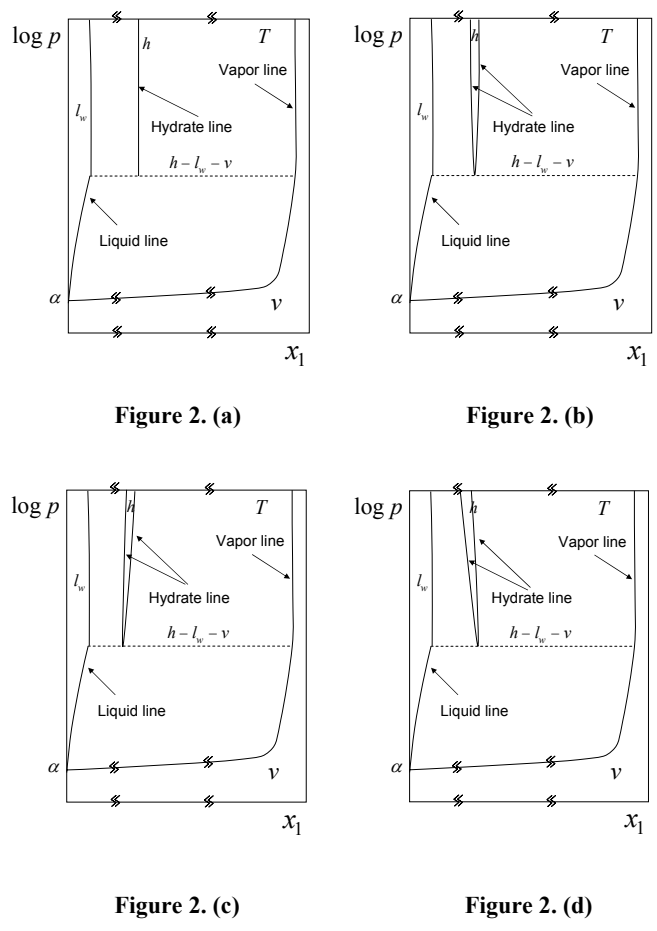

Figure 2. (a) **Figure 2. (b)** **Figure 2. (c)** **Figure 2. (d)**

Figure 2. Possible arrangement of hydrates phases

Qualitative analysis of hydrates' behaviors

Qualitative properties of the hydrates phase can be studied based upon the van der Waals and Platteeuw[1] equations. They derived these equations by applying a grand canonical distribution to guest molecules and a canonical distribution to water molecules. The equations consist of three equations.

$$\log f_w^H = \log f_w^\beta - \sum_{i=1}^{2} \nu_i \log\left(1 + C_i f_1^H\right) \qquad (1)$$

$$\theta_1 = \frac{C_1 f_1^H}{1 + C_1 f_1^H} \qquad (2)$$

$$\theta_2 = \frac{C_2 f_1^H}{1 + C_2 f_1^H} \qquad (3)$$

The equation (1) denotes the difference of fugacity of water in the hydrates phase and in the β lattice. The equation (2) represents the occupancy of CO_2 molecules in small cages, that is, the probability of finding a CO_2 molecule in a small cage, and equation (3) that in large cages. For our purpose equation (2) and (3) are useful.

It is obvious from the equation (2) and (3) that the value of the occupancy approaches to unity with the fugacity in the hydrates phase increasing. It means that the mole fraction of CO_2 in the hydrates phase becomes large and that the density of hydrates also becomes heavy.

If a hydrate phase coexists with a liquid phase, in equilibrium, the fugacity of CO_2 in the hydrate phase becomes equal to that in the liquid phase. Thus it is enough to clarify the dependence of the fugacity of CO_2 in the liquid phase on the pressure.

$$f_1^L = \varphi_1^L x_1^L p \qquad (4)$$

According to the equation (4) the fugacity of CO_2 increases with pressure, where the fugacity coefficient and the mole fraction of CO_2 in the liquid phase can be regarded to be constant comparing with the pressure change. So,

$$p \to \text{large} \quad f_1^H \to \text{large} \quad \theta_1, \theta_2 \to 1 \quad x_1^H \to \text{large}$$

When a hydrates phase coexists with a vapor phase, in equilibrium, the fugacity of CO_2 in the hydrate phase should be equal to that in the vapor phase. The derivative of the fugacity with respect to the pressure is expressed as follows.

$$\frac{\partial f_1^V}{\partial p} = \frac{f_1^V}{RT} v_1^V > 0 \qquad (5)$$

Hence,

$$p \to \text{large} \quad x_1^H \to \text{large}$$

Summarizing the results of qualitative analysis, the inclination of hydrates lines should be both positive.

Quantitative analysis of hydrates' behaviors

To clarify the behaviors of hydrate lines in the two-phase equilibrium such as liquid-hydrate or hydrate-vapor equilibrium under a constant temperature mass balance equations and diffusion stability equations were solved. Differing from the incipient calculation, to achieve this purpose, both equations have to be solved under constant temperature and pressure and mole fractions of water and CO_2 in each phase must be sought simultaneously. Soave-Redlich-Kwong equation was employed for the equation of state, MHV2 for the mixing rule, and van der Waals-Platteeuw equation for the fugacity of water in the hydrates phase. Implicit expression of the fugacity of each gas component in the hydrates phase as a function of mole fractions had been given by Michelsen. Equations necessary for the calculation are as follows.

$$x_w^L + \underline{x_1^L} = 1$$

$$x_w^H + \underline{x_1^H} = 1$$

$$f_w^L = f_w^H$$

$$f_1^L = f_1^H$$

Table 1. Behaviors of a liquid line and a hydrate line

Temperature	Pressure [Mpa]	Mole fraction in liquid phase	Mole fraction in hydrate phase
277.6	2.11	0.0145	0.1421
277.6	4.11	0.0144	0.1423
277.6	6.11	0.0143	0.1424
277.6	8.11	0.0141	0.1425
277.6	10.11	0.0140	0.1426
277.6	12.11	0.0139	0.1427
277.6	14.11	0.0137	0.1428
277.6	16.11	0.0136	0.1430
277.6	18.11	0.0135	0.1431

Table 2. Behaviors of a vapor line and a hydrate line

Temperature	Pressure [Mpa]	Mole fraction in vapor phase	Mole fraction in hydrate phase
277.6	2.11	0.99949	0.1424
277.6	2.61	0.99957	0.1433
277.6	3.11	0.99962	0.1438
277.6	3.61	0.99965	0.1443
277.6	4.11	0.99966	0.1446
277.6	4.61	0.99966	0.1448

Behaviors of the liquid line, the hydrates lines and the vapor line at the temperature of 277.6°K are listed in **Table 1** and **Table 2**. In case of the liquid-hydrate equilibrium, the mole fraction of CO_2 in the hydrate phase altered from 0.1421 to 0.1431 as pressure increased from 2.11MPa to 18.11MPa. In case of the vapor-hydrate equilibrium, the mole fraction of CO_2 in the hydrate phase varied from 0.1424 to 0.1448 with increasing the pressure from 2.11MPa to 4.61MPa.

The results of the quantitative analysis also show that the inclination of hydrates lines is both positive. Other thermodynamic properties like the latent heat, the heat capacity, etc can easily calculated from the phase equilibrium data.

References

(1) van der Walls; Platteeuw,J.C. *Adv.Chem.Phys*.,**1959,** 2, 1.

ACTIVATION OF HYDROGEN OVER SULFIDE CATALYSTS. RELEVANCE TO KINETICS AND MECHANISMS OF HYDROTREATING REACTIONS.

Guy Pérot

Laboratoire de Catalyse en Chimie Organique
Département de chimie
Faculté des Sciences Fondamentales et Appliquées de l'Université de Poitiers
40, Avenue du Recteur Pineau, 86022 Poitiers, France

Introduction

The regulations on transportation fuels regarding sulfur content in particular are more and more severe. This forces the refiners to achieve what is commonly called deep desulfurization. One of the consequences of this requirement is that the demand in the refinery regarding hydrogen is increasing drastically. This is made all the more crucial as at the same time the tendency is to reduce the amount of aromatics in gasoline and consequently the capacity of the reforming units which provide hydrogen in the refinery.

Another reason why it is essential to better understand hydrogen activation on hydrotreating catalysts and the hydrogenation properties of these catalysts is related to the HDS of FCC gasoline in which the objective is to obtain high sulfur removal with a minimum of olefin hydrogenation.

Twenty years ago, Barbour and Campbell [1] reported the results of the hydrogenation of buta-1,3-diene on a D_2S-treated MoS_2 catalyst. They concluded that hydrogen present as SH groups on the surface was involved in the hydrogenation of the diene, which could suggest that the dissociation of H_2 was heterolytic. Later on, in their theoretical approach of the homolytic and heterolytic dissociation of H_2, Anderson et al. [2] concluded that the most stable chemisorption form of hydrogen was heterolytic at edges of MoS_2 crystals. Since then the authors of numerous studies have assumed that the dissociation of hydrogen on sulfides was heterolytic [3-8].

In a recent review, Furimsky et al. [9] examined in detail the reaction of sulfide surfaces with hydrogen and in particular the mechanism of creation of vacancies as well as the nature of the species resulting from the chemisorption of hydrogen. The purpose of this contribution is not to cover all the aspects of the interaction of hydrogen with sulfides, it will focus mainly on the dissociation of H_2. We will review a number of experimental results which are in favor of the heterolytic dissociation of hydrogen and show its relevance to mechanisms and kinetics of hydrotreating reactions. We will also report examples of promoter effects related to hydrogen activation and to the hydrogenation of olefins.

Tracer experiments on the dissotiation of hydrogen on sulfides

To our knowledge no direct proof of the heterolytic dissociation of H_2 over MoS_2 catalysts has been reported yet. However quite a number of experimental facts obtained by various authors are clearly in favor of such a dissociation mode.

Isotopic exchange experiments between H_2 and D_2S. The experiments were carried out at 80°C on $NiMo/Al_2O_3$ catalyst samples which were presulfided with a H_2/H_2S mixture (10 vol.% of H_2S) at 400°C [10].

The formation of HD indicated that isotopic exchange occurred between H_2 and D_2S. Similar results were obtained by Hensen et al. on carbon supported catalysts [11]. Hence,we can suppose that both reactants dissociate in the same maner on the same kind of catalytic centers. If we assume as it is generally accepted that the dissociation of H_2S (D_2S) on sulfides is heterolytic [2,4,12-18], we can suppose that the chimisorption of hydrogen also is heterolytic.

Involvement of support hydrogen in the isotopic exchange between gas phase H_2 and D_2. By carrying out H_2-D_2 exchange experiments on a H_2/H_2S presulfided $NiMo/Al_2O_3$ catalyst or by reacting D_2 on such a catalyst sample, it was shown through isotopic delution that gaseous D_2 could incorporate H-atoms coming from the support [10,19,20]. On a typical commercial catalyst, the amount of support hydrogen which could be incorporated into the deuterium of the gas phase varied depending on the pretreating conditions and could be as high as 90% of the hydrogen held by the solid after sulfidation. It was also shown that the latter resulted mostly from the adsorption of H_2S [20]. Since the isotope exchange between H_2 and D_2 is extremely slow under the same conditions with the pure alumina support, it was concluded that the hydrogen held by the support could only exchange with gas phase hydrogen via the sulfide through a spillover-like process. This was confirmed by FTIR experiments [19,20] which showed that OD bands (2640 cm^{-1}) appeared readily on the alumina support of a presulfided $NiMo/Al_2O_3$ catalyst during its exposure to D_2 while OH bands (3580 cm^{-1}) desappeared. This process barely existed on the pure presulfided support under the same conditions.

Since the H atoms of the hydroxyl groups of the alumina support have undoubtedly an ionic character, this is also good evidence in favor of the heterolytic splitting of D_2 (H_2).

Incorporation of deuterium from D_2S in propane via propene hydrogenation. The hydrogenation of propene over a D_2S-treated $NiMo/Al_2O_3$ catalyst showed that D-atoms from D_2S were involved in the reaction [21]. This is in accordance with the results reported previously by Barbour and Campbell [1] regarding the hydrogenation of buta-1,3-diene over a D_2S-treated MoS_2 catalyst although it is difficult at the moment for us to conclude, as these authors did for butadiene, that D-atoms were incorporated directly from D_2S to propene.

Relevance of the heterolytic dissociation of hydrogen to reaction mechanisms and kinetics

The heterolytic dissociation of H_2 on a catalytic center composed of a sulfur vacancy located on a molybenum atom and of a neighbouring sulfur anion leads to the H-atom having a hydride character adsorbed on the metal ion and the H-atom with a protonic character adsorbed on the sulfur anion [3-6]. However, as shown recently by DFT calculations [22], the hydride bound to the metal seems to be highly unstable with Molybdenum-based catalysts, especially with nickel-molybdenum. Contrary to what was obtained with ruthenium catalysts [18], metal-hydrogen species have not been observed yet. H_2S is supposed to dissociate in the same manner with its proton adsorbed on a sulfide anion and the sulfhydril group on the metal; this leads to two SH groups.

The first step of the hydrogenation of unsaturated substrates can be either the addition of H^+ or of H^-. Kinetic modeling studies bring some information on this point [6,7,23].

In their study of the effect of H_2S on the hydrogenation of toluene over a Mo/Al_2O_3 catalyst, Kasztelan and Guillaume [6] compared various kinetic models supposing molecular, homolytic and heterolytic dissociative adsorption of H_2 and H_2S. By computing the rate laws according to the classical Langmuir-Hinshelwood-Hougen-Watson method, they came to the conclusion that the model which fitted at best the kinetic orders of the reaction with respect to the various reactants, especially H_2S, was the one supposing the heterolytic dissociation of H_2 and H_2S on a vacancy and a sulfur anion. The hydrogenation was found to proceed via addition of a hydride followed by the addition of a proton to the aromatic molecule. The changes in kinetic order with respect to H_2S was

explained by supposing that the rate-limiting step of the reaction was changing from one of these two elementary steps to the other as the H_2S partial pressure increased.

More recently, Blanchin et al. [23] have used the Chemkin/Surface Chemkin II tool to investigate the effect of H_2S and of NH_3 on the same reaction catalysed by a $NiMo/Al_2O_3$ catalyst. They found also that the model involving the heterolytic dissociation of H_2 and H_2S on centers composed of an unsaturated molybdenum ion and of a sulfur anion fitted at best with the experimental data. They confirmed that the hydrogenation of the aromatic molecule started with the addition of a hydride followed by the addition of a proton, the latter being the rate-limiting step of the reaction in the range of H_2S partial pressures investigated. However the rate-limiting character of this step depended very much on the partial pressure of H_2S which in addition to H_2 provides protons to the system.

Orozco and Vrinat used the same approach as Kasztelan and Guillaume to investigate the effect of H_2S on the hydrodesulfurization of dibenzothiophene through kinetic modeling [7]. Like Kasztelan and Guillaume, they concluded that the reaction involved the heterolytic dissociation of H_2 and H_2S and that depending on the partial pressure the rate-limiting step of the reaction could be the addition of a hydride ion to the adsorbed substrate or the attack of a dihydrointermediate by a sulfur anion to achieve carbon-sulfur bond cleavage.

Promoter effects in hydrogen activation and in the hydrogenation of olefins.

The role of the promoters in the hydrogenation process on sulfides was investigated by measuring the effect of cobalt and nickel on the activities of MoS_2–based catalysts in the isotopic exchange between H_2 and D_2 and in the hydrogenation of cyclopentene in the absence of H_2S [24]. The catalyst samples containing the same amount of molybdenum and various quantities of cobalt or nickel were presulfided with a H_2/H_2S mixture (10 vol.% of H_2S) at 400°C then treated at 350°C under helium for 1 hour. Under these conditions, the catalysts containing cobalt were much more active than those containing nickel in the H_2-D_2 isotopic exchange reaction so that the experiments were carried out at 35°C with the former and 80°C with the latter [20]. It was verified that both series of catalysts exhibited the expected synergy effect in the hydrodesulfurization of dibenzothiophene at 340°C under 30 bar of hydrogen [25]. However no sinergy effect was obtained with nickel in the isotopic exchange between H_2 and D_2 while the catalyst containing cobalt with a Co/Co+Mo atomic ratio of 0.3 was found five times more active than the unpromoted catalyst. This is in accordance with other results reported in the litterature [11,26,27] and was interpreted by Travert et al. by a difference in the rate-limiting step of the process [22]. Surprisingly, the reverse was obtained regarding the promoting effect in the hydrogenation of cyclopentene. The promoting effect of cobalt (2 only for a Co/Co+Mo atomic ratio of 0.3) was much weaker than the effect of nickel (about 10 for the same atomic ratio).

While both promoters have similar effects in hydrotreating reactions as well as in the thioreduction of ketones [25], their effect on hydrogen activation and on the hydrogenation of olefins seem to be different. This might be a question of operating conditions but also of kinetics [22] regarding hydrogen activation and hydrogenation or of sulfur coverage connected to the intrinsic properties of the solids.

Conclusions

Various observations (the isotopic exchange between H_2 and D_2S, the contribution of the support to the isotopic exchange between H_2 and D_2) as well as theoretical calculations are definitely in favour of the heterolytic dissociation of hydrogen on sulfides.The best fittings regarding the kinetic modeling of hydrotreating reactions is also obtained when supposing such a dissociation process.

However certain observations like differences in promoting effects with cobalt and nickel in hydrogen activation and hydrogenation have to be rationalize and further experiments are needed.

References

(1) Barbour, J.; Campbell, K.C., *J. Chem. Soc., Chem. Commun.* **1982**, 1371.
(2) Anderson, A. B., Al-Saigh, Z. Y., and Hall, W. K., *J. Phys. Chem*., **1988**, *92*, 803.
(3) Kasztelan, S., *Ind. Eng. Chem. Res.*, **1992**, *31*, 2497.
(4) Kasztelan, S., Prepr. Pap. - *Am. Chem. Soc., Div. Petrol. Chem.*, **1993**, *38*, 642.
(5) Kasztelan, S., In *Hydrotreating Technology for Pollution Control Catalysts, Catalysis, and Processes,* Occelli M. L., Chianelli, R. Eds., Marcel Dekker, Inc., New York, Basel, Hong Kong, 1995, pp 29-45.
(6) Kasztelan, S., and Guillaume D., *Ind. Eng. Chem. Res.*, **1994**, *33*, 2497.
(7) Orozco, O., and Vrinat, M., *Appl. Catal.,* **1998**, *170*, 195.
(8) Mijoin, J., Pérot, G., Bataille, F., Lemberton, J.-L., Breysse, M., Kasztelan, S., *Catalysis Letters,* **2001**, *71*, 139.
(9) Furimsky, E., Breysse, M., Kasztelan, S., Lacroix, M. and Pérot, G., *Catal. Rev.-Sci. Eng.,* in the press.
(10) Thomas, C.; Vivier, L.; Lemberton, J.L.; Kasztelan, S.; Pérot, G. *J. Catal.* **1997**, *167*, 1.
(11) Hensen, E.J.M.; Lardinois, G.M.H.J.; de Beer, V.H.J.; van Veen, J.A.R.; van Santen, R.A. *J. Catal.* **1999**, *187*, 95-108.
(12) Schuit, G. C. A., *Int. J. Quantum Chem.,* **1977**, *12*, 43.
(13) Wright, C. J., Sampson, C. Fraser, D., Moyes, R. B., Wells, P. B., and Riekel, C., *J. Chem. Soc. Faraday Trans. I.,* **1980**, *76*, 1585.
(14) Yang, S. H., and Satterfield, C. N., *J. Catal.* **1983**, *81*, 168.
(15) Yang, S. H., and Satterfield, C. N., *Ind. Eng. Chem. Process Des. Dev.*, **1984**, *23*, 20.
(16) Olalde, A., and Pérot, *Appl. Catal.,* **1985**, *13*, 373.
(17) Lacroix, M., Yuan, S., Breysse, M., Dorémieux-Morin, C., and Faissard, J., *J. Catal.* **1992**, *138*, 409.
(18) Jobic, H., Clugnet, C., Lacroix, M., Yuan, S., Mirodatos, C., and Breysse, M., *J. Am. Chem. Soc*. **1993**, *115*, 3654.
(19) Thomas, C.; Vivier, L.; Travert, A.; Maugé, F.; Kasztelan, S.; Pérot, G., *J. Catal.* **1998***, 179*, 95-502.
(20) Scaffidi, A.; Vivier, L.; Travert, A.; Maugé, F.; Kasztelan, S.; Scott, C.; Pérot, G., *Stud. Surf. Sci. Catal.* **2001**, *138*, 31-38.
(21) Brémaud, M., Vivier, L., Pérot, G., and Harlé, V., *This meeting,* Submitted.
(22) Travert, A., Nakamura, H., van Santen, R. A., Cristol, S., Paul, J.-F., and Payen, E., *J. Am. Chem. Soc*. **2002**, *124*, 7084.
(23) Blanchin, S., Galtier, P., Kasztelan, S., Kressmann, S., Penet, H., and Pérot, G., *J. Phys. Chem*., **2001**, *105*, 10860.
(24) Vivier, L., Mijoin, J., Schneider, S., Lemberton, J.-L., Kasztelan, S., Scott, S., and Pérot,G., to be published.
(25) Mijoin, J., Thévenin, V., Garcia-Aguirre, N., Yuze, H., Wang, J., Li, W. Z., Pérot, G., and Lemberton, J.-L., *Appl. Catal.,* **1999**, *180*, 95.
(26) Thomas, C.; Vivier, L.; Lescanne, M., Kasztelan, S.; and Pérot, G., *Catalysis Letters,* **1999**, *58*, 33.
(27) Lacroix, Dumonteil, C., Breysse, M., and Kasztelan, S.; *J. Catal.* **1999**, *185*, 219.

HYDROGENATION OF PROPENE ON SULFIDE CATALYSTS - H-D ISOTOPIC STUDY

M. Brémaud[a], L. Vivier[a], G. Pérot[a] and V. Harlé[b]*

[a]Laboratoire de Catalyse en Chimie Organique UMR CNRS 6503
Faculté des Sciences – Université de Poitiers
40, avenue du Recteur Pineau, 86022 Poitiers Cedex, France
*e-mail : laurence.vivier@univ-poitiers.fr
[b]Institut Français du Pétrole
1 et 4, avenue de Bois Préau, 92852 Rueil-Malmaison Cedex, France

Introduction

Because of increasing environmental constraints hydrotreating becomes more and more important in refineries for the removal of sulfur and nitrogen impurities from petroleum.

The catalysts have to be more and more efficient in hydrodesulfurization whereas the consumption of hydrogen has to be limited. Moreover, in the case of gasoline hydrotreating, the selectivity in hydrodesulfurization in comparison with the hydrogenation of olefins has to be controlled and has to be improved in order to limit the octane loss.

In order to better understand the factors which influence this selectivity, the hydrogenation of propene in parallel with the isotopic exchange between H_2 and D_2 has been studied on sulfided $NiMo/Al_2O_3$ and the interaction of H_2 with H_2S during the hydrogenation reaction was also examined.

It was shown previously that an exchange of hydrogen atoms between H_2 and D_2S occurred on sulfided hydrotreating catalyst [1-4]. The existence of this exchange reactions seems to indicate that there is a common mode of dissociation, presumably heterolytic, for both reactants on the same catalytic centers as described in Eqs (1) and (2).

$$H_2 + \star\text{–V} + \bullet\text{–}S^{2-} \rightleftharpoons \star\text{–}H^- + \bullet\text{–}SH^- \qquad (1)$$

$$H_2S + \star\text{–V} + \bullet\text{–}S^{2-} \rightleftharpoons \star\text{–}SH^- + \bullet\text{–}SH^- \qquad (2)$$

FTIR studies have confirmed that hydrogen from the gas phase can be exchanged with the hydrogen atoms of hydroxyl groups of the support by the intermediate of the sulfide phase. Under our experimental conditions the amount of exchangeable hydrogen preadsorbed on the support was very significant compared to the amount on the active phase, which represented less than 10% of the total amount [2]. The hydrogen present on the support was essentially due to adsorbed H_2S [5].

The aim of this study is to examine the influence of H_2S on the hydrogenation of propene and to see if the hydrogen present at the surface of the catalyst as preadsorbed H_2S can be involved and incorporated in propene during the hydrogenation.

Experimental

Catalysts. The $NiMo/Al_2O_3$ commercial catalyst contained 2.9 wt% NiO and 12.5 wt% MoO_3 deposited on alumina (230 $m^2.g^{-1}$). The catalyst was presulfided *in situ* with a flow of H_2 (90%) and H_2S (10%) at 400°C for 15 hours. After sulfidation, and before the hydrogenation reaction, the catalyst underwent two different pretreatments : it was either cooled down to 80°C in the presence of the sulfidation mixture and treated for 1h under He at 80°C (pretreatment **1**) or treated for 1h at 350°C and cooled down to 80°C under He (pretreatment **2**). After both pretreatments, the catalyst was treated at 80°C for 1h under a flow of Ar. The treatment under Ar was necessary to remove He which has the same mass as D_2.

Hydrogenation of Propene. The hydrogenation of propene by H_2 or D_2 was carried out at 80°C in a 72 cm^3 recycling reactor. The reactants (H_2 or D_2 plus propene ; 0.5 bar of each) were introduced into the reactor and the recycling pump was started. The apparatus which was described elsewhere [1], was fitted with a gas chromatograph with a FID detector and with a mass spectrometer in order to analyze H_2, HD, D_2, propene and propane, deuterated or not.

Preadsorption of D_2S. After sulfidation and pretreatment **2**, D_2S was introduced in the closed reactor and recycled at 80°C (0.5 bar with 1.5 bar of He) for 1h. The catalyst was then treated under a flow of He at diverse temperatures for 1h, cooled down to 80°C, and then treated under a flow of Ar. The hydrogenation of propene was carried out in the presence of H_2 at 80°C.

Results and Discussion

The rate of the hydrogenation of propene hydrogenation in the presence of sulfided $NiMo/Al_2O_3$ after pretreatment **2** increased when the partial pressure of H_2 and the partial pressure of propene increased from 0.1 bar to 0.5 bar. The kinetic orders deduced from these results are about 1 with respect to H_2 and propene.

In subsequent experiments , the partial pressures of H_2 (or D_2) and of propene were of 0.5 bar each. Table 1 shows the influence of the pretreatment procedure of the sulfided $NiMo/Al_2O_3$ catalyst on the initial rate of hydrogenation of propene by H_2 and by D_2. The rate of propene hydrogenation or deuteration was in the average 100 times greater after pretreatment **2** than after pretreatment **1**. Indeed, pretreatment **2** allows the desorption of a large amount of H_2S present on the catalyst after sulfidation. Table 2 shows the influence of H_2S in the gas phase on the hydrogenation of propene. The reaction was carried out with 0.4 bar of each reactant in the absence or in the presence (0.04 bar) of H_2S. Helium was added to reach a total pressure of 2 bar. H_2S had an important inhibiting effect on the hydrogenation of propene since in its presence the reaction was about two orders of magnitude slower then in its absence.

Table 1. Effect of the Pretreatment Procedure on the Initial Rate of Propene Hydrogenation.

	Hydrogenation $r°(10^{-7}\ mol.s^{-1}.g^{-1})$	Deuteration $r°(10^{-7}\ mol.s^{-1}.g^{-1})$
Pretreatment **1**	0.20	0.12
Pretreatment **2**	14.2	14.6

Table 2. Influence of the Presence of H_2S on the Initial Rate of Propene Hydrogenation.

Composition of the gas phase (plus He to reach a total pressure of 2 bar)	Hydrogenation $r°(10^{-7}\ mol.s^{-1}.g^{-1})$
H_2 (0.4 bar) + propene (0.4 bar)	19.7
H_2 (0.4 bar) + propene (0.4 bar) + H_2S (0.04 bar)	0.23

Table 1 shows also that there was no significant difference between the hydrogenation by H_2 or by D_2 especially after pretreatment **2**. For the experiments with D_2, the incorporation of deuterium atoms in the different products was followed by mass spectrometry. After pretreatment **1**, the hydrogenation was very slow. Nevertheless, HD was formed with an initial rate of 8.6 10^{-7} $mol.s^{-1}.g^{-1}$. Previous experiments, carried out on the same catalyst treated under the same conditions, showed that D_2, introduced alone, was exchanged with hydrogen adsorbed on the catalyst to produce HD with a rate of 8.4 10^{-7} $mol.s^{-1}.g^{-1}$ [1]. The formation of HD occurred with a very similar rate in these two experiments. Mono- and di-deuterated propenes were also formed but since the reaction was very slow (initial rate of about 0.2 10^{-7} $mol.s^{-1}.g^{-1}$) we can conclude that the formation of HD was essentially due to a direct exchange between D_2 and the "H" preadsorbed on the catalyst.

After pretreatment **2**, the major reaction was the deuteration of propene to yield di-deuterated propane (d2) (Figure 1). The

consumption of D_2 was greater than the consumption of propene, which was a consequence of the H-D exchange of D_2 with the hydrogen adsorbed on the catalyst. HD and H_2 formed by isotopic exchange were added to propene to form mono-deuterated and non-deuterated propane (d1 and d0). The existence of tri- and tetra-deuterated propane (not reported in Figure 1) reveals the exchange reaction between D_2 and propene prior to hydrogenation. Actually it was shown that there was no exchange between propane and D_2 under the same conditions.

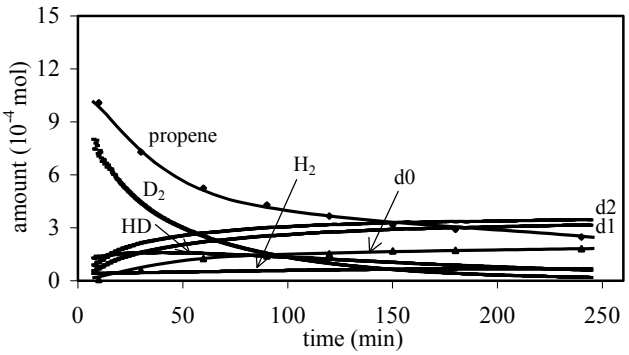

Figure 1. Products present in the gas phase during the reaction of propene with D_2 on sulfided $NiMo/Al_2O_3$ catalyst after pretreatment **2**. (d0 ; d1 ; d2 : non-, mono- and di-deuterated propanes, respectively).

As it was shown above, under our conditions, H_2S inhibited the hydrogenation reaction very much. In order to study the involvement of hydrogen sulfide in the hydrogenation of propene, experiments were carried out on a sulfided $NiMo/Al_2O_3$ catalyst which was pretreated with D_2S at 80°C then treated at various temperatures in order to desorb part of the D_2S. Table 4 shows the influence of the temperature of D_2S desorption on the initial rate of hydrogenation and on the incorporation of deuterium atoms in propane and hydrogen after 2 hours of reaction.

Table 4. Influence of the Temperature of D_2S Desorption on the Hydrogenation of Propene

Temperature of D_2S desorption (°C)	200	280	350
Initial rate of formation of :			
non-deuterated propane (10^{-7} mol.s^{-1}.g^{-1})	4.3	15.2	25.6
mono-deuterated propane (10^{-7} mol.s^{-1}.g^{-1})	0.7	0.8	1.4
Amount of incorporated deuterium atoms into propane and hydrogen after 2 h :			
total amount (10^{-5} mol)	13.2	9.5	7.4

The rate of hydrogenation increased when the temperature of D_2S desorption increased while the amount of incorporated deuterium atoms decreased (Table 4). The formation of mono-deuterated propane was not significantly influenced by the temperature of D_2S desorption and it was very slow compared to the formation of the non-deuterated propane. This is the result of a compensation phenomenon between, on the one hand the increase of the overall rate of hydrogenation of propene following the elimination of D_2S as its desorption temperature increased and, on the other hand, the decrease in concentration of D-atoms (as D_2S) present in the medium.

Nevertheless, it is clear that deuterium atoms adsorbed on the catalyst as D_2S were incorporated into propane via propene hydrogenation. This is in accordance with the results reported by Barbour and Campbell [4] who carried out similar experiment with 1,3-butadiene. However, contrary to what they did, it is difficult to tell at the moment from our experiments whether D-atoms from D_2S are added to propene directly or not. Actually, if one excepts the point at low conversion, the isotopic distribution in dihydrogen and in propane were quite similar (Figure 2), which would not be the case if D-atoms would add directly from D_2S to propene. This means that under our conditions D-atoms from D_2S could exchange with H-atoms of H_2 of the gas phase prior to the addition to propene. Complementary experiments at very low conversion with higher concentration of adsorbed D_2S are necessary to make this point clearer.

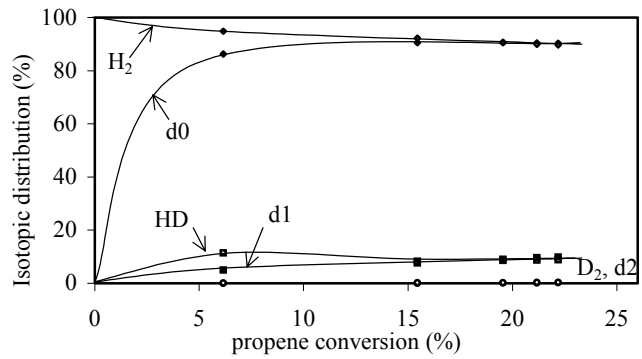

Figure 2. Isotopic distribution in propane and in dihydrogen in the gas phase during the hydrogenation of propene on sulfided $NiMo/Al_2O_3$ catalyst treated with D_2S desorbed at 200°C. (d0 ; d1 ; d2 : non-, mono- and di-deuterated propanes, respectively).

As was the case with the experiments of Barbour and Campbell [4] the presence of H_2 in the gas phase was necessary for the hydrogenation to proceed and for D-atoms to be incorporated in propane. They concluded that hydrogen gas was necessary to replenish the SH groups involved in the hydrogenation. However, if we assume that the dissociation of H_2 and H_2S is heterolytic, another explanation is possible, i.e. that preadsorbed H_2S (D_2S) can only provide H^+ (D^+) to the reaction and that hydrogen gas is necessary to provide H^- via dissociation on the sulfide.

Conclusion

The hydrogenation of propene was very sensitive to the presence of H_2S in the gas phase or to H_2S previously adsorbed on sulfided $NiMo/Al_2O_3$. It was also shown that D-atoms from preadsorbed D_2S were incorporated in propane via propene hydrogenation in the presence of gas phase hydrogen. This is in agreement with the hypothesis that the dissociation of H_2 and H_2S on sulfide catalysts is heterolytic. The presence of gas phase hydrogen is thought to be necessary to provide H^- to the reaction medium.

References

(1) Thomas, C.; Vivier, L.; Lemberton, J.L.; Kasztelan, S.; Pérot, G. *J. Catal.* **1997**, *167*, 1-11.
(2) Thomas, C.; Vivier, L.; Travert, A.; Maugé, F.; Kasztelan, S.; Pérot, G., *J. Catal.* **1998**, *179*, 95-502.
(3) Hensen, E.J.M.; Lardinois, G.M.H.J.; de Beer, V.H.J.; van Veen, J.A.R.; van Santen, R.A. *J. Catal.* **1999**, *187*, 95-108.
(4) Barbour, J.; Campbell, K.C., *J. Chem. Soc., Chem. Commun.* **1982**, 1371-1372
(5) Scaffidi, A.; Vivier, L.; Travert, A.; Maugé, F.; Kasztelan, S.; Scott, C.; Pérot, G., *Stud. Surf. Sci. Catal.* **2001**, *138*, 31-38.

Influence of the Support Acidity on the Sulfided Phase Properties

Françoise Maugé[(a)], Gérald Crépeau[(a)], Arnaud Travert[(a)] and Tivadar Cseri[(b)]

[a] Catalysis and Spectrochemistry Laboratory, CNRS - EnsiCaen - University, 14050 CAEN cedex, France
[b] IFP, Kinetics and Catalysis Department, 1-4 av. de Bois Préau, 92852 Rueil Malmaison cedex, France
email : francoise.mauge@ismra.fr

Introduction

High pressure hydrocracking is a key catalytic refining process used to upgrade low quality feedstocks into high quality middle distillates (kerosene and gasoil). In addition to the cracking of the molecules the ability of the hydrocracking process to ensure the elimination of sulfur and nitrogen compounds and a deep saturation of aromatics, allows to produce high quality diesel fuels that will match the future and more stringent specifications (1). The catalysts used in hydrocracking are bifunctional, associating a hydro-dehydrogenating function (generally a sulfided phase) with an acidic function. The acidity of the catalyst is a key parameter to control the activity and the selectivity of the hydrocracking catalysts. Generally, hydrocracking catalysts are supported on zeolites or amorphous silica-alumina (ASA).

This study concerns sulfided NiW catalysts supported on ASA presenting various Si/Al ratio. Our aim was to describe precisely the acidity of the ASA, the sulfided phase sites and to establish the influence of the acidity of the support on the sulfided phase properties.

Experimental

The ASA used as support are denoted SiXAlY where X and Y represent the weight % in SiO_2 and in Al_2O_3 respectively. Mo and NiW catalysts were prepared by incipient wetness impregnation of salt precursors, dried at 393 K and calcined at 773 K under air.

For IR characterization, the samples were pressed under the form of a disc and activated in situ in the cell. Surface properties of pure ASA were studied after evacuation at various temperatures. Catalysts were characterized after sulfidation under a flow of H_2S(15%vol)/H_2 at 623 K (for Mo catalysts) or 723 K (for W-based catalysts) followed by an evacuation at the same temperature. After activation, acidity of surface sites of the support and of the sulfided phase was characterized by CO adsorption at 100 K. IR spectra are recorded on a Magna Nicolet using a MCT/A detector.

Activity of sulfided NiW catalysts supported on ASA and alumina were tested for the transformation of a feed composed of 74% cyclohexane, 20% toluène and 6% DMDS. The reaction was performed at 623 K under 60 bars with a VVH of 2 h^{-1}.

Results and Discussion

On ASA, CO adsorption shows the presence of two types of Lewis acid sites which present a very strong and a weak acidity (Figure 1). They are attributed to vacancies situated on surface Al(IV) or on surface Al(IV)Al(VI) respectively. Silanol groups are also present on ASA surface. These SiOH groups exhibit mainly a very weak acidity equivalent to that detected on pure silica (type C). However, a small amount of these silanol groups show an acidity as strong as that measured on Hβ zeolite (site A) and on partially exchanged NaY zeolite (site B). These specific OH groups should correspond to silanol groups situated close to an Al atom [2,3]. Results obtained on various ASA show that the Al situated in the vicinity of the silanol should be in a tetrahedral environment. Structures for sites A and B are proposed [4] taking into account the localisation of this Al (surface or bulk) and the number of Al(IV) in the neighbouring of the SiOH. These two types of sites are detected on all the studied ASA but their number increases with SiO_2 content.

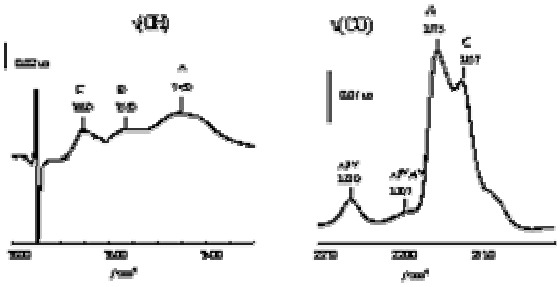

Figure 1 : IR spectra of CO adsorbed (130μmol.g^{-1}) on Si88Al12 activated at 723 K (difference spectra).

After sulfidation of the NiW catalyst, ν(CO) bands specific of coordinative unsaturated sites of the NiW phase are detected at 2135 and 2080(sh) cm^{-1} on the NiW/Si40Al60. The detection of a band at 2108 cm^{-1} indicates that part of the Ni is not in promotion. Similar features are observed for all the studied catalysts. As presented on Figure 2, the ν(CO/NiWS) values vary according to the ASA acidity i.e. the frequency increase with the number of strong acidic OH groups of the ASA. Extention to supports presenting various acidity confirms this sensitivity. Similar trends are also observed in the case of Mo-based catalysts. These results provide evidence for the influence of the acidity of the support on the adsorptive properties of the sulfided phase.

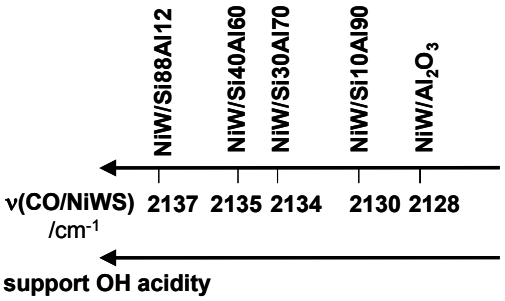

Figure 2 : Variation of the ν(CO/NiWS) frequency for NiW sulfided catalysts supported on oxides presenting various acidity.

On NiW catalysts, catalytic tests show that cyclohexane isomerisation and toluene hydrogenation activities are higher for catalysts supported on ASA than on alumina (Figure 3). Comparison with IR results show that isomerisation activity depends on the number of the most acidic OH groups. Moreover, a linear relationship between CO wavenumber in interaction with the NiW phase and activity for cyclohexane isomerisation is observed (Figure 3). It is concluded that the wavenumber of CO in interaction with the sulfided phase is a good indicator of the global acidity of the support.

Parallel between IR spectroscopy and toluene hydrogenation points out that the catalyst activity depends both on the number of CUS sites of the sulfided phase and also on the "quality" of these sites which is modified by the support acidity.

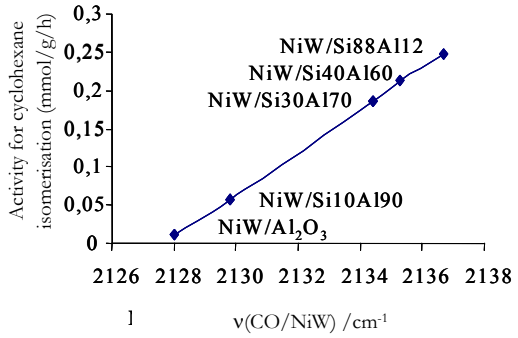

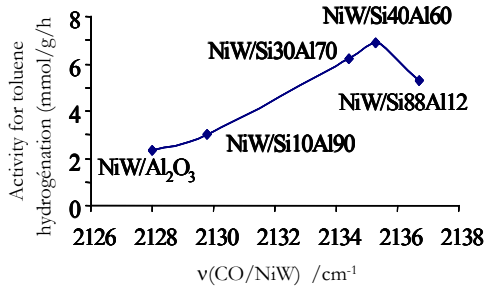

Figure 3 : Activity for cyclohexane isomerisation and toluene hydrogenation versus the wavenumber of CO in interaction NiW sulfided phase deposited on various supports.

Conclusion

This study provides evidence for the influence of the acidity of the support on the adsorptive properties as well as on the reactivity of the sulfided phase.

References

1 P. Marion, D. Duee and E. Benazzi, *Petroleum Technology Quaterly*, summer 2001, page 23.

2 O. Cairon, Th. Chevreau, J.C. Lavalley, *J. Chem. Soc., Faraday Trans*., 94, 3039 (1998).

3 M. Trombetta, G. Busca, S. Rossini, V. Piccoli, U. Cornaro, A. Guercio, R. Catani, R.J. Willey, *J.Catal.*, 179, 581 (1998).

4 G. Crepeau, PhD Thesis, University of Caen, 2002.

Effect of Methyl Groups on the HDN Activities of Indole and Quinoline

*F.E. Massoth and Jack Simons**

Department of Chemical and Fuels Engineering and
*Department of Chemistry
University of Utah, Salt Lake City, UT 84112

Introduction

Catalytic hydrotreating has become an important process for removal of sulfur and nitrogen from petroleum due to increasing environmental constraints. Heterocyclic compounds containing sulfur and nitrogen are relatively stable structures requiring high temperatures and high hydrogen pressures for removal of sulfur and nitrogen.

A number of studies have shown that methyl groups on C-atoms adjacent to the S-atom resulted in lower HDS activity, although only limited studies have been reported on the effect of alkyl substituents on HDN reactivity of N-heteroatom compounds (1).

The HDN of heterocyclic nitrogen compounds generally involves the following reactions: (1) hydrogenation of nitrogen heterorings, (2) hydrogenation of adjacent aromatic rings, and (3) C-N bond cleavage. The aim of the present study was to determine the effect of methyl substituents on the above reactions for indole and quinoline. The numbering systems for these compounds are shown below.

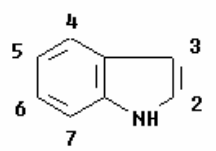

indole

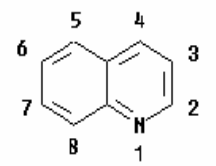

quinoline

Experimental

The catalysts used was Topsøe TK-555, which consisted of 3.8% NiO, and 24% MoO_3 supported on alumina containing 2% phosphorous ($160m^2/g$). Reactions were carried out in a fixed-bed reactor under vapor-phase conditions at 613 K and 3.1 MPa H_2. Liquid feeds consisted of 0.5 wt% of indole or quinoline or their methyl-substituted analogs.Further details are given elsewhere (2,3).

Results and Discussion

Figures 1 and 2 display reaction pathways for the HDN of indole and quinoline. We assume the same apply to the methyl analogs. For all reactants, equilibrium between the parent and its N-ring hydrogenated structure was rapidly achieved. For indole, the equilibrium lies heavily to the left and thus favors the parent compound, while for quinoline, the opposite is true. This equilibrium was also significantly affected by the position of the substituent methyl group, generally suppressing the ratio when methyl groups are on the N-ring (Figure 3).

Subsequent reaction of equilibrium mixtures to intermediate and final products (overall conversion) was also affected by the position of the substituent methyl group. Methyl groups on the N-ring substantially lowered this conversion (except for 2-methylquinoline, which was higher). On the other hand, methyl groups on the aromatic ring had little effect. Similar trends were obtained for HDN.

The reaction of equilibrium mixtures followed two pathways, viz a CNH path (C-N bond cleavage) and a HYD path (aromatic and N-ring hydrogenation). The relative ratios of the HYD/CNH paths were also affected by the methyl group position. The CNH path leading to OEA or OPA was suppressed by methyl groups on the N-ring, and slightly augmented with methyl groups on the aromatic ring; whereas the HYD path to indole hydrogenated products or DHQ was hardly affected by methyl groups.

The quinoline network has an additional important pathway not found for indole, that is, hydrogenation of the aromatic ring in quinoline to THQ5. Compared to hydrogenation to THQ1, this contribution is small. However, it becomes more significant in quinolines in which methyls are in N-ring positions. Since the latter also result in lower equilibrium ratios (THQ1/Q), the lower reactivities appear to be a manifestation of the equilibrium properties, rather than differences in intrinsic rates due to methyl position.

Structural (computational) chemistry calculations of ionization potentials of the methyl-substituted HIND's and THQ1's performed made in order to compare to their respective equilibrium ratios. Reasonably good correlations were obtained in both cases, suggesting that the transition state complex is in the hydrogenated form.

Calculations were also performed relating initial CNH rates (paths in Figs. 1 and 2) to electrostatic potentials on the N atom of the methyl-substituted HIND's and THQ1's, and relating initial HYD rates to ionization potentials. Again, reasonably good correlations were obtained in both cases.

These correlations are in line with the expected properties of the active catalytic sites responsible for hydrogenation and C-N bond cleavage reactions, namely hydrogenation is related to ionization potentials, while bond cleavage is related to the property of the N atom. This would seem to imply that adsorption of the molecule on the active site is via pi bonding during hydrogenation, and adsorption via the N atom for C-N bond cleavage.

Results will be compared to those obtained with a $CoMo/Al_2O_3$ catalyst.

Acknowledgement

Support of this research by Haldor Topsøe A/S is gratefully acknowledged.

References

(1) Topsøe, H; .Clausen, B.S.; Massoth, F.E., Catalysis-Science and Technology, (J.R. Anderson and M. Boudart, eds.), Springer, New York, 1996.
(2) Kim, S.C.; Massoth, F.E., J. Catal. **2000**, *189*, 70.
(3) Kim, S.C.; Simons, Jack; Massoth, F.E., J. Catal. in press

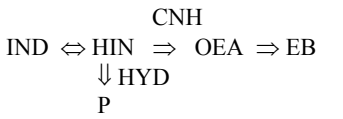

EB	ethylbenzene
HIN	indoline (dihydroindole)
IND	indole
OEA	orthoethylaniline
P	hydrogenated products

Figure 1. Indole reaction network

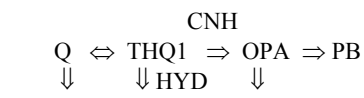

DHQ	decahydroquinoline
OPA	*o*-propylaniline
P	hydrogenated products
PB	propylbenzene
Q	quinoline
THQ1	1,2,3,4-Tetrahydroquinoline
THQ5	5,6,7,8-Tetrahydroquinoline

Figure 2. Quinoline reaction network

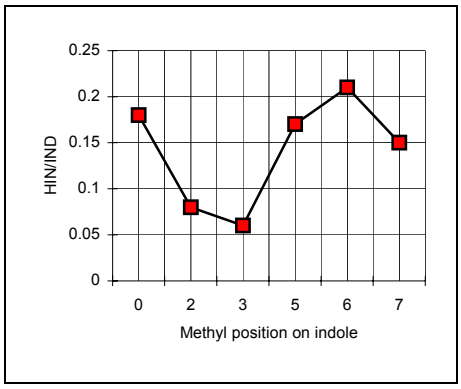

Figure 3a. Equilibrium ratios for methylindoles.

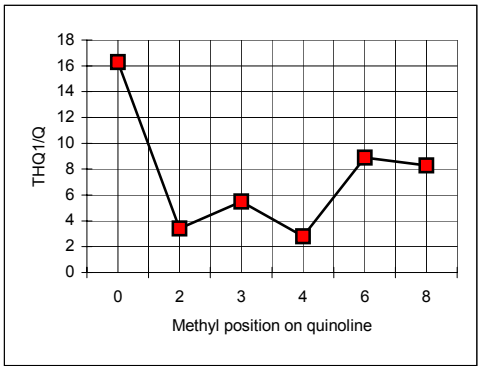

Figure 3b. Equilibrium ratios for methylquinolines.

Effect of Methyl Groups at 4- and 6-Positions on Adsorption of Dibenzothiophenes over CoMo and NiMo Sulfide Catalysts

Xiaoliang Ma, Jae Hyung Kim, Chunshan Song

Clean Fuels and Catalysis Program, The Energy Institute, and
Department of Energy & Geo-Environmental Engineering,
Pennsylvania State University,
209 Academic Projects Building,
University Park, PA 16802

Introduction

Ultra-deep hydrodesulfurization (HDS) of diesel fuel is becoming more and more important because the environmental regulations require producing ultra-low sulfur fuels (1). The major sulfur compounds existing in the current commercial diesel fuels are alkyl dibenzothiophenes (DBTs), especially those with one or two alkyl groups at the 4 and/or 6-positions, for example, 4-methyldibenzothiophene (4-MDBT) and 4,6-dimethyldibenzothiophene (4,6-DMDBT), which are difficult to remove by the conventional HDS processes (1-3).

The major challenge in ultra-deep HDS of diesel fuel is to remove such refractory sulfur compounds. In order to develop novel catalysts and to design more efficient HDS processes, it is necessary to fundamentally understand why and how the alkyl groups at the 4 and 6 positions decrease the HDS reactivity of DBTs. Some researchers attributed the refractory nature of 4,6-DMDBT to the steric hindrance towards the adsorption on the active sites (4,5). On the basis of the heats of adsorption for DBT, 4-MDBT and 4,6-DMDBT, which were obtained by measuring the parameters in a simplified Langmurir-Hinshelwood equation, Kabe and co-workers concluded that 4-MDBT or 4,6-DMDBT can be adsorbed on the catalyst through π-electrons in the aromatic rings more strongly than DBT, and the retarding effect of the methyl substitution on HDS rates of DBTs was not attributed to the inhibition of the adsorption of DBTs on the catalyst but to the steric hindrance in the C-S bond scission of the adsorbed DBTs (6,7). Recently, based on a study on the promoter effect of Co and Ni on HDS of DBTs, Bataille et al. proposed that the lower reactivity of 4,6-DMDBT compared to that of DBT measured on the promoted catalysts could not be attributed to difference in the adsorption strength of the reactants, but to a steric hindrance by the methyl groups to the adsorption of the dihydrointermediates and/or others (8). However, many explanations regarding the adsorption of DBTs are deficient in direct experimental evidence.

In the present study, we directly examined the adsorption of DBT, 4-MDBT and 4,6-DMDBT on two sulfided commercial catalysts, CoMo/alumina and NiMo/alumina, by using a liquid-phase adsorption device. The adsorption capacity and selectivity of DBTs over the two catalysts were measured and compared. We believe that such adsorption information is important for our fundamental understanding of the retarding effect of the alkyl groups at the 4 and 6-positions of DBTs on HDS.

Experimental

Two commercial catalysts, Cr344 ($CoMo/Al_2O_3$, CoO: 3wt%, MoO_3: 14wt% Suface area: 190 m^2/g) and Cr424 ($NiMo/Al_2O_3$, NiO: 3.0wt%, MoO_3: 13wt%, Surface area: 155 m^2/g,), used in the present study, were from Criterion Catalysts and Technologies. A model diesel fuel, which contains the same molar concentration of DBT, 4-MDBT and 4,6-DMDBT, was used in the adsorption experiments. 2-Methylnaphalene (2-MNaph) with the same molar concentration as the sulfur compounds was also added into the fuel for comparing adsorption selectivity. The detailed composition of the model diesel fuel with their purity is listed in Table 1. The sulfur compounds and hydrocarbons contained in the fuel were purchased from Aldrich without further treatment before use.

After presulfidation at 350 ˚C with 10 vol % H_2S in H_2 at a flow rate of 200 ml/min for 4 h, the catalysts were cooled to room temperature under the same atmosphere, and then, kept in hexane before use. The adsorption experiments were performed at ambient pressure using a liquid-phase adsorption device, including a gas control system, HPLC pump, adsorption column in a furnace and a sample collection system. The presulfided catalyst was packed into a stainless column with internal diameter of 4.6 mm and length of 150 mm. The adsorbent bed volume was 2.49 ml. Before feeding the model diesel fuel into the column, H_2 gas was passed through the column at 300 ˚C at a flow rate of 20 ml/min for 1.0 h, and then, the column temperature was reduced to the assigned temperature for adsorption experiment. The model diesel fuel was fed into the column and flow through the adsorption bed without using H_2 gas. The liquid flow rate was 0.2 ml/min. The effluent was collected for analysis using a GC-FID with a capillary column.

Results and Discussion

Figure 1 shows the molar concentration of sulfur compounds and 2-MNaph at the outlet as a function of the effluent amount for the adsorption on the NiMo catalyst at 50 ˚C and 150 ˚C, respectively. No detectable biphenyls and cyclohexylbenzenes were found in the effluent, indicating no HDS reaction takes place at such conditions. At 50 ˚C, the first break-through compound is 2-MNaph with a break-through point at ~0.2 g/g and a saturation point at ~1.6 g/g. The second one is 4,6-DMDBT with a break-through point at ~0.4 g/g. The concentration of 4,6-DMDBT kept below 0.2 mmol/l before the effluent volume reached 2.5 g/g, and then, increased to the saturation point at ~4.4 g/g. Break- through point of 4-MDBT is at 2.5 g/g with a saturation point at ~5.0 g/g. The last break-through compound is DBT with a break-through point at ~3.5 g/g and a saturation point at > 5.5 g/g. It is clear that DBTs exhibit much higher adsorption selectivity than 2-MNaph, indicating that the adsorption of DBTs on the NiMo catalyst not only depend on the interaction through π-electrons on aromatic ring but also depend on the interaction through the S atom in DBTs. As is well known, 2-MNAPH has higher π-electron

density on its aromatic ring than that of DBTs (9), although the aromatic ring size of the former is smaller than that of the latter. However, DBTs exhibit much higher adsorption selectivity, which indicates that interaction between the S atom and the adsorptive sites play an important role in the adsorption of DBTs. Furthermore, by comparing DBT, 4-MDBT and 4,6-DMDBT, the increases of adsorption selectivity in the order of 4,6-DMDBT < 4-MDBT < DBT implies that the methyl groups at the 4 and 6-positions inhibit the interaction between the S atom in DBTs and the active sites on the catalyst, which results in the decrease of adsorption capacities of 4,6-DMDBT and 4-MDBT on the catalyst.

The adsorption capacities corresponding to the saturation point of 4,6-DMDBT, 4-MDBT and DBT were calculated on the basis of data in Figure 1, being ~ 0.062, ~0.064, and ~0.068 mmol/g, respectively. It indicates that at least one tenth of the adsorptive sites on the catalyst are able to adsorb DBT, but fail to adsorb 4,6-DMDBT due to the steric hindrance of the methyl groups at the 4 and 6- positions.

When the column temperature was increased to 150 ˚C, the adsorption selectivity shows the same order: 2-MNAPH < 4,6-DMDBT < 4-MDBT < DBT, which confirms further the effect of the methyl groups on the adsorption of DBTs on the NiMo catalyst. Figure 1 also clearly shows that the adsorption capacity decreases at 150˚C in comparison with that at 50 ˚C. The saturated adsorption capacity for the total sulfur on the NiMo catalyst is 0.068 and 0.045 mmol/g, respectively, at 50 and 150 ˚C. This result confirms further that the low sulfur concentration in the effluent is because the surface adsorption instead of surface reaction. On the other hand, the effect of temperature on the adsorption capacity, observed in the present study, also implies that the adsorption might be weak and reversible.

Figure 2 shows the molar concentration of sulfur compounds and 2-MNaph at the outlet as a function of the effluent amount for the adsorption on the CoMo catalyst at 50 ˚C in comparison with the adsorption on the NiMo catalyst at the same temperature. It was found that the CoMo catalyst exhibits the break-through curves and selectivity similar to those of the NiMo catalyst. However, the CoMo catalyst has higher adsorption capacity than the NiMo catalyst for all examined species, probably because higher surface area of the former than that of the latter. The higher adsorption capacity of the CoMo catalyst indicates it has more adsorption sites on the surface.

In the HDS kinetic study (10), we found that the NiMo catalyst is more active than the CoMo catalyst for HDS of 4,6-DMDBT. If assuming that the HDS takes place at the same sites, the higher activity of the NiMo catalyst than the CoMo catalyst might not be attributed to the number of the active sites but the turnover frequency of the active sites. In general, HDS reactivity (rate constant) of 4,6-DMDBT over CoMo catalysts is lower than that of DBT by more than an order magnitude. However, the effect of the methyl groups at 4 and 6-positions on the adsorption of DBTs is weaker in comparison with their effect on the HDS rate. It might indicate that 1) not all of the adsorptive sites are related to the active sites for HDS reaction, and/or 2) the effect of the steric hindrance by the methyl groups on the adsorption of DBTs is one of the factors but not the only factor that retard the HDS rate of 4,6-DMDBT.

Acknowledgments

This work was supported in part by US Department of Energy, National Energy Technology Laboratory, and US Department of Defense. We gratefully acknowledge the financial support.

References

1. Song, C. , Ma, X. Appl. Catal. B: Env. 2003, 40 (4) in press; Song, C. Am. Chem. Soc. Div. Fuel Chem. Prep., 47(2), 438-444 (2002).
2. Ma, X., Sakanishi, K,, Mochida, I. Ind. Eng. Chem, Res. 33, 218 (1994).
3. Gates, B.C., Topsoe, H. Polyhedron 16, 3213 (1997).
4. Ma, X., Schobert, H. H._Prepr., Div. Pet. Chem., Am. Chem. Soc. 42, 657-661 (1997).
5. Shafi, R., Hutchings, G. J. Catal. Today, 59, 423-442 (2000).
6. Kabe, T., Ishihara, A., Zhang, Q. Appl. Catal. A 97, L1-L9 (1993).
7. Zhang, Q., Ishihara, A., Kabe, T. Sekiyu Gakkaishi, 39, 410-417 (1996).
8. Batail, F., Lemberton, J., Michaud, P., Perot, G. Vrinat, M., Lemaire, M., Schulz, E. Breysse, M., Kasztelan, S. J. Catal. 191, 409-422 (2000).
9. Ma, X., Sakanishi, K,, Isoda, T., Mochida, I. Energy & Fuels 9, 33-37 (1995).
10. Kim, J. H., Ma, X., Song, C. Prepr., Div. Pet. Chem., Am. Chem. Soc. , 48 (1), in press (2003).

Table 1 Composition of Model Diesel Fuel

No.	name	concentration	
		wt %	mmol/l
1	DBT(99+%)	0.095	3.97
2	4-MDBT(96%)	0.102	3.97
3	4,6-DMDBT(97%)	0.109	3.97
4	Naphthalene (99%)	0.067	3.97
5	2-methylnaphthalene (98%)	0.074	3.97
6	n-Hexadecane(99+%)	39.965	
7	n-Dodecane(99+%)	39.500	
8	n-Tetradecane (99+%)	0.109	
9	Decalin(99+%)	9.988	
10	t-Butylbenzene(99%)	9.988	

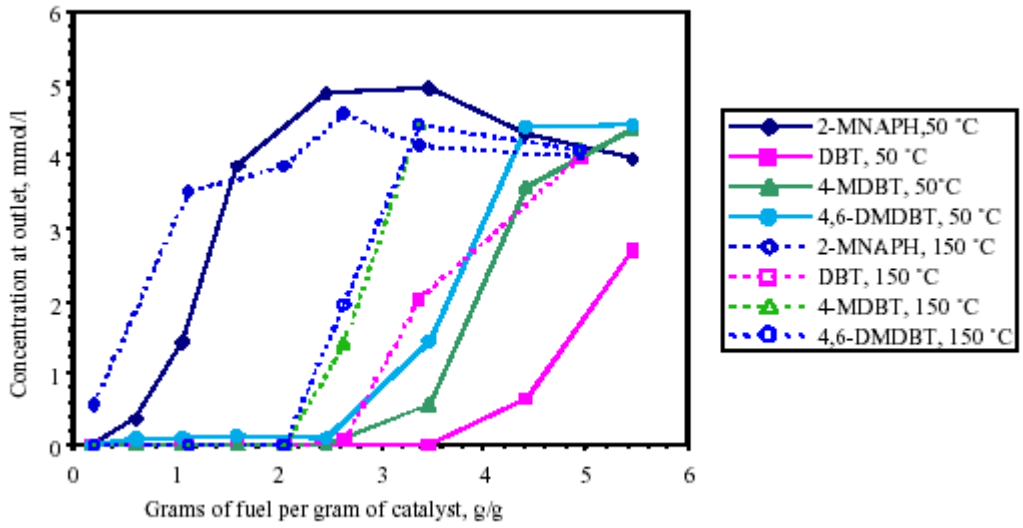

Figure 1. Adsorption profile of DBTs on the NiMo catalyst.

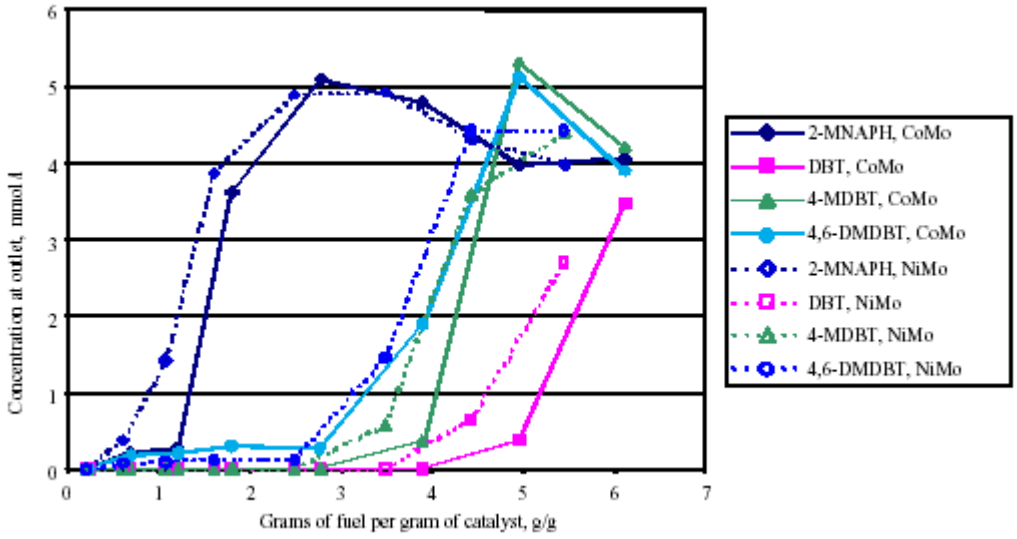

Figure 2. Adsorption profile of DBTs on CoMo and NiMo catalysts at 50 °C.

ADSORPTIVE REMOVAL OF SULFUR AND NITROGEN SPECIES FROM A STRAIGHT RUN GAS OIL FOR ITS DEEP HYDRODESULFURIZATION

*YOSUKE SANO, KI-HYOUK CHOI, YOZO KORAI and ISAO MOCHIDA**

Institute of Advanced Material Study, Kyushu University, Kasuga-koen, Kasuga, Fukuoka 816-8580 JAPAN

*mochida@cm.kyushu-u.ac.jp

INTRODUCTION

World refining industry is facing new and stricter challenges on the heteroatom content in their major products, such as diesel fuel and gasoline. The sulfur content of diesel fuel must be lowered to 15 ppmS from current 500 ppmS and even further regulations may be implemented with accelerated concerns on the atmospheric pollution[1]. Several kinds of new ideas have been proposed and some of them were practically examined to achieve the ultra deep desulfurization. However, more efficient and economic process is still being required in spite of various efforts. Critical barriers in achieving ultra deep desulfurization are refractory sulfur species, which have very low reactivity, and inhibitors such as H_2S, NH_3 and nitrogen species under conventional hydrotreating conditions. The inhibitors retard the desulfurization reaction, very markedly in ultra deep region [2, 3]. There are some suggestions on the pre-treatment of gas oil to remove nitrogen species prior to hydrodesulfurization [4,5]. However, detailed accomplishment of the suggestions has not been clarified yet

Activated carbon and activated carbon fiber have been known to be versatile absorbents of gaseous and liquid molecules. Its surface and properties can be easily controlled.

In this study, sulfur and nitrogen species were removed from straight run gas oil (SRGO) through adsorption by activated carbon materials and treated oil was examined in conventional hydrodesulfurization reaction to evaluate the effects of pre-treatment on the HDS activity.

EXPERIMENTAL

I. ASORPTION

Straight run gas oil (11,780 ppmS and 260 ppmN) used in this study was provided by a japanese commercial refinery. Carbon materials (activated carbons and activated carbon fibers), which were dried at 110 ^oC under vacuum oven prior to adsorption experiment, were packed into the stainless steel tube of 50 mm length and 6 mm diameter. Key properties of carbon materials were listed in Table 1. SRGO was fed into the tube by an HPLC pump at the rate of 0.1 ml/min and at the pressure of 20 psig. The temperature of the adsorption reactor was maintained at 10 - 40 ^oC by water bath. The eluted oil was sampled at every 10 min for 30 sec and analyzed by GC-AED (Atomic Emission Detector, HP5890P, and G2350A).

II. HDS REACTION

The eluted oil was hydrodesulfurized with commercial catalysts in autoclave-type reactor (100 ml internal volume). 10 g oil, 1 g catalyst, which was pre-sulfided by 5% H_2S/H_2 at 360 ^oC for 2 hours, and 50 kg/cm^2 hydrogen gas were charged into the reactor. The temperature of the reactor was raised to 340 ^oC by 50 min and maintained at that temperature for 2 hours. The HDS product was sampled through filter fitted in reactor. and analyzed by GC-AED.

RESULTS AND DISCUSSION

Fig. 1 showed carbon-, sulfur-, nitrogen-specific chromatograms of SRGO feed. Most of the sulfur species in SRGO were benzothiophenes (BT), dibenzothiophenes (DBT). Quinolines, indoles, and carbazoles were found in nitrogen-specific chromatogram of feed gas oil.

Sulfur and nitrogen species removal depended on the types of carbon materials as shown in Fig. 2. MAXSORB-II, which has the largest surface area and oxygen content, showed the largest capacity for sulfur and nitrogen species. Fig. 3 showed that breakthrough time for nitrogen species was much longer than that for sulfur species over MAXSORB-II. The other carbon materials exhibited the same trend with that of MAXSORB-II. Breakthrough points for sulfur and nitrogen contents were estimated to be around 40 and 240 ml-oil/g-absorbent, respectively over MAXSORB II. The calculated capacities of sulfur and nitrogen until breakthrough point were to be 0.095 g-sulfur and 0.029 g-nitrogen/g-absorbent, respectively. The relative affinity for adsorption of nitrogen and sulfur species depended on their size and molecular weight as indicated in Fig.4; DBT was eluted earlier than MDBT and DMDBT.

Carbon materials were regenerated by flowing toluene and drying it at 250 ^oC. As can be seen in Fig. 5, regenerated MAXSORB-II showed almost similar capability for nitrogen and sulfur removal to that of virgin MAXSORB- II. Small difference between them at the range of 20 - 80 ml-oil/g-absorbent could be suggested due to the change of surface area and surface functional group during heat treated at 250 ^oC.

Nitrogen species has been reported to be one of the strong inhibitors in deep range HDS due to its competition with sulfur species for the same active site. HDS products of nitrogen species removed SRGO showed much lower sulfur content. When 70% of nitrogen species was removed, attainable sulfur level was 11 ppmS while 180 ppmS for mother SRGO. Sulfur content of product oil was almost proportional to that of nitrogen in the feed, although the latter content of 39ppm allowed deep desulfurization less than 6ppm-sulfur. From this result, it is clear that partial removal of nitrogen species from SRGO is very effective to achieve sulfur content lower than 10 ppmS by using current catalyst and process conditions. Some of the activated carbon appears feasible on its capacity and rate of nitrogen removal for practical application.

CONCLUSIONS

Carbon material could be applied as an absorbent bed for the removal of sulfur and nitrogen species of gas oil. Adsorption capacity of carbon materials depended on the textural and surface properties of them. Nitrogen species removed gas oil showed significant enhancement of desulfurization.

REFERENCES

1. Halbert, T. R.; Brignac, G. B.; Demmin, R. A.; Roundtree, E. M. *Hydrocarbon Engineering*, June, **2000,** *2*.
2. Whitehurst, D. D.; Isoda, T.; Mochida, I. *Adv. Catal*., **1998,** *42***,** 345.
3. Whitehurst, D. D.; Farag, H.; Nagamatsu, T.; Sakanishi, K.; Mochida, I. *Catal. Today*, **1998,** *45***,** 299.
4. Zeuthen, P; Knudsen, K.G.; Whitehurst, D. D. *Catal. Today*, **2001**, *65,* 307.
5. Min, W-S et. al., U.S.patent 6,248,230, **2001**.

Table 1. The characteristics of carbon materials

Carbon materials	C/H/N/O(%)	Surface area (cm^2/g)	Total pore volume (cm^3/g)
MAXSORB -II	85/0.49/0.14/14.16	2972	1.75
OG-20A	93.83/0.69/0.25/5.15	2000	1.1
MGC-B	80.11/0.6/3.23/7.27	683	0.59

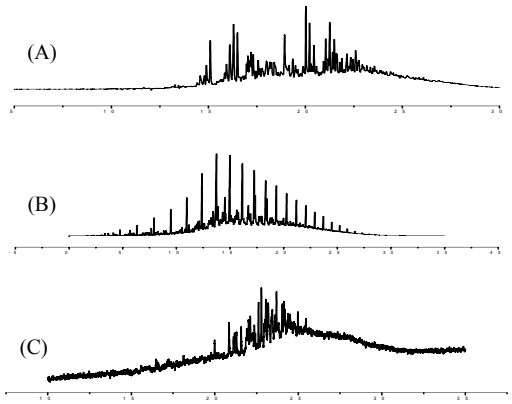

Figure 1. (A) sulfur-, (B) carbon, and (C) nitrogen-specific chromatograms of SRGO

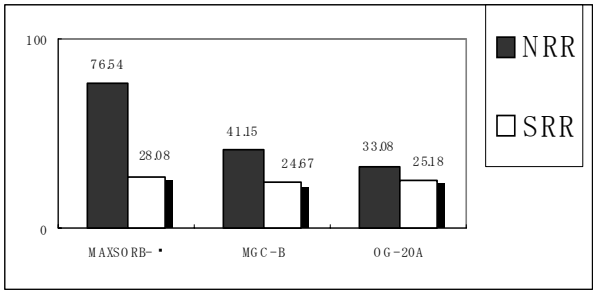

Figure 2. Nitrogen and sulfur removal ratio of carbon materials at 30 ^oC. Oil=72ml, adsorbent=0.3g
*NRR=Nitrogen removal Ratio (%)
*SRR=Sulfur Removal Ratio (%)

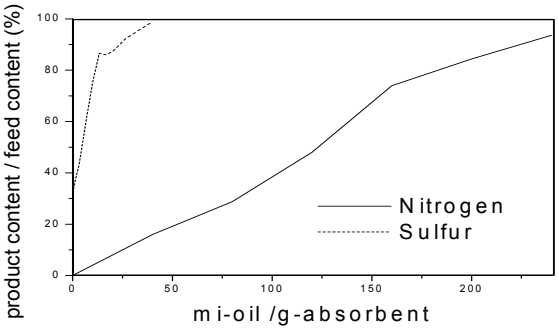

Figure 3. Sulfur and nitrogen breakthrough profile of SRGO on MAXSORB-II at 30 ^oC.

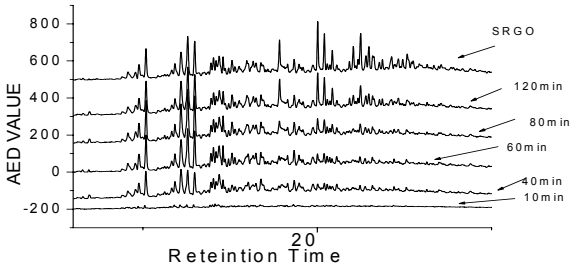

Figure 4. Sulfur-specific chromatograms of eluted SRGO from MAXSORB-II at 30 ^oC.

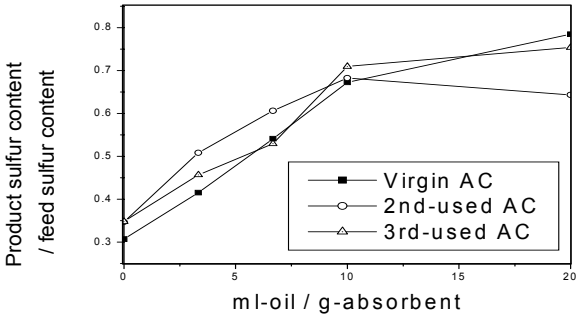

Figure 5-A. Sulfur breakthrough profiles of virgin and regenerated MAXSORB-II at 30 ^oC.

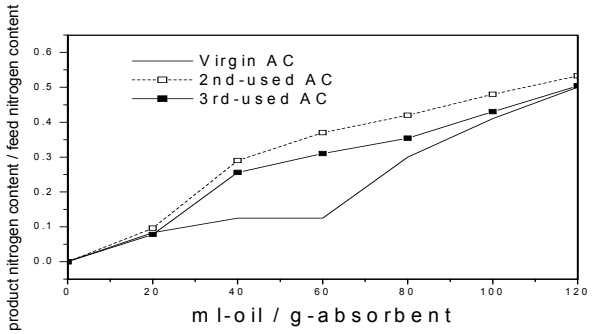

Figure 5-B. Nitrogen breakthrough profiles of virgin and regenerated MAXSORB-II at 30 ^oC.

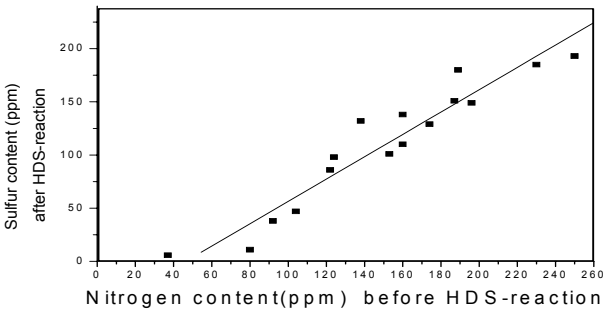

Figure 6. Plot of total sulfur content of HDS products and nitrogen content of feed gas oils.

NUCLEOPHILIC SUBSTITUTION RATHER THAN ELIMINATION IN THE HDN OF ALKYLAMINES

Y. Zhao and R. Prins

Laboratory for Technical Chemistry, Federal Institute of Technology (ETH), Zurich, Switzerland

The hydrodenitrogenation (HDN) of hexylamine, dihexylamine, and trihexylamine was studied at 300-340°C and 3-5 MPa total pressure over a sulfided $NiMo/Al_2O_3$ catalyst. The main products were hexanethiol, hexane, hexene, and disproportionation products of the alkylamines. Disproportionation occurred especially at low H_2S pressure and high alkylamine pressure. The conversions of the hexylamines increased with H_2 pressure and decreased with increasing partial pressure of the amines. The conversion of hexylamine and dihexylamine decreased slightly with H_2S pressure, but that of trihexylamine increased substantially.

The influence of the pressure of thiols, amines, and H_2S in the simultaneous HDN of alkylamines, hydrodesulfurization (HDS) of alkanethiols, and hydrogenation of alkenes was investigated as well. A high H_2S pressure promoted the substitution reaction of hexylamine to hexanethiol, but inhibited the decomposition of the resulting thiol to hexene and hexane. H_2S also strongly inhibited the hydrogenation of alkenes in the absence of amine, but less in its presence.

The simultaneous reactions of thiol and alkene in the presence of amine showed that the decomposition of thiol is much faster than the alkene hydrogenation. Therefore, alkenes, observed in the HDN of alkylamines, may not only be formed by elimination of the alkylamine, but also by substitution of the alkylamine by H_2S and decomposition of the resulting thiol.

The contributions of elimination and nucleophilic substitution to the HDN were determined from the product selectivities at short contact time. The initial alkene selectivities were low and accounted only for a minor part of the alkylamine conversion. A substantial part of this alkene even originated from the reaction of hexanethiol. These results demonstrate that the HDN of alkylamines proceeds mainly by nucleophilic substitution by H_2S and not by elimination. In accordance with this, the hexene/hexane ratio in the HDN of hexylamine was similar to the pentene/pentane ratio in the HDS of pentanethiol.

2-Methylpiperidine reacted by ring opening to 2-aminohexane rather than hexylamine. The same ring-opening pattern was observed for 2-ethylpiperidine, which demonstrates that the piperidine ring opens on the sterically less hindered side of the molecule and not on the side with the most H atoms.

This, and the small percentage of olefins formed, suggests that elimination does not play an important role in the HDN of piperidine either. In accordance with our HDN results for dihexylamine, we therefore assume that also piperidine undergoes HDN mainly by nucleophilic substitution by H_2S, followed by decomposition of the resulting alkanethiol.

CLEAN FUELS FROM COAL: THE PATH TO 1972.

Burtron H. Davis
Center for Applied Energy Research, University of Kentucky
2540 Research Park Drive, Lexington, KY 40511

During its infancy, the United States utilized renewals as its source of energy. With time, coal became the dominant source of energy for home, industry and transportation and gradually replaced renewables during the 1800s. During this period the conversion of coal to gas was developed and grew in use until natural gas subsequently supplanted it. Scientific advances in the utilization of coal began with the establishment of the US Bureau of Mines and the German laboratory in Mulheim, among others, in the early 1900s. The period 1920-40 has been characterized as the flowering era of fuel science and technology. A brief perturbation was superimposed on the research activities for coal by the fear of an oil shortage during 1944-1953 but this emphasis declined with the exploitation of Mid-East oil. The oil crisis of 1972 set the stage for the activities for the period of the current symposium: 1972-2002.

Introduction

Humans, as gatherers, utilized renewable resources. With the use of domestic animals for transportation and agriculture, the utilization of energy by humans increased, but still depended on renewable resources. Growth of human population caused an escalation of energy usage to the point where forests nearly vanished in "developed" countries in the 1600s. In Great Britain, the shortage of forests was overcome by substituting a stored fossil fuel, coal. The high density of energy stored in coal gradually caused developing countries with coal reserves to switch to it for their energy sources. Even so, transportation and agriculture was still accomplished by energy derived from humans and domesticated animals.

With the introduction of the steam engine, the situation changed dramatically. Rather than an evolutionary escalation of the use of energy, there was an abrupt, revolutionary increase in the use of energy. Based on this increased use of energy, the productivity of each human and their ability to travel great distances could also undergo a revolutionary advance, and this happened. As shown in Figure 1, evolutionary and revolutionary advances in mechanical developments and theoretical understanding now permit the efficiency of a steam engine to approach its ultimate value

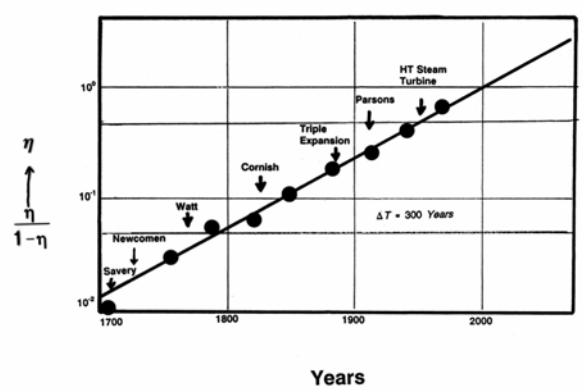

Figure 1. Evolution of steam engine efficiency η (Fisher-Pry notation).

The primary energy in the U.S. in 1800 was wood, a renewable resource. However, as energy use increased coal gradually displaced wood (Figure 2). Coal was at a later time replaced by oil and natural gas. Nuclear was destined to become a dominant source of energy for the U.S., but political controversy led to its loss of favor and no new plants have gone on-stream during the past 20 years.

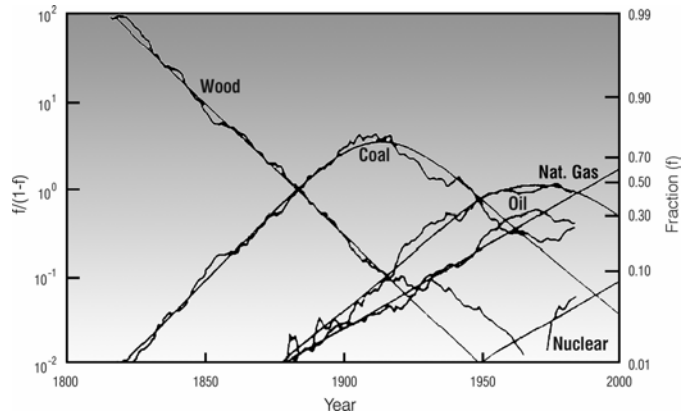

Figure 2. The distribution of fuel usage during 1800 to 2000.

Figure 3 shows the distribution by milage of intercity transportation in the U.S. Early travel was predominantly by canals and this was replaced, first by rail and then by auto/truck traffic. More recently air travel has shown growth and, because of the long distances for plane travel, will soon replace the auto for intercity transportation. Fuel usage by transportation had a significant influence on the form of energy used. Rail transportation was the dominant mode until well into the 20th century. Coal gradually replaced wood as the fuel of choice and maintained this dominance through the WW II period and was then rapidly replaced by diesel powered electric trains. The use of coal in transportation was accomplished with inefficient combustion and the emission of large quantities of ash and soot. Black skies and buildings in major cities resulted from this incomplete combustion without control measures and this was tolerated, or even encouraged, as the cost of the industrial revolution.

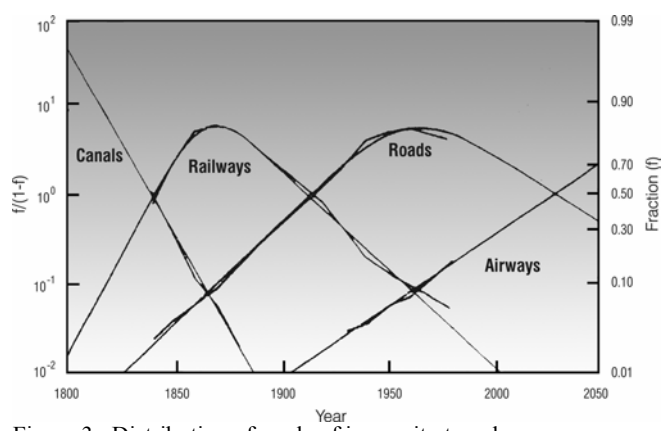

Figure 3. Distribution of mode of inner-city travel.

Coal-based industries developed that were based on the by-product tars from the coke ovens. Coke ovens lining highways and rivers leading into Pittsburgh, for example, emitted sufficient light and smoke that night sky glowed and was described by an observer as

"Hell with the roof off." By 1950 the glow started to dim and petroleum began to become the dominant feedstock for the chemical industry.

During the 1800s the general theme of the U.S. was expansion. As natural resources were reduced so that they could no longer meet demand, the population either concentrated in cities in the eastern U.S. or moved West For example, the population of New York City was about 30,000 people in 1800 but had grown to about 4.5 million by 1900. Coal replaced wood and, as it was used at that time, it was a dirty fuel. But so was the renewable that it displaced: wood. Likewise, transportation depended upon horses, and these also were dirty. New York City had about 200,000 horses in 1900 and each horse produced about 24 pounds of manure and several quarts of urine. During the winter, the accumulation of snow and horse wastes could reach 2 to 6 feet in the streets of NYC. The conditions that the horses were exposed to resulted in a life expectancy of less than three years. The "dirty coal" images lives on but the even dirtier alternatives have been forgotten. The advantages of coal greatly outweighed the disadvantages, judged by the conditions of that time. Thus, the growth of coal usage was rapid up to about 1925.

As research on coal intensified at the beginning of the 20th century, processes were soon developed that could convert the solid into liquid transportation fuels. The Bergius Process for the direct liquefaction of coal using high reaction temperatures and high hydrogen pressures was announced in the 1910s. In the following decade, the process now known as the Fischer-Tropsch synthesis was announced, and coal could be converted first to a synthesis gas and then to liquid hydrocarbons. Today it is easy to overlook the significance of these discoveries. The following extract gives one a flavor of the magnitude of these advances placed in the time of the discoveries (H. Elkwood, J. Chem. Educ., 2, 631 (1925).).

> One of the unsolved riddles of chemistry is the precise constitution of a lump of coal. There are combinations of carbon and hydrogen and oxygen and nitrogen there that go to pieces as soon as we undertake to find out just what they are. Now a German chemist named Bergius has succeeded, prinipally by means of high pressures, in introducing hydrogen into heavy oils and also into bituminous coal so that the latter takes on the liquid character of a crude petroleum. Suppose, then, that some chemist were to discover a catalytic method of hydrogenating bituminous coal so that it becomes liquid and that this method should become economically possible. **Please close the book for a few moments at this point and think what such a discovery would mean. Liquid fuel for everything. No more stoking, no more smoke or cinders, no more worry about the waning supply of petroleum and no more coal bins (emphasis added).**

Since 1925 when Elkwood wrote the above, we have come close several times to attaining his dream only to find an additional source of petroleum, and coal usage continued to decline.

The increasing use of coal and other fossil fuels together with the results from the scientific centers established around the world led to results that could make the period of 1925-1940 the flowering era of fuel science and technology [M. A. Elloit, Preprints, ACS Division of Fuel Chemistry 19(3), 140-161 (1974).] In the field of combustion this period saw the extensive development of the burning of pulverized coal under slagging conditions to generate steam and a greatly improved understanding of the kinetics and mechanism of the combustion of solid fuels. Coal gasification technology was advanced: by the development of gasifiers using oxygen; by operating at elevated pressures, under slagging conditions, and with a fluidized bed; and by demonstrating the feasibility of hydrogasification. During the period the efficient by-product coke oven almost completely replaced the beehive oven for producing metallurgical coke. Coal liquefaction and solvation progressed from the laboratory tot he full-scale commercial plant. The Fischer-Tropsch process was discovered and progressed to the commercial stage during this period. Major advances were made in knowledge of the kinetics and mechanism of the oxidation of gaseous fuels and in knowledge of the properties of fuel-air mixtures. Extensive work was done on the chemical constitution of coal and tar and on their physical properties. These advances are detailed in Elliott's paper.

During 1940-1960, war played a dominant role in the use of fuel during the early years of this period. Based on tonnage, petroleum products were the major export from the U.S. to European Allies. Even so, the Allies were required to make dramatic adjustments in lifestyle. Shown in Figure 4 is an auto on a street in Paris, modified to run on gases generated by the "on-board garbage-can gasifiers" mounted on the front of the auto.

Figure 4. On-board gasifier for auto transportation during WWII in Paris, France.

During this period it was recognized that the U.S. was facing a future supply problem for transportation fuels. The Synthetic Liquid Fuels Act went into effect in 1944 and the research at the Bureau of Mines, started in 1936, underwent a large and rapid expansion. Bench- and pilot-scale plants were operated at the labs in Pittsburgh with emphasis on new catalysts, effects of process variables and reaction mechanisms. These studies were incorporated together with results from

German operations in the demonstration plant that was built in Louisiana, Missouri. The direct coal liquefaction demo plant processed about two tons coal per hour to produce about 200 bbl/day of products. Emphasis was on operability and much progress was made. Fischer-Tropsch synthesis received much support. The high-temperature fluid bed operation to produce mainly gasoline was favored by petroleum companies. A commercial scale plant using a fixed-fluid catalyst bed reactor was built near Brownsville, Texas. Just as operational problems were overcome, the discovery of large quantities of Mid-East oil at low prices caused the plant to be closed. In South Africa, the need for energy independence led the government to support the Sasol plant that utilized circulating fluid-bed reactors. The other approach involved several modifications of low- temperature operations utilizing fixed-bed catalytic reactors, bubble column reactors and variations between these two extremes of operation. A demonstration plant was constructed and operated at the Louisiana, Missouri plant. In Germany, a demonstration plant using

the bubble column reactor was operated. However, these plants were also victims of the increased supply of cheap oil.

During the 1940-60 period, coal gasification was a major topic. A variety of processes advanced up to bench scale units (100-500 pounds of coal per hour). Most of these were designed to operate at pressures that would permit purification and Fischer-Tropsch operation without additional compression. Nearly all of these processes utilized oxygen. However, during this period, only two plants were built at a larger scale. The Bureau of Mines operated at Louisiana, Missouri a Linde-Frankie oxygen plant that produced 25 tons per day and this was fed to a suitably sized Koppers-Totsaek coal gasifier. Du Pont built a plant at Belle, West Virginia to produce 25 million cubic feet of hydrogen per day and this was operated successfully for two years using coal. However, after two years, operations were terminated and natural gas became the source of the hydrogen.

As it was recognized that U.S. demand for liquid hydrocarbons could be met using foreign oil to augment internal production, the Office of Synthetic Liquid Fuels was eliminated in 1953. The demonstration plants were closed, laboratory staff was reduced and the research emphasis was shifter to other topics.

The 1960-1980 period provides two extremes. During the late 1950s and early 1960s gasoline was plentiful and low priced; service station operators, backed by petroleum companies, offered many incentives for customers to buy more of their products. The muscle cars of that era consumed large quantities of gasoline, much as SUVs do today. U.S. petroleum production was subsidized by two means during this period. Petroleum producers were allowed significant tax advantages in the form of allowances for their depletion of U.S. reserves. In addition, refiners were to limit imports to no more than 25% of their production. Thus, U.S. production was artificially priced at about $4.50/bbl when mid-East crude would be obtained for $2.25/bbl at U.S. coast ports. Thus, U.S. government actions were accelerating the depletion of U.S. crude reserves while indirectly subsidizing the oil industry in its completion with coal. The picture dramatically changed as the 1970s two oil price shocks with very high prices and shortage of supplies. The U.S. and other developed countries started crash programs to convert coal to liquid fuels. Pilot plants for direct coal liquefaction were constructed in the U.S. that processed up to 600 tons of coal per day. During this period, one state (Kentucky) had 12 commercial coal-based plants at some stage of design as well as others based on oil shale and tar sands. During the 1970s the public expected the worst and projections supported this fear (Figure 5). The oil shocks also

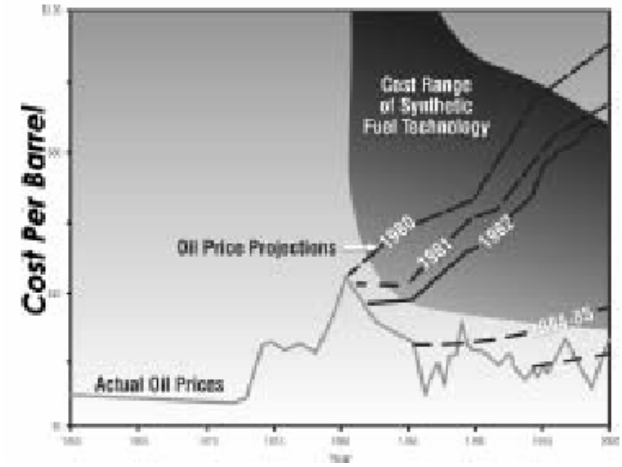

Figure 5. Projected and actual prices for crude.

changed perceptions in other ways. The straight line portion of Figure 6, covering the period 1950-1974 showed a straight line relationship between energy consumption and the U.S. gross national product (GNP). The linear relationship was shown to be one of convenience since the increase in oil prices caused dramatic and rapid changes, determined primarily by conservation and by exporting energy intensive industries to other countries.

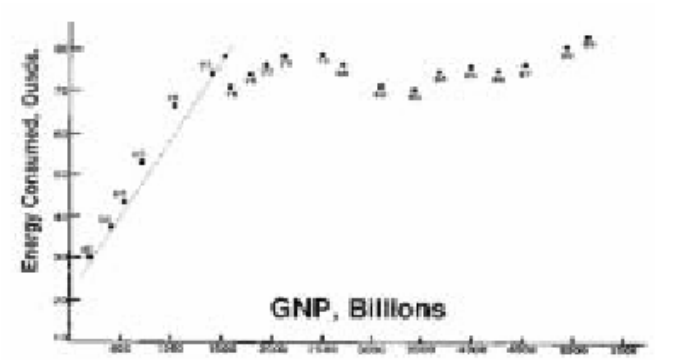

Figure 6. Relation of energy consumption and GNP for U.S. (Numbers in figure are for year; eg., 65 is 1965).

History shows that it has been very difficult to predict the future of coal and of the development of a synfuels industry. Predicting the progress of clean fuels from coal is especially fitted by the quote attributed to Niels Bohr: "It is very difficult to make predictions, especially when it is about the future!!". Clean fuels from coal is here today for the generation of electrical power, and it gets cleaner each year. Coal can provide clean fuels for transportation and this will become necessary for the U.S., the difficulty is to predict when this will occur.

References

1. B.H. Davis, Energeia.
2. H. Elkwood, J. Chem. Educ., 2, 631 (1925).
3. M.A. Elloit, Preprints, ACS Division of Fuel Chemistry 19(3), 140-161 (1974).

Progress of Coal Science in the 20th Century

Karl H. van Heek
Fährenkotten 3, D - 45259 Essen, Germany

Abstract
The Lecture deals with the development and advances of coal science in the last century under the driving forces of politics, economics, and technology and in interaction with the progress achieved by other scientific and engineering disciplines. The growth and status of knowledge is demonstrated choosing examples under the guideline "Structure and Basic Reactions". The contribution is based on the author's publication in Fuel 79 (2000) 1-26.
Keywords: coal science, history, methods, structure, reactions, progress

Coal Science in the Political and Technological Context of the Century

No doubt, the reader will be aware of the fact, that coal has been the dominant source of energy, for coke and for chemicals, throughout the world for long periods in the past two centuries of industrialisation and still is at present and will be in the future in many countries. Thus the readiness of the best technology for its conversion and use has been and still is a prominent, factor for the development of the international economy and consequently the subject of strategic considerations and measures.
At the beginning of the century the enormously increasing demand for energy, for industrial use, transportation and homes in interplay with the nations' efforts for self-sufficiency spurred the industrialised countries to intensify research into improved utilisation of their fossil fuels. The First World War and the post wartime made the strategic and economic rank of coal even more evident, stressing the necessity of intensified relevant research also. New scientific journals appeared e. g.: *"Brennstoff-Chemie"* (Fuel-Chemistry) in Germany and "*Fuel"* in Great Britain both in 1921/22. Economic strategies and political interests and the attraction of coal for science along with methods and instruments under development in physics and chemistry pushed progress of coal technology and research at that period. Their outcome in petrology, characterisation and classification of coal, in developing direct and indirect liquefaction and the first steps to explain mechanisms and kinetics of reactions are admirable. Some outstanding examples must be mentioned:
In 1913 at an age of 27 years *Friedrich Bergius* made studies into the application of high pressure and temperature. In doing so, a pure academic work for clearing up coalification became the immediate fundament of direct liquefaction of coal [1]. In 1921 *Fritz Winkler*, 33 years old, investigated the possibility to produce activated carbons by partial gasification of lignite with steam. Thereby he detected the phenomena of fluidisation in the "Winkler Reactor"[2]named after him . The synthesis of liquid hydrocarbons was discovered by *Franz Fischer* and *Hans Tropsch* in 1926, as a fruit of coal orientated activities [3]. Pioneering work was carried out during the 30ies in the field of kinetics of carbon combustion at the MIT under the direction of *Hoyt C. Hottel* [4 5]. They discovered the principles of macrokinetics of gas-solid reactions occurring in coal combustion, which in the meantime became a well-known theory for gas -solid reactions in porous solids.
The enthusiasm and results of coal research going on from that characterises the situation in the 50s and early 60s also. During this phase a whole series of public or private institutions had been founded, stimulating coal research. A series of in total 7 international biennial conferences with up to say 160 participants started in 1955, a sign of the increased self-confidence of coal scientists. In the late 50s however, oil, natural gas and even nuclear energy had grown up into challenging competitors pushing coal from the first place: Coal and its science lost interest in a dramatically short period of time.
However this wine of seeming abundance of energy and fuel was watered down relatively soon by the message of the "Club of Rome": Supplies of fossil fuels and other resources are limited, especially those of oil and natural gas. Leaders in politics, industry and science reflected on coal again: In the USA it was the program "Substitute Natural Gas (SNG) from Coal" starting in the 60s. New perspectives had been opened for coal science and technology [6]. A large variety of processes and concepts on *hydrogasification* were proposed for development and research [7]. The German development of a nuclear-aided gasification processes was initiated in 1968 [8 9]. The impact of this approach on coal science especially on the investigation of gasification of coal and lignite [10] in Germany at the end of the 60's was enormous.
From October 1973 onwards the banner of coal science seemed to be erected again for good. A sudden shortage of oil along with a dramatic rise in price, unexpectedly for many of us, stimulated energy research in practically all areas. A fresh impetus was given to research into the chemical and physical structure of coal, as well as its gasification and hydrogenation, as the basis of development of new, and optimisation of known, technical processes [11]. Coal science was going strong and as evidence of it the ICCS was revived in 1981 by initiative of the "International Energy Agency-IEA" and its "Working Party on Coal". Financially supported by the public and by private industries of Australia, Germany, Japan, Canada, The Netherlands, Spain, UK, USA and at the beginning also of Sweden, the Conferences took place biennially, hosting often more than 500 participants[12 13 14 15 16 17 18 19 20] . The last one took place in China 99 [21]. - After years of concentration among the publications on coal science publication, new journals appeared. "Fuel Processing Technology" started in 1977, and in 1987 "Energy and Fuels", by the "Fuel Division" of the "American Chemical Society". A novelty has been the well-recognised publications of "IEA-Coal Research" in London, founded in 1975 by the IEA supported by IEA-Member Countries [22].
A political issue that became of high priority in the seventies and eighties was the *protection of the environment*, the aims of which gave a lot of new impulses to coal science. Special attention was given to research into coal combustion with particular regard to the efficient use of coal as well as to the formation and abatement of all kind of pollutants and hazardous species. NOx formation was found to be unexpectedly complicated and, therefore, of special scientific interest [23 24 25]. Relevant investigations included research into the nature of nitrogen-compounds in the chemical structure of coal. Also, coal minerals and their „products", ash and slag, in their different roles as sources of emissions, wastes or raw material for further use, won the interest of scientists. In the last decade the *protection of the earth's climate* has been an additional issue influencing coal science.

Interaction with other Sciences

Regarding its strong connection with chemistry, physics and chemical engineering, it is evident that every suitable progress was used for research on coal:
The exploration of chemical structure of coal has lead to comprehensive and well-defined results on the basis of developments of *spectroscopic methods* only. These are IR- and UV- spectroscopy and X-ray structural analysis in the 50s and 60s and the proton and solid state-NMR and the X-ray absorption spectroscopy in the last 20

years. *Thermal analysis* including Thermogravimetry (TGA) and Differential Thermal Analysis (DTA) had reached a technical status in the 60s that it became a reliable instrument for the investigations into coal pyrolysis, gasification, combustion and others. Small mass-spectrometers, IR-analysers and gas-chromatographs became routine tools for on-line gas analysis and completed these methods. The development of big *mass spectrometers* and an increasingly improved *hydrocarbon gas chromatography* [26] enabled coal scientists to make structural analysis. In order to investigate the porous structure of coal, char and coke methods have been developed since the beginning of the 30s already, to measure *porosity* and to characterise qualities and quantities of the *internal surfaces.* The most important ones are based on the work of Brunauer, Emmett and Teller [27] and Dubinin [28] introducing sorption of gases to characterise micropores and of Ritter and Drake [29] developing mercury intrusion for the characterisation of macropores. The enormous development of *microbiology and biotechnology* has opened the door for fundamentally new methods in coal science in the last decade [30]. All of us experience the progress achieved by the development and application of *computers* and the useful algorithms available for data acquisition and evaluation and the possibilities of *modelling and simulation* of structures, reactions and reactors.

Chemical Structure and Structural Models

Attempts made in the first half of the century resulted hardly in saying much more with regard to chemical structure of coal than elementary analysis and qualitative hints to the main groups present in coal [31]. Later the dynamic development of spectroscopic methods allowed to analyse the products of the different destructive reactions with increasing precision and confidence. *Coal models* were proposed, in which the well-defined fragments were composed again taking into account the knowledge about structures and bonds in macromolecules. Given had made one of the first proposals [32]. Today's knowledge is based on quite a few ideas, which had been published among others by Wiser [33], Wender [34] and Shinn [35]. Their basic assumptions and their main characteristics are reviewed e. g. by Davidson [36], and more recently by Haenel, Collin and Zander[37] [38]. Experiments on coal swelling in organic solvents suggested a 3-dimensionl structure. Spiro has given notice to this by vivid space models [39]. Of importance is the discovery of "guest molecules", hosted by the network, forming the *"mobile phase"* [40].
The progress achieved in the past two decades, has confirmed and completed the picture convincingly. The NMR-studies as performed by the group lead by Pugmire [41] and the investigations into nitrogen functionalities by Burchill and Welch [42] shall be mentioned here as good examples. - The models have been utilised with great success to investigate the mechanisms of pyrolysis, hydrogenation and hydrocracking reactions including the formation of the products and its control by experimental conditions and catalysts.

Reactions based on Bond Cleavage

On the basis of the chemical structure model of coal Jüntgen has developed a reaction scheme for the *mechanism of coal pyrolysis* [43]: Primary breaking of weaker bonds between the aromatic units followed by cracking, hydrogenation or agglomeration resulting in gas, condensable liquids, and char. The coal model and the reaction scheme based on it demonstrate its power in the conclusive explanation of the influence of experimental conditions like rate of heating, pressure and presence of hydrogen, on the distribution and the quality of the products[44]. This progress has opened the door also for the simulation of pyrolysis by computer modelling. Using the results on the macromolecular structure Pugmire [45], Solomon [46] and Niksa [47] each have developed and successfully tested relevant *models*. They predict the pyrolytic behaviour of different coals including the yields of the products at different conditions. The reaction mechanism of *direct coal liquefaction* is almost identical to that of pyrolysis. A scheme published by F. Derbyshire demonstrates the similarities[48].

To describe the kinetics of the products' formation H. Juentgen, K. H. van Heek [49] and co-workers have developed equations, considering the thermal bond-breaking rate determining step, this being the prelude of the non-isothermal kinetics of coal pyrolysis [50] [51]. The equations derived are used for the description of the curves measured and result in kinetic data. The *non-isothermal kinetics* has been used widely to describe and evaluate thermal reactions with solid fuel, for reactor simulation e. g. of gasifiers and furnaces. Over and above that coal science has developed a sturdy method for the evaluation of experimental data, a tremendous enrichment of thermal analysis in general.

Physical Structure of Char and Coke and Heterogeneous Reactions

Coke and char have a distinct *porous structure* [52] reaching down into the dimensions of the molecular units. Important contributions to explain the development of inner surfaces under thermal treatment have been made by H. Marsh, A. Oberlin and others [53] [54] [55]. Concerning the heterogeneous gas-solid-reactions literature till the 30s contains mainly stoichiometric and thermodynamic calculations. Kinetic studies on combustion starting in the third decade were performed on "pure carbons" such as "spectric coal" or graphitic material. The important work of Hottel [4] has been mentioned. His results were further evaluated by Essenhigh and Howard [56], thereby acknowledging its importance for the understanding of *combustion kinetics*. A detailed theory describing the reactions in the different regimes was developed by Wicke, Hedden and Rossberg [57] in the 40ies and 50ies..
Char and coke from different natural coal or lignite, mainly investigated in the last 30 years, show enormous differences in *gasification rates* [58] [59]: The high reactivity of lignite chars is due to the catalytic influence of earth-alkalis, in particular Ca [60].. Chars from coal treated below 1000°C have a medium reactivity, whereas high-temperature-coke shows distinctly lower values. To investigate the influence of temperature during or after pyrolysis P. L. Walker and co-workers at Pennsylvania State University, USA, made essential experiments leading to significant interpretations [61]. - Coal research since long was looking for interactions between amount, properties and accessibility of internal surfaces of char and coke and their reactivity [62]. A simple correlation between total area and reactivity does not exist in general. But the assumption of the existence of special configurations on char/coke surfaces, the *"active centres"*, which react preferentially, was carrying on decisively. [63] [64] [65].

Concluding Remarks

The fundamental knowledge about origin, properties and reactions of coal, their characterisation with respect to scientific or industrial use, and the manifold skills and methods for the treatment of coal related scientific problems hitherto has contributed in many ways and often unseen to the development of efficient and clean coal technologies. But many excellent and promising results got stuck also in the attempt to transfer them into practice, remaining unfulfilled dreams of the researcher, examples are hydrogasification, catalytically aided

gasification, or hydropyrolysis. Even if nowadays coal is world-wide preferably used for electricity production and coke making, we can be pretty sure, that knowledge gained in the fields of liquefaction, gasification and pyrolysis, will become necessary for industrial processes, possibly soon, as inexpensive oil and gas will not last forever and will not be equally accessible for every country. The predictions of the Club of Rome since 1972 are valid generally, even if the chronological order has had to be shifted somewhat into the future. Thus, as a global view, new and especially improved processes for the clean utilisation of coal remain to be a steady task for coming generations of coal scientists and engineers. science and technology will start from there and other developing countries in the future.

References

[1] J. Ivon Graham, H. G. Shatwell, Fuel 2, 1923, p. 54
[2] P. Feiler, Die Wirbelschicht, (The fluidised bed) Schriftenreihe des Firmenarchivs der BASF, Ludwigshafen, Germany, 1972
[3] F. Fischer, H Tropsch, Ber. Dtsch. Chem. Ges. 59, 1926, p. 830
[4] C. M. Tu , H. Davis, H. C. Hottel, Ind. Eng. Chem. 26, 1933, p. 749
[5] J. M. Beer, J. B. Howard, J. P. Longwell, A. F. Sarofim, Combustion and Flame 117, 1999, p. 1
[6] Hottel, H. C. and Howard, J. B., New Energy Technology, MIT Press, Cambridge, Mass. 1971
[7] Clean Fuels from Coal, Sept. 10-14, 1973 - Symposium Papers, Institute of Gas Technology, Chicago
[8] Nuclear Engineering and Design, Special Issues: High Temperature Reactor for Process Heat Applications, 1975, p. 34 and 1984, p. 78,
[9] Kugeler,K., Neis, N. and Ballensiefen,G. Eds., Fortschritte in der Energietechnik, (Progress in Energy Technology) Monographien des Forschungszentrum Jülich, Bd. 8, 1993
[10] van Heek, K. H., Jüntgen. H. and Peters, W., J. of the Inst. of Fuel, 1973, p. 249
[11] Falbe, J., Chemierohstoffe aus Kohle, (Chemical Feedstock from Coal), G. Thieme Verlag, Stuttgart, Germany, 1977
[12] Proceedings International Conference on Coal Science, Düsseldorf, Germany, 7.-9. 1981, Verlag Glückauf Essen, 1981
[13] 1983 International Conference on Coal Science, Proceedings, Pittsburgh, USA,
August 15-19, 1983
[14] Proceedings 1985 International Conference on Coal Science, 28-31 October 1985
Sydney, N. S. W., Pergamon Press, Sydney 1985
[15] Moulijn, J. A., Nater, K. A., and. Chermin, H. A. G., Eds., 1987 International Conference on Coal Science, Maastricht, The Netherlands, Oct. 26-30,1987, Proceedings, Coal Science and Technology 11, Elsevier, Amsterdam, 1987
[16] 1989 International Conference on Coal Science Proceedings Vol. I, II, October 23-27,1989, Tokyo, Japan
[17] 1991 International Conference on Coal Science Proceedings, 16-20 September 1991, Newcastle, U. K.
Edited by the Int. Energy Agency Coal Research Ltd., Butterworth Heinemann Oxford 1991
[18] Michaelian, K. H. Ed., International Conference on Coal Science, September12-17, 1993, Banff, Alb. ,Canada, Conference Proceedings Vol. I, II, ISBN- 0-9697498-0-5
[19] Pajares, J. A. and Tascon, J. M. D. Eds., Coal Science, Proceedings of the Eighth International Conference on Coal Science, Oviedo, Spain, Sept. 10-15, 1995, Vol. I, II, Coal Science and Technology 24, Elsevier Amsterdam, 1995
[20]. Ziegler, A., van Heek, K. H., Klein, J. and Wanzl, W. Eds., Proceedings 9th International Conference on Coal Science, 7-12. 9. 1997, Essen Germany, Vol. I, II, III, DGMK Tagungsbericht 9702, ISBN -931850-20-X3
[21] Bao Qing Li, Zhen Yu Liu, Prospects for Coal Science in the 21st Century, Proc. 10th ICCS, Shanxi Science & Technology Press, Taiyuan , China , 1999
[22] IEA Coal Research The Clean Coal Centre, Annual Report 1997-1998, ISBN 92-90029-309-8
[23] Pohl, J. H. and Sarofim, A. F., Devolatilisation and oxidation of coal nitrogen, 16th Symp. on Combustion,
The Combustion Institute,1976, p. 491
[24] de Soete, G. G., Rev. Gen. Therm. Fr., 1989, No. 330-331, p. 353
[25] Wojtowicz. M. A., Pels, J. R. and Moulijn, J. A., Fuel, 1995, 74, p. 507
[26] A. G. Sharkey Jr, Spectrometry of Fuels, Plenum Press, New York, 1970
[27] S. Brunauer, P. H. Emmett, E. Teller, Journal of the American Chemical Society60, 1938, p. 309
[28] M. M. Dubinin, Chemistry and Physics of Carbon 2 , Marcel Dekker New York, 1966, p. 51
[29] H. L. Ritter, C. L. Drake, Ind & Eng. Chemistry. Analytical Edition 17,1967, p. 782
[30] Klein, J. et al., Coal in Biotechnology in Rehm H.-J. and Reed, G. Eds. Biotechnology Vol. 6b, VCH Verlagsges. Weinheim, 1988, p.499
[31] H. H. Lowry, Ed., Chemistry of Coal Utilisation I, II, John Wiley & Sons New York, 1945, 1947
[32] P. H. Given, Fuel, 39, 1960, p.147
[33] W. H. Wiser, Proc. EPRI Conf .Coal Catalysis Santa Monica, Cal., 1973
[34] I. Wender, Chemical Reactions and the Constitution of Coal in Chemistry of Coal Utilization, 2nd Suppl.
Ed. M. A. Elliott, J. Wiley & Sons New York, 1981, p. 520
[35] J. H. Shinn, Fuel, 63, 1984, p.1187
[36] R. M. Davidson, Molecular Structure of Coal, IEA Coal Research , 1980
[37] M. W. Haenel, G. Collin, M. Zander, Erdöl Erdgas Kohle 105,1989, p.71
[38] M. W. Haenel, Fuel, 71, 1992, p. 1211
[39] C. L. Spiro, Fuel 60, 1981, p. 1121; Fuel 61, 1982, p. 1080
[40] P. H. Given, A. Marzek, W. A. Barton, L. J. Lynch, B. C. Gerstein, Fuel 65, 1986, p.155
[41] M: S: Solum, R. J. Pugmire, D. M. Grant, Energy & Fuels, 3, 1989, p. 187
[42] P. Burchill, L. S. Welch, Fuel, 68, 1989
[43] H. Jüntgen Fuel 63, 1984, p. 731
[44] K. H. van Heek, W. Hodek, Fuel 73 1994, p. 886
[45] T. H. Fletcher, A. R. Kerstein, R. J. Pugmire, M. S. Solum, D. M. Grant, Energy & Fuels 6 1992, p. 414
[46] P. R. Solomon, D. G. Hamblen, M. A. Serio, S. Charpenay, Fuel 72 1993, p. 469
[47] S. Niksa, Combustion & Flame 100, 1995, p. 384
[48] F. Derbyshire et al. ULLMANNS's Encyclopaedia of Industrial Chemistry, Vol.A7, 1986
[49] H. Jüntgen, Erdöl und Kohle, 17.1964, p. 180
[50] H. Jüntgen, K. H. van Heek, Fuel 47 1968, p. 103
[51] H. Jüntgen, K. H. van Heek, Fuel Processing Technology 2, 1979, p. 261
[52] J. W. Patrick Ed., Porosity in Carbons, Edward Arnold, London 1995
[53] H. Marsh, E.A. Heintz, F. Rodrigues-Reinoso, Eds., Introduction to carbon tech., Univ. of Alicante, 1997
[54] H. Marsh, Carbon 29, 1991, p. 703
[55] A. Oberlin, in Chem. and Phys. of Carbon, Ed. P. Thrower, Vol. 22, Marcel Dekker New York, 1989, p. 1
[56] R. E. Essenhigh, R. Froberg, J. B. Howard, Ind. Eng. Chem. 57, 1965, p. 33
[57] E. Wicke, K. Hedden, M. Rossberg, BWK, 8, 1956, p. 264
[58] K. H. van Heek, H. Jüntgen. W. Peters, J. of the Inst. of Fuel, 1973, p. 249
[59] K. H. van Heek, H. J. Mühlen, Fuel 64, 1985, p. 1405
[60] A. Linares-Solano, C. Salinas-Martinez, D. Cazorla-Amoros, J. P. Joly, in reference 55, p. 409
[61] L. R: Radovic, P. L. Walker, R. G. Jenkins, Fuel 62, 1983, p. 849
[62] N. M. Laurendeau, Prog. Energy Combust. Sc. 4,p. 221
[63] N. R. Laine, F: J: Vastola, P. L. Walker, Journal of Physical Chemistry, 67, 1963, p. 2030
[64] E. Hippo, P. L. Walker, Fuel 54, 1975, p.245
[65] J. Lahaye, P. Ehrburger, Ed., Fundamental Issues in Control of Carbon Gasification Reactivity,
NATO ASI Series E: Applied Sciences - Vol. 192, Kluwer Academic Publishers, Dordrecht 1991

Progress in Coal Liquefaction Including a Discussion of Wilsonville Data

Anthony M. Valente* and Donald C. Cronauer**

* BP Products North America Inc., Naperville, IL
** Argonne National Laboratory, Argonne, IL

ABSTRACT

Activity in direct coal liquefaction research has passed through a number of swings since its inception. High activity levels included Germany=s production during WWII and research during the period of 1970 through 1992. A sizeable number of processes have been developed. Effort appears to have evolved toward a two-stage reactor concept with one or both stages containing active hydrogenation catalysts with supplemental and/or recycled mineral matter. A high point of research activity centered upon the Advanced Two-Stage Coal Liquefaction Facility located in Wilsonville, AL. A database was set up to correlate the effect of operating variables in their liquefaction of Illinois No. 6 seam bituminous coal. Overall preferred processing conditions for generating distillable liquids included the use of high reactor temperatures (>430EC) and a high process solvent resid concentration (>50 wt% if mechanically possible). The space rate of coal in the reactors should be set at a point where resid production is minimized. Significant results included lower coal conversion, hydrogen consumption, C_1-C_3 yield, IBP-350EF yield, and C_1-C_3 selectivity when using half-volume over full-volume reactors at similar conditions, including space velocities. These were apparently due to flatter reactor temperature profiles and lower catalyst to thermal volume ratios.

INTRODUCTION AND BACKGROUND

Research in the field of liquefaction of coal has passed through a number of phases since its inception with coking to recover liquids and gases in the 1840's. Direct liquefaction which involved the extraction of coal with a solvent at high temperatures and pressures was patented in 1913 by Bergius and commercialized soon thereafter. Direct liquefaction in combination with other routes to generate liquids was the primary source of fuels in Germany during WWII.

Additional research for this route to liquids followed in the US and elsewhere in the 1950's. Effort and funding decreased into the late 1960's. In the early 1970's crude oil prices rose and availability decreased. At this time, essentially a panic occurred with the amount of funding almost exceeding the number of staff and research and development facilities. Effort peaked in the next decade, and it has now fallen to a low level again. The only remaining effort of a major scale is that of Hydrocarbon Technologies, Inc. (HTI) in combination with China; their work is being discussed by Dr. Peizheng Zhou in this session.

Starting with fundamentals, coal is a solid with a low level of hydrogen (4 – 6 wt%) while the desired product liquid contains 10 to 15% hydrogen. Coal contains a sizeable amount of mineral matter (3 to 20%) and water (5% with bituminous coal to 30+% with subbituminous and lignites). It also contains a wide range of oxygen (2% to 20+%, and organically-bound sulfur (0.2 to 5%). Its level of nitrogen averages about 1%. To generate refinery feedstocks, catalytic hydrogenation is necessary at some step in the process. Common catalysts are molybdenium or tungsten oxides on alumina promoted by cobalt and/or nickel; these catalysts are sulfided prior to use. The pore size distribution and structure of the catalyst are important.

Laboratory and academic research has centered upon chemical structures and reaction mechanisms. Various groupings of products have been reported, such as aromatics, aliphatics, asphaltenes, preasphaltenes, asphaltols, maltenes, etc. In most cases these fractions were dependent upon the separation or identification technique. As far as a refinery feedstock is concerned, emphasis was placed upon distillate cuts, hydrogen and heteroatom contents and solid (or coking) levels.

There are a number of processes available for the direct liquefaction of coal. At least 18 process concepts have been developed, many through pilot plant or semi-works scale operation. A good summary of these processes has been issued by the UK Department of Trade and Industry.1

The overall process scheme is the following: 1. pulverized coal is mixed with coal-derived, recycled solvent; 2. the resulting slurry is reacted in one or more reactors at 350C to 450C (620K - 720K) for a period of about one hour or more; and 3. the resulting product is upgraded. The approach depends upon the type of feed coal, the desired characteristics of the product liquids, the availability of supplemental feed (hydrogen, carbon monoxide, treated solvents), solid separation schemes, gasification processes (by-product solids and/or gases), location and catalysts. To an extent, overall process development has evolved toward a two-stage route with one or both stages containing active hydrogenation catalysts with supplemental and/or recycled mineral matter.

COAL LIQUEFACTION RUNS AT WILSONVILLE, AL

An extensive series of liquefaction runs was made at The Department of Energy Advanced Two-Stage Coal Liquefaction Facility located in Wilsonville, Alabama. The facility was operated by Southern Company Services (SCS) with funding by the United States Department of Energy (DOE), the Electric Power Research Institute (EPRI), and Amoco Oil Corporation. The unit capacity was about 6 tons of coal per day. Operation occurred from 1970 through 1992. A description of the process and a summary of runs made using low rank coals have been reported.2, 3

Liquefaction runs which were made with bituminous Illinois No. 6 coal are discussed herein to show the scope of coal conversion and the distribution of products that can be achieved. Emphasis was placed upon close-coupled, integrated two-stage liquefaction (CC-ITSL) mode with and without interstage separation and "ashy recycle." Ashy recycle refers to the recycle of a portion of the mineral matter and unconverted coal with the recycle solvent to the feed tank of the first reactor. This recycle increased coal conversion and liquid yield due to the catalytic activity of recycled pyritic iron in the coal minerals. Solids separation was achieved using a Kerr-McGee ROSE-SRITM unit, which was placed after the second reactor. For reference, coal conversion and yields were reported on a basis of weight per unit of MAF (moisture ash free) coal.

The addition of a supported catalyst in either the first or second stage or both stages was also studied at Wilsonville. All the runs using Illinois No. 6 seam coals in the close-coupled mode were made with a supported catalyst in either the second stage only (thermal/catalytic or T/C) or in both stages (catalytic/catalytic or C/C). The format in which the Wilsonville pilot plant data was reported has changed over the years. A database design for runs in CC-ITSL mode was developed in order to standardize their data. All runs at the Wilsonville pilot plant have been made in close-coupled mode since 1985 and Illinois No. 6 seam coal has been used in more of these recent runs than any other single coal.

The database consisted of sixteen process variables that were used in a linear regression analysis of unit conversions and yields. Due to the recycle of high boiling liquids to form the coal slurry to the first stage, the two stages were interrelated. The products of the

first stage influenced the products of the second stage and vice versa. For this reason, the focus of this work is on the two-stages as a single unit.

The model suggested that the most influential variables are reactor temperatures, coal space rate, each stage's catalyst age, and process solvent resid concentration. Use of half-volume reactors caused lower C1-C3 yield, IBP-350F yield, C1-C3 selectivity, coal conversion, and hydrogen consumption. This was likely due to the lower catalytic/thermal volume ratio and flatter temperature profile of the half-volume versus the full-volume reactors.

From these models and correlations, an estimate of the optimum conditions for liquefaction of Illinois No. 6 coal was made. The regression equations suggested that increasing temperature in both stages increased the distillable liquid production and increased resid conversion. For reference, the temperature effects in both reactors were similar and essentially overlapped, so only that of the First Stage is included herein as Fig. 1. As the temperatures increased, there was a loss of a distillate product due to gas production; however, the production of distillable liquids increased more than the C1-C3 gas make. A plateau where higher temperatures cause no increase in a distillate liquid yield and an elevated gas make would likely be reached. Wilsonville, however, did not demonstrate this point of diminishing liquid yields. Minimizing the catalyst age (and increasing catalyst replacement) showed improvement in yields (Fig. 2). The yields of hydrocarbon gases and 350-450F liquids did not change significantly as the catalyst age increased. This observation implies that the formation of low boiling hydrocarbons was primarily thermal.

The optimum coal space rate was difficult to surmise. Coal conversion was a very weak function of a space rate (Fig. 3). If converting coal to liquids is the primary goal, then the space rate of coal can be increased significantly from that demonstrated at Wilsonville. The amount of low boiling products would suffer. As space rate was increased, the amount of resid became significant. If an all distillate product slate (no resid production) is desired, then the space rate should be pushed higher at given conditions until resid is produced. At the base conditions shown in Fig. 3, this would be around 35 lb/hr*ft3.

Process solvent resid concentration should be increased to the operability limit. Recycling more resid allows more to convert to distillable liquids, as shown in Fig. 4. Coal conversion also showed a marginal increase as resid concentration in the recycle solvent was increased.

The regression models showed that the Wilsonville reactors when run at half-volume generally demonstrated lower C1-C3 yield, IBP-350F yield, coal conversion, and hydrogen consumption. Distillate yield was, however, not significantly affected by using half-volume reactors. The half-volume reactors exhibited better internal mixing and would thus be more similar to a commercial reactor than full-volume reactors.

ACKNOWLEDGMENT

The authors would like to sincerely thank D. R. Porter for his statistical services, R. J. Torres-Ordonez and A. J. Swanson for many helpful discussions, and J. R. Lerman for her graphics assistance. The authors are indebted to Drs. R. E. Lumpkin, A. Basu, and N. C. Stewart for their aid in the field of coal liquefaction and numerous individuals at DOE and Southern Company Services who participated in the operation of the Wilsonville facility. A portion of this work was performed under the auspices of the U. S. Department of Energy under contract number W-31-109-ENG-38.

REFERENCES

1. Dept. of Trade & Technology, UK, Coal Liquefaction: Technology Status Report 010, Oct. 1999 (See www.dti.gov.uk/ent/coal)
2. Lamb, C. W., Nalithan, R. V., Johnson, T. W., PREPRINTS: ACS Div. Fuel Chem., 1986. 24, 1091.
3. Munkvold, G., Valente, A. M., Cronauer, D. C., PREPRINTS: ACS Div. Fuel Chem., 1994. 39(1), 92.

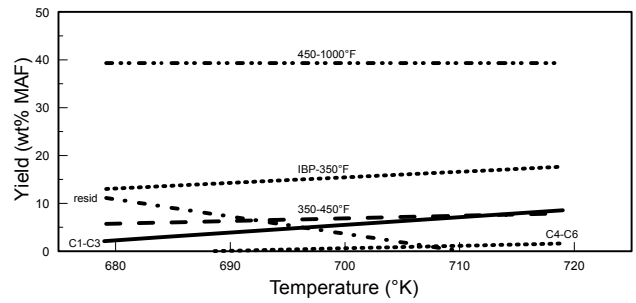

Figure 1. Reactor No. 1 Temperature Effect on Yields

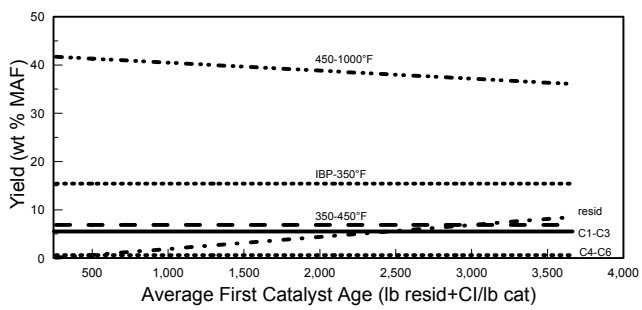

Figure 2. Effect of Reactor No. 1 Catalyst Age on Yields

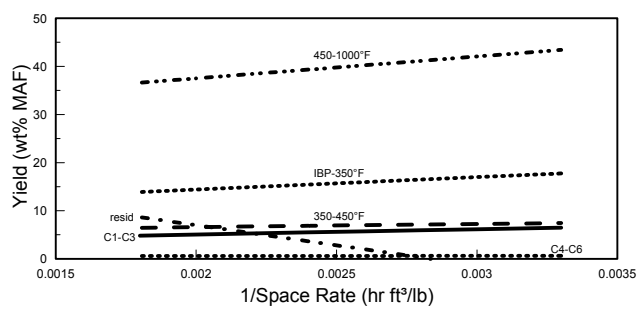

Figure 3. Inverse Space Rate Effect on Yields

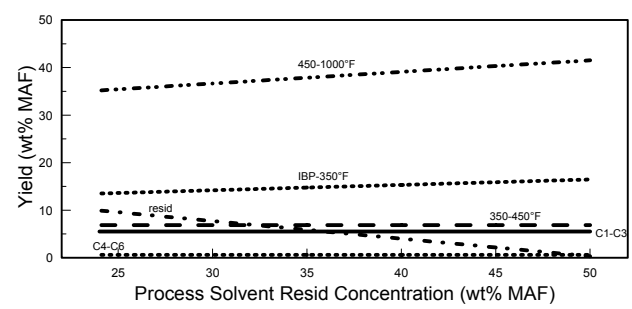

Figure 4. Recycle Resid Concentration Effect on Yields

PROGRESS TOWARD THE COAL-FINERY

Harold H. Schobert

The Energy Institute, Penn State University
University Park, PA 16802

Introduction

The conversion of coal to thermal energy or to other fuel forms has usually been considered in the context of a single product. For example, in the direct liquefaction of coal, the goal might be production of the maximum possible liquid yield. An alternative approach is to recognize that there may be valid technical and economic reasons for pursuing a multiple-product strategy, in which coal would be converted to several products—some combination of thermal energy, synthetic fuels, chemical feedstocks, and carbon materials—in a single plant. Such plants have been called coal refineries, coal-fineries, or coalplexes [1]. This paper provides examples of progress, mostly at a laboratory scale, in developing specific experimental findings that can lead to conceptual design of a coal-finery.

Synthetic Liquids, Phenols, or Both

There has been a large effort at Penn State for more than a decade to develop an aviation gas turbine (jet) fuel that would resist pyrolytic decomposition at temperatures to 480°C for up to two hours. One approach to the formulation of such a fuel is to produce a liquid with high concentrations of decalins, to take advantage of the excellent intrinsic pyrolytic stability of these compounds. The increasing dependence of the U.S. on imported petroleum, and the abundance of two-ring structures in some coals, encourage considering producing this fuel from coal.

The direct liquefaction of coal for the specific purpose of making jet fuel was pioneered by Burgess [2,3]. One of her findings was that careful attention must be paid to the structural features present in the coal, primarily elucidated by pyrolysis/ GC/MS and ^{13}C NMR, for feedstock characterization [4]. Burgess showed the possibility of producing high yields of two- and three-ring compounds (up to 50% on a dmmf coal basis) provided that the appropriate coal was selected. In her work, the best coal was Pittsburgh No. 8 hvA bituminous. Although a high conversion was achieved, and the liquid was rich in two-ring structures, it also contained significant amounts of phenols, about 10–15% yield. Rather than consider downstream hydrodeoxygenation of the whole product, the phenols were removed by a caustic wash.

If one were to focus only on production of jet fuel, then simultaneous formation of phenols in significant yield could be a detriment to Burgess's process. However, Song and I have argued that significant commercial potential exists for coal-derived phenols [5,6]. Therefore, direct liquefaction of Pittsburgh No. 8 coal at the conditions developed by Burgess (two-stage liquefaction with sulfided molybdenum catalyst and dihydrophenanthrene solvent) could lead to the co-production of a synthetic liquid fuel plus phenols that are not a nuisance, but rather have economic value in their own right.

Subsequently, Kirby investigated the possibility of a "one-pot" liquefaction with simultaneous hydrodeoxygenation [7-11], with bimetallic organometallic compounds as catalyst precursors. It was not intended that such compounds be used on an industrial scale (absent remarkable breakthroughs in their synthesis and handling), but rather sought to explore the potential process benefits from bimetallic dispersed catalysts. Kirby's study included three coals that provided a range of rank (subbituminous B to high-volatile A bituminous), oxygen content, and, presumably, oxygen functional groups. He showed that the possibility exists to produce high yields of synthetic liquid fuel, *or* high yields of phenols, *or* to co-produce synthetic fuels *and* phenols, provided that the appropriate selection is made of the coal feedstock and the catalyst used [11]. This finding provides significant flexibility in meeting demand for synthetic liquids, for phenols as chemical feedstocks, or both.

Synthetic Liquids and Coke

The intention to produce an advanced thermally stable jet fuel in a commercial-scale demonstration in 2005-2010 has shifted focus away from direct liquefaction, because no liquefaction plants are under construction in the U.S., nor even appear to be in an advanced planning stage. Instead, development now centers on the addition of coal, or coal tar derivatives, to existing refinery infrastructure. Following a suggestion by E.T. Robinson, then of BP Oil, one process being considered is addition of coal to delayed cokers, along with the customary petroleum feed. We have coined the name "co-coking" for this process.

Conceptually, co-coking would provide a liquid product that, on fractionation and hydrotreatment, could be used as synthetic fuel, along with a coke as a co-product. If some of the desirable two-ring structures in the coal would be liberated into the liquid product, hydrotreating would provide a decalin-rich, pyrolytically stable fuel. If, at the same time, the interaction of the coal with the petroleum stream could produce a coke of use for production of carbon materials (i.e., rather than simply a fuel coke), then the by-product credits for the coke could have an impact on the economics of the overall process. In the most favorable scenario, production of a material like needle coke might be the economic "driver" that would more than compensate the expense of producing the jet fuel.

Initial scouting studies by Martin et al. showed the promise of the idea [12,13]. Her work was followed up by Fickinger [14-17] and now by Escallon [18]. A key has been the use of highly fluid coals, particularly to match the temperature of maximum fluidity, or at least most of the plastic range, of the coal with the temperature in the coker. From optical microscopy, it appears that this temperature matching provides the optimum opportunity for coal-petroleum interactions. Yields from co-coking Powellton hvA bituminous coal with FCC decant oil at 465°C were 55-60% total liquids, with distillate boiling in the jet fuel range being 10–12% of the total product yield [17].

It is important to evaluate the prospective uses of the coke, and to assess its potential application beyond use as fuel coke. The most detailed study undertaken so far by Badger et al., studied the possibility of using the "co-coke" as a replacement for petroleum coke in anodes for aluminum smelting [19]. Laboratory-scale test anodes from this "co-coke" exceeded all specifications for anodes, with the sole exception of ash value. Further work on cleaning the parent coals could potentially allow meeting the ash specification as well. Other possible applications of the "co-coke" remain to be investigated, e.g., production of specialty graphites or molded graphite electrodes.

Anthracite

The future for anthracite in traditional combustion applications appears to be bleak. However, there are remarkable opportunities for use of anthracite in the production of premium carbon materials [20]. In part, this is because anthracite already *is* a carbon material, being ≥90% carbon, most or all of which is in large aromatic structures.

Recently, Pappano has shown that anthracite can be graphitized at temperatures ≥2500°C [21]. However, not all anthracites graphitize to the same extent when heat-treated at

identical conditions. Atria has shown that the difference in behavior of anthracites can be related, at least in part, to structural differences [22]. Pappano and his colleagues have shown the possibility of producing a product meeting the specifications of some specialty-grade graphites by replacing the petroleum coke normally used with a selected anthracite [23]. This finding could represent a potential new market for anthracite.

The conventional approach to producing specialty graphites, in addition to using a petroleum coke as the so-called filler, uses coal tar pitch as the binder for the solid particles. The decline of the metallurgical coke industry, and the prospect that there will never be another by-product coke oven battery built in the U.S., calls into question future availability of coal tar pitch. In collateral work, Andrésen studied the possibility of making from anthracite not just a replacement for coal tar pitch, but actually a superior binder [24]. His work has shown that hydrogenation of anthracite at 300°C in the presence of 7 MPa H_2, sulfided molybdenum catalyst, and tetralin yields a pitch of softening point 207°C and atomic H/C ratio of 0.42 [24]. Test specimens of baked carbon bodies have been made successfully with this pitch.

Currently, there are plans to establish a commercial operation for the production of synthesis gas from anthracite in east-central Pennsylvania. The intent is to use the gas to produce low-sulfur, clean diesel fuel via F-T synthesis. However, shifting the synthesis gas to hydrogen would provide the necessary material for mild hydrogenation to produce Andrésen's binder pitch. That pitch, combined with unreacted anthracite, could be used for production of specialty graphite products. Further, Burgess is now conducting a scouting study on the exfoliation of anthracite to make a hydrogen storage medium, by treatment with strong acids followed by thermal shocking [25]. Thus, future vehicular fuel cell applications could use anthracite-derived hydrogen stored on exfoliated anthracite medium, possibly relying also on carbon components of graphitized anthracite and anthracite pitch.

Conclusions

A substantial amount of work over the past decade, albeit mostly at the laboratory scale, has provided data that show the potential for production of multiple products of bituminous and anthracitic ranks. The range of possible products includes distillate fuels (e.g., pyrolytically stable jet fuel), phenols for chemical feedstocks, coke for anode production, binder pitch, graphites, and hydrogen storage media. All of these products are of substantially higher value than the parent coals. Further development of these, and related, processes could establish the opportunity for coal to move aggressively into markets for specialty chemicals and premium carbon materials.

Acknowledgements. It is a pleasure to the many present and former colleagues who actually did the work discussed in this paper: John Andrésen, Joseph Atria, Mark Badger, Caroline Burgess, Maria Escallon, Anne Fickinger, Stephen Kirby, Shona Martin, Gary Mitchell, Peter Pappano, Chunshan Song, and Jasna Tomic. Funding for various of these studies has been provided by the Air Force Office of Scientific Research, the Air Force Research Laboratory, the Carbon Research Center, the Consortium for Premium Carbon Products from Coal, the U.S. Department of Energy, and the former Pennsylvania Energy Development Authority; I am grateful for this support.

References

[1] Grainger, L.; Gibson, J. *Coal Utilisation: Technology, Economics, and Policy*. Graham and Trotman: London, 1981; Chapter 20.
[2] Burgess, C.E. *Ph.D. Dissertation*. The Pennsylvania State University, University Park, PA, **1994** .
[3] Burgess, C.E.; Schobert, H.H. *Fuel Proc. Technol.* **2000**, *64*, 57.
[4] Burgess, C.E.; Schobert, H.H. *Energy Fuels*. **1998**, *12*, 1212.
[5] Song, C.; Schobert, H.H. *Proc. 16th Intl. Pittsburgh Coal Conf.* **1999**, CD-ROM publication, file 16-4.
[6] Song, C.; Schobert, H.H. *Energeia*. **2001**, *12(1)*, 1.
[7] Kirby, S.R.; Song, C.; Schobert, H.H. *Prepr. Pap.—Amer. Chem. Soc. Div. Fuel Chem*. **1995**, *40*, 993.
[8] Kirby, S.R.; Song, C.; Schobert, H.H. *Proc. 13th Intl. Pittsburgh Coal Conf.* **1996**, 466.
[9] Kirby, S.R.; Song, C.; Schobert, H.H. *Catal. Today*. **1996**, *31*, 121.
[10] Kirby, S.R.; Schobert, H.H. *Prepr. Pap.—Amer. Chem. Soc. Div. Fuel Chem.* **1997**, *42*, 643.
[11] Kirby, S.R. *Ph.D. Dissertation*. The Pennsylvania State University, University Park, PA, **2003**.
[12] Martin, S.C.; Tomic, J.; Schobert, H.H. *Prepr. Pap. Amer. Chem. Soc. Div. Fuel Chem*. **1997**, *42*, 121.
[13] Martin, S.C.; Tomic, J.; Schobert, H.H. *Proc. 9th Intl. Conf. Coal Sci.* **1997**, *3*, 1557.
[14] Fickinger, A.E.; Badger, M.W.; Mitchell, G.D.; Schobert, H.H. *Prepr. Pap.—Amer. Chem. Soc. Div. Fuel Chem.* **1999**, *44*, 106.
[15] Fickinger, A.E.; Badger, M.W.; Mitchell, G.D.; Schobert, H.H. *Prepr. Pap.—Amer. Chem. Soc. Div. Fuel Chem*. **1999**, *44*, 684.
[16] Fickinger, A.E.; Badger, M.W.; Mitchell, G.D.; Schobert, H.H. *Prepr. Pap.—Amer. Chem. Soc. Div. Fuel Chem*. **2000**, *45*, 299
[17] Fickinger, A.E. *M.S. Thesis*. The Pennsylvania State University, University Park, PA, **2000**.
[18] Escallon, M.M.; Mitchell, G.D.; Schobert, H.H. *Prepr. Pap.—Amer. Chem. Soc. Div. Fuel Chem*. **2003**, *48* (in press).
[19] Badger, M.W.; Mitchell, G.D.; Karacan, O.; Herman, N.; Senger, B.; Adams, A.N.; Schobert, H.H. *US Dept. Energy Rept.* No. DE-FC26-98FT40350, **2001**.
[20] Andrésen, J.M.; Burgess, C.E.; Pappano, P.J.; Schobert, H.H. *Fuel Proc. Technol.* **2002** (submitted).
[21] Pappano, P.J. *Ph.D. Dissertation*. The Pennsylvania State University, University Park, PA. **2003**.
[22] Atria, J.V.; Rusinko, F., Jr.; Schobert, H.H. *Energy Fuels*. **2002**, *16*, (in press)
[23] Schobert, H.H.; Pappano, P.J. *US Dept. Energy Rept.* No. DE-FC26-98FT40350, **2000**.
[24] Andrésen, J.M.; Zhang, Y.; Burgess, C.E.; Schobert, H.H. *Fuel Proc. Technol.* **2002** (submitted).
[25] Burgess, C.E. *Unpublished data*. The Pennsylvania State University, University Park, PA. **2002**.

HTI Coal Conversion Technologies in China

Peizheng Zhou and Theo L.K. Lee
Hydrocarbon Technologies, Inc.
Lawrenceville, New Jersey

Introduction

Hydrocarbon Technologies, Inc. (HTI), its predecessor first founded in 1943 and currently a subsidiary of Headwaters Incorporated, has a long history of developing technologies for converting coal and heavy oil into liquid transportation fuels and chemicals. This presentation describes, in particular, development of HTI coal conversion technologies, including direct coal liquefaction and indirect coal liquefaction, and commercialization efforts of these technologies in China.

Direct Coal Liquefaction (DCL)

Direct coal liquefaction is a technology catalytically converting coal directly into liquid transportation fuels under hydrogen pressure and temperature. HTI has developed under the auspices of U.S. Department of Energy (USDOE), a cost-efficient DCL technology, HTI Coal^{TM} Process. This process operates at a moderate 19 MPa system pressure and 425-450°C reactor temperature and has the following features:

- Two-stage back-mixed (slurry-phase) liquefaction reactors, with relatively simple structure, uniform temperature distribution and ease of temperature control;
- highly active and inexpensive dispersed iron-based catalyst, HTI GelCat^{TM};
- Optional interstage separator;
- Ashy recycle to enhance catalytic function;
- Fixed-bed Stabilization hydrotreating, either in-line or off-line, to obtain environmentally friendly, very clean liquid fuel products;
- Solvent de-ashing to reject inert materials and coal ash and to recycle heavy organics (de-ashed oil or DAO) to maximize oil yield.

Figure 1 is a schematic of the HTI Coal Process^{TM}, showing both in-line and off-line hydrotreating options. Features described above make elevated coal conversion and high oil yield achievable, usually 8-12% higher in distillate yield compared with other direct liquefaction technologies without ashy recycle and DAO recycle. By hydrogenation of coal followed by hydrotreatment of the coal-derived distillate, DCL product has very low sulfur and nitrogen content, and is free of metals and non-distillable resid. These features also yield a good site-specific plant economics, making it economically viable when world oil price is above around $22-28/bbl.

The U.S. Department of Energy (USDOE) has funded the development of direct coal liquefaction technology since the 1970's oil crisis. In 1996, as part of its Proof-of-Concept Program, the USDOE recommended HTI's direct coal liquefaction technology to the Sate Science and Technology Commission of China and supported signing of pre-feasibility study and "license in principle" agreements with the Shenhua Group, China's largest coal enterprise, for application of HTI DCL technology. HTI has conducted a number of bench-scale (25 kg/day) and Process Development Unit (PDU)-scale (3 metric tons/day) tests on various coal samples from Shendong coal field, and a pre-feasibility study including conceptual design. As part of the license-in-principle agreement, HTI provided Shenhua Group with a process design package including four sections: coal liquefaction, GelCat catalyst preparation, solvent de-ashing, and distillate hydrotreating; which constitutes an essential part of the official feasibility study of Shenhua coal direct liquefaction plant. In 2001, with the full support of the U.S. Department of Commerce (USDOC), the U.S. Trade Development Agency (USTDA) funded a technology verification testing. In April 2002, following pilot plant validation, China's State Development Planning Commission completed a comprehensive review of the Shenhua Project.

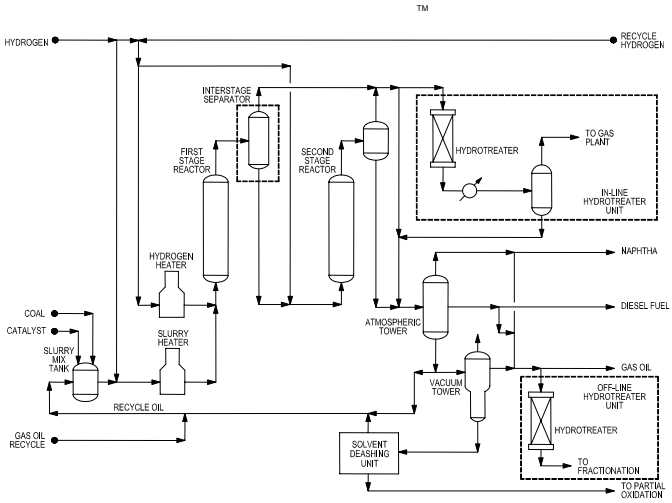

Figure 1. Schematic of HTI Coal Process

Shenhua Group selected the HTI Coal Process^{TM} to build the first large-scale commercial coal-to-liquid-fuels plant in the world, after extensive review of processes offered by competing technology providers around the world. On June 18, 2002, HTI signed a process license agreement with Shenhua Group for a direct coal liquefaction plant to be constructed in China, and a signing ceremony was held in Washington, D.C. U.S.A. Under the agreement, HTI will provide the technology license, process design, and technical services. China's State Council approved the official feasibility study of construction of the first direct coal liquefaction plant in China.

The plant will have an ultimate capacity of 50,000 barrels per day of ultra clean, low-sulfur, diesel fuel and gasoline produced from indigenous coal. The license agreement is for three reactor trains planned for the facility, each of which will process approximately 4,300 metric tons of coal per day. Construction of the first reactor train is expected to begin in early 2003 and the plant is expected to start up in 2005. The $2 billion facility will be located approximately 130 km south of Baotou, at Majiata, Inner Mongolia Autonomous Region of People's Republic of China. In addition to this first facility, Shenhua Group, a 15% owner of the technology, intends to construct three more direct coal liquefaction plants in foreseeable future. Shenhua Group has exhibited foresight in utilizing China's vast coal resources to provide the economy's future energy needs in a highly efficient and environmentally safe manner.

Indirect Coal Liquefaction (Gas-to-Liquids)

Different to direct coal liquefaction, the indirect coal liquefaction (or Gas-to-Liquids) technology first gasifies coal into a mixture of hydrogen and carbon monoxide, called synthesis gas or syngas, which in turn is catalytically converted via Fishcer-Tropsch (F-T) reaction into a spectrum of hydrocarbons and oxygenates spanning from methane to waxes. Based on catalyst function and operating conditions, product distribution can be focused on light hydrocarbons, naphtha fraction, or middle distillate, diesel fuels, or heavy products, waxes. One of the most attractive features of F-T synthesis is that its products are extremely clean, free of sulfur, nitrogen, and aromatics; and its diesel fuel product has an remarkably high cetane number, ranging from 76 to 80. Diesel fuels with such a high quality are extremely difficult and costly for refiners to produce from petroleum, if ever possible.

The state-of-the-art F-T technology uses slurry-phase reactors for uniform temperature control and lower reactor cost, however, harsh hydrodynamic conditions in slurry-phase reactors require F-T catalyst to possess high attrition-resistance in addition to high catalytic activity. Prevalent F-T catalysts are either iron- or cobalt-based. Many iron-based F-T catalysts, usually made by co-precipitation method, quickly breaks down into very fine, even sub-micron size particles which are extremely difficult to separate from wax products. This has been a major obstacle for its commercialization. Cobalt-based catalysts are believed to avoid catalyst breakdown and facilitate catalyst/wax separation problems, however, its high cost is hardly justified.

• HTI ZIP Catalyst

HTI has developed a novel iron-based F-T catalyst, HTI ZIP^{TM} catalyst, which is a promoted skeletal iron catalyst. This catalyst does not breakdown as easily as precipitated iron catalysts (Table 1) and is readily separable from waxy F-T products even by simple gravitation sedimentation (Table 2), thus the catalyst/wax separation difficulty is alleviated. HTI ZIP^{TM} catalyst has a high activity comparable to typical precipitated iron catalysts.

Table 1. Catalyst Particle Distribution (wt%)

Particle size (μm)	Fresh catalyst	HTI ZIP (after 500 hours operation in CSTR)	Precipitated iron (after 500 hours operation in CSTR)
44-74	100	25	40
2.5-44	0	70	48
<2.5	0	5	12

Table 2. Catalyst/Wax Separation by Gravity Sedimentation

	HTI ZIP catalyst	Precipitated iron catalyst
Catalyst in slurry, wt%	15	3.0
Settling temperature, °C	Solids concentration after settling (wt%) and efficiency (%)	
130	0.132 (99.1)	1.372 (54.3)
185	0.085 (99.4)	0.938 (68.7)
205	0.069 (99.5)	0.882 (70.7)

• HTI Slurry-Phase GTL Process

On the basis of the unique properties of HTI ZIP catalyst, a HTI Gas-to-Liquids (GTL) Process has been developed, which employs simple gravity settling for catalyst/wax separation (Figure 2). HTI just completed a feasibility study using HTI ZIP catalyst and slurry-phase GTL process for a Chinese client to convert natural gas-derived syngas to produce petrochemicals.

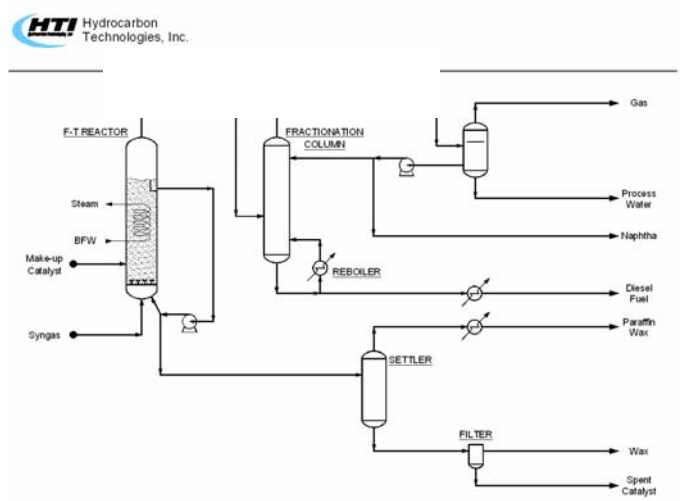

Figure 2. Schematic of HTI Slurry-Phase GTL Process

• HTI Integrated Fuel-Ammonia Co-Production Process

As a new development of HTI GTL technology, HTI has coined an innovative concept of integrating ammonia production with F-T synthesis, thus developed HTI Integrated Fuels-Ammonia Co-Production Process. This process was designed for small-size and medium-size, coal-based in particular, ammonia synthesis plants in countries such as China where imported ammonia fertilizers are threatening survival of local fertilizer producers. By retrofitting existing small- and medium-sized ammonia plants via addition of a GTL unit between syngas manufacture and ammonia synthesis, most of carbon monoxide and a portion of hydrogen in syngas are first converted to hydrocarbon fuels, while remaining hydrogen is further utilized to produce ammonia. Doing so, product slate of these plants is greatly changed to produce high-valued ultra clean diesel fuels and naphtha as major products, which have a broad market, while ammonia production is substantially reduced. Furthermore, the product slate (proportion of fuels and ammonia production) can be adjusted according to seasonal demand, thus providing significant flexibility in plant operation. Plant economics is thus dramatically improved. Preliminary assessment was conducted for eleven (11) small- and medium-sized ammonia plants, and results are very encouraging. Currently we are conducting a feasibility study for a Chinese chemical company to retrofit a small ammonia plant. This process is graphically demonstrated in Figure 3.

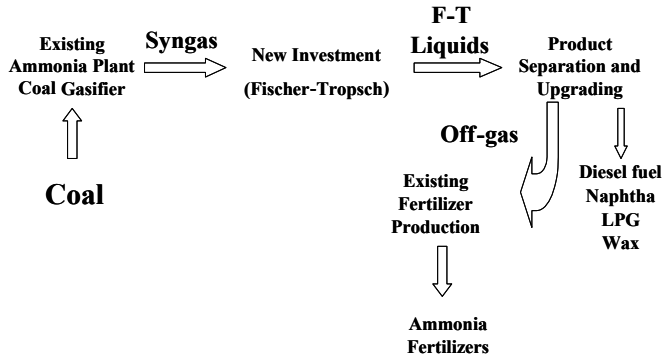

Figure 3. HTI Integrated Fuels-Ammonia Co-Production Process

Concluding Remarks

HTI has successfully developed a direct coal liquefaction technology which is co-owned by Shenhua Group and is currently being applied to the first large-scale commercial direct coal liquefaction plant. HTI is grateful to USDOE, USDOC, and USTDA for their strong support. HTI also developed promoted skeletal iron catalyst that is easy to separate from waxy F-T products, a Slurry-Phase GTL Process based on skeletal iron catalyst, and Integrated Fuels-Ammonia Co-Production Process which is believed to be very useful for retrofitting small- and medium-sized ammonia plants.

COAL-BASED JET FUEL: COMPOSITION, THERMAL STABILITY AND PROPERTIES

Suchada Butnark[1], Mark W. Badger[1], Harold H. Schobert[1] and Geoffrey R. Wilson[2]

[1]The Energy Institute, The Pennsylvania State University, C211 Coal Utilization Lab, University Park, PA 16802
[2]PARC Technical Services, 100 William Pitt Way, Pittsburgh, PA 15238

Introduction

The future use of jet fuel as a primary coolant for on-board heat sources of high-performance jet aircraft flying at high speeds will have an increased thermal stability requirement [1-3]. Currently, the conventional jet fuel for military aircraft, JP-8, is produced from petroleum through well-known refinery processes. However, it has been shown to be less stable in the pyrolytic regime than a coal-derived jet fuel [1]. Unlike long-chain alkanes in petroleum-derived jet fuel such as JP-8, the cyclic structures, such as cycloalkanes and hydroaromatics, in coal-derived material have shown significant improvement of thermal stability and high energy density. Thus, the coal-derived materials can be incrementally incorporated into existing refinery operation for thermally stable coal-based jet fuel production. The fuel, the so-called JP-900, is expected to not decompose when operating at pyrolytic temperatures as high as 900°F (482˚C).

In addition to the thermal stability improvement, the alternative jet fuel production has been developed due to the availability of potential coal resources as a strategic hedge against possible curtailment of petroleum imports. The pilot-scale production of prototype JP-900 has been performed on a petroleum refinery stream (light cycle oil (LCO)) and a coal-derived liquid (refined chemical oil (RCO)) described elsewhere [4]. In the present work, the candidate products from the hydrotreatment and dearomatization processes were studied to obtain the optimum composition that provides prototype JP-900 a highest thermal stability and appropriate physical properties.

Experimental

Samples.

The pilot-scale production of six jet fuel samples used in this work was done by PARC Technical Services, Harmaville, PA. The LCO, RCO and their 1:1 blend underwent severe hydrotreatment in order to achieve an extremely low heteroatom content, thus avoiding the poisoning of the noble metal catalyst used in the aromatic saturation step [4]. Crosfield NiMo catalyst was used for hydrotreatment of LCO, RCO and their 1:1 blend using at 710 psi and 685-725˚C [4, 5]. The hydrotreated products are called HDT LCO, HDT RCO and HDT (LCO/RCO).

The aromatic saturation was performed on each of the hydrotreated samples under 2100 psi and 400-500˚C, using Engelhard Pt-Pd catalyst [4, 5]. These saturated fuels are called SAT LCO, SAT RCO and SAT (LCO/RCO).

Characterization.

Jet fuel candidates was characterized using a Shimadzu GC-17 coupled with Shimadzu QP-5000 MS detector fitted with a Restek XTi-5 column with dimension of 30 m, 0.25 mmID and 0.25 μm df (5% phenyl film thickness). Nine basic compound classes were determined as:

Class 1: alkane
Class 2: alkene, alkyne, and cyclo-alkene
Class 3: cycloalkane
Class 4: hydroaromatic
Class 5: alkylbenzene
Class 6: naphthalene and methylnaphthalene
Class 7: other aromatics (biphenyl and 3-, 4-ring aromatics)
Class 8: decalin and methyldecalin
Class 9: tetralin and methyltetralin

For a quantitative GC analysis, tetrahydrofuran, an internal standard, was used to quantify the weight percentage from GC intensity of nine classes' major compounds.

Thermal Stability in Batch Conditions (Static Test).

The thermal stability tests of JP-900 fuel candidates have been studied in various flow systems in autoxidative and pyrolytic regimes [6, 7]. In this work, the static tests in batch reactors have been performed in the pyrolytic regime at very high temperatures in the absence of oxygen [8]. Pyrolytic stability was determined by heating 5 ml of sample in a 25 ml microautoclave at 480°C under 100 psig of UHP N_2 for 5, 15, 30, 45, 60, 120, 180 and 240 minutes. After completion each pyrolysis run, the micro- autoclave was cooled and the weight percent of the solids, liquids and gases produced was determined. The method is described elsewhere [1, 9] and the error in the measurements is about ± 0.1 wt% [10]. The liquid products were also analyzed by GC/MS.

Physical Properties Testing.

Net heat of combustion, an indication of combustion performance, was measured using a Parr Calorimeter (Model 1563) followed ASTM D 2015. The error associated with the measured value was ± 60 BTU/lb.

Flash point in this study was measured using a continuously closed cup flash point tester (MINIFLASH-FLP from Grabner Instruments), which used 1-mL sample with no open flame and 30-second manipulation time. The repeatability was ± 2˚F.

The measurement of Saybolt universal viscosity was performed at 100˚F in Saybolt universal seconds (SUS). The conversion of Saybolt universal viscosity to kinematic viscosity in centistokes (cSt) followed the ASTM D 2161.

Smoke point is the minimum flame height at which soot comes from a laminar diffusion flame tip generated by a standard wick burner. It was measured under ASTM D 1322 and could predict the soot formation tendency of aviation gas turbine fuels. The repeatability of the test was 2 mm.

Results and Discussion

Chemical Composition of Samples.

Table 1 displays the nine compound classes taken from the conventional JP-8 and six prototype JP-900 fuels. Unlike JP-8, all six fuel candidates have more cyclic structures than long-chain components. The hydrotreated fuels (HDT LCO, HDT (LCO/RCO) and HDT RCO) show a greater distribution of components in different classes and have higher aromatic and tetralin contents. Upon saturation, the major components for saturated fuels (SAT LCO, SAT (LCO/RCO) and SAT RCO) were converted to cycloalkanes, primarily decalin. Decalin and tetralin are preferred components for prototype JP-900 [11-13]; however, it is also important to take the other properties into consideration.

Table 1. The Overall Composition (in weight%) of Conventional JP-8, Hydrotreated and Saturated Fuels.

Fuel	Class 1	Class 2	Class 3	Class 4	Class 5	Class 6	Class 7	Class 8	Class 9
JP-8	72.11	5.65	9.80	0.63	7.92	2.27	1.16	0.00	0.46
HDT LCO	15.30	8.03	2.85	2.71	27.52	11.00	0.41	11.24	20.94
HDT (LCO/RCO)	6.66	0.55	2.54	7.35	10.97	12.06	12.13	11.56	36.17
HDT RCO	0.50	0.00	2.30	7.33	3.77	16.93	17.68	13.13	38.37
SAT LCO	14.61	21.01	19.92	0.00	0.58	1.94	0.00	35.21	6.73
SAT (LCO/RCO)	6.24	7.44	21.92	0.00	0.15	0.00	0.00	61.66	2.58
SAT RCO	3.13	3.07	19.73	0.00	0.04	0.00	0.00	74.04	0.00

Thermal Stability in Batch System.

After thermal stressing of hydrotreated and saturated fuels in pyrolytic regime at different resident times, the solid deposits and gas formed were collected, presented in term of remaining liquids (stressed fuels) in Figure 1.

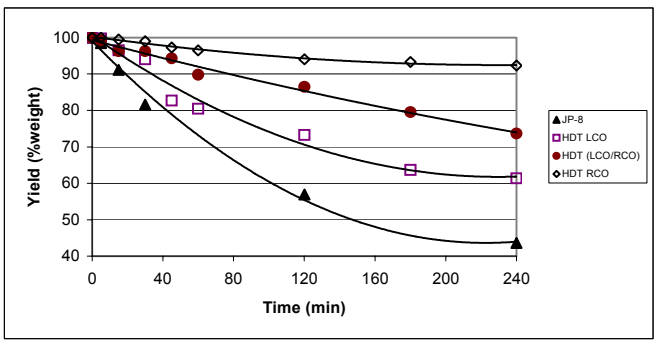

(a)

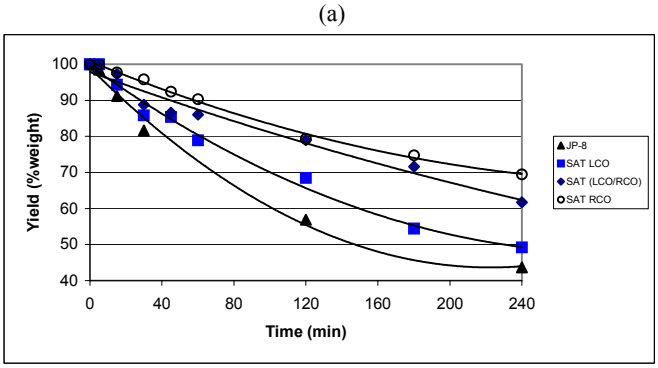

(b)

Figure 1. Remaining liquid after being stressed at 480˚C compared to JP-8: (a) hydrotreated fuels and (b) saturated fuels.

A Simple Kinetic Model.

To study the jet fuel reaction in batch system, simple kinetic models of similar hydrocarbon mixture have been previously discussed [14, 15]. However, it is still impractical to model the chemical changes of all components of a real mixture like jet fuel that is comprised of hundreds of chemical species [16]. For six jet fuel candidates, a simple model is proposed to describe the time dependence of the liquid degradation to gas, solid and remaining stressed liquid (Equation 1). The stressing at 480˚C in batch system at long resident time can represent the most severe thermal stressing that the fuels can experience.

Liquid degradation:

$$\text{Fresh liquid } (l_o) \xrightarrow{k_{app}} \text{Gas } (g) + \text{Solid } (s) + \text{Stressed liquid } (l) \quad (1)$$

The initial concentration (weight) of fresh liquid is denoted by C_{lo} whereas the amount remaining after a particular thermal-stressing time (t) at 480˚C is expressed by C_l. Assuming an apparent first-order equation, the rate of liquid degradation (r_l) can be written in the form:

$$r_l = -dC_l/dt = k_{app}C_l \quad (2)$$

Therefore;

$$C_l = C_{lo} \exp(-k_{app}t)$$
$$\ln [C_l/C_{lo}] = -k_{app}\, t \quad (3)$$

The plot of ln $[C_l/C_{lo}]$ vs t gives a slope $-k_{app}$ (an apparent rate constant). Figure 2(a) and 2(b) show that the degradation rate of JP-8, hydrotreated and saturated fuels behave good fittings with a first-order model. Thus, the apparent degradation rate constant can be quantitatively expressed in the trends of thermal stability for all fuels. As displayed in Table 2, both fuel candidates, especially HDT (LCO/RCO) and HDT RCO, have shown lower apparent rate constants than that of JP-8. Especially, the HDT RCO, dominated by its tetralin component, has exhibited the lowest thermal degradation. Considering the apparent degradation rate constants, all jet fuel candidates are more stable than the JP-8.

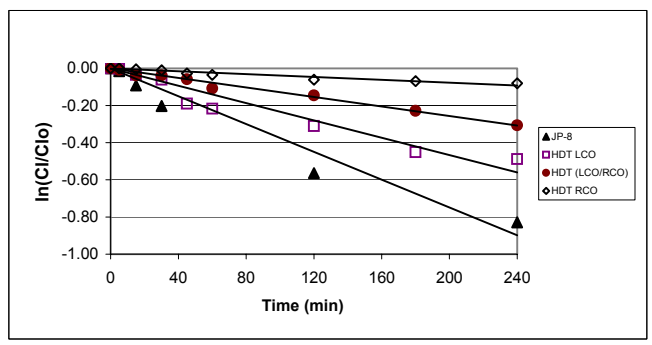

(a)

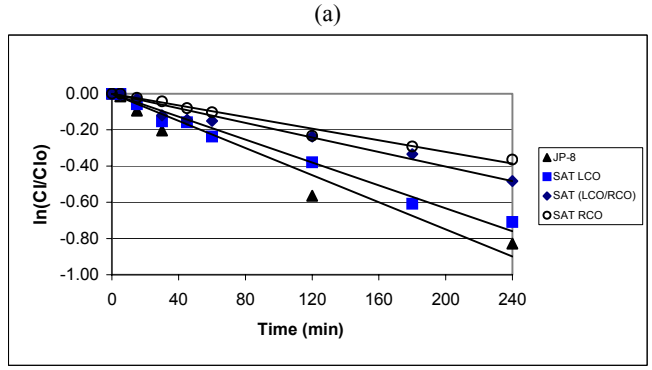

(b)

Figure 2. Plot of ln $[C_l/C_{lo}]$ vs t for (a) hydrotreated fuels and (b) saturated fuels at 480˚C and compared to JP-8.

From general observation, the increasing concentration of refined chemical oil (RCO) to the feedstock blends of both hydrotreated and saturated fuels yielded lower solid deposition and

gas formation (inhibited degradation of liquid). This may be due to a high aromatic content, presence of a hydrogen donor such as tetralin, and the low alkane concentration.

Table 2. k_{app} for Fuel Candidates Obtained from Figure 2.

Fuel	$-k_{app}$ (min^{-1})
JP-8	0.0040
HDT LCO	0.0023
HDT (LCO/RCO)	0.0013
HDT RCO	0.0004
SAT LCO	0.0032
SAT (LCO/RCO)	0.0020
SAT RCO	0.0016

Overall Chemical Changes during Stressing.

Examples of product distribution of a hydrotreated fuel and a saturated fuel have been determined from GC/MS. Figure 3(a) and 3(b) display the chemical changes during stressing HDT (LCO/RCO) and SAT (LCO/RCO) respectively.

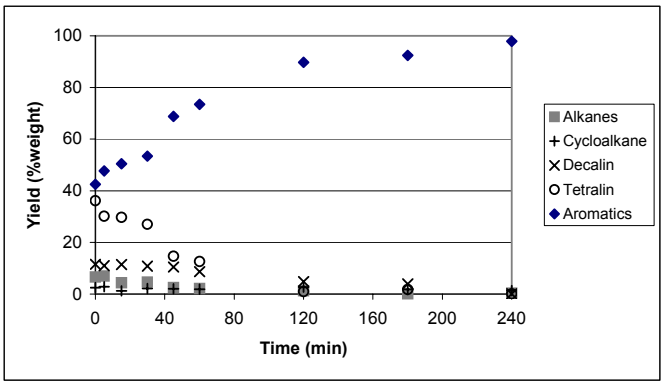

(a)

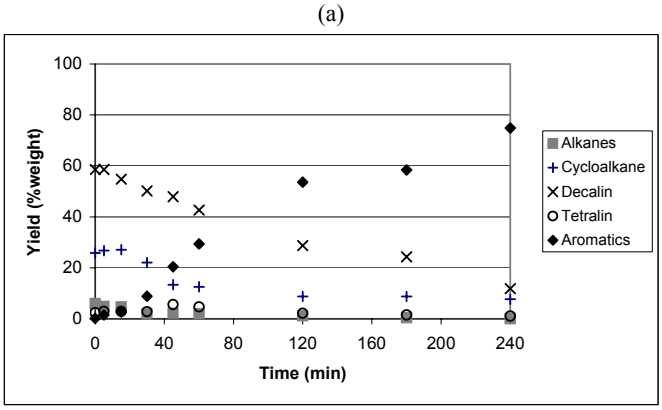

(b)

Figure 3. Distribution of chemical composition for fresh fuels and their liquid products after stressing at 480˚C: (a) HDT (LCO/RCO), and (b) SAT (LCO/RCO).

For stressed HDT (LCO/RCO), the increase in aromatic content was significant, starting from 45 to 240 minutes. Tetralin, a hydrogen donor in hydrotreated fuels, was substantially decreased after the 45-minute reaction. After this time period, the small amounts of alkanes, cycloalkanes and decalin were all converted to aromatic to almost 100% at 240 minutes. Most of converted aromatics (not shown here) are mainly 3- and 4- ring aromatics, followed by naphthalene and alkylbenzenes.

Compared to HDT (LCO/RCO), SAT (LCO/RCO) is mostly comprised of thermally stable compounds such as decalin and cycloalkanes. However, these components were significantly converted to aromatics after 45 minutes, as well as those of HDT (LCO/RCO). Tetralin slightly rose from 5 to 45 minutes and dehydrogenated to naphthalene after 60 minutes. The major aromatic contents for SAT (LCO/RCO) as increase of resident time are naphthalene and alkylbenzenes.

Physical Properties.

Table 2 shows the physical properties of all fuels. The heat of combustion values of six JP-900 fuels do not differ greatly from that of JP-8 despite differences in chemical composition. The hydrotreated fuels appear to be low in net heat of combustion due to highly aromatic and low alkane concentration. However, with the presence of aromatic content, the fuels' density and energy density are significantly high. A heavy fuel of high energy density is desirable when storage volume limits fuel capacity [17].

The other problem associated with high aromatic contents is low smoke point, resulting in high sooting tendencies and emissions [18] as seen from tests with the hydrotreated fuels. The specification for minimum smoke point, 19 mm [19, 20], is achieved only by the saturated fuels.

For other properties, all coal-based jet fuels' flash points and viscosities meet the ASTM D 1655 specification (MIN. 100˚F and MAX 8.0 cst at -20˚C, respectively) [20].

To this point, the most important factor for a new formula of JP-900 would be aromatic contents, including tetralin that helps improve thermal stability in pyrolytic regime but tends to give low smoke point. The current aromatics in conventional jet fuel are about 25 volume% [19, 20]. However, the specification for future jet fuel may have to increase aromatic contents [21] to improve the fuel's thermal stability and energy density.

Table 3. The Physical Properties of JP-8, Hydrotreated and Saturated Fuels.

Fuel	Heat of combustion (BTU/lb)	Density (kg/L)	Energy density (MJ/L)	Flash point (˚F)	Viscosity (cSt)	Smoke point (mm)
JP-8	19880	0.81	37.42	124.1	1.7	23.6
HDT LCO	19140	0.89	39.53	171.1	2.4	8.2
HDT (LCO/RCO)	18750	0.93	40.55	163.0	2.6	6.5
HDT RCO	18260	0.97	41.33	157.1	2.0	5.8
SAT LCO	19886	0.84	38.36	148.0	2.7	24.1
SAT (LCO/RCO)	19500	0.86	39.13	145.0	2.7	22.8
SAT RCO	19440	0.88	39.55	139.1	2.8	19.6

Conclusions

Coal-based jet fuels from hydrotreatment and saturation of light cycle oil and refine chemical oil have shown a great improvement of thermal stability in the pyrolytic regime in batch system. The fuel's physical properties, such as energy density, flash point and viscosity, have also shown encouraging results. However, the main concern of JP-900 is the excess of aromatic content in hydrotreated fuels, resulting in low smoke points or poor combustion performance. To establish the right formula for JP-900, the compromise must be made

on thermal stability, physical properties and distribution of compound classes.

Acknowledgement.

This project is fully supported by the Department of Defense and Air Force Wright-Patterson Laboratory. The authors also would like to thank Koppers Industries for coal-tar feedstock, United Refinery for petroleum feedstock and PARC Technical Services for the production of JP-900 fuel candidates.

References

1. Song, C., Eser, S., Schobert, H.H. and Hatcher, P.G., *Energy & Fuels*, 1993. **7**: p. 234-243.
2. Heneghan, S.P., Zabarnick, S., Ballal, D.R. and Harrison III, W.E., *Journal of Energy Resources Technology, 1996*. **118**: p. 170-179.
3. Edwards, T., AIAA 93-0807, *31st Aerospace Sciences Meeting and Exhibit*, Reno, Nevada, 1993: p. 1-11.
4. Wilson, G.R., *Project Report on AFOSR-Subcontract for Advanced Thermally Stable Coal-Based Jet Fuels for the Pennsylvania State University*. May 2000, PARC Technical Services Inc. (Pittsburgh, PA) to Pennsylvania State University.
5. Badger, M.W., *Preprints of Papers, American Chemical Society Division of Petroleum Chemistry*, 2000. **45**(3): p. 531-533.
6. Roan, M.A. and Boehman, A.L., *Preprints of Papers, American Chemical Society Division of Petroleum Chemistry*, 2002.
7. Andrésen, J.M., Strohm, J.J., Boyer, M.L., Song, C., Schobert, H.H. and Butnark, S., *Preprints of Papers, American Chemical Society Division of Fuel Chemistry*, 2001. **46**(1): p. 208-210.
8. Hazlett, R.N., *Thermal Oxidation Stability of Aviation Turbine Fuels (Monograph: 1),* ASTM 1991, Philadelphia, PA.
9. Strohm, J.J., Andrésen, J. M. and Song, C., *Preprints of Papers, American Chemical Society Division of Petroleum Chemistry*, 1999. **44**(3): p. 386-390.
10. Andrésen, J.M., Strohm, J.J., Sun, L. and Song, C., *Energy & Fuels*, 2001. **15**(3): p. 714-723.
11. Butnark, S., Badger, M. and Schobert, H.H., *Preprints of Papers, American Chemical Society Division of Fuel Chemistry*, 2001. **46**(2): p. 492-494.
12. Butnark, S., Badger, M. and Schobert, H.H., *Preprints of Papers, American Chemical Society Division of Fuel Chemistry*, 1999. **44**(3).
13. Butnark, S., Master Thesis 1999, The Pennsylvania State University.
14. Yoon, E.M., Selvaraj, L., Eser, S. and Coleman, M.M., *Energy & Fuels,* 1996. **10**: p. 812-815.
15. Veytsman, B. and Coleman, M.M. *Preprints of Papers, American Chemical Society Division of Petroleum Chemistry*. 1998.
16. Zabarnick, S., *Energy & Fuels*, 1998. **12**: p. 547-553.
17. Goodger, E.a.V., R., *Aviation Fuels Technology*. 1985, Hong Kong: MacMillan Publishers Ltd.
18. Pande, G.S. and Hardy, D.R., *Energy & Fuels*, 1995. **9**: p. 448-457.
19. Coordinating Research Council, *Handbook of Aviation Fuel Properties, Society of Automotive Engineers, CRC Report No. 530.* 1983.
20. ASTM, *Annual book of ASTM standards*. 2000: Philadelphia, PA.
21. Kirklin, P.W. and David, P., *Aviation Fuel: Thermal Stability Requirements*. 1992, Philadelphia, PA: ASTM.

AN ANALYSIS OF THE ACCOMPLISHMENTS OF THE DOE DIRECT COAL LIQUEFACTION PROGRAM, 1976-2000

[(a)] *R. A. Winschel and F. P. Burke*
[(b)]*D. Gray and G. Tomlinson*

(a) CONSOL Energy Inc., Research & Development,
4000 Brownsville Road, South Park, PA 15129
(b) Mitretek Systems, 3150 Fairview Park Drive South
Falls Church, VA 22042-4519

Summary

The DOE direct coal liquefaction program, conducted between 1976 and 2000, resulted in the development and optimization of a commercially ready technology for the production of petroleum substitutes as refinery feedstocks. An intensive large scale demonstration program in the late 1970s and early 1980s demonstrated overall engineering feasibility. Subsequent process research and development work overcame the major technical and economic obstacles to commercialization of the process. As a result, direct liquefaction products that meet or exceed crude oil qualities can be made for about $30/bbl. The technology was shown to be applicable to a wide range of coals in the United States. Fundamental research supported the process development effort, and provided direction in optimizing process performance. The DOE program met the goal of defining the costs and benefits of direct coal liquefaction as a strategic alternative to imported oil as a source of liquid fuels and petrochemicals.

Introduction

To understand the costs and benefits of the DOE direct coal liquefaction effort, it important to recognize that the program consisted of three main components. The first was the relatively large-scale demonstration of thermal/catalytic hydrogenation processes (referred to below as "Phase I" processes) in the 1970s and early 1980s. These demonstrations were done to accelerate the availability of coal liquefaction technology as a short-term response to the energy crisis of the 1970s. The second component was a more fundamental research program to investigate potential improvements in the thermal/catalytic processes, and to identify potential alternative processes, based on a better understanding of coal and process chemistry. The third component was a broadly based bench-scale and pilot plant process development program to overcome the technical and economic deficiencies encountered in the earlier Phase I demonstration programs. The processes developed in this third component of the program are referred to below as "Phase II" processes.

In 1976, U.S. petroleum imports cost $106 billion (in 1999 dollars), and during the period from 1976 through 1999, the U.S. imported 68 billion barrels of crude oil, at a cost of $2 trillion (1999 dollars). Between 1976 and 1999, the average cost of a barrel of crude oil, in 1999 dollars, has been $29. The overall cost of the DOE direct coal liquefaction program, through the year 2000, was $3.6 billion (1999 dollars), or 0.2% of the imported petroleum cost. As shown in Figure 1, 89% of the total DOE spending occurred between 1976 and 1982. The majority was spent on large plants to demonstrate the Phase I processes. The DOE investment was matched by substantial investments by private industry, state governments, and academic institutions.

In the early 1970s, in a military and international political climate much different than today's, the United States was faced with a shortfall in supplies of petroleum which it was unable to satisfy with domestic sources. The gasoline supply situation was particularly visible and acute, but the electric power industry, which had increased petroleum consumption by 600% between 1963 and 1973, also was seeking reliable domestic oil sources. In an attempt to ensure alternatives to imported oil, a national decision was made to pursue direct coal liquefaction, among other options, as a means to produce domestic supplies of transportation and utility fuels.

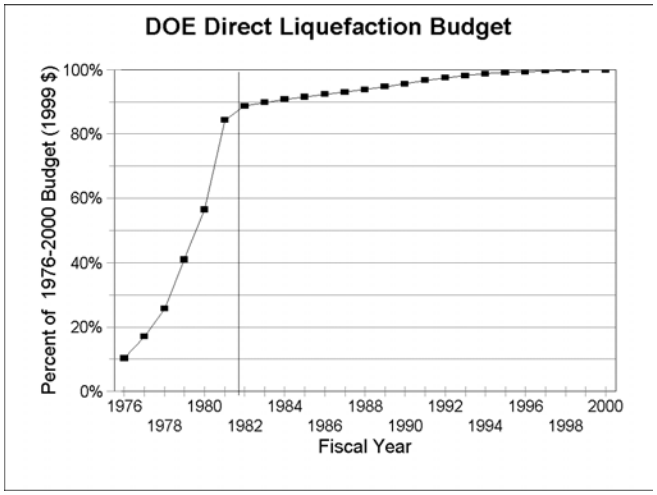

Figure 1. DOE Direct Liquefaction Budget.

The major oil companies (Exxon, Mobil, Chevron, Amoco, Conoco, Gulf and others) and the electric power industry (notably Electric Power Research Institute (EPRI) and Southern Company) actively supported this decision as evidenced by their substantial investment in the development and demonstration of direct liquefaction technology. The majority of the funding in the Phase I direct liquefaction program of the 1970s and early 1980s was focused on large projects to develop and demonstrate the Exxon Donor Solvent (EDS), the Hydrocarbon Research Inc. (HRI) H-Coal and SRC-II distillate fuels processes, and the Solvent Refined Coal (SCR) boiler fuel process.

Concurrently, a much smaller, but significant amount of funding was directed to the universities, private sector and government labs which conducted more fundamental research to determine if better alternatives to the high temperature thermal/catalytic processes like EDS and H-Coal could be identified for further development. This work involved substantial research on the chemistry of coal and associated products.

While the H-Coal and EDS programs demonstrated the technical and engineering feasibility of direct coal liquefaction, many issues were not satisfactorily resolved, including those of process yield, selectivity, product quality, and, ultimately, economic potential. However, process development research had identified a number of options for process improvement that were further developed and demonstrated at the bench and pilot plant scale, principally at Lummus-Crest, HRI (later, Hydrocarbon Technologies Inc. (HTI)) and the Wilsonville facility, during the 1980s and early 1990s. This Phase II development work successfully addressed the outstanding technical issues identified earlier, and largely optimized the process in terms of the most important performance parameters. The principal accomplishments of the program are described below.

Discussion

High Yields of Distillate Fuels Demonstrated. One of the most important accomplishments of the Phase II work was a substantial increase in liquid yields compared to the Phase I processes. High liquid yield is important, because direct liquefaction

is capital-inten-sive. Therefore, increasing liquid yields greatly reduced the capital cost component of the process on a dollars/barrel/stream day basis. As shown below, liquid fuel yields were increased from 45% to 50% (MAF coal basis) for Phase 1 processes to about 75% (more than 4.5 bbl/t of MAF coal) for Phase 2 processes, while the yields of less valuable gaseous and non-distillate fuels were reduced commen-surately, as shown below for mid-western U.S. (Illinois Basin) coal. In the table, ITSL refers to Integrated Two Stage Liquefaction, and CMSL refers to Continuous Multi-Stage Liquefaction.

Table 1. Process Yields with Illinois Basin Coal

Process	SRC-II	H-Coal	EDS	ITSL	CMSL
Year	1980	1981	early 80s	1989	1994
Yield, wt % MAF Coal					
Heterogases	12.9	11.3	17.4	15.2	15.2
C_1-C_3 gas	14.5	12.8	19.0*	5.4	11.4
Naphtha	19.3	22.9	22.8	14.5	20.7
Middle Distillate	25.2	20.0	17.0	21.7	39.1
Gas Oil	4.9	7.6	4.4	29.6	12.5
Total Distillate	47.3	50.5	44.2	65.8	72.3
H Consumption, wt %	5.0	6.0	5.9	6.0	7.5
H Efficiency, lb dist./lb H Consumed	9.5	8.4	7.5	11.0	9.7

* C_1 - C_4 gas

High-Quality Liquids Produced. The liquids made in the Phase I processes were intended to be crude oil replacements, but they were unstable, highly aromatic, and had high heteroatom (sulfur, nitrogen, oxygen) contents. This prompted concern about refinability, storage stability, and human health, principally related to carcino-genicity. In the Phase II work, considerable attention was paid to improving liquid fuel quality. The Phase II process produces liquid fuels containing no resid, no metals, and very low levels of hetero-atoms. These primary products could be refined in conventional refineries to meet then-current specifications for motor and turbine fuels. Product quality evaluations, which were an important element of the Phase II work, ensured that acceptable transportation fuels can be produced by direct coal liquefaction. The Phase 2 processes make a superb quality naphtha that can be processed in conventional refineries into high-quality gasoline. No undesirable blending inter-action with conventional gasolines and naphthas is expected. Direct coal liquefaction middle distillates can serve as blend stocks for the production of diesel fuel and kerosene. The higher hydrogen contents of Phase 2 process products alleviate the carcinogenicity concerns related to Phase 1 process products. The properties of naphthas generated by Phase 1 and Phase 2 processes are compared in Table 2.

Table 2. Comparison of Properties of Naphthas Generated by Phase 1 and 2 Processes

	Illinois Basin Coal				PRB Coal On-Line Hydrotreater
Process	SRCII	H-Coal	EDS	CMSL	CMSL
Year	1980	1981	Late 70s	1996	1996
Naphtha Properties					
b.pt., °F	100-400	180-380	158-392	ibp-350	70-350
°API	39	35	31.1	49.9	53.5
H, wt%	11.5	11.6	10.9	14.0	14.7
S, wt %	0.2	0.2	0.5	0.04	0.02
N, wt %	0.4	0.31	0.2	0.02	0.002
O, wt %	3.9	3	2.8	0.3	<0.1

Process Scale-Up Demonstrated. The Phase I work demon-strated successful continuous operation of plants as large as 200 t/d of coal feed. The Phase II processes are sufficiently similar to the Phase I processes, in terms of process equipment and unit operations, that this experience is directly applicable. In addition, some of the key process equipment, such as the ebullated-bed reactor, is used in petroleum refineries around the world. Materials of construction and equipment designs were found to overcome corrosion, erosion, and fouling problems experienced in Phase 1 plants; these new materials and designs were demonstrated to be suitable. As a result, we can approach the scale-up of the Phase II processes to commercial scale with reasonable confidence. Some specific issues that were origi-nally problem areas, but that were overcome by improved materials, equipment, or process design during the development program include: deashing, product compatibility with conventional fuels, let-down valve erosion, preheater coking, and corrosion in distillation columns. This list is illustrative, rather than comprehensive.

Direct Liquefaction Shown to Apply to a Wide Range of Coals. Lignite, subbituminous, and bituminous coals from the eastern, mid-western, and western U.S. were shown to be suitable feedstocks. These represent the vast majority of U.S. coal resources. One important development was the application of direct liquefaction to low rank coals. In the 1970s, it was generally believed that subbituminous coal was an inferior liquefaction feedstock because of its high oxygen content, and perceived lower reactivity. One emphasis of the Phase II work was to apply direct liquefaction to low-rank coals. This is important, because it proved that the huge reserves of inexpensive western U.S. subbituminous coals make excellent liquefaction feedstocks. The Phase 2 work showed that direct liquefaction is a flexible process. It was shown that direct liquefaction could be applied to a mixed feedstock containing coal and petroleum resids, heavy oil, or bitumen ("coprocessing"), and to coal and waste polymers. This allows a single plant to operate with the most economical feedstock available at a given place and time. The improvement in liquid yields of the Phase 2 processes, relative to Phase 1 processes, with U.S. Powder River Basin subbituminous coal is shown in Table 3.

Table 3. Process Yields with Powder River Basin Coal

Process	H-Coal	ALC/CMSL
Year	1980	1996
Yield, wt % MAF Coal		
Heterogases	19.8	21.3
C_1-C_3 gas	11.0	12.4
Naptha	24.3	23.0
Middle Distillate	14.5	9.7
Gas Oil	11.9	33.4
Total Distillate	50.7	66.1
H Consumption, wt %	5.6	6.8
H-Efficiency, lb dist./lb H consumed	9.0	9.7

Economic Competitiveness Was Significantly Improved. Table 4 shows the economic analysis of conceptual full-scale plant designs employing three levels of technological development. The plants have been analyzed on the basis of a common set of economic assumptions shown below.

Return on Equity	15%	Federal Tax Rate	34%
% Equity	25%	State/Local Property Tax	1%
Loan Interest (16 yr)	8%	Depreciation, DDB, yr	16
Construction Period, yr	4		

Table 4. Economics of Coal Liquefaction

	H-Coal		ITSL	
	1981 $	1999 $	1991 $	1999 $
Hydrogen Source	Coal	Coal	Coal	Coal
Yield, bbls/day	50,000	50,000	69,000	69,000
Coal Feed, T/D AR	26,370	26,370	25,415	26,415
at $/Ton AR	20.5	20.5	20.5	20.5
Plant Cost $MM	$2,769	$4,592	3,543	$4,239
Escalation Factor		1.658		1.197
Capital Cost/@ $MM/yr	$415	$689	$531	$636
Coal Cost, $MM/yr	$178	$178	$172	$172
O&M, $MM/yr	$111	$184	$115	$138
Total Cost/yr	$705	$1,051	$819	$946
MM bbls/yr	16.50	16.50	22.77	22.77
RSP	$42.70	$63.69	$35.95	$41.53
Premium	1.00	1.00	1.07	1.07
Eq Crude RSP	$42.70	$63.69	$33.60	$38.81
Capital/Barrel/Day		$91,841		$61,439

	CMSL		
	1994 $	1999 $	1999 $
Hydrogen Source	NG	NG	Coal
Yield, bbls/day	51,500	51,500	51,500
Coal Feed, T/D AR	13,400	13,400	18,090
at $/Ton AR	20.5	20.5	20.5
Plant Cost $MM	$2,481	$2,714	$2,914
Escalation Factor		1.094	
Capital Cost/@ $MM/yr	$372	$407	$437
Coal Cost, $MM/yr	$91	$91	$122
Natural Gas, $MM/yr	$71	$71	
O&M, $MM/yr	$74	$81	$87
Total Cost/yr	$609	$651	$647
MM bbls/yr	17.00	17.00	17.00
RSP	$35.81	$38.28	$38.06
Premium	1.20	1.20	1.20
Eq Crude RSP	$29.90	$31.96	$31.78
Capital/Barrel/Day			$56,580

All plants employ Illinois 6 coal. The first design, designated H-Coal, is based on an analysis by process developers in 1981.[1] Capital required for a first of a kind plant employing H-Coal technology was estimated at $3.258 billion $1981. We have reduced this figure by 15% to reflect an Nth plant, consistent with the other estimates in Table 4.

The second plant, designated ITSL is based on a detailed preliminary design prepared for DOE by Bechtel in 1991-92.[2] Performance assumed in that study was derived from test results from run 257 at the Wilsonville Pilot Plant.

The plant designated as CMSL is based on bench scale results at HTI. Capital and operating costs are based on preliminary designs prepared by HTI in 1997.[3] The HTI design uses natural gas as a feedstock for some hydrogen production. The design has been modified for coal only input in order to be compatible with the other plants.

Table 4 shows that the Required Selling Price (RSP) of direct liquefaction products on an equivalent crude basis to be about $64, $38, and $32 per barrel for H-Coal, ITSL, and CMSL respectively. Figure 2 shows the contribution of coal, O&M, and capital related charges to the total RSP.

The principal advantage of ITSL vs. H-Coal stems from the substantial increase in yield per ton of coal processed. This, plus improvements in gasification and gas treatment, results in an improvement in yield of about 20% while reducing capital costs by over 5%. Capital cost per daily barrel was reduced from $91,800 to $61,400 (in 1999 dollars).

CMSL technology permits a further reduction in capital cost per daily barrel to $56,600. Some additional savings would result if the plant were scaled to the higher coal input of the other plants shown. CMSL employs less complex reactors and has much reduced catalyst costs. Total catalyst and chemical costs are less than $500/daily barrel of capacity vs. $1,160 for the Bechtel ITSL design. The major advantage of CMSL is improved product quality. Syncrude quality considerations are discussed below.

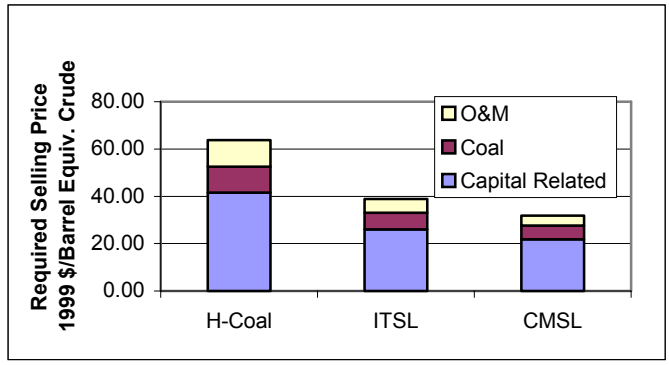

Figure 2. Components of Syncrude RSP.

Table 5 compares the quality of syncrudes from the three configurations to a typical U.S. crude oil. H-Coal liquids were characterized by low hydrogen content and other limitations noted earlier in this report. These limitations counterbalanced their advantage of being all distillate materials that produced a considerable volume gain when refined. The assessment in Table 5 that they had a value to refiners equal to crude (e.g., premium of 1.0) may be optimistic.

Table 5. Properties of Syncrude and Typical Crude

	H-Coal	ITSL	CMSL	Typ. Crude
Carbon, wt %	86.63	85.72	86.57	85.80
Hydrogen, wt %	10.54	11.48	13.08	13.00
Nitrogen, wt %	0.50	0.49	44 ppm	2000 ppm
Sulfur, wt %	0.19	0.07	0.06	1.00
Oxygen, wt %	2.13	2.24	0.44	
Vanadium, ppm	nil	nil	nil	200
650 $^{o}F^{-}$, wt %	83	79	80	53
975 $^{o}F^{+}$, wt %	0	0	0	20
Gravity, ^{o}API	27	22	38	32
Premium	1.00	1.07	1.20	1.00

ITSL products are more similar to petroleum and thus more easily processed. The premium of 1.07 relative to crude oil was determined by Bechtel through extensive refining analysis using the PIMs model.

CMSL liquids contain no residual material and only limited amounts of material boiling above 750 ^{o}F. The premium value of 1.2 relative to crude was assessed by HTI in the referenced study.[3]

Production of Higher Value Chemical Co-Products Demonstrated. Direct coal liquefaction is particularly well suited to the co-production of certain chemicals, many of which preserve the inherent molecular structure of the original coal. The production of cresylics, paraffin wax, sulfur (or sulfuric acid), and ammonia co-products was demonstrated. The Phase 2 process operated with subbituminous coal can yield 9% MAF of mixed cresylics (valued at $0.55/lb, 1999) and 4% MAF of paraffin wax (valued at $0.37/lb, 1999, fully refined). Benzene, toluene, BTX, other aromatics, argon, krypton, nitrogen, and other specialty chemicals also can be co-produced with liquid fuels. A coal liquefaction plant dedicated to producing chemicals, rather than fuels, and integrated into an Integrated Gasification Combined Cycle (IGCC) plant could be operated at less severe conditions and at substantially less cost than a stand-alone

liquefaction plant. This suggests the possible inclusion of a direct liquefaction module in a Vision 21 facility. "Vision 21" refers to DOE's conceptual facility of the future that produces some combination of electric power, clean fuels, and chemicals, with essentially no emissions of pollutants and reduced emissions of carbon dioxide.

Benefits Derived from Fundamental Research Program. A research program, conducted concurrently with the Phase 1 and Phase 2 development programs, evaluated novel process concepts and the fundamental chemistry of coals and catalysts and developed suitable analytical methodology. This program led to better understanding of the process. Some of this understanding, such as the benefits of slurry catalysis, was incorporated in the process development effort that generated the Phase 2 process. This work was sufficiently extensive to conclude that the catalytic/thermal direct liquefaction process, as developed with DOE, is the best liquefaction pathway, and that radical departures are unlikely to result in substantially improved processes Thus, much of the value in the work was in providing indirect confirmation that the process development was near-optimum. The analytical techniques, catalyst development, and catalyst testing methodologies have spin-off value in that they are being applied in other fields or are likely to be in the future.

Conclusions

The DOE direct liquefaction program produced a reasonably mature technology. The intensive effort between 1976 and 1982 (Phase I), when 90% of the program funds were expended, resulted in a demonstration of the technical feasibility of the major process components. The Phase I processes, however, were deficient in terms of product yield and quality. This stimulated further research and development work between 1983 and 1999 (Phase II). The Phase II work was significantly less costly than the earlier demonstration projects, but resulted in substantial improvements in process performance and economics. It now is possible to produce liquids of high quality at yields that approach the theoretical maximum. At the same time, the cost for a barrel of product dropped by 50%, because of process optimization and increased yields. Economic and engineering studies conducted throughout Phase II have reduced the uncertainty and, therefore, the risk associated with commercial deployment of the technology. Many ideas for improving the basic thermal/catalytic process were identified and evaluated. Some of these were incorporated into the process development effort. In addition, considerable research was directed toward a better fundamental knowledge of coal chemistry, and to identify and explore novel liquefaction concepts distinct from the thermal/catalytic processes. The knowledge gained in the fundamental investigations is valuable in assuring that direct liquefaction technology, as it has been developed, represents a likely optimum in terms of process performance and costs. This knowledge would not have been available without the persistent advances in the technology achieved in the DOE direct liquefaction program.

The current technology is well defined in terms of cost and performance. It represents a technically available option for the production of liquid fuels. It can be used domestically in the United States to limit our exposure to oil price increases in the international market or to offset supply reductions. It also can be used by other nations who choose to use domestic coal to meet their transportation fuel needs, thus reducing demands on conventional petroleum sources. It can be used with coal alone, or to co-process a variety of lower value feedstocks. The results of the DOE program allow direct coal liquefaction to be accurately assessed in context to the costs and risks associated with other options for securing liquid fuel supplies should the need arise.

The future of energy supply and energy costs is uncertain. Recent swings in petroleum and natural gas prices serve as timely reminders of our inability to forecast even short-term trends. We now rely on foreign sources for nearly 60% of our petroleum, a greater percentage than in the 1970s. In addition, natural gas imports have increased almost continuously since 1980, and by 1999 accounted for 16% of our natural gas consumption. In contrast to the situation with oil and natural gas, coal is the most stable and abundant fossil energy resource in the United States, and much of the rest of the world. The DOE direct coal liquefaction program represents a prudent investment to mitigate of the risk of future increases in petroleum prices or curtailment of supplies for economic or political reasons.

Acknowledgment. The preprint was derived from Chapter 2 of "Summary Report of the DOE Direct Liquefaction Process Development Campaign of the Late Twentieth Century: Topical Report", Report No. DOE/PC 93054-94, July 2001.

References

(1) Ashland Synthetic Fuels, Inc. and Airco Energy Company, Inc., *The Breckinridge Project Initial Effort Report VIII*, prepared for U.S. DOE under Cooperative Agreement No. DE-FC05-800R, 1981.

(2) Bechtel Corporation, *Final Report on Baseline and Improved Baseline Volume VIII, Design, Capital Cost, and Economics For Improved Baseline*, Contract No. DE-AC22-90PC89857, March 1993.

(3) Hydrocarbon Technologies, Inc., *Direct Liquefaction Proof of Concept Program, DE-92148-TOP-09*, Contract No. DE-AC22-92PC92148, December 1997.

Separation of CO_2 from Power Plant Flue Gas Using a Novel CO_2 "Molecular Basket" Adsorbent

Xiaochun Xu, Chunshan Song, Ronald Wincek, John M. Andresen, Bruce G. Miller, and Alan W. Scaroni*

Clean Fuels and Catalysis Program, The Energy Institute, and Department of Energy & Geo-Environmental Engineering, The Pennsylvania State University, 209 Academic Projects Building, University Park, PA 16802, USA

* Corresponding author. E-mail: csong@psu.edu; Tel: 814-863-4466; Fax: 814-865-3248

Introduction

A considerable increase in the global atmospheric CO_2 concentration has raised concern about climate change and has led to a worldwide effort in research and development on control of CO_2 emissions.[1,2] The main CO_2 emission sources include fossil fuel-based electric power plants, vehicles, manufacturing plants for cement, limestone, hydrogen, ammonia, and commercial and residential buildings.[2] Capture and separation of CO_2 from stationary sources is considered as the first step for the control of CO_2 emission and its cost constitutes about three-fourths of the total cost of the control of CO_2 emission, e.g., carbon sequestration.[3] It is therefore important to explore new approaches for CO_2 separation.

Recently, a novel CO_2 "molecular basket" adsorbent, which showed a high CO_2 adsorption capacity and a high CO_2 selectivity, was developed in our laboratory.[4-6] The adsorbent was successfully applied in the separation of CO_2 from simulated flue gas.[6] In this paper, the separation of CO_2 from flue gas of a gas-/coal-fired power plant is reported.

Experimental

The "molecular basket" adsorbent of MCM-41-PEI-50 (mesoporous molecular sieve of MCM-41 type with the polyethyleneimine PEI loading of 50 wt%) was used in the adsorption separation. The details on the preparation and characterization of this adsorbent are reported elesewhere.[4-6]

The adsorption separation of CO_2 from power plant flue gases was investigated. Both the gas-fired and the coal-fired flue gases were used as feed gases. The composition of the gas-fired flue gas was 7.4-7.7% CO_2, 14.6% H_2O, ~ 4.45% O_2, 200-300 ppm CO, 60-70 ppm NO_x, and 73-74% N_2. The composition of the coal-fired flue gas was 12.5-12.8% CO_2, 6.2% H_2O, ~ 4.4% O_2, 50 ppm CO, 420 ppm NO_x, 420 ppm SO_2, and 76-77% N_2. In a typical adsorption/desorption process, about 30 g of the adsorbent was placed in the central part of a stainless steel adsorption column (O.D., 2'; I.D., 1.7'). The adsorbent was pressed to 18-35 mesh. The top and the bottom of the adsorption column were filled with alumina (~170 g) to decrease the dead volume in the separation system. The adsorption column was heated up to 100 ^oC in a helium atmosphere at a flow of 5 l/min and held at that temperature until there was no CO_2 detected in the effluent gas. The temperature was then adjusted to 80±10 ^oC and the flue gas mixture was introduced at 5-6 l/min. Generally, the adsorption was carried out for 300-600 seconds. After adsorption, the gas was switched to helium at a flow rate of 5 ml/min to perform the desorption at the same temperature. The time for desorption was 300-600 seconds. The flow rate of the effluent gas was measured by a rotameter. The concentration of CO_2, O_2, CO, SO_2 and NO_x in the effluent gas was measured on-line using a model NGA 2000 non-dispersive infrared CO_2 analyzer; a model NGA 2000 paramagnetic oxygen analyzer; a model NGA 2000 non-dispersive infrared CO analyzer; a model 890 ultraviolet SO_2 analyzer; and a model NGA 2000 chemiluminescence NO_x analyzer (Rosemount Analytical, Inc.). The analysis was carried out every 5-6 seconds. (Note that the on-line analysis of the effluent gas composition was carried out after removing the water vapor in the gas mixture. Therefore, the measured gas concentrations were slightly higher than those in the real gas mixture.) Since the alumina also adsorbed the gases, a blank separation test with the column filled only with the alumina (~210 g) was carried out. Therefore, adsorption/desorption capacity of the "molecular basket" adsorbent can be calculated by subtracting the adsorption/desorption capacity between the adsorption experiment and the blank experiment. The adsorption/desorption capacity was calculated from the mass balance before and after the adsorption. The separation factor was defined as the mole ratio of the gases adsorbed over the mole ratio of the gases in the feed.

Results and Discussions

1. Adsorption separation of gas-fired flue gas

Typical CO_2 breakthrough curves for the 'molecular basket" adsorbent and the "blank" alumina are shown in Figure 1 for the gas-fired flue gas. Clearly, both the alumina and the "molecular basket" adsorbent can adsorb CO_2. However, the adsorption performance of the "molecular basket" adsorbent was much better than that of the alumina. The lowest CO_2 emission concentration was ~ 0.8% for alumina and was less than 0.1% for the "molecular basket" adsorbent. The CO_2 adsorption capacity was 1.1 ml (STP)/g adsorbent for the alumina and 26 ml (STP)/g adsorbent for the "molecular basket" adsorbent. In addition, the "molecular basket" adsorbent showed a better selectivity. The "molecular basket" adsorbent did not adsorb O_2, N_2 and CO, while the CO_2/O_2 selectivity was 3.5 for alumina. The "molecular basket" adsorbent adsorbed more NO_x than the alumina. The NO_x adsorption capacity was 0.0505 ml (STP)/g adsorbent for the "molecular basket" adsorbent and $7.5*10^{-4}$ ml (STP)/g adsorbent for the alumina. The selectivity of CO_2/NO_x was 0.45 for the "molecular basket" adsorbent. However, very little NO_x was adsorbed before CO_2 breakthrough. The CO_2 and NO_x adsorption capacity before CO_2 breakthrough was 21 ml (STP)/g adsorbent and $7.1*10^{-3}$ ml (STP)/g adsorbent, respectively. Therefore, the selectivity of CO_2/NO_x was 2.5. Further, while CO_2 was completely desorbed, very little NO_x desorbed.

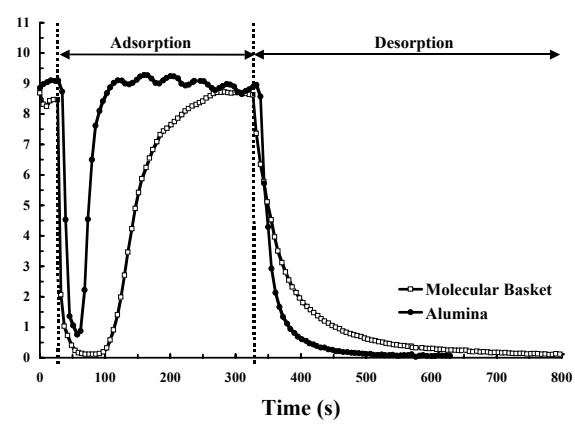

Figure 1 Breakthrough curve of CO_2 for the gas-fired flue gas.

2. Adsorption separation of coal-fired flue gas

The adsorption separation of CO_2 from a coal-fired flue gas was also investigated. In the coal fired flue gas, there was a significant concentration of SO_2. The CO_2 breakthrough curves are shown in Figure 2. Similar trends as for the gas-fired flue gas were observed

for the coal-fired flue gas. The adsorption of N_2 or O_2 by the "molecular basket" adsorbent was below the detection limit of the apparatus. The adsorption capacity for CO_2, SO_2 and NO_x were 36, 0.11 and 0.21 ml (STP)/g adsorbent, respectively. The separation selectivity for CO_2/SO_2 and CO_2/NO_x was 1.07 and 0.57, respectively. The adsorption capacity for CO_2, SO_2 and NO_x before CO_2 breakthrough was 24, 0.0074 and 0.028 ml (STP)/g adsorbent, respectively. Therefore, the separation selectivity for CO_2/SO_2 and CO_2/NO_x was 10.7 and 2.86, respectively, before CO_2 breakthrough. Again, while the desorption of CO_2 was complete, very little NO_x and SO_2 desorbed.

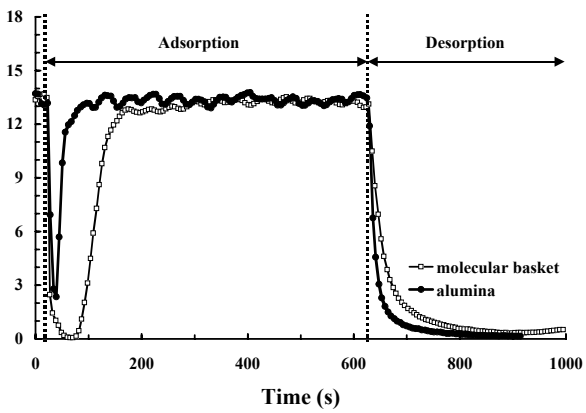

Figure 2 Breakthrough curve of CO_2 for the coal-fired flue gas.

Compared with the CO_2 adsorption capacity in the simulated flue gas condition, the CO_2 adsorption capacity in the power plant flue gas condition was about ~ 30% lower. The adsorption capacity for the coal-fired flue gas was 36 ml (STP)/g adsorbent at 80±10 ^oC with the feed composition of 12.5-12.8% CO_2, ~4.4% O_2, 50 ppm CO, 420 ppm NO_x, 420 ppm SO_2, 6.2% H_2O and 76-77% N_2. The adsorption capacity for the simulated flue gas mixture was 53 ml (STP)/g adsorbent at 75 ^oC with the feed composition of 13.9% CO_2, 3.95% O_2, 6.43% H_2O and 75.7% N_2. There are several reasons which may cause the difference in the adsorption capacity. First, the CO_2 concentration in the coal-fired flue gas mixture was lower than that in the simulated flue gas mixture. At lower CO_2 concentrations, the CO_2 adsorption capacity will be lower.[4] Second, the adsorbent with different physical forms will have different CO_2 adsorption capacities. A comparison study on the CO_2 adsorption by a powder adsorbent and by a pellet (18-35 meshes) adsorbent was carried out and the results are shown in Figure 3. It is clearly shown in Figure 3 that the pellet adsorbent had a lower CO_2 adsorption capacity than the powder adsorbent. The adsorption capacity of the pellet adsorbent was about 10% lower than that of the powder adsorbent. Third, the higher flow rates in the power plant flue gas separation tests resulted in the lower adsorption capacity. The feed flow rate was 167ml/min.g adsorbent in the power plant flue gas separation tests and was only 5 ml/min.g adsorbent in the simulated flue gas separation. Lastly, minor gas components, i.e., NO_x and SO_2, influenced the adsorption of CO_2. Since NO_x and SO_2 are acid gases and the adsorbent is basic in nature, the NO_x and SO_2 are competitive adsorbates for CO_2. Our experimental results showed that the adsorption of NO_x by the "'molecular basket" adsorbent was even stronger than that of CO_2 in some experimental conditions. The pre-removal of NO_x and SO_2 from the flue gas mixture is therefore preferred for the adsorption separation of CO_2 from the flue gas mixture by this "molecular basket" adsorbent.

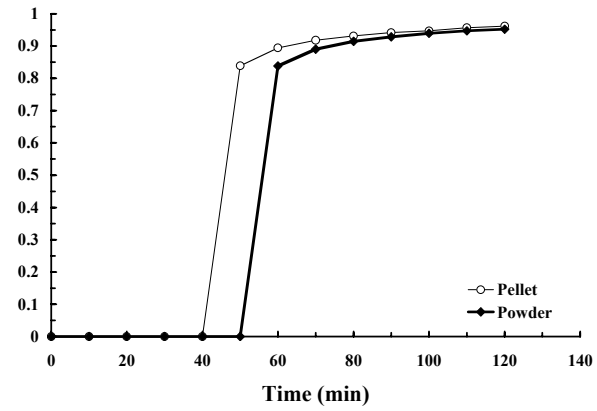

Figure 3 Comparison of the CO_2 breakthrough curve of the "molecular basket" adsorbent in pellet and in powder form. Operation condition: Weight of adsorbent: 2.0 g; Feed composition: 14.9% CO_2, 4.25% O_2 and 80.85%; Temperature: 75 ^oC; Feed flow rate: 10 ml/min.

Conclusions

CO_2 can be selectively separated from the flue gases of power plant by using the novel "molecular basket" adsorbent MCM-41-PEI-50. The adsorbent hardly adsorbs any N_2, O_2 and CO. The selectivity of CO_2/NO_x was 2.5 for gas-fired flue gas and the selectivity of CO_2/SO_2 and CO_2/NO_x were 10.7 and 2.86 for coal-fired flue gas, respectively. Very little NO_x and SO_2 desorbed after adsorption indicating the need for pre-removal of NO_x and SO_2 from the flue gas before capture of CO_2 by the PEI based "molecular basket" adsorbent.

Acknowledgement. Funding for the work was provided by the U.S. Department of Defense (via an interagency agreement with the U.S. Department of Energy) and the Commonwealth of Pennsylvania under Cooperative Agreement No. DE-FC22-92PC92162.

References

(1) Maroto-Valer, M. M.; Song, C.; Soong, Y. (Eds). Environmental Challenges and Greenhouse Gas Control for Fossil Fuel Utilization in the 21st Century. Kluwer Academic/Plenum Publishers, New York, **2002**, 447 pp.

(2) Song, C.; Gaffney, A. M.; Fujimoto, K. (Eds). CO_2 Conversion and Utilization. American Chemical Society (ACS), Washington DC, ACS Symp. Series, Vol. 809, **2002**, 448 pp.

(3) U.S. Department of Energy, Carbon Sequestration-Research and Development,**1999**, http://www.fe.doe.gov/coal_power/sequestration/reports/rd/index.html.

(4) Xu, X.C.; Song, C.; Andresen, J.M.; Miller, B.G.; Scaroni, A.W., Energy & Fuels, **2002,** 16, 1463-1469.

(5) Xu, X.C.; Andresen, J.M.; Song, C.S.; Miller, B.G.; Scaroni, A.W. Am. Chem. Soc., Div. Fuel Chem., **2002**, 47 (1), 67-68.

(6) Xu, X.C.; Song, C.; Andresen, J.M.; Miller, B.G.; Scaroni, Proceeding of the Nineteenth Annual International Pittsburgh Coal Conference, September 23-27, **2002**, Pittsburgh, PA USA. (Paper No. 39-2)

Performance of Solid Amine Sorbents

M. L. Gray[1*], Y. Soong[1], K. J. Champagne[1], H. Pennline[1], J. Baltrus[1],
R.W. Stevens, Jr.[2], R. Khatri[2], S. S. C. Chuang[2], and S. Khan[3]

[1]US Department of Energy, National Energy Technology Laboratory, P.O. Box 10940, Pittsburgh, PA, 15236. Gray@NETL.DOE.GOV. (412) 386-4826, Fax (412) 386-4808.
[2]Chemical Engineering Department, University of Akron, Akron, OH, 44325-3906.
[3]Chemistry and Biochemistry Department, Duquesne University, Pittsburgh, PA, 15282

ABSTRACT

Solid amine sorbents have been successfully prepared by reacting oxygen rich substrates with alkoxy amine compounds. The initial solid sorbents have been proven to be competitive with existing environmental CO_2 controlled life sorbents. It was determined that both silicon and titanium based substrates were very reactive with these alkoxy amine compounds resulting in stable solid amine sorbents. XPS analysis has indicated that the amine group was incorporated onto the surface of these substrates in the range of 3-7 percent. The performance of these silicon and titanium amine sorbents will be described within this paper.

Keywords: carbon dioxide, capture, and amine sorbent.

INTRODUCTION

The concentration of CO_2 in our atmosphere is promoted by the combustion of fossil fuels for the generation of electricity. Capturing CO_2 from flue-gas streams is an essential parameter for the carbon management for sequestrating of CO_2 from our environment. Current technologies[1] being considered for CO_2 sequestration include: disposal of CO_2 in deep oceans; depleted oil and gas fields; deep saline formations (aquifers); and recovery of enhanced oil, gas, and coal-bed methane. However, the current cost for the utilization of these types of technologies has proven to be too expensive. Consequently, reducing the cost for the capture of CO_2 will be a critical step in the overall carbon management program.

The physical and chemical adsorption of CO_2 can be achieved by using solvents, cryogenic techniques, membranes, and solid sorbents. The large-scale operation of these technologies is energy intensive when applied to capturing CO_2 in dilute stream, such as flue gas, which consist of 15% CO_2 by volume for most coal combustion systems. Amine-based, solvent-capture systems are the most energy efficient option, but are energy intensive due to the large amount of water needed in these system. Excessive water is required because of the corrosion and air flow problems created by the use of monoethanolamine (MEA), diethanolamine (DEA), or methyldiethanolamine (MDEA) in these aqueous-based, CO_2-capture systems. The proposed reaction sequences for using primary, secondary, and tertiary alkanolamines reacting with dissolve CO_2 are shown below.

Solid-amine CO_2 sorbents should have similar reactions with airborne CO_2, water vapor, and the amine functional group on its surface. Consequently, these types of sorbents are being used in aircraft, submarine, and spacecraft technologies[2-4]. However, the cost of these sorbents is too expensive for large-scale applications in the utility industry. Consequently, the development of economical amine-enriched sorbents based on reacting oxygen rich substrates with alkoxy amine compounds will be discussed within this paper.

Formation of the zwitterion ion:

(1) $R_1R_2NH + CO_2 \longleftrightarrow R_1R_2NH^+CO2^-$

Formation of amine carbamate:

(2) $R_1R_2NH + R_1R_2NH{+}CO_2 \longleftrightarrow R_1R_2NH^+ + R_1R_2NCO_2^-$

Protonation of amine:

(3) $R_1R_2R_3N + H_2O + CO_2\,(aq) \longleftrightarrow R_1R_2R_3NH^+ + HCO_3^-$

EXPERIMENTAL PROCEDURES:

Samples-- The three alternative oxygen rich solid substrates that were examined as CO_2 capture sorbents were a Tetraethyl orthrosilcate (SBA-15) from Aldrich Chemical Company, a Titanium (II) oxide (TiO-1) from Aldrich Chemical Company and a Immobilized amine sorbent (IAS) from an leading industrial manufacturer.

Amine Treatment Process--The actual conditions for incorporating the amine group into the structure of the oxygen rich substrates will not be discussed in this paper due to pending patent applications.

CO_2 Capture Capacity--The chemical CO_2 capture capacities were determined by the combination of Temperature Programmed Desorption (TPD) and Mass Spectroscopy (MS) analyses. The adsorption of CO_2 was achieved in the presence of moisture at 25 ^oC and the total desorption of CO_2 was achieved over the temperature range of 30 – 60 ^oC. The composition of the experimental gas stream used in these test runs was 10% $CO_2/H_2O/He$. The detailed operating conditions for this procedure were previously described in the literature[5]. The experimental set-up for these test runs is shown in figure 1.

XPS Analysis – The amount of nitrogen of the surface of the amine-enriched sorbent was determined by XPS analysis. The details of this experimental procedure have been reported in the literature[6].

RESULTS AND DISCUSSION:

Initially, the performance of the prepared amine-enriched sorbents (SBA-15 and TiO-1) were compared to the existing industrial solid amine sorbent (IAS). These sorbents were place in a 10% $CO_2/H_2O/He$ stream and TPD, and MS analyses were conducted determined the performance of these CO_2 capture sorbents. The adsorption/desorption of CO_2 for these sorbents were determined over the temperature range of 25 – 60 ^oC. A typical TPD/MS spectra are shown in figures 2. According to the TPD/MS analysis, all of the sorbent were successful in the capture of CO2 the moist experimental gas streams. The comparison of the CO_2 capture performances and XPS results for these sorbents are summarized in Table 1.

Table 1: TPD CO_2 Desorption and XPS Data of the Amine-Enriched Sorbents

Sorbents	XPS %Nitrogen	μmol/g CO_2 Captured
IAS	6.68	1886.6
SBA-15	7.13	2011.4
TiO-1	3.59	1057.2

As shown in Table 1, the best performing sorbent for the capture of CO_2 from these experimental gas streams was SBA-15. With the surface nitrogen value of 7.13 % the total amount of CO_2 captured was 2011.4 μmol/g for the SBA-15 sorbent. The SBA-15 performed slightly better then the IAS sorbent (1886.6 μmol/g) which may indicate that there are potential applications within in the

environmental control CO_2 capture industry for the SBA-15 sorbent. The TiO-1 was least reactive with the alkoxy amine compounds resulting in lower a CO_2 capture capacity of 1057.2 µmol/g with a surface nitrogen value of 3.59%. The overall performance for these sorbents will be determined by multiple regeneration testing (5-10 recycle runs) and these results will be disclosed in future publications.

CONCLUSION

Preliminary results indicate that the SBA-15 sorbent is comparable to the IAS sorbent which is currently being used environmental CO_2 controlled life sorbent. Additional experimental work is now underway to improve the performances of the SBA-15 and TiO-1 as CO_2 capture sorbents.

REFERENCES

1. DOE Report Doe/ER-30194, "Research Needs Assessment for the Capture, Utilization and Disposal of Carbon Dioxide from Fossil Fuel-Fired Power Plants," 1993.
2. US Patent 4,810,266, Zinnen, H. A., Oroskar, A. R., and Chang, C. H."CO_2 Removal using Aminated Carbon Molecular Sieves," 1989.
3. US Patent 5,492,683, Bibara P.J., Naletta T. A. "Regenerable Support Amine Polyol Sorbent," 1996.
4. US Patent 5,876,488, Bibara P. J. Filburn T. P., Nalette T. A. "regenerable Solid Amine Sorbent," 1999.
5. Soong, Y., Gray, M. L., Siriwardane, R. V., Champagne, K. J., Stevens, Jr., R. W., Toochinda, P., and Chuang, S. S. C. "Novel Amine Enriched Solid Sorbents for Carbon Dioxide Capture," Fuel preprint, 46 (1), pp. 285, 2001.
6. Gray, M. L., Champagne, K. J., Soong, Y., Killmeyer, R. P., Baltrus, J., Maroto-Valer, M. M., Andersen, J. M., Ciocco, M.V., and Zandhuis, P.H., ACS Chapter Book, " Environmental Challenges and Greenhouse Gas Control for Fossil Fuel Utilization in the 21 st Century", unpublished.

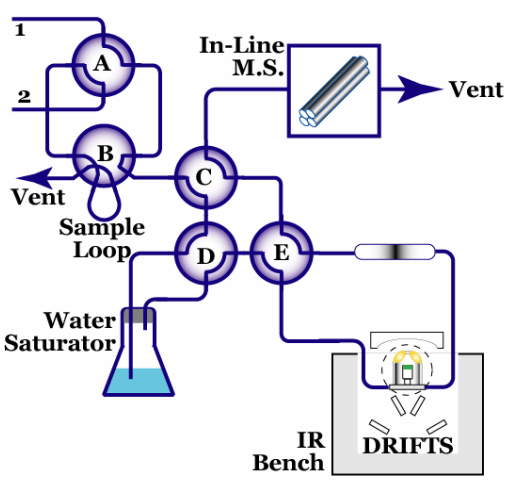

Figure 1: Experimental set-up for TPD/MS analysis

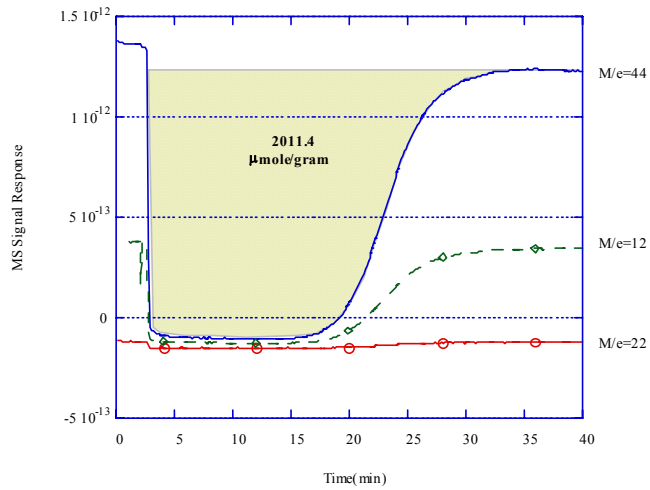

Figure 2: Typical TPD Mass spectra of SBA-15

Development of a CO_2 Affinity Ceramic Membrane

R. J. Ciora, Jr. and P. K.T. Liu
Media and Process Technology Inc.
1155 Willaim Pitt Way, Pittsburgh, PA 15238
T. T. Tsotsis, and M. Sahimi
Department of Chemical Engineering
University of Southern California
Los Angeles, CA 90089-1211

Significance of A CO_2 Affinity Ceramic Membranes

Most CO_2 selective membranes available today can effectively separate CO_2 from combustion off-gas at low temperatures. However, these membranes are not ideal for CO_2 sequestration applications due to (i) the large volume of off-gas that must be processed and (ii) the low partial pressure available in these streams. One way to overcome these intrinsic barriers associated with the use of membrane technology is to separate CO_2 in-situ from the coal gasification off-gas after shift reaction while producing high pressure hydrogen as clean fuel. Thus, the membrane can be used on a stream with a significantly reduced volume at a high pressure. In this presentation we will discuss one of the membrane concepts we are developing: a CO_2-affinity ceramic membrane, which can be used to selectively remove CO_2 from the high temperature stream (e.g., 200 to 400°C).

Characterization of Membrane Material

The material selected as a candidate for the CO_2 selective membrane has been evaluated comprehensively to insure its adequacy as a membrane material. Here we present the characterization results from TG/MS, DRIFTS and cyclic adsorption/desorption to demonstrate its reversibility with respect to its affinity to CO_2. The TG study indicates that significant weight loss from the 25°C to 600°C. However, according to MS, CO_2 weight loss is not significant until ~200°C. Further, the majority of the weight loss takes place at <400°C. To determine its degree of reversibility, we also performed cyclic adsorption and desorption studies using TGA for the temperature ranging from 200 to 350°C. The result shows that a majority of the CO_2 loss is reversible. It appears that the degree of reversibility begins to stabilize after the 5th cycle. Cyclic adsorption/desorption greater than the 5th cycle is presently underway. DRIFTS was performed to characterize the surface change as a result of CO_2 adsorption/desorption. Its trend is consistent with that determined by TGA.

Membrane Synthesis – Preliminary Experimental Results

Several methods have been under investigation for the synthesis of the proposed CO_2-affinity membrane. Some preliminary results obtained from slip casting, one of the methods currently explored by us, are presented here. Slip casting is a common method employed to prepare micro porous membranes with the pore size ranging from ~40Å to microns. To successfully develop a membrane through this approach, a homogenous solution suspended with particles with appropriate size is a prerequisite. In addition, the slip viscosity and the casting time, and many other parameters are important. SEM examination of the unsupported film shows that we are able to prepare a slip with the particles size in the range of 0.03 to 0.05 micron. Figure 1 presents one of the membranes prepared via slip casting. It is clear that a nearly defect free nanoporous membrane has been prepared with this CO_2-affniity ceramic material. Its pore size is estimated in the range of ~100Å in comparison with the reference Al_2O_3 membrane with a pore size of ~100Å shown in Figure 2.

Presently, we are actively pursuing the use of the CVD/I technique to plug the openings of this porous membrane as a post treatment. Thus, CO_2 can selectively permeate through the thin film formed by the selected CO_2-affinity material. This CVD/I technique has been successfully employed by us to seal the commercial 100Å Al_2O_3 membrane to become a nearly non-porous membrane with an ultra thin layer in the range of <1.5 micron. We anticipate this technique can be used here for the same purpose.

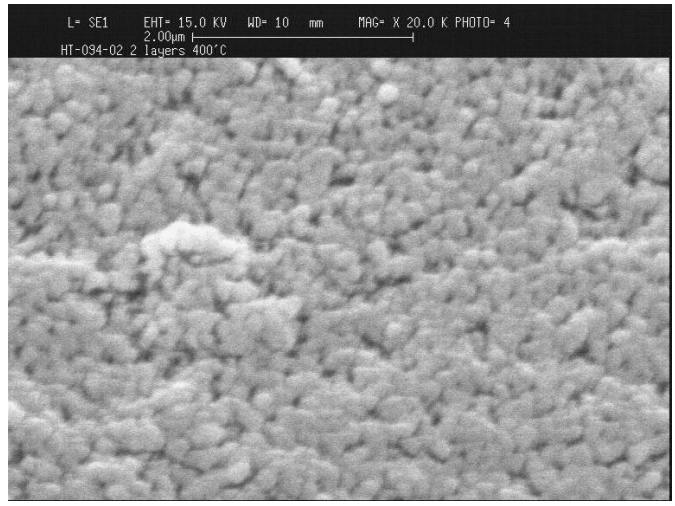

Figure 1 SEM photomicrograph of the porous ceramic membrane prepared with the CO_2-affinity material via slip casting.

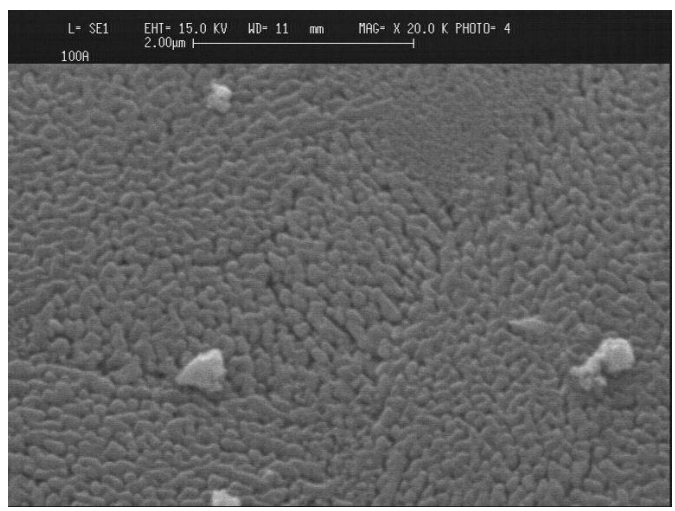

Figure 2 SEM photomicrograph of commercial Al_2O_3 membrane with 100Å pore size.

Sorbent Development for Carbon Dioxide Separation and Capture

Daniel J. Fauth, James S. Hoffman, and Henry W. Pennline

U.S. Department of Energy
National Energy Technology Laboratory,
P.O. Box 10940, Pittsburgh, PA 15236

Introduction

The combustion of fossil fuels emits considerable levels of carbon dioxide, a greenhouse gas proposed to influence global climate warming from human activities. Large stationary sources, such as coal-based electric generating plants, are likely targets for CO_2 capture and sequestration if regulation is deemed necessary for the 21st century and beyond. A number of mitigation technologies, to include CO_2 capture and sequestration, are currently under investigation[1-4]. The majority of these processes require CO_2 in a concentrated form.

A wide range of technologies currently available to separate CO_2 from flue gas include chemical absorption with monoethanolamine (MEA), membrane separation, cryogenic fractionation, and adsorption using molecular sieves[5]. It has been generally established that CO_2 capture for most of these processes is expensive and energy-intensive. Hence, a need exits for developing a range of emerging approaches to separate CO_2 with more cost-effective processes. Such a technique for CO_2 capture may employ dry scrubbing – a process that includes chemical absorption with a solid sorbent. Dry, regenerable sorbent processes are cyclic in the sense that a sorbent can remove the pollutant, be regenerated (and in this step yield a concentrated stream of CO_2), and thus be reused.

The approach undertaken in this study was to investigate the reaction of CO_2 with calcium-based reagents and a number of calcium-based impregnated materials using a thermogravimetric analyzer. The chemical reactions for CO_2 capture using these compounds are illustrated below. The forward reaction pathway depicts absorption of CO_2, whereas regeneration is expressed as the reverse reaction path.

$$CaO + CO_2 \Leftrightarrow CaCO_3 \quad (1)$$

$$Li_2ZrO_3 + CO_2 \Leftrightarrow Li_2CO_3 + ZrO_2 \quad (2)$$

In the thermogravimetric (TG) system, the change in sample weight was recorded as the sample was exposed to gases under conditions representative of absorption and regeneration. The extent of chemical reaction was linked to sample weight change, from which kinetic rate parameters could be estimated.

Experimental

An activated alumina (200 m^2/g) containing lanthanum was obtained from Alcoa Industrial Chemical Division, Vidalia, LA. Lanthanum (3.1 wt%) was added to impart high temperature stability to the alumina. For a given preparation, calcium nitrate tetrahydrate was dissolved in acetone for 1 hour. The alumina support (cylindrical extrudates) was immediately added to the calcium nitrate solution and soaked overnight at room temperature. The mixture was subsequently vacuum filtered and dried at 110°C for 18 hours. Lastly, the calcination step (400°C for up to 48 hours) converted the Ca-based complex into calcium oxide uniformly distributed throughout the carrier as confirmed by SEM-EDX analysis. A CaO loading of 13.8 wt% was determined for the calcined CaO/La_2O_3-doped/Al_2O_3 material.

A number of mesoporous zirconia catalyst supports (Type A and Type B) were purchased from Alfa Aesar. The zirconium oxide substrates were 1/8 inch in diameter having larger pore size and smaller surface area relative to the activated alumina. Both zirconia supports had a bimodal pore diameter distribution. Type A had approximately double the surface area of Type B (90 versus 51 m^2/g); with Type A having a corresponding smaller pore size for both maximums of the pore size distribution. Elemental analysis performed on the calcined CaO/ZrO_2 materials showed CaO loading to be 6.77% and 5.99% for Type A and Type B, respectively. The physical properties of the activated alumina and zirconia oxide carriers are included in Table 1.

Table 1. Physical and Chemical Characterization of Alumina and Zirconium Oxide Carriers

Ga-200L Alumina (Cylindrical Extrudates)	Analysis of Lot No. G2L0C011	
Surface area (M^2/g)	215	
Lanthanum (wt%)	3.1	
Pore volume (cc/g)	0.61	
Thermal Stability aged 1200°C, 3 hrs.		
Surface area (M^2/g)	53	
Zirconia Catalyst Support	**Type A**	**Type B**
Pellet diameter (in)	1/8	1/8
Surface area (M^2/g)	90	51
Median pore diameter, bimodal (Angstrom)	80/400	160/600
Total pore volume (cc/g)	0.31	0.30
Percent purity (metal basis)	99.8	99.8

Thermogravimetric experiments were performed using a microbalance assembly consisting of a Cahn TG-131 Thermogravimetric Analyzer (TGA). A gas cylinder supplied carbon dioxide of stock gas grade (99.99%) to the TGA unit. In a representative test, ~200 mg of sample was initially charged into a quartz sample pan. Slotted apertures in the bottom and sidewall of the sample pan were added to help mitigate gas diffusional resistance. A type K thermocouple located directly below the suspended sample measured and controlled the internal temperature within the thermogravimetric assembly. A gas flow rate of 140 cc/min was employed for all tests. Prior to CO_2 absorption, each sample was preconditioned and dried in nitrogen elevating the reactor temperature to 150°C, followed by subsequent heating to achieve the absorption temperature of interest (typically 500-750°C). Upon achieving steady state in dry nitrogen, the introduction to carbon dioxide was made. A constant CO_2 flow rate of 140 cc/min. was maintained. The CO_2 absorption stage was allowed to proceed until a steady-state weight gain was achieved, or it was otherwise halted if excessive duration of time was required to reach steady state.

Results and Discussion

Calcium-Based Reagents: To help elucidate the chemical behavior of the active metal within the impregnated sorbent, several tests were conducted using pure reagent compounds (CaO, $CaCO_3$). The CO_2 absorption reaction was initially very fast (50% theoretical conversion after an hour), followed by much slower reaction. The absorption reaction appeared favorable between 750-850°C, while regeneration was attainable at 1000°C. By raising the temperature from 850°C to 1000°C in N_2, the calcium-based reagents could be rapidly regenerated within a short period of time (~15 minutes). Thermal regeneration of the product was strongly dependent on the background gas composition. In nitrogen, the

regimes of temperature suitable for regeneration was found to be significantly lower than in pure CO_2. For example, $CaCO_3$ began to decompose at 650°C in nitrogen, whereas in CO_2 it was relatively stable up to 900-950°C.

A multi-cycle test with repeated absorption and regeneration steps was conducted at 750°C starting with $CaCO_3$ (**Figure 1**). Gas composition was switched between carbon dioxide (absorption) and nitrogen (regeneration) at 30-minute increments, resulting in one-hour intervals for a complete cycle. Although the cycles appear very similar, a slight degradation in performance was apparent. For equivalent cycle times, the CO_2 capture (conversion to calcium carbonate) decreased by ~2 percentage points, from 36% to 34% to 32% over 3 cycles. Gupta[6] observed slight degradation of $CaCO_3$ reagent over a 3-cycle test.

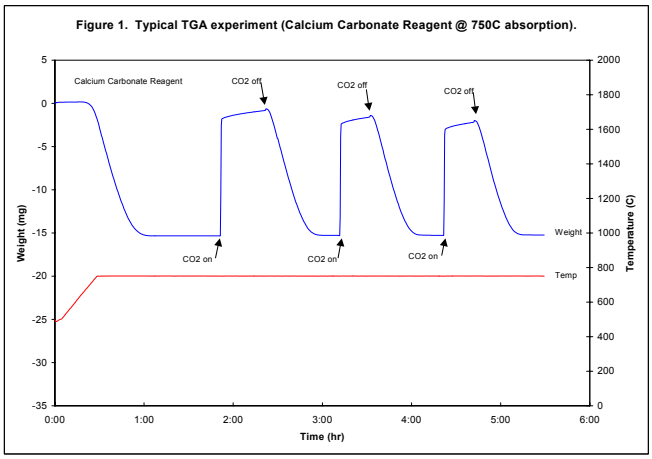

Ca-based/La-modified/Alumina Sorbent: Absorption tests with the Ca-based lanthanum-doped alumina sorbent were performed upon exposure to pure CO_2 at temperatures between 500-750°C (**Figure 2**). The alumina substrate, when tested individually at temperatures between 650-850°C in pure CO_2, showed no appreciable affinity to sorb CO_2. As with calcium-based reagent tests, the initial rate of reaction is very fast, achieving 15-20% sorbent conversion for the $CaO/La_2O_3/Al_2O_3$ material. However, the reaction slows significantly and enters a regime characterized by very long residence time required to achieve minimal increase in sorbent conversion. This regime was partially attributed to increased gas diffusional resistance through a product layer of calcium carbonate.

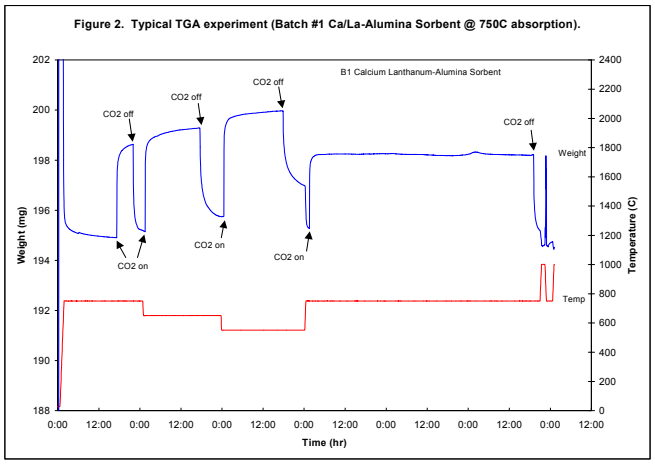

Calcium-based/Zirconia Sorbent: Thermogravimetric testing of the prepared calcium deposited on zirconium oxide substrates were performed at 500°C in pure CO_2. Type A and Type B zirconia carriers, with no calcium deposition, showed a slight weight gain indicating some CO_2 absorption was achieved. However, upon gas switching to N_2, the carriers lost all of the gained weight. It is logical to assume that the captured CO_2 was not due to chemical reaction to form carbonate, but rather another mechanism.

Similar to the calcium reagents and the $CaO/La_2O_3/Al_2O_3$ sorbent tests, the absorption reaction was initially rapid and then entered into a slower kinetic regime. However, the zirconia sorbents performed much better, as characterized by the much higher conversion attained versus the CaO/lanthanum-doped alumina sorbent. Conversions ranging from 50-75% were observed for the Ca/zirconia sorbents versus 15-20% conversion for the CaO/lanthanum-doped alumina sorbent. One obvious explanation for the improved conversion was attributed to the pore size differential between mesoporous zirconia and microporous lanthanum-alumina. Even though the alumina had a higher surface area, pore pluggage and/or increased diffusional resistance through the calcium carbonate product layer appeared to be a plausible cause for the less active calcium/alumina sorbent.

The permanence of the sequestered CO_2 onto the Ca/zirconia sorbents was also in stark contrast to the alumina sorbents. The Ca/zirconia materials exhibited significantly less weight loss and retained a larger fraction of the absorbed CO_2 upon gas switching from pure CO_2 to N_2 at the end of the absorption stage at 500°C. Approximately 70-80% of the sorbed CO_2 remained with the sorbent for the Type B zirconia (larger pore volume and smaller surface area) and roughly half of the sorbed CO_2 with the sorbent for the Type A zirconia. Regeneration of the Ca/zirconia sorbents was quickly achieved by elevating the temperature from 500°C to 750°C under nitrogen.

Conclusion

Dry, regenerable sorbent processes capable of removing carbon dioxide from point generation sources can be used for the capture of CO_2. Cyclic reaction performances of various Ca-based sorbents were investigated using a thermogravimetic analyzer. Incorporating the materials at temperatures expected to be seen under gasification conditions, pure calcium and calcium/alumina systems had good initial reactivity, but the capacity and overall reactivity were poor. Improved results were obtained with calcium/zirconia sorbents. Future work will focus on development of more active, more attrition-resistant materials.

References

1. DOE Report No. DOE/SC/FE-1, "Carbon Sequestration Research and Development" December 1999.
2. Kane, R.L.; and D.E. Klein, Chemical Engineering Progress, pp. 44-52. June 2001.
3. Herzog, H.; Environmental Science and Technology, **35:7**, pp. 148A-153A, April 1, 2001.
4. Rao, A.B.; and E.S. Rubin, Environmental Science & Technology, **36:20**, pp. 4467-4475, October 2002.
5. Herzog, H.; Drake, E.; and E. Adams, CO_2 Capture, Reuse, and Storage Technologies for Mitigating Global Climate Change, Final Report DOE Contract No. DE-AF22-96PC01257, January 1997.
6. Gupta, H.; and L.S. Fan, Industrial & Engineering Chemistry Research, 41:16, pp. 4035-4042, August, 2002.

SIMULATION OF RATE-BASED THEORETICAL MODEL FOR CO_2 CAPTURE: MASS TRANSFER AND HYDRODYNAMIC ASPECTS

Adisorn Aroonwilas and Amornvadee Veawab

Faculty of Engineering, University of Regina,
Saskatchewan, Canada S4S 0A2

Introduction

Carbon dioxide (CO_2) absorption process is an immediate capturing technique suitable for the high-volume waste gas streams from coal-fired power plants. However, the overall cost of this process is relatively high. One reason for this high cost is the use of rule-of-thumb or approximation technique for the process design. Customarily, the absorption column is designed using the lumped mass-transfer and hydrodynamic parameters that are simply assumed to be constant over the entire length of the column, leading to an unnecessary oversized unit. With the advent of the environmental crisis and the economic constraint, the approximation is no longer applicable to process design. It is therefore necessary to obtain a better understanding of the actual phenomena taking place in this particular system so that a more rigorous and accurate column design technique can be developed. This paper presents a mechanistic concept for a rigorous absorber design that describes mass-transfer and hydrodynamic behavior within the CO_2 absorption columns fitted with structured packings.

Mechanistic Concept

The development of mechanistic concept was based on an integration of various theoretical models that aim to determine the distribution pattern of the flowing liquid inside the packing element, effective interfacial area, mass-transfer coefficients and other information such as thermodynamic contributions (vapor-liquid equilibrium-VLE). Each model is briefly described below. Complete details can be found in the thesis of Aroonwilas [1].

Liquid Distribution Model

The liquid distribution model (LDM) was developed in order to evaluate the distribution features of irrigating liquid, at different locations inside the packing element, during the operation of the absorption columns. The model is composed of two major components; i) a distribution structure representing a network of all possible flow-paths (connecting between packing intersections) through which the liquid can travel within the packing element and ii) a distribution intensity that indicates the quantity of irrigating liquid in each path (liquid rivulet). The liquid distribution features were generated by taking into account the details of the packing sheet arrangement and perforation, including dimensions, coordinates and patterns of the opening space on the packing sheets.

Effective Interfacial Area Model

After the flow rates of liquid rivulets in all flow-paths were assigned by the liquid distribution model, the effective area for mass-transfer process was then evaluated from the calculated liquid rivulet dimensions (width and thickness). The calculations were based on the Shi and Marsmann's equations [2]. Such equations take into account physical properties of the associated liquid solution, including density, viscosity, surface tension and contact angle.

Mass-Transfer Coefficient Model

The determination of absorption performance directly involves coefficients of mass-transfer across the gas-liquid boundary. The overall mass-transfer coefficient in the absorption system associated with chemical reactions can be determined from two-film theory. The liquid-phase mass-transfer coefficient (k_L°) can be estimated from Penetration Theory as shown below.

$$k_L^\circ = 2\sqrt{\frac{D_{A,L}}{\pi t}} \qquad (1)$$

where $D_{A,L}$ and t are liquid-phase diffusivity coefficient of component A and gas-liquid contact time, respectively. The gas-phase mass-transfer coefficient (k_G) can be estimated from equation 2 [3].

$$Sh_G = 0.0338(\mathrm{Re}_G)^{0.8}(Sc_G)^{0.333} \qquad (2)$$

where Sh_G, Re_G and Sc_G represent Sherwood number, Reynolds number and Schmidt number, respectively. The enhancement factor due to chemical reactions can be evaluated by using the relationships proposed by DeCoursey & Thring [4].

Thermodynamic Model

The vapor-liquid equilibrium (VLE) behavior of the CO_2 absorption system is another important element of the mechanistic model presented in this study. The equilibrium establishes concentration gradient between the gas and liquid phases, driving the mass-transfer process to proceed. An understanding of the equilibrium behavior is particularly essential for CO_2 absorption using aqueous alkanolamine solutions. In this work, the equilibrium behavior of the CO_2-MEA system was evaluated by using the electrolyte NRTL model proposed by Austgen and colleagues [5]. The model can provide the necessary thermodynamic information, including the speciation (concentrations of different ionic species and molecules) in the CO_2 absorption system. This means that the concentration of free CO_2 in the bulk liquid can be estimated.

MODEL SIMULATION

A Fortran-90 computer program was written for the mechanistic concept in order to simulate the CO_2 absorption performance of columns packed with structured packings. The simulation was based on the theoretical column design procedure for adiabatic gas absorption with chemical reaction. The procedure accounted for heats of absorption, solvent evaporation and condensation, chemical reactions in the liquid phase, and heat-and mass-transfer resistance in both gas and liquid phases.

The simulation of the absorption column was achieved by dividing the column or packing height into a number of sections with height dz. Each of these sections was treated as a non-equilibrium (or rate-based) discrete stage, which was governed by the material and energy equations.

Each run of computer simulation gave essential information for the design of absorption system. These include concentration of CO_2 in the gas-phase, concentration of reactive species in the liquid-phase, system temperature, mass-transfer coefficients and the effective interfacial area at different axial positions along the absorption column. The simulation results were generally presented as plots against the column height to show the extent of the variation in process parameters at different column positions. The simulation also provided the plots, which represent quality of the liquid distribution across the cross-section of the column.

The model was successfully verified by comparing the simulated and experimental CO_2 concentration profiles for CO_2-MEA system under two extreme conditions, depending upon the

significance of thermodynamics contribution in controlling the mass-transfer phenomena.

SIMULATION RESULTS

The simulation was carried out for the absorbers containing stainless-steel structured packings with different specific surface area ranging from 170 to 500 m^2/m^3, i.e. Gempak-1.5A, Gempak-2A, Gempak-3A, and Gempak-4A. The simulation was based on 15%CO_2 in feed gas and 1 m/s gas velocity. Figure 1-(a) shows the concentration profiles for the absorbers with the packing height of 5 m. The Gempak-4A having the surface area of 500 m^2/m^3 provided the highest recovery performance (98%), whereas the Gempak-1.5A having the area of 170 m^2/m^3 gave the lowest value of 57%. The Gempak-3A and -2A provided the recovery values in between the two extremes, i.e. 89% and 76%, respectively. The difference in the recovery performance of these packings is due to the difference in the effective interfacial area shown in Figure 1-(b).

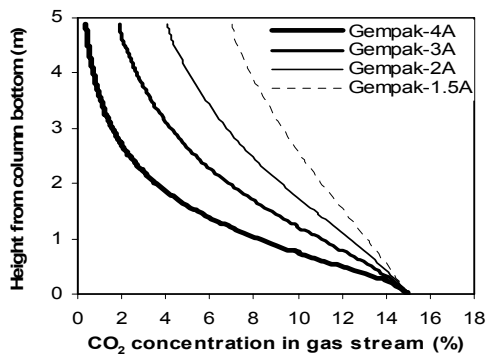

(a)

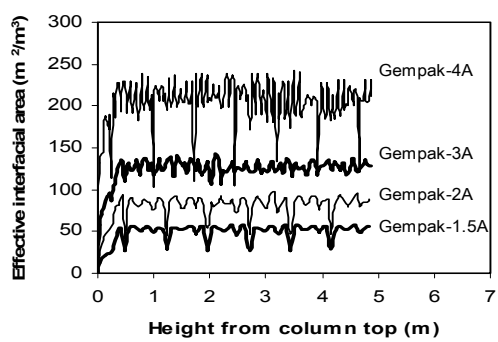

(b)

Figure 1. CO_2 recovery performance of different structured packings.

Figure 2-(a) illustrates the CO_2 concentration profiles for the absorbers used to recover 1075 kg CO_2/m^2-hr. Based on this information, the relationship between the specific surface area of packing and the packing height requirement for a given recovery target can be plotted in Figure 2-(b). The required packing height increases proportionally as the packing surface area decreases from 500 to 233 m^2/m^3. However, the height requirement increases substantially when the surface area is reduced to 170 m^2/m^3.

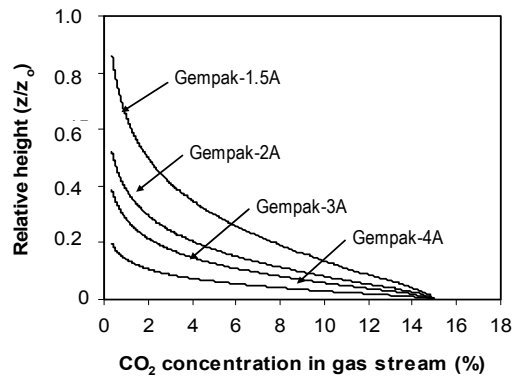

(a)

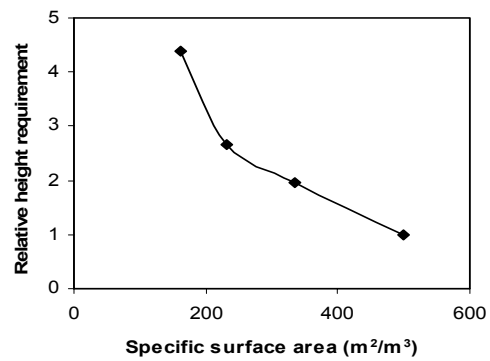

(b)

Figure 2. Height requirement for different structured packings.

Acknowledgement

Financial support from the Natural Sciences and Engineering Research Council of Canada (NSERC) is gratefully acknowledged.

References

1. Aroonwilas, A., Ph.D. Thesis: University of Regina, Canada, 2001.
2. Shi, M. G.; Mersmann, A., *German Chemical Engineering*, **1985**, *8*, 87-96.
3. Bravo, J. L.; Rocha, J. A.; Fair, J. R., *Hydrocarbon Processing* **1985**, *64*, 91-95.
4. DeCoursey, W. J.; Thring, R. W., *Chemical Engineering Science*, **1989**, *44*, 1715-1721.
5. Austgen, D. M.; Rochelle, G. T.; Peng, X. and Chen, C., *Industrial & Engineering Chemistry Research*, **1989**, *28*, 1060-1073.

TRANSITION METAL PHOSPHIDES: NEW CATALYSTS FOR HYDROPROCESSING

S. T. Oyama, Y.-K. Lee

Department of Chemical Engineering
Virginia Tech
Blacksburg, VA 24061

Introduction

Transition metal phosphides are a class of refractory metallic compounds formed from the alloying of metals and phosphorus. They have recently been shown to have excellent activity in hydroprocessing (1,2,3,4), with activity higher than sulfides for hydrodenitrogenation (HDN) and hydrodesulfurization (HDS). The materials can be prepared by the temperature-programmed reduction of phosphate precursors in bulk or supported form. A comparison of the activity of several phosphides indicates that the HDN and HDS activity at 3.1 MPa increases in the order: Fe_2P < CoP < MoP < WP < Ni_2P. Most of the work has been done on Ni_2P/SiO_2 because of its high activity. Analysis of the structure of the fresh catalyst by extended x-ray absorption fine structure (EXAFS) shows the presence of Ni-Ni and Ni-P distances corresponding to the bulk compound. The catalyst after reaction shows the appearance of a signal corresponding to a Ni-S distance, indicating that at high pressure the active phase is a phosphor-sulfide.

Experimental

The synthesis of the phosphide catalysts involved two steps. First, precursor phosphates were prepared by evaporating aqueous solutions of the metal nitrate, and ammonium orthophosphate $(NH_4)_2HPO_4$ (Aldrich, 99 %), followed by calcination at 773 K. Second, the precursors were reduced in a flow of hydrogen in a temperature-programmed manner using a heating rate of $\beta = 0.0167$ K s^{-1} (1 K min^{-1}), following which they were cooled in He, and passivated in 0.1% O_2/He. In the case of supported samples the phosphate precursors were prepared by impregnation of the metal nitrate and ammonium phosphate solutions onto a fumed silica (Cabosil, L90) followed by calcination. Sulfided Ni-Mo/Al_2O_3 (Shell 324) and Co-Mo/Al_2O_3 (Ketjenfine 756) were used as references. The catalysts were routinely characterized by x-ray diffraction, CO uptake, and BET surface area measurements. Irreversible CO uptake measurements, denoted here as *ex situ*, were obtained at room temperature after passivated samples were rereduced at 723 K. For the sulfide references, O_2 uptakes were measured at 195 K.

Hydrotreating activities of the samples were obtained in a three-phase trickle bed reactor for hydrodenitrogenation (HDN) and hydrodesulfurization (HDS) with a model petroleum liquid containing 2000 ppm nitrogen (quinoline), 3000 ppm sulfur (dibenzothiophene), 500 ppm oxygen (benzofuran), 20 wt.% aromatics (tetralin), and balance aliphatics (tetradecane). The operating conditions were close to industrial conditions, 3.1 MPa and 643 K, with a liquid flow rate of 5 cm^3/h and a hydrogen flow rate of 100 μmol s^{-1} (150 cm^3 min^{-1}) corresponding to a gas-liquid ratio of 9800 SCF H_2/barrel. The detailed description of the testing system is reported elsewhere (5). Quantities of catalysts loaded in the reactor correspond to the same amount of *ex situ* CO uptake (70 μmol). Prior to reactivity measurements, the catalyst samples were pretreated in exactly the same manner as before the *ex situ* CO uptake determinations. Hydrotreating samples were collected every two or three hours in sealed septum vials and were analyzed off-line with a gas chromatograph (Hewlett Packard, 5890A) equipped with a 0.32 mm i.d. x 50 m fused silica capillary column (CPSIL-5CB, Chrompack, Inc.) and a flame ionization detector.

The chemicals utilized in the reactivity study were dibenzothiophene (Aldrich, 99.5 %), quinoline (Aldrich, 99.9 %), benzofuran (Aldrich, 99.9 %), tetralin (Aldrich, 99.5 %) and tetradecane (Jansen Chimica, 99 %).

Results and Discussion

A more complete description of the content of this article is presented elsewhere (6). The general properties, structure, and preparation of transition metal phosphides have been described in a number of reviews (7,8). The materials have ceramic character, with high hardness and strength, but also possess metallic properties, such as conductivity. Their structure of phosphides is built up from trigonal prisms, with the phosphorus atoms surrounded by six metal atoms. Examples of structures are shown in Fig. 1. The phosphorus atoms may be isolated, or may interact to form chains or pairs (not shown).

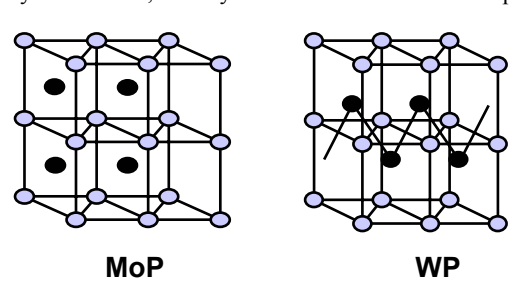

Figure 1. Typical structures of transition metal phosphides.

Characterization of the samples by ^{31}P magic angle spinning nuclear magnetic resonance (9,10) and EXAFS (11) confirms the structural assignements. Results of characterization of the samples by surface area measurements and CO uptakes are shown in Table 1.

Table 1. Surface Area and CO Chemisorption

Catalyst	MoP	WP	Fe_2P/SiO_2 14 wt.%[a]	CoP/SiO_2 9 wt.%[b]	Ni_2P/SiO_2 10 wt.%[b]
SA m^2g^{-1}	8	10	97	87	97
CO uptake μmol g^{-1}	15	10	16	16	28

[a] Metal loading = 2.31 mmol/g SiO_2 [b] Metal loading = 1.16 mmol/g SiO_2

The phosphides are stable and active catalysts for hydroprocessing (Table 2). The most active catalyst was nickel phosphide, with higher HDN and HDS than a commercial Ni-Mo catalyst sulfided *in situ*. The basis of comparison is equal sites loaded in the reactor, as measured by *ex situ* CO uptake for the phosphides and by O_2 uptake for the freshly sulfided Ni-Mo/Al_2O_3 catalyst.

Table 2. Activity in Hydroprocessing

Catalyst	MoP	WP	Fe_2P/SiO_2 14 wt.%[b]	CoP/SiO_2 9 wt.%[a]	Ni_2P/SiO_2 10 wt.%[a]	Ni-Mo/ Al_2O_3
HDS	57	67	4.7	30	98	76
HDN	52	58	1.6	32	81	38

The Ni_2P/SiO_2 (Ni/P = 1/2) catalyst was studied with a real feed to test its performance at realistic conditions (12). The feed was a hydrotreated gas oil with low sulfur (440 ppm) and nitrogen (8 ppm) content, and moderate aromatics content (27 wt%), which mimics that which would be used in a second-stage hydrotreating process. In measurements in a trickle-flow system at 593 K and 3.9 MPa and a WHSV of 4 h^{-1}, the Ni_2P/SiO_2 compared well with a commercial Co-Mo-S/Al_2O_3, with HDS conversion of 85 % vs. 80 %.

The effect of P content on the Ni_2P/SiO_2 was studied (13) with samples prepared with initial Ni/P ratios of 2/1, 1/2, and 1/3. The best material had a Ni/P ratio of 1/2, with the other catalysts showing lower HDS and, especially, HDN. Elemental analysis showed that the actual Ni/P ratio after preparation was closer to the stoichiometric value of 2/1 due to volatilization of the P during reduction.

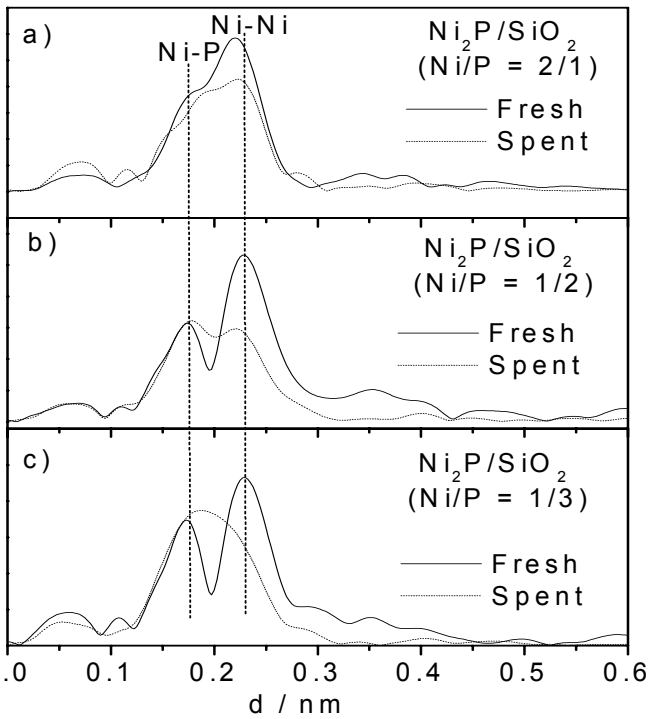

Figure 2. Nickel K-edge EXAFS of the fresh and spent samples with different Ni/P ratios: a) Ni/P = 2/1, b) Ni/P = 1/2, c) Ni/P = 1/3. The Ni/P ratios indicated are initial values. (Ref. 13)

Figure 2 compares the Ni K-edge EXAFS spectra of the fresh and spent samples. For the fresh materials, the sample with initial Ni/P = 2/1 (Fig. 2a) shows a main peak with a shoulder at lower interatomic distance. In contrast, the samples with initial Ni/P = 1/2 and 1/3 (Fig. 2b,c) display two distinct peaks. Comparison with a reference Ni_2P sample shows good agreement in the Ni-Ni and Ni-P distances. There is no such agreement with the features of NiO, $Ni(OH)_2$, and Ni metal, and this demonstrates that the predominant phase in these two supported catalysts is Ni_2P. For the sample with the initial Ni/P ratio of 2/1 (Fig. 2a) the Ni-P peak is reduced to a shoulder and the Ni-Ni peak shifts to the position of metallic Ni. Clearly, the amount of Ni_2P phase is smaller, as expected from the spreading of the metal and phosphorus components on the surface of the support, and this explains the low activity. With the Ni_2P/SiO_2 sample with the excess phosphorus (Initial Ni/P = 1/3), the EXAFS peak positions duly correspond to those of bulk Ni_2P. However, the intensity of the Ni-P relative to the Ni-Ni peak is now increased over that of bulk Ni_2P. The extra phosphorus probably resides on the surface of the highly dispersed particles, breaking up the catalytically active ensembles and again reducing activity.

For the spent catalysts, changes occurred after reaction. For the spent sample with initial Ni/P = 2/1, a small feature appears in between the main Ni-Ni peak and the Ni-P shoulder (Fig. 2a). For the spent sample with initial Ni/P = 1/2, the two-peak structure is retained, but there is a reduction in the Ni-Ni peak intensity (Fig. 2b). For the spent sample with initial Ni/P = 1/3, the Ni-Ni peak is almost entirely attenuated and a broad feature at lower interatomic distance appears (Fig. 2c). Clearly, in all cases there is disruption of the original Ni_2P phase, and this is likely due to the formation of sulfur compounds. The identification of the changes occurring in the spent samples was carried out by comparing their spectra to those of bulk sulfide references (13).

Conclusions

Transition metal phosphides constitute a new class of catalysts for hydrotreating that differ substantially from sulfide materials. The activity of the phosphides in HDS and HDN follows the order: Fe_2P < CoP < MoP < WP < Ni_2P. The most active material is Ni_2P/SiO_2, which compares favorably with commercial sulfided Ni-Mo/Al_2O_3 and Co-Mo/Al_2O_3 catalysts. Phosphorus content has a profound effect on the structure and activity of Ni_2P/SiO_2 catalysts. Samples prepared with initial ratios of Ni/P ≈ 1/2 result in a material with close to stoichiometric proportions of P (Ni/P = 1/0.5) with excellent activity in hydroprocessing. Characterization of the catalysts by EXAFS measurements before and after reaction indicates that the active phase in the catalysts is a phospho-sulfide. Overall results indicated that on these novel, high activity hydroprocessing catalysts, the HDS and HDN reactions are not promoted by nickel on its own, but that phosphorus plays an important role in the reaction.

Acknowledgement. Support for this work came from the U.S.Department of Energy, Office of Basic Energy Sciences, through Grant DE-FG02-963414669, the NEDO International Joint Research Program, the LNLS (National Synchrotron Light Laboratory) in Campinas, Brasil, under Project XAS #592/99, the Tsukuba Photon Factory of the High Energy Accelerator Research Organization under Grant 2001G297, and Brookhaven National Laboratory under grant 4513. Individuals who contributed to this work were W. Li, P. Clark, X. Wang, K. Bando, and F. G. Requejo.

References

(1) Robinson, W. R. A. M.; van Gastel, J. N. M.; Korányi, T. I.; Eijsbouts, S.; van Veen, J. A. R.; and de Beer, V. H. J., *J. Catal.* **1996**, 161, 539.
(2) Li, W.; Dhandapani, B.; Oyama, S. T., *Chem. Lett.* **1998**, 207.
(3) Stinner, C.; Prins, R.; Weber, T., *J. Catal.* **2000,** 191, 438.
(4) Phillips, D. C.; Sawhill, S. J.; Self, R.; Bussell, M. E., *J. Catal.* **2002**, 207, 266.
(5) Ramanathan, S.; Oyama, S. T., *J. Phys. Chem*., **1995**, 99, 16365.
(6) Oyama, S. T., *J. Catal.* **2002**, In press.
(7) Aronsson, B., Lundström, T., Rundqvist, S., *Borides, Silicides and Phosphides*, Methuen, London and Wiley, New York, 1965.
(8) Corbridge, D. E. C., *Studies in Inorganic Chemistry*, Vol. 10, 4th Ed., Elsevier, Amsterdam, 1990.
(9) Clark, P.; Wang, X.; Oyama, S. T., *J. Catal.* **207**, 256 (2002).
(10) Stinner, C.; Tang, Z.; Haouas, M.; Weber, Th.; Prins, R., *J. Catal.* **208**, 456 (2002).
(11) Oyama, S. T.; Clark, P.; Wang, X.; Shido, T.; Iwasawa, Y.; Hayashi, S., Ramallo-López, J. M.; Requejo, F. G., *J. Phys. Chem.* **106**, 1913 (2002).
(12) Oyama, S. T.; Wang, X.; Requejo, F. G.; Sato, T.; Yoshimura, Y., J. *Catal.* **209**, (2002).
(13) Oyama, S. T.; Wang, X.; Lee, Y.-K.; Requejo, F. G., *J. Catal.* **210**, 207 (2002).

NEW CATALYSTS FOR HYDRODESULFURIZATION: CARBIDES, NITRIDES AND PHOSPHIDES

Mark E. Bussell, Stephanie J. Sawhill, Kathryn A. Layman, Autumn W. Burns

Dept. of Chemistry, MS-9150,
Western Washington University
Bellingham, WA 98225

Introduction

Concerns for the environment both in the United States and abroad have led to new regulations which will require dramatically lower sulfur levels in fuels. Considerable effort has been devoted to optimizing molybdenum sulfide-based hydrodesulfurization (HDS) catalysts and nearly a two-fold increase in catalyst activity has been achieved over the last thirty years.[1] When the requirement for lower sulfur levels in fuels is coupled with the need to process lower quality petroleum feedstocks, incremental improvement of the current sulfide-based HDS catalysts may not be sufficient to meet industry needs.

An approach to the development of new HDS catalysts we are exploring is to investigate how main group elements other than sulfur modify the catalytic properties of molybdenum (and other transition metals). Studies in a number of laboratories over the past few years have shown oxide-supported molybdenum carbide ($\exists$-Mo_2C)[2-4] and nitride ((-Mo_2N)[3-7] to be more active HDS catalysts than conventional sulfided molybdenum catalysts. More recently, a few studies have appeared which show that silica-supported molybdenum phosphide (MoP)[8,9] and nickel phosphide (Ni_2P)[10-13] also demonstrate excellent potential for use as HDS catalysts.

In the current study, we describe the synthesis, characterization and HDS evaluation of a number of monometallic and bimetallic carbide, nitride and phosphide catalysts in oxide-supported form. Careful attention has been paid to the role of catalyst pretreatment in determining HDS activity, and the stability of the different catalytic materials under reaction conditions has been investigated.

Experimental

Catalyst Synthesis. Alumina-supported monometallic and bimetallic carbide and nitride catalysts were prepared as described elsewhere.[3,4,14] The syntheses involved carburization or nitridation of alumina-supported oxidic precursors in a CH_4/H_2 mixture or NH_3, respectively, using the temperature-programmed reduction (TPR) method. Silica-supported molybdenum carbide and nitride catalysts were prepared similarly.

Cobalt-promoted molybdenum carbide (Co-Mo_2C/Al_2O_3) catalysts, as well as oxidic precursors (Co-MoO_3/Al_2O_3) of sulfided Co-Mo/Al_2O_3 catalysts were prepared as follows. Promoted catalysts with theoretical molar ratios in the range Co/Mo = 0.15 - 1.5 were prepared by impregnation of MoO_3/Al_2O_3 and Mo_2C/Al_2O_3 catalysts with aqueous cobalt (II) nitrate ($Co(NO_3)_2 \bullet 6H_2O$). The Co-MoO_3/Al_2O_3 and Co-Mo_2C/Al_2O_3 catalysts were then transferred to a vacuum desiccator and vacuum dried overnight at room temperature. Following drying, the catalysts were passivated by back-filling the vacuum desiccator with 1 atm of a 1 mol% O_2/He mixture for 2 h. The Co-Mo_2C/Al_2O_3 catalysts were not calcined following Co promotion to avoid oxidation of the supported β-Mo_2C particles. So that the catalyst preparation procedures were the same, the Co-MoO_3/Al_2O_3 catalysts also were not calcined following addition of the cobalt nitrate.

Silica-supported molybdenum phosphide (MoP/SiO_2) and nickel phosphide (Ni_2P/SiO_2) catalysts were prepared as described elsewhere.[9,13] Briefly, silica-supported metal phosphate-like precursors were prepared by impregnation of the support with aqueous metal salts and diammonium hydrogen phosphate ($(NH_4)_2HPO_4$ followed by calcination at 773 K in air. The oxidic precursors were reduced using TPR in flowing H_2 to give the phosphide catalysts.

The oxide-supported carbide, nitride and phosphide catalysts were characterized with a variety of techniques including X-ray diffraction (XRD), X-ray photoelectron spectroscopy (XPS), transmission electron microscopy (TEM) and chemisorption measurements. The details of these measurements have been described elsewhere.[3,9,13,14] Hydrodesulfurization activity measurements were carried out at 643 or 693 K using a feed consisting of 3.0 mol% thiophene (C_4H_4S) in H_2.[3,9]

Results and Discussion

The successful synthesis of the oxide-supported carbide, nitride and phosphide catalysts was verified using XRD and TEM. Shown in **Figures 1** and **2** are XRD patterns for a series of Ni_2P/SiO_2 catalysts with increasing Ni_2P loadings and a TEM image showing a Ni_2P particle on a 25 wt% of Ni_2P/SiO_2 catalyst, respectively.

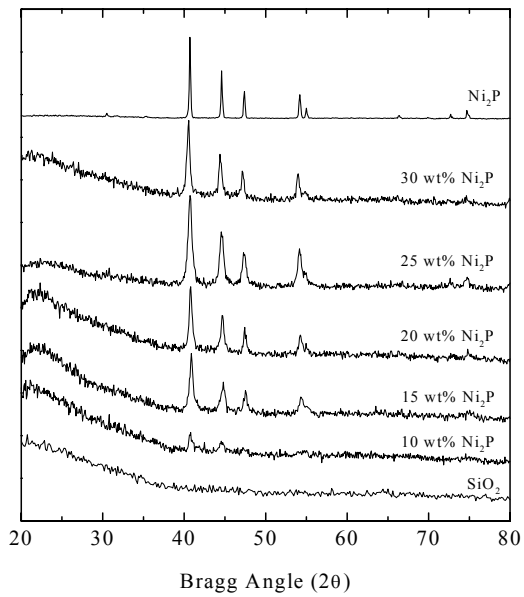

Figure 1. XRD patterns for Ni_2P/SiO_2 catalysts as well as the silica support and unsupported Ni_2P.

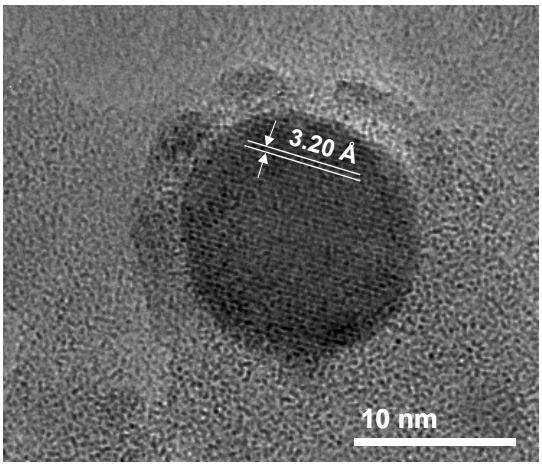

Figure 2. A TEM micrograph of a 25 wt% Ni_2P/SiO_2 catalyst.

The lattice spacing of 3.20 Å is assigned to the {001} crystallographic plane of Ni_2P which is consistent with the XRD patterns. The thiophene HDS activity of a 30 wt% Ni_2P/SiO_2 catalyst as well as of silica-supported molybdenum carbide (β-Mo_2C), molybdenum nitride (γ-Mo_2N), molybdenum phosphide (MoP) and a sulfided molybdenum catalyst are plotted versus time on-stream in **Figure 3**.

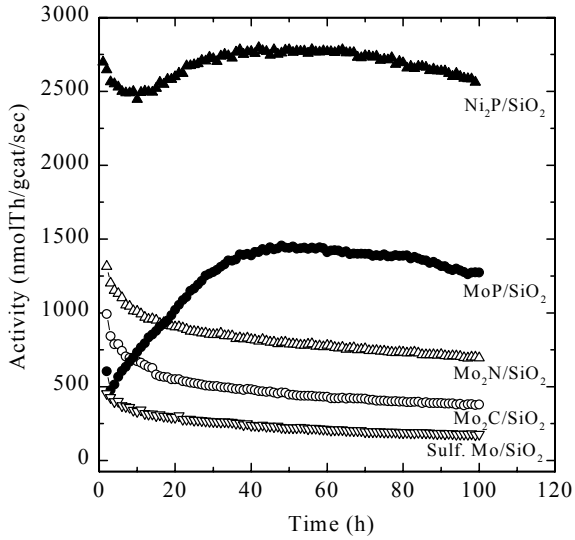

Figure 3. Comparison of thiophene HDS activity data for carbide, nitride and phosphide catalysts with similar data for a sulfided Mo catalyst.

The Mo-based catalysts have similar Mo loadings, corresponding to a 28.5 wt% MoO_3 loading in the oxidic precursor of the Mo carbide, nitride and sulfided Mo catalysts. The catalysts exhibit a wide range of thiophene HDS activities with the carbide, nitride and phosphide catalysts all having higher HDS activities than the sulfided Mo/SiO_2 catalyst. The Mo carbide, nitride and sulfided Mo catalysts display similar trends in HDS activity over time, decreasing over the entire time on-stream but achieving a relatively stable activity at 100 h. In contrast, the HDS activities of the MoP/SiO_2 and Ni_2P/SiO_2 catalysts show a different trend, increasing over approximately the first 50 h on-stream and then decreasing somewhat for the remaining 50 h of the testing period.

Similar to a model presented previously for alumina-supported catalysts,[3,4] the high HDS activities of the Mo_2C/SiO_2 and Mo_2N/SiO_2 catalysts are ascribed to a high density of active sites located on a thin, highly dispersed sulfided Mo layer formed at the surface of the supported carbide and nitride particles under reaction conditions. An understanding of the high HDS activities of the MoP/SiO_2 and Ni_2P/SiO_2 catalysts is less well developed at this time. Infrared spectroscopy studies of adsorbed CO and other probe molecules are currently under way to gain insight into the nature of the adsorption sites on the phosphide catalysts and their stability under reaction conditions.

In addition to our studies of monometallic carbide, nitride and phosphide catalysts, we have also investigated the HDS properties of bimetallic and promoted carbide and nitride catalysts. As recently described elsewhere,[14] the synthesis of alumina-supported bimetallic carbide (Co_3Mo_3C/Al_2O_3) and nitride (Co_3Mo_3N/Al_2O_3, Ni_2Mo_3N/Al_2O_3) catalysts requires care in order to avoid monometallic impurities. The preparation of promoted catalysts is far simpler, involving only impregnation of the carbide or nitride catalyst with the promoting metal salt followed by vacuum drying. The incorporation of a second metal (Co, Ni) to form bimetallic carbide and nitride phases (e.g. Co_3Mo_3C/Al_2O_3) or promoted materials (e.g. Co-Mo_2C/Al_2O_3) yields significantly more active HDS catalysts as summarized in **Figure 4.**

Conclusions

Oxide-supported metal carbide, nitride and phosphide catalysts can be prepared using the TPR method. These materials have high HDS activities and their catalytic properties warrant further investigation.

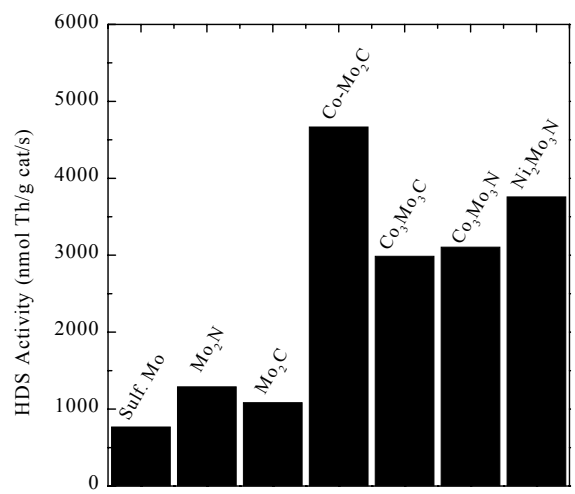

Figure 4. Thiophene HDS activities for alumina-supported carbide and nitride catalysts.

Acknowledgement. This research was supported by the National Science Foundation under grant numbers CHE-9610438 and CHE-0101690. Acknowledgment is also made to the Henry Dreyfus Teacher-Scholar Awards Program of the Camille and Henry Dreyfus Foundation for partial support of this research. A portion of the research described in this paper was performed in the Environmental

Molecular Sciences Laboratory, a national scientific user facility sponsored by the Departments of Energy's Office of Biological and Environmental Research and located at Pacific Northwest National Laboratory.

References

1. Kabe, T.; Ishihara, A.; Qian, W. *Hydrodesulfurization and Hydrodenitrogenation: Chemistry and Engineering*; Wiley-VCH: Weinheim, 1999.
2. Sajkowski, D. J.; Oyama, S. T. *Appl. Catal. A* **1996**, *134*, 339-349.
3. Aegerter, P. A.; Quigley, W. W. C.; Simpson, G. J.; Ziegler, D. D.; Logan, J. W.; McCrea, K. R.; Glazier, S.; Bussell, M. E. *J. Catal.* **1996**, *164*, 109-121.
4. McCrea, K. R.; Logan, J. W.; Tarbuck, T. L.; Heiser, J. L.; Bussell, M. E. *J. Catal.* **1997**, *171*, 255-267.
5. Nagai, M.; Miyao, T.; Tuboi, T. *Catal. Lett.* **1993**, *18*, 9-14.
6. Nagai, M.; Uchino, O.; Kusgaya, T.; Omi, S. In *Hydrotreatment and Hydrocracking of Oil Fractions*; Froment, G., Delmon, B., Grange, P., Eds.; Elsevier: New York, 1997; p 541.
7. Nagai, M.; Kiyoshi, M.; Tominaga, H.; Omi, S. *Chem. Lett.* **2000**, 702-703.
8. Oyama, S. T.; Clark, P.; Teixiera da Silva, V. L. S.; Lede, E. J.; Requejo, F. G. *J. Phys. Chem. B* **2001**, *105*, 4961-4966.
9. Phillips, D. C.; Sawhill, S. J.; Self, R.; Bussell, M. E. *J. Catal.* **2002**, *207*, 266-273.
10. Oyama, S. T.; Wang, X.; Requejo, F. G.; Sato, T.; Yoshimura, Y. *J. Catal.* **2002**, *209*, 1-5.
11. Wang, X.; Clark, P.; Oyama, S. T. *J. Catal.* **2002**, *208*, 321-331.
12. Oyama, S. T.; Wang, X.; Lee, Y.-K.; Bando, K.; Requejo, F. G. *J. Catal.* **2002**, *210*, 207-217.
13. Sawhill, S. J.; Phillips, D. C.; Bussell, M. E. *J. Catal.* **2002**, submitted for publication.
14. Korlann, S.; Diaz, B.; Bussell, M. E. *Chem. Mater.* **2002**, *14*, 4049-4058.

Catalysis by Mo-based Monometallic and Bimetallic Carbides and Sulfides for Simultaneous Hydrodesulfurization, Hydrodenitrogenation, and C-C Hydrogenolysis

Chunshan Song[1], Weilin Wang[1], Boli Wei[1], S. Ted Oyama[2], and Viviane Schwartz[2]*

(1) Clean Fuels and Catalysis Program, The Energy Institute, and Department of Energy & Geo-Environmental Engineering, Pennsylvania State University, 209 Academic Projects Building, University Park, PA 16802, Fax: 814-865-3248, csong@psu.edu
(2) Dept. of Chemical Engineering, Virginia Polytechnic Institute and State University, 140 Randolph Hall, Blacksburg, VA 24061

The present work deals with multi-probe molecular reactions for simultaneous hydrodesulfurization, hydrodenitrogenation, and C-C hydrogenolysis over Mo-based monometallic and bimetallic carbide and sulfide catalysts, in conjunction with the work on single-probe molecular reactions [Song et al., 2003]. Molybdenum based sulfide catalysts are widely used in hydroprocessing of petroleum fractions in refining industry. While these catalyst systems have been extensively studied [Topsoe et al., 1996], some fundamental issues remain to be addressed. Mo based carbide and bimetallic carbides have shown promises as new catalytic materials for hydroprocessing [Schwartz et al., 2000; Oyama et al., 1999; Dhandapani et al., 1998]. Knowledge on functionalities of these catalyst systems is still limited.

Table 1 shows the properties of the Mo-based monometallic and bimetallic carbide and sulfide catalysts. A multi-component model-feedstock was used to test catalytic functions for simultaneous hydrogenation, C-C bond hydrogenolysis, hydrodesulfurization, and hydrodenitrogenation. These reactions are precisely those involved in the conversion and processing of heavy hydrocarbon resources such as heavy oil, coal, and other residual materials. The multi-component feed includes 4-(1-naphthylmethyl)bibenzyl (NMBB), dibenzothiophene (DBT), quinoline, pyrene, and eicosane. The information feedback from model tests should be useful for selecting promising catalysts for hydroprocessing or coprocessing of coal and waste materials as well as petroleum resid in the future.

Table 2 and Tables 3 shows the results of multi-probe reactions at 400 °C and 375 °C, respectively. All the catalysts show certain activity for conversion of the five compounds under the reaction conditions compared to the thermal reaction. From the thermal reaction of 5-component model compounds, we can rank the five compounds in the following sequence in terms of reactivity: quinoline > NMBB> pyrene > DBT > eicosane.

ATTM and Co-Mo/Al_2O_3 and Ni-Mo/Al_2O_3 exhibit high activity on hydrogenolysis and hydrogenation properties. Among the Mo carbide catalysts and the Mo sulfide catalysts, $NbMo_{1.6}C$ showed similar activity on quinoline and NMBB compared to the two commercial catalysts. Moreover, $NbMo_{1.6}C$ exhibit slightly higher activity on the conversion of pyrene, which is consistent with its high hydrogenation ability. Co-reactants significantly influence NMBB conversion and the products derived. Many hydrogenation products from bibenzyl and 4-methylbibenzyl that were observed in single-component NMBB reaction in the presence of $NbMo_{1.6}C$, decline or disappear completely in the 5-component reaction.

It is noticed clearly that Mo_2C, unlike in the single-component reaction, shows low activity on the model compounds, indicating Mo_2C was strongly affected by the existence of other co-reactants.

Given the same active sites per gram reactant charges, $NbMo_{1.6}C$ showed slightly higher hydrogenation ability on pyrene than Co-Mo/Al_2O_3 and Ni-Mo/Al_2O_3 catalysts at 400°C. Compared to the hydrogenation ability in single compound reactions, the co-reactants apparently change the catalytic activities of the various catalysts. The co-reactants significantly inhibit the hydrogenation of the products from NMBB cracking.

For all catalytic runs, quinoline is the most reactive among the 5 compounds, which was almost completely converted at 400°C. For DBT reaction, the two commercial Co-Mo/Al_2O_3 and Ni-Mo/Al_2O_3 catalysts showed high activity compared to ATTM-derived Mo catalyst. ATTM performs as a better catalyst precursor on HDN than even the commercial Co-Mo/Al_2O_3 and Ni-Mo/Al_2O_3 catalysts. However, Co-Mo/Al_2O_3 and Ni-Mo/Al_2O_3 catalysts show higher HDS ability on DBT than ATTM. Between the monometallic carbide Mo_2C and bimetallic carbide $NbMo_{1.6}C$ catalyst, $NbMo_{1.6}C$ catalyst is more active on HDN and HDS. $NbMo_{1.6}C$ shows slightly higher activity on HDN than Ni-Mo/Al_2O_3 catalyst under the reaction condition.

The results from 5-component reactions indicate that the patterns of product distributions strongly depend on the type of catalysts, and the trends do not always parallel with those for single-component tests, indicating the influence of co-reactants. The catalytic properties of Mo_2C are significantly inhibited in the 5-component reaction. ATTM performs as a better catalyst on HDN even than the two commercial Co-Mo/Al_2O_3 and Ni-Mo/Al_2O_3 catalysts. However, Co-Mo/Al_2O_3 and Ni-Mo/Al_2O_3 catalysts show higher HDS ability on DBT than ATTM. $NbMo_{1.6}C$ also shows high activity on hydrogenation and HDN.

The reaction temperature has a great effect on the product distribution. More hydrogenation products and very limited C-C cleavage products were obtained at 375°C, while higher yields of hydrocracking, and hydrogenated C-C cleavage products were detected at 400°C.

Overall, the unique reactivities and selectivities of the $NbMo_{1.6}C$ carbide in hydrogenation and its HDN and HDS performance make the bimetallic Mo-based carbides promising candidates for further study in hydrocarbon processing.

Acknowledgment

This work was supported by the US Department of Energy, National Energy Technology Laboratory through its UCR Program.

References

Dhandapani B, St Clair T.; Oyama S.T. Appl. Catal. A: Gen., 1998, 168 (2), 219
Farcasiu, M.; Smith, C.; Pradhan, V. R.; Wender, I. Fuel Process. Tech. 1991, 29, 199.
Oyama S.T.; Yu C.C.; Ramanathan S. J Catal., 1999, 184 (2), 535.
Schmidt, E.; Song, C.; Schobert, H. H. Energy Fuels, 1996, 10, 597.
Schwartz ,V.; Oyama S.T.; Chen JGG. J. Phys. Chem. B., 2000, 104 (37), 8800.
Song, C.; Wang, W.; Wei, B.; Oyama S.T.; Schwartz ,V. Am. Chem. Soc. Div. Fuel Chem. Prepr., 2003, 48 (1), in press.
Topsoe, H.; Clausen, B. S.; Massoth, F. E. Hydrotreating Catalysis. Science and Technology. Springer-Verlag, Berlin, 1996, 310 pp.
Yoneyama, Y.; Song, C. Catal. Today 1999, 50, 19.

Table 1. Active sites of catalyst by chemisorption

Catalyst	Catalyst/ Support	CoO (wt%)	NiO (wt%)	Mo (wt%)	Active Sites (micro-mol/g) on wt of catalyst used	Active Sites (micro-mol/g) on wt of catalyst recovered
ATTM	$(NH_4)_2MoS_4$	N/A	N/A	36.91	57.30	93.70
CR-344	$Co\text{-}Mo/Al_2O_3$	2.90	N/A	9.0(13.5*)	82.40	85.90
CR-424	$Ni\text{-}Mo/Al_2O_3$	N/A	3.00	8.7(13.0*)	92.30	95.00
Mo2C	Mo_2C	N/A	N/A	94.1	99.00	-
NbMo1.6C	$NbMo_{1.6}C$	N/A	N/A	59.4	22.00	-

* The content of MoO_3 within the commercial catalysts

Table 2 Results of 5-Component Probe Reactions at 400 °C

Catalyst	ATTM	Co-Mo/Al2O3	Ni-Mo/Al2O3	Mo2C	NbMo1.6C	Thermal
Experiment No.	5-017	5-024	5-025	5-028	5-029	5-013
Temperature, oC	400	400	400	400	400	400
Quinoline						
Propylcyclohexane	60.2	34.8	50.0	2.1	25.6	
PropylBenzene	3.9	2.4	3.9	0.4	3.1	
Propenylcyclohexene	0.8	3.1	3.3	2.6	4.3	
1,2,3,4-tetrahydroquinoline		13.8	3.2	50.3	12.4	11.3
5,6,7,8-tetrahydroquinoline		3.3	0.9	12.4	3.6	
Decahydroquinoline				7.0	1.5	
2-propylbenzenamine	6.0	19.7	20.6	3.0	5.4	
Quinoline recovered		1.0	0.9	7.0	1.3	89.0
Conversion	**100.0**	**99.0**	**99.1**	**93.0**	**98.7**	**11.0**
DBT						
Benzene, cyclohexyl-	10.6	4.8	4.7		4.7	
Biphenyl	6.3	72.1	80.5	5.4	40.7	
TH-DBT	15.6					
DBT recovered	53.9	24.1	14.8	95.1	52.3	100.0
Conversion	**46.1**	**75.9**	**85.2**	**4.9**	**47.7**	**0.0**
NMBB						
Methylcyclohexane	5.0		1.8			
Toluene	3.5	3.5	3.8		5.5	1.5
p-Xylene			1.3		2.8	
Tetralin	49.2	23.6	30.7	0.9	25.6	
Naphthalene	15.9	30.9	31.8	25.5	47.9	
1-Methylnaphthalene			0.8		1.5	
Bibenzyl	5.3	2.1	2.2	1.2	3.9	
4-Methylbibenzyl	64.1	47.3	51.6	21.7	64.7	
4-Methyldicyclohexylethane	5.6		2.9		1.2	
1-Naphthyltolylmethane						0.8
TH-NMBB-1		7.7	5.6		2.5	
TH-NMBB-2	9.3	21.9	21.5		8.0	
NMBB recovered	6.1	14.9	6.5	59.9	15.3	96.9
Conversion	**93.9**	**85.1**	**93.5**	**40.1**	**84.7**	**3.1**
Pyrene						
4,5,9,10-tetrahydropyrene	2.5	3.7	3.3	0.5	2.9	
1,2,3,3a,4,5-hexahydropyrene	9.7	6.4	6.7		6.3	
1,2,3,6,7,8-hexahydropyrene	10.7	6.1	7.3	0.8	8.3	
4,5-Dihydropyrene	20.5	29.2	27.2	15.2	24.4	1.8
Pyrene recovered	42.4	60.9	64.7	83.5	53.6	99.1
Conversion	**57.6**	**39.1**	**35.3**	**16.5**	**46.4**	**0.9**
Eicosane						
n-C20 recovered	97.7	91.5	90.1	91.9	88.7	99.5
Conversion	**2.3**	**8.5**	**9.9**	**8.1**	**11.3**	**0.5**

Table 3 Results of 5-Component Probe Reactions at 375 °C

Catalyst	ATTM	Co-Mo/Al2O3	Ni-Mo/Al2O3	Mo2C	NbMo1.6C
Experiment No.	5-019	5-022	5-023	5-026	5-027
Temperature, oC	375	375	375	375	375
Quinoline					
Propylcyclohexane	30.4	10.9	20.2	0.6	13.6
PropylBenzene	2.1	0.4	0.7		2.0
Propenylcyclohexene	5.7	2.1	2.4	1.0	6.6
1,2,3,4-tetrahydroquinoline	16.9	54.0	46.7	77.7	30.3
5,6,7,8-tetrahydroquinoline	0.5	1.4	1.5	5.2	4.6
Decahydroquinoline				4.7	16.9
2-propylbenzenamine	13.1	12.5	17.1	1.8	1.0
Methylquinoline					0.3
Ethyl-THQ isomers				3.6	1.1
Ethylquinoline isomers				1.4	5.7
Quinoline recovered		2.3	1.3	5.7	2.0
Conversion	**100.0**	**97.7**	**98.7**	**94.3**	**98.0**
DBT					
cyclohexylbenzene	0.9	0.8	1.2		
Biphenyl	2.2	32.6	54.4	4.4	21.1
TH-DBT	8.8		0.3		
DBT recovered	88.1	66.3	44.7	95.8	78.9
Conversion	**11.9**	**33.7**	**55.3**	**4.2**	**21.1**
NMBB					
Methylcyclohexane					
Toluene					
p-Xylene					
Tetralin	6.7	2.4	4.8		3.3
Naphthalene	11.4	11.2	12.3	9.7	32.7
1-Methylnaphthalene		1.4	0.8	0.8	
Bibenzyl					1.3
4-methylbibenzyl	16.7	12.6	15.4	8.7	34.7
TH-NMBB-1	21.3	8.0	8.2		4.8
TH-NMBB-2	25.0	15.7	19.7		9.7
NMBB recovered	38.8	51.6	48.6	73.6	45.3
Conversion	**61.2**	**48.4**	**51.4**	**26.4**	**54.7**
Pyrene					
4,5,9,10-tetrahydropyrene	3.9	5.2	3.6	0.2	2.7
1,2,3,3a,4,5-hexahydropyrene	14.8	2.9	1.9		2.9
1,2,3,6,7,8-hexahydropyrene	21.0	2.2	1.9		4.1
4,5-dihydropyrene	27.4	36.1	32.3	7.6	26.8
1,3-dimethylpyrene					
Pyrene recovered	34.9	61.2	65.6	91.8	62.9
Conversion	**65.1**	**38.8**	**39.7**	**8.2**	**37.1**
Eicosane					
n-C20 recovered	90.0	93.9	98.3	98.8	90.4
Conversion	**10.0**	**6.1**	**1.7**	**1.2**	**9.6**

NEW AMINES FOR CARBON DIOXIDE SEPARATION FROM GAS-MIXTURES

Angela Dibenedetto, Michele Aresta and Roberta Girardi*

Department of Chemistry and METEA Research Center, University of Bari, Campus Universirtario, 70126, Bari – Italy.
E-mail: a.dibenedetto@chimica.uniba.it

Introduction

Mono- and di-amines have been used for carbon dioxide separation from gas mixtures. Derivatized diamines bearing a silyl-group have been shown to pick-up one mol of CO_2 per mol of amine, affording intra-molecular carbamates that reversibly release carbon dioxide. The silyl-diamines can be converted into xerogels that are able to adsorb carbon dioxide. The absorption-desorption curves show a good efficiency in CO_2 up-take, that is higher than that of monoamines[1,2] in the same conditions.

Results and Discussion

It is well established that aliphatic amines react with carbon dioxide to afford ammonium carbamates as represented in Eq. 1.

$$2\,RNH_2 + CO_2 \rightarrow RNH_3^{+-}O_2CNHR \qquad (1)$$

In this work we have studied the up-take of carbon dioxide using aliphatic di-amines ($H_2N(CH_2)_2NH(CH_2)_3Si(OMe)_3$ I and $CH_3(CH_2)_2NH(CH_2)_2NH_2$ II) and found that they are able to capture 1 mol of CO_2 per mol of amine. Their behavior has been compared with that of monoethanolamine (MEA), used at industrial level, in the same reaction conditions.

Figure 1 shows the up-take curve by di-amines I and II, and that of MEA.

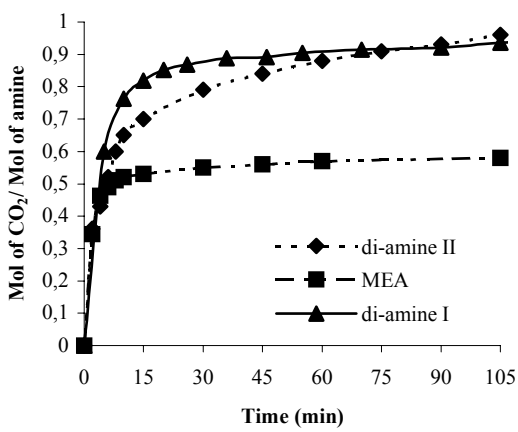

Figure 1. CO_2 up-take of diamines comparing with MEA.

Differently from MEA, one mol of CO_2 per mol of amine was up-taken by amines I and II. This behaviour has been explained considering that, as described in a previous work [3], the amine I affords an intra-molecular carbamate. The reaction was quite fast (less than 20 minutes) and a glassy material difficult to handle was isolated. Nevertheless, by evaporating directly on a single KBr disk the amine solution under CO_2 atmosphere, it was possible to record the IR spectrum which showed the characteristic band at 1540 cm^{-1} due to the carbamate $RHNCOO^-$ moiety [3]. Moreover, the ^1H and ^{13}C NMR spectra of a solution of the amine I under 0.1 MPa of CO_2 confirm the formation of the intra-molecular carbamate.

As shown in Fig. 1, also di-amine II takes-up CO_2 with a 1:1 molar ratio, but, differently from amine I, affords a white light powder more easy to handle.

In both cases, the absorption was reversible and carbon dioxide was completely released at 333 K. In fact, if neat amine was used, the starting material was quantitatively recovered.

Following such discovery, we built a laboratory apparatus to follow the carbon dioxide absorption and desorption using either the neat amines, or their water- or organic solvent-solutions. The absorption/desorption curve when free amine I was placed in contact with a gas mixture (14% of CO_2) is shown in Figure 2.

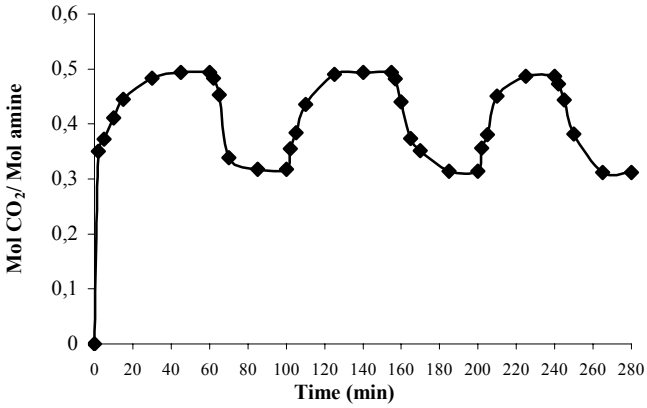

Figure 2. CO_2 absorptio/desorption curve for neat amine I

As Figure 2 shows after few minutes di-amine I was able to up-take carbon dioxide with a 1:1 molar ratio at room temperature. By heating to 333 K, half of the CO_2 absorbed was released. Such amount was then absorbed and desorbed for several cycles (Fig. 2). Most probably the working temperature range is limiting the release of carbon dioxide. The upper limit of the temperature is given by either the use of water or organic solvents or by the vapour pressure of the amine and its thermal stability.

For avoiding losses, we have tried to change the state of the di-amine I from liquid to solid and have transformed the liquid di-amine into a xerogel. The silica xerogel was obtained by condensation of amine I and silicon alkoxydes under hydrolytic conditions.

By using the solid species, the desorption was carried out at temperature higher than that of liquid amine increasing the efficiency of the desorption.

In fact, as shown in Figure 3, the xerogel was able to absorb and desorb CO_2 from a gas mixture in a very short time and for several cycles in a batch system.

Studies are in progress for elucidating how the amine is linked to the silicon alkoxydes in the xerogel and its structure. The next step will be the design of a flow system.

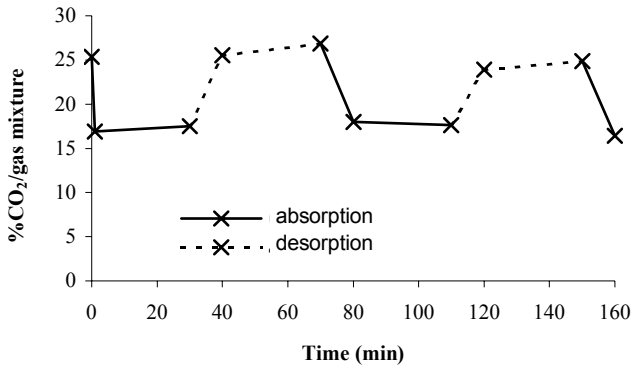

Figure 3. Carbon dioxide absorption/desorption cycles by using diamine I in a xerogel

Conclusions

The use of di-amines for the reversible uptake of carbon dioxide is more efficient than the use of monoamines. In fact, di-amines uptake twice the amount of carbon dioxide per mol from a gas mixture at 0.1 MPa total pressure (14% CO_2).

Moreover, the di-amines converted into a xerogel are more efficient than liquid amines or amine solutions in water or organic solvents for capturing CO_2 from a gas mixture. They can be reused for several cycles and the working temperature is higher than that of free amines..

Acknowledgement. The financial support by MIUR, Project n° 9803026360 and n° MM03027791 are acknowledged.

References

(1) Dibenedetto, A., Aresta, M., Narracci, M. 223rd ACS National Meeting, April 7-11, **2002**, Orlando Florida.

(2) Michele Aresta and Angela Dibenedetto *6th International Conference on Greenhouse Gas Control Technologies* (GHGT-6) 30th September-4th October **2002**, Kyoto, Japan, Book of Abstracts CAABP8.

(3) Dibenedetto, A., Aresta, M., Narracci, M., Fragale, C. *Green Chemistry* **2002**, *4*, Issue 05, 439-443.

Probe Reactions for C-C Bond Cleavage and Aromatic Hydrogenation over Mo-based Carbide and Sulfide Catalysts

Chunshan Song[1], Weilin Wang[1], Boli Wei[1], S. Ted Oyama[2], and Viviane Schwartz[2]*

(1) Clean Fuels and Catalysis Program, The Energy Institute, and Department of Energy & Geo-Environmental Engineering, Pennsylvania State University, 209 Academic Projects Building, University Park, PA 16802, Fax: 814-865-3248, csong@psu.edu
(2) Dept. of Chemical Engineering, Virginia Polytechnic Institute and State University, 140 Randolph Hall, Blacksburg, VA 24061

Introduction

Molybdenum based sulfide catalysts are widely used in hydroprocessing of petroleum fractions in refining industry. While these catalyst systems have been extensively studied [Topsoe et al., 1996], some fundamental issues remain to be addressed. Mo based carbide and bimetallic carbides have shown promises as new catalytic materials for hydroprocessing [Schwartz et al., 2000; Oyama et al., 1999; Dhandapani et al., 1998]. Knowledge on functionalities of these catalyst systems is still limited.

The present work deals with probe molecular reactions for C-C bond cleavage and aromatic ring hydrogenation over Mo-based carbide and sulfide catalysts. It is believed that cleavage of aromatic-aliphatic or aliphatic-aliphatic C-C bonds is very important for catalytic hydroprocessing and upgrading of heavy oil, and liquids derived from coal and coprocessing of heavy materials. There is little literature information on catalytic functionalities of Mo-based carbide and sulfide catalysts on C-C bond cleavage. As has been discussed in our recent report [Schmidt et al., 1996; Yoneyama and Song, 1999], 4-(1-naphthylmethyl)bibenzyl, abbreviated as NMBB, is a good model compound for examining activities and selectivities of various catalysts on hydrogenolysis and hydrogenation, since there are different types of potential cleavage sites of C-C bonds and both monocyclic and bicyclic aromatic moieties in the compound.

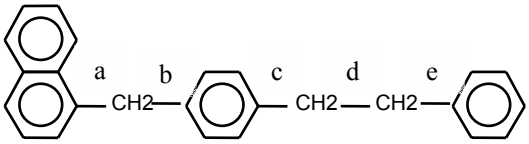

In this work, we employed this model compound to simulate the structure in heavy hydrocarbon resources. Hydrogenolysis and hydrogenation properties of multiple catalysts have been examined on this model structure at 375 °C and 400 °C. Two types of molybdenum catalysts have been tested to study the impact of different catalysts on the catalytic reaction of NMBB at 375°C and 400°C. One type is Mo carbide catalyst including Mo_2C and $NbMo_{1.6}C$, and the other type is sulfide catalyst including Mo sulfide from ATTM, Co-Mo/Al_2O_3, Ni-Mo/Al_2O_3.

Experimental

Three metal sulfide catalysts have been examined, including dispersed MoS_2 catalyst derived in-situ from ammonium tetrathiomolybdate [ATTM, $(NH_4)_2MoS_4$] and sulfided Co-Mo/Al_2O_3 (CR-344) and Ni-Mo/Al_2O_3 (CR-424) catalysts from Criterion. Before using these two commercial catalysts for model compound reaction, they were sulfided in 100 ml autoclave using 6% CS_2 in *n*-tridecane under hydrogen pressure by a temperature-programmed manner: first at 250 °C for 2 h and then at 300 °C for 3 h. Our experience shows that such a procedure is effective for sulfidation in batch reactors. After sulfidation, the catalysts were kept in *n*-tridecane before use.

It should be noted that the molybdenum carbide catalysts were prepared at Virginia Tech and shipped to Penn State in a sealed ampoules with about 0.1 g sample in each ampoule. The carbide catalyst was charged into the reactor in the sealed glass ample, and broken in situ to avoid exposure to air.

All the reactions were conducted in a 25-ml horizontal micro-autoclave reactor under 1000 psig hydrogen pressure for 30 min plus 3 min for heat-up. The reactants charges were 0.2 g NMBB and 1 g solvent (*n*-tridecane) plus a given amount of catalyst for the single component reaction.

The sealed reactor was purged four times with H_2 and then pressurized up to 1000 psi H_2 at room temperature for all experiments. A preheated fluidized sand bath was used as the heating source, and the reactor was horizontally agitated to provide mixing (about 240 strokes/min). After the reaction, the micro-autoclave was quenched in cold water bath. The contents were washed out with 20-30 methylene dichloride, and filtered through a low speed filter paper for subsequent GC analysis.

After the reaction, the liquid was collected and analyzed by GC-MS. Quantitative analysis of products is computed according to the relative response factors that was pre-determined by using the reagent chemicals (relative to an internal standard). In this work, we used Shimadzu GC 17A gas chromatograph coupled with QP-5000 mass spectrometer. The column used for GC-MS was the Crossbond® 5% phenyl – extended temperature and inertness capillary column with 30 m long, 0.25 mm I.D., 0.25 μm. Dibenzofuran (DBF) was selected as an internal standard which has no overlap with the products from the reactions of the 5 different model compounds. The oven for GC-MS was programmed from 40 °C to 290 °C at a heating rate of 4 °C/min, with a initial holding time of 5 min and a final holding time of 10 min.

The conversion of reactants is defined as {[reactant (wt) charged – reactant (wt) recovered]/reactant (wt) charged]} × 100, the molar yields of products are defined as [product (mol)/reactant (mol) charged] × 100.

Results

Table 1 shows the active sites of different catalysts measured by chemisorption. In order to comparatively examine the functionalities of different catalysts on an uniform basis, the amount of catalyst was charged based on the equal number of active sites per gram of reactant feed. The measurements of active sites for the molybdenum sulfide catalysts were done in pulse mode with molecular oxygen in a stream of helium at dry ice/acetone temperature. The samples were pre-sulfided for 2 hrs at 415 °C in 10% H_2S/H_2. The CO uptake data was measured as active sites for the unsupported metal carbides.

Table 2 shows the product distribution of NMBB reactions over four different sulfide catalysts at 400°C. From Table 2, the total yields of naphthalene and tetralin were almost over 70% and 4-methylbibenzyl close to or over 50% in most catalytic runs, indicating that the cleavage of NMBB mainly products from 4-methylbibenzyl were also detected from the GC-occurs on the aromatic-aliphatic bond ***a***. Some further cracking MS spectroscopy, such as toluene, ethylbenzene, *p*-xylene. In addition, some amount of methylnaphthalene, its hydrogenation isomers and bibenzyl also existed in the product pool, which represented that cracking also

Table 1. Active sites of catalyst by chemisorption

Catalyst	Catalyst/ Support	CoO (wt%)	NiO (wt%)	Mo (wt%)	Active Sites (micro-mol/g) on wt of catalyst used	Active Sites (micro-mol/g) on wt of catalyst recovered
ATTM	$(NH_4)_2MoS_4$	N/A	N/A	36.91	57.30	93.70
CR-344	$Co\text{-}Mo/Al_2O_3$	2.90	N/A	9.0(13.5*)	82.40	85.90
CR-424	$Ni\text{-}Mo/Al_2O_3$	N/A	3.00	8.7(13.0*)	92.30	95.00
Mo2C	Mo_2C	N/A	N/A	94.1	99.00	-
MoNb1.6C	$NbMo_{1.6}C$	N/A	N/A	59.4	22.00	-

* The content of MoO_3 within the commercial catalysts

Table 2 Hydrogenolysis of NMBB over Mo-based sulfide and carbide catalysts at 400 **°C**

	ATTM	$S\text{-}Co\text{-}Mo/Al_2O_3$	$S\text{-}Ni\text{-}Mo/Al_2O_3$	Mo_2C	$NbMo_{1.6}C$	Thermal
Experiment No.	1-014	1-023	1-024	1-025	1-026	1-013
Catalyst Amount, g	0.1636	0.0226	0.0203	0.1	0.125	
Active Sites, mcior-mol	9.37	1.86	1.87	9.90	2.75	
Catalyst loading, micro-mol/g	9.37	9.32	9.35	9.37	9.36	
Temperature, ^oC	400	400	400	400	400	400
Reactant, g NMBB	0.9997	0.1999	0.2003	1.0567	0.2939	0.2000
Yields, mol%						
Methylcyclohexane					5.5	
Toluene	4.6	5.1	6.2	6.6	8.7	2.2
Ethylbenzene		2.2	2.4	0.7	2.6	
p-Xylene	1.5	2.2	2.9	3.0	5.3	
Decalin				4.7	7.7	
Tetralin	62.9	43.7	41.5	64.7	46.9	
Naphthalene	8.2	28.9	42.8	4.6	3.6	2.0
MTHN isomers	5.1	4.6	4.8	1.8	2.3	
1-Methylnaphthalene		3.0	4.2	5.7	5.9	
Bibenzyl	9.9	8.7	9.8	5.9	3.4	
4-Methylbibenzyl	63.8	62.5	73.7	39.1	23.6	2.5
4-Methylhexahydrobibenzyl				18.6	16.8	
1,2-Dicyclhexylethane					5.9	
4-Methyl-1',2'-dicyclohexylethane				1.9	6.6	
1-Naphthyl-4-tolylmethane						0.7
NMBB Recovered						96.8
Conversion	**100.0**	**100.0**	**100.0**	**100.0**	**100.0**	**3.2**

Table 3 Hydrogenolysis of NMBB over Mo-based sulfide and carbide catalysts at 375°C

Experiment No.	ATTM 1-016	Co-Mo/Al_2O_3 1-021	Ni-Mo/Al_2O_3 1-022	Mo_2C 1-017	$NbMo_{1.6}C$ 1-018	Thermal Baseline
Catalyst Amount, g	0.0326	0.0229	0.0203	0.1000	0.1140	N/a
Active Sites, mcior-mol	1.87	1.89	1.87	9.90	2.51	N/a
Catalyst loading,micro-mol/g	9.34	9.42	9.35	9.37	9.37	N/a
Temperature, ^oC	375	375	375	375	375	375
Reactant, g NMBB	0.2001	0.2003	0.2005	1.0567	0.2678	0.258
Yields, mol%						
Methylcyclohexane					12.7	
Toluene			1.4	1.9	5.4	
Ethylbenzene					2.1	
p-Xylene					6.0	
Decalin					10.2	
Tetralin	41.7	53.9	68.3	74.6	35.8	
Naphthalene	34.3	31.6	2.9	7.8	6.8	
MTHN isomers	1.8	1.4	1.6	3.7	4.0	
1-Methylnaphthalene	3.6	1.9		1.1		
Bibenzyl	9.8	10.2	9.4	12.0	4.4	
4-Methylbibenzyl	70.4	80.3	60.9	60.3	24.1	
4-Methylbibenzyl isomer	-					
4-Methylhexahydrobibenzyl	9.4		2.3	7.0	11.1	
1,2-dicyclhexylethane					10.0	
4-Methyl-1,2-dicyclohexylethane					8.9	
Tetrahydro-NMBB-1		5.2	4.0	5.9		
Tetrahydro-NMBB-2						
NMBB Recovered	11.0	0.0	0.0	0.0	0.0	
Conversion	**89.0**	**100.0**	**100.0**	**100.0**	**100.0**	**< 3%**

occurred on bond ***b***. It is very obvious that no naphthyltolylmethane product were detected in all the catalytic reactions. In some catalytic runs, small amounts of hydrogenated NMBB products have been detected. Table 3 shows the results of catalytic runs at 375 °C.

Baseline Runs. Reaction of NMBB without added catalyst provides a baseline for comparison of all catalytic reactions. The results in Table 2 show that naphthalene and 4-methylbibenzyl are the main products at 400 °C. They were derived from hydrogenolysis at bond ***a***. Some wall catalytic effect may be responsible for the observed conversion in the non-catalytic (thermal) runs.

The small amount of 1-(naphthyl)-4-tolyl-methane and toluene indicated that bond ***d*** would be another cracking site under non-catalytic atmosphere. Naphthyltolylmethane, which was not found in catalytic reactions, is believed to be a product in non-catalytic reactions at 400 °C. It has been reported that, at least for temperature ≥410°C the dominant cleavage in thermal runs is at bond ***d*** [Farcasiu et al, 1990]. The low conversion observed in this reaction, 3.2%, agrees well with other values reported in our previous literature [Schmidt et al., 1996].

Discussion

The results of single-component NMBB reaction (Table2 and Table 3) reveal that NMBB is a good model compound for examining the activity and selectivity of various catalysts for C-C bond hydrogenolysis and aromatic ring hydrogenation. The product distribution from NMBB catalytic hydrogenolysis indicates that the cleavage of NMBB mainly occurs on the aromatic-aliphatic C-C bond ***a***, which is in distinct contrast to the non-catalytic and computational results which indicate the bond ***d*** in NMBB structure as the weakest linkage among the five potential C-C cleavage sites.

Naphthalene, tetralin and 4-methylbibenzyl are the major products from reactions catalyzed over Mo sulfide catalysts under the specified reaction condition. The temperature has a significant effect on NMBB conversion. The higher the temperature, the higher the hydrogenolysis activity. The two commercial catalysts exhibit high hydrogenolysis activity even at low temperature compared to ATTM.

Compared to Mo sulfide catalysts, Mo carbide catalysts possess different catalytic functionality. Some new hydrogenation products derived from bibenzyl and 4-methylbibenzyl, such as 1,2-

dicyclohexylethane, 4-methylhexahydrobibenzyl and 4-methyl-1,2'-dicyclohexylethane, were formed in the catalytic runs over $NbMo_{1.6}C$ catalyst.

Among the Mo sulfide catalysts, ATTM exhibits highest hydrogenation ability on NMBB reaction at 400°C, while Ni-Mo/Al_2O_3 showed high activity on hydrogenation at 375°C. In addition, Ni-Mo/Al_2O_3 and Co-Mo/Al_2O_3 are more active to hydrogenolysis in terms of the yields of the secondary cracking products. Compared to Mo sulfide catalysts, Mo_2C and $NbMo_{1.6}C$ carbide catalysts are extremely active to NMBB reaction in terms of hydrogenation ability. $NbMo_{1.6}C$ catalyst shows hydrogenation ability twice as high as Ni-Mo/Al_2O_3 based on the same active sites of catalyst per gram NMBB. $NbMo_{1.6}C$ also exhibits highest activity on hydrogenolysis among the examined Mo-based catalysts.

Acknowledgment

This work was supported by the US Department of Energy, National Energy Technology Laboratory through its UCR Program.

References

Dhandapani B, St Clair T.; Oyama S.T. Appl. Catal. A: Gen., 1998, 168 (2), 219

Farcasiu, M.; Smith, C.; Pradhan, V. R.; Wender, I. Fuel Process. Tech. 1991, 29, 199.

Oyama S.T.; Yu C.C.; Ramanathan S. J Catal., 1999, 184 (2), 535.

Schmidt, E.; Song, C.; Schobert, H. H. Energy Fuels, 1996, 10, 597.

Schwartz ,V.; Oyama S.T.; Chen JGG. J. Phys. Chem. B., 2000, 104 (37), 8800.

Topsoe, H.; Clausen, B. S.; Massoth, F. E. Hydrotreating Catalysis. Science and Technology. Springer-Verlag, Berlin, 1996, 310 pp.

Yoneyama, Y.; Song, C. Catal. Today 1999, 50, 19.

IR investigations on the surface sites of MoP/SiO_2 and their evolution under hydrodesulfurization conditions

Zili Wu, Weicheng Wu, Zhaochi Feng, Qin Xin, Can Li**

State Key Laboratory of Catalysis, Dalian Institute of Chemical Physics, Chinese Academy of Sciences, P.O. Box 110, Dalian 116023, China. Email: ziliwu@dicp.ac.cn; canli@ms.dicp.ac.cn, Fax: 86-411-4694447

Introduction

In the last decades, there grows considerable interest in the development of new hydroprocessing catalysts because of the more stringent environmental legislation and the need of efficient conversion of low quality stocks into clean fuels. Since 1980s, transition metal nitrides and carbides has been attracted much attention as they show potential use in hydrotreating processes.[1] Recently, increasing studies show that transition metal phosphides have high catalytic activity for hydrodenitrogenation (HDN) [2,3] and hydrodesulfurization (HDS).[4,5] Among this class of catalysts, molybdenum phosphides, MoP, MoP/SiO_2 and MoP/Al_2O_3, were frequently studied and show better activity than conventional Mo sulfide catalysts in both HDN and HDS. It is interesting to note that molybdenum phosphides even increase in activity in the HDS of thiophene with steam on time,[5] which is different from the case of molybdenum nitride and carbide catalysts that readily deactivate in the presence of sulfur species.[6] In this work, in order to get insight into the nature of working surface of molybdenum phosphides under HDS reaction conditions, the surface sites of MoP/SiO_2 and their evolution in the presence of sulfur species were studied by IR spectroscopy using CO as the probe molecule.

Experimental

The precursor sample with Mo loading of 10 wt% was prepared by incipient wetness impregnation of SiO_2 with an aqueous solution of $(NH_4)_6Mo_7O_{24}$ and $(NH_4)_2HPO_4$. MoP/SiO_2 was prepared by reducing the oxide precursor in flowing hydrogen using temperature-programmed method.[2, 5] The freshly prepared sample was passivated in a stream of 1% O_2/N_2 at room temperature (RT) and the passivated MoP/SiO_2 was obtained. In the IR study, a passivated sample was reduced in H_2 at different temperatures and then subjected to CO adsorption. The reduced sample was treated by thiophene (4 Torr), a mixture of thiophene/H_2 (4/400 Torr), or H_2S (5 Torr) at different temperatures, and the surface sites were probed by CO adsorption. All infrared spectra were collected on a Fourier transform infrared spectrometer (Nicolet Impact 410) with a resolution of 4 cm^{-1} and 64 scans.

Results and Discussion

Figure 1 presents the IR spectra of CO adsorbed on MoP/SiO_2 reduced at different temperatures. No IR band of adsorbed CO can be observed on the sample reduced at 673 K. Great changes of the spectra take place for the sample reduced at 723 K, a main band at 2050 cm^{-1} together with a weak shoulder at 2075 cm^{-1} appears. The band at 2050 cm^{-1} continues to increase in intensity with the elevated reduction temperatures, indicating that more surface sites for CO adsorption are generated owing to the deeper reduction. This band slight shifts to 2045 cm^{-1} and become the predominant band for the sample reduced at 923 K. According to the preparation process, the passivated MoP/SiO_2 reduced at 923 K can be regarded as fresh phosphide and it will be used in the following experiments. Therefore, adsobed CO on the surface of fresh MoP/SiO_2 owns an characteristic band at around 2045 cm^{-1}. This band can be assigned to the linearly adsorbed CO on the surface molybdenum atom of MoP/SiO_2, which may be positively charged, i.e. $Mo^{\delta+}$ ($0<\delta<2$).[7,8] To our knowledge, this is the first IR report for the nature of the surface sites of molybdenum phosphide.

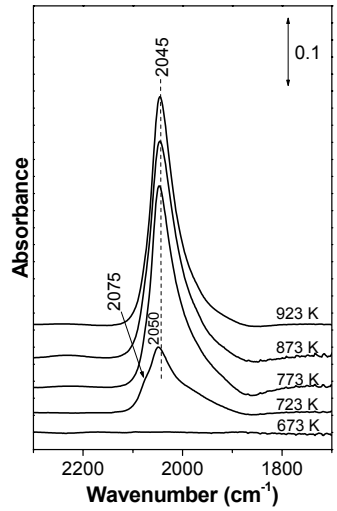

Figure 1. IR spectra of CO adsorbed on MoP/SiO_2 reduced by H_2 at different temperatures.

Figure 2 exhibits the IR spectra of CO adsorbed on MoP/SiO_2 sample treated with a thiophene/H_2 (4/400 Torr) mixture at different temperatures. The band at 2045 cm^{-1} shifts to higher frequencies when the treatment temperature is increased, e.g., to 2047 cm^{-1} at 373 K, to 2049 cm^{-1} at 473 K, to 2058 cm^{-1} at 573 K, and to 2096 cm^{-1} at 673 K. Meanwhile, a shoulder band at 2060 cm^{-1} is present for the sample treated at 673 K. The appearance of 2096 cm^{-1} indicates the sulfidation of the phospide surface because this is a characteristic band of CO adsorbed on sulfided Mo catalyst and has been assigned to linearly adsorbed CO on *cus* Mo^{2+} sites.[8] The results clearly show that the surface of the fresh MoP/SiO_2 catalyst is partially sulfided when treated with the thiophene/H_2 mixture at temperatures above RT.

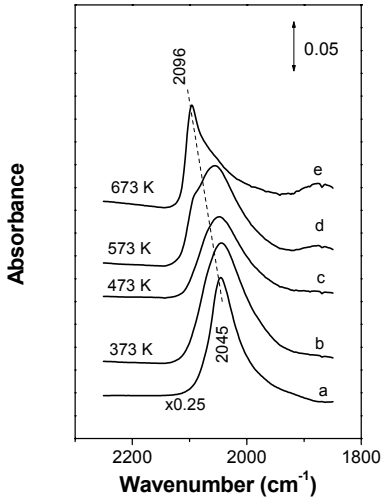

Figure 2. IR spectra of CO adsorbed on MoP/SiO_2 pretreated by a thiophene/H_2 mixture at different temperatures.

When MoP/SiO_2 sample was treated by thiophene alone, IR spectra of adsorbed CO imply that the surface keeps its phosphide nature even when it was treated by thiophene at 673 K, indicating that thiophene alone is quite stable on the surface of MoP/SiO_2.

The influence of H_2S on the nature of surface sites of MoP/SiO_2 is also studied by CO adsorption using IR spectroscopy. IR results show that the surface of MoP/SiO_2 is completely sulfided at the treatment temperature of 473 K.

Conclusions

The surface $Mo^{\delta+}$ ($0<\delta<2$) sites of MoP/SiO_2 catalyst has been probed by adsorbed CO using IR spectroscopy. IR results indicate that the surface of MoP/SiO_2 catalyst will be sulfided under HDS reaction conditions. With the presence of P atoms in the bulk of MoP, the composition of the sulfided MoP catalyst is somewhat similar to that of conventional Mo sulfides that adopt P as an additive. This could be the reason why MoP catalysts show good activities in HDS reactions.

Acknowledgement. Financial supports from the National Nature Science Foundation of China (NSFC, No. 29625305) and the State Key Project of the Ministry of Science and Technology of China (Grant No. G2000048003) are appreciated.

References

(1) Oyama, S. T. *Catal. Today* **1992**, *15*, 179.
(2) Li, W.; Dhandapani, B.; Oyama, S. T. *Chem. Lett.* **1998**, 207.
(3) Stinner, C.; Prins, R.; Webber, T. *J. Catal.* **2001**, *202*, 187.
(4) Clark, P.; Wang, X.; Oyama, S. T. *J. Catal.* **2002**, *207*, 256.
(5) Phillips, D. C.; Sawhill, S. J.; Self, R.; Bussell, M. E. *J. Catal.* **2002**, *207*, 266.
(6) Wu, Z.; Chu, Y.; Yang, S.; Wei, Z.; Li, C.; Xin, Q. *J. Catal*. **2000**, *194*, 23.
(7) Yang, S.; Li, C.; Xu, J.; Xin, Q. *J. Phys. Chem. B* **1998**, *102*, 6986.
(8) Müller, B.; van Landeveld, A. D.; Moulijn, J. A.; Knözioger, H. *J. Phys. Chem*. **1993**, *97*, 9028.

HYDRODESULFURIZATION BEHAVIOR OF Mo_2N CATALYST

Shuwen Gong, Haokan Chen, Wen Li, Baoqing Li

State Key Laboratory of Coal Conversion
Institute of Coal Chemistry Chinese Academy of Sciences
Taiyuan, China, 030001

Introduction

Since Volpe[1] synthesized γ - Mo_2N by temperature-programmed reaction of MoO_3 with NH_3, γ - Mo_2N as effective and selective hydrotreatment catalysts had been extensively studied[2-4]. Nagai[2] and co-workers reported the nitrided Mo/Al_2O_3 catalyst to be 1.1-1.2 times more active than a sulfided Mo/Al_2O_3 in the hydrodesulfurization(HDS) of dibenzothiophene and to be extremely selective in the C-S hydrogenolysis to form biphenyl. Also, Sajkowski and Oyama[3,5] found unsupported γ - Mo_2N to be nearly twofold as active as the commercial Ni-Mo/Al_2O_3 catalyst for HDS of coal-derived feed. Markel et al[6]. reported that unsupported molybdenum nitride was presented despite the sulfidation conditions in the catalytic reactor.

However, up to now, preparation of γ - Mo_2N is difficult, because all the reaction gases must be very high purity. Markel[6] synthesized γ - Mo_2N using matheson ammonia(99.9999%). Wise and his colleagues[7] synthesized γ - Mo_2N using mixture of N_2 and H_2(N_2 or H_2 is matheson and 99.9995%).

In this paper, we studied the HDS behavior of molybdenum nitride catalysts synthesized using low purity of reaction gases compared with previous reports in order to make the synthesis easy. Effects of reaction temperature and pretreatment method on the activities and structures of Mo_2N were also examined.

Experimental Section

Catalyst Synthesis. Mo_2N was produced by reaction of MoO_3(99%) and flowing mixture of N_2(99.9%) and commercial H_2. The gases were controlled using rotameters. MoO_3 powder was loaded in the center of 15mmID×20mmOD×60mm quartz tube reactor. The temperature was increased in three steps: first rapidly from room temperature to 300℃, then from 300℃ to 500℃ at 0.6℃/min, finally from 500℃ to 700℃ at 2℃/min and held at 700℃ for 2h. After the nitridation reaction, the reactor was cooled down to room temperature under N_2, and then passivated with a mixture of 1%O_2 in N_2 for 2h. We called it as passivated molybdenum nitride. Passivated Mo_2N was sulfided by the mixture of 3wt% CS_2 in cyclohexane and H_2 as the carrier gas at 350℃, which we called pre-sulfided Mo_2N. Passivated Mo_2N was employed in H_2 at 400℃ for 2h, which we called it as pre-reduced Mo_2N.

X-Ray Diffraction. The crystal structures of catalysts were determined using XRD, The diffraction patterns were collected using a DMAX-rA diffractometer and CuK α radiation(λ =1.542Å).

Evaluation of HDS Activities of Catalysts. The measurements of catalytic activities of Mo_2N were carried out using an atmospheric pressure flow reactor. A gas chromatograph equipped with a flame ionization detector was used to analyze thiophene and hydrocarbon products. Catalyst samples(≈ 0.2g) were loaded in the reactor. Thiophene was carried by H_2 using a bubbler apparatus. The major HDS products (1-butene, butadiene, cis-2-butene, trans-2-butene and butane) were calibrated with analytical gas standards to facilitate conversion calculations.

Results and Discussion

XRD Patterns of Passivated and After-reacted Mo_2N. The diffraction pattern for passivated Mo_2N showed peaks at 37.8°, 43.2°, 45.2°, 62.6°, 64.2°, 75.5°, 78.2°, and 80.5°(**Figure 1a**), which were assigned to the {111}, {200}, {002}, {220}, {202}, {311}, {113} and {222} reflections of bulk Mo_2N, respectively. They were obvious difference with γ - Mo_2N by JCPDS standard data and references[6-7]. There were not peaks attributed to Mo oxides and γ - Mo_2N, indicating that MoO_3 all transformed into Mo_2N, and passivation had no effects on bulk structure of Mo_2N. Therefore, it was concluded that passivation produced a protective, amorphous, surface oxide film which was slightly greater than one-monolayer thick like passivated γ - Mo_2N.

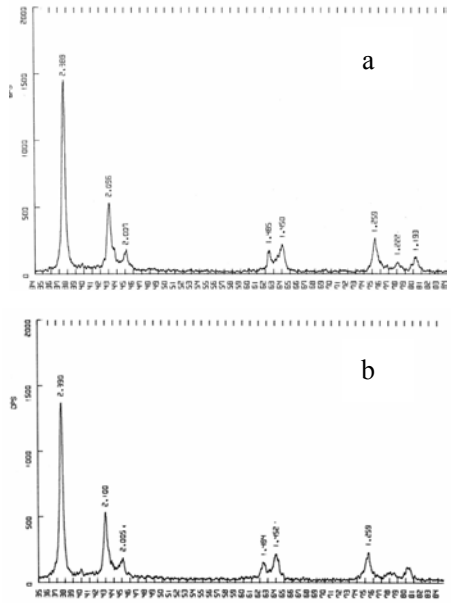

Figure1. XRD patterns of Mo_2N a: before-reaction
b : after-reaction.

After HDS reaction, Mo_2N was removed from the reactor and analyzed by X-ray diffraction. Diffraction pattern was presented in **Figure 1b**. Peak locations and relative intensities showed that the bulk structure of Mo_2N was unchanged, which meant that no traces of impurities, such as Mo sulfide, were found. This suggested that Mo_2N had strong resistance to sulfidation.

HDS Behavior of Mo_2N. HDS activity of passivated Mo_2N without pretreatment under different reaction temperature was showed in **Figure 2**. At 400℃ and 360℃ the HDS activities of Mo_2N deactivated with reaction time in the initial stage, and then retained about a constant. Because the bulk structure of Mo_2N was retained in the whole reaction, the deactivation of catalyst might be resulted from the change of Mo_2N surface properties.

It was also found that with the increase of the reaction temperature the amount of C4 products converted from thiophene was high(**Figure 2**). However, at 320℃ the HDS activities of Mo_2N were a little low.

Effect of Pretreatment on Mo_2N HDS Behavior. **Figure 3** showed the effect of pre-treatment on Mo_2N HDS activity. The

activity order was passivated nitride>sulfided nitride>reduced nitride, which indicated that pre-reduction and pre-sulfidation did not improve the activity of Mo_2N. But the sulfidation could improve the stability of catalytic activity. After 9h reaction, pretreated Mo_2N were removed from the reactor and analyzed by X-ray diffraction.

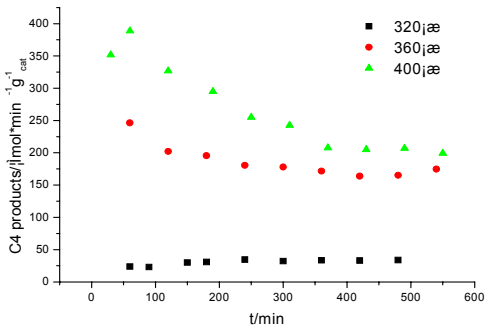

Figure 2. Catalytic activities of Mo_2N in HDS reaction at different temperature.

XRD spectra of pre-reduced Mo_2N catalyst was presented in **Figure 4**. There were not obvious changes of peak locations compared with **Figure 1**, which indicated that no impurities such as Mo sulfide or Mo were found and pre-reduction had no effects on bulk structure of Mo_2N. Thus, pretreatment might affect the surface character of Mo_2N and deactivate the catalytic activity of Mo_2N. A possible reason might be that very thin metal Mo species film was formed on the surface. Logan[8] and Liu[9] reported similar result for the nitride catalysts which were reduced in H_2. Pre-sulfidation did not change the bulk structure of Mo_2N either. It suggested that Mo_2N had strong resistance to sulfidation. Sulfidation might only affect the surface properties which had great influence on the catalyst HDS activity. Markel[6] and McCrea[10] thought that a thin film of Mo sulfide formed on the surface of molybdenum nitrides in sulfidation condition. However, it should be noted that there were no satisfied explanation why deactivation of Mo_2N catalyst was also discovered after its pre-reduction and pre-sulfidation treatment.

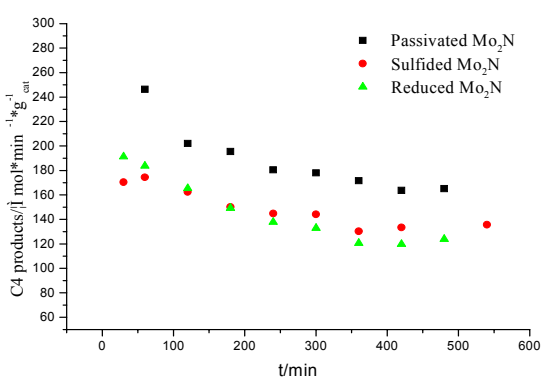

Figure 3. Catalytic activities of Mo_2N pretreated by different methods.

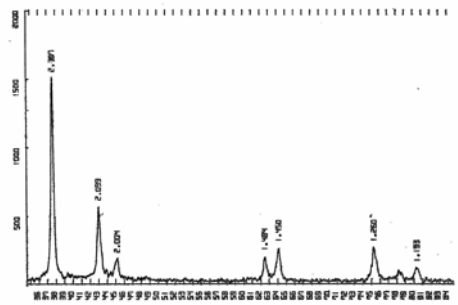

Figure 4. XRD pattern of pre-reduced molybdenum nitride.

Conclusions

1. Another crystal type Mo_2N that different from γ one was synthesized by temperature-programmed reaction between MoO_3(99%) and the mixture of N_2(99.9%) and commercial H_2. It had high thiophene HDS catalytic activity like γ - Mo_2N.

2. Mo_2N deactivated with reaction time at the initial stage of reaction, and then retained about a constant. The catalytic activity increased with increasing reaction temperature. X-ray diffraction pattern suggested that bulk structure of Mo_2N did not have change after reaction.

3. The HDS action of nitride catalyst was strongly dependent on the pretreatment of the catalyst. Pre-reduction and pre-sulfidation could deactivate the catalytic activity. However, the bulk structure of Mo_2N remained unchanged after pretreatment. The pretreatment might affect the surface properties of catalyst to deactivate the activity.

Acknowledgment. We are grateful to the Shanxi Youth Foundation, P. R. China, Grant No. 20001014.

References

1. Volpe, L.; Boudart, M., J Solid State Chem., 1985, 59(3): 332-347
2. Nagai, M., Miyao, T.; Tuboi, T., Catal. Lett., 1993, 18(1): 9-14
3. Sajkowski, D. T.; Oyama, S. T., Appl. Catal. A, 1996, 134(1-2): 339-349
4. Colling, C. W.; Thompson, L. T., J. Catal., 1994, 146(1): 193-203
5. Sajkowski, D. T.; Oyama, S. T., Prepr. Am. Chem. Soc. Div. Pet. Chem., 1990, 35(2): 233-236
6. Markel, E. J.; Van Zee, J. W., J. Catal., 1990, 126 (2): 643-657
7. Wise, R. S.; Markel, E. J., J. Catal., 1994, 145(2): 344-355
8. Logan, J. W. Heiser, J. L., McCrea, K. R., Gates, B. D., Bussell, M. E. Catal., Lett., 1998, 56(4): 165-171
9. Liu, Y. Q., Liu, C. G., Que, G. H., Energy & Fuels, 2002, 16(3): 531-535
10. McCrea, K. R., Logan, J. W., Tarbuck, T. L., Heiser, J. l., Bussell, M. E., J. Catal., 1997,171(1):255-267

INVESTIGATION OF CO ADSORPTION ON THE ZIRCONIA POLYMORPHS

Zhongyi Ma, RunXu, Cheng Yang, Wei Wei, Yuhan Sun

State Key Laboratory of Coal Conversion, Institute of Coal Chemistry, Chinese Academy of Sciences, Taiyuan, P.R.China 030001

Introduction

In recent years, interest has grown in the surface properties of microcrystalline zirconia, in view of its wide use as a catalyst, metal catalyst support, and precursor for ceramic applications. The most used probe molecule for testing the chemical properties of oxides in particular of zirconia, is CO. Different zirconia phase have great difference in adsorption CO because of different surface chemical properties. In this present the interactions of CO with amorphous, monoclinic and tetragonal zirconia are investigated by both infrared spectroscopy and temperature-programmed spectroscopy to determine the influence of bulk phase on adsorption capacity and species formed by CO reaction with hydroxyl on zirciona surface.

Results and discussion

Figure1 showed that the infrared spectra of CO adsorption on the am-ZrO_2 with temperature increasing. Below 523 K, obvious spectra could not be seen. With temperature increasing, CO adsorption bands at 2132cm^{-1}could be detected. The bands at 1558cm^{-1} and 1369cm^{-1} are considered to the formate bands, which could be proved with bands at 2973cm^{-1} and 2888cm^{-1} for CH (not show). There were different from what W.Hertl[1] observed in which formate was not detected while carbonate formed. Figure 4 showed that TPD spectra of am-ZrO_2 adsorption of CO at temperatures at 673K. Three species desorbing in this case were CO, CO_2 and H_2O, which could attribute to the thermal decomposition of formate and desorption of adsorption CO.

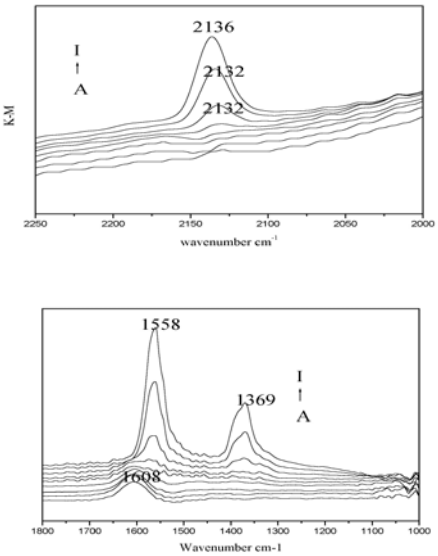

Figure1.Spectra of CO adsorption on am-ZrO_2.A-303K,B-323K,C-373K,D-I-423-673K

CO adsorption spectra on the m-ZrO_2 with temperature increasing were showed in Figure2. Two weak bands at 2121cm^{-1} and 2105cm^{-1} were detected at 473K, when temperature increased, two bands merge and only one band at 2109 was seen. At low temperature bidented bicarbonate with bands at 1631cm^{-1} and 1481cm^{-1} were observed while formate bands at 1573cm^{-1}, 1384cm^{-1} and 1361cm^{-1} formed when temperature increased up to 576K, which were similar to what Konstantin Pokrovski reported[2]. TPD-MS species were same to the am-ZrO_2 and only three species could be detected. But three CO_2 peaks were showed and CO desorption temperature was lower than that of am-ZrO_2. IR spectra showed that the bicarbonate and formate species formed when CO adsorption on m-ZrO_2, with temperature increasing, these species were decomposed.

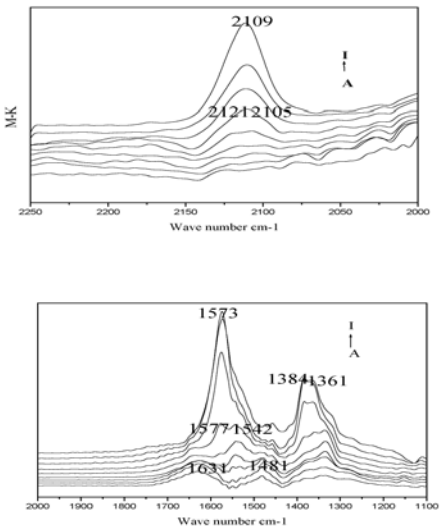

Figure2. Spectra of CO adsorption on m-ZrO_2. A-303K,B-323K,C-373K,D-I-423-673K

IR spectra of CO adsorption on the t-ZrO_2 were showed in Figure3. Below 573K obvious bands could hardly be seen. When temperature increased, two bands in 2183cm^{-1} and 2090cm^{-1} were detected, which differ from what detected on the am-ZrO_2 and m-ZrO_2. When temperature was below 623K, bidented carbonate with bands in 1658cm^{-1} and 1288cm^{-1} were obvious, bidented bicarbonate with bands in 1612 cm^{-1} and 1357cm^{-1} were formed when temperature up to 623K. But polydentate reported by Konstantin Pokrovski[2]could hardly be detected. CO-TPD-MS(Figure4) showed that the different species were desorbed when CO adsorption at 623K, besides H_2O CO and CO_2, H_2 was desorbed . We could speculate that there were different chemical properties in the zirconia polymorphs.

In addition, the concentration and basicity of hydroxyl groups were different on the zriconia polymorphs and as well as Lewis acidity of Zr^{4+} cation and Lewis basicity of O^{2-}, which exerted great influence on CO adsorption and species formed on different zirconia phase when CO reacted with hydroxyl on zriocnia polymorphs. The detail mechanism was under investigation.

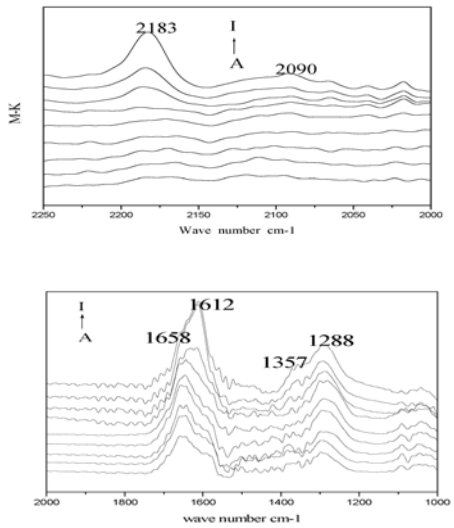

Figure3. Spectra of CO adsorption on t-ZrO_2. A-303K, B-323K,C-373K, D-I-423-673K

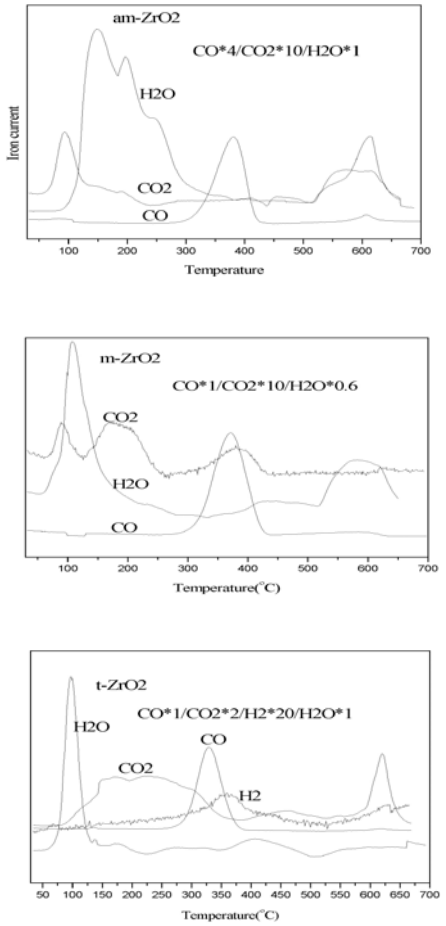

Figure 4 CO-TPD-MS spectra of am-ZrO_2, m-ZrO_2 and t-ZrO_2. Adsorption CO at 623K

Reference:
(1) W. Hertl *Langmuir* **1989**, 5(1), 96-100.
(2) Konstantin Pokrovski, Kyeong Taek Jung, and Alexis T. Bell, *Langmuir*.**2001**,17 (14) 4297-4303

REMOVAL OF HETEROATOM CONTAINING SPECIES IN COAL LIQUID DISTILLATES FROM SOUTH BANKO COAL BY CATALYTIC HYDROTREATMENT OVER NiMo SUPPORTED ALUMINA CATALYST

*SRI DJANGKUNG SUMBOGO MURTI[1], KINYA SAKANISHI[2], OSAMU OKUMA[3], YOZO KORAI[1] and ISAO MOCHIDA[1]**

1. Institute of Advanced material Study, Kyushu University, Kasuga, Fukuoka 816-8580, Japan
2. National Institute of Advanced Industrial Science and Technology, Tsukuba, Ibaraki 305-8569, Japan and
3. The New Industry Research Organization, 1-5-2, Minatojima-minamimachi, Chuo-ku, kobe 650-0047, Japan

INTRODUCTION

Coal liquid distillates ranging in the boiling point from naphtha to gas oil fractions tends to contain more heteroatoms such as nitrogen and oxygen than the corresponding petroleum product [1]. Removal of these heteroatom is required before using as feedstock for existing refineries, because these elements are sources of air pollution and causes for severe deactivation catalysts.

Heteroatom, S, N and O, in aromatic rings required sulfided NiMo, CoMo or NiW catalysts for their extensive removal to required levels in petroleum refining. Sulfur is eliminated directly by the catalyst to form H_2S, although sterically hindered S compounds are hardly removed unless the hydrogenation of neighboring aromatic ring releases the hindrance [2]. In contrast, denitrogenation and deoxygenation required complete hydrogenation of aromatic rings because of strong C-N and C-O bonds [3]

In the present study, hydrotreatment of South Banko coal liquids was carried out over commercially available NiMo/Al2O3 catalysts. The effect of reaction conditions such temperature, contact time and amount of catalyst on heteroatom removal was studied. HDS, HDN and HDO reactivities of some heteroatoms containing species were also investigated.

EXPERIMENTAL

I. Feedstocks.

Coal liquid used in the present study was obtained from coal liquefaction pilot palnt in Japan. The boiling range of the sample is < 300 ^oC, and contained 0.84wt% of N, 3.74wt% of O and 900ppm S.

II. Hydrotreatment

The coal liquid was hydrotreated over a commercial $NiMo/Al_2O_3$ catalysts in autoclave-type reactor (100 ml internal volume). 10 g oil, 1 g catalyst, which was pre-sulfided by $5\%H_2S/H_2$ at 360^oC for 2 hours, and 10 kg/cm^2 hydrogen gas were charged into the reactor. The reactor was heated to prescribed temperature and maintained for 2h. The hydrotreated product was filter and analyzed by GC-AED to qualify and quantify all the heteroatom containing compounds.

RESULTS AND DISCUSSION

Fig. 1 showed carbon, sulfur, nitrogen and oxygen chromatograms feed analyzed by GC-AED. Most of sulfur species in SBCL were thiophenes (TH) and benzothiophenes (BT). Pyridines, aniline quinolines, and indoles were found as nitrogen, phenols, benzofurans and dibenzofuran were as oxygen compounds. Hump on the nitrogen chromatogram due to nitrogen species was observed in this feed, indicating basic nitrogen species in the SBCL.

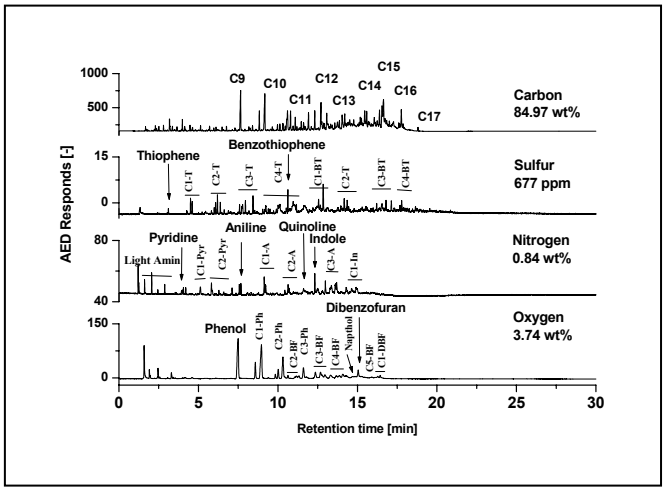

Figure 1. GC-AED chromatograms of SBCL.

The reactivity of sulfur species after hydrotreatment over $NiMo/Al_2O_3$ catalysts are shown in Figure 2. All sulfur species found in SBCL showed the high reactivity over the NiMo catalyst, and removed by 360 ^oC for 60 min.

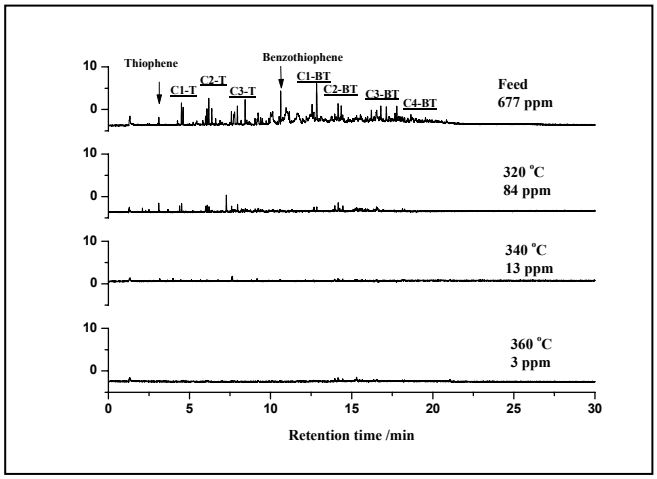

Figure 2. Sulfur chromatogram of hydrotreated SBCL.

In contrast, nitrogen species exhibited a wide range of reactivity. Pyridines exhibited high reactivity, however, anilines and quinoline were much less reactive. Nitrogen conversion after HDN is listed in Table 1. The surprising result of this study is that at high HDN conversions the majority of the compounds remaining in the hydrotreated products are alkylated anilines. Thus, alkylated anilines are the compounds most difficult to convert from coal liquid. At a higher temperature of 400 ^oC, alkylated anilines were as the lowest reactivity, lower even than quinolines. It is surprising since anilines has an aliphatic C-N bond whereas quinolines have the nitrogen atom included in the six-membered ring structure. Another study has noted that 3-ethyl aniline showed a lower reactivity than quinoline when both were present in the reaction mixture while it showed a higher reactivity than quinoline when reacted alone.

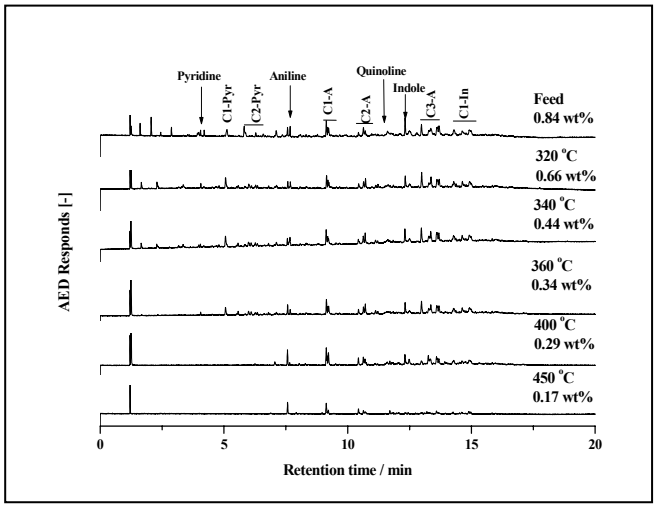

Figure 3. Nitrogen chromatograms of hydrotreated SBCL.

Table 1. Nitrogen species conversion (ppm).

	Feed	320	340	360	400	450
Light Amin	547	368	256	232	336	176
Pyridine	143	185	50	0	0	0
c1-Pyr	310	334	261	173	0	0
c2-Pyr	587	399	301	225	45	0
Aniline	155	136	101	151	239	197
c1-A	629	444	432	293	366	284
c2-A	951	746	545	506	588	334
c3-A	2606	2014	1302	1070	888	387
Quinoline	322	244	141	120	115	88
Indole	427	342	210	184	179	48
c1-In	1385	1118	506	448	391	319
Un-known	884	686	569	185	40	28
Total	8418	6649	4418	3356	2851	1687

Oxygen species, 3.74 wt% of feed, exhibited low reactivity over NiMo catalyst especially dibenzofuran as showed in Figure 4.

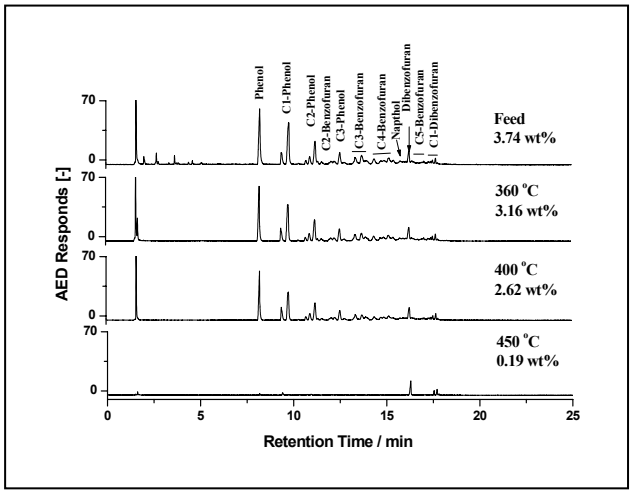

Figure 4. Oxygen chromatograms of hydrotreated SBCL.

References

1. Yanai, S., Komatsu, N., Shimasaki, K., *proceedins the 6th Japan China Symposium on Coal and C1 Chemistry*, Miyagi, Japan (1998) 196
2. Ma, X., Sakanishi, K., Mochida, I., *Ind. Eng. Chem. Res*. **33** (1994) 218
3. Girgis, M.J., Gates, B.C., *Ind. Eng. Chem. Res*. **30** (1991) 2021.

STUDY OF THE LIQUIDS DERIVED FROM CO-COKING IN A LABORATORY SCALE DELAYED COKER

María M. Escallón, Gareth Mitchell, Harold H. Schobert and Mark W. Badger

The Energy Institute, the Pennsylvania State University, PA 16802

KEYWORDS: Co-coking, Jet Fuel, Gasoline

Introduction

Co-coking is the simultaneous coking of a bituminous coal and petroleum product, such as decant oil. The advantage of co-coking relative to the better-known co-processing is that co-coking can be carried out a relatively low-pressures and that hydrogen is not required in the process [1]. Delayed coking of petroleum streams has been widely used for the conversion of heavy distillates into lighter ones. By the use of an appropriate aromatic feedstock, in addition to the conversion into lighter distillates, this process produces needle coke. Extensive work at our Institute has shown that the inclusion of coal-derived components brings more pyrolytic stability to the distillates [2-6].

Many studies have been performed in order to improve the quality of the jet fuel by blending coal and petroleum [7-20]. It has been seen that these blends give to the distillates thermal stability because of the production of hydroaromatic or naphthenic compounds. This is desirable for the jet fuel to reduce formation of deposits that can lead to the obstruction of the aircraft's fuel lines or burner nozzles.

For the future characterization, S.A.R.A analysis (saturates, aromatics, resins, asphaltenes) will be carried out to dtermine the contribution of the coal to the final liquid yield with respect to reaction time in co-coking. The components of each fraction will be identified by mass spectrometry. A blank of decant oil (100%) at 6 h was run in order to compare the contribution of the coal to the final liquid yield.

Experimental

The experimental procedure has been described iin a companion preprint in this volume. The reactor has three sections, bomb, transfer pipe and catchpot. Approximately 20 g of the mixture decant oil / coal (2:1) was added to the bomb of the reactor. A blank with 20g of pure decant oil was run at six hours to compare the coke obtained with those of co-coking.

The reactor is assembled and purged with N_2. The reactor is heated in a sand bath at a constant temperature of 465°C, varying the reaction time from 2 up to 12 hours. When the reaction at each specific temperature has finished, the reactor is allowed to cool at room temperature. After reaching this temperature, the three sections are disconnected.

The solid product which is in the bomb goes through Soxhlet extraction with THF and the insoluble material is dried for 1 hour at 100°C in an oven. The weight of the coke before and after the extraction was recorded to get the amount of THF- solubles in the coke. For the mass balance, the THF-solubles were added to the liquid yield.

The characterization of jet the liquid was carried out using a Hewlett Packard 5800 GC with flame ionization detector .Simulated distillation, following ASTM D2887. This is useful to explore boiling point distributions in complex mixtures, usually fuel related.

Samples. Decant oil: Obtained from Seadrift Coke in Texas. This feed is used for making premium needle coke.

Coal: A number of compatible coals with regard to thermoplastic properties, ash and sulfur values were evaluated in past investigations [1,7-10,12,13,18]; this work has led to the selection of Powellton coal as a feedstock of choice. This coal was obtained previously cleaned by mechanical process; this coal is called "whole clean Powellton".

Results and Discussion

For the mass balance, the THF -solubles or liquids trapped in the coke were determined; the values have been normalized at 10g of coke. As is shown in Figure 1, as reaction time increases, liquids present in the coke decreases. This means that the contribution to the liquid yield from the coke is higher as reaction time is increased.

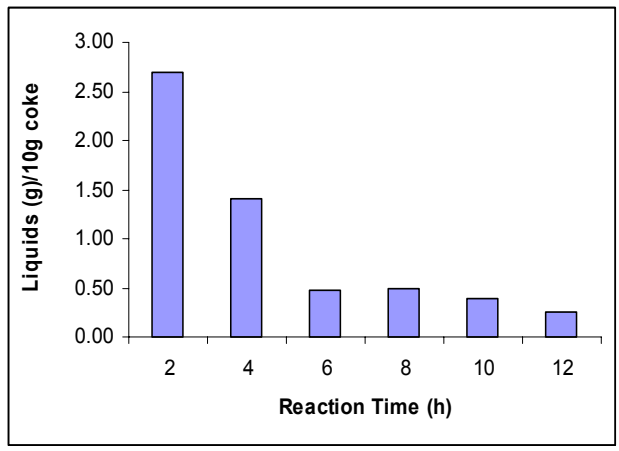

Figure 1. Variation of the liquids trapped in the coke (g)/10 g of coke with the time

The THF-solubles present in the decant oil (100%) run at 6h are much higher than the solubles present at the same reaction time but with the blend decant oil/coal. The amount of THF -solubles is 2.64 g/10g coke (decant oil 100%); this amount is comparable to that from reaction time at 2 hours (blended). We can conclude that the addition of coal acts to reduce the liquids trapped in the coke (increasing of the liquid yield) at lower reaction times.

Figure 2 shows the boiling point of the fraction <350C (i.e., potential gasoline and jet fuel). It is observed that at zero reaction time the percentage of the boiling point at <350C is 5%. Then, the percentage reaches a maximum value at 2-4 h and slightly decreases at 10-12 h.

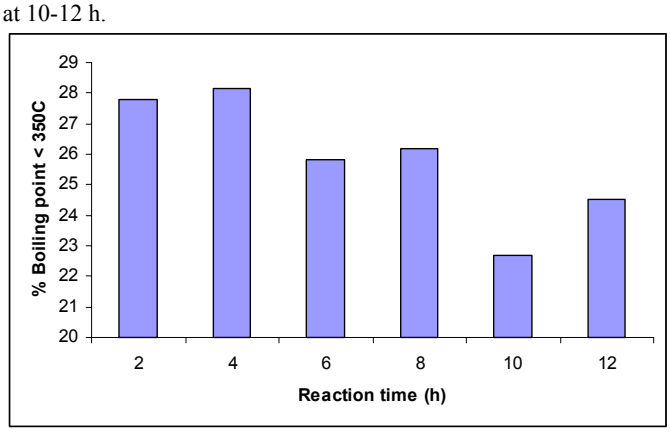

Figure 2. Fraction at boiling point <350C variation with the time

By comparing the boiling point fraction of the run at 6 h between decant oil (100%), 23.28%, and 2;1 decant oil:coal mixture,

25.80%, we can say that the additional 2.52% of the fraction <350C is provided by the coal volatiles. Therefore, the presence of the coal contributes to enhance the yield of the liquids at that specific cut point at 6h. The percentage of the particular cut <350C has been enhanced by 10% through the coal addition.

Conclusions

The addition of coal to the decant oil enhances the percentage of liquids to the fraction <350C. This indicates that the liquid obtained by the delayed coking process at laboratory scale contains coal-derived liquids, which provide cyclic and aromatics improving the stability of the jet fuel.

Acknowledgement. The authors are pleased to acknowledge the financial support for this work provided by the Air Force Office of Scientific Research. We thank Seadrift Coke for the sample of decant oil used in this work.

References

[1] Fickinger, A.E. *M.S. Thesis*. The Pennsylvania State University, University Park, PA. **2000.**

[2] eser, S.; Song, C.; Copenhaver, R.M.; Perison, J.; Schobert, H.H. *US Air Force Rept.* AFWAL-TR-87-2042, **1990**.

[3] Song, C.; Eser, S.; Schobert, H.H.; Hatcher, P.G. *Prepr. Pap.—Amer. Chem. Soc. Div. Petr. Chem.* **1992**, *37*, 540.

[4] Song, C.; Eser, S.; Schobert, H.H.; Hatcher, P.G. *Energy Fuels* **1993**, *7*, 234.

[5] Coleman, M.M.; Schobert, H.H.; Song, C. *Chem. Britain*. **1993**, *29*, 760.

[6] Badger, M.W.; Santoro, R.J.; Schobert, H.H. *Newsletter, Intl. Assoc. Stabil. Handling Liq. Fuels*. **2001**, *(26)*, 10.

[7] Martin, S.C.; Tomic, J.; Schobert, H.H. *Prepr. Pap.—Amer. Chem. Soc. Div. Fuel Chem.* **1997**, *42*, 121.

[8] Martin, S.C.; Tomic, J.; Schobert, H.H. *Proc. 9th Intl. Conf. Coal Sci.* **1997**, *3*, 1557.

[9] Badger, M.W.; Fickiinger, A.E.; Martin, S.C.; Mitchell, G.D.; Schobert, H.H. *Proc. 8th Austral. Coal Sci. Conf.***1998**, 245.

[10] Fickinger, A.E.; Badger, M.W.; Mitchell, G.D.; Schobert, H.H. *Prepr. Pap.—Amer. Chem. Soc. Div. Fuel Chem.* **1999**, *44*, 106.

[11] Butnark, S.; Badger, M.W.; Schobert, H.H. *Prepr. Pap. Amer. Chem. Soc. Div. Fuel Chem.* **1999**, *44*, 662.

[12] Fickinger, A.E.; Badger, M.W.; Mitchell, G.D.; Schobert, H.H. *Prepr. Pap.—Amer. Chem. Soc. Fuel Chem.* **1999**, *44*, 684.

[13] Fickinger, A.E.; Badger, M.W.; Mitchell, G.D.; Schobert, H.H. *Prepr. Pap.—Amer. Chem. Soc. Div. Fuel Chem.* **2000**, *45*, 299.

[14] Butnark, S.; Badger, M.W.; Schobert, H.H. *Prepr. Pap.—Amer. Chem. Soc. Div. Petr. Chem.* **2000**, *45*, 493.

[15] Andrésen, J.M.; Strohm, J.J.; Boyer, M.L.; Song, C.; Schobert, H.H.; Butnark, S. *Prepr. Pap.—Amer. Chem. Soc. Div. Fuel Chem.* **2001**, *46*, 208.

[16] Butnark, S.; Badger, M.W.; Schobert, H.H. *Prepr. Pap.—Amer. Chem. Soc. Div. Fuel. Chem.* **2001**, *46*, 492.

[17] Strohm, J.J.; Butnark, S.; Keyser, T.L.; Andrésen, J.M.; Badger, M.W.; Schobert, H.H.; Song, C. *Prepr. Pap.—Amer. Chem. Soc. Div. Fuel Chem.* **2002**, *47*, 179.

[18] Badger, M.W.; Mitchell, G.D.; Herman, N.; Senger, B.; Schobert, H.H. *Prepr. Pap.—Amer. Chem. Soc. Div. Fuel Chem.* **2002**, *47*, 179.

[19] Badger, M.W.; Butnark, S.; Wilson, G.R.; Schobert, H.H. *Prepr. Pap.—Amer. Chem. Soc. Div. Petr. Chem.* **2002**, *47*, 198.

[20] Butnark, S.; Badger, M.W.; Schobert, H.H.; Wilson, G.R. *Prepr. Pap.—Amer. Chem. Soc. Div. Petr. Chem.* **2002**, *47*, 201.

A COAL TO HYDROGEN PLANT

Phil Amick, Global Energy Inc.
Robert Geosits, Bechtel Corporation
Sheldon Kramer, Nexant, Inc.

Introduction

In late 1999, as part of the Vision 21 program, the National Energy Technology Laboratory awarded Nexant, Inc. (a Bechtel-affiliated company) and Global Energy, Inc. (which acquired the gasification related assets of Dynegy Inc., of Houston, Texas including the E-GAS™ gasification technology, formerly the Destec Gasification Process) a contract to optimize IGCC plant performance.[1] Task 1 of this contract developed optimized IGCC plant configurations: (1) petroleum coke gasification for electric power with/without the coproduction of hydrogen and industrial-grade steam, (2) coal gasification for electric power generation only, and (3) a Coal to Hydrogen Plant. Figure 1 is a schematic diagram of Task 1 showing the steps used to develop the various coal and petroleum coke gasification plants.

This paper summarizes the optimization and cost reduction techniques that were used, presents the optimized design, and describes plant performance. It also provides cost information and presents a financial analysis.

The Wabash River Coal Repowering Project

In 1990, Destec Energy, Inc. of Houston, Texas and PSI Energy, Inc. of Plainfield, Indiana formed the Wabash River Coal Gasification Repowering Project Joint Venture to participate in the Department of Energy's Clean Coal Technology Program by demonstrating the coal gasification repowering of an existing 1950's vintage generating unit. In September 1991, the project was selected by the DOE as a Clean Coal Round IV project to demonstrate the integration of the existing PSI steam turbine generator and auxiliaries, a new combustion turbine, a heat recovery steam generator, and a coal gasification facility to achieve improved efficiency and reduced emissions. In July 1992, a Cooperative Agreement was signed with the DOE.[2] Under terms of this agreement, the Wabash River Coal Gasification Repowering Project Joint Venture developed, constructed and operated the coal gasification combined cycle facility. The DOE provided cost-sharing funds for construction and a three-year demonstration period.

The participants jointly developed, separately designed, constructed, owned, and operated the integrated coal gasification combined-cycle power plant, using Destec's coal gasification technology to repower the oldest of the six units at PSI's Wabash River Generating Station in West Terre Haute, Indiana. The gasification process integrated a new General Electric 7FA combustion turbine generator and a heat recovery steam generator (HRSG) to repower the 1950s-vintage Westinghouse steam turbine

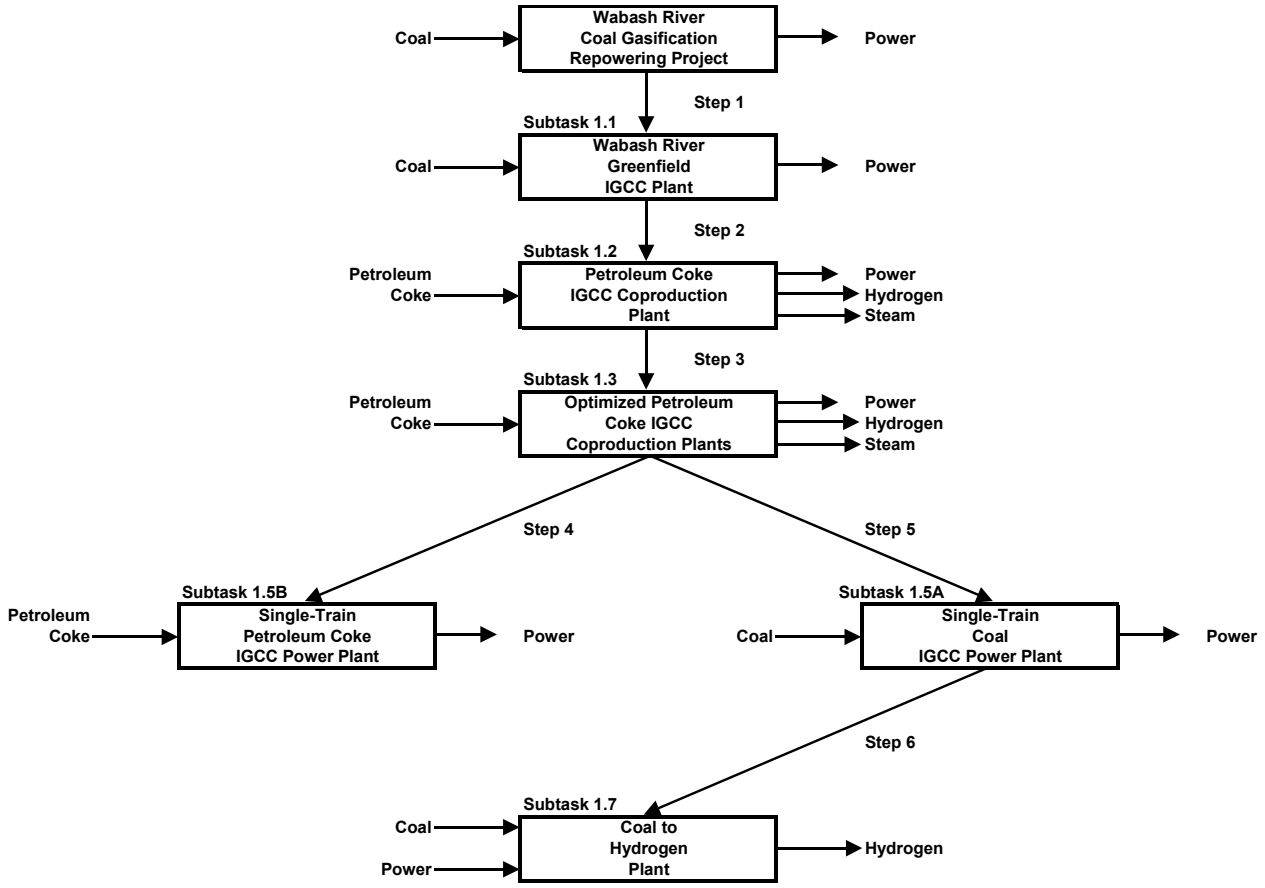

Figure 1. Schematic Diagram Showing the Chronological Development of the Coal to Hydrogen Plant

[1] Task 1 Topical Report, "Gasification Plant Cost and Performance Optimization," Contract No. DE-AC26-99FT40342, May 2002, http://www.netl.doe.gov/coalpower/gasification/projects/systems/docs/40342R01.PDF.

[2] Contract No. DE-FC21-92MC9310, "Wabash River Coal Gasification Repowering Project"

generator using some of the pre-existing coal handling facilities, interconnections, and other auxiliaries.

Based on the Wabash River Coal Gasification Repowering Project, Global Energy, Bechtel and Nexant contributed their combined design, engineering, construction, and operating expertise to develop optimized designs for state-of-the-art gasification plants for either coal or petroleum coke.

The Wabash River Greenfield Plant

The gasification optimization work began by reviewing and assessing performance data and cost information from the existing Wabash River Project facility. From this basis, design and cost engineers adjusted the plant's scope – equipment, materials, and process operation – so that the Wabash River project design was transformed into a Greenfield IGCC design as shown in Step 1 of Figure 1. Figure 2 is a simplified train diagram showing the major process blocks in the Wabash River Greenfield Plant developed in Step 1. The plant processes 2,260 tpd of dry Illinois No. 6 coal and exports 269.3 MW of power. It also produces 356 tpd of slag and 57 tpd of sulfur. The export power of the greenfield facility is greater than the 262 MW of the Repowering Project because a newer steam turbine that is a better fit with the gasification block is used. The plant has a heat rate of 8,912 Btu (HHV)/kW-hr or a 38.3% thermal efficiency (HHV) to power.

Capital cost is a key part of IGCC economics and profitability. A three-stage cost estimating methodology was employed to develop a reliable mid-year 2000 total installed cost for the Greenfield Plant equivalent to the Wabash River Coal Gasification Repowering Project, but located at a generic site in a typical Mid-Western state.[3] The plant would have an EPC cost of 452.6 MM$ (mid-year 2000) or 1,680 $/kW of export power. All plant costs cited in this paper are EPC costs which exclude contingency, taxes, licensing fees, and owners costs (such as land, operating and maintenance equipment, capital spares, operator training, and commercial test runs).[4]

The Optimization Process

Step 2, converted the Greenfield Plant to a petroleum coke IGCC coproduction plant located on the Gulf Coast. The next step optimized the petroleum coke IGCC plant. Process and project optimization was guided by Bechtel's Value Improvement Practices (VIPs) methodology using the following VIPs:

- Technology Selection
- Process Simplification
- Classes of Plant Quality
- Process Reliability Modeling
- Design-to-Capacity
- Predictive Maintenance
- Traditional Value Engineering
- Constructability and Schedule Optimization

Initially, Bechtel and Global Energy prepared a Value Improvement Plan. This plan determined that the above practices were most applicable to this study. "Champions" were assigned to each applicable practice, and these champions along with the Value Improvement Plan administrator were responsible for implementation of the VIP process as well as documenting the results. Bechtel and Global Energy thoroughly analyzed the Value Engineering ideas generated during the brainstorming sessions to determine which were applicable for improving the project by assessing their benefits.

The VIP efforts were concentrated in the gasification area, specifically on the gasification and waste heat recovery section, the particulate removal section, the raw gas cooling area, and the syngas cleanup area. Lessons learned from plant operations showed that these areas are critical to reliable operations and high on-stream factors. In the Traditional Value Engineering VIP, almost 300 different ideas were generated in several brainstorming sessions. These ideas are based on (1) actual operations and maintenance experience at the Wabash River plant, (2) construction of the Wabash River Repowering Project, and (3) Bechtel's experience in other gasification and power generation projects with similar equipment. Personnel from the Wabash River facility proposed many of these ideas.

In conjunction with the Value Improvement Plan, Bechtel used the COMET plant layout program to evaluate and optimize equipment layout arrangements and minimize piping requirements for a given area or between areas. By changing the location of any piece of equipment in a given area, COMET readjusts the interconnecting piping and recalculates new quantities. This optimization tool is especially beneficial in cases where a large percentage of the piping is large bore or high cost alloy material. Additionally, the COMET program also is capable of automatically generating plot plans and three-dimensional architectural renderings of the plant.

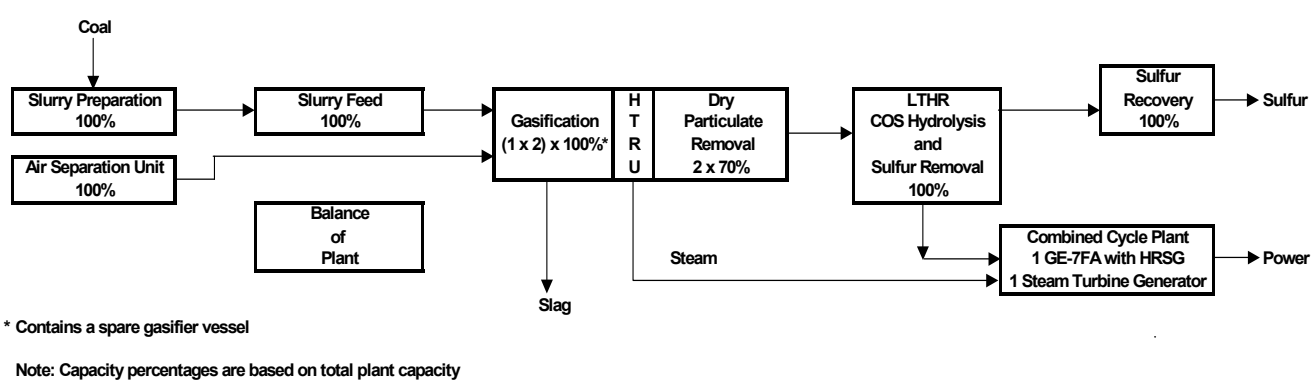

Figure 2. Simplified Block Flow Diagram of the Wabash River Greenfield Plant

[3] Amick, P. et al., "An Optimized Petroleum Coke IGCC Coproduction Plant", Gasification Technologies Council Conference, San Francisco, CA, October 7-10, 2001.

[4] These excluded items are included in the subsequent discounted cash flow financial analysis.

For several years now, Bechtel has been optimizing the heat integration of their standard coal and gas-based power plant designs. As a consequence, Bechtel has developed a *Powerline* suite of templates for combined cycle, pulverized coal, and fluidized bed power plant designs.[5] These *Powerline* plants incorporate the most advanced technologies and best practices from Bechtel's engineering portfolio. Designing plants using standard templates saves engineering and procurement costs resulting in higher quality plants that are less expensive and require less time for construction. The lessons learned during the development of the *Powerline* templates also were applied to optimize the various subtask designs.

Bechtel has created a number of supplier alliances, not only for major equipment manufacture and fabrication, but also for bulk materials. In addition to reducing the price of equipment, these alliances also shorten the engineering and procurement cycle resulting in shorter overall project schedules and reduced EPC costs which translate into faster payback and increased profitability. These ideas also were applied to optimize the designs.

The resulting optimized Subtask 1.3 plant design has been previously described in Reference 3. Not only does the optimized petroleum coke coproduction plant have significantly improved performance, reduced emissions, and a substantially higher return on investment, it is 11% less costly than the original design.

The Subtask 1.5A Coal IGCC Power Plant

In Step 5, the design for a single-train coal-fueled IGCC power plant was developed based on the Subtask 1.3 Optimized Petroleum Coke IGCC Coproduction Plant. In this plant, the hot syngas leaving the gasifier goes to a hot residence vessel to allow further reaction. Following this, it is cooled in the high temperature heat recovery (HTHR) section before most of the particulates (98+%) are removed from the syngas by a cyclone. The remaining particulates and water soluble impurities are removed simultaneously by wet scrubbing with water. The particulates are concentrated and recovered from the wash water by a filter system before being recycled to the gasifier for further reaction. Filtered water is recycled to the wet scrubber or is sent to the sour water stripper.

Figure 3 is a train diagram of the Subtask 1.5A Coal IGCC Power Plant. The plant consumes 2,335 TPD of dry Illinois No. 6 coal and produces 284.6 MW of export power, 60 TPD of sulfur, and 364 TPD of slag. The plant has a heat rate of 8,717 Btu (HHV)/kW-hr, or a 39.1% thermal efficiency (HHV). The plant cost 375 MM$ (mid-year 2000) or 1,318 $/kW of export power.[6] Additional improvements have been identified to further reduce the plant cost.

The Subtask 1.5A Single-Train Coal IGCC Power Plant costs over 75 MM$ less than the Subtask 1.1 Greenfield Plant and produces more export power showing the result of the optimization process and use of a larger and more efficient combustion turbine. On a $/kW basis, the Subtask 1.5A plant costs over 22% less than the Subtask 1.1 plant. Furthermore, the Subtask 1.5A plant is less polluting than the Wabash River Greenfield Plant. On a lb/MW-hr basis, SO_2 is reduced by 56%, CO is reduced by 33%, and NOx is reduced by 60%. Sulfur removal is increased from 96.8% to 98.5%.

The Subtask 1.7 Coal to Hydrogen Plant

The gasification section of the Subtask 1.7 Coal to Hydrogen Plant produces 142 MMscfd of 99.0% hydrogen from 3,007 TPD of dry Illinois No. 6 coal. It also produces 76 TPD of sulfur and 474 TPD of slag, and consumes 18.4 MW of imported power. The plant satisfies all applicable environmental laws. The plant occupies about 38 acres. Figure 4 is a simplified block flow diagram of the Subtask 1.7 Coal to Hydrogen Plant

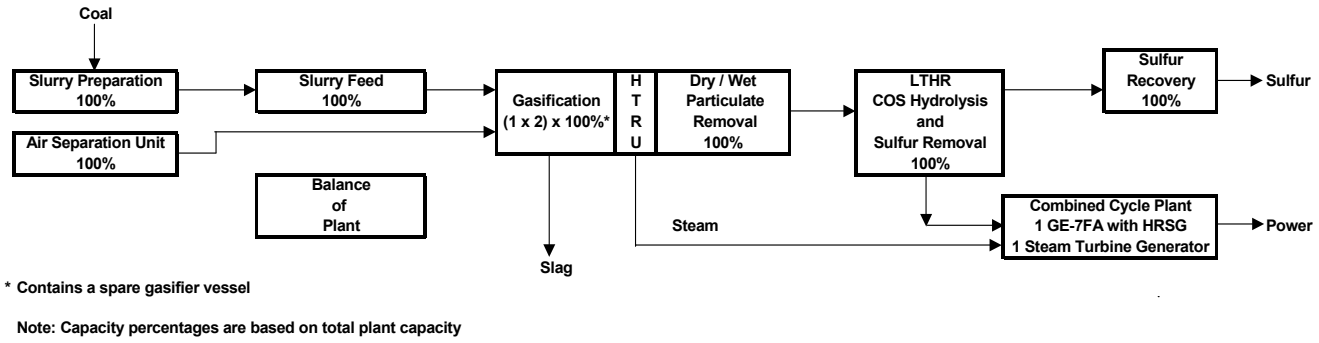

Figure 3 Simplified Block Flow Diagram of the Subtask 1.5A Single-Train Coal IGCC Plant

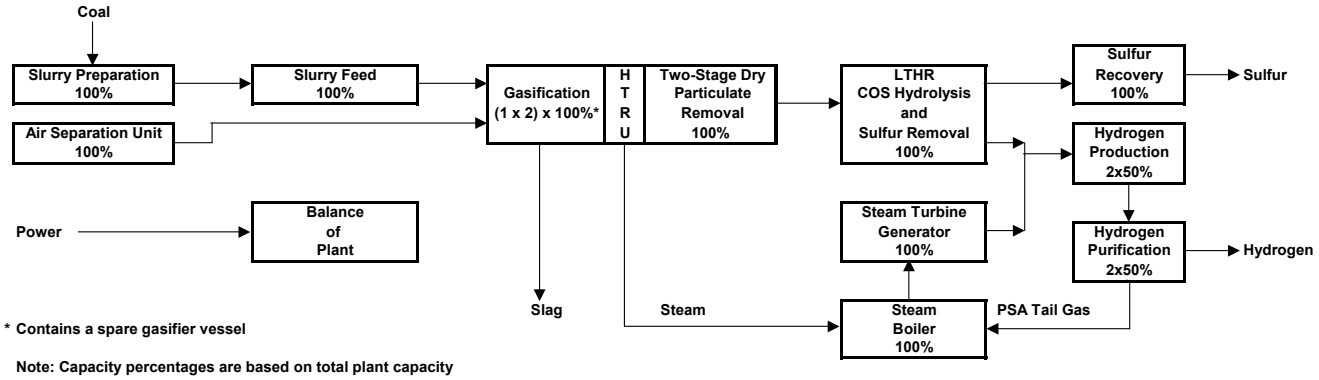

Figure 4. Simplified Block Flow Diagram of the Subtask 1.7 Coal to Hydrogen Plant

[5] *Powerline* is a registered trademark of the Bechtel Corporation.

The Air Separation Unit (ASU) supplies about 2,522 TPD of 99.5% oxygen to Global Energy's two-stage E-GAS™ gasifier which employs full slurry quench to control the second stage outlet temperature. The plant contains a spare gasifier vessel that can be placed in service to minimize the downtime whenever refractory replacement is required.

Char and unreacted coal particles that leave the gasifier in the syngas are collected downstream and recycled back to the first stage of the gasifier. Coal slurry, recycled char and oxygen are fed substoichiometrically into the first stage at elevated temperature and pressure to produce hot, raw syngas. Additional coal and slurry is added in the second stage, lowering the temperature of the gas through quenching and endothermic reactions; thereby, generating more syngas with a higher heating value. Particulates are removed from the syngas in a two-step system. First, a hot cyclone removes over 90% of the particulates, and the remainder is removed by an advanced dry char filtration system.

A Recitsol system is used for acid gas removal rather than an amine system for two reasons. First, it provides better sulfur removal from the syngas than an amine system so that a "sweet" shift process can be used to produce hydrogen from the CO in the syngas. The "sweet" CO shift system has the advantage of allowing higher CO conversions than the "sour" shift process. Secondly, the Rectisol system can be used to remove the bulk of the CO_2 from the shifted syngas for possible sale or sequestration, and it allows the downstream PSA unit to produce a 99.0% pure hydrogen stream containing only trace amounts of CO. However, a Rectisol system is more expensive and auxiliary power intensive than the amine systems that are used for the other subtasks.

The hydrogen production area consists of two parallel trains. Each train contains three CO shift reactors in series with cooling between them. The first two reactors are high temperature shift reactors that are sized to control the maximum outlet temperature. The third reactor is a low temperature reactor for maximum conversion. CO conversion is over 99%.

After the bulk of the CO_2 has been removed by the second stage of the Rectisol unit, two parallel PSA units purify the hydrogen. Hydrogen recovery from the shifted syngas is 90% to the 99.0% pure hydrogen product.

PSA sweep (off) gas is used to generate steam for the steam turbine. Medium pressure steam is extracted from the steam turbine for the CO shift reactors. The steam turbine produces 70.6 MW of power. The internal power consumption of the plant is about 89.0 MW. Thus, the plant imports about 18.4 MW of power. Table 1 shows the design feed and product rates for the Subtask 1.7 Coal to Hydrogen Plant.

The Coal to Hydrogen Plant has low emissions. The CO_2 vent gas emissions are free of SOx and NOx. However, the vent gas contains 0.51 mole% CO. At a 3% oxygen concentration and on a dry basis, the incinerator and steam boiler stack emissions contain 84 ppmv SOx, 40 ppmv NOx, and 50 ppmv CO. Combined, both stacks result in total emissions of 37 lb/hr of SOx (as SO_2), 27 lb/hr of NOx (as NO_2), and 1,846 lb/hr of CO. Sulfur removal is 98.5%.

The Coal to Hydrogen Plant costs 529.8 million mid-year 2000 dollars.[6] This EPC cost is about 3.7 MM$ per MMscfd of hydrogen production. Cost reductions could be obtained by relaxing the CO specification in the product hydrogen thereby allowing the use of a lower cost MDEA acid gas removal system. The cost of the hydrogen plant on a per unit of hydrogen also could be lowered by building larger, multiple train plants or coproduction plants where electric power is the major product as was done in the Subtask 1.3 Petroleum Coke IGCC Coproduction Plant.

Table 1. Design Feed and Product Rates of the Subtask 1.7 Coal to Hydrogen Plant

Ambient Temperature, °F	59
Coal Feed, as received, TPD	3,517
Dry Coal Feed to Gasifiers, TPD	3,007
Total Fresh Water Consumption, gpm	2,457
Hydrogen, 99.0%, MMscfd	142.1
Sulfur, TPD	76.4
Slag Produced, TPD (15% moisture)	474.3
Total Oxygen Feed to the Gasifier, TPD of 99.5% O_2	2,507
Heat Input to the Hydrogen Plant (HHV), Btu/hr x 10^6	3,195
Cold Gas Efficiency to Clean Syngas (HHV), %	76.5
Steam Turbine Output, MW	70.6
Gasification Plant Power Consumption, MW	(53.6)
ASU Power Consumption, MW	(35.4)
Net Power Consumption (Power Import), MW	(18.4)

Availability. In Table 5.0A of the Final Report for the Wabash River Wabash River Repowering Project, Global Energy reported downtime and an availability analysis of each plant system for the final year of the Demonstration Period.[7] During this March 1, 1998 through February 28, 1999 period, the plant was operating on coal for 62.37% of the time. There were three scheduled outages for 11.67% of the time (three periods totaling 42 days), and non-scheduled outages accounted for the remaining 25.96% of the time (95 days).

After adjustments, this data was used to estimate the availability of the Coal to Hydrogen Plant using the EPRI recommended procedure.[8] Table 2 presents the design (stream day), average availability, and average daily (calendar day) input and product rates for the Coal to Power Plant. As the table shows there are significant differences between the calendar day rates and the stream day rates for all the input and output flows. The average hydrogen production rate is 116.7 MMscfd or 81.32% of the design rate.

Discounted Cash Flow Financial Analysis. A financial analysis was performed using a discounted cash flow (DCF) model that was developed by Nexant Inc. (formerly Bechtel Technology and Consulting) for the DOE as part of the Integrated Gasification Combined Cycle (IGCC) Economic and Capital Budgeting Practices Task.[9] This model calculates investment decision criteria used by industrial end-users and project developers to evaluate the economic feasibility of IGCC projects. The IGCC financial model consists of 18 coupled spreadsheets in a Microsoft Excel workbook format. The model spreadsheets are organized into four main sections; (1) data input sheets, (2) supporting analysis sheets, (3) financial statements, and (4) projects summary result sheets.

[6] All plant EPC costs mentioned in this report are mid-year 2000 order of magnitude cost estimates which exclude contingency, taxes, licensing fees, and owners costs (such as land, operating and maintenance equipment, capital spares, operator training, and commercial test runs). It also assumes that process effluent discharge is permitted.

[7] "Wabash River Coal Gasification Repowering Project, Final Technical Report," U. S. Department of Energy, Contract Agreement DE-FC21-92MC29310, http://www.lanl.gov/projects/cctc/resources/pdfs/wabsh/Final%20_Report.pdf, August 2000.

[8] Research Report AP-4216, *Availability Analysis Handbook for Coal Gasification and Combustion Turbine-based Power Systems,* Research Project 1800-1, Electric Power Research Institute, 3412 Hillview Avenue, Palo Alto, CA, August 1985.

[9] Nexant, Inc., "Financial Model Users Guide – IGCC Economic and Capital Budgeting Evaluation," Report for the U. S. Department of Energy, Contract No. DE-AM01-98FE64778, May 2000.

Table 2. Design and Daily average Feed and Product Rates of the Subtask 1.7 IGCC Coal to Hydrogen Plant

Inputs	Design Rate	Daily Average Rate
Dry Coal, TPD	3,007	2,470
Electric Power, MW	18.4	15.1
River Water, gpm	2,457	2,018
Products		
Hydrogen, 99.0%, , MMscfd	142.1	116.7
Sulfur, TPD	76.4	62.8
Slag, TPD (15% moisture)	464.3	389.6
CO2, TPD	7,125	5,795

At the base economic conditions shown in Table 3, the Subtask 1.7 plant requires a hydrogen selling price of 2.790 $/Mscf to generate a 12% return on investment. These conditions are based on an 80% loan amount at a 10% interest rate with a 3% up front financing fee.

Table 3 shows the sensitivity of some individual component prices and financial parameters for the Subtask 1.7 Coal to Hydrogen Plant starting from a 12% ROI (with a hydrogen price of 2.79 $/Mscf). Each item was varied individually without affecting any other item. Most sensitivities are based on a ±10% change from the base value except when either a larger or smaller change is used because it either makes more sense or it is needed to show a meaningful result. The hydrogen selling price has the greatest impact on the ROI with a 10% increase resulting in a 4.32% increase in the ROI to 16.32%, and a 10% decrease resulting in a 4.59% decrease in the ROI to 7.41%. Changes in the sulfur and slag prices have only a small influence on the ROI.

A 10% decrease in the dry coal price of 2.2 $/ton from the base price of 22.0 $/ton to 19.8 $/ton will increase the ROI by 0.62% to 12.62%, and a 10% increase in the coal price to 24.2 $/ton will lower the ROI by 0.62% to 11.38%. A 10% change in the imported power price has a lesser effect on the ROI.

A 5% decrease in the plant EPC cost to 503.3 MM$ will increase the ROI by 1.59% to 13.58%, and a 5% increase in the plant cost to 556.3 MM$ will decrease the ROI by 1.45% to 10.55%. A 10% change in the plant cost will have about double the effect of a 5% change

The loan interest rate is the most sensitive of the financial parameters that were studied. A 20% decrease in the loan interest rate to 8% from the base interest rate of 10% will increase the ROI to 15.30% from 12.00%, and a 20% increase in the interest rate to 12% will lower the ROI to 8.68%. A 20% decrease in the loan amount from 80% to 72% will lower the ROI by 0.52% to 11.48%, and a 20% increase in the loan amount to 88% will increase the ROI by 0.83% to 12.83%. Decreasing the income tax rate by 10% from 40% to 36% will increase the ROI to 12.48%, and a 10% increase in the tax rate to 44% will lower the ROI by 0.52% to 11.48%.

Effect of Loan Interest Rate. At a 8% loan interest rate and with the 3% up front financing fee, a 12.0% ROI can be obtained at a hydrogen selling price of 2.590 $/Mscf. This is a drop of 0.20 $/Mscf from the 2.790 $/Mscf price required with a 10% loan interest rate. Figure 5 shows the effect of the hydrogen selling price on the ROI for the Subtask 1.7 Coal to Hydrogen Plant at both 8% and 10% loan interest rates. The two curves are very similar with the ROI for the 8% loan interest rate having about 3.3% higher return than that for the 10% loan interest rate.

Table 3. Sensitivity of Individual Component Prices and Financial Parameters for the Subtask 1.7 Coal to Hydrogen Plant Starting from a 12% ROI (with a Hydrogen Price of 2.79 $/Mscf)

	Decrease			Base	Increase		
	ROI	Value	% Change	Value	% Change	Value	ROI
Products							
Hydrogen	7.41%	2.511 $/Mscf	-10%	**2.790 $/Mscf**	+10%	3.069 $/Mscf	16.32%
Slag	11.80%	-5 $/t	---	**0 $/t**	---	5 $/t	12.20%
Sulfur	11.98%	27 $/t	-10%	**30 $/t**	+10%	33 $/t	12.02%
Feeds							
Coal	12.62%	19.8 $/t	-10%	**22.00**	10%	24.2 $/t	11.38%
Power	12.12%	24.3 $/MW-hr	-10%	**27.0 $/MW-hr**	+10%	29.7 $/MW-hr	11.88%
Financial							
EPC Cost	13.58%	503.3 MM$	-5%	**529.8 MM$**	+5%	556.3 MM$	10.55%
EPC Cost	15.29%	476.8 MM$	-10%	**529.8 mm$**	+10%	582.8 MM$	9.20%
Interest Rate	15.30%	8%	-20%	**10%**	+20%	12%	8.68%
Loan Amount	11.48%	72%	-20%	**80%**	+20%	88%	12.83%
Tax Rate	12.48%	36%	10%	**40%**	+10%	44%	11.48%

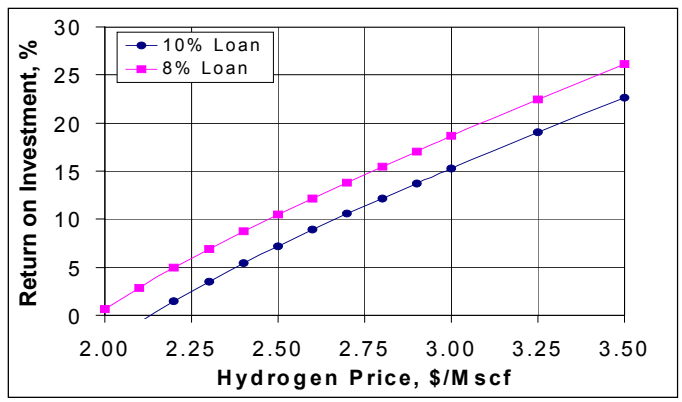

Figure 5. Effect of Hydrogen Selling Price on the Return on Investment

Effect of Syngas Availability. After commissioning all plants undergo a "learning curve" during which problem areas are corrected, inadequate equipment is replaced, and adjustments are made. Consequently, performance improves as measured by increased capacity and/or improved on-stream factors. At a 10% loan interest rate, Figure 6 shows the effect of improved hydrogen availability on the ROI for the plant at a hydrogen selling price of 2.79 $/Mscf. Increasing the hydrogen availability from the expected 81.3% to 85% increases the ROI to 13.68% from 12%.

Figure 7 shows the effect of improved hydrogen availability on the required hydrogen selling price for a 12% ROI for both 8% and 10% loan interest rates. Increasing the hydrogen availability from 81.3% to 85% reduces the required hydrogen selling price by about 0.10 $/Mscf in each case.

These two figures show the importance of designing, constructing and operating the plant to obtain a high hydrogen availability. Care should be taken in the design and selection of process equipment so that they will have a high reliability and require minimum scheduled downtime for maintenance.

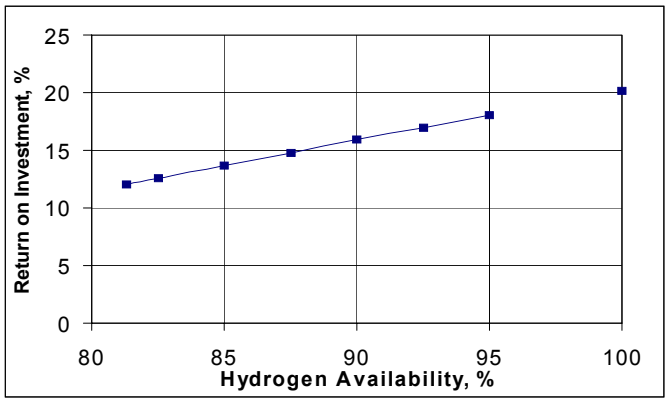

Figure 6. Effect of Hydrogen Availability on the Return on Investment with Hydrogen Price of 2.79 $/Mscf and a 10% Loan Rate

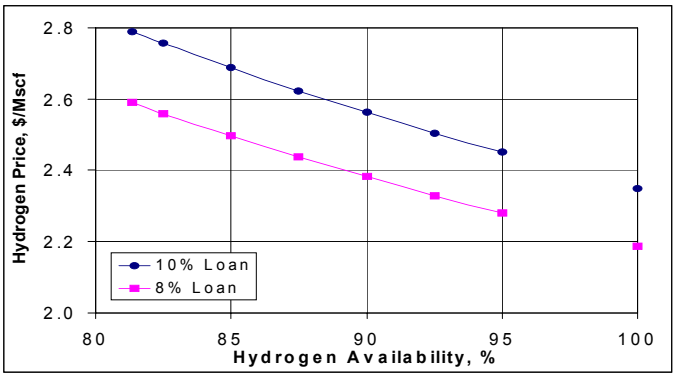

Figure 7. Effect of Hydrogen Availability on the Required Hydrogen Selling Price for a 12% Return on Investment

Effect of Plant Cost. Figure 8 shows the effect of the plant EPC cost on the required hydrogen selling price for the plant to produce a 12% return on investment. At a 10% loan rate, a 5% reduction in the plant EPC cost from 529.8 MM$ to 503.3 MM$ will reduce the required hydrogen selling price from 2.790 $/Mscf to 2.695 $/Mscf, a reduction of about 0.09 $/Mscf or 3.4%. At a 8% loan interest rate, a 5% reduction in the EPC cost reduces the required hydrogen selling price from 2.590 $/Mscf to 2.505 $/Mscf, a reduction of about 0.08 $/Mscf or 3.3%.

Summary

The objective of this study was to design a single-train coal to hydrogen plant. The design presented in this report satisfies that objective. It processes 3,007 TPD of dry Illinois No. 6 coal and produces 142.1 MMscfd of 99.0% hydrogen at 1,000 psig. It has an installed cost of 529.8 million mid-year 2000 dollars.

For the plant to generate a 12% ROI, the required hydrogen selling price must be in the 2.50 to 2.80 $/Mscf range. The exact value depends upon the financing assumptions. However, there are several possibilities for reducing the required hydrogen selling price.

First, the hydrogen purity specification can be relaxed allowing a higher concentration of oxygen containing impurities in the hydrogen. This would not be harmful if the hydrogen were to be used for hydrotreating in a refinery environment, but could be detrimental for certain petrochemical applications. In this situation, the Rectisol system would be replaced by an amine system, a "sour" shift would be employed, the hydrogen production would be reduced by 9.4%, the plant would become a net electric power producer exporting 39 MW, and the capital cost would be reduced by about 58 MM$. The net effect is that the required hydrogen selling price for a 12% ROI would drop by about 0.19 $/Mscf to 2.60 $/Mscf with a 10% loan interest rate.

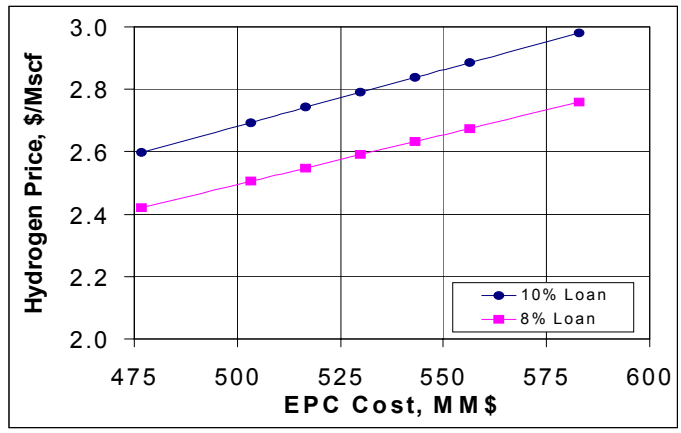

Figure 8. Effect of EPC Cost on the Required Hydrogen Selling Price for a 12% Return on Investment

Second, switching to the use of a lower cost fuel, such as petroleum coke, as was used in the Subtask 1.2 and 1.3 cases. Approximating this situation by using a zero cost coal would reduce the required hydrogen selling price for a 12% ROI by about 0.40 $/Mscf.

Third, instead of using a single gasification train with a spare gasifier vessel, a complete spare gasification train (without a spare gasifier vessel) could be installed to increase the hydrogen availability. Although this would increase the plant cost, the hydrogen availability would be increased to about 91.7%, and the required hydrogen selling price for a 12% ROI would drop by about 0.11 $/Mscf to 2.684 $/Mscf. This design philosophy was demonstrated during the Subtask 1.3 studies (see references 1 and 3).

Fourth, if the plant were located where the captured CO_2 could be utilized for enhanced oil recovery, the economics would be substantially improved. Assuming the CO_2 could be sold for 12 $/ton, the required hydrogen selling price for a 12% ROI would drop by about 0.6 $/Mscf to 2.194 $/Mscf.

By combining three of the above cases (1. the zero cost feedstock, 2. the increased availability of a spare gasification train, and 3. the opportunity to sell CO_2 for enhanced oil recovery) with an 8% loan rate will significantly reduce the required hydrogen selling price for a 12% ROI to about 1.50 $/Mscf.

Building a larger plant with coproduction of power (similar to that of Subtask 1.3) should allow the advantages of economies of scale primarily by reducing the apportioned cost of the utilities and other OSBL areas that are attributable to the hydrogen plant. Also, a multiple train plant would provide a more reliable source of some hydrogen (although not at the rated capacity) since it is unlikely that the entire plant would be shut down at the same time. This should make the cost of hydrogen competitive with that from steam methane reforming of natural gas.

The Fischer-Tropsch process to clean fuels and chemicals.

Mark E. Dry
University of Cape Town.

For close on fifty years Sasol has been producing a variety of fuels and chemicals from synthesis gas produced by coal gasification. Two types of Fischer-Tropsch (FT) operations are used to convert the synthesis gas to the desired products, namely, the low temperature (LTFT) and the high temperature (HTFT) process.

The LTFT process is carried out in either multitubular, or preferably, in slurry bed reactors. The catalyst used can be either cobalt or iron based. At similar conditions cobalt based catalysts are capable of higher conversions. The main product is high value linear paraffin wax, which is used in a variety of applications. Alternatively the wax can be hydrocracked under mild conditions to produce a high yield of high quality diesel which combined with the straight-run FT diesel yields a fuel virtually free of aromatic and ring compounds and having a cetane number of about 70.

The HTFT process is carried out in fluidised bed reactors. The straight-run gasoline contains less than one percent benzene, the total aromatic content being only about 5%. The olefin content is about 70%. In order to increase the octane rating to the required level the naphtha is hydrotreated, the C_7+ cut is reformed and the C_5/C_6 cut can be hydroisomerised. Extracting the highly valuable linear olefins as such or by converting them to valuable linear alcohols and then removing these naturally increases the octane rating of the remaining naphtha and hence less severe upgrading is required to meet the octane number specification.

Fischer-Tropsch Catalysts Supported on Sol-Gel Derived Silica

Brian C. Dunn, Paul Cole, Daniel J. Covington, Emily C. Heider, Jennifer Gasser, Edward M. Eyring, Henk L. C. Meuzelaar, and Ronald J. Pugmire

Departments of Chemistry and Chemical and Fuels Engineering
University of Utah
Salt Lake City, UT 84112

Introduction

Fischer-Tropsch synthesis has traditionally employed heterogeneous catalysts supported on metal oxides such as alumina, silica, or titania.[1] The metallic catalyst is typically loaded onto the support using either an impregnation or coprecipitation technique. Neither of these methods allows for strict control over the support properties which can play a crucial role in the Fischer-Tropsch synthesis.[2] Employing the sol-gel method to prepare amorphous silica from the polycondensation and hydrolysis of a suitable precursor, such as tetramethoxysilane, allows for control and manipulation of bulk support properties such as density, strength, pore diameter, and pore volume.[3] The properties of the silica are determined by molar ratio of reactants, time required for gelation, aging period, drying technique, and drying time. Silica prepared by the sol-gel route can range from relatively dense, microporous xerogel to non-dense, mesoporous aerogel and can be controlled at all points in this continuum.

Heterogeneous catalysts prepared using sol-gel derived supports include platinum,[4] iron,[5] silver,[6] gold,[7] cobalt,[8] and palladium.[9] Fischer-Tropsch synthesis is typically performed utilizing either a cobalt or iron-based catalyst and the support properties greatly influence the product distribution by influencing heat and mass transport near the active metal catalyst particles. Sol-gel derived silica provides a unique opportunity for controlling the support properties and thus influencing the product distribution.

Experimental

Catalyst Preparation. The catalysts employed for Fischer-Tropsch synthesis were prepared by the sol-gel method. Water, methanol, and tetramethoxysilane (TMOS) were combined in a 16:4:1 molar ratio. An appropriate metal salt ($Co(NO_3)_2$, $Fe(NO_3)_2$, $RuCl_2$) was dissolved in the water to yield 5-30% by weight of the final material. The mixture was sealed in glass vials and allowed to gel and age for 14 days. The xerogels were obtained by allowing the methanol and water to evaporate under ambient conditions over a period of 14 days. The xerogels were then crushed, reduced by heating in a stream of hydrogen, and sieved for size.

Fischer-Tropsch Synthesis. The reaction between H_2 and CO was carried out in a continuous flow reactor, 6 inches by 0.25 inch in diameter. Approximately 2 g of catalyst was used for each trial and discarded after the experiment. The flow of the reactants and carrier gas were maintained with appropriate mass-flow controllers (MKS Model 1179A) and the entire reactor system, including the transfer line, was heated to ensure that no condensation of the reaction products occurred. Routine measurement of reaction products was performed with online GC monitoring and reaction product identification was performed by condensing into cold *n*-octane, and analyzing by off-line GC/MS.

Results and Discussion

Catalyst Characterization. One of the catalysts was examined to determine some of the porosity properties of the sol-gel derived silica and the nature of the active metal catalyst, cobalt. **Table 1** lists the specific surface areas of three different xerogel catalysts: unreduced $Co(NO_3)_2$, metallic cobalt, and a mixture of metallic cobalt and iron.

Table 1. BET Surface Areas

Catalyst	Surface Area (m^2 / g)
$Co(NO_3)_2$	134
Co^0	338
Co^0 / Fe^0	245

As can be seen from **Table 1**, the xerogel-based catalysts possessed a significant amount of surface area. The apparent increase in surface area upon reduction of the catalyst is most likely caused by expulsion of water and methanol, produced in the sol-gel reaction, from the pores of the catalyst when the catalyst was heated in a stream of hydrogen.

During reduction with hydrogen, the catalyst noticeably changed color from red (hydrated $Co(NO_3)_2$) to black and became ferromagnetic. This visual indication of reduction was confirmed by XRD analysis which indicated the presence of metallic cobalt and cobalt oxide. The XRD analysis also showed that the cobalt particles were about 6 nm in diameter.

Fischer-Tropsch Synthesis. Four different catalysts were employed to convert a mixture of hydrogen and carbon monoxide into higher hydrocarbons. Initial experiments were conducted using the cobalt xerogel and condensing the reaction products in cold *n*-octane. **Figure 1** shows an offline GC/MS chromatogram of the product mixture. Hydrocarbons lower than C_9 were not observable due to their volatility and the presence of the octane. The apparent product distribution is centered around C_{15} and the heaviest hydrocarbon observed was C_{32}. Each hydrocarbon consisted primarily of the *n*-alkane, but significant amounts of single unsaturated hydrocarbons were seen for the lower hydrocarbons (C_9 – C_{15})

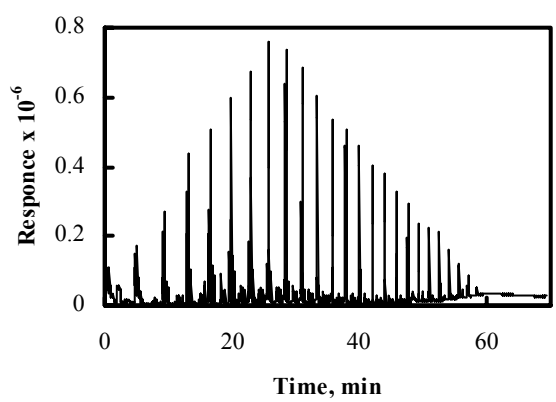

Figure 1. GC/MS chromatogram of Fischer-Tropsch product using 25% by weight cobalt xerogel catalyst. Reaction temperature was 225 °C and pressure was 30 psi.

Routine experiments were performed with online GC/FID detection of reaction products. **Figure 2** shows a chromatogram of the reaction products using an identical catalyst as that used in **Figure 1**. The lowest hydrocarbons, C_1 through C_4, are not well resolved with C_5 appearing at about 7 minutes. The heaviest hydrocarbon observed with online monitoring was C_{18} rather than C_{32} as seen previously. Either the heavy products were not present in

high enough concentration for detection or the products were condensing somewhere in the reactor system prior to GC analysis.

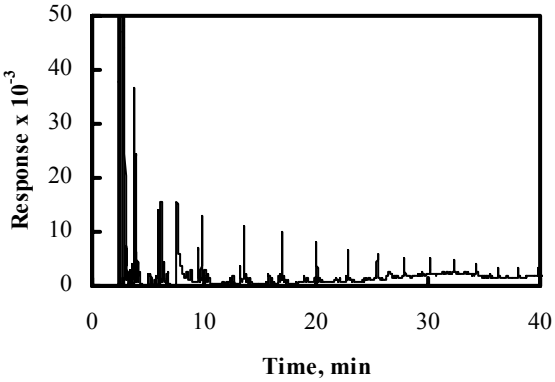

Figure 2. Online chromatogram of Fischer-Tropsch product using 25% by weight cobalt xerogel catalyst. Reaction temperature was 225 ^{o}C and pressure was 30 psi.

A mixed cobalt/iron catalyst was used in the reactor and the product distribution is shown in **Figure 3**. The lower hydrocarbons can be seen prior to five minutes and appear to be somewhat resolved. Only a trace of heavy hydrocarbons was produced using this catalyst. Overall, the mixed cobalt/iron catalyst is much less active compared to the catalyst that contains only cobalt, although this may simply be caused by the different loadings of the cobalt.

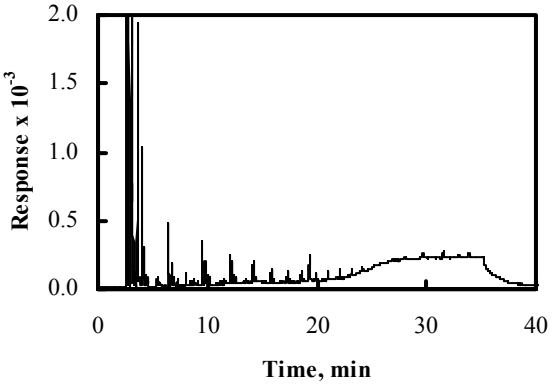

Figure 3. Online chromatogram of Fischer-Tropsch product using 15% by weight cobalt and 15% by weight iron xerogel catalyst. Reaction temperature was 225 ^{o}C and pressure was 30 psi.

Nickel and cobalt were combined during the sol-gel preparation of another catalyst and the Fischer-Tropsch product distribution appears in **Figure 4**. Very small amounts of hydrocarbon products were detected using this catalyst. However, the catalyst appears to be more selective for the heaviest hydrocarbons compared with either the cobalt only or cobalt / iron catalyst.

All of the catalysts have high selectivity towards the lower hydrocarbons, C_1 through C_4, which is undesirable. It should be possible to alter the reaction conditions (temperature, pressure, reactant flow rate, residence time) to decrease the selectivity for the lower hydrocarbons and increase the selectivity for higher hydrocarbons. It is possible that these sol-gel silica supported catalysts may be more sensitive to reaction conditions than traditional catalysts. The cobalt likely resides in pores of the amorphous silica rather than simply on the outside surface of the support. This should provide for mass and heat transfer properties which are different than traditional catalysts.

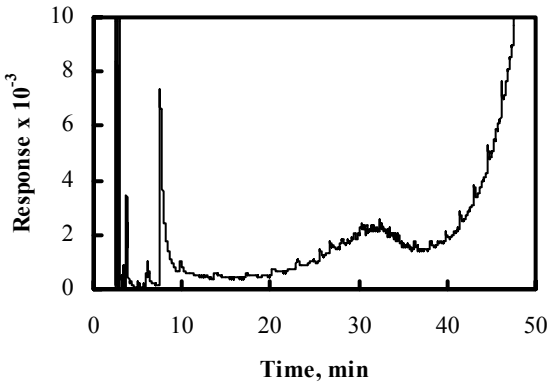

Figure 4. Online chromatogram of Fischer-Tropsch product using 15% by weight cobalt and 15% by weight nickel xerogel catalyst. Reaction temperature was 225 ^{o}C and pressure was 30 psi.

Additional experiments are currently underway to more fully characterize the support properties and to prepare a series of catalysts with a range of pore sizes and volumes to determine their effects on the Fischer-Tropsch synthesis.

Conclusions

The sol-gel technique for preparing amorphous silica is capable of incorporating metal salts into the structure of the support and, after reduction, the catalysts are active for Fischer-Tropsch synthesis. The unique nature of the sol-gel chemistry should allow for strict control and manipulation of the support properties in order to tune the catalyst for a desired product distribution.

Acknowledgement. The authors would like to thank Dr. M. Seehra and Dr. A. Punnoose of West Virginia University for performing the XRD analysis and Dr. R. Cutler and Lyle Miller of Ceramatec, Inc. for performing the BET analysis. The financial support of the Consortium for Fossil Fuel Science (CFFS) is gratefully acknowledged.

References

(1) Jacobs, G.; Das, T. K.; Zhang, Y.; Li, J.; Racoillet, G.; Davis, B. H. *Appl. Cat. A* **2002**, *233*, 263-281.
(2) Li, S.; Krishnamoorthy, S.; Li, A.; Meitzner, G. D.; Iglesia, E. *J. of Catalysis* **2002**, *206*, 202-217.
(3) Bryans, T. R.; Brawner, V. L.; Quitevis, E. L. *J. Sol-Gel Sci. Tech.* **2000**, *17*, 211-217.
(4) Anderson, M. L.; Stroud, R. M.; Rolison, D. R. *Nano Letters* **2002**, *2*, 235-240.
(5) Leventis, N.; Elder, I. A.; Long, G. J.; Rolison, D. R. *Nano Letters* **2002**, *2*, 63-67.
(6) Morley, K. S.; Marr, P. C.; Webb, P. B.; Berry, A. R.; Allison, F. J.; Moldovan, G.; Brown, P. D.; Howdle, S. M. *J. Mater. Chem.* **2002**, *12*, 1898-1905.
(7) Pietron, J. J.; Stroud, R. M.; Rolison, D. R. *Nano Letters* **2002**, *2*, 545-549.
(8) Bae, D. S.; Kim, D. J.; Han, K. S.; Adair, J. H. *J. Ceram. Proc. Res.* **2002**, *3*, 38-40.
(9) Tanaka, S.; Mizukami, F.; Niwa, S.; Toba, M.; Maeda, K.; Shimada, H.; Kunimori, K. *Appl. Cat. A* **2002**, *229*, 165-174.

HYDRODESULFURIZATION OF THIOPHENE OVER CARBIDED MOLYBDENA-ALUMINA CATALYSTS

Masatoshi Nagai,[1] Hiroyuki Tominaga, Ryouko Abe, and Shinzo Omi

Graduate School of Bio-applications and Systems Engineering
Tokyo University of Agriculture and Technology
2-24 Nakamachi, Koganei, Tokyo 184-8588, Japan

Introduction

Molybdenum carbides supported on alumina and unsupported carbides with high surface area are recently being studied in order to prepare catalysts with high performance for hydrodesulfurization (1–3) and hydrodenitrogenation. McCrea *et al*. (1) studied the activities of Mo nitride, carbide, and sulfide supported on alumina in thiophene HDS and compared the order of the catalytic activity. The HDS activity depended on a high site density measured by CO adsorption as follows: β-Mo_2C > γ-Mo_2N > MoS_2. Miyao *et al*. (4) studied the relationship between the surface properties of carbided Mo/Al_2O_3 and the activity in carbazole HDN and reported that the Mo/Al_2O_3 carbided at 973 K was about 2.2 times more active than the reduced catalyst (per catalyst weight). Thus, Mo carbide was the most active catalyst of the three types of molybdenum catalysts during the hydrogenolysis reactions. However, few studies have been made at a higher activity of carbided Mo/Al_2O_3 per g-catalyst, then compared to sulfided Mo/Al_2O_3 and $CoMo/Al_2O_3$ catalysts for the HDS reaction. Furthermore, some of the sulfur removed during the HDS reaction accumulated on the surface to form a thin layer of sulfided molybdenum on the Mo carbide catalysts after 24 h (1). Little attention has been paid on how sulfur is adsorbed and changes the surface properties and activities during the HDS reaction, or on the behavior of the molybdenum and carbidic carbons of the Mo carbide catalysts. In this study, the activity of the carbided Mo/Al_2O_3 catalysts with various Mo loadings was studied during the HDS of thiophene at atmospheric pressure and compared to the sulfided Mo/Al_2O_3 and commercial CoMo catalysts. The relationship between the HDS activity and the atomic ratios of the molybdenum, carbidic carbon, and sulfur to aluminum and Mo oxidation states on the surface using X-ray photoelectron spectroscopy (XPS) is studied during the HDS reaction. The active species of the carbided Mo/Al_2O_3 during thiophene HDS are also discussed.

Experimental

Hydrogen was dried by passing it through a Deoxo unit (SUPELCO Co. Oxysorb) and a Linde 13X molecular sieve trap. 20% CH_4/H_2 and thiophene were used without further purification. 1.0–18.7 wt% MoO_3/Al_2O_3 were prepared as follows: γ-alumina (CSJ Reference catalyst, AL-04) was added to an aqueous solution of ammonium paramolybdate and the solution was boiled while being stirred. The MoO_3/Al_2O_3 sample was dried at 473 K for 24 h and calcined in air at 823 K for 3 h. After the MoO_3/Al_2O_3 catalyst (0.2 g) treated with 20% CH_4/H_2 from 573 to 973 K at a rate of 0.0167 K s^{-1} and held at the final temperature for 3 h. After the carburizing treatment, the catalyst was cooled to room temperature in flowing 20%CH_4/H_2 for surface property measurements or cooled to 623 K for HDS activity measurement. For the sulfided catalysts, $CoMo/Al_2O_3$ (Kejenefine124) and fresh and carbided 11.6 wt% MoO_3/Al_2O_3 were sulfided at 623 K for 3 h in flowing 10% H_2S/H_2 and they were purged with helium at 623 K. After the sulfiding treatment, the catalyst provided activity measurement at 623 K or the XPS measurement after it was cooled to room temperature in flowing helium. The rate of the HDS of thiophene over the carbided catalyst was measured at 623 K using a flow microreactor system at atmospheric pressure. A 0.134 mol% thiophene in hydrogen mixture was introduced into the microreactor at 3.0 L h^{-1}. The reaction products were quantitatively analyzed using an FID gas chromatograph with a 2% Silicone DC-550 column for thiophene and tetrahydrothiophene at 393 K and a VZ-8 column for C4 hydrocarbon products.

The surface properties of the Mo/Al_2O_3 catalysts were analyzed before the reaction or at 0.167, 1, 3, and 8 h after the start by interrupting the reaction. The reactor was cooled to room temperature, both ends of the reactor closed, and then transferred to a glovebox which was pumped and backfilled with argon three times. The catalysts were removed from the reactor in argon and introduced to the XPS prechamber without exposure to air. The specific surface area (BET) of the catalysts was measured by nitrogen adsorption using a BET apparatus after the catalysts were evacuated at 473 K and 0.1 Pa for 2 h. The Mo loading (wt%) was measured using an atomic absorption spectroscope and represented as MoO_3-gram per sample-g. The quantity of chemisorbed CO on the catalysts was determined by the volumetric analyzer (Omnisorp 100CX) during evacuation. XPS spectra were obtained using a Shimadzu ESCA 3200 spectrometer with monochromatic MgK_α exciting radiation (1253.6 eV, 8 kV, 30 mA). The binding energies for the samples were referenced to Al 2p at 74.7±0.2 eV. The analysis was done by argon etching using a nonlinear square method with a 100% Gaussian function, according to previously published XPS studies (5,6).

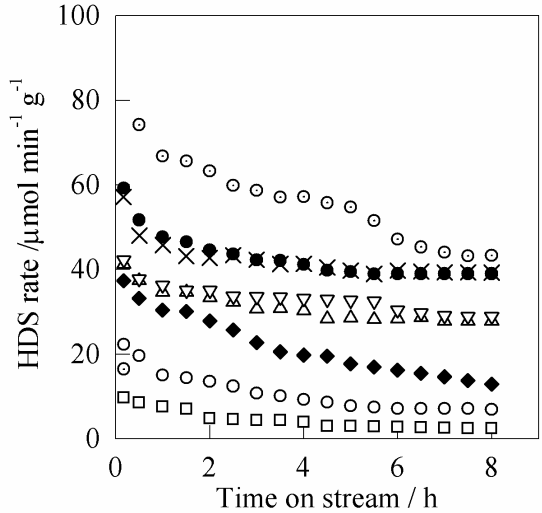

Figure 1. The HDS of thiophene over various Mo/Al_2O_3 catalysts with time on stream at 573 K and a total pressure of 10.1 MPa. (□) 3.6 wt%, (○) 4.8 wt%, (△) 6.6 wt%, (▽) 8.5 wt%, (●) 11.6 wt%, and (✕) 18.7 wt% Mo/Al_2O_3 carbided at 973 K. (◆) 11.6% Mo/Al_2O_3 and (⊙) $CoMo/Al_2O_3$ sulfided at 623 K.

Results and Discussion

HDS Activity of Carbided Mo/Al_2O_3. The rates of the HDS of thiophene over the 1.0–18.7 wt% Mo/Al_2O_3 catalysts carbided at 973 K with time on stream at 623 K and atmospheric pressure are shown in Fig. 1. The HDS rates for the 11.6 and 18.7 wt% Mo/Al_2O_3 catalysts were the highest of any carbided catalysts. As far as the same 11.6 wt% Mo loading was concerned, the HDS rate of the

carbided catalyst was 3 times higher than that of the sulfided catalyst. Although the HDS rate of the sulfided $CoMo/Al_2O_3$ catalyst was the highest of all the catalysts, it was decreased more rapidly than the carbided catalysts and then reached to a level similar to the carbided 11.6 and 18.7 wt% Mo/Al_2O_3 catalysts at 8 h on stream. The carburizing of the sulfided 11.6 wt% Mo/Al_2O_3 (sulfided/carbided) catalyst at 973 K improved the HDS activity of the sulfided catalyst. McCrea *et al.* (1) reported that the HDS rate (based on a weight) for a series of passivated 1.5–20 wt% Mo/Al_2O_3 catalyst carbided at 950 K was 1.5 times higher than that for a sulfided Mo/Al_2O_3 at atmospheric pressure. Moreover, the reaction products for thiophene HDS at 623 K were primarily *n*-butane and butenes with a trace of tetrahydrothiophene.

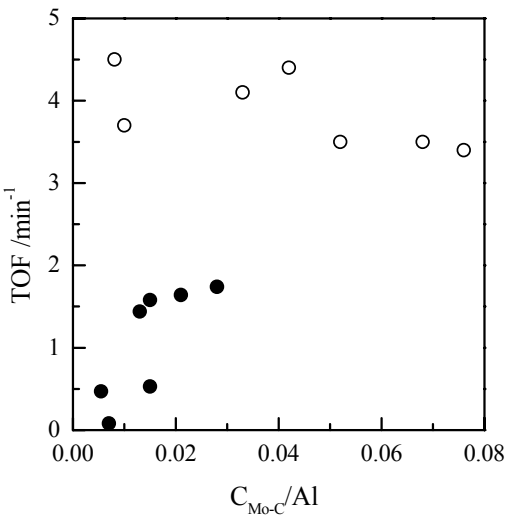

Figure 2. The relationship between TOFs and C_{Mo-C}/Al ratio of the carbided 1.0-18.7% Mo/Al_2O_3 (○) before the reaction and (●) at 8 h after the start.

Change in Surface Properties by XPS Analysis. X-ray photoelectron spectroscopy was used to provide information about the surface compositions of molybdenum, carbidic and carboneous carbons, and sulfur of the carbided and sulfided catalysts. The Mo/Al ratios were proportional up to an 11.6 wt% Mo loading, before raction. Mo carbides were dispersed on the surface except for the 18.7 wt% Mo catalyst that was agglomerated. Large Mo carbide particles were generated and agglomerated during the carburizing treatment but small Mo carbides were more likely dispersed during reaction, compared to those before the reaction. The C_{Mo-C}/Al ratio decreased 0.25-fold at 8 h after the start for more than 4.8 wt% Mo loadings. The C_{Mo-C}/Mo ratio was constant at 0.76±0.04 for the carbided catalysts in the entire range of Mo loading, indicating that the carbided catalysts before the reaction contained a similar type of molybdenum carbide species such as $Mo_2C_{1.5}$ or Mo oxycarbide. In combination of the TOF with the C_{Mo-C}/Al ratio (Fig. 2), the TOFs for the carbided catalysts were almost constant for various C_{Mo-C}/Al ratios before the reaction, while the TOFs and C_{Mo-C}/Al ratios decreased at 8 h after the start. As a result, the TOF of the catalysts with the 1.0–4.8 wt% Mo loadings were much lower than the higher Mo loadings catalysts. Two types of carbides of the carbided Mo/Al_2O_3 catalysts are present on the surface: Mo carbide and oxycarbide which interacted with alumina.

Molybdenum Oxidation States and Active Species. The distribution of the Mo oxidation states of the carbided 1.0–18.7 wt% Mo/Al_2O_3 catalysts, Mo^{3+} was mainly distributed at 26.6–39.3% together with Mo^{4+} and Mo^{5+} ions before the reaction. Mo^0 and Mo^{2+} were distributed at only a small percentage. In a previous paper (6), the carburization of 100% MoO_3 exhibited the total distribution of Mo^0 and Mo^{2+} at 80% in fresh carbided catalysts. As a result, higher values of the Mo oxidation state in the carbided Mo/Al_2O_3 catalysts are due to the interaction of molybdenum and alumina that are resistant to carbide. Furthermore, because the carbided 11.6 wt% Mo/Al_2O_3 was sulfided and had a S/Mo atomic ratio of more than 0.34 at 0.167 h after the start, the Mo 3d-S 2s envelope for the carbided catalysts during the reaction and the sulfided catalysts were curve-fitted. The Mo^{4+} species was also mainly distributed at 77.4% for the sulfided 11.6 wt% Mo/Al_2O_3 catalysts. This result is in good agreement with the Mo distribution obtained from the deconvolution of the Mo 3d spectra of MoS_2. The Mo^{4+} ion increased at 0.167 h after the start on the basis of the deconvolution of both the carbides and sulfides. Mo^{3+} ion was present on the carbided Mo/Al_2O_3 catalyst before the reaction and turned into Mo^{4+} (Mo sulfide) on the catalyst surface within 0.167 h. The TOF_{8h} (number of thiophene molecules converted per exposed Mo atom per min at 8 h after the start) of the catalysts was linearly correlated with the presence of Mo^{4+} ion. Mo^{3+} on the carbided Mo/Al_2O_3 catalyst might be an active center at short time on stream but turned into Mo^{4+} (Mo sulfide) on the surface as a newer less active center than the Mo carbide, especially from 0.167 h after the start.

Conclusions

The activities of 1.0-18.7 wt% Mo/Al_2O_3 catalysts for thiophene HDS at 623 K and atmospheric pressure was correlated with the results of the XPS measurement. The HDS rates for the 11.6 and 18.7 wt% Mo/Al_2O_3 catalysts were the highest of any carbided catalysts. Concerning the same 11.6 wt% Mo loading, the HDS rate of the carbided catalyst was 3 times higher than that of the sulfided catalyst. Although the HDS of the sulfided $CoMo/Al_2O_3$ catalyst was the highest of all the catalysts, it was more rapidly reduced than the carbided catalysts and decreased to a level similar to the carbided 11.6 and 18.7 wt% Mo/Al_2O_3 catalysts at 8 h on stream. Carburizing of the sulfided 11.6 wt% Mo/Al_2O_3 catalyst at 973 K improved the HDS activity of the sulfided catalyst. The TOF_{8h} of the catalysts was linearly correlated with the presence of the Mo^{4+} ion.

Acknowledgment

This work has been carried out as a research project with a Grant-In-Aid for Scientific Research on Priority Areas from the Ministry of Education, Culture, Sport, and Science, Japan.

References

1. McCrea, K. R., Logan, J. W., Tarbuck, T. L., Heiser, J. L., and Bussell, M. E., *J. Catal.* **171**, 255 (1997).
2. Da Costa, P., Potvin, C., Manoi, J.-M., Lemberton, J.-L., Perot, G., and Djega-Mariadassou, G., *J. Mol. Catal. A* **184**, 323 (2002).
3. Dhandapani, B., Clair, T. St., and Oyama, S. T., *Appl. Catal. A* **168**, 219 (1998).
4. Miyao, T., Oshikawa, K., Omi, S., and Nagai, M., *Stud. Surf. Sci. Catal.* **106**, 255 (1997).
5. Quincy, R. B., Houalla, M., Proctor, A., and Hercules, D. M., *J. Phys. Chem.* **94**, 1520 (1990).
6. Oshikawa, K., Nagai, M., and Omi, S., *J. Phys. Chem.B* **105**, 9124 (2001).

In situ FT-IR spectroscopic studies of sulfur effect on Mo_2C/Al_2O_3 catalyst

*Weicheng Wu, Zili Wu, Can Li**

State Key Laboratory of Catalysis, Dalian Institute of Chemical Physics, Chinese Academy of Sciences, P.O. Box 110, Dalian 116023, China

Introduction

Molybdenum carbide seems to be one of the most promising catalysts because it shows excellent catalytic activity for hydrogen-involved reactions.[1, 2] Especially, they have potential applications in hydrodesulfurization (HDS) [3-9] processes. However, transition metal carbides are found to be sensitive to sulfur species. Aegeter et al.[3] found by IR spectroscopy that Mo_2C/Al_2O_3 became sulfided at HDS temperatures. Their discussions were concentrated on the results of passivated carbide. It is noted that the passivation procedure causes a dramatic change in the carbide surface, i.e., from carbide to oxycarbide. Therefore, it is of significance to study how fresh carbide works under the reaction conditions. Thiophene is a typical representative of sulfur-containing hydrocarbons in hydrotreating reactions, so it is necessary to study the influence of thiophene on the surface property of carbide catalysts in order to get insight into the sulfur effect on the catalytic performance. In this work, we use *in situ* IR spectroscopy to characterise the surface nature of fresh Mo_2C/Al_2O_3 catalyst pretreated by thiophene/H_2. CO was employed to probe the sulfur effect of the catalyst surface.

Experimental

A MoO_3/Al_2O_3 sample with 10 wt % Mo was prepared by incipient impregnation method, a γ-Al_2O_3 (Degussa, S_{BET} = 108 m^2 g^{-1}) impregnating with an aqueous solution of ammonium heptamolybdate, followed by a drying at 397 K overnight and calcination at 773 K for 4 h. The MoO_3/Al_2O_3 sample was pressed into a self-supporting wafer with a weight of approximately 15 mg/cm^2. The wafer was placed in a quartz IR cell equipped with CaF_2 windows, in which *in situ* carburization could be performed, and then carburized in a flowing 20% CH_4/H_2 mixture. The temperature was increased from room temperature to 573 K in 30 minutes and from 573 to 1033 K in 460 minutes, and then the temperature was maintained at 1033 K for 60 minutes. The carburized sample was cooled down to room temperature in flowing 20% CH_4/H_2 mixture.

The sample in the IR cell was treated with a thiophene/H_2 mixture (5/100 Torr) for 60 min at different temperatures (298, 373, 473, 573, 673 and 773 K) and detected by FT-IR spectroscopy, then evacuated to 10^{-5} Torr at 773 K for 60 min. Then the sample was cooled to RT and 10 Torr CO was introduced. The system was evacuated to 10^{-3} Torr in order that we could get the spectrum of chemisorbed CO.

All IR spectra were collected at room temperature on a Fourier transform infrared spectrometer (Nicolet Impect 410) with a resolution of 4 cm^{-1} and 64 scans in the region 4000-1000 cm^{-1}.

Results and Discussion

To investigate the sulfiding effect on Mo_2C/Al_2O_3 catalyst under different conditions, the catalyst was treated with a thiophene/H_2 mixture (5/100 Torr) at given temperatures for 60 min and then its surface nature was probed by CO adsorption at RT. Figure 1 exhibits the IR spectra of CO adsorbed on a fresh Mo_2C/Al_2O_3 sample and that sample treated with a thiophene/H_2 mixture. CO adsorbed on a fresh Mo_2C/Al_2O_3 sample gives two *characteristic* IR bands at 2055 and 2197 cm^{-1}. The detailed discussion will be done elsewhere.[10] The intensity of the 2055-cm^{-1} band decreased dramatically. The 2197-cm^{-1} band disappeared and a strong band at 2100 cm^{-1} was observed when fresh sample was treated with the thiophene/H_2 mixture at 298 K. With the elevated treatment temperature, the intensity of the 2055-cm^{-1} decreased gradually and the 2100-cm^{-1} band become dominant. The band at 2100 cm^{-1} can be assigned to adsorbed CO on sulfide catalyst.[5, 11, 12] The results strongly suggest that the surface of the fresh Mo_2C/Al_2O_3 catalyst is significantly changed when treated with the thiophene/H_2 mixture above room temperature. The surface of the fresh Mo_2C/Al_2O_3 catalyst was partially sulfided.

The changes in the thiophene itself were also detected when the fresh Mo_2C/Al_2O_3 catalyst was treated with a thiophene/H_2 mixture at different temperatures (Figure 2). Upon exposure of a fresh Mo_2C/Al_2O_3 catalyst to a mixture of 5 Torr of thiophene and 100 Torr of H_2 at 473 K, the IR spectrum in the ν_{CH} region contains absorbance features at 2958, 2933, and 2879 cm^{-1}, and these are assigned to thiophene hydrodesulfurized on the catalyst surface.[13, 14] When treated at 673 K, a series of new bands at 3037, 3016, 2976, 2966, 2947, and 2922 cm^{-1} was observed. The two bands at 3037 and 3016 cm^{-1}, which can be assigned to the formation of alkene species, grow in intensity with the increase of treatment temperature. The process of hydrodesulfurization produced the bands at 2976, 2966, 2958, 2947, 2933, 2922, and 2879 cm^{-1}, which can be due to the attribution of saturated alkanes.[13, 14] These results indicated that when the fresh Mo_2C/Al_2O_3 catalyst was treated with a thiophene/H_2 mixture above 473 K, one or more hydrogenated species, exhibiting IR bands in the region 2870-2980 cm^{-1}, are produced. When the treatment temperature was increased to 673 K, some alkene species were formed. These species may be due to the decomposition of thiophene.

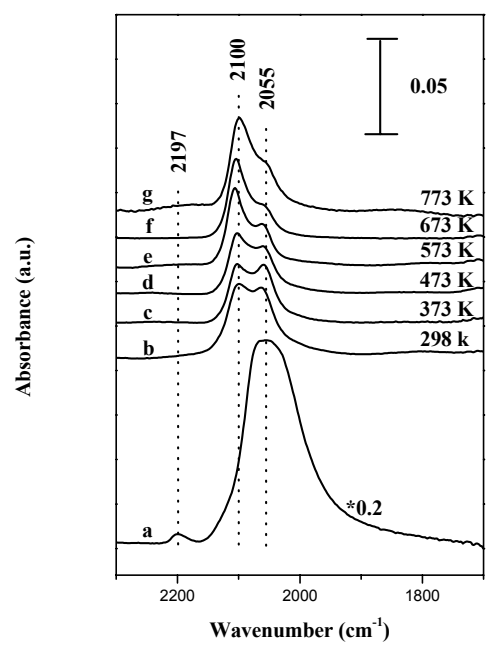

Figure 1. IR spectra of CO adsorbed at RT (a) on fresh Mo_2C/Al_2O_3 catalyst, and on the same catalyst after it was treated with a thiophene/H_2 (5/100 Torr) mixture at (b) 298 K, (c) 373 k, (d) 473 K, (e) 573 K, (f) 673 K, and (g) 773 K for 60 min.

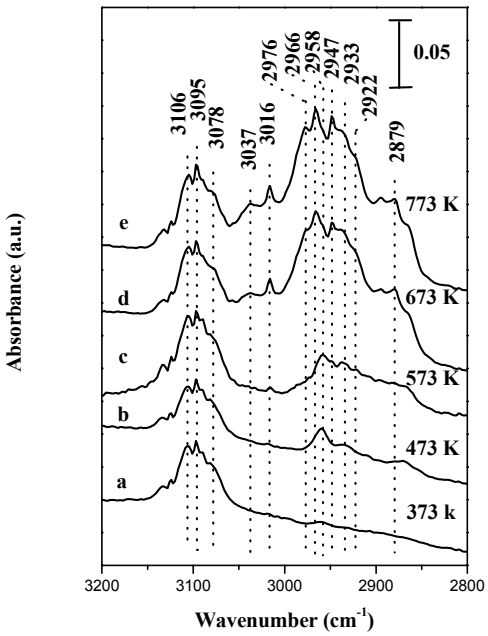

Figure 2. IR spectra in the ν_{CH} region for the fresh Mo_2C/Al_2O_3 catalyst treated with a thiophene/H_2 (5/100 Torr) mixture at (a) 373 k, (b) 473 K, (c) 573 K, (d) 673 K, (e) 773 K for 60 min.

Conclusions

The influence of thiophene on the surface state of the fresh Mo_2C/Al_2O_3 catalyst in the presence of H_2 has been studied by FT-IR spectroscopy combined with CO adsorption. The IR spectra of adsorbed CO suggest that thiophene can be easily hydrodesulfurized in the presence of H_2 on fresh Mo_2C/Al_2O_3 catalyst at temperatures as low as 473 K, at the expense of the sulfidation of the carbide catalyst.

Acknowledgement. This work was supported by the State Key Project of the Ministry of Science and Technology of China (Grant No. G2000048003 & G1999022407) are appreciated.

References

(1) Oyama, S. T. *Catal. Today* **1992**, 15, 179.
(2) Chen, J. G. *Chem. Rev.* **1996**, 96, 1477.
(3) Lee, J. S.; Boudart, M. *Appl. Catal.* **1985**, 19, 207.
(4) Sajkowski, D. J.; Oyama, S. T. *Appl. Catal. A.* **1996**, 134, 339.
(5) Aegerter, P. A.; Quigley, W. W. C.; Simpson, G. J.; Ziegler, D. D.; Logan, J. W.; McCrea, K. R.; Glazier, S.; Bussell, M. E. *J. Catal.* **1996**, 164, 109.
(6) McCrea, K. R.; Logan, J. W.; Tarbuck, T. L.; Heiser, J. L.; Bussell, M. E. *J. Catal.* **1996**, 171, 255.
(7) Dhandapani, B.; Clair, T St.; Oyama, S. T. *Appl. Catal. A.* **1998**, 168, 219.
(8) Li, S.; Lee, J. S. *J. Catal.* **1998**, 178, 119.
(9) Costa, P. Da.; Potvin, C.; Manoli, J.-M.; Lemberton, J.-L.; Pérot, G.; Djéga-Mariadassou, G. *J. Mol. Cata. A: Chem.* **2002**, 184, 323.
(10) Manuscript in preparation.
(11) Müller, B.; Van Langeveld, A. D.; Moulijn, J. A.; Knözinger, H. *J. Phys. Chem.*, **1993**, 97, 9028.
(12) Mills, P.; Phillips, D. C.; Woodruff, B. P.; Main, R.; Bussell, M. E. *J. Phys. Chem.*, **2000**, 104, 3237.
(13) Tarbuck, T. L.; McCrea, K. R.; Logan, J. W.; Heiser, J. L.; Bussell, M. E. *J. Phys. Chem.*, **1998**, 102, 7845.
(14) Wu, Z.; Chu, Y.; Yang, S.; Wei, Z.; Li, C.; Xin, Q. *J. Catal.* **2000**, 194, 23.

CLEAN AND EFFICIENT COAL BASED ELECTRIC POWER GENERATION

Janos M. Beér

Department of Chemical Engineering
Massachusetts Institute of Technology
77 Massachusetts Ave
Cambridge, MA.,02139 USA

Background

The provision of electric power is one of the prerequisites of prosperity; there is strong correlation between electric power generating capacity and per capita GDP. Because of the large coal reserves in the major developing countries such as China, India and Indonesia, where most of the new power generating plants will be installed, it can be expected that coal will remain the dominant source of power generation world wide, at least during the first half of this century. According to US Energy Information Administration data for 1999,[1] of the around 800 GW electric power generating parks in the USA, 54% are fueled by coal, 16% by natural gas (increasing to an estimated 36% by 2020), and about 1% by oil. The rest are by nuclear power (18%), hydro power (9%), and by renewable solar, wind or biomass (2%). Across the world economic indicators signal continued growth and increased electricity demand. 1200 GW of new capacity is projected during the next fifteen years to be added to the world's present electric generating capacity of about 3500 GW. A large proportion of this new capacity will be installed in China, India and Indonesia, and will be coal based. Coal as an energy source has the advantages of broad availability with large reserves in several countries over the world, safe and secure supply, low cost, and economic utilization by mature technologies. The disadvantages are due mainly to combustion generated pollution. Clearly, as coal is going to be used in the future it has to be used cleanly and efficiently, to minimize adverse environmental impact.

Pollutant Emission Control

In the 1970s, applied combustion research has taken a turn from high output, high intensity combustion towards combustion process modifications for reduced pollutant emissions. The combustion generated pollutants of concern are oxides of sulfur, of nitrogen and carbon, and fine organic and inorganic particulates (**Figure 1**).

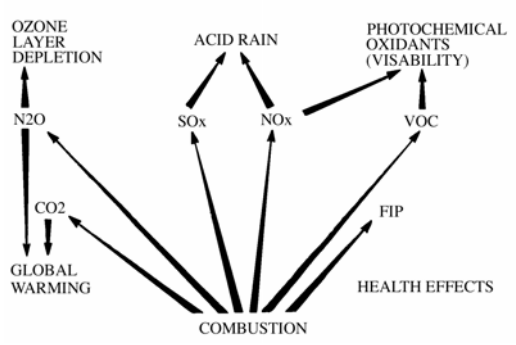

Figure 1. Combustion Generated Pollutant Emissions.

Sulfur in the coal oxidizes during combustion mainly to SO_2, an acid rain precursor. Methods of sulfur capture in the combustion process involve the reactions of additive sorbents such as calcined limestone, CaO, with SO_2 to produce $CaSO_4$, a stable, disposable solid waste. In the high temperature, fuel-lean environment of pulverized coal flames (Tpeak~2000K), however, $CaSO_4$ is unstable; it decomposes, which leaves flue gas desulfurization as the viable option of sulfur capture in PC combustion.

The development of Fluidized Bed Combustion (FBC) for steam generation, in the 1960s[2] provided the opportunity to retain sulfur in the combustion process, because $CaSO_4$, is stable at FBC operating temperatures of 1050-1170K. One of the difficulties of FBC technology is that it does not lend itself well to scale-up to the 700-1000 MW utility size range, mainly because of the large number of feed points it requires to ensure uniform distribution of the coal across the fluidized bed. Conditions for scale up are more favorable in Circulating Fluidized Bed Combustion (CFBC) where the gas velocities are higher and the cross sectional area of the bed for a given thermal performance of the boiler is smaller than for a conventional bubbling fluidized bed. This, on the other hand, helps to reduce the number of coal feed points, which is an operational convenience. Also, smaller size limestone particles can be used which improves the sulfur capture and reduces the Ca/S mole ratio necessary for reaching a target value of sulfur capture, typically 90-95%.

Sulfur dioxides emissions from utility plants in the U.S. have been reduced 40% since 1980 even though electricity production increased by 35% during the same period. This was achieved by switching to coals of lower sulfur content, and by retrofitting some of the existing coal fired power plants with scrubbers. This process will have to continue to satisfy the constraints of the Clean Air Act Amendment 1990 which require further continuing reductions in SO_2 emissions in its Phase 2 implementation that began in the year 2000.

Nitrogen oxides as pollutants deserve special attention because of their wide ranging effects on the environment**,** including contribution to acid rain, reduction of atmospheric visibility, production of tropospheric ozone, and in the case of N_2O, depletion of stratospheric ozone. It is also noteworthy that NOx emissions are well amenable to reduction by combustion process modifications;[3] nitrogen compounds organically bound in the coal and NOx formed in the course of combustion can be converted to molecular nitrogen in fuel-rich pyrolysis reactions. The chemistry of nitrogen compound interconversions in high temperature coal pyrolysis, and of NO formation in fuel lean combustion[4] are the bases of the design protocol for low NOx combustion technology**.**

In coal combustion, where the major part of the NOx is formed by the oxidation of nitrogen compounds organically bound in the coal, the design protocol requires:

i) sequential fuel-rich and fuel-lean combustion zones achieved by staged air or staged fuel supply to the combustion process,
ii) maintenance of high temperature in the fuel–rich flame zones, and
iii) reduced peak flame temperatures in fuel-lean flame regions.

Low NOx combustion technologies include: Over Fire Air (OFA), low NOx Burners (LNB), and NO Reburn.

In the method of **Over Fire Air (OFA)** a fuel-rich pyrolysis zone is created in the lower part of a furnace with only 70-80% of the stoichiometrically required combustion air. For effective conversion of the fuel nitrogen to N_2, high temperature and sufficient residence time for the pyrolysis reactions to run their course (>300ms), are required. The rest of the combustion air needed for complete combustion is then injected in the upper furnace in the form of high velocity air jets (OFA). Fast admixing of the overfire air can reduce the formation of thermal NO during this fuel-lean combustion stage. OFA is capable of reducing NOx by 40-60% from uncontrolled

emission levels. To date, approximately 39 GWe coal fired capacity in the USA has been fitted with OFA.

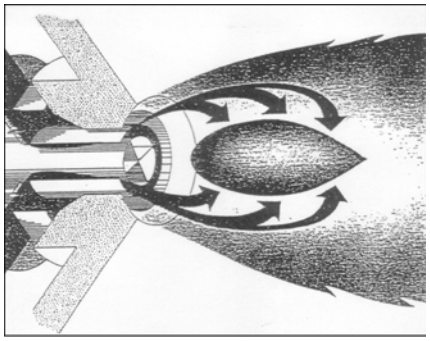

Figure 2. Low NOx Burner Schematic

In **Low NOx Burners (LNB**) the staged admixing of air to the pulverized coal jet occurs by aerodynamic control **(Figure 2)**. Both the fuel and the air are introduced through the same burner. Application of Low NOx Burners can reduce emissions typically by 50%. There are a number of engineering designs that offer retrofits with no changes to pressure parts, and minimal or no changes to wind boxes of the boilers. LNBs represent the most cost effective NOx reduction technology. Since 1995, more than 35 GWe of a total of 325 GW coal fired capacity in the USA has been retrofitted with LNBs.[5]

In **NOx Reburning** the NOx reduction is effected by the injection of a hydrocarbon fuel, about 15-20% of the total heat input, into the fully burned combustion products of the coal flame.[6] NOx can be reduced by about 60% in the slightly fuel rich flame created by the injection of the reburning fuel. Tertiary air has then to be added for completing combustion. The Reburning fuel can be Natural Gas or a High Volatile Bituminous Coal. NO reburning technology has been successfully applied in the USA for cyclone fired boilers,[7] and for wall- and tangentially-fired pulverized coal combustion with dry ash removal.[8] The above mentioned technologies can be effectively combined to increase NOx reductions:

LNBs	30-55%
LNB+OFA	35-70%
Reburning (Nat.gas)	~60%
LNB+Reburning (Nat.gas)	60-70%

The reduction of NOx emission by combustion process modification, a science based technology, has been successfully applied in industry**;** more than 188 GW of electric power generating capacity currently in operation internationally has been fitted by these "primary combustion measures".[5]

Further reductions in NOx emissions can be obtained by the injection of additive ammonia into the combustion products. At high temperature (1060K-1350K) no catalyst is needed in the **Selective Non Catalytic Reduction (SNCR)** process for the removal of up to 40% of the NO formed during coal combustion.

In **Selective Catalytic Reduction (SCR)** the ammonia vapor is injected over a catalyst bed situated at the boiler economizer outlet where the flue gas temperature ranges from 600K to 650K. In the presence of the catalyst, the ammonia chemically reacts with NOx to form water vapor and N_2. The costs of SRC installation are higher than that of the SNCR, but much less ammonia has to be injected, and NOx reductions in excess of 90% can be obtained, depending on the type of coal burned.

Coal based high efficiency power cycles

The efficiency of existing power plants in the U.S. is in the range of 33-36%. Advanced cycles of power generation, some of them mature technologies, others at the stage of demonstration or R&D, hold the promise to generate electricity at significantly increased efficiency (in the range of 50% and above). These technologies ought to be commercially available in the U.S. soon, as it will be necessary to replace older plants beginning 2010. Higher efficiency is the key to the reduction of all of the pollutants and is presently the practical route for mitigating CO_2 emissions. In the near term there are several options for clean and efficient electric power generation, including the following technologies:

- Pulverized coal combustion (PCC) in Supercritical steam boiler in a single Rankine Cycle (4500 PSI/2x 1200F),
- Pressurized Fluidized Bed (PFBC) with Topping Combustor,
- Integrated Gasification Combined Cycle (IGCC) with coal, refinery waste, or biomass as fuel.

Pulverized coal fired supercritical steam boilers have been in use since the 1930s but improvements in materials and increasing demand for higher efficiency are making this system presently the choice of new coal fired utility plant world wide. The increase in efficiency is due to the higher mean temperature of heat addition in the supercritical steam cycle. Comparison of design parameters of a new 300 MW subcritical steam cycle plant with a supercritical plant of the same performance shows an efficiency gain of 1.7% with a fuel saving of 50.000t/y and a CO_2 emission reduction of 137.000t/y for the supercritical unit.[9] The efficiency of a pulverized coal fired steam plant can be increased in small steps to beyond 45% using supercritical steam parameters as shown in **Figure 3**.[10]

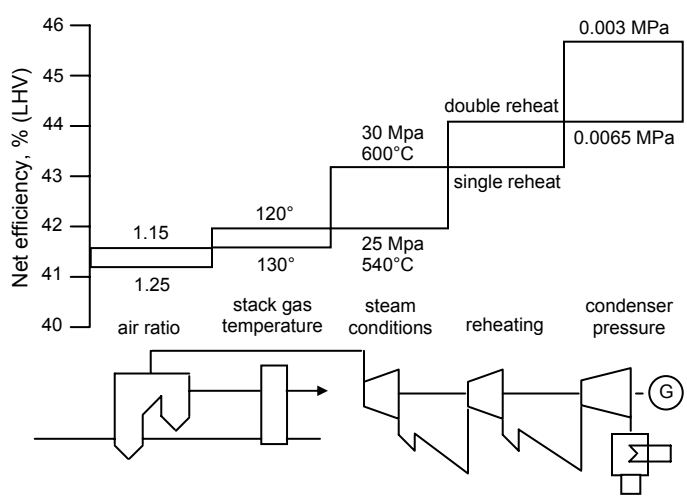

Figure 3. Improving efficiency in P.C. power plants.[10]

Pressurized Fluidized Combustion[11] has grown out of the early development at BCURA in Leatherhead UK in the 70s, the Grimethorp Experimental Facility in the UK in the 80s funded by Germany, the UK, the USA and the IEA; and R&D at the Stal Laval Company in Sweden in preparation of the 70MWe demonstration plant built for the American Electric Power Co. Compared to AFBC, the heat release rate per unit bed area in PFBC is about an order of magnitude higher, and the bed height is 3-4 meters instead of the typical bed height of 1 m in AFBC. Under atmospheric pressure conditions the bed height is limited by the acceptable pressure drop of about 100 mbar across the bed. In the PFBC–GT Cycle the 300 mbar pressure drop represents less than 3% of the total pressure ratio.

A consequence of the increased bed height is a larger carbon inventory in the bed and lower NO emission due to the reduction of the formed NO by solid carbon.[12] The high carbon load does not, however, reduce the emission of the N_2O which is still stable at the relatively low temperature of the PFBC. The temperature in the PFBC is also too low for an efficient gas turbine application. The thermodynamic efficiency of the PFBC Combined Cycle units in operation is about 40%.

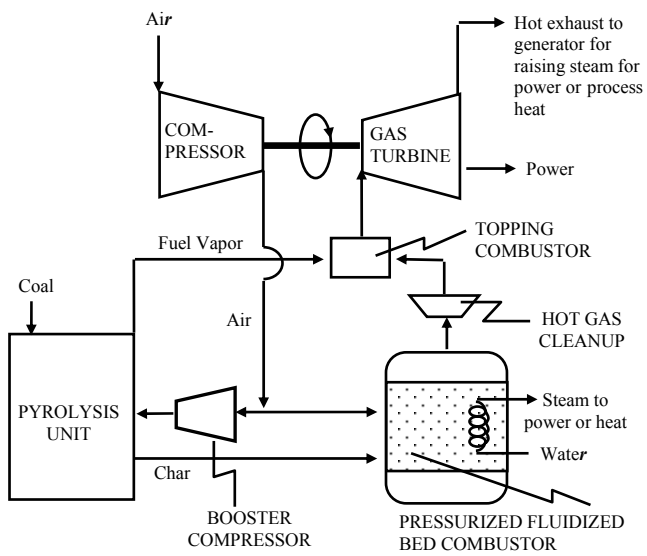

Figure 4. Pressurized Fluidized Bed Combined Cycle.

Further increases in efficiency can be obtained by the use of a **Topping Combustor**. In this latter cycle **(Figure 4)**, coal, usually in the form of coal-water slurry is injected into a pressurized fluidized bed carbonizer where it undergoes partial gasification to produce a low calorific value gas, and char. The char is burned in a Pressurized Fluidized Bed (PFBC) and the flue gas is cleaned of particulates and alkali at high temperature. Sulfur is captured both in the fluidized bed carbonizer and combustor by additive dolomite. The syngas produced in the carbonizer is cleaned of particulates and alkali by hot gas cleanup. It is then mixed with the oxygen rich combustion products of the PFBC in the Topping Combustor where it is burned to raise the temperature at the inlet to the gas turbine to 1623K. This temperature rise increases the cycle efficiency to about 47%. Further improvements in efficiency can be obtained by the application of advanced gas turbine technology, and on the steam side, by supercritical steam parameters with high temperature double reheat. An additional advantage of this cycle is that the N_2O emission is eliminated because the N_2O formed in the Pressurized Fluidized Combustor decomposes at the elevated temperature in the Topping Combustor.[13]

Integrated Gasification Combined Cycle (IGCC)

IGCC involves the total gasification of coal with oxygen and steam to produce a high calorific value fuel gas for combustion in a gas turbine. The gasifier also produces steam for a steam power cycle. The fuel gas has to be cleaned of particulates, alkali and sulfur compounds; the fuel-nitrogen bearing gas is burned in a low NOx combustor. The main features of IGCC are shown in **Figure 5**.[14]

IGCC is the cleanest advanced coal technology. It is also demonstrated to be working with no major operational problems. The future of IGCC depends on whether it will be possible to reduce its first cost and to increase its cycle efficiency. The cost is presently high, mainly because of the oxygen plant necessary for the oxygen blown gasifier and because of the less than complete integration of the various subsystems such as the gasifier air separation system, fuel gas cooler and cleanup, gas turbine and steam plants.

Existing IGCC demonstration plants in the USA have design efficiencies of 40%, but two more recently commissioned European IGCC demonstration plants, the one in Buggenum in the Netherlands, and the other, the Puertollano plant in Spain, both of which began operation in 1993, have higher design efficiencies of 43% and 45%, respectively. The higher cycle efficiencies are due to improved gas turbine and steam plant efficiencies and better sub-system integration. An example of such an improved sub system integration

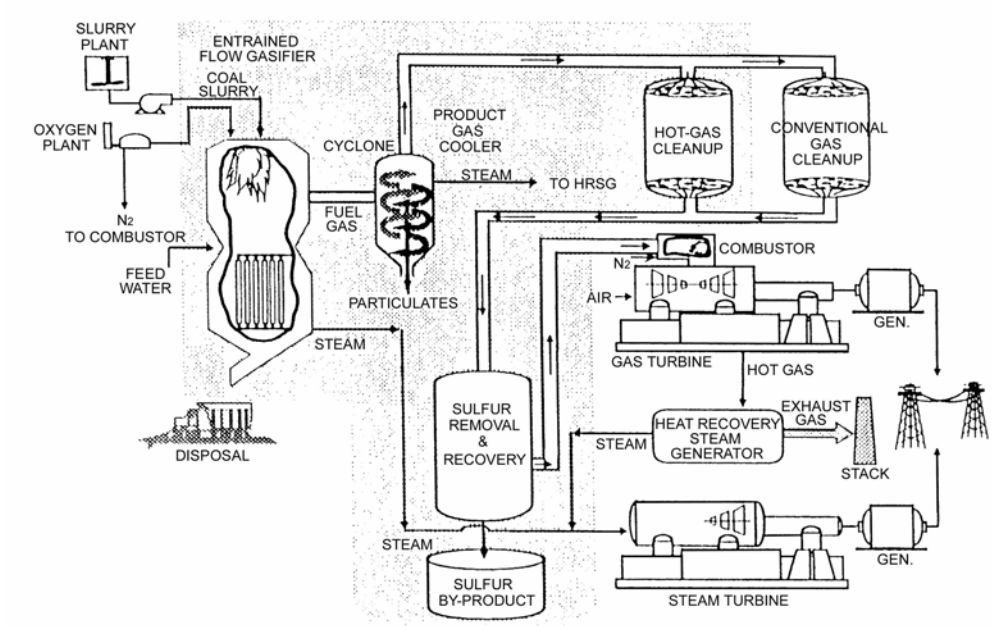

Figure 5. Integrated gasification combined cycle schematic.

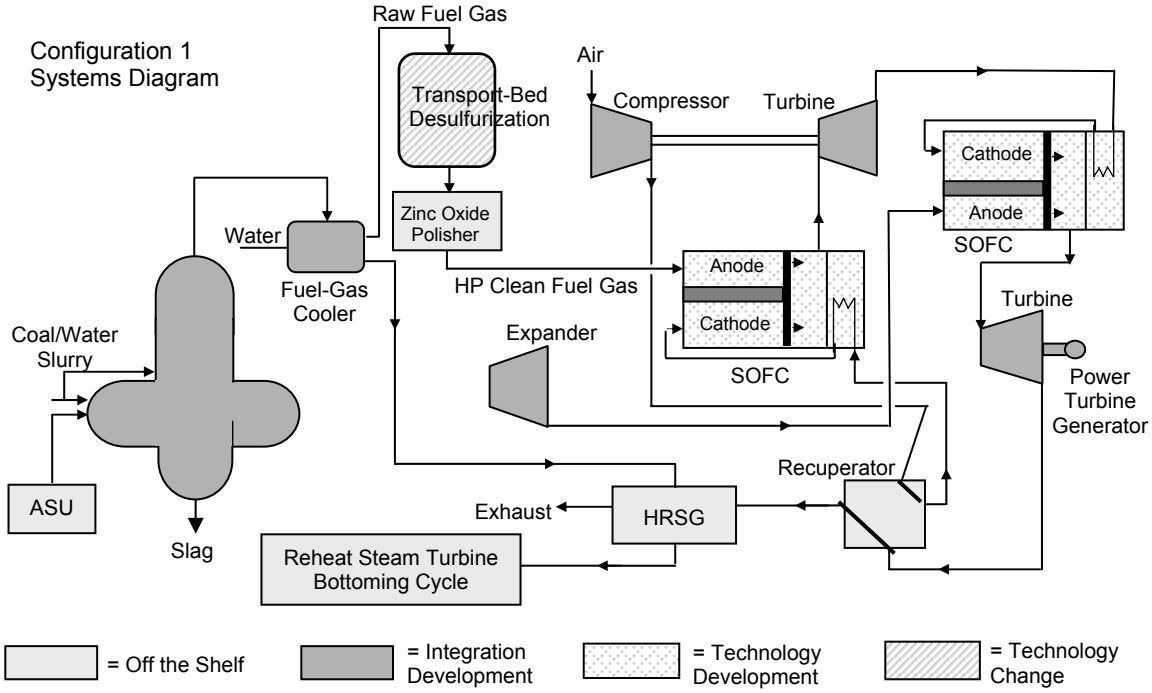

Figure 6. Vision 21 fuel cell / gas turbine cycle.

occurs at the boundary of the oxygen blown gasifier and the gas turbine combustor. The air separation unit produces oxygen for the gasifier in the Portollano plant at 13 bar pressure. The nitrogen, which is also available at high pressure, is mixed with the clean gas to feed the gas turbine combustors; this helps to control NOx emission and increases the mass flow rate through the turbine raising thereby the turbine performance. The NOx is further lowered through the saturation of the coal gas by water (condensate from the steam cycle) heated up by the sensible heat of the compressed air (673K) at the compressor outlet.

While the first cost of IGCC at present is higher than PC/supercritical steam, the balance may be tilted towards IGCC in the future because:

- IGCC lends itself for the efficient removal of mercury and CO_2 from the high pressure fuel gas;
- with the strongly increasing volume of refinery wastes (heavy residual oils, petroleum coke, Orimulsion) IGCC could become attractive for using fuels of very low or even "negative" cost. (The waste fuel cost is negative if it stands against the cost of disposal);
- the cycle efficiency could exceed 50% in schemes of producing hydrogen in the gasification process and combining the Brayton -Rankine Cycles with Fuel Cells. An example, the US DOE's Vision21 Gasification /Gas Turbine/Fuel Cell Cycle Schematic is shown in **Figure 6.**[15]

Table 1. Environmental performances at full load (mg/N m^3, 6% O_2).

Technology	PCC + FGT	CFBC	PFBC	PCFBC	IGCC	TC
Nitrogen oxides						
Intrinsic	800-1300	150-250	200-300	100-200	150-200	150-300
Low-NOx burners	400[a]					
In project		75-120	70-200	40-100		
With SCR	100-200					50-150
Nitrous oxide	0-5	20-100	20-100	20-100	0-5	0-5
Sulfur dioxide (1.0% S)		[b]	[b]	[b]		[b]
Intrinsic	2000	200	200	200	10-25	200
Ca/S ratio	1.05	2.5	2.2	1.5		2.0
With FGD	200					
Dust	50	50	50 10[c]	10[c]	10[c]	10[c]

[a] For new boilers 400mg/N m^3; from 500 to 700 mg/N m^3 for existing ones.
[b] With ceramic filters.
[c] It is possible to reach emission levels below 200 mg/N m^3 by simply increasing the quantity of limestone injected into the furnace, and consequently the Ca/S ratio.

Comparison of Clean Coal Technologies

Several studies attempted to compare the emerging Clean Coal Technologies with PCC +Flue Gas Treatment from the points of view construction cost, operating cost, cost of electricity fuel flexibility, pollutant emission, and cycle efficiency (CO_2 emission). Efficiency is becoming an important factor as it is the main determinant of CO_2 emission. For a comparison of these technologies it is also important to forecast the development of some enabling technologies such as new superalloys for gas turbine blades and for superheaters in supercritical steam boilers.

It is generally agreed that PCC + FGT has an edge over the coal fired combined cycle systems in the short and medium term mainly because it is a mature technology and also because competition and R&D in recent years has reduced its first cost to below $1100/kW installed capacity.

Comparisons of environmental performance data at full load (estimated by Delot et. al.[16]) are shown in **Table 1**. The low temperature fluid bed systems, except of the PFBC with Topping combustor, have a problem with N_2O emission while PCC may face some future regulation on fine particulate (PM 2.5) and HAP (e.g., mercury) emissions. IGCC is the potentially cleanest of the advanced coal fired cycles and has also the special advantage that it is amenable to the efficient capture of CO_2 from the high pressure syngas stream.. This is further underlined by the comparative illustration of environmental advantages of advanced power cycles shown in **Figure 7**.[17] IGCC can be seen to have lower NOx emission than a Gas Turbine Combined Cycle, and with sequestration its CO_2 emission compares also favorably with that from a natural gas fired combined cycle.

CO_2 Sequestration

In addition to current strategies of improving the efficiency of power generation, greenhouse gas emission can be mitigated by CO_2 sequestration.[18] CO_2 capture and sequestration technology used to reduce the CO_2 concentration in North Sea natural gas is based on chemical absorption with monoethanolamine (MEA). This process is expensive and prohibitively wasteful in energy use for CO_2 capture from flue gas in power plant. The problem of efficient CO_2 capture hinges on increasing the CO_2 concentration in, and reducing the volume flow rate of, the gas to be treated. There are combustion measures which by increasing the CO_2 concentration in the flue gas can reduce the costs associated with CO_2 separation. One such technique applicable to atmospheric-pressure boilers is oxygen enrichment of the combustion air and recirculation of high CO_2 bearing flue gas through the burners.[19] While such a scheme has to bear the cost of an air separation unit to produce the oxygen, there is some compensation in the reduced volume of the flue gas, which reduces the cost of flue gas clean up equipment and improves the boiler efficiency. CO_2 capture becomes more favorable when the gas to be treated is at elevated pressure and is a syngas rather than flue gas, the product of partial or total coal gasification such as in the cases of PFBC with Topping Combustion or IGCC.

Conclusions

- Coal is the prevailing fuel of power generation world wide, and it is likely to remain important well into this century,
- Because of coal's pollution, and especially due to the expected future limitations on CO_2 emissions, clean coal utilization technology with high thermodynamic efficiency will have to be applied in the new generation of coal fired central power stations to be built in OECD countries.
- Pulverized Coal Combustion in Supercritical Steam Boilers (240atm 2x 838 K) is the likely choice for new central power plants in the short and medium term because of the relatively high efficiency (42-45% LHV) and the long experience with pulverized coal combustion. Also, the cost of these plants is continually getting reduced (presently about $ 1100/kW) There are more than 30 SC plants being commissioned at present in Europe, Australia Japan, S.Korea and Taiwan. Further developments towards Ultra Supercritical Coal Plants (300 atm 3 x 923 K) with 50% single cycle efficiency is dependent on progress in materials R&D; applications are expected past 2010.

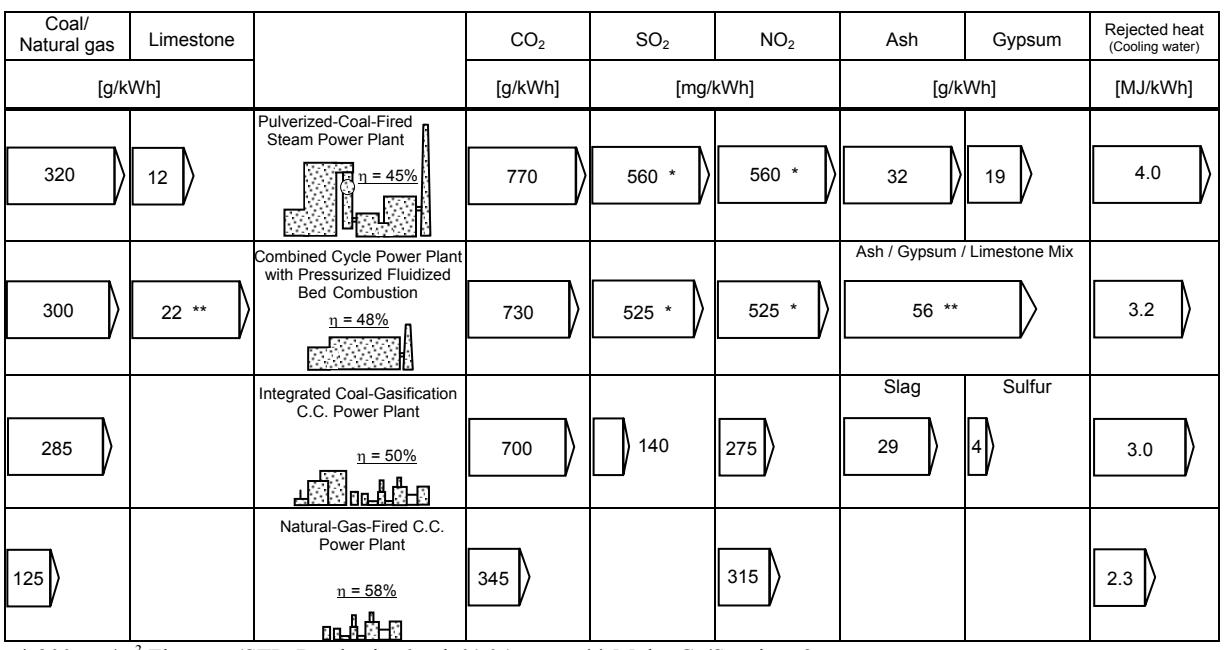

* 200 mg/m^3 Flue gas (STP, Dry basis, 6 vol. % 0_2) ** Molar Ca/S-ratio = 2

Figure 7. Comparison of supply flows, emissions and byproducts of different 600 MW-class power plants.[17]

- Pressurized Fluidized Combustion Combined Cycle in several plants of 70 MWe have been operating satisfactorily since 1991 and a larger plant (360MWe) is starting up in 1999 in Japan. Low alkali coal permits the use of higher pressure ratio with 850C gas turbine entry temperature. Efficiency is around 40% (LHV). Emissions are low, except N_2O (50 –100 ppm).
- PFBC Topping Combustor Cycle Pregasification produced syngas raises turbine inlet temperature to 1570 K with efficiency increase to 47%. N_2O is eliminated at the elevated temperature in the Topping Combustor. Enabling technologies are: Hot Gas Cleanup and Topping Combustor. Demonstration is expected by 2010.
- Integrated Gasification Combined Cycle is the cleanest of advanced coal fired technologies. The demonstration plants in the US were designed with relatively low cycle efficiency (~40%) but IGCC is capable of higher efficiencies through the application of advanced gas turbine technology and better subsystem integration. The disadvantage of presently higher installation cost compared to PC fired plant could be compensated for in the future by lower cost of mercury removal and more favorable conditions for CO_2 capture.
- Interest in gasification has risen also because of favorable prospects for achieving in the near future a "zero emission" and near 60% efficient cycle by combinations of hydrogen production in coal gasification and use of fuel cell and gas turbine technology (Vision21).
- While the cost of high efficiency power generation is expected to be reduced with time, it will likely to remain higher than that of a conventional plant mainly because of the low price of the saved coal. The real value of efficiency is environmental. In order to achieve diversity of fuel supply consistent with environmental quality, application of advanced coal based power generating technology would need to receive governmental financial incentive.

Acknowledgement

Thanks are due to Mr Don McGaffigan for his valuable assistance in the production of the manuscript and illustrations.

References

1. Annual Energy Outlook 2001 Energy Information Administration, Office of Integrated Analysis and Forcasting U.S. Department of Energy, Washington, DC.
2. Skinner, D.G., The Fluidized Combustion of Coal, Review of the Findings of Research up to the beginning of 1969 National Coal Board R&D Department, London, UK, January 1970.
3. Beér, J.M., H.C. Hottel Plenary Lecture, 22nd Symposium (International) on Combustion, The Combustion Institute, Pittsburgh, Pa., pp.1-16 (1988).
4. Bowman, C.T., Progr. in Energy and Combustion Sci. p. 35, Pergamon Press (1975).
5. Couch, G.R., OECD Coal Fired Power Generation IEAPer/33 (1997).
6. Wendt, J.O., C.V. Sternling, M.A. Mafovich, 14th Symposium (International) on Combustion, The Combustion Institute, Pittsburgh, Pa., pp. 897-904 (1973).
7. Borio, R., Lewis, R., Keough, M.B., Booth R.C., Hall, R.E., Lott, R.A., Kokkinos, A., Gyorke, D.F., Durrant, S., Johnson, H.J., Kienkle, J.J., Proceedings of the 1991 Joint Symposium on Stationary Combustion NOx Control, EPRI, Palo Alto, Ca., USA., Rep. TR103265-V2 ,pp.49-68.
8. Folsom, B., Hong, C., Sommer, T., Pratapas, J.M., in the Proceedings of the 1993 Joint Symposium on Stationary Combustion NOx Control, EPRI, Palo Alto, Ca., USA, Rep. TR103265-V2 pp. 7A , 15-34.
9. Hauser, U., OECD/IEA Paris France pp 381-395 (1993).
10. Schilling, H.D., VGB Kraftwerkstechnik (73) 8., pp.564-576 (1993).
11. Roberts, A.G, K.K. Pillai and J.J. Stantan, Pressurized Fluidized Combustion in Fluidized Beds (J.R. Howard Ed.) Applied Science Publishers London (1983).
12. Chan, L.K., A.F. Sarofim, J.M. Beér, Comb. Flame 52, pp.37-45 (1983).
13. Beér, J.M. and R.V. Garland, Coal Fueled Combustion Turbine Cogeneration System with Topping Combustion, Trans. ASME J. of Engnr. for Gas Turbines and Power Vol. 119, no1,pp. 84-92 (1997).
14. Pruschek, R.,Goettlicher, G., Oeljeklaus, G.,Haupt, G., Zimmermann, G., Power-Gen Europe 98 Milan, June 1998.
15. Ruth L.A., US DOE Vision 21 Workshop FETC Pittsburgh, Pa., Dec 1998.
16. Delot, P., DiMaggio, I., Jaquet, L., Roulet V., EDF Comparative Study of Clean Coal Technologies, Electricite de France Thermal Dept. (1996).
17. Haupt,G. and Karg, J., Proc. of the 12th Conf. on the Electric Supply Industry (CEPSI) Pattaya/Thailand Nov. 1998.
18. Herzog, H.J. and E.M. Drake, IEA/93/0E6, IEA Greenhouse Gas R&D Program, Cheltenham, UK (1993).
19. Thambimuthu, K.V. and E. Croiset, Proc. Advanced Coal Based Power and Environmental Systems '98 Conference USDOE Morgantown. Paper 4.4. July 1998.

SYNTHESIS OF MIXED ALCOHOLS OVER ADM CATALYSTS PROMOTED BY Ni AND Mn

Li Debao Qi Huijie Ma Yugang Li Wenhuai
Sun Yuhan Zhong Bing

State Key Laboratory of Coal Conversion, Shanxi Institute of Coal Chemistry, Chinese Academy of Sciences, Taiyuan, P.R. China 030001

Introduction: Many attentions have been paid on the developments of catalysts for mixed alcohol synthesis from syngas in recent years. Among the various catalysts, alkali-doped molybdenum sulfide (ADM) catalyst was considered as one of the most promising systems because of its high selectivity towards alcohols and high activity of water-gas shift reaction, in particular, resistance of S poisoning in the feed gas [1-4]. ADM catalyst modified by Ni and Mn was prepared and the performance for higher alcohols synthesis was investigated in this paper. It was found that the Ni element could promote the activity and selectivity to C_2^+OH, however the selectivity to hydrocarbons also increased. Mn-ADM catalyst showed different performance from Ni-ADM catalyst. Modified by Mn and Ni, the catalyst showed high selectivity to alcohols because of the inhibition of formation of hydrocarbons and the selectivity to C_2^+OH increased sharply. It implied that the structure of Ni played an important role for the performance of higher alcohols synthesis The characterizations such as XRD, SEM, EPMA were carried out to illustrate the influence of the promoters on the performance of higher alcohols synthesis.

Experimental: The Ni (Mn)-ADM and Ni-Mn-ADM catalysts were prepared by co-precipitation from a solution of aqueous $(NH_4)_2MoS_4$, $Ni(C_2H_3O_2)_2$ and (or) $Mn(C_2H_3O_2)_2$ under pH=3-4. The precipitate was dried and mixed with a mount of K_2CO_3 and then decomposed in nitrogen. The compositions was as follows: Mo:K:Ni:Mn=1:0.7:0.33:0.03 (mole ratio). The reactions were carried out in a stainless fixed-bed reactor. The reaction condition was: 10.0MPa, GHSV=5000h-1, 300℃, H_2/CO=2.0. The products were analyzed by gas chromatographs. The data were taken at steady-state after 100hr on-stream. X-ray powder diffraction (XRD) patterns of the tested catalysts were obtained using a Rigaku D/Max 2500 powder diffractometer using Cu Kα radiation as the X-ray source. SEM imagines and X-ray maps were obtained using a LEO 438VP SEM (20KV) and a KEVEX energy dispersive X-ray spectroscopy (probe current 1.5nA).

Results and Discussion:

The results of carbon monoxide hydrogenation were listed in Table1 and Table2. It can been seen that for Ni-ADM catalyst, the CO conversion and the selectivity of both higher alcohols and hydrocarbons increased compared with that of ADM catalyst. The remarkable effect of Ni promoter might be ascribed to the intrinsically nature that nickel is activity element for carbon monoxide hydrogenation especially methanation. It was apparently that Ni was bi-functional, the first is the promotion effect for chain propagation for higher alcohols, and the second is the higher activity for synthesis of hydrocarbons, especially CH_4. The dual effects of Ni promoter implied that it could offer different activity sites for higher alcohols and hydrocarbon simultaneously. Recent investigation on nickel catalyst showed that Ni containing catalyst had excellent ability for CO insertion, which was extremely important significance for higher alcohol synthesis [5]. Studies of metal catalysts for syngas reaction with varying dispersion revealed that the structure of some active element (such as Ni, Pd) played an important role for the reaction of CO hydrogenation: catalysts with small crystallites produce alcohol while larger crystallites produce methane [6-7]. As a result, the increasing of CO conversion and selectivity of alcohols especially C_2^+OH over Mn-Ni-ADM catalyst might suggested that the promoter Mn had strong influence on the distributions and morphology of Ni that were closely related to the active sites for synthesis alcohols.

The XRD patterns (Fig.1) showed that ADM-based catalysts all had phase of poorly crystalline hexagonal MoS_2, the values of 2θ were 14.4、33.5、39.5 and 58.4. The pattern of Ni-ADM showed strong crystal phases of NiS_x, the 2θ were 26.1、29.8、30.8 and 53.6, however for Mn-Ni-ADM catalyst, such diffraction peaks as that of NiS_x disappeared clearly. Fig.2 showed the SEM images and element maps of Ni of Ni-ADM and Mn-Ni-ADM catalysts. The X-ray maps showed that lateral distributions of Mo、S、K had little difference of the two catalysts, however the distribution of Ni was changed greatly due to the addition of Mn. It was clear that for Ni-containing ADM catalysts, the structure and the dispersion of Ni on the catalyst surface had great influence on performance of synthesis alcohols. The promoter Mn inhibited forming of larger crystal of NiS_x and improved the dispersion of Ni species due to the interaction between Ni and Mn. The strong synergy effect of Ni and Mn could offer more active sites for synthesis alcohols.

Table1 Performance of CO hydrogenation over ADM catalysts

Catalyst	CO conv. (mol%)	STY (g/(ml • h))		Selectivity (mol%-freeCO_2)	
		ROH	C2+OH	Alcohols	Hydrocarbons
ADM	11.4	0.321	0.091	68.27	31.73
Ni-ADM	28.8	0.465	0.181	53.5	46.5
Mn-ADM	10.5	0.37	0.092	75.49	24.51
Mn-Ni-ADM	24.3	0.39	0.206	76.19	23.81

Table2 Product distributions of CO hydrogenation

Catalyst	Hydrocarbons (mol.%)				Alcohols (wt%)				
	C1	C2	C3	C4+	C1	C2	C3	C4	C5+
ADM	74.01	20.20	4.71	1.09	70.64	19.77	7.40	2.02	0.16
Ni-ADM	93.32	4.75	1.92	/	70.10	25.10	3.94	0.81	0.05
Mn-ADM	76.80	19.81	2.98	0.41	77.02	17.01	3.84	1.68	0.45
Mn-Ni-ADM	81.00	15.79	2.71	0.51	41.97	36.88	14.93	5.03	1.20

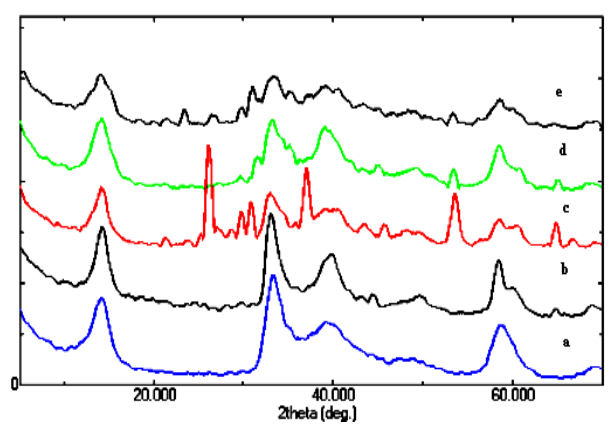

Fig.1. The X-Ray Diffraction Patterns of Molybdenum Sulfides-based catalysts
a. MoS_2; b. ADM; c. Ni-ADM; d. Mn-ADM; e. Mn-Ni-ADM

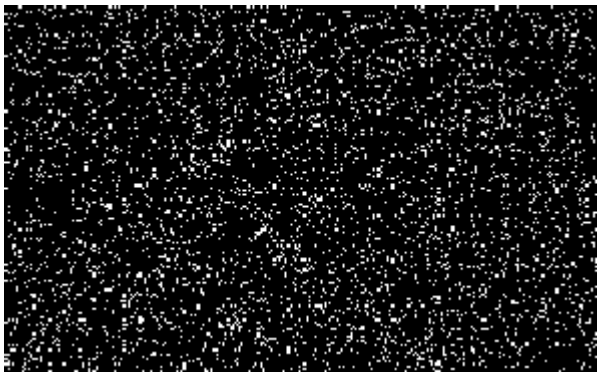

(a) Ni-ADM

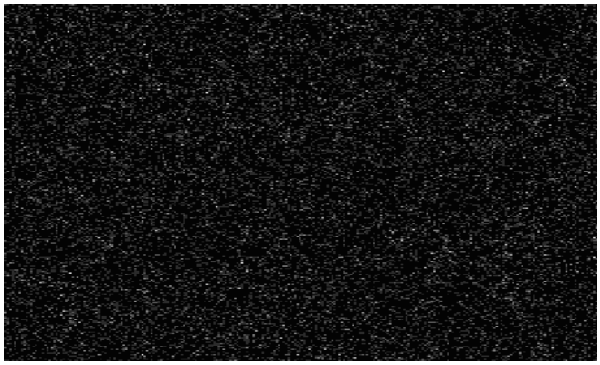

(b) Mn-Ni-ADM

Fig.2. Electron probe analysis of Ni-ADM and Mn-Ni-ADM catalysts (1000×) X-ray map of Ni

References:

1.Xu X.D., et al., Catal. Today. 2(1987)125.
2.Zhenyu Liu, Xianguo Li, et al., Ind.Eng.Chem.Res. 36(1997)3085.
3.Murchison,C.B., Conway, M.M.,Stevens,R.R. and Quarderer,G.J., in "Proceedings,9th International Congress on Catalysis,Cagary,1988" (M.J.Phillips and M.Ternan,Eds.), Vol.2,p.626.Chem.Institute of Canada,Ottawa,1988.
4.Santiesteban,J.G.,Bogdan,C.E.,Herman,R.G.,and Klier,K., in "Proceedings,9th International Congress on Catalysis,Cagary,1988" (M.J.Phillips and M.Ternan,Eds.), Vol.2,p.561.Chem.Institute of Canada,Ottawa,1988.
5. Steven S.C.CHUANG and Shyh-Ing PIEN, Catal. Lett. 3(1989)323.
6. zhongrui Li, Yilu Fu et al., Catal. Lett. 65(1989)43.
7. V.Ponec, Catal.Today. 12(1992)227.

Steam Reforming for Hydrogen. The Process and the Mechanism

Jens R.. Rostrup-Nielsen and Jens Sehested
Haldor Topsøe A/S
Lyngby, Denmark

Introduction

Steam reforming has been a well-established process in industry for more than 70 years and it will play an important role in future applications related to a new hydrogen economy[1,2]. There is also a fast growing need for more hydrogen production capacity in refineries, as the hydrogen balance is negative which means that more hydrogen has to be produced at the refinery or being imported. In spite of efforts to produce hydrogen by schemes involving solar energy, wind energy and biofuels, fossil fuels remain the most feasible feedstock for hydrogen generation in the near term[2].

The choice of hydrogen technology is dictated by the cost and availability of feedstock, and by the scale of operation.

Other parameters than efficiency play a role for small units such as simplicity, compactness and (for automotive units) short start-up time. Air blown catalytic partial oxidation (CPO) fulfils these requirements in particular for fuel cell applications where it is normally acceptable that the hydrogen stream contains nitrogen[3]. However, for commercial scale production of pure hydrogen, steam reforming remains the most economic and efficient technology for a wide range of hydrocarbon feedstocks.

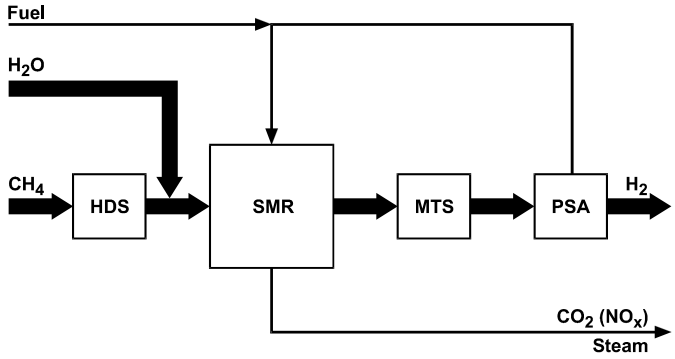

Figure 1. Hydrogen plant. Simplified scheme.

A typical lay-out of a hydrogen plant is shown in **Figure 1**. The reforming process is followed by water gas shift at 410-625 F to ensure high conversion of carbon monoxide and clean-up of the hydrogen product in a PSA-unit.

In many situations when natural gas is not available, higher hydrocarbons become the preferred feedstock for the reforming process. Many refineries can benefit from flexibility in feedstock, taking advantage of the surplus of various hydrocarbon streams in the refinery. Steam reforming of liquid hydrocarbons is also considered for hydrogen generation for fuel cells[4] with diesel and jet fuel considered as "logistic fuels".

The steam reforming process may appear straightforward from an overall consideration as the product composition is determined by simple thermodynamics, but in reality it is a complex coupling of catalysis, heat transfer and mechanical design. In recent years, there has been progress in steam reforming technology resulting in less costly and more efficient plants, in part because of better materials for reformer tubes, better control and understanding of carbon limits, and better catalysts and process concepts with high feedstock flexibility. This progress has been accompanied by a better understanding of the reaction mechanism.

Results

Efficiency and costs. With no steam export, theoretical energy consumption of 300 BTU/scf H_2 (11,8 MJ/Nm^3) on LHV (lower heating value) basis (using liquid water as feed). The industrial value[2] for natural gas based plants is about 320 BTU/scf H_2 (12.6 MJ/Nm^3H_2) corresponding to 94% of the theoretical efficiency. At locations with high natural gas prizes, the energy efficiency becomes critical. For a natural gas price of 4 USD MM BTU, the feedstock and utility costs makes about 65% of total operating costs.

High temperature and high steam to carbon ratio favor high conversion of the endothermic steam reforming reactions. However, modern hydrogen plants are normally designed for low steam-to-carbon ratios (1.8-2.5 mole/C-atom). A low steam-to-carbon ratio reduces the mass flow through the plant and thus the size and costs of equipment[2]. Furthermore, low steam-to-carbon ratios result in a more energy-efficient plant and thus a lower operating cost. In principle, a low steam-to-carbon ratio increases the amount of unconverted methane from the reformer, but is compensated for by increasing the reformer outlet temperature, typically to ca. 1700°F.

- High heat flux
- Low steam to carbon ratio and high exit temperature
- Prereformer and high inlet temperature

Figure 2. Parameters resulting in lower reformer costs

The thermal efficiency of the tubular reformer and waste heat recovery section approaches 95%. The heat transferred to the process is about 50% of the heat input to the reformer and the remainder is recovered from the flue gas. This heat is used for steam production and for preheating of the reformer feed, combustion air, etc. The same is true for the heat contained in the hot product gas exiting the reformer. Very often, there is little need for export steam and today's design aims at minimum steam production.

It is possible to increase the amount of heat transferred to the process gas in the reformer from about 50% to about 80% of the supplied heat when using a convective heat exchange reformer[5], in which the flue gas as well as the hot product gas are cooled by heat exchange with the process gas flowing through the catalyst bed. This results in a more compact piece of equipment. In all types of heat-exchange reformers, however, the heat exchange is by convection, which generally leads to lower heat fluxes than in reformers with radiant heat transfer. However, the compact heat exhange reformer is well suited for small skid-mounted) hydrogen plants. For large scale reforming, tubular reforming remains the most economic solution.

There have been strong efforts to minimize the costs of the tubular reformer. A smaller size is achieved by improving the heat transfer and hence reducing the number of tubes[6]. Tubular reformers today are designed for operation at average heat fluxes exceeding 37000 BTU/sqft/h) (100,000 kcal/m^2/h) almost two times higher than what was industrial practice 20 years ago. Such reformers are built today for capacities up to 270 MM SCFD H_2 (300,000 Nm^3/h).This can be achieved by using a side wall fired furnace with better control of the tube wall temperatures.

Prereformer. Steam reforming generally involves the risk of carbon formation[1]. Whisker carbon may be formed on the catalyst and at high temperatures, ethylene from the pyrolysis of higher

hydrocarbons may lead to pyrolytic coke, which may encapsulate the catalyst pellets.

These constraints are eliminated when a prereformer[7] is installed before the tubular reformer. All higher hydrocarbons are converted in the prereformer in the temperature range of 750-1000 F. After a prereformer, it is possible to preheat to temperatures around 1200 F. The prereformer offers great feedstock flexibility ranging from natural gas and refinery off-gas to liquid fuels and it also serves as an effective sulfur guard for down-stream catalysts.

Catalyst. The typical steam reforming catalyst contains nickel[1]. The catalyst properties are dictated by the severe operating conditions in the reformer with high temperatures an steam partial pressures. Sintering is an important cause of deactivation of nickel-containing steam reforming catalysts[8]. The most important parameters are the temperature and the atmosphere in contact with the catalyst. The catalyst support can affect the sintering in various ways by loss of surface area. The sintering ceases when the nickel particle size exceeds a given size. This maximum size increases with temperature[8].

The catalyst activity is rarely a limiting factor. The catalyst volume (space velocity) is fixed from the tubular reformer design. The equilibrium conversion at high reforming temperatures is achieved at very high space velocities (above 10^6 vol CH_4/vol cat/h) when extrapolating the intrinsic rates[1]. In practice, however, the utilization of the activity (as expressed through the effectiveness factor) is smaller than 10% because of transport restrictions. It can be shown by computer simulations that the catalyst is not the limiting factor for the design of a tubular reformer. An increase of the heat flux and the load at a given exit temperature by a factor of two results in an increase in methane leakage by only 10%[7.]

Discussion

The mechanism of steam reforming. Recent studies of the fundamentals of the steam reforming reactions have lead to a more consistent understanding of the mechanism of the main reactions and the competing reactions for carbon formation[1,9]. The dissociation of methane on nickel surfaces has been investigated extensively, and several details of the reaction pathway are known from fundamental studies, in-situ high resolution electron microscopy and theoretical calculations.

In-situ high resolution electron microscopy has provided new information on sintering mechanisms and for the importance of steps in nucleation of whisker carbon. DFT-calculations have quantified the energetics of methane activation and shown that activation barriers are smaller on surface steps where also carbon is the most stable surface species.

Fig. 3 shows the full potential energy diagram of the steam reforming reaction. The figure shows the energies of the intermediates on the surface and activation barriers separating the intermediates along the reaction path. Two different nickel surfaces were considered. The Ni(111) surface represents the stable dense packed surface, whereas the Ni(211) surface contains steps.

The steps are much more reactive than the close packed surface. All intermediates are also more strongly bound at the steps than on the terraces. For example, adsorbed atomic carbon is much more stable at the steps than at the terraces[1]. Consequently, the steps should be better nucleation sites for graphite than the terraces. The availability of step sites is therefore important both for a high reaction rate and for graphite formation. This raises the question of where promoters (such as potassium) are located on the surface during the catalytic reaction. Again, these were found to be considerably more stable at a step than on a terrace[1,9].

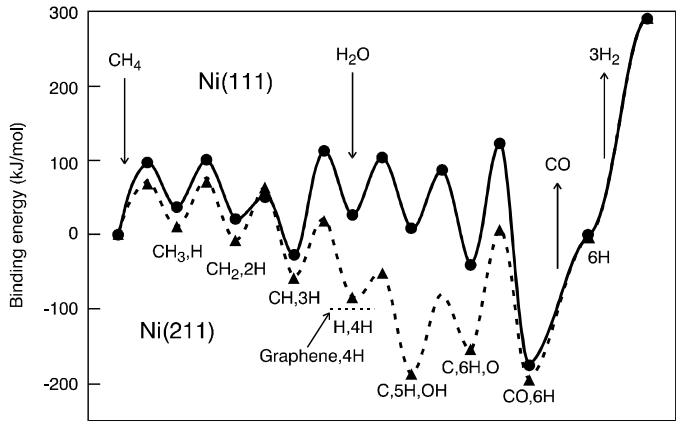

Figure 3. Potential energy curves for steam reforming of methane reaction on Ni(111) and Ni(211) surfaces[9]

Conclusions

Fundamental studies of the steam reforming reactions have led to a more consistent understanding of the mechanism of the main reactions and the competing reactions leading to carbon formation. This forms a more solid basis for development of better catalysts and for their optimum use in advanced reforming technologies. It remains a challenge to take advantage of the huge surplus of catalyst activity in present reformer designs and there is still room for developing catalysts being better in withstanding the risk for carbon formation and sulfur poisoning.

References

1. Rostrup-Nielsen, J.R.; Nørskov, J.K; Sehested, J., *Adv.Catal.* **2002,** *47* (2002), 65 (in print).
2. Rostrup-Nielsen, J.R.; Rostrup-Nielsen, T. *Cattech*, **2002,** *6* (4) 150 (2002).
3. Rostrup-Nielsen, J.R.; Aasberg-Petersen, K. in: "Fuel Cell Handbook" (John Wiley & Co.) (in press).
4. Rostrup-Nielsen, J.R. *Phys. Chem. Chem. Phys,*. **2001,** *3*, 283.
5. Dybkjær, I.; Winter Madsen, S.E.L. *Int. J. Hydrocarb. Eng.* 3 (1) 56 (1997/1998).
6. Rostrup-Nielsen, T. *Hydrocarb.Eng,*, .**2002**, *7* (8) 51.
7. Aasberg-Petersen, K.; Bak Hansen, J.-H.; Christensen, T.S.; Dybkjær, I.; Seier Christensen, P.S.; Stub Nielsen, C., Winter Madsen, S.E.L.; Rostrup-Nielsen, J.R. *Appl.Catal*. A. **2001,** *221*, 379.
8. Sehested, J.; Carlson, A.: Janssens, T.V.W.; Hansen, P.L.; Datye, A.K. *J. Catal,*. **2001,** *197*, 200.
9. Bengaard, H.S., Nørskov, J.K.; Sehested, J.; Clausen, B.S.; Nielsen, L.P.; Molenbroek, A.M.; Rostrup-Nielsen, J.R., *J. Catal.* **2002,** *209*, 365.

A GREEN AND SUSTAINABLE ENERGY SYSTEM BUILT UPON BIOLOGICAL HYDROGEN PRODUCTION

Bruce E. Logan, Steven W. Van Ginkel, Sangeun Oh

COE Environmental Institute, 212 Sackett Bldg, Pennsylvania State University, University Park, PA, 16802

Introduction

The production of petroleum products from oil reserves is expected to peak during the next 10 to 20 years. While vast reserves of other forms of carbon-based materials are well known, these will be costly to obtain. In addition, there is a global drive to reduce carbon dioxide emissions in order to slow or reverse global warming. Only energy sources that do not produce a net gain in CO_2 release will be useful in addressing global warming. New energy sources that can be used will include wind, solar, geothermal, hydraulic, tidal, and other non-carbon based processes to produce electricity. There will still remain a need for more mobile sources of energy, and hydrogen gas can be an important contributor to this energy area. However, in order for hydrogen to become a truly "green" source of energy, more environmentally sustainable techniques must be developed for its production.

Hydrogen is currently manufactured primarily using non-sustainable technologies such as hydrocarbon reforming and electrolysis. However, hydrogen can be formed and recovered in large quantities during anaerobic fermentation of organic substrates. Up to one-third of the energy in a sugar-based material can be recovered as hydrogen in a fermentation process. This hydrogen can then be used to generate electricity in high efficiency fuel cells. The remaining energy value of the material can be biologically converted to methane and recovered either through methane combustion or through methane-reforming fuel cells. Fermentation of sugars to produce hydrogen release CO_2 and volatile fatty acids (specifically acetic and butyric acid), but there is no net change in CO_2 if crop based products are used in the process. During the later stages of the fermentation, the culture may switch its metabolism and produce other final products such as ethanol, acetone, and butanol. These latter products have been commercially produced for profit using anaerobic reactors. For example, acetone and butanol were produced from maize and used as solvents and fuel extenders during World War II (1). Commercial production of ethanol is currently not economical, but part of the reason is that products such as ethanol have less energy than hydrogen.

The infrastructure for biological hydrogen production does not yet exist, so research is needed on methods to maximize hydrogen production from fermentation processes. This must be done in an economical method so that the cost of producing the hydrogen is competitive with other energy production methods. The main costs in biological hydrogen production are for the substrate and the fermentation infrastructure.

We have been examining biological hydrogen production from wastewaters produced by food processing industries for two reasons. First, many of these industries already spend money on wastewater treatment to reduce the oxygen demand of their wastewaters. Thus, the treatment of these wastewaters represents an expense to the company, and any value derived from the wastewater represents a benefit to the company and a potential profit. Second, many companies already have the necessary pipes and plumbing needed for biological treatment. Thus, the cost of producing hydrogen represents only additional materials that must be added onto the system, not the cost of a complete system.

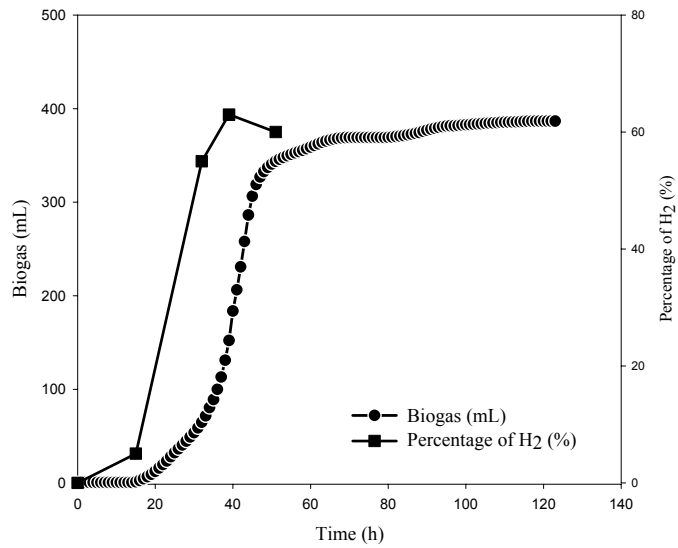

Figure 1. Biogas production and hydrogen percentage curves using apple processing wastewater as the substrate.

In order to investigate the potential for hydrogen production from food processing wastewaters, we conducted a series of batch and chemostat experiments with simulated and real wastewaters. We did not use pure cultures, but instead found it was sufficient to use ordinary soil as an inoculum for hydrogen producing processes.

Methods

Tests were conducted using various substrates and a heat-shocked soil inoculum (2). The soil was baked for two hours at 100°C to kill non-spore-forming, hydrogen-consuming methanogens (3). The spore-soil suspension was then sieved through a #20 mesh (850 μm) mesh and 10 grams of this spore suspension was used to inoculate 250 mL serum bottles. In tests with defined substrates we added substrates to the bottles at a concentration of 4 g-COD/L (1 g-COD per bottle). For the experiments using real wastewaters, we used concentrations around these values. For example, with an apple wastewater we used a concentration of 7.2 g-COD/L. Solutions were buffered with 0.05 M 2-(N-morpholino)ethanesulfonic acid monohydrate (MES) (J.T. Baker) and adjusted to a pH=6.0 using 1M NaOH.

Results and Discussion

An example of our results using apple processing wastewater is shown in Figure 1. Hydrogen in the headspace reached a maximum of 62% (by volume), with a total of 240 mL of pure hydrogen gas produced during the batch test. With defined substrates, the highest volumes of hydrogen were produced with glucose and sucrose, 158 mL and 142 mL, respectively. The fermentation of molasses produced 151 mL of hydrogen, which is comparable to the amounts produced using glucose and sucrose. Molasses has been extensively used in the production of ethanol, acetone, and butanol as discussed previously. Less hydrogen was produced using the other substrates.

The chemical oxygen demands (CODs) of the wastewaters ranged from 2000 to 20,000 mg/L. Conversion efficiencies of four industrial wastewaters ranged from 23% to 209% based on the sugar content of these wastewaters. The values larger than 100% reflect biohydrogen production from materials not detected as glucose in our tests. In all cases, high hydrogen concentrations were measured in the headspace. Based on the wastewater production rates at these four industries, over a billion liters of hydrogen gas and over 10 billion BTUs (from methane combustion) could be produced from organic matter in the wastewaters.

Our current research is directed at maximizing the conversion of renewable substrates to hydrogen in a continuous reactor system. We will present in our talk the results of these different tests and show how different chemicals produced during fermentation can control the switch from hydrogen to solvent production.

Acknowledgement. This research was supported by the National Science Foundation Grant BES-0124674.

References

(1) Jones, D.T. and Woods, D.R. **1986**. Acetone-Butanol Fermentation Revisited. *Microbiological Reviews*. *50*, 484-524.
(2) Logan, B.E., S. E. Oh, I.S. Kim, and S. Van Ginkel. 2002. Biological hydrogen production measured in batch anaerobic respirometers. *Environ. Sci. Technol.* 36(11):2530-2535.
(3) Van Ginkel, S.W., Sung, S., Lay, J.J. 2001. Biohydrogen production as a function of pH and substrate concentration. *Environ. Sci. Technol.* 35 (24): 4726-4730.

Hydrogen Generation from Methane and Water by Nonthermal Plasma

Kanji Irie
Research And Development Laboratory,Daido Steel Co.,Ltd., 2-30, Daido-cho, Minami-ku,Nagoya,Japan457-8545

The decomposition of methane and water was investigated in a dielectric-barrier discharge-plasma(SDR). Effects of new electrodes named Spiral Electrode Silence Discharge Reactor(SESDR) and Micro Arc Jet Electrode(MAJ) were studied in new plasma system. It is convinced that high product hydrogen >500mL/min could be acquired from methane 1L/min in atmosphere and room temperature by small reactor.

1. Introduction

Fuel cells are invesigated to apply to the future automobile. In a fuel cell, Reformer need high temperature to generate hydrogen and cooling system to send to fuel cell. In order for the fuel cells to become more competitive, the hydrogen generation system has to work even at lower as room tempererature. Automobile need high startability fewer than 10 seconds. The production of hydrogen by plasma destruction of water and/or methane might meet the above demand and prove more economical than previous methods.

2. Experimental and Results

In these experiments a copper/gold electrode in a tubular reactor was used to produce the plasma with water and methane as the reactant gases (in balance nitrogen when necessary). The water level is set at 2.3 % in all experiments. Flow rates from 200 to 4000 mL/min were examined at a peak-to-peak voltage of 1.022 kV to 20 kV. The hydrogen production was monitored by a Agilent micro GC .

The decomposition of methane was investigated in a dielectric-barrier discharge-plasma system with conventional electrode of tubular type.

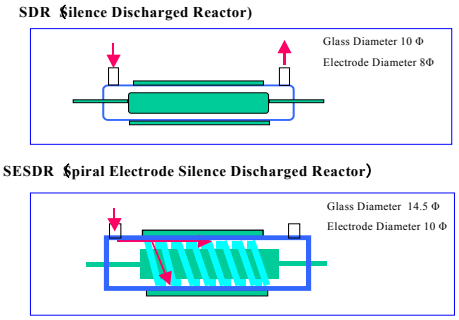

Figure 1 . Reactor SDR and SESDR

It is difficult to get high hydrogen yield and high hydrogen vol.-% by using SDR as shown Figure 2. although methane concentration is increased.

So we advanced to next stage to develop new electrode named Spiral Electrode Silence Discharge

Reactor(SESDR) which composed of spinning gas around electrode and direct gas turbulence.

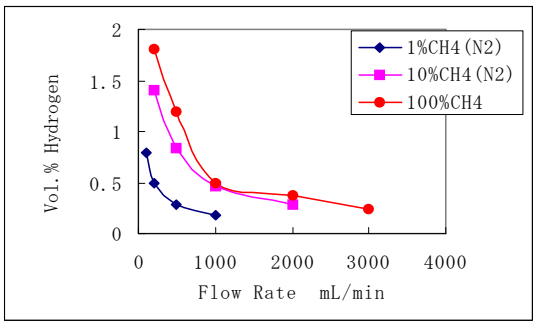

Figure 2. Hydrogen Production in volume-% in relation to the applied CH4 flow rate with non-thermal plasma SDR. H2O: 2.3%. Current:20mA. Voltage:10kV

Hydrogen yield and vol.-% are improved by using SESDR. The discharge can be formed between the 0.3mm gap with about 20 kVp-p sin-wave (~20 kHz). We found frequency affect hydrogen yield more prominent by applying SESDR than SDR as shown Figure 3. Most effective frequency was 20kHz to generate hydrogen from methane with water. The maximum methane conversion rate(90%) into hydrogen was achieved in the absence or presence of water. The other major products observed were CO and CO_2.

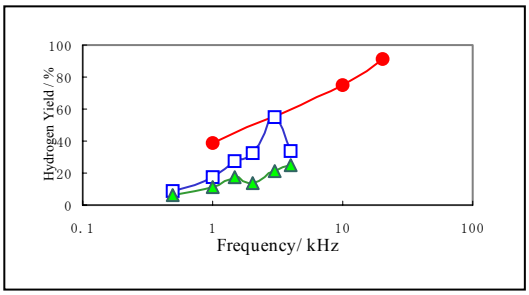

Figure 3. Hydrogen Yield from Methane by SESDR and SDR.
●SESDR50mA, □ SESDR20mA, ▲ SDR20mA
1%$CH_4(N_2)$, Q= 200mL/min, H_2O2.3%

Even though by using SESDR, hydrogen yield degraded on the condition of high velocity of gas .

With the aim of high yield of hydrogen, new type plasma methods are developed and experimented as shown Table 1.

Table 1.

	SDR	SESDR	SESDR	Double	Corona	MAJ
Diameter	10	14.5	46	46	46	10
Volume(cm3)	2.8	13.9	128.4	226.4	249	0.39
Surface (cm2)	59	114	367	524	217	2.2
Gas velocity(cm/sec)	59	18	2	2(3.4)	1	21
Time of flight (sec)	0.17	0.83	7.5	13.4	15	0.02
H2 Yield (%)	1.5	4.1	4.0	6.4	14.9	22.3

Q=1000mL/min I= 50mA, V= 6kV(MAJ = 20mA,1kV)

It is notable that hydrogen yield are not much increased even though by using double layer non-thermal plasma which is expected to be

more effective. It is also notable that corona and arc type pseudo non-thermal plasma developed by us generates hydrogen effectively and hydrogen yield increases as shown table 1. Newly designed arc plasma MAJ which works with comparatively lower voltage (<30W) and simple sin wave electric power can keep hydrogen at room temperature. MAJ is like Needle-Needle electrode plasma. MAJ can endure high velocity of gases more than 4L/min. MAJ can generate high concentration hydrogen (400,000ppm) at flow rate of methane 500mL/min.

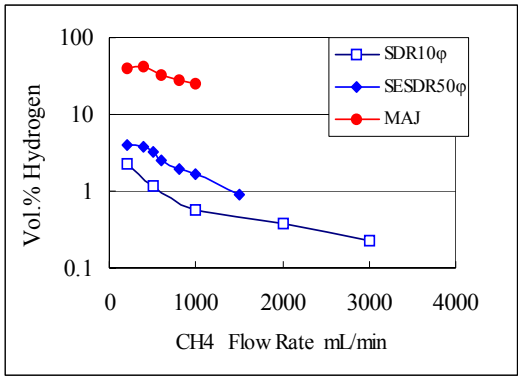

Figure 4. Hydrogen Production in volume-% in relation to the applied CH4 flow rate.
SDR, SESDR: 10kV, 20mA.. MAJ:1kV, 20mA, H2O:2.3%

We obtained hydrogen at rate 250mL/min by MAJ under 30W power expense and produced hydrogen energy as value of 45W on the assumption of hydrogen burning rate as 242kJ/mole shown Table 2. Energy consumption is calculated 21.9MJ/kgH2 for 10% methane and 80.6MJ/kgH2 for 100% methane. The reason of above difference is due to nitrogen existence which may avoid of carbon generating.

Table 2. Energy Consumption of Hydrogen Generation

	Electric Power W	O/C	H2O/C	H2 Yield %	H2 Product mL/min	Product Power W	Energy Consumption MJ/kgH2
10% CH4(N2)	3	0	0.2	42.0	92	16.5	21.9
100% CH4	30	0	0.02	12.5	250	45.0	80.6

Reactor: MJ

Q=1000mL/min, H2 Burning Rate=242kJ/mole

We concluded energy consumption can be raised further more by using cascade equipment developed by us. It is expected that large amount of hydrogen >20L/min) are produced in case of using gasoline for methane and transfer reaction from endothermic to exothermic by using oxygen and water . Plasma reformer can be expected to apply to fuel cell vehicle in near future.

THE ROLE OF IRON PROMOTER IN HIGHER ALCOHOLS SYNTHESIS: EFFECT OF PREPARATION PARAMETER ON THE $Cu/Mn/Fe/ZrO_2$ CATALYST

Xu Run, Ma Zhongyi, Yang Cheng, Wei Wei, Sun Yuhan

State Key Laboratory of Coal Conversion, Institute of Coal Chemistry, Chinese Academy of Sciences, TaiYuan, China, 030001

Introduction

The elucidation of the effect of the preparation on the nature and structure of a catalyst is of considerable importance for catalyst design. In previous work [1], Cu/ZrO_2 catalysts prepared by different method were tested by carbon monoxide hydrogenation and characterized by means of various surface and structure. And it was found that a proportion for higher alcohols was reached over iron, cobalt and nickel modified Cu/ZrO_2 catalysts [2]. Among them, iron modified $Cu/Mn/ZrO_2$ catalysts showed good performance in higher alcohol synthesis. The role of iron has been described promoted carbon chain growth in the literature. Therefore, the effect of iron on the catalysts was investigated by different prepared method.

Results and Discussion

Carbon monoxide hydrogenation was investigated on Fe-modified $Cu/Mn/ZrO_2$ catalysts. The catalysts were prepared by wetness impregnation method (CMZF-i) and co-precipitation (CMZF-c) method. When Fe was added as a promoter, CO hydrogenation products over the catalyst exhibited an obvious change from methanol to $C_{2+}OH$. The alcohol yield of 0.26g/(mL•h) with a $C_{2+}OH$ selectivity of about 22% was obtained over CMZF-i catalyst under the moderate reaction condition (573K, 6.0MPa, $3000h^{-1}$). The activity and selectivity of CMZF-i catalyst was obviously higher than CMZF-c. The curves of CO conversion – higher alcohol selectivity was showed in Fig.1 and 2. It was found that the methanol selectivity decreased and the iso-butanol selectivity increased sharply regular with the CO conversion raise up in CMZF-c catalyst (Fig 1). However, it was not that in CMZF-i catalyst. The linear alcohol selectivity increased synchronously expect methanol. The experimental results indicated that there have different mechanisms of alcohols synthesis on catalysts in CO hydrogenation [3]. So the effect of iron was different. The catalysts have been characterized by the TEM (Fig. 3). It was found the CMZF-i catalyst could get smaller particles than the CMZ sample; the particle size distribution of the CMZF-i catalyst was in 80-120 nm. And the particle of CMZF-c was same as the CMZ catalyst with an average particle size of 180-220 nm. So the iron in CMZF-i catalyst could increase the dispersal of catalyst. Fig. 4 illustrates TPR curves for the copper catalyst with different prepared method. Only one peak was seen during the reduce process. This peak was considered to the reduction of CuO to Cu [4]. The curve of CMZF-c was similar to the CMZ. But the peak shifted to higher temperature in the CMZF-i catalyst. The reduction of CuO in catalysts became harder. The results indicate that Fe loaded by an impregnation method could improve the dispersal of catalysts. On the other hand, the strong interaction occurred because of highly dispersed Cu, Fe or Mn. So the reduction of CuO in catalysts became harder. It is suggested that the effect of iron in catalysts was not only promoted carbon chain growth but also modified the structure of catalysts.

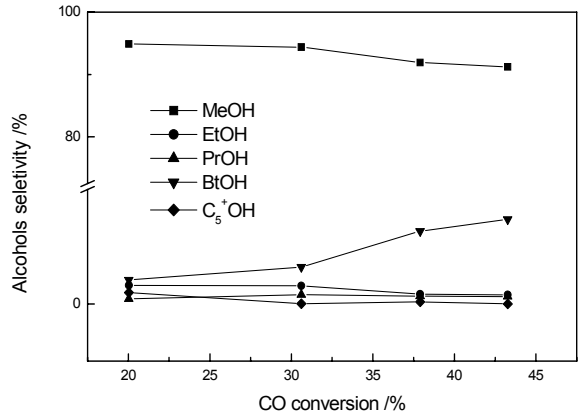

Fig 1 The performance of CMZF-c catalyst in higher alcohol synthesis

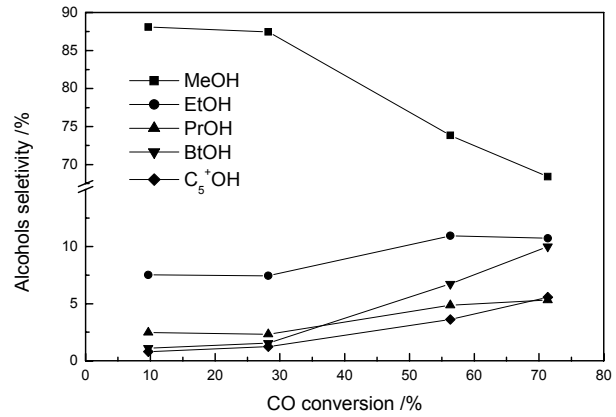

Fig 2 The performance of CMZF-i catalyst in higher alcohol synthesis

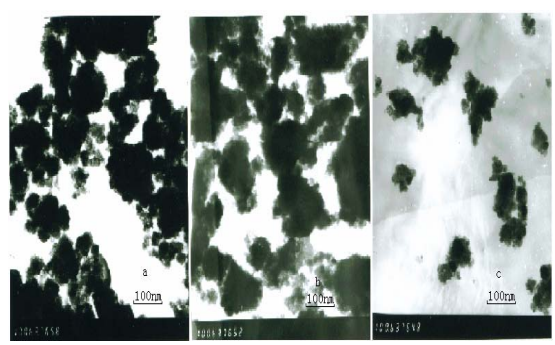

Fig 3 The TEM photo of catalysts a: CMZ, b: CMZF-c, c: CMZF-I

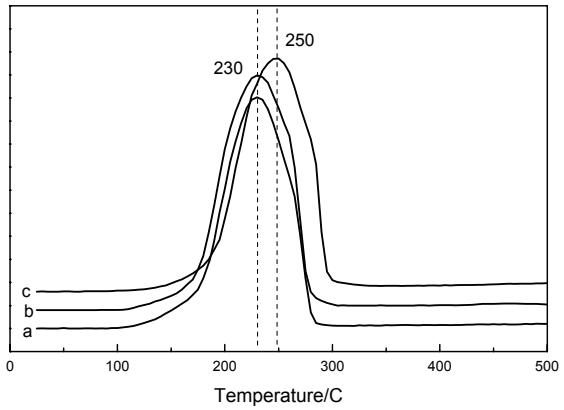

Fig 4 The H_2-TPR curve of catalysts
a: CMZ, b: CMZF-c, c: CMZF-I

References

(1) Yuhan Sun and P.A.Sermon, *J.C.S.Chem.Commum.* , 1 (**1993**) 242
(2) Ning Zhao, Run Xu, Wei Wei and Yuhan Sun, *React. Kinet. Catal. Lett.*, 75 (**2002**) 297
(3) Xiaoding Xu, E. B. M.Doesburg, J. J. F. Scholten, *Catal. Taday*, 2 (**1987**) 125
(4) M. Shimokawabe, H. Asakawa, N. Takezawa, *Appl. Catal.*, 59 (**1990**) 45

HIGHLY ACTIVE STEAM REFORMING CATALYST FOR NATURAL AND JUST ACTIVITY EVALUATION METHOD

T.Numaguchi

Technology Research Center, Toyo Engineering Corporation
1818 Fujimi, Togo, Mobara, Chiba, 297-0017, JAPAN

Introduction

In these years, Gas-to-Liquid (GTL) and DME technologies from SynGas is strongly required from the environmental viewpoint. These requirements widen the basic demand of hydrogen and SynGas from conventional uses for NH3, H2, and CH3OH. Under the circumstance, realizations of these new technologies wholly depend on economical efficiency, that is, it strongly depends on how cheaply the SynGas section, the most costly section, can be built. One solution is an application of a highly active steam reforming catalyst [1].

Toyo Engineering Corporation (abbreviate to TEC) developed a highly active steam reforming catalyst, named ISOP catalyst, for hydrogen and SynGas production from light to moderate hydrocarbon level natural gas. ISOP catalyst is 3 – 4 times as active as currently available other commercial catalysts. The cost impact of the highly active catalyst on the process was precisely confirmed [2] by reviewing our constructing experience of over 10 % of steam reforming facilities on a basis of total hydrogen production rate in the world. The technology on the developed catalyst had licensed to Catalysts and Chemicals Inc., Far East (now, Sued-Chemie Catalyst Japan Inc.), and Sued Chemie Inc., and they put it on the market. Nickel containing ISOP catalyst and ruthenium containing one have more than 10 years experience in fuel cell market in Japan (*ca.* 70 % share), and nickel containing ISOP catalyst in a spoke shape suitable for large scale plants has commercial experiences of 4 years in the longest case in 1500 t/d class NH_3 plant.

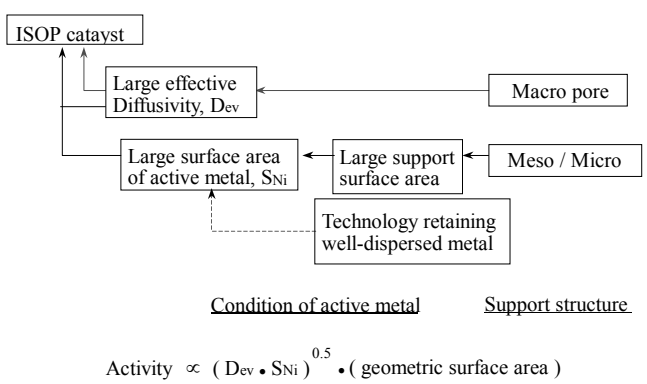

Figure 1. Concept of high activity in ISOP

The concept of ISOP catalyst is shown in **Figure 1**. The higher activity is realized by a larger effective diffusivity (Dev) due to macro pores as shown in **Figure 2** and a larger metal surface area due to a larger BET surface area contributed by meso/micro pores as shown in **Figure 3**. Thus, ISOP catalyst is realized by a bimodal structure. Technology relevant to the retaining the condition is written in elsewhere [3].

Activity of the developed catalyst was evaluated by a pilot plant, installing a reformer tube with a commercial size, precisely heated by electric heaters. The problem to measure the activity in a small scale

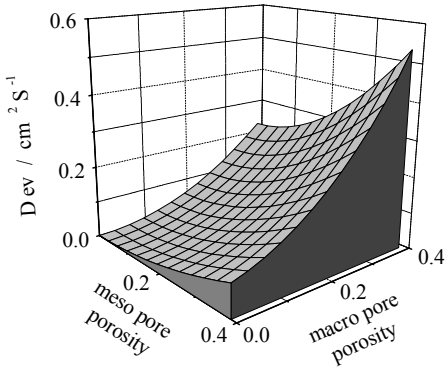

Figure 2. Bimodal structure and effective diffusivity

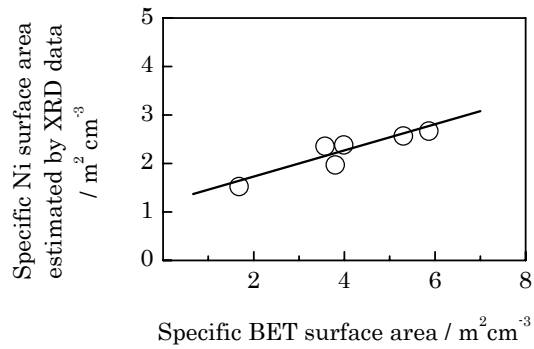

Figure 3. Relation between specific BET surface area and Ni surface area. Ni content (8.2 wt%) is controlled as the same each other.

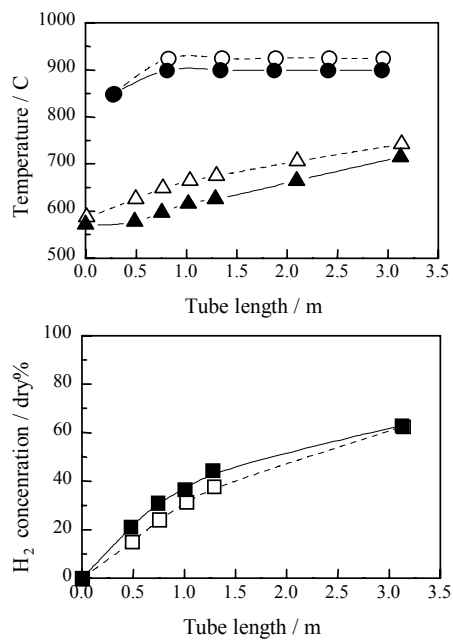

Figure 4. Confirmation of temperature decrease of tube wall using highly active catalyst in electrically heated pilot plant with similar tube diameter to that in commercial use. Operating conditions; P=2.1MPa, S/C=3.0, W/F=750(g/g s).

Conventional catalyst; ○tube, △gas, □H_2 concentration
ISOP catalyst; ●tube, ▲gas, ■H_2 concentration

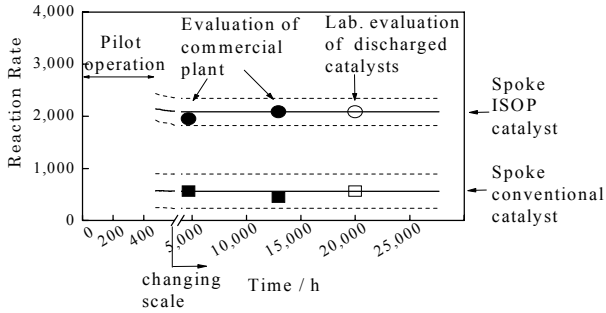

Figure 5. Activity of ISOP catalyst. Solid lines are estimated activities from the pilot operations. Dotted lines mean a 95% confidence limit range.

is discussed later, but on the other hand, it is also true that the precise temperature measurement of tubes, which is indispensable, in a commercial plant requires substantial know-how and experience because of fluctuation of the tube temperature due to not always perfectly adjusted hundreds of burners, unstable flue gas flow under a delicate pressure balance in a box furnace, etc. In consequence, the most reliable evaluating method of is measuring temperature decrease due to endothermic reaction using a tube similar to a commercial size and a precise heating by electrical heaters. By the pilot plant, as a matter of course, the precise temperature measurement is required by checking out Shunt Error problem, etc. **Figure 4** shows that the tube having lower surface temperature by 25 C using ISOP catalyst, decreasing lower process temperature by 60 C, produced the same hydrogen to that by the conventional catalyst at the outlet. The highly active catalyst, thus, proved to decrease the tube temperature as estimated by the simulation result.

After confirming the activity precisely using the pilot plant, ISOP catalyst was charged in a reformer of a 1500 ton/day-class commercial NH3 plant and operated for four years successfully as shown in **Figure 5**, only indicated for two years performance. The mechanical strength was higher than conventional one after two years operation [1] and carbon content was less than the conventional one as indicated in **Table 1**. Not only in this experience, but also ISOP catalyst charged in other commercial plants has been successfully operated.

Through the development of the catalyst, it became clear that the activity evaluation of the steam reforming catalysts is much more

Table 1. Carbon contents in spent catalysts in 2 years

	Conventional Catalyst	ISOP Catalyst
Carbon contents	0.12 wt %	0.038 wt %

difficult than our own estimate, especially by laboratory scale experiments and just evaluation is hardly executed in many cases. Further, this is not well recognized even by researchers concerned in the steam reforming. For example, discussions on benefit estimation require precise reaction rate from a viewpoint of chemical engineering.

We evaluated the activities in the laboratory, the pilot and the commercial scales. As seen in **Figure 5**, every evaluated activity in these scales agrees one another because experimental data were analyzed according to chemical engineering methods [4]. Without analysis from the chemical engineering viewpoint, the observed apparent reaction rate in the laboratory experiment has 100% of error to that in the pilot operation very close to the commercial scale. It was concluded [1] that there are only two ways to evaluate the steam reforming catalyst correctly enough to estimate commercial performance: one is to analyze and evaluate data obtained in the laboratory scale experiments by making the most of the chemical engineering methods. The other is just to measure data in the pilot scale experiments close to commercial conditions. In the latter case, the observed result is directly applicable to the benefit estimation.

This is true but the both methods are not handy. In this paper, reason why conventional evaluation in laboratory scale is not suitable for predicting performance in a commercial scale is discussed. A next-best method, that is, appropriate conditions in laboratory scale are also discussed for a just evaluation through simulation works.

Methods

The following kinetics and simulating conditions are applied to obtain temperatures of the reforming tube, process gas, catalyst surface and reaction rate in commercial plants and laboratory scale experiments for the discussion of the appropriate conditions in laboratory scale.

Kinetics. Rate equations of the steam reforming reaction and shift reaction of a conventional catalyst (abbreviated as "ConvCat") in a shape of multi-holes with a size of 5/8 x 1/4 in. applied to **Figure 5** are set on the basis for the simulation of commercial reformer. That of the steam reforming for a catalyst having three times higher activity (abbreviated as "3ActCat") is obtained by triplication of that of ConvCat. For the laboratory scale evaluation assuming use of a fresh catalyst divided into several pieces, the activities are assumed to have a three times higher activity than that after a deactivation in the plant.

Simulation. According to a designing procedure [2] of the reformer tube to balance the activity and the heat transfer performance, which is basically common in any reformer design, temperature profiles and reaction rate profiles of the both catalysts are simulated under typical commercial conditions of a top firing reformer for a 1500 ton/day class NH3: Tube ID = 80.5 mm (3.17 inch), Feedstock = light natural gas (CH4 = 94.6 %), Process gas Temperature at inlet = 410C (770F), P = 35.0 atom (514.4 psiA), S/C = 3.0, GHSV0 ("0" means at 0C, 1atom) = 7900 (1/h).

For the evaluations in the laboratory scale, the following conditions are applied. These are examined under adiabatic conditions for an easy judgment, which means a comparison of the activities can be basically obtained from a comparison of temperature decreases between inlet and outlet of a catalyst bed.

(1) Typical conditions conventionally used in a small laboratory: Tube (3/4 inch) ID = 21.4mm (2.75 inch), Feedstock = CH4 (99.9 %), Process gas Temperature at inlet = 600 C (1112F), P = 10.0 atom (147.0 psiA), S/C = 3.0, GHSV0 = 15000 (1/h) [accordingly Inlet gas velocity: Ug = 0.1 m/s].

(2) Conditions increasing GHSV0 by 30 times from the conditions (1): GHSV0 = 300000 (1/h), the others are the same as conditions (1) [Inlet Ug = 2m/s].

(3) Conditions increasing GHSV0 by 30 times and decreasing the process gas temperature from the conditions (1): GHSV0 = 300000 (1/h), process gas Temperature at inlet = 500 C (932F), the others are the same as conditions (1).

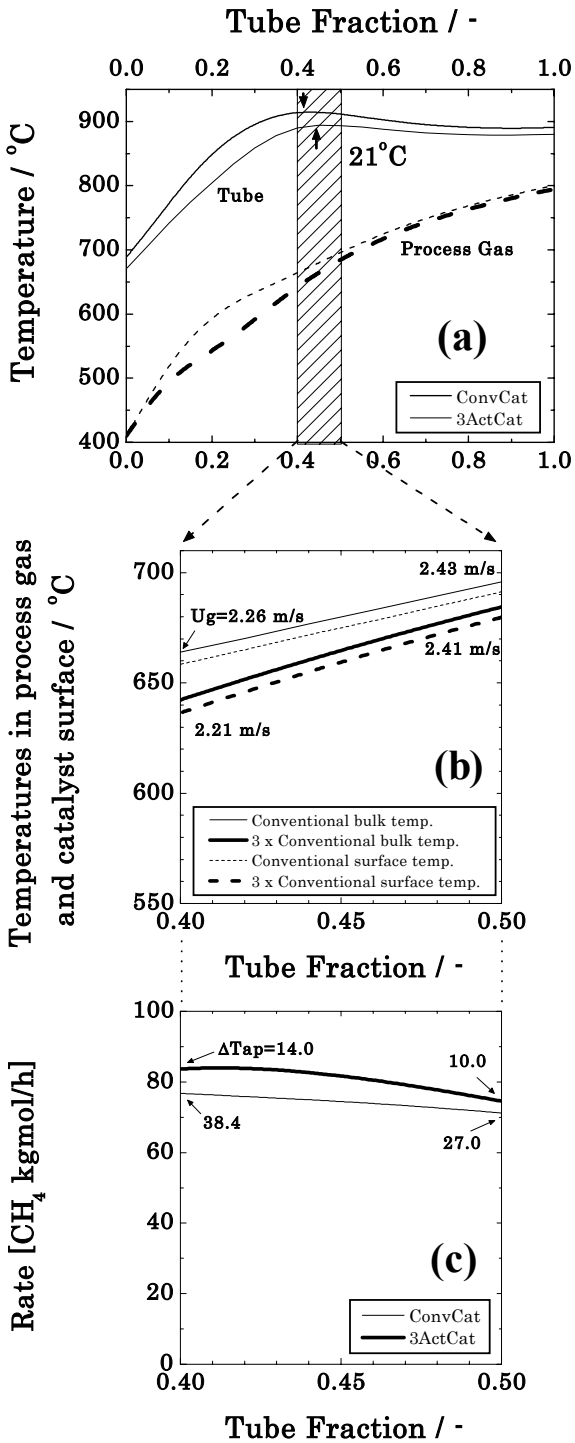

Figure 6. Temperature profiles and rate profiles in commercial plant. Tube length is 9.6 m [31.5 ft].

Results and Discussion

Figure 6-a shows temperature profiles of the tube surface and the process gas in the cases of the both catalysts in the commercial conditions. The figure shows that active 3ActCat (bold lines) decreases the process gas temperature due to the larger reaction rate especially around 0.2 of tube fraction, which decreases the tube wall temperature. An important tube temperature is the highest one in the tube, or a peak temperature of the tube, abbreviated as (Two)max.

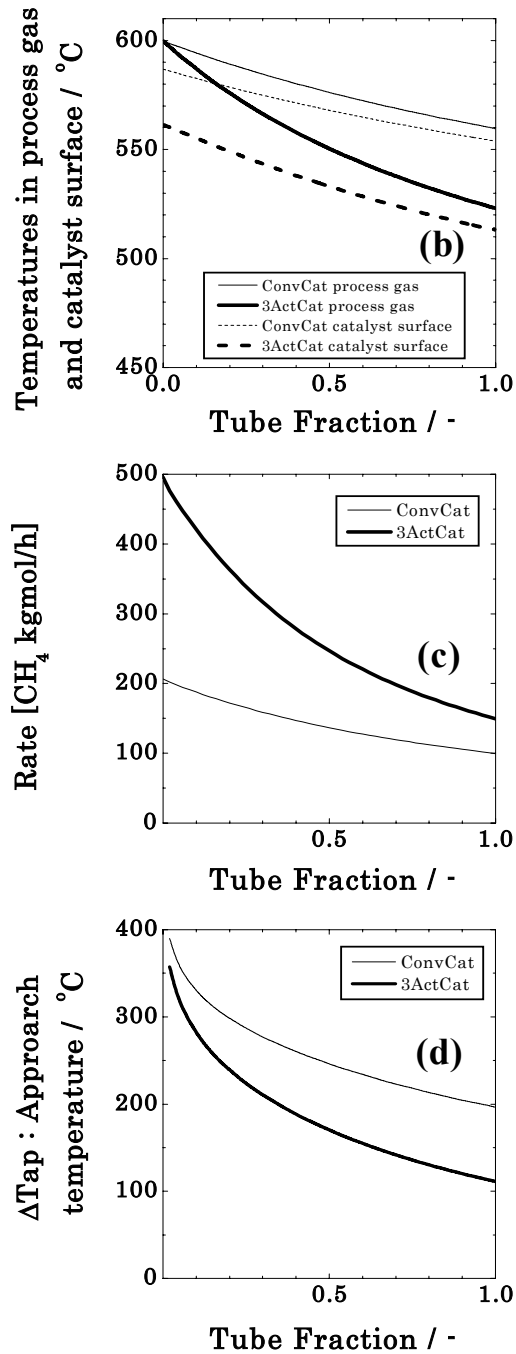

Figure 7. Temperature and rate profiles under typical conditions (1) used in a laboratory scale. Tube length is 70 mm [2.75 in].

(Two)max appears around 0.45 of the tube fraction in the both cases and 3ActCat decreases (Two)max by 21 C, which leads the good deal of profits. The shaded area in the figure from a tube fraction 0.4 to 0.5 is in this paper called "peak zone". The peak zone is enlarged and expressed in detail in **Figure 6-b** and-**c**.

The interfacial gradient of temperature in the solid-fluid film, well known to be large [5], is described by the heat balance equation [4]. By solving the equation catalyst surface temperatures are calculated. **Figure 6-b** shows the process gas temperatures and the catalyst surface temperatures.

In **Figure 6-b** a temperature difference between the process gas temperatures and the catalyst surface temperature in each catalyst is close, 4.5 - 6.0C. Reaction rates corresponding to them are close each other and values are in a range of 70 - 85 [CH4-Kgmol/h] shown in **Figure 6-c**. This is understood that conditions of them are relatively close to equilibriums at the inlet of the "peak zone" as judged from each "approach temperature", abbreviated as delta-Tap in the figure. The approach temperature, represented by the difference between the gas temperature and the equilibrium temperature corresponding to the gas composition, indicates degree of approach to equilibrium by temperature. The larger is the approach temperature, the more far from equilibrium is the state. Zero means the state of equilibrium. While the process gas temperatures are high such as 640 – 700C, the approach temperatures of them are small enough to explain the small rates due to small Drive term in the rate equations: cf. Rate = (Arrhenius term) x (Drive term) / (Adsorption term).

In the commercial plant, thus, a value of the Drive term around the peak temperature is small, by which the reaction rate is not so large, while the process gas temperatures are high in the both, and this leads the interfacial temperature gradient small along with higher gas linear velocity (Ug) of above 2 m/s in the both cases. This is a reason why the highly active catalyst demonstrates its true abilities in the commercial plant. A similar conclusion is obtained in a side-firing reformer as well.

Results under (1) typical conditions used conventionally in laboratory scale are shown in **Figure 7**. 3ActCat almost reaches to the equilibrium showing approach temperature less than 1C in a half part of the catalyst bed, which is so different from the state in the commercial plant shown in **Figure 6-c** that no just evaluation is carried out.

To avoid the state under the conditions (1) commonly applied in the laboratory evaluation, GHSV0 is by 30 times increased in the conditions (2). Under the conditions, the approach temperatures become much larger than those in conditions (1) and the rates at the inlet are about 3 – 6 times as large as those of ConvCat and 3ActCat in conditions (1) as shown in **Figure 8**. This leads the catalyst surface temperature of 3ActCat by 40 C lower than that of the process gas at the inlet despite of a close Ug value to that in the commercial conditions, while that of ConvCat is 12 C: *cf.* 4.5 – 6.0 C for the both catalysts in the commercial plant. This means that 3ActCat is evaluated with a handicap of 28 C compared with ConvCat under conditions (2). Too large rates due to the larger Drive term are a reason of this situation. If the evaluation would be carried out using a mixed gas having a similar composition to that at the inlet of the peak zone in the commercial plant, the rates would be appropriate and a just evaluation would be possible.

Since preparation of the mixed gas is not handy so that a decreasing temperature by 100 C is selected as condition (3) in order to decrease Arrhenius term. Results are shown in **Figure 9**. Rate for ConvCat at the inlet is 34.8 [CH4-Kgmol/h] and that for 3ActCat 114.2, that is, each ratio of the rate in conditions (3) to that in commercial conditions is 34.8/76.8 = 0.45, 114.2/83.9 = 1.4 respectively. While the conditions (3) are still tough to the highly active catalyst, 3ActCat, and tender to ConvCat, the conditions are acceptable. A ratio of average rate of each is 91.6/31.6 = 2.9, which corresponds to a ratio of an adiabatic temperature decrease of each, 22.7/8.0 = 2.8.

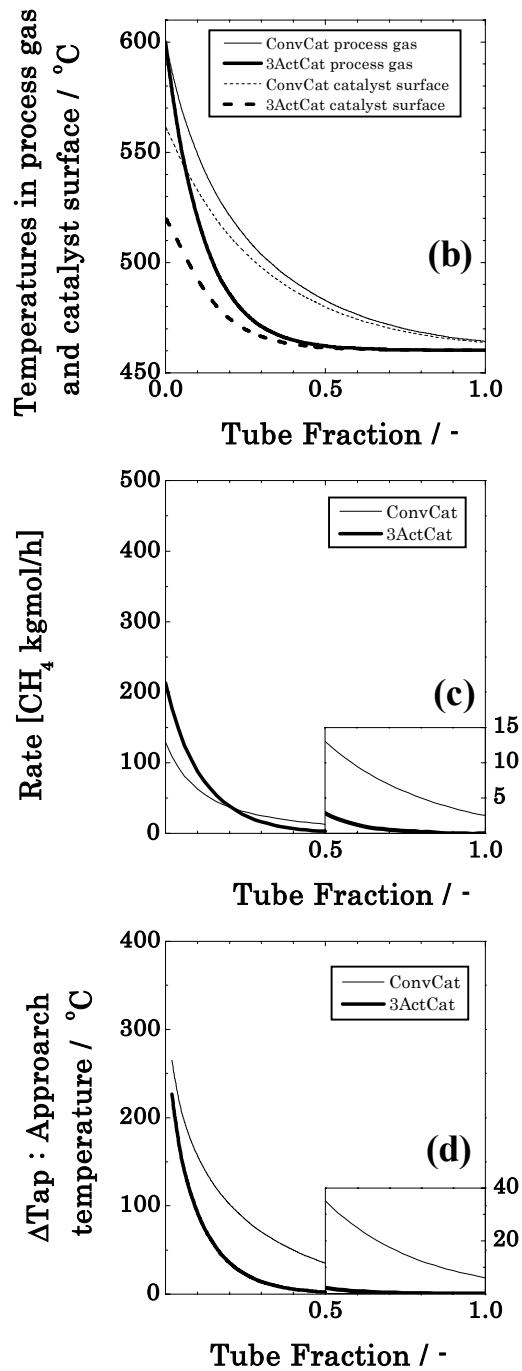

Figure 8. Temperature and rate profiles under conditions increasing GHSV0 by 30 times from conditions (1).

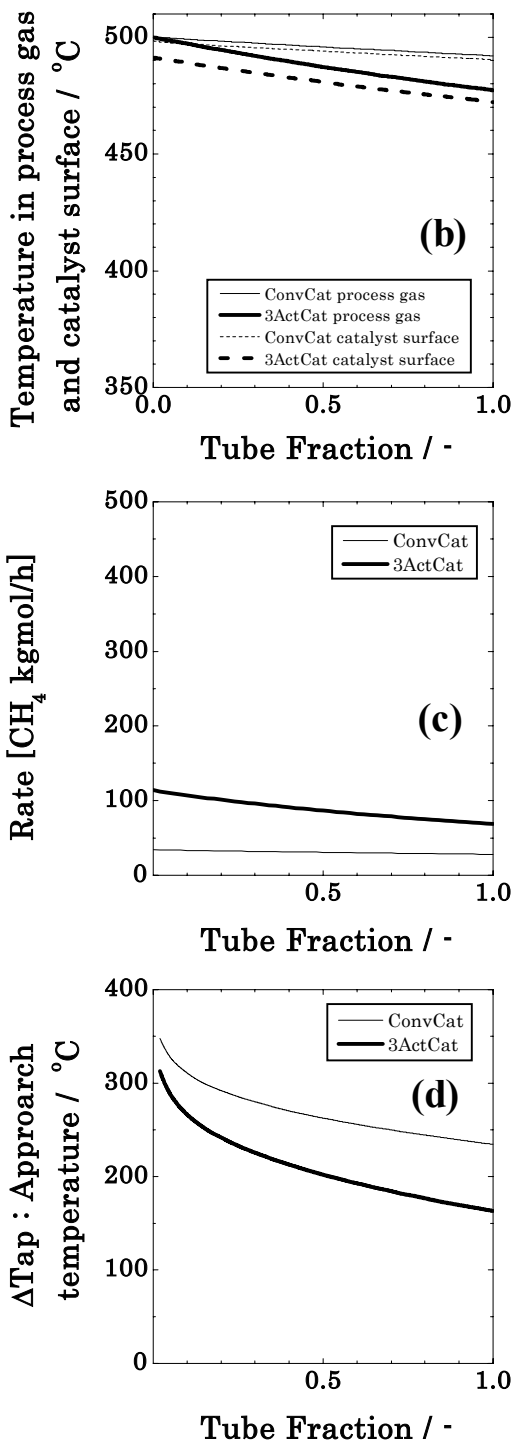

Figure 9. Temperature and rate profiles under conditions increasing GHSV0 by 30 times and decreasing process gas temperature to 500C from conditions (1).

Thus, under typical conditions conventional in a laboratory evaluation such as GHSV0 = 15000 (1/h), 600C using steam and CH4, the reaction rate of steam reforming is too large to evaluate the activity observed in the peak zone of the commercial plant, especially for the highly active catalyst. To avoid the situation, selecting conditions realizing a similar reaction rate to that in the commercial plant is required. Increasing GHSV0 in order to avoid too close state to equilibrium, and decreasing the process gas temperature in order to make the interfacial temperature gradient similar to that in the commercial case, are effective conditions, for example.

Conclusions

The activity evaluation of the steam reforming catalysts is much more difficult than our own estimate, especially by laboratory scale experiments and just evaluation is hardly executed in many cases.

This is caused by the following situation. The reaction rate in a commercial tube where temperature shows the maximum value in the tube is not so large in the commercial plant because the reaction proceeds to some extent before reaching the position, which makes Drive term in a rate equation small. This leads the interfacial temperature gradient small along with a higher gas linear velocity even for a highly active catalyst, which is a reason why the highly active catalyst demonstrates its true abilities in the commercial plant.

On the other hand, typical evaluating conditions in laboratory scale are not infrequently those that make the reaction rate too fast, which makes the state too close to equilibrium to evaluate, or make the interfacial temperature gradient too large derived from much more proceeding of the endothermic reaction than that in commercial operations and give much handicap to a highly active catalyst.

Besides the best evaluating method using the pilot plant electrically heated, the next-best method in a laboratory scale, it's handy, is selecting conditions realizing a similar reaction rate to that in the commercial plant by increasing GHSV0 and/or decreasing the process gas temperature in order to make the interfacial temperature gradient similar to that in the commercial case.

References

(1) Numaguchi, T. *Catalysis Survey from Japan* **2001**, *5 (1),* 59.
(2) Shoji, K.; Hirota, Y.; and Numaguchi, T. *Stud. Surf. Sci. Catal*. **1999**, *121*, 449.
(3) Numaguchi, T. *Catalysts & Catalysis* **2001**, *43 (4)*, 287.
(4) Numaguchi, T.; and Kikuchi, K. *Chem. Eng. Sci***. 1988**, *43*, 2295.
(5) Rostrup Nielsen, J. R. *NATO Advanced Study Workshop*, Nov. 1-6, **1992**, Vauclause, France.

Syngas Production by Direct Oxidation of Methane in a Reverse-Flow Reactor

Dirk Neumann and Götz Veser

Chemical Engineering Dept.
1249 Benedum Hall, University of Pittsburgh
Pittsburgh, PA 15261

Introduction

The catalytic conversion of methane to synthesis gas is a key technology in the petrochemical industry, with its importance further increasing in coming decades due to the increasing significance of natural gas as a feedstock for petrochemical processes. Currently, syngas is typically produced via steam reforming of methane, a strongly endothermic reaction in which methane reacts with water over Ni-based catalysts to CO and H_2 at a molar ratio of 1:3:

$$CH_4 + H_2O \Xi CO + 3\ H_2 \quad (\Delta H_R = +\ 206\ kJ/mol)$$

This primary reforming stage is then typically followed by one or several secondary water-gas-shift stages to adjust the H_2/CO ratio to the stoichiometric value of 2.0, which is needed for most downstream processes like methanol synthesis and Fischer-Tropsch processes.

An interesting alternative for the production of syngas is the direct partial oxidation of methane [1]. Here, methane reacts directly with oxygen or air to form CO and H_2 in a one-step reaction, directly yielding an H_2/CO ratio of 2:

$$CH_4 + 0.5\ O_2 \Xi CO + 2\ H_2 \quad (\Delta H_R = -37\ kJ/mol)$$

The reaction is catalysed by noble metals (Pt, Rh) and is characterized by extreme reaction temperatures exceeding 1000°C, which results in very high reaction rates and thus extremely short residence times in the millisecond range [2].

The extreme temperatures observed at autothermal conditions arise due to a complex interaction of total and partial oxidation pathways: A preferential adsorption of oxygen on the catalyst surface results in a local over-oxidation at the catalyst front edge, which leads to the strongly exothermic total oxidation of parts of the methane feed. While this is by definition detrimental for syngas yields, it also leads to the high reaction temperatures which are thermodynamically necessary to shift the reaction route towards the mildly exothermic partial oxidation of methane. The need for sufficiently high temperatures therefore effectively limits the syngas yields attainable at autothermal reactor operation [3].

This thermodynamic limitation can be overcome through heat-integration in a multifunctional reactor configuration. We have previously been able to show that a counter-current heat-exchange reactor leads to improved methane conversions and syngas selectivities [4]. We have now extended these studies onto the study of direct oxidation of methane in a dynamically operated reverse-flow reactor (RFR). In this reactor configuration, a very efficient heat-integration is achieved by periodically switching the flow-direction of the gases through the reactor, while heat-reservoirs (so-called inert zones) before and after the catalyst as well as the catalyst bed itself act as regenerative heat-exchangers. The experimental investigation and the feasibility of syngas production via direct oxidation of methane in a small-scale RFR is the focus of this paper.

Experimental

The experimental setup used for the investigations is shown in figure 1. The reactor consists of a quartz-glass tube with catalyst and inert-zones, which is then inserted into a metal housing. The catalyst used was a Pt-coated alumina foam monolith (45 ppi, 1.7cm diameter, 1cm long), which had been prepared by standard impregnation procedures. The inert zones consisted of cordierite extruded monoliths (1.7 cm diameter, 11cm long). The flow-reversal was accomplished with 4 valves, positioned as indicated in figure 1. Reactor operation and data acquisition were computer controlled.

The reactants (CH_4 and air) were fed with standard mass-flow controllers and product gases were analyzed with mass spectrometry for time-resolved qualitative measurements and gas chromatography for quantitative measurements. For direct comparison of the results at reverse-flow operation with results from a conventional reactor, the same reactor setup was used for steady-state experiments. In this way, it was assured that all differences between the steady-state results ad the results at unsteady conditions were exclusively due to the differences in reactor operation rather than differences in the experimental setup.

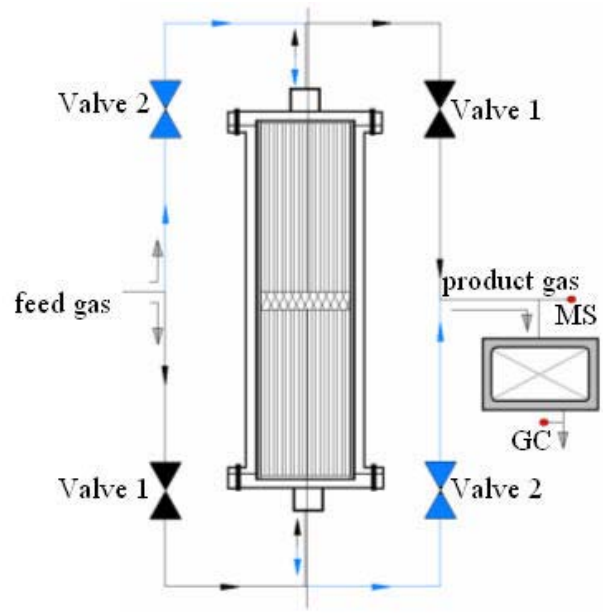

Figure 1: Schematic of the experimental Reverse-Flow Reactor system used for investigating the partial oxidation of methane

Using this reactor setup, syngas selectivities as well as methane conversions were investigated as a function of the CH_4/O_2-ratio of major reactor operating parameters, such as the feed gas composition, cycling periodicity and total gas flow-rate.

Results and Discussion

Variation of the CH_4/O_2 feed gas ratio. Figure 2 shows selectivities towards the partial oxidation products as well as methane conversion as a function of the CH_4/O_2 ratio of the feed gas (flow-rate 4slm, cycling period $\tau/2$ = 15s; the stoichiometric point for partial oxidation is at CH_4/O_2 = 2.0, for total oxidation at 0.5). The results for the RFR are shown in comparison to results obtained at conventional steady-state operation.

The non-stationary process shows a strong increase in syngas selectivities as well as methane conversion over the whole range of CH_4/O_2 ratios investigated when compared to a steady-state reactor without heat-integration. CO selectivities are raised by about 5%, H_2 selectivities by up to 30%, and CH_4 conversions by about 20%. This strong increase in syngas yields can be traced back to the elevated temperatures attained though the excellent heat-integration resulting from the dynamic reactor operation.

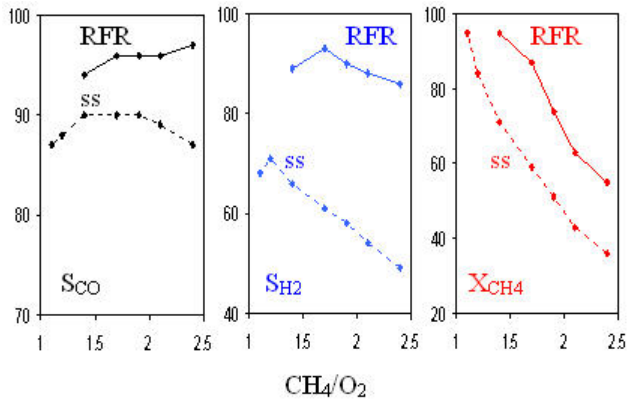

Figure 2: S_{CO}, S_{H2} and X_{CH4} as a function of the CH_4/O_2-ratio of the feed gas; comparison between reverse-flow operation (RFR, solid lines) and a steady-state conventional reactor (ss, dotted lines)

Variation of the flow-rate. One of the main advantages in high temperature catalysis is the high space-time yields attainable due to the fast reaction-rates. Figure 3 shows the syngas yields as a function of the flow-rate for the RFR as well as the steady-state reactor.

Again, the strongly increased syngas yields at reverse-flow operation are apparent. Furthermore, it can be observed that this increase becomes even more pronounces with increasing flow-rates: While the steady-state process exhibits a maximum between 2 and 3slm, syngas yields steadily increase with higher flow-rates in the dynamic reactor operation. Maximum attainable syngas yields are thus shifted towards even higher flow-rates and shorter contact times when compared to the conventional reactor.

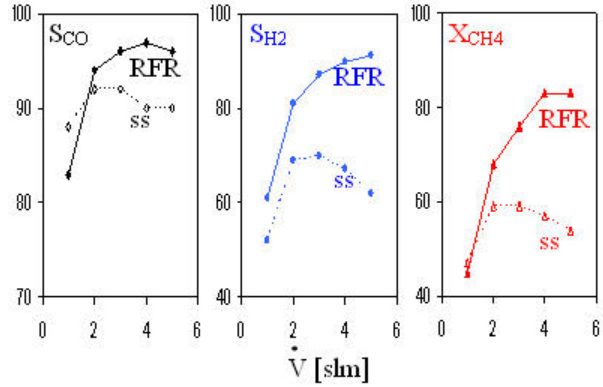

Figure 3: Syngas selectivities and methane conversion as a function of the flow-rate; comparison between RFR (solid line) and steady-state conventional reactor (ss, dotted line).

The reason for this behavior can be found in the temperature profiles (figure 4): With increasing flow-rates, the reaction front is pushed further into the catalyst bed, leading to decreasing catalyst entrance and increasing catalyst exit temperatures with increase flow-rate in the steady-state operation. Particularly the cooling of the catalyst front edge is detrimental for syngas yields since it leads to the total oxidation of the methane in this area [5]. In contrast to that, dynamic reactor operation leads to a steady increase in maximum as well as mean catalyst entrance temperatures. This is due to the fact that increasing flow-rates lead to an increase in the amount of heat generated by the reaction per unit time and thus to an increase in sensible heat leaving the catalyst zone, which is then integrated through the internal heat-exchange in the inert zones.

Finally, it seems noteworthy that the mean catalyst exit temperatures in the RFR are roughly the same as the catalyst exit temperatures at steady-state operation, even though the catalyst entrance temperatures are strongly increased. This indicates that in fact a large amount of the heat integrated in the RFR is effectively converted into chemical energy in form of an increase in syngas yields.

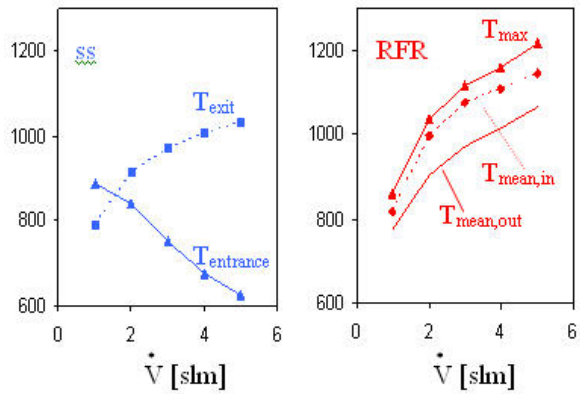

Figure 4: Catalyst entrance (solid line and triangles) and exit (dashed line and squares) temperatures in the steady-state reactor (ss, left graph), maximum (solid line and triangles), mean catalyst entrance (dashed line and diamonds) and mean catalyst exit temperatures (solid line) in the RFR (right graph) as a function of the flow-rate.

Conclusions

Direct catalytic oxidation of methane in a heat-integrated RFR leads to a strong increase in catalyst entrance temperatures and a pronounced increase in syngas yields compared to conventional steady-state reactor operation. Maximum attainable syngas yields could be shifted towards even higher flow-rates or shorter contact times due to the changed temperature profiles at dynamic reactor operation, indicating that this reactor configuration could also be an interesting for other high-temperature short contact-time reactions.

Future Work. A problem related to the harsh operating conditions in the high-temperature RFR concerns a possible enhanced catalyst deactivation. To investigate this problem in more detail we are currently performing long term runs with the laboratory-scale RFR. First results indicate that the heat-integration also leads to a partial compensation some of these deactivation problems. An extension onto partial oxidation of higher hydrocarbons is planned for the near future.

Acknowledgement. The financial support by the German Science Foundation (DFG) as well as the Fund of the Chemical Industry is gratefully acknowledged.

References

(1) Prettre, M., C. Eichner, and M. Perrin, *Trans. Faraday Soc.*, **1946**. 43: p. 335.
(2) Hickman, D.A. and L.D. Schmidt, *Science*, **1993**. 259: p. 343.
(3) Veser, G. and J. Frauhammer, *Chemical Engineering Science*, **2000**. 55: p. 2271-2286.
(4) Friedle, U. and G. Veser, *Chemical Engineering Science*, **1999**. 54(10): p. 1325-1332.
(5) Witt, P.M. and L.D. Schmidt, *Journal of Catalysis*, **1996**. 163(2): p. 465-475.

HYDROGEN PRODUCTION BY WATER DISSOCIATION USING MIXED-CONDUCTING MEMBRANES

U. (Balu) Balachandran, T. H. Lee, S. Wang, and S. E. Dorris

Energy Technology Division
Argonne National Laboratory
Argonne, IL 60439, USA

Introduction

Currently, hydrogen is mainly used as a chemical feedstock in the petrochemical and food industries. Concern about using hydrogen as a fuel for the electric power and transportation industries is growing rapidly because of the climate impact of CO_2 and other gases such as NO_x and SO_x generated from fossil resources. Most of the hydrogen demands are met by fossil-based technologies such as steam reforming of natural gas and coal gasification, which produce CO_2 and other gases. Therefore, hydrogen production from renewable clean hydrogen resources, in particular, water, is of significant interest. Water dissociates into oxygen and hydrogen at high temperatures, and the dissociation increases with increasing temperature:

$$H_2O(g) \Leftrightarrow H_2 + \frac{1}{2}O_2 .$$

Because of the small equilibrium constant of this reaction, the concentrations of generated hydrogen and oxygen are very low, even at relatively high temperatures, e.g., 0.1 and 0.042% for hydrogen and oxygen, respectively, at 1600°C (1). However, significant amounts of hydrogen or oxygen could be generated at moderate temperatures if the reaction were shifted toward dissociation by removing either oxygen or hydrogen with a mixed-conducting membrane. While hydrogen can also be produced by high-temperature steam electrolysis, mixed-conducting membrane offers the advantage of requiring no electric power or electrical circuitry. Hydrogen production with a mixed oxygen ion-electron conducting membrane is shown schematically in **Figure 1**. The rate at which oxygen is removed from the sweep gas depends on the oxygen permeability of the membrane, which is a function of the ambipolar conductivity and surface oxygen exchange kinetics of the membrane, and on the oxygen partial pressure (pO_2) gradient across the membrane (2-4). Therefore, membranes should have high ambipolar conductivity, as well as good surface exchange properties and be exposed to a high oxygen partial pressure gradient in order to obtain a high hydrogen production rate on the sweep side. Previous studies of hydrogen production from water splitting with mixed-conducting membranes showed only a modest hydrogen production rate above 1500°C (5, 6), e.g., 0.6 cm^3/min-cm^2 (STP) at 1683°C (5), mainly because of the low electronic conductivity of those membranes.

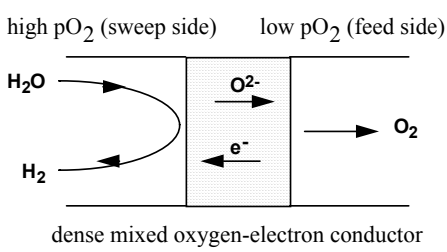

Figure 1. Hydrogen production from water dissociation with a mixed oxygen ion-electron conducting membrane.

We made composites of metal and oxygen ion conductor to develop mixed oxygen ion-electron conducting membranes. In our study of hydrogen production from water splitting with these membranes, we used hydrogen as a model feed gas to obtain a high pO_2 gradient across the membrane. Alternatively, another reducing feed gas such as methane could be used to maintain a high pO_2 gradient across the membrane, in which case hydrogen and syngas could be produced in the sweep and feed gas, respectively. This paper presents the results of hydrogen production from water splitting with cermet membranes.

Experimental

Acceptor doped ceria (CMO) powder was obtained from Praxair Surface Technologies Specialty Ceramics. Membranes designated as ANL-1b (7) were prepared from a mixture of CMO powder and a metal (40 vol.%) with a low hydrogen permeability. Powder mixtures for the membranes were prepared in isopropyl alcohol using a mortar and pestle. After the powder mixtures were dried, they were pressed into disks at 200 MPa and sintered for 10 h at 1400°C in a reducing atmosphere. For measurement of the hydrogen production rate, sintered disks were polished to desired thickness with 600-grit SiC polishing paper. A polished disk was then affixed to an Al_2O_3 tube by using an assembly described elsewhere (7). A gas-tight seal formed when the assembly was heated to 900°C, and spring-loaded rods squeezed a gold ring between the membrane and the Al_2O_3 tube. Gas concentrations in the sweep gas were analyzed with an Agilent 6890 GC using a thermal conductivity detector. The flow rates of both the sweep and feed gases were controlled with MKS mass flow controllers. Water partial pressure in the sweep gas was controlled by bubbling the sweep gas through water at various temperatures.

Results and Discussion

The temperature dependence of hydrogen production was determined with 80% H_2/balance He feed and 49% H_2O/balance N_2 sweep gases. The hydrogen production rate was measured between 700 and 900°C at constant sweep and feed gas flow rates, and the results are shown in **Figure 2**. The production rate increased with temperature and showed Arrhenius-type behavior, with an apparent activation energy (Ea) of 0.85 eV.

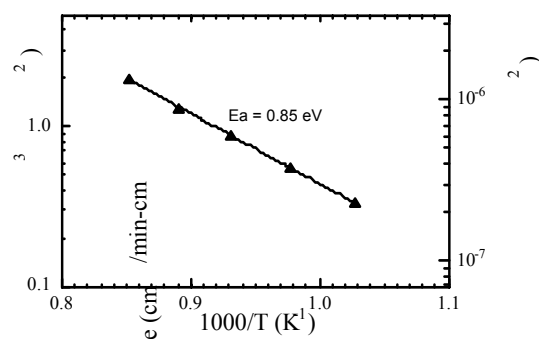

Figure 2. Dependence of H_2 production rate on temperature. Membrane thickness = 0.97 mm.

The hydrogen production rate for the ANL-1b membrane was measured as a function of water partial pressure (pH_2O) in the sweep gas. Measurements were at 900°C in the pH_2O range from 0.03 to 0.49 atm with dry 80% H_2/balance He feed gas and 100 ppm H_2/balance N_2 sweep gas. Results of these measurements are shown in **Figure 3**. The hydrogen production rate increased from 1.1 to 2.0 cm^3 (STP)/min-cm^2 as the sweep pH_2O increased from 0.03 to 0.49

atm; the hydrogen production rate showed a logarithmic dependence on pH_2O in the sweep gas. As the pH_2O in the sweep gas increases, the pO_2 increases, and this effect increases the driving force for oxygen permeation from the sweep to the feed side. As a result, the hydrogen production rate increases as the pH_2O in the sweep gas increases.

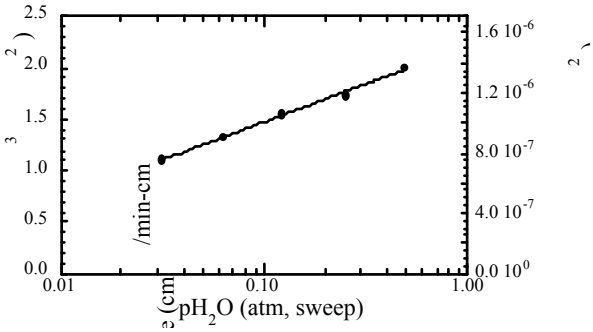

Figure 3. Dependence of H_2 production rate on the pH_2O in the sweep gas. Membrane thickness = 0.97 mm.

The influence of feed-side pH_2 on the hydrogen production rate is shown in **Figure 4**. The hydrogen production rate increased with increasing pH_2 in the feed gas, showing a logarithmic dependence. As the hydrogen concentration in the feed gas increases, the pO_2 on the feed side decreases, thus increasing the driving force for oxygen permeation from the sweep to the feed side. As a result, the hydrogen production rate on the sweep side increases as the pH_2 in the feed gas increases.

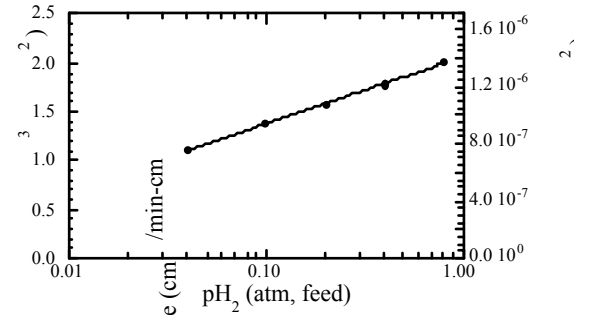

Figure 4. Dependence of H_2 production rate on the pH_2 in the feed gas. Membrane thickness = 0.97 mm. Sweep pH_2O = 0.49 atm.

Previous study (8) showed that the hydrogen production rate increases with decreasing membrane thickness, but surface kinetics becomes important as the membrane thickness decreases below ≈0.5 mm and dominates oxygen permeation through thin (≈0.1 mm) membranes. To increase the hydrogen production rate further, surface kinetics should be enhanced either by increasing the surface area of the membrane (9, 10) or by applying an active catalyst to the surfaces of the membrane. In an effort to enhance surface kinetics and thereby increase the hydrogen production rate, we increased the surface area by applying porous ANL-1b layers on both sides of a dense membrane. By applying the porous layers, the triple phase boundary area increases and extends beyond the surface of the membrane, which may facilitate the oxygen exchange at surfaces. **Figure 5** compares the hydrogen production rate for a surface-modified membrane with that for a nonmodified membrane. Measurements were made at 900°C using 80% H_2/balance He as the feed gas and 49% H_2O/balance N_2 as the sweep gas. As shown in **Figure 5**, the porous layers significantly increased the hydrogen production rate. The maximum hydrogen production rate for a 0.13-mm-thick membrane modified with porous ANL-1b layers was 6.0 cm^3 (STP)/min-cm^2. Compared with nonmodified membranes, the relative rate increase of membranes with porous layers becomes larger as the membrane thickness decreases. This is because the hydrogen production rate, which is directly related to the oxygen permeation through the membrane, is mainly determined by the surface oxygen exchange rate as the membrane thickness decreases. The non-linear increase in hydrogen production rate with the inverse of membrane thickness indicates that the hydrogen production is still largely determined by surface reactions for surface-modified membranes as the membrane thickness decreases.

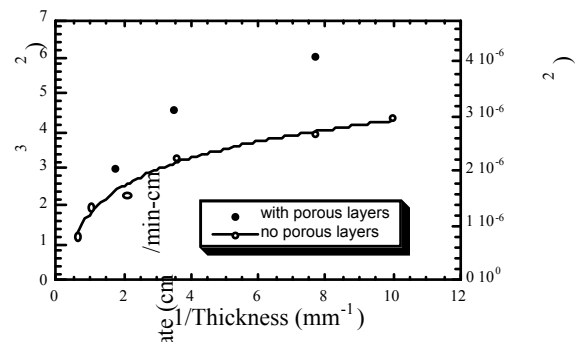

Figure 5. Hydrogen production rates vs. inverse of membrane thickness. The hydrogen production rate of a membrane with porous layers is compared with that of a nonmodified membrane.

Conclusions

Novel mixed oxygen ion-electron conducting cermet membranes were developed to produce hydrogen through water dissociation. We obtained a maximum hydrogen production rate of 6.0 cm^3 (STP)/min-cm^2 with a surface-modified, 0.13-mm-thick membrane. Because of the increased driving force for oxygen permeation from the sweep to the feed side, the hydrogen production rate increased with the pH_2O in the sweep gas and with the pH_2 in the feed gas. The hydrogen production rate also increased with decreasing membrane thickness, but surface kinetics began to dominate the process at a membrane thickness < 0.5 mm.

Acknowledgment. This work is supported by the U.S. Department of Energy, National Energy Technology Laboratory, under Contract W-31-109-Eng-38.

Refrences

(1) Ihara, S. *Bull. Electrotech. Lab.*, **1977**, *41*, 259.
(2) Lee, T. H.; Yang, Y. L.; Jacobson, A. J.; Abeles, B.; and Zhou, M. *Solid State Ionics*, **1997**, *100,* 77.
(3) Qiu, L; Lee, T. H.; Liu, L. M.; Yang, Y. L.; and Jacobson, A. J. *Solid State Ionics*, **1995**, *76,* 321.
(4) Bouwmeester, H. J. M. and Burggraaf, A. J. In *The CRC Handbook of Solid State Electrochemistry*, Gellings, P. J. and Bouwmeester, H. J. M., Ed, CRC Press, Inc. **1997**; pp. 481.
(5) Naito, H. and Arashi, H. *Solid State Ionics*, **1995**, *79*, 366.
(6) Etievant, C. *Solar Energy Materials*, **1991**, *24*, 413.
(7) Balachandran, U.; Lee, T. H.; Zhang, G.; Dorris, S. E.; Rothenberger, K.S.; Howard, B. H.; Morreale, B.; Cugini, A. V.; Siriwardane, R. V.; Poston Jr., J. A.; and Fisher, E. P. In *Proc. 26th Intl. Technical Conf. on Coal Utilization and Fuel Systems,* Clearwater, FL, March 5-8, **2001**. Coal Technical Association, Gaithersburg, MD, pp.751-761.
(8) Lee, T. H.; Wang, S.; Dorris, S. E.; and Balachandran, U. In *Proc. 201st Meetings of the Electrochemical Society*, Philadelphia, PA, May 12-17, **2002**.
(9) Lee, T. H.; Yang, Y. L.; Jacobson, A. J.; Abeles, B.; and Milner, S. *Solid State Ionics*, **1997**, *100,* 87.
(10) Deng, H.; Zhou, M.; and Abeles, B. *Solid State Ionics*, **1994**, *74*, 75.

DEACTIVATION OF SUPPORTED GOLD WATER GAS SHIFT CATALYSTS

Chang Hwan Kim and Levi Thompson

Department of Chemical Engineering
University of Michigan
2300 Hayward St.
Ann Arbor, MI, 48109-2136

Introduction

An emerging application for the water gas shift (WGS) is in the production of hydrogen-rich gas for proton exchange membrane (PEM) fuel cells. The WGS is used to remove most of the CO, a poison to most fuel cell electrocatalysts, from the steam reforming and/or partial oxidation exhaust. The WGS reactor dominates the fuel processor mass, volume, and cost.

Catalysts composed of nanocrystalline gold particles supported on reducible oxides have been demonstrated to be highly active for a number of reactions including WGS[1]. With regard to the activity, the gold particle size is very important[1], and its size must be small enough to lose metallic character and increase its electronegative character[2]. The particle size dependency requires delicate preparation methods. The preferred method is deposition-precipitation[3]. The support usually does not contribute to the catalytic activity, but synergetic effects have been observed in reducible oxide supported gold catalysts[1].

In some cases supported gold catalysts have been report to be substantially more active for WGS than commercial Cu based catalysts[3]. It has, however, also been observed that supported gold catalysts are very susceptible to deactivation and therefore may not be suitable for commercial application. It is claimed this deactivation is due to over-reduction of the support by the reformate[4]. Results from our work are not consistent with this deactivation mechanism. These results along with a tentative mechanism for deactivation will be presented in this paper.

Experimental

Sample preparation. A 10 wt% Au/CeO_2 catalyst was prepared using the deposition-precipitation method. A gold precursor ($HAuCl_4 \cdot 3H_2O$) was deposited and precipitated onto the CeO_2 support. The support was suspended in 100 ml of water with stirring. A $NaCO_3$ solution was used to keep the pH at 10 during precipitation. The catalyst was aged, carefully washed at 60 °C then dried at 80°C under vacuum for 6 h. The resulting material had a surface area of $120 m^2/g$. The commercial Cu-Zn-Al catalyst was obtained from Süd Chemie Ltd.

Activity measurement. Approximately 15-30 mg of catalyst was loaded in a quartz microreactor. Silica was used as an inert diluent. The catalyst was reduced prior to the activity measurement with a mixture containing 4% H_2 in N_2. The catalytic properties were measured at atmospheric pressure and temperatures ranging from 200 to 240 °C using a reactant gas whose composition simulates reformate from gasoline partial oxidation (CO, H_2O, CO_2, H_2 and N_2 concentrations of 10, 22, 6, 43 and 19 mol%, respectively). An HPLC pump was used to feed H_2O (0.04ml/min *liq.*) to the reactant. The space velocity was high enough to minimize transport limitations, and the particle size was adjusted to minimize the pressure drop as well as transport limitations. The effluents were analyzed using a SRI gas chromatograph with single Carboxen 1000 column.

Characterization. The catalyst was characterized using x-ray diffraction (XRD), Fourier Transform Infrared Spectroscopy (FT-IR) and sorption analysis. The XRD analysis was carried out using a Rigaku Rotaflex DMAX-B rotating anode x-ray diffractometer with a CuK_α radiation source operated at 40 kV and 100 mA. *In-situ* FT-IR analysis was performed using a Mattson Galaxy 5000 spectrometer equipped with a Harrick high temperature reaction cell. The sample pellet included inert silica. A Micromeritics AutoChem 2910 was used for all sorption techniques.

Results and Discussion

The initial WGS activity for the Au/CeO_2 catalyst was three times higher than that of a commercial Cu-Zn-Al catalyst, however, its activity decreased by more than 50 % during the first 12 hours on-stream when the CO conversion was limited to 15%. The deactivation rate was significantly slower when the catalyst was evaluated at CO conversions near 95%. Considering the excesses of H_2O, H_2, N_2 and CO_2, this result suggested that the CO content had the most significant effect on the deactivation behavior.

To explore the effect of CO, the Au/CeO_2 catalyst was pretreated with H_2, CO, and a mixture of H_2 and CO (20% each balanced with N_2). **Figure 1** shows that H_2 and CO alone didn't affect to the initial deactivation behavior, however, the catalyst was deactivated severely when pretreated with the H_2/CO mixture.

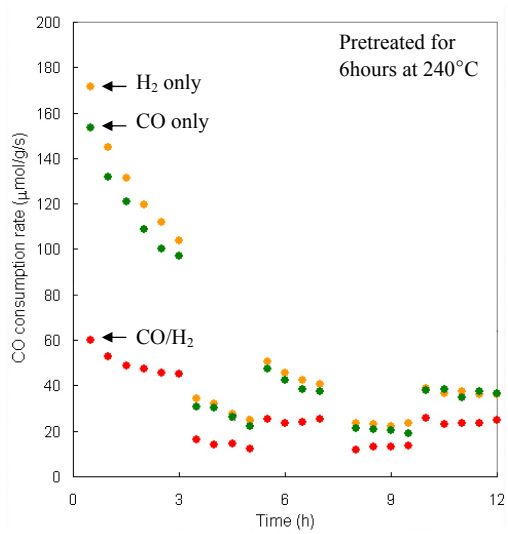

Figure 1. The effect of H_2/CO on deactivation of the WGS activity

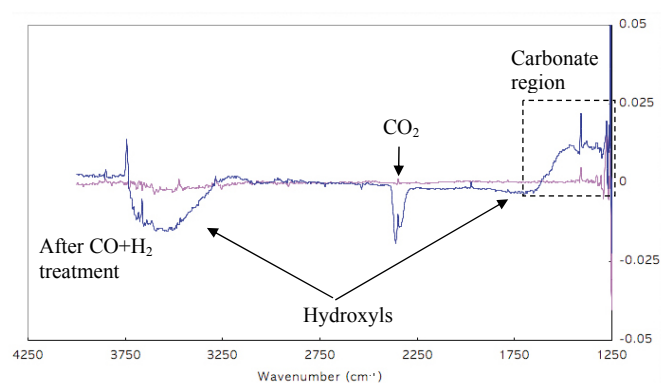

Figure 2. *In-situ* FT-IR spectra after CO/H_2 treatment

We used FT-IR spectroscopy to investigate the surface chemistry after the treatment with the CO/H_2 mixture. The spectra are shown in **Figure 2**, and they illustrate an increase in the amount of carbonate on exposure to the reactant or H_2/CO mixture. There are two possible mechanisms for carbonate formation. Consumption of the hydroxyls and CO_2 could explain the formation of Au-HCO_3 on the surface. Cerium carbonates could also be produced under the experimental conditions employed. Cerium carbonates have been identified on the surfaces of other supported noble metal catalysts during WGS[5].

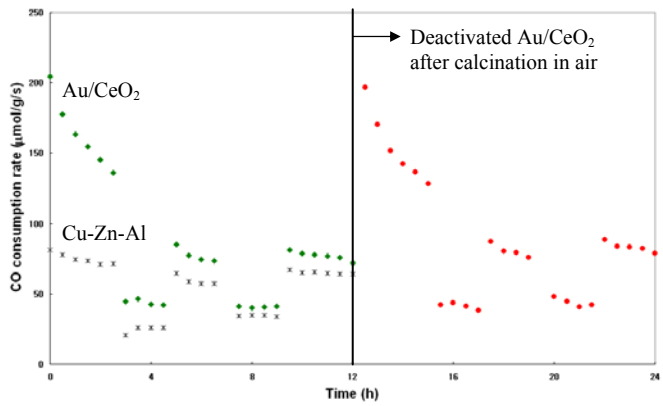

Figure 3. Reaction rates for fresh and reactivated Au/CeO_2 catalyst

We propose that deactivation of the Au/CeO_2 catalyst was caused by poisoning of the active sites by carbonates formed during the WGS reaction. If carbonates deactivated the surface, calcinations should regenerate the activity. In **Figure 3**, the typical deactivation trend during the first 12 hour on stream is illustrated. Subsequently, we calcined the sample with air at 400 °C followed by reduction with 4% H_2/N_2, the same reduction treatment as that used for the fresh sample. The catalyst was regenerated, and in particular more than 95% of the initial activity was recovered following calcination.

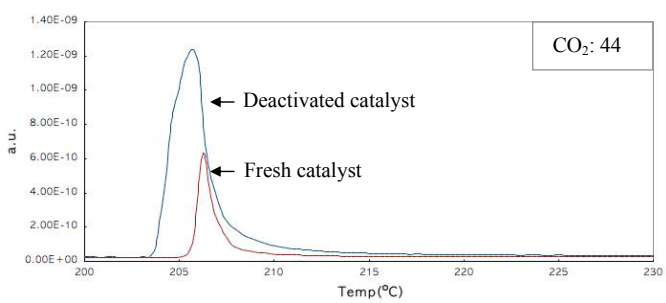

Figure 4. Desorption of CO_2 during calcination of fresh and deactivated catalysts.

We monitored the CO_2 produced using calcinations using a mass spectrometer. A significant amount of CO_2 was measured as shown in **Figure 4**. This observation is inconsistent with calcination simply resulting in a re-oxidation of the over-reduced support. It suggests that adsorbed carbonates on the active sites reacted with oxygen in the air to produce CO_2. Reductions in the NO uptakes are also consistent with carbonates decreasing the density of active sites.

Conclusions

The gold catalyst was more active than a commercial Cu-Zn-Al catalyst, but deactivated very fast. We believe that this deactivation was due to formation of carbonates on the surface. Formation of the carbonate is typically reversible, and they were removed by calcination. The initial activity was fully recovered after the carbonates were removed.

Acknowledgment

This work was financially supported by the U.S. Department of Energy.

References

1. Haruta, M., Tsubota, S., Kobayashi, T., Kageyama, H., Delmon, B., J. Catal, **1993**, *144*, 175
2. Bond, G.C., Thompson, D. T., Catal. Rev.-Eng. Sci., **1999**, *3&4*, 41
3. Andreeva, D., Idakiev, V., Ilieya, L., Travlos, A., Catalysis Today, **2002**, *72*, 51
4. Zalc, J. M., Sokoloyskii, V., Loffler, D. G., J. Catal. **2002**, *206*, 169
5. Hilaire, S., Wang, X., Luo, T., Gorte, R. J., Wagner, Appl. Catal, **2001**, *215*, 271

Particle-Film Structured Dense Dual-Phase Membrane

Weishen Yang[a,], Haihui Wang[a], Y.S. Lin[a,b]*

[a] State Key Laboratory of Catalysis, Dalian Institute of Chemical Physics, Chinese Academy of Sciences

Dalian 116023, China

[b] Department of Chemical Engineering, University of Cincinnati, OH 45221-0171, USA

Dual-phase composite inorganic materials, such as inorganic membranes consisting of an oxygen-ionic conducting ceramic phase and electronically conducting metal or ceramic phase, can find many applications including as membrane separator for oxygen production[1-4], solid oxide fuel cells for power generation[5], and membrane reactors for catalytic conversion of light hydrocarbons[6-11]. If both phases are percolated, such dual-phase membranes offer many unique properties unattainable by the separate single phase. For example, the oxygen permeability for an oxygen ionic conducting (OIC) ceramic membrane (ionic transference number close to one) or an electronic conducting (EC) inorganic membrane (ionic transference number close to zero) is very low because oxygen permeability is determined by the charged species with a lower mobility (conductivity). Combining the two phases would result in a dual-phase membrane with much higher oxygen permeability.

Several research groups[12-18] have reported preparation of dual-phase membranes containing an OIC phase of stabilized zirconia or bismuth oxides and an EC phase of noble metals, such as Ag, Pd. The structure of these dual-phase membranes is defined by random packing of particles of both OIC and EC phases. This structure gives a percolation threshold for the expensive noble metal phase of about 40%, i.e., at least 40 vol% of the electronic conducting phase is required in order to obtain a dual-phase membrane with continuous metal and ceramic phases. This renders the dual-phase membranes too expensive for practical application. Furthermore, the structure of packing particles of two phases of very different properties presents a compatibility issue making such composite membrane mechanically unstable under the conditions of swinging temperature and oxygen pressure.

Kim and Lin [13] reported preparation of dual-phase membrane with an OIC phase formed by close packing of yttria-stabilized-zirconia particles (YSZ) and a continuous phase of Pd as a film covering YSZ particles or filling in the interparticle space of the YSZ phase. They first prepared a mesoporous YSZ membrane by the sol-gel method, and then coated Pd onto the grain surface of YSZ particles by dip-coating and solvent evaporation. Though the Pd phase becomes continuous at low Pd loading they could not obtain a dense dual-phase membrane for effective oxygen transport. In this communication, we report a new structure of dense dual-phase membrane and its preparation method. This new dual-phase membrane consists of an OIC ceramic phase defined by compact packing of OIC ceramic particles and a three dimensional film of an EC phase covering the surface (or grain boundary) of the OIC ceramic particles. This dual-phase membrane requires much lower loading of the EC phase and may also offer improved chemical and mechanical stability.

The primary idea for the formation process of this dual-phase membrane and its structure is shown in Scheme 1 in which the gray particles are an OIC phase and the black one an EC phase. The initial green-body of the dual-phase membrane includes an OIC phase and an EC phase with different but close melting points. It is preferred that the more expensive phase has a lower melting point. The green-body containing particles of two phases are sintered at a temperature between the two melting points. As shown in Scheme 1, the small particles (Scheme 1a) of the OIC-Phase are sintered together to form connected larger grains with clear grain boundaries (Scheme 1b) because the sintering temperature is lower than, but close to, its melting point. At same time, the EC-phase (black one in Scheme 1a) becomes molten and spread over the grain surface of the larger EC particles. Finally, the sintered grains of the OIC-phase develop to a dense bulk particle and the liquid EC-phase forms a continuous three-dimensional film running through the grain-boundaries of the connected OIC phase, as shown in Scheme 1c. Both the EC and OIC phases are expected to be percolated.

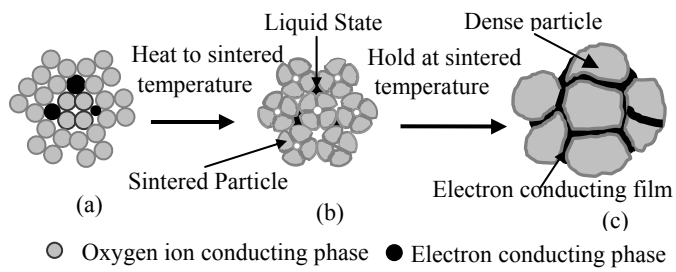

Scheme *1* schematic illustration of structure and formation process of the dual-phase membrane

To verify this concept, we selected $Ba_{0.5}Sr_{0.5}Fe_{0.2}Co_{0.8}O_{3-\delta}$ (BSCF)[3] and $La_{0.15}Sr_{0.85}Ga_{0.3}Fe_{0.7}O_{3-\delta}$ (LSGF)[19] as the OIC and EC phases respectively. BSCF is a mixed oxygen ionic and electronic conductor with electronic-conductivity much higher than the oxygen ionic conductivity[3]. In contract, LSGF developed recently by Eltron[19] exhibits very high oxygen ionic conductivity, low electronic conductivity, and good chemical stability in a reducing atmosphere. But it has very low electronic conductivity and therefore offers very low oxygen permeability. More importantly, the melting point of LSGF (~ 1250°C) is higher than, but close to, that of BSCF (~ 1180°C). We expected that a dual-phase membrane containing a dense LSGF phase and a thin three-dimensional film of BSCF could be prepared from the powders of these two ceramics.

Experimentally, we prepared dual-phase LSGF-BSCF composites by mixing LSGF powder[20] with BSCF powder[3] at a volume ratio of 12.8:1. The powder mixture was ball-milled, pressed into disk-shaped membrane, and then sintered in stagnant air at 1200°C for 10 hours (with a heating and a cooling rate of 1.5°C/min). Low magnification SEM (JEM-5600 LV) analysis of the two dimensional surface of the dual-phase membrane clearly shows a two-dimensional view of the membrane surface characterized by a continuous netlike "wire" running between the boundaries of many grains of about 30-50 μm in size, reassembling the schematic shown in Scheme 1c.

**Corresponding author. Tel: +86-411-4379073; Fax: +86-411-4694447. E-mail address: yangws@dicp.ac.cn (W.S.Yang)*

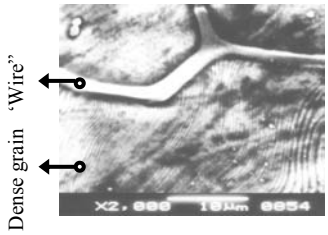

Figure 1 SEM picture of dual phase membrane

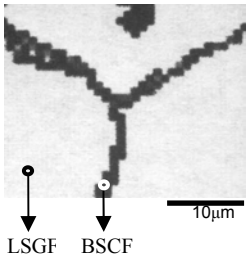

Figure 2 EPMA picture of dual phase membrane

Figure 1 is a higher magnification SEM micrograph of the top view of the dual-phase membrane. This figure shows a section of the continuous netlike "wire" running in the boundaries of three larger ceramic grains. It is important to note that the continuous netlike "wire" is very fine (only 2.5 μm) and uniform throughout the membrane surface observed. Composition of the surface of the dual-phase membrane analyzed by electron probe microanalysis (EPMA, Shimadzu-1600) shows different compositions for the netlike "wire" region and the region of the grains, as shown in Figure 2. The EPMA picture of the two-dimensional view of the dual-phase membrane is very similar to the SEM picture in Figure 1, i.e., a continuous netlike "wire" (black region) running along the boundary of bulk grains (white region). Quantitative EMPA analysis shows only the elements of La, Sr, Ga, Fe, O in the white region, and Ba, Sr, Co, Fe, O in the black region, confirming that the white grains are the LSGF phase and the netlike "wire" is the BSCF phase.

The LSGF-BSCF composite membrane was mechanically fairly strong. It was hermetic to non-oxygen containing gas such as nitrogen or helium. The oxygen permeation flux of the dual-phase LSGF-BSCF membrane was measured in air/helium gradient, and the results are given in Figure 3. Oxygen permeation flux for pure LSGF and BSCF membranes, after being multiplied by the percentage of the phase in the dual-phase composite (92.8% for LSGF and 7.2% for BSCF), are also given in Figure 3 for comparison. As shown the oxygen permeation flux for the dual-phase composite membrane is about one order of magnitude larger than that for the membrane of either pure phase. Such substantial increase in oxygen permeation indicates formation of both percolated phases in the composite membrane and effective electronic transport between the LSGF and BSCF phases and within the BSCF phase.

In conclusion, the above experimental results confirmed successful

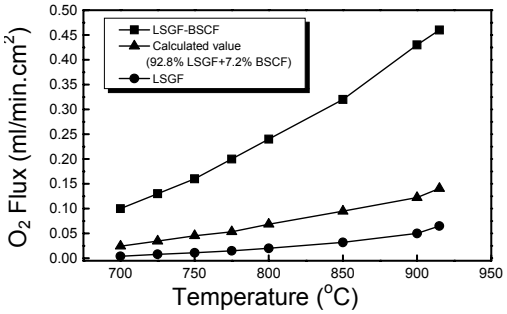

Figure 3 Comparison of oxygen permeation flux at different temperature for the dual-phase membrane with the pure phase membrane.

synthesis of a dual-phase LSGF-BSCF composite membrane with a structure defined by the percolated packing of oxygen ionic conducting LSGF grains with a three-dimensional thin electronic conducting BSCF film running between the boundaries of the connected LSGF grains. The film phase is percolated at a volume percent as low as 7%. Since the majority phase is the chemically more stable LSGF and the second phase is made of a mechanically and chemically compatible BSCF, rather than a metal, the dual phase composite membrane not only exhibit a higher oxygen permeability but also may offer better chemical/mechanical stability than the highly oxygen permeable BSCF membrane. After their structure is further optimized and chemical and physical properties are better understood, the dual-phase membranes will offer many applications including in membrane oxygen separators, fuel cells, and membrane reactors. The concept of the dual-phase membrane and its synthesis method can also be extended to composite materials for other applications.

Acknowledgment. The authors gratefully acknowledge financial supports from the National Advanced Materials Committee of China (Grant No.715-006-0122) and the Ministry of Science and Technology, China (Grant No. G1999022401).

References

(1) Thorogood, R.M.; Srinivasan,R.; Yee,T.F.; Drake,M.P. *U.S.Patent*. 1993, 5240480
(2) Qiu, L.; Lee, T.H.; Liu, L.M.; Yang, Y.L.; Jacobson, A.J. *Solid State Ionics.* 1995, 76, 321
(3) Shao, Z.P.; Yang, W.S.; Cong, Y.; Dong, H.; Tong, J.H.; Xiong, G.X. *J Membr Sci.* 2000, 172, 177
(4) Zeng, Y.; Lin, Y.S.; Swartz, S.L. *J Membr Sci.* 1998, 150, 87
(5) Minth, N.Q. *J.Am.Ceram.Soc.* 1993, 76(2), 563
(6) Balachandran, U.; Dusek, J.T.; Mieville, R.L.; Poeppel, R.B.; Kleefish, M.S.; Pei, S.; Kobylinski, T.P.; Faber, J.; Bose, C.A. *Appl. Catal.A:General.* 1995, 133, 219
(7) Elshof, J.E.; Bouwmeester, H.J.M.; Verweij, H. *Appl Catal A: General.* 1995, 130, 195
(8) Xu, S.; Thomson, W.J.; *AIChE J.* 1997, 43, 2731
(9) Dong, H.; Shao, Z.P.; Xiong, G.X.; Tong, J.H.; Sheng, S.S.; Yang, W.S. *Catal Today.* 2001, 67, 3
(10) Zeng, Y.; Lin, Y.S. *J Catal.* 2000, 193, 58
(11) Tsai, C.Y.; Dixon, A.G.; Moser, W.R.; Ma, Y.H. *AIChE J.* 1997, 43, 2741
(12) Kim, J.; Lin, Y.S. *J Membr Sci*., 2000, 167, 123
(13) Kim, J.; Lin, Y.S. *Ind. Eng. Chem. Res*., 2000, 39, 2124
(14) Chen, C.S.; Kruidhof, H.; M.Bouwmeester, H.J.; Verweij, H.; Burggraaf, A.J.; *Solid State Ionics* 1997, 99, 215.
(15) C.S.Chen, B.A.Boukamp, H.J.M.Bouwmeester, G.Z.Cao, H.Kruidhof, A.J.A.Winnubst, A.J.Burggraaf, *Solid State Ionic.* 1995, 76, 23
(16) Shen, Y.S.; Liu, M.; Taylor, D.; Bolagopal, S. in Proceedings of the 2nd international Symposium on ionic and Mixed Conducting ceramics Vols94-112 (Eds: T.A.Ramanarayanan, W.L. Worrell, H.L.Tuller) *The Electrochemical Society.* Penningeon, NJ, 1994, P. 574
(17) Mazanec, T.J.; Cable, T.L.; Fryer, J.G. *Solid State Ionics* 1992,53-56, 111
(18) Mazanec, T.J.; *Electrochem.Soc.Proc.* 1996, PV95-24, 16.
(19) Schwartz, M.; White, H.James.; Sammells, F.A. *International Patent* WO 1999, 99/21649
(20) Cong, Y.; Shao, Z.P.; Yang, W.S.; Xiong, G.X.; Lin, L.W. *Science in China B.* 2001, 44, 294

ITM Oxygen Membrane Performance and Properties

M. Watson[1], P. Armstrong[1], M. Carolan[1], R. Cutler[2], J. Gordon[2], D. Shelleman[3], R. Tressler[3]

[1]Air Products and Chemicals, Inc.
7201 Hamilton Boulevard
Allentown, PA 18195-1501

[2]Ceramatec, Inc.
2425 South 900 West
Salt Lake City, UT 84119

[3]Department of Materials Science and Engineering
The Pennsylvania State University
110 Steidle Bldg.
University Park, PA 16802

Introduction

Ion Transport Membranes (ITMs) are ceramic materials that conduct oxygen ions at elevated temperatures. The ITM Oxygen process, in which an ITM is used to separate high-purity oxygen from high-pressure air, (Figure 1) has the potential for significant advantages when integrated with power generation cycles. The separation process occurs under high temperature and pressure and places severe demands on the performance and property requirements of the ITM Oxygen material. Air Products and Chemicals has joined with the US Department of Energy, Ceramatec, Penn State University and other partners to develop, scale-up and commercialize this technology.

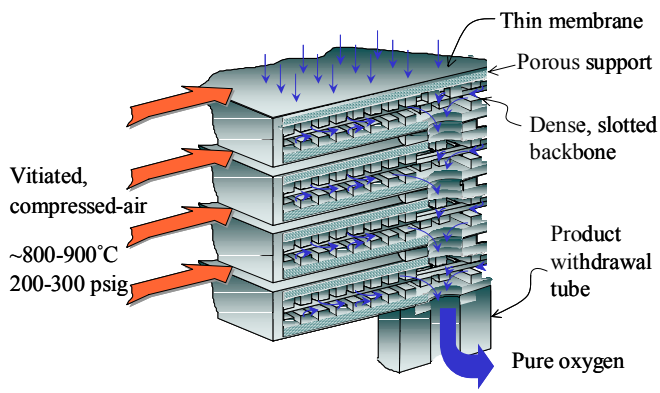

Figure 1. Section of planar membrane modules showing functional layers and process flows.

ITM Oxygen is a pressure-driven process, and the membrane separates oxygen by conducting oxygen ion vacancies from the low-pressure permeate side of the membrane to the high-pressure feed side, causing a counter flow of oxygen anions. Under isothermal conditions, the steady state oxygen flux, N, can be expressed as:[1]

$$N = \frac{D}{4VL}\int_{\ln(P'')}^{\ln(P')} \delta(\ln(P)) \cdot \partial(\ln(P))$$

where V is the material molar volume, D is the vacancy diffusion coefficient, L is the thickness of the separating layer, and δ is the vacancy concentration, expressed as a function of the solid-state oxygen partial pressure, ln(P), integrated between the feed and permeate oxygen partial pressures, P' and P'', respectively. The oxygen flux is inversely proportional to the separating layer thickness, L, and proportional to the thermodynamic driving force for separation, which is the integrand in the above equation.

Experimental

Membrane and Sample Fabrication. ITM powder processing is carried out by Ceramatec, Inc., and is produced by calcining oxides and carbonates of the cationic species. The calcined powders are milled and mixed with binder/plasticizer/solvent to form a slurry suitable for tape casting. Samples suitable for creep testing are cut from green tape. The membrane consists of multiple functional layers, shown in Figure 1, which are featured and laminated together. The green wafer is then sintered, and one or more wafers are joined to a manifold tube to create an ITM Oxygen module, (Figure 2).

The progression in membrane area from 1996 – 2001 is shown in Figure 2. The disk shaped membrane, first tested in 1996, has approximately 0.9% of the area of a single commercial wafer. Each wafer in the module built in 2001 is commercial scale.

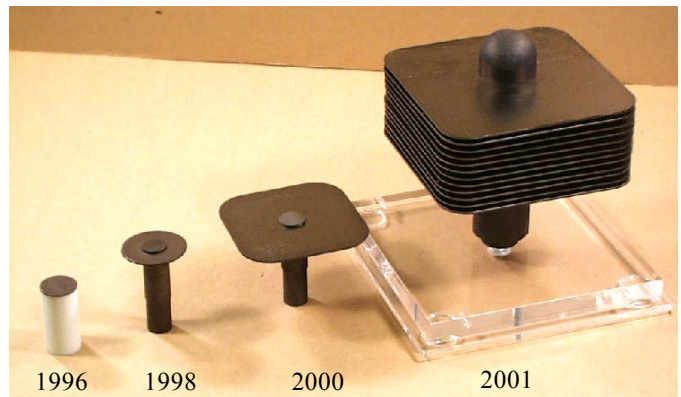

Figure 2. Size-progression of ITM Oxygen modules from 1996 – 2001.

Creep Testing. Rectangular bars were cut from green tape and sintered to full density. Four point flexural creep testing was carried out at Penn State University using standard methods,[2] to ensure the material is able to withstand extended exposure to the high-pressure, high-temperature operating environment without excessive plastic deformation.

Membrane Testing. The ITM wafer is flux tested inside a heated pressure vessel. Hot, pressurized air passes on the outside of the membrane while pure oxygen is collected in the manifold tube, as shown in Figure 1. The flux is measured as a function of feed-side pressure, permeate-side pressure, and thickness of the outermost dense layer of the wafer.

Results

The results presented in this section are given in terms of units relative to the commercial targets. For example, relative flux is the ratio of measured flux to commercial flux target; relative thickness is the ratio of measured thickness to the commercial target for the thickness of the outermost dense layer, and so forth. This approach

[1] H.J.M Bouwmeester and A.J. Burggraaf, "Dense Ceramic Membranes For Oxygen Separation," Chapter 14, pp 527, in P.J. Gellings and H.J.M. Bouwmeester (Editors), *CRC Handbook of Solid State Electrochemistry*, CRC Press, Boca Raton, Florida, 1997.

[2] D. C. Crammer, and D. W. Richerson, *Mechanical Testing Methodology for Ceramic Design and Reliability*, Marcel Dekker, Inc. New York, 1998, p. 171-222

enables the comparison of a number of data sets that have been generated under different experimental conditions.

The effect of the thickness of the outermost dense layer on membrane performance is shown in Figure 3. The membrane performance is expressed in terms of relative flux normalized to relative driving force. As expected from the equation describing flux, (flux)/(driving force) is proportional to the inverse of thickness of the separating layer thickness, and Figure 3 shows that the commercial flux target can be reached and exceeded when the commercial membrane layer thickness is used.

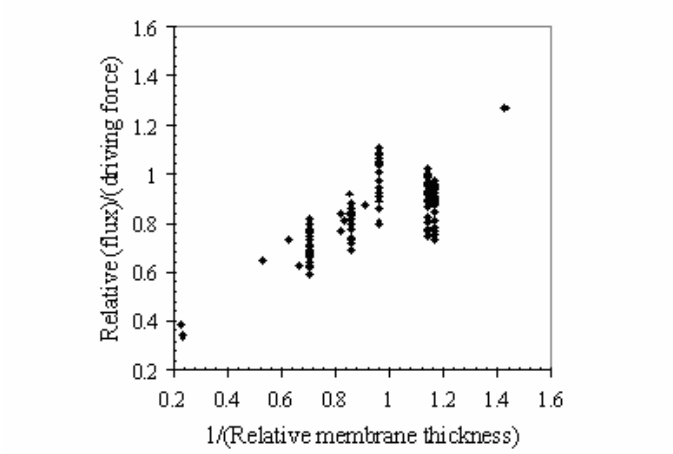

Figure 3. Effect of membrane layer thickness on performance.

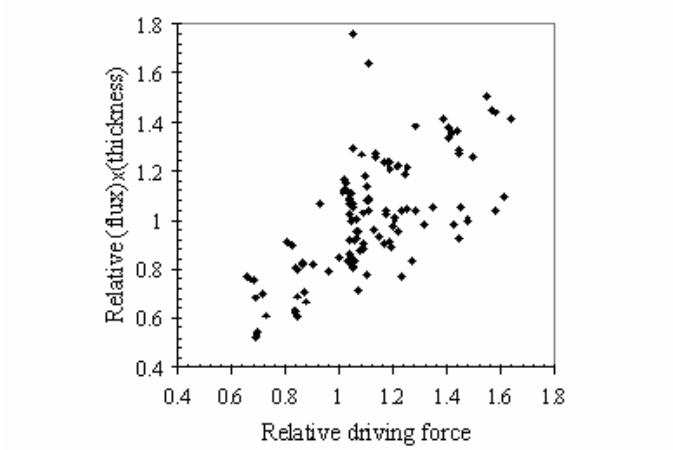

Figure 4. Effect of driving force on performance.

The effect of thermodynamic driving force on the membrane performance is shown in Figure 4. The membrane performance is expressed as relative flux multiplied by the thickness of the dense separating layer. As expected from the equation above (flux)•(thickness) is proportional to the driving force for separation, and Figure 4 shows that the commercial flux target can be reached and exceeded when the commercial driving force is used.

It is important to check that the scale-up from a laminate to wafer module geometry does not negatively impact the membrane performance. During the scale-up, the driving force was increased from ambient pressure to a full commercial pressure gradient; and the thickness of the separating layer decreased to the commercial target. Figure 5 shows that relative flux of the membrane is unchanged by the different geometry. In fact, the sub-scale wafer flux lies within a tighter flux band, which may indicate a more controlled ceramic process.

The scale up of the membrane fabrication and testing processes has occurred simultaneously with the materials development effort. One important property of the membrane material is the ability to withstand extended exposure to a high-pressure, high-temperature environment without excessive plastic deformation, or creep. Figure 6 shows that the latest generation of membrane material (Generation 2) is an order of magnitude more creep resistant than an earlier generation of material (Generation 1).

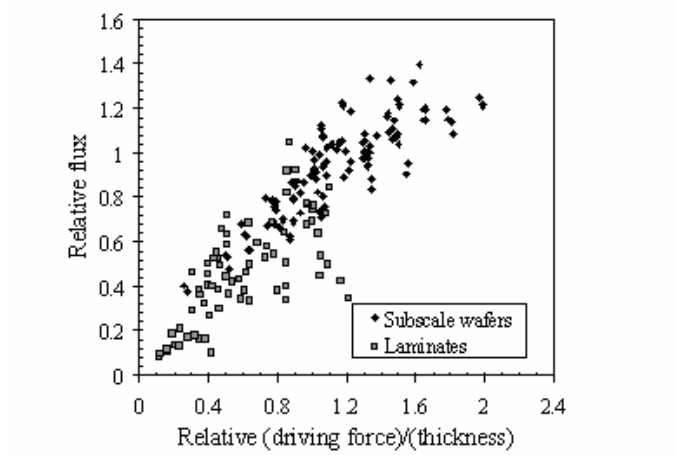

Figure 5. Effect of relative membrane geometry on performance.

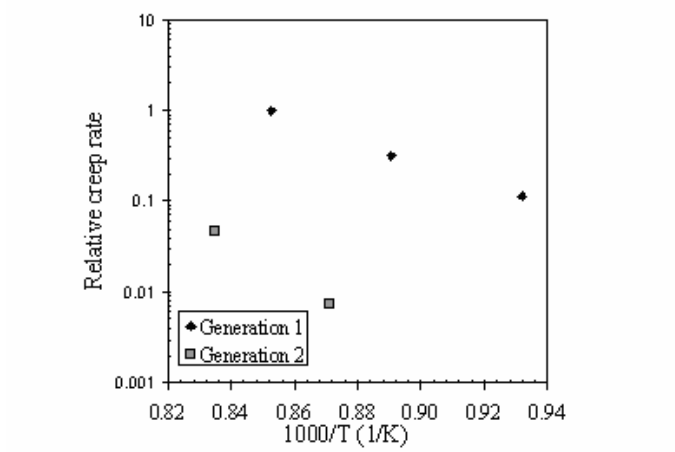

Figure 6. Improvement in creep properties with material development.

Conclusions

The commercial flux target can be reached and exceeded when commercial driving force conditions and separating layer thickness are used. The latest generation of membrane materials are an order of magnitude more creep resistant than an earlier generation.

Disclaimer

A significant portion of this report was prepared by Air Products and Chemicals, Inc. pursuant to a Cooperative Agreement partially funded by the United States Department of Energy, and neither Air Products and Chemicals, Inc. nor any of its contractors or subcontractors nor the United States Department of Energy, nor any person acting on behalf of either:

1. Makes any warranty or representation, express or implied, with respect to the accuracy, completeness, or usefulness of the information contained in this report, or that the use of any information, apparatus, method, or process disclosed in this report may not infringe privately owned rights; or

2. Assumes any liabilities with respect to the use of, or for damages resulting from the use of, any information, apparatus, method, or process disclosed in this report. Reference herein to any specific commercial products, process, or service by trade name, trademark, manufacturer, or otherwise, does not necessarily constitute or imply its endorsement, recommendation, or favoring by the United States Department of Energy. The views and opinions of authors expressed herein do not necessarily state or reflect those of the United States Department of Energy.

This paper was written with support of the U.S. Department of Energy under Contract No. DE-FC26-98FT40343. The Government reserves for itself and others acting on its behalf a royalty-free, nonexclusive, irrevocable, worldwide license for Governmental purposes to publish, distribute, translate, duplicate, exhibit and perform this copyrighted paper.

OXYGEN TRANSPORT KINETICS IN MIXED IONIC AND ELECTRONIC CONDUCTING MEMBRANE MATERIALS

Allan J. Jacobson, Susan Wang and Jiho Yoo

Department of Chemistry, University of Houston, Houston, TX

Introduction

Mixed conducting oxides with high oxygen ion conductivities have potential application in membrane reactors that can produce synthesis gas ($CO + H_2$) by direct conversion of hydrocarbons such as methane (1, 2). A number of perovskites (1-7) and non-perovskite oxide materials (8-10) have been evaluated for membrane reactors. Many of these compositions suffered from poor stability due to phase changes and differential thermal expansion in low oxygen partial pressures. At the present time, iron based compositions are the materials of choice.

The performance of mixed ionic and electronic conducting oxides (MIECs) in oxygen separation membranes is related to the oxygen transport kinetics that include contributions from the surface oxygen exchange rate at the gas-solid interface and oxygen diffusion within the bulk material. For MIEC oxides, electrical conductivity relaxation (ECR) is convenient technique with which to study the kinetics. By analyzing the time dependence of the relative change of the conductivity after an abrupt change in the ambient pO_2, the chemical diffusion coefficient and the surface exchange coefficient can be obtained.

The application of ECR to investigate and compare the oxygen transport kinetics of several perovskite oxide materials with the general composition $(La,Sr)(M,M')O_3$ (M = Fe, Co and M' =Cr, Ga, Co) is described. The long-term stability and the effects of CO_2 on the oxygen transport, which are concerns in practical applications, are discussed for the specific case of $La_{0.2}Sr_{0.8}Fe_{0.8}Cr_{0.2}O_3$.

Experimental

Samples. Sample powders were obtained either from Praxair Specialty Ceramics, or prepared in house by either conventional solid-state methods or by self-propagating high temperature synthesis (11). Phase purity was determined by powder X-ray diffraction and by electron microprobe analysis. Dry powder was pressed into a cylindrical shape by cold isostatic pressing at 40,000 psi. Thin disks were cut using a diamond saw and sintered in air with heating and cooling rates of 1 ºC/min. The sintered disks typically had a density of >95% of the theoretical density. In typical experiments, rectangular samples were used for conductivity relaxation experiments. These were cut from the sintered disks and wound with 4 gold wires (0.025mm, Alfa), which serve as electrodes.

Electrical Conductivity Relaxation. The theory of ECR of MIEC oxides has been described previously (12). Model calculations show that a square bar geometry gives better sensitivity than a thin plate (13). When the ratio of the length to the width is greater than ~10, the sample can be approximated as infinitely long. Analysis of the transients, gives D_{chem} and k_{chem}, the transport parameters measured in a chemical process. They are related to the equilibrium values for MIEC oxides with dominant electronic conductivity by $D_{chem} = \Gamma_O D_{O=}$ and $k_{chem} = \Gamma_O k_{ex}$ where $D_{O=}$ is the self-diffusion coefficient of the oxygen ion, k_{ex} is the surface exchange coefficient at thermal equilibrium and Γ_O is the thermodynamic factor.

Electrical conductivities were measured using the 4-probe method with gold wires as current and voltage electrodes. A model SR830 dual-phase lock-in amplifier (Stanford Research System) with built-in oscillator was used for applying and measuring the AC voltages at a frequency of 13 kHz in the ECR experiments. Instrument control and data acquisition used LabVIEW (National Instruments).

The volume of the ECR apparatus was minimized by using a fine quartz tube (i.d. = 1.0 mm, length = 15 cm, volume = 0.47 cm^3) as the gas inlet line. Gas switching between two streams at the same measured flow rate was performed using a 4-way valve connected to the inlet line through a 3 cm long tube (i. d. = 3 mm). A 6-bore Al_2O_3 tube was used as the sample holder. The holder accommodates a sample with maximum length of 2.5 cm and holds all four gold electrodes and an R-type thermocouple. The gas change-out time in the ECR apparatus was determined by measuring the high temperature conductivity relaxation behavior of a thin film of $La_{0.5}Sr_{0.5}CoO_{3-x}$ (LSCO, ~5000Å) prepared on a $LaAlO_3$ single crystal substrate by laser deposition (14). The results show gas change-out times of <1 second.

Results and Discussion

Oxygen transport kinetics. The results of electrical conductivity measurements for two compositions, $La_{0.5}Sr_{0.5}MO_{3-x}$ (M= Fe, Co), are shown in Figure 1. Because of the differences in conductivity between the two compositions and in the relative magnitudes of D and k, it is not possible to obtain data over the same temperature range. Nevertheless, a comparison can be made. The difference in the diffusion coefficient between the iron and cobalt composition arises in part from differences in the thermodynamic factor but mainly from differences in the vacancy concentration. The extrapolated vacancy diffusion coefficients at the same temperature, determined from the relation $c_O D_O = c_V D_V$, are closely similar (30% difference at 750 °C). In contrast, the equilibrium surface exchange coefficient for $La_{0.5}Sr_{0.5}CoO_{3-x}$ is an order of magnitude higher than for $La_{0.5}Sr_{0.5}FeO_{3-x}$, a difference that cannot be explained solely by the difference in vacancy concentrations.

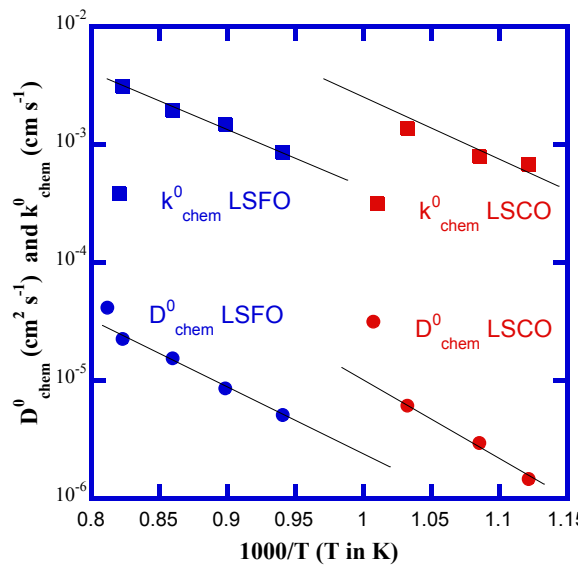

Figure 1. A comparison of the chemical diffusion coefficients and surface exchange rates for $La_{0.5}Sr_{0.5}MO_{3-x}$ (M= Fe, Co), the 0 suffix refers to 1atm oxygen partial pressure.

Long-term performance and surface segregation. The long-term behavior of the oxygen transport kinetics of $La_{0.2}Sr_{0.8}Cr_{0.2}Fe_{0.8}O_{3-x}$ was studied by measuring periodically the relaxation behavior for 1% - 5% O_2 gas switches over a period of

12 d. While the measured surface exchange coefficient was found to decrease monotonically with time, the oxygen chemical diffusivity remained almost constant. The bulk electrical conductivity also remained constant as seen in Figure 2. The behavior indicates a time dependent slow transformation in the sample, which affects the surface exchange kinetics adversely but does not affect bulk transport.

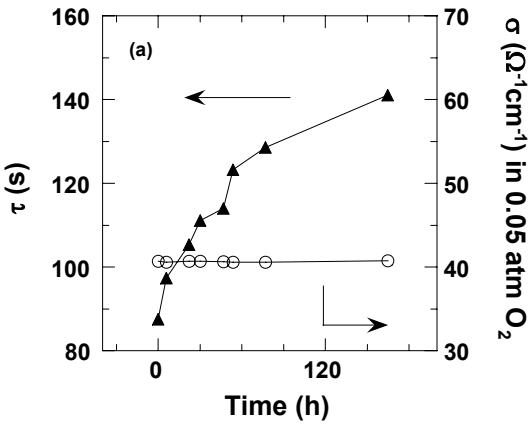

Figure 2. Long time variation of the ECR time constant and the total conductivity for $La_{0.2}Sr_{0.8}Cr_{0.2}Fe_{0.8}O_{3-x}$.

XPS data (15) indicate that the change in the surface exchange kinetics is due to time variations in the surface concentrations of chromium and strontium. Assuming that a varying surface concentration of chromium is responsible for the observed behavior and using a simple analysis of the kinetics of segregation, the diffusivity of chromium can be estimated. We assume that the measured surface exchange coefficient is inversely proportional to concentration of chromium in the surface layer, the thickness of the surface layer is the order of 2 - 3 nm as estimated from the XPS results, and that evaporation of chromium species at the present experimental conditions are negligible. Figure 3 shows the time dependent changes in surface exchange coefficient fitted to the model. The chromium diffusivity, D, in $La_{0.2}Sr_{0.8}Cr_{0.2}Fe_{0.8}O_{3-x}$ is estimated to be ~10^{-19} cm^2/sec at 821 °C.

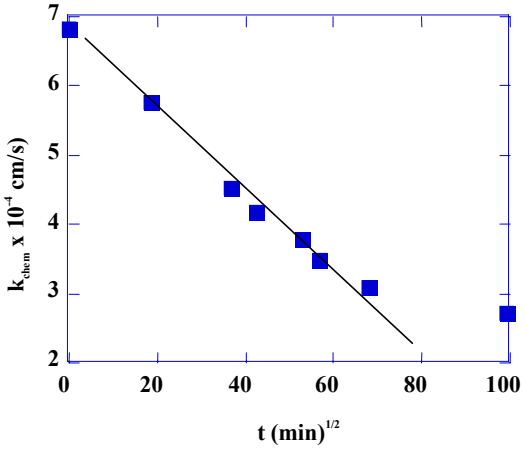

Figure 3. Dependence of k_{chem} at 821°C for $La_{0.2}Sr_{0.8}Cr_{0.2}Fe_{0.8}O_{3-x}$.

A decrease in surface exchange coefficient was also found in a separate study where gas switches where made between 5% O_2 and 15% O_2 over a period of 12 d. During this period, the sample was also exposed to pure CO_2 for short periods. As seen in Figure 4, the exposure of CO_2 temporarily accelerates surface kinetics of the sample. However, the exchange kinetics revert to the original behavior after a short time once the CO_2 is removed.

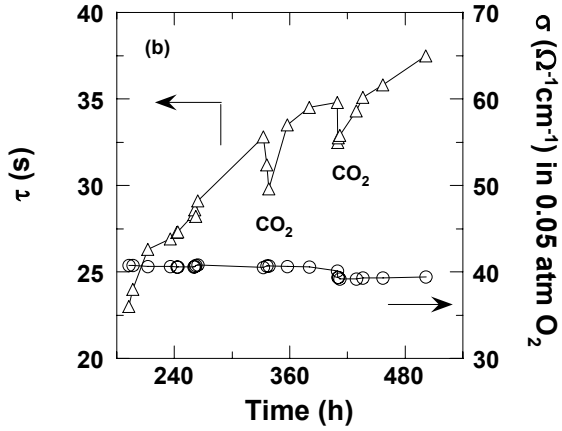

Figure 4 Influence of CO_2 on the ECR time constant and the total conductivity for $La_{0.2}Sr_{0.8}Cr_{0.2}Fe_{0.8}O_{3-x}$ at 821 °C.

Conclusions

Electrical conductivity relaxation is shown to be a useful technique for the determination of the transport properties of mixed electronic ionic conducting membrane materials. Results for $(La,Sr)(M,M')O_3$ (M = Fe, Co) are compared and the long-term stability and the effects of CO_2 are discussed for the specific case of $La_{0.2}Sr_{0.8}Fe_{0.8}Cr_{0.2}O_3$.

Acknowledgement. The work was supported by the Department of Energy, DOE-DE-FC26-99FT40054 and the Robert A. Welch Foundation

References

(1) Mazanec, T. J., *ElectroPox Gas Reforming, Ceramic Membranes*; Anderson, H. U.; Khandkar, A.C.; Liu, M. Eds.; The Electrochem. Soc., 1997; pp 16-28.
(2) *The CRC Handbook of Solid State Electrochemistry*, Eds. P. J. Gellings, P. J.; Bouwmeester, H. J. M., Eds.; CRC Press, USA, 1997, p 413.
(2) Mizusaki, J.; Tabuchi, J.; Matsuura, T.; Yamauchi, S.; Fueki, K. *J. Electrochem. Soc.* **1989**, *136*, 2082.
(4) Kilner, J.A.; De Souza, R.A.; Fullarton, I. C. *Solid State Ionics* **1996**, *86-88*, 703.
(5) Stevenson, J. W.; Armstrong, T. R.; Carneim, R. D.; Pederson L. R.; Weber, W. J. *J. Electrochem. Soc.* **1996**, *143*, 2722.
(6) ten Elshof, J. E.; Lankhorst, M. H. R.; Bouwmeester, H. J. M. *Solid State Ionics* **1997**, *99*, 15.
(7) ten Elshof, J. E.; Lankhorst, M. H. R.; Bouwmeester, H. J. M. *J. Electrochem. Soc.* **1997**, *144*, 1060.
(8) Ma, B.; Balachandran, U.; Park, J.-H.; Segre, C. U. *Solid State Ionics* **1996**, *83*, 65.
(9) Kim, S.; Yang, Y. L.; Christoffersen, R.; Jacobson, A. J. *Solid State Ionics* **1998**, *109*, 187.
(10) Lee, T. H.; Yang, Y. L.; Jacobson, A. J.; Abeles, B.; Zhou, M. *Solid State Ionics* **1997**, *100*, 77.
(11) Ming, Q.; Nersesyan, M.; Wagner, A. L.; Ritchie, J.; Richardson, J. T.; Luss, D.; Jacobson, A.J.; Yang, Y.L. **1999**, *122,* 113.
(12) Yasuda, I; Hishinuma, M. *Solid State Ionics* **1995**, *80*, 141.
(13) Wang, S.; Abeles, B.; Jacobson, A. J. *Mater. Res. Soc. Symp. Proc.* **1999**, *548*, 557.
(14) Kim, S.; Wang, S.; Chen, X.; Yang, Y. L.; Wu, N.; Ignatiev, A.; Jacobson, A. J.; Abeles, B. *J. Electrochem. Soc.* **2000**, *147*, 2398.
(15) van der Heide, P.A.W.; Wang, S.; Verma, A.; Jacobson, A. J. to be published.

ISOTOPE TRANSIENTS ON OPERATING LSCO OXYGEN SEPARATION MEMBANES

Charles A. Mims and Linjei Hu

Department of Chemical Engineering and Applied Chemistry
University of Toronto, Toronto Ontario CANADA M5S 3E5

Introduction

Mixed oxide ion-electron conducting (MIEC) oxide materials are under intense development for use in membrane processes for air separation, syngas generation and others (1). The performance of the membrane depends on the surface and bulk properties of the material and the membrane geometry. The membrane operates under an oxygen potential gradient, which is in turn shaped by the various surface and bulk resistances.

Isotope exchange - depth profiling (IEDP) has been extensively used to study the kinetics of oxygen activation at the surface and diffusion in the bulk of oxides in the absence of a chemical gradient.(2). Surface exchange coefficient, k*, and tracer diffusion coefficient, D*, are extracted from the isotope distribution profile. Other relaxation techniques measure similar properties under small potential gradients. These techniques provide an accurate and relatively simple way to get valuable parameters for mixed ion-electron conducting (MIEC) materials. Since these parameters are measured under gradientless conditions for oxygen and net oxygen flux is zero, the behavior of the membrane with oxygen chemical gradient may be different from those that are calculated from k* and D*. Conversely, it is not easy to determine the relative contributions of surface and bulk resistances under operating conditions.

Dynamic isotope tracing techniques, which are extensively used in catalysis research, involve placing isotopic labels on reacting atoms. Monitoring these labeled atoms as they become incorporated into reaction intermediates and eventually into reaction products will yield information on the steady state operation of the membrane under a gradient and allow surface and bulk resistances to be separated. An experiment is typically performed by establishing two identical reactant streams (one is fed to the reactor and the other is vented), except that the isotopic labels of one or more of the constituents are different. The transient is initiated by switching feeds while maintaining steady state reactions and monitoring the change in the isotopic composition of products.

We report results here from the first study of isotope transients on MIECs to investigate the oxygen transport parameters across a functioning the membrane. A a pulse of $^{18}O_2$/Ar while maintaining a constant O_2 partial pressure, was introduced to the air side of the sample while maintaining the steady state conditions. The ^{18}O diffuses into the sample as a result of both the existing ^{18}O chemical gradient and oxygen gradient across the membrane. The isotopic ratio $^{18}O/^{16}O$ in the permeated O_2 reveals the residence time distribution of the oxygen transiting the membrane. By fitting the obtained isotopic composition in the permeated oxygen using mathematical models, the surface activation rate, its degree of reversibility (related to the potential drop across the surface, and the bulk mobility under operating conditions can be obtained.

Experimental

The tubular sample of $La_{0.6}Sr_{0.4}Co_{0.2}Fe_{0.8}O_{3-\delta}$ was approximately 6.2 mm outer diameter, 1.0 mm wall thickness, and 8.8 mm length. The both sides of the tube were ground with 800 grit silicon carbide paper to a desired flat and smooth surface. Prior to installing into the reactor, the sample was rinsed and ultrasonically cleansed with distilled water and then acetone to remove any residue and contaminant.

Experimental setup. Figure 1 illustrates the configuration of the internals of the reactor. To minimize the undesired wall reactions, all parts which may contact gas mixture inside and outside of the perovskite membrane in the hot zone of the reactor are made of quartz except the gold seal. The temperature of furnace was controlled by a Omega Type I/32 PID temperature controller with an accuracy of ±0.5 ^{o}C. Before and after each measurement, the temperature of the sample was measured by a K-type thermocouple as illustrated in Figure 1.

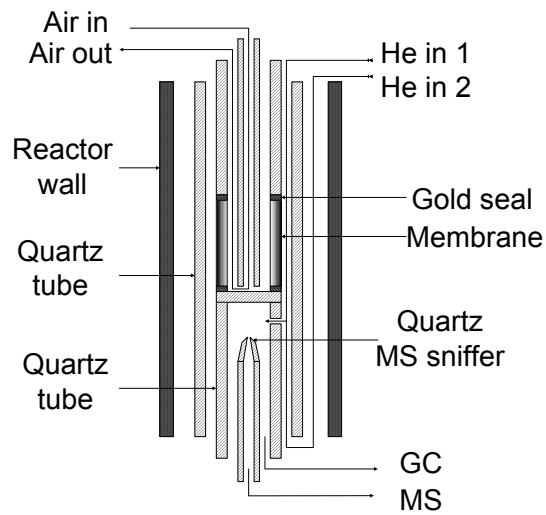

Figure 1: Experimental apparatus for isotope transients

Oxygen permeation measurements. The sample was heated at a ramping rate of ca. 2 ^{o}C/min to 750 C. The flow rates of air and the sweeping gas He were basically 20 ml/min in our experiments. As illustrated in Figure 1, another He flow (He in 2) was introduced to purge the dead volume between the reactor wall and outer quartz tube, and the flow rate is fixed at 5.0 ml/min. The composition of sweeping gas was analyzed by a SRI 8610C Gas Chromatograph with a 5A molecular-sieve column. A Helium Ionization Detector (HID) was used to measure the oxygen and nitrogen content.

Oxygen isotope transient experiments. The synthesized air, O_2:N_2 = 20:80, was provided by Praxair Products Inc.. The ^{18}O-containing gas, $^{18}O_2$:Ar = 20:80, was supplied by Icon Isotopes. The ^{18}O isotope purity is 97%. The sample was equilibrated at the experimental conditions for at least 24 h in the natural abundance isotope version of the gas mixture. Following this equilibration the gas mixture O_2/N_2 in the air side of the membrane was switched to the ^{18}O containing mixture (^{18}O2/Ar) and maintained for 15 min or 60 min. The flow rates of $^{18}O_2$/Ar were 1-3 ml/min for the duration of isotope pulse to avoid depletion of the isotope oxygen, which depend on the experimental temperature and oxygen flux. A "pulse" of ^{18}O was then obtained in the oxygen-rich side. At the end of the pulse, the gas mixture was switched back to O_2/N_2 and kept the same experimental conditions as before for 4-6 days. The sweeping gas was analyzed with an on-line UTI Model 100C Quadrupole Mass Spectrometer (MS). The oxygen fluxes were obtained simultaneously by an on-line GC analysis.

Results

Modelling. The results were simulated by 1-D constant properties computer model to extract values for the transport parameters. The following equations govern the isotope transport:

Transport from gas to air surface (z=0):

$$(k_f^{'}\chi_g^* - k_r^{'}\chi_s^*\Big|_{z=0} = \frac{j_O}{C_O}\frac{\partial\chi^*}{\partial z}\Big|_{z=0} - D_O\frac{\partial^2\chi^*}{\partial z^2}\Big|_{z=0} \quad (1)$$

where * denotes the infusing isotope, χ^* is the isotope fraction, C (mol/cm^3) the bulk oxygen atom concentration, j mol/cm^{2}s the oxygen atom flux, D (cm^2/s) is the oxygen diffusion coefficient, k(cm/s) is the transfer coefficient, f = forward, r = reverse. The surface corresponds to $z = 0$. The net oxygen flux is given by C times (k_f - k_r) and the subscripts g and s denote gas and surface respectively. L is the membrane thickness.

Transport in the membrane: (0 # z # L)

$$\frac{\partial\chi_f^*}{\partial t} = D_O\frac{\partial^2\chi_f^*}{\partial z^2} - \frac{j_O}{C_O}\frac{\partial\chi}{\partial z} \quad (2)$$

and the isotope transport from membrane to the helium sweep side is simply given by $j_O^*\chi_f^*\Big|_{z=L}$.

Figure 2 shows the results of simulations of ^{18}O isotope transients delivered to the sweep side of an oxygen separation

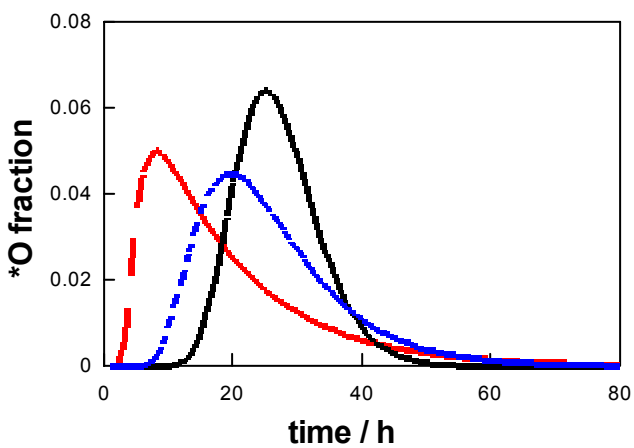

Figure 2: Simulations of isotope transient son delivery (helium sweep) side of an operating membrane at similar flux conditions to this study. Oxygen diffusion coefficient decrease for curves peaking from left to right – 10^{-7}, 10^{-8} and 10^{-9} cm^2 s^{-1} respectively. Oxygen molecule flux = 0.05 sccm for 1 cm^2 area. Air side surface reaction was 50% reversible (forward rate of oxygen activation was twice that of the reverse.

membrane. As the diffusion coefficient is reduced, the residence time distribution becomes more and more "plug-flow"–like. Another interesting observation from the simulations is that the shape changes as the reversibility of the air-side reaction changes, thus providing a measure of the reversibility of the air-side surface reaction. The reverse of the air-side oxygen activation provides another path for the isotope to leave the membrane and shortens the residence time distribution of the isotope.

Isotope transient data. Figure 3 presents the time dependent ^{18}O fraction of permeated oxygen in the oxygen-lean side after introducing a pulse (15 min) of 20% $^{18}O_2$ (97% isotopic purity at atom) at 800 ^{0}C . Also shown is a fit to the data by the model described above with the following values. D_O = 1.3 x 10^{-7} cm^2 s^{-1}, $k_{forward}$ = 4 x 10^{-6} cm s^{-1}, $k_{reverse}$ = 2.6 x 10^{-6} cm s^{-1}. The net flux is 0.05 sccm per cm^2. The substantially reversible surface activation rate and the bulk diffusion coefficient are consistent with IEDP measurements on the same material ().

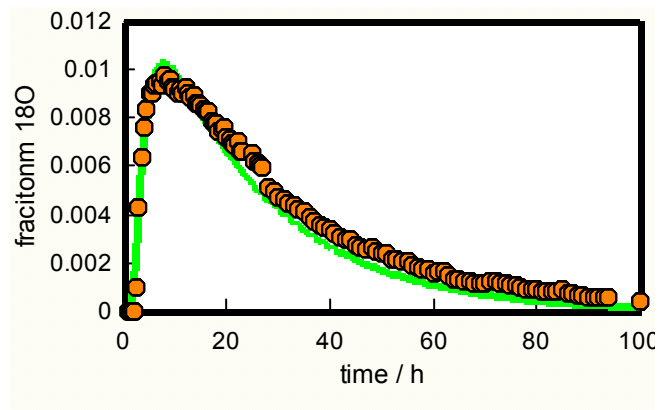

Figure 3: Isotope transient ($^{18}O_2$) on operating membrane. Solid line is given by 1-D model described in text. Natural abundance (0.002) has been subtracted.

Conclusions

The reversibility of the surface reaction together with a finite value fit to the diffusion coefficient shows that both the surface and bulk processes contribute to the overall resistance to oxygen flux through this membrane. The characteristic distance D*/k* measured for this material in IEDP experiments (2,3) is similar to the membrane thickness used here and the substantial reversibility seen in both processes here is consistent with the modest oxygen potential gradients. Future experiments will examine the large gradients present in membranes for syngas production.

Acknowledgments. Support for this work from the UAF membrane consortium under DOE-DE-FC26-99FT40054, the NSF-MRSEC program, and the Natural Sciences and Engineering Research Council (Canada) is gratefully acknowledged.

References

(1) Bouwmeester, H. J. M. and Burggraaf, A. J., Dense Ceramic Membranes for Oxygen Separation. [14], The CRC Handbook of Solid State Electrochemistry, 481-553. Gellings P.J. and Bouwmeester H. J. M, Editors, CRC Press 1997

(2 J.A. Kilner, B.C.H. Steele, L. Ilkov, *Solid State Ionics* **12** (1984) 89. J.A. Kilner, R.A. De Souza, I.C. Fullarton, *Solid State Ionics* **86-88** (1996) 703.

(3) Lane, J.A., Benson, S.J., Waller, D. Kilner, J.A., *Solid State Ionics* 121 (1999) 201: Xu, J.X., Thomson, W.J., *Chemical Engineering Science* **54** (1999) 3839: Li, S. J. , *et.al. J. Membrane Science* **166** (2000) 51.

ATOMIC SCALE CHARACTERIZATION OF OXYGEN VACANCY ORDERING IN OXYGEN CONDUCTING MEMBRANES

R.F. Klie*, N. D. Browning[1]

* Brookhaven National Laboratory, Dept. of Applied Science, Upton, New York 11973

[1] University of Illinois at Chicago, 845 West Taylor Street, Chicago, IL 60607-7059

Introduction

Mixed conductors have been the focus of many studies in the last decade, leading to a detailed understanding of many of the macroscopic bulk properties of these materials.[1] Of particular interest are perovskite oxides for applications as oxygen conducting membranes in syngas reactors. However, there are still many issues that need to be addressed on the fundamental atomic scale. In particular, although the reduced low temperature phase in rare earth perovskite oxides is commonly explained in terms of ordered Brownmillerite (BM) structured micro-domains, the transition to the high temperature phase remains elusive. Here we present an investigation of this transition through atomic resolution annular dark field imaging and electron energy loss spectroscopy of (La, Sr)FeO_3 prepared under different reducing conditions.

Experimental

The STEM and EELS results presented in this paper were obtained using a JEOL 2010F STEM/TEM, having a Schottky field emission gun-source and being operated at 200 kV.[2,3] The microscope is equipped with a standard ultra high resolution objective lens pole piece, a JEOL annular dark-field detector and a post column Gatan imaging filter (GIF).[2] The lens conditions in the microscope were defined for a probe size of 0.2 nm, with a convergence angle of 13 mrad and a collection angle of 52 mrad. With these settings the Z-contrast image is incoherent; i.e., a direct image of the interface is acquired. The experimental setup for this microscope allows us to use low-angle scattered electrons that do not contribute to the Z-contrast image for EELS.[4] As the two techniques do not interfere, Z-contrast images can be used to position the electron probe at the desired spot in the sample to acquire spectra.[5,6,7] This allows us to obtain direct images (spatial resolution of 2 Å) of the atomic structure and to correlate this information with the atomically resolved EELS information (acquisition time 3s, energy resolution 1.2 eV). The in-situ heating experiments performed here utilize a double tilt heating stage with a variable temperature range between 293 K and 1273 K. If the holder is operated above 773 K a water recirculation must be connected, to prevent heat transfer through the rod of the stage. Turbulent flow of water through the recirculation system makes it impossible to achieve atomic resolution for temperatures higher than 773K. The oxygen partial pressure in the microscope column is $P_{O_2} \sim 5*10^{-8}$ Pa during the experiment, which means that at 724 K the oxide samples are in a highly reducing environment. [8]

For (La, Sr)FeO_3 we are primarily interested in the bonding between oxygen and the B-site transition metal atoms. To investigate this, the near edge fine structure of the oxygen K-edge contains valuable information about the nearest neighbor bonding (O 2p with metallic 3d) and the hybridization with the metal sp band.[9] The formal valence-state of the transition metal elements in the structure can be determined from the analysis of the L_2 and L_3 white lines that are visible due to the spin-orbit interaction. More specifically, the L_3 and L_2 lines are the transition of $2p^{3/2} \rightarrow 3d^{3/2}3d^{5/2}$ and $2p^{1/2} \rightarrow 3d^{3/2}$, respectively. However, it needs to be stated that the computed L_3/L_2 white line intensity ratios, used to determine the numerical value for the valence must be compared either with results from the literature or parametric fits calculated from well known materials under similar conditions, to convert the intensities into numerical ionization values.

Results and Discussion

In **Figure 1**, a Z-contrast image of the atomic structure of the sintered but untreated material is shown. The cubic symmetry is clearly visible and the brightest spots represent the mixed (La, Sr), whereas the less bright spots are the Fe-O columns. The pure O-columns are not visible in the image due to the low scattering amplitude of oxygen compared to La, Sr, and Fe. **Figure 1a** also shows a planar defect, commonly found the bulk of the untreated material. Upon investigation, the atomic structure of these planar defects, which run irregularly through the grains, can be identified. The regular lattice above and below the dark line is shifted by half a unit-cell along the direction of this dark feature. EEL spectra taken from the center of the dark line and the adjacent bulk exhibit a significantly lower La M-edge signal (**Figure 1b**). In addition to the decrease of La-M edge intensities, the Fe-$L_{3,2}$ ratio as well as the oxygen K-edge pre-peak is decreased in the defect. The measured Fe valence in the dark lines of 2.4±0.1, as well as the changed O K-edge fine structure originates from the different local atomic environment.

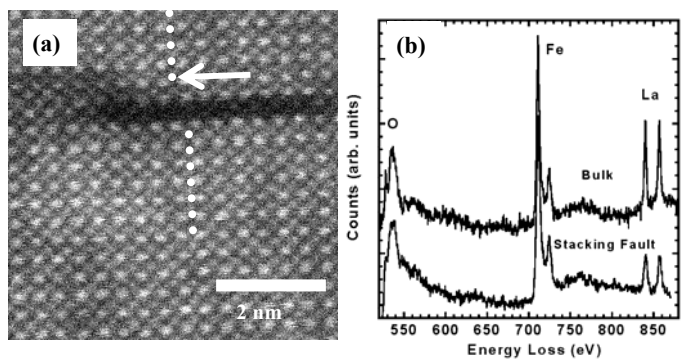

Figure 1. a) Z-contrast image of sintered (La, Sr)FeO_3 [001] showing the cubic perovskite structure and one dark line, revealing the internal structure of this feature and the shift between the adjacent bulk crystal structures. b) EEL spectra from the stacking fault and from the surrounding bulk. The spectra are normalized to the Fe-$L_{3,2}$ intensities.

Figure 2 shows a Z-contrast micrograph of the material after heating to 1023 K in an oxygen partial pressure of $P_{O_2} = 10^{-2}$ Pa for 27h. Ordered structures in the form of contrast variations in every second column can be seen, and one can show that the dark columns represent the reduced valence columns (+2.6± 0.1), whereas in the bright columns the valence is close to +(2.8± 0.1). The results indicate that in the dark FeO_2 lines the point-defect concentration is higher.

After the sample was heated and allowed to stabilized at 724 K for 12 hours in the microscope, the contrast changes appear more distinct in the sample, and can be clearly identified in the

power spectrum of the acquired image (**Figure 3**). We can now observe small micro-domains of 8-16 unit cells width (2.4 nm – 4.8 nm); with no preferential orientation of the boundaries. Note that the EEL spectra at elevated temperatures from the dark and the bright FeO_2 columns (**Figure 3b**), normalized to the intensity of the La M-edges, display different fine structures and intensities of the O K- and Fe L-edges. The pre-peak of the O K-edge in the dark columns of the domains is reduced with respect to the bright ones, indicating a decreased number of available O 2p - Fe 3d orbits, and therefore a lower valence. Also the Fe white line intensity ratios reveal a reduction of the transition metal valence from +(2.8 ± 0.1) in the bright to +(2.3 ± 0.1) in the dark columns respectively. Additionally, the intensity ratio of the iron L-edge to the oxygen K-edge is increased in the dark lines by 10% with respect to the bright line ratio, again showing the lower oxygen content in the dark columns.

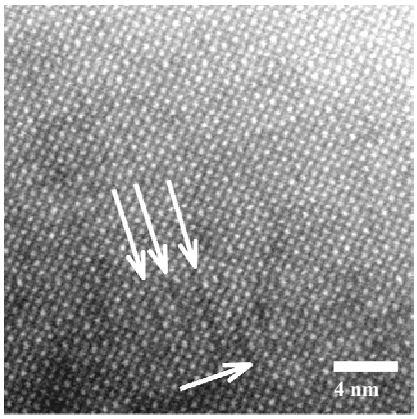

Figure 2. Z-Contrast image showing marked change in contrast in every second FeO_2 column

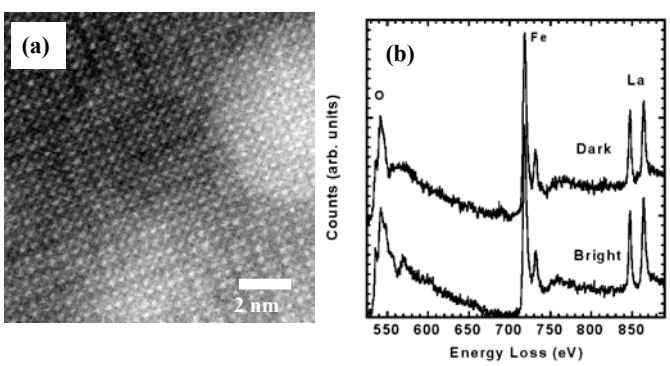

Figure 3. a) Z-Contrast image at 724 K with clearly visible ordered domain. b) EELS of bright and dark columns in LSFO [001] at 724 K.

Following this characterization, the reducing conditions were increased by heating the specimen to 1074 K for 3 hours at an constant oxygen partial pressure of $P_{O_2} = 5*10^{-8}$ Pa in the microscope. **Figure 4** shows a Z-contrast image in which the ordered domains and the interwoven domain-boundaries can be seen very clearly. (Note: The picture appears blurred due to the increased contamination layers from the heating process.) This image suggests that the size of the micro domains is increased dramatically in this environment (~20nm), and also the domain boundaries are more clearly defined. The stronger distinction between the bright and dark columns suggests that the difference in the oxygen concentration between the bright and the dark lines is even higher than before the reduction process. An analysis of the acquired EEL spectra at 724 K reveals that the already reduced, dark columns have an even lower iron valence of +(2.0± 0.1), whereas the bright columns remain at a constant valence of +(2.9± 0.1).

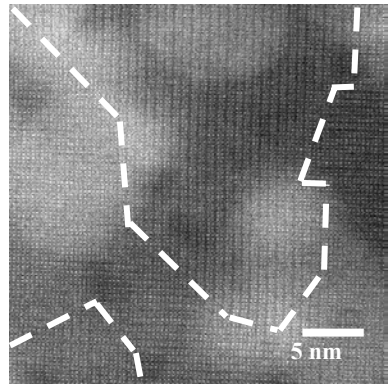

Figure 4. Z-Contrast image of LSFO at 724 K after heating at 1073 K, showing the change in domain size. The diffuse white blobs in the image are caused by contamination built up on the surface during the heating process.

Figure 5 shows the micrographs of the sample at room temperature, after a heat treatment of 1073K at 10^{-10} Pa. The image displays some features that were not observed in the bulk of the untreated or lesser-reduced samples. Two dark lines of one unit cell width, separated by one bright line in the center are oriented along the [010] direction. The EEL data acquired from the dark feature and from the surrounding bulk material is shown in **Figure 5b**. Due to the different Fe/La ratio in these spectra, all the spectra are now normalized to the Fe L-edge intensities. The most striking difference between the bulk spectra and the spectra taken from the defect structure is the drastic decrease in the La M-edge intensity. Hence, it appears to be most likely that the dark lines are caused again by a stacking fault, containing a double layer of FeO_2. The different atomic environment in the stacking fault also gives rise to the observed difference in the O K-edge fine structure. Parallel to these stacking faults the reduced columns form huge domains.

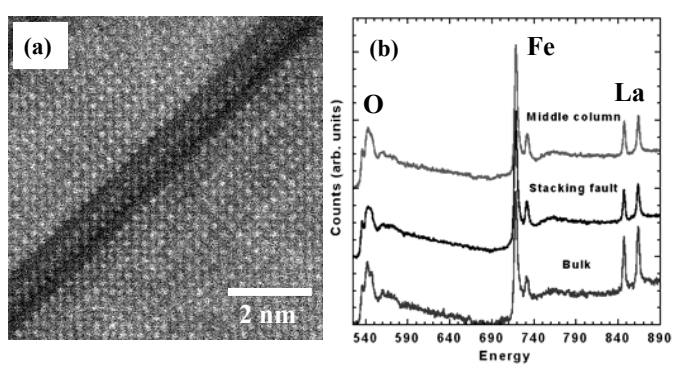

Figure 5. a) Z-Contrast image of LSFO, previously treated at 1073 K in 10^{-10} Pa showing stacking faults and revealing its structure The sandwiched structure of one brighter atomic column surrounded by two darker one can clearly be identified. b) EELS of LSFO from bulk and stacking fault, normalized to oxygen and iron core- loss edge intensity.

Discussion

The atomic scale analysis of (La, Sr)FeO_3 under various ambient pressure and temperature conditions illustrates the formation and evolution processes of ordered vacancy structures in the reduced perovskite oxides. The freshly sintered samples exhibit the ideal cubic perovskite structure in the majority of the grains. However, some grains contain linear stacking faults (**Figure 1**), which can be identified as a Ruddelsden-Popper (RP) phase.[10] These planar defects are usually formed in connection with the planar-type accommodation of excess alkaline-earth oxides by interleaving slabs of the rock-salt structure within the perovskite structure. Here the images suggest that the planar defect formed in the (La, Sr)FeO_3 ceramic is the interleaving a single-layered FeO_2 block within the perovskite structure with a shear vector ½ [110]. Therefore, the occurrence of these RP-phases is closely linked to a deviation from the ideal ***cation*** stoichiometry of the bulk matrix and compensates for the local non-stoichiometry. Most importantly, these defects are not related to oxygen vacancies and are found not to exist in the subsequently annealed samples. The formation of the RP phase in the as sintered materials is clearly not related to changes in ionic conductivity at elevated temperatures.

In fact, the conductivity of the reduced materials appears to be controlled by the formation of the BM- phase. The Z-contrast and EELS results clearly demonstrate that the planar structures observed under reducing conditions are caused by the ordering of oxygen vacancy clusters in every second FeO_2 column (**Figure 2** and **Figure 3**). At temperatures below 1073 K and $P_{O_2} = 1*10^{-6}$ Pa the oxygen vacancy ordered domains are randomly oriented throughout the bulk. Due to the arbitrary direction of this ordering, with no preferential orientation or clustering into larger ordered domains, the overall diffusion performance of the material should be very high (as the reduced planes act as conductivity channels). A disordered arrangement (on the scale of a few nm) of the ordered vacancies is therefore essential for the high oxygen transport material performance. Under higher reducing conditions (lower oxygen partial pressure and higher temperatures) more oxygen vacancies are created. However, the formation of these vacancies does not occur in every position with identical probability. It seems that the already reduced (dark) columns have an increased vacancy formation rate, or from the opposite point of view, a lower vacancy formation energy. The iron valence data for this situation show a decrease in the iron valence from +2.6 to +2.3. The bright columns on the other hand remain mostly unchanged or even a slight increase in the iron valence (i.e. oxygen content) is measured. This means that the two atomic layers in the same material have a different thermodynamic behavior.

A further increase in temperature causes even more oxygen to diffuse out of the material and leave behind continuously growing micro domains of ordered vacant oxygen lattice sites. The oxygen of the already reduced columns is decreased even further, as the iron valence drops from +2.3 to +2.0, while the unreduced columns (bright) keep their original oxygen content (iron valence +2.8). The dark lines represent a further reduction of the BM-phase. At this point the micro domains start to exhibit a distinct bulk and boundary behavior. Under these conditions the huge ordered domains are assumed to not act as high conductivity paths anymore, as oxygen flow is only possible in one direction. Rather than flowing along the shortest line of the concentration gradient, the oxygen atoms must move in the direction of the ordered domains. The grains oriented perpendicular to the oxygen gradient do not contribute to the overall oxygen current across the membrane and the oxygen ions must flow long a percolative path. Four probe conductivity measurements seem to confirm this hypothesis.

At temperatures of 1350 K and pressure around 10^{-9} Pa the concentration of oxygen vacancies in the dark (vacancy containing) columns reaches a critical value. Here the already highly reduced columns cannot host any more oxygen vacancies without losing their structural integrity. Consequently these columns collapse and form the observed stacking faults of double FeO_2 layers, or the Aurivillius phase. [11] These second phases then act as nucleation sites/barriers to preferentially orient the ordered domains, thereby forming huge ordered domains. Four-probe conductivity measurements under these conditions indicate a sudden drop in the ionic and electronic conductivity, consistent with this effect. The decrease in conductivity can be explained by the preferential flow direction in the bulk of a single grain and that fact that practically no oxygen transport occurs perpendicular to the stacking faults.

Conclusions

In conclusion, the ability to observe the structure, characterize the composition and to map valence state changes at atomic resolution in various thermodynamic environments provides an unparalleled capability to understand the effects of oxygen vacancy ordering in electronic and ionic conducting perovskite. This ordering of oxygen vacancies gives rise to the ionic conductivity of the material at elevated temperatures, but the decline in the conductivity can be explained by the progressive growth of the ordered domains. Although we are not able to acquire atomic resolution images at temperatures higher than 724 K, we now have the opportunity to test the predictions of conventional defect chemistry on the atomic scale. The results presented here clearly show that the oxygen formation energy is not constant from one atomic column to another: the defect chemistry differs dramatically from one FeO_2 layer to the next. Ultimately the structure becomes unstable and forms stacking faults, which will prohibit the oxygen diffusion through this grain. Correlations of this structural analysis with conductivity measurements will exhibit this proposed relationship.

Acknowledgements

This research was sponsored by the U.S. Department of Energy under grant numbers DE-FG02-96ER45610 and No. DE-FC26-99FT40054. The experimental results were obtained on the JEOL 2010F operated by the Research Resources Center at UIC and funded by NSF under grant number DMR-9601796. We thank H.U. Anderson and T.J Mazanec for the provision of the samples and A.C. Palanduz for the discussions and conductivity measurements.

(1) Huang, K, Tichy, RS and Goodenough, JB, *J. Am. Ceram. Soc.* **81**, 2565-75 (1998)
(2) James, EM and Browning, ND, Ultramicroscopy 78, 125 (1999)
(3) James, EM Browning, ND Nicholls, AW, Kawasaki, M, Xin, Y, and Stemmer, S, J. Electr. Micr. 47(6), 561 (1998).
(4) Egerton, RF, Electron Energy Loss Spectroscopy in the Electron Microscope, Plenum, New York (1986).
(5) Browning, ND, Chrisholm, MF, and Pennycook, SJ, Nature 366, 143 (1993)
(6) Nellist, PD, and Pennycook, SJ, Ultramicroscopy 78, 111 (1999).
(7) Jesson, DE, and Pennycook, SJ, Proc. R. Soc. Lond. A 449, 273 (1995)
(8) Klie, RF, and Browning, ND, Appl. Phys. Lett., **77 (23)**, 3737, 2000
(9) Browning, ND, Buban, JP, Moltaji, HO, Duscher, G, Pennycook, SJ, Rodrigues, RP, Johnson, K, and Dravid, VP, *Appl Phys Lett.* **74**, 2638-2640. (1999)
(10) Ruddlesden, SN, and Popper P, *Acta Crystallogr.*, **11**, 54 (1958)
(11) Aurivillius, B, *Ark. Kemi*, **2**, 519 (1950)

A novel heterogeneous catalyst for synthesis of dimethyl carbonate by transesterification

Tong Wei, Mouhua Wang, Wei Wei, Yuhan Sun, Bing Zhong*

State Key Laboratory of Coal Conversion,
Institute of Coal Chemistry,
Chinese Academy of Sciences,
Taiyuan, 030001, P.R.China

Introduction

Dimethyl carbonate (DMC) is an important precursor of polycarbonate resins as well as a useful carbonylation and methylation agent [1]. Because of the negligible toxicity of DMC, it is promising as a substitute for phosgene, dimethyl sulfate, or methyl iodide. DMC can be prepared by the oxidative carbonylation of methanol, carbonylation of methyl nitrite or transesterification of cyclic carbonate with methanol [2,3]. Because of the moderate reaction conditions and the use of CO_2 as raw material, transesterification method, as shown follow, has gained increasing attention in recent years [4]. In our previous work, CaO prepared from the dissociation of $CaCO_3$ at elevated temperature was found very effective for synthesis of DMC from methanol and propylene carbonate, even at room temperature [5]. However, ultra fine CaO prepared from $CaCO_3$ are difficult to be separated from the products and reused. Therefore, CaO-carbon composites were prepared in present paper; the structure, basicity and the catalytic performance of such catalyst were also investigated.

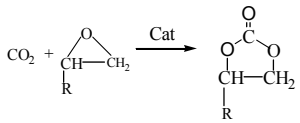

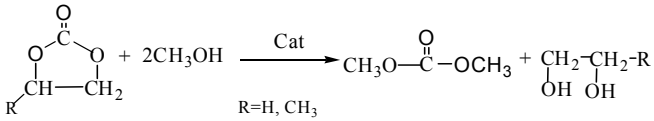

Experimental

CaO was prepared by heating $CaCO_3$ at 1173K for 1 h in N_2 atmosphere. CaO-C composite was prepared from phenolic and $CaCO_3$ (weight ratio=5:1:5), which were grounded and mixed homogeneously. The mixture then was pumped at 20 MPa and solidified at 473K for 10 h in N_2 atmosphere. After being broken into small particles ranging from 60 to 80 mesh, the solidified mixture was activated at 1173K for 1 h in N_2 atmosphere to prepare final catalyst (CaO-C composite, CaO: 50 wt%). The reaction was carried out in a 250 mL flask equipped with reflux condenser, water bath and strong magnetic stirring. The mole ratio of MeOH to PC for all evaluation reaction was 4:1, and the catalyst used were 0.90 wt% (CaO) or 1.80 wt% (CaO-C). The product was analyzed on a gas chromatograph with a TCD after centrifugal separation from the catalyst.

Result and discussion

The XRD shows that the structure of CaO in CaO-C composite hardly changes (both are cubic CaO). As a result, the basic property of CaO-C almost remains as that of pure CaO, which is illustrated by CO_2-TPD of CaO and CaO-C (see **Figure 1**). This indicates that no chemical interaction takes place between carbon and CaO, and carbon mainly acts as the inert supporter. The pore distributions of CaO-C and carbon are illustrated in **Figure 2**. It can be seen that although there are two kinds of pores, micropores and mesopors in CaO-C samples, only mesopores are effective for the catalysis of CaO loaded on carbon.

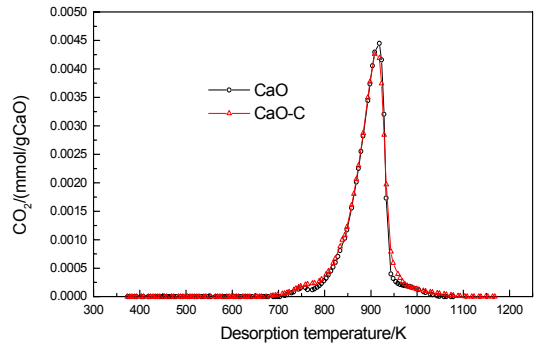

Figure1 CO_2 TPD of CaO and CaO-C

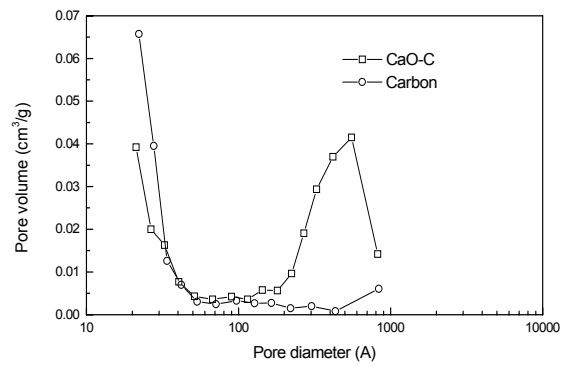

Figure 2 Pore distribution of CaO -C and carbon

The catalytic performance of CaO-C is illustrated in **Figur 3**, and that of CaO is also given for comparison. For CaO-C as catalyst, with the rise of temperature, reaction rate increase greatly, the reaction reach equilibrium in 60 min at 323K. Whereas, the reaction rate over CaO-C catalyst is still slower than that over pure CaO. Because the crystal structure, base strength and basicity of CaO-C are similar to that of pure CaO, the catalytic performance difference between CaO and CaO-C may come from the mass transfer of them. CaO used in this paper are ultra fine particles with diameter about 10-20nm, and the reaction mainly proceeds on the surface of the powders under strong mixing. Thus the reaction rate is intrinsic. Whereas the CaO-C catalyst used is particles of 60~80 mesh, the reaction, therefore, proceeds on outer surface and especially inner surface. Furthermore, this reaction proceeds in liquid phase and the viscosity of reactants and products especially that of propylene glycol are very high under low temperature, which make reactant and product molecules, particularly propylene glycol move very slowly in the pores of CaO-C catalyst. To illustrate the reusability of the catalyst, CaO-C was reused two times (see **Figure 4**), after each reaction the catalyst was separated by filtration and reused. It can be seen that the catalytic activity hardly changes when CaO-C catalyst is used for three times.

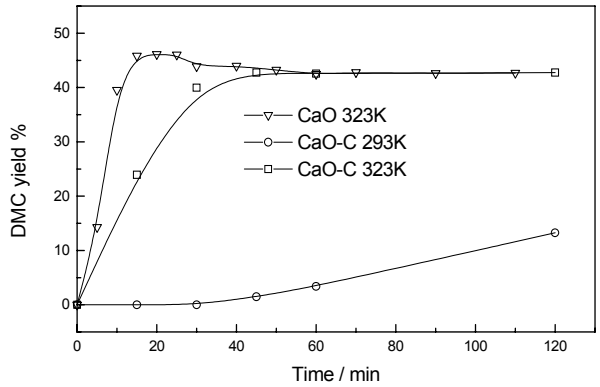

Figure 3 Catalytic performance of pure CaO and 50% wt CaO-C with the same CaO content.

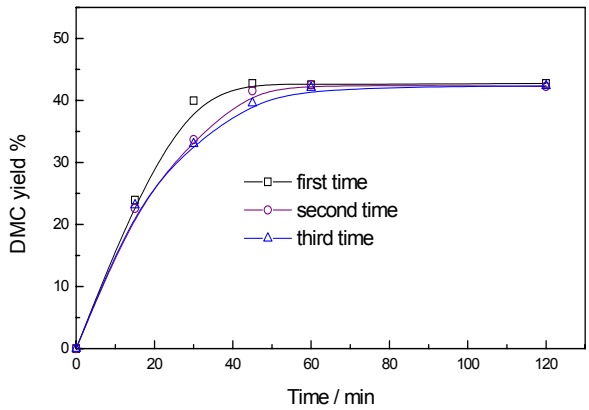

Figure 4 Reusability of CaO-C for synthesis of DMC. temperature: 323K

Conclusion

In conclusion, CaO-carbon composite serves as an efficient and convenient heterogeneous catalyst for synthesis of dimethyl carbonate from methanol and propylene carbonate. Compared with pure CaO, the CaO-C shows the same basic property and then high performance. Furthermore, the catalyst is easily recovered and reused without a significant loss of its efficiency.

References

(1) Sato Y.; Yamamoto T.; Souma Y. *Catal. Letters,* **2000**, 65**,** 123.
(2) Pacheco M. A.; Marshall C. L. *Energy & Fuels,* **1991**, 11**,** 2.
(3) Fujita S.; Bhanage B. M.; Ikushima Y. and Arai M. *Green Chemistry,* **2001**, 3**,** 87.
(4) Ikedal Y.; Sakaihori T.; Tomishige K.; Fujimoto K. *Catal. Letters*, **2000**, 66**,** 59.
(5) Wei T.; Wang M.; Wei W.; Sun Y. and Zhong B. *Preprints of Fuel Chemistry,* **2002**, 312.

Overview of Advanced Gas Separation Technologies for Gasification-Based Energy Systems

Gary J. Stiegel
National Energy Technology Laboratory
U. S. Department of Energy
P.O. Box 10940
Pittsburgh, PA 15236

Jay Ratafia-Brown
SAIC
8301 Greensboro Dr.
McLean, VA 22102

Massood Ramezan
SAIC
P.O. Box 18689
Pittsburgh, PA 15236

INTRODUCTION

Gasification-based energy systems offer a stable, affordable energy supply for the nation, providing high-efficiency conversion and near zero pollutants, and flexibility in the production of a wide range of commodity and premium products. Perhaps just as important, flexible gasification systems provide for operation on low-cost, widely available feedstocks, such as coal, petroleum coke, and biomass. Building on current operating experience, gasification-based technologies can be refined and improved via application of advanced gas separation technologies that are being developed through DOE's programs. Improved gas separations involving oxygen (O_2), hydrogen (H_2), and carbon dioxide (CO_2) can lead to reduced capital and operating costs, as well as improvements in thermal efficiency and superior environmental performance.

Most of the current commercial gasification projects, as well as those planned for the future, are oxygen-blown and require cryogenic air separation units to provide large quantities of oxygen. These gasifiers allow for lower pressure operation, lower synthesis gas (syngas) volumetric flow rates, and easier adaptability to syngas cleanup systems, which helps reduce the size (and cost) of gas cleanup equipment and improves integration into complete gasification and combined cycle power systems. Unfortunately, the air separation unit can typically represent 12 to 15 percent of the total capital cost of a plant and requires a significant amount of auxiliary power for operation. Thus, air separation represents a major area of opportunity for both cost reduction and performance improvement, making it a key part of DOE's gasifier R&D program. DOE is currently sponsoring projects to develop Ion Transport Membrane Technology (ITM) and Oxygen Transport Membranes (OTM), both of which operate at high temperature and provide a high level of thermal integration with the gasification process. DOE studies indicate that they will offer substantial cost reduction compared with the cryogenic air separation methods now employed.

There is also increasing interest in gasification-based hydrogen production, as well as the capture of CO_2 to help reduce emissions of this climate change agent. Therefore, separation of the H_2 and CO_2 syngas constituents may become vitally important to future applications of gasification. These separations will be of increasing importance for integration with downstream processes, such as fuel cells and Fischer-Tropsch conversions, and producing gas compositions suited to these applications. Significant opportunities to improve upon current separation techniques can result from the use of advanced membrane technologies, and much of the work that DOE supports involves further developing membranes to be consistent with the temperature and pressure requirements of power plant applications, as well as required product specifications. Development of a high-pressure, non-membrane CO_2 separation technology is also being supported.

NETL's gas separation projects primarily support DOE's Vision 21 Program. Two industrial teams are focusing on advanced ceramic membranes for air separation and will begin their first major scale-up effort on the path to commercialization. Development of high temperature membranes for hydrogen separation continues, with two new industrial teams leading the effort. Another industry team has been developing palladium-based composite membrane reactor module for separation of hydrogen and carbon dioxide. This paper describes these technologies and associated R&D projects.

DOE's AIR SEPARATION MEMBRANE PROJECTS

The use of oxygen instead of air in gasification processes is currently burdened by: 1) the high cost of oxygen production, and 2) the loss of thermal efficiency inherent in the low temperatures of the current technology - cryogenic separation. In partnership with the DOE's National Energy Technology Laboratory (NETL), two industry teams are developing advanced, ceramic-based membranes that are well suited for thermal integration with the gasification cycles to achieve major cost reductions and efficiency improvements.

Mixed conductors, which transport both oxygen ions and electrons, can be operated in a pressure-driven mode, negating the need for the electrodes and external circuits that are required for purely ionic-type of conductors. The oxygen chemical potential difference across the membrane provides the driving force for oxygen transport. Oxygen atoms adsorb on the cathode (high oxygen partial pressure side of the membrane), and dissociate into atoms/ions as they pick electrons. These ions travel from cathode to anode (the low oxygen partial pressure side) by jumping through lattice sites and vacancies until they reach the anode side of the membrane. On the anode side, the oxygen ions give up their electrons to become atoms/molecules, which are then desorbed into the gas phase. Electrons from the anode side are carried through the membrane to the cathode side to complete the circuit. The rate of oxygen transport through such membranes is temperature sensitive, and can be very fast at high temperatures. Also, since the flux through the membrane is inversely proportional to the thickness, thin films can enable higher fluxes, leading to compact systems. Thus, the ability to produce pure oxygen at high permeation rates, combined with the thermal integration enabled by high temperature operation, results in significant benefits for integration with gasification-based power systems.

Ion Transport Membrane Technology (ITM) – Air Products and Chemicals, Inc.

ITM technology makes use of non-porous, mixed ion and electron-conducting ceramic membranes operating at high temperature, typically 80-900 ^{o}C. The oxygen ions and electrons flow countercurrent through the membrane, with the driving force for oxygen separation being the relative oxygen partial pressure gradient across the membrane. A thin-film, multi-layer membrane structure has been developed to support the pressure load imposed by gasifier operating conditions.

NETL's Ion Transport Membrane (ITM) Oxygen project will develop, scale-up, and demonstrate this technology for large-scale production of oxygen from air with the co-production of power, and for the integration of ITM Oxygen with IGCC and other advanced power generation systems. The R&D program is being conducted in three phases, with the goal being to cut the cost of oxygen production

by approximately one-third compared to conventional, competing technologies and demonstrate all necessary technical and economic requirements for commercial scale-up in the 2006 to 2008 time-frame. Phase I, initiated in October 1998, focused on materials and process R&D and the design, construction, and operation of a 0.1-TPD Technology Development Unit (TDU) to validate the ITM oxygen process concepts, ITM Oxygen integration schemes with IGCC and other advanced power generation systems, and obtain scale-up data. The work successfully addressed all technical and economic requirements for scale-up by reconfirming the economic benefits of ITM technology, a 30-45% reduction in capital cost; exceeding the target flux with a newly developed material by 25% over baseline; achieving an 8-fold increase in the monthly yield of membrane structures; and demonstrating over 2,300 hours of long-time performance and stability of thin-film membrane structures in several experiments.

The Phase II and Phase III activities will build upon Phase I results to further develop, scale up, and demonstrate the ITM Oxygen technology to an approximately 5-ton-per-day (TPD) design capacity sub-scale engineering prototype facility and a pre-commercial-scale demonstration facility approximating 25-TPD, and obtain materials, engineering, membrane fabrication, operating, performance, and economic data necessary for technology commercialization.

A recent study of IGCC economics, comparing the use of ITM Oxygen technology against a state-of-the-art cryogenic air separation unit (ASU), projects a 7% reduction in overall plant installed capital cost, a 7% improvement in power output, a 35% savings in the installed specific cost of the air separation unit compared to the cryogenic ASU, a 37% improvement in the power requirement of the oxygen plant, and a 2.2% improvement in the overall power plant efficiency.

The project team includes Air Products and Chemicals, Inc., Eltron Research, Inc., Ceramatec, Inc., ChevronTexaco Inc., Concept NREC Inc., McDermott International, Inc., The Pennsylvania State University, and the University of Pennsylvania.

Ceramic Oxygen Transport Membranes (OTM) - Praxair, Inc.

OTM technology is based on ceramic materials that can rapidly and selectively transport oxygen ions at high temperatures (600°C - 1000°C). NETL's OTM project is comprised of a three-year Phase I and two-year Phase II components. The goals are to advance critical technologies for the commercial deployment of OTMs for IGCC oxygen production to enable significant improvements in process economics, efficiency and environmental benefits. Phase I has been completed and has achieved a number of critical milestones. A new, high-performance material has been invented which greatly improves the mechanical properties of the OTM element while maintaining the superior flux performance of an earlier lead candidate. Composite OTM technology capable of high-performance, gas-tight composite OTM membranes capable of sustained operation at 900°C and high-pressure differential has been developed. These elements have demonstrated the production of >99% pure oxygen at fluxes 120% of commercial target in tests conducted at 900°C with a 275 psi pressure differential. A 1000 hr life test and >10 complete thermal cycles were demonstrated on such elements under simulated IGCC conditions with virtually no membrane degradation. Significant progress is also being made in scaling up the manufacturing of the elements. Seal technology has advanced to the point where leak rates are much below commercial target and adverse interactions with the OTM membrane are absent. A multi-element pilot reactor is operational and is being used to understand operational characteristics of the OTM reactor module and validate design concepts for scale-up.

Phase II activities, currently underway, includes advancing OTM reliability to ensure 10-year life, manufacturing of full-size elements for a pilot plant, development of critical components required for efficient thermal and power integration, assessment of advanced process integration concepts, economic modeling and business and marketing studies. This will culminate in the design, construction, and operation of a multi-element pilot reactor that is sufficiently large to confirm scale-up issues, and will feature the elements and design concepts anticipated in the commercial design. It will validate the engineering design basis, startup and shutdown protocols and demonstrate safety, and provide cost data to verify that economic targets are met when scaled to full size. The project team includes Praxair, Inc., and the University of Missouri, Rolla.

DOE's ADVANCED HYDROGEN SEPARATION MEMBRANE PROJECTS

Hydrogen separation in gasification-based systems can be a significant source of low-cost H_2 for use in refineries, as fuel for fuel cells, and for H_2 product gas. These techniques must be suitable for the rapid, selective removal of hydrogen from high-temperature, high-pressure syngas streams, while remaining resistant to chemical impurities such as sulfur. Various ceramic membranes, including both high- and low-temperature membranes, are being tested at laboratory-scale to obtain design and scale-up data.

Mixed-Conducting Dense Ceramic Membranes

Mixed-conducting membranes transport via ion and electron conducting mechanisms. Hydrogen separation is achieved in a non-Galvanic mode without the need for an external power supply to drive the separation, thereby offering potential economic advantages over existing technologies. The membranes are non-porous and therefore, are 100% selective to hydrogen. A hydrogen-permeable membrane must exhibit high electronic and protonic conductivities.

Composite membranes are being developed at Argonne National Laboratories (ANL) containing a metal phase dispersed in a ceramic phase. A preliminary test result using a composite has shown an hydrogen flux of 20 $cm^3/min\text{-}cm^2$ through a 40 micron thick membrane at 900°C using 100% H_2 as the feed gas.

Eltron Research is employing dense ceramic membranes based in part on Eltron-patented materials with a demonstrated ability for rapid proton and electron conduction. Eltron has prepared thick membrane materials that are greater than 95% dense and demonstrated hydrogen separation rates that are roughly 20% of the target (10 $ml/min/cm^2$), and nearly an order of magnitude higher than doped ceramic membranes. These composite materials have been prepared with distinct ceramic and metallic phases by precipitating metal onto a ceramic powder. A tubular-type design concept for this membrane is shown in Figure 1 below.

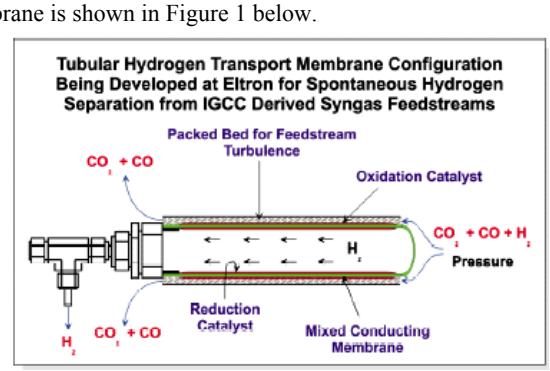

Figure 1

This project was initiated in October of 2000 and will conclude in September 2003 after construction and testing of a sub-engineering scale prototype separation unit. The project team includes Coors Tek, Sud Chemie, McDermott Technologies, and Argonne National Laboratory.

Ion Conducting Ceramic Membranes (ICCM) – ITN Energy Systems

A team led by ITN Energy Systems is pursuing a novel approach to hydrogen separation membrane technology based on Ion Conducting Ceramic Membranes (ICCM) where fundamental engineering material development is fully integrated into module fabrication designs by combining functionally-graded materials, monolithic module concepts and thermal spray manufacturing techniques. The membrane process will also result in a stream of concentrated, sequestration-ready carbon dioxide. (see Figure 2.) The membranes are composed of composites of a proton conducting ceramic and a second metallic phase to promote electrical conductivity.

Functional grading of the membrane components allows for the fabrication of individual membrane layers of different materials, microstructures, and functions directly into a monolithic module. Plasma spray techniques will be used for fabricating ICCM hydrogen separation modules inexpensively, yielding compact membrane modules amenable to large, continuous manufacturing techniques at low costs. The goal of the research program is to demonstrate industrially significant H_2 flux rates of 50 ml/min/cm^2 in a laboratory-scale prototype in the 600 ^oC -900 ^oC temperature range using thin film design. The project was initiated in October of 2000 and will conclude in April 2004 after construction and testing of a sub-engineering scale prototype separation unit. The project team includes Nexant Consulting, Praxair, Argonne National Laboratory, and Idaho National Engineering and Environmental Laboratory.

NETL Hydrogen Gas Separation Program

The overall goal of this project is to develop hydrogen gas separation technology for applications in both the DOE Fuels Program and the Gasification Program. Of particular emphasis are robust hydrogen separation membranes that are suitable for the rapid, selective removal of hydrogen from high-temperature, high-pressure gas streams, while remaining resistant to chemical impurities such as sulfur. This effort comprises four tasks: 1) membrane development, 2) membrane testing, 3) membrane reactor concepts, and 4) computational modeling.

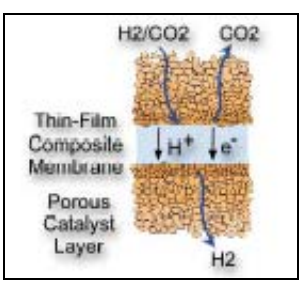

Figure 2 Separation of H2 from Syngas Stream Using an ICCM Membrane Technology

Project activities are centered around two NETL Hydrogen Membrane Testing (HMT) units. These units provide the unique capability of high-pressure, high-temperature hydrogen membrane flux measurements at conditions of up to 400 psi at 900 ^oC. The units can accommodate membrane sizes of 1/4" to 1/2" in both disk and tubular configurations, with a wide range of flow rates for process gases. In addition, they have the flexibility to be used for both membrane separation testing and membrane reactor testing.

CARBON DIOXIDE SEPARATION PROJECTS

Operation of high-pressure, oxygen-blown gasification systems with both high (~350 ^oC) and low (~200 ^oC) temperature shift reactors in series can yield a syngas stream primarily composed of H_2 and CO_2, with some residual CO and H_2O. The concentration of CO_2 in the shifted gas should be about 40%. This syngas composition provides an opportunity to use the previously described hydrogen-selective membranes to separate the H_2 and CO_2 into separate streams.

Palladium-Silver Alloy Composite Membrane - RTI

Research Triangle Institute (RTI) is developing an inorganic palladium-based composite membrane rector that is structurally stable under the fuel reforming conditions with a high selectivity and flux rate for hydrogen permeation through the membrane. The focus of this project is on developing thin palladium-silver alloy composite membranes with a thin protective noble metal coating. Preliminary results form simplified model simulations of the membrane reactor concept has shown hydrogen permeances range from 16 to 80 gmoles/m^2-min (40 to 180 scc/cm^2-min) at 500-600 ^oC temperature and 40 psi hydrogen partial pressure differential depending upon the film thickness and substrate pore size.

CONCLUSIONS

Advanced gas separation research offers the potential for substantial improvement in the thermodynamic, environmental, and cost performance of gasification based energy systems. A major DOE program objective is the development of cost-effective ceramic membranes that can provide substantial cost reduction for oxygen separation, compared to conventional cryogenic methods. Both ITM and OTM types of ion-conducting ceramic membranes offer significant potential to reduce costs by as much as 30 percent and are well suited to integration into plant systems. Based on the current schedules for DOE-sponsored projects, commercial scale-up of the oxygen separation membrane technologies is scheduled to occur in the 2006 – 2008 time frame.

Improved hydrogen recovery and CO_2 removal are also becoming important. Currently, the program is developing high-temperature ceramic membranes and palladium-based dense membrane for H_2 recovery from syngas streams, which can also serve to separate CO_2 when shift reactors are employed with oxygen-blown gasification systems. The hydrogen separation projects are currently operating at the laboratory-scale and further scale-up will depend upon performance results achieved in the current efforts.

For more information visit
http://www.netl.doe.gov/coalpower/gasification/

Effects of ZrO_2 addition on structure, oxygen permeation and stability of $SrCo_{0.4}Fe_{0.6}O_{3-\delta}$ oxides

Li Yang, Liang Tan, Xuehong Gu, Lixiong Zhang, Nanping Xu

Membrane Science & Technology Research Center,
Nanjing University of Technology, Nanjing 210009, P. R. China

Introduction

Mixed-conducting oxides have received considerable attention as possible candidate materials for application in oxygen separation membranes and catalytic membrane reactors. Although the bright future of electronic conducting membrane reactor in the POM reaction, the commercial application of mixed-conductive membranes is often limited by specific disadvantages of the membrane materials known at the present time, for instance, the order-disorder phase transition in the oxygen sublattice. Such a transition is characteristic of most perovskites derived from the strontium cobalites $SrCoO_{3-\delta}$.[1] In addition, a high oxygen chemical potential gradient in the Sr(Co, Fe)$O_{3-\delta}$ type membranes results in a crystal lattice mismatch inside the ceramic, leading to the fracture of the membranes. [2] Thus, the disadvantages of $SrCoO_{3-\delta}$ based ceramics create a necessity to develop new materials and optimizing known materials for oxygen separation and catalytic membrane reactors.

Recently, a novel perovskite-related oxide membrane, which was prepared by addition of 9 wt% ZrO_2 into $SrCo_{0.4}Fe_{0.6}O_{3-\delta}$ (SCFZ), has been reported in our laboratory.[3] The oxygen nonstoichiometry, transport properties and structure stability of SCFZ have been investigated. [4] It showed that the stability of $SrCo_{0.4}Fe_{0.6}O_{3-\delta}$ (SCF) was greatly improved with the addition of ZrO_2, while the oxygen permeability was slightly reduced. The aim of the present study was to investigate the effect of various amounts of ZrO_2 additions on structure, oxygen permeation and stability of SCF in an attempt to search for a suitable composition exhibiting high oxygen flux as well as structural stability in reducing atmosphere.

Experimental

ZrO_2-$SrCo_{0.4}Fe_{0.6}O_{3-\delta}$ (SCFZ) powders with the ZrO_2 additions of 0, 1, 3, 5, 7 and 9 wt% were prepared by conventional solid-state reaction. The required amounts of $SrCO_3$, Co_2O_3, Fe_2O_3 and monoclinic ZrO_2 were mixed and milled for 24 h followed by calcination in air at 1223 K for 4 h. The calcined powders were pressed into disks of 16 mm in diameter with an oil pressure of 200 MPa and then sintered in air at 1473 K for 5 h to form the dense membranes. X-ray diffraction (XRD) was collected on a Bruker D8 Advance diffractometer with Cu Kα radiation. Scanning electron microscopy (SEM) and energy dispersive X-ray (EDX) analysis was performed using a JSM 6300 scanning microscope equipped with a Sigma energy dispersive X-ray microanalysis system. SEM images were recorded in back-scattered electron modes.

Oxygen permeation measurements were performed using a permeation apparatus reported previously. [2] The membrane samples were sealed by two gold rings. Before beginning of the oxygen permeation measurement, the assembly was heated to 1313 K and held for 4 h to form the bonding. One side of the membrane was exposed to air (P_h = 0.209 atm) at a flow rate of 200 ml min^{-1} while the other side was exposed to a lower oxygen partial pressure (Po_2) that was controlled by regulating the He flow rate by mass flow controllers (Models D07/ZM, Beijing Jianzhong Machine Factory, China). A gas chromatograph (GC, Model Shimabzu GC-7A) equipped with a 5 A molecule sieve column was connected to the exit of the sweep side. The amount of oxygen passing through the membrane was calculated from the measured outlet flow rate and the oxygen content.

Results and Discussion

Crystal structure characterization

XRD patterns of the as-synthesized powders with ZrO_2 additions of 1-9% showed the existence of SCF and $SrZrO_3$ phase. But for the sintered membrane (Figure 1), the second phase $SrZrO_3$ was reabsorbed into the perovskite for the compositions with ZrO_2 additions ≤ 7 wt%. Small amount of Co_3O_4 was also detected by XRD analysis. The formation of Co-rich phase may attribute to two parts: the segregation of Co at high temperature[5] and the precipitate of Co to maintain the stoichiometry because of Zr dissolution in SCF as will be discussed below. The presence of these phases in the samples was confirmed by SEM-EDX analysis for the sintered membranes. The results are shown in Figure 2 taking 1% and 9% ZrO_2 addition as examples. Besides, EDX analysis performed on the region corresponding to the SCF phase showed the presence of Zr, indicating the dissolution of Zr in SCF phase took place. The ratio between Sr, Co, Fe, and Zr in five membranes with ZrO_2 addition from 1% to 9% were1:0.48:0.84:0.027, 1:0.42:0.77:0.067, 1:0.38:0.75:0.099, 1:0.51:0.77:0.15, 1:0.38:0.76:0.19, respectively, indicating Zr content in SCF phase increased directly with amount of ZrO_2 additions.

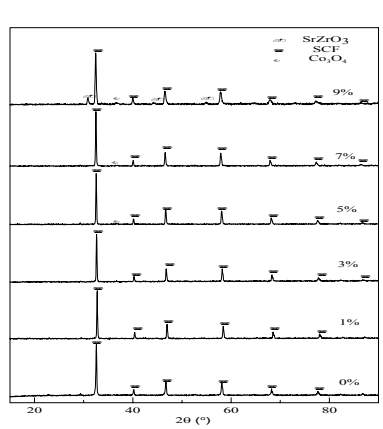

Figure 1. XRD patterns of sintered membranes.

Unit cell dimensions for SCF phase calcined at 1473 K with various amount of ZrO_2 additions are shown in Figure 3. The expanded lattices of SCF phase were found for powders with the addition of ZrO_2 and the lattice parameters increased directly with amount of ZrO_2 addition. Increase of lattice parameter of SCF phase with increasing amount of ZrO_2 addition in these systems could be due to increasing amount of Zr dissolution in B site of SCF phase as indicated by the SEM-EDX analysis. The larger ionic radii of dopant ion Zr^{4+} (0.84 Å) in comparison to the host ions Fe^{3+} (0.65 Å) and Co^{3+} (0.61 Å) resulted in an expanded SCF lattice.

Effect of amount of ZrO_2 addition on phase stability

To study the phase behavior under reducing atmospheres, SCFZ membranes with various amount of ZrO_2 additions were crushed and annealed in helium at 1123 K for 3 h and then applied for XRD analysis. The results are shown in Figure 4. Comparing with the XRD patterns of the fresh powders shown in Figure 1, we could see that the crystal structure of SCF had changed from cubic phase to an oxygen-vacancy ordered, orthorhombic phase Sr_2CoFeO_5. Structure stability of the materials seemed improved with increasing amount of ZrO_2 addition due to increasing amount of Zr dissolution in SCF phase, and when ZrO_2 addition was ≥ 3%, samples could maintain their structure in reducing atmospheres.

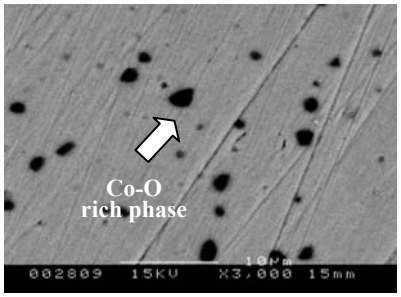

(a)

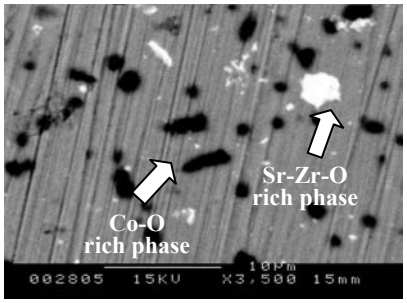

(b)

Figure 2. Back-scattered electron SEM images of membranes for ZrO_2 additions with (a)1%, (b)9%.

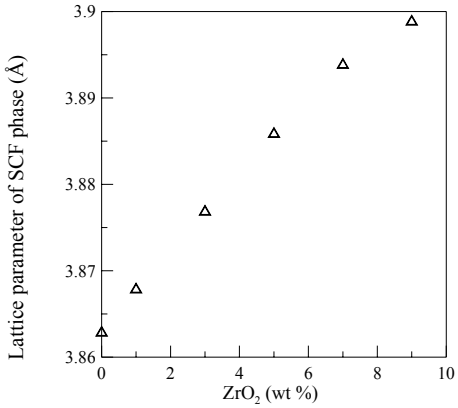

Figure 3. Unit cell dimensions for SCF phase calcined at 1473 K with various amount of ZrO_2 additions.

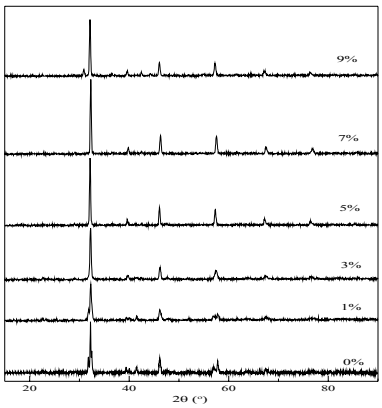

Figure 4. XRD patterns of SCFZ membranes annealed in helium at 1123 K for 3 h.

3.3. Effect of amount of ZrO_2 addition on oxygen permeation

The temperature dependence of oxygen flux through SCFZ membranes is shown in Figure 5 for the ZrO_2 additions of 0, 1, 3, 5, 7 and 9 wt%. The flow rate of He was controlled at 30 ml/min. The oxygen flux was found to decrease monotonically with the increasing amount of ZrO_2 addition due to the more amount of Zr dissolution in SCF phase. Solid solution of Zr in B sites of SCF increased the M-O bonding energy and reduced the concentration of oxide ion vacancies, both leading to a decrease in the oxygen permeability.

Another factor for evaluating the oxygen permeability of the membrane is the activation energy for oxygen permeation. As shown in Figure 5, two activation energies for oxygen permeation in the range of 973-1223K were observed for the compositions with ZrO_2 additions <3%, which was related to the order-disorder transition of oxygen vacancies.[1] In contrast, single activation for oxygen permeation was observed for samples with ZrO_2 addition >3%. The results were in accordance with the XRD analysis of the annealed samples shown in Figure 4. From the dependence of stability and oxygen permeability on the amount of ZrO_2 addition described above, the optimum ZrO_2 addition to greatly improve the structure stability without deleteriously affecting the oxygen permeability has been identified as 3 wt %.

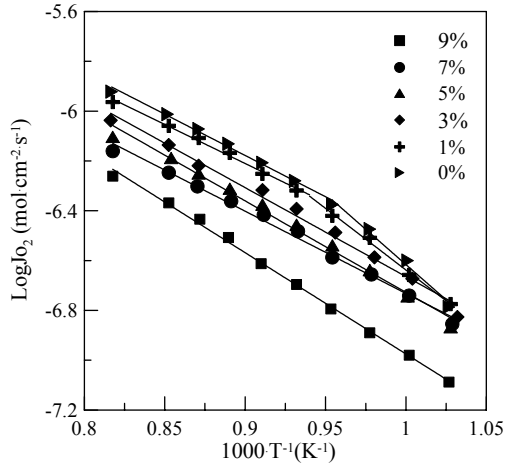

Figure 5. The Temperature dependence of oxygen permeation flux through SCFZ membranes with various ZrO_2 additions.

Acknowledgment

This work is supported by the National Natural Science Foundation of China (NNSFC, No. 20125618) and the Key Laboratory of Chemical Engineering and Technology of Jiangsu Province.

References

1.Kruidhof, H., Boumeester, H. J., Doorn, R. H. E. v., Burggraaf, A. J. *Solid State Ionics* **1994**, ***63-65***, 816-822.

2. Pei, S., Kleefisch, M. S., Kobylinski, T. P., Faber, J., Udovich, C. A., Zhang-Mccoy, V., Dabrowski, B., Balachandran, U., Mieville, R. L., Poeppel, R. B. *Catal. Lett.* **1995**, ***30***, 201-212.

.3. Li, S. G., Jin, W. Q., Huang, P., Xu, N. P., Shi, J., Hu, Z. C., Payzant, E. A., Ma, Y. H. *AIChE J.*, **1999**, ***45***, 276-284.

4. L. Yang, X.H. Gu, L. Tan, W.Q. Jin, L.X. Zhang, N.P. Xu, *Ind. Eng. Chem. Res.* **2002**, *41*, 4273-80.

5. Takeda, Y., Kanno. R., Takada, O., Yamamoto, O., Takano, M., Bando, Y. *Z. Anorg. Allg. Chem.*, **1986**, *9-10*, 259-263.

Joining $LaMO_3$ Perovskite Ceramics to Nickel-based Super Alloys using Brazing/TLPB Techniques

Raymundo Arroyave, Thomas W. Eagar, Harold Larson*

Massachusetts Institute of Technology
77 Massachusetts Ave. Room 4-134
Cambridge, MA 02139
*raymundo@mit.edu

ABSTRACT

Alternatives to mechanical sealing of perovskite/metal interfaces are explored. Experimental results demonstrating the possibility of using conventional TLPB/brazing techniques for the joining of $LaMO_3$ ceramics with Ni-based super alloys are presented. The nature of the chemical reactions occurring at the $LaMO_3$/metal interfaces is investigated. It is shown that the localized reduction of the perovskite substrate has important consequences regarding the integrity of the joints.

INTRODUCTION

Due to their mixed electronic-ionic conductivity properties, $LaMO_3$ (where M is a transition metal) perovskite ceramics constitute a promising material for emerging energy-related applications such as oxygen transfer membranes (OTM) [1] and electrodes for solid oxide fuel cells (SOFC) [2]. Despite the fact that such applications have been proved to be technically feasible, several engineering challenges must be met in order to make them commercially viable. In both SOFC and OTM-based technologies, the sealing of the process gases and their isolation from the outer environment constitutes a critical step to be resolved.

In particular, OTM technologies used in Gas-to-Liquid (GTL) applications rely heavily on the successful isolation of the syngas from the oxygen-rich external environment. Additionally, the product of the GTL reactors must be transported to further stages of the process and therefore requires the interfacing with metallic pipes capable of withstanding the mechanical stresses undergone in any industrial scale facility.

In this work, we describe the ongoing efforts by our research group regarding the development of reliable alternative sealing techniques for Oxygen Transfer Membrane technologies applied in GTL processes. Particularly, we describe the research aimed at understanding the interactions between Nickel-based brazing alloys and $LaMO_3$ perovskite membranes.

PEROVSKITE/METAL SEALING FOR GTL APPLICATIONS

Mechanical Seals. In GTL technologies using OTM, a perovskite-based membrane separates two regions of highly different oxygen chemical potentials. In order to ensure the proper functioning of the process, it is required to effectively seal the OTM perovskite/metal arrangement. Currently, mechanical compression has been the only effective technique through which this sealing can take place. In order for OTMs to be effective oxygen conductors, the operating temperatures of the GTL reactors must be relatively high ($>900^0$ C) [1] so high oxygen transport rates across the membrane are obtained.

Mechanical seals that rely on compression of the subcomponents of the seal (perovskite and metal substrates) undergo creep processes when subjected to such elevated temperatures for extended times. As time progresses, these creep processes may result in a loss of the compressive force necessary for maintaining a gas-tight seal. In practice, such problems are usually solved by over loading the seals in order to compensate for such mechanical relaxations. However, excessive overloading of the ceramic materials can lead to premature failure of the seals.

Sealing Alternatives. A possible alternative to such mechanical sealing approaches could be the use of liquid-phase based joining techniques such as brazing or transient liquid phase diffusion bonding (TLPB) so that (upon cooling) solid interface between the perovskite membrane and the metallic substrate can be obtained.

Brazing consists of the use of an interlayer with lower melting point than the substrates to be joined [3]. The joint assembly is brought up to a temperature slightly above the melting point of the interlayer so the resulting liquid wets the substrates to be joined. The resulting joint is subsequently cooled down so a solid joint is obtained. TLPB, on the other hand, relies on the isothermal solidification of the interlayer placed between the substrates to be joined and relies on the use of a melting point depressant (MPD) that is also a fast diffuser at least in one of the parent materials [4]. As the joint is held at elevated temperatures for long enough periods of time, the MPD diffuses out of the interlayer and into the base materials, allowing a higher re-melting temperature of the whole joint assembly.

Ceramic/Metal Liquid-based Joining. For brazing or TLPB joining techniques to work, the resulting liquid interlayer must wet both substrates to be joined, since the wetting angle between the liquid and the solid surface is inversely related to the Work of Adhesion, i.e. the energy that must be exerted on the interface to separate both surfaces.

In general, due to the highly different nature of their interatomic bonds, molten metals do not wet ceramic substrates [5] (especially highly stable ones, such as MgO, ZrO_2, Al_2O_3), since the resulting interfaces have a much higher energy than that of the un-joined surfaces. An exception occurs when a chemical reaction between the metal and the ceramic substrate takes place, since this chemical reaction lowers the overall surface energy of the system and therefore increases its stability [6]. In many ceramic/metal joining applications, the promotion of the necessary interfacial reactions is achieved by modifying the interlayer by the addition of active elements, such as titanium, hafnium, zirconium. These active elements ensure the formation of a interfacial reaction product, thus resulting in a chemically stable ceramic/metal interface[7]. In a few cases, particularly when the ceramic substrate has a relatively high surface energy, wetting can be ensured without the use of active elements. As will be seen below, conventional, non-reactive TLPB alloys wet $LaMO_3$ perovskite substrates without the addition of reactive elements. This can be correlated with the relatively low thermodynamic stability (compared to highly stable oxides such as MgO, ZrO_2, etc.) of this family of ceramic materials.

USE OF TLPB ALLOYS FOR JOINING $LaMO_3$ PEROVSKITES TO METALS

In order to select a proper interlayer material for the joining of two particular substrates, special attention must be paid to three different aspects:

a) The melting range of the interlayer material must be lower than that of the parent substrates.

b) The solidus point of the interlayer must lie above the expected operating temperature of the joint.

c) The interlayer material must be able to withstand the operating conditions, such as temperature, chemical environment, etc. of the joint.

As noted above, the melting range of the interlayer material must be above at least 900^0C, which is the minimum temperature in order to ensure fast enough oxygen transfer rates across the perovskite membrane. Moreover, the liquidus of the alloy in question must lie below the solidus of the metallic substrate to be joined to the OTM (for most Ni-based super alloys, the solidus lies somewhere around 1350^0C). This leaves us with a rather limited temperature range of 900^0C-1350^0C.

Of the broad range of commercial metallic brazing and TLPB alloys, copper and nickel-based alloys are the most promising ones. Previously, it has been shown that copper-based brazing alloys do wet perovskite-based substrates [8]. Unfortunately, the poor oxidation resistance of these alloy systems [9] precludes their utilization under the highly oxidizing environments occurring at GTL reactors.

Given the constraints outlined above, it was decided that Ni-based alloys constituted the only commercial alloy system that could lead to the development of a reliable perovskite/metal joint. In general, Ni-based TLPB alloys relay on the use of melting point depressants such as boron, silicon or phosphorus to depress the liquidus surface to temperatures well below the melting point of pure nickel[10].

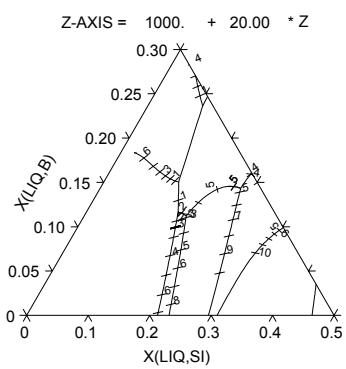

Figure 1. Primary surface of crystallization for the Ni-B-Si system, calculated using the models developed by [10]

Figure 1 shows the liquidus surface for the B-Ni-Si based on the models developed by [10]. As can be seen in the figure, the melting point of the Ni-rich alloys can be reduced by almost 400^0C when considerable amounts of both B and Si are added. Due to the fact that the metallic substrate is a Ni-based super alloy and that boron is a fast interstitial diffuser in nickel, it is expected that by using these alloys it is possible to isothermally solidify the interlayer and thus its re-melting temperature can be even higher than the processing temperature. By modifying these alloys through the addition of chromium their oxidation resistance is increased markedly, which constitutes a clear advantage, given the operating conditions within the GTL reactors.

In the remaining of the paper, we describe the analysis of the nature of the interactions between $LaMO_3$ perovskite substrates and Ni-based super alloys.

EXPERIMENTAL

Perovskite-based ceramic $(La,Sr)FeO_3$ discs were cut from a 0.8 in DIA solid hot-isostatically pressed powders. The discs were cut using a diamond saw and polished down to a 1μm finish using ethanol as the suspension media (water may attack the perovskite materials). Haynes-230® was the Ni-based super alloy selected to work as the metallic substrate due to the fact that its coefficient of thermal expansion (CTE) closely matches (although there is still a difference of about $2x10^{-6}$ /^{0}C) that of the perovskite ceramics used in the present work (~12 x 10^{-6} / ^{0}C at RT). The parent rod was machined down to 0.8" DIA and discs were cut and later polished using standard metallographic techniques. As the TLPB interlayer, a commercial B-Ni5 brazing alloy (3 wt. % Fe, 4.5 wt. % Si, 3.2 wt.% B, 7 wt. % Cr, Ni-balance) in its amorphous foil (2 mils) presentation was used. Both substrate materials and the Ni-based interlayer were ultrasonically cleaned in acetone for about 60 minutes.

Once the joint components were cleaned, a Perovskite/TLPB Alloy/ Haynes230® sandwich assembly was placed inside a high-temperature, high-vacuum furnace (1 x 10^{-6} torr). The temperature of the furnace was increased at a 5 ^{0}C/min rate up to 1090^0C (above the liquidus temperature of the TLPB alloy) and held at that temperature for 30 min. Afterwards, the joint arrangement was cooled at 5 ^{0}C/min until room temperature was reached.

The resulting samples were examined and sectioned. Analyses using optical microscopy, SEM and EDS were performed in order to characterize and understand the reaction mechanisms occurring at the perovskite/braze interfaces.

RESULTS AND DISCUSSION

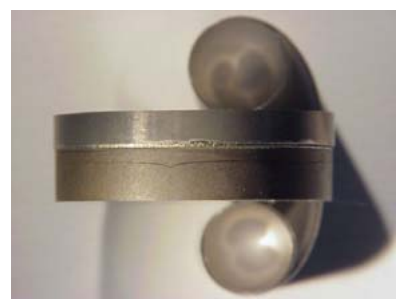

Figure 2. $(La_{0.6}Sr_{0.4})FeO_3$/Haynes230® joint. Joining conditions: 1090^0C, $1x10^{-6}$ torr.

Figure 2 presents typical flat joints created using the TLPB approach. As can be seen, it was possible to create large contact area (disc diameter of approx. 0.8 in) joints. The Ni-based alloy used as an interlayer wetted both substrate materials without the addition of active elements. However, it was observed that cracks appeared in a direction parallel to the ceramic/metal interface. To test the influence of the vacuum pressure on the final integrity of the joints, assemblies were also joined at reduced vacuum pressures of about 10^{-3} torr. In general, cracking of the samples at these reduced vacuum pressures was significantly reduced, as can be seen in Figure 3.

Figure 3. . $(La_{0.6}Sr_{0.4})FeO_3$/Haynes230® joint. Joining conditions: 1090^0C, $1x10^{-3}$ torr.

The effect of the different vacuum pressures may be interpreted as follows: It is well known that perovskite-based ceramics of the $LaMO_3$ class tend to change volume not only with temperature but with the amount of oxygen vacancies present in the lattice. By decreasing the environmental pressure, the oxygen potential was decreased, increasing the degree of non-stoichiometry of the perovskite material. This increased volumetric expansion increased the already present thermally-induced stresses due to the differences in CTE. The greater residual stresses made the formation of cracks parallel to the ceramic/metal interface more likely. However, the fact that a relatively minor change in vacuum pressure had such an effect on the integrity of the resulting joints indicated that the ceramic/metal interfaces created were not stable enough. In order to further examine what was the nature of the perovskite/Ni-based brazing alloy interaction, samples were sectioned and analyzed under SEM.

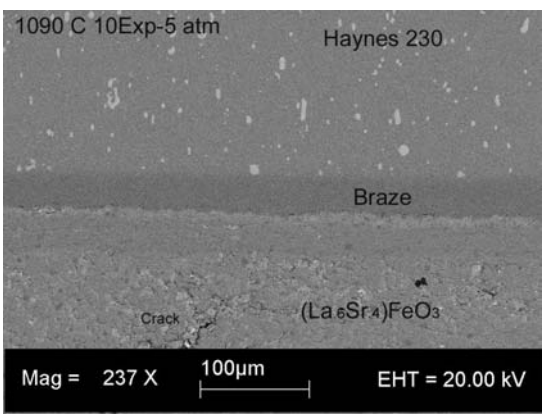

Figure 4. $(La_{0.6}Sr_{0.4})FeO_3$/Haynes230® joint. Joining conditions: 1090^0C, $1x10^{-3}$ torr. SEM Backscattered Image micrograph.

As can be seen from Figure 4, even for some of the samples (approx. 10%) that were joined at reduced vacuum pressures, crack initiation was observed. By using backscattering imaging, it is possible to observe contrast due to differences in composition. From the contrast observed, several regions can be identified. Moreover, it is clear that on the perovskite substrate (below the "Braze" label), at least three clearly identifiable regions have formed due to interactions between the Ni-based brazing alloy and the La-Sr-Fe-O substrate. It can also be seen that cracks tend to nucleate within a region that is relatively far away from the perovskite/braze interface.

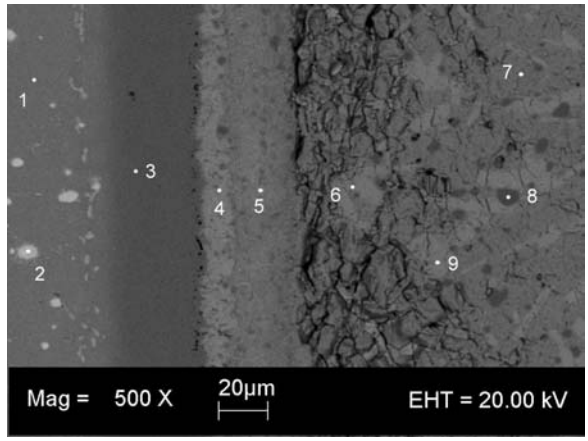

Figure 5. $(La_{0.6}Sr_{0.4})FeO_3$/Haynes230® joint. Joining conditions: 1090^0C, $1x10^{-3}$ torr. SEM Backscattered Image micrograph

Based on Figure 5 and Table 1 it can be seen that the Ni-based alloy reacted with the perovskite substrate in a rather excessive manner. From the compositional analysis (it is important to note that EDS analyses tend to overestimate the presence of light elements such as oxygen) it is possible to determine that the braze/perovskite reaction led to the precipitation of several distinct phases out of the originally single phase ceramic.

Table 1. Compositions through EDS Analysis corresponding to Figure 5 (at %).

	1	**2**	3	4	5	6,9	7	**8**
Ni	56	21	70	0	0	0	0	0
Cr	25	30	9	0	0	0	0	0
W	13	40	0	0	0	0	0	0
Mo	1	0	0	0	0	0	0	0
Ti	0	0	0	0	0	0	0	0
Si	0	0	3	0	0	0	0	0
Fe	2	1	7	1	1	14	15	69
La	0	0	0	23	2	13	15	1
Sr	0	0	8?	1	37	8	8	2
O	0	0	0	76	60	65	62	29
Mn	4	4	0	0	0	0	0	0

The layering of the phases identified as 4 (La_2O_3) and 5 (SrO?) indicates that an oxygen chemical potential gradient was established across the perovskite/braze interface. By establishing this oxygen chemical potential gradient, the original $(La_{0.6}Sr_{0.4})FeO_3$ perovskite substrate close to the interface was decomposed. The localized oxygen potential at that interface must have decreased below $1x10^{-16}$ atm, which is the stability limit of such materials [11]. Under such reducing conditions, the formation of more stable oxides, such as SrO and La_2O_3 becomes thermodynamically favorable. These reducing conditions can be explained by the presence of Fe and Cr dissolved into the Ni-based liquid, since these two elements have

relatively high chemical activities in Ni [12], [13] and additionally have a relatively high oxygen affinity [14]. Although for more stable ceramics, such as ZrO_2 and Al_2O_3, this braze alloy would not have been considered as "active", that is, capable of reducing the ceramic substrate, the relatively low thermodynamic stability of $(La_{0.6}Sr_{0.4})FeO_3$ accounts for the observed decomposition.

Based on purely mass conservation arguments, the formation of La-O and Sr-O compounds must have also led to the segregation of Fe ions. Fe could have been dissolved into the Ni melt, as indicated by the slight increase in the Fe content, compared to the pre-brazing composition. Figure 5, however, shows the formation of Fe-O "islands" within the perovskite matrix (identified as number 8). Thus, the decomposition of $(La_{0.6}Sr_{0.4})FeO_3$ due to the oxygen potential gradient across the perovskite/braze interface led in the first place to the precipitation of La-O and Sr-O layered reaction products and the accompanying segregation of Fe ions both towards the Ni melt and within the perovskite matrix. This localized decomposition of the perovskite matrix led to the formation of an extensive porous network in a well-defined region between points 5 and 6 in Figure 5.

When the joint is created, it can be considered that is stress-free. However, as the joint is cooled, residual stresses generated due to both the CTE mismatch build up. Moreover, since an oxygen potential gradient exists close to the perovskite/braze interface, there should also be a gradient in chemical volumetric expansion, which also contributes to the overall state of stress. Under normal conditions, and given that the actual CTE mismatch between the perovskite and metallic materials used is not significant, one could expect that the joint created would be relatively stable. However, the presence of a localized region of high porosity promotes the nucleation of cracks, which during the normal operating conditions of the interface could grow and eventually would lead to the failure of the seal.

CONCLUSIONS

In the present paper it has been demonstrated that Ni-based liquid alloys wet $LaMO_3$ perovskite substrates without additions of active elements such as Ti, Zr, etc. Moreover, relatively large contact area ceramic/metal joints have been created using such alloys. Under certain joining conditions (low vacuum environments), crack-free specimens were obtained. However, it was observed that, even in these cases, micro-cracks were likely to nucleate in regions close to the ceramic/metal interface.

Through analysis of the interfacial reaction zone it was concluded that the presence of oxygen-active elements such as Cr and Fe in the Ni braze created a relatively large oxygen chemical potential across the ceramic/metal interface. Such a large chemical potential caused the localized decomposition of the perovskite matrix and the formation of a high-porosity region parallel to the ceramic/metal interface.

Approaches such as the use of effective diffusion barriers that would prevent the migration of oxygen ions into the Ni-based melt are under investigation. Alternatively, changes in the chemistry of the Ni-based brazing alloys are being explored so the oxygen affinity of the braze can be reduced. By controlling the extent of the interfacial reactions, it will be possible to use liquid phase-based joining techniques to successfully create $LaMO_3$/metal seals.

REFERENCES

[1] Mazanec, T. Proc. Electrochem. Soc. **1995**, *95*, 24
[2] Skinner, S. J. Int. J. Inorg. Mater. **2001**,*3*, 113-121
[3] Passerone, A.; Muolo, M. L. Mater. Manif. Processes, **2000**, *15*,631-648
[4] McDonald, W. D.; Eagar, T. W. Metall. Trans. A, 1998, *29A*, 315-318
[5] Li, J-G., J. Am. Ceram. Soc., **1992**, *75*, 3118-26
[6] Schwartz, M. M. Ceramic Joining, ASM International, Metals Park, Ohio, 1990.
[7] Eustathopoulos, N.; Drevet, B. Mater. Res. Bull. **1993**, *314*, 15-25
[8] Wilkenhoener, R.; Buckremer, H. P.; Stoever, D.; Stolten, D.; Koch, A. New Materials for Batteries and Fuel Cells, MRS, Warrendale, PA,2000 pp.295-302.
[9] Kapoor, R. R.; Eagar, T.W. J. Am. Ceram. Soc. **1989**, *72*, 448-456.
[10] Tokunaga, T.; Nishio, K.; Hasebe, M. J. Phase Equilib.**2001**, *22*,291-299.
[11] Nakamura, T.; Petzow, G.; Gauckler, L. J. Mater. Res. Bull. **1979**, *14*,649-659
[12] Schuster, J. C.; Du, Y. Metall. Mater. Trans. A. **2000**, *31A*,1795-1803
[13] Larrain, J. M. CALPHAD: Comput. Coupling Phase Diagrams Thermochem. **1980**, *4*, 155-171
[14] Laag, T.; Phser, J.; Janke, D. Steel Res. **1997**, *68*, 341-344

DEGRADATION OF AQUEOUS ALKANOLAMINE SOLUTIONS CONTAINING CO_2 AND H_2S

Kwang-Joong Oh[1], Sang-Sup Lee[1], Byung-Hyun Shon[2], Sang-Wook Park[3], and Dae-Won Park[3]

(1) Department of Environmental Engineering, Pusan National University, Pusan, 609-735, Korea (2) Department of Environmental Engineering, Hanseo University, Choongnam, 356-820, Korea (3) Department of Chemical Engineering, Pusan National University, Pusan, 609-735, Korea

Introduction

The removal of CO_2 and H_2S from natural, refinery, and synthesis gas stream plays an important role in gas processing. Aqueous alkanolamine solutions are frequently used for the removal of CO_2 and H_2S, and the alkanolamines include MEA (monoethanol-amine), DIPA (diisopropanolamine), DEA (diethanolamine), MDEA (*N*-methyldiethanolamine). Recently, the sterically hindered amine such as AMP (2-amino-2-methyl-1-propanol) has been suggested as an attractive solvent for the removal of acid gases, and the advantage of AMP includes high equilibrium loading capacity (1.0mol of CO_2 per mole of amine). In addition, aqueous MDEA solution is frequently used as a solvent for selectively absorbing H_2S because of its instantaneous reaction with H_2S.

However, in removing acid gas by alkanolamines and regenerating them, undesirable compounds can be produced by the irreversible transformation of alkanolamines, which is called degradation. Degradation causes a loss of alkanolamine, and it may also contribute to operational problems such as foaming, corrosion and fouling. To understand the mechanism of degradation and to find the method to suppress it is required.

In this study, AMP 30wt%+MDEA 3wt%, which had high absorption capacity of CO_2 and H_2S in former study, AMP 30wt%, MDEA 30wt%, and DEA 30wt% were degraded in 120, 160, and 200℃ for 30days. And then, the degradation rates and degradation products of alkanolamines were measured.

Experimental

Materials and Apparatus. AMP (99%) was purchased from Acros, MDEA (99%) was from Tokyo chemical, and DEA (99%) was from Katayama chemical. The carbon dioxide (99.9%), the nitrogen (99.99%), and the hydrogen sulfide (99.9%) were obtained from Daeyounggas Co.(Korea).

The reactor was made of stainless steel with about $10cm^3$ volume (13cm height, 1cm diameter). We poured silicon oil into oil bath and then heating oil bath with temperature controller to maintain the reaction temperature, and confirmed the temperature by thermometer.

Procedure. We prepared all the solutions with distilled water and then made 6wt% CO_2 and H_2S absorbed into the solutions respectively by using absorption instrument. After we poured 5ml of the solutions into reactor, we heated the reactor to 120, 160, and 200℃. The degraded solutions were acquired for scheduled days, and analyzed by GC (DS6200). The GC (DS6200) was composed of FID (Flame Ionization Detector) and packed column (Tenax TA 60-80mesh, 1/8in. O.D., and 9ft. long). The operating conditions of GC were as follows; Helium gas was carried at 20ml/min flow rate, and oven temperature was increased from 150 to 300℃ by 6℃/min rate, and maintained at 150℃ for 0.5 minutes and at 300℃ for 3 minutes. The temperature of injector and detector was 300℃ and 1μl of degraded solution was instilled by a syringe.

Results and Discussion

When AMP 30wt%+MDEA 3wt% solution containing 6wt% CO_2 was degraded at 120, 160, and 200℃, AMP concentration of the solution decreased with time for the beginning part of it at constant rate as shown in **Figure 1**. Therefore, initial degradation can be assumed as first order reaction as Polderman and Steele presented in their study. After degradation in three kinds of temperature for 10 days, the concentrations of AMP decreased to about 83% of basal AMP concentration at 120℃, 67% at 160℃, and 31% at 200℃.

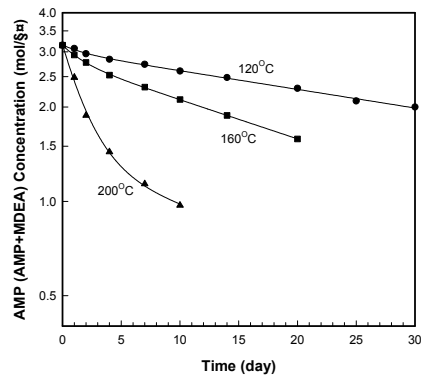

Figure 1. AMP concentration as a function of time and temperature. (AMP 30wt%+MDEA 3wt%+H_2O 61wt%+CO_2 6wt%).

6wt% CO_2 was absorbed into the aqueous alkanolamine solutions such as AMP, MDEA, and DEA, and then the solutions were degraded at 120, 160, and 200℃ respectively. Initial degradation rate constants could be measured with degradation temperature, and **Figure 2** shows this result by Arrhenius plots. Initial degradation rate constants of AMP 30wt% solutions containing 6wt% CO_2 were 0.0212, 0.0801 and $0.2481day^{-1}$ and those of MDEA 30wt% solutions were 0.0331, 0.1254 and $0.3151day^{-1}$.

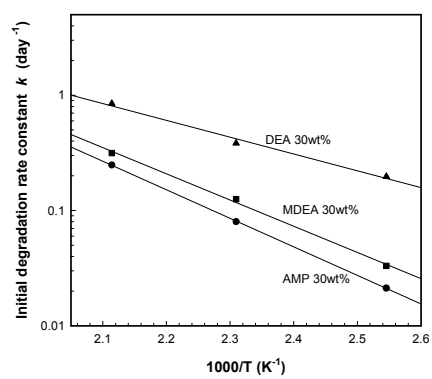

Figure 2. Arrhenius plots for k at various alkanolamines degraded with CO_2.

The constants were much lower values than those of DEA 30wt% solutions (0.1972, 0.3841 and $0.8470day^{-1}$at 120, 160, and 200℃ respectively). It is considered that AMP 30wt% and MDEA 30wt%

containing 6wt% CO_2 are degraded much more slowly than DEA 30wt% are at the temperature from 120 to 200 ℃.

The addition of MDEA 3wt% into AMP 30wt% significantly increased the absorption capacity of CO_2 and H_2S in former study. Therefore, in this study, AMP 30wt%+MDEA 3wt% solutions containing 6wt% CO_2 and H_2S were degraded in 120, 200℃ and analyzed by GC, and the chromatograms are also shown in **Figure 3** and **Figure 4** respectively. **Figure 3** shows the chromatograms of the solution containing CO_2 after degradation at 120℃ for 7days and 30days. **Figure 3 (A)** shows the result of the degradation for 7days. Peak 5 is considered as AMP, peak 6 as the salt of AMP, peak 10 as MDEA, and peak 1, 13, and 14 as compounds produced by degradation. Sixteen degradation compounds were produced, and the peak areas of AMP and MDEA were decreased due to the degradation for 30days as shown in **Figure 3 (B)**.

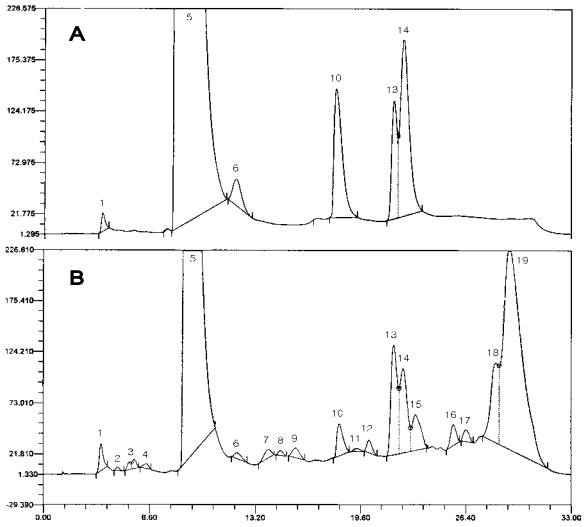

Figure 3. Chromatograms of partially degraded aqueous AMP+MDEA solutions. (AMP 30wt%+MDEA 3wt%+H_2O 61wt%+CO_2 6wt%, (A) Temp. =120℃, t=7days; (B) Temp. =120℃, t=30days).

Figure 4 (A) is the chromatogram of AMP 30wt%+MDEA 3wt% containing H_2S after degradation at 120℃ for 30days. The solution containing H_2S produced an only degradation compound while the solution containing CO_2 produced sixteen degradation compounds after the degradation at 120℃ for 30days. It is considered because the amount of H_2S absorbed into alkanolamine is less than that of CO_2 due to higher solubility of H_2S into water than that of CO_2. In addition, twelve degradation compounds were produced for 1-day degradation at 200℃ as shown in **Figure 4 (B)**.

Figure 5 shows the peak area of main degradation products transformed from AMP 30wt%+MDEA 3wt% containing 6wt% CO_2 at 120℃ for 30days. The area of peak 13 was increased for about 14days, and then it was almost constant. The area of peak 14 was the largest on degradation for about 15days. In addition, that of peak 19 was significantly increased for degradation from 25days to 30days. Therefore, it is considered that the degradation product of peak 14 may be converted to that of peak 19.

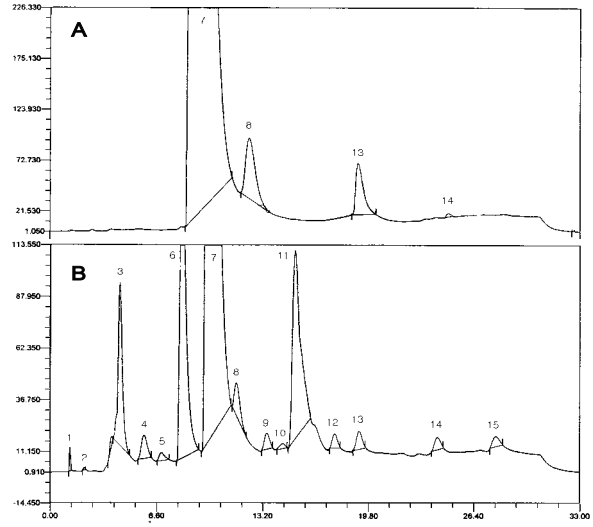

Figure 4. Chromatograms of partially degraded aqueous AMP+MDEA solutions. (AMP 30wt%+MDEA 3wt%+H_2O 61wt%+H_2S 6wt%, (A) Temp. =120℃, t=30days; (B) Temp. =200℃, t=1-day).

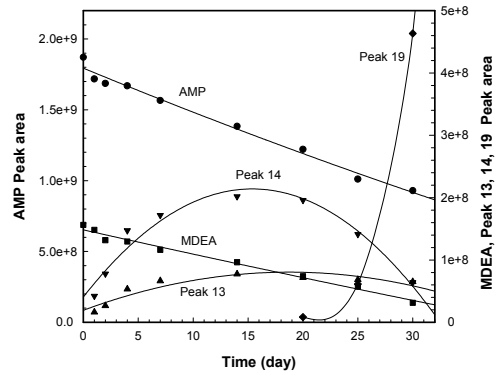

Figure 5. Rates and products of AMP+MDEA degradation. (AMP 30wt%+MDEA 3wt%+H_2O 61wt%+CO_2 6wt%, Temp. =120℃).

Acknowledgment

This work was supported by The Korean Science and Engineering Foundation under contract R01-2000-00326

References

1. Pani, F., Gaunand, A., Richon, D., Cadours, R., Bouallou, C., *J. Chem. Eng. Data*, **42**, 865～870(1997).
2. Kennard, M. L., Meisen, A., *Ind. Eng. Chem. Fundam.*, **24**, 129～140(1985).
3. Dawodu, O. F., Meisen, A., *Ind. Eng. Chem. Res.* **33**, 480～487(1994).
4. Polderman, L. D., Steele, A. B., *Oil and Gas Journal*, **54**(65), 206～214(1956).
5. Oh, K. J., Choi, W. J., Lee, J. J., Cho, S. W., Shon, B. H., *J. of KSEE*, **23**(8), 1337～1347(2001).

ENERGY FROM MACRO-ALGAE

Michele Aresta, Angela Dibenedetto and Immacolata Tommasi*

Department of Chemistry and METEA Research Center, University of Bari, Campus Universirtario, 70126, Bari – Italy.
E-mail: aresta@metea.uniba.it

Introduction

80% of the energy used today at the world level is derived from carbon based fuels, that increases the concentration of carbon dioxide in the atmosphere, rising serious concerns about the effects on global warming and climate change. To limit the emissions, alternative sources of energy have to be considered. Biomass represents an environmentally and economically feasible alternative to fossil fuels.

As a matter of fact, the forecast is that biomass may contribute to the energy balance with a share of more than 10% by 2030, with a fivefold increase with respect to the actual 2%, essentially represented by terrestrial or residual biomass utilization.

Aquatic biomass may represent a convenient solution, because it has a higher growth-rate than terrestrial plants. Micro-algae have been extensively studied so far, as they can grow both in fresh- and salty-waters [1, 2]. More recently, marine macro-algae have been considered with increasing attention [3, 4].

In this paper, the potential of macro-algae for the production of energy will be estimated.

Macro-algae for energy production

The use of macro-algae for energy production received less attention so far, despite the fact that macro-algae are cultivated since long for several purposes (food production, chemicals extraction) in China, Korea, Philippines, and Japan. The productivity is in the range 1-15 kg m^{-2} y^{-1} dry weight (10-150 t_{dw} ha^{-1} y^{-1}) for a 7-8 month culture. Either brown algae (Laminaria, Sargassum) or red algae have been used so far for such purposes.

Interestingly, macro-algae are effective in nutrients (N, P) uptake from sewage and industrial waste water, for example for the treatment of fishery effluents or agriculture drain off [5, 6]. The use of macro-algae for cleaning up effluents from fisheries is quite important as macro-algae can reduce the concentration of nitrogen derivatives like urea, amines, ammonia, nitrite or nitrate to a level that is not toxic for fishes, allowing the recycling of water. This will reduce the economic cost of growing fish as will improve the quality of the effluent water, avoiding penalties if it is discharged into the sea and making it of such quality to be recycled into fish-ponds.

In Europe macro-algae are grown in experimental fields, and natural basins. The capacity of macro-algae as bio-filters or nutrient uptake has been tested in the north-western Mediterranean Sea, along French coasts [7] using *Ulva lactuca* or *Enteromorpha intestinalis* that adapted to non-natural basins. Also in colder climate, macro-algae grow at a interesting rate. For example, in Denmark the Odjense Fiord produces ca. 10 kg per day of dry-weight-biomass, equal to a productivity of ca 10 t per year per hectare. Although macro-algae can grow in both hemispheres, the climatic factors may affect the productivity by reducing either the rate of growth or the growing-season. The Mediterranean area has ideal climatic conditions for a long growing season, with good solar irradiation intensity and year duration, and correct temperature. Moreover, along the coasts of several Countries (Italy, Spain, France, Greece) fishponds exist that may be the ideal localization of algae-ponds. Therefore, we have recently started a Project [8] aimed at assessing the potential of macro-algae as source of biofuel considering fishpond effluents as growing media.

Our objective is the use of recovered carbon dioxide from power plant flue gases or industrial plants as source of carbon.

A number of algae have been selected that, due to their adaptability to variable conditions and presence throughout the year, can be good candidate for cultivation in ponds. The selected algae have been investigated for the definition of the best conditions for their growth in a pond. The influence of temperature, irradiance, weight/volume ratio on the growth, and oxygen production has been followed during one year. Also, the production of oxygen by a freshly collected sample has been seasonally monitored as a function of the temperature. In this way, the best period for harvesting the algae can be defined and the wet collectible mass estimated.

Five algae have been treated so far, namely *C. linum, P. capillacea, U. rigida, C. vermilaria and G. bursa-pastoris.* Five different treatments can be used for the extraction of products. In this report we focus on the use of SC-CO_2 extraction, SC-CO_2 with methanol as co-solvent and the extraction with an organic solvent.

The equipment used for SC-CO_2 extraction was a SITEC apparatus, which temperature and pressure are fully computer controlled. The range of the working conditions is: temperature up to 500 K, pressure up to 33 MPa.

The organic solvent extraction was carried out with a Soxhlet apparatus using hexane as solvent. Because of the different permeability and resistance of the cell membrane of the tested algae, the use of either technique was not equally possible for all algae.

The cost of energy production from macro-algae depends on the biofuel content and the extraction technology. The estimate cost of feedstock may vary over a large interval, depending on the cultivation technique: typical values of 5 to 60 US$ per GJ of produced energy are usual. Such values are well over those of coal, oil, and LNG. Most recent revision of energy cost from macro-algae are as old as 1987 [9]. The productivity for macro-algae ranges from 150 to 600 t per hectare per year fresh weight, that is much higher than the typical value for sugarcane that ranges from 70 to 170 t_{fw} ha^{-1} y^{-1}. This means that under the best operative conditions macro-algae would be a better energy source than terrestrial biomass.

The minimum target value for a seaweed farm to be economically valuable is around 200 t per ha per year, that is higher than the productivity of micro-algae.

Interestingly, because of their edible use, several macro-algae have been fully characterized for their lipid content and nutritional properties. Consequently, a number of macro-algae are better characterized for their composition with respect to micro-algae. This also has contributed to gather useful information from the perspective of the evaluation of the biofuel productions. Noteworthy, depending on the algae species, a different composition of the extract is observed, that gives a different heat content to the fuel. It must be emphasized that methyl esters of acids may be used as fuels without any major problem.

The energetic value of the algae depends on the amount of compounds extracted that may be used as fuels. The content of fuels is very variable with the species considered, as it is the lipid content. A content of 10-20 % dw is quite usual, with a peak value up to 40%. Another key parameter to be evaluated for the assessment of the economic value of the macro-algae as source of biofuel is the energy that can be obtained from the extracted fuel. Such value allows to calculate the net energy (NE) obtainable from the algae, once it is known the energy needed for their growth (Eg), harvesting (Eh) and processing (Ep), Eq. 1.

$$\text{Net Energy} = \Delta H - (Eg + Eh + Ep) \qquad 1$$

We have also developed a tool for the evaluation of the approximate value of the heat content of the extracted material from algae and for evaluating the energetic yield of algae, not considering the dry residual material. Is worth to recall that, the residual algal mass after SC-CO_2 extraction is practically water free, and can, thus, find a use as fuel.

Taking into consideration the composition as acids and hydrocarbons, the average heat content of the algae used in this work was calculated to range around 11 500-13 500 kJ mol^{-1}, that corresponds to 24 000-30 000 kJ m^{-2} of sea surface.

Conclusions

Macro-algae are a promising source of renewable energy. In order to grow algae with an economic convenience for fuel extraction, R&D is necessary that will allow to establish the optimal growing condition, optimizing yield and minimizing costs. At least a fivefold reduction is necessary with respect to the actual cost for algae could be seriously considered as energy feedstock. Large ponds (10-20 hectare per pond, 1000 hectare surface) may produce a scale economy that will make convenient algae cultivation for energy extraction. The most convenient extraction technology must be selected for minimizing costs and for a better use of the entire algae mass.

Acknowledgement. The financial support by CNR-Rome Project CNRC008EBF is gratefully acknowledged.

References

(1) Kadam, K. L. *Energy Convers. Mgmt*., 1997, ***38***, PS 505-510.
(2) Wilde, E. W., Benemann, J. R.*Biotechnology Advances*, 1993, ***11***, 781-81.
(3) Gao, K., McKinley, K. R.,*J. Appl. Phycol*., 1994, ***6***, 45-60.
(4) Aresta, M., Dibenedetto, A., Tommasi, I., Cecere, E., Narracci, M., Petrocelli, A., Perrone, C., Elsevier 2002, Special Issue Dedicated to GHGT-6, Kyoto, October 2002.
(5) Cohen, I., Neori, A. *Bot. Mar.,* 1991, ***34***, 977-984.
(6) Hirata, H., Xu, B. SUISANZOSHOKU, 1990, ***38***, 177-182.
(7) Sauze, F. in "*Energy from Biomass*", Stub, A., Chartier, A., Schleser, P., Schleser, G. Eds, Elsevier Applied Science, London, 1983, p. 324-328.
(8) CNR-Rome, Agenzia 2000, Project CNRC008EBF
(9) Bird, K.T. in "*Seaweed Cultivation for Renewable Resources*", Bird, K. T. , Benson, P.H. Eds., Elsevier, Amsterdam, 1987, p. 327-350.

Production of Synthesis Gas from H_2O and CO_2 with Nonthermal Plasma

Shigeru Futamura and Hajime Kabashima

National Institute of Advanced Industrial Science and Technology
AIST Tsukuba West, 16-1 Onogawa, Tsukuba, Ibaraki, 305-8569 Japan

Introduction

The average global ground temperature has been increasing by 0.6±0.2˚C since 1861, and the contribution of CO_2 occupies ca 64 %.[1] Recognition of the CO_2 influence on the accelerated global warming[1] stimulated researches relevant to the development of technologies for the capture, sequestration,[2] and fixation of CO_2 along with those for energy conservation.

Many of CO_2 fixation technologies are still in the phase of fundamental research. Photochemical reduction of CO_2 to CO is achieved with some of rhenium complexes,[3] but UV light is necessary in the complicated processes of CO_2 reduction and the quantum yield is lower than unity. Direct methanol synthesis from CO_2 is possible with Cu/ZnO based catalysts at 200 ~ 300˚C.[4] However, this reaction is not cost-effective because a high pressure of H_2 [5.0 MPa of H_2/CO (3:1 v/v)] derived from electrolysis is assumed to be the H_2 source.

Recently, we have been applying nonthermal plasma to H_2 production from small molecules such as water,[5,6] methane,[6] and methanol,[6] and steam reforming of light paraffins such as methane, [7,8] ethane,[8] propane,[8] and 2,2-dimethylpropane.[8] In H_2 production, the substrate reactivity decreases in the order: methanol > methane > water. In the steam reforming of light paraffins, methane is the most desirable substrate because the highest H_2 yield is obtained with almost quantitative recovery of carbon atoms in the presence of sufficient water. The technical merits of nonthermal plasma consist in rapid start-up time and convenient operation at ambient temperature. It has been shown that the energy efficiency of the reactor is highly affected by the plasma-generating methods.[5-8]

These results urged us to explore the possibility of H_2O-CO_2 as an alternative substrate system to give synthesis gas in the reforming with nonthermal plasma. This paper will present the novel results on the reactor effect on the reaction behavior of H_2O-CO_2, product yields as functions of SED, water concentration dependence of product yields, [H_2]/[CO], and carbon balance, and the successful results of a continuous operation.

Experimental

A ferroelectric packed-bed reactor (**FPR**) and a silent discharge reactor (**SDR**) used in this research were described in detail elsewhere.[9,10] Gas flow rate was set at 100 mL min^{-1} (residence time 44.5 s) and 50 mL min^{-1} (residence time 3 s) for **FPR** and **SDR**, respectively. The both reactors employed 50 Hz ac and high voltage up to 8 kV was applied to both of them. No breakdowns occurred during operations within their maximum voltages. CO_2 balanced with N_2 in a standard gas cylinder was introduced to the reactor through a Teflon tube by adjusting the CO_2 concentration and flow rate with sets of mass flow controllers after humidification in a water-bubbler in a thermostatic bath. Water concentrations were determined with a dew point hygrometer, and they were controlled within the range of 0.5 ~ 2.5 %. The gas streams passed through the entry tube (1/8 inch in diameter) and dispersed into the plasma zone as shown in Fig. 1. Reforming of H_2O and CO_2 was carried out at room temperature and an atmospheric pressure by using a conventional mass flow reaction system.

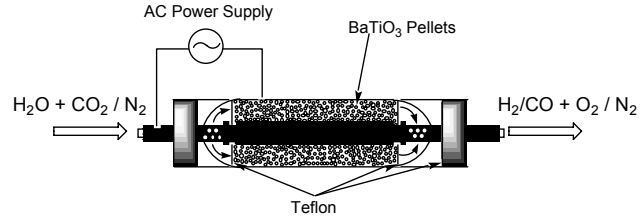

Figure 1. Schematic of ferroelectric pellets packed-bed reactor (**FPR**).

H_2 and methane were quantified by a TCD-GC with a packed column of Molecular Sieve 13X. CO, CO_2, ethane, ethylene, and acetylene were quantified by a GC equipped with a TCD and a FID with a packed column of Porapak Q+N and Molecular Sieve 13X.

Results and Discussion

Definitions of SED and the yields of H_2, CO, and O_2. As a measure of energy density for **FPR** and **SDR**, specific energy density (SED) will be used later (1), where Power denotes the plug-in power. The yields of H_2, CO, and O_2 are defined in (2), (3), and (4), respectively.

$$\text{SED (kJ L}^{-1}) = \text{Power (kW) / [Gas flow rate (L/min) / 60]} \quad (1)$$

$$H_2 \text{ yield (mol\%)} = 100 \text{ X [}H_2 \text{ concentration (ppm) / initial } H_2O \text{ concentration (ppm)]} \quad (2)$$

$$\text{CO yield (mol\%)} = 100 \text{ X [CO concentration (ppm) / initial } CO_2 \text{ concentration (ppm)]} \quad (3)$$

$$O_2 \text{ yield (mol\%)} = 200 \text{ X [}O_2 \text{ concentration (ppm) / \{[}H_2O]_{initial} + [CO]_{initial} \text{ (ppm)\}]} \quad (4)$$

Reactor Effect on the Reaction Behavior of H_2O-CO_2. Table 1 shows the reactor effect on the reaction behavior of H_2O - CO_2 in N_2 at 12 kJ L^{-1}. The gas flow rates for **FPR** and **SDR** were set at 100 mL min^{-1} and 50 mL min^{-1}, respectively.

Table 1. Reactor Effect on CO_2 Conversion and Product Distribution

Reactor	CO_2 Conv. (mol%)	Product yield (mol%)			[H_2]/[CO]
		H_2	CO	O_2	
FPR	12.3	12.4	11.8	2.8	2.1
SDR	0.5	0.7	>0.5	-	-

Initial concentrations of H_2O and CO_2 were 2.0 % and 1.0 %, respectively. Background gas N_2; SED 12.0 kJ L^{-1}.

A 24.6-fold higher CO_2 conversion was obtained with **FPR** than with **SDR**. Since the lifetime of the energetic electron is shorter than 100 ns, these data cannot be rationalized by the residence time difference between **FPR** and **SDR**. Similar types of barrier discharge plasmas are attained in both the reactors, but it is considered that electrons with higher energies are more highly populated in **FPR** than in **SDR**.[5-8] Based on these results, only **FPR** was used as a reactor in the subsequent reactions.

Irrespective of the reactor type, comparable yields were obtained for H_2 and CO. In the case of **FPR**, the O_2 yield was much lower than that of H_2. In the case of **SDR**, the O_2 amount was below the detection limit.

The yields of H_2, CO, and O_2 increased with SED. Irrespective of SED, almost the same yields were obtained for H_2 and CO. The O_2 yield was much lower than those of H_2 and CO.

H_2O Concentration Effect on the Product Distribution. Figure 2 shows the plot of CO yield vs. CO_2 conversion. The slope of the dotted line is unity, and the data points on this line show that the carbon atoms in the reacted CO_2 are quantitatively recovered as CO. In the absence of H_2O, CO yield saturates at 85 % with an increase in SED. Meanwhile, a good carbon recovery is obtained on addition of H_2O. The stoichiometry of the CO_2 deoxygenation process shows that a half amount of O_2 is produced compared to that of CO, but the data in Fig. 2 suggest the occurrence of the further deoxygenation of CO, resulting in lower carbon recovery. H_2O itself or its oxygen atoms may be involved in the oxidation of carbonaceous materials derived from CO_2.

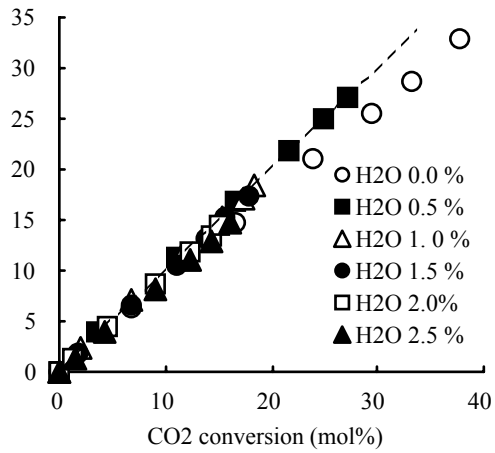

Figure 2. Carbon Balance in the Reaction of H_2O-CO_2 in N_2.
Reactor **FPR**; CO_2 1.0 %; gas flow rate 100 mL min^{-1}.

Figure 3 shows the molar ratio of H_2 to CO as a function of SED. This ratio depends on the H_2O concentration, but almost the same ratios are obtained, irrespective of SED. These data suggest that compositions of synthesis gas from H_2O-CO_2 mixtures can be controlled by selecting pertinent ratios for initial concentrations of H_2O and CO_2. This trend sharply contrasts with those observed in the steam reforming of light paraffins.[5-8] In this reaction, deoxygenations of CO_2 and H_2O proceed independently from each other.

Continuous Production of H_2 and CO from H_2O-CO_2. Continuous operation of **FPR** in the reforming of H_2O-CO_2 in N_2 for 5 h (SED at 11.9 to 12.6 kJ L^{-1}) gave constant yields of H_2 and CO in about 12 % and 10 %, respectively, as observed in the steam reforming of methane.[5]

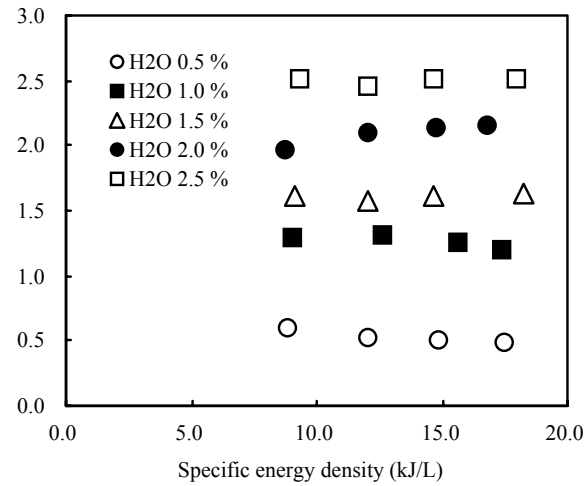

Figure 3. Effect of H_2O Concentration on the Molar Ratio of H_2 to CO in the Reaction of H_2O and CO_2.
Reactor **FPR**; CO_2 1.0 %; gas flow rate 100 mL min^{-1}.

In this process, target compositions of synthesis gases could be obtained by selecting pertinent ratios of H_2O and CO_2 depending on purposes such as H_2 utilization and preparation of a feedstock for methanol synthesis. At this moment, initial concentrations of H_2O and CO_2 cannot be increased due to the occurrence of the backward reaction of H_2 and O_2. Rapid separation of the products is mandatory to increase the potential of this method.

Conclusions

It has been shown that a versatile process of synthesis gas production from H_2O-CO_2 can be constructed with nonthermal plasma. Good carbon balances are obtained, and the molar ratio of H_2 to CO can be facilely controlled by changing the initial concentration ratios of H_2O and CO_2. Continuous operation of **FPR** for 5 h assured the constant yields of H_2 and CO.

Acknowledgment. This work was partly supported by the Grants-in-Aid from New Energy and Industrial Technology Development Organization of Japan (NEDO).

References

(1) 2nd Assessment Report of IPCC, 1997.
(2) Kajishima, T.; Saito, T.; Nagaosa, R.; Kosugi, S. *Energy*, 1997, **22**(2/3), 257.
(3) Hawecker, J.; Lehn, J.-M.; Ziessel, R. *Helv. Chim. Acta*, 1986, **69**, 1990.
(4) Saito, M.; Fujitani, T.; Takeuchi, M.; Watanabe, T. *Appl. Catal. A: General*, 1996, **138**, 311.
(5) Kabashima, H.; Einaga, H.; Futamura, S. *Chem. Lett*., 2001, 1314.
(6) Kabashima, H.; Einaga, H.; Futamura, S. *IEEE Trans. Ind. Applicat*., in press.
(7) Kabashima, H.; Futamura, S. *Chem. Lett*., 2002, in press.
(8) Futamura, S.; Kabashima, H.; Einaga, H. *IEEE Trans. Ind. Applicat*., submitted for publication.
(9) Futamura, S.; Zhang, A.; Yamamoto, T. *IEEE Trans. Ind. Applicat*., 2000, **36**(6), 1507.
(10) Einaga, E.; Ibusuki, T.; Futamura, S. *IEEE Trans. Ind. Applicat*., 2001, **37**(5), 1476.

STUDY OF CARBON FORMATION ON Ni-MgO CATALYST DURING REFORMING OF $^{13}CH_4$ WITH CO_2

Abolghasem Shamsi

U.S. Department of Energy
National Energy Technology Laboratory
P. O. Box 880
3610 Collins Ferry Road
Morgantown, WV 26507-0880

Introduction

Reforming is a critical technology that is necessary for generating cleaner fuels such as pure hydrogen and synthesis gas from coal, natural gas, and carbonaceous wastes. It is also compatible with the technologies used for capturing and sequestering CO_2. SynGas and hydrogen produced from fossil and renewable sources will play an important role in the 21st century, powering high-efficiency electricity generating systems, which are essential for reducing greenhouse gas emissions. SynGas could be converted to pure hydrogen (for fuel cells), low-sulfur liquid fuels, chemicals, and fuel additives. It has been reported that syngas production routes are efficient, but still expensive and the major problem is avoiding carbon formation.[1] Carbon is the major cause of catalyst deactivation and since the rate of carbon formation is greater than the rate of carbon gasification, carbon accumulates in the catalyst bed, causing catalyst deactivation and plant shutdown. Industrially, this problem is solved by addition of excess steam or oxygen, which increases the cost of syngas production. The cost of syngas production in a system that converts natural gas to liquid fuels is more than 60-70% of the total cost.[2] And the higher cost is mainly due to addition of excess steam or oxygen to the process for preventing carbon formation. Therefore, the challenge is to expand our understanding of the reforming process and to develop technologies that produce cheaper and cleaner energy in an environmentally acceptable manner.

It has been reported that a cost-reduction of 25% in syngas production would allow the gas-to-liquids processes to become more competitive with oil refining.[3] Therefore, developing catalysts and processes that operate at low steam/carbon and/or oxygen/carbon ratios would have a significant impact on the cost of syngas production. Increasing the life and the efficiency of the catalyst can also lower the cost of syngas production. Therefore, studies attempting to explain catalyst deactivation by carbon formation have intensified in recent years.

Numerous research groups have focused their efforts on reducing carbon formation during reforming reactions and their efforts have been carried out mainly at atmospheric pressure. However, several groups studied carbon formation at higher pressures. For example, Tomishige et al. have studied the effect of pressure on the reaction of methane with CO_2 over a Ni0.03Mg0.97O solid solution which, under atmospheric pressure, is resistant to carbon formation.[4,5] Our earlier studies with Pt/ZrO_2, $Pt/Ce\text{-}ZrO_2$, and Rh/Al_2O_3 catalysts also showed similar results.[6] With increasing pressure, methane and CO_2 conversion rates decreased, H_2/CO ratio decreased, and the rate of carbon formation increased. Higher rates of carbon formation at high pressure leads naturally to the question of whether the source of carbon at elevated pressures is the same as at 1 atmosphere. It is well known that most of the carbon deposited on the catalyst during reforming of methane with CO_2 comes from CO disproportionation and methane decomposition. Understanding which of these carbon sources is the major contributor at high pressure is necessary information in developing processes that will prevent or reduce carbon formation under industrial reaction conditions. Therefore, we have undertaken a ^{13}C-labeling study, using $^{13}CH_4$, to compare the relative contributions of methane and CO_2 as the sources of carbon formation at low and high pressures.

Experimental

The Ni-MgO catalyst was prepared by dissolving Mg(NO3)2.6H_2O and Ni(NO3)2.6H_2O (Ni/Mg = 0.5) in de-ionized water and mixing the solution on a hotplate until the excess water was removed. The resulting powder was heated in air at 850°C for two hours to decompose nitrates into oxides of MgO, NiO, Mg0.4Ni0.6O, and $MgNiO_2$ as indicated by x-ray diffraction. Before reaction the samples were reduced for two hours at 600°C under flowing hydrogen (30 ml/min) and tested at 800°C in a fixed-bed reactor with $^{13}CH_4/CO_2$ = 1:1.

Temperature-programmed oxidation (TPO) of deposited carbon was performed after the reaction by heating the sample from 30 to 900°C at a rate of 20°C/min in flow of 2% oxygen in helium (40 ml/min). Pulse reactions were performed by injecting 22.31 μmoles of reactant into He carrier gas (40 ml/min) at 800°C and pressures of one and 10 bar. The reaction products were analyzed and quantified by a quadrupole mass spectrometer using internal and external standards.

Results and Discussion

Reaction of $^{13}CH_4$ with CO_2 over reduced Ni-MgO at steady state conditions

Ni-MgO catalyst has been extensively studied for reaction of methane with CO_2 and it appears to be more resistant to carbon formation than other Ni-based catalysts, specifically in solid solution form.[5] Although there are some studies conducted at higher pressure the majority of the results are obtained at atmospheric pressure. Most of the downstream processes using syngas or hydrogen require compressed gases. Therefore it is more economical to conduct reforming reactions at higher pressure, which causes a serious problem due to high amount of carbon deposition. The Ni-MgO catalyst was tested at 800°C and at pressures of one and 10 bar. The carbon formed on the catalyst was quantified by oxidation of carbon and measuring the amount of CO and CO_2 produced. The results of temperature-programmed oxidation of carbon to CO_2 are shown in Figure 1, indicating that a significant amount of oxygen consumed by the catalyst at about 380°C compared to that consumed by carbon. As the time on stream increased the amount of carbon also increased at a rate of 15.7 mg-C/g-cat.h. The catalyst was regenerated and tested six times without any significant loss of activity or selectivity. Methane and CO_2 conversions of 96 and 94% were obtained, respectively, with a H_2 /CO ratio of 0.76.

Pulse reaction of $^{13}CH_4$ with CO_2 over reduced and oxidized Ni-MgO catalyst at 10 bar

A gas mixture with $^{13}CH_4/CO_2$ = 1:1 was injected over reduced and oxidized Ni-MgO catalyst at 800 °C and 10 bar (He at 40 ml/min used as carrier gas). Figure 2 shows the product distribution for the first pulse over the reduced catalyst. The H_2 concentration over the reduced sample was about 44% compared to 8% for the oxidized sample. The CO concentration (47%) was also higher for the reduced sample compared to that of oxidized one (15%). The peak maxima for H_2 and CO were delayed about 23 seconds compared to that of CO_2. Similar results were obtained with the oxidized sample with a time delay of about 16 seconds. The ratios for $^{12}CO_2/^{13}CO_2$ and $^{12}CO/^{13}CO$ were about 0.95 for both the reduced and oxidized samples. On the first pulse about 95% of methane and 80% of CO_2

were converted over the reduced sample compared to 80% of methane and 19% of CO_2 over the oxidized sample as shown in Figure 3. Methane and CO_2 conversions and the concentrations of H_2 and CO were increased with the second and third pulse over the oxidized sample. As a higher amount of CO_2 converted the concentrations of $^{12}CO_2$ and $^{13}CO_2$ decreased with increasing number of pulses. The product distributions over reduced sample showed smaller changes with increasing number of pulses. Methane appears to react readily with the oxidized sample where as CO_2 requires reduced sites for reaction to occur. Equal amounts of $^{12}CO_2$ and $^{13}CO_2$ were detected over both the reduced and the oxidized samples and the concentration of $^{13}CO_2$ follows the same trend as $^{12}CO_2$, indicating that the oxygen exchange reaction is very fast as reported earlier.[8]

$$^{12}CO + {}^{13}CO_2 = {}^{13}CO + {}^{12}CO_2$$

Five pulses of oxygen (22.31 7moles each) were introduced after the reaction to oxidize the deposited carbon on the catalyst and about 688 7moles/g.cat. were consumed by the catalyst. The major products were H_2 and H_2O with no significant amounts of carbon oxides, indicating that carbon deposition in the presence of CO_2 at 800°C and 10 bar was insignificant. Similar results obtained for the oxidized sample except that the catalyst consumed less oxygen (491 7moles/g.cat) after 4 pulses of oxygen. It appears that methane reacts with surface oxygen, reducing NiO to metallic nickel, and forming adsorbed CH_x, H_2, and OH. However, CO_2 requires reduced sites in order to dissociate into adsorbed oxygen (Oad) and CO or the CO_2 reacts with adsorbed hydrogen via reverse water gas shift reaction forming H_2O and CO. Furthermore, CO could also form from interaction of adsorbed CH_x and OH.[9] The results indicated that carbon deposited on the catalyst formed from both methane and CO_2, possibly via disproportionation of CO which is produced from both $^{13}CH_4$ and $^{12}CO_2$. The time delay observed for H_2 and CO could result from strong adsorption of these species on the reduced nickel sites.

Conclusions

Catalytic reaction of $^{13}CH_4$ with CO_2 over reduced and oxidized Ni-MgO catalyst was studied to obtained mechanistic information at low and higher pressures. No significant amount of carbon was deposited with reaction time of less than 60 minutes. However, as the time increased the amount of carbon deposited on the catalyst increased. The carbon deposited on the catalyst during the first hour of reaction appears to be very active and was removed by reacting with 2vol% oxygen in He at temperature of about 660°C. The catalyst maintained its original reactivity and selectivity after removal of carbon.

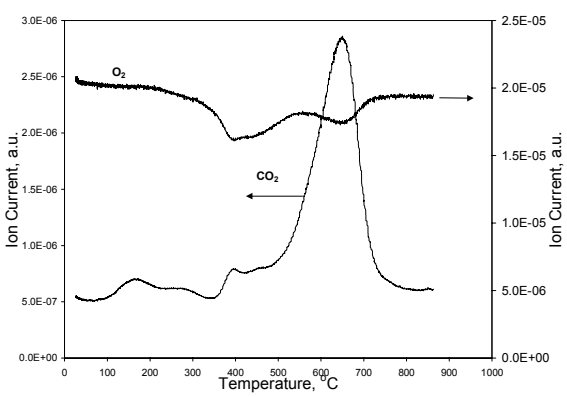

Figure 1. TPO of deposited carbon on Ni-MgO catalyst reacted at 800°C and 1 bar

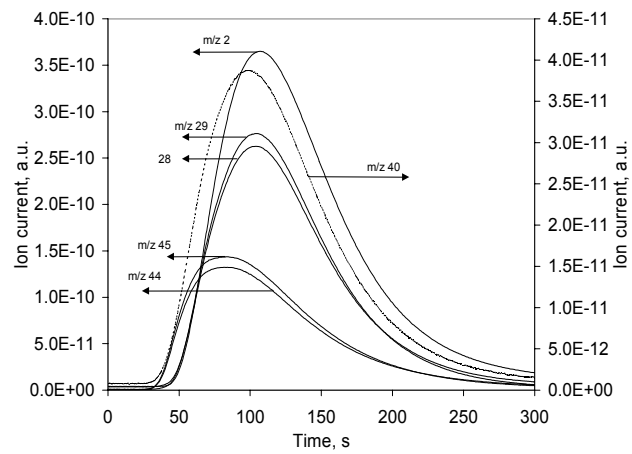

Figure 2. Pulse reaction of $^{13}CH_4/CO_2$ = 1:1 over reduced Ni-MgO catalyst at 800°C and 10 bar

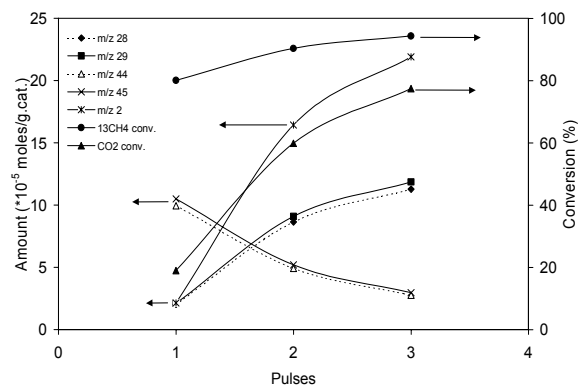

Figure 3. Pulse reaction of $^{13}CH_4/CO_2$ =1:1 over oxidized Ni-MgO catalyst 800°C and 10 bar

References

1. Jens R. Rostrup-Nelson, New aspect of syngas production and use, Catalysis Today 63 (2000) 159-164.
2. L. Basini and L. Piovesan, Ind. Eng. Chem. Res. 37 (1998) 258-266.
3. L. P. Lange and P.J.A. Tijm, Process for Converting Methane to Liquid Fuels: Economic Screening Through Energy Management, Chem. Eng. Sci. 51 (1996) 2379.
4. K. Tomishige, Y. Himeno, O. Yamazaki, Y Chen, T. Wakatsuki, K. Fujimoto, Kinetics and Catal. 40(3) (1999) 388-394.
5. K. Tomishige, Y. Himeno, Y. Matsuo, Y. Yoshinaga, K. Fujimoto, Ind. Eng. Chem. Res. 39 (2000) 1891-1897.
6. A. Shamsi, C.D. Johnson, Am. Chem. Soc., Div. Fuel Chem., Preprints, 46 (2001) 94-96.
7. D.Qin, J. Lapszewicz, Catalysis today 21 (1994) 551-560.
8. E. P. J. Mallens, J. H. B. J. Hoebink, and G. B. Marin, Journal of Catalysis 167 (1997) 43-56).
9. M.C.J. Bradford and M.A. Vannice, Applied Catalysis A: General 142 (1996) 97-122.

SYNTHESIS OF DIMETHYL CARBONATE AND PROPYLENE CARBONATE FROM UREA

Wang Mouhua, Zhao Ning, Yang Jinhai, Wei Wei, and Sun Yuhan

State Key Laboratory of Coal Conversion Institute of Coal Chemistry, Taiyuan 030001, China

Introduction:

Synthesis of urea was a traditional industrial process for CO_2 utilization. As a CO_2 carrier, urea was cheap and widely available, so it was thought to be a potential route for the synthesis of important organic compounds, such as dimethyl carbonate or propylene carbonate from urea.

Dimethyl carbonate(DMC) was environmentally benign in organic synthesis as intermediates substituting the poisonous phosgene and dimethyl sulfate. In addition, DMC could also be used as fuel additives to improve the combustion efficiency[1,2]. Propylene carbonate(PC) was important as an organic solvent, a processing agent for synthesis fibers, a raw material for a pharmaceutical composition or an intermediate for the synthesis of dimethyl carbonate[3]. At present, DMC was produced industrially by phosgene or by liquid-phase or gas-phase oxidative carbonylation of methanol; PC was produced by cycloaddition of CO_2 and propylene oxide. As a result, DMC and PC synthesis from urea has a lot of advantageous which was considered to be an alternative method such as cheap feedstock and low toxicity.

The known catalysts for the synthesis of DMC were organotin compound and alkali metal compounds. The known catalysts for the synthesis of PC were metal oxide. Cho reported the using of alkali metal compound or quaternary ammonium compound as catalyst, but the DMC yield was low[3]. The yield of DMC was 36.4% over LiH catalyst according to West[4]. Saleh obtained higher DMC yield and selectivity over dibutyl methoxy isocyanato tin catalyst[5]. High yield and selectivity of DMC was reached by using dibutyl dimethoxy tin and high boiling electron donor compound(triglyme) as cocatalyst[6]. However, the preparation of these catalysts was difficult and expensive. In addition, the separation of the products was also very complex. Thus, homogeneous catalysts should be disadvantageous to industrialization. The synthesis of propylene carbonate from urea and propylene glycol also had the same problems. The present paper investigated the performance of different metal oxide for the synthesis of dimethyl carbonate and propylene carbonate from urea.

Experimental:

A serious of metal oxides had been prepared and the catalytic activity for synthesis of DMC and PC were evaluated. The solid base MgO, ZnO, CaO were prepared by calcination of the corresponding hydroxide. The Bu_4Sn was used as commercial product prepared by Fluka. The synthesis of DMC was carried out in a novel reactor. In order to promote the selectivity and the yield of the products, the ammonia which was the by-product in the two reactions should be removed efficiently.

Results and discussion:

Figure 1 showed the effect of the catalyst on the yield of DMC from urea and methanol. It could be seen that the catalyst showed different performance on the synthesis of DMC from urea and methanol. When little catalyst was used, MgO showed the better results than ZnO. However, with the increasing of the catalyst weight, the DMC yield over ZnO increased dramatically which was higher than that of MgO and Bu_4Sn reported by Ryu. The different activity of these catalysts could be related to the base strength and base density of the catalysts.

Figure 2 illustrated the influence of the solid catalyst on the producing of PC from urea and propylene glycol. It was found that the metal oxide catalyst(MgO, ZnO) showed high yield to PC. Higher yield of PC over $Ca/K/SiO_2$ catalyst was also obtained while $Pb(Ac)_2$ and NaCl showed poor performance. It was obvious that the reaction results were also related to the basicity of the catalyst. How the basicity of the catalyst influence the reaction was under research

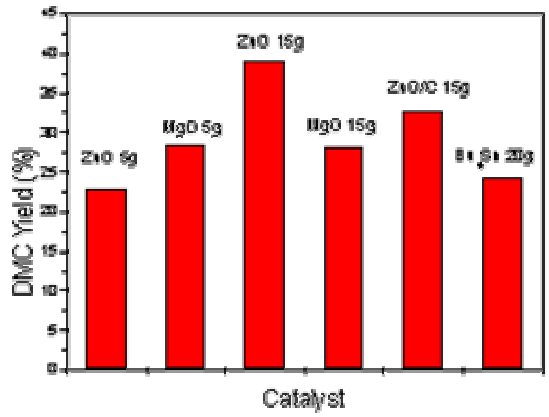

Fig.1 Effect of the catalyst on the DMC yield

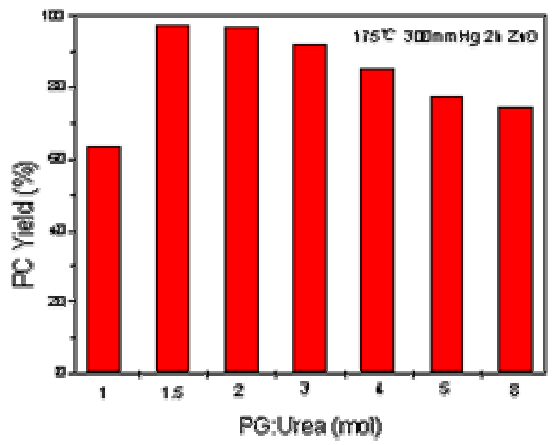

Fig.2 Effect of molar ratio of PG to urea on the reaction

It could be seen from the results that the solid base had the ability to promote the formation of PC and DMC from urea though the activity was different. The activation of the reactant might obey the same mechanism. The removal of the by-product ammonia was necessary to promote the selectivity and yield of the products. The novel reactor should be used. The synthesis of DMC and PC was thought to be a promising process for the utilization of CO_2.

References

(1) Ono.Y, *Applied Catalysis A*, **1997**, 155, 133.
(2) M,Ratzenhofer, *Angew.Chem. Int. Ed. Engl.,* **1980**, 19,317
(3) Cho, T. US 5534649 (**1994**)
(4) West. U. JP 10-109960 (**1998**)
(5) Saleh. R, WO 9517369 (**1995**)
(6) Ryu, J US 5902894(**1999**)

RECENT DEVELOPMENTS ON HYDROGEN STORAGE SYSTEMS

Hironobu Fujii, Jürgen I. Gottwald, Takayuki Ichikawa

Faculty of Integrated Arts and Sciences
Hiroshima University
1-7-1, Kagamiyama
Higashi-Hiroshima
739-8521 JAPAN

Introduction

Protection of earth is one of the main issues to be solved for human race. However, the fast growing world population, an increasing globalization and the emerging nations on the threshold to a highly mobile society will yield more and more atmospheric pollution. Thus, hydrogen energy systems have been proposed as a means to reduce greenhouse gas and other harmful emissions from stationary and mobile sources, also aiming at a higher energy independence from the short-running fossil fuels and their uncertain sources. Moreover, the car manufactures would like to increase their rate of "zero-emission vehicles" in their car fleet.

For realizing hydrogen energy systems in near future, we have to establish suitable energy storage and transportation technologies. One of the key technologies on that way is the development of high performance hydrogen storage (H-storage) systems.

For stationary applications, weight is not a key problem. But especially for mobile applications, e.g. in fuel-cell electric vehicles (FCEV), or cars with hydrogen-fueled internal combustion engine, fuel tanks have to be a compact, lightweight, safe and affordable containment as an on-board H-storage system. As technical realizations, high-pressure hydrogen, liquid hydrogen, absorbed hydrogen in metal hydrides, chemical hydrides and nano-structured carbons will be discussed, omitting on-board reforming of hydrogen from methanol or other liquid fuels.

High-pressure hydrogen

Classical high-pressure gas cylinder tanks made of inexpensive steel are regularly filled up to 15 or 25 MPa in most countries. To run a compact car for 400 km, approximately 4 kg of hydrogen for a FCEV or 8 kg for an internal combustion engine are required[1]. If 4 kg of hydrogen is stored in its gaseous form and compacted at a pressure of 20 MPa, an internal volume of 220 liters would be necessary, a space clearly not available in standard compact cars.

Therefore, novel high-pressure tanks involving fiber-reinforced composite materials are being developed; normally these new tanks consist of an inner liner, onto which the fibers are wound. They are tested up to a maximum pressure of 60 MPa and for regular use filled up to 35 MPa (5,000 psi)[2]. However, even for that pressure, the fuel tank would have a too large volume for a compact FCEV. To overcome this disadvantage, very-high-pressure tanks up to 70 MPa (10,000 psi) for mobile and 82.5 MPa (12,500 psi) for stationary application[3] have been considered and exist as prototypes. These tanks are envisaged to have a weight of 110 kg, equivalent to a technical efficiency of 0.70 m^3/kg[4]. But even at these high pressures, at the current technical status, the gas cylinders will be a factor of three more inefficient than liquid hydrogen tanks[4]. However, besides the fact that there remains always a considerable risk in using very-high-pressure vessels, the most dangerous and complicated part is the compression itself. In addition, compressing the hydrogen up to 70 MPa (10,000 psi) would require almost the same energy as its liquefaction and some problems concerning the high-pressure container itself remain to be solved[5].

Liquid hydrogen

Liquid hydrogen has an over 800 times higher density than in its gaseous state. Therefore, liquefaction of hydrogen is particularly attractive from the point of view of improving the mass per volume ratio. However, the condensation temperature of hydrogen at 0.1 MPa is -253 °C and the unavoidable heat transfer even through a super-insulated container leads directly to loss of hydrogen due to boil-off. Larger containers have a better surface to volume ratio than smaller ones, reducing the loss of hydrogen due to evaporation. Therefore, huge hydrogen containers are used for commercial transportation of liquid hydrogen inside ships and delivery by trailers or for stationary storage systems. For small tanks inside sedans, the manufactures are currently working on reducing the boil-off rate[6]. For example, Linde AG, Germany, is using a newly patented re-cooling system, so the loss due to evaporation can be minimized. The stand-by time of a parked car can so be extended from before 3 days to more than 12 days, before evaporation losses occur[6]. Additionally, major advances in motor development like direct fuel injection and new valve generations for hydrogen have been made, improving the maximum available torque and power of the car engine, by simultaneously reducing the fuel-consumption[7].

Metal-hydrides

It is well known that metal-hydride (MH) systems can store more hydrogen than in liquid hydrogen in a safe and efficient way. However, those materials with good storage capabilities and reversibility only desorb hydrogen at relatively high temperatures, too high for fuel cell application. On the other hand, materials fitting these requirements are too heavy or too expensive for a commercial application.

Therefore, all over the world hydrogen research teams have been initiated: In 1996, the IEA (International Energy Agency) program[8] has established an international hydrogen storage task force to search for innovative materials with high H-storage capacity. Since 1995, the DOE (Department of Energy) is progressing the research program on hydrogen storage materials[9]. In Japan, since 1994 the R&D-program of developing hydrogen storage and transportation systems using metal hydrides has been set up in the WE-NET (World Energy-Network) project[10]. In addition, the research program on new advanced H-storage materials has been launched in the Priority Areas Project "New Protium Functions in Materials" by the Ministry of Education, Science, Sports and Culture of Japan. The above projects are aiming at the development of high performance H-storage materials applicable to FCEV. To overcome the disadvantages in conventional heavyweight metal hydrides, new materials using lighter elements have been investigated in the recent years.

One attractive light-element metal hydride is MgH_2, since it is directly formed from the reaction of bulk Mg with gaseous hydrogen, reaching hydrogen concentrations up to 7.6 wt.% of hydrogen. However, like in many other metal hydrides, the reaction is too slow and needs 300 °C for progressing the hydrogen desorption reaction.

A reduction of the metal grain sizes to nanocrystalline dimensions can significantly improve the thermodynamic and diffusional properties in MgH_2 and enhances the H-storage features[11]. Therefore, different processes to obtain micro- or nano-structured Mg have been investigated to overcome the above-mentioned drawbacks.

Recently, Pd-coated nano-structured Mg films prepared by a RF sputtering method have been reported to absorb ~5 wt.% at 100 °C under hydrogen atmosphere of 0.1 MPa and to completely desorb below 100 °C in vacuum[12]. These catalyzed nano-structured Mg composites are now developed as one of the H-storage materials aiming at large-scale production. Moreover, in another work, the kinetics of MgMH with a maximum H-storage capacity of 7.5 wt.%

could be drastically improved by ball-milling Mg together with nanometer size catalysts of Ni and Fe under an H_2-atmosphere of 1 MPa. The grinding time could be shortened from 10 hr to 15 min by simultaneously optimizing the Ni nanoparticle amount to 0.5 at%[13].

Recently, it has been found that Cr-Ti-V bcc alloys absorb and desorb effective hydrogen up to 2.6 wt% at 313 K under ambient pressure, which is the highest hydrogen capacity in the metal hydrides applicable for fuel cell cars at present[14].

Carbon-related storage materials

In the first work on H-storage in single-walled nanotubes (SWNT) in 1997, a H-storage capacity between 5 to 10 wt.% was reported[15]. This, and the stunning result of up to 67 wt.% at room temperature in carbon nanofibers by another group[16], have triggered many laboratories around the world to focus their research on that class of materials. (For a review on the vast area about H-storage in carbon nanostructures, see [17, 18] and [19]). Unfortunately, these first experimental results could not be repeated or confirmed independently in other laboratories up to now. Some of the reported storage capacities could be even solely caused by Ti-alloy impurities introduced by the special sonication process, which is applied to open the caps of the nanotubes[20]. Currently, the opinions about the ability of H-storage in carbon nanotubes and –fibers are still controversially discussed[21] and are as widespread as the experimental results.

Instead, nano-structured graphite, mechanically milled under a hydrogen atmosphere of 1 MPa, has been reported and confirmed to absorb hydrogen up to 7.4 wt.%[22, 23]. However, still some progress should be done in improving the yet too high desorption temperature for H storage.

Chemical hydrides

Complex metal hydrides, also called chemical hydrides, have a high theoretical H-storage capacity (e.g. the "alanate" $NaAlH_4$: 5.6 wt.%) and their feedstock is relatively cheap. But for complex aluminum hydrides, for example, the comprised hydrogen was presumed to be stored irreversibly. The material was only used, after being added to water, as a "one-shot" hydrogen releasing material[24]. Additionally, hydrogen was released only at temperatures above their melting point. Therefore, the chemical hydrides were assumed an unsuitable material for reversible H-storage. In 1995, Bogdanović et al. have shown in their pioneering work, that Ti-doping of $NaAlH_4$ renders the reaction reversible and kinetically enhances the hydrogen release already at near-ambient temperatures[25]. At present, research groups are now investigating improved catalysts for optimizing the dehydriding characteristics not only of the alanates. However, a H-storage system applicable to FCEV has not been established yet because the reaction rate and temperatures are still too inadequate for application in an on-board storage system. Moreover, it is currently still unknown what the effective catalyst mechanism is and how it contributes to the process[26]. In addition, the hydrogen release is not yet optimized, because either the full storage capacity is lost after the first cycle or the initial H capacities are low[26]. However, if the reaction is improved and becomes significantly fast, the chemical hydrides will play a dominant role as H-storage media in mobile applications.

Conclusion

Currently, in the hydrogen research laboratories all over the world new non-traditional and nano-technological techniques are applied to design high performance H-storage materials. We believe that, due to this research effort, one day better hydrogen-storage materials, which absorb and desorb at least 5 wt.% hydrogen at temperatures below 100 °C, will be discovered and developed.

Acknowledgement

One author (J.G.) would like to thank for his financial support by the Japanese Society for the Promotion of Science fellowship program.

References

1 Schlapbach, L., *MRS Bulletin*, **2002**, *27* (09), 675
2 Quantum technologies, Inc, "Quantum Technologies, Trishield™ Composite Cylinder", http://www.qtww.com/pdf/TriShield.pdf
3 Dynetek, http://www.dynetek.com/
4 Irani, R. S., *MRS Bulletin*, **2002**, *27* (09), 680
5 Verdugo-Peralta, C., *Proc. 14th World Hydrogen Energy Conf.*, Montréal, **2002**
6 Wolf, J., *MRS Bulletin*, **2002** *27* (09), 684
7 Wetzel, F.-J., *Proc. 14th World Hydrogen Energy Conf.*, Montréal, **2002**
8 IEA (International Energy Agency) Hydrogen Program, http://www.eren.doe.gov/hydrogen/iea/
9 U. S. DOE (Department of Energy), Hydrogen, Fuel Cells, and Infrastructure Technologies Program, http://www.eren.doe.gov/hydrogen/
10 WE-NET (World Energy Network), http://www.enaa.or.jp/WE-NET/
11 Zaluska, A.; Zaluski, L.; Ström-Olsen, J. O., *J. Alloys Compd.*, **1999**, *288*, 217
12 Fujii, H.; Higuchi, K.; Yamamoto, K.; Kajioka, H.; Orimo, S.; Toiyama, K., *Mater. Trans*., **2002**, *43* (11), 2651
13 Kanoya, I.; Hosoe, M.; Suzuki, T., *Honda R&D Technical Review*, **2002**, *14* (2), 91
14 Okada, M.; Kuriiwa, K.; Tamura, T.; Takamura, H.; Kamegawa, A., *J. Alloys Compd.*, **2002**, *330-332*, 511
15 Dillon, A. C.; Jones, K. M.; Bekkedahl, T. A.; Klang, C. H.; Bethune, D. S.; Heben, M. J., *Nature*, **1997**, *386*, 377
16 Chambers, A.; Park, C.; Terry R.; Baker, K.; Rodriguez, N. M., *J. Phys. Chem. B*, **1998**, *102*, 4253
17 Züttel, A; Sudan, P.; Mauron, Ph.; Kiyobayashi, T.; Emmenegger, Ch.; Schlapbach, L., *Int. J. Hydrogen Energy*, **2002**, *27*, 203
18 Dillon, A. C.; Heben, M. J., *Appl. Phys. A*, **2001**, *72*, 133
19 Züttel, A.; Orimo, S., *MRS Bulletin*, **2002,** *27* (09), 705
20 Hirscher, M; Becher, M; Haluska, M.; Dettlaff-Weglikowska, U.; Quintel, A.; Duesberg, G. S.; Choi, Y.-M.; Downes, P.; Hulman, M.; Roth, S.; Stepanik, I.; Bernier, P., *Appl. Phys. A*, **2001**, *72*, 129
21 Atkinson, K.; Roth, S.; Hirscher, M.; Grünwald, W., *Fuel Cells Bulletin*, **2002**, *38*, 9
22 Orimo, S.; Majer, G.; Fukunaga, T.; Züttel, A.; Schlapbach L.; Fujii, H., *Appl. Phys. Lett.*, **1999**, *75* (20), 3093
23 Orimo, S., Matsushima, T.; Fujii, H.; Fukunaga, T.; Majer, G., *J. Appl. Phys*., **2001**, *90* (03), 1545
24 Jensen, C. M.; Zidan, R.; Takara, S.; Guthrie, S. E.; Thomas, G. J., IEA Task 12, Final Task Report, Project 10, **2001**, 53
25 Bodanović, B.; Schwickardi, M. J., *J. Alloys Compd*., **1997**, *253*, 1
26 Bogdanović, B.; Sandrock, G., *MRS Bulletin*, **2002,** *27* (09), 712

PERFORMANCE OF A METAL HYDRIDE HYDROGEN STORAGE SYSTEM

*Sarang A. Gadre, Armin D. Ebner and James A. Ritter**

Department of Chemical Engineering
University of South Carolina
Columbia, SC 29208 USA

Introduction

Hydrogen is considered to be the ultimate fuel for the future, not only because of its renewable and nonpolluting nature, but also because water is the only byproduct during combustion. However, there are many roadblocks to the implementation of the hydrogen economy, such as the lack of refueling and storage infrastructures. Hence, a considerable effort is being put fourth worldwide to alleviate some of these roadblocks.[1] For example, the Savannah River Technology Center (SRTC) has developed a novel metal hydride hydrogen storage container for niche transportation applications.[2] In fact, despite their low gravimetric density, metal hydrides as a means to store hydrogen have been under consideration for many years[2-7] because they have the ability to store hydrogen reversibly in the solid state at relatively low pressures and ambient temperature.

However, a metal hydride hydrogen storage container can be complicated and may contain heat transfer tubes as well as a heat transfer medium to overcome the enthalpic effects during charge and discharge. The SRTC container is an excellent example.[8] It contains aluminum foam and a u-tube heat exchanger for heat transfer, it is only three-fourths filled with metal hydride powder to compensate for expansion during hydrogenation, and the sintered metal feed tube runs axially along the top of the container to ensure a uniform flux of hydrogen into the vessel. These complications present quite a challenge to the development of a mathematical model that can be used for design and optimization.[8] To this end, experimental data are needed over a wide range of hydrogen charge and discharge conditions to calibrate and/or validate such a mathematical model.

Therefore, the objective of this paper is to present some of the results from a simple two level fractional factorial design study that reveals the effect of seven factors on the discharge performance of the SRTC hydrogen storage container from only sixteen different experimental runs. These results are used to further test the models developed previously under diverse operating conditions. Select experimental and modeling results are presented to show how a relatively simple model is able to capture the dynamic discharge behavior of a complex hydrogen storage container.

Table 1. Fractional Factorial Study Operating Conditions

Factors	Factor Levels	
Surface Insulation	No	Yes
Water Flow Rate (gpm)	2	4
Water Temperature (^oC)	25	55
Initial Bed Temperature (^oC)	25	55
Initial Bed Pressure (atm)	12	20
H_2 Discharge Flow Rate (SLPM)	10	30
Hysteresis	No	Yes

Experimental

Seven process factors were identified as the critical factors for this study. They are the container insulation (In), u-tube water flow rate (Qw), u-tube water temperature (Tw), initial bed temperature (Ti), initial bed pressure (Pi), hydrogen gas flow rate (Qg), and hysteresis (Hy). These factors and their high and low levels are given in Table 1. The conventional "study one factor at a time" approach was inefficient here as it is incapable of quickly assessing the relative importance of each factor and how it interacts with the other factors. At the same time, a full factorial design for these seven factors was also impractical, as it would take considerable time to carry out 128 experiments. Hence, a two-level resolution IV fractional factorial design ($1/8^{th}$ fraction) comprising 16 runs was devised for these factors.[9] The experiments were carried out as described elsewhere.[8]

Results and Discussion

To understand the effects of these factors on the discharge performance of this container, several performance indicators or response variables of practical relevance were identified. However, due to space constraints, only a couple of them are discussed here. To isolate the factors or factor interactions that have significant effects, normal probability plots and Pareto charts were constructed for each response variable using MINITAB. The results for the time until the discharge flow rate is constant, and for the standard volume of H_2 discharged are shown in Figures 1 and 2.

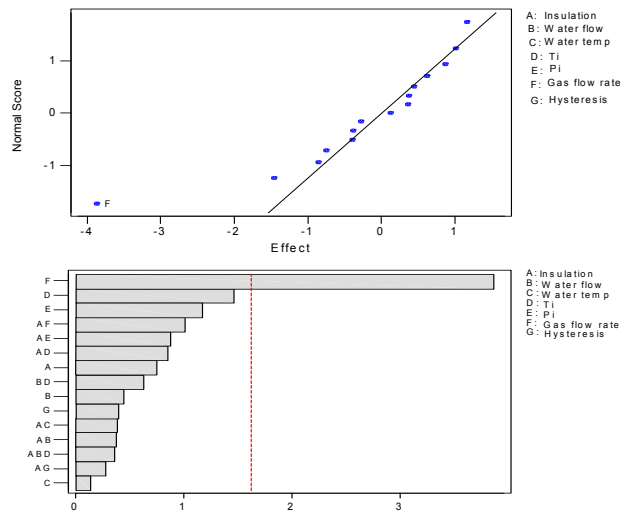

Figure 1. Normal probability plot and Pareto Chart for the estimated effects of the time until the discharge flow rate is constant.

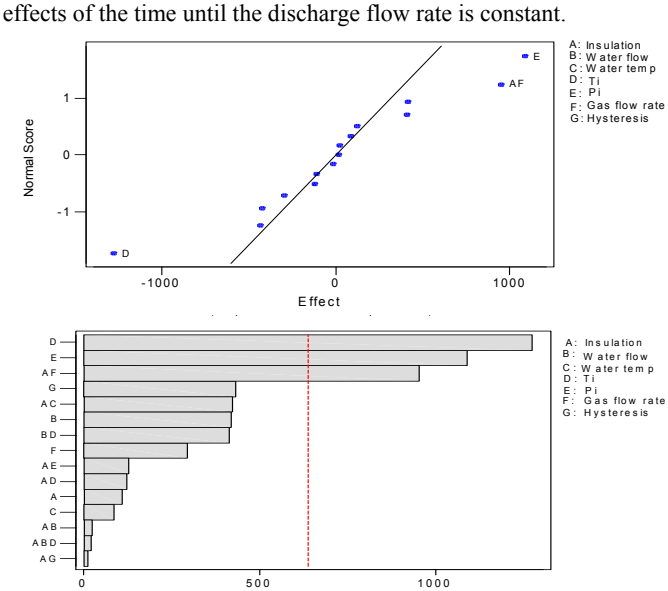

Figure 2. Normal probability plot and Pareto Chart for the estimated effects of the standard volume of H_2 discharged.

The time duration for which the molar flow rate stays constant is an important variable for assessing the performance of the hydrogen storage system as it provides information on how long the bed can be operated at the desired flow rate. Figure 1 shows the effects of the factors and the factor interactions for an alpha value of 0.10, which corresponds to a 90% confidence level. The only factor that had any significant effect was the hydrogen gas discharge flow rate.

The standard volume of hydrogen discharged, which also represents the bed capacity, is important for knowing how much hydrogen can be stored in the solid state and taken out during discharge. This quantity was based on the volume discharged up until 20 % of the set value was reached. From Figure 2 it is evident that the factors influencing this variable were the initial pressure (Pi), initial temperature (Ti) and interaction between insulation (In) and gas flow rate (Qg). Since this was a resolution IV fractional factorial design, two-factor interactions were confounded with each other. Hence, In-Qg had an alias with two other factor interactions, namely Qw-Hy and Ti-Pi, and since real interaction effects are not likely to occur unless at least one of the factors involved in the interaction has a main effect,[9] it was safe to assume that the alias structure of the two-factor interaction was dominated by the interaction between Ti-Pi, as they both occurred as significant main effects.

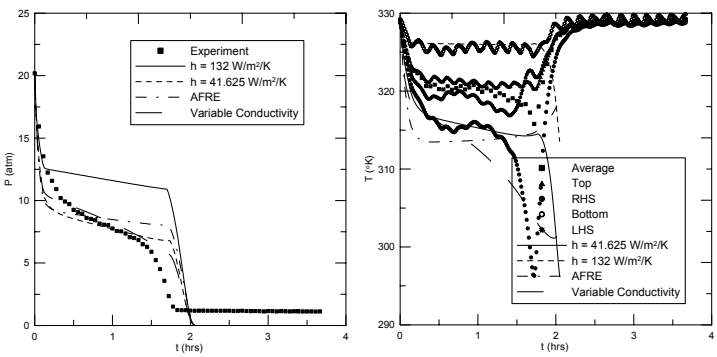

Figure 3. Comparison of the experimental pressure and temperature histories during discharge with different model predictions.

Mathematical Model Simulations

The models developed in a previous work[8] were calibrated with a standard discharge run to obtain the heat and mass transfer coefficients; it was then used to predict other experimental runs at different hydrogen gas discharge flow rates. The same set of heat and mass transfer coefficients was able to predict the performance of all the runs with the same, reasonable accuracy. However, to understand the real potential of these models, they need to be tested under diverse conditions, such as used in this fractional factorial study. Thus, 8 runs, all corresponding to the insulation on condition, were used to test various models under very diverse conditions.

Figure 3 shows the predictions from several models for one of the runs from this study under extreme conditions. Here, the water flow rate was kept at its high value, while using hot water as the heat exchanger fluid. The initial bed pressure, temperature and discharge flow rate were also set at their high levels; and the hysteresis "yes" condition was used (recall, however, that its effect was insignificant). The predictions from the axial model with the same value of heat and mass transfer coefficients obtained from the previous study[8] (132.4 $W/m^2/K$) resulted in poor predictions; the value of heat transfer coefficient had to be adjusted to 41.625 $W/m^2/K$ to obtain a good fit. Nevertheless, the axial flow, radial energy (AFRE) model, using the same value of the bed conductivity (2.78 W/m/K) from the previous work,[8] was able to predict the pressure discharge characteristics with reasonable accuracy. However, these predictions were improved by making the bed conductivity a linear function of loading. This trend was also evident in the temperature histories, where the variable conductivity model gave the best predictions among all the models.

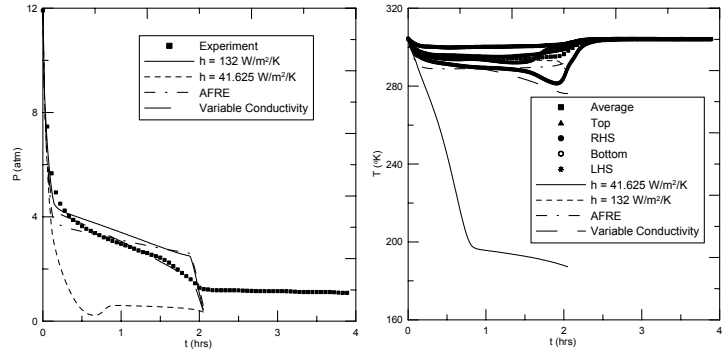

Figure 4. Comparison of the experimental pressure and temperature histories during discharge with different model predictions.

Similar results were observed for another experimental run obtained at extreme conditions, as shown in Figure 4. The water flow rate was again high, but cold water was used as the heat exchanger fluid. The initial bed temperature and pressures were set at the low values, and the discharge flow rate was set at the high value. Again, the hysteresis "yes" condition was set. This time the old value of the heat transfer coefficient was able to predict the discharge characteristics. Typically, the lower value of 41.625 $W/m^2/K$ was needed when hot water was used, and the value of 132.4 $W/m^2/K$ was needed when cold water was used. Just like the previous case, the AFRE model with the same value of the bed conductivity predicted the pressure discharge curve with reasonable accuracy, which was further improved with the variable conductivity model. The temperature curves followed a similar trend. The AFRE predictions were good but they did not capture the characteristic dip in temperature just before the bed became exhausted. Interestingly, the variable conductivity model did capture this dip, at least qualitatively. Similar trends were observed with all the other experimental runs from this fractional factorial design study.

Acknowledgements

Financial support provided by the National Reconnaissance Office under contract NRO-00-C-0134 is greatly appreciated.

References

1. National Hydrogen Energy Roadmap, US DOE, November 2002, http://www.eren.doe.gov/hydrogen/features.html.
2. Heung, L. K. *Hypothesis II conference proceedings,* Norway, **1997**, 1.
3. Mat, M. D.; and Kaplan, Y. *Int. J. Hydro. Energy*, 2001, 26, 957.
4. Levesque, S.; Ciureanu, M.; Roberge, R.; and Motyka, T. *Int. J. Hydro. Energy,* **2000**, 25, 1095-1105.
5. Das, L. M. *Int. J. Hydro. Energy,* **1996**, 21, 789-800.
6. Jemni, A.; Nasrallah, S. B.; and Lamloumi, J.; *Int. J. Hydro. Energy,* **1999**, 24, 631-644.
7. Nakagwa, T.; Inomata, A.; Aoki, H.; and Miura, T. *Int. J. Hydro. Energy,* **2000**, 25, 339-350.
8. Gadre, S. A.; Ebner, A. D.; Al-Muhtaseb, S. A.; Ritter, J. A. *Ind. Eng. Chem. Res.,* submitted, 2003; unpublished results.
9. Lochner, R. H.; Mater, J. E. *Designing for Quality: An Introduction to the Best of Taguchi and Western Methods of Statistical Experimental Design*. Quality Resources, New York; ASQC Quality Press, Wisconsin, 1990.

GENERATION OF NANOPOROUS THIN POLYMER FILMS VIA FOAMING WITH CARBON DIOXIDE

S. Siripurapu,[a] J.M. DeSimone,[a,b] R.J. Spontak[a] and S.A. Khan[a]

[a] Dept. of Chemical Eng., North Carolina State University, Raleigh, U.S.A.
[b] Dept. of Chemistry, University of North Carolina, Chapel Hill, U.S.A.

Abstract

We report the use of geometrical confinements to generate novel nanoporous thin polymer films with supercritical carbon dioxide ($scCO_2$). Poly(methyl methacrylate) films measuring on the order of 75-100 μm in thickness, when constrained between impenetrable plates in the foaming process yield a variety of diffusion-controlled foamed micro/nanostructures. Results obtained here demonstrate that the foamed cell size can be systematically reduced in such systems by applying high CO_2 saturation pressure and low temperature (near the T_g of the $scCO_2$-plasticized polymer). Cell sizes can also be lowered, and cell densities increased at lower CO_2 pressures, through the addition of a nanoscale filler or a tailored surfactant. Addition of such fillers enhances foaming through concurrent heterogeneous nucleation and/or decreasing the polymer- CO_2 interfacial tension, revealing that nanoporous polymers can be controllably generated through the synergistic use of diffusion control and filler/surfactant addition.

Introduction

The microcellular foaming process has been developed in the past to manufacture foamed products aimed at replacing their unfoamed analogs without compromising desired application-specific properties. In a typical microcellular foaming procedure [1], a polymer sample is saturated with an inert gas such as supercritical carbon dioxide $scCO_2$ at high pressures and desired foaming temperature. On reaching equilibrium of the gas uptake into the polymer, the gas is released in a controlled fashion near isothermal conditions to yield separation of the gas phase via nucleation and growth of gas bubbles to foam a stable foam structure. Microcellular foams of different thermoplastic materials have been generated in the past with $scCO_2$ in batch [1,2] and continuous [3,4] processes. Most studies in the past have concentrated on understanding the effects of foaming variables such as CO_2 saturation pressure, saturation time and foaming temperature on final foam cell sizes and nucleation densities [1]. Synthesis of nanoporous thin polymer films has become of significant interest recently due to potential novel applications such as low-*k* dielectrics, membranes and drug delivery vehicles [5]. Different synthesis approaches are being pursued utilizing block copolymers, nanotemplating and dentritic macromolecules [6]. The thin film geometry presents a challenge in achieving uniform nanoporous morphology in a foaming process due to depletion of the available CO_2 for nucleation through surface diffusion to the external environment. The main purpose of this work is (i) to investigate the use of simple geometrical constrains to incorporate uniform porosity in thin polymer films using a $scCO_2$-based foaming process and (ii) to study the effect of nanoscale fillers and tailored surfactants to achieve higher nucleation rates at lower CO_2 saturation pressures.

Experimental

Materials. The PMMA (Plexiglas VM-100) employed in this study was provided by Elf Atochem N.A. (King of Prussia, PA, U.S.A.) in pellet form and was purified before use in experimentation. Specific material properties are listed in Table 1. Carbon dioxide (>99.8% pure) was obtained from National Specialty Gases (Durham, NC, U.S.A.). Colloidal silica (particle diameter = 10-12 nm) dispersed as 30 wt% solution in methyl ethyl ketone was purchased from Nissan Chemicals Ltd. (Houston, Texas, U.S.A.). The non-ionic surfactants used in this study were synthesized using different techniques that will be described elsewhere. Table 2 gives specific details of the surfactant architectures.

Table 1: Polymer Characteristics

Polymer	M_n (kg/mol)	M_w (kg/mol)	M_w/M_n	Density (g/cm^3)	T_g (°C)
PMMA	70,000	107,000	1.53	1.18	101

Table 2: Surfactant Characteristics

Surfactant	M_n (kg/mol)	M_w/M_n
PMMA-*g*-PDMS (GCP)	40,000	1.46
PMMA-*b*-PFOMA (BCP1)	29k-b-3.5k	1.14
PMMA-*b*-PFOMA (BCP2)	110k-b-50k	1.2

Sample Preparation. Solutions of PMMA with/without the surfactants were prepared by dissolving 30 wt% polymer in toluene. Samples that included the nanoscale filler (colloidal silica) were prepared in methyl ethyl ketone. Thin films measuring 75-100 μm thick were formed by solution casting on a glass plate and drying under vacuum. The polymer films are separated from the glass plate under water and subsequently vacuum dried for an additional 12 h.

Foaming Experiments. The polymer films were cut into 1.3 cm x 2.5 cm samples for foaming experiments. A schematic of the foaming setup is shown in Figure 1. A sample film is sandwiched in the foaming die or placed alone in the foaming vessel. Once the vessel is heated to a desired foaming temperature in an oven, the sample is then saturated with CO_2 from an ISCO pump for a desired amount of time (6 h) at an elevated pressure (1000-5000 psi). The foaming vessel is finally depressurized rapidly to yield the final product.

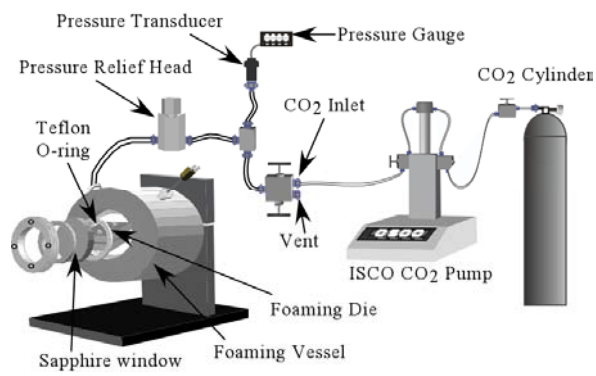

Figure 1. Schematic of the foaming setup

Foam Characterization. Foamed samples were dried under vacuum for 24 h at 50°C, fractured in liquid nitrogen and examined by scanning electron microscopy (SEM) with a Hitachi S3200N variable-pressure microscope. Backscattered electron images of uncoated foams were acquired at an accelerating voltage of 21 kV and a chamber pressure of 60 Pa. The images were subsequently analyzed for cell diameters, cell densities and the thickness of the unfoamed outer skin. While the cell diameter was taken as the

average of two dimensions in the cell, the cell density was determined using the method described elsewhere [2].

Results and Discussion

As a natural extension of the microcellular foaming process of bulk polymers, similar experiments have been attempted using thin polymer films. Figure 2 (a) shows a micrograph of a PMMA film foamed at 5000 psi and 40˚C. The foamed film is characterized by three regions, (i) a microcellular core, (ii) a transition region between the core and unfoamed skin and (iii) relatively thick unfoamed skins accounting for almost 70% of the film thickness. The microcellular core has a mean cell diameter of 1 μm and a cell density of *ca*. 10^{11} cells/cm^3 of material. Figure 2 (b) is an enlargement of the same sample showing the transition region and the unfoamed skin morphology. Attempts to optimize the process by varying process parameters such as foaming temperature and saturation pressure do not yield a substantial improvement in the ultimate foam morphology.

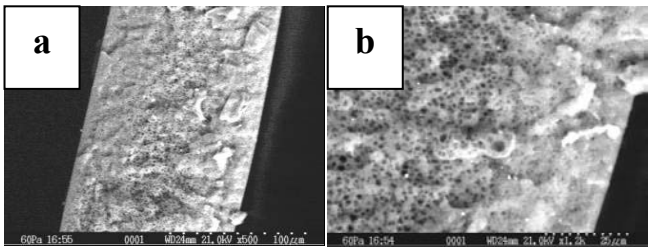

Figure 2. PMMA film foamed at 5000 psi and 40˚ C

Foaming with Diffusion Control. The fundamental difference between foaming bulk polymers and thin polymer films lies in the kinetics of the foaming process. Depressurization of the foaming cell results in nucleation of billions of microvoids in the polymer matrix. As a subsequent step, cell growth occurs wherein remaining gas in the polymer migrates to nuclei, thereby leading to the final microcellular structure upon retrograde vitrification of the polymer. In the case of thin films, there is competing gas diffusion occurring on the order of the same time scale as cell growth from the film surfaces. Such diffusion depletes available gas for cell growth. These two opposing transport mechanisms account for a high degree of heterogeneity in material properties such as viscosity, T_g, gas concentration and diffusion coefficients along the film thickness. This heterogeneity in combination with varying processing conditions, such as differences in foaming temperature, yield highly non-uniform foamed structures. Restricting surface CO_2 diffusion is anticipated to allow for greater gas availability for cell growth and higher uniformity of cell distribution.

To test the above hypothesis, a foaming die has been designed and machined with smooth surfaces that, when sandwiching the polymer film, serves as a physical constraint to CO_2 diffusion from the film surfaces. Figure 3(a) shows a micrograph of a PMMA film foamed under the same conditions as the sample in Figure 2, but in the presence of a diffusion barrier. The foamed film is characterized by extreme uniformity in cell size distribution and a ultrathin layer (corresponding to a single layer of cells) of unfoamed skin with a smooth integral surface, as seen in Figure 4(b). Confinement of the film in the foaming die eliminates property gradients across the film and promotes uniform cell growth, yielding a nanoporous foamed film with ultrathin unfoamed skin.

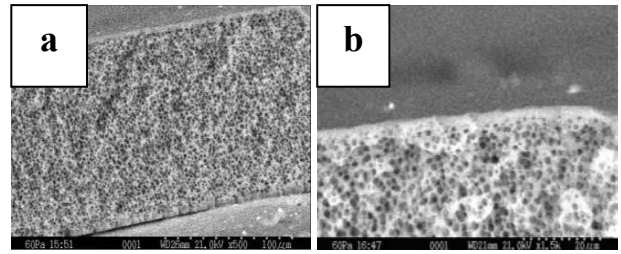

Figure 3. PMMA film foamed at 5000 psi and 40˚ C with diffusion control

Addition of nanoscale fillers and tailored surfactants. Nucleating agents such as talc are normally used in the foaming industry to achieve higher nucleation rates. We have attempted a synergistic combination of external confinement in the foaming die and nanoscale internal confinements via addition of colloidal silica (particle diameter = 10-12 nm) and the above-mentioned surfactants to enhance gas nucleation under various foaming process conditions. The rationale behind using the above surfactants is to have a block that is miscible in the polymer and a second block that has a strong CO_2-philicity (PDMS or PFOMA). We find the highest improvement in cell nucleation densities and uniform cell growth with the addition of the lower molecular surfactant (BCP1), even with liquid CO_2. Results from these studies will be discussed and guidelines for ideal surfactant architectures for different foamed morphologies will be given.

Conclusions

We have developed a new processing strategy to produce nanoporous thin polymer films using a gas foaming process with CO_2. The strategy involves physical restriction of gas diffusion from the film surfaces, allowing for higher gas availability for growth of stable nuclei. The resultant foams not only exhibit remarkably uniform pore morphologies at different length scales depending on the processing conditions, but also possess amazingly thin unfoamed skins. This process methodology has been improved to promote higher nucleation rates at lower CO_2 pressures via addition of a nanoscale filler or a tailored non-ionic surfactant that can influence the polymer- CO_2 interface.

Acknowledgement. This study was supported by the Kenan Center for the Utilization of Carbon Dioxide in Manufacturing and the STC Program of the National Science Foundation under Agreement No. CHE-9876674.

References

(1) Goel S.K. and Beckman E.J. *Polym. Eng. Sci.* **1993**, *34*, 271.
(2) Kumar V. and Weller J. E. *Polymeric Foams: Science and Technology* **1997**, American Chemical Society, Washington DC.
(3) Behravesh A.H., Park C. B. and Venter R. D. *Proc. ANTEC '98* **1998**, 1958.
(4) Siripurapu S., Gay Y. J., Royer J. R., DeSimone J. M., Spontak R. J. and Khan S. A. *Polymer* **2002**, *43*, 5511.
(5) Krause B., Mettinkhof R., van der Vegt N. F. A and Wessling M. *Macromolecules* **2001**, *34*, 874.
(6) Hawker C.J., Hedrick J.L., Miller R.D. and Volksen W. *MRS Bulletin 2000*, *25*, 54.

SELECTIVE CONVERSION OF CO_2 TO ETHYLENE BY THE ELECTROLYSIS AT A THREE-PHASE(GAS/LIQUID/SOLID) INTERFACE IN AN ACIDIC SOLUTION CONTAINING CUPRIC IONS

Kotaro Ogura, Hiroshi Yano, and Fukutaro Shirai

Department of Applied Chemistry, Yamaguchi University,
Tokiwadai Ube 755-8611, Japan

Introduction

We have previously reported that the electrochemical reduction of CO_2 at the three-phase (gas/liquid/solid) interface on a Cu-mesh electrode leads to the formation of major products such as CO, C_2H_4 and CH_4 with high current efficiencies and the deposition of poisoning species is extremely suppressed during the reduction.[1] These beneficial results are caused by the maintenance of high concentration of CO_2 at the three-phase interface in acidic solution. Hitherto, the electrochemical reduction of CO_2 has been performed mainly at the two-phase (liquid/solid) interface with an electrode wholly immersed into electrolyte in which CO_2 is supplied to the electrode through solution. Although a copper electrode shows a high catalytic activity toward the conversion of CO_2 to hydrocarbons with such an electrode in a neutral buffer solution,[2,3] the faradaic efficiencies are known to rapidly decrease after the start of electrolysis and the catalytic activity to disappear almost completely at longer times. This is caused by the deposition of poisoning species.[4,5] In general, neutral buffer solution has been used in such an electrolysis at the two-phase interface, because the hydrogen evolution is predominant in acidic solution and the reduction of CO_2 is difficult due to the insufficient concentration of protons in alkaline solution. As previously pointed out, however, the poisoning process including the deposition of graphitic carbon is expedient in a neutral solution.

In the present study, the electrolysis of CO_2 at the three-phase interface on a copper-mesh electrode was carried out in acidic halide solutions containing cupric ions, and the selective formation of ethylene was observed with a maximum Faradaic efficiency of 73.5% at –2.4V vs Ag/AgCl in a KBr solution of pH 3.

Experimental

The electrolysis cell used was schematically shown in **Figure 1**. The three-phase interface was constructed on a pure copper-mesh (purity 99.99%, 50 mesh, Nilaco Co.). The copper mesh put on a glass filter (average pore size, 20μm) was bound to a Teflon cylinder tightened with a Teflon cap. The cylinder with the copper-mesh was attached to a cathode compartment via an O-ring, which was separated from an anode compartment by a cation-exchange membrane (Selemion CMV 10, Asahi Glass Co.). The bottom of the Teflon cap was fixed to a reservoir containing the same solution as that used in the cathode compartment via an O-ring. The purified CO_2 gas was blown up onto the Cu-mesh through the glass filter from the bottom of the cell, and the reaction gas was circulated via the cathode compartment with a circulating pump. The gas/liquid/solid phase provided on the Cu-mesh electrode was sustained during the electrolysis by adjusting the rate of CO_2 flow, and the net surface area was 10.2cm^2. Before each experiment, the Cu-mesh electrode was immersed to remove Cu oxide in concentrated HCl, and washed with doubly distilled water and then with electrolytic solution in an ultrasonic bath. A platinum plate and an Ag/AgCl/saturated KCl electrode were used as the counter and reference electrodes, respectively. The electrolytes used were 3M KCl or KBr solutions

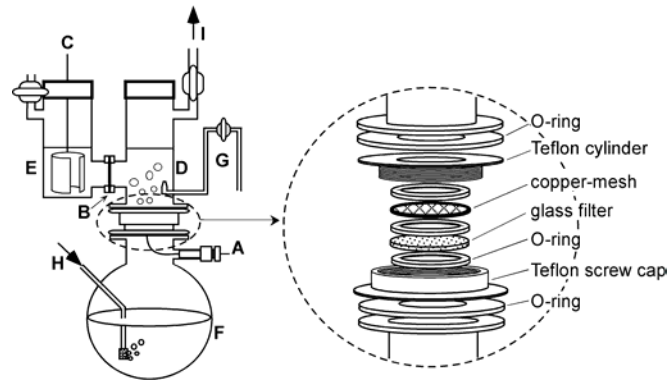

Figure 1 Schematic diagram of an electrolysis cell. A, working electrode (copper-mesh); B, cation-exchange membrane; C, counter electrode; D, cathode compartment; E, anode compartment; F, reservoir; G, Luggin capillary; H, gas inlet; I, gas outlet.

containing various concentrations of $CuSO_4$. The anolyte was always a 0.5M $KHSO_4$ solution of pH 0.

Gaseous products were analyzed with a Shimazu GC-8AIT and a GC-8AIF gas chromatograph. A Shimazu GC-MS spectrometer and an organic acid analyzer were used to analyze aqueous products. The electrode surface after the electrolysis was observed by FE-SEM and EPMA techniques.

Results and Discussion

The electrolysis of CO_2 was performed at the three-phase interface on a Cu-mesh electrode in a KCl solution of pH 3.0, and the Faradaic efficiency for each product is shown in **Figure 2** where the current density observed was : e. g., at –1.8V, 9.1~9.4mA/cm^2. The onset potential for the reduction of CO_2 was –1.4V, and the major products were C_2H_4, CH_4 and CO. Maximum Faradaic efficiencies for C_2H_4, CH_4 and CO were obtained at –1.8V: 46.3% (C_2H_4); 19.9% (CH_4); 18.0% (CO). The Faradaic efficiency for H_2 decreased with

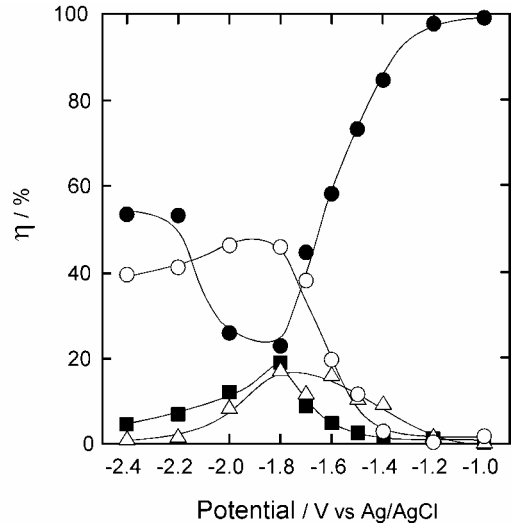

Figure 2 Plot of the Faradaic efficiencies for C_2H_4 (○), CO (△), CH_4 (■) and H_2 (●) versus the electrode potential in a 3M KCl solution of pH 3. Electrolysis time at each potential, 30 min.

Table 1 Faradaic efficiencies for the products obtained in the electrochemical reduction of CO_2 in a 3M KCl solution of pH 3 containing various concentrations of $CuSO_4$ on a Cu-mesh electrode[a)]

$CuSO_4$	Faradaic efficiency / %									Conversion[b)]	Selectivity[c)]	Q[d)]	η[e)]
mmol dm^{-3}	Ethylene	Methane	CO	Ethane	EtOH	Formic	Acetic	Lactic	H_2	%	%	C	%
0	46.3	19.9	18.0	1.1	0.0	2.5	0.4	0.0	23.1	4.5	37.3	177	111
0.01	49.9	20.2	11.3	0.6	0.0	2.6	0.6	0.8	24.3	6.9	45.6	205	110
0.05	52.4	6.1	9.5	1.2	0.2	3.2	0.3	0.2	26.9	7.1	54.0	242	100
0.3	56.5	4.8	5.5	1.0	0.0	3.0	0.2	0.1	33.1	7.0	64.8	267	104
0.5	58.1	4.0	4.6	1.3	0.3	3.7	0.6	0.0	35.5	7.2	65.8	274	108
1.0	61.0	5.5	4.6	1.0	3.5	3.4	0.7	0.6	37.9	7.2	64.0	262	118
1.5	50.5	0.9	4.9	2.6	1.2	2.7	0.4	0.3	41.5	7.5	64.5	358	105

a) Electrolyte,3M KCl containing $CuSO_4$, initial pH, 3.0; the area of a copper-mesh substrate, 10.2 cm^2; electrolysis potential, -1.8V vs Ag/AgCl; electrolysis time, 30 min; initial volume of CO_2, 480 cm^3; catholyte, 205 cm^3.
b) Conversion percentage in the electrolysis at 30 min.
c) Selectivity for the formation of ethylene on the basis of C content.
d) Amount of the electric charge passed in the electrolysis.
e) Total current efficiency in the reduction.

decreasing the potential and showed a minimum value of 20% at –1.8V. Beyond this potential, however, the formation of H_2 was again enhanced, and η reached 52.1% at –2.4V. The total Faradaic efficiency including that for hydrogen evolution was about 100% at each potential. Hence, it is indicated that there was neither unknown product nor poisoning species except for the compounds measured here.

As shown in **Table 1**, the product distribution is considerably affected by the addition of cupric ions to the electrolyte. The Faradaic efficiency for C_2H_4 increased with an increase in concentration of Cu^{2+} until 1mM, and the maximum value of η was 61.0%. Conversely, η for CH_4 and CO were about one fourth as large as those in the absence of Cu^{2+}. On the other hand, the Faradaic efficiency for C_2H_4 was always larger than that for H_2, although the hydrogen evolution was also enhanced by the addition of Cu^{2+}. The results also indicate that the addition of cupric ions was not accompanied by any poisoning reaction. This was supported from the EPMA data in which no any element except copper atom was detected on the electrode after the electrolysis.

In **Figure 3**, the conversion percentage of CO_2 and the Faradaic efficiency of each product are shown versus the electrode potential in a 3M KCl solution containing 1mM $CuSO_4$. The onset potential for the reduction of CO_2 was found to be –1.4V, and the conversion percentage increased linearly as the potential was shifted to the negative side. The current efficiency for ethylene reached a constant value of 65% at about –1.8V, but that for the hydrogen evolution dropped below 20% at –2.4V. Similar result was obtained for the electrochemical reduction of CO_2 in a 3M KBr solution with cupric ion. In a KI solution, however, the conversion percentage of CO_2 and the faradaic efficiency for C_2H_4 both were rather higher than those obtained in KCl solution (**Figure 3**); e. g., conversion percentage: 23.8% (KI), 20.5% (KCl) at –2.4V; faradaic efficiency for C_2H_4: 72.6% (KI), 66.0% (KCl) at –2.4V. Electron probe microanalysis of the electrode which had been used for the electrolysis of CO_2 in halide solutions containing $CuSO_4$ proved that cuprous halides were deposited on the copper-mesh electrode during the electrolysis. Especially, the existence of CuI was extremely evident from a definite EPMA spectrum. Hence, it is suggested that a cuprous halide is deposited *in situ* during the cathodic reduction and this species is involved as a catalyst in the conversion of CO_2 to ethylene.

Thus, the electrochemical reduction of CO_2 at the three-phase

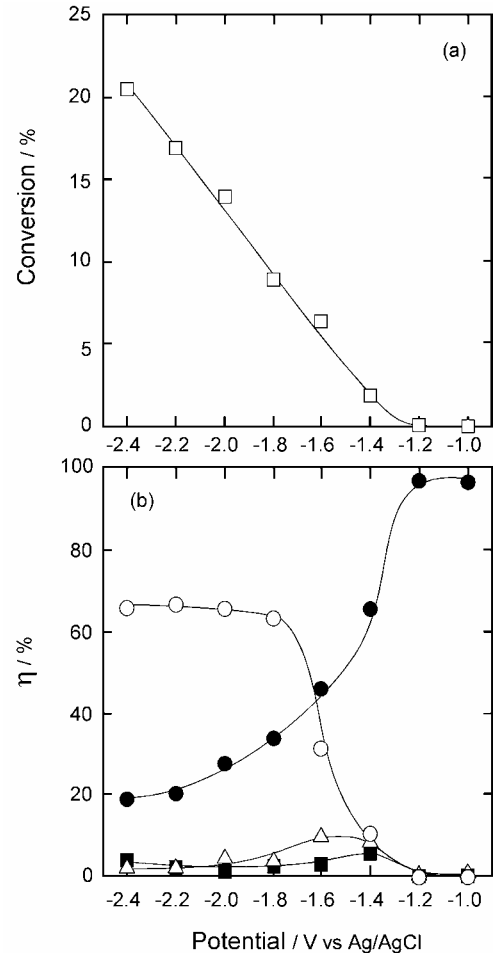

Figure 3 Plots of the conversion percentage of CO_2 (a) and the Faradaic efficiencies (b) for C_2H_4 (○), CO (△), CH_4 (■) and H_2 (●) versus the electrode potential in a 3M KCl solution of pH 3 containing 1mM $CuSO_4$. Electrolysis time at each potential, 30 min. Initial volume of CO_2, 480 cm^3.

interface led to the selective formation of C_2H_4 in a halide solution containing cupric ions. The probable reaction scheme is considered as: CO_2(g) is first reduced to CO(g) at the three-phase interface, CO adsorbs on a newly formed copper surface, and the electrochemical hydrogenation of CO to :CH_2 and the coupling of methylene radicals to C_2H_4 are followed. This would be brought about by the ability of copper halide which can combine reversibly with CO and C_2H_4 through their π bonds.[6]

References

1. H. Yano, F. Shirai, M. Nakayama, K. Ogura, *J. Electroanal. Chem.*, **2002**, 519, 93.
2. Y. Hori, K. Kikuchi, S. Suzuki, *Chem. Lett.*, **1985**, 1695.
3. J. J. Kim, D. P. Summers, K. W. Frese Jr., *J Electroanal. Chem.*, **1988**, 245, 223.
4. G. Kyriacou, A. Anagnostopoulos, *J. Electroanal. Chem.*, **1992**, 328, 233.
5. B. D. Smith, D. E. Irish, P. Kedzierzawski, J. Augustynski, *J. Electrochem. Soc.*, **1997**, 144, 4288.
6. H. Y. Huang, J. Padin, R. T. Yang, *Ind. Eng. Chem. Res.*, **1999**, 38, 2720.

On the mechanism of synthesis of acetic acid directly from CH_4 and CO_2 Using Dielectric-barrier Discharges

Chang-jun Liu[1], Jian-guo Wang[1], Yu Wang[1] and Baldur Eliasson[2]

[1]ABB Plasma Greenhouse Gas Chemistry Laboratory, State Key Laboratory of C1 Chemistry and Technology, Tianjin University, Tianjin 300072, China
[2]ABB Switzerland Ltd., CH5405, Baden, Switzerland

Introduction

The synthesis of acetic acid directly from methane and carbon dioxide is a 100% atomic economic reaction:

$$CH_4+CO_2 \rightarrow CH_3COOH, \quad \Delta G^\circ_{400\,K} = 19.2 \text{ kcal/mol} \qquad (1)$$

The reaction is not favored thermodynamically. Huang et al. proposed a two-step conversion of methane into acetic acid [1]. With the first step, methane is adsorbed in the catalyst. Then, in the second step, the adsorbed methane species react with carbon dioxide to make acetic acid. The main obstacle is presented by thermodynamics rather than kinetics. A periodic operation has been proposed to break the thermodynamic limitations [1]. Regarding this thermodynamic limitation, the gas discharge plasma can be applied for thermodynamically un-favored reactions. We previously reported a direct synthesis of acetic acid from methane and carbon dioxide using dielectric-barrier discharges (DBDs) [2,3]. A yield of up to 2.7% of acetic acid has been achieved. The discharge plasma has been confirmed to be an effective way to make the reaction (1) become true even at ambient conditions. However, the reaction mechanism for such acetic acid synthesis remains unclear. To improve the synthesis, it is very necessary to investigate the reaction mechanism theoretically. In this work, we use the three hybrid DFT methods to study the reaction mechanism of the formation of acetic acid. Several routes of dissociation of CO_2 have been discussed. The main reaction pathways for acetic acid synthesis have been analyzed by using the three hybrid DFT methods. To confirm the mechanism, an experimental investigation has been conducted.

Computations

All the calculations have been performed with the Gaussian98 package [4]. The Becke's three parameters exchange functional [5] were used to combine with three different correlation functions: LYP [6,7], Perdew 86[8] and Perdew and Wang's 1991 gradient-corrected correlation functional[9,10]. The structures of all kinds of molecules and radical were optimized at the B3LYP, B3P86 and B3PW91 level with 6-311G(d, p) basis set. Vibrational frequency calculations were performed for each structure at the same level used for the geometrcal optimization. The potential energy surface was obtained by the Scan calculation.

Results and discussion

The simulation results show that there are two pathways for the synthesis of acetic acid directly from methane and carbon dioxide using dielectric-barrier discharges. One pathway is via CO_2^-, and the other is via the formation of CO. The first pathway requires less energy. Therefore the mechanism can be described as following.

When the reactants are fed into the discharge region, they can be dissociated due to the existence of electrons with energies ranged from 1 to10 eV [11,12]. The reaction is thereby initiated from the dissociation reactions of CH_4 and CO_2:

$$CH_4 \rightarrow CH_3+H \qquad (2)$$
$$e^-+CO_2 \rightarrow CO_2^- \qquad (3)$$
$$e^-+CO_2 \rightarrow O^-+CO \qquad (4)$$
$$e^-+CO_2 \rightarrow O+CO+e^- \qquad (5)$$

The reactions to produce acetic acid via the CO_2^- include:

$$CO_2^-+H \rightarrow COOH^- \qquad (6)$$
$$CH_3+COOH^- \rightarrow CH_3COOH+e^- \qquad (7)$$

Acetic acid can also be synthesized via CO:

$$CH_3+CO \rightarrow CH_3CO \qquad (8)$$
$$CH_3CO+O \rightarrow CH_3COO \qquad (9)$$
$$CH_3CO+O^- \rightarrow CH_3COO^- \qquad (10)$$
$$CH_3COO+H \rightarrow CH_3COOH \qquad (11)$$
$$CH_3COO^-+H \rightarrow CH_3COOH+e^- \qquad (12)$$
or
$$O+H \rightarrow OH \qquad (13)$$
$$O^-+H \rightarrow OH^- \qquad (14)$$
$$CH_3CO+OH \rightarrow CH_3COOH \qquad (15)$$
$$CH_3CO+OH^- \rightarrow CH_3COOH+e^- \qquad (16)$$

The detailed energy parameters calculated will be presented in the future publications.

We have previously reported the direct synthesis of acetic acid from methane and carbon dioxide using dielectric-barrier discharges [2,3]. The experiment has confirmed indirectly the first reaction pathway. To confirm the second reaction pathway, we conducted an experimental investigation using methane and carbon monoxide as the co-feed gases using the same reactor system as reported previously [2,3]. Table 1 presents the conversion of methane and carbon monoxide. It can be seen that the conversion is very high. Table 2 shows the composition of liquid product. Obviously, acetic acid can be produced this way. This confirms the second pathway experimentally.

Table 1. Conversions of methane and carbon monoxide

Ratio of CH_4/CO	2/1	2/1	1/1
Input power/W	50	100	100
Conversion of CH_4	43.74	62.45	72.92
Conversion of CO	14.70	20.02	18.51

Temperature of reaction: 338K; flow rate of feed: 40 ml/min

Table 2. Component of liquid products

Component	w%
Methanol	1.54
Ethanol	2.08
1-Propanol	2.51
2-Butanone	1.81
2-Butanol	3.07
Acetic acid	21.60
Propanoic acid	19.56
Butanoic acid	3.04
Pentanoic acid	1.22
Hydrocarbons	8.25

Temperature of reaction: 338K; flow rate of feed: 40 ml/min

Acknowledgments

The authors are grateful for supports from the Major Research Foundation of Ministry of Education of China (under the contract No. Major 0212) and ABB Corporate Research Ltd., Switzerland.

References

[1] W. Huang, K.-C. Xie, J.-P. Wang, Z.-H. Gao, L.-H. Yin and Q.-M. Zhu, J. Catal. **2001,** 201, 100.

[2] Y. Li, C.-J. Liu, B. Eliasson and Y. Wang, Energy Fuels **2002**, 16, 864.

[3] C.-J. Liu, Y. Li, Y.-P. Zhang, Y. Wang, J. Zou, B. Eliasson and B. Xue, Chem. Lett. **2001**, 1304.

[4] M. J. Frisch, G. W. Trucks, H. B. Schlegel, G. E. Scuseria, M. A. Robb, J. R. Cheeseman, V. G. Zakrzewski, J. A. Montgomery, Jr., R. E. Stratmann, J. C. Burant, S. Dapprich, J. M. Millam, A. D. Daniels, K. N. Kudin, M. C. Strain, O. Farkas, J. Tomasi, V. Barone, M. Cossi, R. Cammi, B. Mennucci, C. Pomelli, C. Adamo, S. Clifford, J. Ochterski, G. A. Petersson, P. Y. Ayala, Q. Cui, K. Morokuma, D. K. Malick, A. D. Rabuck, K. Raghavachari, J. B. Foresman, J. Cioslowski, J. V. Ortiz, A. G. Baboul, B. B. Stefanov, G. Liu, A. Liashenko, P. Piskorz, I. Komaromi, R. Gomperts, R. L. Martin, D. J. Fox, T. Keith, M. A. Al-Laham, C. Y. Peng, A. Nanayakkara, M. Challacombe, P. M. W. Gill, B. Johnson, W. Chen, M. W. Wong, J. L. Andres, C. Gonzalez, M. Head-Gordon, E. S. Replogle, and J. A. Pople, Gaussian 98, Revision A .9, Gaussian, Inc., Pittsburgh PA, 1998.

[5] A. D. Becke, J. Chem. Phys. **1993**, 98, 5648

[6] C. Lee, W. Yang and R. G. Parr, Physical Review B **1988**, 37, 785.

[7] B. Miehlich, A. Savin, H. Stoll and H. Preuss, Chem. Phys. Lett. **1989**, 157, 200.

[8] J.P.Perdew, Phys. Rev. B **1986**, 33, 8822.

[9] J. P. Perdew, in Electronic Structure of Solids '91, Ed. P. Ziesche and H. Eschrig (Akademie Verlag, Berlin, 1991) 11.

[10] J. P. Perdew, J. A. Chevary, S. H. Vosko, K. A. Jackson, M. R. Pederson, D. J. Singh and C. Fiolhais, Phys. Rev. B **1992**, 46.

[11] B. Eliasson, M. Hirth, U. Kogelschatz. J.Phys.D:Appl.Phys. **1987**, 20, 1421

[12] B. Eliasson, U. Kogelschatz. IEEE Trans.Plasma Sci. **1991**, 19, 309

HYDROGEN STORAGE USING COMPLEX HYDRIDES

Darlene K. Slattery,[1] Michael D. Hampton,[2] Janice K. Lomness,[2] Nahid Najafi-Mohajeri,[1] and Mirna Franjic[2]

[1]Florida Solar Energy Center, 1679 Clearlake Rd., Cocoa, FL 32922
[2]Dept. of Chemistry, University of Central Florida, Orlando, FL 32816-2366

Introduction

The storage of hydrogen has long been acknowledged as a primary obstacle to the implementation of a hydrogen economy. To be considered acceptable by current DOE targets, any storage system must contain 6.0 wt% hydrogen or 2000 w-h/kg and 1100 w-h/L and be capable of reversible hydriding. Additional requirements include a cost of $5/kw-h, a decomposition temperature of less than 80°C, a hydrogen release rate of 1.5 g/sec and a recharge time of less than 5 minutes. Currently no system meets all of these requirements.

Complex hydrides of aluminum are attractive as hydrogen storage compounds due to their large hydrogen content. Their application in this manner has been impractical as a result of the great difficulties in reversing the hydrogen release reaction. Interest in these materials as hydrogen storage media has been rekindled by reports from several laboratories that a number of catalysts improve the rehydriding of some complex hydrides of aluminum.

The recent advances in hydride storage by the research groups of Bogdanovi,[1] Jensen,[2] Zaluski,[3] and Gross[4] have illustrated the reversibility of $NaAlH_4$, and Na_3AlH_6. However, these complex hydrides have not been shown to contain the required amount of hydrogen. Furthermore, the mechanism by which the reported catalysts function is a matter of debate and mystery. For example, one study by Jensen,[5] reported that Ti doping of $NaAlH_4$ with $Ti(OBu)_4$ resulted in the formation of a red-violet substance, suggesting the reduction of the titanium from +4 to +3. Elemental analysis showed virtually no carbon in the samples and x-ray data indicated the presence of non-metallic Ti on the surface, suggesting the presence of a titanium hydride species and the loss of the organic groups as butanal. A later work[6] reported that the hydrogen desorbed from $NaAlH_4$ doped with liquid catalysts such as $Ti(OBu)_4$, is contaminated with hydrocarbons.

In this paper, the hydrogen interaction properties of an alanate with a hydrogen capacity greater than that of $NaAlH_4$ will be presented. The effects of catalysts, such as Ti, $TiCl_4$, and $TiCl_3$ will also be presented and discussed from a fundamental chemical viewpoint.

Experimental

Lithium aluminum hydride, powder 97%, was obtained from Lancaster and was used as received, with no additional purification, unless it was to be used as a reagent in a synthetic procedure. All other reagents were obtained from Fisher Scientific and purified using standard procedures.

Differential Scanning Calorimetry. The compounds characterized via differential scanning calorimetry were studied using a SETARAM DSC111, equipped with high pressure cells. The high pressure cells are made of Hastelloy C22 and are equipped with quick disconnects and pressure transducers. This instrumentation allows simultaneous pressure, temperature, and heat flow measurement. Hydrogen release was studied in an argon atmosphere, initially at ambient pressure. Hydrogen uptake was studied in an atmosphere of hydrogen at 120 psi. In all analyses, the furnace temperature was changed at a rate of 2°C/min from ambient to 450°C.

Thermovolumetric Analysis. Thermovolumetric analysis was obtained using one gram samples of each hydride. The TVA is a modified Sievert's apparatus and the high pressure vessel is constructed of Monel. The sample was loaded in the TVA, under a nitrogen atmosphere. The temperature of the reactor was ramped from ambient to 300 °C, at 2°C/minute. Data for temperature and pressure was acquired using National Instruments hardware and LabView software. Data were plotted with weight percent hydrogen released as a function of temperature.

Ball milling. All samples to be ball milled were loaded into a stainless steel vial under an inert atmosphere in a glove box. Stainless steel balls were added at a 17:1 ratio and samples were run for one hour using a SPEX 8000M mixer/mill.

Results and Discussion

To study the effect of the method of catalyst loading and to determine if residual by-products could be eliminated, we used the methods outlined by Jensen and compared them to results obtained by simple ball milling of an alanate with elemental Ti. If Ti is added as an alkoxide or as $TiCl_4$, some of the alanate is decomposed as the Ti^{4+} is reduced and H_2 is evolved, decreasing the amount of hydrogen containing material. In addition, if $TiCl_4$ is used, one of the by-products will be a chloride salt, thereby further reducing the wt% of hydrogen containing material. The experiments conducted in this study showed that the undoped material released over 7 wt% hydrogen while the $TiCl_4$ doped material only released about 2 wt% hydrogen. On the other hand, the addition of elemental Ti was found to have the same effect on lowering release temperature and improving kinetics, **Figure 1**. Since the titanium was already in the zero valent state, no alanate was consumed to reduce it and the hydrogen content was preserved

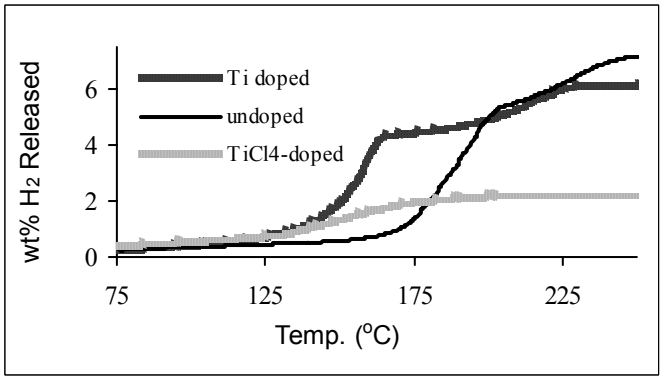

Figure 1. The Dehydriding of Undoped and Undoped $LiAlH_4$.

In an additional attempt to understand the effect of the initial form on dehydriding characteristics, $TiCl_3$ was also added via ball milling with $LiAlH_4$. For this sample, the dehydriding temperature, determined using DSC, was nearly 75 °C lower than that of the undoped material. Unfortunately, the wt% of hydrogen released was less than 1.5.

Because mechanical milling was used to incorporate the catlysts into samples, the effect of ball milling alone was first determined. **Figure 2** shows the hydrogen release curves for unaltered and ball milled $LiAlH_4$. It is clear that ball milling caused a decrease of approximately 25 °C in the hydrogen release temperature relative to the unaltered material. .

Additional studies are ongoing with regard to the reversibility of the dehydriding reaction and the exact nature of the catalytic species.

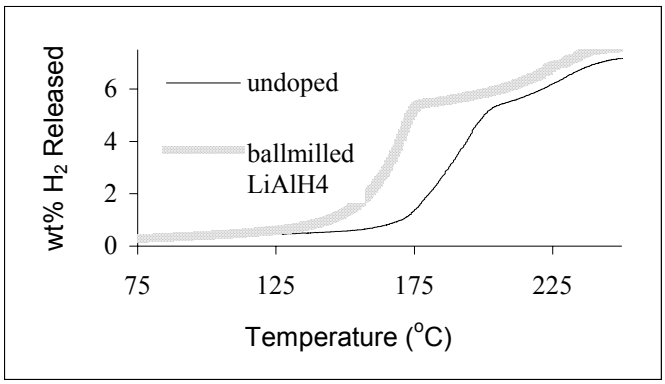

Figure 2. The Dehydriding of Ball Milled and Unaltered $LiAlH_4$

Conclusions

The influence of the method of addition and the form of the titanium added to $LiAlH_4$ were studied. Titanium added in the form of $TiCl_3$ lowered the release temperature by the greatest amount but the quantity of hydrogen released was also the lowest. Adding elemental titanium via ball milling decreased the release temperature by 30 ^oC while maintaining the weight content of hydrogen. Ball milling in the absence of a catalyst was also shown to decrease the release temperature, increase kinetics and preserve hydrogen content.

Acknowledgement. The authors gratefully acknowledge funding from the Department of Energy under cooperative agreement DE-FC36-01GO11094.

References

[1] Bogdanovi, B., Brand, R. A., Marjanovic, A., Schwickardi, M. and Tolle, J. *J. Alloys and Compounds*, **2000,** 302, 36.

[2] Jensen, C. M., Zidan, R., Mariels, N., Hee, A. and Hagen, C. *Int. J. Hydrogen E.*, **1999,** 24, 461.

[3] Zaluski, L., Zaluska A., and Ström-Olsen, J.O. *J Alloys and Compounds,* **1999,** 290, 71.

[4] Gross, K.J., Guthrie, S., Takara, S., and Thomas, G. *J. Alloys Comp.,* **2000**, 297, 270.

[5] Jensen, C. M., Zidan, R., Mariels, N., Hee, A., and Hagen, C. *Int. J. Hydrogen E.*, **1999,** 24, 461.

[6] Gross, K.J., Thomas, G.J., and Jensen, C.M. *J. Alloys and Compounds*, **2002,** 330-332, 683.

PERFORMANCE OF METAL-DOPED SODIUM ALUMINIUM HYDRIDE FOR REVERSIBLE HYDROGEN STORAGE

Jun Wang[1], Armin D. Ebner[1], Keith R. Edison[1], James A. Ritter[1], and Ragaiy Zidan[2].

[1]Department of Chemical Engineering
University of South Carolina
Columbia, SC 29208 USA

[2]Westinghouse Savannah River Company
Savannah River Technology Center
Aiken, SC 29804 USA

Introduction

Metal-doped $NaAlH_4$ is becoming a very promising material for H_2 storage because it contains a high concentration of useful hydrogen (5.6 wt%). At standard conditions, the dehydrogenation of $NaAlH_4$ is thermodynamically favorable, but it is kinetically slow and takes place at temperatures well above 200°C in a two-step process involving the following reactions:[1-4]

$$3NaAlH_4 \rightarrow Na_3AlH_6 + 2Al + 3H_2 \quad (1)$$

$$Na_3AlH_6 \rightarrow 3NaH + Al + 3/2H_2 \quad (2)$$

The first work on the doping of $NaAlH_4$ with Ti used solution chemistry techniques, whereby nonaqueous solutions of $NaAlH_4$ and either $TiCl_3$ or $Ti(OBu^n)_4$ catalyst precursors were decomposed to solid Ti-doped $NaAlH_4$.[1] Zidan et al.[2] and other investigators[3-5] discovered later that a further lowering of the dehydrogenation temperature was highly dependent on the doping and homogenization procedures. They also found that Zr when mixed with Ti improved the dehydrogenation reversibility of $NaAlH_4$ over Ti alone. These favorable effects of using mixed metals as the dopant generated interest in trying other combinations of mixed metal catalysts. The objective of this study is to show the effects of Ti, Fe, Zr and their combinations on the H_2 desorption kinetics of $NaAlH_4$.

Experimental

$TiCl_3$ (Aldrich), $FeCl_3$ (Aldrich, 99.99%, anhydrous) and $ZrCl_4$ (Aldrich, 99.9%) were used as received as the catalyst precursors. Crystalline $NaAlH_4$ (Fluka) was purified from a THF (Aldrich, 99.9%, anhydrous) solution and vacuum dried. The dried $NaAlH_4$ was mixed with a predetermined amount of catalyst in THF to produce a doped sample in the desired concentration up to 4 mole% total metal. Samples containing a single catalyst or a combination of them were all prepared in this manner. The THF was evaporated while the $NaAlH_4$ and the catalyst were mixed manually for about 30 minutes using a mortar and pestle, or until the samples were completely dry. These mixtures were then ball-milled for 2 h, using a high-energy SPEX 8000 mill. The above procedures were carried out in a N_2–laden glove box free of oxygen and moisture.

A Perkin-Elmer thermogravimetric analyzer (TGA) was used to determine the hydrogen desorption kinetics at atmospheric pressure. This instrument was located in another glove box under nitrogen atmosphere to prevent any exposure of the samples to air and moisture. Samples were heated to 250°C at a ramping rate of 5°C/min under 1 atm of He, using an initial 1 minute delay to ensure an environment of pure He. Approximately 10 mg of sample were used in the TGA.

Results and Discussion

Figure 1 shows the TGA results for catalyzed $NaAlH_4$ with 1 to 4 mole% $TiCl_3$. The 4 mole% Ti sample exhibits the best behavior with respect to the H_2 desorption kinetics, while the 1 mole% Ti sample has the highest H_2 capacity. In the recent study by Sandrock et al,[6] they found that the $TiCl_3$ was completely reduced by Na in the $NaAlH_4$ to form NaCl and most likely zero-valent Ti. This solid state reaction can be written as: [6]

$$(1-x)NaAlH_4+xTiCl_3 \rightarrow (1-4x)NaAlH_4+3xNaCl+xTi+3xAl+6xH_2 \quad (3)$$

where x is the mole fraction of $TiCl_3$ in the $NaAlH_4$. This reaction shows that the H_2 capacity depends on the amount of $TiCl_3$ in the sample. Theoretically, after doping with 4 mole% Ti, the H_2 capacity decreases to 4.6 wt%; the experimental value obtained here is very close to this value at 4.5 wt%. Clearly, the $TiCl_3$ loading has a negative effect on the H_2 capacity. In contrast, the $TiCl_3$ loading has a positive effect on the H_2 desorption kinetics, which increases with increasing $TiCl_3$ loading.

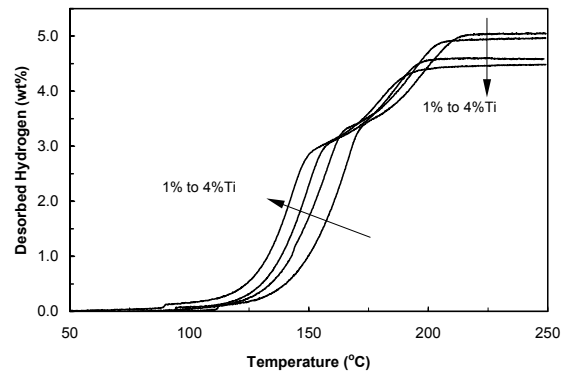

Figure 1. TGA analyses of $NaAlH_4$ doped with 1 to 4 mole% Ti.

Figure 2 shows the TGA analyses for $NaAlH_4$ doped with 4 mole% each of the three different metal chlorides. The 4 mole% Ti sample exhibits the best behavior with respect to the H_2 desorption kinetics, followed by 4 mole% Zr and then 4 mole% Fe. This result confirms that Ti by itself is the best catalyst with respect to the kinetic behavior. Figure 3 shows the TGA analyses for $NaAlH_4$ catalyzed with 4 mole% metal, but in different combinations and with each containing with 1 mole% Fe. The 1 mole% Fe-3 mole% Ti sample exhibits the best behavior with regard to the H_2 desorption kinetics and again the kinetics increase with increasing Ti loading. Figures 4 to 6 compare the 1 to 3 mole% Ti samples with different amounts of Fe and Zr and Ti itself. All the mixed metal samples with the same Ti loading have similar profiles, i.e., the samples with 1 or 2 mole% Ti exhibit similar kinetics and H_2 capacity. However, by comparing with Ti alone at the same loading, the 1 or 2 mole% Ti mixed with different metals show an improved kinetic profile, while losing some H_2 capacity. Surprisingly, the 1 mole% Fe-3 mole% Ti sample is better than the 4 mole% Ti sample with respect to H_2 desorption kinetics, but it does nothing for improving the kinetics of the second reaction depict in eq 2. This synergistic behavior with the Fe-Ti mixed catalyst system is very interesting and needs to be explored in more detail. In general, however, all the samples containing Ti exhibited the best behavior.

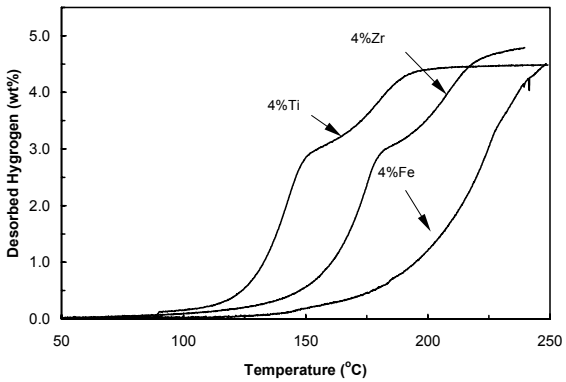

Figure 2. TGA analyses of $NaAlH_4$ doped with varying amounts of the three pure metal chloride catalysts.

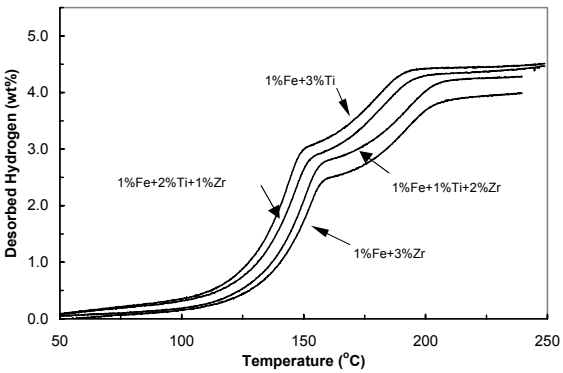

Figure 3. TGA analyses of $NaAlH_4$ doped with 4 mole% metal, but in different combinations and with each containing with 1 mole% Fe.

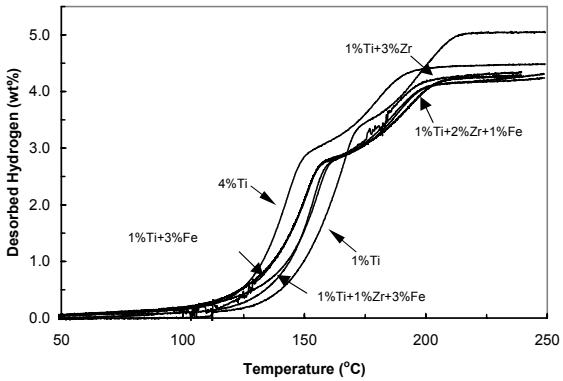

Figure 4. TGA analyses of $NaAlH_4$ doped with 4 mole% metal, but in different combinations and with each containing with 1 mole% Ti.

Conclusions

In an ongoing effort to reduce the kinetic limitation of the dehydrogenation of $NaAlH_4$, while maintaining sufficient H_2 capacity, the effect of different transition metal catalysts (Ti, Zr, Fe) in various combinations have been investigated using thermogravimetric analyses. The Ti doped systems, in all cases, exhibited the lowest H_2 desorption temperature, with the H_2 desorption kinetics improving with an increase in the Ti loading, but at the expense of decreasing the H_2 capacity. In all samples doped with 4 mole% combinations of Ti, Zr and Fe, the Ti played the most important role; however, an interesting synergistic behavior was revealed when doping $NaAlH_4$ with 1 mole% Fe and 3 mole% Ti.

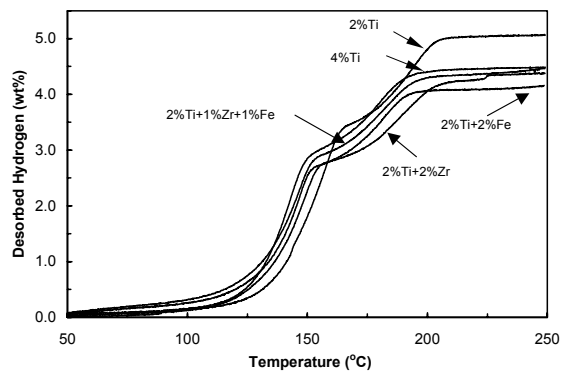

Figure 5. TGA analyses of $NaAlH_4$ doped with 4 mole% metal, with at least 2 mole% Ti and varying amounts of Fe and Zr.

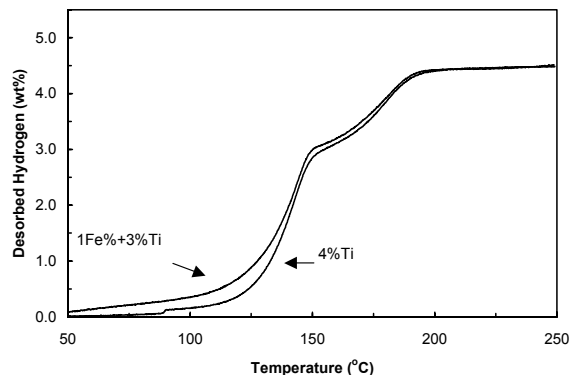

Figure 6. TGA analyses of $NaAlH_4$ doped with 1 mole% Fe-3 mole% Ti and 4 mole% Ti.

Overall, these results continue to prove that doping $NaAlH_4$ with transition metals, especially Ti, improves the H_2 dehydrogenation kinetics. However, more research still needs to be done to lower the dehydrogenation temperature even further, especially for the second reaction depict in eq 2. In this study, the effect of the different transition metals played an insignificant role in reducing the dehydrogenation temperature or increasing the kinetics of the second reaction. Other metals and metal combinations are currently being explored for this purpose, as well as to further reduce the dehydrogenation temperature of the first reaction.

Acknowledgements

Financial support provided by SCUREF/WSRC/DOE under contract WEST052, KG09725-O, and the National Reconnaissance Office under contract NRO-00-C-0134 is greatly appreciated.

References

1. B. Bogdanovic, M. Schwickardi, J. Alloys Comp. 253 (1997) 1.
2. B. Bogdanovic, R. A. Brand, A. Marjanovic, M. Schwickardi, J. Tölle, J. Alloys Comp. 302 (2000) 36.
3. R. A. Zidan, S. Takara, A. G. Hee C. M. Jensen, J Alloys Comp. 285 (1999) 119.
4. C. M. Jensen, R. Zidan, N. Mariels, A. Hee, C. Hagen, Inter. J. Hydrogen Energy 24 (1999) 461.
5. C. M. Jensen, K. J. Gross, Appl. Phys. A: Mat. Sci. Proc. 72 (2001) 213.
6. G. Sandrock, K. J. Gross, G. Thomas, J Alloys Comp. 339 (20002) 299.

Hydrogen Separation by Zeolite Membranes

Xiaochun Xu[,1,2], Weishen Yang[*,2], Chunshan Song[*,1], Jie Liu[2], and Liwu Lin[2]*

1. Clean Fuels and Catalysis Program, The Energy Institute, and Department of Energy & Geo-Environmental Engineering, The Pennsylvania State University, 209 Academic Projects Building, University Park, PA 16802, USA
2. State Key Laboratory of Catalysis, Dalian Institute of Chemical Physics, Chinese Academy of Sciences, Dalian 116023, China
* Corresponding author: Xiaochun Xu (E-mail: xux1@psu.edu; Tel: +1-814-865-6617; Fax: +1-814-234-8461); Weishen Yang (E-mail: yangws@ms.dicp.ac.cn; Tel: +86-411-4379073; Fax: +86-411-4694447); Chunshan Song (E-mail: csong@psu.edu; Tel: +1-814-863-4466; Fax: +1-814-865-3248)

Introduction

Hydrogen is a potential ultra-clean energy for the future and an important chemical for the chemical and refining industries.[1] With the introduction of fuel cells for vehicular propulsion and power generation, the demand of hydrogen may increase significantly.[2] Using hydrogen in these areas will contribute to the reduction of energy-related environmental impacts, including anthropogenic carbon emissions; mobile source emissions such as CO, NO_x, SO_x, and particulates. Hydrogen can be produced from fossil fuels or non-fossil fuels such as biomass. The separation of hydrogen from its source gas mixtures is often the first step for the hydrogen applications. Membrane separation is one of the promising methods for hydrogen separation. Currently, palladium (or palladium alloy) membranes[3] are widely studied and mixed protonic-electronic conducting membranes[4] was reported recently. Palladium and mixed conducting hydrogen membrane showed high hydrogen selectivity. However, they have the disadvantage of the low flux. In addition, the palladium membrane shows hydrogen brittleness and may not be applied for long-term use.[3]

The molecular size of hydrogen is 2.89 Å, and is much smaller than those of the other gases, e.g., 3.64 Å for N_2 and 4.3 Å for normal alkanes.[5] Zeolite is a kind of crystalline materials with uniform-sized pores between 3-10 Å. Therefore, hydrogen can be separated from gas mixtures through molecular sieving or configuration diffusion mechanism if zeolite can be configured into membrane form. Here, we report the synthesis and hydrogen separation properties of MFI and NaA zeolite membrane.

Experimental

1. Support A self-made porous α-Al_2O_3 disk (30 mm in diameter, 3 mm in thickness, 0.1~0.3 μm pore radius, about 50% porosity) was used as the support. The surface of the support was polished with sand paper on both sides, after which the support was cleaned with deionized water in an ultrasonic cleaner for ca. 3-5 min to remove the loose particles created during polishing. Before hydrothermal synthesis or coating the nucleation seeds, the cleaned support was calcined in air at 673 K for 3 hours with a heating and cooling rate of 4 K/min to burn off the organics on the support surface.

2. MFI Zeolite Membrane Synthesis The synthesis mixture was prepared from silica sol, sodium hydroxide, tetrapropylammonium bromide (TPABr) and water. The molar ratio of the resultant solution mixture was $4Na_2O$:5TPABr:$100SiO_2$: $10000H_2O$. The crystallization was carried out at 453 K for 24 hours in a stainless steel autoclave with the support held vertically in the synthesis mixture by a Teflon holder. After synthesis, the membrane was washed several times with deionized water, dried at 373 K and calcined at 773 K in the air to remove TPABr which occluded the zeolite channels.

3. NaA Zeolite Membrane Synthesis One side of the support was coated with NaA zeolite crystals as nucleation seeds before synthesis.[6] The synthesis mixture was prepared by mixing sodium aluminate, sodium silicate solution, sodium hydroxide and water. The molar ratio of the resultant gel mixture was $3Na_2O$:$2SiO_2$:Al_2O_3: $200H_2O$. The synthesis was carried out at 363 K for 24 hours in a stainless steel autoclave with the seeded support held vertically in the synthesis mixture by a Teflon holder. After synthesis, the membrane was washed several times with deionized water until the pH of the washings became neutral, then dried at 423 K for 3 hours. In order to obtain a high quality NaA zeolite membrane, the synthesis was repeated two times (refer to as three-stage synthesis).

4. Characterization The structure of the as-synthesized membranes were determined by X-ray diffraction (XRD) patterns. XRD was carried out on a Ragaku D max/b powder diffractometer using Cu K_α (λ=1.54 Å) radiation operating at 40KV and 50mA. The morphology and thickness of the as-synthesized membrane were examined by scanning electron microscope (SEM). The SEM photographs were obtained on a JEM-1200E scanning electron microscope.

5. Gas Permeation Measurement The as-synthesized membranes were sealed in a permeation module with the zeolite membrane on the high-pressure side. The gas permeances (flux) of the membranes were measured by a soap-film flowmeter under a pressure difference of 0.10 MPa at different temperatures. The permselectivity of A/B is defined as the permeance ratio of the gas A and the gas B.

Results and Discussions

1. MFI zeolite Membrane The as-synthesized membrane was characterized by XRD and SEM. The XRD patterns (not shown) represented the sum of the diffraction patterns of MFI zeolite and α-Al_2O_3 support, which indicated that pure MFI zeolite membrane was synthesized on the support surface. SEM images (Figure 1) showed that the zeolite crystals inter-grew well and the thickness of the MFI zeolite membrane was about 35 μm.

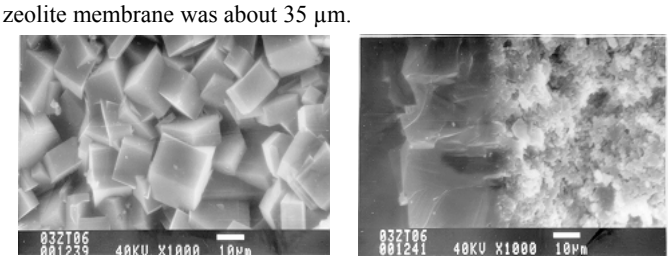

(a) (b)

Figure 1. Top view (a) and cross-section (b) SEM image of MFI zeolite membrane.

Gas permeation property of the MFI zeolite membrane was shown in Figure 2. Before synthesis, the α-Al_2O_3 support showed a H_2 permeance of 1.69×10^{-5} mol/m^2.s.Pa, and H_2/N_2, H_2/n-C_4H_{10} permselectivity of 2.68 and 1.51 at 298 K (Figure 5). After synthesized the MFI zeolite membrane on the support, the H_2 permeance decreased to 5.98×10^{-8} mol/m^2.s.Pa, which was only 0.35% of the α-Al_2O_3 support. The H_2/N_2 permselectivity slightly increased to 3.08 and the H_2/n-C_4H_{10} permselectivity sharply increased to 47.8. With the increase in permeation temperature, gas permeances increased. The H_2/N_2 permselectivity hardly changed and the H_2/n-C_4H_{10} permselectivity gradually decreased.

2. NaA zeolite Membrane XRD patterns of the as-synthesized membrane showed that only diffraction patterns of NaA zeolite and the α-Al_2O_3 support appeared in the diffraction diagram (not shown),

which indicated that only NaA zeolite membrane was synthesized on the support surface. SEM images (Figure 3) showed that the zeolite crystals highly inter-grew and the thickness of the NaA zeolite membrane was about 18 µm.

Gas permeation property of the NaA zeolite membrane was shown in Figure 4. The NaA zeolite membrane showed a H_2 permeance of 2.86×10^{-7} mol/m^2.s.Pa. The H_2/N_2 and H_2/n-C_4H_{10} permselectivity was 23.8 and 106, respectively, at 298 K. With the increase in permeation temperature, gas permeance increased. The H_2/N_2 and H_2/n-C_4H_{10} permselectivity gradually decreased with the increase in permeation temperature.

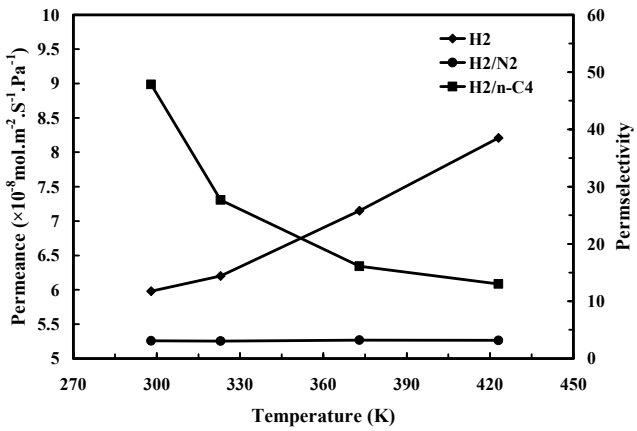

Figure 2. Gas permeation Properties of MFI zeolite membrane.

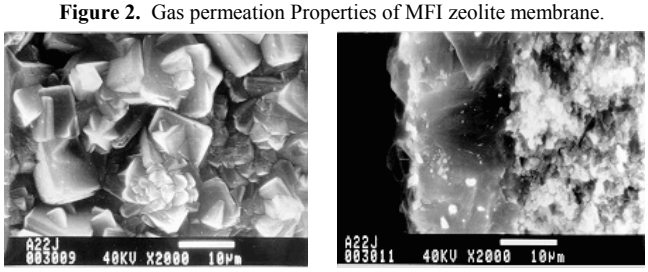

(a) (b)

Figure 3. Top view (a) and cross-section (b) SEM image of NaA zeolite membrane.

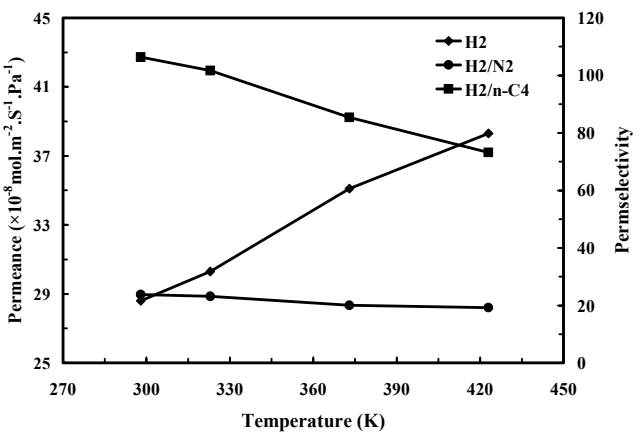

Figure 4. Gas permeation Properties of NaA zeolite membrane.

3. Comparison

Gas permeation properties of the α-Al_2O_3 support, MFI zeolite membrane and NaA zeolite membrane are compared in Figure 5. Compared the MFI zeolite membrane with NaA zeolite membrane, the NaA zeolite membrane showed not only a high permeance but also a large permselectivity. The higher permeance of NaA zeolite membrane than that of MFI zeolite membrane can be explained by the formation of a thinner membrane for NaA zeolite membrane than for MFI zeolite membrane. The membrane thickness was 18 µm and 35 µm for NaA zeolite membrane and for MFI zeolite membrane respectively. The difference in permselectivity can be related to the different pore size of NaA zeolite and MFI zeolite. The molecular size for H_2, O_2, N_2, n-C_4H_{10} and i-C_4H_{10} are 2.89 Å, 3.46 Å, 3.64 Å, 4.3 Å and 5.0 Å respectively. The pore size of NaA zeolite is 4.1 Å and the pore size of MFI zeolite is ~ 5.5 Å. Therefore, n-C_4H_{10} should not permeate through a defect-free NaA zeolite membrane and n- C_4H_{10} can permeate through the MFI zeolite channels. The gas separation of H_2/n-C_4H_{10} was controlled by molecular sieving for NaA zeolite membrane and by configuration diffusion for MFI zeolite membrane. This can explain the higher H_2/n-C_4H_{10} permselectivity of NaA zeolite membrane than that of MFI zeolite membrane. Since the pore size of MFI zeolite is much larger than the molecular size of N_2 and the pore size of NaA zeolite is near the molecular size of N_2, the H_2/N_2 separation showed a configuration diffusion mechanism for NaA zeolite membrane and a Knudsen diffusion behavior for MFI zeolite membrane. This can explain the higher H_2/N_2 permselectivity of NaA zeolite membrane than that of MFI zeolite membrane. Worthy to mention is that, n-C_4H_{10} and i-C_4H_{10} can all permeate through the MFI zeolite channels. Due to the configuration diffusion, MFI zeolite membrane showed a high n-C_4H_{10}/i-C_4H_{10} permselectivity. However, since n-C_4H_{10} and i-C_4H_{10} all permeate through the defects in NaA zeolite membrane, NaA zeolite membrane did not show any separation on n-C_4H_{10} and i-C_4H_{10}.

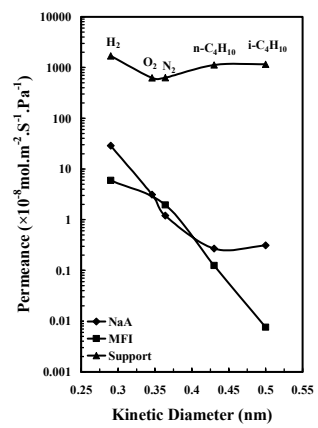

Figure 5 Comparison of the gas permeation properties of α-Al_2O_3 support, MFI zeolite membrane and NaA zeolite membrane.

Conclusions

MFI membrane and NaA zeolite membrane were successfully synthesized on the porous α-Al_2O_3 support. Both the MFI and NaA zeolite membrane showed a high H_2/n-C_4H_{10} permselectivity. Since NaA zeolite has a smaller pore size than MFI zeolite, the NaA zeolite membrane has a higher H_2/n-C_4H_{10} permselectivity.

References

(1) Song, C. Catalysis Today, **2002**, 77, 17-50; Song, C.; Gaffney, A. M.; Fujimoto, K. (Eds). *CO_2 Conversion and Utilization*. American Chemical Society (ACS), Washington DC, ACS Symp. Series, Vol. 809, **2002**, 448 pp;
(2) Armor, J.N. Applied Catalysis A: General, 1999, 176 (2), 159-176; U.S. DOE. *Carbon Sequestration-Research and Development.* 1999, http://www.fe.doe.gov/coal_power/sequestration/reports/ rd/index.html.
(3) Paglieri, S.N.; Way, J.D. Innovations in palladium membrane research, *Separ. Purif. Meth.,* **2002**, *31*, 1-169.
(4) Bose, A.C.; Richards, R.E.; Sammells, A.F.; Schwartz, M. Beyond state-of-the-art gas separation processes using ion-transport membranes, *Desalination*, **2002,** *144*, 91-92.
(5) Breck, D.W. (Eds). *Zeolite Molecular Sieves: Structure, Chemistry and Use*, John Wiley & Sons, New York, 1974.
(6) Xu, X.C.; Yang, W.S.; Liu, J.; Lin, L.W. Synthesis of NaA zeolite membrane from clear solution, *Microporous and Mesoporous Materials*, **2001**, *43*, 299-311.

MECHANISM OF PERMEATION IN HYDROGEN SELECTIVE SILICA MEMBRANES

S. T. Oyama, D. Lee

Environmental Catalysis and Materials Laboratory
Department of Chemical Engineering
Virginia Tech
Blacksburg, VA 24061

Introduction

Composite membranes formed by the deposition of a thin SiO_2 layer on a porous Vycor glass support are well known (1-9). In this work we analyze in detail the permeation mechanism of small gas species through this silica layer. The order of permeance through the silica layer is highly unusual, He > H_2 > Ne, following neither molecular weight nor size. This is the same order as observed in vitreous silica glass, but occurs with lower activation energies in the silica layer. The order of permeation is explained for the first time using a statistical approach, which takes into consideration the density of solubility sites for the various species and the vibrational frequency of the species within the sites.

The membranes are generally prepared by chemical vapor deposition of a silica precursor at low temperatures using H_2O, O_2 or O_3 as co-reactants. This work describes the preparation of a special highly hydrogen permeable silica membrane, referred to as Nanosil, obtained by an adaptation of the method. Instead of using low temperatures, the SiO_2 layer is deposited at high temperatures by thermal decomposition. This gives rise to a composite membrane with excellent selectivity (~10^4) for the small gas molecules (He, Ne and H_2) over other larger gas molecules (CO_2, CO, and CH_4). The gas permeance on the deposited silica layer was obtained by applying a series analysis of gas permeation on the combined silica layer and Vycor support composite system. The experimental gas permeation data on Vycor glass support alone could be explained by a mechanism involving Knudsen diffusion in parallel with surface diffusion.

Experimental

The Nanosil membrane was prepared by depositing a thin silica layer on a porous Vycor support by the chemical vapor deposition (CVD) of tetraethylorthosilicate (TEOS) at 873 K in an argon stream. Vycor glass (7930 glass, Corning, Inc.) with a 4 nm nominal average pore size was used as a substrate for the silica deposition. It had a tubular geometry with an outside diameter of 10 mm and a thickness of 1 mm. A 4 cm section of the Vycor glass was connected to two pieces of quartz tubing by glassblowing joints. This substrate was installed concentrically inside another piece of tubing of 14 mm inside diameter using machined Swagelok fittings with Teflon ferrules. After placing the assembly in an electric furnace, argon gas flows were introduced on the outer shell side (20 μmol s^{-1}) and inner tube side (8 μmol s^{-1}) of the reactor (flow rates in μmol s^{-1} may be converted to cm^3 min^{-1} (NTP) by multiplying by 1.5), and the temperature was raised to 873 K. A flow of tetraethylorthosilicate (TEOS, Aldrich, 98%) was introduced on the inside of the Vycor substrate through a bubbler (at 298 K) using argon (3 μmol s^{-1}) as a carrier gas. This stream was premixed with the tube stream of argon before introducing it to the tube side to produce a stream with a TEOS concentration of 0.03 mol m^{-3} (0.07 mol %).

General gas permeation measurements were conducted in the temperature range of 300 – 873 K by flowing 20 μmol s^{-1} of a pure gas at 123 kPa in the outer shell side. The permeation rate of each gas exiting from the inside of the membrane tube was measured with a sensitive bubble flow meter at atmospheric pressure. The permeance of gas was obtained from $Q_i = F_i / A\ \Delta P$, where Q_i is the permeance (mol m^{-2} s^{-1} Pa^{-1}), F_i is the gas flow rate on the tube side (mol s^{-1}), A is the surface area (m^2) of the membrane section, and ΔP is the pressure difference (Pa) between the shell and tube side.

For higher sensitivity the permeance of the gases was also measured with a gas chromatograph (GC) equipped with a thermal conductivity detector (SRI, Model 8610B). The shell side gas flow rates and pressure conditions were the same as above, however, on the tube side an argon flow was introduced as a sweep gas for the permeated gas. The tube side outlet gas flow rate was measured using a bubble flow meter, and the flow was injected into the GC to obtain the concentration of the permeated gas. The permeance was then calculated using the outlet gas flow rate and the concentration of the permeated gas on the tube side.

Results and Discussion

It is found that the Nanosil membrane has 100% selectivity to the small gas molecules He, H_2 and Ne. Larger species like CO2, CO, CH_4 are completely excluded. This is likely to be a size effect. The structure of the silica layer can be viewed as a disordered form of cristobailite containing rings formed from connected SiO_4 units. The rings contain between 5-8 units and the limiting size is 0.3 nm. Thus, the larger species (Fig. 1) cannot pass through because their molecular size exceeds this limit.

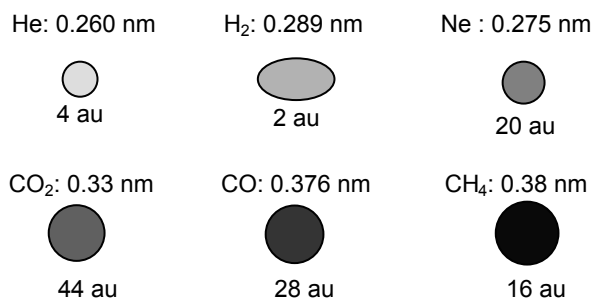

Figure 1. Sizes and molecular weights of permeating species.

Careful studies have been made on the permeation of these species on the Vycor support (10). The permeance is typical for this type of membrane, of the order of ~10^{-8} mol m^{-2} s^{-1} Pa^{-1}. It is found that the small gas species He, H_2, and Ne permeate by a Knudsen diffusion mechanism. The larger species, CO_2, CO, and CH_4 permeate by a parallel Knudsen diffusion and surface diffusion mechanisms. This is reasonable, as the interaction of these condensable molecules with the surface of the membrane is stronger.

In a previous paper, atomic force microscopy (AFM) images of the Vycor and the Nanosil membrane surface were reported (11). The thickness of the silica layer deposited on the Vycor was deduced to be approximately 10 nm from the change in surface topology after the silica deposition. Therefore, it appears that the unusually high H_2 selectivity on the Nanosil membrane originates from the thin defect free SiO_2 layer, with only the small gas molecules (He, Ne and H_2) being able to pass through the silica layer. Considering the pore size of the Vycor support (3.6 nm), this 10 nm thickness of the silica layer may be of the order of the smallest thickness level that can be achieved by the CVD technique. This thickness is much smaller than the thickness (500 nm) obtained by conventional CVD of silica (12).

The Nanosil membrane can be viewed as a composite system composed of the Vycor support and a the thin layer of silica on top. A schematic is shown in Fig. 2.

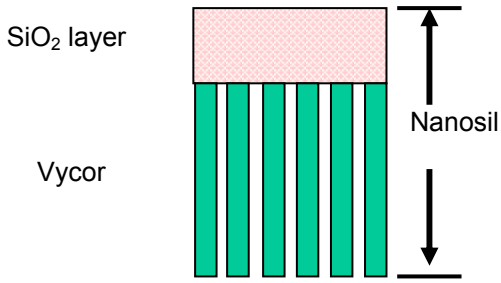

Figure 2. Schematic of Nanosil membrane.

The gas permeance of He, Ne, and H_2 on the silica layer in the Nanosil membrane can be obtained using a series analysis of gas diffusion, where the total resistance for gas permeation on the Nanosil membrane is a summation of the resistance on the Vycor support and the silica layer.

$$\frac{1}{Q_{\text{Nanosil}}} = \frac{1}{Q_{\text{Vycor}}} + \frac{1}{Q_{\text{silica}}}$$

where Q is the permeance (mol m^{-2} s^{-1} Pa^{-1}). Since the gas permeance of He, H_2 and Ne on the Vycor alone is known, the permeance on the top silica layer can be calculated.

The permeance order obtained is He > H_2 > Ne, which follows neither size nor mass of the species. This unusual order of gas permeance may be explained using a statistical gas permeance model on vitreous silica glass (13).

$$Q = \frac{1}{6L}\left(\frac{d^2}{h}\right)\left(\frac{h^2}{2\pi m k T}\right)^{\frac{3}{2}} \frac{(N_S / N_A)}{(e^{h\nu^*/2kT} - e^{-h\nu^*/2kT})^2} e^{-\Delta E_K/RT}$$

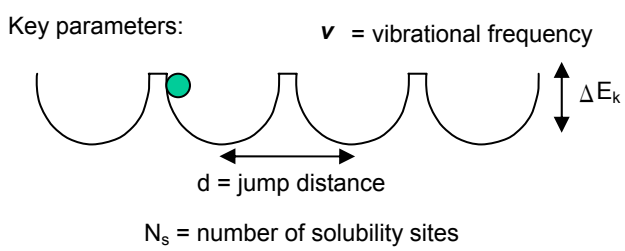

The silica layer thickness, L, and the jump distance, d, used for the calculation were 10 nm and 0.3 nm respectively. The adjustable parameters were the number of solubility sites (N_s) and the activation energy of permeation (ΔE_K). The model fitting was carried out using the Nelder-Mead simplex method. The fitting results and the best-fit parameter values are shown in Figure 3 and Table 1. The results showed a good fit between the model analysis and the experimental data with a permeance order of He > H_2 > Ne that agreed with the observations. The model analysis was able to account for the unusual order of the small gas permeance on the silica layer of the Nanosil membrane. The order is due to a tradeoff between the number of solubility sites and the vibrational frequency (ν*). The number of solubility sites in the silica layer is larger than that found in vitreous glass, consistent with a more open structure. The number of solubility sites is also physically realistic. The inverse cube root of the quantity gives a value of ~ 1 nm, which is of the same order of magnitude as the jump distance. Further details are presented in a full paper (10).

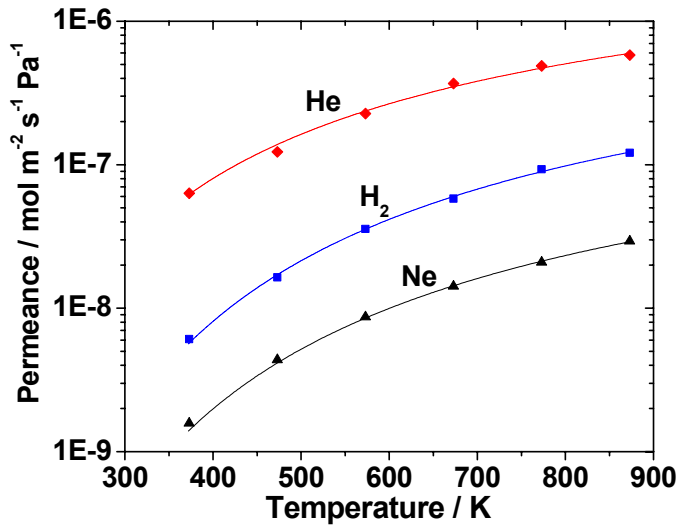

Figure 3. Experimental and calculated permeance in the silica layer.

Table 1. Results of Model Fitting.

Gas	Solubility sites N_s (m^{-3})	ν* (s^{-1})	Activation energy E_a (kJ mol^{-1})
He	3.4×10^{27}	6.90×10^{12}	9.7
H_2	1.4×10^{27}	1.22×10^{13}	13.6
Ne	1.4×10^{27}	4.38×10^{12}	14.0

Conclusions

The permeation characteristics of the gas molecules, He, Ne, H_2, CH_4, CO and CO_2, on the composite Vycor-supported silica membrane, referred to as Nanosil, were investigated. The gas transport characteristics on the Vycor and Nanosil membranes were discussed with relevant diffusion models. Surface diffusion enhanced Knudsen diffusion was a good model for the gas transport on the Vycor support. Gas transport on the deposited silica layer was successfully described by a statistical solid state diffusion model.

Acknowledgement. The authors thank the Director of the Division of Chemical and Thermal Systems (Grant CTS-9815041) of the National Science Foundation for the support of this project.

References

(1) Okubo, T.; Inoue, H., *J. Membr. Sci.* **1989**, 42, 109.
(2) Gavalas, G. R.; Megiris, C.E.; Nam, S.W., *Chem. Eng. Sci.* **1989**, 44, 1829.
(3) Ha, H.Y.; Nam, S.W.; Hong, S-A.; Lee, W. K., *J. Membr. Sci.* **1993**, 85, 279.
(4) Levy, R. A.; Ramos, E. S.; Krasnoperov, L. N.; Datta, A.; Grow, J. M., *J. Mater. Res.* **1996**, 11, 3164.
(5) Nakao, S-I.; Suzuki, T.; Sugawara, T.; Tsuru, T.; Kimura, S., *Micropor. Mesopor. Mat.* **2000**, 37, 145.
(6) Morooka, S.; Yan, S.; Kusakabe, K.; Akiyama,Y., *J. Membr. Sci.* **1995**, 101, 89.
(7) Sea, B.K.; Kusakabe, K.; Morooka, S., *J. Membr. Sci.* **1997**, 130, 41.
(8) Nair, B.N.; Yamaguchi, T.; Okubo, T.; Suematsu, H.; Keizer, K.; Nakao, S-I., *J. Membr. Sci.* **1997**, 135, 237.
(9) de Vos, R.M.; Verweij, H., *Science* **1998**, 279, 1710.
(10) Lee, D.; Oyama, S. T., *J. Membr. Sci*. **2002**, 210, 291..
(11) Oyama, S.T.; Lee, D.; Sugiyama, S.; Fukui, K.; Iwasawa, Y., *J. Mater. Sci.* **2001**, 36, 5213.
(12) Tsapatsis, M.; Gavalas, G. R., *J. Membr. Sci.* **1994**, 87, 281.
(13) Masaryk, J.S.; Fulrath, R.M., *J. Chem. Phys.* **1973**, 59,1198.

HYDROGEN TRANSPORT CATALYTIC MEMBRANE REACTORS

Anthony F. Sammells, Michael V. Mundschau, Richard Mackay, and Shane E. Roark

Eltron Research Inc.
4600 Nautilus Court South
Boulder, CO 80301
www.eltronresearch.com

Introduction

Eltron Research Inc. is developing low cost, multi-phase membranes for separating hydrogen from hydrogen containing feedstreams. This is being addressed using material composites which facilitate high proton and electron conduction. Membranes are being developed for high (>750°C) and low (<425°C) temperature applications and have been successfully operated under a high pressure differential (250 psi) for extended times. Under ambient pressure, hydrogen transport rates >25mL/cm^2/min have been achieved at 400°C.

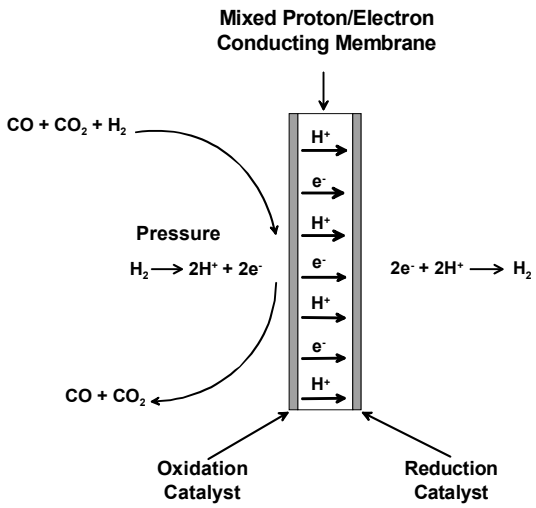

Figure 1. Schematic diagram of the ceramic membrane process for separating hydrogen from a mixture of gases.

Experimental

Doped perovskites $A_{1-x}A_x'B_{1-y}B_y'O_{3-\delta}$, where x and y are the fractions of dopants in the A and B sites, respectively, and δ is the number of oxygen vacancies,[1-3] were prepared using conventional high temperature solid state synthesis techniques. Corresponding cermets $A_{1-x}A_x'B_{1-y}B_y'O_{3-\delta}$/M were prepared by sequential pressing and sintering at elevated temperatures under controlled atmosphere conditions.

The inlet hydrogen source was initially diluted with helium. This facilitated determination of the membrane seal quality. H_2 and He fractions within inlet and sweep streams were determined by TCD-GC using a Shimadzu GC 14-A with a 12-ft. by 1/8-in. stainless steel Carbosphere column. Ultra-high purity Ar was used as the carrier gas to optimize detection limits for hydrogen and helium.

Results and Discussion

Cermet membranes under development at Eltron consist of a proton conducting ceramic phase and a low cost hydrogen permeable metallic phase. Figure 2 shows an SEM image of a cermet membrane.

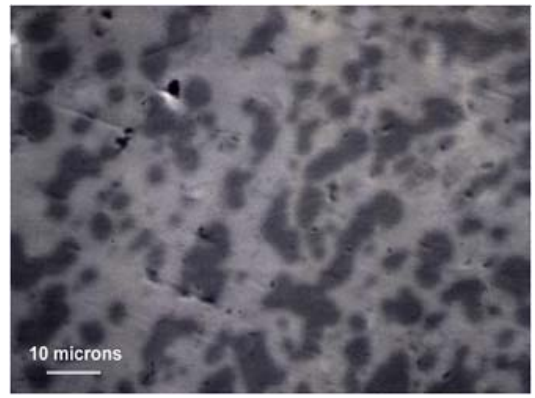

Figure 2. SEM image of a cermet membrane containing 46 wt.% metal phase. The proton-conducting ceramic appears as the light regions and the metal phase as the dark regions.

Hydrogen flux, *J*, through dense mixed proton/electron conducting membranes in the absence of surface kinetic limitations is dependent on the membrane thickness, *t*, according to,

$$J = \frac{\sigma_{amb} E}{t}$$

where *E* is the Nernst potential. Figure 3 contains a plot of theoretical hydrogen transport rates versus membrane thickness.

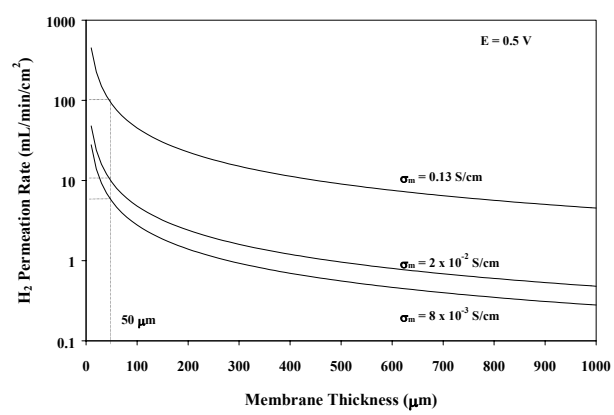

Figure 3. Plot showing H_2 transport rates as a function of membrane thickness for a range of bulk conductivities and a H_2 concentration gradient equivalent to 0.5V.

Several approaches currently are being pursued at Eltron for fabrication of thin film hydrogen separation membranes. The most straightforward strategy is to deposit a thin layer of dense membrane material on a porous support of the same composition. The challenge for this approach is to match the shrinkage rates of the support and thin film to enable sintering without membrane cracking. Shrinkage of the thin film was controlled by varying the surface area of the powder prior to sintering, whereas, shrinkage of the support was controlled by adjusting the material porosity. Using this strategy, the shrinkage mismatch between the thin film and support was

minimized to a only a few percent, and homogenous crack-free thin films approximately 100 Φm thick routinely are prepared. An example is shown in the SEM image in Figure 4.

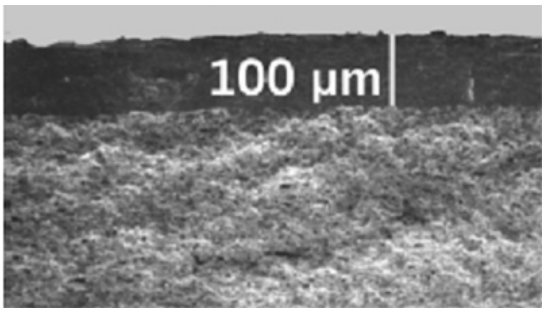

Figure 4. SEM image showing a cross section of a 100 µm thick dense membrane deposited onto a porous support of the same composition.

Hydrogen separation membranes have been operated at 250 psi pressure differential between the hydrogen feed and sweep side at elevated temperatures continuously for >1000 hrs. The performance of our low cost membranes operating under ambient pressure conditions as a function of temperature (Figure 5) and Ar sweep rate (Figure 6) on the hydrogen permeate side are shown below. As can be seen, hydrogen diffusion fluxes >25 mL/cm^2/min have been achieved at 400°C.

A simplified block diagram of a hydrogen separation unit installed in an integrated gasification combined cycle (IGCC) plant is shown in Figure 7. The diagram shows three options for installation, indicated as baseline, alternative 1, and alternative 2. The alternative 1 option assumes the membrane materials will be tolerant to sulfur and particulate material, and that the raw syngas from coal gasification can be sent directly to the unit. The baseline option also assumes sulfur tolerance, but the gas stream must be filtered prior to entering the unit. If the membrane materials are not sulfur tolerant, then alternative 2 will be necessary, and the unit will be inserted after desulfurization. This condition will require reheating the gas stream through a heat exchange prior to entering the hydrogen separation unit.

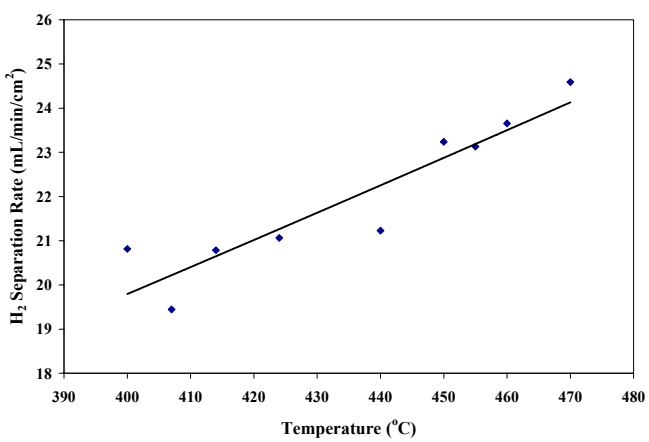

Figure 5. Hydrogen diffusion as a function of operating temperature under ambient pressure conditions. Ar sweep rate on permeate side 300 mL/min.

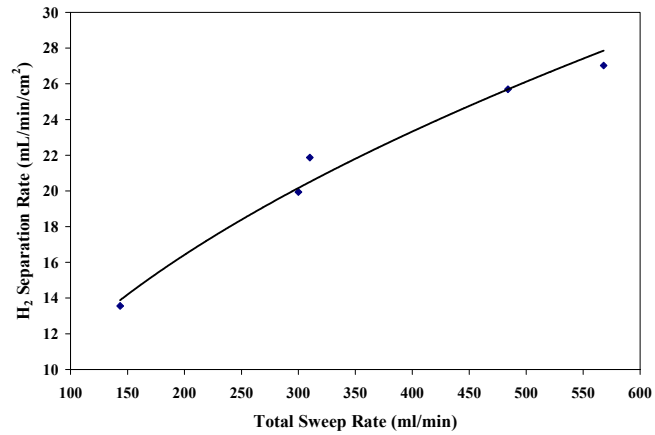

Figure 6. Hydrogen diffusion as a function of Ar sweep rate on the permeate side at 400°C. Ambient pressure conditions.

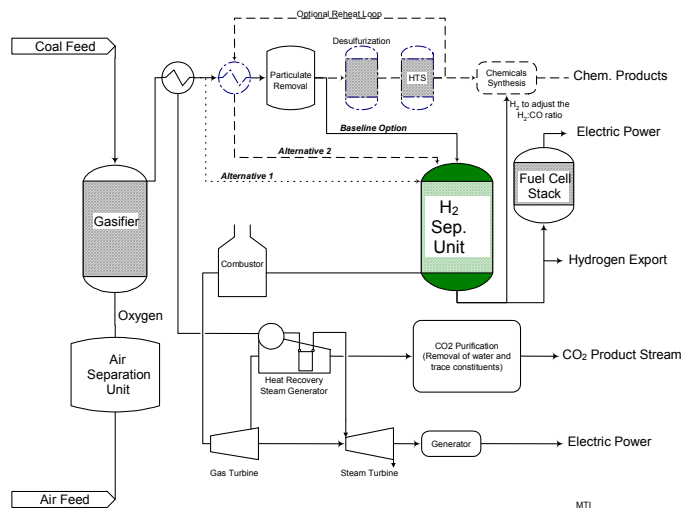

Figure 7. Diagram of an IGCC plant with three installation options for a hydrogen separation unit.

Acknowledgment

This work is supported by DOE/NETL under Contract Number DE-FC26-00NT40762.

References

(1) White, J. H.; Schwartz, M.; and Sammells, A. F. U.S. Patent 5,821,185, October 13, 1998.
(2) White, J. H.; Schwartz, M.; and Sammells, A. F. U.S. Patent 6,037,514, March 14, 2000.
(3) White, J. H.; Schwartz, M.; and Sammells, A. F. U.S. Patent 6,281,403, August 28, 2001.

Novel Composite Membranes for Hydrogen Separation from Coal Gasification Streams

Michael Schwartz, Brian S. Berland, Sabina K. Gade and Ronald W. Schaller

ITN Energy Systems, Inc.
8130 Shaffer Parkway
Littleton, CO 80127

Introduction

Hydrogen separation membranes have been identified by the Department of Energy as an "enabling" technology for future "Vision 21" power plants – plants that will be substantially cleaner and more efficient than today's power plants. ITN Energy Systems, Inc. is developing composite membranes for the separation of hydrogen from coal gasification streams for use in the "Vision 21" plant. The fundamental approach is based on Ion Conducting Ceramic Membranes (ICCM) that remove hydrogen from the gasification streams. The membrane process also results in a stream of concentrated carbon dioxide suitable for subsequent sequestration.

The technical approach for achieving the program objectives is three-fold: novel materials development, the integration of materials, module design and fabrication techniques and plant engineering design. The basic building block of the membrane system is a tri-layer consisting of the thin-film, mixed proton and electron conducting membrane and a porous catalyst layer on each side. This structure is illustrated in Figure 1.

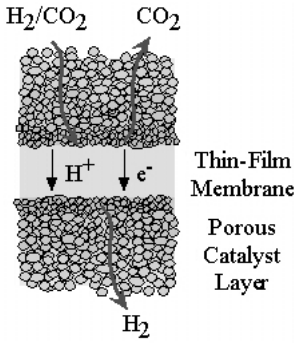

Figure 1. Schematic illustration of hydrogen separation process using an ion conducting ceramic membrane.

As illustrated in Figure 1, the H_2 separation membrane needs to conduct both protons and electrons. In this program, the focus is on cermets consisting of a proton conducting ceramic combined with a metal for electrical conductivity. For proton conducting materials, previous work has focused primarily on rare-earth-doped strontium cerate, strontium zirconate and barium cerate.[1-8] These materials have high ionic conductivities, ~10^{-2} S/cm at 600-800 ^oC. However, they are poor electrical conductors, precluding their use in H_2 separation membranes.

Recently, Balachandran and co-workers at Argonne National Laboratory have developed cermet membranes utilizing strontium and barium cerates as the proton conducting phase and nickel as the electron conducting phase.[9,10] They reported quite high H_2 flux rates, $9x10^{-2}$ $cm^3/min\text{-}cm^2$, at 750 ^oC with relatively thick membranes, ~0.5 mm. Since the flux rate is inversely proportional to the membrane thickness, commercially attractive flux rates could be achieved with membranes of thickness on the order of tens of microns.

One major concern of membranes comprised of strontium and barium cerates is their chemical stability. Specifically, barium oxide, and to a lesser extent, strontium oxide, react with both water and carbon dioxide, major components of gasification streams, to form hydroxides and carbonates, respectively. This reaction is less of a problem at high temperatures but still can be the deleterious to membrane chemical and mechanical stability during the membrane fabrication process and during membrane module startup and shutdown processes.

To overcome this problem with membrane reactivity, ITN is developing alternate proton conductors that are based on pyrochlore phases with little or no barium or strontium content. Pyrochlore phases are attractive for this application for several reasons. Recent work has pointed to specific pyrochlore phases that exhibit proton conductivity.[11-13] The pyrochlore crystal structure is based on the fluorite structure with additional oxygen vacancies that promote proton conductivity. The fluorite structure typically shows high chemical and mechanical stability which is not expected to be degraded by the presence of additional oxygen vacancies. As an example, the well-known oxide conductor, yttria-stabilized zirconia, crystallizes in the fluorite structure. In this program, ITN is developing new materials by rationally doping the base pyrochlore materials. The goal is to obtain materials which exhibit high ionic conductivity and maintain high chemical and mechanical stability.

Experimental

Pyrochlore membrane powders were prepared by the Pechini process.[14-16] This method starts with an aqueous solution of metal nitrates. Citric acid and ethylene glycol are then added and heated and a gel is formed through a polymerization reaction. The resulting gel is then fired at relatively low temperatures, 700-900 ^oC, to yield a fine, homogenous powder of the desired metal oxide phase.

Composite membrane disks were fabricated by uniaxial pressing. In this process, the ceramic powder was ball-milled with Ni powder. An aqueous binder solution (2wt% polyvinyl alcohol) was added and the resulting slurry dried in air. The dried mixture was then passed through a 48 mesh sieve, placed in a cylindrical die and then pressed uniaxially. The resulting membrane disks were then fired at 300 ^oC in air for binder burnout followed by sintering at 1400-1450 ^oC in 3% H_2 in Ar. Membranes prepared in this manner were typically >90% dense.

Membranes were tested for hydrogen flux by first brazing the membranes into gas-tight holders machined from Inconel 600. Mixtures of H_2, N_2, H_2O and CO_2 were passed over one surface of the membrane while He was passed over the opposite surface. The H_2 concentration in the He stream was determined by gas chromatography. The H_2 flux was determined from the concentration and measured He flow rate. Any leak through the membrane or seal was determined by measuring the N_2 or CO_2 in the He stream. H_2 flux through the membrane was adjusted for this leakage which typically was a few percent of the H_2 flux.

Results and Discussion

Approximately twenty doped pyrochlore materials have been identified as potential proton conductors. To date, several doped pyrochlore phases have been prepared using powders synthesized as above. Figure 2 shows the X-ray diffraction (XRD) pattern of one particular sample. The pattern shows no reflections due to any of the constituent metal oxides, indicating that it is single-phased. Additionally, the broad reflections are indicative of a very fine powder.

The H_2 flux rate through a cermet membrane is shown in Figure 3. This is one particular composition which consists of a pyrochlore proton conductor with 50wt% Ni. The membrane was tested under

several feedstreams containing H_2, N_2, CO_2 and H_2O. Specific feedstreams are shown in Figure 3. At 50% H_2 in N_2, a flux rate greater than 0.3 ml/min-cm^2 (normalized to 1 mm thickness) was achieved. The membrane was stable over operation at 900 ^oC for several days. The sample was also thermally cycled several times over this period with no loss of flux rate. One important point is that these membranes did not have any catalysts on the surfaces and in fact had been polished smooth for the sealing procedure. This would tend to result in lower flux rates as the surface area would be greatly reduced by a lack of roughness.

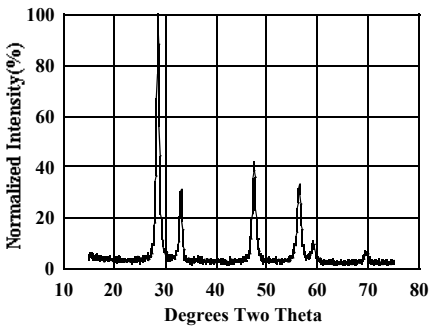

Figure 2. XRD pattern of a doped pyrochlore prepared using the Pechini process.

Figure 3 also shows the effect of the introduction of both CO_2 and H_2O. Here the flux was decreased relative to the dry H_2 in N_2 feedstream. This drop was attributed to a decrease in the H_2 concentration in the feedstream due to the presence of water and the reverse water-gas shift reaction:

$$H_2 + CO_2 \rightarrow H_2O + CO \qquad (1)$$

Measurement of the gases in the feedstream indicated that CO was being produced. At this point, the exact concentration of CO in the feedstream due to the reverse water-gas shift reaction has not been measured. The results in Figure 3 also indicate that the membrane is stable over at least several days with both H_2O and CO_2 in the feedstream.

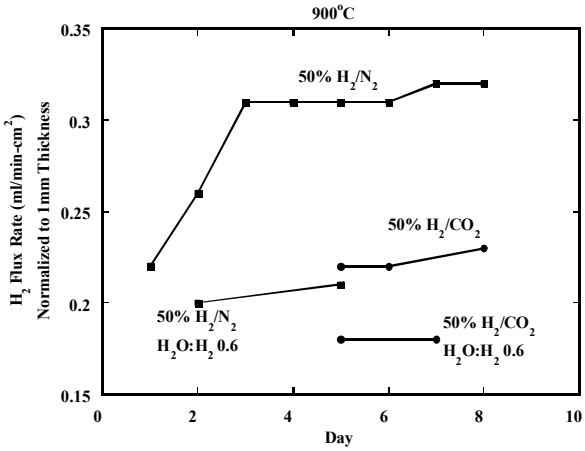

Figure 3. Plot of H_2 flux rate vs. time in different feedstreams.

Conclusion

In conclusion, ITN has identified novel proton-conducting pyrochlore phases. These materials have been incorporated into cermet membranes for the separation of H_2 from mixed gas streams. Initial experiments indicate that these materials do in fact conduct protons and appear to be stable to both H_2O and CO_2 at least over a several day period. The flux rates are roughly a factor of eight lower than what will be required in a commercial process. To enhance the observed flux rates, work is continuing at ITN in two areas. One area is the continued development of novel pyrochlore phases. Here selective doping is being used to increase the overall protonic conductivity. Second, the use of surface catalysts will also be investigated to enhance the surface exchange rates.

Acknowledgement. This work was supported by the U.S. Department of Energy through contract DE-FC26-01NT40793, Dr. Arun Bose, Program Manager.

References

(1) Iwahara, H.; Esaka, T.; Uchida, H.; Maeda, N. *Solid State Ionics* **1981,** *3/4*, 359.
(2) Iwahara, H. *Solid State Ionics* **1988,** *28*, 573.
(3) Lee, W.; Nowick, A.S.; Boatner, L.A. *Solid State Ionics* **1986**, *18/19*, 989.
(4) Iwahara, H.; Uchida, H.; Ono, K.; Ogaki, K. *J. Electrochem. Soc.* **1988**, *135*, 529.
(5) Iwahara, H.; Uchida, H.; Morimoto, K. *J. Electrochem. Soc.* **1990**, *137*, 462.
(6) Taniguchi, N.; Hatoh, K.; Niikura, J.; Gamo, T. *Solid State Ionics* **1992**, *53-56*, 998.
(7) Bonanos, N.; Ellis, B.; Knight, K.S.; Mahmood, M.N. *Solid State Ionics* **1989**, *35*, 179.
(8) Bonanos, N.; Ellis, B.; Mahmood, M.N. *Solid State Ionics* **1991**, *44*, 205.
(9) Balachandran, U.; Lee, T.H.; Zhang, G.; Dorris, S.E.; Rothenberger, K.S.; Martello, D.V.; Cugini, A.V.; Siriwardane, R.V.; Poston, Jr., J.A.; Fisher, E.P. Presented at the 6th Natural Gas Conversion Symposium, Girdwood, AK, June 2001.
(10) Balachandran, U.; Lee, T.H.; Wang, S.; Dorris, S.E.; Rothenberger, K.S. Presented at the 18th Annual International Pittsburgh Coal Conference, Newcastle, Australia, Dec. 2001.
(11) Shimura, T.; Komori, M.; Iwahara, H. *Solid State Ionics* **1996**, *86-88*, 685.
(12) Labrincha, J.A.; Frade, J.R.; Marques, F.M.B. *Solid State Ionics* **1997**, *99*, 33.
(13) Omata, T.; Otsuka-Yao-Matsuo, S. *J. Electrochem. Soc.* **2001**, *148*, E252.
(14) Duran, P.; Capel, F.; Tartaj, J.; Moure, C. *J. Mater. Res.* **2001**, *16*, 197.
(15) Xu, Y.; Chen, X.M.; Wu, Y.J. *J. Mater. Sci.: Mater. Elect.* **2000**, *11*, 633.
(16) Tai, L.-W.; Lessing, P.A. *J. Mater. Res.* **1992**, *7*, 502.

A NOVEL PROCESS FOR HYDROGEN SEPARATION USING MIECS: THEORETICAL ANALYSIS

Srikanth Gopalan and Cui Hengdong

15 St.Mary's Street, Department of Manufacturing Engineering,
Boston University, Boston, MA 02215

Introduction

Hydrogen separation from hydrocarbon reformate using mixed proton and electron conductors is presently an active area of research [1-3]. In this process, a pressure differential is maintained across the membrane and hydrogen is transported from the higher hydrogen partial pressure (reformate side) to the lower hydrogen partial pressure side. A few selected examples based on this approach include Balachandran et al. [1], Wachsman and Jiang [2] and White et al. [3]

A different approach described here employs a mixed oxygen ion and electron (or hole) conductor and has not been reported widely in the literature. In this approach, reformate consisting of CO and H_2 is fed to one side of the membrane and water vapor to the other side. Dissociation of water vapor into hydrogen and oxygen ions occurs on the water vapor side of the membrane, followed by ambipolar transport of oxygen across the membrane where the reformate is oxidized to water vapor and carbon dioxide. Thus hydrogen is segregated on the water vapor side. This approach has the potential to generate higher hydrogen fluxes than possible using the mixed proton and electron conductors.

Hydrogen Separation Using Oxygen Ion Conducting MIECs

The concept of using O^{2-} conducting MIECs to separate hydrogen is shown in Figure 1.

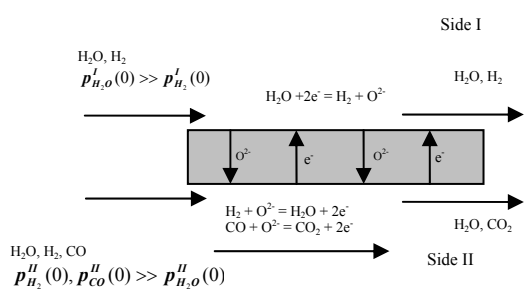

Figure 1. Principle of hydrogen separation using a mixed oxygen ion and electron conductor

Equivalent Circuit Analysis

We have modeled the process shown schematically in Figure 1 using a simple equivalent circuit shown in Figure 2. To simplify the analysis it is assumed that electronic and ionic conductivities (or resistivities) are independent of the partial pressure of O_2, p_{O_2}. In reality these conductivities will depend on the local p_{O_2} in the membrane. However, this complicates the analysis and is not required for a first level estimation of the hydrogen fluxes. The driving Nernst potentials $E_{0,i}$ are a function of position along the direction of gas flow. Each individual leg of the equivalent circuit containing a driving Nernst potential, electronic resistor R_{el} and an ionic resistor R_i has an incremental current dI_x.

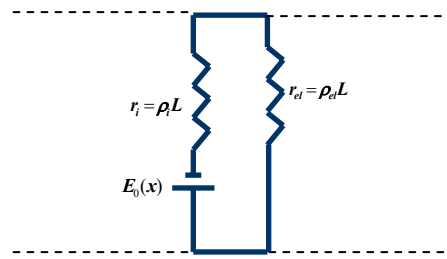

Figure 2. Equivalent circuit model for hydrogen separation using MIECs.

The incremental current is given by,

$$dI_x = \frac{E_0(x)}{R_{el} + R_i} \tag{1}$$

The resistances R_{el} and R_i are given by,

$$R_{el} = \frac{t\rho_{el}}{B.dx} \tag{2a}$$

$$R_i = \frac{t\rho_i}{B.dx} \tag{2b}$$

In equations (2a) and (2b), t is the thickness of the membrane, ρ_{el} and ρ_i are the electronic and ionic resistances which are assumed to be independent of p_{O_2}, B is the width of the membrane (i.e. membrane dimension perpendicular to the plane of the paper) and dx is the incremental dimension in the direction of gas flow. Substituting equations (2a) and (2b) in (1) and summing over the length of the membrane, we get,

$$I_{total} = \sum \frac{E_0(x).B.dx}{t(\rho_{el} + \rho_i)} \tag{3}$$

Since the driving Nernst potential is a function of p_{O_2} which is a continuous function of the position x, the summation can be replaced by an integral as given below.

$$I(x) = \int_{x=0}^{x=x} \frac{E_0(x).B.dx}{t(\rho_{el} + \rho_i)} \tag{4}$$

In equation (4), $I(x)$ represents the cumulative current from the inlet to an arbitrary position along the direction of gas flow. Note that the net current through the membrane is zero, i.e. the current flux due to the transport of the O^{2-} is exactly balanced by the concurrent current flux of holes (or the countercurrent current flux of electrons). The driving Nernst potential is given by,

$$E_0(x) = \frac{RT}{4F} \ln[\frac{p^I_{O_2}(x)}{p^{II}_{O_2}(x)}] \quad (5)$$

For the purposes of this analysis it is assumed that the inlet gas on side II comprises of a mixture of CO and H_2 with trace amounts of H_2O and the inlet gas on side I comprises of H_2O with trace amounts of H_2. The local p_{O_2} s in equation (5) will be determined by the gas phase equilibria. We define two more terms which we use in the analysis, namely the flow ratio λ and the degree of conversion ζ. The flow ratio λ is ratio of the inlet steam flow on side I to the H_2 and CO flow on side II. The degree of conversion ζ is the ratio of exit flow of H_2 on side I to the H_2 and CO flow on side II. It can be shown that assuming that no surface exchange limitations exist,

$$\zeta = \frac{\lambda}{1+\lambda} \quad (16)$$

Results and Discussion

Figure 3 shows the variation of Nernst potential with dimensionless position Γ in the direction of gas flows, for various values of λ. At smaller values of Γ, the Nernst potential is higher for higher values of λ. Further, the slope of the Nernst potential versus Γ is smaller for higher values of λ. This is to be expected since a higher H_2O flow on side I results in a higher Nernst potential. The slower decrease of Nernst potential at higher λ values signifies slower consumption of the driving force for O^{2-} flux (and thus H_2 flux).

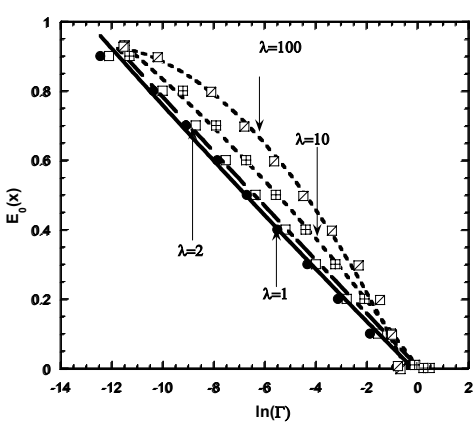

Figure 3. Variation of Nernst potential with dimensionless position for various flow ratios

Figure 4 shows the degree of conversion as a function of the flow ratio calculated from equation (16). As can be seen, the degree of conversion approaches unity only at very large λ values. High values of λ imply higher input of steam which will translate to a higher cost. However, fairly high degrees of conversion (~ζ =0.75) can be achieved at modest flow ratios (λ=3). Table 1 shows the maximum obtainable degree of conversion and hydrogen fluxes (shown as equivalent current density).

Table 1. Maximum Obtainable Degree of Conversion and Current Density (Flux) for Various Flow Ratios

λ	ζ	$J(\max)$: A/cm^2
1	0.5	11.8
2	0.67	12.5
10	0.91	19.7
100	0.99	46.6

The flux calculations shown in Table 1 are based on ionic and electronic conductivities representative of the well known perovskite mixed conductor $La_{1-x}Sr_xCo_yFe_{1-y}O_{3-\delta}$ [4].

Conclusions

A new process for selective separation of hydrogen from reformate using dense MIECs that conduct oxygen ions and electrons (or holes) has been analyzed. The analysis shows that potentially high hydrogen fluxes can be obtained from this process.

Acknowledgment: Seed funding from Boston University for this work is gratefully acknowledged.

References

(1) Balachandran, U.; Guan, J.; Dorris, S.E.; Bose, A.C.; and Stiegel, G.J;and Xu, L. Proc. 5th Int. Conf. on Inorganic Membranes. – Nagoya, Japan, **1998**, p. 192.
(2) Wachsman, E.; and Jiang, N. US Patent # **6,296,687**
(3) White, J.H; Schwartz, M; and Sammels, A.F. US Patent # **6,281,403**
(4) Minh N, Science and Technology of Ceramic Fuel Cells, Elsevier **1995**

DENSE CERMET MEMBRANES FOR HYDROGEN SEPARATION

U. (Balu) Balachandran, T. H. Lee, S. Wang, J. J. Picciolo, J. T. Dusek, and S. E. Dorris

Energy Technology Division
Argonne National Laboratory
Argonne, IL 60439, USA

Introduction

The U.S. Department of Energy's Office of Fossil Energy sponsors a wide variety of research, development, and demonstration programs that aim to maximize the use of the vast domestic fossil resources and ensure a fuel-diverse energy sector while responding to global environmental concerns. Development of cost-effective, membrane-based reactor and separation technologies is of significant interest for applications in advanced fossil-based power and fuel technologies. The purpose of this work is to develop dense hydrogen-permeable membranes for separating hydrogen from mixed gases at commercially significant fluxes under industrially relevant operating conditions. Of particular interest is the separation of hydrogen from product streams that are generated during coal gasification, methane partial oxidation, and water-gas shift reactions.

Membrane development efforts at Argonne National Laboratory (ANL) and the National Energy Technology Laboratory (NETL) have resulted in various ceramic/metal composite (i.e. cermet) membranes that are classified on the basis of the hydrogen transport properties of the ceramic and metal phases. The cermet membranes in this paper are classified as ANL-1, -2, or -3, based on the hydrogen transport properties of the metal and matrix phases. The first class of membranes, ANL-1, contains a metal with low hydrogen permeability in a matrix of $BaCe_{0.8}Y_{0.2}O_{3-\delta}$ (BCY), a mixed proton-electron conductor (1-4). ANL-2 membranes also have a BCY matrix but contain a metal with high hydrogen permeability. In this type of membranes, the metal phase also serves as an additional path for the hydrogen transport. In ANL-3 membranes, the BCY matrix is replaced by a ceramic with superior mechanical properties and thermodynamic stability, e.g., Al_2O_3 or ZrO_2. Specific membranes are identified by a number and a letter, where the number represents the type of the membrane, and the letter indicates a specific combination of metal and matrix phase. For example, ANL-1a is an ANL-1 membrane that contains "metal a" in a matrix of BCY. In this paper, we discuss the results from hydrogen permeation tests of the various cermet membranes.

Experimental

Cermet membranes prepared in this work contain 40 vol.% metal phase unless otherwise noted. BCY powder was prepared at ANL as described elsewhere (5). Powder mixtures were prepared in isopropyl alcohol using a mortar and pestle. They were then pressed uniaxially to prepare disks (22 mm diameter x 2 mm thick) for sintering. ANL-1a and -2a membranes were sintered at 1420°C for 5 h in 4% H_2/balance Ar. ANL-3a membranes were sintered at 1400°C for 5 h in 4% H_2/balance He. ANL-3b membranes were sintered at 1350°C for 12 h in air. For measurement of the hydrogen permeation rate, sintered disks were polished to desired thickness with 600-grit SiC polishing paper. A polished disk was then affixed to an Al_2O_3 tube by using an assembly described elsewhere (6). For the wet condition, feed gas was bubbled through a water bath at room temperature to give ≈0.03 atm H_2O; for the dry condition, feed gas was introduced directly into the furnace from the gas cylinder.

Results and Discussion

The hydrogen permeation rates for ANL-1a, -2a, and -3b are compared in **Figure 1** for a feed gas of 4% H_2/balance He. Among these membranes, ANL-3b exhibited the highest permeation rate, approximately three times that of ANL-1a over the whole temperature range (600-900°C). ANL-3b gave the highest permeation rate because its metal phase had the highest hydrogen permeability of the various metals tested to date.

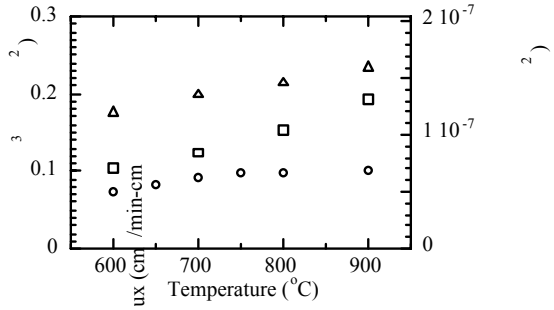

Figure 1. Hydrogen permeation rates through ANL membranes. (○): 0.5-mm-thick ANL-1a. (□): 0.46-mm-thick ANL-2a. (Δ): 0.43-mm-thick ANL-3b.

Figure 2 shows the temperature and thickness dependence of the hydrogen flux through ANL-3b membranes with wet 100% H_2 feed gas. For the 0.1-mm-thick membrane the leakage was high at lower temperatures; therefore, the permeation rate is shown only at 900°C. The hydrogen permeation rate increased with temperature and was proportional to the inverse of membrane thickness, as shown by the inset of **Figure 2**. The inverse dependence of flux on thickness indicates that the bulk diffusion of hydrogen through the metal phase is rate-limiting for thicknesses >0.1 mm.

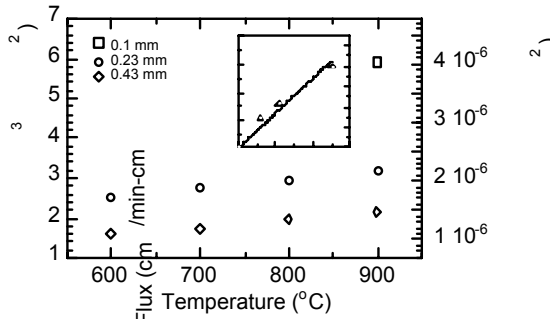

Figure 2. Hydrogen permeation rate through ANL-3b membranes. Inset shows the thickness dependence of permeation rate.

The bulk-limited hydrogen diffusion was further confirmed by measuring the pressure dependence of hydrogen permeation through ANL-3b membrane. **Figure 3** shows the effect of hydrogen partial pressure on the permeation rates through a 0.23-mm-thick ANL-3b membrane at 800 and 900°C. At both temperatures, the flux varies linearly with the difference in square root of hydrogen partial pressure of the feed gas and sweep gas; this relationship is characteristic of bulk-limited hydrogen diffusion through metals (7).

Figure 4 shows the temperature dependence of hydrogen fluxfor a 40-μm-thick ANL-3a membrane, which contained 50 vol.% hydrogen transport metal, before and after it was conditioned in air. Before the conditioning, the membrane gave high hydrogen flux [16.2 cm^3 (STP)/min-cm^2 at 900°C]. However, the flux at 400°C [0.8 cm^3 (STP)/min-cm^2] was much lower than expected based on the known hydrogen permeabilities for the materials in the membrane.

Previous study of the hydrogen transport metal in the ANL-3a membrane suggested that conditioning it in oxygen may increase its hydrogen flux, so it was heated for ≈250 h in air at 800°C. While it is not presently understood how conditioning in oxygen influences the hydrogen flux, the flux increased to 20.0 and 7.6 cm^3 (STP)/min-cm^2 at 900 and 400°C, respectively; the flux at 600°C increased only marginally. Although this membrane contained a higher concentration (50 vol.%) of metal phase, which was different from the one used in ANL-3b membrane, its significantly higher permeation rate can be related primarily to its reduced thickness.

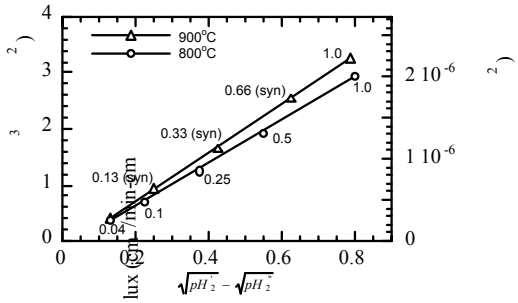

Figure 3. Hydrogen flux through ANL-3b vs. partial pressure of hydrogen (pH_2). pH_2' = pH_2 of feed gas; pH_2'' = pH_2 of sweep gas; values for pH_2 of feed gas is shown on curves; syn = gas mixtures made with simulated syngas.

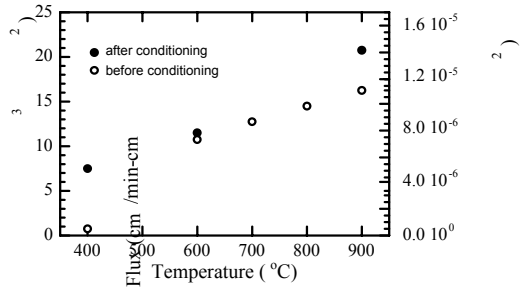

Figure 4. Hydrogen flux through ANL-3a membrane before and after conditioning in air.

The chemical stability of membranes was investigated in simulated syngas. **Figure 5** shows the permeation rates through ANL-2a and -3d as a function of time at 900°C in dry syngas of composition 2.0% CH_4, 19.6% H_2, 19.6% CO, and 58.8% CO_2 (mol.%). The permeation rate through ANL-2a decreased dramatically after only several minutes, whereas the hydrogen flux through ANL-3d was stable for >3 h. Examination of the ANL-2a surface by scanning electron microscopy and X-ray diffraction after the permeation measurements showed that the BCY matrix had decomposed to form $BaCO_3$ and other phases. These results indicate that a chemically stable matrix such as Al_2O_3 or ZrO_2 will be required for application of the membrane in atmospheres with high CO_2 concentrations. The chemical stability of 0.43-mm-thick ANL-3b in simulated syngas (66% H_2, 33% CO, and 1% CO_2) was tested by measuring its hydrogen flux at several temperatures for times up to 190 h. As can be seen in **Figure 6**, no noticeable decrease in flux was observed during testing. Similar tests with 0.23-mm-thick ANL-3b showed no decrease in the hydrogen flux during 120 h of exposure to syngas at 900°C.

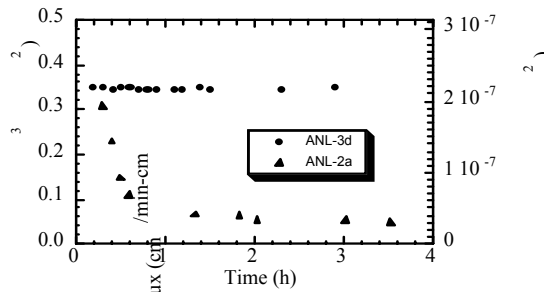

Figure 5. Permeation rates through Al_2O_3-based ANL-3d and BCY-based ANL-2a. Thickness of ANL-3d membrane was 0.53 mm; thickness of ANL-2a, 0.43 mm.

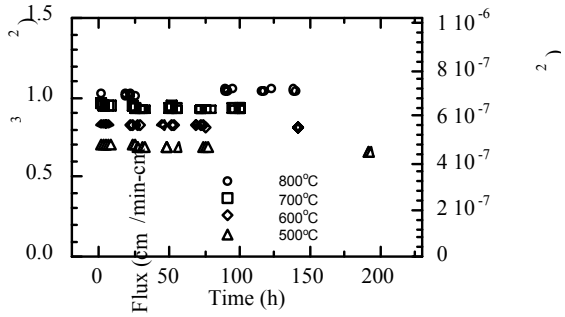

Figure 6. Hydrogen permeation rates through ANL-3b membrane vs. time in simulated syngas at various temperatures.

Conclusions

Various types of cermet membranes have been developed at ANL. The highest measured hydrogen flux was 20 cm^3 (STP)/min-cm^2 for an ANL-3a membrane at 900°C. For ANL-3 membranes with thickness of 0.04-0.5 mm, the permeation rate is limited by the bulk diffusion of hydrogen through the metal phase. The permeation rates in a syngas atmosphere for times up to 190 h showed no degradation in performance, indicating that ANL-3 membranes may be suitable for long-term, practical hydrogen separation.

Acknowledgment This work is supported by the U.S. Department of Energy, National Energy Technology Laboratory, under Contract W-31-109-Eng-38.

References

(1) Iwahara, H.; Yajima, T.; and Uchida, H. *Solid State Ionics*, **1994**, *70/71*, 267.
(2) Iwahara, H. *Solid State Ionics*, **1995**, *77*, 289.
(3) Guan, J.; Dorris, S. E.; Balachandran, U.; and Liu, M. *Solid State Ionics*, **1997**, *100*, 45.
(4) Guan, J.; Dorris, S. E.; Balachandran, U.; and Liu, M. *J. Electrochem. Soc.*, **1998**, *145*, 1780.
(5) Guan, J.; Dorris, S. E.; Balachandran, U.; and Liu, M. *Ceram. Trans.*, **1998**, *92*, 1.
(6) Balachandran, U.; Lee, T. H.; Zhang, G.; Dorris, S. E.; Rothenberger, K. S.; Howard, B. H.; Morreale, B.; Cugini, A. V.; Siriwardane, R. V.; Poston Jr., J. A.; and Fisher, E. P. In *Proc. 26th Intl. Technical Conf. on Coal Utilization and Fuel Systems*, Clearwater, FL, Mar. 5-8, **2001**, Coal Technical Association, Gaithersburg, MD, pp. 751-761.
(7) Buxbaum, R. E. and Marker, T. L. *J. Membr. Sci.*, **1993**, *85*, 29.

MIXED CONDUCTING MEMBRANES FOR PRESSURE-DRIVEN HYDROGEN SEPARATION FROM SYNGAS

S. Elangovan, B. Nair, J. Hartvigsen and T. Small
Ceramatec Inc.
Salt Lake City, UT

Introduction

Integrated Gasification Combined Cycle (IGCC) systems show tremendous potential for very efficient, environmentally friendly power generation.[1] In IGCC systems, a combined cycle is employed in which syngas ($CO+H_2$) is used to drive a gas turbine and the exhaust gases are then used to heat water/steam to generate superheated steam that drives a steam turbine. IGCC systems typically operate at efficiencies higher than 40%, whereas coal-burning plants that employ flue gas desulfurization processes reach a maximum efficiency of 34%. A number of demonstration projects, such as the Wabash River Coal Gasification Repowering Project in Indiana and the Pinon Pine IGCC Power Project in Nevada, have been carried out as part of the Department of Energy (DOE) Clean Coal Technology Program.[2,3]

Despite the significant potential of IGCC systems, economic considerations still limit their wide-spread commercial applicability. Fortunately, the total hydrogen in raw syngas is usually greater than 200% of the required amount. Thus, one critical advance that would significantly enhance the commercial viability of IGCC systems is the recovery of hydrogen fuel from syngas as a by-product.[4] There are a number of technologies and combinations of technologies being considered as alternatives for recovery of hydrogen from syngas. These technologies include membrane separation, pressure swing adsorption (PSA), methanation and nitrogen wash techniques. Each of these techniques has its strong points, and the choice of the specific technique is usually dictated by the economics of the process and the purity of hydrogen desired. Since ultra-high purity (>99 %) H_2 is a high value commodity, a technique that could generate such a high purity gas stream would be most attractive from an economic standpoint.

Technical Approach

Membrane separation, especially with ceramic membranes that separate H_2 by selectively transporting H+ ions (protons), offers the potential for generation of very high purity hydrogen (>99.9%), and is clearly superior in this regard compared with the other techniques mentioned above. Studies at SK Corporation in Ulsan, Korea have shown that the highest purities attainable by other techniques such as PSA, methanation and nitrogen wash techniques are only 97%, 85% and 97% respectively.[4]

A high-temperature, pressure-driven membrane-based separation system would be ideal for separation of hydrogen from the hot, high-pressure syngas stream typical of IGCC systems. Ceramic membranes are the only alternatives for operation under the high-temperature, high-pressure environment expected in IGCC systems, and can be designed to have very good thermomechanical and thermochemical stability under IGCC operating conditions. Our approach is to use a dense ceramic mixed-conducting membrane that can generate a stream of very high-purity H_2. The proposed concept, when fully developed, will be compatible with the temperature and pressure conditions in IGCC systems, and thus will be amenable for process and physical system integration.

One category of ceramic membranes that has received a good deal of attention in the preceding decade is mixed protonic/electronic conducting perovskite type oxide ceramics.[5,6] The stoichiometric chemical composition of perovskites can be represented as ABO_3, where A is a bivalent ion (A^{2+}) such as calcium, magnesium, barium or strontium and B is a tetravalent ion (B^{4+}) such as cerium or zirconium. While simple perovskites such as barium cerate ($BaCeO_3$) and strontium cerate ($SrCeO_3$) have some proton conductivity, it is now well known that doping these perovskites at the B sites can significantly enhance their protonic conductivities. The most common examples are structures of the form $AB_xD_{1-x}O_{3-\delta}$ formed by doping ABO_3 with trivalent ions such as yttrium (Y^{3+}) and ytterbium (Yb^{3+}). For example, $BaCe_{0.95}Y_{0.05}O_{3-\delta}$ has been shown to have a proton conductivity as high as 1.27×10^{-2} S/cm at 800°C in a H_2/H_2O atmosphere.[7]

In a pressure driven system, both hydrogen ions and electrons generated by dissociation of H_2 molecules at the high-pressure surface must be transported through the membrane to recombine at the low-pressure surface. Since these two are parallel kinetic processes, the overall kinetics are limited by the slowest process. In the case of a conventional mixed conducting membrane, the paths for proton conduction and electron conduction are the same. However, the electronic conductivity of mixed perovskites is very low and therefore is usually the limiting factor to these materials being used effectively as pressure-driven hydrogen separation membranes. For example, Phillips et al have shown that the electronic conductivity of $SrCe_{1-x}Y_xO_\delta$ was 2 to 3 orders of magnitude lower than its protonic conductivity at 800°C.[8] Our approach is to increase the electronic conductivities of these perovskite-based membranes through compositional and microstructural modifications.

In addition to being a good electronic conductor at these temperatures, the membrane material should also possess good thermomechanical and thermochemical stability at testing conditions involving temperatures as high as 900°C and high pressures of up to 5-10 atm. It has been reported that barium and strontium cerates are thermochemical unstable in H_2O and CO_2 containing atmospheres, due to carbonate formation as indicated in Equation (2).[9]

$$BaCeO_3 + CO_2 \rightarrow BaCO_3 + CeO_2 \qquad (2)$$

We are also addressing methods of increasing the thermochemical stability of the cerate-based membranes in CO_2-containing atmospheres. A membrane system that displays good mixed conductivity and thermochemical stability has been chosen for a proof-of-concept demonstration using said perovskite-ceria composite mixed conducting membranes for pressure-driven gas separation.

Experimental Approach

Membrane materials were synthesized with optimized compositions for mixed conductivity and thermochemical stability, using conventional powder processing routes. The powders were uniaxially pressed with appropriate binder additions in the shape of bars for conductivity measurements and as pellets for thermochemical stability measurements in simulated syngas. The bars and pellets were subjected through a prescribed sintering schedule and the densities of the sintered parts was measured through an Archimedes measurements, to ensure that the porosities in all parts was less than 1%, and that the densities corresponded to expected values for the chosen compositions. The specimens were studied by x-ray diffraction and scanning electron microscopy respectively to ensure that the targeted phases and microstructures were obtained in the sintered pellets.

The conductivity of the baseline cerate compositions and the modified compositions were evaluated using a conductivity test station, which is schematically shown in Figure 1. The apparatus has the ability to measure conductivities of bar specimens in various dry or wet gases. Conductivities of various bar specimens were measured at 800°C, 850°C and 900°C in wet hydrogen, and dry argon so that the protonic and electronic conductivities of the material could be assessed.

Membrane material stability under conditions expected in an IGCC system will be tested using a simulated syngas produced by steam reforming of natural gas. A mixture of steam/methane (2:1 ratio), and carbon dioxide (CO_2/CH_4=1.4) calculated to match the carbon/hydrogen ratio found in IGCC syngas, will be passed over a commercial nickel steam reforming catalyst at 800°C and 7.8 bar. Space velocity of less than 500 volume methane (stp conditions) per volume catalyst per hour will be used. This is low enough that the reformate composition is expected to closely match the equilibrium composition (1.5% CH_4, 21.4% CO, 15.3% CO_2, 36.2% H_2, 1.1% N_2, 24.5% H_2O) calculated for a steam/CO_2 reformed natural gas.

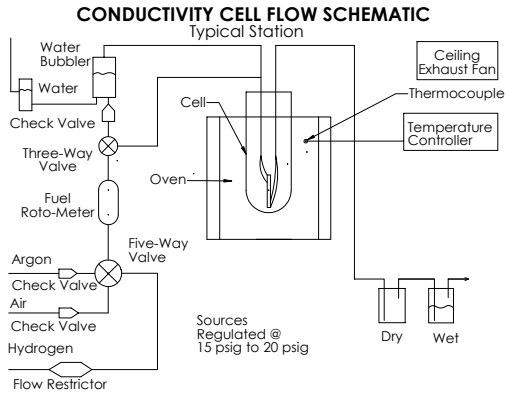

Figure 1. Schematic of test set-up for measuring conductivity of perovskite-based materials in various atmospheres.

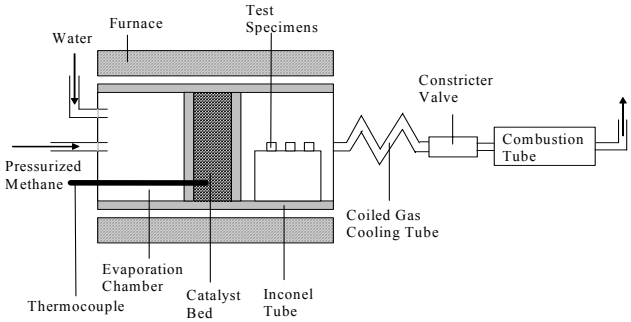

Figure 2. Schematic of test set-up for performing thermochemical stability experiments on perovskite-based membrane materials in pressurized syngas environment.

Results and Discussion

The results of preliminary conductivity testing of BaCeO3 and SrCeO3 based materials in moist H_2 are shown in Figure 3. The protonic conductivities of $\approx 0.9\text{-}1.3\times10^{-2}$ S/cm in the temperature range of 800-900°C obtained for our baseline compositions (c.f. Figure 3(a)) of doped $BaCeO_3$ compare very favorably with conductivity values reported for similar compositions in the literature.[8] Based on the slopes of Arrhenius plots shown in Figure 3(b), we calculated activation energies of 50-75 KJ/mol for these perovskite compositions, which also compares very favorably with values reported in the literature.

Ongoing work includes measurement of conductivities of baseline and modified perovkite-based candidate membrane materials in dry argon and moist H_2 to study the effect of our microstructural/ compositional modifications on electronic and protonic conductivity. In parallel, experiments to study thermochemical stability of the baseline and modified compositions will be carried out. Based on the conductivity measurements and thermochemical stability studies, compositions will be selected for membrane fabrication on porous supports. Experiments will then be carried out to demonstrate the feasibility of H_2 separation from simulated syngas by use of these mixed conducting membranes.

Summary

A novel, dense, mixed-conducting ceramic membrane is being developed. These membranes will allow pressure-driven hydrogen separation at 800-900°C, resulting in a very high purity hydrogen stream. The electronic conductivity and thermochemical stability of cerate-based perovskite membranes is enhanced through compositional/microstructural modifications. Hydrogen separation membranes were fabricated and protonic and electronic conductivity through the membrane will be characterized. The thermochemical stability of candidate membranes materials under simulated operating

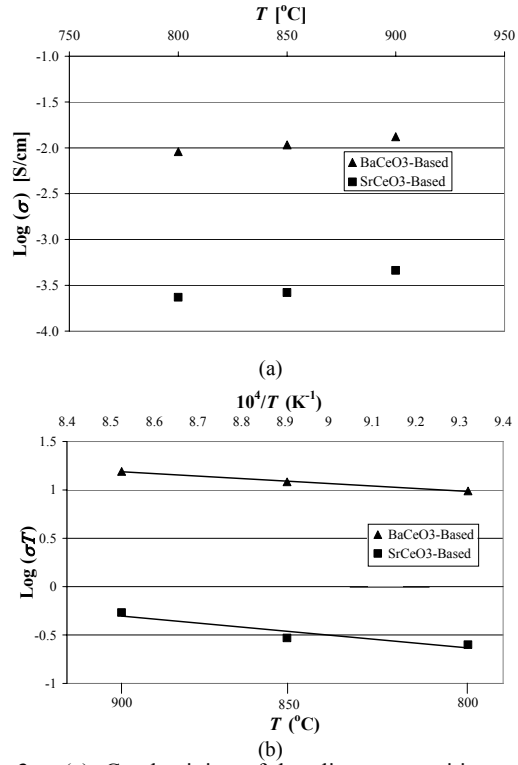

Figure 3. (a) Conductivity of baseline compositions of doped $BaCeO_3$ and $SrCeO_3$ in moist H_2 as a function of temperature; (b) Arrhenius plots of the data in (a).

conditions will be evaluated. The performance of the membrane as a mixed ionic-electronic conducting membrane will be evaluated through feasibility studies of pressure-driven hydrogen separation from simulated syngas. This hydrogen separation technique is expected to have a major impact on enhancing the commercial feasibility of IGCC systems.

Acknowledgement

This work was funded by the U.S. Department of Energy (DOE) through SBIR Grant No. DE-FG03-02ER83386.

References

(1) Campbell, P. E., McMullan, J. T. and Williams, B. C. *Fuel* **2000** *79* [9] 1031.
(2) Brdar, R. D., and Cicero, D. C., DOE Report No: DOE/METC/C-69/7231.
(3) Ness, H. M. and Brdar, R. D., DOE Report No. DOE/METC/C-96/7236.
(4) Kwon, S H., Shin, J. W., Oh, J. K., Heaven, D. L., and Condorelli, P. *Hydrocarbon Processing*, **1999** *78* [4] 73.
(5) Norby, T. and Larring, Y., *Solid State Ionics* **2000** *136-137* 139.
(6) Sata, N., Yugami, H., Akiyama, Y., Sone, H., Kitamura, N., Hattori, T., and Ishigame, M., *Solid State Ionics* **1999** *125* 383.
(7) Guan, J. Dorris, S. E., Balachandran, U., and Liu, M., *Solid State Ionics*, **1997** *100* 45.
(8) Phillips, R. J., Bonanos, N., Poulsen, F. W., and Ahlgren, E. O., *Solid State Ionics* **1999** *125* 389.
(9) Bhide, S. V., and Virkar, A. V., *J. Electrochem. Soc.* **1999** *146* [6] 2038.

THERMOCHEMISTRY OF HYDROGEN STORAGE BY MAGNESIUM METALIN THE NANOMETER AND SUB-NANO METER REGIME: ARE WE SURE THAT THE THERMOCHEMISTRY IS NOT CHANGED COMPARED TO THE BULK?

Jian-jie Liang

Accelrys Inc.
9685 Scranton Rd
San Diego, Ca 92121

Introduction

Magnesium, forming ionic, transparent MgH_2 containing 7.6 mass% hydrogen, is among those that are most-promising in hydrogen-storage materials for mobile applications[1]. However, the formation from bulk Mg and gaseous hydrogen is not only extremely slow, but requires elevated temperatures (300 °C at 1 bar pressure) as well, with the reverse process requiring similar conditions[2]. One school[3] of thought had been focusing on reducing the Mg particle sizes to micro- or nano-range, including precipitation from metal-organic solutions and high-energy ball milling of Mg. More efforts had been devoted to alloying Mg before hydride formation[4-6]. For example, Mg_2Ni forms, fairly rapidly, a ternary complex hydride Mg_2NiH_4, probably owing to the presence of Ni as catalysts for the dissociation of molecular hydrogen. Many other alloys, e.g., Mg_2Cu, $Mg_{17}La_2$ and MgAl, also react readily with hydrogen. However, in spite of improved kinetics in hydrogen uptake, the required reaction temperatures in most case were not lowered significantly. The alloying approach also suffers sharply lowered mass percentage of hydrogen in the hydrides (e.g., there is only 3.6 mass% hydrogen in Mg_2NiH_4, as oppose to 7.6 mass% hydrogen in pure MgH_2).

It's already been established[3-6] that reducing the particle size to nanometer regime doesn't change the thermochemistry notably. This is conceptually inconceivable, as the finer the individual particles, the greater the surface area, and hence the greater the structural modification due to the increasing importance of the surface relaxation that happens at the particle surfaces. Is there a critical point on particle size at which the thermochemistry will change remarkably? Also, what might the system go through in terms of crystal chemistry during the H-absorption/desorption process? What's the associated thermochemistry? These are questions the present paper tries to address, using the computational tool of Density Functional Theories (DFT).

Details of the Calculations

Details of the DFT calculations. Dmol3[7], a Density Functional Theory (DFT) method available in the software package, Materials Studio, was used in the calculations. The setup parameters in data collections were given in Table 1.

The bulk structures of Mg and MgH_2. Experimental structures of Mg[8] and MgH_2[9] were used as starting models to obtain the DFT relaxed structures. Unit cell dimensions were varied systematically to obtain the Energy – volume relationship (Fig 1). A polynomial was fitted to the set of data points, and the cell dimension corresponding to the minimum of the polynomial was taken as the calculated cell dimension. Parameters pertinent to the bulk samples are given in Table 2.

The Mg and MgH_2 thin films. DFT optimized bulk structures were used as the basis for constructing the thin films. The thickness of each thin film corresponds to an integral number of the bulk unit cell dimension along the direction perpendicular to the cleaving surface. The surfaces were used as cleaved, with no capping on either sides of the surface slab. The cleaved unit cell was extended laterally using the 2D periodic condition to form an essentially infinitely extending thin film. A vacuum slab of 20 Å was added on top of the surface such that 3D periodic conditions can be used in the summation of the energy terms in the DFT calculations. Pertinent parameters of the thin films are given in Table 3.

Table 1. Setup parameters in the Dmol[3] calculations

Basis Set	DND
Functional	GGA (P91)
Core treatment	All electron
Hamiltonian integration accuracy	fine
SCF convergence	10^{-6}
k-point separation (1/Å)	0.04 (fine)
Real space cut off (Å)	3.5
Spin_polarization	restricted

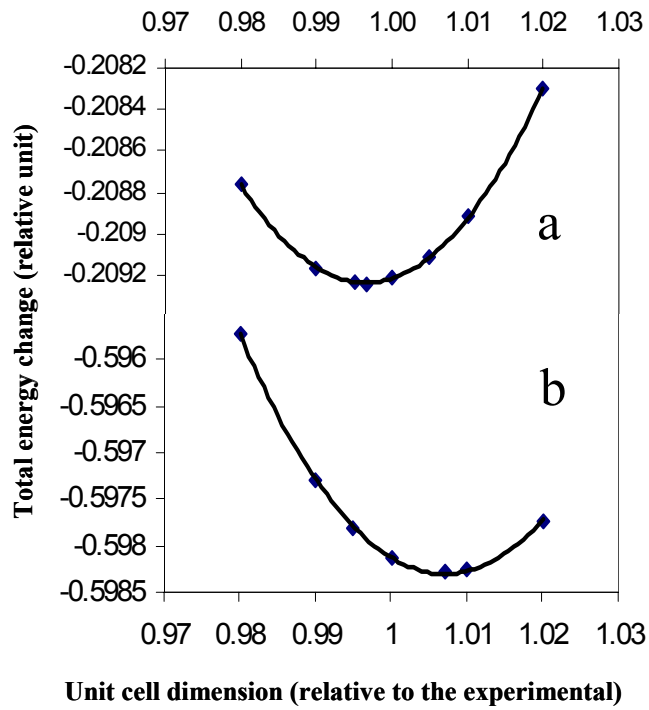

Figure 1. Potential energy change as a function of unit cell dimensions relative to the experimental dimensions. a. Mg; b. MgH2.

Table 2. Bulk Samples used in the Dmol[3] calculations. All quantities are with respect to 0 K.

	Formula	Dimension (Å)	ΔH_f (kJ/mol)
Hydrogen gas	H_2	0.751	-431.5_{H2}
Mg crystal	Mg_2	*a*: 3.198 *c*: 5.193	-118.4_{Mg}
MgH_2 crystal	Mg_2H_4	*a*: 4.533 *c*: 3.031	-621.0_{MgH2}

Table 3. Mg and MgH_2 surface slabs used in the Dmol[3] calculations

Cell Depth	Formula	Thickness (Å)	$\Delta H_f(0K)_{Mg}$ (kJ/mol)
Mg 110			
1	Mg_2	1.599	-60.855
2	Mg_4	3.198	-89.317
3	Mg_6	4.798	-99.477
4	Mg_8	6.397	-105.053
5	Mg_{10}	7.996	-108.001
6	Mg_{12}	9.595	-110.029
7	Mg_{14}	11.194	-111.458
8	Mg_{16}	12.794	-112.621
9	Mg_{18}	14.393	-113.523
MgH_2 001			
1	Mg_2H_4	3.031	-563.267
2	Mg_4H_8	6.062	-578.529
3	Mg_6H_{12}	9.093	-591.243
4	Mg_8H_{16}	12.124	-598.410
5	$Mg_{10}H_{20}$	15.155	-602.856
6	$Mg_{12}H_{24}$	18.186	-605.871
7	$Mg_{14}H_{28}$	21.217	-608.030
8	$Mg_{16}H_{32}$	24.248	-609.652
9	$Mg_{18}H_{36}$	27.279	-610.916

Calculation of enthalpy of formation. Dmol[3] calculations give binding energy, E_B, the energy to separate the constituent elements to infinity at 0 K, corrected with the zero point vibration term[10]:

$$E_{vib} = 1/2\,h \sum_{i}^{\substack{normal \\ modes}} \nu_i \qquad (1)$$

where h is the Planck's constant, ν the frequency of a normal mode. By definition, E_B is the enthalpy of formation of the compound under consideration from elements. For a given reaction, e.g.,

$$Mg\ (crystal) + H_2\ (gas) = MgH_2\ (crystal) \qquad (2)$$

a thermochemical cycle (Table 4) can be constructed to calculate the enthalpy of formation, based on the enthalpies of formation of the individual compounds given by the Dmol[3] calculations. Note that the enthalpy of formation in this example corresponds to that at 0 K. With the set of normal modes also given by the DMol[3] calculation, corrections can be made to account for the finite temperature effects[10] such that the enthalpy of formation at a given temperature can be obtained.

In the present paper, enthalpy of formation all referred to the 0 K state, unless specifically specified otherwise.

Results and Discussions

Bulk Materials. The optimized unit cell dimensions based on the energy – volume relation (Fig. 1) are within –0.4 and 0.7% to the experimental values for bulk Mg and MgH_2, respectively. The good agreement between the calculated and the experimentally observed cell dimension is an indication that the DFT functional and the basis set chosen are appropriate for the systems under study.

Table 4. Thermochemical cycle used in the calculation of enthalpy of formation at 0 K of MgH_2 from gaseous H and crystalline MgH_2

Reaction		ΔH (kJ/mol)
(1)	H (element) + H (element) → H_2 (gas)	-431.5
(2)	H (element) + H (element) + Mg (element) → MgH_2 (crystal)	-621.0
(3)	Mg (element) → Mg $_{(crystal)}$	-118.4
	Mg (crystal) + H_2 (gas) → MgH_2 (crystal) $\Delta H_f = -\Delta H_1 + \Delta H_2 - \Delta H_3$	-71.1

The enthalpy of formation at 0 K (Table 4) for MgH_2 is –71.1 kJ/mol. The value is well within the experimental uncertainty to the observed value[11] of –68.00 ± 9.2 KJ/mol.

Thin Films. Table 3 gives the enthalpies of formation from elements of the Mg and MgH_2 thin films of various thickness obtained directly from the Dmol[3] calculations. For both Mg and MgH_2, the enthalpy of formation becomes steadily less negative as the film thickness decreases, and , in the range of 9 to 1 unit-cell thickness, the net enthalpy change amount to ~ 50 kJ/mol_{Mg}. It is apparent that, as the film thickness decreases, the structural stability of the materials decreases considerably.

Based on these enthalpies of formation from elements, the enthalpies of hydridation were calculated and plotted in Figure 2.

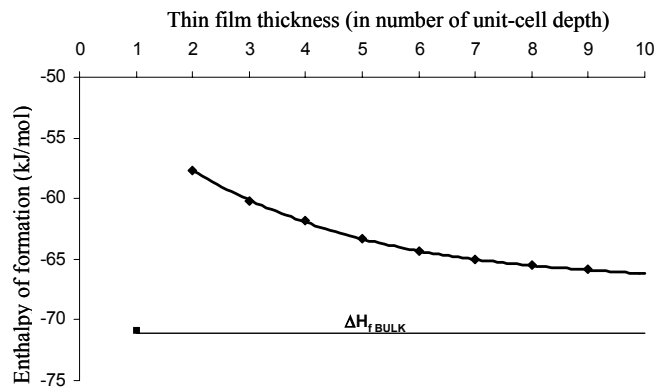

Figure 2. Variation of enthalpy of formation of hydriding Mg thin films as a function of Mg film thickness. Solid squares represent data points derived from the DFT calculation results.

The smallest enthalpy change, corresponding to 2 unit-cell thickness (1.6 Å Mg / 3.0 Å MgH_2) of the film, is 57.7 KJ/mol_{Mg}. This enthalpy change is over 10 KJ/mol smaller than that of the bulk. In addition, it is important to note that the upper bound of enthalpy change for systems that are suitable for mobile storage is 24 kJ/mol_H[1]. As there are 2 H per MgH_2, the enthalpy change corresponding to films of 2 unit-cell thickness is 57.7/2 = 28.9 kJ/mol_H, a mere 5 kJ/mol_H over the desired value.

Excluding the case of thin film thickness of 1 unit-cell depth, there's a clear trend that, as the film thickness increases, the enthalpy change also increases steadily. When the film thickness increased to that of 9 cell depth (14 Å Mg / 27 Å MgH_2), the enthalpy

change becomes 65.9 kJ/mol$_{Mg}$, approaching that of the balk of 71.1 kJ/mol$_{Mg}$. Therefore, it's not surprising that, even when the particle sizes were reduced to the nanometer range, there's still no apparent change in the enthalpy of formation[3-6].

The thin film of thickness of just 1 unit-cell depth behaves differently from the other films of greater thickness, by breaking the trend of decreasing change of enthalpy of formation and giving a value close to that of the bulk (Fig. 2). This behavior can be explained as a result of MgH_2 loosing its identity structurally compared to the bulk (Fig. 3). While Mg and H are 6- and 3-coordinated, respectively, in the bulk structure, they are 4- and 2-coordinated in the film of 1 unit-cell depth. In fact, attempts to cap the surfaces of the film with H only resulted in the stoichometrically excess hydrogen to be driven away from the surfaces to form molecular hydrogen in a Dmol[3] geometry optimization.

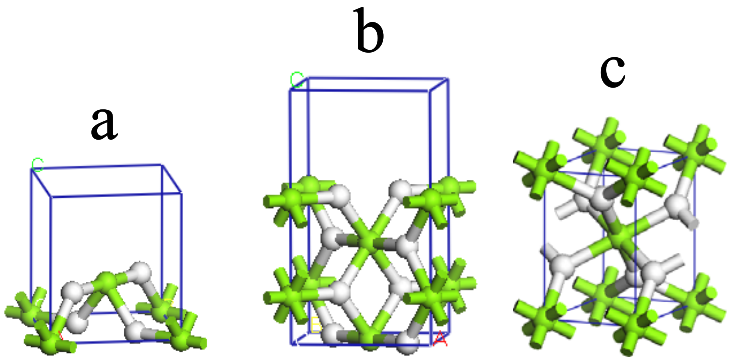

Figure 3. Structure models of MgH_2. a. Dmol[3] optimized 2D repeating unit of 1 unit-cell depth cleaved along the 001 surface; b. Dmol[3] optimized 2D repeating unit of 2 unit-cell depth cleaved along the 001 surface; c. Bulk unit cell.

How will the thermochemistry change if there is cohesive addition/subtraction to the layers in the hydrogen absorption/desorption processes? Using the same set of thermochemical data in Table 3 and the thermochemical cycle similar to that in Table 4, thermochemistry of such hypothetical combinations can be mapped out (Fig. 4). Two important points can be drawn. First, be it a forward (absorption) or reverse (desorption) reaction, if there is a decrease in film thickness of the product (e.g. in a decrepitation), the enthalpy change will increase significantly (by as much as 50 kJ/mol$_{Mg}$ in the present system). While such change is unfavorable in the desorption process, it may be beneficial in the absorption process. Secondly, if there is a cohesive increase of film thickness of the product, the enthalpy change decreases steadily. For example, when the MgH_2 films of 2 unit-cell thickness desorb and forms Mg films that are structurally coehsive in 9 unit-cell thickness, then the enthalpy change becomes 33 kJ/mol$_{Mg}$, or 17 kJ/mol$_H$, well within the range suitable for mobile storage, of 15 - 24 kJ/mol$_H$[1].

Conclusions

The DFT method reliably reproduced the known value of enthalpy of formation of bulk MgH_2 formed from gas-phase H and crystalline Mg. The same method was extended to thin films of Mg and MgH_2 of thickness ranging from 1 to 9 unit cell depths (sub-nanometer to low nanometer thickness). A clear trend was observed that, as the thickness of the film decreases, so does the enthalpy change, to a smallest value of 29 KJ/mol$_H$ at 2 unit-cell depth, close to the upper bound (24 KJ/mol$_H$) of the desired enthalpy change for systems that are suitable for mobile storage. On the other hand, the enthalpy change approaches that of the bulk value (or to within the error limit of experimental observations) as the thin film thickness increases towards the high nanometer regime. The results also suggested that it is thermo- chemically advantageous if there is cohesion of the products during the desorption process.

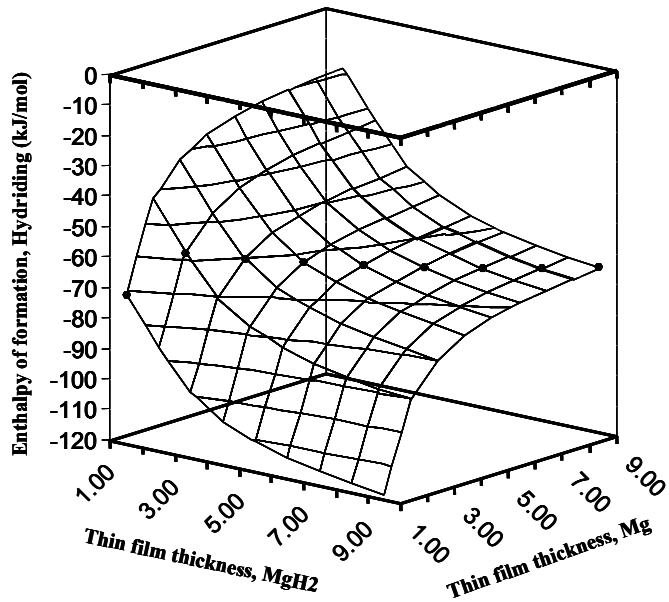

Figure 4. Variation of enthalpy of formation of hydriding Mg thin films. The thin films hypothetically assumes arbitrary thickness (in term of the number of unit-cell depth) before and after hydridation. Solid dots represent data points of comparable thin film thickness before and after hydridation (e.g. 1 unit-cell depth before and after hydridation).

References

1. Schlapbach, L. & Zuttel, A., Nature, 2001, 414, 353
2. Schlapbach, L. (e.d.) Hydrogen in Intermetallic Compounds I. Electronic, Thermodynamic, and Crystallographyic Properties (Topics in Applied Physics Vol 63) (Springer, 1988)
3. Zaluska, A., Zaluski, L., & Stroem-Olsen, J. O., Appl. Phys. A, 2001, 72, 157
4. Akiba, E. & Iba, H., Intermetallics 6, 1998, 461
5. Kuriiwa, T. et al., J. Alloys Compounds, 1999, 295, 433
6. Tsukahara, M. et al., J. Electrochem. Soc., 2000, 147, 2941
7. Delley, B., J. Chem. Phys., 1990, **92**, 508
8. Wyckoff, R.W.G., in *Crystal Structures*, volume 1, Interscience, John Wiley & Sons, 1963.
9. Zachariasen, B.H., Holley, C.E., Jr, and Stamper, J.F., Jr., Acta Cryst., 1963, 16, 352
10. Hehre, W.J., Radom, L., Schleyer, P.v.R., Pople, J.A., AB Initio molecular orbital theory (John wiley & Sons, 1986)
11. Gurvih, L.V., Veyts, I.V., and Alocock, C.B. (eds*)* Thermodynamic properties of individual substances, 4th ed; Vol. 2, Part I, II. (Hemisphere, New York, 1990)

HYDROGEN SEPARATION THROUGH DENSE MIXED PROTONIC-ELECTRONIC CONDUCTING MEMBRANES

Eric D. Wachsman, Sun-Ju Song and Jamie Rhodes

Department of Materials Science and Engineering
University of Florida, Gainesville, FL 32611-6400

Introduction

Membrane reactor technology holds the promise to circumvent thermodynamic equilibrium limitations by *insitu* removal of product species, resulting in improved chemical yields. Recent advances in mixed-conducting oxide-membrane technology present the possibility for a dramatic reduction in the cost of converting petroleum and coal derived feed stocks to hydrogen and other "value added" hydrocarbons. We have developed mixed protonic-electronic conducting materials for use as solid-state dense high temperature hydrogen permeation membranes. These membrane materials are perovskite ($BaCe_{1-x}M_xO_3$ and $SrCe_{1-x}M_xO_3$) based high temperature protonic conductors Both protonic and electronic conductivity are necessary to achieve hydrogen permeation through the solid-state. Therefore, we are modifying the chemistry of $BaCe_{1-x}M_xO_3$ and $SrCe_{1-x}M_xO_3$ by substitution of a multivalent dopant cation (M = $Eu^{+2/+3}$) in the Ce lattice site to obtain electronic conductivity.

We have studied the defect chemistry of these materials to determine regions of $P_{H2}/P_{H2O}/P_{O2}$ where the membrane exhibits both protonic and n-type electronic conductivity [1-4]. Using this defect chemistry information and conductivity data we determined mobilities and calculated the H_2 flux through 1 mm thick $SrCe_{0.95}Y_{0.05}O_{3-\delta}$ [3,4]. At 700°C the calculated maximum H_2 flux was between 1.5 x10^{-9} and 2.3 x 10^{-8}, depending on feed and sweep $P_{H2}/P_{H2O}/P_{O2}$ conditions [4].

In this paper we report on measured H_2 flux of $BaCe_{1-x}M_xO_3$ and $SrCe_{1-x}M_xO_3$ and compare it to calculated flux.

Experimental

Polycrystalline samples of multivalent and univalent $SrCe_{1-x}M_xO_3$ ($SrCe_{0.95}Eu_{0.05}O_{3-\delta}$ and $SrCe_{0.95}Sm_{0.05}O_{3-\delta}$) and $BaCe_{1-x}M_xO_3$ ($BaCe_{0.85}Eu_{0.15}O_{3-\delta}$ and $BaCe_{0.85}Gd_{0.15}O_{3-\delta}$) were prepared by conventional solid-state reaction methods. High-purity oxide powder of $SrCO_3$ or $BaCO_3$ (99.9% Alfa Aesar), CeO_2 (99.9% Alfa Aesar), and Eu_2O_3, Gd_2O_3 or Sm_2O_3 (99.99%, Alfa Aesar) were mixed, ground in a ball mill with stabilized zirconia balls in ethanol and calcined at 1573K for 10h in air. The calcined oxides were then crushed, sieved to < 45microns, ground in a ball mill again, pressed into pellets, cold-isostatic-pressed, and sintered at 1773K for 10h in air. The densities of the resultant disks were 96% of the theoretical. X-ray diffraction spectra confirmed that all specimens obtained in this way exhibit a single phase perovskite structure.

Hydrogen permeation measurements were performed on dense disks, 24 mm diameter × 1-2 mm thickness. The planar surfaces of the disk were polished down to #1200 grit SiC paper. Polished disks were sealed with ceramic sealant to alumina tubes so that the open surface was exposed to feed gas (H_2/N_2 mixtures). The sweep side had a constant flow of 20ccm helium. The hydrogen content of the permeate stream was measured using a mass spectrometer (Q100MS Dycor Quadlink Mass Spectrometer). Leakage of neutral gas through pores in the sample or through an incomplete seal was checked by measuring the argon content of the permeate stream. No discernible leak was detected. See references 4 and 5 for details.

Results and Discussion

From the hydrogen concentration measurements in the helium sweep side of the permeation assembly and the helium flow rate, the total hydrogen permeation fluxes (mol/sec) were calculated, assuming ideal gas law, and then the permeation fluxes (mol/cm^{2}sec) calculated from the effective surface area of the membrane disks.

The variation in hydrogen flux with temperature for Eu-doped and Sm-doped $SrCeO_3$ is given in Fig. 1. The hydrogen fluxes increase with temperature for both systems and the $SrCe_{0.95}Eu_{0.05}O_{3-\delta}$ exhibits higher permeability in comparison with $SrCe_{0.95}Sm_{0.05}O_{3-\delta}$ over the entire temperature range investigated.

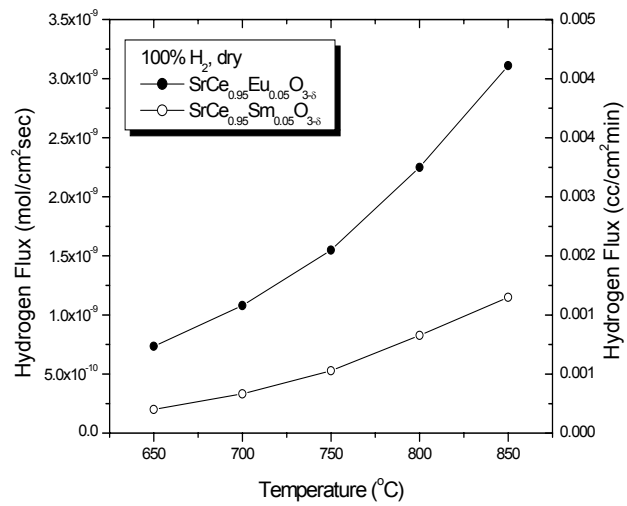

Figure 1. Comaprison of H_2 fluxes through $SrCeEuO_3$ and $SrCeSmO_3$ as a function of temperature.

The influence of an applied hydrogen chemical potential gradient at various P_{H2O} on the hydrogen permeability was also studied [5]. The hydrogen permeation flux of the Eu-doped specimen consistently showed higher hydrogen permeability compared to that of the Sm-doped specimen. The dopant dependence of hydrogen permeability can be explained by the increase in n-type electronic conduction by the multivalent cation under low P_{O2} conditions [1-4].

$BaCeO_3$'s have higher protonic conductivity than $SrCeO_3$'s. Therefore, we investigated the H_2 permeation of multivalent doped $BaCe_{0.85}Eu_{0.15}O_{3-\delta}$ vs. that of univalent doped $BaCe_{0.85}Gd_{0.15}O_{3-\delta}$ [5]. The $BaCe_{0.85}Eu_{0.15}O_{3-\delta}$ exhibited significantly higher H_2 permeation than $BaCe_{0.85}Gd_{0.15}O_{3-\delta}$ due to it's higher n-type electronic conduction. Further, the $BaCe_{0.85}Eu_{0.15}O_{3-\delta}$ had higher H_2 permeation than $SrCe_{0.95}Eu_{0.05}O_{3-\delta}$ due to it's higher protonic conductivity.

Conclusions

Hydrogen permeability of $BaCe_{1-x}M_xO_3$ and $SrCe_{1-x}M_xO_3$ membranes were studied by gas permeation measurements as a function of temperature, P_{H2} gradient, and P_{H2O} gradient. The measured fluxes with the $SrCe_{1-x}M_xO_3$ membranes are in good agreement with our earlier modeling results [4].

The effect of dopant ion on hydrogen permeability through 1-2 mm thick membranes was investigated. In both cases the membrane

with the multivalent $Eu^{+2/+3}$ dopant exhibited higher hydrogen permeability. Further effort is required to enhance electron conductivity of Eu-doped cerates by adjusting doping level, increasing the effective surface area and/or improving hydrogen exchange properties at the surface.

Acknowledgement. This work was supported by the U.S. Department of Energy, Contract W-31-109-Eng-38, NASA, Contract NAG3-2750, and CANMET, Contract 23341-8-3222/001-SS.

References

(1) S. J. Song, E. D. Wachsman, S. E. Dorris, and U. Balachandran, *Solid State Ionics*, **149**, 1-10 (2002).
(2) S. J. Song, E. D. Wachsman, S. E. Dorris, and U. Balachandran, *J. Electrochem. Soc.,* accepted
(3) S. J. Song, E. D. Wachsman, J. Rhodes, S. E. Dorris, and U. Balachandran, *J. Electrochem. Soc.,* submitted
(4) S. J. Song, E. D. Wachsman, J. Rhodes, S. E. Dorris, and U. Balachandran, *J. Electrochem. Soc.,* submitted
(5) J. Rhodes and E. D. Wachsman In *Solid State Ionic Devices II - Ceramic Sensors*, Proc. Electrochem. Soc., E.D. Wachsman, W. Weppner, E. Traversa, M. Liu, P. Vanysek, and N. Yamazoe, Ed., **2000-32**, 137-147 (2001).

SORPTION IN PROTON EXCHANGE MEMBRANES: AN EXPLANATION OF SCHROEDER'S PARADOX

Pyoungho Choi and Ravindra Datta

Fuel Cell Center, Department of Chemical Engineering, Worcester Polytechnic Institute, Worcester, MA 01609, USA.

Introduction

Fuel cells based on the proton-exchange membranes (PEMs) are of great potential as efficient and largely pollution-free power generators for mobile and stationary applications.[1] The PFSA membranes typically consist of a polytetrafluoroethylene (PTFE) backbone with side-chains terminating in SO_3H groups. They possess little porosity in the dry state. However, in the presence of water or other polar solvents, the membrane swells and the sulfonic acid groups ionize protonating the sorbed solvent molecules that are responsible for conducting the protons. The conductivity of Nafion® is highly dependent upon hydration level[2] being essentially an insulator below a threshold and rising through several orders of magnitude to about 0.07 ~ 0.1 Siemens/cm at 80 ºC when it is fully hydrated.

The water uptake in Nafion® expressed in terms of λ, the number of moles of water per equivalent of polymer, upon contact with liquid or its saturated vapor as reported in the literature[3] There is an unexplained discrepancy in the water uptake in Nafion® from pure liquid ($\lambda_{i,L} \approx 22\sim23$) versus that from its saturated vapor ($\lambda_{i,V} \approx 13.5\sim14.0$), even though both possess unit activity. In fact, when a liquid water-equilibrated membrane was removed and exposed to saturated water vapor, λ dropped from 22 to 14, thus indicating that the two states are thermodynamically stable. The phenomena, known as Schroeder's paradox,[4] is apparently not uncommon in polymer systems, but has not so far been satisfactorily explained although many different explanations have been advanced.

A sorption model of water in Nation® is proposed here based on that the sorption isotherm is controlled by the swelling pressure determined by the matrix and surface forces of the polymer membrane and sorbed solvent.

Model Description

When the ion exchange membrane, *e.g.,* Nafion®, is in equilibrium with a solvent, *e.g.,* water, some of the sorbed solvent molecules are in a physicochemical state that is different from the bulk solvent molecules depending upon their interaction with surroundings. The model developed here simply assumes that the sorbed solvent molecules are of two types; *i*) those that are strongly, or chemically, bound to the acid sites, akin to chemisorption, and *ii*) others that are physically equilibrated between the fluid and the membrane phases, akin to physisorption. It is further assumed that as the membrane swells due to solvent uptake, the solvent molecules meet increasing resistance from the hydrophobic backbone as well as the stretched polymer chains resulting in a swelling pressure on the pore liquid. The model, thus, involves a balance of forces.[5] Equilibrium is achieved when the elastic forces of the polymer matrix counterbalance the increased pressure within the pore liquid in an effort of solvent molecules to equalize the chemical potential of the fluid inside and outside of the pore. The spring constant κ of the spring is assumed to depend upon the temperature (*e.g.,* proximity to the glass-transition temperature, T_g), and pretreatment procedures.

Liquid-Membrane Phase Equilibria For equilibration between a liquid and membrane phases for an uncharged species *i*

$$\ln\frac{a_{i,M}^{F}}{a_{i,L}} = -\left(\frac{\overline{V}_i}{RT}\right)\Pi_{\mathrm{M}} \tag{1}$$

where the membrane swelling, or osmotic pressure, $\Pi_{\mathrm{M}} = P_M - P_L$, is the pressure rise within the membrane exerted by the membrane polymer matrix due to stretching to accommodate the imbibed pore liquid The activity of species *i* within the membrane $a_{i,M}^{F}$ corresponds to the 'free', or non-chemically bound, molecules of *i*, as denoted by the superscript *'F'*.

Vapor-Membrane Phase Equilibria. When the membrane equilibrates with a vapor phase, assuming that the pressure changes within the condensed phase in the pore is caused both due to the stretching of the polymer chains upon solvent uptake, Π_{M}, as well as that exerted by the curved vapor-liquid interface within the pores, Π_σ,

$$\ln\frac{a_{i,M}^{F}}{a_{i,V}} = -\left(\frac{\overline{V}_i}{RT}\right)\left(\Pi_{\mathrm{M}}+\Pi_\sigma\right) \tag{2}$$

where the vapor phase activity $a_{i,V} = P_i/P_i^{sat}$ and Π_σ is provided by the equation of Young and Laplace[6]

$$\Pi_\sigma = -\frac{2\sigma\cos\theta}{r_p} \tag{3}$$

where θ is the liquid-membrane contact angle and r_p is the mean pore radius of liquid-filled pores. For the case of saturated vapor, $P_i = P_i^{sat}$, then Eq. (2) gives

$$\ln a_{i,M}^{F} = -\left(\frac{\overline{V}_i}{RT}\right)\left(\Pi_{\mathrm{M}}+\Pi_\sigma\right) \tag{4}$$

whereas for the case of pure liquid solvent *i*, from Eq. (1)

$$\ln a_{i,M}^{F} = -\left(\frac{\overline{V}_i}{RT}\right)\Pi_{\mathrm{M}} \tag{5}$$

It is then clear from the Eq. (4) and (5) that, in general, the amount sorbed from a saturated vapor would be different from that sorbed from a pure liquid, both possessing unit activity. This simple result, thus, provides a reasonable explanation for the Schroeder's paradox for the sorption in polymers.

The final expression for the liquid-phase sorption in the proton exchange membrane is obtained as

$$\left\{\lambda_{i,L} - \frac{\lambda_{i,m}K_1 a_{i,L}}{(1-a_{i,L})}\left[\frac{1-(\nu+1)(a_{i,L})^{\nu}+\nu(a_{i,L})^{\nu+1}}{1+(K_1-1)a_{i,L}-K_1(a_{i,L})^{\nu+1}}\right]\right\}^{-1} =$$

$$a_{i,L}^{-1}\exp\left\{\frac{\overline{V}_i}{RT}\left[\frac{\kappa\lambda_{i,L}}{\lambda_{i,L}+\overline{V}_M/\overline{V}_i}\right]\right\} - 1 \tag{6}$$

where $\lambda_{i,m}$ is the monolayer coverage being bound, K_1 is the equilibrium constant of water molecules with ion exchange site of the polymer and ν is the number of equilibrium steps chemical equilibrium between the ion exchange site and each water molecules.

For the vapor-phase sorption, surface energy term is included in the isotherm expression as

$$\left\{\lambda_{i,V}-\frac{\lambda_{i,m}K_1 a_{i,V}}{(1-a_{i,V})}\left[\frac{1-(\nu+1)(a_{i,V})^{\nu}+\nu(a_{i,V})^{\nu+1}}{1+(K_1-1)a_{i,V}-K_1(a_{i,V})^{\nu+1}}\right]\right\}^{-1}=$$

$$a_{i,V}^{-1}\exp\left\{\frac{\overline{V}_i}{RT}\left[\frac{\kappa\lambda_{i,V}}{\lambda_{i,V}+\overline{V}_M/\overline{V}_i}-(S\sigma\cos\theta)\left(1+\frac{\overline{V}_M}{\overline{V}_i}\frac{1}{\lambda_{i,V}}\right)\right]\right\}-1 \quad (7)$$

For given $\lambda_{i,m}$, K_1, ν, $\overline{V}_i$, κ, S, σ, θ and $\overline{V}_M$, thus, the sorption isotherm, namely versus a_i can be determined for vapor or liquid phase sorption. Further, it is then clear from the Eq. (6) and (7) that the solvent loading in liquid sorption, $\lambda_{i,L}$, would in general be different from the solvent loading from the vapor sorption $\lambda_{i,V}$.

Results and Discussion

In order to apply this model into water sorption in Nafion®, the parameters of the equations, K_1, $\lambda_{i,m}$, and ν, are obtained based on the following considerations. The equilibrium constant K_1 between water and the side chain of SO_3^- ion is approximated by that of sulfuric acids in water for the first ionization. The solvent loading parameter, $\lambda_{i,m}$, is taken as a monolayer coverage being bound in the proton exchange membrane. The number of equilibrium steps, ν, for hydration of the ions is related to the number of solvent molecules in the hydration shell. For sulfonated styrene-type ion exchanger, six hydration number for SO_3H group is reported experimentally and recent molecular modeling studies also results in 5 to 6 hydration number for SO_3H. The activity of water in Nafion®, which is osmotically active, is limited to the water molecules that are outside of the first hydration shell.[7] In the dry or low humidity conditions, a few water molecules are in the hydration shell and are not enough to shield the ions and as the humidity of the membrane increases, more water molecules are involved in the shielding of sulfonic acid and hydronium ion.

Figure 1 shows the predicted isotherm of water in Nafion® by Eq. (7), the solid line, as well as the experimental data. The model represents the sorption of water in Nation® and predicts quite precisely all the features of the isotherm throughout the entire range of vapor phase activity; it predicts the high initial slope, gradual increase of the slope after the sorption of the first a few molecules and high slope at high activities after about $a_{i,V}$ = 0.7 ~ 0.8.

In order to explain the Schroeder's paradox for the sorption of water in Nafion®, Eq. (6) and (7) can be further modified for the sorption of pure liquid *i*, $a_{i,L}$ = 1.0. The model predicts the loading of water in water solution $\lambda_{i,L}$ = 22 ~ 23 and $\lambda_{i,V}$ = 15 ~ 16 for saturated vapor condition. There is a clear difference in solvent loading between liquid and saturated vapor sorption; *that is*, the solvent loading of vapor phase sorption is less than that of liquid phase, in this case the difference is about seven. This means that seven water molecules per acid site on average are less sorbed in Nafion® when the molecules are sorbed from the vapor compared with the liquid molecules contacting the membrane. The reason for this difference is that the surface energy of the sorption phase affects the chemical potential of the sorption phase in different extents in the liquid and saturated vapor sorption.

The simplified model presented here predicts the isotherms, the solvent loadings from the vapor and liquid phase sorption, and explains the Schroeder's paradox for the water sorption in Nafion® satisfactorily. It is based on the difference in the states, which are stable in thermodynamic means, of the sorption phases where the sorption phases interact with different environments of the bulk liquid and its saturated vapor phases.

Conclusions

A theoretical model is developed for the sorption of solvent in proton exchange membrane. This model predicts isotherm of water in Nation® quite precisely and provides insight into the sorption phenomena in the ion exchange polymer. The sorption isotherm is a result of equilibrium conditions that are established between the elastic forces of the polymer matrix and swelling pressure in the membrane. The swelling pressure is derived from the solvent activity inside of the polymer membrane and the dissociation characteristics of the solvent in the presence of the acid exchange site.

The isotherm equations clearly show the difference in the sorption amount from liquid and its saturated vapor, which is known as Schroeder's paradox. The paradox could well be explained in terms of surface energy that leads different energy states of sorption molecules for the liquid immersion and saturated vapor conditions.

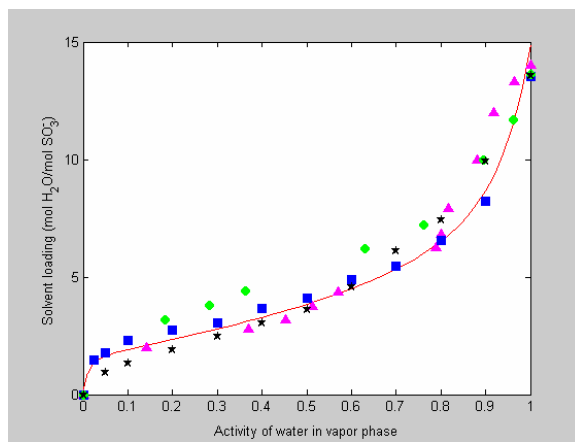

Figure 1. Isotherm of water vapor in Nafion: experimental reports (symbols) from four different groups with model prediction (solid line).

References

1. Perry. M. L.; Fuller. T. F. *J. Electrochem. Soc.* **2002**, 149, S59.
2. Anantaraman, A. V.; Gardner, C. L. *J. Electroanal. Chem.,* **1996**, 414, 115.
3. Zawodzinski, T. A.; Springer, T. E.; Davey, J.; Jestel, R.; Lopez, C.; Valerio, J.; Gottesfeld, S. *J. Electrochem. Soc.,* **1993**, 140, 1981.
4. Schroeder, P. V. *Z. Phys. Chem.,* **1903**, 45, 75.
5. Gregor, H. P. *J. Am. Chem. Soc.,* **1951**, 73, 642.
6. Adamson, A. W.; Gast, A. P. *Physical Chemistry of Surfaces*; John Wiley & Sons, Inc.: NY, 1997.
7. Helfferich, H. *Ion Exchange*; McGraw-Hill; NY, 1960.

CHEMICAL STABILITY OF BARIUM CERATE–BASED HIGH-TEMPERATURE PROTON CONDUCTORS

R. D. Carneim and T. R. Armstrong

Metals and Ceramics Division
Oak Ridge National Laboratory
PO Box 2008
Oak Ridge, TN 37831

Introduction

Proton conducting ion transport membranes are required to extract absolutely pure hydrogen from mixed gas streams in the processing of fossil fuels and other petroleum and petrochemical processes. Ceramic materials are required to withstand these high-temperature processes. Yttrium-doped barium cerate ($BaCe_{0.80}Y_{0.20}O_{3-\delta}$) is currently one of the best materials when considering only proton conductivity. However, this material is very sensitive to the carbon dioxide (CO_2) and sulfur (H_2S) contamination found in the fossil fuel process stream. Barium cerate will decompose into barium carbonate ($BaCO_3$) and ceria (CeO_2) in the presence of CO_2; and CeO_2 reacts with H_2S to produce a sulfided phase, particularly in the highly reducing fuel environment. Two approaches for improving the stability of barium cerate are examined: manipulation of the A- to B-site stoichiometry and partial substitution of Ce with Zr. Individually these techniques have been previously shown to enhance stability. In the present work, the effect of applying both modifications simultaneously is explored. High-temperature x-ray diffraction (HTXRD) and thermogravimetric analysis (TGA) are used to determine decomposition temperatures, extent of decomposition, and reaction kinetics of various yttrium-doped barium cerate compositions in CO_2-contaminated environments.

Experimental

Sample preparation. Small batches (≈ 10 g) of powders were prepared by the glycine–nitrate process (GNP).[1] The resulting ash was sieved (100-mesh) and calcined for 20 min to 30 min at 1200 °C to produce the desired single-phase perovskite. The following compositions were synthesized:

BCY—: Four barium-deficient compositions: $Ba_xCe_{0.80}Y_{0.20}O_{3-\delta}$ with x = 1.00, 0.98, 0.95, and 0.90; designated BCY108, BCY88, BCY58, and BCY08, respectively.

BCZ—: Three barium-deficient, non-acceptor-doped zirconium-substituted compositions: $Ba_{0.98}Ce_{1-y}Zr_yO_{3-\delta}$ with y = 0.15, 0.10, and 0.05; designated BCZ885, BCZ89, and BCZ895, respectively.

BCZY: One barium-deficient, acceptor-doped, zirconium-substituted composition: $Ba_{0.98}Ce_{0.65}Zr_{0.15}Y_{0.20}O_{3-\delta}$; designated BCZY.

High-temperature x-ray diffraction. The bulk of the HTXRD measurements were conducted in a Phillips X'Pert diffractometer with a Pt-Rh strip heater/sample stage in an environmentally controllable sample chamber (HTK 16 High-Temperature Camera) with Capton x-ray windows.

Resistance to degradation due to the presence of CO_2 was determined by measuring the temperatures at which $BaCO_3$ formed during heating and cooling of the single-phase perovskite in flowing CO_2 ($p[CO_2] = p$ = 101 kPa [1 atm]). The procedure used was: heat sample in N_2 to t = 1400 °C and cool to room temperature; perform scan; change sample environment to flowing CO_2 and hold 20 min; perform scan; raise temperature by 50 °C and hold 5 min; perform scan; repeat preceding two steps until t = 1400 °C; lower temperature by 100 °C and hold 10 min; perform scan; repeat preceding two steps until t = 500 °C. Measurements were taken over the range from 2θ = 20° to 2θ = 44°.

The HTXRD data is presented by plotting the common logarithms of the peak ratios (areas under peaks attributable to only the perovskite phase vs. those attributable to only non-perovskite phases; background intensity and noise ensure finite results), , versus temperature during heating and cooling (figure 1). A cut-off value of $\lg(r_{p/c}) = -0.25$ was used to define transition temperatures ($\lg(r_{p/c}) > 0$ indicates no observable $BaCO_3$ and $\lg(r_{p/c}) < -0.5$ indicates the presence of a significant amount of $BaCO_3$). The temperatures at which carbonate phase forms and disappears on heating, and forms again on cooling can be easily seen and compared. Additionally, the relative extent of conversion to $BaCO_3$ can be seen by the magnitude of the deflection into the carbonate side of the plot.

An additional feature that stands out in this representation of the data is hysteresis in the high-temperature transition (i.e., the temperature at which $BaCO_3$ disappears on heating or appears on cooling). The high-temperature transition hysteresis, Δt_{hyst}, is defined as the difference between the transition temperatures measured during heating and cooling. This quantity may be used for comparing reaction kinetics between related materials undergoing the same reaction at comparable temperatures.

Thermal analysis. Simultaneous thermogravimetric analysis and differential thermal analysis (TGA and DTA) were performed on the three modified compositions BCY88, BCZ885, and BCZY (T/A Instruments). Sample and α-Al_2O_3 reference powders of $m \approx 25$ mg each were used. Multiple scans were performed on each composition at different heating/cooling rates (ϕ = 4 °C·min^{-1}, 10 °C·min^{-1}, and 20 °C·min^{-1}) to allow estimation of the reaction activation energies using the Kissinger method.[2, 3] Derivatives of the TGA data were used for these calculations rather than the DTA data due to significantly greater signal intensity.

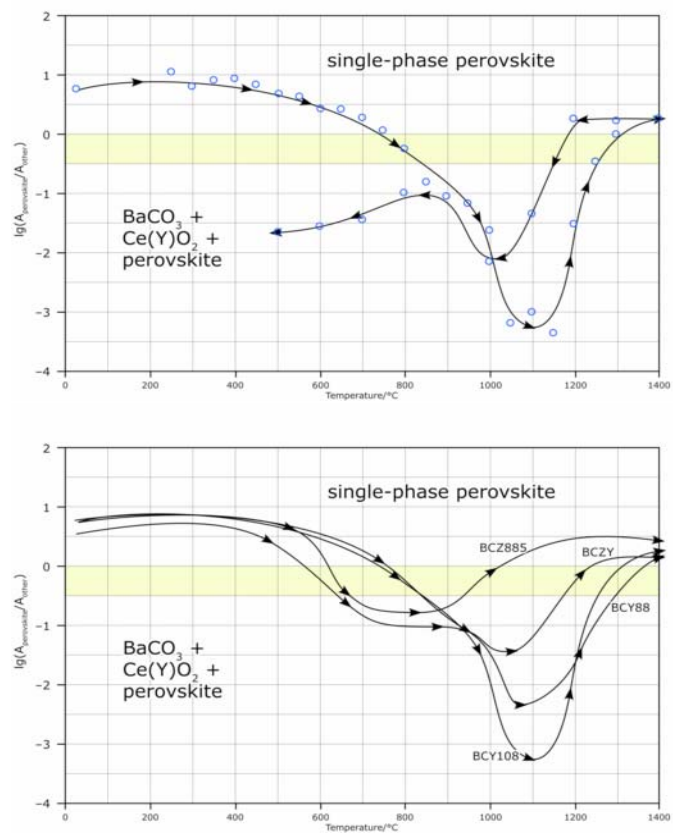

Figure 1. The results of HTXRD in CO_2 are represented as the common logarithm of the ratio of perovskite to non-perovskite (i.e., $BaCO_3$) peak areas. Values > 0 indicate no detectable $BaCO_3$ and values < –0.5 indicate significant $BaCO_3$ formation. ***Top:*** sample complete data set for BCY108, heating and cooling. ***Bottom:*** data on heating only for BCY108 and the three modified compositions BCY88, BCZ885, and BCZY.

Results and Discussion

Barium Stoichiometry. Earlier cursory measurements showed no difference in the behavior of the three barium-deficient compositions (BCY88, BCY58, and BCY08). For the purpose of stability in CO_2, any of the barium-deficient compositions would serve to realize the improvement over the stoichiometric composition and stay well clear of a barium-excess situation (which previous work reports as detrimental [4]); however, an extreme barium deficiency would result in severe degradation of electrical properties[4]. Therefore, the least (non-zero) barium-deficient composition was chosen for propagation through this study: $x = 0.98$.

The measurements reported here for BCY108 and BCY88 reveal details of the differences in behavior of the stoichiometric and barium-deficient compositions with respect to degradation in CO_2. The various transition temperatures are nearly identical for these two compositions. The temperature range in which $BaCO_3$ is present and the high-temperature transition hysteresis were similar for these two materials. The consequential difference between these two compositions is the extent of transformation: the peak ratio, $\lg(r_{p/c})$, is nearly one order of magnitude larger (i.e., indicating significantly less $BaCO_3$ formation) for BCY88 than for BCY108.

Zirconium substitution, undoped. Published work[5] and previous experiments indicated that the BCZ samples showed significantly less carbonate formation relative to the BCY samples, though the carbonate appears at higher temperatures in the BCZ samples than in the BCY samples. The highest zirconium-content composition, BCZ885, had no measurable $BaCO_3$ peaks on cooling, though on heating BCZ885 clearly showed $BaCO_3$ formation at approximately the same temperature as the BCY compositions ($t \approx 550$ °C).

Current results clearly reveals considerable improvements in the chemical stability of BCZ885 over the most similar non-zirconium-substituted composition, acceptor-doped BCY88. The data barely enters the $BaCO_3$ region of the $\lg(r_{p/c})$ vs. t plot during both heating and cooling. Furthermore, the temperature range in which $BaCO_3$ is present is smaller and occurs at lower temperatures (Table 1).

The high-temperature transition hysteresis, however, is greater: $\Delta t_{hyst} \approx 230$ °C for BCZ885 vs. $\Delta t_{hyst} \approx 150$ °C for BCY88. Such an increase in this quantity indicates a slowing of the reaction kinetics. It is not clear at this point whether this effect on the kinetics is a direct result of the chemical effects of the Zr_{Ce} substitution or merely due to the fact that the transition occurs at a lower temperature (an *indirect* result of the Zr_{Ce} substitution).

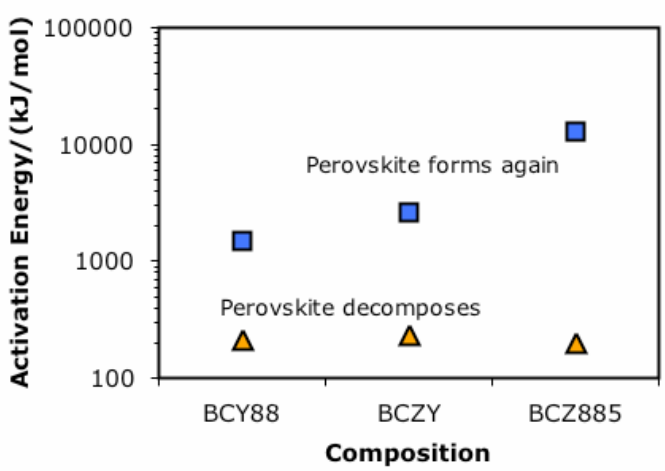

Figure 2. The activation energies are shown for the three modified barium cerate compositions: (▲) initial decomposition of the single phase perovskite into $BaCO_3$ and CeO_2, (■) formation of perovskite as CO_2 is lost at high temperature. Values were calculated using the Kissinger method from TGA data on heating in $p = p(CO_2) = 101$ kPa (1 atm).

Table 1. Summary of Transition Temperatures from HTXRD*

Composition	$BaCO_3$ appears on heating: t/°C	$BaCO_3$ disappears on heating: t/°C	$BaCO_3$ temperature range: t_{range}/°C	$BaCO_3$ appears on cooling: t/°C	High-temperature transition hysteresis: Δt_{hyst}/°C	Maximum $\lg(r_{p/c})$ peak deflection to $BaCO_3$†
BCY108	780	1280	500	1160	120	–3.25
BCY88	780	1330	550	1180	150	–2.35
BCZ885	640	980	340	750	230	–0.80
BCZY	600	1200	600	950	250	–1.45

* Tabulated values were extracted from data as in figure 1 using $\lg(r_{p/c}) = -0.25$ cutoff.
† N.B., $\lg(r_{p/c}) < -0.5 \equiv$ significant formation of $BaCO_3$

Zirconium substitution, yttrium-doped. The composition BCZY incorporates all the stability-enhancing modifications examined earlier, plus the standard 0.20 Y doping. On heating, BCYZ possesses characteristics of both component compositions (i.e., BCY88 and BCZ885): a minor excursion into the $BaCO_3$ field at $t \approx 600$ °C, similar to BCZ885; then further $BaCO_3$ formation above $t \approx 1000$ °C, approximately the temperature of maximum conversion to $BaCO_3$ of BCY88. The extent of conversion also falls between that of the two simple compositions. On cooling, BCZY behaves slightly differently. Barium carbonate begins to form at a temperature approximately midway between the onset temperatures for BCY88 and BCZ885. But rather than distinct peaks in the $\lg(r_{p/c})$ data, BCZY displays a gradual, monotone decrease in $\lg(r_{p/c})$ to the lowest temperature.

Since BCZY behaves approximately as a combination of the two component compositions, the magnitudes of the $BaCO_3$-presence temperature range and high-temperature transition hysteresis are approximately equal to the greater of the two corresponding values for the simple compositions: $t_{range} \approx 600$ °C, comparable to the t_{range} value for BCY88; and $\Delta t_{hyst} \approx 250$ °C, similar to the Δt_{hyst} value of BCZ885. Furthermore, the high-temperature transition temperatures of BCZY fall between those of BCY88 and BCZ885 while the hysteresis is still comparable to that of BCZ885. This indicates that the effect on the kinetics is principally due to chemical differences resulting from the Zr_{Ce} substitution. This is corroborated by the calculated activation energies shown in figure 2. While activation energy of the low-temperature transition (▲ in figure 2) is nearly independent of the composition, the high-temperature transition (■ in figure 2) has a significantly higher energy barrier in the BCZ885 composition.

Conclusions

Two methods for improving the stability of yttrium-doped barium cerate in CO_2 have been investigated. Producing slightly barium-deficient compositions and partial substitution of Zr for Ce have previously and in this work been shown to increase the resistance to decomposition in the presence of CO_2. The effects of the individual modifications as well as their combined effects have been shown utilizing thermal analysis and high-temperature x-ray diffraction. While definite improvements in CO_2-tolerance were observed, absolute immunity was not achieved at the levels of modification studied. Since it is known[4, 5] that significant amounts of Zr_{Ce} substitution or Ba-deficiency severely decrease conductivity, the prospect of producing a practical, durable high-temperature proton conductor in this system with these techniques is unlikely.

Acknowledgement. Research at Oak Ridge National Laboratory sponsored by the Office of Fossil Energy, U.S. Department of Energy under contract DE-AC05-00OR22725 with UT–Battelle, LLC.

References

(1) Chick, L. A.; Pederson, L. R.; Maupin, G. D.; Bates, J. L.; Thomas, L. E.; Exarhos, G. J. , *Materials Letters,* **1990,** *44* (1, 2) 6–12.
(2) Kissinger, H. E., *J. Res. National Bureau of Standards,* **1956,** *57*(4), 217–21.
(3) Kissinger, H. E., *Anal. Chem.,* **1957,** *29* (11), 1702–6.
(4) Ma, G.; Shimura, T.; Iwahara, H., *Solid State Ionics,* **1998,** *107,* 221–29.
(5) Ryu, K. H.; Haile, S. M., *Solid State Ionics,* **1999,** *125,* 355–67.

HIGH CATALYTIC PERFORMANCES OF LOW RANK COAL CHARS IN AMMONIA DECOMPOSITION AT HIGH TEMPERATURES

Yasuo Ohtsuka, Chunbao Xu, Dapeng Kong, Naoto Tsubouchi

Institute of Multidisciplinary Research for Advanced Materials,
Tohoku University
Katahira, Aoba-ku, Sendai 980-8577, Japan

Introduction

To develop a novel hot gas cleanup method to efficiently remove heteroatom compounds from coal gasification products is important to achieve high power-generation efficiency in integrated gasification combined-cycle technologies.[1] The present authors have recently found that fine particles of Fe or CaO supported on chars, prepared by carbonizing brown coals with Fe or Ca ions added, promote the decomposition of 2000 ppm NH_3 diluted with He at 750 – 850°C, and the high performance of the Fe catalyst is comparable to those of Ni- and Ru-based catalysts.[1),2)]

Since Fe and Ca ions are naturally present mainly as ion-exchanged forms in low rank coals, the present work focuses on the utilization of such cations as catalyst sources for NH_3 decomposition from a practical point of view. The inherently present, exchanged Fe ions have been reported to provide nanoscale particles of metallic Fe upon carbonization[3] and are thus expectable to show high catalytic activity for this reaction.

Experimental

Five kinds of low rank coals from different countries with size fraction of 150 – 250 μm were used as catalyst sources. The carbon contents were 66 – 72 wt%(daf). These coals were carbonized with a fluidized bed reactor at 900°C in a stream of He. The resulting chars had carbon contents of 88 – 92 wt%(daf) and BET surface areas of 100 – 230 m^2/g.

Catalytic decomposition of 2000 ppm NH_3 diluted with high purity He was carried out mainly at 750°C with a quartz-made fixed bed reactor. To examine the effect of actual gas components, a simulated gas containing H_2, CO, and CO_2 was also used. In a typical run, the char charged into the reactor was first treated with pure H_2 at 500°C for 2 h, then heated at 15 K/min up to 750°C under flowing high purity He, which was finally replaced with feed gas, the space velocity being 45000 h^{-1}. The concentration of NH_3 or N_2 in the outlet gas was on line analyzed with a photoacoustic multi-gas monitor or a high speed micro GC, respectively. Conversion of NH_3 to N_2 was calculated by using the amount of N_2 determined.

Some chars before and after reaction were characterized with a transmission electron microscope (TEM) equipped with an energy dispersive analyzer (EDX), by the X-ray diffraction (XRD) measurement with Ni-filtered Cu-Kα radiation, and by the temperature programmed desorption (TPD) technique.

Results and Discussion

Performances of Different Coal Chars. Figure 1 shows NH_3 conversion at 750°C against time on stream. All of five chars used promoted NH_3 decomposition, though the efficiency depended strongly on kind of char. NH_3 conversion decreased with increasing time to be almost steady in most cases. When the value after 3 – 4 h reaction was compared among all of the chars, it increased in the sequence of AD < ZN ≈ SB < AB < RB and reached 80 % with RB char. It is evident that such performances of coal chars originate from the catalytic activity of Fe and Ca species naturally present in them, since Fe and Ca ions added to brown coals are active for this reaction,[2] as mentioned above.

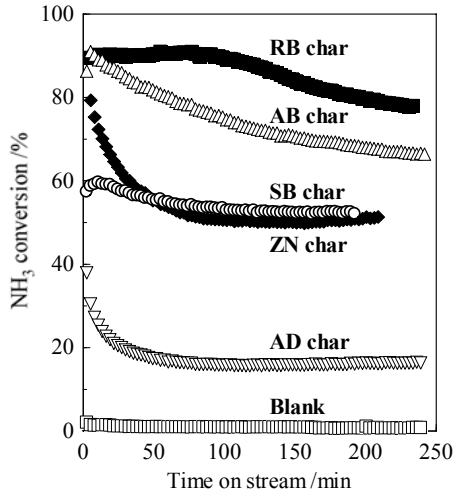

Figure 1. Catalytic performances of different coal chars in NH_3 decomposition at 750°C.

Figure 2A shows the result for the life test at 750°C of RB char with the largest performance. Although the initial conversion of about 95 % was decreased to less than 80 % after 2 – 3 h reaction, the conversion level was almost unchanged even when time on stream was further prolonged to 25 h. The activity of RB char was thus very stable under the present conditions.

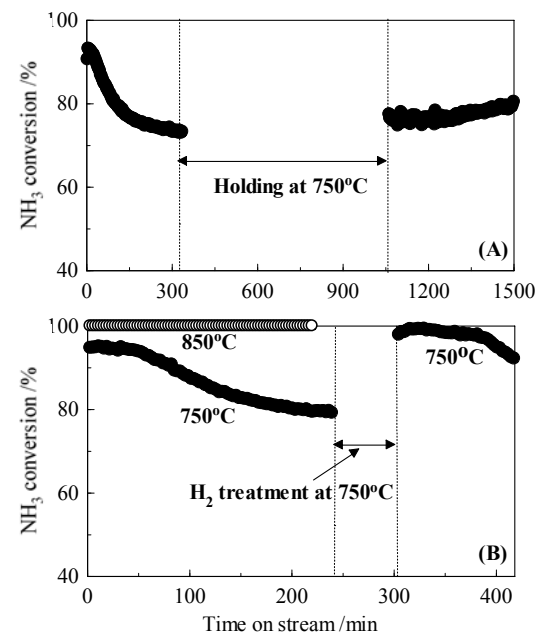

Figure 2. Catalyst life of RB char (A) and the effect of H_2 treatment of the char on NH_3 conversion (B).

To make clear the reason for the decrease of the initial activity of RB char, the char used was treated with H_2 at 750°C for 1 h. The result is shown in Figure 2B. When feed gas was first stopped after 4 h, then replaced with pure H_2, and finally passed again over the char, NH_3 conversion was restored to the initial state. A significant amount of CH_4 was formed during H_2 treatment. These observations strongly suggest that the surface of metallic Fe as the catalytically active species is partly carburized by the reaction with carbon atoms

in the char in the process of NH_3 decomposition, and H_2 treatment can restore the carbide species to the original metallic form. As is seen in Figure 2B, RB char showed no significant deactivation at 850°C. The H_2 evolved by NH_3 decomposition may prevent the iron surface from being carburized because possibly of larger reaction rate of the carbide species and H_2 at 850°C.

Catalysis by Inherent Fe and Ca in Char. Figure 3 shows a TEM picture of the fresh RB char. Fine particles with the size of 10 – 20 nm existed on the char. The EDX analysis of this field revealed the dominant presence of Fe and Ca elements, as is expectable. Although no significant XRD peaks of Fe species were detectable in the char, it is reasonable to see that inherent Fe ions in RB coal are reduced to the metallic form during carbonization. With Ca species, very weak diffraction lines of CaO were observed in not only RB char but other chars. The formation of nanoscale particles of metallic Fe and CaO accounts for high catalytic performance of RB char.

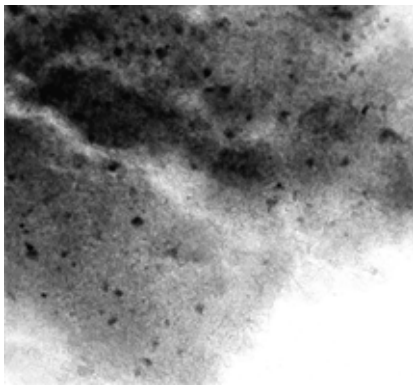

Figure 3. TEM picture of RB char before NH_3 decomposition.

To examine the relationship between NH_3 conversion and the content of Fe or Ca inherently present in char, these elements were chemically determined. The results are provided in Figure 4. The conversion at 750°C increased with increasing Fe or Ca content, and the correlation was stronger with the Fe. When Fe or Ca cations were externally added to brown coals, followed by carbonization, the Fe is much more effective for NH_3 decomposition than the Ca. It is thus likely that the inherent Fe in char plays more crucial role in this reaction than the Ca.

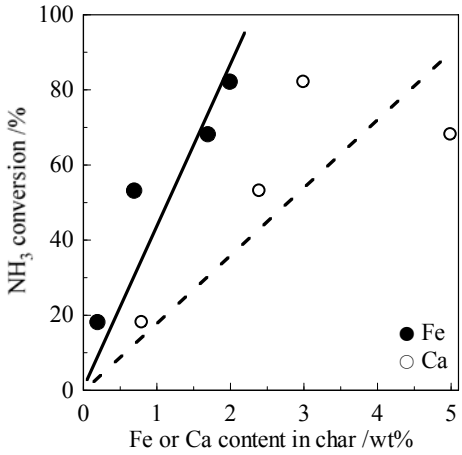

Figure 4. Relationship between the content of inherent Fe or Ca in char between NH_3 conversion at 750°C.

It has been proposed that NH_3 decomposition with Fe catalysts supported on brown coal chars proceeds through a following cycle mechanism involving α-Fe and the nitride species.[2)]

$$8Fe + 2NH_3 \rightarrow 2Fe_4N + 3H_2 \quad (1)$$
$$2Fe_4N \rightarrow 8Fe + N_2 \quad (2)$$

Thus, the inherent Fe in char can also promote NH_3 decomposition via the same mechanism as above. Although the XRD peaks of Fe_4N could not be detected in RB char after reaction, the TPD measurements revealed that, when the used char was quenched to room temperature and then heated in a stream of high purity He, the formation of N_2 started around 600°C, suggesting the decomposition of the nitride species to N_2.

With Ca species after reaction, very weak diffraction lines of $CaCN_2$ appeared in RB and AB chars. This species was also observed after NH_3 decomposition with Ca catalyst added. The $CaCN_2$ may be formed according to the following equation:

$$CaO + 2C + 2NH_3 \rightarrow CaCN_2 + 3H_2 + CO \quad (3)$$

Since the standard free energy changes are estimated to – 27 kJ/mol, eq. (3) is thermodynamically favorable. The TPD measurements showed that the decomposition of $CaCN_2$ to N_2 occurred at higher temperatures of > 700°C than observed for Fe_4N. These results suggest that the Ca-catalyzed NH_3 decomposition proceeds via the mechanism involving $CaCN_2$.

When a simulated gas including H_2, CO, and CO_2 as well as 2000 ppm NH_3 was used in place of NH_3 diluted with He alone, the initial activity of RB char was low, but, in contrast to the profile observed in Figure 1, NH_3 conversion increased with increasing time on stream and was finally comparable to that in Figure 1. To make clear the catalytic effectiveness of coal chars in the coexistence of a large concentration of syngas should be the subject of future study.

Conclusions

Some chars prepared from low rank coals work efficiently as the catalysts for decomposition at 750°C of 2000 ppm NH_3 diluted with He. The presence of fine particles of metallic Fe and CaO, formed from Fe and Ca ions naturally present in low rank coals, accounts for such catalytic performances. There is a stronger correlation between NH_3 conversion to N_2 and Fe content in char. The char with the largest content of 2 wt% Fe shows the stable activity during 25 h reaction and achieves complete decomposition of NH_3 at 850°C. It is likely that the catalytic decomposition proceeds through the mechanisms involving Fe_4N and $CaCN_2$ as intermediate species.

Acknowledgement. The present work was supported by a Grant-in-Aid for Scientific Research on Priority Areas (B) from the Ministry of Education, Science, Sports, and Culture, Japan (No. 11218202). One of the authors (CX) gratefully acknowledges Japan Society for the Promotion of Science for the Postdoctoral Fellowship.

References

(1) Mitchell, S.C.. In *Hot Gas Cleanup of Sulfur, Nitrogen, Minor and Trace Elements*; IEA Coal Research, London, 1998.
(2) Ohtsuka, Y.; Xu, C.; Kong, D.; Tsubouchi, N. Prepr. Pap. - *Am. Chem. Soc., Div. Fuel Chem.*, **2001**, *46*, 152.
(3) Wu, Z.; Ohtsuka, Y. *Energy Fuels* **1997**, *11*, 902-908.

EFFECT OF IRON AND CALCIUM COMPOUNDS ON NO EMISSION DURING COAL COMBUSTION

Rengui Guan, Wen Li, Haokan Chen and Baoqing Li

State Key Lab of Coal Conversion, Institute of Coal Chemistry, Chinese Academy of Sciences, Taiyuan, 030001, China

Introduction

Millions tons of NO_x are released into atmosphere per year by the coal-fired power stations, which causes serious environmental pollution. During coal combustion, the major proportion of NO_x is NO which can be formed by three ways: thermal NO, prompt NO and formation from fuel-bound nitrogen (Fuel-N) [1]. Not all the Fuel-N thoroughly turned into NO and the conversion rate is dependent on the combustion conditions. Fuel-N partly turns into NO through two possible processes: oxidation of volatile and oxidation of char. The later was the main source of NO. The formed NO can be reduced by reductive agents such as CO, char etc. The ultimate NO emission concentration is determined by the competitive results of oxidation of fuel-N and reduction of the formed NO.

Minerals in coal affect many coal utilization processes. They also have evident influence on both formation and reduction of NO, which play an important role in NO emission [2]. Calcium and iron, the highly active components in minerals, are paid more attention during coal combustion. Calcium-based compounds are widely used as SO_2 retention agents for their high efficiency and low cost, which are found to be responsible for higher NO emission in fluidized bed combustion. On the other hand, calcium compounds under reductive atmosphere catalytically accelerate NO reduction reactions as well. The impregnated iron is well known as an effective NO reduction catalyst, while the high content iron in mineral matters does not show high catalytic reactivity. It is important to obtain further understanding of their effects on NO emission in order to reduce the NO pollution, which is the aim of this study.

Experimental

Coal samples. Neimeng bituminous coal (abbreviated as NM) was used in this study. In order to exclude the influence of inherent minerals in coal, NM (60-100mesh) was deeply demineralized by HF and HCl. The mineral-free sample was further depyrited by newly formed $CrCl_2$. The treated sample was dried in vacuum and denoted as NMDM. **Table 1** was the property of NMDM. To clarify the effects of iron and calcium compounds on NO emission during coal combustion, calcium compounds including CaO, $Ca(OH)_2$, $CaCO_3$, $CaSO_4$ and $Ca(CH_3COO)_2$, and iron compounds including $FeCl_2$, $FeCl_3$, $FeSO_2$ and $Fe_2(SO_4)_3$ were introduced to NMDM by mechanic mixing. The introduced compounds are all chemical agents. The ratio of each additive was 2% wt in coal.

Table 1. Characteristics of NMDM (wt%)

Ash (ad)	0.5	N (daf)	0.95
Water (ad)	0.4	S (daf)	0.21
C (daf)	76.53	O^* (daf)	17.74
H (daf)	4.57		

O^*: by difference

Procedure. The combustion experiments of samples were performed in a fixed-bed quartz reactor. 0.0500g samples were combusted in Ar mixed with 5.3% O_2 at heating rate of 10K/min. The gas flow rate was 325ml/min. NO, CO and O_2 in the flue gas were determined on line by Gas Analyzer (Kane-May 9106).

Results and Discussion

Emission profiles of NO and CO. During coal combustion, carbon was firstly oxidized to form CO which was further oxidized to CO_2. The total concentration of CO and CO_2 represented the rate of coal oxidation. We did not measure the CO_2 for the limitation of the Gas Analyzer, hence the exact rate of coal combustion could not be known, but we could gain a general idea by analyzing the concentration of O_2 and CO. **Figure 1** shows the emission profiles of NO, CO and O_2. It was clearly seen that there were a major peak of O_2 reduction at nearly 600^0C and a shoulder peak at about 450^0C. The shoulder peak resulted from the combustion of volatile, and the main peak was due to the combustion of char. The peak temperature for CO formation is at around 500^0C, which is mainly due to the oxidation of volatile matters. After that, with rising the temperature the oxidation of CO accelerated, at the same time the oxidation of char to form CO became difficult because of the bad reactivity of char compare to that of volatile matters, the CO concentration was decreased and formed a shoulder peak at about 550^0C.

Very little NO was formed during volatile oxidation. After 500^0C, the NO concentration increased linearly upto 650^0C, then decreased sharply. The peak temperature of NO emission was nearly 50^0C higher than that of O_2 consumption, which indicated that the combustion reactivity of nitrogen was lower than that of carbon as a whole. John also observed the peak temperature of NO formation is higher than that of CO_2 [3].

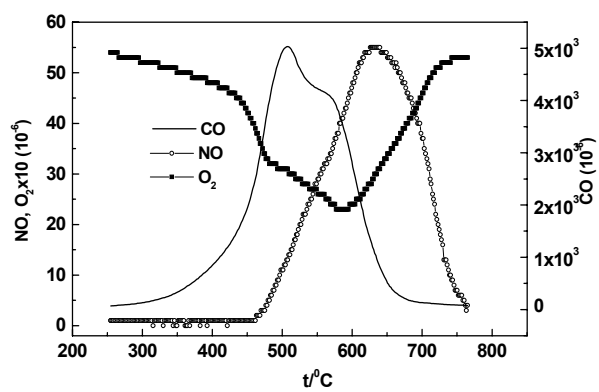

Figure 1. The emission profiles of NO, CO and O_2 during combustion of NMDM coal.

Effects of iron and calcium compounds. The iron compounds were widely used catalysts during coal gasification and combustion. They could accelerate both the formation and oxidation of CO. There are also many researches focused on their catalytic NO reduction under reduced atmosphere and catalytic NO formation under oxidation atmosphere [1]. It was well known that the added iron showed high catalytic activity under CO or other reductive atmosphere, but the inherent iron in minerals of coal showed much low catalytic effect [4], which suggested that the existing form of iron was very important for its catalytic activity.

CO emission profile during combustion of samples added with iron compounds was shown in **Figure 2.** Under our combustion conditions, the O_2 was superfluous to coal, hence the added iron compounds showed much catalytic activity of further oxidation of CO. Although the emission profile of CO was different with the different iron compounds added, especially in the second peaks, the total amount of CO emission was all decreased compared with that of

iron-free sample. It was also found that the peak temperature of CO emission of samples added with iron compounds moved to low range, which was due to catalytic effects of iron compounds on combustion of volatile and char.

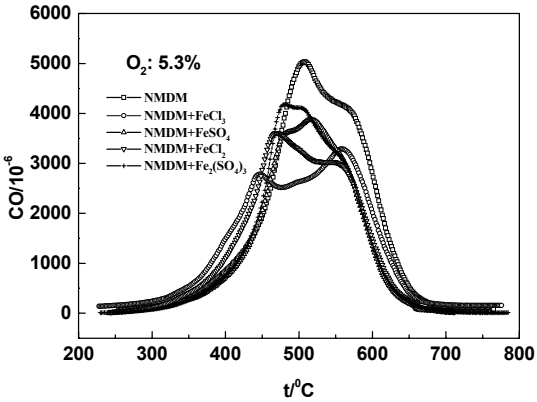

Figure 2. Emission profiles of CO during combustion of samples with and without iron compounds.

Figure 3 was the NO emission profiles during combustion of samples added with iron compounds. The added iron compounds catalyzed the combustion of carbon, and exposed the fuel-N to O_2, which resulted in decrease in both the peak temperature and the amount of NO evolution. This is believed to be due to the fact that iron compounds catalyzed the NO reduction by CO and char surface [5]. Although the iron compounds were different from each other, they showed the same catalytic tendency. This might infer that the added iron compounds turned into the same form (maybe FeO) during coal combustion.

Figure 4 compared the NO emission during combustion of different Ca-added samples. The calcium compounds showed the similar catalytic effects on both CO and NO emission with iron compounds. As a whole, the added calcium compounds decreased the NO emission [6].

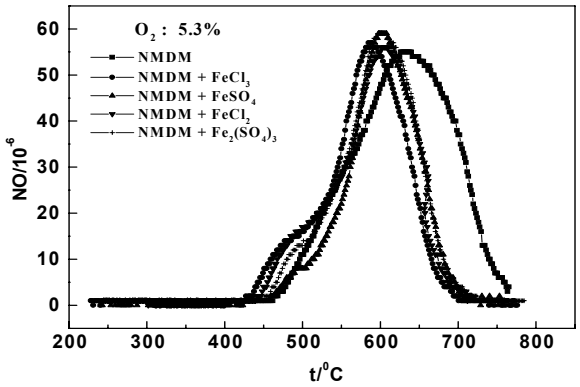

Figure 3. Emission profiles of NO during combustion of samples with and without iron compounds.

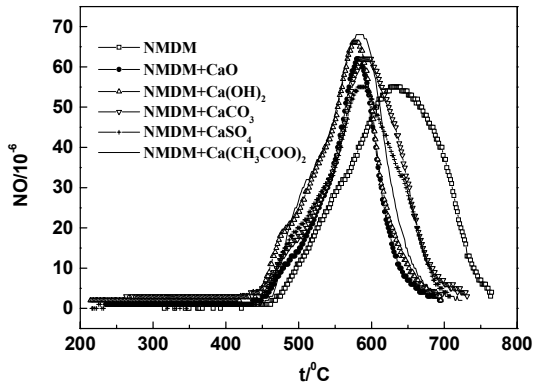

Figure 4. Comparative of NO emission during samples combustion added with calcium compounds.

Table 2 was the NO conversion during combustion of different samples under **5.3%** O_2 concentration. It was found that iron compounds had higher catalytic activity in reducing NO emission than calcium compounds. This difference of catalytic reactivity between two kinds of compounds probably was due to their ability to form active intermediates and to provide active sites.

Table 2 NO Conversion for Different samples

Sample	NO conversion
NMDM	37.77
NMDM+$FeCl_3$	28.23
NMDM+$FeSO_4$	26.39
NMDM+$FeCl_3$	28.75
NMDM+$Fe_2(SO_4)_3$	29.72
NMDM+CaO	33.62
NMDM+$Ca(OH)_2$	30.61
NMDM+$CaCO_3$	34.19
NMDM+$CaSO_4$	29.86
NMDM+$Ca(CH_3COO)_2$	32.20

Acknowledgment

This work was subsidized by the Special Funds for Major State Basic Research projects (G1999022102).

Reference:

(1) Johnsson, J. E. Fuel, **1994**, 73(9), 1398.
(2) Ralf, F. W. K.; Sven, H. Fuel, **1997**, 76(4), 345.
(3) John, C. C.; Thomas, K. M.; Marsh, H. Fuel, **1993**, 72, 349.
(4) Ana, I. G. A.; Thomas, K. M. Fuel, **1994**, 73(5), 635.
(5) Illan-Gomez, M. J.;Linares-Solano, A.; Salinas-Martinez de Lecea, C. Energy and Fuel, **1995**, 9, 540.
(6) Illan-Gomez, M. J.;Linares-Solano, A.; Salinas-Martinez de Lecea, C. Energy and Fuel, **1995**, 9, 976.

Simultaneous reduction of NOx and N_2O emissions from a bubbling fluidized bed coal combustor using alternative bed material

Tadaaki Shimizu,Jun Asazuma, Masayuki Shinkai, Sayako Matsunaga, Kazuaki Yamagiwa, Naoki Fujiwara***

*: corresponding author, Department of Chemistry and Chemical Engineering, Niigata University, 2-8050 Ikarashi, Niigata, 950-2181, Japan
**: Idemitsu Kosan Co. Ltd

Introduction

Fluidized combustion has been developed as a coal combustion technology that can capture SO_2 by limestone feed without external wet scrubbing system. The temperature in the bed is usually maintained at approximately 1123 K so that SO_2 capture efficiency can be maximized. However, such low temperature is not advantageous for reduction of N_2O emission, which is known to be a greenhouse effect.

One approach to reduce N_2O emission is the use of catalyst as bed material to decompose N_2O. However, the use of catalysts has been reported to increase NOx emission; red-mud (Fe-containing solid)[1], γ-alumina[1], Fe_2O_3[2], and MgO[3] have been tested but the increase in NOx with decreasing N_2O was reported. Limestone is also well known as a catalyst of N_2O decomposition but it also increases NOx emission.[2,4,5,6,7] The increase in NOx during limestone feed is attributable to catalytic activity of limestone for NOx formation through oxidation of NH_3 and HCN, both of which are released from coal during devolatilization.[7,8,9] Thus the increase in NOx with other catalytic bed materials is considered to be attributable to the oxidation of volatile-N by the catalyst.

Recently, Liu and Gibbs[10] reported that a kind of alumina decreased N_2O emission without increase in NOx during char combustion in a bench-scale BFBC. However, it is possible that their results are limited only for char combustion, where contribution of volatile-N to NOx and N_2O emissions is less pronounced than that during coal combustion. A catalyst which reduces N_2O without increasing NOx during coal combustion has not yet been found.

In the present study, two kinds of porous alumina particles were tested as bed materials during bubbling fluidized bed combustion of four kinds of coal. The emissions of NOx and N_2O were compared with those during combustion in the inert sand bed.

Experimental

A bench-scale BFBC of 1.3 m in height and 5.4 cm in inner diameter was employed. The reactor was heated by electric heaters and the temperature in the bed and the freeboard was maintained at 1123 K. Primary air was fed through the distributor at the bottom of the bed. Secondary air was not injected. The superficial gas velocity was 20 cm/s at 1123 K.

Two kinds of porous alumina particles, MS-1B (Mizusawa Industrial Chemicals Ltd.) and activated bauxite (Engelhard Co. Ltd.) were used as alternative bed materials, the analysis of which is shown in Table 1. Non-porous quartz sand (QS), which is known to be inert for the reactions of NOx and N_2O, was used as control. The minimum fluidizing velocity (U_{mf}) of each porous particle was nearly the same as that of the sand. The static bed height was 10 cm.

Four kinds of coals with different volatile matter content, from high volatile bituminous coals (HVB1 and HVB2), medium volatile bituminous coal (MVB) to semi-anthracite (SA), were employed as fuels. The analyses of the fuels are shown in Table 2. The size of the fuel was between 0.3 and 1.0 mm. The fuel was continuously fed through a vibration feeder, conveyed pneumatically in air stream, and then injected into the bottom of the bed about 1 cm above the distributor. The feed rate of coal was controlled so that the desired O_2 concentration in the flue gas was attained.

Concentrations of O_2, total NOx (=NO+NO_2), CO_2, and CO in the flue gas were continuously measured by a magnetic oxygen analyzer for O_2, a chemical luminescence analyzer for NOx, and NDIR adsorption analyzers for CO_2 and CO, respectively. A portion of the dried sample gas was stored in Tedler (R) gas bags. Concentration of N_2O in the gas was measured by gas chromatography with a thermal conductivity detector.

Table 1. Composition, Size, and Surface Area of Bed Materials

Composition [wt-%]	MS-1B (MS) 0.39mm	Activated Bauxite (AB) 0.40mm	Quartz sand (QS) 0.27 mm
Al_2O_3	84.7	69.4	-
SiO_2	2.2	7.2	100
MgO	0.0	0.0	-
CaO	0.8	0.3	-
TiO_2	1.1	13.0	-
Fe_2O_3	5.8	8.4	-
SO_3	3.8	0.8	-
Others	1.6	0.9	-
Surface area [m^2/g]	195	124	Non-porous

Table 2 Analyses of Coals

	Ultimate analysis (daf, wt%)					Proximate analysis(dry, wt%)		
Fuel	C	H	O[a]	N	S[b]	V.M.[c]	F.C.[d]	Ash
HVB1	80.1	6.1	11.7	1.5	0.6	38.3	47.5	14.2
HVB2	78.1	6.3	13.4	1.3	1.0	41.4	43.5	15.1
MVB	85.9	4.9	7.0	1.7	0.5	27.0	57.7	15.4
SA	89.7	4.2	3.6	1.9	0.7	15.9	72.3	11.2

a: by diff.; *b*: combustible S; c: Volatile matter; *d*: Fixed carbon

Results and Discussion

Figure 1 shows the effect of bed material and flue gas oxygen concentration on emissions of NOx and N_2O. Both alumina particles (MS and AB) employed for the present work were effective for N_2O reduction in comparison to the sand bed. This is attributable to the catalytic activity of present alumina particles to decompose N_2O.

However the role of bed material to NOx emission was different between MS and BA; MS bed material reduced NOx emission whereas BA increased it. At this moment, the mechanism of the difference in NOx emission between the two bed materials is not clear. One possibility is that the selectivity of volatile-N to NOx is different between two particles. In the following part, the results obtained by use of MS bed material will be shown since AB was not effective to the reduce NOx.

In Figure 1, the effect of oxygen concentration on emissions of N_2O and NOx is also shown. For the sand bed, both N_2O and NOx emissions increased with increasing flue gas O_2 concentration. The sensitivity of N_2O and NOx emissions to flue gas O_2 concentration was weak for the MS bed. This is advantageous not only for suppression of NOx and N_2O emissions but also suppression of SO_2 emission. SO_2 capture by limestone is known to be inhibited by reduction of O_2/fuel ratio since the low O_2 atmosphere or reducing gases such as CO reduce SO_2 capture rate by CaO or enhance decomposition of $CaSO_4$ to CaO and SO_2.[11,12] Thus operation with higher O_2/fuel ratio is preferred for SO_2 reduction but it increases NOx and N_2O emissions for the conventional bed material. The

present bed material (MS) is considered to enable operation at higher O_2/fuel ratio without increasing NOx and N_2O emissions.

Figure 2 shows the effect of fuel type on conversions of fuel bound nitrogen (fuel-N) to N_2O and NOx. For all the fuels tested, the present MS bed material reduced N_2O emission without increasing NOx emission. But its effect was different among fuels. The reduction of N_2O by MS was more remarkable for fuels with lower fixed carbon content. On the other hand, the reduction of NOx by MS was more effective for higher fixed carbon content fuel.

The present results were obtained using a small-scale reactor and it is necessary to discuss if the present results are applicable to large-scale FBCs. Under the present condition, the static bed height (H_S) was 10 cm and the superficial gas velocity (U_0) was 20 cm/s and the contact time, H_S/U_0, was 0.5 s. In large-scale BFBCs, the static bed height and the superficial gas velocity are approximately 1 m and 1 m/s, respectively, and the contact time in the large BFBCs is approximately 1 s. Therefore the contact between gas and solid in the large-scale BFBCs is sufficient and the suppression of N_2O and NOx emissions by the present MS bed material is expected to occur in the large-scale plant.

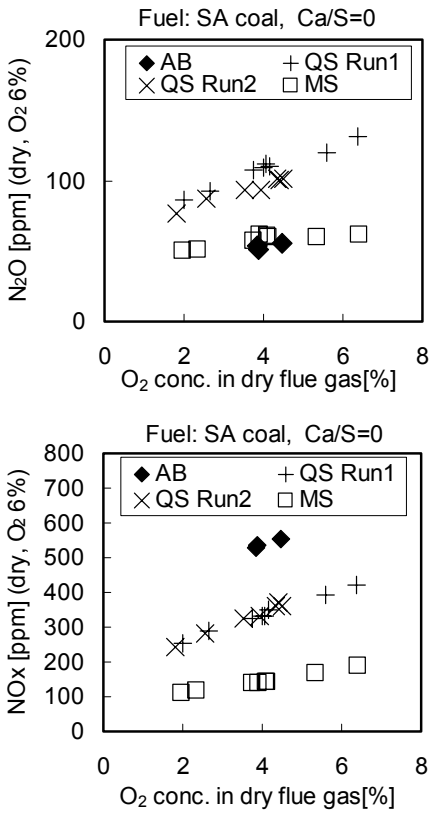

Figure 1. Effect of bed material and O_2 concentration in the flue gas on N_2O and NOx emissions during semi-anthracite combustion.

Conclusion

The present work found one kind of porous alumina particle which was effective not only for N_2O reduction but also suppression of NOx emission during coal combustion in a bubbling fluidized bed.

Acknowledgement. T.Shmizu express his thanks to the T. Shimizu thanks The Ministry of Education, Culture, Sports, Science and Technology for Grant-in-Aids (No.11218204).

References

1. Hirama, T., Hosoda, H. Moritomi, H., Suzuki, Y., Harada, M., Shimizu, T., Naruse, I., *Nihon-Energy-Gakkai-Shi (J. Jpn. Inst. Energy)*, **1993**, *72*, 252-262
2. Shimizu, T., Togashi, T., Miura, M., Karahasi, E., Yamaguchi, T., Tonsyo, M., Inagaki, M., *Proc.6th Int. Workshop on N_2O Emissions (Turku, Finland, 1994)*, **1994**, 115
3. Klein, M., Rotzoll, G., *Proc.6th Int. Workshop on N_2O Emissions (Turku, Finland, 1994)*, **1994**, 239
4. Gavin, D.G. and Dorrington, M. A., *Proc. 1991 International Conference on Coal Science, (Newcastle, UK)*, Ed. by International Energy Agency Coal Research Ltd., Butterworth-Heinemann, Oxford, UK, **1991**, 347
5. Åmand L-E., B. Leckner, S. Andersson and L. Gustavsson, *European workshop on N_2O emissions LNETI/EPA/IFP (Lisbon, Portugal)*, **1990**, 171
6. Moritomi H., Y. Suzuki, N. Kido and Y. Ogisu, P*roceedings of 1lth International Conference on Fluidized Bed Combustion (Montreal, Canada)*, ASME, New York, **1991**, 1005
7. Shimizu, T., Tachiyama, Y., Fujita, D., Kumazawa, K., Wakayama, O., Ishizu, K., Kobayashi, S., Shikada, S., Inagaki, M., *Energy & Fuels*, **1992**, *6*, 753
8. Hirama, T., Kochiyama, Y., Chiba, T., Kobayashi, H. *Nenryo-Kyokai-Shi (J. Fuel Soc. Japan)*, **1982**, *61*, 268
9. Furusawa, T., Tsujimura, M., Yasunaga, K., Kojima, T. *Proc. 8th International Conference on Fluidized Bed Combustion (Houston, USA)*, DOE/METC-85/6021, U.S. Department of Energy, Office of Fossil Energy, Morgantown, West Virginia, U.S.A., **1985**, 1095
10. Liu, H., Gibbs, B.M., *Proc. 15th Int. Conf. on Fluidized Bed Combustion* (Savannah, GA, USA), ASME, **1999**, Paper No. FBC99-0114
11. Kojima, T., Take, K, Furusawa, T. and Kunii, D. *J. Chem. Eng. Japan*, **1985**, *18,* 432
12 Hansen, P.F.B.; Dam-Johansen, K.; Bank, L.H.; Ostergaard, K., *Proc. 11th International Conference on Fluidized Bed Combustion* (Montreal, Canada), ASME: New York, **1991**; 73

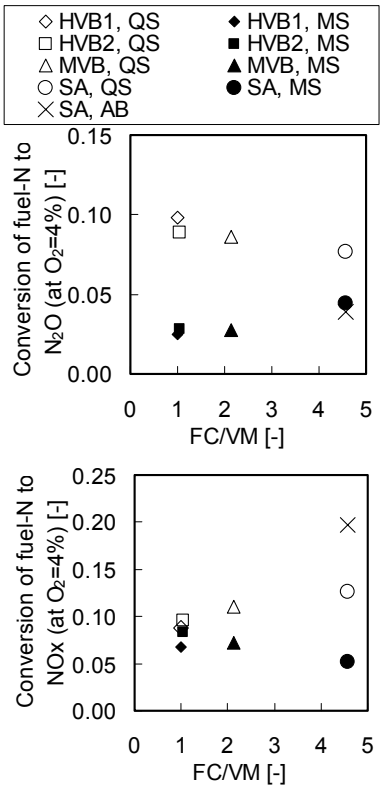

Figure 2. Effect of coal type on conversions of fuel-N to N_2O and NOx at flue gas O_2 concentration of 4.0%

CONTINUOUS REMOVAL OF NO_2 INTO HNO_3 BY PITCH AND PAN BASED ACTIVATED CARBON FIBER

Takashi Enjoji[a], Noriaki Shirahama[a], Seoung-Ho Yoon[a], Yozo Korai[a], Isao Mochida[a], Akinori Yasutake[b], Masaaki Yoshikawa[c] and Takaaki Shimohara[d]

a) Institute of Advanced Material Study, Kyushu University
6-1 Kasugakoen, Kasuga, Fukuoka 816-8580, JAPAN
b) Mitsubishi Heavy Industries Ltd., 5-717-1 Fukahori
Nagasaki 851-0392, JAPAN
c) Osaka Gas Co. Ltd., Torishima, Konohana
Osaka 554-0051, JAPAN
d)Fukuoka Institute of Health and Environmental
39 Mukaizano, Dazaifu, Fukuoka 818-0135, JAPAN

Introduction

SO_2 removal by wet scrubbing after NO selective reduction over V_2O/TiO_2 honeycomb has been established in the power plant to protect atmospheric environment. Nevertheless more efficient and deeper reduction of NOx is still wanted. NOx of very low concentration leaked to the environment causes photochemical smog and acid rain, NOx must be removed from environmental air. Exhausted NO from automobile and boiler is oxidized in atmosphere gradually into NO_2. The most harmful species of the NOx in atmosphere is NO_2. The 20ppm of NOx is detected at busy cross-section. Reduction of low concentration NO_2 in atmosphere can be one of direct caution for the environmental protection.

The present authors reported that pitch based activated carbon fiber(ACF) was very effective to remove SO_2 completely at 30℃ in the flue gas(1000ppm SO_2, 5vol.% O_2, 10vol.%H_2O).[1,2] Pitch based ACF was calcined in argon gas at 1100℃ for 1hr to increase its activity for SO_2 removal. PAN-ACF showed the high activity of adsorption and oxidation of NO_2 with oxygen at ambient temperatures when the fiber was also calcined in argon gas as an inert gas at 800℃ for 1hr.[3]

In the present study, NOx of 20ppm in air was attempted to be fixed as HNO_3, which was continuously recovered from the ACF bed. The pitch based ACF was calcined at 400～1100℃ to increase activity. Influence of humidity in air was studied to simulate real atmosphere.

Experimental

Pitch-based ACF(OG20A) and polyacrylonitrile-based ACF(FE300) were manufactured and supplied by Osaka Gas Co. and Toho Tenax Co., respectively. The ACF was further heat-treated in argon gas at 400～1100℃. The oxidation and hydration of 20ppm NO_2 with O_2 were carried out in dry and wet air using a flow type glass reactor (8mm diameter). 0.1～0.5g of ACF was closely packed in the reactor. The total flow rate(F) and the contact time(W/F) were 300 ml/min and 3.3×10^{-4}～1.7×10^{-3}g·min/ml, respectively. NO_2 and NO concentrations were analyzed continuously at the inlet and outlet of the reactor, using a NO_X meter (ECL-77, Yanagimoto Co., Kyoto). Stationary NO_2 conversion was determined when NO_2 concentration at the outlet of the reactor became stationary. Adsorption and oxidation of NO_2 appeared to continue for several hours after the reaction started.

Results and Discussion

Effect of heat-treatment temperature of ACFs

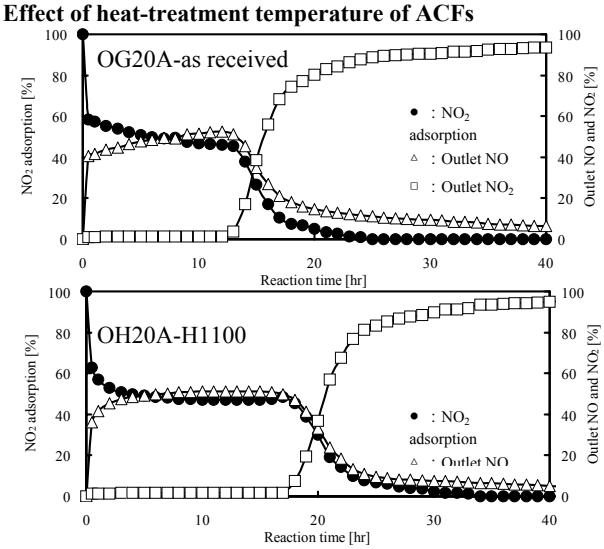

Figure 1. Profiles of NO_2 oxidation over Pitch-ACF OG20A and its heat-treatment in dry.
ACF：0.1g, NO_2：20ppm, O_2：21%, Flow rate：300ml/min
Relative humidity：0%, Reaction temperature：30℃

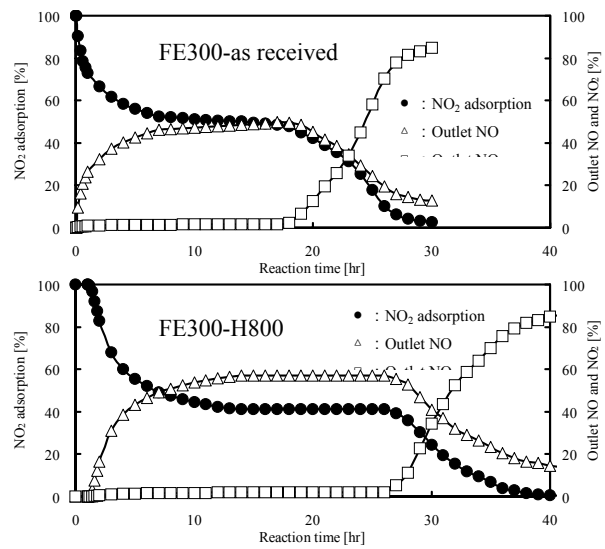

Figure 2. Profiles of NO_2 oxidation over PAN-ACF FE300 and its heat-treatment in dry.
ACF：0.1g, NO_2：20ppm, O_2：21%, Flow rate：300ml/min
Relative humidity：0%, Reaction temperature：30℃

Figure 1 illustrates reactivity of 20ppm NO_2 in dry air at 30℃ over as-received and heat-treated OG20As. NO_2 was converted to give NO in a gaseous product over OG20A series. NO_2 concentration at the outlet continued zero for 13hrs while 50% of NO_2 appeared to give NO. The some amount of NO_2 must be adsorbed on the ACF probably in form of NO_3. Hence 2 molecules of NO_2 in dry air were found to be dispropotionated into NO and adsorbed NO_3 over pitch based ACF. Outlet NO concentration decreased shapes to 20% by 17hrs with an increase of outlet NO_2 concentration. After 17hrs, the outlet NO concentration decreased very slowly to be 5% by 40hrs, while no NO_2 adsorption was found.

Thus, NO_2 disproportionation continued for 23hrs. No apparent oxidation of NO_2 was observed under the condition.

Disproportionation increased with an increase of calcination temperature of ACF up to 1100℃. OG20A-H1100 continued the disproportionation for 32hrs, while the conversion of NO_2 gradually decreased to be zero, although the period of balanced NO_2 adsorption and NO outlet continued for 22hrs.

Figure 2 illustrates the reactivity of 20ppm NO_2 in dry air over as-received and heat-treated PAN-FE300 at 30℃. Over as-received FE300, outlet of NO was observed immediately when the gas started to flow. The outlet concentrations of NO and NO_2 were equivalent through disproportionation after 10hrs. The calcination of the ACF enhanced disproportionation. FE300-H800 showed the highest activity among PAN-FE300s, continuing stationary disproportionation reaction for 26hrs. The conversion of NO_2 started gradual decrease to be zero after 40hrs. Further higher calcination temperature shortened period of NO_2 adsorption and disproportionation.

Effect of humidity on NO_2 reaction in air

Figure 3 shows reactivity of 20ppm NO_2 in wet air over OG20A-H1100, varying relative humidity in the range of 0～100%. Humid air extended the period of disproportionation, its conversion to decreasing 20% by 70hrs, which appeared to continue stationary. Thus the wet air hydrates adsorbed NO_3 into aq.HNO_3 which flowed out from the bed to regenerate continuously active site of NO_3 adsorption.

Figure 4 shows reactivity of 20ppm NO_2 over PAN-FE300-H800 by varying relative humidity in the range of 0～100%. Wet air continued the removal of NO_2 at least for 60hrs while the disproportionation and oxidation reactions continued although the conversion decreased. It was found that formed HNO_3 over ACF was drained from the reactor to regenerate the active site.

Conclusions

Reactivity of 20ppm NO_2 in air was studied at 30℃ over pitch based activated carbon fiber (OG20A) and polyacrilonitrile based activated carbon fiber (FE300) by varying the calcinations temperature of ACF as well as relative humidity in the reaction gas to find the continuous removal of NO_2 in atmosphere in form of HNO_3. The calcination of ACF at a temperature up to 800～1100℃ in inert atmosphere increased significantly adsorption and oxidation of NO_2 as observed for continuous removal of SO_2 into H_2SO_4 over the some ACFs. The OG20A and FE300 ACFs were calcined at 800℃ and 1100℃ to enhance its activity. NO_2 in dry air was found to be disproportionated into NO and adsorbed NO_3 over as-received and calcined ACF. NO_2 was oxidized and disproportionated into NO_3 to be absorbed over the ACF, the latter reaction producing also NO. The disproportionation reaction was terminated by the saturation of NO_3 adsorption over ACF. Oxygen in air enhanced the oxidation of NO_2 into adsorbed NO_3, reducing NO formation through the disproportionation. The same amount of adsorbed NO_3 terminated the both oxidation and disproportionation regardless of O_2 contents.

The humidity prolonged both oxidation and disproportionation reactions, before the breakthrough of NO_2 allowing stationary NO_2 removal in form of aq.HNO_3 at the release of some NO. Higher humidity increased the stationary NO_2 removal by eluting out adsorbed NO_3 in aq.HNO_3. Higher humidity increased the NO_2 removal adsorbed NO_3 to regenerate the active site. It must be noted that the oxidation of NO_2 was limited on pitch based ACF. Large amount of PAN ACF extended the period of complete NO_2 removal and increased stationary NO_2 removal rate in air with less NO formation. Pitch based ACF appeared to promote disproportionation more than oxidation.

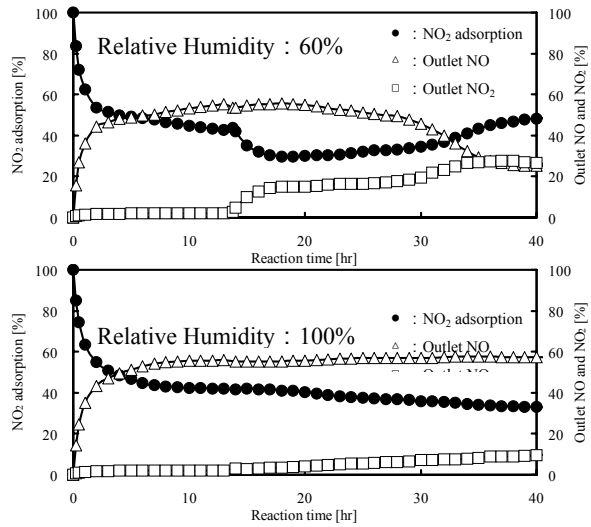

Figure 3. Reactivity of NO_2 over Pitch-ACF OG20A-H1100 at variable humidity.
ACF：0.1g, NO_2：20ppm, O_2：21%, Flow rate：300ml/min
Relative humidity：60%,100%, Reaction temperature：30℃

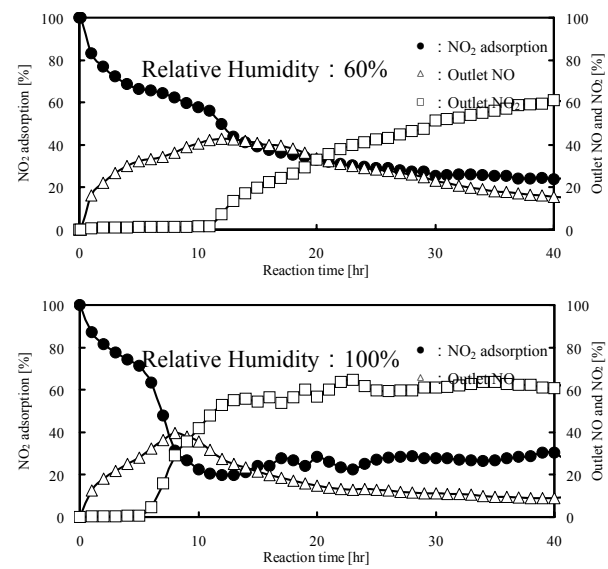

Figure 4. Reactivity of NO_2 over PAN-ACF FE300-H800 at variable humidity.
ACF：0.1g, NO_2：20ppm, O_2：21%, Flow rate：300ml/min
Relative humidity：60%,100%, Reaction temperature：30℃

References

1. Mochida, I.; Kuroda, K.; Miyamoto, S.; Sotowa, C.; Korai, Y.; Kawano, S.; Sakanishi, K.; Yasutake, A.; and Yoshikawa, M. *Energy & Fuels*, **1997**, 11, 272.
2. Mochida, I.; Miyamoto, S.; Kuroda, K.; Kawano, S.; Sakanishi, K.; and Korai, Y. *Energy & Fuels*, **1999**, 13, 374
3. Mochida, I.; Kawano, S.; Hironaka, M.; Yatsunami, S,; Korai, Y.; Matsumura, Y.; and Yoshikawa, M. *Energy & Fuels*, **1995**, 9, 659

Reduction of NOx by Activated Lignite Char

H. Gupta[1], S. A. Benson[1], L. –S. Fan[2], J.D. Laumb[1], E. S. Olson[1], C. R. Crocker[1], R. K. Sharma[1]

[1]Energy and Environmental Research Center, 15 North 23rd Street, Grand Forks, ND 58203
[2]Department of Chemical Engineering, The Ohio State University, Columbus OH 43210

Introduction

Nitric oxide (NO) adsorbs physically and reversibly on graphite below ambient temperature.[1] It was observed that the extent of physisorption on a thermally pretreated activated carbon surface reduces with increasing sorption temperature in the 25-215 ^oC temperature range.[2] However, Teng and Suuberg observed that the contribution of chemisorption of NO on a thermally cleaned phenol-formaldehyde derived char increases with temperature in the 50-150 ^oC temperature range.[3] Physisorption of NO leads to the formation of C(NO) type surface species that emit NO molecules upon thermal desorption. In contrast, chemisorption of NO occurs by the dissociation of NO molecules to form C(N), C(O), and $C(O_2)$ type surface.[4] Oxygen from the NO molecules form relatively stable surface complexes while nitrogen atoms from NO molecules pair up and exit the reaction system as nitrogen molecules.[5] Saturation of the carbon surface prevents further interaction between NO molecules and carbon due to the non-availability of free carbon sites. Further increase in reaction temperature beyond 600-700 ^oC leads to the breakdown of surface complexes releasing CO and CO_2 from the surface and creating new carbon sites that sustain carbon-NO reaction. Desorption of chemical complexes, being a thermally activated process, increases with rising temperature. NO reduction is complete when the rate of desorption exceeds the rate of NO entering the carbon bed. This two-step mechanism has gained wide acceptance as the has been widely accepted as the mechanism of the high temperature carbon-NO reaction.[6] The activation energy of the high temperature desorption of complexes (28-59 kcal/mol) was usually much higher than that involved in the low temperature dissociative chemisorption of NO (4.5-19 kcal/mol).[7]

When operated beyond the transition temperature (), sustained NO reduction occurs as the reaction is no longer limited by the desorption of surface complexes according to the reactions below:

$$C + 2NO \rightarrow N_2 + CO_2 \qquad (1)$$
$$2C + 2NO \rightarrow N_2 + 2CO \qquad (2)$$

However, carbon is consumed parasitically by the presence of oxygen that exists in higher concentration and has a higher oxidizing power than NO.[8] At low concentrations of oxygen (0.1-2%), the temperature required for sustained NO reduction decreases due to gasification of carbon by oxygen leading to the creation of active surface sites that in turn react with NO and convert it to nitrogen.[9] In this process a major fraction of carbon is consumed by oxygen and the primary challenge in commercializing this carbon based NO reduction process involves reducing the consumption of carbon by improving the selectivity of the carbon-NO reaction in the face the carbon-oxygen reaction. This study provides an insight into the efficacy of activated lignite char for its reduction of NO as measured by a global parameter for selectivity (mg NO reduced/g carbon) that can be obtained from the integral experiments conducted here.

Experimental Section

Reactor Assembly

An inlet gas mixture of preset concentrations was obtained by from mixing metered flow of helium, NO and oxygen. The gas mixture was preheated and allowed to floe through a bed consisting of 1000 mg of char housed in a stainless steel reactor. The gases exiting from the sorbent bed are analyzed for NOx and oxygen by a host of online gas analyzers. A chemiluminescence NOx analyzer (from The Advanced Pollution Inc., Model 200 AH) provided the on-line measurement of NO concentration. Oxygen was monitored using a Teledyne Model 3000 PA percent oxygen analyzer that generates an electric current as a function of oxygen concentration through its electrochemical galvanic micro fuel cell. Non-dispersive infrared analyzers tracked the online concentrations of CO and CO_2.

Char Synthesis

Samples of lignite coal were obtained from North Dakota, since it is well known that the lignite coal contains a large amount of sodium in it. Its combustion in air in a TGA indicated the presence of 19.8% ash, with the sodium content being about 9% as revealed by ICP-AES analysis. The initial surface area of HSLC was 16 m^2/g. The role of surface area on the selectivity for carbon-NO reaction over the competing carbon-oxygen reaction was studied by conducting experiments on a series of activated lignite char differing in their structural properties. Lignite coal samples were first dried in air and then devolatilized at 750 ^oC in flowing helium for 2 hours. Higher surface area and porosity in HSLC was obtained by controlling the reaction time between HSLC and pure CO_2. 2 g samples of HSLC were placed in a flow through reactor and nitrogen was passed through the system till the furnace brought the bed temperature to 700 ^oC. Then the gas was switched to pure CO_2 and after a preset reaction time, the flow was switched back to nitrogen. The activated HSLC was allowed to cool and analyzed for conversion and morphological properties. Four samples were obtained after an exposure time of 21, 42, 60 and 90 minutes. Conversion of HSLC was obtained by taking a ratio of final and initial weight of char. **Table 1** shows the surface area and pore volumes developed in the char as a function of % burnoff in the lignite coal.

Table 1: Structural properties due to lignite char activation by CO_2.

Reaction time (min)	%burnoff	Surface Area (m2/g)	Pore Volume (cc/g)
0	0	16	0.012
21	12	260	0.13
42	24	333	0.19
60	31	397	0.23
90	44	414	0.25

Results and Discussion

The effect of surface area on the NO reduction in the presence of 2% oxygen is quantified in **Figure 1**. The isothermal reaction data were obtained at 525 ^oC. It can be seen that the extent of NO reduction increases monotonically with the surface area (and its associated porosity). The presence of higher surface area allows greater contact between the gas and solid for the reaction to occur, resulting in lower NO concentration in the outlet. However, an unexpected increase in selectivity (mg NO/g HSLC) was observed

with increasing surface area as shown in **Figure 2**. The selectivity for inactivated HSLC was 81.26 mg NO/g HSLC. The selectivity increased steadily with higher surface area (93.92, 98.30, 101.52, 104.32 mg NO/g HSLC for initial surface area of 260, 332.8, 397, 414.4 m^2/g.). The increase in selectivity with initial surface area can be explained on the following basis. In these experiments, the outlet oxygen concentration remains close to zero almost throughout the hour. Hence, once the oxygen is depleted, higher surface area in the remaining activated HSLC would reduce NO to a higher extent compared to an inactivated HSLC.

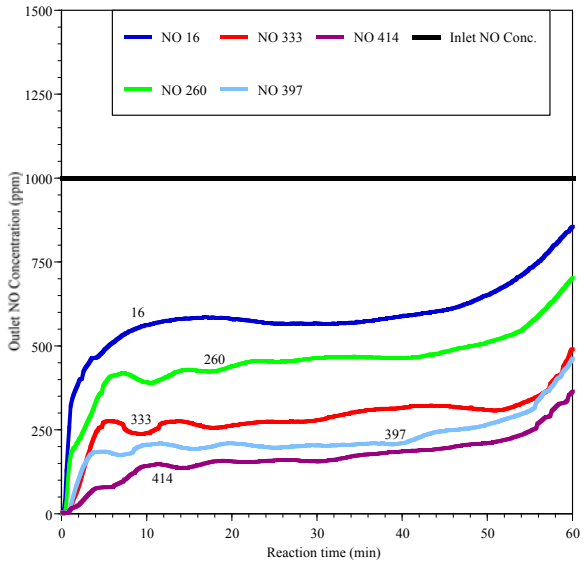

Figure 1. Effect of initial surface area of HSLC on the HSLC-NO reaction [Flow: 1000 ml/min; Inlet NO Conc.: 1000 ppm; Wt. Of Carbon: 1000 mg; Oxygen Conc.: 2.0%]

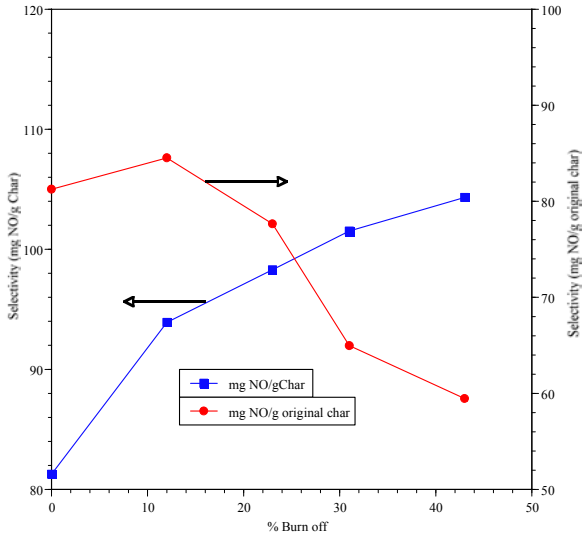

Figure 2. Effect of %burnoff on the selectivity of HSLC-NO reaction based on actual and initial char weight

Data analysis on the effect of surface area on NO reduction revealed that higher initial surface area and porosity led to higher selectivity. However, activation of char also leads to a loss in weight. Hence, the selectivity should also be compared on the basis of similar initial weight of char. Such a comparison is shown in Figure 2. From the data, we can conclude that pore volume of about 0.13 cc/g provided the optimal selectivity with respect to the original char.

Conclusions

From the experimental data we can conclude that higher sodium content leads to enhanced rate of gasification for both the carbon-NO and carbon-oxygen reactions. The lignite char provided higher degrees of activation in the form of higher pore volume and surface area compared to the sub-bituminous char. Although higher initial pore volumes lead to better NO selectivity, 0.13 cc/g pore volume provided the best selectivity among the carbons activated in this study.

Acknowledgement.

The authors acknowledge the financial support provided by the US Department of Energy and North Dakota Industrial Council for co-funding this pilot scale feasibility study.

References

(1) Brown, C. E.; Hall, P. G. Physical Adsorption of Gases on Graphite. *Trans. Farad. Soc.* **1971**, *67*, 3558-3564.

(2) Agnihotri, R.; Chauk, S. S.; Gupta, H.; Jadhav, R. A.; Mahuli, S. K.; Fan, L. -S. Reduction of NOx Emissions using Carbon and/or Carbon containing species. In *Proceedings of the Fifteenth Annual International Pittsburgh Coal Conference: Coal-Energy and the Environment*, Pittsburgh, PA, USA, 14-18 Sep 1998.

(3) Teng, H.; Suuberg, E. M. Chemisorption of Nitric Oxide on Char. 2. Irreversible Carbon Oxide Formation. *Ind. Eng. Chem. Res.* **1993**, *32*, 416-423.

(4) Smith, R. N.; Swinehar N.; Lesnini, D. The Oxidation of Carbon by Nitric Oxide. *J. Phys. Chem.* **1959**, *63*, 544-547.

(5) Mochida, I.; Ogaki, M.; Fujitsu, H.; Komatsubara, Y.; Ida, S. Reduction of nitric oxide with activated PAN fibers. *Fuel* **1985**, *64*, 1054-1057.

(6) Furusawa, T.; Kunii, D.; Oguma, A.; and Yamada, N. Rate of reduction of nitric oxide by char. *International Chemical Engr.* April **1980**, *20(2)*, 239-244.

(7) Aarna, I.; Suuberg, E. A review of the kinetics of the nitric oxide-carbon reaction. *Fuel* **1997**, *76(6)*, 475-491.

(8) Chan, L. K.; Sarofim, A. F.; Beer, J. M. Kinetics of the NO-Carbon Reaction at Fluidized Bed Combustor Conditions. *Combustion and Flame* **1983**, *52*, 37-45.

(9) Suzuki, T.; Kyotani, T.; Tomita, A. Study of the Carbon-Nitric Oxide Reaction in the Presence of Oxygen. *Ind. Eng. Chem. Res.* **1994**, *33*, 2840-2845.

Thermal Behaviors of Dioxines Captured on a Mesophase Pitch Based Active Carbon Fiber.

Keiichi Kuroda [a], Ken-ichi Tobo [a], Nobuaki Matsuoka [a], Yuji Kawabuchi [b], Yozo Korai [c], Isao Mochida [c]

a) Kyushu Environmental Evaluation Asociation
1-10-1 Higashikumatsukadai, Fukuoka, Fukuoka pref
813-0004, JAPAN
b) Kashima Oil Co.,ltd
4 Touwada, Kamisumachi, Kashima, Ibaraki pref
314-0102, JAPAN
c) Institute of Advanced Material Study, Kyushu University
6-1 Kasugakoen, Kasuga, Fukuoka pref 816-8580, JAPAN

Introduction

Dioxines, which are produced in the combustion of organic substances containing chlorine compounds, are now strictly regulated not to be liberated from any combustors. Complete capture at the end of the flue is one of the most reliable technologies, being applicable to any forms of dioxines for their complete removal from the flue even if the control of combustion and post-combustion is recognized effective to reduce the liberation of dioxines at its formation and decomposition. Hence it is the most feasible procedure to achieve no liberation of dioxines to install the active carbon bed in the flue. The problem is how to deal the active carbon, which has captured dioxines.

In the present paper, thermal behaviors of adsorbed dioxines were studied on a particular active carbon fiber produced for a mesophase pitch through KOH activation (MP-ACF). Its very large surface area and high hydrophobicity are recognized to show high capacity for dioxine adsorption. The adsorbed dioxines on the MP-ACF were extracted at their as-adsorbed or heated forms in an inert atmosphere up to 400°C. A series of 10 dioxine species were analyzed by a high resolution GC-MS, which told us their acurate concentrations and some of products through their thermal reactions on the MP-ACF. Such a post-treatment of used ACF allows the conversion of adsorbed dioxines into unharmful forms and its regeneration for the repeated use.

Experimental

1. Dioxines, their adsorption and heattreatment (HT)

A series of ^{13}C-labeled dioxines in acetone listed in Table 1 were used as the standard samples. Their concentrations are also listed in Table 1.

2. Extraction of dioxines and their derivatives adsorbed on MP-ACF and their analysis.

Table 1. The amount of introduced ^{13}C-labeled dioxins (unit:pg)

Compound	Amount of standard	Compound	Amount of standard
^{13}C-2378-TeCDD	1000	^{13}C-2378-TeCDF	1000
^{13}C-12378-PeCDD	1000	^{13}C-12378-PeCDF	1000
^{13}C-123478-HxCDD	1000	^{13}C-123478-HxCDF	1000
^{13}C-1234678-HpCDD	1000	^{13}C-1234678-HpCDF	1000
^{13}C-12346789-OCDD	2000	^{13}C-12346789-OCDF	2000

Results

1. Extraction of Adsorbed Dioxines on MP-ACF

Extracted amounts of Dioxines which have be adsorbed from acetone onto MP-ACF are listed in Table 2 where the experiments (R1~3) were repeated three times to confirm the reproduciality. The amounts were fairly well reproduced at the pg level of analysis, 47~67% of adsorbed species being recovered. Strong adsorption of dioxines is indicated on the ACF. Among dioxines, 123478-Hexa(Hx)CDD, 1234678Hepta(Hp)CDD, and especially 12346789Octa(Oc)CDD were much less extractable, less than 50% of adsorbed species being extracted their strong adsorption being noted on the active carbon fiber. CDDs with chlorine atoms more than 6 appeared less extractable than CDF with the same numbers of chlorines. CDFs were extracted at 53~60% of adsorbed amounts, although more chlorines may increase slightly the extraction.

Table 2. Extracted amounts of Dioxines from MP-ACF wituout HT (unit:pg)

Compound	Amount of standard	R-1	R-2	R-3	Average
^{13}C-2378-TeCDD	1000	810	560	630	670
^{13}C-2378-TeCDF	1000	650	460	480	530
^{13}C-12378-PeCDD	1000	760	520	550	610
^{13}C-12378-PeCDF	1000	720	520	530	590
^{13}C-123478-HxCDD	1000	640	420	420	490
^{13}C-123478-HxCDF	1000	620	470	480	530
^{13}C-1234678-HpCDD	1000	510	380	530	470
^{13}C-1234678-HpCDF	1000	700	490	570	590
^{13}C-12346789-OCDD	2000	720	490	710	640
^{13}C-12346789-OCDF	2000	1300	900	1300	1200

2. Extraction of Adsorbed Dioxines on the ACF After the Heattreatment at 200~400°C for 1~2h.

Table 3 summarizes extracted amount of CDDs and CDFs adsorbed on the ACF after the heattreatment. The heattreatment was performed in the closed bottle to be cooled down to room temperature. Extraction was carried with the ACF and vessel. Hence non-volatile dioxines with chlorine more than 4 must stay in the catalyst on the vessel to be extracted. Such extracted amounts after the heattreatment were compared to those without heattreatment. The heattreatment at 200°C and 300°C for 1h decreased extracted amounts of tetra-, penta-, and hexa-CDDs and CDFs whereas it did not change or even increased the amounts of hepta- and octa- CDDs and CDFs. The heattreatment at 400°C reduced significantly the extracted amounts of all CDDs and CDFs, indicating the deconposition of major adsorbed CDDs and CDFs.

Table 3. Extracted amounts of Dioxines from MP-ACF witu HT (unit:pg)

Compound	Amount	200℃ -1h	200℃ -2h	300℃ -1h	300℃ -2h	400℃ -1h	400℃ -2h
^{13}C-2378 -TeCDD	1000	500	540	480	440	6	5
^{13}C-2378 -TeCDF	1000	380	410	350	320	6	5
^{13}C-12378 -PeCDD	1000	460	500	410	360	8	6
^{13}C-12378 -PeCDF	1000	430	450	440	360	9	7
^{13}C-123478 -HxCDD	1000	360	390	320	260	5	4
^{13}C-123478 -HxCDF	1000	420	430	380	320	7	3
^{13}C-1234678 -HpCDD	1000	500	600	530	420	0	13
^{13}C-1234678 -HpCDF	1000	590	690	690	550	8	28
^{13}C-12346789 -OCDD	2000	990	1000	680	550	0	9
^{13}C-12346789 -OCDF	2000	1700	1900	1200	900	0	49

The decomposition rates by the heattreatment were calculated according to a following equation to be summarized in Table 4.

$$\text{Decomposition}(\%) = \frac{\text{Extracted without HT - Extracted with HT}}{\text{Extracted without HT}} \times 100$$

According to the decomposition rates, CDD and CDF with chlorines less than 6 decomposed significantly at 200°C, the rates being 17~30%, whereas CDD and CDF with more than 7 hardly decomposed. The heattreatment at 300°C decomposed the former CDDs and CDFs at 27~36% for 1h and 23~47% for 2h, respectively while the latter CDDs and CDFs were hardly decomposed by 1h, but 7~23% by 2h. The heattreatment at 400°C decomposed all CDD and CDF almost completely, the decomposition rates being above 95% at least.

Table 4. Decomposition rates of Dioxins by the HT (unit:%)

Compound	200℃ -1h	200℃ -2h	300℃ -1h	300℃ -2h	400℃ -1h	400℃ -2h
^{13}C-2378-TeCDD	24.8	19.8	28.1	33.8	99.1	99.2
^{13}C-2378-TeCDF	29.4	22.6	33.8	40.1	98.9	99.1
^{13}C-12378-PeCDD	24.5	18.7	33.0	41.2	98.7	99.0
^{13}C-12378-PeCDF	26.5	23.3	26.3	39.0	98.6	98.8
^{13}C-123478-HxCDD	27.4	20.8	36.1	46.6	98.9	99.2
^{13}C-123478-HxCDF	20.9	17.3	27.0	39.4	98.7	99.4
^{13}C-1234678-HpCDD	0	0	0	11.0	100	97.3
^{13}C-1234678-HpCDF	0	0	0	6.2	98.7	95.2
^{13}C-12346789-OCDD	0	0	0	14.6	100	98.6
^{13}C-12346789-OCDF	0	0	0	22.5	100	95.8

3. Unlabeled Dioxines Found in the Extracts

Tables 5 and 6 summaries extracted amounts of unlabeled dioxine families and their particular species, respectively, after the heattreatment at 300°C for 1~2h. The heattreatment at 300°C for 1h produced large amounts of unlabeled CDDs and CDFs. Among there very large amounts of penta to octa CDFs were extracted. Such amounts of unlabeled dioxines produced by the heattreatment carried more chlorines than those of the adsorbed labeled dioxines. Chloride ions on the ACF which had remained after HCl washing must produced extra amount of dioxines.

CDFs with more chlorines tend to be produced than CDDs with the same numbers of chlorines. Some particular CDDs and CDFs appear certainly more produced. The locations of chlorines found in the standard species may stabilize the particular structure of the isomers.

Heattreatment for 2h at 300°C reduced very much the extractable unlabeled CDDs and CDFs, smaller chance of chlorine transfer from the labeled to unlabeled CDD and CDF species being suggested due to the preference of decomposition.

Table 5. Extracted amounts of unlabeled dioxine isomers (unit:pg)

Compound(isomer)	300℃-1h	300℃-2h
2378-TeCDD	4	0
2378-TeCDF	90	0
12378-PeCDD	38	0
12378-PeCDF	2000	0
23478-PeCDF	600	0
123478-HxCDD	250	0
123678-HxCDD	30	0
123789-HxCDD	120	0
123478-HxCDF	3800	0
123678-HxCDF	1300	1
234678-HxCDF	630	0
123789-HxCDF	360	5
1234678-HpCDD	220	64
1234678-HpCDF	6800	42
1234789-HpCDF	4800	14
12346789-OCDD	75	150
12346789-OCDF	5900	38

Table 6. Extracted amounts of unlabeled dioxine families (unit:pg)

Compound(Families)	300℃-1h	300℃-2h
TeCDD	680	0
TeCDF	3100	0
PeCDD	1700	0
PeCDF	16000	0
HxCDD	580	5
HxCDF	13000	21
HpCDD	470	130
HpCDF	18000	77
OCDD	75	150
OCDF	5900	38
Tolal amount	59000 (1400pgTEQ)	430(2.6pgTEQ)

Discussion

The present study clarified the adsorption strength and reactivity for chlorine transfer ask decomposition over particular ACF of CDDs and CDFs with variable numbers of chlorines at variable locations on the their ring systems. They are stable up to 200°C but reactive to loose their chlorine atoms to other CDD and CDF rings above 300°C and very much to decompose above 400°C.

Such adsorption strength and reactivity appear to depend on the ring system and number of chlorines on the ring. Tetra to hexa and hepta to octa chlorine species behaved as two groups, respectively, in their adsorption and reactivity. The latter groups are certainly less extractable and less reactive than the former group. Nevertheless, heattreatment above 400°C decomposes all of them so far examined. The extraction level after the heattreatment stays below a few percents of introduced dioxines at 1000~2000pg levels.

At 300°C, chlorines are proved to go around among the CDD and CDF rings on the ACF. Native, not labeled, CDDs and CDFs families with variable numbers of chlorines were found in the extract after the heattreatment at 300°C. CDFs with more than five chlorines were produced more than those with four chlorines. CDFs are certainly more reactive to receive chlorines than CDDs. Native DDs and DFs at this level of concentration may be present in the ACF as the structural ring units in the carbon skeleton. Chlorination may fission their connection in the skeleton to be extractable. Chlorines feed in native DDs and DFs are definitely more than those introduced by labeled CDDs and CDFs. Chlorines present on ACF reactive to produce dioxines at 300°C. It must be noted that all of CDDs and CDFs lost their chlorines by the heattreatment at 400°C.

The adsorption, reactivity for decomposition and production of CDDs and CDFs appeared to depend on the location of chlorines on their rings. The sequence of location appears to receive more chlorines as typically indicated by the case of hexaCDFs where more amounts of 123478(3,800pg), 123678(1,300pg), 234678(630pg), and 123789(360pg) hexaCDFs were found in the extract. The most abundant native hexaCDF is noted to carry the chlorines at the same locations to those of introduced labeled hexachlorides. Although so far governing rules are not clear, stability of the product or copying reaction between mother and product dioxines may govern the distribution of product native CDFs.

Conclusions

In conclusion, dioxines are effectivity and rather strongly fixed on the ACF. Heattreatment can remove or transfer chlorines of CDD and CDF rings according to the heattreatment temperatures.

Heattreatment above 400°C decomposes almost completely all of adsorbed CDFs and CDDs. Hence ACF is an excellent material to fix the dioxines in the flue gas below 150°C and decompose them by the heattreatment at 400°C for its safe disposal or regeneration for the second use. ACF may decompose catalytically any dioxines in the exhaust at 400°C, if oxygen concentration is limited.

THE INFLUENCE OF MINERAL MATTERS IN COAL ON THE REACTION OF NO-CHAR IN THE PRESENCE OF SO_2

Hui Chang, Baoqing Li, Wen Li, and Haokan Chen

State Key Laboratory of Coal Conversion, Institute of Coal Chemistry, Chinese Academy of Sciences, Taiyuan, China 030001

Introduction

The emission of NO_x from coal combustion has become one of the greatest challenges in environmental protection. It is well known that NO_x is one of the main contributors of acid rain and N_2O is the greenhouse gas and depletes the ozone layer indirectly. So great effort has been made to reduce NO economically and effectively. The reduction of NO by char *in situ* is an important reaction that determines the fuel-N converse to NO during coal combustion.

It is desirable to clarify the catalytic activities of mineral matters of coal on the reaction of NO-char. Many active components coexist in coal and their activities can be enhanced or abated each other, and the active components may have the potential synergistic activity in the reaction of NO-char. Recently, the effect of mineral matters in coal on the reaction of NO-char has been reported[1]. Illan-Gemez *et al*[2-4] studied the reduction of NO by carbon materials loaded with K, Ca and Fe in inert atmosphere. The reduction of NO by coal chars loaded with Ca and Fe in various atmosphere (O_2 and CO) was also conducted[5]. Li *et al*[6] found the catalyst of Na-Fe has the synergistic activity in NO-char reaction.

CO, O_2 and SO_2 are inevitable in the real exhaust gases. However, the effect of mineral matters on the reaction of NO-char in the presence of SO_2 has not been addressed. The principal motive of the present work is to investigate the catalytic characteristics of mineral matters in the presence of SO_2. Furthermore, the study will also provide some valuable information about char as the reducing agent and catalyst supporter in flue gas cleaning technology.

Experimental

Chinese longkou(LK) lignite, wulong(WL) bitumituous coal and yangquan(YQ) anthracite were used in the study. The characteristics of coal samples are shown in **Table 1** and **Table 2**. The deashed coals were prepared by demineralization using concentrated HF and HCl subsequently. The chars of deashed coals and raw coals were obtained in a quartz fluidized bed (i.d.50mm) at 900℃ for 30min in N_2 atmosphere.

Table 1. Proximate and Ultimate Analyses of Coal Chars

Sample	Ash/w%, d	Ultimate Analysis /w%, daf				
		C	H	S	N	O*
LK	13.20	92.58	0.73	0.44	2.07	4.18
WL	13.92	94.56	0.69	0.79	1.74	2.22
YQ	11.37	96.00	0.73	0.30	1.27	1.70
LK-de	0.42	92.90	0.68	0.39	2.55	3.48
WL-de	0.89	94.73	0.70	0.51	1.69	2.37
YQ-de	1.02	95.33	0.73	0.23	1.26	2.45

*** By difference**

Table 2. The Analyses of Mineral Matters in Chars (w%)

Sample	SiO_2	Al_2O_3	Fe_2O_3	TiO_2	CaO	MgO	K_2O	Na_2O
LK	7.63	3.10	0.52	0.07	0.69	0.27	0.11	0.59
WL	7.66	2.52	1.92	0.12	0.51	0.10	0.24	0.08
YQ	6.77	3.29	0.20	0.14	0.12	0.08	0.23	0.09

NO-char reaction was performed in a quartz tube (i.d.20mm) fixed bed reactor with a fused quartz sieve-plate in the center as the gas distributor and supporter of the reactant char.

Each sample was pretreated at 900℃ for 30min before each experiments. Two methods were conducted in this study: (i) Temperature programmed reaction (TPR): The pretreated samples decreased to 400℃, and then Ar was switched to Ar/NO/SO_2 (NO: 560ppm, SO_2: 1000ppm). When the NO concentration reached to the stable level, TPR was performed at the heating rate of 5℃/min; and (ii) Isothermal reaction: When temperature was lowed to certain level, Ar was switched to Ar/NO/SO_2 and reacted for 20min, then switched off SO_2, and kept the same total flow rate by balance gas of Ar. After reaction for 20min, above step was repeated.

Results and Discussion

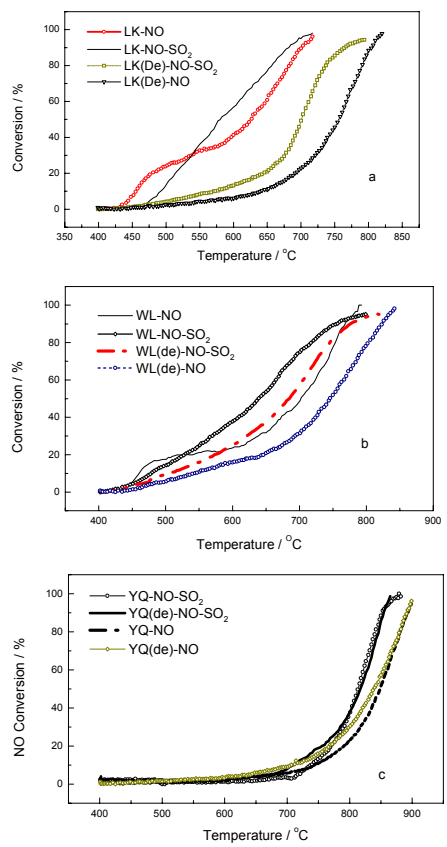

Figure 1.TPR of deashed chars and raw chars.

The effectiveness of mineral matters on the reaction of NO-char in the presence of SO_2 by TPR is presented in **Figure1**. The result shows that the conversion of NO is enhanced with increasing temperature. The three coals have a common phenomenon, *i.e.*, the conversion of NO is higher in the SO_2-containing system at the higher temperature (>530℃ for LK and WL, and >650℃ for YQ) for raw char. Apart from the effect of mineral matters in char, the gas-gas reaction of NO and SO_2 become an another main contributor to NO conversion, which is in agreement with Angelidis and Kruse[7]. They found that all possible nitrogen oxides can oxidize SO_2 to SO_3 at 480 ℃ since the respective equilibrium reactions are thermodynamically spontaneous:

$NO_2+SO_2 \Leftrightarrow NO+SO_3$, $*\ G_{480} = -6.47 Kcal.mol^{-1}$

$2NO+SO_2 \Leftrightarrow N_2O+SO_3$, $*\ G_{480} = -12.26\ Kcal.mol^{-1}$

$N_2O+SO_2 \Leftrightarrow N_2+SO_3$, $*\ G_{480} = -39.75\ Kcal.mol^{-1}$

We also found that at high temperature(＞600℃) the NO-SO_2

reaction can happen easily as shown in **Figure 2**. However, SO_2 can suppress the conversion of NO at low temperature. It was known that the active components in their reduced state after the pretreatment can accept oxygen from NO and form the intermediate $M_xO_y(O)$[8] during the process of NO conversion. $M_xO_y(O)$ is less stable and can transfer O to active sites of the char. Sumiya *et al*[9] found that with the addition of SO_2 the active components cannot catalyze the reduction of NO due to the formation of sulfates on the catalyst. The deashed chars have the similar phenomenon in the presence of SO_2. The suppression of NO at low temperature is resulted from the occupation of the active sites by SO_2.

Comparing with deashed char, LK and WL raw chars have higher activity obviously on NO reduction in the presence of SO_2 because of the catalytic effect of mineral matters in the char. As shown in **Table 2,** LK raw char contains more active components, especially sodium (Na_2O: 0.59%) and WL char more Fe (1.92%), which can catalyze the NO-char reaction effectively[3,10], Thus, the conversion of NO is higher for LK and WL raw chars than their deashed chars. However, YQ char shows the different phenomenon, because too much inert components exist in the char, leading to the abatement of the catalytic activities of the active components.

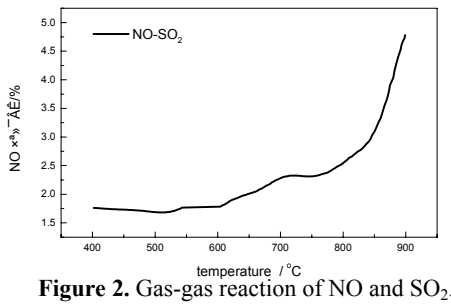

Figure 2. Gas-gas reaction of NO and SO_2.

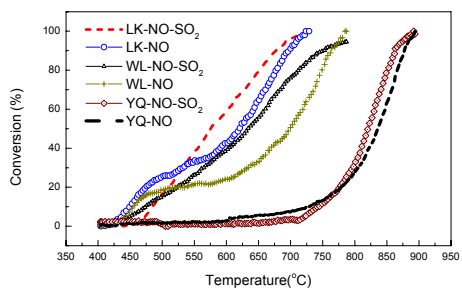

Figure3. TPR of raw char of different coal.

NO conversion of various chars with or without presence of SO_2 is different as shown by TPR in **Figure 3.** The order of activity is LK char ＞WL char ＞YQ char. During the temperature range of NO reduction, NO conversion is mainly determined by two factors: NO-SO_2 reaction and the catalytic activities of mineral matters in char. Thus, the conversion of NO is higher for LK and WL raw chars than their deashed chars. Because of the high contents of Na and Fe in LK coal, the highest activity of LK char may imply that Na and Fe as active components have synergistic function in NO reduction.

The isothermal experiments were carried out at 700℃ and 550 ℃ for deashed chars and raw chars. The results are presented in **Figure 4**. It is proved that the effect of SO_2 on the NO-char reaction is different at different temperature. For both deashed and raw chars, SO_2 suppress the reduction of NO at low temperature, because of the occupation of SO_2 and the formation of sulfates on active sites, while at high temperature NO conversion is promoted by the NO-SO_2 reaction and the effect of active components. Furthermore, high temperature can enhance the activity of the active sites on the surface of the chars.

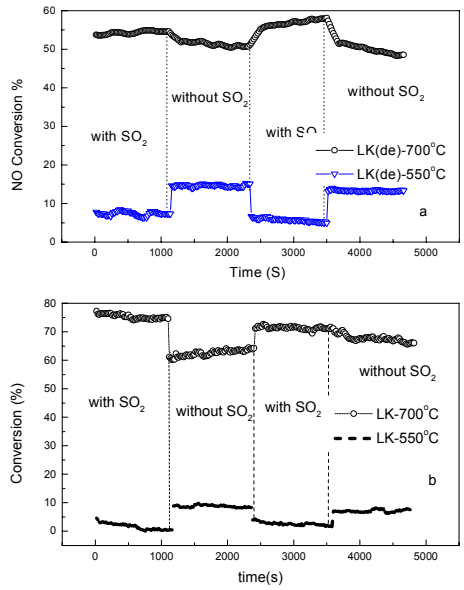

Figure 4.Effect of SO_2 on the activities of LK chars.

Conclusions

(1) The reduction of NO is enhanced with increasing temperature during the range of 400℃-900℃;

(2) The effect of SO_2 on the NO-char reaction is changed with temperature. At low temperature SO_2 can suppress the conversion of NO, while at high temperature NO conversion is enhanced by the reaction of NO-SO_2;

(3) The effect of mineral matters is closely related to the content of active components and its dispersion. If the char contains more active components in mineral matters, it can catalyze the NO-char reaction effectively (like LK and WL chars), otherwise it will abate the NO-char reaction (like YQ char).

Acknowledgment.

The authors thanks for the financial support of Natural Science Foundation of China (29936090) and Special Founds for Major State Fundamental Research Project of China (G1999022102).

References

1 Zhao, Z. B., Li, W., Li, B. Q., 11th International Conference on Coal Science, U.S., 2001,9.

2 Illan-Gomez, M. J., Linares-Solano, A., Radovic, L. R., and Salinas-Martinez de lecea, Energy & Fuels, 1995,9,112-118.

3 Illan-Gomez, M. J., Linares-Solano, A., Radovic, L. R., and Salinas-Martinez de lecea, Energy & Fuels, 1995, 9,540-548.

4 Illan-Gomez, M. J., Linares-Solano, A., Salinas-Martinez de lecea, Energy & Fuels, 1995,9,976-983.

5 Zhao, Z. B., Li, W., Li, B. Q., Fuel, 2002, 81,1559-1564.

6 Li, B. Q., Zhao, Z. B., Li, W., Fuel Chemistry Division Preprints, 2001, 46(1), 163-166.

7 Angelidis, T. N., Kruse, N., Appl. Catal. B: Environ., 2001, 34(3):201-212.

8 Yamashita, H., Yoshida, S., Tomita, A., Energy & Fuels, 1991, 5(1)，52-57.

9 Sumiya, S., Saito, M., He, H., Feng, Q.-C., Takezawa, N., Yoshida, K., Catal. Lett., 1998,50-87.

10 Kapteijn, F., Alexander, J. C., Mierop, G. A., Moulijn, J. A., J. Chem. Soc. Chem. Commun., 1984, 1085-1086.

NUMERICAL ANALYSIS OF PULVERIZED COAL COMBUSTION CHARACTERISTICS USING ADVANCED LOW-NOx BURNER

Ryoichi Kurose[1], *Hisao Makino*[2] *and Akira Suzuki*[3]

[1]Yokosuka Research Laboratory, Central Research Institute of Electric Power Industry (CRIEPI), 2-6-1 Nagasaka, Yokosuka, Kanagawa 240-0196, Japan
[2]CS Promotion Office, CRIEPI, Otemachi Bldg., 1-6-1 Otemachi, Chiyoda-ku, Tokyo 100-8126, Japan
[3]CD-adapco JAPAN Co., LTD, Nisseki Yokohama Bldg. 16F, 1-1-8 Sakuragicho, Naka-ku, Yokohama, Kanagawa 231-0062, Japan

Introduction

Coal is an important energy resource to meet the future demands of electricity, because its reserves are more abundant than that of other fossil fuels. The major utilization method of coal in thermal power plants is pulverized coal combustion for which the reduction of environmental pollutants, especially NOx emissions, is indispensable. In utility boilers, the most effective technology for NOx reduction is the staged combustion method. However, this method generally causes another problem: the increase in unburned carbon.

To overcome this situation, we have investigated pulverized coal particle motion, thermal decomposition, NOx formation and reduction and so on near the burner in a furnace, and developed an advanced low-NOx burner called the CI-α (CRIEPI-IHI advanced Low Pollution High Ability) burner[1]. The concept of the CI-α burner is that the residence time of pulverized coal particles in high temperature fields near the burner is lengthened by the recirculation flow and the thermal decomposition of coal particles is accelerated. The CI-α burner achieved a further 30% NOx reduction compared to the conventional low-NOx burners without any increase in the unburned carbon. However, the behaviors of the flow and coal particles in the furnace have not been sufficiently evaluated yet because of the difficulty to measure them.

The purpose of this study is, therefore, to apply a three-dimensional numerical simulation to the pulverized coal combustion field in the furnace installed with the CI-α low-NOx burner, and to investigate the detailed combustion characteristics.

Numerical Simulation

Computational Domain and Conditions. The test furnace used was one at Yokosuka Research Laboratory of CRIEPI, in which the CI-α burner with a coal combustion capacity of about 0.1 t/h was installed. The furnace was a cylindrical furnace with a diameter of 0.85 m and a length of 8 m. The configurations of the computational domain and the CI-α burner are shown in **Figure 1**. The computational domain was half of the furnace. The combustion air was injected through the burner and through the staged combustion-air ports mounted at 3.0 m from the burner outlet. The air through the burner was divided into primary air, secondary air and tertiary air. The primary air moved in a straight motion, and the secondary and tertiary air moved in a strong swirling motion. The swirl vane angles for the secondary and tertiary air were set at 81 deg. and 72 deg. respectively, which were optimum values for bituminous coal. The pulverized coal was carried with the primary air.

The combustion conditions were the same as in our recent experiments[2]. The value of the thermal input was 2.725×10^6 kJ/h. The air ratio was 1.24, and the excess O_2 concentration was 4.0%. The staged combustion air ratio was set at 30 %. The mass ratio of the pulverized coal (dry base) to the sum of the air and moisture in the primary air was 1:2.2, and the mass ratio of the secondary air to the tertiary air was 1:6. The test fuel was Newlands coal (bituminous coal).

Mathematical Models and Numerical Method. The computation was performed using the STAR-CD code. The gas-phase turbulence was represented by the renormalization group (RNG) k-ε model[3,4], and the continuity and momentum equations were solved using the SIMPLE algorithm. The motion of the representative coal particles was calculated by Lagrangian formulation. The particle temperature was calculated by considering the heat transfer due to convection, radiation, heat loss due to vaporization of moisture in coal, and heat gain due to char combustion. The radiative heat transfer among the gas, particles and wall were simulated by the discrete transfer radiation method of Lockwood and Shah[5].

The concept of pulverized coal combustion simplified for this calculation is shown in **Figure 2**. Coal devolatilisation [arrow (1)] was simulated by first-order single reaction model[6]. The gaseous combustion between the volatilized fuel and the air was calculated using the combined model of kinetics and eddy dissipation models [arrows (3)－(5)]. As a chemical mechanism, 2 global reactions, $C_aH_bO_c+0.5O_2 \rightarrow \alpha\ CO+\beta\ H_2O$, $CO+0.5O_2 \rightarrow CO_2$, were used. Here a, b, c, α and β were determined by the coal constituent. Regarding the kinetics, the rate of the reaction for reactants of $C_aH_bO_c$ and CO was given by Arrhenius expression[7]. Char burning [arrow (2)] was simulated using Field et al.'s model[8].

For the NOx formation, three different mechanisms were employed, namely Zeldovich NOx, prompt NOx and fuel NOx [arrows (6)－(9)]. The Zeldovich NO was evaluated by applying a quasi-steady state approximation for N species to the extended Zeldovich mechanisms with the rate constants of Baulch et al.[9]. The prompt and fuel NO were predicted using the models of De Soete[10,11].

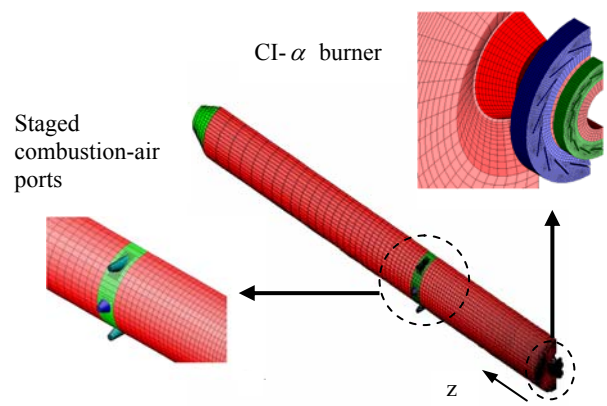

Figure 1. Computational domain and burner.

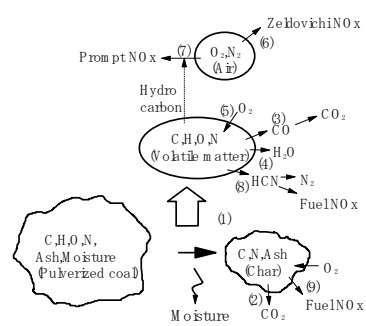

Figure 2. Concept of Pulverized coal combustion.

Results and Discussion

Gas velocity vectors and particle trajectories near the CI-α burner in the furnace are shown in **Figure 3**. As expected in the previous experiments[1], recirculation flow is generated and the residence time of coal particles is lengthened by being caught in the flow. It was also found that the residence time in this recirculation zone tends to be longer for intermediate coal particles with diameters of 20 and 40 μm than that for smaller or larger coal particles. This is attributed to the fact that the coal particles with smaller diameters instantly vanish due to devolatilisation, and those with larger diameters are not caught by the recirculation flow because of their large inertias.

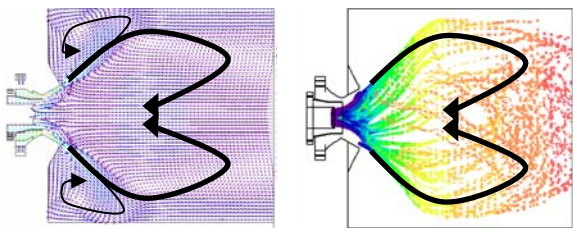

Gas velocity vectors Particle

Figure 3. Gas velocity vectors and particle motions.

Figures 4 and 5 show the comparisons of axial distributions of the gas temperature and the O_2 mole fraction. The axial distribution of the gas temperature is in general agreement with the measurements[2], whereas that of the O_2 mole fraction indicates a greater value than the measurements[2] around the region where the staged combustion air is injected (z=3.0m). The discrepancy is considered to be due to the inlet condition of the staged combustion air and/or the limitation of the RNG k-ε turbulent model[3,4]. That is, there are possibilities that the maximum velocity of the injected air is less than that of the experiments[2] because a non-slip condition was not set on the wall boundary of the ports, and that the numerical method using the RNG k-ε turbulent model[3,4] overestimates the swirl strength, which prevents the air (O_2) from reaching the center region in the furnace. However, the specified feature that the extreme low-O_2 zone is found near the burner can be simulated well.

Figure 6 shows the comparisons of axial distribution of the NO mole fraction. Although the calculated value near the burner nearly corresponds with the experimental value[2], the rate of decrease with the axial distance is much less than that for the experiments[2]. This means that the NO reduction which is observed in the experiments[2] does not function in the present computation. The reason for this can be explained as follows. As indicated by arrow (8) in **Figure 2**, the formation of the fuel NO from the nitrogen in volatiles are modeled under the assumption that the fuel-bond nitrogen is released as HCN and HCN transforms to NO or N_2. However, to account for the NO reduction in the low-O_2 (fuel-rich) zone, the destruction of NO to HCN by hydrocarbon radicals ($NO \rightarrow HCN$) should be added in this model. Magel et al.[12] compared the NO emissions for staged and unstaged combustion conditions between experiment and calculation and found that the NO destruction mechanism played an important role especially for the staged combustion condition.

Conclusions

The pulverized coal combustion characteristics in a furnace installed with the CI-α burner was numerically investigated. It was observed that the recirculation flow and the extreme low-O_2 zone appeared near the burner. To improve the accuracy of the numerical prediction for the NOx emissions, it is necessary to account for the NO destruction mechanism in the fuel NO formation model.

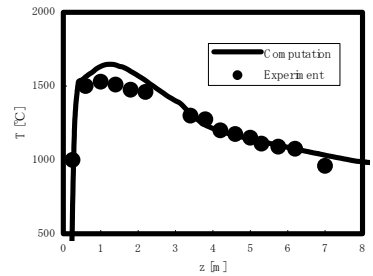

Figure 4. Axial distribution of gas temperature.

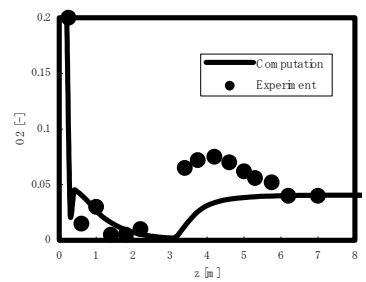

Figure 5. Axial distribution of O_2 mole fraction.

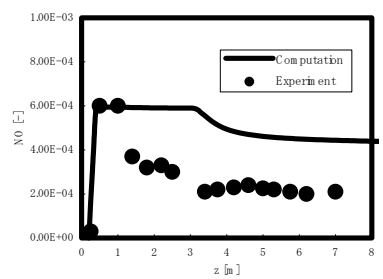

Figure 6. Axial distribution of NO mole fraction.

Acknowledgment

The authors are indebted to Mr. M. Kimoto, Dr. H. Tsuji and Mr. M. Ikeda of CRIEPI for their help in providing the experimental data. The authors also would like to thank Mr. M. Sato of CD-adapco JAPAN CO., LTD. for many helpful discussions.

References

1. Makino H et al., *EPRI-ODE-EPA Combined Utility Air Pollution Control Symp.: The MEGA Symp.*, vol.2. Atlanta, USA: EPRI, 1999. p.11. **2**. Ikeda M et al., *JSME Int. J., Ser. B*, 2002;45:506. **3**. Yakhot V et al., *Sci. Comp.*, 1986;1:1. **4**. Yakhot V et al., *Phys. Fluids*, 1992;4:1510. **5**. Lockwood FC et al., *18th Symp. (Int.) on Comb., The Combustion Institute*, 1981, p.1405. **6**. Van Krevelen DW et al., *Fuel*, 1951;30:253. **7**. Borman GL et al., *Comb. Engng.*: McGRAW-HILL. 1998. p.120. **8**. Field MA et al., *The Combustion of Pulverised Coal, British Coal Utilisation Research Association*: Leatherhead, Surrey, 1967. **9**. Baulch DL et al., *Evaluated Kinetic Data for High Temperature Reactions*: Butterworth, 1973. **10**. De Soete GG, *15th Symp. (Int.) on Comb., The Combustion Institute*, 1975, p.1093. **11**. De Soete GG, *23th Symp. (Int.) on Comb., The Combustion Institute*, 1990, p.1257. **12**. Magel HC et al., *NOx-reduction with Staged Combustion – Comparison of Experimental and Modelling Results, Joint Meeting of the Portuguese, British, Spanish and Swedish Section of the Combustion Institute*, Maderia, 1996.

ADVANCES IN FUEL PROCESSING FOR PEM FUEL CELLS

Levi T. Thompson

University of Michigan,
Department of Chemical Engineering,
Ann Arbor, MI 48109

Introduction

Proton Exchange Membrane (PEM) fuel cells have emerged as leading candidates to provide primary and auxiliary power for stationary, automotive and portable electronic device applications. A key challenge to their use is the availability of sufficiently small and cost-effective H_2 sources. Hydrogen can either be stored or produced from suitable fuels. The H_2 loadings for pressurized containers or in adsorbent materials are relatively low. Chemical sources are able to yield the equivalent of more than 5 wt% H_2. Work described in this paper focuses on H_2 production via hydrocarbon "reforming" or fuel processing reactions. The reforming of liquid hydrocarbons like methanol and gasoline is attractive because of their high energy densities.

The principal functions accomplished by the fuel processor are the production of syngas and CO removal (see **Figure 1**). Syngas, a mixture principally of H_2 and CO, is most often produced using steam reforming and/or partial oxidation reactions. The amount of CO must typically be reduced because the noble metal fuel cell electrocatalysts are very susceptible to poisoning by as little as 10-100 ppm CO.[1,2] While significant advances in PEM fuel cell technology are expected through the development of poison-tolerant electrocatalysts and/or high temperature membranes, more selective reforming and/or partial oxidation processes, and improved CO removal catalysts will have to be developed.

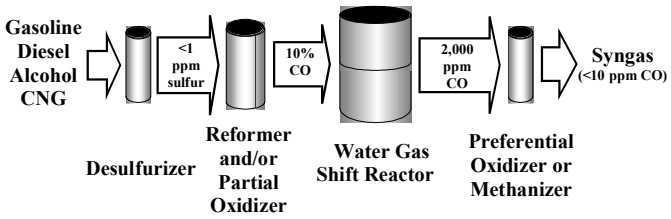

Figure 1. Schematic of key steps in the conversion of hydrocarbons into syngas for fuel cells (CNG=compressed natural gas).

Presently carbon monoxide removal is accomplished via water gas shift and preferential oxidation or methanation reactions. Many commercial and military applications including automobiles and soldier individual power favor the use of gasoline, diesel and/or logistic fuels as H_2 sources. These fuels contain deleterious amounts of sulfur and present important challenges because most of the CO removal catalysts are susceptible to poisoning by sulfur.

The University of Michigan has been engaged in projects to significantly improve hydrocarbon fuel processors via the integration high performance catalysts into low-cost micro-reactor systems. This talk will describe the properties of carbide and nitride based fuel processing catalysts including characteristics of the active sites. In addition, their deposition on engineering supports, and their integration into micro-reactor systems will be discussed.

Discussion

We have developed a series or carbide and nitride based materials and evaluated their use as methanol steam reforming and water gas shift (WGS) catalysts. These materials were typically prepared in high surface area form using temperature programmed reaction methods and characterized using a variety of methods including sorption analysis, x-ray diffraction, x-ray photoelectron spectroscopy and infrared spectroscopy.

The carbide and nitride based catalysts were very active for methanol steam reforming. For example, methanol conversion rates for one of the Mo_2N based catalysts were comparable to those for a commercial Cu-Zn-Al catalyst, however, the CO_2 selectivities were lower (**Figure 2**). The selectivities and rates improved when the CH_3OH:H_2O was increased suggesting competition between CH_3OH and CO for active sites. The carbide and nitride based catalysts were also much more stable at high temperatures (up to 400 °C)_than the Cu-Zn-Al catalyst.

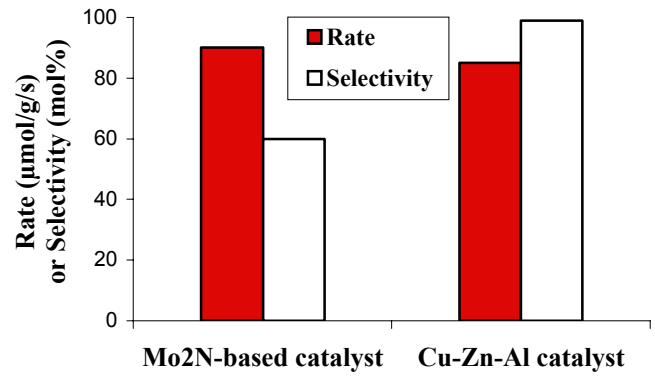

Figure 2. Methanol conversion rate and CO_2 selectivity for Mo_2N based and Cu-Zn-Al catalysts at 230 °C, atmospheric pressure and a CH_3OH:H_2O molar ratio of 1:1.

The carbides and nitrides were also very active for the WGS. In fact, several of the formulations substantially outperformed a commercial Cu-Zn-Al WGS catalyst (**Figure 3**).

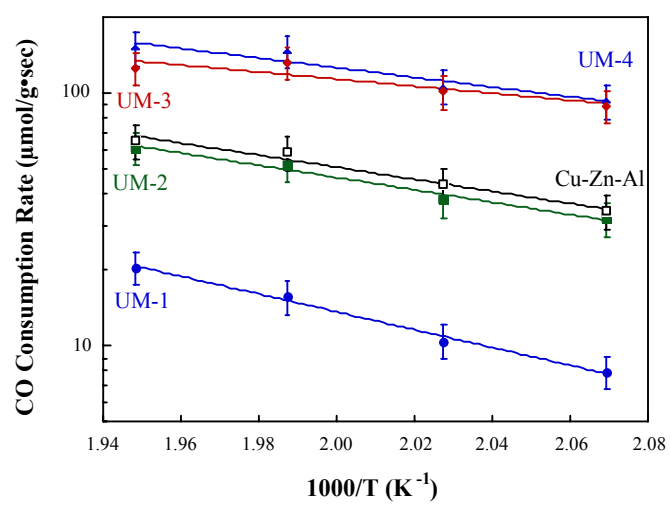

Figure 3. Comparison of WGS rates for selected carbide and Cu-Zn-Al catalysts at atmospheric pressure.

The carbides were more active than the nitrides, and the performance was a function of the pretreatment conditions employed. For example, pretreatment in the CH_4/H_2 mixture typically resulted in catalysts that were more active than those same catalysts pretreated in pure H_2. *In situ* x-ray photoelectron spectroscopic results suggested that active sites on the carbide surfaces were linked to carbidic carbon. In particular, the WGS rates increased proportionally with the amount of carbidic carbon (**Figure 4**).

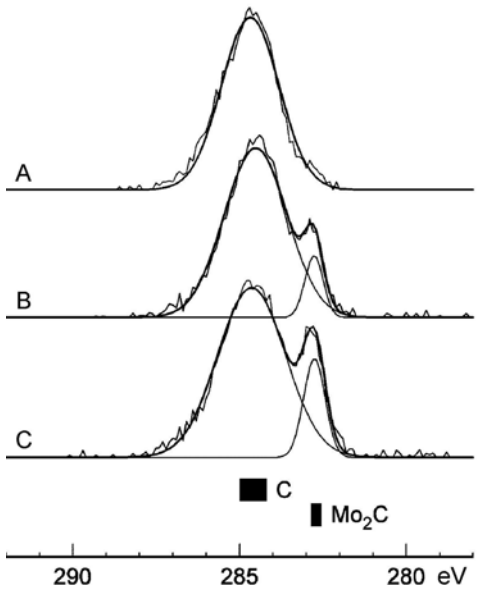

Figure 4. X-ray photoelectron spectra (C 1s region) for an Mo carbide catalyst following A) passivation in 1% O_2 in He, B) pretreatment in H_2/Ar at 500 ˚C, and C) pretreatment in CH_4/H_2/Ar at 500 ˚C.

We have also demonstrated that the carbide and nitride based catalysts can be washcoated onto engineering supported including cordierite monoliths and ceramic foams (**Figure 5**), and infiltrated into micro-reactor systems. These and other results will be discussed during the presentation.

Figure 5. Carbide washcoated ceramic foam.

Acknowledgement

Financial support from the Department of Energy and Osram Sylvania was used to carry out work described in this paper.

References

(1) Appleby, A.J. and Foulkes, F.R., *Fuel Cell Handbook*, Van Nostrand Reinhold, NY (1989).
(2) Kordesch, K. and Simander, G., *Fuel Cells and Their Application,* VCH Publishers, NY (1996).

HYDROGEN PRODUCTION FROM PROPANE THROUGH PARTIAL OXIDATION AND AUTOTHERMAL REFORMING IN MICROSTRUCTURED REACTORS

Torbjørn Gjervan[1], Hilde Venvik[1], Ingrid Aartun[2], Anders Holmen[2], Oliver Görke[3], Peter Pfeifer[3], Klaus Schubert[3]

[1] SINTEF Applied Chemistry, N-7465 Trondheim, Norway
[2] Department of Chemical Engineering, NTNU, N-7491 Trondheim, Norway
[3] Institute for Micro Process Engineering (IMVT), Forschungszentrum Karlsruhe (FZK), Postfach 3640, D-76021 Karlsruhe, Germany

Introduction

The size and compactness of microstructured reactors makes them interesting for application in small-scale fuel reformer units for distributed hydrogen production. Because of the small linear channel dimension and thus the high surface to volume ratio, efficient mass and heat transfer is possible. In addition, well-defined flow conditions facilitate narrow residence time distribution. Manufacturing the catalyst system in metal results in high thermal conductivity. This is favorable for combination of exothermic partial oxidation and endothermic steam and CO_2 reforming, since the heat from the exothermic oxidation reactions is effectively transported along the flow direction.

The present work aims at studying the effect of varying catalyst material, addition of steam/oxygen, and residence time on the selectivity and yield of hydrogen during partial oxidation (POX) and autothermal reforming (ATR) of propane. Reactors of two different lengths have been tested. These were either made from rhodium or from the high temperature alloy Fecralloy [1]. The latter material was oxidized and impregnated with catalytic particles prior to testing.

Experimental

The experimental work has been done both at IMVT in Germany and SINTEF/NTNU in Norway using different reactor housings. The experimental set up at IMVT is described elsewhere [2]. At IMVT, the reactor housing contained a ceramic holding unit for the microstructured reactor. This unit was equipped with a heating wire for rapid heating of the reactor. In Trondheim the microstructured reactor was placed in a quartz tube situated in a Thermcraft Trans Temp furnace. In both cases the temperature was measured with a thermocouple at the reactor exit. At IMVT, the temperature was also monitored with a pyrometer through a quartz window. The product gas mixture was measured by gas chromatography.

The reactors have been manufactured from rhodium or Fecralloy (72.6% Fe, 22% Cr, 4.8% Al) at IMVT, Karlsruhe, with channels of small linear dimensions (approximately 120×130 μm^2). Each reactor is made of several microstructured foils that are stacked and welded to a compact honeycomb reactor through diffusion bonding. The reactors were manufactured in two different lengths in order to study different contact times. Table 1 gives the physical data for the different reactors.

The Fecralloy reactor was oxidized at high temperature in air in order to form a thin α-Al_2O_3 surface layer and then subsequently impregnated with nickel or rhodium. After oxidization, the specific surface area of reactor 2 was measured by Kr-BET and was found to be approximately 146 cm^2 (> 8 times larger than the geometric area). Nickel was deposited on the reactor by allowing a saturated aqueous solution of $Ni(NO_3)_2 \cdot 6H_2O$ to flow through the channels several times. This was followed by drying at 120°C over night, calcination at 600°C for 4 hours in flowing air, and reduction in hydrogen at 600°C for 1 hour. Rhodium was similarly impregnated using an aqueous solution (0.03 M) of $RhCl_3$, drying at 120°C over night, and reduction at 800°C for 3 hours in hydrogen. The mass increase after impregnation was found to correspond to approximately 50 mg Ni and 5 mg Rh deposited on the channel walls of the two reactors (Reactor 3).

Table 1: Physical Data of the Microstructured Reactors

Reactor no.	1	2	3
Material	Rhodium	Fecralloy	Fecralloy
H×W×L [mm]	5.5×5.6×20	5.5×5.6×5.0	5.5×5.6×20
Channels	644	675	675
Channel dimension [μm^2]	120×130	120×130	120×130
Geom. surface of channel [cm^2]	67.8	17.3	67.8
Porosity	0.34	0.33	0.34
Residence time (τ) at 1 Nl/min	10.5	3.0	10.5

The reactor/catalyst was installed in the reactor holder unit and reduced before the first experiment. The furnace temperature was raised to 300°C, and the premixed gases were introduced. Partial oxidation was performed keeping a C/O ratio of 0.8 using synthetic air as oxygen source (10 vol. % C_3H_8, 71 vol. % N_2, and 19 vol. % O_2). For ATR experiments steam was added to the reactant gas. The C/O ratio was thereby decreased to 0.5, keeping the total flow and C_3H_8 concentration constant. The furnace temperature was increased stepwise until a maximum temperature of 1000°C was reached.

In order to compare hydrogen selectivity from different experiments, it has been calculated as follows:

$$S(H_2) = \frac{F_{tot,out}}{F_{tot,in}} \cdot \frac{C_{H_2,out}}{4 \cdot C_{C_3H_8,in} \cdot X_{C_3H_8}} \qquad (1\text{-}1)$$

where $S(H_2)$ = hydrogen selectivity, $F_{tot,in}$ = total volumetric gas flow at reactor inlet, $F_{tot,\ out}$ = total volumetric gas flow at reactor exit, $C_{H2,out}$ = hydrogen concentration in product gas, $C_{C3H8,in}$ = propane concentration in feed gas, and X_{C3H8}= conversion of propane.

Hydrogen may be produced both from propane and water, and the selectivity can therefore exceed one on the ATR.

Results and discussion

The results show that partial oxidation gives the highest hydrogen yield is using the Rh/Fecralloy reactor. The product composition as a function of temperature for reactor 2 is shown in Figure 1, where the gas flow is 1 Nl/min giving a residence time of 3.0 ms. It can be observed that below 600°C total oxidation to water and CO_2 is dominant. Further increase in the temperature favor endothermic reforming reaction, increasing the production of hydrogen. At 1000°C complete conversion of propane is reached,

and a hydrogen yield of approximately 60% is obtained. The hydrogen selectivity is higher than obtained using the rhodium reactor (reactor 1). This indicates that having the catalyst dispersed as small particles on the surface is beneficial. Characterization of the impregnated Fecralloy reactor by XPS and SEM/EDX has confirmed that Rh (and Ni) is present as metal particles on the alumina surface. Using the Rh/Fecralloy reactor, complete conversion of propane was obtained in the range 900 - 1000°C in POX, depending on the residence time.

Complete conversion of propane is also obtained at 900°C when using the Ni/Fecralloy reactor; however, the hydrogen yield is lower than when using the Rh/Fecralloy reactor.

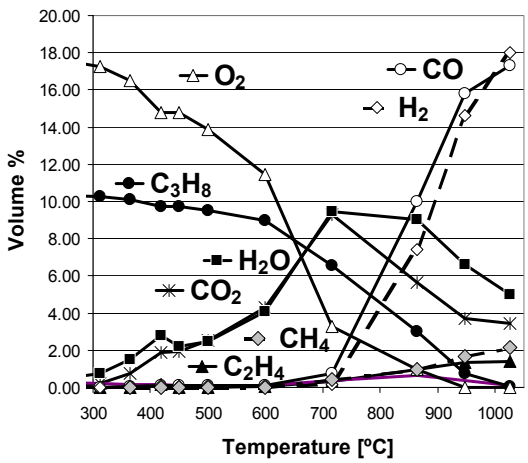

Figure 1. Production composition as a function of temperature after partial oxidation of propane in reactor 2 (τ = 3.0 ms).

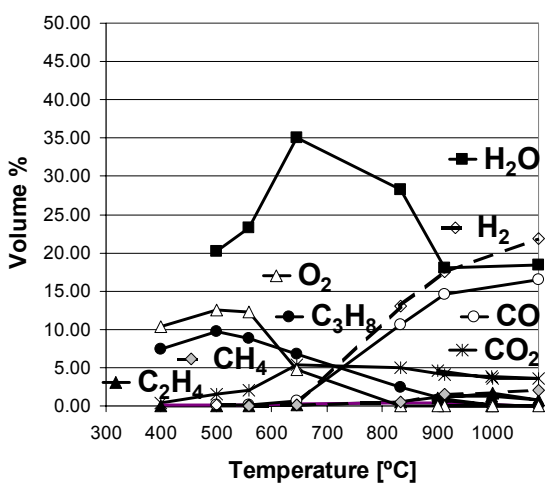

Figure 2. Production composition as a function of temperature after autothermal reforming of propane in reactor 2 (τ = 3.0 ms).

Figure 2 shows the product composition after autothermal reforming of propane using reactor 2. Here, total oxidation producing water and CO_2 is present below 600°C. At higher temperatures water is consumed through steam reforming, increasing hydrogen production. The highest yields of hydrogen were obtained for the Rh/Fecralloy reactor also in these experiments. Addition of steam increases the hydrogen production, and hydrogen selectivity higher than 70% were obtained. The hydrogen yield is clearly dependent on the residence time, which can be explained by the slow kinetics of the reforming reactions. It is therefore planned to scale up the Fecralloy reactors, allowing higher residence times while maintaining the same gas flows.

The performance of the Ni/Fecralloy reactor is rather poor in comparison with the Rh/Fecralloy indicating that sintering of the Ni particles during autothermal reforming deactivates the catalyst. Alternative methods for impregnating the Fecralloy reactor with Ni particles will therefore be considered.

As can be observed in Figures 1 and 2, there is some ethylene and methane are produced by unwanted pyrolysis both during POX and ATR experiments. This is due to the high temperature applied for complete conversion of propane. In spite of the small channel dimension of the reactors, no problem with pressure build up due to coke formation was observed.

Conclusions

- Microstructured reactors of rhodium and Fecralloy have been manufactured and tested for their activity in partial oxidation and autothermal reforming reactions. Both Rh and Ni have been impregnated on the oxidized Fecralloy reactor channel walls, resulting in a catalyst system with good activity for partial oxidation of propane
- Fecralloy reactors impregnated with Rh are found to be the most active catalyst systems for partial oxidation and autothermal reforming.
- Using the Rh/Fecralloy reactor for autothermal reforming of propane at elevated temperatures (>950°C), hydrogen selectivity higher than 70 % can be obtained.

Acknowledgement

The Norwegian Research Council through the KOSK Program is greatly acknowledged for their financial support.

References

(1) http://www.goodfellow.com/csp/active/static/E/FE08.HTML
(2) Fichtner, M.; Mayer, J.; Wolf, D.; Schubert, K. *Ind. Eng. Chem. Res.* **2001** *40*, 3475.

THE STABILITY OF MOLYBDENUM CARBIDE CATALYSTS IN METHANE REFORMING

David C. LaMont, Anna R. S. Darujati, Benjamin N. Gallaher, William J. Thomson

Department of Chemical Engineering
Washington State University
Pullman, WA 99164-2710

The application of bulk molybdenum carbide catalysts to the reforming of hydrocarbon fuels for fuel cell hydrogen production, has been a subject of research ever since a group at Oxford showed that these catalysts could be operated at stoichiometric feed conditions and maintain stability for 70 hours. However, despite these remarkable results, they are potentially susceptible to deactivation by both oxidation and coking.

Catalyst Characterization

The molybdenum carbide catalyst used in this study was a commercial Alfa Aesar Mo_2C lot# K17J11 (99.5% metals purity, <325 mesh), with a BET surface area less than 2 sq. m/g. The high surface area catalysts were synthesized via Temperature Programmed Reaction, producing a surface area of 70 sq m/g and by a "solution derived" technique, which produced surface areas as high as 240 sq m/g.

Effect of Molybdenum Carbide Surface Area

The high and low surface area catalysts were compared under identical conditions of steam reforming at 950 C, 8 bars pressure, using a stoichiometric steam-methane feed in a packed bed reactor. Whereas the high surface area catalyst began deactivating after 40 hours on stream, the low surface area catalyst maintained equilibrium conversions for 100 hours. Analysis of the spent high surface area catalyst showed a high level of refractory carbon, suggesting that the excess synthesis carbon on the fresh catalyst may have acted as nucleation sites for refractory coke deposition. There was no sign of catalyst oxidation under these conditions.

Controlled Oxidation Experiments

The low surface area catalysts were placed in a Dynamic X-Ray Diffractometer and scanned for both the carbide and oxide peaks as the temperature was ramped from 500 C to 850 C in the presence of oxidizing gases (steam, carbon dioxide), as well as those gases with various concentrations of hydrogen and carbon monoxide. It was found that the oxidation commenced at 625 C but that the rate of oxidation increased dramatically at about 750 C. It is hypothesized that the high temperature path includes decomposition to the metal, which is then immediately oxidized. It was also found that hydrogen and carbon monoxide was able to eliminate the first stage of oxidation and significantly hinder the oxidation at the higher temperature.

Effect of Sulfur

In order to evaluate the effect of sulfur on these catalysts, dimethyl sulfide (DMS) was chosen as a model sulfur compound for methane reforming and experiments were performed in a TGA/MS unit as well as in a packed bed reactor. The data from the TGA/MS unit indicated that DMS decomposes in the gas phase at about 550 C. In the absence of hydrogen, the primary sulfur product was carbon disulfide and in the presence of sulfur, it was hydrogen sulfide. At 900 C the carbon disulfide readily adsorbed on the catalyst whereas sulfur was not detectable on the catalyst in the presence of hydrogen, indicating that hydrogen sulfide does not readily adsorb at these temperatures. In separate dry reforming experiments at 1050 C and atmospheric pressure, the catalyst was allowed to reach steady state methane equilibrium conversion values (95%) and then exposed to methane/carbon dioxide in the presence of 1000 ppm DMS. The conversion immediately dropped to levels between 65 and 45%, depending on the hydrogen concentration in the reactor, and remained at these levels for at least 7 hours with no further loss in activity. In one experiment, after suffering a loss of conversion in the presence of sulfur, the sulfur concentration was lowered to zero and the conversion returned to its equilibrium value after about one hour. This indicates that the catalyst is capable of being regenerated, in-situ, once exposed to sulfur.

Partial methane oxidation on yttria and ceria supported platinum catalysts

Fabio B. Passos[1], *Elaine R. Oliveira*[1], *Carlos E.E.L. Rego*[1], *Lisiane V. Mattos*[2], *and Fabio B. Noronha*[2]

[1] Departamento de Engenharia Química, Universidade Federal Fluminense, Rua Passo da Patria, 156. São Domingos, Niteroi RJ 24210-240, Brazil, Fax: 552127174446, fbpassos@engenharia.uff.br
[2] Laboratório de Catálise, Instituto Nacional de Tecnologia

Introduction

Partial methane oxidation of methane is an interesting alternative for synthesis gas production. The reaction is exothermic and produces a synthesis gas mixture with a H_2/CO ratio to 2, which is more adequate for the subsequent Fischer-Tropsch synthesis[1-3] . A two-step mechanism has been proposed for the partial oxidation of methane. According to this mechanism, in the first step, combustion of methane takes place, producing CO_2 and H_2O. In the second step, synthesis gas is produced via carbon dioxide and steam reforming reaction of unreacted methane[2] . On the other hand, a direct mechanism was claimed to occur on Ru/TiO_2[4] , Ni/CaO.2Al_2O_3[5] and on ytria-zirconia[6].

In this work, we investigate the use of platinum supported different oxides (Al_2O_3, ZrO_2, CeO_2 and Y_2O_3) in the partial oxidation of methane. The effect of the oxygen storage capacity of the catalysts on the stability of the catalysts is reported as well as the effect of the support on the controlling mechanism of the reaction.

Experimental

The Al_2O_3, CeO_2 , ZrO_2 and Y_2O_3 supports were prepared by calcination of γ-Al_2O_3, $(NH_4)_2Ce(NO_3)_6$, $Zr(OH)_4$ and $Y(NO_3)_3$, respectively, at 800°C for 1 h in flowing . Another sample of ceria (CeO_2 ppt) was prepared by precipitation as described by Hori et al[7].

The catalysts were prepared by incipient wetness impregnation of the supports with an aqueous solution of $H_2PtCl_6.6H_2O$. All samples contained 1.5 wt.% of Pt and were calcined under air (50 mL/min) at 700°C for Pt/Al_2O_3 catalysts and at 400°C for the other. The catalysts were characterized by Oxygen Storage Capacity (OSC) measurements and the mechanism investigated by Temperature Programmed Superficial Reaction (TPSR). Partial oxidation of methane was performed in a system previously described[8].

Oxygen Storage Capacity (OSC). Oxygen storage capacity (OSC) measurements were carried out in a micro-reactor coupled to a quadrupole mass spectrometer (Balzers, Omnistar). The samples were reduced under H_2 at 500°C for 1h and heated to 800°C in flowing He. Then, the samples were cooled to 650°C and a 5%O_2/He mixture was passed through the catalyst until the oxygen uptake was finished. The reactor was purged with He and the dead volume was obtained by switching the gas to the 5%O_2/He mixture. Finally, N_2 pulses were injected in order to calculate the amount of oxygen consumed on the catalysts taking into account a previous calibration of the mass spectrometer.

Temperature Programmed Superficial Reaction (TPSR). Temperature Programmed Surface Reaction (TPSR) experiments were performed in the same apparatus used for TPR. After reduction at 500°C under H_2 for 1 h , the sample (300 mg) was purged in He at 800°C for 30 min, and cooled to room temperature. Then the sample was submitted to a flow of CH_4/O_2/He (2:1:27) at 30 cm^3/min while the temperature was raised up to 800°C at a heating rate of 20 K/min.

Partial Oxidation of Methane. Reaction was performed in a quartz reactor at atmospheric pressure. Prior to reaction, the catalyst was reduced under H_2 at 500°C for 1h and then heated to 800°C under N_2. The reaction was carried out at 800°C and WHSV = 523 h^{-1} over all catalysts. A reactant mixture with CH_4:O_2 ratio of 2:1was used with a flow rate of 100 cm^3/min. The exit gases were analyzed using a gas chromatograph (Agilent 6890) equipped with a thermal conductivity detector and a CP-carboplot column (Chrompack).

Results and Discussion

Oxygen storage capacity (OSC) results for the several catalysts are presented on Table 1. Pt/Al_2O_3 and Pt/Y_2O_3 catalysts have not showed any OSC uptakes, while for Pt/ZrO_2 e Pt/CeO_2 ppt the values were quite low. Pt/CeO_2 catalyst was the only catalyst that presented a considerable OSC uptake. Several studies reported that cerium oxide has a very high oxygen exchange capacity[9,10]. This capacity is associated to the ability of cerium to act as an oxygen buffer by storing/releasing O_2 due to the Ce^{4+}/Ce^{3+} redox couple[9].

Table 1. Oxygen Uptakes of Pt catalysts

Catalysts	O_2 Uptake (μmol/g_{cat})
Pt/Al_2O_3	0
Pt/ZrO_2	9
Pt/CeO_2	194
Pt/Y_2O_3	0
Pt/CeO_2 ppt	18

The Temperature Programmed Superficial Reaction results indicated different mechanisms for Pt/CeO_2 and Pt/Y_2O_3 catalysts. Pt/Al_2O_3, Pt/ZrO_2, Pt/CeO_2 and Pt/CeO_2 ppt catalysts presented TPSR profiles consistent to the indirect mechanism. Figure 1 presents a representative profile for Pt/CeO_2. For temperatures between (300°C and 400°C) platinum is covered with oxygen and the catalyst is active for total oxidation of methane to carbon dioxide and water. After this step, the catalyst is active for steam and CO_2 reforming of methane, forming the synthesis gas.

The TPSR profile for Pt/Y_2O_3 is shown in Figure 2. The reaction starts at 480°C, yielding H_2, CO, H_2O and CO_2 as products. H_2O is not consumed indicating there is not a steam reforming step for this catalyst. CO_2 formation is consumed at higher temperatures indicating a additional dry reforming reaction. .

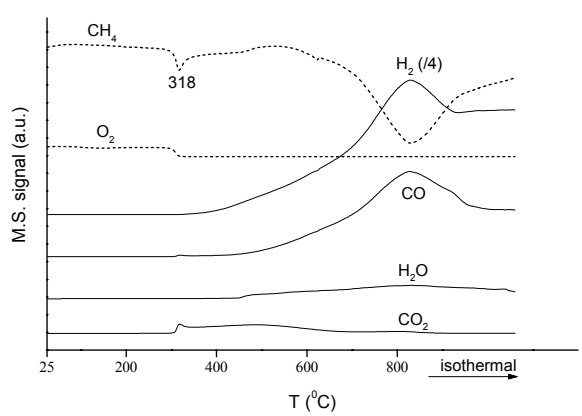

Figure 1. Temperature Programmed Superficial Reaction of Pt/CeO_2 catalyst.

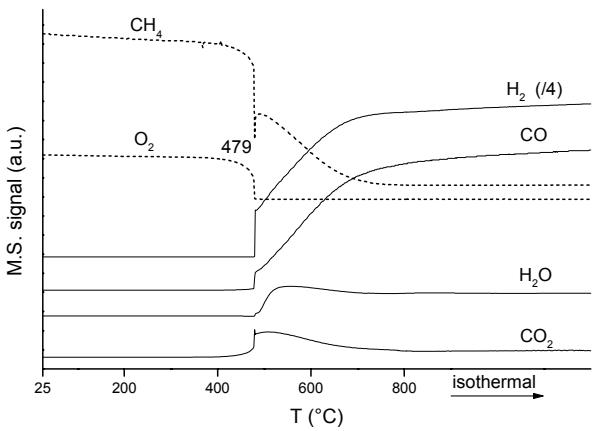

Figure 2. Temperature Programmed Superficial Reaction of Pt/Y_2O_3 catalyst.

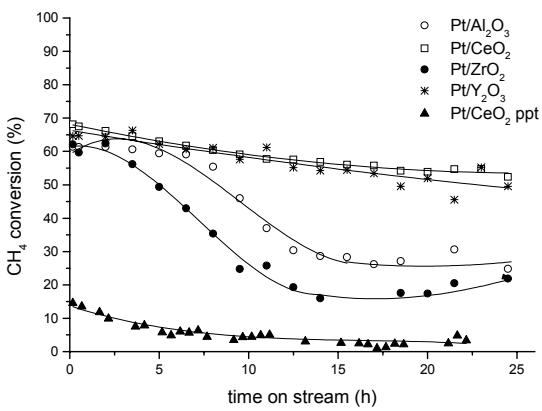

Figure 3. Methane conversion on partial oxidation of methane versus time on stream at 800°C and CH_4:O_2=2:1. (WHSV = 523 h^{-1})

Figure 3 shows the methane partial oxidation results for the several catalyts. For the catalysts that followed the indirect mechanism, Pt/Al_2O_3 and Pt/ZrO_2 presented high initial conversions but deactivated during time on stream. Pt/CeO_2 ppt was neither active nor stable. On the other hand Pt/CeO_2 was quite active and stable during the time of reaction. This result was explained by the high oxygen storage capacity of CeO_2 that promotes the removal of carbon from the surface of catalyst. First, CH_4 decomposes on the metal particle, resulting in the formation of carbon and hydrogen. Carbon formed can partially reduce the support near the metal particles. Then, on the second step of the reaction, CO_2 dissociates on the support followed by the formation of CO and O_2 which can reoxidize the support.

Pt/Y_2O_3 presented a high initial conversion, and was as stable as Pt/CeO_2. For Pt/Y_2O_3, the stability cannot be explained by the same mechanism of Pt/CeO_2 and Pt/Y_2O_3 has not shown any OSC uptake. This stability is related to the change of mechanism, when Y_2O_3 is used as support. When yttria-zirconia was evaluated in the partial oxidation of methane, a direct mechanism was also observed[6], with a Mars van Krevelen type mechanism being proposed.

Figure 4 shows the variation of the selectivity to CO for the several catalysts. The selectivity to CO decreased as the conversion decreased for the catalysts that showed the indirect mechanism, as the carbon formation suppressed the consequent reforming of methane with carbon dioxide. Pt/CeO_2 and Pt/Y_2O_3 catalysts presented similar CO selectivities that were not affected during the course of the reaction.

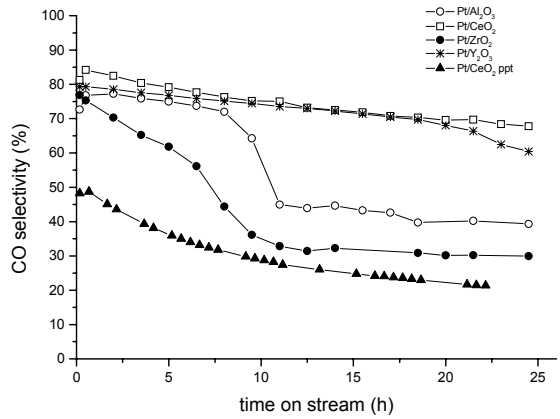

Figure 5. Selectivity towards CO versus time on stream at 800°C and CH_4:O_2 = 2:1. (WHSV = 523 h^{-1})

Conclusions

For Pt/Al_2O_3, Pt/ZrO_2 and Pt/CeO_2, temperature programmed surface reaction (TPSR) studies showed partial oxidation of methane comprehends two steps: combustion of methane and CO2 and steam reforming of unreacted methane, while for Pt/Y2O3 a direct mechanism was observed. Oxygen Storage Capacity (OSC) evaluated the reducibility and oxygen transfer capacity of the catalysts. Pt/CeO2 catalyst showed the highest stability on partial oxidation. The results were explained by the higher reducibility and oxygen storage/release capacity which allowed a continuous removal of carbonaceous deposits from the active sites, favoring the stability of the catalyst. For Pt/Al2O3 and Pt/ZrO2 catalysts the increase of carbon deposits around or near the metal particle inhibits the CO2 dissociation on CO2 reforming of methane. Pt/Y_2O_3 was active for partial oxidation of methane and the stability was explained by the change in the reaction mechanism, with the participation of a lattice oxygen in a Mars Van Krevelen Mechanism.

Acknowledgement. Financial support from CNPq, Finep (CT-PETRO), Faperj and Petrobras is gratefully acknowledged.

References

(1) Torniainen, P.M.; Chu, X.; Schmidt, L. D. *J.Catal.* 1994 , 146, 1.
(2) Dissanayake, D.; Rosynek, M. P.; Kharas, K.C.C.; Lunsford, J. H. *J.Catal*,. **1991**, 132, 117.
(3) Vernon, P.D.F.; Green, M.L.H; Cheetham, A.K.; Ashcroft, A.T. *Catal. Lett.*, **1990**, 6, 181.
(4) Boucouvalas, Y.; Zhang. Z.; Verykios, X. E. *Catal. Lett.* **1996**, 40, 1989.
(5) Lemonidou, A. A.; Stambouli, A.E.; Tjatjopoulos, G. J., Vasalos, I.A. *Catal. Lett.*, **1997**, 43, 235.
(6) Steghuis, A.G.; van Ommen, J.G.; Lercher, J.A. *Catal. Today*, **1998**, 46, 91.
(7) Hori, C. E.; Permana, H.; Simon Ng, K.Y.; Brenner, A.; More, K.; Rahmoeller, K.M.; Belton, D. *Appl. Catal. Envir. B*, **1998**, 16, 105.
(8) Mattos, L.V.; Oliveira, E.R.; Resende, P.D.; Noronha, F.B.; Passos, F.B., to be published in *Catalysis Today*.
(9) Kaspar, J.; Fornasiero, P.; Graziani, M. *Catal. Today*, **1999**, 50, 285.
(10) Yao, M.H.; Baird, R.J.; Kunz, F.W.; Hoost, T.E. *J. Catal*., **1997**, 166, 67.

METHANOL STEAM REFORMIMG OVER NITRIDE BASED CATALYSTS

Shyamal K. Bej, Easwar S. Ranganathan and Levi T. Thompson

Department of Chemical Engineering, University of Michigan, Ann Arbor, MI-48109

Introduction

Methanol is emerging as a potential fuel for the production of hydrogen for fuel cell applications. Hydrogen is easily extracted from methanol through the steam reforming reaction. This reaction takes place in two steps. The first stage is the endothermic decomposition of methanol into CO and H_2 followed by the exothermic water gas shift reaction.

$$CH_3OH \longrightarrow CO + 2H_2$$
$$CO + H_2O \longrightarrow CO_2 + H_2$$

The concentration of CO and CO_2 in the outlet gas depends on the water gas shift activity of the catalysts. The Cu-Zn-Al catalyst is commonly used for this reaction. However, it has number of limitations considering vehicular applications. For example, Cu-Zn-Al catalysts are very sensitive to the reduction procedures and the transient conditions typical of vehicular applications. Moreover, it loses its activity slowly upon frequent exposure to condensed water. Membrane based separation processes are gaining importance to produce pure H_2 from mixtures of H_2, CO_2 and CO. Generally, the membrane based H_2 separation processes are carried out in the temperature range of 300–350 °C. For use in conjunction with membranes, the methanol steam reforming catalyst must be active and stable in this temperature range. Presently available Cu-Zn-Al catalysts are not stable at temperatures higher than approximately 300 °C.

There is growing interest in the development of better methanol reforming catalysts. In this work, we report the performance of high surface area Mo_2N based formulations. Since early transition metal carbides and nitrides have been reported to be good catalysts for water gas shift reaction, it is expected that these materials would also be very active for the methanol steam reforming reaction[1]. The results obtained for the Mo_2N based catalysts were compared with those for a commercial Cu-Zn-Al catalyst.

Experimental

High surface area Mo_2N based catalysts were prepared by the temperature programmed reaction method. Details regarding synthesis of the catalyst are given elsewhere[2, 3]. In brief, about 1.5 g of ammonium paramolybdate was placed in a quartz reactor and heated in a programmed manner in presence of ammonia. The temperature program was defined based on the results of a thermogravimetric analysis experiment. The Cu-Zn-Al catalyst was obtained from Sud Chemie Ltd. The BET surface area of the Mo_2N based catalysts were typically 130 m^2/g while that of the Cu-Zn-Al was 60 m^2/g.

The methanol steam reforming experiments were performed using a 4 mm ID quartz reactor. A mixture of methanol and water in appropriate proportions was pumped using a HPLC pump. Nitrogen was used as a carrier gas. Analysis of the effluents of the reactor was performed with an on-line gas chromatograph (HP 5890) equipped with a TCD and Carboxen-1000 column.

Before measuring the catalytic activity, the Mo_2N based catalyst was reduced at 480 °C for 4 hrs using a mixture of 15% CH_4 in H_2. The Cu-Zn-Al catalyst was reduced at 200 °C for 4 hrs using a mixture of 4% hydrogen in nitrogen. The catalytic activity measurements were conducted at 230-330 °C. The higher temperature limit was selected to be consistent with operating temperatures for membrane reactors. Experiments were conducted at methanol to water molar ratios of 1:1 to 1:3.

Results and Discussion

Low temperature methanol steam reforming:

Methanol conversion rates and selectivities towards CO_2 for selected catalysts at 230 °C and a methanol to water molar ratio of 1:1 are shown in **Figure 1**. The methanol conversion was limited to ~25 mol%. The methanol conversion rate for the Mo_2N based catalyst was comparable to that for the Cu-Zn-Al catalyst, however, the selectivity was lower.

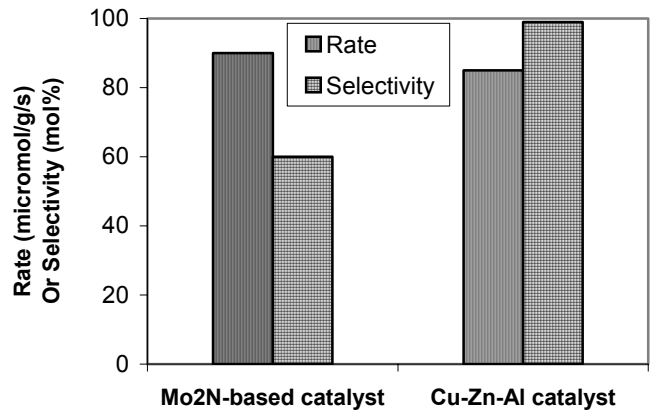

Figure 1. Methanol conversion rate and CO_2 selectivity for Mo_2N based and Cu-Zn-Al catalysts at 230 °C and a methanol:H_2O molar ratio of 1:1.

Since the selectivity toward CO_2 for the Mo_2N based catalyst was low, the methanol to water molar ratio was varied in order to understand its role on CO_2 selectivity. The results are shown in **Figure 2**. Again, the conversions were limited to ~ 25 mol%.

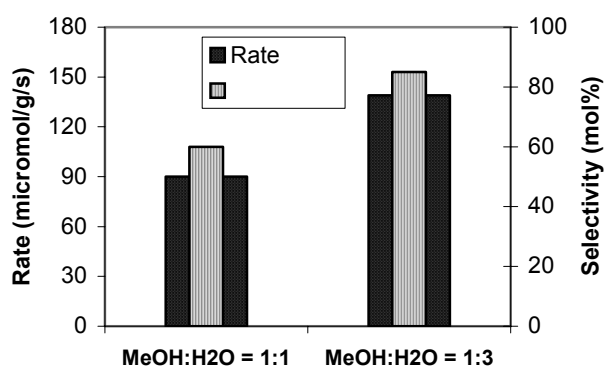

Figure 2. Effect of methanol to water molar ratio on methanol conversion rate and CO_2 selectivity for Mo_2N based catalyst at 230 °C.

The higher concentration of water increased the rate of methanol conversion and CO_2 selectivity significantly. A comparison of the results shown in **Figures 1 and 2** suggests that the surface of the Mo_2N based catalyst had a lower affinity for water as compared to that of the Cu-Zn-Al catalyst. Therefore, a relatively higher concentration of water was necessary to achieve high selectivities.

Experiments were also conducted over the Mo_2N based catalyst at methanol conversions near 60 mol% to assess the effect of lower methanol partial pressures on the activity and CO_2 selectivity. The temperature and the methanol to water molar ratio were kept constant at 230 °C and 1:1, respectively. The results are compared with those obtained at lower conversions. As the conversion was increased, the rate decreased from 90 to 50 µmol/g/s. This is expected for a reaction having a positive dependency on the partial pressure of the reactant (in this case on the partial pressure of methanol).

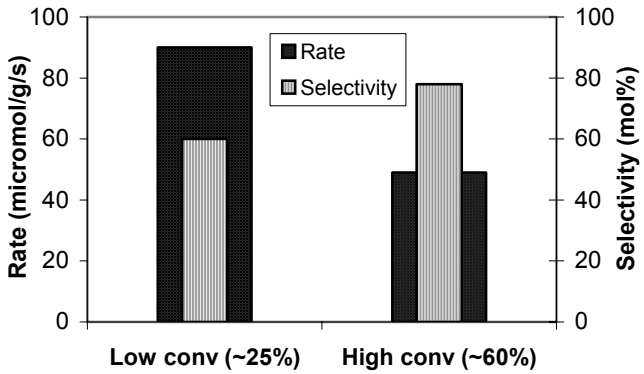

Figure 3. Methanol conversion rate and CO_2 selectivity over Mo_2N based catalyst at low and high conversion at a temperature of 230 °C and a methanol to water molar ratio of 1:1.

The CO_2 selectivity increased on increasing the conversion. Two reasons could explain this observation. First, the longer CO contact time with the catalyst could produce more CO_2. However, as the contact time was increased, more CO was also generated from methanol. The average contact times of CO with the catalyst were calculated and found to be in the similar range for both the case of low and high conversions. The second and possibly the most plausible explanation is that methanol competed with CO for active sites. At high conversions, the partial pressure of methanol was lower and as a result more sites were available for the adsorption and reaction of CO.

High temperature methanol steam reforming:

The rates and selectivities as a function of time for the Mo_2N based formulation at a temperature of 330 °C and a methanol to water molar ratio of 1:1 are compared with those for the Cu-Zn-Al catalyst in Figure 2. The initial methanol conversions for both the catalysts were ~75 mol%. For the Mo_2N based catalyst, the activity decreased during the first 5 hrs on stream, however, after this period the change in activity was not very significant. On the other hand, the activity of the Cu-Zn-Al catalyst decreased sharply during the initial 8 hrs. In addition, this catalyst deactivated slowly beyond this period of initial deactivation. The CO_2 selectivity for the Mo_2N based catalyst did not change significant and was about 30 mol% after 12 hrs, whereas selectivity for the Cu-Zn-Al catalyst was nearly 100% and steady. The lower selectivity toward CO_2 for the Mo_2N based catalyst may not be a problem for membrane based systems.

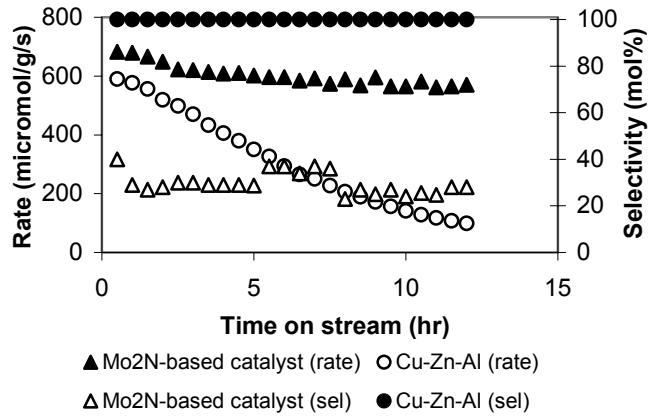

Figure 4. Time on stream methanol conversion rate and CO_2 selectivity over Mo_2N based catalyst and Cu-Zn-Al catalyst at 330 °C and at a MeOH:H_2O molar ratio of 1:1.

Conclusions

The activity for the Mo_2N based catalyst was comparable with that of the Cu-Zn-Al catalyst for low temperature methanol steam reforming reaction. However, the selectivity towards CO_2 was lower as compared to that of the Cu-Zn-Al catalyst. At higher temperature, the pseudo-steady state rate for methanol conversion for the MO_2N based formulation was about fives time than that of the Cu-Zn-Al catalyst.

Acknowledgement. The authors would like to acknowledge financial support from the Osram Sylvania.

References

(1) Patt, J.; Moon, D. J.; Phillips, C.; and Thompson, L. T. *Catal. Letters* **2000**, 65, 193.
(2) Neylon, M. K.; Kwon, H. H.; Choi, S.; Curry, K. E.; and Thompson, L. T. *Appl. Catal.A: General* **1999**, 183, 253.
(3) Neylon, M. K.; Bej, S. K.; Bennet, C. A.; Thompson, L. T. *Appl. Catal. A: General* **2002**, 232, 13.

NON-NOBLE METAL WATER-GAS SHIFT CATALYSTS FOR AUTOMOTIVE FUEL CELL APPLICATIONS

Valery D. Sokolovskii, Jeffrey M. Zalc, Damodara Poojary, Tek Ho, Douglas J. Taube, Grigoriy Malukhin, and Ralph A. Dalla Betta

Catalytica Energy Systems
430 Ferguson Drive
Mountain View, CA 94043

Introduction

In light of the distribution and storage issues associated with hydrogen, on-board fuel processing is the likely route of H_2 delivery for PEM fuel cells in automotive applications. Generation of a hydrogen-rich stream from a gasoline feed is achieved by steam reforming (SR) or autothermal reforming (ATR) with the resulting reformate containing about 10 mole % carbon monoxide. The CO level in the fuel cell feed must be less than 10 ppmv to prevent irreversible poisoning of the anode electrocatalyst. This reduction in CO can be accomplished by sequential water-gas shift (WGS) and preferential oxidation (PrOx) reactors.

The target for the WGS unit is to convert 90% of the carbon monoxide via the reaction $CO + H_2O = CO_2 + H_2$. Although high temperatures favor high catalytic activity, the equilibrium level of CO conversion decreases with increasing temperature. A viable water-gas shift catalyst must be highly active at temperatures around 250-300ºC and have a useful lifetime of 2000-5000 hours. In addition, the catalyst must be non-pyrophoric and not require long or high temperature *in-situ* pre-reduction. It is widely acknowledged that the WGS unit poses the greatest technical challenge to the development of a commercial fuel processing system.

Previous work by our group demonstrated that precious metal/ceria WGS catalysts possessed low activity, had poor durability, and would result in excessive cost of the WGS unit[1]. The poor catalyst stability appeared to be due to the high hydrogen concentration in the reactant stream. Other researchers have recently shown that Pt-CO interactions are affected by the extent of ceria reduction[2]. Although addition of a small concentration of oxygen to the reactant feed stream may help stabilize the catalyst activity, precious metal costs would still make such catalysts impractical even if there were no catalyst deactivation, considering the long-term Department of Energy goal that the entire fuel processor have a cost of $10/kW, or $500. The use of even small amounts of precious metals is incompatible with meeting this objective. Consequently, efforts have been focused on developing non-noble metal water-gas shift catalysts suitable for use in an automotive fuel processor.

Experimental

A series of non-noble metal catalyst materials were formulated using Cu as the active component with Cu loading between 6 and 12 wt%. Catalysts were tested in a dilute-bed reactor using an approximate feed stream molar composition of 46.5% H_2, 11% CO, 7.5% CO_2, and 35% H_2O. Experiments were performed at temperatures of 230-260ºC with gas hourly space velocities of 200,000-300,000 hr^{-1}. Effluent gas was analyzed by gas chromatography to determine CO conversion. Deactivation studies were performed on promising materials by monitoring CO conversion over several hundred hours.

Catalysts were also characterized using XRD and N_2O adsorption. XRD was performed using a XDS 2000 Powder X-ray diffractometer on both the as prepared catalyst and catalyst samples after WGS testing followed by inert gas purge and passivation in air. Cu dispersion was measured by N_2O adsorption on Micrometrics AutoChem 2910 using a pulse adsorption technique. The catalyst sample was reduced in hydrogen at 250ºC, then hydrogen was replaced by Ar, cooled to 85ºC, and then pulses of N_2O added to the argon flow over the catalyst sample. Adsorption was monitored by mass spectrometry, recording intensity of molecular mass of N_2O. The amount of Cu on the catalyst surface was calculated based on the assumed stoichiometry:

$$N_2O + 2Cu(s) = Cu(s)_2O + N_2.$$

Results and Discussion

These developed catalysts do not require not require a special or extensive reduction. Typical conversion versus time-on-stream data are shown in Fig. 1 for a fresh catalyst. The CO conversion rises slightly at short times, apparently due to rapid *in-situ* reduction of the catalyst by the reaction mixture, and then stabilizes.

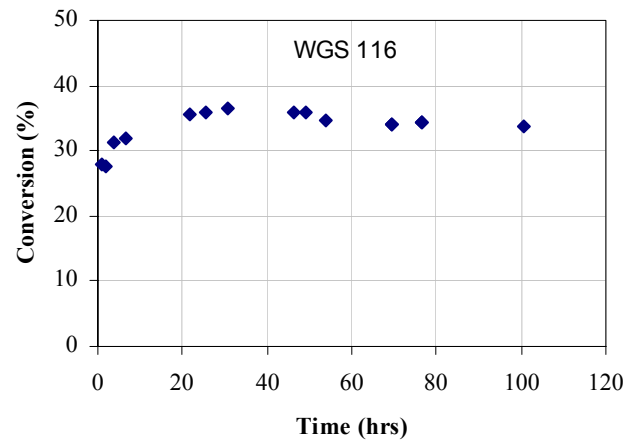

Figure 1. Data for CO conversion versus time-on-stream are shown for the start-up of one of our catalysts operated at 248ºC and 275,000 hr^{-1}. The molar composition of the feed is 11% CO, 7.5% CO_2, 46.6% H_2, 34.9% H_2O.

Also, these catalysts are air-tolerant, which is a beneficial characteristic because it makes material handling easier. Conversion versus time-on-stream data are shown in Fig. 2 for normal operation and after air exposure.

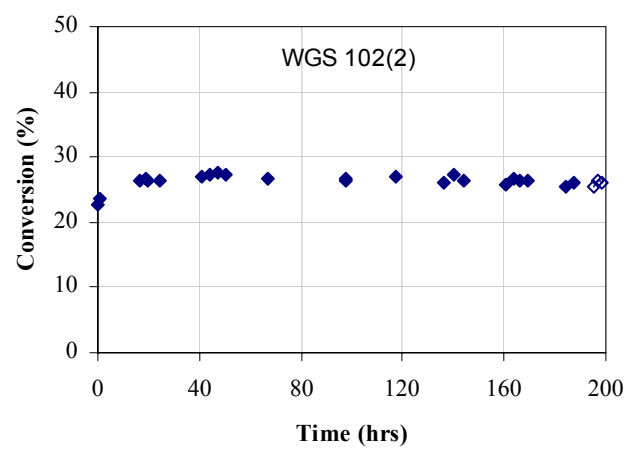

Figure 2. The effect of air exposure on the catalyst performance is illustrated for operation at 246ºC and 275,000 hr^{-1}. Feed composition is the same as in Fig. 1 and open symbols represent data recorded after exposure to air.

For the results shown in Fig. 2, the catalyst was tested under normal reaction conditions for almost 200 hours, at which time the catalyst was purged with inert gas (N_2), exposed to air, purged again with inert, and then the reaction mixture was re-started. The data collected after this air exposure reveal negligible influence on activity. The addition of a small amount of air into the reaction mixture also did not result in catalyst deactivation. Fig. 3 shows conversion versus time-on-stream data for a case in which 1% air was added to the reaction mixture.

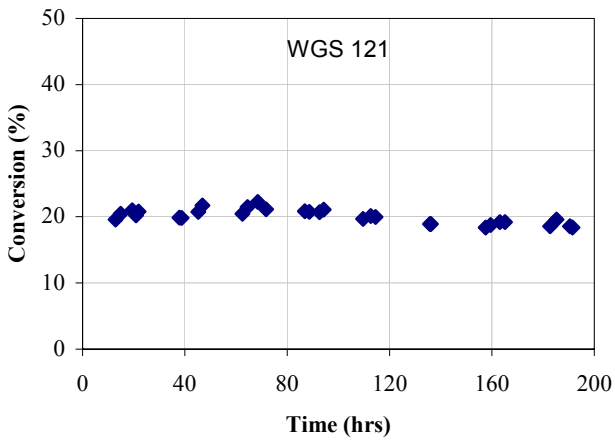

Figure 3. Data for CO conversion versus time-on-stream are shown for operation at 255ºC and 279,000 hr^{-1}. Here, the reaction mixture consisted of 1% air, 10.9% CO, 7.4% CO_2, 46.1% H_2, and 34.6% H_2O.

It can be seen that the presence of air did not harm catalyst performance. As before, the activity increased slightly during the first 100 hours on-stream, beyond which a very slight decrease in activity was observed.

XRD characterization of fresh and used catalyst revealed that freshly prepared materials contain copper in the form of CuO, while after exposure to the reaction mixture and subsequent purge with inert and passivation in air, the XRD analysis showed the copper exists as Cu metal. The reduced catalyst can be re-oxidized to yield results almost identical to those of the fresh material. Dispersion of Cu on the fresh and used catalysts was determined by N_2O decomposition and results are shown in Table 1.

Table 1. Copper Dispersion of Fresh and Used Catalysts

Catalyst	Cu dispersion (%)
WGS 80, fresh	8.2
WGS 80, used	8.0
WGS 89, fresh	10.7
WGS 89, used	11.6
WGS 92, fresh	5.8
WGS 92, used	6.2
WGS 94, fresh	9.7
WGS 94, used	9.0

To better assess catalyst durability, a long term test was run. Results are shown in Fig. 4.

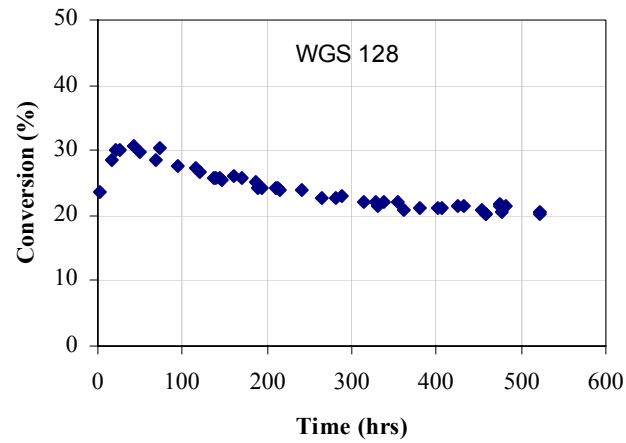

Figure 4. Data for CO conversion versus time-on-stream are shown for one of our non-noble metal catalysts operated at 245ºC and 275,000 hr^{-1}. Feed composition the same as in Fig.1.

The data indicate that the catalyst activity becomes nearly constant after about 350 hours. The activity at the end of this durability run corresponds to approximately 5 kg of WGS catalyst for a 50 kWe fuel processor operating with a CO conversion of 90%.

Conclusions

A class of Cu-based water-gas shift catalysts have been developed that appear very promising for use in automotive fuel processing applications. These catalysts are non-pyrophoric and do not require long or special *in situ* pre-reduction; their relatively low metal content allows washcoating as well, which is desirable since the use of packed beds in automotive applications can lead to pellet abrasion and poor long-term performance. These catalysts also exhibit rather good stability over the course of a 500-hr test and their activities translate into catalyst requirements of roughly 5 kg for a 50 kWe fuel processing system. The lack of any precious metal components also leads to low materials and preparation costs.

Acknowledgement

This work was supported by the U.S. Department of Energy, under contract DE-FC04-01AL67605.

References

(1) Zalc, J.M.; Sokolovskii, V.; and Löffler, D.G. *J. Catal.*, **2002**, 206, 169-171.
(2) Mullins, D.R.; and Zhang, K.Z. *Surf. Science*, **2002**, 513, 163-173.

ON-SITE PRODUCTION OF HYDROGEN FROM HYDROCARBON FUELS WITH MINIMAL GREENHOUSE GAS EMISSIONS

Nazim Z. Muradov

Florida Solar Energy Center, University of Central Florida,
1679 Clearlake Road, Cocoa, FL 32922

Introduction

Fossil fuel based power systems are major producers of greenhouse gas (primarily, CO_2) emissions, which are linked to the global climate change and other serious environmental and health-related problems. Hydrogen is seen by many as an answer to these environmental problems; however, the main question is how to produce hydrogen from fossil fuels without CO_2 emissions. Special devices, called "fuel reformers" are being developed for extracting hydrogen from different hydrogen-containing fuels, e.g., natural gas (NG), gasoline, methanol, etc. Conventional fuel reformers are based on methane steam reforming (MSR), partial oxidation (POx) and autothermal reforming (ATR) processes. Although being energy efficient, these reformers are complex, multi-stage and expensive. They include several (3-4) catalytic stages, which make them prone to catalyst deactivation/replacement problems. POx- and ATR-based reformers produce low quality hydrogen gas ($[H_2]$< 40 v%). Furthermore, the conventional reformers produce large amounts of CO_2 emissions, which significantly diminish an environmental appeal of hydrogen-based energy systems. CO_2 sequestration (underground or under the ocean) is envisioned by many as a potential solution to this environmental problem; however, it is better suited to large centralized hydrogen plants. Removing CO_2 from relatively small sources, collecting it, transporting it, and sequestering it are daunting tasks.[1]

One alternative to conventional fuel reforming technologies is to produce hydrogen via single-step thermal (or thermocatalytic) decomposition of hydrocarbon feedstock (e.g., NG):

$$CH_4 \rightarrow C + 2H_2 \qquad \Delta H^o = 75.6 \text{ kJ/mol } (CH_4)$$

No carbon oxides are formed during the process, due to the absence of oxidants (e.g., H_2O and/or O_2) in the reactor. Methane decomposition is a moderately endothermic reaction. The energy input requirements (per mole of H_2) for the decomposition process is significantly less than that of MSR (37.5 and 63.3 kJ/mol H_2, respectively).

It is well known that the use of transition metal catalysts (e.g., Ni, Fe, Co) significantly reduces the maximum temperature of the methane decomposition process. However, there is a catalyst deactivation problem associated with the carbon build-up on the catalyst surface. The fuel reformers have been developed where carbon produced during hydrocarbon decomposition stage was combusted, providing heat for the endothermic reaction.[2] This, however, decreases the overall energy efficiency of the process and results in the production of large amounts of CO_2 (comparable with that of conventional reformers). The main objective of this work is to develop an efficient and economical process for the on-site (decentralized) production of hydrogen with minimal CO_2 emissions.

Experimental

Methane (99.99 v.%, Air Products and Chemicals, Inc.) and propane (99.0 v.%, Praxair) were used without further purification. Samples of activated carbons were obtained from Barneby Sutcliffe Corp. and NORIT Americas. Cabot Corp. provided different samples of carbon black. All carbon samples were used in the form of fine powder (<100μm). The experimental set-up for hydrocarbon fuel decomposition consists of 3 main subsystems: (1) a fluidized bed thermocatalytic reactor (with temperature-controlled electric heater and pre-heater), (2) a hydrocarbon metering and delivering sub-system, and (3) an analytical sub-system. The catalytic reactors were made out of a fused quartz in order to reduce the effect of the reactor material on the rate of hydrocarbon decomposition. The analysis of the products of hydrocarbon decomposition was performed gas chromatographically: SRI- 8610A (a thermal conductivity detector, Ar carrier gas, a silica gel column, temperature programming from 25 to 180°C), and Varian-3400, flame ionization detector, He-carrier gas, stationary phase- Hysep D_B.

Results and Discussion

The concept is based on thermocatalytic decomposition of methane or other hydrocarbons using carbon-based catalysts in an air/water-free environment. This results in the following advantages: (i) no concurrent CO/CO_2 production and, hence, no need for water gas shift, preferential oxidation, and other stages, (ii) no catalyst deactivation due to sulfur poisoning, (iii) production of a valuable byproduct carbon, and (iv) significant reduction in CO_2 emissions. The detailed information on the catalytic properties of carbon catalysts for methane decomposition reaction has been published elsewhere.[3]

Fig. 1 depicts kinetic curves of methane and methane-propane (3:1 by volume) decomposition over carbon black (BP2000) catalyst using fluidized bed reactor.

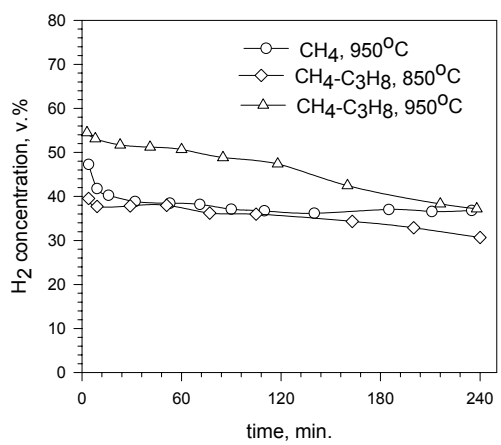

Figure 1. Methane and methane-propane (3:1 by volume) decomposition over carbon black (BP2000) catalyst using fluidized bed reactor

It can be seen that H_2 concentration in the effluent gas gradually decreases which can be explained in terms of carbon catalyst deactivation due to the deposition of catalytically inactive form of carbon and the reduction in catalytic surface area. It was determined earlier that carbon particulates produced by thermal decomposition of different hydrocarbons exhibit dissimilar catalytic activities in methane decomposition reaction.[4] The catalytic activity of carbons produced from different hydrocarbons can be arranged in the following order: naphthalene > benzene > ethylene > propane > methane. Thus, carbon produced from methane is least catalytically active in methane decomposition reaction, which agrees with the above experiment. On the other hand, the enhanced catalytic activity of carbon particles produced from ethylene and other unsaturated and aromatic hydrocarbons could potentially be used for the accelerating

methane decomposition process (via in-situ generation of catalytically active carbon species).

In principle, the surface area of carbon particulates can be increased via their surface treatment with activating agents at elevated temperatures. High temperature steam, CO_2 or their mixtures are the most common activating agents in the production of activating carbons from a variety of carbonaceous materials. This approach was applied to increase the surface area and, consequently, catalytic activity of carbon particulates in methane decomposition reaction. The deactivated carbon samples (after exposure of a carbon catalyst to methane at 850°C for more than 6 h) were subjected to the treatment by equimolar amounts of steam, steam-CO_2, CO_2 and O_2 (air) at 950°C. The effect of carbon activation on methane decomposition rate is shown in Fig. 2.

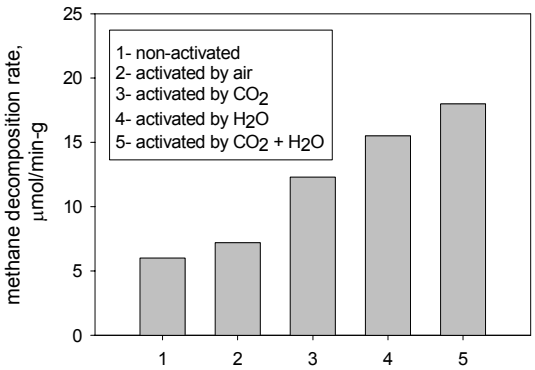

Figure 2. Effect of carbon catalyst activation by different activating agents on methane decomposition rate at 850°C.

It is evident that the treatment of carbon particles with steam and steam-CO_2 (1:1 by volume) mixtures resulted in significant increase in methane decomposition rate. Air exhibited a relatively low carbon activating efficiency.

Fig. 3 depicts a simplified schematic diagram of the proposed TCD process for the decentralized (on-site) production of hydrogen and carbon. A preheated stream of a hydrocarbon feedstock enters the reactor (1) where it is pyrolyzed at the temperature range of 800-900°C, and the pressure of 1-10 atm over the fluidized bed of catalytically active carbon particulates. The resulting hydrogen-containing gas is directed to a gas separation unit (e.g., a polymeric membrane, or pressure swing adsorption system) (4), where hydrogen gas with the purity of >99.0 v.% is separated from the gaseous stream and directed to a hydrogen end-user. Non-permeate gas is recycled back to the reactor (1). Non-permeate gas is enriched with ethane, propane, ethylene and other high hydrocarbons that upon decomposition produce carbon particles with enhanced catalytic activity (compared to carbon produced from methane). Carbon product is continuously withdrawn from the reactor, and portion of it is ground in a grinder (3), heated in a heater (2) and returned to the reactor (1). The activation of carbon particles with steam and CO_2 is accomplished in the heater (2) where temperature conditions (900-1000°C) are suitable for the activation process. Thus, the above scheme allows to apply both modes of catalyst activation (i.e., in-situ generation of catalytically active carbon species and increase in catalyst surface area) which contributes to the improvement in the process sustainability.

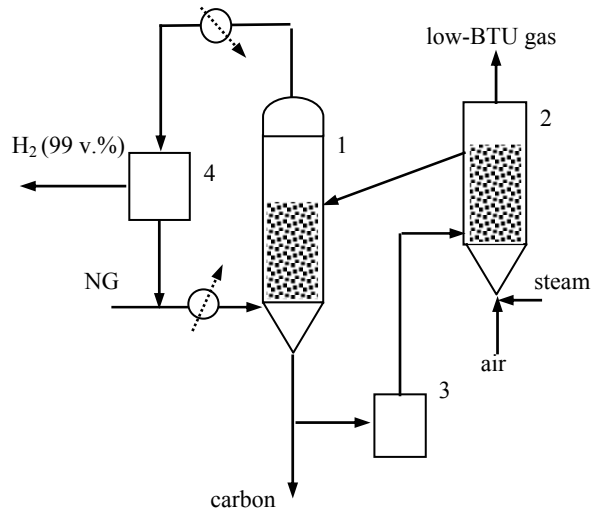

Figure 3. Schematic diagram of the process for on-site production of hydrogen from natural gas. 1-TCD-reactor, 2- Heater, 3- Grinder, 4- Gas separation unit

Although the TCD process produces certain amount of CO_2 emissions, its quantity is small compared to MSR reformers due to relatively low endothermicity of the process and the lack of energy intensive steam generating and gas conditioning units. It is evident that most of the carbon in the feedstock ends up in the form of carbon. According to Steinberg, the overall net energy efficiencies of TCD and MSR processes become close (58 and 60%, respectively) after accounting for 15% energy loss due to CO_2 sequestration.[4] One should consider that TCD produces a valuable byproduct carbon, whereas, in MSR process 40% of the energy is lost irreversibly due to high endothermicity and CO_2 sequestration. Carbon can be sold, thus, reducing cost of hydrogen production.

Conclusions

The production of hydrogen from renewable energy sources would be an ultimate solution for energy and environmental problems. It is understood, however, that it would take two-three or even more decades before these technologies will come on the stage. Meantime, new technological approaches, such as TCD, could play an important role as transitional technologies bridging the gap between fossil fuel and renewable energy based economies. The technical feasibility of TCD of methane with the production of CO/CO_2-free hydrogen-rich gas and carbon byproduct is demonstrated in this paper.

Acknowledgement. This work is supported by U.S. DOE Hydrogen Program.

References

(1) Ogden, J. *Physics Today*, **2002**, 13, 94
(2) Calahan, M. *Proc. Conf. Power Sources,* **1974,** 26, 181.
(3) Muradov, N. *Catalysis Communications*, **2001**, 2, 89
(4) Muradov, N. *Energy & Fuels*, **1998,** 12, 41
(5) Steinberg, M. *Int. J. Hydrogen Energy*, **1999**, 24, 771

Composite Palladium and Palladium-alloy Membranes for High Temperature Hydrogen Separations

Yi Hua Ma, Erik E. Engwall and Ivan P. Mardilovich

Center for Inorganic Membrane Studies
Department of Chemical Engineering
Worcester Polytechnic Institute
Worcester, MA 01609

Introduction

As we are approaching the era of the hydrogen economy, hydrogen is not only an important industrial chemical but also becoming one of the future's key energy resources. It is expected that the future worldwide demand for hydrogen will increase greatly. Dense composite Pd and Pd/alloy membranes supported on a porous substrate, in particular, porous stainless steel (PSS), are especially suited for high temperature hydrogen separation and membrane reactor applications.

Most early work on hydrogen permeation in palladium involved the use of palladium foils as summarized in detail by Lewis (1). However, there are a number of advantages of using composite palladium membranes supported on porous substrates, in particular, porous stainless steel, over palladium foils and tubes. These advantages include thinner membrane layer, better mechanical strength and higher hydrogen flux. Furthermore, there are additional main advantages for using porous stainless steel (PSS) supports that include the resistance to cracking and the simplicity of module construction. Composite Pd/PSS membranes, welded from both ends with non-porous stainless steel tubes, can be very easily assembled and integrated into a process. Additionally, the thermal expansion coefficient of stainless steel is very close to that of palladium, insuring good mechanical properties of the composite membrane during temperature cycling.

This paper reviews the synthesis by electroless plating and characterization of composite Pd and Pd-alloy with a special emphasis on porous stainless steel (PSS) support, and long-term thermal stability. In addition, the unique features of the controlled in-situ oxidation technique to create an intermetallic diffusion barrier are discussed.

Electroless Plating

The advantages of electroless plating include uniform deposition on complex shapes and large substrate areas, hardness of the deposited film, and very simple equipment. Electroless plating (2) generally consists of pre-treatment of the porous stainless steel (PSS) support, surface activation and plating. The pre-treatment of the PSS support includes complete removal of foreign contaminants (grease, oil, dirt, corrosion products) while surface activation consists of seeding the support surface with palladium nuclei, which during the electroless plating initiate an autocatalytic process of the reduction of a metastable Pd salt complex on the target surface. Electroless plating is carried out at constant temperature with a plating solution typically consisting of a plating agent $(Pd(NH_3)_4)Cl_2H_2O$, stabilizing agent Na_2EDTA, and a reducing agent H_2NNH_2 with NH_4OH for pH adjustment.

One of the problems associated with electroless plating of palladium on porous metal substrates is the intermetallic diffusion of metal elements into the palladium layer at high temperatures causing deterioration of the hydrogen flux. We have developed a unique technology to create an intermediate intermetallic diffusion barrier layer by controlled in-situ oxidation prior to the plating (3). Furthermore, there are added benefits that the intermediate barrier layer also provides surface sites for easy activation and plating as well as improved adhesion (4). Typical Pd/PSS membranes plated by the electroless plating technique with an in-situ barrier layer are shown in Fig.1. Non-porous stainless steel tubes of the same diameter were welded to the membrane tubes on both ends and the white sleeves were used to facilitate the handling of the membranes.

Figure 1. Composite Pd/PSS membranes 1" OD (2.54 cm), Membrane area: 24.7 in^2 (159 cm^2)

Hydrogen Permeation Flux as a Function of Membrane Thickness

Since the permeation of hydrogen through Pd and Pd/alloy is by the solution and diffusion mechanism and is, in most cases, controlled by the diffusion of dissociated hydrogen molecules through the Pd bulk, the hydrogen flux is proportional to the difference of the square root of the pressures, known as the Sievert's law. A typical plot of permeance vs. the difference of the square root of pressure (Sievert's law) is shown in Figure 2 for a membrane of

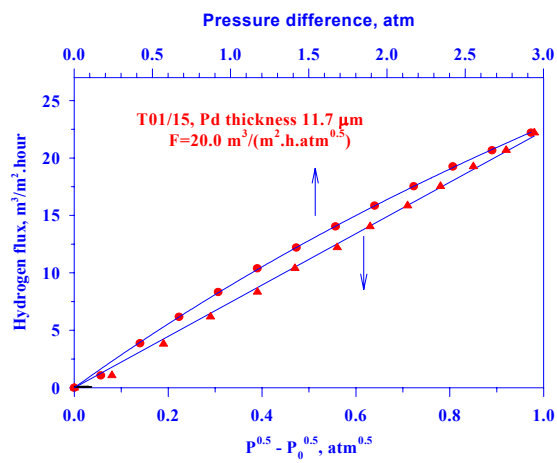

Figure 2. The hydrogen Flux as a function of the difference of the square root of the pressure (Sievert's law) at 350°C)

thickness of 11.7 µm at 350°C. In addition, when the permeation is controlled by the diffusion of hydrogen in the bulk palladium layer, the permeation flux and thus the permeance, is inversely proportional to the membrane thickness. We have performed a systematic study of the permeation of hydrogen through composite Pd/PSS membranes with different Pd layer thickness and showed the inverse relationship between the hydrogen permeance and the Pd layer thickness at 350°C[4]. As shown in Fig. 3, these experimental

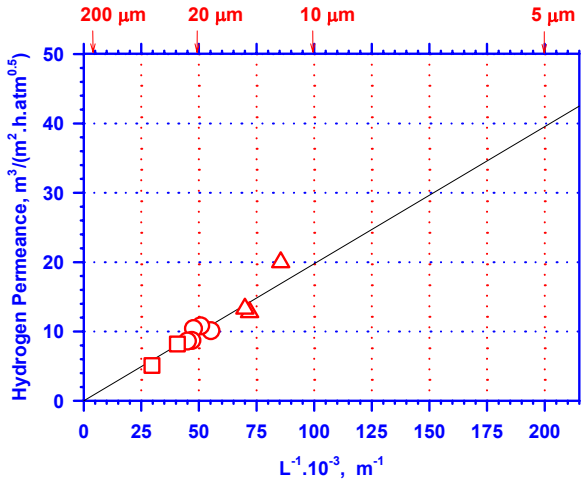

Figure 3. Hydrogen permeance versus reciprocal palladium thickness for a pressure difference of 1 atm and a temperature of 350 ºC. The Pd layer thickness is indicated along the top. The grade of the supports from Mott Metallurgical Corporation were: **squares**-grade 0.5 µm; **circles**-grade 0.2 µm; **triangles**-grade 0.1µm.

results covered the range of the Pd layer thickness between 11.7 µm and 33.8 µm, an almost three-fold difference in membrane thickness. This inverse relationship provides additional evidence that even at such small membrane thickness, the flux was still controlled by the hydrogen permeation through the Pd bulk without any influence by the mass transport at the membrane surface or through the pores of the support.

Palladium Alloys for Improving Hydrogen Permeation Flux and Thermally Stability

It has long been recognized that Pd alloys may have advantages over Pd for use in hydrogen separation and membrane reactor applications. In general, Pd alloys have a reduced critical temperature for the α-β phase transition (1). For example, Pd/Ag alloy membranes may be operated in the presence of H_2 at temperatures below 300ºC without the hydrogen embrittlement observed for pure Pd membranes (6). In some cases, the hydrogen permeability of alloys is greater than that of Pd. This is true for binary palladium alloys with yttrium, cerium, silver, copper and gold for the appropriate compositions as shown in Table 1 based on data from Knapton (7). Several tertiary Pd alloys such as Pd-Ru-In, Pd-Ag-Ru and Pd-Ag-Rh reported to have high hydrogen permeability as well (7, 8) are also included in the table. Finally, some Pd alloys may produce membranes with enhanced chemical resistance. It has been suggested that both the Pd-Cu and Pd-Au systems can be used to produce membranes with enhanced resistance to H_2S (9, 10).

Of the metals listed above for binary palladium alloys, Cu and Ag represent the least expensive alternatives from the standpoint of materials costs. Palladium-silver alloys are attractive because they have good hydrogen permeability relative to pure palladium. In the case of Pd-Ag alloys, the solubility of hydrogen increases with increasing Ag content reaching a maximum at an Ag content between 20-40 wt % (1). However, the diffusivity of hydrogen in Pd-Ag alloys decreases with increasing silver content. The simultaneous changes in solubility and diffusivity result in a maximum in the hydrogen permeability of 1.7 times the permeability of pure palladium, at a silver content of 23 wt % and a temperature of 350 ºC (10). Recently, Roa et al. (11) also reported highest hydrogen permeability for a Pd(60)/Cu(40) alloy membrane on porous ceramic supports.

Table 1. Improvement in hydrogen permeability of various binary Pd alloys at 350 ºC (7, 8)

Alloy Metal	wt % for Maximum Permeability	Normalized Permeability (P_{alloy}/P_{Pd})
Y	10	3.8
Ag	23	1.7
Ce	7.7	1.6
Cu	40	1.1
Au	5	1.1
Ru, In	0.5, 6.0	2.8
Ag, Ru	30, 2	2.2
Ag, Rh	19, 1	2.6
Pure Pd	-	1.0

Palladium-copper alloys are attractive from the standpoint of relatively high permabilities coupled with their enhanced sulfur resistance. In the case of Pd-Cu alloys, the formation of a solid phase with a BCC structure at 40 wt % copper, leads to an increase in the hydrogen diffusivity of two orders of magnitude, and thus a sharp maximum in permeability for this composition (6). More detailed discussion can be found in Ma et al. (12).

Conclusions

Dense composite palladium, especially palladium/alloy, membranes will play an important and essential role in the production of pure hydrogen in the 21st century of hydrogen economy. The use of porous metal as substrates will facilitate the membrane module fabrication and process integration. Many technical issues, such as producing thin membranes with good separation characteristics and long term thermal and mechanical stability, remain to be solved. Further exploration of the use of palladium alloys to increase the hydrogen permeability and at the same time, to enhance the thermal stability can expedite the implementation of these composite membranes into hydrogen production processes.

References

(1) Lewis, F.A., The Palladium Hydrogen System, **1967**, Ac. Press. London.
(2) Mardilovich, P. P., She, Y. and Ma, Y. H., AIChE J, **1998**, 44, 310.
(3) Ma, Y.H., Mardilovich, P. .P. and She, Ying, **2000**, US Patent 6,152,987.
(4) Akis, B. C., Engwall, E. E., Mardilovich, I. P. and Ma, Y. H., **2003**, Fuel Chemistry Preprints, 47(1), the 225th ACS National Meeting, New Orleans, LA, March 23-27, 2003.
(5) Mardilovich, I. P., Engwall, E. E. and Ma, Y. H., Desalination, **2002**, 144(1), 85.
(6) Shu, J., B.P.A. Grandjean, A. Van Neste and Kaliaguine, S., Can. J. Chem. Eng.. **1991**. 69: 1036-1060.
(7) Knapton, A.G.. Plat. Met. Rev., **1977**, 21: 44.
(8) Gryaznov, V.M.. Separation and Purification Methods. **2000**. 29: 171-187
(9) McKinley, D.L. and Nitro, W.Va., **1967**. US patent 3,350,845.
(10) McKinley, D.L. and Nitro, W.Va., **1969**. US patent 3,439,474.
(11) Roa, F., Block, M. J. and Way, J. D., Desalination, **2002**, 144(4), 411.
(12) Ma, Y.H., Mardilovich, I.P. and Engwall, E.E., Annals of the New York Academy of Science, **2002**, In press.

EFFECTS OF THE IN-SITU FORMATION OF AN INTERMETALLIC DIFFUSION BARRIER LAYER ON THE PROPERTIES OF COMPOSITE PALLADIUM MEMBRANES

B. Ceylan Akis, Erik E. Engwall, Ivan P. Mardilovich and Y.H. Ma

Center for Inorganic Membrane Studies
Department of Chemical Engineering
Worcester Polytechnic Institute
Worcester, Massachusetts 01609

Introduction

Composite palladium and palladium/alloy membranes are especially suited for high temperature hydrogen separation and membrane reactor applications. However, when porous metal supports are used at high temperatures, the intermetallic diffusion between metal elements in the substrate and the palladium separation layer causes the hydrogen flux to deteriorate. One way to improve the membrane stability is to create an intermediate intermetallic diffusion barrier layer. This barrier layer can be created by the in-situ controlled oxidation of the substrate prior to plating, developed recently by Ma *et al*. (1). The technique consists of the oxidation of the metal substrate (e.g., porous stainless steel) followed by electroless plating. A detailed description of the technique can be found in Ma *et al*. (1).

The objective of this work was to investigate the effect of oxidation time and temperature on the surface of porous stainless steel (PSS), thus on the thickness of the Pd dense layer and hydrogen flux. Specifically, the effects of the oxidation temperature and time on the pore size and porosity of the porous stainless steel support were systematically investigated. In addition, the effects of the oxidized layer on the surface sties required for activation and plating were studied by scanning electron microscopy (SEM) to provide better understanding of plating mechanisms on the oxidized layer.

Experimental

Electroless plating was used to plate Pd on porous stainless steel supports of Grade 0.5 μm produced by Mott Metallurgical Corporation. Both porous cups and cups welded to non-porous stainless steel tubes were used in the study. The porous stainless steel supports were oxidized in a high temperature furnace at constant temperature. The uniformity of the temperature in the furnace was carefully monitored and controlled. The cups were oxidized at three different temperatures: 400, 600 and 800°C for six hours. An additional cup was oxidized at 400°C for 18 hours to study the effect of the oxidation time. The procedure for cleaning, activation and electroless plating has been described in detail by Mardilovich *et al*. (2). The surface of the support was examined by SEM (AMRAY model 1610).

Results and Discussion

For the PSS supports, a high He flux before plating indicates low resistance to hydrogen permeation. Table 1 shows the mass gains Δm, changes in He flux ΔJ, median pore size D_p and porosity ε of the 0.5 μm grade PSS cups after oxidation at various temperatures. There were no significant changes in porosity and He flux, between the unoxidized blank and the support oxidized at 400°C. Between the oxidation temperatures of 400 °C and 800 °C the pore size and porosity decrease slightly with increasing T_{ox}. However, between the oxidation temperatures of 400°C and 800°C the reduction in He flux was too drastic to be explained by the changes in porosity. This is particularly true for changes observed between 600 and 800°C. As the oxidation temperature was increased, the weight gain increased indicating the formation of more oxide at higher temperatures. The formation of greater quantities of oxide gave a larger resistance to the He permeation.

The oxidation of PSS supports of smaller grades resulted in higher declines in the He flux after oxidation. With a 0.2 μm grade support over 90% reduction in He flux was observed after oxidizing at 800 °C for 4h. The characterization of this membrane showed that the maximum H_2 flux that could be achieved was limited by the reduced support porosity.

Table 1. Flux Decline and % Weight Gain of the Supports After Oxidation.

T_{ox} [°C]	Time [h]	Δm [%]	D_p [μm]	ε	Δ J [%]
25	-	unoxidized	3.9	0.22	0.0
400	6	~0.0	4.1	0.22	0.0
600	6	0.5	3.9	0.21	-10.4
800	6	1.4	3.7	0.20	-73.5
400	18	~0.1	-	-	0.0

Figure 1 shows the scanning electron micrographs of the four PSS cups oxidized at different temperatures for 6h. It can be seen from Figure 1 that higher oxidation temperatures appeared to increase the surface roughness. Figure 2 shows the scanning electron micrographs of the same oxidized cups after 1 hour of the Pd deposition. As shown in the figure, the size of the Pd clusters was bigger on the supports oxidized at higher temperatures. Aggressive oxidation caused enhanced formation of a porous oxide layer which provided more surface area. Furthermore, the oxidized surface appeared to enhance the absorption of $SnCl_2$ and nucleation of Pd seeds during activation and increased the surface roughness for easy attachment of Pd ions during plating.

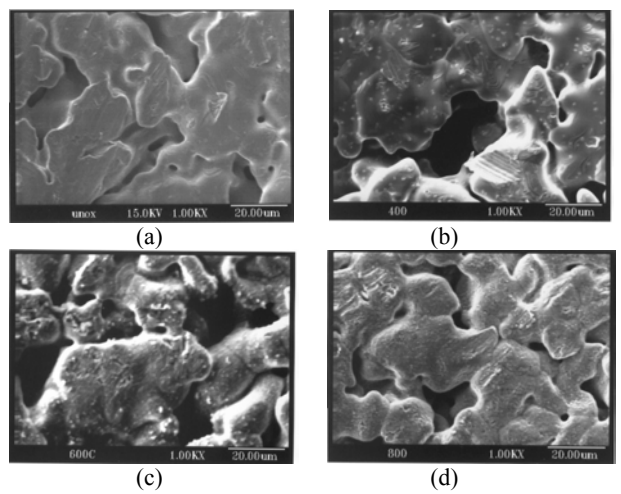

Figure 1. Scanning electron micrographs of PSS cups after oxidation: (a) unoxidized, (b) 400°C, (c) 600°C and (d) 800°C.

Another support was oxidized at 400°C for 18 h to study the effect of longer oxidation time on the surface morphology, thus the microstructure of the Pd layer. The surface morphology and cluster size of Pd deposited on cup5 were almost the same as the one oxidized at 400°C for 4 h. Furthermore, as shown in Table 1, the weight gain and He flux decline also are essentially the same as those of cup2.

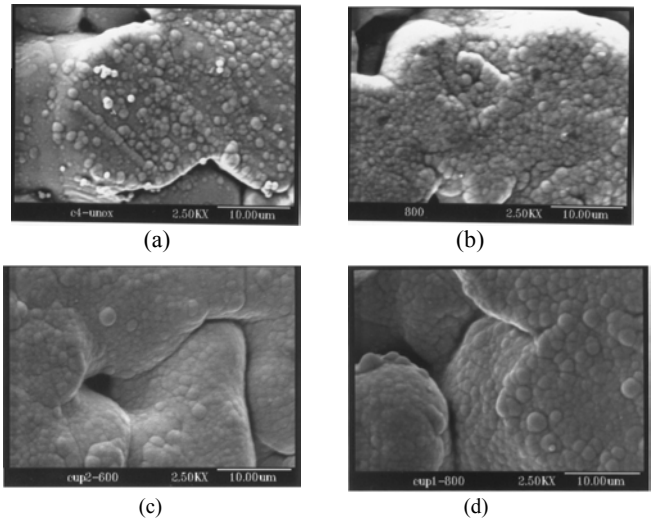

Figure 2. Scanning electron micrographs of oxidized cups after 1 hour Pd plating: (a) unoxidized (1.8μm), (b) 400°C (2.7μm), (c) 600°C (2.8μm) and (d) 800°C (2.54μm). Note: Numbers in the parentheses indicate the Pd layer thickness at the end of one hour plating.

The He flux was used to check if the Pd layer was dense. The membrane is deemed 'dense' when there was no He flux at room temperature under a pressure difference of 1 atm. Three PSS supports welded to nonporous tubes were oxidized at three different temperatures, 400°C, 600°C, 800°C, and electroless-plated with Pd until they were dense. As shown in Figure 3, the He flux declines after oxidation showed similar behavior as the cups shown in Table 1. The final thicknesses of the dense Pd layers were about the same for the supports oxidized at 600 and 800°C and appeared independent of the oxidation temperature as shown in Table 2. The slightly thicker Pd layer for the support oxidized at 400°C appeared to be due to the lower extent of oxidation that provided less active oxide area for absorption and plating.

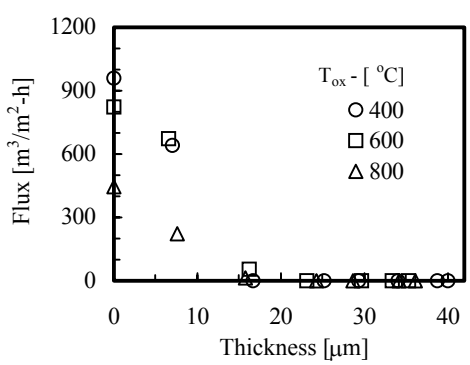

Figure 3. He flux at 1 atm difference as a function of Pd layer thickness for membranes oxidized at different temperatures.

The typical behavior of the He flux as a function of the Pd layer thickness is shown in Figure 3 for the three prepared membranes. The curves can be divided into two parts. The first part is the linear decline of He flux with the plated Pd thickness, where all the small pores were being plugged. All three membranes had different initial He fluxes as a result of the oxidation at different temperatures, however they intersected the abscissa at essentially the same point. The second part of the curves is the exponential decline of the He flux with the thickness, where the largest pores were being gradually plugged. The fact that the exponential decline starts at a similar Pd layer thickness for all oxidation conditions indicates that the pores being blocked in this portion of the curve are too large to be significantly affected by the oxidation conditions. These pores may be regarded as defect pores for the purpose of Pd membrane fabrication. Our previous works also showed that the dense Pd layer thickness was dependent on the largest pore size (3). Therefore, for large grade supports, the oxidation temperature will not affect the size of the pore enough to cause a significant reduction of the plated Pd layer thickness.

Table 2. Thickness of Dense Pd Layer on Supports Oxidized at Different Temperatures.

#	T_{ox} [^{0}C]	Time [h]	l [μm]
1	400	6	40.00
2	600	6	35.32
3	800	6	36.16

Although the oxide layer is used as a barrier for the intermetallic diffusion, it could also act as a barrier for hydrogen diffusion through the pores if the oxide layer were too thick. Therefore, the thickness of the oxide layer should be thick enough to prevent intermetallic diffusion, thereby increasing the thermal stability of the membrane but thin enough not to block the flow of hydrogen through the pores of the PSS support.

Conclusions

The oxidation of PSS supports should have an optimum time and temperature at which stable, uniform oxide layer is formed without plugging pores, thus without producing a hydrogen diffusion barrier, yet sufficient to prevent intermetallic diffusion. For relatively low oxidation temperatures, the time of oxidation does not affect the He flux appreciably.

Higher oxidation temperatures cause a larger reduction of the He flux resulting possibly from either the pores been blocked or the formation of a thicker oxide layer. Although the final thickness of the dense palladium layer does not appear to be affected appreciably by the oxidation temperature, the oxide layer not only acts as a diffusion barrier but also provides surface sites for easy activation and plating and improved adhesion.

References

(1) Ma, Y.H., Mardilovich, P. .P. and She, Ying, **2000**, US Patent 6,152,987.
(2) Mardilovich, P. P., She, Y. and Ma, Y. H., AIChE J, **1998**, 44, 310.
(3) Mardilovich, I.P.; Engwall, E.; & Ma, Y.H. *Desalination*. **2002**, *144*, 85.

NOVEL METHOD FOR FABRICATION OF SUPPORTED PALLADIUM MEMBRANES FOR MEMBRANE REACTOR

Shigeyuki Uemiya[1], Shogo Mishima[2], Yutaka Makino[2], Ikumi Miyazaki[1], Hiroshi Moritomi[2], Makoto Nishimura[1]

1) Department of Human and Information Systems, Faculty of Engineering,
2) Environmental and Renewable Energy Systems Division, Graduate School of Engineering,
Gifu University
Yanagido 1-1, Gifu, 501-1193 JAPAN

Introduction

In most chemical reactions there is the thermodynamically limited level of conversion attainable for a given reaction condition. Among them hydrogen producing reactions, for example steam reforming and dehydrogenation of hydrocarbon, require relatively high reaction temperatures; however, in some cases the level of equilibrium conversion is not so high even at high temperatures that the recycle operation of unconverted reactant is required in industrial-scale plants.

Membrane reactor has been proposed as one of novel reactors that will be able to solve the problems existing in thermodynamically limited reactions. Membrane reactor is defined as a reactor incorporating with a functional membrane, and enables the simultaneous separation of product with chemical reaction. Membrane reactor leads to an environmentally friendly compact and simple chemical process. Development of novel membrane material, fabrication technique of thin film, and screening of highly active catalyst even at milder reaction conditions are required for the realization and commercialization of novel membrane reactor system. We have reported the fabrication technique of supported palladium and palladium-alloy membranes[1,2] and the applicability of hydrogen permeable palladium membrane reactor[3], and have experimentally demonstrated importance of improving hydrogen permeance of supported palladium-based membranes. In this paper we will present novel methods for fabrication of a supported palladium membrane in order to decrease the thickness of palladium film.

Experimental

A porous alumina tube with asymmetric structure (o.d., 10 mm; mean pore size of effective layer, 0.2 μm) was used as a supporting material for palladium thin film. First, the tube was cleaned using a solvent in an ultrasonic condition. Palladium thin film was formed on the outer surface of the tube by the electroless-plating technique. Just before plating, the surface was activated and catalyzed in two step activation involving repeated immersing into stannous chloride and palladium chloride aqueous solutions with pure water washing between them. During this procedure, palladium ions were reduced into metallic form. The deposited utrafine palladium particles worked as a catalyst for the electroless-plating. The plating conditions are shown in Table 1.

In the improved procedure of membrane fabrication proposed here, there were five different points:

1. The temperature of activation procedure was changed from room temperature to 35°C.
2. The immersion procedure of the support into distilled water was added just before the activation procedure.
3. The immersion into hydrazine aqueous solution was added just before electroless-plating.
4. The time of the repeated activation procedure was decreased from 10 to 3.

Table 1. Composition of Electroless Plating, Sensitization and Activation Solutions

Electroless plating solution	
$Pd(NH_3)_4Cl_2$	5.4 g L^{-1}
EDTA 2Na	67.2 g L^{-1}
NH_3 H_2O [28%]	651.3 mL L^{-1}
N_2H_4 H_2O	0.35 mL L^{-1}
Sensitization solution	
$SnCl_2$ $2H_2O$	1.0 g L^{-1}
HCl [37%]	1.0 mL L^{-1}
Activation solution	
$PdCl_2$	0.1 g L^{-1}
HCl [37%]	1.0 mL L^{-1}

Plating temperature, 50°C

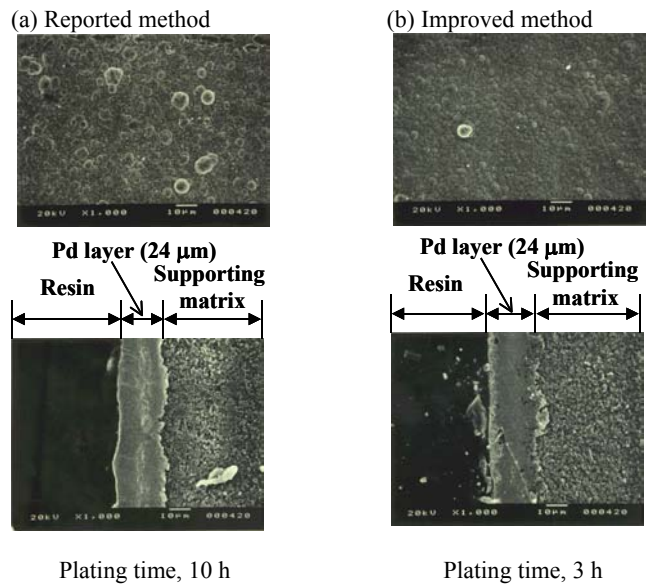

Plating time, 10 h Plating time, 3 h

Figure 1. Surface and cross section view of supported palladium membranes.

5. Bath load, namely the ratio of the surface area of a support to the volume of the plating bath, was changed from 785 cm^2 L^{-1} to 167 cm^2 L^{-1}.

Furthermore, the effect of hydrazine concentration in the immersion procedure conducted just before electroless-plating was investigated.

The resulting membranes were characterized by SEM, XPS, and gas permeation tests. For the purpose of checking formation of pinholes and cracks, gas leakage test was conducted using helium. Hydrogen permeance of the membrane was evaluated by a traditional permeation test using pure hydrogen.

Results and Discussion

The surface of the porous alumina tube used as a support was completely covered without any pinholes by 10-hour electroless plating in the previously reported method. On the other hand, only 3 hour plating was required in the improved method. The morphology of the surface and the cross section of the both supported palladium membranes were almost same, as shown in Figure 1. The difference is found to be only plating rate.

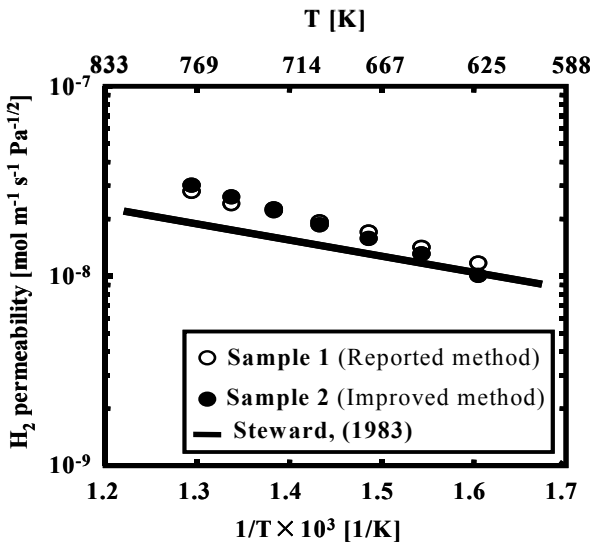

Figure 2. Comparison in hydrogen permeability between the supported palladium membranes prepared by reported and improved methods.

Table 2. Effect of Hydrazine Concentration on the Thickness of Palladium Film

Hydrazine conc. [mol L^{-1}]	Palladium thickness[1)] [μm]	Standard deviation
3.6 x 10^{-3}	3.02	0.27
7.2 x 10^{-3}	2.83	0.12
14.4 x 10^{-3}	4.66	0.21

1) Ten data obtained from the cross section view were averaged.

Figure 2 demonstrates the comparison in hydrogen permeability between two membranes. Here, hydrogen permeability means hydrogen permeance per unit area, unit thickness, unit transpressure, and unit thickness. The line in the figure indicates reported values refereed from Steward's review article[4]. The plots of hydrogen permeability are overlapped and the values are nearly equal to the reported ones. This indicates that hydrogen permeance is independent of preparation procedure.

The effect of plating method on palladium plating rate has not investigated yet; however, we may speculate that the immersion into hydrazine aqueous solution greatly affects the plating rate among five different factors between the reported and improved fabrication methods. In the reported method, a considerable amount of palladium ions, which were not reacted with stannous ions, still existed on the surface of support besides active palladium metallic ultrafine particles in electroless plating. On the other hand, in the improved method, most palladium ions were probably reduced by the reaction with hydrazine; therefore, active palladium fine particles worked as a catalyst for electroless-plating adsorbed densely on the surface, leading to the shorten preparation time of a dense supported palladium membranes applicable to membrane.

As aforementioned, the density of palladium ultrafine particles was increased in case of the improved method. This means that the adoption of the improved method possibly leads to decrease the thickness of palladium film for covering the surface of the support completely. Table 2 summarizes the effect of hydrazine concentration in the immersion procedure conducted just before electroless-plating on the thickness of palladium film. Here, a porous

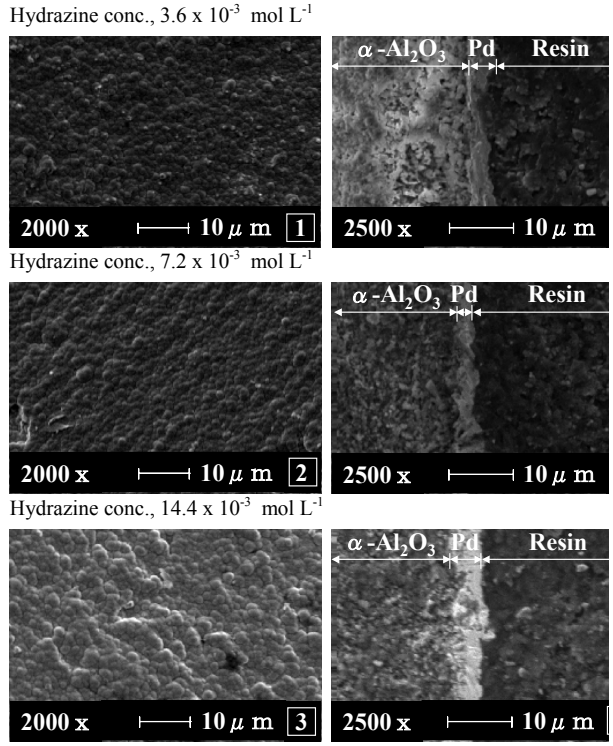

Figure 3. Surface and cross section view of supported palladium membranes prepared by improved method with different hydrazine concentration.

alumina tube with relatively short length (5 cm) was used. Fortunately, helium leakage was hardly observed in these membranes, indicating that the thickness of 2.8 μm will be enough to cover completely the surface of the porous alumina support with the mean pore size of 0.2 μm. When hydrazine concentration is 14.4 x 10^{-3} mol L^{-1}, the plating time will be shorten for the fabrication of thin palladium film with the thickness of 2.8 μm. However, stannous ions still coexisted with active palladium fine particles. Paglieri et al. demonstrated that the amount of tin presented at the interface of palladium and porous support was qualitatively related to stability of a resulting supported palladium membrane at high temperatures. Further study will be necessary to remove stannous ions from the surface of the support.

Acknowledgement. This work has been partly carried out as a research project of The Japan Petroleum Institute commissioned by the Petroleum Energy Center with the subsidy of the Ministry of Economy, Trade and Industry, and partly supported by Grants-in-Aid for Scientific Research from the Ministry of Education, Culture, Sports, Science and Technology and Japan Society for the Promotion of Science.

References

(1) Kikuchi, E.; Uemiya, S, *Gas Separation & Purification*, **1991**, 5, 261-266.
(2) Uemiya, S.; Kajiwara, M.; Kojima, T., *AIChE J.,* **1997**, 43(11A), 2715-2723.
(3) Kikuchi, E.; Uemiya, S.; Matsuda, T.; *Stud. Surf. Sci. Catal.,* **1991**, 61, 509-515.
(4) Steward, S.A.; Lawrence Livermore National Laboratory Report UCRL-53441 (1993).
(5) Paglieri, S.N.; Foo, K.Y.; Way, J.D.; Collins, J.P.; Harper-Nixon, D.L.; *Ind. Eng. Chem. Res.,* **1999**, 38, 1925-1936.

CATALYTIC MEMBRANE REACTORS FOR GAS, LIQUID AND SOLID REFORMING TO SYNGAS

Anthony F. Sammells, Thomas F. Barton, and Michael V. Mundschau

Eltron Research Inc.
4600 Nautilus Court South
Boulder, CO 80301
www.eltronresearch.com

Introduction

Catalytic Membrane Reactor (CMR) technology, under development at Eltron Research Inc., facilitates the exclusive mediation of oxygen from the atmosphere to a desired reaction site. As a consequence of this, many CMR-driven hydrocarbon partial oxidation chemistries become exothermic while at the same time eliminating the need for a separate oxygen plant - a significant reduction in overall production costs compared to currently available technology. An additional feature is that in such chemical processing NO_x emissions are eliminated, since N_2 in the air is separated from O_2 via the membrane.

In particular, this technology is being developed for the respective spontaneous reforming of natural gas, liquid fuels and coal into synthesis gas. Principles behind the membrane technology and its current status for the partial oxidation of these feedstocks will be discussed.

Experimental

Proprietary oxygen deficient metal oxides possessing the general stoichiometry $A_{2-x}A'_xB_{2-y}B'_yO_{5+z}$ were prepared following conventional high temperature solid-state synthesis techniques until subsequent XRD analysis indicated that the desired single phase material had been obtained. Membranes were prepared into closed-one-end tubes using isostatic pressing techniques followed by sintering at elevated temperatures in the atmosphere. Mixed conducting catalysts were then subsequently deposited on respectively the oxidizing and reducing membrane surfaces using either dip coating, silk screening or spray pyrolysis techniques. Following incorporation of the resulting CMR into experimental test stands, a seal was formed at the open-end of the membrane tube to ensure gas-tight separation between respective membrane compartments. Hydrogen, carbon monoxide, methane, and carbon dioxide gas constituents were analyzed using a Gow-Mac series 580 TCD gas chromatograph equipped with a carbosphere column. Helium was used as the carrier gas. Pre-analyzed standard gas samples were used for calibration purposes in order to quantify all products. Gas analyses from each membrane compartment were performed with the aid of air tight syringes (Pressure-Lok, Alltech Associates). The amount of products measured was compared to the feed in order to calculate the overall conversion efficiency of the membrane reactor system towards promoting the subject partial oxidation reactions.

Results and Discussion

Dense mixed oxygen anion and electron conducting ceramic membranes are derived from oxygen-deficient metal oxides possessing the general stoichiometry $A_{2-x}A'_xB_{2-y}B'_yO_{5+z}$. This CMR technology will facilitate spontaneous reforming of respectively natural gas (methane), liquid hydrocarbon fuels and coal into synthesis gas feeds, as shown schematically in Figure 1.

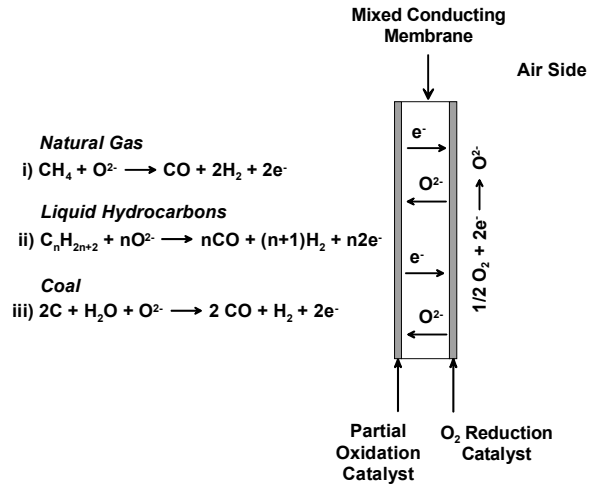

Figure 1. Schematic of spontaneous processes occurring on the membrane partial oxidation surface for the respective reforming of i) natural gas, ii) liquid hydrocarbons, and iii) coal into synthesis gas.

To achieve high oxygen flux in membrane materials which possess high stability, Eltron[1-6] has developed mixed oxygen anion and electron conducting membranes $A_{2-x}A\rho_xB_{2-y}B\rho_yO_{5+z}$ where:

A is an alkaline earth metal ion or mixture of alkaline earth metal ions; Aρ is a metal ion or mixture of metal ions where the metal is selected from the group consisting of the lanthanide series or is yttrium; B is a metal ion or mixture of metal ions wherein the metal is selected from the group consisting of 3d transition metals, and the group 13 metals; Bρ is a metal ion or mixture of metal ions where the metal is selected from the group consisting of the 3d transition metals, the lanthanides and yttrium.

The rationale for selecting specific A and B lattice substituents has evolved from work performed at Eltron which identified clear correlations between crystallographic and thermodynamic parameters relating to the activation energy for ionic transport. These parameters include: 1) the average metal-oxygen bond energy within the lattice, 2) lattice free volumes, obtained by subtracting the ionic volumes of cations and O^{2-} in the unit cell from the overall crystallographic unit cell, 3) the parameter $r_{critical}$ (r_c) which corresponds to the radius of the opening between the two A site cations and one B site cation through which the mobile anion must pass, and 4) lattice polarizability towards ionic migration.

Of all the potential applications for mixed oxygen anion and electronic conducting materials, the partial oxidation of methane to syngas is one of the most commercially important. Syngas can serve as a precursor for a variety of products such as methanol, higher alcohols or Fischer-Tropsch products. Current commercially available technology for syngas production from natural gas is based on the endothermic steam reforming reaction which may be represented by:

$$CH_4 + H_2O \rightarrow 3H_2 + CO$$

with CO also reacting with water via the water-gas shift reaction:

$$CO + H_2O \rightarrow CO_2 + H_2$$

In contrast, the methane partial oxidation reaction:

$$2CH_4 + O_2 \rightarrow 2CO + 4H_2$$

proceeding across mixed conducting membranes is exothermic, with oxygen being separated from the atmosphere at the membrane reducing surface for subsequent participation in the natural gas partial oxidative reforming reaction at the membrane oxidizing surface.

CMRs have been successfully operated under ambient pressure conditions for over one year at 900°C for natural gas reforming with no evidence of instability. Performance realized for ambient pressure CMRs may be summarized as: Syn Gas Production Rate - 60 mL/min•cm^2, Equivalent O_2 Flux 10-12 mL/min•cm^2 (corresponding oxygen anion conductivity > 1S cm$^{!1}$), H_2: CO Ratio - ~ 1.9 - 2.0, CO Selectivity - >96%, Throughput Conversion - 90% CH_4, 70% O_2 (air). Additionally, Eltron has accumulated over eight years of experimental experience for CMRs operating at elevated temperatures with a 250 psi pressure differential between the hydrocarbon and the air side of the membrane.

The spontaneous reforming of liquid hydrocarbon fuels into H_2/CO mixtures provides a feedstock compatible for subsequent electrochemical oxidation in the anode compartment of a Solid Oxide Fuel Cell (SOFC). The overall reforming process may be represented by:

$$C_nH_{2n+2} + n/2O_2 \rightarrow nCO + (n+1)H_2$$

Ceramic membrane partial oxidation process operating conditions have been systematically evaluated using: i) the respective logistic fuel model constituents dodecane, hexadecane, octane, branched chain hydrocarbons and aromatic hydrocarbons, and ii) representative diesel and jet fuels. At 900°C, synthesis gas production rates approaching 40 mL/min-cm^2 were achieved when converting dodecane as a simulant for diesel fuel. Throughput conversions were 99%. This corresponded to an oxygen flux rate across the membrane >6.3 mL/min-cm^2. CMRs were also operated directly on both diesel and jet fuels. For diesel fuel, the synthesis gas production rate was >27mL/min-cm^2 with stoichiometric (100%) throughput conversion. In the case of jet fuel, the synthesis gas production rate was >22 mL/min-cm^2 with a throughput conversion of >80%. Diesel fuel partial oxidation to synthesis gas at a rate of 27 mL/min-cm^2 when used for SOFC fuel would produce an equivalent current of 3.9A/cm^2. Assuming the SOFC operates at 0.75V per cell, this would correspond to a power output of 2.9W/cm^2 of membrane reactor surface area.

Eltron's CMR technology is also being applied towards oxygen separation for reaction with coal fines. Membrane-based coal gasifiers are being developed for both the direct catalytic gasification of coal with mediated oxygen anions as well as for coal gasification with molecular oxygen evolved from the membrane's oxidation catalyst. This is requiring the development of two catalysis strategies. Gasification reactions occurring between coal and mediated oxygen are a combination of the partial oxidation and complete combustion of coal as shown below:

$$C + ½O_2 \rightarrow CO$$

$$C + O_2 \rightarrow CO_2$$

where C is used as an empirical representation for coal. Using coal as the sole component of the feedstream requires consideration of two issues. The first is that since the above reactions are highly exothermic (ΔH = -110.5 J/mol and -393.8 J/mol respectively), any reactor system using this approach must be designed to account for proper heat transfer. Secondly, the sole product of this process is not very versatile, useful only as a fuel or as a feedstock in chemical processes requiring carbon monoxide.

In order to address these two issues, steam is being added to the coal feedstream. Since the steam reforming of coal, given below,

$$C + H_2O \rightarrow H_2 + CO$$

is endothermic in nature (ΔH = 175.4 J/mol), this process can then be used to absorb the heat generated by the exothermic coal oxidation process.

Furthermore, the introduction of steam serves to form hydrogen. The resulting product, a mixture of hydrogen and carbon monoxide, has a high BTU value making it more valuable as a fuel or as a feedstock for the production of liquid fuels such as methanol or diesel.

The following reaction, which is a combination of the partial oxidation and steam reforming of coal, summarizes the catalytic process being developed at Eltron utilizing CMRs with a humidified coal feed stream to yield a product containing hydrogen and carbon monoxide.

$$2C + ½O_2 + H_2O \rightarrow 2CO + H_2$$

For the process to be self-sustaining it needs to be operated at the thermoneutral point or exothermically. The thermoneutral point is represented by:

$$1.8\ C + 0.5\ O_2 + 0.8\ H_2O \rightarrow 0.8\ H_2 + 1.8\ CO$$

which yields a product gas with a H_2:CO ratio of 0.44:1.

For fixed-bed coal gasifiers, coal gasification rates as high as 4.9 mL/min/cm^2 (61.3 ml/min) were obtained. A corresponding oxygen depletion of greater than 60% was found on the air side confirming the utility and role of the mixed conducting membrane. There was never any sign of melting of the coal ash which was recovered following experimentation. This indicates that this membrane-based gasifier operates below the slagging temperature. Coal gasification production rates of up to 17.8 mL/min/cm^2 (188 mL/min) were achieved with a continuous feed reactor operating at 900°C. Experimentation without an oxidation/reforming catalyst on the surface of the membrane showed similar results to when a catalyst layer was deposited on the oxidation surface. This indicates that intimate contact between coal, oxygen anions, and steam on the membrane surface is not essential, greatly simplifying future gasifier designs.

Acknowledgment. This work is supported by the U.S. Department of Energy (DOE) and the Defense Advanced Research Projects Agency (DARPA).

References

(1) Schwartz, M.; White, J. H.; and Sammells, A. F. U.S. Patent 6,033,632, March 7, 2000.
(2) Mackay, R.; Schwartz, M.; and Sammells, A. F. U.S. Patent 6,165,431, December 26, 2000.
(3) Mackay, R.; and Sammells, A. F. U.S. Patent 6,146,549, November 14, 2000.
(4) Schwartz, M.; White, J. H.; and Sammells, A. F. U.S. Patent 6,355,093, March 12, 2002.
(5) Schwartz, M.; White, J. H.; and Sammells, A. F. U.S. Patent 6,214,757, April 10, 2001.
(6) Van Calcar, P.; Mackay, R.; and Sammells, A. F. U.S. Patent 6,471,921, October 29, 2002.

HYDROGEN RECOVERY FROM FLUID CATALYTIC CRACKING UNITS USING MEMBRANES OR CATALYTIC MEMBRANE REACTORS

Christophe CHAU, Thierry GAUTHIER°*

Institut Français du Pétrole,
1 & 4, avenue de Bois-Préau, 92852 Rueil-Malmaison - France,
*Catalysis and Separation Division, christophe.chau@ifp.fr
°Process Development Division, Chemical Engineering Department

Introduction

Hydrogen consumption and demand are increasing, due to more severe specifications on gasolines and highly hydrogen consuming units like hydrotreating, hydroconverting and hydrocracking. To face this increasing demand, refiners can invest in hydrogen production units (methane to naphtha steam reforming and partial oxidation) and/or optimize hydrogen consumption and recycle (*e.g.* catalytic reforming). In this context, hydrogen recovery from refining and petrochemical off gases has a great potential.

Fluid catalytic cracking (FCC) units are used worldwide to convert heavy hydrocarbons (typically with boiling points above 360°C at atmospheric pressure) into lighter products. Among the reaction products, dry gas contains the lighter molecules typically lighter than C3. After postreatment (absorption and further washing), dry gas contains typically 0.2 to 0.5 t/h of hydrogen (*e.g.* 0.4 t/h for FCC units with a 65,000 BPSD capacity and 27% mol. hydrogen) and this dry gas is generally used as fuel gas. Besides hydrogen, light olefins (25% mol.) and carbon oxides (0.6%) are found in these hydrogen containing gaseous streams. Considering the high FCC capacities in refineries, hydrogen recovery from dry gas can be of great economical and technical interest. A schematic flowsheet of a R2R catalytic cracking unit, licensed by Axens (of IFP's Group) and SWEC is depicted in Fig. 1.

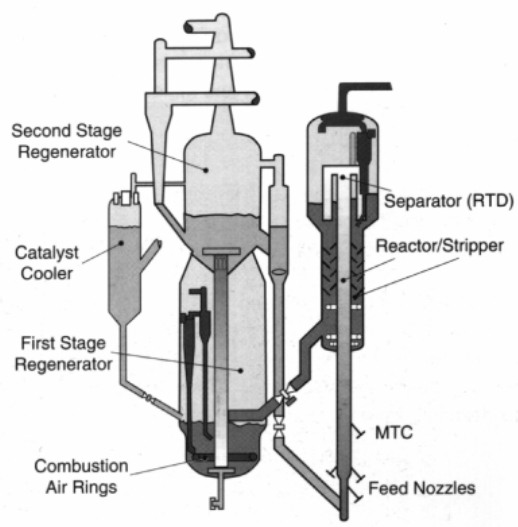

Figure 1. Flowsheet of a R2R Fluid Catalytic Cracking unit

Experimental

Hydrogen recovery from FCC units can be considered using either a separation unit with a membrane module used alone (gas permeation) or in combination with a catalyst (catalytic membrane reactor). In this latter case, the permeation driving force can be considerably increased by hydrogen consumption through a catalytic hydrogenation. The coupling effect gas permeation/catalytic reaction can compensate for the low or moderate pressures of hydrogen and the moderate permeation driving force. IFP highlights a new process flowsheet that integrates a hydrogen selective membrane and a catalytic hydrogenation of aromatics from a reforming unit.

Simulation has been carried out using Matlab software. Membrane performances were taken from literature, industrial or commercial data. Kinetic data were determined in previous IFP's studies on heterogeneous catalysis at pilot scale.

Results and discussion

Gas permeation. Requirements on hydrogen selective membranes are related to selectivity (in the presence of *e.g.* olefins, CO and H_2S), permeability (necessarily high, due to high gas flowrates) and commercial availability. Dense metallic membranes with hydrogen specificity are too expensive and their manufacture is strongly limited by palladium availability and fabrication technology. To date, only hollow fibers made of polymeric materials can be considered for this application, with their high surface to volume ratio and their commercial availability and maturity.

Our studies revealed that a sweep gas is required to increase hydrogen recovery, unless a compression stage of the hydrogen streams from FCC units is used (with high associated CAPEX and OPEX). Moreover a sweep gas would have to be integrated in the full-scale industrial process, separated from hydrogen and recycled. This alternative is seemingly not economically feasible.

Separation/catalytic reaction coupling. To improve the separation process, we have considered an integrated flowsheet (disclosed in IFP's patent applications) based on: a selective hydrogen separation using a membrane, contacting this hydrogen with a hydrogenation catalyst and a naphtha reforming containing *e.g.* 15% of aromatics. Part of these aromatics is hydrogenated and this hydrogen consumption favors hydrogen transfer through the hydrogen selective membrane by increasing permeation driving force. Lastly hydrogenated aromatics are converted in a reforming unit, thus allowing aromatics recycle and hydrogen recovery. Hydrogen is therefore recovered at a higher pressure with a high purity for further use (see Fig. 2), without any compression stage.

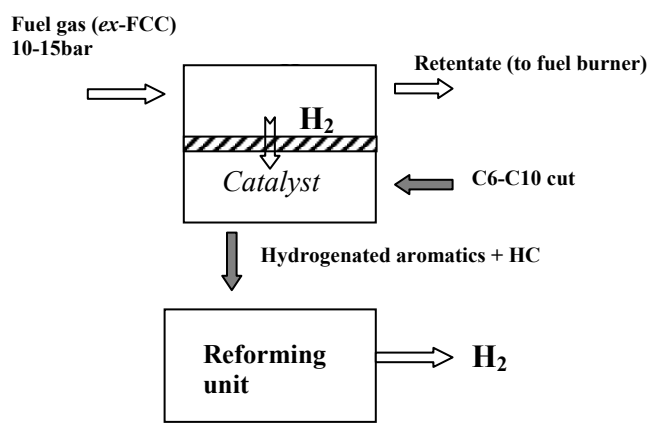

Figure 2. Hydrogen recovery from FCC units using membrane reactors

The membrane implemented has a high selectivity to hydrogen and thus limits the permeation of unsatured hydrocarbons and carbon oxides, which can affect catalyst activity. Operating conditions allow both hydrogen permeation and catalytic conversion in the catalytic membrane reactor.

A sensitivity study has been carried out and highlighted operating conditions to increase the synergetic effect of hydrogen separation (by membrane) and catalytic reaction. Space velocity at the reaction side and membrane performances determines the efficiency of hydrogen recovery. Co-current and counter-current modes are of great importance in the combined system and affect membrane surface area. Moreover, the catalytic activity can limit hydrogen recovery.

Conclusions

In hydrogen-containing streams from refining and petrochemistry, gas permeation allows partial hydrogen recovery, as soon as the hydrogen selective membrane performances (permeability, high selectivity) and the modular compacity and membrane specific surface area are very high. With hydrogen streams from FCC units, delivered at moderate to low pressures, hydrogen compression is required to reach hydrogen recoveries that are economically feasible.

Membrane/catalyst coupling allows increased hydrogen recovery rates by hydrogen consumption through a catalytic reaction. IFP proposed flowsheet is an integrated and combined system in which hydrogen recovery is higher than that of a permeation system. Catalyst activity is of significant importance as it affects hydrogen permeation driving force and the closer the coupling effect, the higher the hydrogen recovery rate.

Oxygen transport membranes for ultra-clean fuel production

E.T. Robinson
Torix, Inc.
7165 Hart. St., Ste. B, Mentor, Oh. 44060

Introduction

Natural gas is an abundant, inexpensive hydrocarbon resource that can be converted to clean burning liquid fuels. Most gas to liquid (GTL) processes require two steps: conversion of natural gas to a mixture of hydrogen and carbon monoxide (syngas), followed by an upgrading process such as Fischer-Tropsch (FT) synthesis, methanol synthesis or water-gas shift to hydrogen. The Fischer – Tropsch process converts syngas to a highly paraffinic synthetic crude oil that is free of sulfur and aromatics. The synthetic crude can be refined to yield a clean, high cetane diesel fuel. In the overall GTL process scheme, the syngas production consumes about 60% of the capital and therefore has been the focus of extensive research to reduce costs. The conventional syngas process, autothermal reforming, requires high purity oxygen, which is normally produced by cryogenic distillation. Ceramic oxygen transport membranes can replace cryogenic oxygen and thus offer a potentially lower cost, higher efficiency method for producing syngas from natural gas in ultra-clean fuel applications.

Oxygen Transport in Mixed Conducting Membranes

A commercial OTM process exploits the unique properties of mixed conducting ceramic materials, which transport both oxygen ions and electrons across a gas impermeable membrane. The membranes are typically made of inorganic crystalline metal oxides with the general composition ABOx, where A and B are cations and x is a number that satisfies the valences of A and B. Numerous compositions have been patented for various oxygen separation and oxidation applications[1, 2].

The oxygen separation process, **Figure 1**, involves at least four steps: 1) molecular oxygen diffuses to the membrane surface on the air side, 2) molecular oxygen dissociates to oxide ions, consuming electrons, 3) oxide ions diffuse across the membrane by moving through oxygen vacancies, electrons move in the opposite direction, and 4) oxygen ions recombine or react with process gas on the fuel side, liberating electrons. The driving force for oxygen transport is the chemical activity or oxygen partial pressure gradient from the air to fuel side. However, other factors can be rate limiting. At high oxygen flux rates, diffusion or mass transport of oxygen to the membrane surface, or oxidation products away from the membrane surface, can be rate controlling. The electronic and ionic conductivity of the ceramic membrane materials are rate determining at lower temperatures. Most materials require temperatures in excess of 700C and partial pressure gradients (pO2 air/pO2 fuel) exceeding 10,000 to achieve commercial significance.

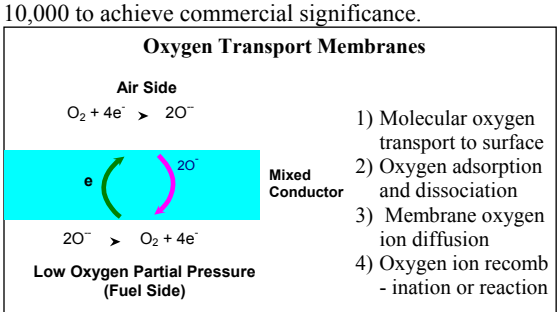

Figure 1. Ceramic membrane oxygen ion transport

Application of OTM to Syngas Production

The benchmark syngas technology for the Fischer Tropsch (FT) process is autothermal reforming (ATR). ATR reacts high purity oxygen with natural gas and steam at pressures of 15 to 40 bar and temperatures above 950C. The ATR process employs a catalyst to ensure the product gases achieve equilibrium conversion. Product gas composition is determined by the process conditions, (temperature and pressure) and relative amounts of steam, oxygen and carbon dioxide fed to the reactor. For FT, a H_2/CO ratio of about two is desired, with minimum quantities of CO_2. The major cost component for ATR is the air separation unit, which includes air compression to about 6 bar, cryogenic oxygen distillation and product oxygen compression to about 30 bar.

OTM can in principal reduce or eliminate the cost of all three of these unit operations if the mixed conducting materials can achieve certain oxygen flux and durability targets. A significant advantage of OTM is the ability to transport oxygen from a low pressure air source to a high pressure fuel stream without mechanical compression. Oxygen partial pressure on the fuel side of the membrane is on the order of 10^{-12} to 10^{-16} bar, regardless of total pressure of the fuel gas. Thus, a substantial driving force is established across the membrane, irrespective of the actual pressure differential. With OTM, air compression is minimal, just enough to overcome the pressure drop through the OTM reactor and air heat exchangers. Obviously no oxygen compressor is required if the membrane is operated above the FT pressure. And, of greatest significance, OTM eliminates cryogenic distillation.

Oxygen Transport Membrane and Reactor Design Challenges

The critical performance factors for an OTM based syngas process are oxygen flux and membrane durability. Oxygen flux, often reported in units of standard cubic centimeter of oxygen per minute per square centimeter (scc/min./cm^2), directly determines the surface area of oxygen transport membrane required to achieve the target oxygen flow rates. Fluxes exceeding 10 scc/min/cm^2 have been reported as minimum requirements for an economical syngas process[3]. A much greater challenge is to build an OTM element that can withstand the extreme temperatures and stresses of an ATR environment, while resisting creep, corrosion and poisoning.

In an ATR or OTM syngas reactor, at least five reactions are occurring:

1) $CH4 + ½ O2 \rightarrow CO + 2H2$
2) $H2 + ½ O2 \rightarrow H2O$
3) $CO + ½ O2 \rightarrow CO2$
4) $CH4 + H2O \rightarrow CO + 2 H2$
5) $CO + H2O \rightarrow CO2 + H2$

The first three oxidation reactions are exothermic, the steam methane reforming (SMR) reaction (4), is endothermic, and the water gas shift reaction (5) is about thermally neutral, depending on operating conditions.

Oxidation on the fuel side is very rapid and has an "autocatalytic like" effect: oxidation reduces the oxygen partial pressure and increases the temperature, both of which increase oxygen flux. With no controls, thermal runaways and formation of local hot spots are major concerns. The steam methane reforming reaction will adsorb the heat of oxidation. Catalyst deployment to promote SMR in the hot zones is a primary design consideration. Adequate temperature monitoring and control mechanisms must be in place to ensure safe and reliable operation.

OTM Element

The element is the means of deploying the oxygen transport membrane in a chemical reactor. Both planar and tubular designs have been considered. Both must withstand the pressure load across the membrane of 15 to 40 bars and be capable of achieving a reliable

seal. The OTM Alliance has selected a tubular element design, primarily because successful seals have been developed, and many manufacturing hurdles have already been overcome.[4] Eight foot tubular elements have been made and 5 foot elements have been tested in a mutli-tube pilot plant reactor.

However, the most serious challenge facing these elements is the capability to withstand the stresses created by the process pressure, mechanical loads and the thermal and chemical gradients inherent in the system. The trans- membrane pressure of 15 to 40 bars is a significant, yet static force on the membrane. Membranes can be made thick enough to withstand the pressure, but at the expense of oxygen flux. At high operating temperatures, creep is a concern. An extremely low creep material is needed to achieve element life times in excess of 5 years.

Of greater concern are the stresses created by thermal and chemical gradients. Thermal stresses are dynamic and can be enormous. Thermal stresses are created by temperature gradients or connected materials with different thermal expansion properties. In the former case, a temperature gradient causes one part of the membrane to expand more than the cooler side, creating stresses in the element. Another issue is supporting the element and providing room for thermal growth. A closed end tubular element requires only one seal and allows unimpeded expansion in the axial direction.

An OTM element made of materials with dissimilar rates of thermal expansion can generate considerable stresses, even if all materials are at the same temperature. As a rule of thumb, the coefficient of thermal expansion (CTE), measured as parts per million per degree C, should match within ~< 1 ppm/C over the entire temperature range, from a cold start to full operation. Managing these same types of thermal stresses is also a major issue for planar solid oxide fuel cells.[5]

A third source of stress in an OTM element is the volumetric change of the material under different oxygen partial pressures. As the oxygen partial pressure decreases, an OTM material will lose oxygen ions, creating vacancies in the crystalline lattice. Oxygen vacancies are the mechanism for ionic transport through the membrane. The penalty however is the crystal will expand, creating internal stresses.

An example of dynamic stress creation and relaxation is shown in **Figure 2.** A rapid, short change in oxygen partial pressure[4] will develop significant stress gradients that decay with time. Under steady state conditions, a significant stress gradient can also be created in response to the large oxygen partial pressure drop across the membrane, as shown in **Figure 3**. In both cases the inherent strength of the materials must exceed the stresses created, or the element will fail.

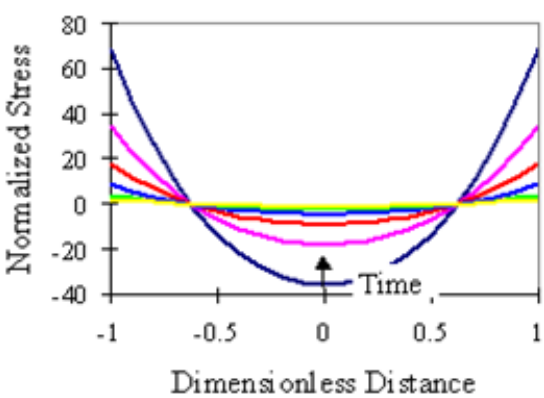

Figure 2. Calculated stress response to a pulse change in oxygen partial pressure. Zero distance is the membrane centerline

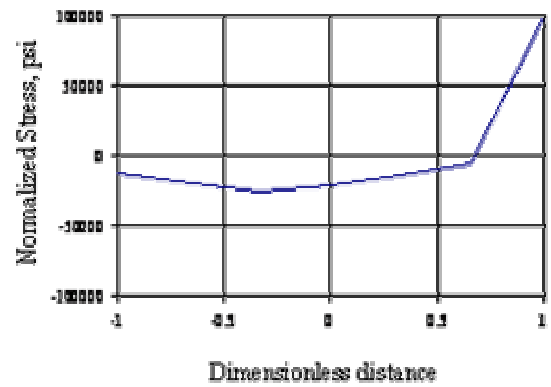

Figure 3: Steady state stress gradient with air on one side and process gas on the opposite side

In addition, an OTM element must resist attack by carbon dioxide and steam. Some metal oxides will form carbonates at elevated CO_2 partial pressures and moderate temperatures. Long term ionic diffusion and phase stability may also be issues, especially in the high temperature region of the element.

Technical Solutions to Challenging Problems

As discussed above, the technical challenges of an OTM based syngas technology are formidable. It is unlikely that a single breakthrough or development will resolve all of the issues. We have therefore adopted a systems approach that focuses on three aspects of the technology:

- Process and reactor design
- Materials development
- Element development

Process and Reactor Design

The broad objectives of the process and reactor design program are: 1) achieve cost and performance targets and 2) ensure safe operation with responsive control. Obviously, the OTM syngas process must reliably and economically deliver a high quality product gas. Key targets are high methane conversion (>97%), consistent H_2/CO ratio of two, high oxygen utilization (~80%) and a competitive capital cost. The reactor and control system must minimize hot spots, prevent thermal runaways, be responsive to load changes, and be entirely safe under both normal and abnormal operating conditions and scenarios.

Reactor development has focused on a progressive scale-up from bench units to pilot plants, coupled with concurrent development and verification of mathematical models. Computational fluid dynamic models have been successfully linked with gaseous diffusion and solid state kinetic models to provide a fairly accurate view of the complex chemical and physical phenomenon in the OTM element and reactor. Thermal and chemical composition maps from the CFD kinetic models are inputs to finite element models to predict stress gradients in OTM elements. The kinetic models assist the development of catalysts and catalyst deployment strategies, which are essential for achieving the close-coupled thermal integration required to control local temperature and achieve maximum efficiency. These tools are important for scale-up, troubleshooting and guiding the technical program.

Materials Development

The OTM material is the "secret ingredient" of the OTM syngas process. The key hurdle is developing a material or suite of materials that collectively are stable, strong, and creep resistant and can deliver

high oxygen flux. The OTM approach has been to develop combinations of materials that can complement each other without compromising performance. These materials will be in close proximity and thus must be physically and chemically compatible. We have successfully developed suites of materials that have similar thermal expansion properties, are minimally reactive, and yet are strong and creep resistant. Several "suites" have completed test runs exceeding 2000 hours and tens of thermal and chemical cycles without degradation. One example is shown in **Figure 4**. Note that even after 10 thermal cycles, numerous compositional cycles and almost 2500 hours on-stream, the flux has not degraded.

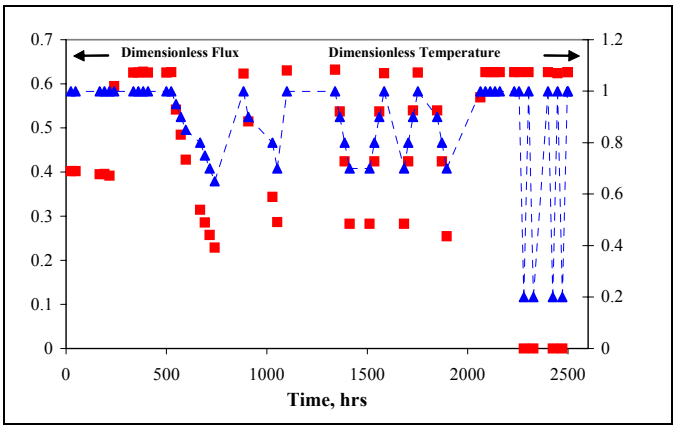

Figure 4: Life and cycle test of an advanced OTM material system

Element Development

The element is the means of deploying the OTM materials in a reactor. Element architecture (design) can have a profound impact on material durability, reactor performance, control and safety. An advanced element design has been developed that exhibits a flat response of oxygen flux to temperature as shown in **Figure 5**. This clearly reduces the risk of thermal runaway. Other architectures have been developed that resist creep or improve flux. We believe architecture also plays a key role in managing the mechanical, thermal and chemical gradient induced stresses.

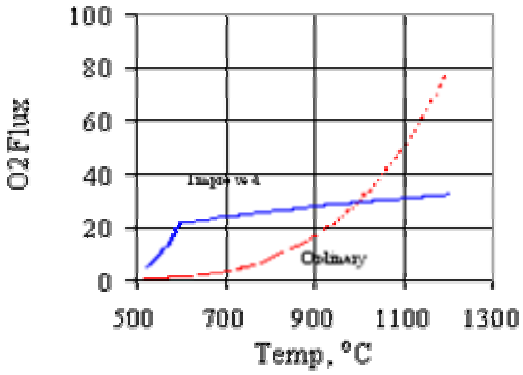

Figure 5: Oxygen flux versus temperature

In addition, element development includes the means to commercially fabricate the elements. Several techniques are under study. High quality tubular elements five feet long can be routinely manufactured as shown in **Figure 6**. Work continues on improving quality and reducing costs and building alternative architectures.

Figure 6: Large scale OTM elements

Conclusions

Exploiting the unique properties of ceramic oxygen transport membranes to develop a syngas process that is more economical than large scale autothermal reforming is a formidable, but achievable goal. Parallel and systemic improvements in the OTM materials, reactor and process design, and element architecture and element manufacturing processes are required for commercial success. Significant advances in all of these arenas have been achieved by the OTM Alliance. OTM syngas coupled with other clean fuel technologies is a promising path for energy independence and a cleaner environment.

Acknowledgements

This work was supported by the National Energy Technology Laboratory, U.S Department of Energy under contract DE-FC26-01NT41096.

The author is grateful for the contributions from all of the OTM alliance scientists and engineers, and in particular Siv Aasland, Morten Brustad, Bente Krogh, Kjersti Kleveland of Statoil; Jack Chen, Hancun Chen, Prasad Apte, Bart van Hassel, John Sirman and Jon Lane of Praxair , Charles Besecker, Sherman Xu, and Mark Kleefisch of BP and John Hemmings of Foster Wheeler.

References

[1]Cable, T.L., Frye, T.G., Jr., Kliewer, W.R., Mazanec, T.J., U.S. Patent 5,591,315, 1997

[2] Cable, T.L., Mazanec, T.J., U.S. Patent 5,788,748, 1998

[3] Bredesen, R; Sogge, J; "A Technical and Economic Assessment of Membrane Reactors for Hydrogen and Syngas Production" presented at Seminar on the Ecol. Applic. Of Innovative Membrane Technology in the Chemistry Industry", Cetraro, Calabria, Italy, May 1-4, 1996

[4] Mazanec, T.J., Prasad, R., Steyn, C., Robinson, E., "Oxygen Transport Membranes for Syngas Production", 6th Natural Gas Conversion Symposium, June, 2001

[5] Chen, Emmeline, Science & Technology Review, Sept. 2002, p. 19

LEACHING BEHAVIORS OF TRACE ELEMENTS IN COAL ASH AND CHAR

Jie Wang, Akira Takaya and Akira Tomita
(Institute of Multidisciplinary Research for Advanced Materials, Tohoku University, Katahira 2-1-1, Aoba-ku, Sendai 980-8577, Japan)
email: tomita@tagen.tohoku.ac.jp

Introduction

Trace elements are of environmental concerns with respect to their emissions during coal combustion. Numerous studies have reported the physical and chemical fates of trace elements during coal combustion. However, there remain some important questions. For example, in what forms the trace elements exist in coal and how they are transformed with the thermal conditions are still not well known. The staged leaching method is widely used to determine the modes of occurrence of trace elements in coal.[1] We have recently proposed a determination method by leaching not only raw coal but also ashes.[2] In this paper, we examine the leaching behaviors of coal ash and char. This provides the further information on the modes of trace elements in coal as well as on the transformations of trace elements during coal combustion and pyrolysis.

Experimental

Coal combustion and pyrolysis were carried out in a horizontal tubular reactor. In combustion, some 1.5 g of coal sample loaded was heated in an air flow of 1 L/min at 10 °C/min, and held at the final temperature for 1 h. In pyrolysis, a nitrogen gas was used in place of air. The maximum temperature used in this experiment was 1150 °C. Quantification of the major and trace metallic elements in raw coal, char and ash was conducted on an inductively coupled plasma atomic emission spectroscope (Optima 3300XL ICP-AES instrument, Perkin-Elmer).[2] Coal or its resultant ash (or char) was leached in a sealed polyethylene container with 30 mL of 6% hydrochloric acid. After leaching, the solution was filtered and then used for ICP-AES analysis. Taiheyo (THY) sub-bitumunous, Ermelo (EL) and Datong bituminous coals were used in this study.

Results and Discussion

Leaching of Major Metallic Elements. Figure 1 shows the leaching percentage of the major metallic elements in hydrochloric acid from ash and char, where the left figure represents the data for EL ashes and the right figure represents those for EL coal chars. For comparison, leaching results of the raw coal are also illustrated. The leaching percentage is referred to as the amount of an element leached from coal, ash, or char divided by the amount contained in the original coal. Analysis of the ashes and chars showed that the major elements were not lost by volatilization during the combustion and pyrolysis under the used experimental conditions. XRD showed that the crystalline mineral phases in EL coal were kaolinite, quartz, calcite, dolomite, pyrite, and gypsum.

Ca and Mg were highly leached out from the raw coals, 550-950 °C ashes, and 550-950 °C chars; this is because the major Ca- or Mg-containing carbonates in coal and their decomposed species are soluble in hydrochloric acid. Mg in the 1150 °C ashes and chars was relatively stable. Fe in the 550-750 °C ashes was greatly soluble as compared with that in the raw coal, while the leaching percentage of Fe significantly decreased from the 950-1150 °C ashes. Pyrite turned to hematite upon the ashing. Hematite in the 550 °C ash was readily soluble in hydrochloric acid; however, hematite was well crystallized with increasing temperature, resulting in a low solubility. Fe in all chars was greatly soluble. This is due to the transformation of pyrite to pyrrhotite. Al in the raw coal was hardly dissolved, whereas it was fairly leached out from the 550-750 ashes and chars. This is due to the breakage of the structure of clay by the dehydration. The formed species such as meta-kailinite become partly extracted by hydrochloric acid. However, with increasing the ashing temperature to 1150 °C, the leaching percentage of Al is significantly reduced; this is because of the formation of some stable species such as mullite, examined by XRD. The leaching features of K were similar to those of Al.

Leaching of Non-vaporized Trace Elements. In a previous study, we found that Zn and Pb was vaporized,[3] whereas the trace elements as shown in Figure 2 entirely remained in the ashes or chars under the used combustion and pyrolysis conditions. Figure 2 shows the leaching results of the non-vaporized elements in EL coal. The leaching percentage of Mn in the raw coal, ashes and chars was relatively high; this is because Mn exists mainly as carbonate. Mn turned to a stable phase at 1150 °C in both the combustion and pyrolysis. Be, V, Co, Cr, and Ni in the raw coal and chars were hardly soluble, whereas these elements in the 550-750 ashes were significantly soluble. These elements are postulated partly as the organic associations. When the organic matter burns out, the liberated species become soluble in hydrochloric acid. In pyrolysis, these elements are not liberated. With the exception of V, the elements including Be, Co, Cr and Ni in the ashes were hardly soluble as the temperature increased to 1150 °C. The leachability of As in the ashes was higher than that in the raw coal. Arsenic easily forms oxyanion in an oxidizing atmosphere that may be soluble in acid. In pyrolysis, Arsenic appeared to form a less-soluble species.

Leaching of Volatile Trace Elements. Figure 3 show the results of Zn and Pb in EL coal. For clarify, the volatilization loss is denoted in the figure; it is referred to as the difference in the amount of an element between the coal and the residual ash or char, divided by the amount of the element containing in the original coal. Zn and Pb significantly volatilized during the pyrolysis above 950 °C, whereas in the combustion, only Pb volatilized slightly at 1150 °C. Zn and Pb exists mainly as sulfide in coal. In pyrolysis, their oxide and sulfides are reduced by carbon; these reduction reactions lead to the vaporization of the two elements as metals.[3] However, such reduction reactions can not occur in the slow-heating combustion because of the burn-out of carbon ahead of 550 °C. Leaching results showed that both Zn and Pb in the ashes became less soluble with increasing temperature. This probably implies the interaction of these trace elements with other mineral matter to form less soluble species

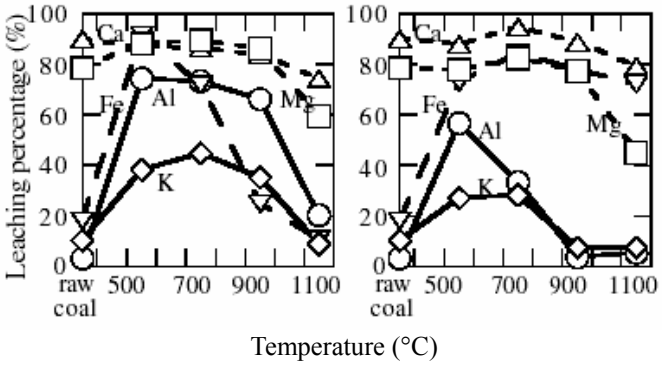

Figure 1. Leaching of major metallic elements from EL raw coal, its ashes (the left figure), and its chars (the right figure). The ashes and chars were obtained from the slow-heating combustion and pyrolysis at different temperatures.

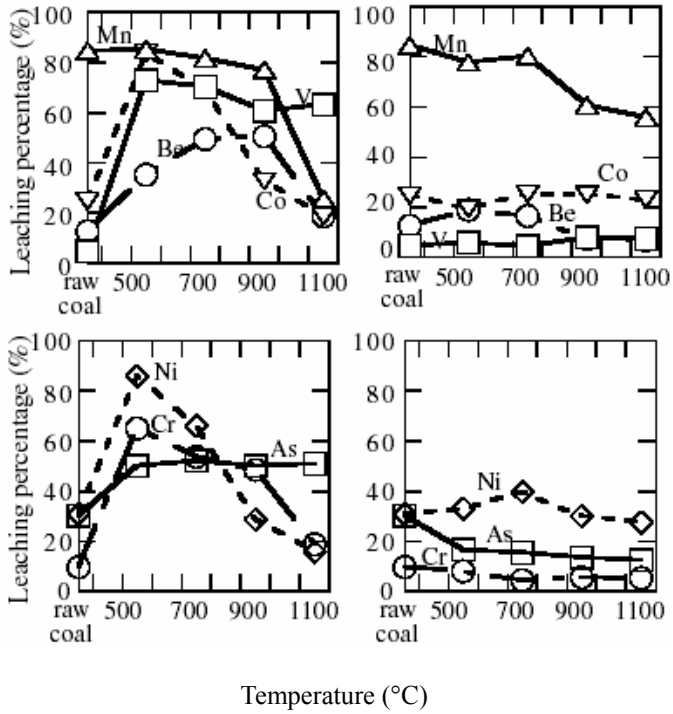

Figure 2. Leaching of non-vaporized trace elements from EL raw coal, its ashes (the left figures), and its chars (the right figures). The preparation of the ashes and chars is noted in Figure 1.

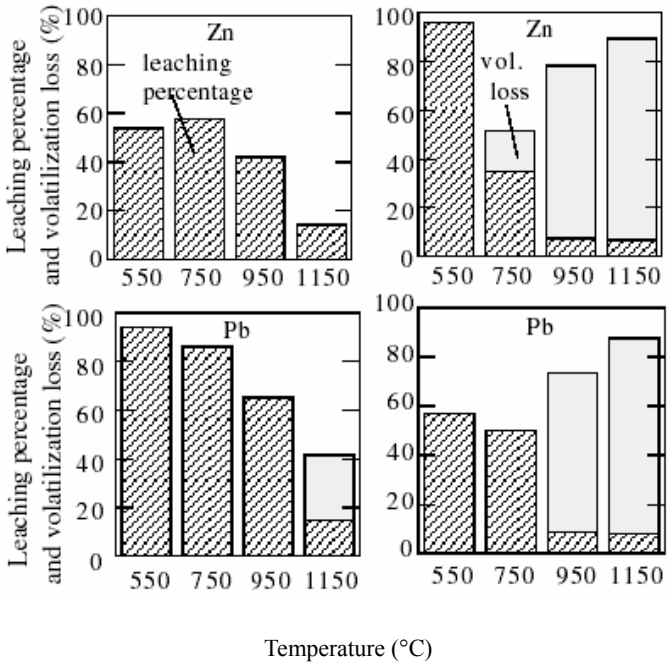

Figure 3. Leaching of volatile trace elements from EL coal ashes (the left figures) and chars (the right figures). The preparation of the ashes and chars is noted in Figure 1.

Conclusions

Leaching behaviors of the major metallic elements in the raw, coal, ashes and chars are well explained by their existing form in coal and their transformations during the combustion and pyrolysis. Leaching results of trace elements showed that Mn is easily dissolved from the raw coal, ashes and chars, implying its existing form of carbonate. Be, Co, V, Cr, Ni in 550-750 ashes were more soluble than those in the raw coal and chars, suggesting their organic association. The liberated species of Be, Co, Cr and Ni in the ashes became less soluble at higher temperatures. Arsenic in the ashes is more soluble than that in the chars, implying a different transformation of As between the combustion and pyrolysis. Zn and Pb significantly volatilized during pyrolysis but little volatilized in the combustion.

Acknowledgements.

This work is partly supported by a Grand-in-Aid for the Scientific Research on Priority (No. 11218201).

References

(1) Davidson, R. M. *Modes of Occurrence of Trace Elements in Coal*; CCC/36, IEA Coal Reasearch: London, UK, 2000; pp1-36.

(2) Wang, J.; Sharma, A.; Tomita, A. *Energy & Fuels* (in press,)

(3) Wang J.; Tomita, A. *Energy & Fuels* (submitted).

REMOVAL OF MERCURY FROM COAL BY MILD PYROLYSIS AND CHELATE EXTRACTION

Akira Ohki, Akira Iwashita, Shomei Tanamachi, Tsunenori Nakajima, and Hirokazu Takanashi

Department of Bioengineering,
Faculty of Engineering, Kagoshima University,
1-21-40 Korimoto, Kagoshima 890-0065, Japan

Introduction

Coal contains many kinds of elements which include hazardous heavy metals, such as As, Hg, Pb, and Se. Among these metals, Hg is the most concerned because the element is quite volatile, so that 30-75% of Hg in coal will be released to air when coal is burned in coal-fired power plant.[1] It is reported that coal combustion is a great source for the global emission of Hg.[1] Therefore, many studies have been devoted to the problem of Hg in coal, including the occurrence of Hg in coal, its emission behavior, and the reduction of Hg emission.[2] There have been many studies about the removal of Hg after the combustion of coal. However, only a few studies have been done about the advanced and precombustion removal of Hg from coal. Keener et al. reported that 40-80% of Hg in coal was removed by mild pyrolysis, in which coal was heated under nitrogen flow at 300-400°C, for several American coals.[3,4] However, the effect of varying the brand of coal upon the Hg removal and detailed mechanism have not yet been clear.

There have been several studies about the removal of heavy metals from coal fly ashes[5,6] incineration ashes,[7] and contaminated soil[8] by use of chelate extraction. However, for the heavy metals in coal, chelate extraction has not been so far applied.

In this paper, the removal of Hg from coal by mild pyrolysis as well as that by chelate extraction were examined. The dependence of the ease of Hg removal upon the brand of coal was discussed in terms of the removal efficiency for mild pyrolysis and that for the chelate extraction.

Experimental

Coals. Nine Japanese standard coals (SS coals) distributed from the Japan Coal Energy Center (JCOAL) and a certified reference material from the SA Bureau of Standards, Republic of South Africa (SARM20) were used. **Table 1** presents the analyses of these coals. The particle sizes of SS coals were under 149 μm while that of SARM20 was under 106 μm and no further pulverization was performed.

Determination of Hg in coal. Powdery coal (ca. 0.25 g) was precisely weighed and was acid-digested with HNO_3+H_2O_2 (5+3 ml) using a microwave processor (Milestone ETHOS1600). After cooling and the addition of further HNO_3+H_2O_2 (2+1 ml), microwave processing was performed again. After cooling and filtration, the filtrate was diluted to a fixed volume (25 ml) and was subjected to cold vapor atomic absorption spectrometry (CVAAS) using a Nippon Jarrel Ash AA855 with a Hg reduction system AMD-D2 for the determination of Hg concentration.

Mild pyrolysis. Powdery coal (0.5 g) was placed in a alumina board and heated by a horizontal tubular furnace at a rate of 1 °C/s to a desired temperature under N_2 flow (100 ml/min) and the temperature was kept for 1 h. Then the resulting coal was digested and analyzed for the Hg content. The value of % Hg removal was defined as [1-(Hg content in treated coal)/(Hg content in raw coal)] X 100.

Chelate extraction. An aqueous solution (20 mL) containing a chelating agent was shaken with 0.25 g of powdery coal for 24 h in a stoppered centrifuge tube at a room temperature (24-25°C), and the filtration was performed to separate the coal. For the chelating agent, ethylenediaminetetraacetic acid (EDTA, 2Na salt), nitrilotriacetic acid (NTA), dimercaptosuccinic acid (DMSA), mercaptopropionic acid (MPA), and mercaptoethanol were used. In case of NTA and DMSA, two equivalent of NaOH was further added in the aqueous solution, while for MPA one equivalent of NaOH was added. The resulting coal was dried and analyzed for Hg content.

Results and Discussion

The nine SS coals were subjected to Hg analysis by CVAAS, and the results are recorded in **Table 1**, together with the data for SARM20. The Hg content of those ten coals varies from 0.04 to 0.25 μg/g, for which SARM20 has the highest value while SS002 has the lowest.

Table 1. Analyses of Coals

Sample coals (Producing country)	Ultimate (wt%, d.b.)			Proximate (wt%, d.b.)		Hg content
	C	N	S	V. M.	Ash	(μg/g)
SS001 (AUS)	72.7	1.4	0.4	27.0	15.4	0.08
SS002 (AUS)	69.1	1.3	0.5	38.9	14.9	0.04
SS003 (AUS)	75.6	1.7	0.3	29.3	8.8	0.10
SS004 (CHN)	74.4	1.0	0.7	29.7	10.0	0.08
SS006 (AUS)	72.2	1.6	0.5	36.3	12.2	0.10
SS020 (ZAF)	71.1	1.8	0.7	32.0	13.4	0.20
SS026 (USA)	66.2	1.2	0.3	38.7	13.9	0.06
SS027 (CHN)	71.6	0.9	0.6	29.2	10.8	0.08
SS028 (AUS)	74.0	1.7	0.3	28.2	8.4	0.05
SARM20	-	-	0.5	-	-	0.25 [1)]

[1)] Certified value

The ten coals were treated by mild pyrolysis at 300 and 400°C, and the results for % Hg removal are shown in **Figure 1**. The removal efficiency varied from 14% to 80% depending upon the brand of coal when the mild pyrolysis was carried out at 300°C. SS004 and SS020 coals provided high % Hg removal values of ca. 80%, whereas the % removal for SS006 was quite low (14%). For coals which give lower % Hg removal, greater increases in the % removal tend to be observed when the pyrolysis temperature is raised from 300°C to 400°C. When 400°C-pyrolysis was carried out, the values of % Hg removal for SS004 and SS006 were 88% and 42%, respectively. The weight loss (dry base) of coal during the mild pyrolysis varied from 0.8% to 7.5% for 300°C and from 1.9% to 20.8% for 400°C. There is no evident correlation between the weight loss values and the % Hg removal values.

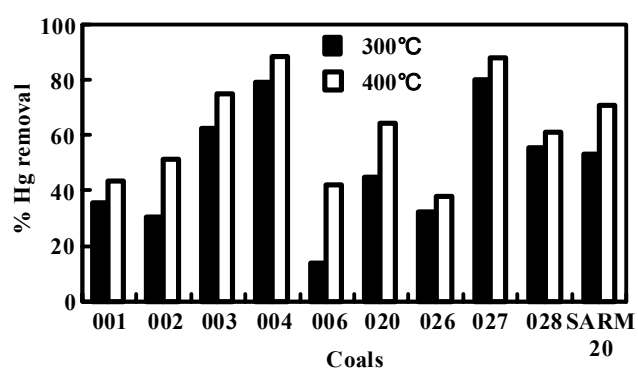

Figure 1. Removal of Hg from SS coals and SARM20 by mild pyrolysis (1 h).

When the % Hg removal values for the mild pyrolysis were plotted against the specific surface areas for those coals, almost no correlation was observed. The effect of varying the particle size of coal upon the Hg removal was assessed when SS004 was subjected to 300°C-pyrolysis (1 h). For the particle sizes of under 1000, 149, and 74 μm, the values of % Hg removal were 79, 79, and 67%, respectively. When SS001 and SS020 were examined, similar results for the effect of varying the particle size were obtained. Consequently, the Hg removal efficiency is dependent neither on the specific surface area nor on the particle size. Therefore, it is anticipated that the difference in % Hg removal for each coal is ascribed not to the difference in physical structure of coal matrix but to that in the mode of occurrence for Hg in coal.

Figure 2 shows the plot of % Hg removal against the pyrolysis temperature for SS004 and SS006. When the temperature was 200°C, both coals gave small values of % Hg removal. For SS004, the % removal rapidly increased when the temperature was raised to 300°C, and kept almost constant at higher temperatures. However, for SS006, the % removal was quite low even at 400°C, and increased to ca. 95% when the temperature was elevated to 500°C. Consequently, it is found that the Hg removal efficiency is greatly different in those two coals when the mild pyrolysis at 300-400°C is performed, although those two coals have similar Hg contents (see **Table 1**).

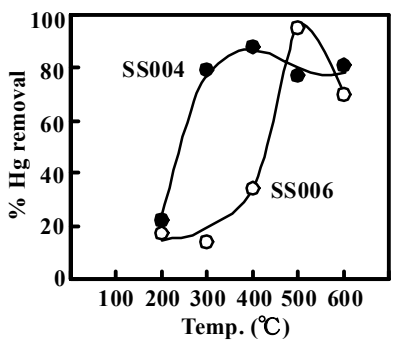

Figure 2. Dependence of Hg removal upon pyrolysis temperature.

The chelate extraction of Hg from SS004 using various chelating agents was performed, and the results of % Hg removal are summarized in **Table 2**. Ordinary chelating agents, such as EDTA and NTA, gave % Hg removals of 18 and 14%, respectively, whereas sulfur-containing chelating agents, such as DMSA and MPA, provided higher % removals of 57 and 44%, respectively. It is reasonable that the chelating agents possessing soft coordination sites give higher Hg removal because Hg ions are typical soft acids.

Table 2. Removal of Hg from SS004 by Chelate Extraction [1)]

Agents (50 mM)	% Hg removal
DMSA [2)]	57
MPA	44
2-Mercaptoethanol	27
EDTA	18
NTA	14
NaOH	16
Water	0

[1)] L/S = 80, 24-25℃, 24h ; [2)] 25 mM

The ten coals shown in **Table 1** were subjected to the chelate extraction using MPA. The % Hg removal varied depending on the coal brand, and interestingly, there is an apparent correlation between the values of % Hg removal for the MPA extraction and those for the mild pyrolysis, as illustrated in **Figure 3**. Taking into account of the above result as well as that for the effects of specific surface area and particle size previously mentioned, it appears that the mode of occurrence for Hg in coal is the greatest factor which affects the ease of Hg removal both for the mild pyrolysis and for the chelate extraction.

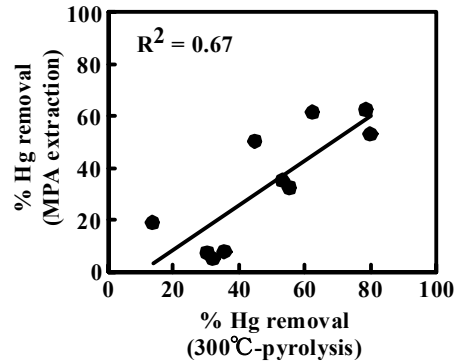

Figure 3. Correlation between Hg removal by MPA extraction and that by mild pyrolysis at 300℃.

Conclusions

The removal of Hg from coal was effectively attained by mild pyrolysis and chelate extraction. For chelate extraction, sulfur-containing agents were superior to ordinary chelating agents. The Hg removal efficiencies of the two removal methods were greatly dependent upon the coal brand, and there is an apparent correlation between those of the two methods. Detailed mechanism about this phenomenon is now under study.

Acknowledgment

This work was supported by a Grant-in-Aid for Scientific Research (No.11218209) from the Ministry of Education, Culture, Sports, Science, and Technology, Japan.

References

(1) Clarke, L. B.; Sloss, L. L. "Trace elements-emission from coal combustion and gasification", IEA Coal Research, IEACR/49, 1992.
(2) Sloss, L. L. "Mercury-emissions and control", IEA Coal Research, CCC/58, 2002.
(3) Merdes, A. C.; Keener, T. C.; Khang, S.-J.; Jenkins R. G. *Fuel*, **1998**, *77*, 1783.
(4) Wang, M; Keener, T. C.; Khang, S.-J. *Fuel Process. Technol.*, **2000**, *67*, 147.
(5) Xu, Y.-H.; Nakajima, T.; Ohki, A. *Toxic. Environ. Chem.* **2001**, *81*, 55.
(6) Xu, Y.-H.; Nakajima, T.; Ohki, A. *Toxic. Environ. Chem.* **2001**, *81*, 69.
(7) Hong, K.-J.; Tokunaga, S.; Kajiuchi, T. *J. Hazard. Mater.* **2000**, *B75*, 57.
(8) Sun, B. ; Zhao, F. J.; Lombi, E.; McGrath, S. P. *Environ. Pollut.*, **2001**, *113*, 111.

ALLOY COMPOSITION EFFECT ON THE N-VALUE FOR H_2-SELECTIVE Pd MEMBRANES

Fernando Roa, J. Douglas Way

Colorado School of Mines, Chemical Engineering Department
1500 Illinois St, Golden, CO 80401-1887

1. Introduction

Hydrogen is known to be highly soluble in palladium and in some of its alloys [1]. This characteristic makes those Pd alloys suitable to be used as hydrogen selective membranes [2].

For reasonably thick Pd membranes (thickness ≥ 10μm), the H_2 flux can be calculated from Sievert's Law [3]:

$$J_{H_2} = \frac{\rho_{H_2}}{X_{metal}}\left(P^n{}_{H,feed} - P^n{}_{H,perm}\right) \qquad (1)$$

The dependence of the H_2 flux on feed and permeate pressures is represented in Equation 1 by the exponent 'n'. For thick Pd films, the rate-controlling step for the permeation process is the bulk metal diffusion of atomic hydrogen, for which the n-value should be 0.5 [4]. Changes in the crystalline structure of the membrane, large external mass transfer resistances, very thin films, gradients in alloy composition or the dominance of other transport mechanism have shown to cause deviations from that value [5].

Pure palladium, however, presents an embrittlement problem if in contact with H_2 at temperatures below 310°C, is easily poisoned by sulfur compounds and doesn't withstand temperature cycling. The Pd-Cu alloy has been found to show improved resistance to all of these problems while exhibiting superior permeation to cost performance at the $Pd_{60}Cu_{40}$ composition [6-8]. N-values and fluxes were calculated for a $Pd_{60}Cu_{40}$ and a $Pd_{90}Cu_{10}$.

Pd membranes should show infinite H_2 selectivity. However the presence of grain boundaries, cracks and pinholes, as well as imperfect seals cause finite permeation of insoluble species[9]. We discuss why differences in plating procedures led to a membrane exhibiting H_2/N_2 ideal selectivity over 7000.

2. Experimental

Materials. Composite Pd alloy membranes were fabricated by sequential deposition of commercially available palladium and copper electroless plating baths onto asymmetric 0.05 cut-off zirconia coated α-alumina tubes (US Filter, T1-70). All gases used were nominally 99.999% pure (UHP grade).

Preparation. A seeding procedure has to be used prior to the palladium plating. That step involves impregnation of the ceramic support with an organic Pd salt solution, followed by calcination and reduction in flowing hydrogen.

Pd and Cu electroless plating baths were then used in combination with osmotic pressure gradients to deposit films ranging from 1 to 5 microns in thickness. The osmotic pressure, generated by circulating concentrated sucrose solutions on the outside of the tubes, insured reduced porosity and promoted surface homogeneity and densification of the plated Pd film [10].

High Temperature Permeation Tests. The membrane to be tested was loaded into a stainless steel module, which in turn was mounted in a tube furnace. To avoid embrittlement, the membranes were heated under helium and no H_2 was introduced until the membrane reached 350°C. Annealing the two metals was achieved while conducting the single gas permeability tests, run at transmembrane pressure differentials of 345 and 172 kPa and temperature varying from 350°C to 500°C. Permeate pressure was local atmospheric pressure (~83 kPa) and no sweep gas was used.

Characterization. Scanning electron microscopy (SEM) was carried out to determine film thickness; Atomic Force Microscopy (AFM) was used to study surface morphology; X-ray diffraction (XRD) and energy dispersive X-ray spectroscopy (EDAX) were used to study crystal structure and determine Pd alloy composition.

3. Results and Discussion

Alloy Composition and Flux. For Pd-Cu membranes, the H_2 flux is strongly influenced by the alloy composition and it has a maximum at about 40-wt% Cu. This behavior is attributed to a favorable phase transition occurring at about this composition in the solid phase [11]. We targeted that specific composition; however, given that our current membrane fabrication procedure mandates each metal to be deposited separately and that we could only calibrate the deposition time after testing the membrane, several membranes of different compositions were made.

Table 1. Permeation Data for Pd-Cu Membranes at 350°C

Membrane	Metal Thickness (μm)	Pd/Cu Alloy Composition (wt%)	Max. Permeance $\left(\frac{mol}{m^2 mmHg^{0.5} s}\right)$	Max. Selectivity
20	1.0± 0.2	90/10	0.061	2000
22	1.5± 0.2	70/30	0.138	48
25b	1.5± 0.2	60/40	0.312	93
28	3.5± 0.5	90/10	0.035	≥7000

Table 1 summarizes the permeation experiments results for our recent membranes. Of the membranes shown there, membrane 25b clearly exhibits the highest permeance; in agreement with the literature, it has a $Pd_{60}Cu_{40}$ alloy as its selective layer. Figure 1 shows the influence of alloy composition on the permeance values for membranes studied in this work. Hydrogen permeance values for 10-25μm-thick Pd-Cu foils from the literature are also plotted on Figure 1 for comparison. As can be seen in that plot, both membrane 25b and the $Pd_{60}Cu_{40}$ foils exhibited higher hydrogen permeance than their comparable membranes having different alloy compositions. Moreover, the H_2 permeance of membrane 25b is more than twice that of an equivalent foil.

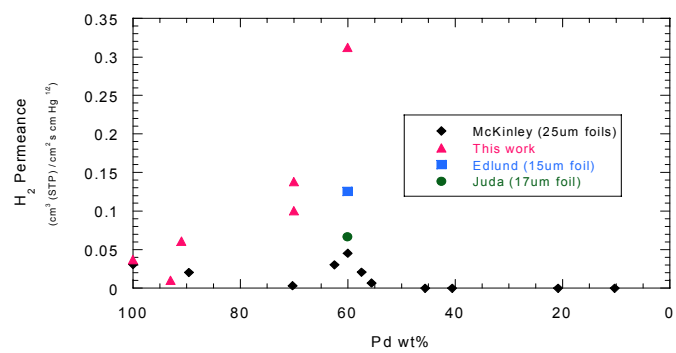

Figure 1. Alloy composition influence on H_2 permeance for Pd-Cu composite membranes and Pd-Cu foils.

Among the factors contributing to the differences in permeance are: the use of supports for making our membranes; these being thinner than the foils; that their surface morphologies are different according to AFM images, and that their bulk crystalline structures are also different as our membranes exhibit domains for both the fcc and bcc phases as opposed to just bcc for the foils (from XRD data).

N-value and Temperature. Figure 2 presents the transport data for membrane 25b at 350°C. Non-linear regression of the data gives an n-value of 0.515. Given that the experimental n-value is very close to the theoretical value of 0.5, it is likely that the H_2 transport through this membrane is controlled by the diffusion of hydrogen atoms through the metal bulk film. By contrast, the n-value for nitrogen permeation through the same membrane was 1.05; presumably indicating that nitrogen transport occurred mainly by Knudsen diffusion through defects in the metal film and seals. The ideal H_2/N_2 separation factor at 350°C for a feed pressure of 25 psig was 100.

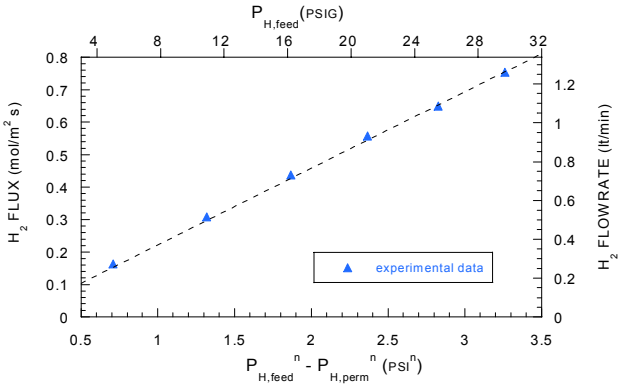

Figure 2. Permeation data for membrane 25b at 350°C. The dotted line shows predicted H_2 fluxes using eq. 1 with n equal to 0.515.

The n-value dependence on temperature was observed for membrane 28 and it is plotted in Figure 3. This membrane was not typically prepared, as it had to be plated again because it failed after air was accidentally let in for an extended period, during the high temperature experiments. As seen in Figure 3, the n-values for membrane 28 departed significantly from the ideal value, 0.5, in contrast with membrane 25b. Moreover, the ideal H_2/N_2 ideal selectivity for membrane 28 was very high, well over 7000.

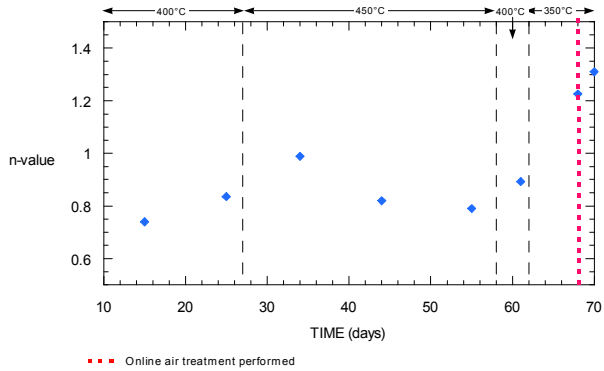

Figure 3. Effect of temperature and time in the n-value for #28.

That discrepancy may be related to the different preparation histories for the two membranes. Based on recently published results for controlled oxidation of on palladium films [12], it is thought that the prolonged air exposure made the original metal film rearrange to form a pattern of conically shaped structures, much like a range of hills and valleys, schematically illustrated in Figure 4, creating a metal oxide layer of very small pore size on top of the ceramic support. These micropores in the sieve-like structure developed would then be easily and completely covered with the subsequent metal depositions, essentially forming a pore-free film, which would thus explain the high selectivity membrane 28 showed. Note, however, that inside those micropores the formation of micro voids underneath the newly deposited film was likely, due to less than perfect wetting between the metallic and oxidized layers, a consequence of the different electronic nature of each surface.

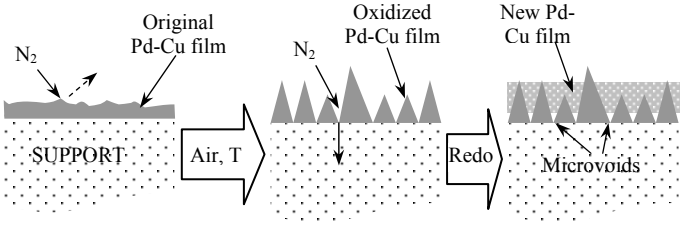

Figure 4. Sketch of what is thought happened to membrane 28.

As a consequence, we hypothesize that there are two different rate processes in series limiting the permeation through the metal film in membrane 28 rather than just one as was the case for membrane 25b: proton diffusion through the metal film and gas phase mass transfer resistance in the voids; each would in turn become dominant depending on the transport conditions.

4. Conclusions

A range of Pd-Cu composite membranes of different alloy composition were fabricated and they exhibited a hydrogen permeation trend consistent with the literature.

A $Pd_{60}Cu_{40}$ membrane was made that showed higher permeance than other composite membranes of different alloy composition and than $Pd_{60}Cu_{40}$ foils. A $Pd_{90}Cu_{10}$ exhibited selectivity over 7000.

The transport mechanism for H_2 through Pd-Cu membranes is affected by alloy composition, temperature and preparation history.

Acknowledgements. This work was supported by the U.S. Dept. of Energy (DOE) University Coal Research Program under grant No. DE-FG2699 – FT 40585. The authors are grateful to Dr. David Edlund of IdaTech, LLC for donating the $Pd_{60}Cu_{40}$ foil membrane used in this work. The authors are also grateful to Michael J. Block for his help with membrane preparation and transport experiments.

5. References

1. Linkov, V. Membrane Technology, 2001. **132**: p. 4-8.
2. Paglieri, S., D. Way, and J. Collins. Ind. Eng. Chem. Res., 1999. **38**(10): p. 1925-1936.
3. Ward, T. and T. Dao. J. Membrane Sci., 1998. **153**(1): p. 211-231.
4. Uemiya, S., T. Matsuda, and E. Kikuchi. J. Membr. Sci. 1991. **56**: p. 315-325.
5. de Rosset, A.J. 1960: U.S. Patent 2,958,391
6. McKinley, D.L. 1967: U.S. Patent 3,439,474
7. Edlund, D.J. and D.T. Friesen. 1993: U.S. Patent 5,217,506
8. Juda, W., Krueger, C.W., and Bombard, R.T. 2000: U.S. Patent 6,103,028
9. Roa, F., D. Way, and S. Paglieri. Chem. Eng. J., 2002. **4047**: p. 1-12.
10. Varma, A. and R. Souleimanova. J. Membrane Sci., 2000. **166**(4): p. 249-257.
11. Piper, J. J. Appl. Phys., 1966. **37**(2): p. 715-21.
12. Aggarwal, S., *et al.* Science, 2000. **287**: p. 2235-2237.

DEVELOPMENT OF THE CERAMIC MEMBRANE ITM SYNGAS/ITM HYDROGEN PROCESS

Michael F. Carolan, Christopher M. Chen and Steven W. Rynders*

Advanced Gas Separation Department
Air Products and Chemicals, Inc.
7201 Hamilton Boulevard
Allentown, PA 18195

Introduction

The ITM Syngas Team led by Air Products and Chemicals and including Ceramatec, ChevronTexaco, Eltron Research, McDermott Technology and other partners, in collaboration with the U.S. Department of Energy, is developing ceramic Ion Transport Membrane (ITM) technology for the production of synthesis gas and hydrogen from natural gas. The ITM Syngas technology is in the fifth year and Phase 2 of a co-funded $90 MM, nine year, three phase development program.

ITM membranes are fabricated from non-porous, multi-component metallic oxides that operate at high temperatures and have exceptionally high oxygen flux and selectivity. A conceptualization of the ITM Syngas process is illustrated in Figure 1. The membrane structure incorporates a non-porous ITM and reduction and reforming catalyst layers. The membrane material must show long-term stability in reducing and oxidizing atmospheres, and long-term compatibility with the reduction and reforming catalysts.

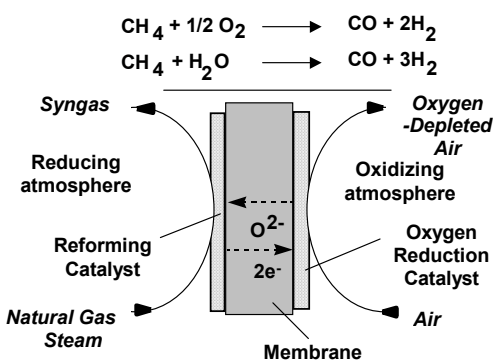

Figure 1. The conceptual ITM Syngas technology.

ITM Syngas Process Design

The ITM Syngas process combines air separation and high-temperature syngas generation processes into a single, compact ceramic membrane reactor, resulting in significant savings when compared to conventional technology. In contrast to conventional oxygen-blown Autothermal Reformer (ATR) processes that require high-pressure oxygen typically supplied by a cryogenic Air Separation Unit (ASU), the ITM process uses low pressure air directly, resulting in significant capital and operating cost savings. The ITM Syngas process is outlined in Figure 2 [1-4]. The process has several important features: production of syngas at high pressure while consuming air delivered at low pressure, use of an upstream prereformer, non-isothermal operation of the ITM Syngas reactor, and integration with the downstream Fischer-Tropsch (FT) process. The ITM Syngas reactor operates in the 200 to 500 psig pressure range, and produces syngas at pressure suitable for downstream Fischer-Tropsch processes without the need for further compression. The air supplied to the ITM Syngas reactor is delivered at low pressure (approximately 5 to 10 psig), resulting in additional significant capital and operating cost savings.

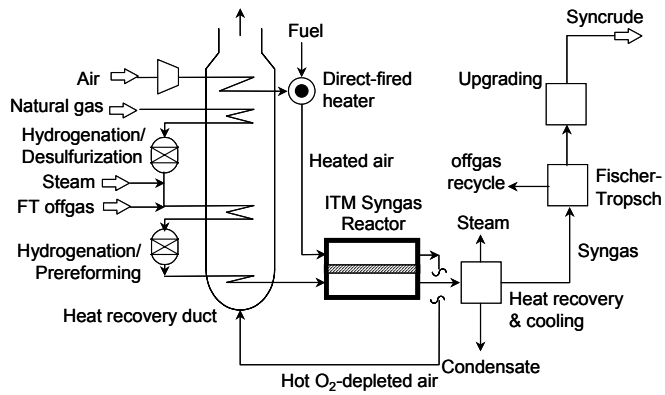

Figure 2. The ITM Syngas process with adiabatic prereformer.

The natural gas feed is converted into syngas in a two-stage process comprising a steam reforming step followed by conversion to syngas in the ITM Syngas reactor. The prereforming step converts a portion of the methane and essentially all of the heavier hydrocarbons into hydrogen, carbon monoxide, carbon dioxide, and methane. This step minimizes processing problems, such as carbon formation, in the downstream heat exchanger and the ITM Syngas reactor.

The ITM Syngas reactor operates non-isothermally, with a prereformed natural gas inlet temperature of 550 – 750 °C and a syngas exit temperature of > 800 °C. The exit temperature is in the preferred range for oxidative reforming while the cooler inlet temperature minimizes carbon formation in the inlet piping and permits a wider choice of piping materials.

CO_2-containing offgas from a downstream Fischer-Tropsch plant may be recycled to the feed of the ITM Syngas process to adjust the product syngas H_2/CO molar ratio to about 2, suitable for FT GTL. This avoids an acid gas removal system to recycle CO_2; instead, the FT offgas containing CO_2 is recovered at high pressure along with other useful components to be recycled, such as light hydrocarbons, hydrogen, and carbon oxides.

Economic Analysis

Air Products, ChevronTexaco, and McDermott developed an ITM Syngas process design and cost estimate for an offshore GTL facility that processes 55 million SCFD of associated gas and produces approximately 6,400 barrels per day of syncrude. The economic evaluation compared an ITM Syngas process to an oxygen-blown ATR process that included a cryogenic ASU. Capital cost savings of greater than 30% are predicted with the ITM Syngas process over a conventional ATR with ASU. Other advantages of the ITM Syngas process include an increase in overall fuel efficiency to 61% versus 58% for ATR/ASU; and up to 40% less deck space required for syngas process and power generation equipment.

Ceramic Fabrication and Testing

The ITM Syngas/ITM Hydrogen team has developed stable ITM Syngas material compositions and successfully fabricated planar membranes from these materials. The membranes are based on microchannel device designs developed by Air Products, Ceramatec, and McDermott and are fabricated at Ceramatec using methods that provide good scalability for commercial application.

Laboratory-scale membranes have been used extensively to evaluate the properties and performance of candidate ITM materials

developed by Air Products, Ceramatec, and Eltron Research. Several generations of ITM Syngas material compositions have been evaluated and compositions that achieve the commercial flux targets have been identified.

Pilot-scale membranes are used to evaluate membrane performance at commercial process conditions. The membranes are assembled into single or multi-membrane modules and are mounted into superalloy holders using double U-ring ceramic/metal seal assemblies developed by Air Products and Ceramatec [5]. A representative pilot-scale membrane module, prior to installation, is illustrated in Figure 3.

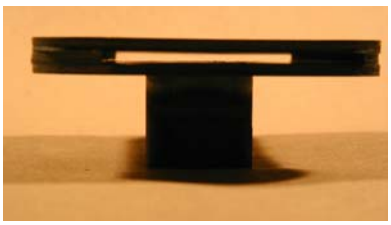

Figure 3. A pilot-scale Membrane Module

Development activities at Ceramatec have also focused on the implementation of fabrication processes to produce large area membranes. These activities have led to a rapid development of scalable fabrication processes and a nearly 200 fold increase in the area of membranes that can be fabricated. Figure 4 illustrates the significant increase in the area of membranes, up to and including full-sized membranes, fabricated using the processes developed at Ceramatec.

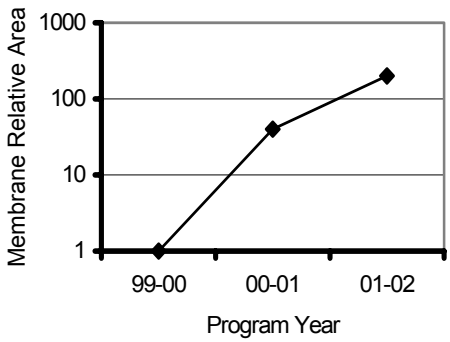

Figure 4. Progression of ITM Syngas/ITM H_2 Ceramic Membranes from Laboratory-scale to Full-sized Components.

Air Products and McDermott have jointly developed and installed a 24,000 SCFD ITM Syngas/ITM H_2 Process Development Unit (PDU) to evaluate membrane performance throughout the full range of ITM Syngas and ITM H_2 process conditions. The PDU, illustrated in Figure 5, is suitable for testing pilot and full-sized membranes and is currently in use for membrane performance testing and membrane design verification.

Conclusions

Significant progress has been made to develop the ITM Syngas/ITM H_2 technology. Membrane modules and seal assemblies have been fabricated for testing in the PDU and ceramic fabrication scaleup is continuing the progression from lab-scale to full-size membranes. A database is being built up of performance data from membrane testing in the laboratory and PDU. Excellent progress

Figure 5. The ITM Syngas/ITM H_2 Process Development Unit.

continues to be made against the remaining technical challenges in the demonstration and scale-up of the ITM Syngas and ITM H_2 technology.

Acknowledgement The authors gratefully acknowledge the work of ITM Syngas team members at Air Products and Chemicals Inc., Ceramatec Inc., ChevronTexaco Energy Research and Technology Co., Eltron Research Inc., and McDermott Technology Inc. The co-funding by the U.S. DOE (DE-FC26-97FT96052) is also gratefully acknowledged.

Disclaimer A significant portion of this report was prepared by Air Products and Chemicals, Inc. pursuant to a Cooperative Agreement partially funded by the United States Department of Energy, and neither Air Products and Chemicals, Inc. nor any of its contractors or subcontractors nor the United States Department of Energy, nor any person acting on behalf of either:

1. Makes any warranty or representation, express or implied, with respect to the accuracy, completeness, or usefulness of the information contained in this report, or that the use of any information, apparatus, method, or process disclosed in this report may not infringe privately owned rights; or
2. Assumes any liabilities with respect to the use of, or for damages resulting from the use of, any information, apparatus, method, or process disclosed in this report. Reference herein to any specific commercial products, process, or service by trade name, trademark, manufacturer, or otherwise, does not necessarily constitute or imply its endorsement, recommendation, or favoring by the United States Department of Energy. The views and opinions of authors expressed herein do not necessarily state or reflect those of the United States Department of Energy.

References

(1) Nataraj, S.; Moore, R. B.; Russek, S. L. U.S. Patent 6048472, **2000**.
(2) Nataraj, S.; Russek, S. L. U.S. Patent 6077323, **2000**.
(3) Nataraj, S.; Russek, S. L. U.S. Patent 6110979, **2000**.
(4) Nataraj, S.; Dyer, P. N.; Russek, S. L. U.S.Patent 6114400, **2000**.
(5) Minford, E.; Rynders, S. W.; Taylor, D. M.; Tressler, R. E. US Patent 6302402, **2001**.

Copyright © 2003 Air Products and Chemicals, Inc.
This paper was written with support of the U.S. Department of Energy under Contract no. DE-FC26-97FT96052. The Government reserves for itself and others acting on its behalf a royalty-free, nonexclusive, irrevocable, worldwide license for Governmental purposes to publish, distribute, translate, duplicate, exhibit and perform this copyrighted paper.

TRANSFORMATION OF ARSENIC IN YIMA COAL DURING FLUIDIZED-BED PYROLYSIS

Hailiang Lu, Haokan Chen, Wen Li & Baoqing Li

State Key Laboratory of Coal Conversion, Institute of Coal Chemistry, Chinese Academy of Sciences, Taiyuan, China 030001

Introduction

Arsenic is one of the most concerned trace element in coal because of its toxicity and environmental persistence. The mode of occurrence of arsenic in coal strongly affects its transformation behaviour during coal conversion. There are many directly and indirectly methods[1,2,3,4] for determining the mode of occurrence of elements in coal, such as X-ray absorption fine structure(XAFS) spectroscopy, scanning electron microscopy- energy dispersive X-ray (SEM-EDX) analyzer, and sequential chemical extraction. Previous work has shown that pyrite is the principal source of arsenic in coal.[1,2] The partitioning of arsenic during coal conversion depends on many factors including coal composition, reaction conditions and the mode of occurrence of arsenic in coal. Papers[3,5,6] show that arsenic belongs to semi-volatile elements, and most of arsenic is bound to fine particulates during coal combustion or gasfication. The behaviour of arsenic is greatly influenced by its coexisting coal major and minor elements. However, there is little information about the transformation behaviour of arsenic under pyrolysis conditions. The volatilization behaviour of arsenic in Yima coal and the influence of coexisting mineral matters during pyrolysis in fluidized-bed reactor are investigated in this paper. The mode of occurrence of arsenic in Yima coal and its char were determined using three methods including density fractionation, demineralization and sequential chemical extraction.

Experimental

Coal Sample and Demineralization. The coal used in this study was a young bituminous coal. Coal sample was ground and sieved to 147 μm~246 μm. To determine arsenic affinities in Yima coal and study the effect of mineral matters on arsenic volatility during pyrolysis, demineralization was carried out. This demineralization procedure was following the method of Chen et al.[7] Proximate and ultimate analyses for Yima raw coal (Yima) and its demineralized sample (YimaD) were given in **Table 1**.

Table 1. Proximate and Ultimate Analyses of Samples / Wt%

Sample	M_{ad}	A_d	V_{daf}	C_{daf}	N_{daf}	H_{daf}	S_{daf}
Yima	8.82	17.3	40.2	78.1	0.86	3.90	0.40
YimaD	2.92	2.73	36.6	78.2	0.85	5.20	0.40

Density Fractionation. Density fractionation had been used frequently to determine the trace element organic/inorganic affinities in coals. Most organic matters in coal occurred in <1.6g/cm^3 density fractions[8]. Three density fractions including <1.3 g/cm^3(YM1), 1.3 g/cm^3~1.6 g/cm^3(YM2) and >1.6 g/cm^3(YM3) were obtained from Yima raw coal by using analytical reagent CH_2Cl_2 and CCl_4. Occurrence of arsenic in coal is obtained through coupling with other two methods, demineralization and sequential chemical extraction. Ash content of different density fractions were analyzed by using Chinese standard method (GB/T212-91).

Pyrolysis Experiment. Yima and YimaD were used for pyrolysis experiment at temperature ranging from 500°C to 900°C, respectively. The pyrolysis conditions are the same as reference 9. Chars were collected for analysis after pyrolysis.

Sequential Chemical Extraction. Sequential chemical extraction was used to determine the mode of occurrence of trace elements in coal, which represented the chemical mobility in environment of the element. The binding forms of arsenic in Yima raw coal and its char were determined by this method. The char samples were obtained at 600°C and 900°C, and ground to <74 μm. During the sequence of extraction steps, arsenic associated with various parts of the coal or char would be extracted in the following order: (1) water soluble and ion exchangeable cations were extracted by 1M CH_3COONa; (2) primarily associated with carbonates were extracted by 1M CH_3COONH_4, (3) associated with sulfates and monosulfides were extracted by 4M HCl at 100 ^{o}C; and (4) associated with disulfides were extracted by 2M HNO_3. After each step of extraction, aqueous solution was separated from the solid residue by centrifugation for 20 min. The solid was dried at 60 ^{o}C for next step. Arsenic remained in extraction residue was labeled "stable forms" in this paper, which had little chemical mobility in environment. Stable forms of arsenic in coal may be present in the organic matrix, or occur in insoluble phases such as zircon, titanium dioxide, silicate and occur in crystal lattice of other insoluble mineral matters.

Determination and Calculation method. Arsenic contents in coal or its char and their extracted solutions were determined by Atomscan16, inductively coupled plasma-atomic emission spectroscopy(ICP- AES), made in TJA company of America. The calculation method of arsenic volatility was similar to that of fluorine in reference 9.

Results and Discussion

Table 2 showed the arsenic contents in density fractions. Ash content of YM1 and YM2 were 5.06% and 6.94%, only 1/3 of that in raw coal(17.3%). The ash content of the heaviest density fraction(YM3) was 61.02%, which was much higher than that of raw coal. So most of YM3 was mineral matters, and large part of YM1 and YM2 should be organic matters. Compared with that in raw coal, arsenic contents of YM1 and YM2 were very low, while arsenic content of YM3 was very high. More than 75% of arsenic enriched in the heaviest density fraction. It indicated that most of arsenic in Yima coal was associated with mineral matters. The mass balance of arsenic is about 85%.

Table 2. Arsenic Contents in Density Fractions Obtained from Yima Coal (dry basis)

Sample	Yield/%	HTA*/%	As / μg·g^{-1}	Fraction /%
Yima	100	17.32	33.0	100
YM1	5.91	5.06	3.8	0.68
YM2	74.38	6.94	4.0	9.02
YM3	19.61	61.02	127.6	75.81

* high temperature ash (820 ^{o}C)

During the demineralization process of raw coal by hydrochloric acid and hydrofluoric acid, almost all mineral matters, except pyrite, could be dissolved. **Table 3** gave the arsenic contents and sulfur forms in Yima raw coal and its demineralized coal. As shown in **Table 3**, the content of pyritic sulfur in deminerlized coal was a little higher than that in raw coal, which indicated that pyrite almost all remained in demineralized coal. Arsenic content of demineralized coal was close to that of raw coal. Combined the results of density fractionations with those of demineralization, we could infer that the major arsenic in Yima coal was associated with pyrite, maybe arsenopyrite(FeAsS) or arsenical pyrite($FeAsS_2$)[2].

Table 3. Arsenic Content and Sulfur Forms of Samples

Sample	As/μg·g^{-1}	Sulfur Forms /Wt%			
		$S_{t,d}$	$S_{p,d}$	$S_{s,d}$	$S^*_{o,d}$
Yima	33.0	2.04	1.65	0.06	0.33
YimaD	32.1	2.14	1.72	0.03	0.39

* by difference

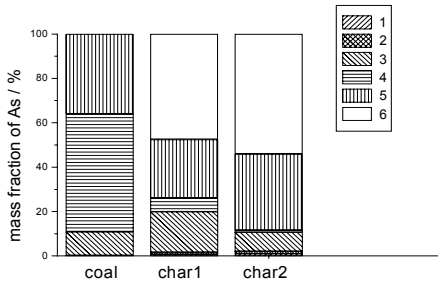

1−water soluble and ion exchangeable 2−associated with carbonates 3−associated with sulfates & monosulfides 4−associated with disulfides 5−stable forms 6-volatility(volatilized into gas & tar)
Figure 1. Mode of occurrence of arsenic in Yima coal and pyrolysis chars.

Figure 1 showed the results of sequential chemical extraction of Yima raw coal and its chars. The pyrolysis temperature of char1 and char2 were 600°C and 900°C, respectively. Arsenic contents occured in water soluble, ion exchangeable and associated with carbonates were below 2% in all samples. It was difficult to compare with each other for these two kinds of forms of arsenic. It could be seen that about 65% of arsenic in raw coal was extracted, and more than 75% was extracted by HNO_3. 35.95% of arsenic in Yima coal occured in stable forms. After pyrolysis, only a little arsenic associated with disulfides still remained in char1(6.13%) and char2(0.98%). It demonstrated that the forms of arsenic associated with pyrite were unstable during coal pyrolysis. A little increase was observed for mass fraction of arsenic associated with sulfates and monosulfides from 10.61% in raw coal to 18.25% in char1, while that in char2(8.54%) was a little decrease. Because of incomplete decomposition of pyrite at 600°C, some arsenic associated with disulfides maybe transformed into the forms associated with monosulfides. The mass fraction of stable forms of arsenic in char2 (34.26%) was higher than that in char1 (26.43%). Maybe some arsenic was transformed into stable forms before it could volatilize at high pyrolysis temperature.

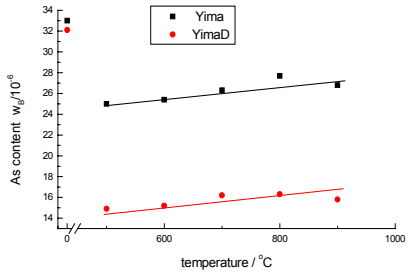

Figure 2. Effect of pyrolysis temperature on As content in char

The relationship between the arsenic content of char and the pyrolysis temperature was shown in **Figure 2**. The arsenic content in coal was indicated at 0°C. The arsenic contents of char were lower than those of coals, especially for that of YimaD. For Yima and YimaD , in the experiment temperature range, the arsenic content of char tended to slightly increase with increasing pyrolysis temperature.

The relationship between pyrolysis temperature and arsenic volatility was plotted in **Figure 3**. It could be seen that arsenic volatility was not strongly susceptible to pyrolysis temperature, which only had slightly changes in the temperature range from 500 °C to 800 °C. But there was a great increase for arsenic volatility at 900 °C, which were about 54.0% and 72.8% for Yima and YimaD in comparison with 47.6% and 69.4% at 800 °C, respectively. It was evident that large amount arsenic already volatilized before 500 °C. Arsenic behaviour at low pyrolysis temperatures might take important role.

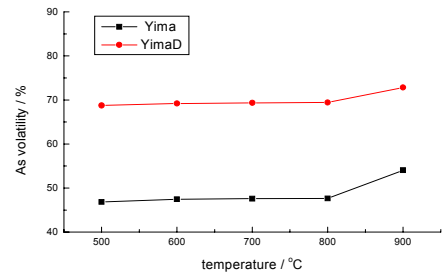

Figure 3. Effect of pyrolysis temperature on arsenic volatility

The ash composition of Yima raw coal was as following (Wt%): SiO_2: 44.17; Al_2O_3:18.88; Fe_2O_3:14.77; CaO: 10.42; MgO:2.33; TiO_2:1.15; K_2O:1.40; Na_2O:0.25; P_2O_5:0.31. From **Figure 3**, we also could see that arsenic volatility of YimaD was much higher than that for Yima during pyrolysis. From **Table 3**, it clearly showed that demineralization only had little influence on arsenic content of Yima coal. All these suggested that the vaporization of arsenic during Yima raw coal pyrolysis might be retarded by its coexisting mineral matters.

Conclusions

Arsenic in Yima coal was mainly associated with pyrite, which was unstable during coal pyrolysis. Arsenic volatility was not susceptible to pyrolysis temperature in the range studied. The vaporization of arsenic in Yima raw coal during pyrolysis might be retarded by its coexisting mineral matters. Arsenic volatility at low pyrolysis temperatures would be studied in the next stage.

Acknowledgement. Financial support for this work by the Special Funds for Major State Basic Research Project of China (Contract No. G1999022107) and Natural Science Foundation of China (29936090) are gratefully acknowledged.

References

1. Koler, A.; Huggins, F. E.; Pamlmer, C. A.; Shah, N.; Crowley, S. S.; Huffman, G. P.; Finkelman, R. P. Fuel Process. Technol., 2000, 63, p. 167-178.
2. Huffman, G. P.; Huggins, F. E.; Shah, N.; Zhao, J. Fuel Process. Technol., 1994, 39, p. 47-62.
3. Galbreath, K. C.; Toman, D. L.; Zygarlicke C. J.; and Pavlish J. H. Energy & Fuels., 2000, 14(6), p. 1265-1279.
4. Querol, X.; Klika, Z.; Weiss, Z.; Finkelman, R. B.; Alastuey, A.; Juan, R.; Lopez-Soler, A.; Plana, F.; Koler, A.; Chenery, S. R. N. Fuel., 2001, 80, p. 83-96.
5. Richaud, R.; Lachas, H.; Healey A. E.; Reed, G. P.; Haines, J.; Jarvis, K. E.; Herod, A. A.; Dugwell, D. R.; and Kandiyoti, R. Fuel., 2000, 79, p. 1077-1087.
6. Yan, R.; Gauthier, D.; Flamant, G. Fuel., 2001, 80, p. 2217-2226.
7. Chen, H. K. Doctoral Dissertation. Chinese Academy of Sciences: Taiyuan, 1998.
8. Guo, C. T. Chemical Industry Press: Beijing, 1992; pp.45-46.
9. Lu, H. L.; Chen, H. K.; Li, W.; and Li, B. Q. 19th Pittsburgh Coal Conference: Pittsburgh, Sep. 23-27, 2002: CD-ROM.

TRACE ELEMENTS IN COAL AND RELEASE OF TRACE ELEMENTS DURING PYROLYSIS

Ruixia Guo, Jianli Yang, Dongyan Liu, Zhenyu Liu

State Key Laboratory of Coal Conversion, Institute of Coal Chemistry, Chinese Academy of Sciences, P.O. Box 165, Taiyuan, Shanxi 030001, P.R. China

Introduction

Environmental problem resulted from the release of hazardous trace elements during coal processing have attracted attention of many researchers. Their studies have been focused on the physico-chemical form of trace elements in coal, the toxicity and partitioning behavior in the combustion/ environmental control system [1-4]. It has been shown that the emission behavior of trace elements during coal process varies with element and coal type, chemical form presented in coal and process conditions significantly. Pyrolysis is the most important stage of coal utilization processing such as gasification, combustion, or liquefaction [5]. It is thus of great important to understand the behavior of trace elements during pyrolysis to guide for the effective control of the emission of the toxic trace elements during coal processing.

The attempt was made in this paper is to understand the release behavior of As, Pb, Cd, Cr and Mn at different pyrolysis temperature, atmosphere and holding time. Their chemical forms transformation during pyrolysis was also investigated.

Experimental

2.1 Coal sample and pyrolysis prededure. A Chinese bituminous coal, named Datong coal, was crushed and sieved to 0.16~0.27mm, and dried under vacuum at 110°C with a nitrogen purge. The characteristics of Datong coal are shown in Table 1.

Table 1. Analysis of Datong coal，wt%

Proximate analysis			Ultimate analysis，daf				
V_{ad}	A_{ad}	M_{ad}	C	H	N	S	O^a
26.91	10.00	0.26	88.18	5.17	1.05	1.64	3.96

A schematic representation of experimental apparatus was shown in Fig.1. It consisted mainly of a rotary furnace and a pyrolysis reactor. Prior to a reaction，about 2.5g of coal sample was placed at the top of the reactor. Then it was sealed and filled with the desired gas to certain pressure. The furnace with the reactor was in the horizontal position first. The fast heating experiment was obtained by quickly rotating the furnace with the reactor to the vertical position. After desired holding time, the reactor was pulled out from the furnace and quenched in the cold water. Gases were released slowly. Char was collected from the bottom of the reactor. Amount of gases produced was determined by the weight difference of the reactor with the samples before and after reaction. Amount of tar produced was calculated by subtraction of char and gas produced from weight of original coal.

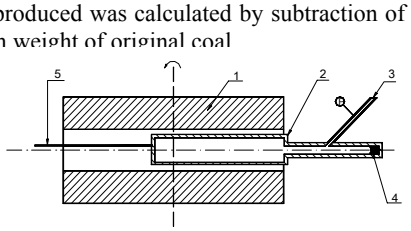

1 furnace, 2 reactor, 3 gas inlet and outet, 4 coal sample 5 thermocouple

Fig.1. The diagram of high pressure closed fast pyrolysis apparatus

2.2 Analysis of the elements. The elements (As、Pb、Cr、Cd and Mn) in raw coal and chars were separated into five chemical forms by a sequential chemical extraction procedure. Through the sequence leaching steps, elements associated with various parts of the coal were removed in the following order: (1) Ion exchangeable element (named form 1), including water soluble or cations associated with ion exchange sites in organic and inorganic matter, and being removed by 1N NaOAc (PH~8.2) at room temperature for 1h; (2) Element bound to carbonates (named form 2), including cations primarily associated with carbonates, and being removed by 1N NaOAc (PH~5.0) at room temperature for 5h; (3) Element bound to iron and manganese oxides (named form 3), including Fe-Mn oxide associated, well–crystallized sulfides or organosulfur compounds, and being removed by 0.04 N $NH_2OH{\cdot}HCl$ in 25%(v/v) HOAc; (4) Element bound to organic matter (named form 4), consisting of paraffin-like material and resistant structural (nonhumified) organic matter residues, and being removed by HNO_3/H_2O_2 (PH~2) and NH_4OAc; (5) Element remaining in the residual after the four preceding extractions (named form 5), consisting essentially of detrital silicate minerals, resistant sulfides, and a small quantity of refractory organic material, and being dissolved into solution by using $HF\text{-}HClO_4$ mixture after ashing. The sequential extraction procedure used in this study was described else where in detail [6-7]. Elements content of the raw coal, the corresponding chars after pyrolysis, and the samples from leaching processing were measured by inductively coupled plasma-atomic spectroscopy (ICP-AES).

Bleeding ratio (Br) used to evaluate the release extent of trace element in coal during pyrolysis defined as:

$$Br(\%) = \frac{\text{concentration in coal - concentration in char} \times \text{char yield}}{\text{concentration in coal}} \times 100\%$$

Results and Discussion

3.1 Effect of pyrolysis temperature on release of trace elements. Fig.2 shows the bleeding ratios of trace elements at various pyrolysis temperatures for Datong coal. It was found that the bleeding ratio of trace elements increased with the increasing of pyrolysis temperature, especially for As, Pb and Cd at 700~1000°C. However, the emission of As reached to a higher level at relative lower temperature. More than 67% of releasable As was released at the temperature of 300 °C. The significant release of Pb and Cd did not occur until 700°C. Cr and Mn released from coal only slightly in the temperature range of 300~1000°C. It can be concluded that the release ability of As, Cd and Pb is higher than that of Cr and Mn. This may be related to the properties of the element itself and their chemical form transformation during pyrolysis.

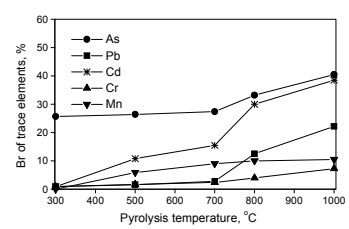

Fig.2. Effect of pyrolysis temperature on bleeding ratio of trace elements under N_2 pressure of 0.1MPa with the holding time of 20s

3.2 Effect of atmosphere and holding time on release of trace elements. Fig.3 illustrates the bleeding ratios of trace elements at different atmospheres and holding times. H_2 atmosphere resulted in the higher bleeding ratio of trace elements than N_2 atmosphere. The

difference in bleeding ratio of the elements between both atmospheres increased with the increasing of the holding time. Among the five elements, the relative volatile elements (As, Pb and Cd) were greatly influenced by atmosphere and holding time. Fig. 4 gives the corresponding volatiles yield at different atmospheres and holding times. H_2 atmosphere and longer holding time led to more volatiles release from coal. In one hand, the release of more volatiles can assist the transportation of the elements from the pore of coal and decrease the possibility of the element retention in the char. In the other hand, as the higher heating rate used in this study, coal may not be heated sufficiently at relatively short holding time. This resulted in incomplete release of the elements from coal. As further increasing the holding time, enough energy was obtained to break strong affinity of the elements to coal matrix structure. Both effects resulted in the more trace elements emitted from coal.

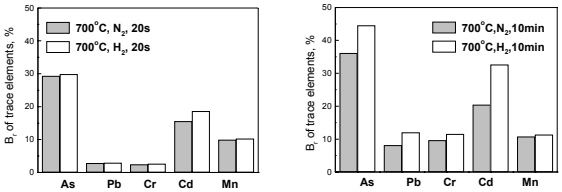

Fig.3 Effect of atmospheres and holding time on release of trace elements at 700°C under 0.1MPa

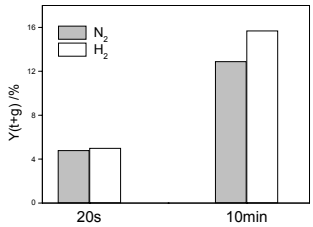

Fig.4 Effect of atmospheres and holding time on volatile (tar +gas) yield at 700°C under 0.1MPa

3.2 Chemical forms transformation of trace elements upon heating. Fig.5 presents the chemical form distribution of As, Pb, Cd, Cr and Mn in Datong coal and char. Char was obtained by pyrolyzed at 1000°C under N_2 pressure of 0.1MPa with the holding time of 20s. It can be seen that As, Pb, Cd and Cr in the raw coal are mainly presented as form 5 with the small amount of forms 2 to 4 but Mn as form 3. Form 1 represents ion exchangeable element. It was only observed for Mn in the raw coal and showed the same value after pyrolysis. Form 2 represents the element bound to carbonates. It was found in raw coal less than 5% for Cr and Mn, and about 10-18% for Pb and Cd. It disappeared for Cd, almost unchanged for Pb and Cr, and increased for Mn after 1000°C heat treatment. There was no observation of As in both raw coal and char. Form 3 represents the element bound to Fe-Mn oxides. This form was observed for all the elements tested in the raw coal (15-20% for As, Pb and Cd, less than 2% for Cr and more than 55% for Mn). It decreased generally after the heat treatment except for the case of Cr. Form 4 represents the element bound to organic matter. Although it was not the major form, it was found for all the elements tested. The element in this form disappeared or decreased after 1000°C pyrolysis. For form 5, residual elements, contained 60% of As, around 50% of Pb and Cd, more than 90% of Cr and 21% of Mn originally. It decreased for As, Pb and Cr after pyrolysis, and slightly increased for Cd and Mn. Form 6 represent the elements went to the volatile phase. Comparing to the less than 10% of Cr and Mn released into volatile phase, As, Pb and Cd have higher volatility and are considered as the primary toxic trace elements in coal. Clearly, trace elements in coal not only emitted into volatile phase but also transformed from one form to another in solid phase significantly during pyrolysis.

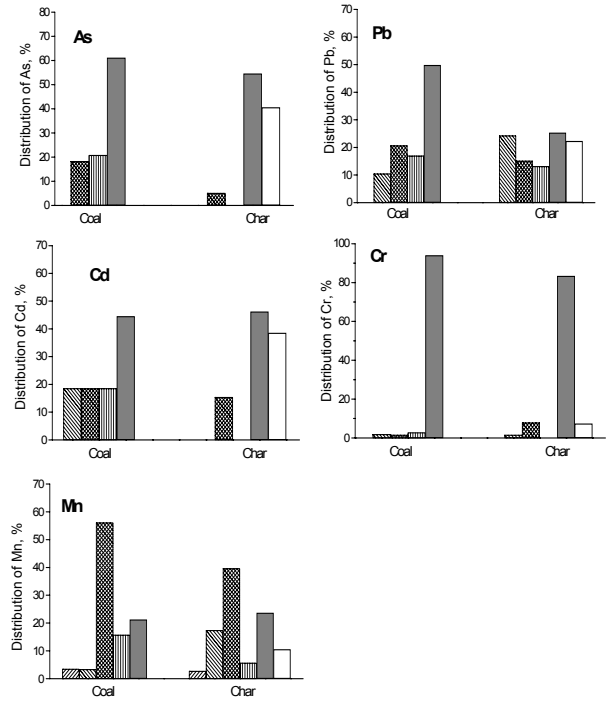

Form 1: Ion exchangeable ; Form 2: Bound to carbonates;
Form 3: Bound to Fe-Mn oxides; Form 4: Bound to organic matter;
Form 5: Residual element; Form 6: Element went into volatile phase.

Fig.5 The distribution of trace elements in coal and char (1000°C, N_2)

Conclusions

The effects of temperature, atmosphere and holding time on trace elements release behavior in a closed fast pyrolysis reactor were investigated. The bleeding ratio of trace elements increased with increasing temperature and holding time. H_2 atmosphere promotes the release of trace elements. During pyrolysis, As, Pb and Cd show the higher emission ability than Cr and Mn. Form 1 element was only found for Mn in the raw coal and was not affected by heat treatment. Change of forms 2 and 5 was dependent on the type of the elements. Elements in form 3 and 4 decreased generally after pyrolysis.

Acknowledgement. The authors gratefully acknowledge the financial support from the Special Founds for Major State Basic Research Project (G19990221), the Chinese Academy of Sciences, and the Natural Science Foundation of China (20076049).

References

(1). Helble, J.J.; Mojtahedi, W.; Lyyränen, J.; and Jokiniemi, J. *Fuel*, **1996**, *75*(8), 931.
(2). Dismukes, E.B. *Fuel Processing Technology*, **1994**,*39,* 403.
(3). Yan,R.; Gauthier, D.; and Flamant, G. *Fuel*, **2001**, *80*, 2217
(4). Querol, X.; Fernández-Turiel, J.L.; and López-Soler, A. *Fuel*, **1995**, *74* (3), 331.
(5). Gryglewicz, G. *Fuel Processing Technology*, **1996**, *46*, 217.
(6). Zhao, F.H. Ph. D. Thesis, in *Chinese with English abstract. Beijing graduate School, China University of Mining and Technology*, **1997**, p.63.
(7). Tessler, A.; Campbell, P.G.C.; and Bisson, M. *Analytical Chemistry*, **1979**, *51*(7), 844.

THE BEHAVIOR OF TRACE ELEMENTS FROM HIGH TEMPERATURE COAL COMBUSTION PROCESS

Yasushi SEKINE, Tomohiro KAWABATA, Kunihisa SAKAJIRI, Eiichi KIKUCHI, Masahiko MATSUKATA

Department of Applied Chemistry
Faculty of Science and Engineering
WASEDA University
3-4-1 Ohkubo, Shinjyuku,
Tokyo, Japan 169-8555

Introduction

Coal has great advantage that deposits are abundant as compared with other fossil fuels. On the other hand, coal includes much kind of trace elements with several 10 ppm concentrations. They volatilize at the combustion and gasification of coal, and are released into the atmosphere. Moreover, on the occasion of the reclamation by coal ashes, they elute into drainage, and become the cause of environmental pollution. Especially it worries about the bad influence to a human body, so it is important to elucidate the releasing behavior of the trace elements in coal. In this study, how the combustion temperature and existence of the steam in combustion atmosphere influence the releasing behavior of the trace elements from coal was investigated.

Experimental

In this study, we employed Wallarah coal as the sample first. It was crushed into particle and sieved under 150 μm before the combustion experiment. The combustion experiment was conducted under the temperature range of 573~1573 K, and the contents of the trace elements in the coal in each temperature was measured. The schematic diagram of experimental apparatus is shown in **Fig. 1**. The proximate analysis and ultimate analysis of Wallarah coal is shown in **Table 1**. About 0.1 g of coal sample was put into the platinum basket, and it inserted into the reactor which was preset at 573~1573 K beforehand. The alumina tube (i.d. 42 mm and length 1 m) was used for the reactor. Combustion atmosphere was air; 5.6 l min^{-1} and 0 or 10 % of steam was supplied together. The coal or ashes which remained in the platinum basket after 10 min combustion were collected carefully, and it was dissolved into acid media using microwave sample pretreatment equipment (Ethos Plus, by Milestone General; solvent; HNO_3 7 ml, HF 1.5 ml in the first step, and HNO_3 2 ml, HF 0.5 ml, and $HClO_4$ 3 ml in the second step was added). Raw coal was also dissolved by just the same method. The contents of the trace elements (Be, V, Cr, Mn, Co, Ni, Zn, As, Se, Cd, Sb, Hg, Pb) in the solution was determined by ICP-AES (CIROS). About Hg, Se, Sb, and As, their amount was measured by the hydride generation method.

Results and discussion

The residual ratio of the trace elements in the coal or ash which remained in the platinum basket after 10 min combustion (573~1573 K, air atmosphere) was defined as follows.

$$\text{Residual ratio}\ [\%] = \frac{\text{Contents in ash}\ [\mu g \cdot g\text{-coal}^{-1}]}{\text{Contents in raw coal}\ [\mu g \cdot g\text{-coal}^{-1}]} \times 100$$

Table 1 Proximate and ultimate analysis of Wallarah coal

Proximate analysis	Water Content	3.0
	Ash Content	13.7
	Volatile Matter	29.4
	Fixed Carbon	53.9
Ultimate analysis	Carbon	71.9
	Hydrogen	4.2
	Nitrogen	1.4
	Sulfur	0.3
	Oxygen	8.1

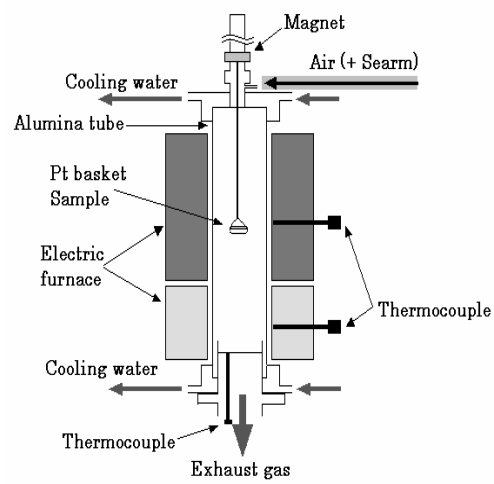

Fig. 1 Schematic diagram of experimental apparatus.

As for Zn, Se, Sb, Hg, and Pb, residual ratios in coal changed with the rise of temperature. A change of residual ratio was not observed about other elements. The relation between the residual ratios of Zn and Pb and temperature (573~1573 K) is shown in **Fig. 2**, and the relation between the residual ratios of Se, Sb, and Hg and temperature is also shown in **Fig. 3**. In Figs. 2~3, the vapor pressure curves of the compounds containing Zn, Pb, Se, Sb, and Hg were also shown together. Residual ratios of Zn and Pb decreased at 1173 K or more, irrespective of existence of steam. Considering that boiling point of metal-Zn is 1181 K, it is thought that Zn compounds in coal decomposed and released from coal as a metal-Zn form. Moreover, considering that boiling point of $PbCl_2$ is 1223 K, it is thought that Pb compounds in coal released as $PbCl_2$. Even if it was in the presence of steam, residual ratios of Zn and Pb were same as the case where it was in the absence of steam. On the other

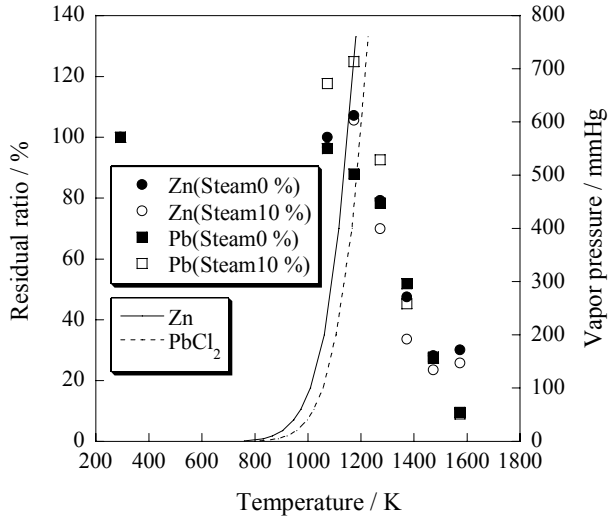

Fig. 2 Relation between temperature and the residual ratios of Zn and Pb in comparison with vapor pressure.

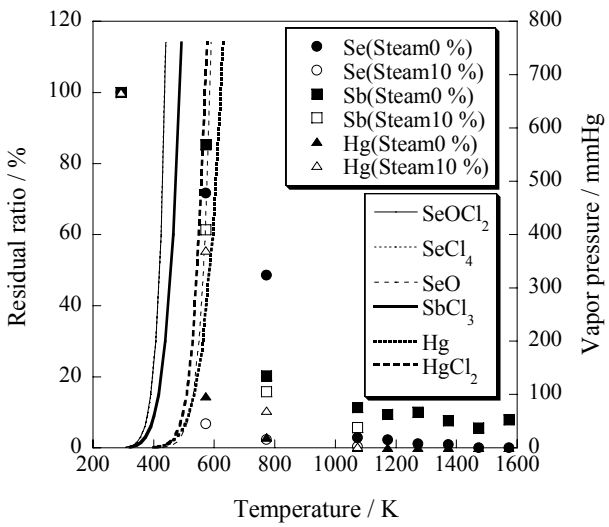

Fig. 3 Relation between temperature and the residual ratios of Se, Sb and Hg in comparison with vapor pressure.

hand, as for Se, Sb, and Hg, the residual ratios in coal decreased greatly at low temperature (573~773 K). It is thought that Se released as $SeOCl_2$, $SeCl_4$, and SeO, Sb released $SbCl_3$, Hg released as metal-Hg and/or $HgCl_2$.

The residual ratios of Se, Sb, and Hg in coal changed in the presence of steam unlike Zn and Pb. As for Se and Sb, residual ratios decreased in the presence of steam. This is considered because it released from coal via a hydroxide form under low temperature region. However, residual ratios of Hg increased in the presence of steam conversely. Considering that boiling point of Hg is 630 K, boiling point of $HgCl_2$ is 577 K, Hg released from coal as metal-Hg and/or $HgCl_2$ under low temperature region in the absence of steam. On the other hand, under steam existing condition, it will be converted into $Hg(OH)_2$ at low temperature, then decomposed to HgO at high temperature. HgO is decomposed into Hg and O_2 at 773 K. Therefore, release of Hg depressed in the presence of steam.

Conclusion

Zn and Pb were released from coal at high temperature (1173 K~), and were not influenced by steam. Se, Sb, and Hg were released from coal at low temperature (573~773 K), steam influenced the releasing behavior of these elements. Whereas Se and Sb enhanced, that of Hg depressed in the presence of steam. They are considered that their existence form has correlation.

Acknowledgement

This work was partly supported by the fund of National Department of Science and Technology Japan (its group leader; Prof. K.Miura from Kyoto Univ.).

CO-PYROLYSIS OF COAL AND WOODY BIOMASS

Behdad Moghtaderi, Chatphol Meesri, and Terry F Wall

Co-operative Research Center for Coal in Sustainable Development
Discipline of Chemical Engineering, School of Engineering
Faculty of Engineering & Built Environment
The University of Newcastle
Callaghan, NSW 2308
Australia

Introduction

Fears of climate change and increasing concern over the global warming have prompted a search for new, cleaner methods of electrical power generation. Co-firing of biomass fuels (e.g. wood chips, straw, bagasse, peat and municipal solid waste) and coal is presently being considered as an effective means of reducing the global CO_2 emissions[1]. Demonstrations have been performed in a number of utility installations across the world, including Australia, Europe and the United States. All types of combustion technologies have been used but a particular attention has been given to pulverised fuel (PF) boilers, as they constitute the bulk of power generation hardware in many countries. Despite the simplicity of the co-firing concept, its application in PF boilers is associated with many technical issues including combustion related problems such as fuel ignition, flame stability, temperature, and geometry as well as char burnout. There is still no fundamental understanding of the underlying mechanisms that cause such technical problems. In particular, Studies on fundamental issues such as pyrolytic behaviour of biomass/coal blends or biomass char reactivity are scarce[1].

Previous investigations on co-pyrolysis of biomass/coal mixtures have mostly concentrated on the mechanism of production of the gas phase species. There has also been a handful of studies[2-3] on the impact of synergistic effects (i.e. chemical interaction between the two fuels) on the yield of major pyrolysis products, in particular, volatile matter. However, much less attention has been given to the influence of synergistic effects on the composition of the pyrolysis products. In addition, most previous studies focused on examining the impact of various controlling parameters (e.g. heating rate, temperature, blending ratio, etc) in isolation.

The objective of this study was to address these shortcomings through a comprehensive investigation of the pyrolytic behaviour of woody biomass/coal blends over a wide range of heating rates and temperatures relevant to PF boilers. The fundamental knowledge gained from this project is essential for the proper understanding of co-firing in practical PF based systems. For example, the knowledge of the low heating rate pyrolysis of biomass/coal mixtures may help to prevent the accidental fires, which sometimes occur in fuel handling units (e.g. mills or pulverisers) of typical PF boilers during co-firing exercises[4]. Similarly, the knowledge of the high heating rate pyrolysis of biomass/coal blends, may help to understand and predict the impact of co-firing on the combustion related phenomena in PF boilers.

Experimental

Equipment. Two sets of experiments were carried out to investigate the pyrolytic behaviour of biomass/coal blends under the low and high heating rate conditions. The low heating rate experiments were conducted to understand the pyrolytic characteristics of coal, woody biomass, and their mixtures under conditions pertinent to the pulveriser units (i.e. mills) of typical PF boilers. That is a heating rate between 10-50°C/min and a temperature between 200–400°C. The high heating rate experiments, on the other hand, were performed to study the pyrolytic behaviour of the individual solid fuels and their blends at heating rates often observed in pulverised fuel combustors (10^4 ^{o}C/s ≤). The low heating rate experiments were carried out in a horizontal tubular reactor consisting of a horizontal alumina tube (reactor), a carbolite horizontal tube furnace, a mass flow controller, a pressure regulating valve, a pressure transducer, a data acquisition system, several thermocouples and controllers.

The high heating rate experiments were conducted at atmospheric pressure in a 330 mm by 50mm ID electrically heated drop tube furnace (Astro Model 1000A graphite vertical furnace) equipped with a Honeywell temperature controller/programmer (Model DCP 7700). The set-up included the tubular furnace, furnace controllers, a solid fuel delivery system, and a char collection device consisting of a cyclone and a water-cooled probe.

A gas analysis train was employed in conjunction with both low and high heating rate set-ups for on-line measurements of the gaseous pyrolysis products. The train comprised of a gas manifold, a fast response micro gas chromatograph (VARIAN, model CP-2003) equipped with a thermal conductivity detector, a cold trap for removing tar compounds, and a data acquisition system.

Materials. Experiments were conducted on blends of Radiata pine sawdust and Drayton coal, which were prepared by manual mixing of the two fuels. To eliminate the effect of moisture content, prior to each test sufficient amounts of fuel samples were oven dried at 105 ^{o}C for several hours and then stored in a desiccator. Particle size measurements indicated a range of particle sizes between 0.045-0.063 mm for coal and 0.09-0.125 mm for pine sawdust. These size ranges are consistent with those produced in practical milling systems used in pulveriser units of PF boilers[1]. While blending ratios (weight of biomass to that of coal/biomass mixture) of 5%, 10%, 25%, 50%, and 75% (w/w) were used in the low heating rate experiments, for the high heating rate investigation, only two blending ratios of 5% and 10% w/w were employed. The details characteristics of both fuels (eg ultimate and proximate analysis) were given in one of our earlier works[2].

Methods and Techniques. The high heating rate experiments were conducted in the temperature range of 900-1400°C. High purity nitrogen (99.5% purity) was used as a carrier gas. Before commencing the experiment, the system was purged with nitrogen for 15 min, after which the concentration of oxygen within the system was continuously monitored by the Micro GC. Once the oxygen concentration approached zero, a 2 L/min flow rate of the carrier gas (primary N_2, 0.5 L/min and secondary N_2, 1.5 L/min) was introduced into the reactor. This provided a residence time of approximately 1 (s) for the individual pulverised fuel particles. The fuel particles were next fed at a uniform rate, depending on the type of material. For the coal and blend samples, the feed rates were about 2-3 g/h whereas for the sawdust samples a feed rate of 0.5 g/h was employed to avoid the blockage of the fuel feeding system. The above-mentioned flow rates were controlled by mass flow controllers and uniformly maintained by a suction pump equipped with a flow regulator. The flow of the gas inside the furnace was maintained at a uniform rate by replacing a filter membrane at 20 minute intervals.

The char was collected in the sample receiver of the cyclone and weighed at the end of the experiment. The ultimate volatile yields % (w/w, daf) of the coal and the blended materials were determined by employing the ash-tracer techniques (ASTM D 1102). For sawdust, the extent of mass loss during devolatilisation was ascertained by determining the content of inorganic metals[5] (average of SiO_2, TiO_2, and Al_2O_3) of the collected char assuming that the mass of these metals is conserved. This was done using the X-ray fluorescence (XRF) technique to minimise the inaccuracy that

would have occurred due to the vaporisation of alkali and alkali earth components of the biomass ash had the ash tracer method been used.

The details of the low heating rate experimental procedures and techniques have been given elsewhere[2] and are not repeated here.

Results and Discussion

Figure 1(a) illustrates the yield of volatiles of coal and sawdust as a function of furnace temperature under the low heating rate condition of 10°C/min. The devolatilisation processes of both coal and sawdust follow a similar trend under these conditions. In the temperature range of 300<T< 600°C the cellulose content of the woody biomass, which accounts for 40% of its weight, undergoes thermal decomposition and transforms primarily into levoglucosan. While almost 80% (w/w) of the woody biomass is converted in the second stage, coal exhibits only 35% (w/w) conversion at this stage and yields much less volatiles. The striking distinction is attributed to the difference in the strength of the molecular structure of the two fuels[2].

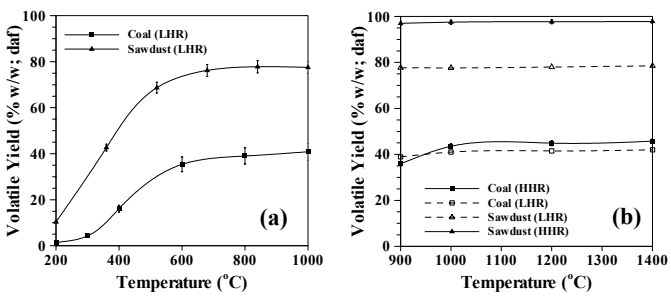

Figure 1: Yield of volatiles as a function of temperature under (a) low heating rate, 10 °C/min, and (b) high heating rate conditions.

Figure 1(b) depicts the yield of volatiles from coal and sawdust over a temperature range of 900 to 1400°C under the high heating rate regime. For comparison, the results extrapolated from the low heating rate experiments (for T > 1000°C) are also shown in the same figure. Both coal and sawdust show similar behaviours and produce higher yields of volatiles compared to those produced under low heating rate conditions. The difference between the two fuels, however, can be seen in the quantity of the volatile yields and the temperature range at which the bulk of devolatilisation takes place. The pulverised woody biomass generates much higher volatile yields (about 98% w/w, daf) compared to that of the coal under the same conditions. This can be attributed to the stronger effects of the temperature and heating rate on the depolymerisation reaction, which leads to the rapid evolution of volatile content of the woody biomass. The yield of volatiles for coal under the high heating rates, however, is not much higher than those of the low heating rate regime. This is most likely due to the stronger molecular structure of coal.

To investigate the behaviour of blends, the yields of pyrolysis products (gas, tar, and char) were plotted against the blending ratio for both low and high heating rate regimes. The amounts of pyrolysis products from a particular blend appeared to be linear functions of the blending ratio (e.g. see **Figure 2** for char). This implies, for instance, that the yield of char at any given blending ratio (Y_{char}) is equal to the algebraic sum of the normalised char yields of the parent fuels. That is:

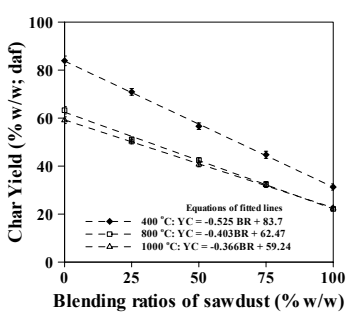

Figure 2: Yield of char as a function of blending ratio under a low heating rate of 10 °C/min.

$$Y_{char} = \frac{k}{100} \times [Y_{Biomass,char}] + \frac{(1-k)}{100} \times [Y_{Coal,char}] \qquad (1)$$

where k is the blending ratio in percentage, $Y_{Biomass,char}$ is the yield of biomass char (correspond to k = 0%), and $Y_{Coal,char}$ is the yield of coal char (correspond to k = 100%). Similar linear relationships can be applied to tar and gaseous products. This even applies to the individual constituents of the gas phase (eg CH_4, CO_2, CO, etc), as shown in **Figure 3**.

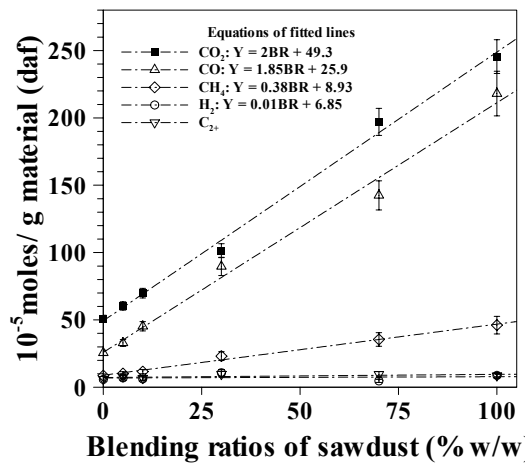

Figure 3: Composition of the gaseous products at a temperature of 400°C and a low heating rate of 10 °C/min.

Similar to the low heating rate results, the blended materials followed the same trend as the parent fuels in the high heating rate regime. More importantly, the yield of the volatiles of the blends seemed to be proportional to the blending ratios of the parent materials. In addition, much like the low heating rate regime, the composition of the gaseous products generated from the blended materials under the high heating rate and the high temperature (900-1400°C) conditions were linearly proportional to the composition of the parent materials (not shown here).

Acknowledgment

The authors wish to acknowledge the financial support provided by the Co-operative Research Centre for Coal in Sustainable Development, which is funded in part by the Co-operative Research Centres Program of the Commonwealth Government of Australia.

References

1. Sami, M., Annamalai, K., and Wooldridge, M., *Progress in Energy and Combustion Science*, **2001**, 27, 171-214.
2. Meesri, C., and Moghtaderi, B., *Biomass & Bioenergy*, **2002**, 23(1), 55-66.
3. Pan, Y.G., Velo, G., Puigjaner, L., *Fuel*, **1996**, 75(4), 421-418.
4. Moghtaderi, B., *Journal of Loss Prevention in Process Industries*, **2001**, 14(3), 161-165.
5. Mitchell, R.E., Hurt, R.H., Baxter, L.L., Hardesty, D.R., Milestone Report SAND92-8208., Sandia National Laboratories, California, USA, **1992**.

EFFECT OF INORGANIC MATTER ON REACTIVITY AND KINETICS OF COAL PYROLYSIS

Quanrun Liu[a], Haoquan Hu[a], Qiang Zhou[a], Shengwei Zhu[a]*
Guohua Chen[b]

[a]Institute of Coal Chemical Engineering, Dalian University of Technology, 129 Street, Dalian 116012, China
[b]Department of Chemical Engineering, The Hong Kong University of Science & Technology, Clear Water Bay, Kowloon, Hong Kong SAR
*hhu@chem.dlut.edu.cn

Introduction

Coal pyrolysis is one of the most important aspect of coal behavior for its occuring in all major coal conversion processes, such as combustion, gasification, carbonization and liquefaction etc. Many works have examined the relationship between inorganic components in coals and their reactivity. Because of the differences in composition and properties for different coal, there were many discrepancies in the results obtained by different researchers for different coal samples[1]. Moreover, there is little on the relationship between inorganic matter and the kinetics of coal pyrolysis has been reported.

In this work, two Chinese coals, Shenfu bituminous coal (SF) and Huolingele lignite (HLGL), were used as samples. The coal was demineralized, then several inorganic matters were added to the demineralized coals. The raw, demineralized and inorganic matters added coals were pyrolysed by using thermogravimetry to investigate the effects of mineral matter on the reactivity and kinetics of coal pyrolysis.

Experimental

Coal Samples Coal sample, with particle size of -120mesh, was demineralized by HCl/HF. The procedure of demineralization followed the method used by Oztas[2]. After the acid treatment, the content of ash in coals are below 1wt%. Three inorganic matters, including Al_2O_3, the main constituents of kaolinite and illite; CaO, the production of calcium carbonate during coal pyrolysis; K_2CO_3, the famous catalyzer for gasification, were ground to 120 mesh and baked at 800°C for 2h, then added to the demineralized coals by co-slurrying with water in concentrated suspension for 24h and dried in vacuum oven. The content of the inorganic matters additive in coal is 10wt%.

Pyrolysis Pyrolysis was carried out with a thermogravitry (SDTA851e). About 20mg raw, demineralized or inorganic matter added samples were placed with an aluminum crucible and pyrolysed under N_2 flow at the heating rate of 10K/min from 110°C to 800°C.

Results and Discussion

Effect on reactivity The effects of inherent mineral and the mineral additive on the weight loss during coals pyrolysis as a function of temperature are shown in **Figure 1**. From the results it can be seen that the conversion of organic matters in the demineralized coal is almost the same as raw coal. This indicates that the inherent mineral matter has no effect on the reactivity of coal pyrolysis. Upon 550°C, the weight loss of raw HLGL is a little higher than that of its demineralized coal, which might be due to the mineral itself decomposition[3].

When Al_2O_3, CaO or K_2CO_3 was added into the demineralized coal, the weight loss curve changed greatly, which indicated the effect of this mineral matter on coal pyrolysis. The trend of effect of Al_2O_3 and CaO is more evident than that of K_2CO_3 with temperature increasing, but upon 450°C, they have same trend with little change.

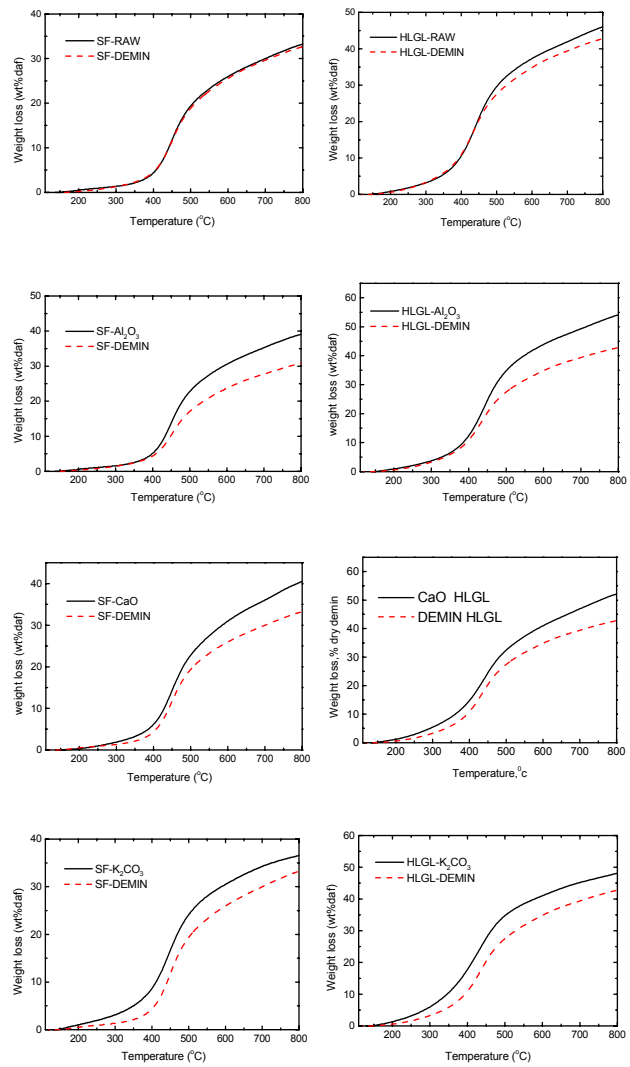

Figure 1 Weight loss of coal samples as a function of temperature

CaO and K_2CO_3 affect the reactions as soon as the beginning of coal pyrolysis, while the effect of Al_2O_3 only occurs upon the temperature of 450°C. These phenomena make out that different inorganic matter has different catalytic nature. The mechanism of the effect of inorganic matters on coal pyrolysis is not very clear, but it may be explained from the nature of these mineral matters. Clay, which exists in coal, affects the coal gasification and catalyzes hydrogen transfer to coal[4], therefore, it is not surprising that Al_2O_3, the main active component of clay, has catalytic effect on coal pyrolysis. CaO is active in effect on cracking oxygen functional groups in coal[4]. A large portion of oxygen in bituminous coal exists in acidic functional groups such as phenol carboxylic acids. CaO might react with these groups. The interaction of K_2CO_3 with –COOH and -OH functional groups possibly resulted in the formation of K-oxygen surface groups or clusters. These surface functional groups have been considered as the active sites on the coal surface[2]

Effect on the kinetics The kinetic parameters, activation energy (E) and pre-exponential factor (A), of coal pyrolysis were determined by Coats-Redfern method[5]. As shown in **Figure 2**, the reaction of coal pyrolysis can be described by multi-step first order reaction.

During processing the data, the relative conversion, x, was defined as: $x=(w_0-w)/(w_0-w_f)$, where w_0 is the sample weight at the beginning of pyrolysis; w is the weight of the instantaneous residue; w_f is the weight of the residue at the end of coal pyrolysis.

Figure 3 is the typical TG and DTG curves of coal pyrolysis. In the figure some characteristic temperature of pyrolysis has been lined out. The beginning temperature of coal pyrolysis T_o is defined as temperature at x=5%; T_P is the temperature at maximum weight loss rate and the end temperature T_F is that at x=85%.

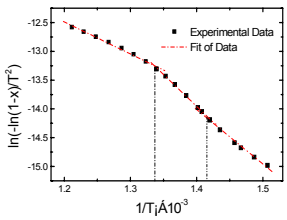

Figure 2 Plot of $\ln[-\ln(1-x)/T^2]$ *vs* 1/T of coal prolysis

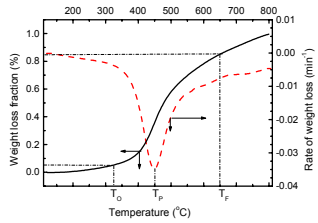

Figure 3 The characteristic temperature of coal pyrolysis

Table 1 Kinetic parameters and characteristic temperatures of coal pyrolysis

Sample	Temp (°C)	Tp (°C)	E (KJ/mol)	A (min^{-1})	-R*
	326-406		61.2	1.39E+3	0.999
SF-DEMIN	406-478	446	97.2	1.28E+6	0.999
	478-549		45.1	1.40E+2	0.998
	307-380		26.5	1.16E+0	0.999
SF-CaO	380-467	450	54.4	2.85E+3	0.999
	467-592		20.9	8.90E-1	0.997
	250-369		18.4	2.90E-1	0.999
SF-K_2CO_3	369-467	444	50.2	2.90E+2	0.996
	467-540		24.8	2.50E+0	0.998
	324-369		56.3	8.40E-1	0.997
SF-Al_2O_3	369-467	450	54.2	1.51E+4	0.999
	467-580		16.9	1.25E+0	0.997
	270-406		41.3	5.04E+1	0.998
HLGL-DEMIN	406~479	440	73.3	2.73E+4	0.999
	479-530		42.9	1.23E+2	0.999
	224-371		22.7	1.06E+0	0.999
HLGL-CaO	371-467	438	38.4	3.29E+1	0.998
	467-574		14.6	2.70E-1	0.998
	234-369		17.4	4.20E+0	0.998
HLGL- K_2CO_3	369-467	438	37.3	3.64E+1	0.999
	467-535		17.4	6.70E-1	0.997
	270-371		38.5	9.10E-1	0.999
HLGL-Al_2O_3	371-467	436	36.7	6.18E+2	0.999
	467-555		12.4	8.90E-1	0.998

*correlation coefficient

Table 1 shows the kinetics parameters and the characteristic temperature of coal pyrolysis**.** The kinetics parameters are calculated in the range from x=5% to x=85%. The experimental and calculating results indicated that the raw and its demineralized coal has almost same kinetic parameters and characteristic temperature, so the results of raw coal aren't listed in the table. The good correlation coefficient indicated that Coats-Redfern model fit the experimental data very well.

From **Table 1,** it can be seen that addition of inorganic matters, the characteristic temperature, activation energy and pre-exponential factor are different from those of raw and deminaralized coals. This makes out that addition inorganic matters alter the course and mechanism of coal pyrolysis. Moreover, the influences are different by different coals.

T_p is related to coal structure[6]. Usually, the same structure of coals have same T_p. **Table 1** shows that addition of inorganic matters has little effect on T_p during coal pyrolysis, which indicate that the procedure of demineralization and addition of inorganic matters didn't change the coal structure very much. T_o and T_F are related to the difficulty of chemical reaction. For the two demineralized coal samples, addition of CaO gives rise to T_o decrease about 20 to 30°C and T_F increase about 40 to 50°C. For demineralized SF coal, addition of K_2CO_3 leads to T_o descend for 70°C and 40°C for demineralized HLGL coal. This indicates that the influence of K_2CO_3 is very different from different coals. But K_2CO_3 has little effect on T_F of coal pyrolysis for both coals. Addition of Al_2O_3 has no effect on the T_o, but make T_F increase about 20 to 30°C.

Reaction with high activation energy needs high temperature or long reaction time[7]. For coal pyrolysis, high activation energy means that the reaction needs more energy offered by exterior. As shown in **Table 1**, there is highest activation energy in the middle temperature range for all samples. Compared to raw and demineralized coal samples, addition of CaO, K_2CO_3 or Al_2O_3 results in the decrease of activation energy at the corresponding temperature range. At low temperature, activation energy of inorganic matter added coals follows the order K_2CO_3< CaO< Al_2O_3 indicates that K_2CO_3 has the highest catalytic effect on coal pyrolysis; At the middle temperature, the activation energy of the three inorganic matters is similar order, which indicate that they have similar catalytic nature at this temperature range; At high temperature, the activation energy of Al_2O_3 added coal is the least. The change of activation energy shows that different inorganic matter has different catalytic nature at different temperature.

Conclusion

In the conditions studied, **t**he inherent mineral in coal has no effect on the reactivity and kinetics of coal pyrolysis. When some inorganic matters, such as CaO, K_2CO_3 and Al_2O_3, were added into the demineralized coal, they showed the positive effect on reactivity of coal pyrolysis. The pyrolysis process of all samples studies can be described by multi-step first order model. Addition of inorganic matters makes the activation energy decreased and the characteristic temperature of coal changed.

Acknowledgment The work was supported by fund of the National Key Fundamental Research and Development Project of China (G1999022101)

References

[1] Lemaignen, L.; Zhuo, Y.; Reed, G.; Dugwell, D. R.; Kandiyoti; R., Fuel, 2002, *81*, 315-326.
[2] Oztas, N.A.; Yurum, Y., Fuel, 2000, *79*, 1221-1227.
[3] Coats, A. W.; Redfern, J. F., Nature, 1964, *68*, 201.
[4] Crpres, R.; and Furfari, S., Fuel, 1982, *61*, 76.
[5] Slaghuis, J. H.; Ferreira, L.C.; and Judd, M. R., Fuel, 1991, *70*, 471.
[6] Xu, Y., Coal Chem. Ind., 1995, *72*, 62-65.
[7] Lazaro, M.J.; Moliner, R.; and Suelves, I., J. of Analytical and Applied Pyrolysis, 1998, *47*, 111-125.

PREREFORMING OF NATURAL GAS

Rune Lødeng[1], De Chen[2], Kjersti O. Christensen[2], Henrik S. Andersen[3], Morten Rønnekleiv[4], Anders Holmen[2]

[1]SINTEF Applied Chemistry, N-7465 Trondheim, Norway. [2]Dept. of Chemical Engineering, Norwegian University of Science and Technology (NTNU), N-7491, Norway. [3]Norsk Hydro, PO. Box 2560, N-3901 Porsgrunn, Norway. [4]Statoil, Postuttak, N-7005 Trondheim, Norway.

Introduction

A prereforming step is common in modern plants for production of synthesis gas to increase feed flexibility, reduce energy consumption, and lower investments. Adiabatic prereforming is basically low temperature steam reforming, combined with equilibration of water-gas shift and hydrogenation [1]. The process is endothermic for natural gas.

$$C_nH_m + nH_2O \rightarrow nCO + (n+1/2m)\,H_2 \quad -\Delta H^0_{298} < 0$$
$$CO + H_2O \rightleftharpoons CO_2 + H_2 \quad -\Delta H^0_{298} = 41.2 \text{ kJ/mol}$$
$$CO + 3H_2 \rightleftharpoons CH_4 + H_2O \quad -\Delta H^0_{298} = 206.2 \text{ kJ/mol}$$

Poisoning and coke (gum) formation are the most common reasons for deactivation [2]. Poisoning are caused by inorganic elements like S, Si, K, and Na. Other causes of deactivation include sintering of nickel and of the support [3].

Different types of carbon forming on nickel [4,5,6,7,8] include filamentous, gum, and more or less ordered encapsulating carbon. The gum and filament formation has been described [2] as follows:

$$C_nH_x - * \rightarrow -CH_2CH_2- * \rightarrow \text{gum (aromatic)}$$
$$C_nH_x - * \rightarrow C- * \text{ (atomic C)} \rightarrow \text{filaments}$$

While gum carbon is encapsulating the active nickel surface, filaments are breaking up the pellets without covering the surface. Carbon can be avoided by operating at high steam to carbon ratios and by adding alkali metals and basic oxides like MgO and CaO to the catalyst.

The aim of the present work was to study prereforming of natural gas over commercial nickel catalysts and in particular the conditions for catalyst deactivation.

Experimental

An industrial prereforming catalyst (PR) with 45 wt% nickel, 10 wt% MgO and 10 wt% α-Al_2O_3 was used. Most of the tests were performed with catalyst (PR-S) which had been stabilized prior to the experiments by exposing the fresh catalyst (PR-F) to a mixture of natural gas and steam for 600 hours at a S/C ratio of 2 at 490°C. Surface areas (BET) are 26 m^2/g for the stabilized catalyst and 155 m^2/g for the fresh catalyst. Tests with a fresh steam reforming catalyst (SR-F) containing 11 wt% Ni, and 9 wt% CaO in spinel with Al_2O_3 (BET surface area: 5 m^2/g) were performed for comparison.

The experiments were carried out using a Tapered Element Oscillating Microbalance (TEOM) reactor which has been described in detail previously [9]. The catalyst bed consisted of 3-10 mg of 0.3-0.5 mm catalyst particles diluted with similar α-Al_2O_3 grains and held in place by $Nextel_{610}$ alumina wool. Materials containing SiO_2 were avoided because of instability in presence of steam. Catalyst reduction was done with an equimolar H_2/Ar mixture heated to 550 °C at a rate of 2 °C/min.

The following conditions were used: Total pressure 20 bar, temperatures 450–580 °C, steam to carbon ratios in the range 0.3-1.3, and gas hourly space velocities (GHSV) of $7.4\cdot10^5$–$3.3\cdot10^6$ ml (reactants)/g_{cat},h. Different sulfur free mixtures of methane and C_2/C_3 hydrocarbons have been used as feed (Ar as balance).

The mass was followed continuously with the TEOM and the products were analyzed on-line with a HP5890 SII GC using N_2 as an internal standard.

Results and Discussion

A prereforming catalyst is designed for low temperature service. It has normally high nickel loading, reasonable porosity, and relatively high surface area. The average crystallite size is relatively small (<50 nm) compared to catalysts designed for high temperature service (200–1000 nm). Nickel catalysts can sinter seriously at high temperature, especially in presence of steam [3]. Recent results [10] indicate that a steam reformer catalyst also can sinter seriously at low temperature, 500 °C, in a H_2O/H_2 = 10 mixture at 30 bars pressure. The rates of sintering were initially high and gradually stabilizing over 300 hours. The present work indicates a significant decrease in BET surface area after 600 h in steam/natural gas even at 490 °C.

Figure 1 shows a comparison of PR-F, PR-S, and SR-F at 460°C. While no visible carbon forms on the fresh catalyst (for 30 hours on-stream), carbon is readily formed on the sintered sample.

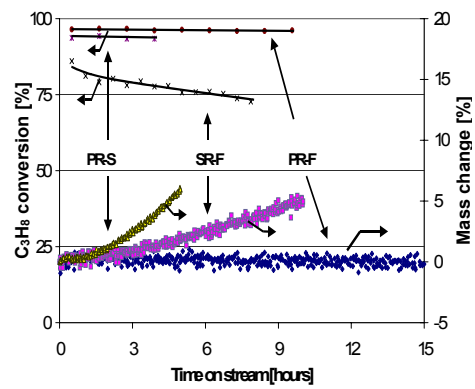

Figure 1. Comparison of fresh (PR-F) and stabilized (PR-S) pre-reformer catalyst and a fresh steam reformer catalyst (SR-F). T=460 °C, P_T=20 bar, P_{H2}=0.1 bar. Feed composition for PR-S and PR-F: P_{CH4}=3.3 bar, P_{C2H6}=0.4 bar, P_{C3H8}=0.18 bar, P_{H2O}=1.46 bar. Feed composition for SR-F: P_{CH4}=3.8 bar, P_{C3H8}=0.15 bar, P_{H20}=1.2 bar

The feed composition is important for carbon formation and deactivation. Previous results have shown [11|] that for steam reforming of CH_4 or CH_4 + C_3H_8 mixtures at 650 °C and 20 bar and at conditions where carbon formation is possible, large amounts of filamentous carbon can be formed resulting in only a very small deactivation following the initial carbon. However, the deactivating effect of carbon seems to be stronger at prereforming conditions as shown on Figure 2 where the conversion of C_3H_8 and C_2H_6 dropped from about 90 % to about 75 % after a coke deposition of 100 wt%. Adding olefins to the feed increases strongly the deactivating effect of carbon. Adding 800 ppm C_3H_6 to the feed resulted in a drop in the conversion of C_3H_8 from about 90 % to about 60 % after a coke deposition of only 40 wt%. Experiments at different temperatures also clearly indicate that most of the deactivating effect of carbon formed on the catalyst is due to C_3H_6 favoring encapsulating carbon.

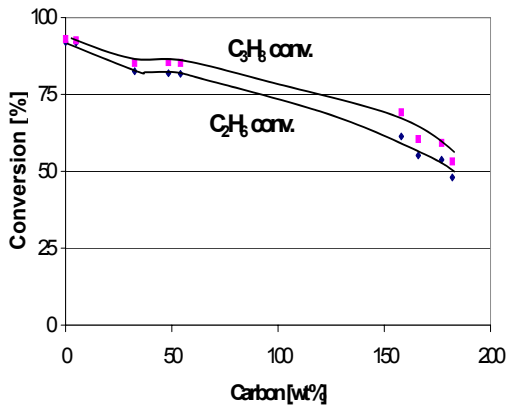

Figure 2. Conversion of C_3H_8 and C_2H_6 as a function of the amount of coke deposited for stabilized prereformer catalyst (PR-S). P_T=20 bar, T=580 ^oC, P_{CH4}=3.36 bar, P_{C2H6}=0.4 bar, P_{C3H8} =0.18 bar, steam to carbon ratio=1, P_{H2}=0.24 bar.

Figure 3 shows that addition of 800 ppm C_2H_4 or 800 ppm C_3H_6 to the feed leads to considerably higher carbon formation rates, and also a higher kinetic threshold, i.e. a higher steam to carbon ratio for carbon free operation.

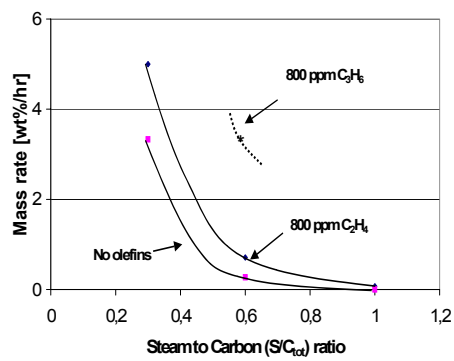

Figure 3. The effect of adding 800 ppm C_2H_4 or 800 ppm C_3H_6 on the rate of carbon formation. For stabilized prereformer catalyst (PR-S). T=520°C, P_t=20 bar, P_{CH4}=3.36 bar, P_{C2H6}=0.4 bar, P_{c3h6}=0.18 bar, P_{H2}=0.08 bar.

The effect of adding CO_2 to the feed has also been studied. Figure 4 indicates that carbon formation starts and the conversion of C_2H_6 and C_3H_8 drops immediately when CO_2 is added. The results in Figure 4 also indicate that the deactivation seems to proceed faster in the presence of CO_2. In the presence of H_2 the hydrogenation of CO_2 will take place:

$$CO_2 + 4\ H_2 \rightleftharpoons CH_4 + 2\ H_2O \quad -\Delta H^0_{298} = 165\ \text{kJ/mol}$$

The correlation between CO_2 and H_2 has also been studied by adding different amount of H_2 to the feed. The results show that the conversion of C_2H_6 and C_3H_8 is largely unaffected, but that the CH_4 formation is favored at increasing H_2 content. Thus, while hydrogenation of carbon oxides proceeds fast, hydrogenolysis seems to be of minor importance for the reactant conversion.

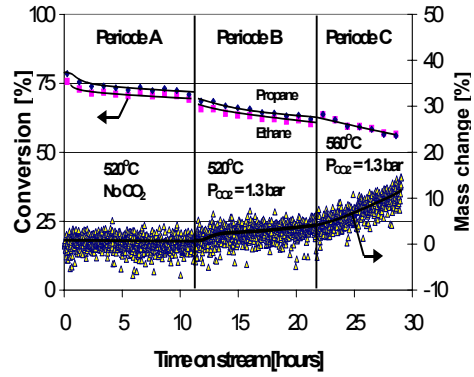

Figure 4. The effect of adding CO_2 to the feed for the stabilized prereformer catalyst (PR-S). P_T=20 bar, P_{CH4}=3.36 bar, P_{C2H6}=0.41 bar, P_{C3H8} =0.18 bar, P_{H2O}=2.7 bar, P_{H2}=0.24 bar.

Conclusions

The most likely reasons for deactivation are apparently sintering and encapsulating carbon formation. Both filamentous and encapsulating carbon seem to form. Carbon initiates more easily on a sintered than on a fresh catalyst sample, probably because of larger crystallites and ensembles. Thus, an aged catalyst requires a higher steam pressure for carbon free operation. Both CO_2 and olefins are increasing the deactivation rate. Part of the encapsulating carbon formed might be a precursor for gum carbon.

Acknowledgement. Norsk Hydro ASA, Statoil ASA and the Norwegian Research Council (NFR) are acknowledged for supporting this work.

References

1) Rostrup-Nielsen, J.R. In *Catalysis, Science and Technology, Vol 5*; Anderson, J.R, Boudart, M., Eds.; Springer, Berlin, 1984; pp. 1.
2) Christensen, T.S.; Rostrup-Nielsen, J.R., ACS Symp. Ser. 634 (Deact. and Testing of Hydro. Proc. Catalysts), 1996; 186 – 200.
3) Bartholomew, C.H. Appl. Catal., A: General, **1993** 107, 1-57.
4) Rostrup-Nielsen, J.R.; Trimm, D.L. J. Catal., **1977**, 48, 155-165.
5) Alstrup, I. J. Catal., **1988**, 109, 241 – 251.
6) Rostrup-Nielsen, J.R.; Sehested, J.,Stud. Surf. Sci. Catal., **2001**, 139, 1-12.
7) De Chen; Lødeng, R.; Omdahl, K.; Anundskås, A.; Olsvik, O.; Holmen, A. Stud. Surf. Sci. Catal., **2001,** 139, 93-100.
8) De Chen; Lødeng, R.; Anundskås, A.; Olsvik, O.; Holmen, A. Chem. Eng. Science, **2001**, 56, 1371 – 1379.
9) De Chen; Grønvold, A.; Rebo, H.P.; Moljord, K.; Holmen. A. Appl. Catal., **1996,** 137, L1
10) Sehested, J.; Carlsson, A.; Janssens, T.V.W.; Hansen, P.L.; Datye, A.K. J. Catal., **2001**, 197, 200 – 209.
13) Lødeng, R.; De Chen; Christensen, K.O; Holmen, A. In preparation.

Operating Experience of a Small Hydrogen Plant by Steam Reforming of Natural Gas

Mou Jian, and Larry Czarnecki

Alstom Power, Inc.
1409 Centerpoint Blvd
Knoxville, TN 37932

Introduction

Small amount of hydrogen is needed for operating a flue gas deNOx system at a 58 MW gas turbine and combined cycle power plant. This requirement posed unique challenges to implement the most economical as well as environmental friendly technologies to meet the hydrogen demand, as the process requirements are unique and customer preference in the electric power industry differs from that of the chemical industry.

Design Considerations

To meet the process and environmental requirements, the generated hydrogen has to be free of oxygen and carbon monoxide (CO), but carbon dioxide (CO_2) is of beneficence to the deNOx process. Therefore, steam reforming of natural gas followed by water-gas shifting is the primary choice because this combined process generates both hydrogen and carbon dioxide, and because natural gas is readily available in this power plant (Figure 1).

Figure 1. The Steam Reformer Installation.

A Platinum-Rhodium based catalyst is selected for the reforming and shifting reactions. The catalyst is of the shape of corrugated plate.

Operating Conditions

Major operation parameters are given in Table 1. Since steam is readily available in the plant, it is supplied to the hydrogen plant not only for the chemical reactions, but also as carrier gas for the process, which requires substantial amount of inert carrier gas flow. As a consequence, the reaction temperature at the steam reformer is mainly determined by the available steam temperature.

Table 1. Operating Parameters of the Steam Reformer

Parameters	Unit	Value
Catalyst Charge	ft3	27
Inlet Temperature	°F	665
Operating Pressure	psig	2.5
Dilution Steam Flow	lb/hr	6,500
Natural Gas Feed Rate	lb/hr	75

Performance Characteristics

Since the combined reaction of steam reforming / water-gas shifting is highly endothermic, and since the reactor has no supplementary heating devices attached, temperature drop across the reactor is used to continuously monitoring the natural gas conversion through the reactor (Figure 2).

$$CH_4 + 2H_2O \rightarrow CO_2 + 4H_2 \qquad -\Delta H^o_{298} = -165 kJ/mol$$

Separate measurement of hydrogen concentration has confirmed the hydrogen yield calculations from the temperature drop.

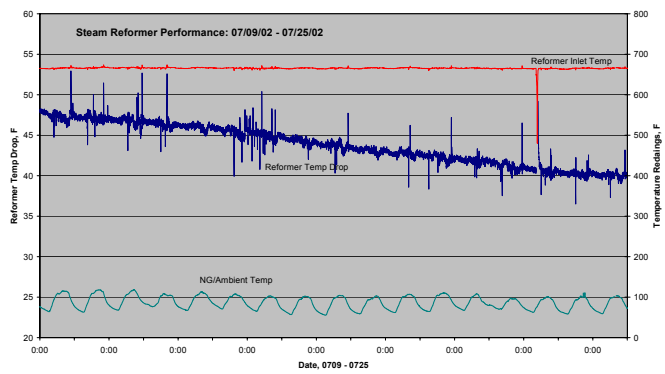

Figure 2. Operating History of the Steam Reformer in July 2002.

40% natural gas conversion was achieved initially. At this conversion level, production of hydrogen was marginally sufficient to meet the process requirement. However, sooner afterward it turned out that the conversion of natural gas across the reactor started decreasing and that hydrogen production could not meet the process demand (Figure 2).

Figure 2 shows that although the steam reformer inlet temperature had been stable, the temperature drop across the steam reformer had dropped continuously, indicating that performance of the hydrogen plant had been degrading. In addition, it was noted that ambient temperature at this plant location had been extremely high in summer months.

Sulfur Contamination

Extensively investigations pointed out that sulfur poisoning of the reformer catalyst was the possible cause of the performance degradation, although sulfur compounds were not detected from the natural gas feed to the steam reformer. However, sulfur was detected on the deactivated catalyst.

It was concluded that due to the high ambient temperatures, the capacity of the sulfur scavenger filter had been significantly reduced. Furthermore, due to the large variations of ambient temperature between day and night, sulfur slippage from the scavenger filter

could have well occurred only in a very short time window, which was very difficult to detect.

Although most noble metal based steam reformer catalyst is said to be able to tolerate a few ppmv of sulfur, it is certainly not the case for the present installation, possibly due to the low operating temperatures. In addition, certain sulfur compounds in the natural gas feed to the steam reformer may be easier to slip through the scavenge filter than others, such as hydrogen sulfide (H_2S) and carbonyl sulfide (COS), both exist in the current natural gas feed.

Upon successfully regeneration of the steam reformer catalyst, initial catalytical activity has been restored, and furthermore, additional operation margin has since been implemented for further operations.

Conclusions

Temperature drop across the steam reformer reactor has been successfully used to monitor the performance of the steam reforming/WGS reactions.

Sulfur slip from scavenger sorbent may easily occur at extreme weather conditions, and certain sulfur-containing compounds are earlier to escape the sulfur trap than others.

EMISSION OF ALKALI AND TRACE ELEMENTS IN CO-COMBUSTION OF COAL WITH SEWAGE SLUDGE

Y. Ninomiya, L. Zhang, M. Ito and A. Sato*

Department of Applied Chemistry, College of Engineering,
Chubu University, Matsumoto-cho, 1200, Kasugai, Aichi, Japan
Tel: +81-568-51-9178, Fax: +81-568-51-3833
*: Corresponding author, Email: ninomiya@isc.chubu.ac.jp

Introduction

Co-combustion of coal with sewage sludge has the potential to overcome the drawbacks of firing pure coals. The most attractive advantage of it is to significantly reduce the net CO_2 emissions [1,2]. Besides of it, the use of sewage sludge can diversify the power plant`s fuel portfolio by adding a potentially less expensive non-fossil fuel [2]. Furthermore, it had been reported that cofiring can also reduce the SO_x and NO_x emissions since in one hand, the biomass fuels including sewage sludge generally contain less sulfur than coal. On the other hand, the alkali and calcium in biomass fuels can react with gaseous sulfur to form deposition on the slag [3]. In addition, the biomass fuels contain high volatile matter contents than coal that tend to form less NO_x in low-NO_x burners.

Co-combustion is generally carried out by cofiring coal with biofuel in the existing pulverized coal boiler. Experience showed that co-combustion could significantly impact on the pulveriser performance. The major subjects of concern are related to the problems of ash and particulate matters in co-combustion [4]. Since the mineralogical of biomass fuels including sludge has the distinct compositions and association compared to coals, co-combustion inevitably incurs the new ash-related problems. Emission of alkali and trace elements played important roles in the process [2,4].

The purpose of this paper is to investigate the fate of alkali and trace elements in co-combustion of coal with sewage sludge in laboratory-scaled drop tube furnace. The reaction temperature was kept at 1200°C; three coals were used to study the influence of coal type. The combustion residues including char and fly ash were collected by cyclones to probe the existence of alkali and trace elements within them. In addition, the particulate matters (PM) were collected by using low-pressure impactor for concerning on the volatized elements.

Experimental

Properties of coals and sludge

Three coals and one sludge were used in this study, they are pulverized to <125 μm and dried before use. Their proximate and ultimate properties were shown in ***Table 1***. Compared to coals, sludge is lean in fixed carbon, bur rich in moisture and ash. The oxide composition in ashes shown in ***Table 2*** indicated a distinct ash composition in sludge. CaO, MgO and P_2O_5 are of most prevalence in the ash of sludge, whilst SiO_2 and Al_2O_3 are the main compounds in the ash of coals. In addition, as to the alkali elements, they have relatively high contents in coals. The trace elements are more abundant in sludge than in coals. Zn, Cu, and Ti are the most prevalent in the former fuel [5].

Experimental procedure

Combustion of fuel alone and co-combustion were carried out in drop tube furnace (DTF), the combustion procedure and conditions are similar to used previously [6]. The weight ratio of coal to sludge was kept as 50:50 in co-combustion. O_2 10% and N_2 being the balance was used as the atmosphere, reaction temperature was selected at 1200°C, while reaction time varied from 0.6 to 2.4 seconds. The combustion residues having micron-ordered size were collected by a water-cooled, rapid N_2 quenching probe and cyclones, which roughly have the particle cut-off size of 1.0 μm. On the other hand, the PM, existing in the exiting gas, was collected by low-pressure impactor (LPI), which is composed of 11 stages having the aerodynamic cut-off diameters ranging from 0.06 to 12.1 μm.

Table 1. Proximate and ultimate analysis on three coals and sludge

	Sludge	THY	DT	YZHS
Proximate analysis, dry, wt%				
Moisture	21.8	0	7.8	2.5
VM	37.0	45.7	24.7	38.8
Ash	15.8	12.6	12.8	9.7
FC	25.4	41.7	54.7	49
Ultimate analysis, daf, wt%				
C	34.4	78.7	78.6	76.4
H	5.5	6.2	4.9	5.6
N	7.5	1.2	0.8	1.4
S	0.8	0.1	1.7	5.7
O	51.8	18.3	14.2	11

Table 2. Ash compositions in three coals and sludge

	Sludge	THY	DT	YZHS
SiO2	26.91	50.3	45.1	48.2
Al2O3	13.04	23.5	15.3	10.7
Fe2O3	8.89	6.2	8.9	17.4
CaO	15.81	9.6	1.5	9.8
MgO	1.98	2	0.5	0.4
Na2O	0.37	1.3	0.3	0.4
K2O	0.53	1.1	1.2	0.6
SO3	9.92	4.0	13.3	11.6
P2O5	24.85	-	0.33	0.02

Characterization methods

The combustion residues, collected by both probe and cyclones, were analyzed by several methods including ICP, XRD, SEM-EDX and CCSEM. The size-segregated PM was digested with filter together in a $15HNO_3$: 2HF: $5HClO_4$: $28H_2O$ solution. The filtered solution was analyzed by ICP for the elemental composition. Furthermore, PM was also observed by SEM-EDX for probing the chemical formations within it.

The novel CCSEM categories were developed for alkali elements and zinc in the combustion residues, which were listed in ***Table 3***. For the Na-based compounds, they were defined as $Na(Ca/Fe)PO_4$, Na/al-si, Na(Ca,Fe)/al-si and $Na(Ca,Fe)PO_4$/al-si. The first one refers to sodium phosphate containing calcium/iron or not; similarly, the third one refers to sodium aluminosilicate containing calcium/iron together, and the fourth being the molten sodium phosphate/aluminosilicate containing calcium/iron or not. The same definition was used for potassium-based compounds. For the zinc-based compounds, they include $Zn(Ca,Fe)PO_4$, Zn/al-si, Zn(Ca,Fe)/al-si and $Zn(Ca,Fe)PO_4$/al-si. The first definition was used considering of the alloys formed in residues, whilst the second refers to the reaction of Zinc with aluminosilicate, and the third and fourth ones were defined for the possible capturing of Zn in slag.

Table 3. CCSEM categories for alkali elements and Zinc

	Category	Wt%
Na- based or K- based	Na(Fe)PO4	Na≥1, P≥5, Si≤10, Ca≤5
	Na(Ca)PO4	Na≥1, P≥5, Si≤10, Fe≤5
	Na/ al- si	Na≥1, Ca≤5, Fe≤5, Si≥10, P≤5
	Na(Ca, Fe)/ al- si	Na≥1, Ca(Fe)≥5, Si≥10, P≤5
	Na(Ca, Fe)PO4/ al- si	Na≥1, Ca(Fe)≥5, Si≥10,P≥5
Zn- based	Zn(Ca, Fe)PO4	Zn≥0.1, Ca(Fe)≥5, P≥5, Si≤10
	Zn/ al- si	Zn≥0.1, Si≥10, Ca≤5, Fe≤5
	Zn(Ca, Fe)/ al- si	Zn≥0.1, Ca(Fe)≥5, Si≥10, P≤5
	Zn(Ca, Fe)PO4/ al- si	Zn≥0.1, Ca(Fe)≥5, Si≥10, P≥5

Results and discussion

Retention of alkali and trace elements in combustion residues

In combustion, the alkali and trace elements would undergo partitioning, a portion of which would be kept in the residues whilst the other would vaporize, suspending in the gas atmosphere and becoming into PM. The retention of alkali and trace elements during co-combustion in 2.4 s (more than 98% of carbon burnt out) was illustrated in ***figure 1***, which was expressed as the comparison of the experimental to calculated values. The calculated value was the arithmetic average of data obtained in combustion of coal or sludge alone. Clearly, the retention of alkali and trace elements varied with coal type. Cofiring YZHS and sludge led to more of these elements kept in the residues than calculated, whilst cofiring DT with sludge resulted in less of these elements kept in residues. On the other hand, cofiring THY had little effect on retention of these elements.

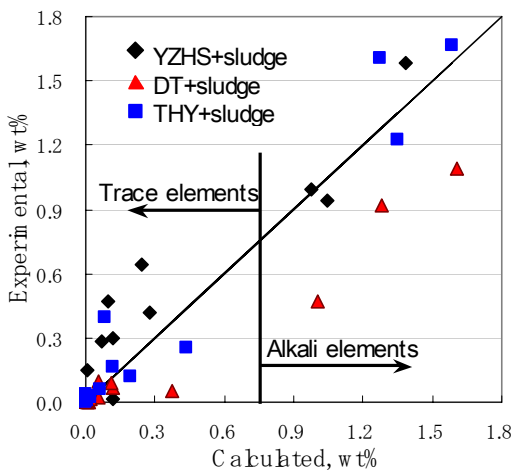

Figure 1. Retention of alkali and trace elements in residues

The distributions of alkali and Zinc were shown in ***figure 2*** for co-combustion of YZHS with sludge at 2.4s. For alkali based compounds, almost all them were reduced in co-combustion, especially for Na/K(Fe)PO_4 and Na/K(Ca,Fe)PO_4/al-si. Conversely, the Zinc-based compounds in residues were enhanced obviously. The above results implied the strong interaction of coal with sludge in co-combustion. The reduction of alkali elements in residues was caused by deterioration of the wall of chars. Cofiring YZHS (being rich in excluded minerals) in one hand changed the ash layer around sludge particle; a more porous char was formed as a result. Furthermore, reaction of CaO/Fe_2O_3, aluminosilicate with P_2O_5 in sludge resulted in formation of more apatite and molten (Ca,Fe)PO_4/al-si, both of them are capable of capturing trace elements [5,7].

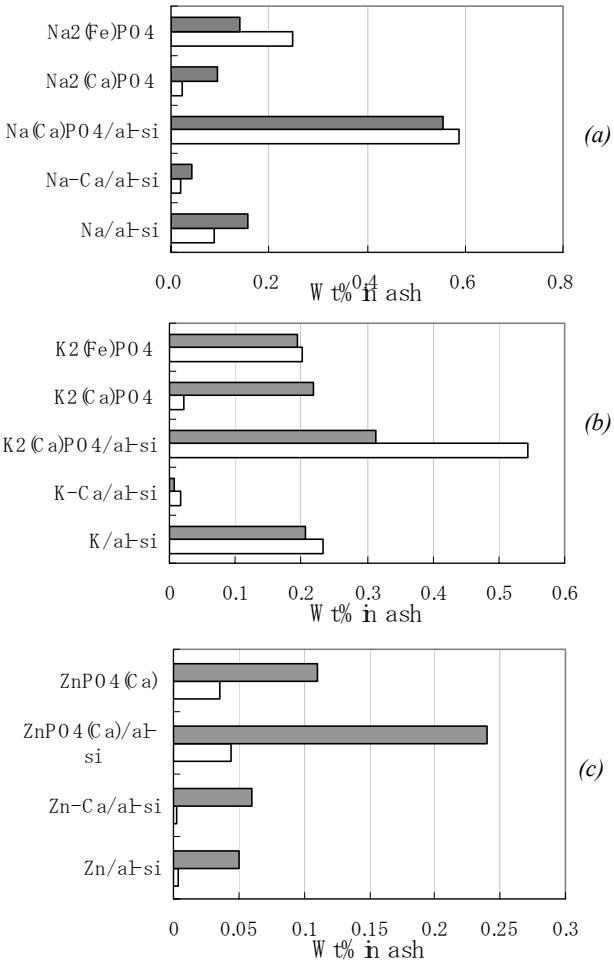

Figure 2. Distribution of alkali and Zinc in residues after co-combustion of YZHS with sludge in 2.4s

Vaporization of alkali and trace elements

The vaporized alkali and trace elements in PM were illustrated in ***Figure 3***. It substantiated the conclusions in above section. For both trace elements including Born and Zinc, the fine particles having size of ca. 0.3 *μm* disappeared due to condensation of them on molten phases. On the other hand, for the alkali elements in PM, both particles having mean size of 0.3 and 2.0 *μm* were enhanced. The former one was caused by formation of alkali sulfate/chlorium/phosphate in PM, whilst the latter one mainly contains alkali with other refractory elements; it functioned as the nuclei for the growth of aerosols by heterogeneous nucleation.

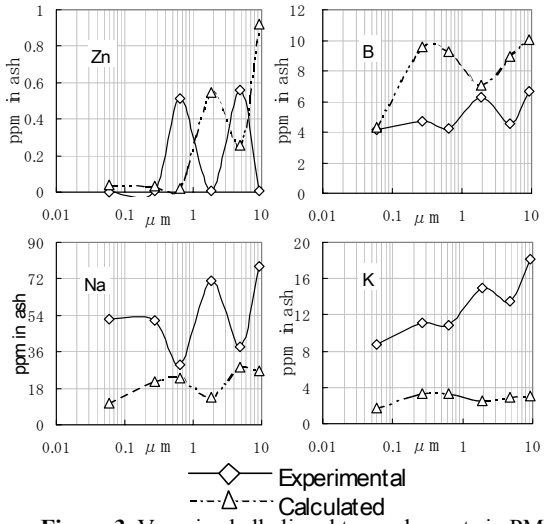

Figure 3. Vaporized alkali and trace elements in PM

Acknowledgements

The authors would like to thank Grant-in-aid for Scientific Research on Priority Areas (B), 11218211, the Ministry of Education, Culture, Sports, Science and Technology of Japan for the financial support. The special appreciation is also given to Mr. M. Masui, Actree cooperation in Ishikawa prefecture, Japan for supplying the sewage sludge.

References

1. Smith I.M., and Rousaki K., IEA Coal Research, UK, May 2002.
2. Fernando Rohan, IEA Coal Research, UK, Oct. 2002.
3. Robinson A. L., Junker H., and Baxter L.L., *Energy & Fuels* 2002, 16, 343-355.
4. Hein K.R.G., Wolski N., and Hocquel M., Trace element workshop 2002, 141-154. Japan.
5. Zhang L., Ito M., Sato A., and Ninomiya Y., proceedings of the 39th coal science symposium, 2002, 10.29-30, Japan.
6. Zhang L., Sato A., and Ninomiya Y., Fuel, 2002, 81, 1499.
7. Yoshiie R., Nishimura M., and Moritomi H., Fuel, 81(2002), 1335-1340.

FUNDAMENTALS ON CO-COMBUSTION CHARACTERISTICS OF LOW-GRADE COAL WITH BIOMASS

Ichiro Naruse, Kunihiro Nishikawa and Keiju Morishita

Department of Ecological Engineering
Toyohashi University of Technology
Tempaku-cho, Toyohashi 441-8580, Japan

Introduction

In some developing countries, low-grade coals, which contain high fixed carbon, sulfur, nitrogen and/or ash contents, are necessitated to be utilized as fuels due to its cost and so forth. However, it is hard for the low-grade coals to be burnt completely in current combustors. Additionally, emission control devices for de-NOx and de-SOx are not placed sufficiently in those countries. On the other hand, biomass resources have become more attractive even in developed countries. This is because the biomass is one of carbon-neutral fuels, which do not increase CO_2 emission in the atmosphere. Although inventory of biomass resources, energy consumption for collection and conveyance of biomass and so forth are still unknown, the biomass must be one of candidates to make up for energy produced by fossil fuels.

From this viewpoint, co-combustion technology of coal with biomass has been applied in several practical coal boilers in order to reduce CO_2 emission, fuel cost and so forth. Furthermore, the biomass may be able to enhance the combustion performance and to control NOx emission since the biomass contains much volatile matter and evolves NH_3 as volatile-N species[1]. However, fundamental combustion and NOx emission characteristics for biomass alone and mixture of coal with biomass have not been elucidated precisely yet. In this study, the fundamental pyrolysis and combustion characteristics for several kinds of biomass were discussed first, using a thermobalance. Second, the combustion behaviors of biomass alone, coal alone and biomass-coal mixture were tested, using an electrically heated drop tube furnace. In the combustion test, the ignition behavior, combustion efficiency and NOx (NO and N_2O) emission behavior were focused, based on the results of gas compositions along the furnace axis. Furthermore, effect of co-combustion on the size of ash particles at the exit was also discussed, sampling the particles and observing them by a scanning electron microscope (SEM).

Experimental

Fundamental tests on pyrolysis and combustion for several kinds of biomass were carried out, using a thermobalance. Experimental conditions in the thermobalance test are summarized in Table 1. The pyrolysis and combustion experiments are operated in the N_2 and air atmosphere, respectively. Five kinds of biomass, which are derived from agricultural or lumbering wastes, were used as a sample. Properties of the biomass employed are shown in Table 2. From the table all of the biomass contain high amount of volatile matter content and little amount of ash content.

The co-combustion test was performed, using an electrically heated drop tube furnace. The furnace mainly consists of a feeder, a process tube made of quartz, electrical heaters and a sampling line. The experimental conditions in the co-combustion test are shown in Table 3. From the table the furnace temperature and combustion stoichiometry are kept constant an all experiments. The mixture ratio of coal to biomass is set at 1 to 1 as mass basis. The input heating value are controlled to keep constant by changing the total feed rate even when varying the coal type. The coal tested in the co-combustion experiments are also shown in Table 2. Three types of coal were burned as a sample. In three types of coal SH coal is classified as a low-rank coal since the content ratio of fixed carbon to volatile matter is the highest of the three as shown in Table 2. NL and TH coals were chosen as a reference to elucidate the effect of volatile matter content on the ignition and combustion behaviors. The biomass tested in the co-combustion is Hinoki sawdust. Mean particle size of coal is about 80 μm, which corresponds to pulverized coal. For the biomass, on the other hand, the particles shifted less than 1000 μm were used.

Table 1. Experimental conditions in thermobalance experiments

		Conditions
Sample		Hinoki, Rice straw, Rice husks, Larch bark, Corn stalk
Temperature increasing rate		20 K/min
Sample weight		7mg
Gas flow rate		120ml/min
Thermal decomposition	Gas	N_2
	Final holding temp.	900℃
Combustion	Gas	Air
	Final holding temp.	815℃

Table 2. Properties of coal and biomass tested

Sample				Coal			Biomass				
				SH	NL	TH	Sawdust Hinoki	Larch bark	Rice straw	Rice husks	com stalk
Low heating value		MJ/kg	air dry	29.16	26.82	25.75	18.02	12.03	11.75	13.54	9.20
Proximate analysis	Moisture	wt %	air dry	1.7	1.8	5.2	11.0	9.4	5.8	7.2	7.4
	Ash			13.8	17.0	11.8	1.2	3.4	19.2	19.3	1.9
	VM			11.2	27.0	45.4	86.6	87.2	75.0	73.4	82.1
	FC			73.3	54.2	37.6	1.2	≒ 0	≒ 0	≒ 0	8.5
Fuel ratio		-	-	6.54	2.01	0.83	0.01	0.00	0.00	0.00	0.10
Total S		wt %	dry	0.40	0.35	0.22	0.00	0.02	0.05	0.02	0.00
Ultimate analysis	C	wt %	d. a. f.	90.12	84.57	77.84	55.87	47.07	47.50	52.	40.10
	H			3.95	4.91	6.17	7.06	5.5	6.49	6.89	5.20
	N			1.16	1.79	1.13	0.24	0.23	1.21	0.29	2.10
	S			0.47	0.25	0.06	0.00	0	0.02	0.01	0.00
	O			4.30	8.47	14.81	36.83	47.20	44.79	40.64	52.60
H/C (mole ratio)		-	-	0.53	0.70	0.95	1.52	1.40	1.64	1.58	1.56

Table 3. Experimental conditions in co-combustion

	Conditions						
Sample	SH	NL	TH	BM	SH+BM	NL+BM	TH+BM
Furnace temperature [℃]	800						
O_2 concentration [vol%]	21						
Lower heating value [kW]	0.225	0.218	0.215	0.224	0.362	0.194	0.224
Sample feed rate [g/min]	0.46	0.49	0.5	0.75	0.92	0.52	0.62
Air ratio	1.2						

BM :Biomass (Sawdust)
Mixing ratio= 50 :50 (wt%)

Results and Discussion

Fundamental pyrolysis and combustion characteristics of biomass. Figures 1 show the decrease curves of unburnt fraction for two kinds of biomass and lignin and cellulose under pyrolysis conditions. From the figure, the pyrolysis begins at about 200 degree C for all samples. After about 500 degree C, however, pyrolysis behavior for bark differs from that for rice husks. This phenomenon is caused by the composition difference in the biomass. In order to elucidate the effect of chemical composition on the pyrolysis behavior, pyrolysis experiments for cellulose and lignin were done under the same experimental conditions. For the cellulose the mass rapidly decreases at about 200 degree C, and almost mass is evolved as volatile matter. For the lignin, while, the mass gradually decreases, and the residual matter remains even at 900 degree C. This result suggests that the lignin has the content of fixed carbon. Comparing the results for the cellulose and lignin with those for two types of biomass, Bark may contain more lignin component than Rice husks. Consequently, lignin content in the biomass may affect the combustion characteristics.

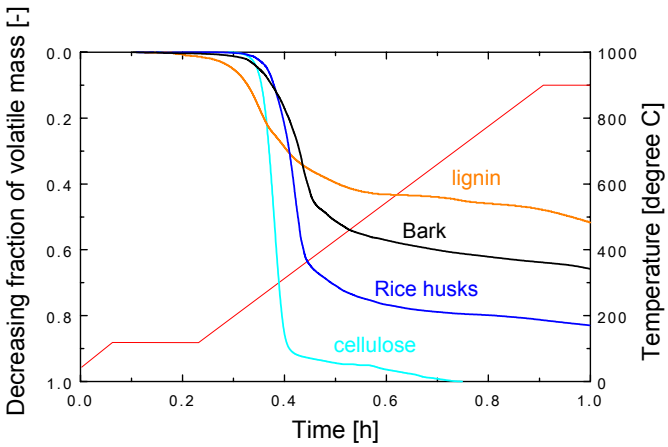

Figure 1. Decreasing profiles of volatile mass for cellulose and lignin, compared with two kinds of biomass

Co-combustion characteristics of coal with biomass. In the co-combustion experiments the reaction gas was sampled along the furnace axis, and the reacting particles were sampled at only the exit of furnace. In order to evaluate the co-combustion characteristics, both biomass alone and coal alone were also burnt under the same experimental condition. O_2 and CO_2 profiles and CO profile along the furnace axis for SH coal, which is categorized as a low-grade coal, are show in Fig. 2. Comparing the results for biomass and SH coal co-combustion with those for SH coal alone, the ignition point, where O_2 concentration rapidly decreases and CO_2 produces approaches the burner and O_2 is also consumed more during the combustion. Those phenomena suggest the effect biomass addition. For CO profile, biomass produces high concentration of CO during the initial stage of combustion. For SH coal the position of the maximum CO concentration comes near to the burner due to the co-combustion with biomass.

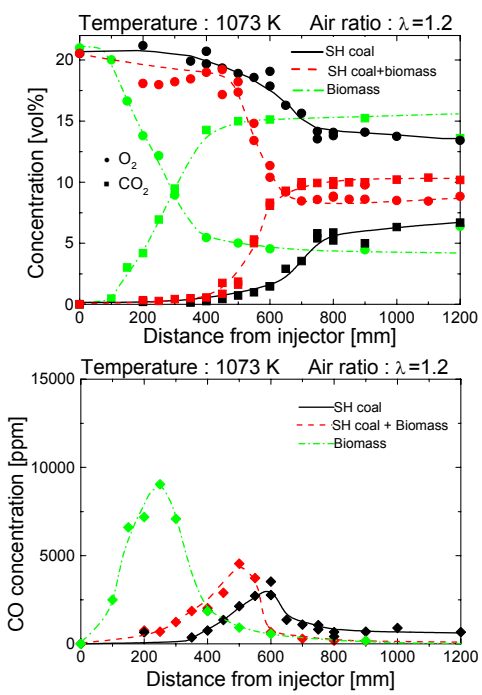

Figure 2. CO_2 and O_2 profiles and CO profile along the furnace axis for biomass alone, coal alone and co-combustion for SH coal

Some reports[2] have presented that biomass addition played a role for NOx reduction since biomass tends to evolve NH_3 as volatile nitrogen species. However, the effect of NOx reduction depends on combustion conditions, furnace type, fuel type and so forth[1]. From this viewpoint, NOx and N_2O were also measured along the furnace axis during the combustion in this study. Figure 3 shows NO and N_2O profiles along the furnace axis for biomass alone, coal alone and co-combustion for SH coal. Both NO and N_2O under the co-combustion condition are not intermediate between those under coal-alone and biomass-alone condition, but are similar to those under coal-alone combustion. Fuel-N input for the co- combustion is half as much as that for the coal-alone. Thereafter, both NO and N_2O emissions for the co-combustion are biased to those for the coal-alone. At the initial combustion stage under the co-combustion N_2O concentration is a little larger than that under the coal-alone combustion condition. Base on those experimental results obtained, the following reaction scheme may be dominant to produce NO and N_2O under the co-combustion condition.

$$NH_3 + CO = HCN + H_2O$$
$$HCN + O_2 = NCO + OH$$
$$NCO + OH = NO + CO + H$$
$$NCO + O = NO + CO$$
$$NCO + NO = N_2O + CO$$

The reason why the scheme above was proposed is caused by production of high CO concentration at the initial stage during biomass combustion. It is necessary to confirm the scheme by means of chemical kinetic theory since the first reaction of $NH_3 + CO = HCN + H_2O$ is not generally adopted in elementary reaction group relating to NO and N_2O.

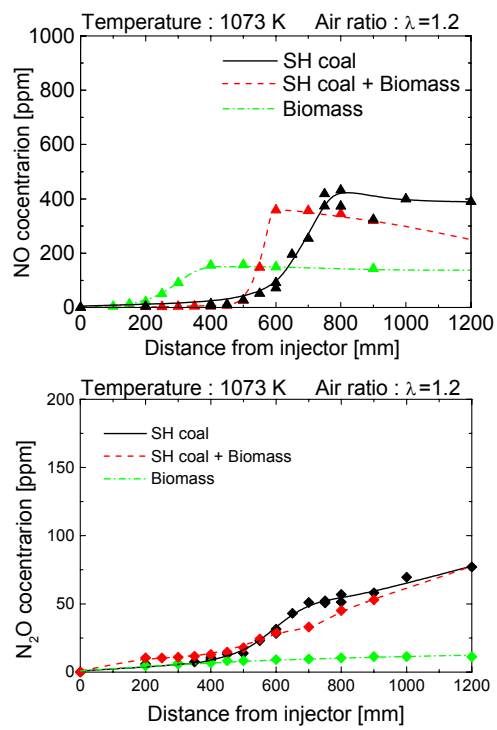

Figure 3. NO and N_2O profiles along the furnace axis for biomass alone, coal alone and co-combustion for SH coal

Recently, fine particulates exhausted from combustion processes, so-called $PM_{2.5}$, have been focused in terms of health effect. Biomass, especially for agricultural biomass, usually contains a small amount of ash content, as shown in Table 2. Therefore, when biomass is burnt out, fine particulates may be produced during the combustion. Figure 4 shows SEM photos of ash collected by a filter for (a) biomass alone and (b) co-combustion of NL coal with biomass. In (a), fibers of the filter are also observed. When the biomass is burnt out, only fine particulates are captured in the filter. Mean particle diameter of those fine particulates was about 1.3 μm. Under the co-combustion condition, on the other hand, co-combustion of coal with biomass contributes to have those fine particulates adhered during the combustion.

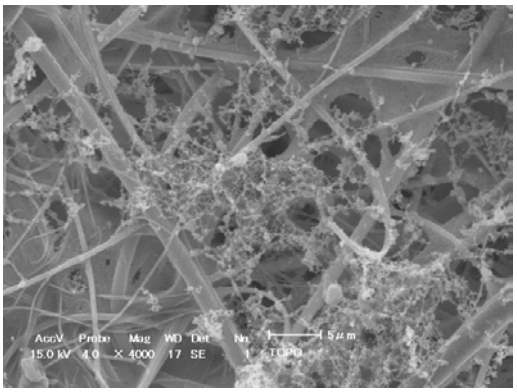

(a) Biomass alone

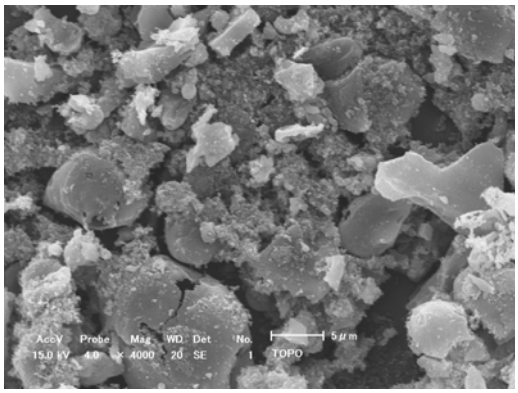

(b) Co-combustion

Figure 4. SEM photos of ash collected by a filter for biomass alone and co-combustion of NL coal with biomass

Acknowledgement This study has been partly supported, as Priority Areas Research of Grants-in-Aid for Scientific Researches and COE project, by Monbu Kagaku-sho.

References

(1) Davidson, R. M. (1999) *IEA Coal Research*, Feb.
(2) Morgan, D. J. and van de Kamp, W. L. (1995) "Combined combustion of biomass/sewage sludge and coals", Bemtgen, J. M. *et al.* (eds.), 35.

ULTRA RAPID REFORMING OF HYDROCARBONS BY THERMO-NEUTRAL REACTION METHOD ON A MULTI-FUNCTIONAL CATALYST FOR HYDROGEN PRODUCTION AND FUEL CELL SYSTEMS

Tomoyuki Inui

Senior Consultant
Air Water Inc.
6-40, Chiko Shinmachi, 2-Cho,
Sakai, Osaka 592-8331, Japan

Introduction

Hydrogen production is increasing importance from the viewpoints of ultimate clean and high caloric energy source, and especially for the use of fuel cell. However, the dead rock is its expensive cost. Among more than two dozen of known methods for hydrogen-production, the large-scale commercialized production is almost limited in steam reforming of natural gas or methanol. The most conventional steam reformers are consisted of the catalytic reactor with heating from outside of the reactor wall to inject the large endothermic heat of the reforming reactions. Even at a high furnace temperature level such as 950ºC, the amount of heat conducted from the reactor wall is limited in considerably low level. Therefore, the reaction is usually operated with a very low space velocity of the feed gas around 1,500 - 2,000 h^{-1}. In other words, a huge reactor for the steam reforming is employed. It is obviously a neck of application to the compact H_2-supplying systems such as fuel-cell equipping cars and co-generation systems for domestic use. In addition to these difficulties, conventional commercial reforming catalysts, consisted of Ni as the major catalytic component, suffer from deactivation owing to the coke deposit on the active sites of the catalyst. In order to moderate the coke deposition, excessive steam in the reaction feed is used, anticipating the reaction between deposited coke and water to form CO. The use of excessive steam lowers energy efficiency. To avoid coke formation, Ru catalyst used as an advanced catalyst, but it has a lower sulfur tolerance.

In order to supply the large heat for steam reforming, auto thermal methods are apt to be employed. However, the most of them are that a part of the natural gas in the feed is priori combusted before the catalytic reformer, and then the heated gas is introduced to the catalyst bed. Therefore, the heat supply is limited in a level of heat capacity of the reactant gases, and it does not achieve essential improvement. Recently, a partial catalytic oxidative reforming of natural gas is operating in some pilot plants for GTL processes. In these cases, one of the advantages is that the syngas having lower H_2/CO molar ratio can be directly used for successive catalytic converters to produce liquid products. Therefore, regulation process of H_2/CO molar ratio can be eliminated. Although the large endothermic heat for the steam-reforming of natural gas is avoided by the exothermic partial oxidation heat, the hydrogen atoms in water, i.e., the cheap and plenty resources for hydrogen, is not utilized as a part of hydrogen source. Therefore, for the purpose of hydrogen production, this method is not sufficient. Furthermore, this process cannot avoid combustion of the fed gas and produced gases, resulting the decrease in the selectivity to H_2 and/or CO.

A number of studies on developing coke-resisted catalysts have been done in the past decade. To this purpose, CO_2 reforming has been focused[2], because coke formation occurs much easier than in steam reforming. A solid solution of Ni-magnesia and a Ni-based composite catalyst, Ni-Ce_2O_3-Pt-Rh[3], are very successful ones for the purpose. The catalyst structure of the latter had been designed as highly enhancing hydrogen spillover effect to avoid both coke formation and sulfidation of the catalyst metals. The catalyst has not only the functions of the reforming but also the catalytic combustion. Therefore, more easily combustible hydrocarbons such as C_2 - C_4 paraffins contained in the natural gas react with O_2 fed at considerably lower temperatures and generate large exothermic reaction heat. This reaction heat elevates catalyst-bed temperature up to 800 - 900ºC. Simultaneously, the CO_2-reforming[4] and/or H_2O-reforming[5] of CH_4 are induced while suppressing excessive raise of catalyst temperature. This automatic thermo-neutralization on the catalyst surface can maintain the reactions very fast and stable.

In this keynote lecture, typical results obtained by the thermo-neutral reaction method in a pilot plant test of hydrogen production by steam reforming of natural gas is presented putting the focus onto feature and performance of the novel reformer. As an extension steam reforming of LP gas for hydrogen supply to polymer electrolyte fuel cell and other applications will be presented.

Experimental

Catalyst. The Ni-Ce_2O_3-Pt-Rh catalyst was prepared by incipient impregnation method by step wise in the order of Rh, Pt, and then (Ni + Ce) simultaneously. The atomic ratio was consistently kept in Ni:Ce:Pt:Rh = 100:20:3:1, irrespective of different loading on various supports. Fiber Flax (ceramic fiber texture), cordierite honeycomb, and high-temperature calcined alumina spherical particles were applied to the support. In case of the former two, alumina-washcoat was made to increase the surface area. The detail procedures for preparation are described in elsewhere[4, 5].

Reaction methods. Reforming of methane or NG (Natural gas) was conducted by three steps, 5 $l/h^{4, 5}$, 2 m^3/h, and 20 m^3/h as expressed with volume rate of produced H_2. The former was operated under atmospheric pressure, and the later two were operated under 0.8 MPa. Reforming of LPG (liquid petroleum gas) was conducted 1m^3 H_2/h scale under atmospheric pressure for the purpose of supplying to 1 kW class PEFC (polymer electrolyte fuel cell). In case of pure hydrogen (99.999% purity) production, desulfurization catalyst, H_2O-CO shift catalyst, and PSA units were employed from commercial ones, respectively. Larger scale reactor systems were fully controlled by computers. Analyses of reactants and products were made by using on-line micro-gas chromatographs.

Results and Discussion

20 Nm^3/h scale pilot plant for 99.999% H_2 production. As the catalyst of reformer, the Ni-Ce_2O_3-Pt-Rh catalyst supported on spherical theta-alumina of 2.4-4.0 mm in diameter was used. Loading of Ni was 6%. Loading of other components were the same as mentioned above. A reactor for the reforming was made of Inconel 800HT and has an inner diameter of 50 mm. The catalyst was packed in the reactor by 196 ml, or the catalyst-bed length was 10 cm. a city gas, A city gas A-13 (calorie-enhanced natural gas), composed of 88.71%CH_4, 5.29%C_2H_6, 3.05%C_3H_8, 2.70%C_4H_{10}, and 0.24% H_2 was added to remove the organic sulfur compounds in the city gas through the desulfurization catalyst bed. One of the typical compositions of the feed gas to the reformer was settled at 23.48%NG, 15.50%O_2, and 61.50%H_2O. The feed gas was fed to the reformer with a space velocity (SV) of 203,800 h^{-1} under 0.77 MPa, and at an entrance temperature of 407ºC. The reforming reactor was heated by an electric furnace at 800ºC for only to maintain the surrounding temperature. The order of feed-gas introduction to the to the reformer was in the order of steam, desulfurized NG and O_2. The introduction of O_2 was done while gradually increase of the concentration within ca. 10 - 20 minutes. As shown in **Figure 1,** catalyst-bed temperature of the reformer instantaneously raised to

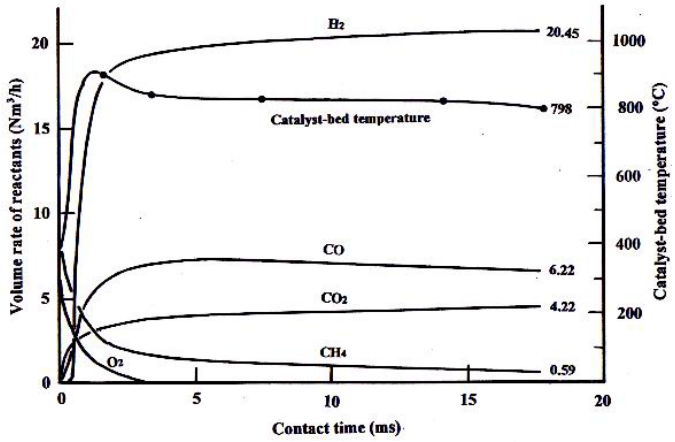

Figure 1. A time course of the reforming of NG with the thermo-neutral reaction method. Conditions are described in the text.

900 ± 28ºC at the 10 mm position from the entrance, and gradually decreased to 826 ± 17ºC at 80 mm position. The catalyst temperature was very stable within the fluctuation of ± 28ºC. Oxygen and C_2 –C_4 hydrocarbons in the NG fed were totally converted, and conversion of CH_4 was 92.8%. The formed gas was composed of 64.97% H_2, 19.76% CO, 13.40%CO_2, and 1.87% CH_4 as expressed by dry-gas basis. The space-time yield (STY) in the reformer was 4,730 mol/l/h, which is two-order magnitude larger than that in conventional reformers equipped with a heating furnace of the reactors.

The formed gas was cooled to 218ºC by passing through a couple of heat exchangers, and then it was introduced to a shift reactor to convert CO to H_2 and CO_2. The conversion of CO was 86.5%. The formed gas was introduced a pressure-swing adsorption units to separate other gases. The recovering H_2 was 90%. Thus, 99.999% purity H_2 was obtained with a flow rate of 20.0 Nm^3/h. Life test of the catalyst for continuous 914 h showed its stability.

Reforming of LPG for 1kW polymer electrolyte fuel cell.
The same catalyst used in the NG reforming was used for LPG reforming. An Inconel 800HT tubular reactor having 20 mm in inner diameter was used under atmospheric pressure condition. The catalyst was packed in the reactor by 4.1 – 78.5 ml, or catalyst-bed

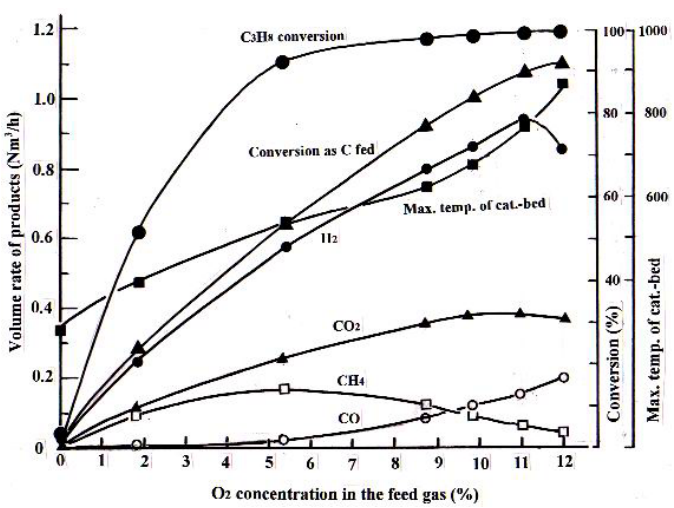

Figure 2 Dependence of O_2 concentration on the reforming of LPG

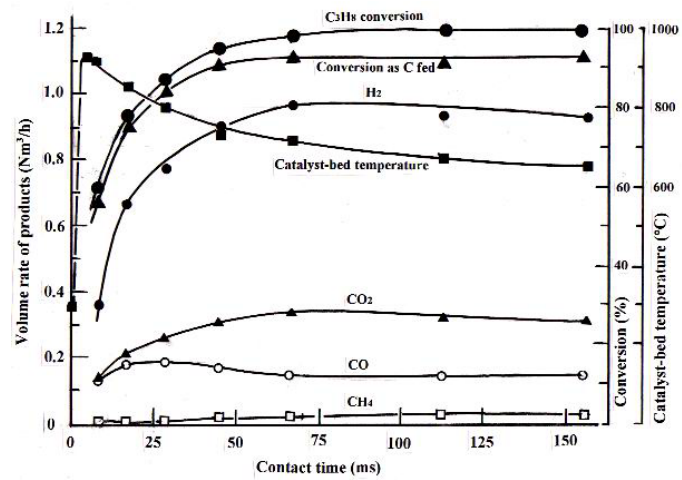

Figure 3. A time course of the reforming of LPG with the thermo-neutral reaction method. Conditions are described in the text.

length of 13 – 250 mm. Oxygen concentration in the feed gas was varied from 0 to 12.75%, with keeping the volume rates of LPG and $H_2O_{(gas)}$ at 165.6 *l*/h and 1,404 *l*/h, respectively. LPG used involves 96%C_3H_8, 2% C_2H_6, 3% C_4H_{10}, and ca.5 ppm of sulfur compounds. Dependence of O_2 concentration on the steam reforming of LPG at the catalyst volume 33.3 ml or 106 mm in packed length was shown in **Figure 2**. Space velocity was changed from 47,750 to 54,730 h^{-1} by the increase of O_2 concentration. Above 11% of O_2 concentration C_3H_8 conversion almost attained to 100%. The increase O_2 concentration enhanced while elevating catalyst-bed temperature, however, above 12% O_2, part of CO and H_2 formed were combusted and the maximum catalyst-bed temperature beyond 900 – 950 ºC, resulting the decrease in H_2 yield. With lower O_2 concentration CH_4 formed from C_3H_8 remains in the product. A time course of the reforming was presented in **Figure 3.** Compared with the case of NG reforming as shown in **Figure 1,** since absolute partial pressure of O_2 in the NG reforming was lower in LPG reforming, by ca. 1/10, due to the condition of total pressure, time course of the reactions is extended; however, essential reaction courses were the same. From the detailed reaction analyses on material balance and heat balance, precise reaction passes have been elucidated. Application to reforming of n-hexane, gasoline, and methanol will be mentioned.

Conclusions

By keeping the good balance between exothermic catalytic combustion and endothermic catalytic reforming, extra ordinary reforming rate was realized using the non-coke deposited catalyst.

Acknowledgement

The work of LP gas reforming was supported by NEDO and LPG Center under contact of a 5-years national project "Development of Fuel Cell System with Liquefied Petroleum Gas".

References

(1) Inui, T. Catalysis, Royal Soc. Chem., **2002**, 16, p.133-154.
(2) Inui, T., CO_2 Conversion and Utilization, ACS Symp. Ser. 809, Amer. Chem. Soc., Song, et. al., edits., **2002**, p. 133-154.
(3) Inui, T., *Stud. Surf. Sci. Catal.*, **1993**, 77, 17-26..
(4) Inui, T., *Appl. Organometal. Chem.* **2001**, 15, 87-94.
(5) Inui, T., Takeguchi, T., Matsuoka, I., *Current Topics in Catal.*, **1999**, 2, 73-82.

Reforming of Liquid Hydrocarbon Fuels for Micro Fuel Cells. Steam Pre-reforming of Jet Fuel over Supported Metal Catalysts

Jian Zheng, Jian-Ping Shen, Chunshan Song, Wei Pan, James Jon Strohm*

Clean Fuels and Catalysis Program, The Energy Institute and Department of Energy & Geo-Environmental Engineering, Pennsylvania State University, University Park, PA 16802
*Email: csong@psu.edu; Tel: 814-863-4466; Fax: 814-865-3248

Introduction

Fuel cell has been identified as a potential device for portable power supply because it is convenient, quiet and energy efficient. In general, all the fuel cells operate without combusting fuel and with few moving parts, and thus they are very attractive from both energy and environmental viewpoints. Inside a fuel cell there are separate reactions at the anode and the cathode, and charged ions move through the electrolyte, while electrons move round an external circuit. Fuel processing is applicable to both high-temperature fuel cells such as solid-oxide fuel cell (SOFC, operating at about 800-1000°C) and low-temperature fuel cells such as proton exchange membrane fuel cells (PEMFC, operating at about 80°C).

The strategy of fuel processing depends on the nature of fuel and type of fuel cells. The choice of liquid fuels such as jet fuel and diesel fuel as logistic fuels is an important consideration for portable fuel cells, because they are widely available and have lower volume and higher energy density.

On the other hand, the choice of fuel cells has a significant impact on the fuel processing strategies for on-board fuel pre-processor. The general status of fuel cells and fuel processing are described in a book by Larminie & Dicks[1]. The challenges and opportunities on fuel processing for fuel cell applications have been discussed in a recent review[2].

Some recent advances in laboratory research has made it possible to make a solid oxide fuel cell for direct electro-chemical oxidation of light hydrocarbons such as methane and ethane[3]. However, it is widely known that the use of heavy hydrocarbons of > C_4 can cause significant deactivation and coking problem associated with most anode catalysts for SOFC[1]. A series of work by our group has also demonstrated that JP-8 type jet fuels can easily undergo thermal decomposition to form carbonaceous solid deposits both in batch reactor[4-6] and in flow reactor[7-9] in the temperature range (400-700°C).

Therefore, one of the main problems in developing fuel pre-processor for micro-fuel cell application using liquid fuel such as JP-8 jet fuel is how to eliminate the carbon formation from higher hydrocarbons during reforming.

Our approach to solving this problem is to conduct catalytic fuel reformation in two stages with a pre-reformer (oxygen-assisted if necessary) to break-down most C_8-C_{13} hydrocarbons to C_1 to C_2 molecules plus CO and H_2, followed by steam reforming (possibly also oxygen-assisted) in main reformer to produce reformates (H_2, CO, CO_2). The present paper reports on our preliminary work on the pre-reforming of model jet fuel (also desulfurized real jet fuel in the near future) in a lab-scale reforming system. The reforming work (following pre-reforming) is reported in a companion paper at this meeting.

Experimental

Noble metals such as Rh, Ru, etc. supported on MgO and CeO_2-Al_2O_3 have been prepared and tested as catalysts. Normal dodecane ($C_{12}H_{26}$) has been used as a model jet fuel.

Reaction system. A catalyst (1.0 gram with particle size of 18~35 mesh) is placed into the middle of stainless steel reactor tube (Inconel 800H alloy, with 0.54" O.D. X 0.375" I.D. and 24" long), with the remaining tube filled with α-Al_2O_3 beads. Before introducing the fuel, the catalyst is heated up to a certain temperature (500˚C) under the hydrogen flow of 20 ml/min, which is controlled by the mass flow controller system, and kept at this temperature for two hours. Then the carrier gas is switched to nitrogen. At the same time, the pre-heater is turned up to certain temperature high enough for vaporizing of the fuel ($C_{12}H_{26}$, b.p. 216˚C) and water before entering the reactor.

To start the test, water was first introduced for 30 minutes before opening the fuel flow to ensure that there is always steam accompanying fuel flow in the reactor lines. The fuel is then introduced with one of the two HPLC pumps through the pre-heater into the reactor with a volumetric flow rate of 1.38 ml/hr. The water flow is kept at 4.02 ml/hr with a steam to carbon ratio of 3:1.

During the reaction, the liquid products are collected every hour by a liquid condenser with volume measured for the calculation of total conversion; the gas products are analyzed on-line by a multi-gas analyzer GC-TCD for the calculation of product distributions. The reactor system is pictured in **Figure 1**.

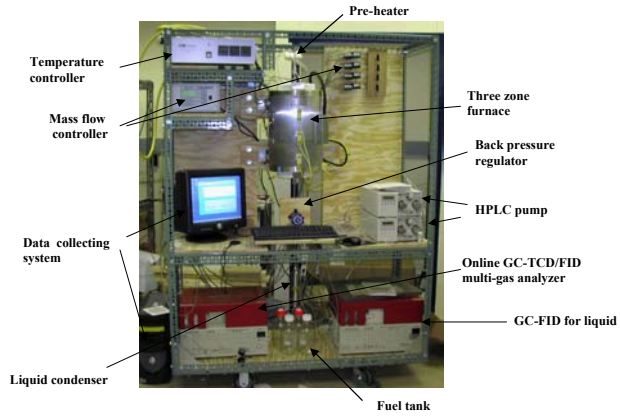

Figure 1. Schematic photo of the integrated reforming system

Results and Discussion

Based on our experience in the thermal decomposition of jet fuels[4-9], we expect that proper pre-mixing of feed fuel and steam is important for the prevention of coke formation prior to the pre-reforming.

In order to improve the pre-mixing, we added a wick material (made of quartz) into the stainless steel tube between the outlet of fuel line and the inlet of reactor (the pre-mixing zone). We then examined the effects of using wick mixer for feed introduction on carbon formation at different temperatures. Interestingly we find that, in order to prevent carbon formation in the pre-mixing zone as revealed by the color of wick, the fuel line should be kept at lower temperature (160ºC-200°C) before fuel meets steam, i.e., rather than allowing the fuel to evaporate at the wick, the steam must serve to vaporize the fuel, which also results in more homogeneous pre-mixing.

The conventional pre-reforming of natural gas or light naphtha is usually run in an adiabatic reactor, i.e., there is no external heat supply during the reaction[10]. It is therefore important for us to set up suitable temperature profiles for pre-reforming of model jet fuels using our tubular furnace as shown in **Figure 1**.

In general, higher temperature will result in higher conversion of the fuels, since the steam reforming alone is endothermic. However, there is also a risk for carbon formation. We carried out blank run by flowing n-dodecane and steam with same ratio through only α-Al_2O_3 beads without any catalyst in the reactor. It is found that if reaction temperature reaches as high as 600ºC, there is a significant amount of carbon deposition during the reaction, since the alumina beads unloaded from the pre-reformer were dark in color. This result indicates that thermal cracking of fuel can take place in the pre-reformer, leading to the formation of carbon on these beads. Therefore, in order to prevent carbon formation, the pre-reforming temperature should be below 600ºC.

Although base-metal catalysts (e.g. Ni) are of interest in terms of lower cost, our results on pre-reforming of dodecane using a commercial Al_2O_3-supported Ni (G-91 from Süd Chemie) shows that the initial conversion is only around 57% at 550˚C, yet rapid deactivation was observed and the reaction has to be stopped due to serious carbon formation (tube fouling) after a few hours. Subsequently, we prepared noble-metal catalysts in order to identify more active and stable catalysts for micro-fuel processor.

Figure 2 shows the pre-reforming results of n-dodecane on 1% Rh/MgO at 500˚C. It can be seen that the initial activity is very high (almost total conversion), however, it gradually deactivates with time on stream. An addition of certain amount of O_2 can recover the activity, but due to the co-existence of combustion reaction, the H_2 yield is reduced.

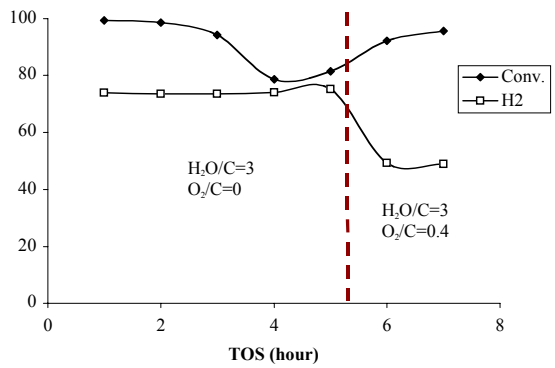

Figure 2. Pre-reforming of dodecane at 500˚C on 1% Rh/MgO catalyst (steam/carbon ratio=3, GHSV=3200h^{-1}) with or without the presence of O_2 (O_2/carbon ratio=0.4)

By increasing the amount of metal loading from 1 wt% to 2 wt% for Rh, we achieved a more effective pre-reforming of n-dodecane at 485˚C, as seen in **Figure 3**. It is clear that the 2% Rh/MgO shows a more stable activity for pre-reforming of the model jet fuel for 10 hours.

Figure 4 shows the TPO-IR spectrum of the used 2% Rh/MgO after pre-reforming of dodecane at the conditions described above for 10 hours. There are a few peaks shown in the TPO-IR temperature ranges of <400˚C, which can be attributed to the desorption of CO_2 previously adsorbed on the used catalyst. There is almost no peak appearing in the range of 400˚C-600˚C that may be attributed to filament carbon, indicating no significant carbon formation on the laboratory-prepared supported 2% Rh/MgO catalyst.

Conclusions

Proper pre-mixing of feed liquid fuels and steam has been found to be important for the prevention of coke formation prior to pre-reforming. As compared with commercial Ni supported Al_2O_3

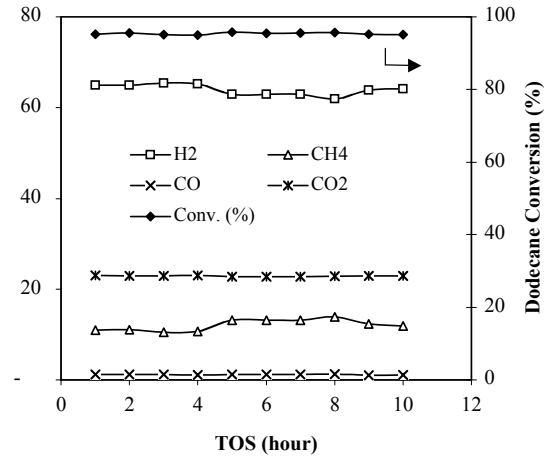

Figure 3. Pre-reforming of dodecane on 2% Rh/MgO catalyst (steam/carbon ratio=3, GHSV=3200h^{-1}) at 485˚C, atm.

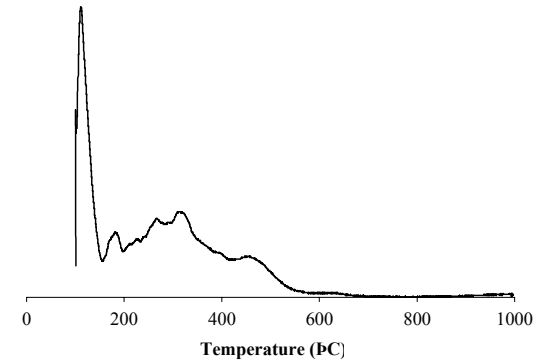

Figure 4. TPO-IR results of used 2% Rh/MgO catalyst after pre-reforming of dodecane at 485˚C for 10 hours.

catalyst, supported rhodium catalysts show not only very high activity but also high resistance to deactivation due to carbon formation. The reformates from the current pre-reformer contain little or no higher hydrocarbons, besides significant amount of CH_4, which can be further converted to H_2 and CO by subsequent reforming.

Acknowledgement. We are grateful to the Palm Power Program of DARPA/DoD for supporting this work. We also wish to thank Dr. Mehdi Namazian of Altex Technologies Inc. for helpful discussions on the pre-mixing. Thanks also go to Mr. Ronald Copenhaver of PSU for help in setting up the reactor system.

References

(1) Larminie, J.; Dicks, A. In *Fuel cell Systems Explained;* John Wiley: New York, **2000**, pp.308.
(2) Song, C. *Catalysis Today*, **2002**,77, 17-49.
(3) Park, S. D.; Vohs, J.M.; Gorte, R.J. *Nature*, **2000**, *404 (6775),* 265-267.
(4) Song C.; Eser, S.; Schobert, H.H.; Hatcher, P.G. *Energy & Fuels*, **1993**, *7 (2),* 234-243
(5) Song, C.; Lai, W.C.; Schobert, H.H. *Ind. Eng. Chem. Res.* **1994**, *33 (3)*, 548-557.
(6) Lai, W.C.; Song, C. *Fuel. Proc. Technol.*, **1996**, *48 (1)*, 1-27.
(7) Andrésen, J. M.; Strohm, J.J.; Coleman, M.M.; Song, C. *Prepr. Pap. - Am. Chem. Soc., Div. Petrol. Chem.*, **2000**, *45 (3)*, 454-458.
(8) Andrésen, J. M.; Strohm, J.J.; Song, C.S. *Prepr. Pap. - Am. Chem. Soc., Div. Petrol. Chem.*, **1999**, *44 (3)*, 562-566.
(9) Strohm, J.J.; Andrésen, J. M.; Song, C. *Prepr. Pap. - Am. Chem. Soc., Div. Petrol. Chem.*, **2000**, *45 (3)*, 465-469.
(10) Christensen, T.S. *Appl. Catal. A: Gen.*, **1996**, *138*, 285-309.

METHANOL AUTOTHERMAL REFORMING OVER OXIDE SUPPORTED NOBLE METAL CATALYSTS

Easwar S. Ranganathan, Shyamal K. Bej, and Levi T. Thompson

Department of Chemical Engineering
University of Michigan
2300 Hayward Ave.
Ann Arbor, MI 48109

Introduction

The apparently conflicting demands of high performance and environmental protection, in the design of vehicles, can be overcome by using fuel cells to generate electricity on-board. This concept would obviate the Carnot efficiency limitation faced by internal combustion engines, thus increasing the overall well to wheel fuel efficiency. Unfortunately, progress in producing hydrogen on-board is not matched by the advanced development of fuel cells.

Methanol steam reforming (SR) and autothermal reforming (ATR) are gaining interest for use in generating hydrogen for portable and automobile fuel cells.[1] Methanol has several advantages over other candidate fuels. It is easier to transport than methane and other gaseous fuels, does not require desulfurization like present gasoline and diesel formulations, can be reformed at much lower temperatures (200-400 °C) than other hydrocarbons, and has a high energy density. Methanol SR is an endothermic reaction requiring external heating resulting in long start up times and poor transient responses, characteristics that are not desirable for most applications.[2] Autothermal reforming combines endothermic steam reforming and exothermic partial oxidation to produce a near zero reaction enthalpy. The feed methanol/oxygen ratio can be varied to achieve the desired start-up times. For vehicular applications, the catalyst must have good activity at low temperatures to light off the reaction and it should also be stable at high temperatures to maintain the activity. In this paper, we report methanol ATR rates for a series of reducible oxide supported noble metal catalysts.

Experimental

Several oxide supported noble metal based catalysts were prepared. The oxide supports included ZnO, CeO_2, ZrO_2, ZnO-ZrO_2, ZnO-CeO_2, TiO_2, and ZnO-TiO_2. In addition to the monometallic catalysts, several bimetallic catalysts containing Pd, Cu and Pt were prepared. All of the catalysts were prepared using a wet impregnation method that is described elsewhere.[3] The ATR activities were measured at 185-230 °C. In-depth activity measurements included testing the catalyst in the temperature range of 110-330 ^oC and atmospheric pressure with varying methanol to water ratios and varying oxygen to methanol ratios.

Reaction rate measurements were performed in a continuous flow system with a 4 mm ID quartz U-tube reactor, using 25-35 mg of catalyst diluted with 30-35 mg of inert silica. The catalyst bed was held between quartz glass wool plugs. The temperature of the reactor was maintained using a controller which powers an electric furnace. The thermocouple was placed 1 mm into the catalytic bed. The combined methanol-water mixture was fed using a HPLC pump at a rate of 1.8 ml/h and then preheated in a vaporizer. The air and nitrogen (diluent) flow rates were adjusted using mass flow controllers. The total flow was 100 ml(STP)/min, with a methanol molar concentration of 11.6% and oxygen to methanol ratios in the range of 0 to 0.5. The water to methanol molar ratio was varied in the range of 0 to 3. Experiments excluding water correspond to methanol decomposition or methanol partial oxidation, depending upon whether or not oxygen was added. The samples were reduced *in situ* in a 4% H_2/N_2 stream at 200-400 ^oC. The exact reduction temperatures were determined by temperature programmed reduction (TPR). Analysis of the reactor effluents was performed using an on-line gas chromatograph (HP 5890) with a thermal conductivity detector and Carboxen 1000 column, using argon as the carrier gas.

Reaction runs for the commercial Cu-Zn-Al_2O_3 were performed to benchmark rates for the noble metal based catalysts.

Results and Discussion

For SR, the commercial Cu-Zn-Al_2O_3 catalyst out-performed the noble metal catalysts at all temperatures tested as shown in **Figure 1**. For ATR, the Cu-Zn-Al_2O_3 and 2% Cu/ZnO catalysts did not light-off until approximately 200 °C, therefore they were significantly less active than the noble metal catalysts below this temperature. Some of the noble metal catalysts were active for ATR at temperatures as low as 110 °C.

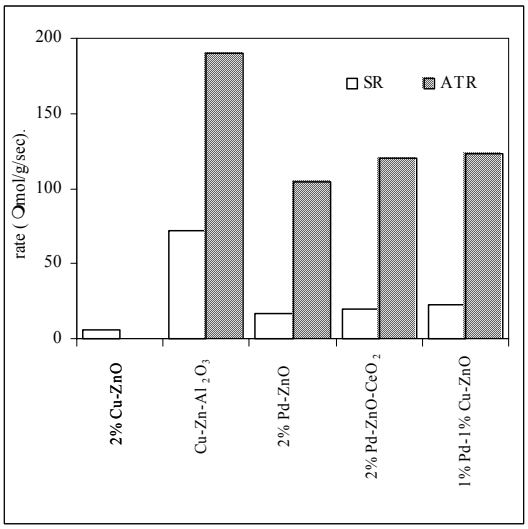

Figure 1. Methanol conversion rate during steam reforming and autothermal reforming for various catalysts at 230 ^oC; MeOH:H_2O = 1:1, O_2:H_2O = 0.2:1(ATR)

We observed some evidence of synergy between Pd and Cu when supported on ZnO. The 1%Pd-1%Cu/ZnO catalyst was significantly more active than either the 2% Pd/ZnO or 2% Cu/ZnO catalysts as indicated by **Figure 2**. A mechanical mixture of 2% Pd/ZnO and commercial Cu-Zn-Al_2O_3 catalyst gave rates similar to those for the 1%Pd-1%Cu/ZnO for ATR at 185 °C. Similar activities were achieved when 2% Pd was impregnated onto the commercial Cu-Zn-Al_2O_3 catalyst suggesting that Pd helps light-off the Cu sites at lower temperatures. The CeO_2 supported catalysts were also highly active for methanol SR and ATR, however, these materials typically had low CO_2 selectivities. The CeO_2-ZnO mixed oxide supported catalysts had low CO_2 selectivities.

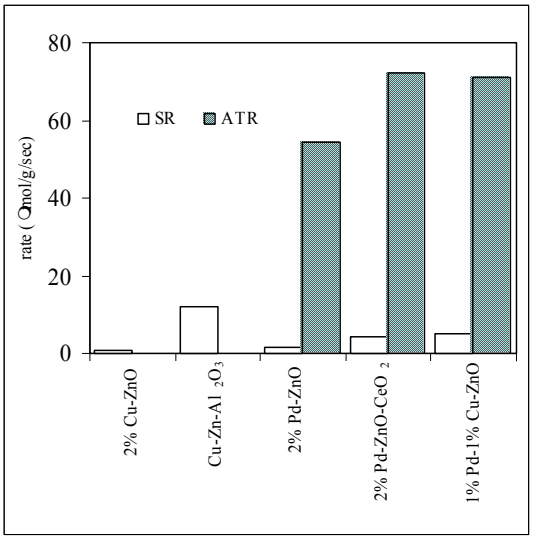

Figure 2. Methanol conversion rate during steam reforming and autothermal reforming for various catalysts at 185 °C; MeOH:H_2O = 1:1, O_2:H_2O = 0.2:1(ATR)

The noble metal-based and commercial Cu-Zn-Al_2O_3 catalysts were evaluated for SR and ATR at 330 °C. Reaction temperatures in this range would allow these catalysts to be used in combination with membrane reactors. The Pd/ZnO catalysts were very active and possessed good thermal stabilities at this temperature as shown in **Figure 3**. The Cu-Zn-Al_2O_3 catalyst was initially very active but deactivated rapidly due to thermal sintering. We also observed that the fresh catalysts (prior to reduction) were active for both methanol SR and ATR, though the activity was slightly lower as shown in **Figure 4**.

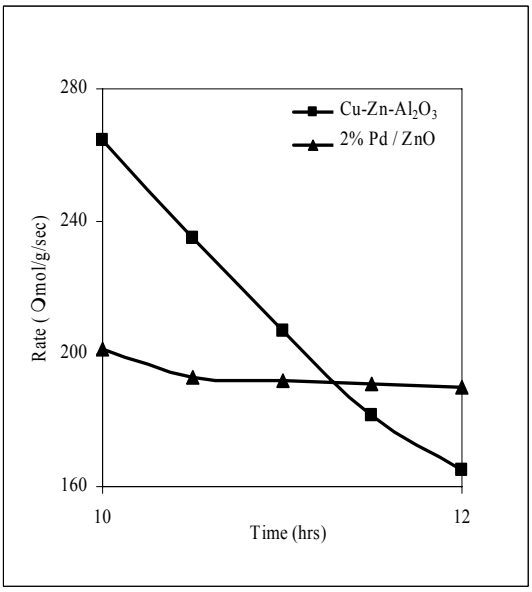

Figure 3. Comparison of steam reforming activities of commercial Cu-Zn-Al_2O_3 and 2% Pd / ZnO at 330°C; MeOH:H_2O = 1:1.

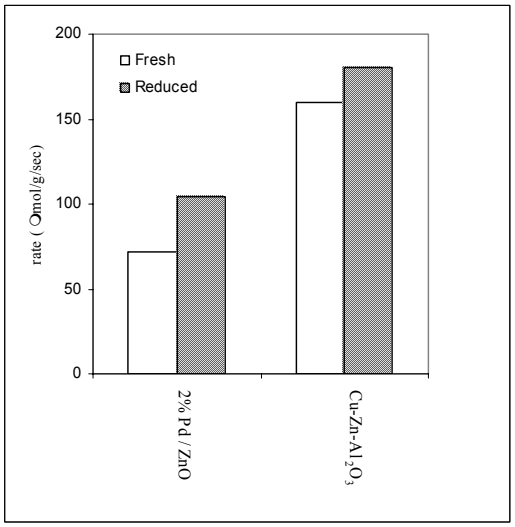

Figure 4. Comparison of autothermal reforming activities of reduced and fresh catalysts at 230°C; MeOH:H_2O = 1:1, O_2:H_2O = 0.2:1

Conclusions

Our preliminary results indicated that the ZnO supported Cu-Pd bimetallic catalyst was highly active for methanol autothermal reforming, in particular at low temperatures. This will assist in lighting off of the ATR reactor at lower temperatures. Currently, we are investigating the effect of Pt as well as the effect of other mixed oxides on the methanol ATR activity and selectivity.

Acknowledgement.

This work was funded by the U.S. Department of Energy.

References

(1) D.L. Trimm.; Z.I. Onsan, *Catal. Lett.* **2001**, 43(1&2), 31.
(2) M. Schuessler.; O. Lamla.; T. Stefanovski.; C. Klein.; D. Megede., *Chem. Eng. Technol.*, **2001**, 24, 1141.
(3) N. Iwasa.; S. Masuda.; N. Ogawa.; N. Takezawa., *Appl. Catal. A: Gen.*, **1995**, 125, 145.

Hydrogen-butane separation through MFI-type zeolite membrane grown by a secondary growth method

Masahiko Matsukata, Hikokazu Akimoto, Yasushi Sekine and Eiichi Kikuchi

Department of Applied Chemistry
Waseda University
3-4-1 Okubo
Shinjyuku-ku
Tokyo, 169-8555, Japan

Introduction

Zeolite is an inorganic membrane material which has heat resistance, chemical resistance, durability, mechanical strength, and selective adsorption properties. Zeolite membrane attracts attention as an inorganic membrane with which separation on a molecular level is possible.

The secondary growth method is a method of growing up seed crystals secondarily and obtaining a compact membrane. In order to obtain a compact membrane, it is necessary to control a mount of and a density of seed crystals on a surface of support. But, researches that are focused on seeding conditions are few.

In this study, the conditions which can synthesize a compact membrane were established and the influence of the seeding conditions on membrane properties was examined. The membrane structure and its permeation properties were examined. In the present study, a dip coating method was used for seeding the surface of a porous alumina support. The effect of the seed concentration in a suspension and the speed of the suspension on membrane property were focused on.

Experimental

Membrane preparation. Silicalite-1 seeds approximately 100 nm in size were hydrothermally synthesized. A mixture with a molar composition of TPAOH (tetrapropylammonium hydroxide): SiO_2:H_2O:NaOH = 2.4 : 10 : 110 : 1.0 was prepared and crystallized[1] at 408 K for 4 h. In order to obtain seed particles with a uniform size, seeds in a suspension was separated by using a centrifuge. The seed concentration in a suspension and the speed of the suspension were changed in the ranges of 3-107 g/l, and 0.08-3.0 cm/s, respectively. Seeding an α-alumina tubular support with the average pore size of the outer top layer of 0.1μm and 3 cm long was performed by a dip coating method. A clear solution with the composition of TPAOH:SiO_2:H_2O=3:25:1500 was prepared[2]. The seeded support was immersed in the clear solution and crystallized at 448 K for 24 h. As-synthesized MFI-type zeolite membranes were calcined in air at 798 K for 5 h.

Characterization. Support surfaces before and after the seeding were observed by field emission scanning electron microscopy (FE-SEM). The structure of product was analyzed by X-ray diffraction (XRD) with Cu Kα radiation. The morphology of product was examined by scanning electron microscopy (SEM). For evaluating the compactness of all MFI-type zeolite membranes, N_2 single gas permeation was carried out at 423 K. The separation properties of membrane were tested by using binary gas mixtures, H_2/iso-butane(i-C_4) and H_2/n-butane(n-C_4), at 423-673 K. Before starting the binary gas mixtures tests, distilled water was charged into both feed and permeate sides of membrane. The membrane was then dried in air for 30 min.

Results and Discussion

Figure 1 shows the relation between the seed crystal concentration and the compactness of membrane prepared. Figure 2 gives the effect of the speed of the suspension on the compactness of membranes. The compactness of membrane was evaluated by the N_2 single gas permeation. Figures 1 and 2 led us to a conclusion that seeding conditions significantly influenced the permeation property. When the seeding was performed with a seed concentration of 22 g/l or above and a speed of the suspension of 0.5 cm/s or above, the membranes became compact.

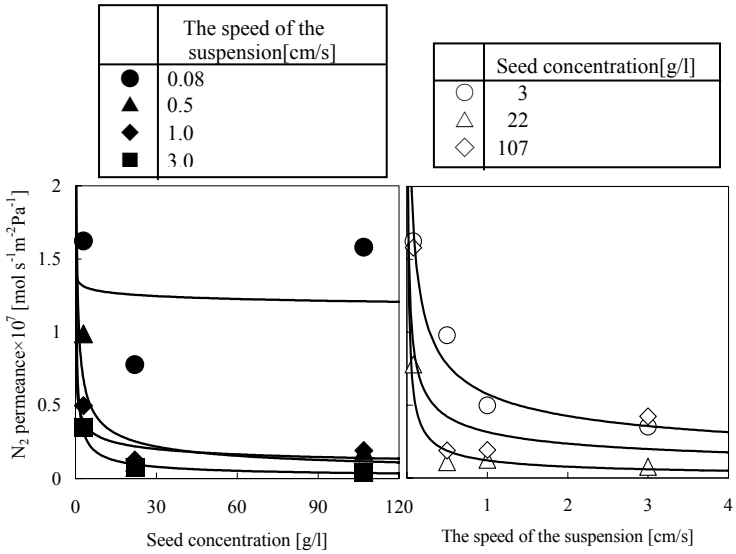

Figure 1. Relation between seed concentration and N_2 permeance.

Figure 2. Relation between the speed of suspension and N_2 permeance.

The seed crystals attached on the surface of support were observed. Figure 3 gives a typical FE-SEM image of the seeded support. In the cases of seeding performed under the conditions determined above, a sufficient amount of seed crystals was densely loaded on the support surface, as shown in Fig. 3. Such seeds could grew up secondarily during crystallization, resulting in the formation of compact membrane.

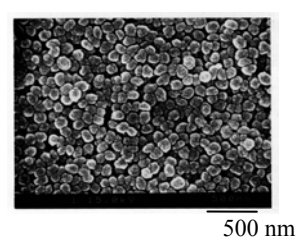

Figure 3. Typical FE-SEM image for the top view of seeded support (seed concentration : 22 g/l, speed of the suspension : 3.0 cm/s).

The formation of MFI-type zeolite on the porous alumina support was confirmed by using XRD, as shown in Figure 5. Irrespective of the compactness of membrane, the (002) plane of MFI-type zeolite was oriented in parallel with the surface of support, that is, its c-axis was grown vertically against the support surface, as

often observed in literature[1,2]. The top surfaces and the cross sections of membranes prepared under different seeding conditions were observed by using SEM. A typical SEM image of MFI-type zeolite membrane is shown in Figure 4. The structure of all the membranes observed was quite similar. As described above, it was difficult observe obvious structural and morphological differences between compact and incompact membranes.

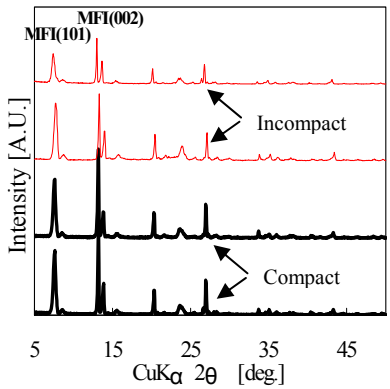

Figure 4. XRD patterns for MFI-type zeolite membranes.

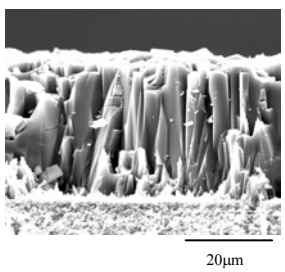

Figure 5. SEM images of the cross-section of MFI-type zeolite membrane (seed concentration : 22 g/l, speed of the suspension : 1.0 cm/s).

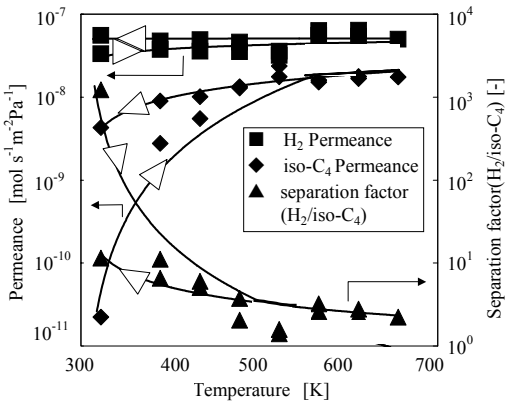

Figure 6. Temperature dependence of the permeances of H_2 and i-C_4 in the binary (50:50) mixture permeation.

The separation properties of the most compact membrane were evaluated. Figure 6 shows the permeation results of a binary 50:50 gas mixture, H_2/iso-C_4. The permeation test was started at 303 K after the water treatment of membrane. The temperature was raised up to 673 K and then fell to 303 K. The permeances of H_2 and i-C_4 were measured after the permeation reached a steady-state at each temperature. The maximum of separation factor as high as 1,200 was observed at 323 K before raising temperature. It is considered that water adsorbed in the membrane blocked i-C_4 permeation. The separation factor decreased with increasing temperature because the permeance of i-C_4 markedly increased with temperature. During cooling, the H_2 and i-C_4 permeances were greater than those observed during heating. The difference in the permeances measured during heating and cooling the membrane would be caused by the desorption of water adsorbed in advance. The permeation of i-C_4 was strongly hindered by the adsorbed water in comparison with H_2 permeation.

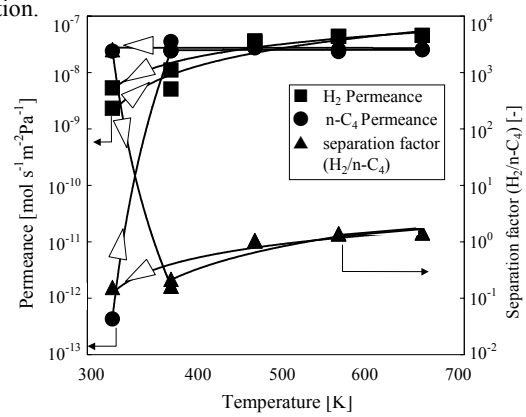

Figure 7. Temperature dependence of the permeances of H_2 and iso-C_4 for mixture.

The binary gas mixture of H_2/n-C_4 was also used for evaluating the separation properties of membrane. The experimental procedure was the same as that for the H_2/n-C_4 permeation test. The results were shown in Figure 7. Similarly to the case of H_2/i-C_4 permeation, the maximum of separation factor of 2,500 was observed at 323 K before raising temperature. It is suggested that the water adsorbed in the membrane also blocked n-C_4 permeation. It is worth noting that upon heating to 373 K the separation factor became less than unity and such a n-C_4 selectivity was held at 323 K after the removal of water. We presume that n-C_4 is strongly adsorbed in the micropore of MFI-type zeolite and thus hinder the H_2 permeation at lower temperature while micropore blockage with n-C_4 was interfered with water.

Conclusions

In the present study, seeding conditions were successfully optimized to prepare a compact MFI-type membrane by the secondary growth method. In the permeation tests of the binary gas mixtures of H_2/i-C_4 and H_2/n-C_4, both i- and n-C_4 permeation was remarkably decreased by the adsorption of water in the membrane, resulting in very high separation factors exceeding 10^3 at 323 K. After the removal of adsorbed water, the membrane was H_2 selective in the H_2/i-C_4 mixture and n-C_4 selective in the H_2/n-C_4 mixture.

References

1. M. C. Lavollo, M. Tsapatsis, *AIChE J.* , 42, 3020, **1996**
2. G. Xomeritakis, S. Nair, M. Tsapatsis, *Micropor. Mesopor. Mater.* , 38, 63, **2000**

CHARACTERIZATION OF SULFONATED CATION-EXCHANGE MEMBRANES MODIFIED WITH POLYANILINE

Sophie Tan, Alexis Laforgue, and Daniel Bélanger

Département de Chimie, Université du Québec à Montréal, C.P. 8888, Succursale Centre-Ville, Montréal (QC) H3C 3P8

Introduction

Different types of membrane surface modifications have been studied in order to obtain selective transport of molecules or ions. For example, membrane surfaces were modified to improve membrane filtration performance,[1] biocompatibility,[2] membrane selectivity for specific proteins,[3] for protons versus solvent[4] or other ions.[5-8]

For some of these applications, a recent approach consisted in the formation of a composite membrane based on a commercially available ion-exchange membrane and electronically conducting polymers such as polypyrrole[5] and polyaniline.[6-8]

In this study, commercial cation-exchange membranes bearing sulfonate groups are modified on a single side by chemical polymerization of aniline. The composite membranes prepared under different polymerization parameters are characterized by several techniques including X-ray photoelectron spectroscopy (XPS), scanning-electron microscopy, cyclic voltammetry and exchange-capacity measurements. Their permselectivity is evaluated by electrodialysis (ED) in acidic media.

Experimental

Materials and Chemicals. Neosepta® CMX membranes were stored in 0.5 M NaCl prior to modification. $(NH_4)_2S_2O_8$, HCl, HNO_3, NaCl, H_2SO_4, $ZnSO_4{\cdot}7H_2O$ and $CuSO_4{\cdot}5H_2O$ were of A.C.S. reagent grade and used as received. Aniline was distilled twice or until a colorless monomer is obtained prior its to use. Millipore water (18 MΩ) was used for the preparation of all solutions.

Modification of cation-exchange membranes. Single-side modifications were done in a two-compartment cell containing the reagents in one compartment and water in the other. The chemical polymerization was performed in two steps: 1) protons within the membranes are exchanged with charged aniline (10 % aniline in 1 M HCl solution) and 2) polymerization is induced by chemical oxidation with ammonium peroxodisulfate, $(NH_4)_2S_2O_8$.

X-ray photoelectron spectroscopy. After conditioning the membranes in 1 M HCl and drying these membranes under vacuum at room temperature, XPS analyses were performed using a VG Escalab 220i-XL system equipped with an hemispherical analyzer and an Al anode (Kα X-rays at 1486.6 eV) used at 10 kV and 15 mA. The data were recorded at room temperature and at a pressure below 10^{-8} Torr.

Electrodialysis experiments. Electrodialysis was performed in a two-compartment cell which contained, in the anodic compartment, 15 g/L of $ZnSO_4{\cdot}7H_2O$ or $CuSO_4{\cdot}5H_2O$ in 0.5 M H_2SO_4 and in the cathodic compartment, 0.5 M H_2SO_4. A current density of 100 mA/cm^2 was applied between two platinum plates for 3 hours. The surface of the membrane exposed to the solutions is 5.1 cm^2.

Results and Discussion

Using various modification parameters, we have obtained two main types of CMX-PANI composite membranes. The XPS survey spectra of these two types of composite membranes along with the spectrum of the unmodified CMX are given in Figure 1. The XPS spectrum of the bare CMX membrane exhibits the following characteristic peaks: O1s at 531 eV, S2s at 228 eV and S2p at 169 eV from the sulfonate (SO_3^-) groups, Cl2s at 271 eV and Cl2p at 200 eV attributed to the poly(vinyl chloride) (PVC) support. The peak at 400 eV indicates the presence of a small amount of nitrogen at the surface of the unmodified CMX membrane. When a PANI layer covers the surface of the membrane, the peaks attributed to PVC and sulfonate groups nearly disappear and are replaced by an enhancement of the nitrogen peak, confirming the presence of polyaniline on the surface of the membrane. It should be recalled here that XPS analysis only allow measurements down to 5-10 nm depth which explains the disappearance of the peaks attributed to the bare CMX membrane upon coverage with PANI chains. The top XPS spectrum shows an intermediate case between the first two spectra where there is still nitrogen attributed to PANI as well as chlorine and sulfur attributed to PVC and the sulfonate groups of the basal membrane.

Hence, the first type of CMX-PANI composite membranes can be described as a three-section membrane:[8] 1) an outermost layer consisting of PANI chains doped with chloride ions 2) an intermediate layer in which PANI chains are doped with sulfonate groups present on the bare membrane and 3) the bulk of the CMX membrane. The second type of composite membranes is obtained under longer polymerization times and at higher concentration of oxidant. In this case, the outermost layer of PANI is almost completely degraded and we believe that more PANI chains and/or oligomers are found within the membrane. Indeed, less nitrogen is found at the surface by XPS, and exchange capacity results demonstrate the presence of a larger PANI content inside the membrane. Therefore, for this second type of CMX-PANI membranes, most of the PANI chains and/or oligomers are found within the bulk of the membrane.

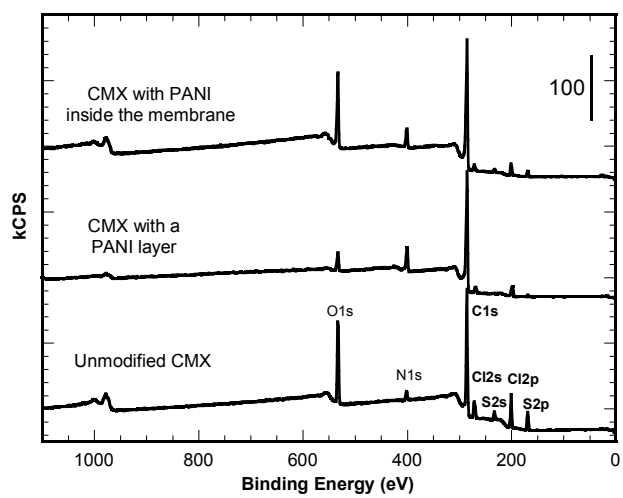

Figure 1. XPS survey spectra of an unmodified CMX membrane, a CMX-PANI composite membrane with PANI at the surface, and a CMX-PANI composite membrane with PANI within the membrane.

In addition, these two types of composite membrane show different permselectivity behaviors. Figure 2 compares metal leakage after electrodialysis in acidic medium for the unmodified CMX, CMX-PANI (type 1) and CMX-PANI with a degraded layer (type 2). It is demonstrated that the presence of a PANI layer on a CMX membrane decreases the Zn^{2+} and Cu^{2+} transport from about

10% to less than 0.5%. However, when the PANI found on the surface is degraded, the permselectivity of the composite membrane for protons decreases significantly with a metal leakage increasing back to 7.4% and 8.6% for Cu^{2+} and Zn^{2+}, respectively. These results suggest that in order to obtain good permselectivity behaviors for protons against bivalent cations in acidic solution, a good PANI surface coverage is required. Nevertheless, the CMX-PANI composite membrane that possesses a higher PANI content within the membrane can be studied for its blocking behavior towards other types of reagents or solvents such as methanol for methanol fuel cells.

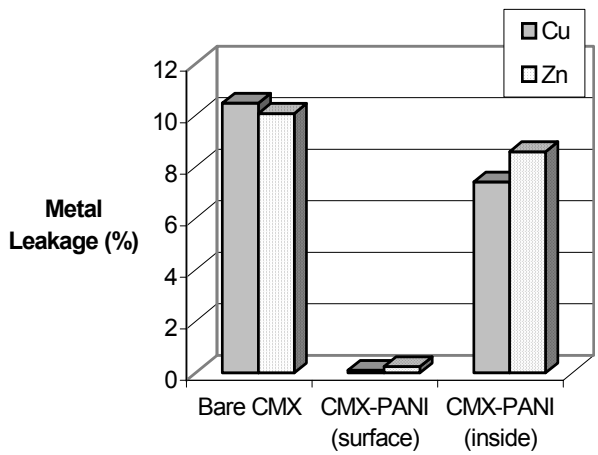

Figure 2. Metal leakage after a 3 h electrodialysis at 100 mA/cm^2 using a bare CMX, and CMX-PANI membranes (with PANI found on the surface and inside the CMX membrane).

Conclusions

We have demonstrated that two main classes of CMX-PANI composite membranes can be prepared under different polymerization times. These two type of membranes are distinguished by the location of the PANI chains or oligomers at the surface or inside the CMX membrane and exhibit very different permeability properties.

To improve our understanding of the structural effect of PANI composite membranes on the permselectivity behavior, the polymerization of aniline will also be studied on Nafion.

Acknowledgments. This research was funded by the Natural Science and Engineering Research Council of Canada through a strategic grant (234959-00) and an equipment grant for an XPS spectrometer (to D.B. and nine others. S.T. acknowledges the "Fonds Québécois de Recherche sur la Nature et les Technologies" for a graduate student fellowship. The financial contribution of UQAM is also acknowledged.

References

(1) Ma, H.M.; Nielsen, D.R.; Bowman, C.N.; Davis, R.H. *Separation Science and Technology*, **2001**, *36*, 1557.
(2) Song, Y.Q.; Sheng, J.; Wei, M.; Yuan, X.B. *J. Appl. Polym. Sc.*, **2000**, *78*, 979.
(3) Li, R.H.; Barbari, T.A. *J. Membr. Sci*., **1994**, *88*, 115.
(4) Easton, E.B.; Pickup, P.G. *Electrochem. and Solid-State Lett.*, **2000**, *3*, 359.
(5) Sata, T; Sata, T.; Yang, W., *J. Membr. Sci.*, **2002**, *206*, 31.
(6) Sata, T.; Ishii, Y.; Kawamura, K.; Matsusaki, K. *J. Electrochem. Soc.* **1999**, *146*, 585.
(7) Tan, S; Laforgue, A.; Bélanger, D., *Electrochem. and Solid-State Lett.*, **2002**, *5*, E55.
(8) Tan, S; Laforgue, A.; Bélanger, D. *Langmuir*, **2003**, in press.

PHASE CHANGE OF $SrCo_{0.5}FeO_X$ OXIDE ION CONDUCTOR IN REDUCING AND OXIDIZING ATMOSPHERE

Rajesh Sharma[1], David Caldwell[2], David A. Lindquist[2], Caner U. Yurteri[1], and Malay K Mazumder[1]

[1]Department of Applied Science
[2]Department of Chemistry
University of Arkansas at Little Rock
Little Rock, AR 72204

Introduction

Ceramic membranes exhibiting both electronic as well as ionic conductivity have generated a significant interest due to their potential applications in high temperature electrochemical devices such as electrodes in solid oxide fuel cell (SOFC) and oxygen separation membranes. Mixed conducting perovskite oxides such as La-Sr-Co-Fe (LSCFO) were extensively studied followed by their discovery by Teroaka et al (1,2). Further Balachandran et al (3) showed that Sr-Fe-Co oxides (SFCO) not only have high ionic and electronic conductivity, but also have structural stability. Extruded tubes of these materials have successfully operated in methane conversion reactors at 850°C for more than 1000 hrs (4). Most of these materials have been studied for their oxygen permeation properties as well as structural stability in oxidizing and reducing atmospheres (5,6). But a limited work has been reported on the effect of microstructure on electrochemical properties of these materials. Zhang et al (7) commented on the effect of surface microstructure on oxygen permeation flux of LSFCO and SFCO. They found out that the microstructure of SFCO exhibited good stability at elevated temperature for as long as 7 days. Since surface exchange kinetics is equally important to bulk diffusion in oxygen permeation through these membranes, the effect of high temperatures on surface microstructure of reducing side of the membranes is of significant interest. In this work we report on the effect of reducing conditions at elevated temperature on the microstructure of Sr-Fe-Co membranes, which simulates the oxygen lean side of the membranes in oxygen permeation reactor. We also report some preliminary results on the reversibility of the effects caused by reducing conditions.

Experimental

SFCO samples were synthesized using solid-state reaction method. Appropriate amounts of $SrCO_3$, $Co(NO_3)_2$. $6H_2O$ and Fe_2O_3 were mixed in isopropanol and ball milled using WC media for 24 hrs. The mixture was dried to remove isopropanol. The powder obtained was ground followed by calcination at 850°C for 8 hrs. The heating and cooling rates were 5°C/min. The calcined powder was ground and mixed with the binder. The binder was comprised of 2 wt% Butavar® B-98 as binder and 0.5 wt% stearic acid as plasticizer dissolved in isopropanol. The mixture with binder system was allowed to dry off isopropanol. This powder was again ground and used for pressing pellets. The resulting powder was then pressed into 13-mm diameter disks by applying a uniaxial pressure of 675 Mpa. These green disks were then sintered at 1250°C for 8 hrs. The heating and cooling rates were 2°C/min.

These pellets were exposed to a reducing atmosphere at 850°C. Two sets of samples were taken out after 24, 48, 72, 96 and 168 hrs of exposure. One set of these samples was observed under scanning electron microscope (Aspex personal SEM 2000). The SEM pictures were used to calculate average grain size using linear intercept method. Another set of the samples was used for X-ray diffraction (XRD) analysis. X-ray patterns for these membranes were obtained using a Rigaku Geigerflex X-ray generator equipped with a theta – theta goniometer and sample rotator (step size 0.05° 2θ, 1 second per step, range 10° to 75° 2θ).

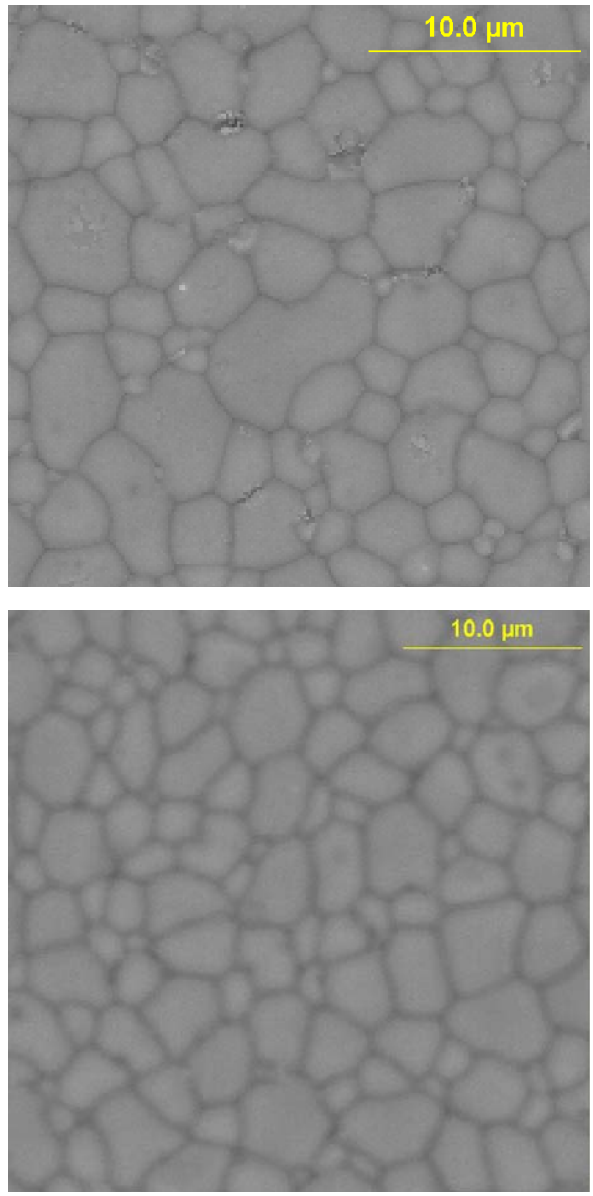

Figure 1. SEM micrograph of membrane surface before (upper plate) and after reduction (lower plate).

To study the reversibility of this composition, the powder was exposed to reducing atmosphere at 850°C. The powder was heated in oxidizing conditions at 850°C and samples were taken after 1, 2, 5, 10 and 30 minutes. These samples were used for generating X-ray patterns.

Results and Discussion

The SEM images of the membrane surfaces show little changes in surface microstructure when exposed to reducing atmosphere at elevated temperature. Figure 1 shows the microstructure of the unmodified and reduced membrane surface. A bimodal grain size distribution is observed for all these images. Although there was no significant change in average grain size, the grain boundaries of reduced surface are coarser than unmodified surface. Probably this

reflects the poor integrity of the membranes during prolonged exposure to reducing conditions in oxygen permeation reactors. The membranes were exposed to reducing atmosphere for different durations up to 168 hrs, but there was no significant change in average grain size. Figure 2 shows the phase behavior of SFCO. The material was cubic perovskite in it original state. When exposed to reducing conditions at 850°C the cubic phase transformed into an oxygen-vacancy-ordered phase.

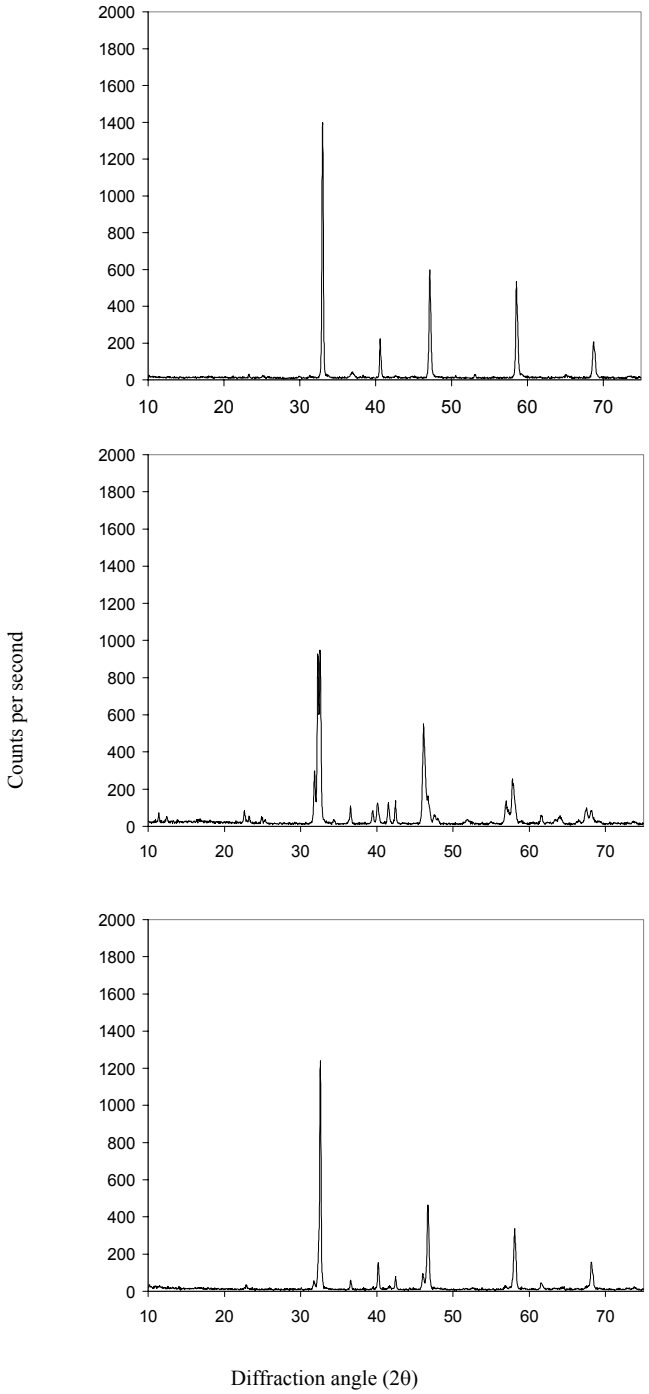

Figure 2. XRD patterns of original SFCO membrane surface (upper plate), after reduction (middle plate) and after oxidation of reduced surface (lower plate).

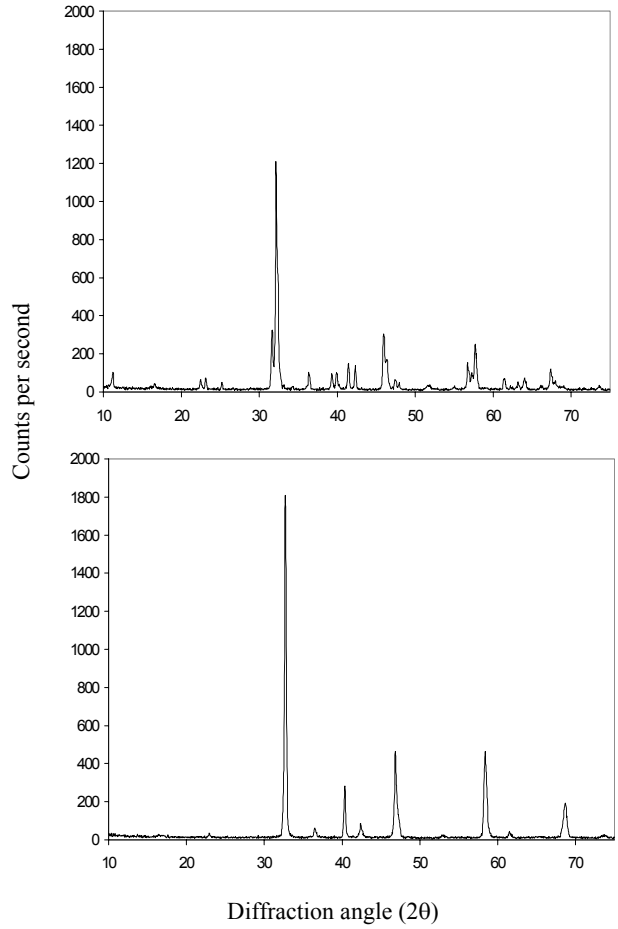

Figure 3. XRD patterns of SFCO powder sample reduced for 24 hrs (upper plate) and after 2-minute oxidation (lower plate).

XRD patterns show new reflections were formed for every characteristic peak of the cubic phase perovskite. Similar patterns were observed when the material was exposed to reducing conditions for various durations between 24 and 168 hrs. When this reduced material was oxidized at 850°C, it reverted back to the original cubic perovskite phase. This reversibility of the membrane surface crystal structure could play an important role in increasing the life span of these membranes.

Another set of experiments was performed to determine the kinetics of oxidation. SFCO membranes were crushed and the powder obtained was reduced at 850°C for 24 hrs. This powder was then oxidized 850°C for different durations between 1 and 30 minutes. Figure 3 shows the XRD patterns of powder, which was reduced and then oxidized. It was observed that there was no change in XRD patterns of the powder, which was oxidized for 1 minute. But XRD patterns of the powder that was oxidized for 2 minutes show that the crystal structure reverts back to its original state. There were no more changes in the XRD patterns with further oxidation.

Conclusions

SEM micrographs of SFCO membranes, exposed to reducing conditions at elevated temperature, show coarser grain boundaries, reflecting deterioration of the membrane surface. The SFCO powder samples were reduced for 24 hrs, followed by oxidation. XRD patterns showed that crystal structure of oxidized samples reverted back to its original state.

Acknowledgement. This work was supported by U.S. Department of Energy/EPSCoR Grant # DE-F602-01ER45865. The authors would also like to acknowledge Dr. Rahul Mehta of SEM Lab at University of Central Arkansas for helping with SEM imaging.

References

(1) Teroaka, Y., Zhang, H., Furukawa, S., Yamazoe, N., Chem. *Lett*., **1985**, 1743.
(2) Teroaka, Y., Zhang, H., Okamoto, K., Yamazoe, N., Mater. Res. Bull., 23, **1988**, 51.
(3) Balachandran, U.; Ma, B.; Maiya, P. S.; Mieville, R. L.; Dusek, J. T.; Picciolo, J. J.; Guan, J.; Dorris, S. E.; Liu, M., *Solid State Ionics*, **1998**, 108, 363-370.
(4) Balachandran, U; Dusek, J. T.; Maiya, P. S.; Ma, B.; Mieville, R. L..; Kleefisch, M. S.; Guan, J.; Udovich, C. A., *Catalysis Today*, **1997**, *36*, 265.
(5) Minh, N. Q., *J. Am. Ceram. Soc.,* **1993***,* 76,563.
(6) Kruidhof, H., Bouwmeester, H. J. M., Doorn, R. H. E. V., Burggraff, A. L., *Solid State Ionics*, **1993**, 816, 63-65.
(7) Zhang, K., Yang, Y. L., Jaconson, A. J., Salama, K., Mater. Res. Soc. Symp. Proc., **1998**, 496, 341-346.

ORDERED MESOPOROUS SILICA MEMBRANES FOR CO_2 SEPARATION FROM FLUE GAS

Sangil Kim, Vadim V. Guliants, Junichi Ida, and Y.S. Lin

Department of Chemical and Materials Engineering
University of Cincinnati
Cincinnati, OH 45221-0171

Introduction

Reducing CO_2 emissions for addressing climate change concerns is becoming increasingly important as the CO_2 concentration in the atmosphere has increased rapidly since the industrial revolution. Most of currently investigated mitigation processes require CO_2 in a concentrated form. However, CO_2 is emitted from large sources, such as coal-fired power plants, at ~15% concentration. Therefore, capturing CO_2 from dilute streams is an important step for many mitigation methods. Membrane separation methods are particularly promising due to potentially high CO_2 selectivities and fluxes.[1] By a proper choice of the pore size and surface properties, the CO_2 transport across a membrane can be facilitated with respect to those of N_2 and O_2 leading to an efficient CO_2 separation process. However, current membranes suffer from a poor control over the pore size on the 2-4 nm scale and surface properties required for CO_2 separation.[2]

We describe here novel mesoporous silica membranes containing surface-attached amino groups promising for CO_2 separation from dilute sources. Defect-free mesoporous silica membranes on porous alumina supports exhibiting 26~28Å pores were obtained by spin-coating (~5-7 μm thick) and solution growth methods. Several kind of amino groups were attached to the membrane surface using amino-containing silicon alkoxides, such as 3-aminopropyltriethoxysilane.

Smaller pores (~18-22Å) were obtained by silylating the original calcined membranes with silane coupling agents. The characterization of the silylated silica membranes by BET surface area measurements, N_2 adsorption pore size analysis and TGA confirmed that silylation technique was successful in decreasing the membrane pore size by ~8 Å which is required for completely filling the pore volume with surface attached aminopropylsilyl groups and achieving facilitated transport of CO_2.

CO_2/N_2 separation on amine-modified silica membranes was investigated at 20-70°C and transmembrane pressure drop of 0.2-1 atm as a function of the pore size and the nature of the amino group using a Wicke-Kalenbach permeability cell. The membrane performance was evaluated with respect to permeance and separation selectivity, determined by a GC/MS analysis of the feed, permeate, and retentate streams.

Experimental

Membrane synthesis and amino group attachment. Mesoporous 3D hexagonal/MCM48 silica membranes were fabricated on disc-shaped porous alumina supports by a spin coating and solution grown method according to a previously published procedure.[3,4] In the spin-coating method, the polymeric silica sol was prepared under acidic conditions by mixing TEOS, water (pH=1.25) and ethanol in the 1:5:3.8 molar ratio. After stirring for 10h, CTAB diluted with ethanol was added to the sol. and the sol was aged at room temperature for 10h. The final molar composition of solution was 1.0 TEOS: 0.1 CTAB: 13.6 ethanol: 5.0 H_2O. Porous alumina supports were spin-coated at ~1000 rpm with this solution. Typically, 4-5 coats were required to obtain ordered mesoporous membranes ~2-6 μm thick. The pores of the silica membrane were opened by the thermal removal of the organic surfactant at ~500 °C in air, which left an ordered array of ~1-3 nm pores.

The MCM-48 membranes were prepared by the solution-growth technique as follows. A porous alumina support was placed in TEOS. Then, a solution containing CTAB, NaOH and water was added to TEOS. The molar composition of the mixture was 1.0 TEOS: 0.59 CTAB: 0.5 NaOH: 61 H_2O. After the mixture was stirred for 2 h, the mixture and alumina support were transferred to an autoclave. The reaction was carried out at 90 °C for 96 h. The membranes were washed with deionized water and dried at room temperature in air. Then, the membranes were calcined in air at 500 °C for 5h with heating and cooling rate of 1 °C /min.

3-aminopropyl groups, NH_2-$(CH_2)_3$-, were attached to the membrane surface by reacting the surface silanol groups with aminopropyltriethoxysilane in toluene under reflux. After distillation of a toluene fraction containing ethanol, the heating and distillation sequences were repeated two times. The functionalized membranes were washed in a Soxhlet apparatus with dichloromethane, and then dried at 100 °C.[5]

Silylation of Mesoporous Membranes. The silylation of the original calcined MCM-48 membranes was carried out at room temperature for 48hr in a liquid phase of trimethylchlorosilane.[6] The membranes were washed several times with n-hexane to remove the residual silylating agent. After silylation and washing, the membranes were calcined at 530 °C to oxidize surface trimethyl silyl groups into silanol groups, and a second silylation treatment was conducted in order to further decrease the pore diameter.

Membrane Characterization. The structure, the absence of "pinhole" defects and the presence of amino groups in mesoporous silica membranes were characterized by the X-ray diffraction, SEM, and He permeation studies. The presence and surface concentration of amino groups in the silica membrane upon attachment was investigated by IR spectroscopy and TGA. For the TGA analysis, samples were heated to 700 °C at a rate of 10 °C /min under O_2. In order to investigate the effect of trimethyl silyl and amino groups in silica membrane on pore size, pore volumes, N_2 adsorption/desorption isotherms and BET surface areas were investigated using Micromeritics TriStar 3000 porosimeter.

Results and Discussion

The X-ray diffraction patterns of calcined mesoporous membranes synthesized on porous alumina support indicated that the presence of low angle reflections corresponding to the ordered mesoporous MCM-48 structures.

The gas permeation properties of as-synthesized, calcined, and amine-attached membranes were characterized by He and CO_2 permeation tests under unsteady state at room temperature. **Figure 1** indicated that the as-synthesized mesoporous membranes were gas-tight prior to the removal of the organic surfactant from the pores as expected with the absence of "pinhole" defects. The He permeation increased dramatically after the pores of the silica membrane were opened by the thermal removal of the surfactant. In addition, the CO_2 permeation data showed higher CO_2 flux, $P(CO_2)$~$7\cdot10^{-7}$ $mol/m^2\cdot s\cdot Pa$, than the DOE target of $3\cdot10^{-7} mol/m^2\cdot s\cdot Pa$.

The SEM image of a silica membrane prepared by 5-fold spin coating the γ-alumina/α-alumina support showed that the support surface is covered with a continuous ~6 μm thick mesoporous silica layer.

The presence of amino groups in the silica membrane upon attachment was confirmed by IR spectroscopy. **Figure 2** shows IR spectra of the silica membranes before and after amino group

attachment. The presence of amino groups is indicated by strong IR peaks in the 1300-1700 cm^{-1} range.

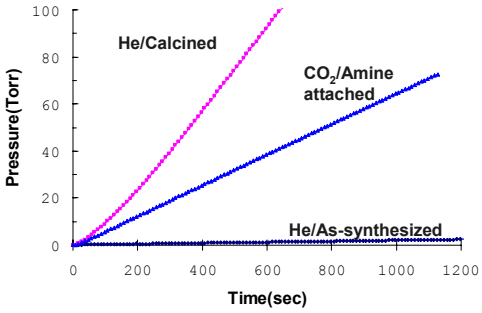

Figure 1. He and CO_2 permeation data for spin coated silica membrane.

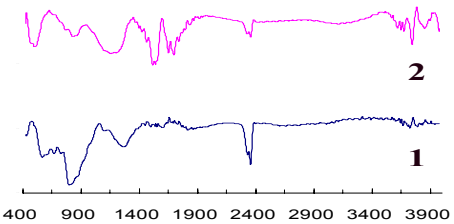

Figure 2. IR spectra of silica membrane prepared by spin-coating the γ-alumina/α-alumina support (1) before and (2) after amino group attachment.

The surface concentration of amino groups was investigated by TGA. **Figure 3** shows TGA derivative data for the mesoporous silica before and after amino group attachment. Above 100 °C, MCM-48 suffered very little weight loss, while the amine-modified MCM-48 showed a rather pronounced weight loss at 300~500°C. This can be explained by the combustion of the amino groups. Derivative TGA curves in **Figure 3** indicated that the attached amino groups are stable up to at least 250 °C. Therefore, the surface concentration of amino groups attached to MCM-48 can be measured from the weight loss in this temperature range. TGA indicated high surface amine concentration of ~0.88 mmol/g.

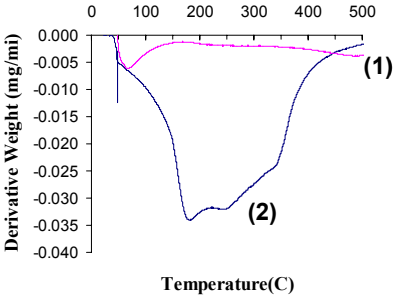

Figure 3. TGA derivative data MCM-48 type membrane (1) before and (2) after amino group attachment.

Single component CO_2 and N_2 studies and binary permeation studies showed that CO_2 and N_2 displayed similar trans-membrane fluxes indicating that the pore size needs to be reduced in order to achieve facilitated transport of CO_2 and its separation from N_2. In order to enhance the CO_2/N_2 separation, the membrane pore was decreased by the silylation process using silane coupling agents.

Figure 4 shows the pore size distributions determined by the BJH method using N_2 adsorption isotherms. The original MCM-48 powder and once-silylated and calcined materials showed the presence of mesoporosity; however, after the second silylation procedure the pore diameters decreased to below 20Å, which is the smallest pore size detectable by the TriStar 3000 porosimeter. The pore size after each silylation was reduced by ca. 6Å and increased slightly after calcination to remove the bulky trimethyl groups. There were no considerable changes in the BET surface areas for the original and silylated materials. These results indicated that the trimethyl silyl groups were uniformly dispersed on the pore surface of MCM-48 samples. These findings further indicated that the pore diameter in mesoporous silica membranes can be fine-tuned by sequential silylation/calcination steps.

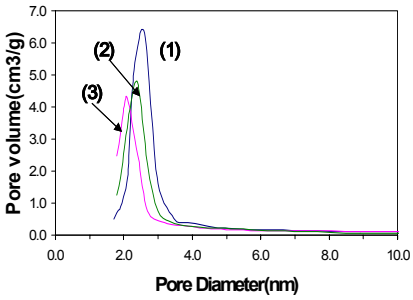

Figure 4. Pore size distribution in the (1) original MCM-48, (2) once silylated MCM-48, and (3) once silylated and calcined MCM-48.

The TGA data for the silylated MCM-48 samples in air indicated that the decomposition of the trimethylsilyl group of once-silylated MCM-48 occurred at ~520 °C, but the decomposition of the trimethylsilyl group of twice-silylated material started at a much lower temperature (~325 °C). The single component and binary CO_2/N_2 permeation studies of these silylated membranes are currently under investigation

Acknowledgment. This work was supported by the Ohio Coal Development Office grant OCRC3-00-1.C3.14.

References

(1) Feron, P.H.M; Jansen, A.E.; Herzog, H.J., *Energy Conversion and Management*, 1997, 38, S98
(2) Hsieh, H.P. *Inorganic Membranes for Separation and Reaction*, Elsevier: New York, 1996
(3) Besson, S.; Ricolleau, C.; Gacoin, T.; Jacquiod, C.; Boilot, J.-P., *J. Phys.Chem.B*, **2000**, 104(51), 12095
(4) Nishiyama, N.; Park, D.; Koide, A.;Egashira, Y.; Ueyama, K, *J.Mem.Sci.*, **2001**, 182(2), 235
(5) Lin, X.; Chuah, G.K.; Jaenicke, S., *J.Mol.Cat.A: Chemical*, **1999**, 150(2), 287
(6) Park, D.; Nishiyama, N.; Egashira, Y.; Ueyama, K., *Ind. Eng. Chem. Res.*, **2001**, 40, 6105

MFI-alumina composite membrane. Influence of the support porous structure on the separative performance.

E. Landrivon[1], S. Miachon[1], I. Kumakiri[1], M. Matsukata[2] and J-A. Dalmon[1]

[1]Institut de Recherches sur la Catalyse, 2 av. A. Einstein
69626 Villeurbanne Cedex France
[2]Waseda University, 3-4-1 Okubo, Shinjyuku,
Tokyo, 169-8555, Japan

Introduction

Owing to their very narrow pore-size distribution, zeolite-based membranes are currently considered for separative applications. Besides A-zeolite membranes, mainly developed for pervaporation processes, MFI-based membranes have been the subject of numerous studies, mostly in relation with gas separation applications. Gas separations require high quality materials, as the selectivity of the transport through the membrane is deeply dependent on the presence of defects in the separative layer.

Most of the materials combine a porous support (ceramic, metallic, carbon) and a thin continuous zeolite film deposited on top of it. In the present paper, we report on a composite MFI-alumina membrane obtained by growing zeolite crystals inside the pores of the support (pore-plugging method). Such systems, made of discrete zeolite particles embedded in the alumina matrix, may present advantages on the viewpoint of thermal stability (no long-range stresses in the zeolite phase). The present study analyses the influence of the support porous structure on the membrane separative performance.

Experimental

Supports were commercial macroporous alpha-alumina tubes obtained from Pall-Exekia (T1-70 type). They consist of concentric layers, with pore sizes decreasing from the outside. The external layer, thickness 1500 µm, pore size 12 µm, is present in all samples. Support 1 is obtained after coating this material with a 40 µm thick inner layer, average pore size 0.8 µm. Supports 2 and 3 are obtained after application on Support 1 of a final 20 µm thick toplayer, average pore size 0.5 µm (Support 2) or 0.2 µm (Support 3).

Tubes (15 cm length) have endings enameled on 1 cm to ensure gas-tight sealing (carbon seals + compression fittings) in the test module.

The precursor solution of the MFI zeolite was obtained by mixing silica (Aerosil 380) and a template (tetrapropylammonium hydroxide, TPAOH). After a 3-day ageing period at room temperature, that solution was poured in a Teflon-lined autoclave containing the Pall-Exekia porous ceramic tube. Hydrothermal synthesis was then performed at 443 K for 3 days. It was then checked that no gas permeation could occur through the precursor-plugged tube. The membrane was calcined at 773 K under a flow of 5% O_2 diluted in N_2, in order to remove organics coming from the template [1].

Pure gas permeation and mixture separation experiments were carried out in the 20-450°C temperature range. The shell side was used as permeate side.

For pure gas permeation measurements, hydrogen was used at 120 kPa feed pressure and 7.6 kPa pressure difference across the membrane, for n-butane these parameters were 148 and 39 kPa.

In gas mixture separation experiments, a mixture of 15% n-butane, 12% hydrogen and 73% nitrogen at about 120 kPa, was used in Wicke-Kallenbach mode in order to determine the separation factor Sf of n-butane over hydrogen, defined as the ratio:

$$Sf = (XC_4H_{10,permeate}/XC_4H_{10,feed}) / (XH_{2,permeate}/XH_{2,feed})$$

where X is the molar fraction. Permeate composition was analyzed by GC. Sf has been used as a reference for measuring the performance of the membrane.

Scanning Electron Microscopy analyses were performed using a Hitachi S800 microscope equipped with a EDX analyzer. Tubes were broken using a hammer and small pieces were glued to a sample holder.

Results and Discussion

Electron Microscopy. In all cases, after zeolite hydrothermal synthesis, SEM micrographs showed the presence of typical MFI crystals on top of the final internal (smallest pores) toplayer. However, it is quite clear these crystals are not well connected. Therefore, they do not form a continuous supported film that might act as a separative layer.

Separated MFI crystals are also observed on top of the very large alumina particles of the external (12 µm pore size) layer. However, the large pores of this layer are still undoubtedly open and this zone also cannot contribute to the separative performance.

According to these SEM observations, if existing, the separative zone should be located in the 0.8 - 0.2 µm pore area. Though SEM micrographs did not allow a clear identification of zeolite crystals in these layers, EDX analyses revealed the presence of Si in all this 0.8 - 0.2 µm pore area. Moreover, an analytical probe including both the material present in these pores and the support, gave a Si/Al ratio close to that calculated on the basis of the complete filling of the porous volume by the MFI phase. In another recent study [2], TEM-FFT structure analysis confirmed the presence of MFI zeolite in the toplayer pores of the host material.

Gas Transport Experiments. The transmembrane transfers were studied using both adsorbing (n-butane) and non-adsorbing (hydrogen) species. Figure 1 shows typical results of single gas measurements obtained with a MFI membrane formed with Support 3 (0.2 µm toplayer).

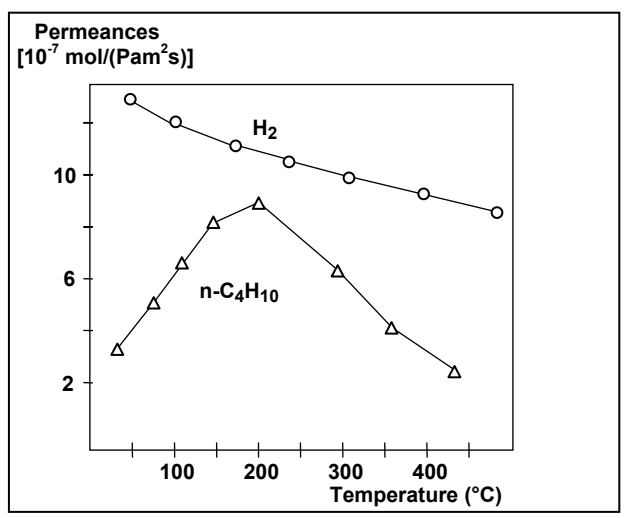

Figure 1. Typical single-gas permeances of a MFI membrane obtained with Support 3. Feed pressure and pressure difference across the membrane (kPa), H_2: 120, 7.6; n-C_4H_{10}: 125, 39.

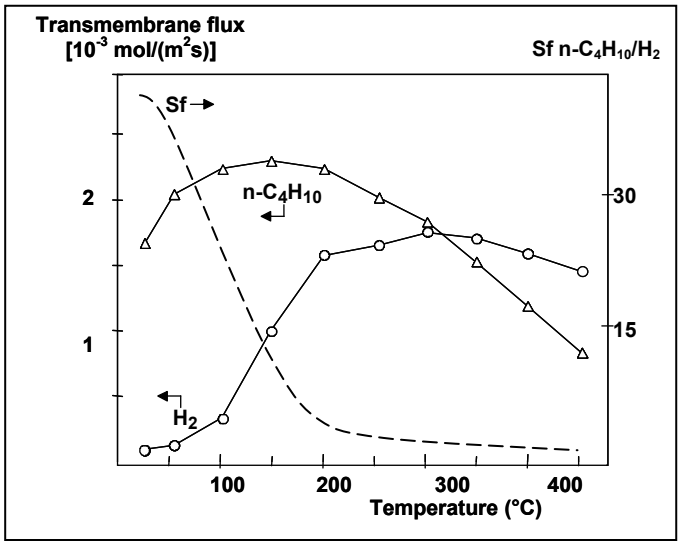

Figure 2. Typical n-C_4H_{10}/H_2 separative performance of a MFI membrane obtained with Support 3. Conditions: P=125 kPa, ΔP=0, Feed flow: 5.410^{-5}mol.s^{-1} (H_2 :n-C_4H_{10} :N_2 =12 :15::73), Sweep flow (countercurrent) 5.410^{-5}mol.s^{-1}.

Figure 2 gives permeating fluxes and Sf (n-C_4H_{10}/H_2) as a function of the temperature.

In single gas permeation experiments (Figure 1), the hydrogen permeance is higher than that of n-butane, which shows a maximum, typical of adsorbing species [3].

However, when mixtures of the two gases are considered (Figure 2), mainly n-butane permeates at room temperature [1, 3]. This is due to the strong adsorption of n-butane, which, owing to its molecular size close to that of the MFI pores, hinders the hydrogen penetration in the zeolite structure. When temperature increases, n-butane adsorption decreases, and the hydrogen flux increases progressively and finally overtakes that of n-butane (however, even at 450°C, there is still some n-butane hindering effect, as the H_2 /n-C_4H_{10} selectivity is much lower than that calculated from single-gas permeances).

If, at low temperature, the strong n-butane adsorption completely blocks hydrogen permeation through the zeolite pores, the value of Sf obtained at room temperature can be used as a quality measurement of the material. As a matter of fact, hydrogen will only permeate through defects of the zeolite separative layer. However, this is only true if n-butane, due to capillary condensation phenomena, does not also block at room temperature pores larger than those of the MFI zeolite. Though, in principle, only valid for larger pores, the Kelvin equation indicates that n-butane should, for the present conditions, only condensate in micropores. It seems therefore that the room temperature value of Sf is a way to evaluate the quality of the membrane, as hydrogen would only permeate through pores larger than micropores.

This Sf criterion has been used for the optimization of the MFI membrane synthesis. This resulted in a net progress in the membrane performance.

Among the various parameters involved in the membrane preparation, the porous structure of the support may play an important role. This should be especially the case in the present synthesis, where zeolite crystals are growing in the porous volume of the support, till plugging the pores. As a matter of fact, it seems reasonable to think there is a critical pore diameter above which the complete pore plugging will not occur.

A comparative study of Sf performances of MFI-alumina composite membranes prepared using Supports 1 (smallest pores 0.8 µm) , 2 (0.5 µm) or 3 (0.2 µm) undoubtedly showed that complete pore plugging did not occur in supports 1 and 2. As a matter of fact, typical Sf values with Support 3 are in the 20-50 range, when Sf is close to 1 (no separation) when the zeolite synthesis is performed in presence of Supports 1 or 2.

The definition of a critical pore diameter (the largest pore size where plugging by zeolite crystals occurs) is not easy. If it is likely between 0.5 and 0.2 µm, it seems difficult to be more precise, as all supports present a pore size distribution. It is clear that both Supports 1 and 2 have a large part of the pore distribution above the critical diameter.

Contrariwise, Support 3 has certainly most of its pores under the critical value. The fraction of pores above the critical value should affect negatively the separative performance of membranes based on Support 3. Moreover, these supports may present some small variations in the pores size distribution. This could contribute to the reproducibility problems observed during the zeolite membrane preparation. Verification of such hypothesis would require a detailed study of the pore distribution of several samples of Support 3 and comparison with the observed values of Sf. However, there are certainly many other parameters that may affect the final separative performance.

Conclusion

The preparation of composite MFI-alumina membranes by growing zeolite crystals inside the pores of a macroporous alumina host material (pore-plugging method) has been successfully achieved. Among other parameters, the porous structure of the alumina support has a great influence on the final separative performance of the composite membrane. There is a critical support pore diameter above which the pore plugging does not occur. As a consequence, the thickness of the layer with pores under the critical diameter should control the thickness of the separative layer. This can be used for further optimization of the zeolite membrane.

References

(1) Giroir-Fendler, A.; Peureux, J.; Mozzanega, H.; Dalmon J-A. *Studies Surf. Sc. Cat.*, **1996**, *101(A)*, 127.
(2) Aouine, M.; Miachon, S.; and Dalmon J-A. *to be published.*
(3) Kapteijn, F.; Bakker, W.J.W.; Zheng, G.; Moulijn J.A..; van Bekkum, H. *Catal. Today*, **1995**, *25 (3-4)*, 213.

THERMAL MECHANOCHEMICAL STABILITY OF OXYGEN TRANSPORT PEROVSKITE MEMBRANES

N. Nagendra[1], W.F. Haslebacher[2], V.K. Venkataraman[2] and S. Bandopadhyay[1]

[1]School of Mineral Engineering, University of Alaska Fairbanks
Fairbanks, AK 99775-5800 USA
[2]US Department of Energy/National Energy Technology Laboratory,
3610 Collins Ferry Road, Morgantown, WV 26507-0880

Introduction

In recent years, mixed conducting perovskites of the general composition $La_xSr_{1-x}M_xM'_{1-y}O_{3-\delta}$ (where M = Co, Mn and Cr and M' = Fe and Al) have attracted considerable attention for possible applications as high temperature electrochemical oxygen membranes – devices that serve to separate oxygen containing gas mixtures due to difference in oxygen partial pressures on the two sides of the membrane. This concept is utilized in membrane reactors that can produce synthetic gas by direct conversion of hydrocarbons [1,2]. For the above-mentioned applications, the ABO_3 type oxides have to be dense and importantly show high ionic and/or electronic conductivity. To achieve this, the A-site cations are often substituted by a lower valence state, effectively forming oxygen vacancies and causing a change of valence state in B-site cation to maintain charge neutrality. The concentration of oxygen vacancies can also be tailored by substituting ions of smaller size but lower valence B sites. It has also been observed that the oxygen vacancies in many of these materials can be created by exposure to an environment having a sufficiently low thermodynamic oxygen activity. The formation of oxygen vacancies so essential for the functional properties in the material often leads to dimensional instability and strength degradation under reducing conditions. Thus, one of the important issues that need to be addressed is the structural, chemical and mechanical stability and reliability of these materials in application environments that are severely reducing ($P(O_2) \approx 0.2$ to10^{-16} atm.).

Much of the available literature has focused on membrane synthesis, characterization and functional properties such as: ionic-electronic conductivities [3], oxygen permeability [4], oxygen transport and diffusion [5]. However, there has been only a limited characterization of the thermo-mechanochemical behavior of these materials. In this paper, the thermomechanical and chemical stability of one such perovskite $La_xSr_{1-x}M_xM'_{1-y}O_{3-\delta}$ (where M = Cr and M' = Fe) membranes is examined. The perovskites processed as tubes are potential candidate material for membrane reactors for direct reduction of methane to syngas. The perovskites are evaluated for strength and toughness through C-ring tests and the fracture surfaces analyzed by X-ray diffraction (XRD) and Scanning Electron Microscopy (SEM).

Experimental

Two sets of membranes of the general composition $La_{0.2}Sr_{0.8}Fe_{0.8}Cr_{0.2}O_{3-\delta}$ and varying in particle size (LSFCO1 ≈ 1μm and LSFCO2 ≈ 5μm) were provided for testing by BP chemicals Inc., USA. The tubes were prepared by a proprietary process involving cold-isostatic pressing and sintering between 1250-1350°C for 4 hours in flowing air and then cooled to room temperature in flowing nitrogen. C-rings Rings cut from the tubes in were tested in diametral compression between two alumina platens in a hydraulic testing frame (MTS 858 MiniBionix II) [6]. The fracture strength (σ_f) and toughness (K_c) of the membranes tubes were evaluated in the temperature range (25-1000°C) and pressure (1 and 1.7 atm) in three different environments: air, 100% N_2 and 90%CO_2/10%CO. These test conditions at 1000°C in 0.17 MPa N_2 and in 0.17 MPa CO_2/CO (90/10) corresponded to oxygen partial pressure of $\log_{PO_2}$ = -4 atm and $\log_{PO_2}$ = –12.1 atm. respectively. After testing, the fracture surfaces were examined under SEM to identify the dominating flaws and possible fracture mechanisms. The surfaces were also examined by X-ray analysis to verify for any possible phase separation.

Post fracture hardness (H) and fracture toughness (K_C) of the membranes were measured. Measurements were made in a Vickers microhardness tester (Buehler, Micromet II) on ground and polished surfaces (< 0.5μm) with loads of up to 10N applied for 15s. The diagonal and crack lengths of ten indents were used to evaluate fracture toughness using the formula [7]

$$K_C = 0.016\left(\frac{E}{H}\right)^{1/2}\frac{P}{c^{3/2}} \qquad (1)$$

Where *2c* is the crack size, P is the indent load, E is the Young's modulus, H is the hardness.

Results and Discussion

The maximum and the average strength of sample set LSFCO-2 (429 MPa and 307 MPa respectively) were twice of that in LSFCO-1 (210 MPa and 167 MPa respectively). Microscopic analysis indicated that surface and volume flaws were the primary failure origins. However, although the fracture in both the sets were by cleavage, the morphology was distinct in observed features. In set LSFCO-1, the surfaces were smooth with apparent lack of features while in set LSFCO-2 microscopic cleavage planes and pore opening at triple point grain boundaries could be observed.

The strength of the oxide membrane tube decreases with increase in temperature and severity of reducing environment (Fig. 1). The strength degradation was markedly more severe in air (Log pO_2 = -0.7 atm) and CO_2/CO (Log pO_2 = -12 atm) in comparison with N_2 (Log pO_2 = -4 atm.) environment. However, LSFCO-1 indicated a higher resistance to strength degradation in comparison with LSFCO-2. Strength of the LSFCO-1 tubes decreased from 167 MPa to 108 MPa and 139 MPa in air and N_2 respectively, while in LSFCO-2, strength in N_2 (178 MPa) decreased rapidly to nearly half its value at the ambient condition. In air (113 MPa) and CO_2/CO (107 MPa), rapid degradation in strength was observed. Although similar trends in toughness (Kc) were seen, the recorded values were not as sensitive to the environment as strength measurements. A drastic drop in toughness in air followed by a slight recovery in N_2 and CO_2/CO was recorded. Fractographic observations indicated a breakdown of grain structure along with distinct relief in grain boundaries [6] in all conditions.

The hardness (*H*) and indentation toughness (K_{ind}) of LSFCO-1 was in the range of 5.2±0.5 GPa and 0.5-0.8 MPa√m respectively. In comparison, LSFCO-2 showed a slightly reduced hardness of 4.4±0.5 GPa but increased toughness of 1-1.5 MPa√m respectively. At room temperatures, the hardness increased in samples after testing with a concomitant decrease in toughness. The trends observed in indentation toughness values confirmed the similarly observed loss of toughness in air and recovery in N_2 and CO_2/CO [8].

At room temperature, X-ray analysis of the membranes indicated that the dominant phase in both the tubes was the primitive cubic perovskite phase. As shown in figure 3, mechanical testing at room temperature did not alter the structure. At elevated temperatures, traces of decomposition products were observed. In LSFCO-1, samples tested in air at 1000°C showed traces of

$(La,Sr)CrO_3$ and no decomposition in N_2. On the other hand, LSFCO-2 samples (decomposed to form $(La,Sr)CrO_3$ and $(La,Sr)Fe_{12}O_{12}$ in air and $(La,Sr)CrO_3$ in N_2 respectively.

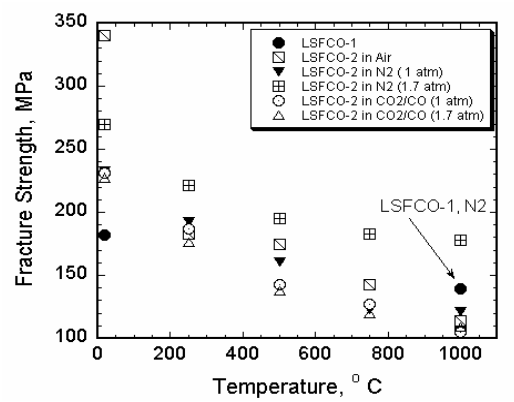

Figure 1. Effect of temperature and pressure on strength of LSFCO membrane tubes.

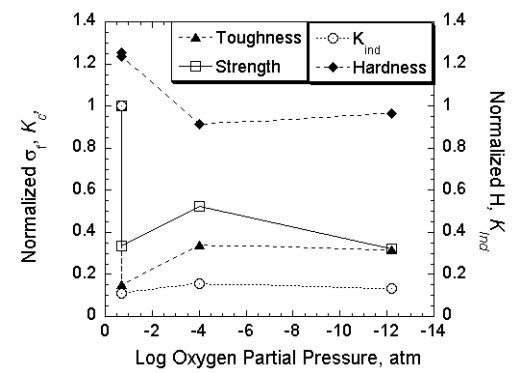

Figure 2. Strength, hardness and toughness of LSFCO membrane tubes as a function of environment

In the present study, the parent $SrFeO_{3-\delta}$ perovskites show a large oxygen deficiency even at room temperature in air. At elevated temperatures, enrichment of Sr at the grain boundaries and surfaces occur via a high diffusive path and leads to the additional formation of point defects. The formation of point defects enhances the diffusion of oxygen or metal component via grain boundary and often governs the oxygen permeation, reaction and degradation of perovskites [8]. Fracture surfaces of specimens tested below 750°C do not indicate an enrichment of Sr at the grain boundaries. This agrees well with an earlier observation indicating that below 800°C, vacancies are not mobile in many of the perovskites. The other point of interest is that at temperatures above 800°C, the vacancy populations in the perovskites are partly mobile and often lead to some local (micro domain) ordering. Studies involving Z-contrast imaging and EEL spectra have shown extended ordering in LSFCO analyzed as Brownmillerite like oxygen vacancy structures, with additional defects produced at elevated temperatures. Although, these transitions are reported above ~500°C, it has been observed that non stoichiometry in the oxide can increase considerably with increasing temperature and reducing conditions. Also, the ordered domains are observed to progressively grow with increasing temperatures until the reduction of the cubic perovskite structure cause some areas to collapse, thereby forming Aurvillus phases in the bulk that may restrict oxygen conductivity. Although, these transitions could not be directly linked to the distinctive morphological features observed in the fractured surfaces by an SEM it is highly probable they bear significant influence on the fracture process.

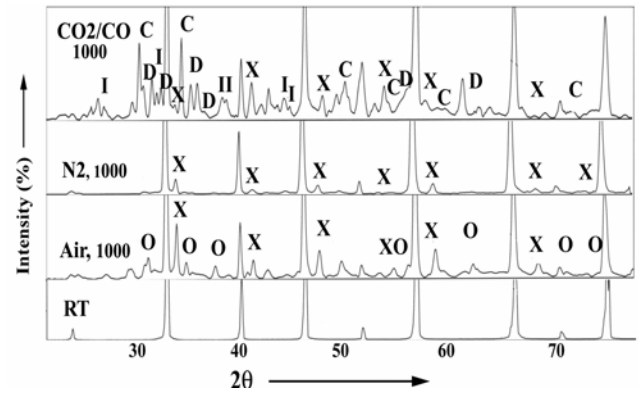

Figure 3. Phase separation upon mechanochemical degradation of LSFCO membrane tubes. The major phases formed are (X)-$(La,Sr)CrO_3$, (O) -$(La,Sr)Fe_{12}O_{12}$ and (C)- SrO. LSFCO-1 is more resistant to degradation in N_2

Conclusions

Oxygen transport perovskite membranes in reducing environment can undergo thermo-mechanochemical degradation that is significantly different from those observed in stress free conditions. The observed behavior has important significance in designing of reliable structures for gas separation and their long-term properties.

Acknowledgment

This research was sponsored by National Energy Technology Laboratory, US Department of Energy under grant number DE-FC26-99FT40054. We thank T.J. Mazanec and W.T Stephens for providing the samples.

References

1. T.J. Mazanec, *Solid State Ionics,* **70/71**, 11 (1994).
2. K. Huang, R.S. Tichy and J.B. Goodenough, *J. Am. Ceram. Soc*., **81**, 2565 (1998).
3. Y. Teraoka, H.M. Zhang, K. Okamoto and N. Yamazoe, *Mater. Res. Bull*. **23**, 51-58 (1988)
4. W.T. Stephens, T.J. Mazanec and H.U. Anderson, *Solid State Ionics,* **129**, 271 (2000).
5. C. Tsai, A.G. Dixon, Y.H. Ma, W.R. Moser and M.R. Pascucci, *J. Am. Ceram. Soc.,* **81**, 1437-44 (1998).
6. N. Nagendra, R. F. Klie, N.D. Browning and S. Bandhopadhyay, *Mat. Sci. Eng A* 341/1-2, 236-246, 2002
7. G.R. Anstis, P. Chantikul, B.R. Lawn and D.B. Marshall, *J. Am. Ceram. Soc*., **64,** 533-28 (1981)
8. N. Nagendra and S. Bandopadhyay, *Scripta Materialia***, 48/1**, 37-42, 2003
9. R.H.E. van Doorn and A.J. Burggraaf, *Solid State Ionics,* **128** , 65-78 (2000).

Reforming of Liquid Hydrocarbon Fuels for Micro Fuel Cells. Steam Reforming of Pre-reformate from Jet Fuel over Supported Metal Catalysts

*Jian Zheng, Chunshan Song**

Clean Fuels and Catalysis Program, The Energy Institute and Department of Energy & Geo-Environmental Engineering, Pennsylvania State University, University Park, PA 16802
*Email: csong@psu.edu; Tel: 814-863-4466; Fax: 814-865-3248

Introduction

Recently, increasing attention has been paid on exploring compact and efficient fuel processors for fuel cell applications around the world[1,2]. We are exploring a fuel-cell fuel processor using logistic fuel (such as JP-8 jet fuel) for portable fuel cell application. As mentioned in a preceding paper[2], our approach to solving the potential problem of carbon formation during reforming of higher hydrocarbon fuels is to conduct catalytic fuel reformation in two stages, with a pre-reformer (oxygen-assisted if necessary) to break-down most C_8-C_{13} hydrocarbons to C_1 to C_2 molecules plus CO and H_2, followed by steam reforming (possibly also oxygen-assisted) in main reformer to produce reformats (H_2, CO, CO_2). Our preliminary studies on pre-reformer are discussed elsewhere[2].

The target for the main reformer sub-section in our integrated fuel-cell fuel processor is to convert smaller hydrocarbons (mainly C_1, with some C_2-C_4) from the pre-reformer into carbon monoxide and hydrogen without any significant carbon formation. The main concern here is that gas mixtures including also H_2 and CO_2, instead of pure CH_4 and/or C_2-C_4, will be the feed for the main reformer, since there will be no gas separation device between pre-reformer and reformer. The presence of H_2, CO_2 and CO produced from pre-reformer inevitably affects the activity and the carbon formation behavior of catalysts used for reformer. Furthermore, the compositions of the effluent from pre-reformer are uncertain, considering that different catalysts and reaction conditions in the pre-reformer are also being screened and tested. Therefore, we began the study of reforming using some model gas mixtures to simulate both the better and worse cases of products from pre-reformer.

Most industrial steam reforming of light hydrocarbons (C_1-C_4) uses a supported Ni catalyst. While the studies on steam reforming using noble-metal catalysts are limited, there are evidences indicating that these materials can be more active and more resistant to carbon formation than conventional Ni catalysts[3-11]. However, the metal activity over various supported materials for steam reforming under different conditions results in some contradictory trends in the literature. The specific activities of metals supported on alumina or magnesia have generally been found to be[3]: Rh ~ Ru > Ni ~ Pd ~ Pt > Re > Co. Turnover numbers have also been reported for steam reforming of methane and ethane on noble metals relative to Ni. For silica-supported catalysts used for methane steam reforming, the relative activities are[4]: Rh (1.6) > Ru (1.4) > Ni (1) > Pd (0.6) > Pt (0.5), whereas for alumina-supported systems with ethane[5, 6]: Rh (13) > Ru (9.5) > Pd (1.0) ~ Ni (1.0) > Pt (0.9). For the steam reforming of propane/propene mixtures, the order of activity is[7]: Rh ~ Ir > Pt > Co > Ru > Ni ~ Re. While the order of activity per metal site (on the base 100 for Rh) for the toluene steam reforming is[8]: Rh (100) > Pd (29) > Pt (19) > Ni (17) > Ir (13). It seems that rhodium has been generally found to be the most active metal, whereas no common agreement and knowledge has been achieved on the activity of iridium as catalyst for steam reforming of hydrocarbons.

With the need for on-board reforming for fuel cell applications, there has been renewed interest in developing more active catalysts that can operate under more severe conditions and lower steam to carbon ratios for steam reforming of hydrocarbons. Instead of using Al_2O_3 as support, some new materials (e.g., CeO_2, ZrO_2, etc.) especially those having unique features, such as stabilization of noble metal dispersion and the ability to improve the storage of oxygen, have been utilized[9-13]. Catalytic properties of CeO_2 and CeO_2-containing materials have been studied extensively[12]. Noble metal based catalysts (Pt, Pd and Rh) deposited on various support such as Al_2O_3, CeO_2 and ZrO_2, have been tested in various reforming processes, and they provide good catalytic activity in methane, propane or n-butane steam reforming reactions[9, 13-14]. The presence of CeO_2 as a promoter has also been found to confer high catalytic activity to the alumina-supported Pd catalyst for methane steam reforming[11]. Furthermore, the catalytic activity and the synergetic effect for the Pd/CeO_2/Al_2O_3 catalysts are strongly dependent on the crystallinity, dispersion and stoichiometry of the CeO_2 promoter deposited. Highly crystalline CeO_2 increases the catalytic activity of a Pd-supported catalyst when used in methane steam reforming[11].

In the present work, various noble metals have been supported on CeO_2 modified Al_2O_3 for the steam reforming of two gas mixtures simulating the effluents from pre-reformer. Interestingly, iridium shows the highest activity for the steam reforming under severe conditions.

Experimental

CeO_2-Al_2O_3 (containing 20wt% CeO_2) support was prepared by wet impregnation of γ-Al_2O_3 (LaRoche, 155 m^2/g) with $Ce(NO_3)_3 \cdot 6H_2O$ (Aldrich) followed by calcinations at 800˚C in air for 3 hours. Various noble metals (such as Pt, Pd, Ru, Rh, Ir) have been supported on $CeO_2.Al_2O_3$ by wet impregnation, with nominal metal content fixed at 1 wt%.

Commercial SMR catalyst (G-91) was obtained from Süd Chemie, with 15-25% NiO, 45-60% Al_2O_3, 5-15% $CaAlO_2$, 5-15% CaO and 1-10% K_2O (as per the data provided by vendor).

Simulated gas mixtures. SGM-1 (34.2% CH_4, 16.2% H_2, 15.5% CO_2, and 34.2% Ar) was prepared to simulate a scenario where the pre-reforming is complete and has converted all higher hydrocarbons into C1 species and H_2 in the pre-reformer. According to the literature[15], the equilibrium gas composition from adiabatic pre-reforming is 51.7% CH_4, 24.3% H_2, 23.4% CO_2, and 0.6% CO. We considered two factors in selecting the SGM-1. First, since the CO concentration is very low in the equilibrium gas composition, it was neglected. Another modification is that we added same amount of argon as that of CH_4, which is to simulate the nitrogen concentration in the use of air for the purpose of "oxidative" pre-reforming.

SGM-2 (47.5% CH_4, 35.5% H_2, 7.0% CO_2, 9.0% C_2H_6, and 1.0% C_3H_8) is chosen as an example for the reformats from incomplete pre-reforming, since there is a significant concentration of higher hydrocarbons (C_2H_6 and C_3H_8).

Reaction conditions. A given amount of catalyst sample (0.4 g or 0.1g, depending on the reaction need) was loaded in the middle of the stainless steel reactor tube (Inconel 800H alloy, with 0.54" O.D. X 0.375" I.D. and 24" long), with the remaining tube filled with α-Al_2O_3 beads. CH_4 feed flow rate was chosen to be 13.7 ml/min. This is to simulate the real conditions defined by the calculations for 20 watts solid-oxide fuel cell.

Before starting the reforming, water was introduced for 30 minutes before opening the gas mixtures to ensure that there is always steam accompanying hydrocarbon flow in the reactor lines. Catalyst screening is then performed in a laboratory continuous-down-flow tubular reactor (as described in our previous paper[3]) at atmospheric pressure in the temperature range of 600-800°C, and

steam to carbon ratio from 1.5 to 3.0. During the reaction, the gas products after condensing of remaining steam are analyzed on-line by a multi-gas analyzer GC-TCD for the calculation of conversion and product distributions.

Results and Discussion

Figure 1 shows methane conversion for steam reforming of SGM-1 and SGM-2 on a commercial G-91 catalyst (Ni supported on Al_2O_3 with some promoters) at temperatures of 600-800˚C. It can be seen that, for the steam reforming of the simulated effluents from the complete pre-reforming (SGM-1), the non-precious metal catalyst can reach almost equilibrium conversions. For SGM-2, since there are significant amounts of higher hydrocarbons (C_2H_6 and C_3H_8), which can produce CH_4 during the reaction, the conversion of CH_4 itself has been decreased as compared to the steam reforming of SGM-1, especially at lower temperatures. However, reacting at 800˚C, the non-precious metal catalyst can still achieve nearly complete conversion.

These results indicate that these reforming conditions (including the temperature of 800°C and space velocity) are sufficient for the main reforming even using commercial Ni catalysts.

In order to identify more active catalysts for reforming, we then reduced the catalyst amount to 0.1g under the same feed flow, so that the space velocity can be increased. Also the steam to carbon ratio was reduced from 3.0 to 1.5 to give us more flexibility for future potential applications.

Figure 2 shows the steam reforming results of SGM-2 at 800˚C over different metal supported catalysts. It can be seen that, while some of the noble metal catalysts (such as Pt and Pd) show even lower activity than that of commercial Ni supported G-91 catalyst (around 85%), the Ru supported catalyst shows similar activity to Rh (around 90%). Interestingly, the Ir supported on CeO_2-Al_2O_3 shows the highest activity, which is as high as 95% conversion for CH_4 out of the simulated gas mixtures (SGM-2).

The trend of metal activity for converting the lower hydrocarbons in the presence of H_2 and CO_2 (as in the case of SGM-2) is as follows:

Ir > Ru ~ Rh > Ni ~ Pd ~ Pt.

Figure 3 shows the 10-hour steam reforming experiment of SGM-2 over 1% Ir supported on CeO_2-Al_2O_3 under the above-mentioned conditions. It is clear that the catalyst has high activity and is stable during the 10-hour run, with H_2 being the dominant product (70%), together with some CO (25%) and small amount of CO_2 (3%).

We further studied the behavior of this catalyst under various temperatures, and found that we could achieve even higher conversion at slightly higher reaction temperatures. Furthermore, by carrying out TPO-IR, we detected no carbon formation on this catalyst. Therefore, Ir/CeO_2-Al_2O_3 is a promising reforming catalyst for our proposed integrated fuel processor for micro-solid oxide fuel cells.

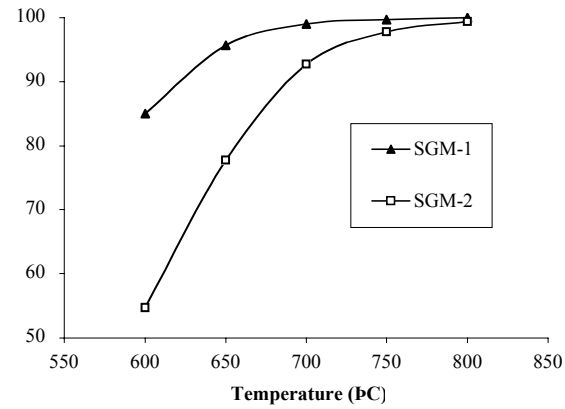

Figure 1. Steam reforming of SGM-1 and SGM-2 on G-91 catalyst (0.4g of catalyst, GHSV=13250h^{-1}, S/C=3, atm)

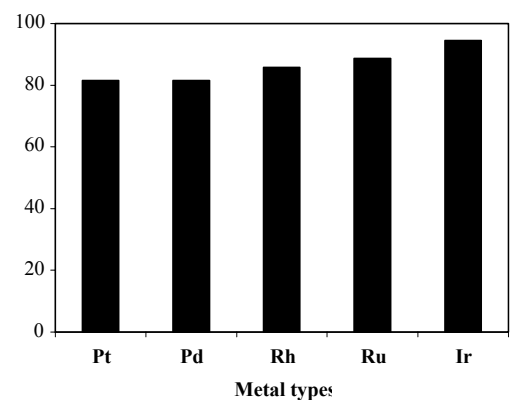

Figure 2. Steam reforming of SGM-2 over different metal catalysts supported on CeO_2-Al_2O_3 (0.1g catalyst, GHSV=21500h^{-1}, 800˚C, S/C=1.5, atm)

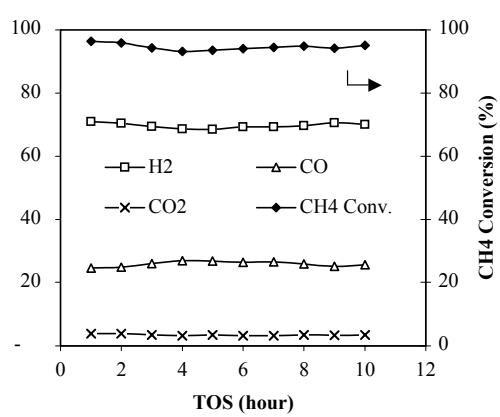

Figure 3. Steam reforming of SGM-2 on 1% Ir supported on CeO_2-Al_2O_3 (0.1g of catalyst, GHSV=21500h^{-1}, 800°C, S/C=1.5, atm)

Conclusions

The reforming reaction can reach equilibrium conversion under sufficiently higher temperature and lower space velocity even on commercial Ni catalyst. However, under more demanding conditions (lower catalyst amount, higher space velocity and lower steam to carbon ratio), Ir/CeO_2-Al_2O_3 catalyst shows the highest activity among all the CeO_2-Al_2O_3 supported noble metal catalysts. The novel noble catalysts are stable for relatively long-duration laboratory tests, which are promising for use in a fuel processor for micro-fuel cell applications.

Acknowledgement. We are grateful to the Palm Power Program of DARPA/DoD for supporting this work. We also wish to thank Dr. Mehdi Namazian of Altex Technologies Inc., Dr. Wei Pan and Mr. J. Jon Strohm of PSU for helpful discussions on fuel reforming. Thanks also go to Dr. Jian-Ping Shen and Mr. Ronald Copenhaver of PSU for help in setting up the reactor system.

References

(1) Song, C. *Catalysis Today*, **2002**,77, 17-49.
(2) Trimm, D.L.; Onsan, Z.I. *Catal. Rev.*, **2001**, *43 (1,2)*, 31-84; Larminie, J.; Dicks, A. In *Fuel cell Systems Explained;* John Wiley: New York, **2000**, pp.308.
(3) Zheng, J.; Shen, J.P.; Song, C.; Pan, W.; Strohm, J.J. *Prepr. Pap. - Am. Chem. Soc., Div. Fuel. Chem.*, **2003**, *47 (1)*, in press.
(4) Kikuchi, E.; Tanaka, E.; Yamazaki, Y.; Morita, Y. *Bull. Japan Petrol. Inst*., **1974**, *16*, 95.
(5) Rostrup Nielsen, J.R. In *Catalysis Science and Technology*; Andersen, J.R.; Boudart, M., Ed.; Springer-Verlag, New York, **1984**; Vol. 4, pp.34.
(6) Grenoble, D.C. *J. Catal.* **1973**, *51*, 203.
(7) Gandhi, H.S.; Piken, A.G.; Stepien, H.K.; Shelef, M.; Delosh, R.G.; Heyde, M.E. *SAE Techn. Pap. Ser. No. 770166*, in SAE Automotive Engineering Congress, Detroit, **1977**.
(8) Duprez, D.; Pereira, P.; Grand, M.; Maurel, R. *J. Catal.*, **1982**, *75*, 151.
(9) Igarashi, A.; Ohtaka, T.; Motoki, S. *Catal. Lett.*, **1991**, *13*, 189-194.
(10) Wang, X.; Gorte, R.J. *Catal. Lett.*, **2001**, *73 (1)*, 15-19.
(11) Craciun, R.; Daniell, W.; Knozinger, H. *Appl. Catal. A: Gen.*, **2002**, in press.
(12) Hofstad, K.H.; Rokstad, O.A.; Holman, A. Catal. Lett., 1996, 36, 25.
(13) Barbier, J.Jr.; Duprez, D. Appl. Catal. B: Environ. 1993, 4, 105.
(14) Kikuchi, E.; Nemoro, Y.; Kajiwara, M.; Uemiya, S.; Kojima, T. Catal. Today, 2000, 56, 75.
(15) Steinfeld, G.; Sanderson, R.; Ghezel-Ayagh, H.; Abens, S. In *AICHE Spring 2000 Meeting*, March, **2000**.

TRANSPORT RESISTANCE FOR OXIDE DIFFUSION BARRIERS ON POROUS METAL SUPPORTS USED IN COMPOSITE Pd AND Pd-ALLOY MEMBRANES

Erik E. Engwall, Ivan P. Mardilovich and Y.H. Ma

Center for Inorganic Membrane Studies
Department of Chemical Engineering
Worcester Polytechnic Institute
Worcester, MA 01609

Introduction

Thin oxide layers may be used as barriers to prevent intermetalic diffusion between a porous stainless steel support (PSS) and the dense Pd layer of a composite Pd-PSS membrane (1,2). An oxide diffusion barrier may be created by heating the PSS support in air prior to application of the Pd layer. The simplicity of this in-situ oxidation (1) approach and the benefits of the barrier must be weighed against an increase in transport resistance caused by oxide formation. In this study, the effects of the oxidation temperature were experimentally evaluated for a series of 316L PSS supports oxidized at 400, 500 and 600°C. The effects of oxidation conditions were determined experimentally by the measurement of support helium flux versus pressure drop at room temperature, before and after oxidation.

For the simple case where a Pd-PSS membrane is used in hydrogen separations with no sweep gases, the contribution of the support to the transport resistance of the membrane may be measured by the trans-support pressure drop ΔP. The measurement of ΔP at process conditions (H_2, 350-450°C) prior to Pd plating, is not convenient as a routine step during membrane synthesis. However, the helium flux of the supports is routinely measured at room temperature before and after support oxidation. It is therefore convenient to have a means to predict the behavior of the support at process conditions from the data taken during synthesis. This was done for the porous disks using a model based on Darcy's law.

Experimental

The supports for this study were disks of 0.1μ grade porous 316L stainless steel with a thickness (z) of 0.071 in. and a diameter of 1.17 in. The pore size and porosity of these disks was determined prior to oxidation by Hg porosimitry on a representative sample. The disks were subjected to the same cleaning procedures as applied to membrane supports used in this laboratory (2). Following cleaning, the disks were oxidized at 400, 500 and 600°C in air. The oxidation treatments were 6 hours in duration with 10°C/min heating and cooling ramps. Three samples were oxidized at each temperature. The sample mass and helium flux versus ΔP at 25°C were obtained before and after oxidation for all samples.

Results and Discussion

Mercury porosimitry on a single unoxidized support indicated a median pore diameter of 1.86 μm and a porosity of 0.31. This result is consistent with Mardilovich *et al*. (2) who have observed that the pore sizes obtained by mercury porosimetry for 316L PSS supports from Mott are typically about an order of magnitude larger than the reported grade, which is determined by other criteria.

The mass of the samples increased following oxidation as indicated in Table 1. These increases in mass indicate the formation of oxide on the support surface and on the pore walls of the support. The increases in mass were relatively small and the composition of the oxide was not determined experimentally. Additionally, the the estimation of ΔP at process conditions does not require the estimation of pore size and porosity for the oxidized supports. For these reasons no effort was made to calculate change in pore size and porosity based on changes in sample mass.

Table 1. Mass increase following oxidations of PSS supports

Oxidation Temperature [°C]	Mass Increase [%]
400	0.12 ± 0.01
500	0.32 ± 0.04
600	1.21 ± 0.04

Figure 1 shows the helium flux J $[m^3/m^2\text{-}h]_{STP}$ before and after oxidation, over a range of trans-support pressure drops for a sample oxidized at 600 °C. There was an excellent linear fit between the flux J and the product of the trans-support pressure drop ΔP and the average of the upstream and downstream pressures P_M. This was typical of all the support samples studied and indicates that the He flux followed a viscous mechanism described by Darcy's law for compressible fluids (3), which may be expressed as follows:

$$\mathbf{J = (B/\eta RT)(\Delta PP_M/z) = m(\Delta PP_M/z)} \qquad \mathbf{(1)}$$

where B is a constant dependent on the geometry of the pore system, η is the viscosity of the gas, R is the gas constant and m is the slope of a plot of J versus ($\Delta PP_M/z$).

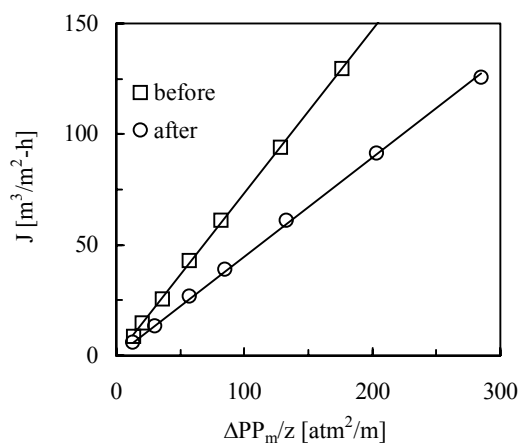

Figure 1. The He flux versus ($\Delta PP_m/z$) measured at 25°C for a PSS disk oxidized at 600°C for 6 hours. Excellent linear fits for these coordinates confirm Darcy's law behavior, m = (B/ηRT).

The effect of oxidation temperature on He permeability at 25°C may be seen in Figure 2. The permeability, indicated as the group (B/ηRT), decreases by 2, 14 and 40 % for oxidation temperatures of 400, 500 and 600°C respectively. This indicates an increase in support resistance with increasing oxidation temperature. To evaluate the significance of the loss in permeance at process conditions, the Darcy's law slope m_1 obtained with He at room temperature was used to predict the slope m_2 for H_2 at the process temperature.

$$\mathbf{m_2 = m_1(\eta_1 T_1/\eta_2 T_2)} \qquad \mathbf{(2)}$$

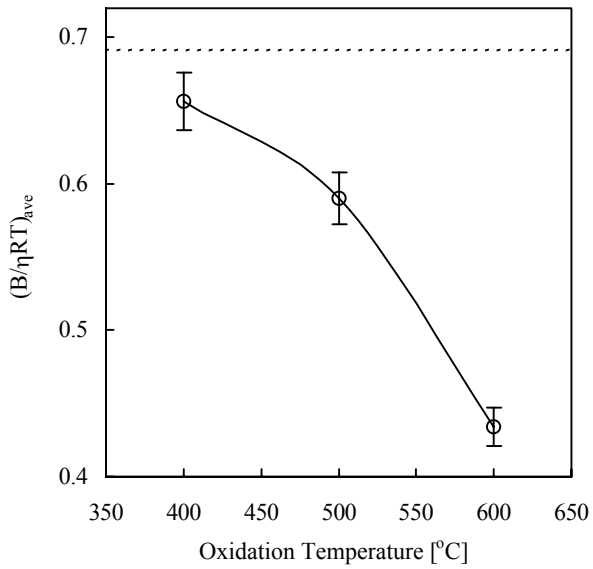

Figure 2. Average He permeability at 25°C $(B/\eta RT)_{ave}$ versus support oxidation temperature. The dashed line indicates the $(B/\eta RT)_{ave}$ for all nine supports before oxidation.

Equation 2 was used in conjunction with published data for the temperature dependence of the viscosities of He and H_2 (4). In this way an estimate for m_2 or $(B/\eta RT)$ was obtained for H_2 at 350°C for each of the oxidized supports. Based on previous results from this laboratory (2), a H_2 flux of 3 $[m^3/m^2\text{-}h]_{STP}$ could be expected from a membrane with a Pd layer thickness of about 30μm at total membrane pressure drop ΔP_T of 1 atm and an permeate side (tube side) absolute pressure P_P of 1 atm. This performance estimate is based on measurments using pure hydrogen on the retante side (shell side). Note that in the case of an actual membrane assembly the pressure drop across the support ΔP could not be determined directly from experimental data because the pressure at the interface between the Pd and the support could not be measured. However, with an estimated of m_2 at process conditions, the following equation may be solved for ΔP, if z, P_P and J are also known.

$$\mathbf{J = (m_2/2z)(\Delta P)(\Delta P + 2P_P)} \qquad \mathbf{(3)}$$

Figure 3 gives the estimates for the expected trans-support pressure drop for oxidized supports based on equation 3, and the realistic process conditions listed above. The predicted trans-support pressure drop for supports oxidized at 600 °C was 0.019 atm. This is nearly double the value expected for unoxidized supports. The total membrane pressure drop for this flux was 1 atm. The estimated support contributions to the total membrane pressure drop are 1.3, 1.4 and 1.9 % of the total membrane pressure drop for supports oxidized at 400, 500 and 600°C respectively. For applications where pure hydrogen is being obtained as a permeate stream from a Pd-PSS membrane module, the trans-support pressure drop provides a good measure of the resistance of the support. Based on these calculations even a 40% reduction of the permeability of the support will not have a significant impact on membrane performance.

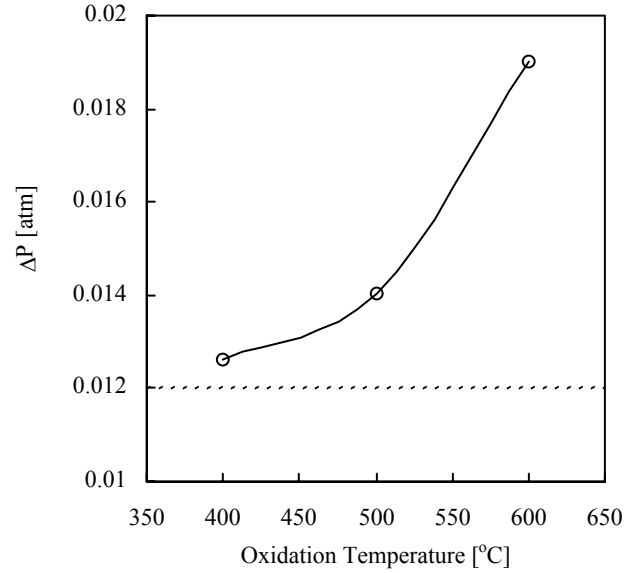

Figure 3. Predicted support pressure drop ΔP for typical hydrogen flux conditions (2). H_2 flux: 3 m^3/m^2-h, temperature: 350°C, total membrane ΔP_T: 1 atm. The dashed line indicates the expected behavior of unoxidized supports.

Conclusions

The He flux vs ΔP behavior of Mott 0.1μ grade 316L PSS supports follows Darcy's law before and after oxidation, over a wide range of flux values. Air oxidation treatments at 400, 500 and 600°C were effective in producing an oxide covering on the supports as indicated by the increasing mass and decreasing helium permeability of the supports after oxidation. The degree of oxidation increases dramatically for this support material at higher oxidation temperatures. At an oxidation temperature of 600°C the room temperature He permeability was decreased by 40%. While this represents a partial blockage of the pore system, the support contribution to the total membrane pressure drop was estimated to be only 1.9% under these conditions. This indicates that higher oxidation temperatures should not cause a significant increase in relative support resistance for applications where a pure hydrogen permeate is withdrawn from the membrane.

References

(1) Ma, Y.H.; Mardilovich, P.P.; & She, Y. *US Patent 6,152,987*, **2000**
(2) Mardilovich, I.P.; Engwall, E.; & Ma, Y.H. *Desalination*. **2002**, *144*, 85.
(3) Cunningham, R. E.; & Williams, R.J.J. In *Diffusion in Gases and Porous Media*; Plenum Press: New York, 1980; pp. 47-48.
(4) *Perry's Chemical Engineers' Handbook Sixth Edition*; Green D.W., Ed.; McGraw-Hill: New York, 1984; pp. 3-247.

CO_2 Remediation via O_2/CO_2 Combustion Utilizing an O_2 Permeable Membrane

Howard G. McIlvried
Massood Ramezan

Science Applications International Corporation
PO Box 18689
Pittsburgh, PA 15236-8689

Arun Bose

National Energy Technology Laboratory
U.S. Department of Energy
PO Box 10940
Pittsburgh, PA 15236-0940

Introduction

Electric power generation is a major CO_2 emitter in the United States; roughly one third of the United States' carbon emissions come from power plants. Since electricity generation is expected to grow and fossil fuels will continue to be the dominant fuel source, fossil fuel based power generation can be expected to produce even greater amounts of CO_2 in the future. Thus, if power generation is to be done in an environmentally acceptable way, new approaches that reduce emissions of CO_2 (including capture and sequestration) must be developed. One promising concept is the use of oxygen-based combustion, using recycled flue gas to moderate combustion temperature. This approach produces a concentrated CO_2 stream that is much easier to prepare for sequestration than a typical flue gas stream. This concept is further enhanced by using an efficient oxygen permeable membrane for the production of O_2 in place of a conventional cryogenic air separation unit (ASU).

In a typical pulverized coal (PC) fired boiler, flue gas is produced with a CO_2 content of about 15% at essentially atmospheric pressure. Thus, the driving force for absorption of CO_2 from such a stream is quite low, requiring the handling of large gas volumes in large equipment. The result is not only increased capital costs but a significant increase in parasitic power requirements and a consequent decrease in efficiency.

Oxygen Transport Membranes

One option for increasing the CO_2 content of the flue gas is to use pure oxygen for combustion. This eliminates most of the nitrogen, which is the major component of flue gas. However, because combustion in pure oxygen results in temperatures higher than existing materials of construction can withstand, it is necessary to recycle some of the CO_2 rich flue gas as a temperature moderator.

The major difficulty with oxygen combustion is supplying the necessary oxygen. Large volume oxygen is typically supplied by cryogenic air separation units. These units are big power consumers, requiring up to 20% of the gross power production, and can have a significant impact on unit efficiency. A promising alternative to a cryogenic ASU is the use of oxygen selective ion transport membranes (ITM).

ITMs are ceramic membranes that, at the proper temperature, are selective for the diffusion of oxygen. Oxygen disassociates at the high pressure side of the ITM and diffuses through the membrane as oxygen ions. These ions recombine into molecular oxygen at the low pressure side of the membrane. However, if there is a reactive material, such as a fuel, at the low pressure side, the oxygen atoms may react rather than recombine. This can result in very efficient combustion.

There are two major options for incorporating membrane oxygen production into an oxygen-fired combustion system. The first option is to build the membrane unit external to the furnace, similar to the situation with a cryogenic ASU. The other much more interesting option is to place the ITM membrane directly in the furnace. This has two advantages. First, as indicated above, membranes may increase combustion efficiency. The second reason is that membranes require a high temperature to operate, and since high temperatures exist in the furnace, that is a logical place to locate them.

This can conveniently be accomplished in a fluidized bed combustor because of its uniform temperature and its high heat and mass transfer capabilities. In a fluidized bed combustor, it would be easy to intersperse membrane tubes and steam generation tubes. A typical membrane reactor consists of a ceramic tube, with compressed air being passed through the tubes. Oxygen passes through the membrane to the shell side, and depleted air exits the tube.

Case Studies

Three cases for incorporating an ITM-based oxygen unit into a power plant were evaluated using an ASPEN process simulator: (1) a base case, (2) a case using recycled CO_2 as a sweep gas in the ITM oxygen unit, and (3) an all coal case.

Base Case

Figure 1 presents a block flow diagram of the base case. Compressed air is heated to a temperature suitable for a membrane oxygen separation unit (1560°F). Pure oxygen from this unit is mixed with cleaned recycle flue gas and used as the oxidant for combustion in a coal-fired boiler. The depleted air from the oxygen separation unit is sent to a gas turbine for power recovery, and the exhaust from the gas turbine goes through a heat recover steam generator (HRSG) to produce steam before it is vented to the atmosphere. The gross efficiency of the 273 MW_e cycle is approximately 31% (HHV). The flue gas is over 95 wt% CO_2 and can easily be prepared for sequestration.

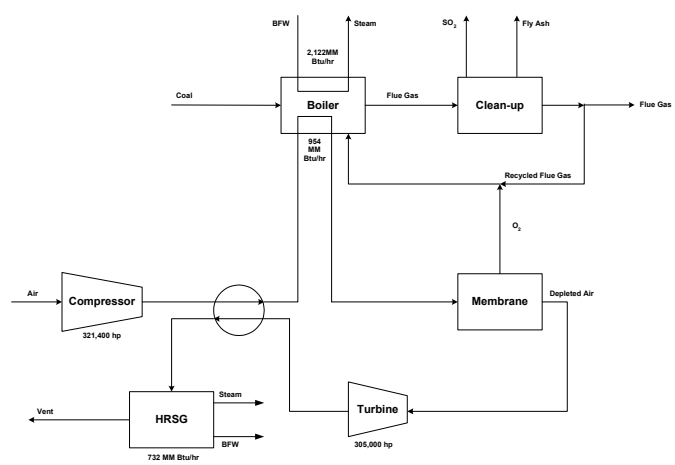

Figure 1. Block flow diagram for base case showing incorporation of an ITM oxygen unit with a PC fired boiler.

Case Using CO_2 Sweep Gas

This case, illustrated in Figure 2, is similar to the base case. The differences are that part of the recycled flue gas is heated in the furnace and utilized as a sweep gas in the membrane unit to reduce the partial pressure of oxygen and increase the oxygen flux in the

membrane separation unit and natural gas is used to increase the temperature of the depleted air which is then sent to an advanced gas turbine. The gross efficiency of this 491 MW_e cycle is approximately 36% (HHV).

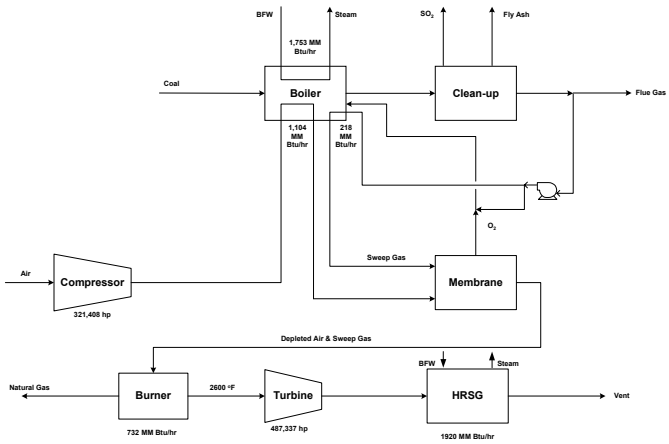

Figure 2. Block flow diagram for case showing utilization of a sweep gas to increase oxygen permeation rate.

All Coal Case

This case, as illustrated in Figure 3, is similar to the previous case, except that the depleted air gas turbine working fluid is heated inside the boiler, similar to a high temperature air furnace (HITAF) rather than using a natural gas burner. The gross efficiency of this 285 MW_e cycle is approximately 32% (HHV).

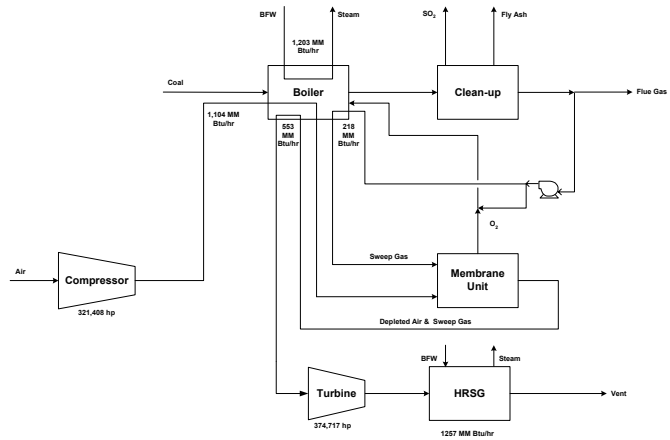

Figure 3. Block flow diagram for case utilizing coal as the only fuel.

Discussion

These preliminary case studies have shown considerable promise for the concept of using oxygen permeable membranes as a source of oxygen for coal combustion. Although these case studies did not include CO_2 sequestration, it is clear that a significant improvement in efficiency will result from sequestering the high concentration CO_2 stream from these cases compared to the low concentration CO_2 flue gas from a conventional pulverized coal fired boiler. After sulfur oxides removal from the flue gas, about all that will be required to prepare for CO_2 sequestration is drying, oxygen separation, and compression.

Theoretical Study on the Hydrogen Absorption Behavior of Palladium and its Alloys

Hitoshi Kurokawa [1], Yuhsuke Makino [1], Mutsumi Takahasi [1], Akira Endou [1], Seiichi Takami [1], Momoji Kubo [1], Naotsugu Itoh [2], Parasuraman Selvam [3], and Akira Miyamoto [1, 3]

[1] Department of Materials Chemistry,
Graduate School of Engineering, Tohoku University,
Aoba-yama 07, Sendai 980-8579, Japan

[2] Catalysis & Membrane Systems Group,
National Institute of Advanced Industrial Science and Technology,
AIST Tsukuba Central 5, Tsukuba, Ibaraki 305-8565, Japan

[3] New Industry Creation Hatchery Center, Tohoku University,
Aoba-yama 04, Sendai 980-8579, Japan

Introduction

Historically, the Pd-H system is a model system to study the most common regularities of hydrogen interaction with metals, and that the hydrogen separating capability of Pd and its alloy membranes is well known. Further, these membranes show very high selectivity for the permeation of hydrogen. Other applications include hydrogenation and dehydrogenation reactions, recovery, purification, and storage of hydrogen, hydrogen sensor, etc. [1-5]. The alloys of Pd, e.g., Pd-Ag, Pd-Cu, Pd-Au, etc., posses certain important characteristics, which may alleviate some of the shortcomings of pure Pd by lowering the β-hydride phase formation temperature and membrane cost as well as increasing the permeability of hydrogen as well as the mechanical properties. In the past, a great deal of experimental work has been carried out about the solubility and diffusivity of hydrogen in bulk materials. Nevertheless, the theoretical studies are interesting from a basic viewpoint. It is, in this context, the understanding of the metal/alloy-hydrogen systems, at the atomic level, is of paramount importance with respect to the development of membrane reactor, hydrogen recovery from petrochemical plants, fuel cell technologies and hydrogen storage systems.

In recent years, computational chemistry has become a powerful tool to design and develop new materials as well as to understand the mechanism of the interactions for the various processes at the atomistic level by taking the advantage of the tremendous progress made on both the theory and the computation spend. Several theoretical methods such as molecular dynamics (MD), Monte-Carlo (MC), quantum chemical calculation, etc. have been employed to extract information at the atomic and molecular scale. The first-principles calculations based on the density functional theory (DFT) have been performed for Pd-Ag-H system in order to understand the properties like the energetics of the hydrogen absorption, the energetic preference of hydrogen absorption site, equilibrium lattice constant, etc. [6]. Romanowski et al. [7] have also studied the interaction between hydrogen and transition metals and their alloys by DFT. Although, the first-principles calculations are quite useful to investigate the metal-hydrogen systems due to its accuracy and reliability, it may, however, force us to use extremely small cluster systems owing to the exorbitant computation time. Thus, it is not attractive for the real systems involving larger models such as the simulation of the storage processes of metal/alloy-hydrogen systems. Thus, a large-scale simulation method is imperative to elucidate the absorption behavior of hydrogen into the pure metals and their alloys.

In a previous study [8], we reported the successful development and demonstration of the new MC program for the hydrogen absorption characteristics of pure Pd and Pd-Ag alloys. The results were in good agreement with the experimental as well as the first-principles studies. In the present investigation, we further extend the study of the hydrogen absorption behavior of Pd-Ti and Pd-Cr alloys using MC program [8].

Computational Details

Monte-Carlo (MC) Method

The equilibrium absorption of hydrogen in metals and alloys may be calculated by the grand-cannonical Monte-Carlo (GCMC) method, employing our originally developed GCMC simulator "MONTA" [9]. However, the conventional as well the GCMC cannot treat the dissociative adsorption of hydrogen molecule and the subsequent absorption process. On the other hand, we have improved our GCMC program [8], in order to perform MC simulation, which takes into account of both the dissociation adsorption of hydrogen molecule and consequent absorption characteristics in metal/alloy-hydrogen systems.

Models, inteatomic potentials

As for the models of Pd and its alloys are concerned, a 4 × 4 × 4 super-cell having fcc structure and a lattice constant of 3.89 Å was considered. In the case of Pd metal, we used 256 atoms model. However, accurate atomistic models for Pd-Ti and Pd-Cr alloys may be difficult to consider, in particular the position of metal atoms in the unit cell. However, they can be modeled by partial substitution of Pd by Ti or Cr in the lattice. As a first step of the atomistic simulation using GCMC method, the effect of both the expansion of the unit cell and the strain in atomic level around the absorbed hydrogen atoms were ignored. The interatomic potentials are estimated by the Morse-type two-body potential function, which is described as:

$$U_{ij} = D\left[x^2 - 2x\right]$$

$$x = \exp\left[-\frac{\gamma}{2}\left(\frac{r_{ij}}{r_e} - 1\right)\right]$$

where r is the interatomic distance, D is the well depth, r_e is the equilibrium interatomic distance, and γ is the parameter, which determines the effective range of the potential. The interaction between hydrogen atoms is the almost repulsive one.

Solubility based on Sieverts' law

In order to evaluate the solubility of hydrogen in metals, we used the Sieverts' law, as described below:

$$\sqrt{\frac{p}{p^0}} = K_s x$$

$$\ln K_s = -\frac{\Delta S_s}{R} + \frac{\Delta H_s}{RT}$$

where p, p^0, K_s, ΔS_s, ΔH_s, and R are the hydrogen pressure, the standard pressure, the Sieverts' constant, the solution entropy of hydrogen, the solution enthalpy of hydrogen, and the gas constant, respectively.

Results and discussion

Parameter fitting

In order to determine the parameters for the interatomic potentials, we attempted to reproduce the solubility of the hydrogen in pure metals such as Pd [8], Ag [8], Ti, and Cr with a hydrogen pressure of 0.1 MPa, and the results are depicted in Figure 1. From this figure, it clear that the calculated values, by our improved GCMC program, for the hydrogen solubility in pure metals are in

excellent agreement with those obtained by Sieverts' law. Further, ΔH_s values were also calculated from the temperature dependent solubility of hydrogen, and ΔH_s were deduced from this data for the various metal-hydrogen systems. The computed ΔH_s values for the various system, viz., Pd, Ag, Ti, and Cr are – 9.5 [8], 67.7 [8], – 50, and 56.8 kJ / mol H, respectively. The corresponding experimental values are –10, 68, – 53, and 58 kJ / mol H, respectively. These results strongly indicate that the parameters employed for the interatomic potential functions are valid and hence they can be used for the MC simulation on the absorption of hydrogen in metal/alloy systems. The various parameters determined in this study are listed in the Table 1.

Table 1. Parameters for the Morse-type two-body potential function.

Atom pair	D [kJ / mol]	r_e [Å]	γ [Å^{-1}]
H-H	0.1848	2.886	11.429
H-Pd	17.3000	1.940	4.300
H-Ti	26.1000	2.069	5.000
H-Cr	12.5000	1.610	3.390

Hydrogen absorption in Pd alloys

In our previous study [8], we have investigated the energetic characteristics of Pd metal and Pd-Ag alloy towards hydrogen absorption. It was found that the most (energetically) favorable site for the hydrogen location is octahedral site in Pd lattice, which clearly reproduces the experimental results [1] as well as the theoretical findings using first-principles calculations [6]. Thus, the above studies clearly reveal that our improved GCMC simulator can perform the simulation of hydrogen absorption behavior and that the method can very well be extended to other Pd alloy-hydrogen systems. Therefore, in the present study, we investigate the hydrogen absorption characteristics of Pd-Ti and Pd-Cr alloys with 5 atom % of the dopant, i.e., $Pd_{0.95}Ti_{0.05}$ and $Pd_{0.95}Cr_{0.05}$. The conditions of GCMC simulation, viz., temperature and hydrogen pressure are set to 473 K and 0.1 MPa, respectively.

Figure 2 shows the integrated coordination number of hydrogen atoms absorbed in Pd-Ti alloy system. It is clear from this figure that the integrated coordination number of H-Ti system is close to 1. On the other hand, it almost 5 for H-Pd. These results suggest that the majority of hydrogen atoms absorbed into the octahedral sites consisting of at least one Ti atom. On the other hand, the integrated coordination number in H-Cr is practically zero (the figure is not reproduced here) and the integrated coordination number in H-Pd is 6. These results indicate that the hydrogen atoms tend to avoid Cr containing octahedral sites in the lattice. Our findings on the hydrogen absorption behavior of Pd-Ti and Pd-Cr alloys are clearly in line with their observation Berlag et al. [10]. They have suggested that when the alloying metals have a higher hydrogen solubility compared to Pd, they act as 'traps' for hydrogen in the Pd matrix. However, further investigations for various kinds of Pd-based alloys are required to understand clearly the various complicated phenomena in the hydrogen absorption behavior in metals and alloys. Such studies are currently in progress.

Conclusions

The hydrogen absorption behavior of Pd and its alloys, viz., Pd-Ti and Pd-Cr, were studied by GCMC simulator. The simulations were conducted at 473 K under the H_2 pressure of 0.1 MPa. The parameters for the Morse-type two-body potential function used here were determined so as to reproduce the solution enthalpy of hydrogen in pure metals. The present results suggest the different roles of Ti and Cr in Pd alloys with respect to the hydrogen absorption characteristics. Further work will be helpful in order to understand and design new alloy materials so as to achieve higher performance on the storage of hydrogen.

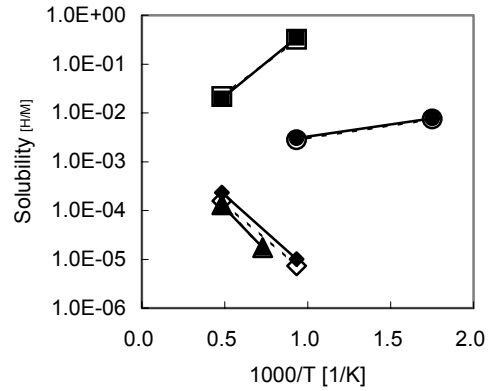

Figure 1. Solubility of hydrogen into the pure metals (○,●: Pd; △,▲: Ag; ◇,◆: Cr; □,■ : Ti). Open symbols: Sieverts' law; Filled symbols: MC simulation (this work).

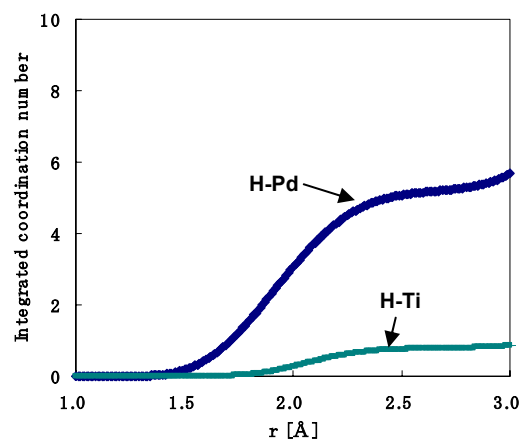

Figure 2. Relation between integrated coordination number and interatomic distances in Pd-H and Ti-H systems.

References

(1) Alefeld, G.; Völkl, J. *Hydrogen in Metals I. Basic Properties*, Springer-Verlag, Berlin, 1978.
(2) Alefeld, G.; Völkl, J. *Hydrogen in Metals II. Application-oriented Properties*, Springer-Verlag, Berlin, 1978.
(3) Wipf, *H. Hydrogen in Metals III. Properties and Applications*, Springer-Verlag, Berlin, 1997.
(4) Fukai, Y. *The metal-hydrogen system*, Springer-Verlag, Berlin, 1993.
(5) Lewis, F. A. *The Palladiumu Hydrogen System*, Academic Press, London, 1967.
(6) Løvvik, O. M.; Olsen R. A. *J. Alloys Comp.* **2002**, *330-332*, 332.
(7) Romanowski, S.; Bartczak,, W. M.; Wesolkowski, R. *Langmuir* **1999**, 15, 5773.
(8) Kurokawa, H.; Nakayama, T.; Kobayashi, Y.; Suzuki, K.; Takahashi, M.; Takami, S.; Kubo, M.; Itoh, N.; Miyamoto, A. submitted to *Catal. Today.*
(9) Hirotani, A.; Mizukami, K.; Miura, R.; Takaba, H.; Miya, T.; Fahmi, A.; Stirling, A.; Kubo, M.; Miyamoto, A. *Appl. Surf. Sci.* **1997**, 120, 81.
(10) Berlag, H.; Opara, L.; Züchner, H. *J. Alloys Comp.* **2002**, *330-332*, 434.

An Overview of the U.S. Department of Energy's Gasification Technologies Program

Gary J. Stiegel
National Energy Technology Laboratory
U.S. Department of Energy
P.O. Box 10940
Pittsburgh, PA 15236

Massood Ramezan
Science Applications International Corporation
P.O. Box 18689
Pittsburgh, PA 15236

Introduction

Coal gasification is a well-proven technology that started with the production of coal gas for urban areas, progressed to the production of fuels, chemicals, and most recently to large-scale power generation. More than 160 commercial gasification plants (equivalent to nearly 61,000 MW_{th} syngas capacity) are currently in operation, under construction, or in planning and design stages in 28 countries worldwide.

Gasification-based technologies can be used to convert coal or other carbon-containing resources into a clean gas with high value as a fuel for combined cycle power generation or as a feedstock for the production of liquid fuels and chemicals. Moreover, these systems have the advantage of being capable of co-generating electricity and fuel/chemical efficiently, economically, and in an environmentally acceptable manner. Environmental performance of these systems can be tailored to any specific requirements. In addition, due to the high efficiency nature of these plants, the emissions of CO_2 are inherently low. The DOE Gasification Technologies Program hasa history of success in technology development and demonstration. The R&D portfolio of today's program will enable deployment of the clean and affordable energy systems required for growing energy markets.

Program Drivers and Goals

The nation's energy mix is dependent primarily on fossil energy. According to the public- and private-sector forecasts, the nation's electricity and transportation fuels will continue to be fossil-fuel based for the next 20 years — and well beyond. This continued use, however, must be matched by combining energy availability at reasonable prices with increasingly clean environmental performance throughout the energy life cycle of production, conversion, and end-use. In the foreseeable future, the cornerstone of our energy will remain fossil-fuel based, but it will be cleaner and sustainable.

Goals for Growing Markets

To capture the opportunity for broad public benefits — and to enable market development for gasification technologies — the program focuses on process efficiency, environmental performance, and plant economics. The program goals are:

- near-zero emissions
- feedstock flexibility
- multiple, high-value products
- efficiency greater than 60% by 2015
- cost competitive

Related technical objectives such as modularity and standardization of plant design, improved plant availability and the capability for CO_2 capture will help make gasification the choice for a range of markets. Achieving these goals can provide the clean, secure, and affordable energy the nation requires.

The Gasification Process

Gasification utilizes virtually any carbon-containing material to produce a gaseous product "syngas". This syngas (made up primarily of H_2 and CO) can be used in many ways, including the production of electricity, chemicals, fuels, hydrogen, and as a source of substitute natural gas. Possible feedstocks include coal, petroleum coke and other residue from petroleum processes, biomass, and municipal and industrial waste. The feedstock enters the gasifier, where it encounters steam and oxygen at high temperatures and pressures. These conditions cause the feedstock to be broken down into syngas and a solid ash/slag product. The ash/salg is removed from the bottom of the gasifier while the syngas enters a purification system. Gas cleaning removes impurities including sulfur, particulates, and related products, the majority of which are saleable by-products. Additional separation units can recover H_2 and remove CO_2. While gasification systems are not new, most applications have focused on single products, generally electric power or chemicals. For a new generation of gasification systems, the program strategy is to enhance the flexibility of gasification in meeting new and growing markets. Achieving a combination of improvements in process efficiency, economics, and environmental performance will enable gasification to be the preferred technology in a wide range of markets. Figure 1 depicts a simplified flow chart illustrating gasification-based energy conversion options.

Program Technology Areas

The program implements strategic, time-phased R&D such as: lower-cost, lower-risk technologies to improve the economic environmental performance of existing systems by 2005, advanced technologies for a new generation of gasification systems by 2010, and advanced integrated energy plants by 2015. The program is currently structured in five technology areas:

1) **advanced gasification –** To further develop fuel flexibility, higher efficiency and reliability, and improved economic and environmental performance. Advances in the gasifier itself to enhance efficiency, reliability and feedstock flexibility and economics are crucial for gasification system improvements. Research is being conducted on advanced gasifiers, such as the transport gasifier, so higher performance goals can be reached and the variety of possible feedstocks can be further expanded. Advanced refractory materials and new process instrumentation are being developed to improve system reliability and availability, operational control, and overall system performance. Studies of alternative feedstocks (biomass and waste from refineries, industries, and municipalities) will improve gasifier flexibility and utility. Data from fluid dynamic models are being used to develop and improve advanced gasifiers. Promising developments will be tested and evaluated in large demonstration and/or commercial-scale gasifiers.
2) **gas cleaning and conditioning** – To evaluate novel concepts to meet rigid syngas quality specifications for fuel cells and catalytic conversion processes. In the gas cleaning and conditioning area, the goal is to achieve near-zero emissions while simultaneously reducing capital and operating costs. Novel gas cleaning and conditioning technologies are undergoing development to reach this goal. Processes that operate at mild to high temperatures and incorporate multi-contaminant control to parts-per-billion levels are being explored. These include process for trace metals, H_2S, HCl, and particulates removal; membrane processes for control of H_2S and CO_2; and sorbents for NH_3 control. Both ceramic and

metallic filters are being assessed for particulate control. Promising technologies will be scaled-up and integrated into existing demonstration facilities. Furthermore, investigation of technologies for mercury removal is currently underway.

3) **advanced gas separation** – To investigate alternatives to energy intensive separation methods, such as cryogenic separation. Advanced gas separation research offers the potential for substantial improvement in environmental and cost performance. These technologies will also enhance process efficiency. A major program objective is the development of cost-effective air-separation membranes. These can provide substantial cost reduction for oxygen production compared to conventional cryogenic methods. Improved hydrogen recovery and CO_2 removal are also important. Currently, the program is developing high-temperature ceramic membranes for hydrogen recovery from gas streams, as well as low-temperature approaches to recovery and removal. Other novel approaches for H_2, CO_2, and O_2 separation will be investigated under different operating conditions.
4) **product and by-product utilization** – To enhance project revenues and eliminate waste streams. The economics of gasification can be improved by fully utilizing all outlet streams of the process. Sale of value-added by-products from waste streams and minimization of waste disposal can substantially improve the economics of gasification processes. By-products include pressurized CO_2 ash/slag, sulfur and/or sulfuric acid, and ammonia. Program activity seeks to expand market options, such as improving the quality of slags and improving the use of sulfur. The program is developing a bench-scale demonstration of a direct sulfur-reduction process. The development of advanced concepts for warm-gas desulfurization technology are targeted as well as a one-step process for elemental sulfur. Methodology is also being developed to produce a lightweight aggregate from gasification ash.
5) **Systems Analysis/Technology Integration -** To achieve improvements in plant economics. The Systems Analysis/Technology Integration area targets integration of all relevant gasification technologies, regardless of the end products. Economic analyses, performance assessments, and market studies provide guidance for future R&D and deployment opportunities. Barriers to deployment are identified and system performance targets are developed. Studies are conducted on topics such as novel warm gas cleaning, membrane-based separation, and co-feeding applications. Also, product outreach activity focuses on the public benefits of gasification today and in the future. Stakeholders include the public, industry officials, environmental groups, and local, state, and Federal legislators and regulators. Efforts are underway through industry stakeholders to identify technology and environmental issues, and to facilitate commercialization.

The Clean Coal Projects

First-generation Integrated Gasification Combined Cycle (IGCC) plants have demonstrated the efficiency and environmental performance benefits. Working with a broad range of industrial, university, and national laboratory stakeholders, the program will establish the technology capability to expand the success to a new generation of technology that will serve broader markets - power, chemicals, hydrogen, and steam - with improved economics.

- **The Wabash River Coal Gasification Repowering Project** located in Vigo County, Indiana was the first full-size commercial gasification combined cycle plant built in the U.S. that repowered an existing pulverized coal plant. It is one of the world's largest single train gasification combined cycle plants operating commercially.
- **The Tampa Electric Polk Station Project** located in Polk County, Florida is the Nation's first "Greenfield" commercial gasification combined cycle power station. The power plant is one of the world's cleanest. The plant's gas cleaning technology removes more than 98% of the sulfur in coal, converting it to a commercial product. Nitrogen oxide emissions are reduced by more than 90%.
- **The Kentucky Pioneer Energy IGCC Demonstration Project** located in Clark County, Kentucky is currently in design phase with construction start up scheduled for 2003. This plant will demonstrate and assess the reliability, availability, and maintainability of utility-scale IGCC systems. It will use a high-sulfur bituminous coal and municipal solid waste blend in an oxygen-blown, slagging gasifier.
- **The Air Products' Liquid Phase Methanol Project** located in Sullivan County, Tennessee has successfully demonstrated the production of methanol from coal gas at commercial scale. The methanol can be used directly as a fuel product or as an intermediary for a wide range of petrochemical products.

Technical Successes

The program builds on this history of success by producing results that will enable clean, affordable energy systems. Improvements in gasifier design and efficiency, in gas-stream cleanup and by-product quality, and in systems integration will provide both enhanced environmental performance and process economics. Recent successes in the R&D program point to the future deployment of new technologies for both current and new markets.

- ***Air Separation Membranes*** Recent process analyses on a variety of gasification-based processes continue to show significant cost and efficiency advantages with the application of high-temperature membranes for oxygen production compared to conventional cryogenic technology.
- ***Hydrogen Production From Coal Gasification*** New technology using ceramic membranes are being developed that have increased the hydrogen permeation rates of dense ceramic membranes at high temperature by over an order of magnitude.
- ***Coal-Based Hydrogen Production and CO2 Capture Technology*** The feasibility of separating CO_2 and hydrogen from coal-derived shifted synthesis gas has been confirmed in laboratory testing of the CO_2 hydrate process.
- ***Gasification Design Optimization*** The application of value engineering to the design of gasification-based processes resulted in the identification ideas that had potential for significant capital and O&M cost savings. Furthermore, significant strides have been made toward successful demonstration in of oxygen-blown gasification using the transport gasifier at the Power Systems Development Facility in Wilsonville, Alabama.
- ***Advanced Materials to Enhance Gasifier Reliability*** A new slag resistant refractory material has been developed that has potential for increasing the lifetime by five to ten times that of current refractories.
- ***Advanced Gas Cleaning Technology*** A novel gas cleaning technology developed to achieve ultra-low levels of emissions. The technology has shown potential to achieve sulfur levels of <1 ppm in the fuel gas to the gas turbine at capital costs of much below than that of existing commercial technologies.
- ***Co-Production of Electricity and Fuels*** Industrial teams are currently assessing the technical and economic feasibility of co-producing electricity and fuels from coal. A low heating value

coal-derived gas, representative of the fuel gas expected to be produced in a co-production process, has been successfully combusted in a GE 6FA turbine.

Clean, Affordable Energy Options for the Future

New markets are emerging that will benefit significantly from the flexibility, environmental improvements, economic successes, and efficiency of gasification. Two examples of emerging markets are repowering, and multi-production.

- **Repowering of existing coal plants** As demand for power production increases, the nation's coal plants — the heart of stable and affordable electric power in the United States — face the need for ever-cleaner power production. Repowering of these plants with gasification can offer major benefits: improved environmental performance, reduced capital investment, feedstock flexibility, and capacity increases due to improved process efficiency. Also, gasification can be used to repower existing gas-fired facilities. A gasifier placed upstream of existing natural-gas-fired turbines can provide an alternative to natural gas with long-term price stability.
- **Multi-production facilities for industry** Feedstock and product options will become increasingly important as the nation continues to make the difficult transition from a regulated environment to one having market-based energy options. Gasification offers the most flexible route to using variable feedstocks and producing electric power, fuels, hydrogen, chemicals, or steam. Feedstock flexibility, with feedstocks that include coal, biomass, petroleum "bottoms" (coke and residuum), and waste materials, will ensure that stable, low-cost fuel sources are available. The ability to vary the product slate will both improve plant economics *and* support market stability.

Gasification: Technology of Choice for Markets Today and Tomorrow

Markets and market drivers are changing at a rapid pace. Environmental performance is a greater factor as emission standards tighten and market growth occurs in areas where total allowable emissions are capped. Also, reduction of carbon dioxide emissions is one of the challenges in response to global climate change. Industries have expressed a need for more environmentally sound processes, more efficient and reliable systems, and an ever-present demand for higher profitability. They need a technology that can match these requirements — a means to remain flexible, reduce risk, decrease emissions, increase stockholder return on investment, and consume fewer resources. Gasification is the technology that can meet these requirements. Today, the majority of existing applications have been geared toward the production of a single product or a constant ratio of two or more products per facility. Tomorrow, the potential of gasification in expanding markets is in its use of low-cost and blended feedstocks and its multiproduct flexibility. With deregulation, rapidly changing market demands, fluctuation in natural-gas prices, and increased environmental concerns, gasification will become the cornerstone technology for market flexibility.

For more information visit
http://www.netl.doe.gov/coalpower/gasification/

Figure 1. GASIFICATION-BASED ENERGY CONVERSION SYSTEM CONCEPTS

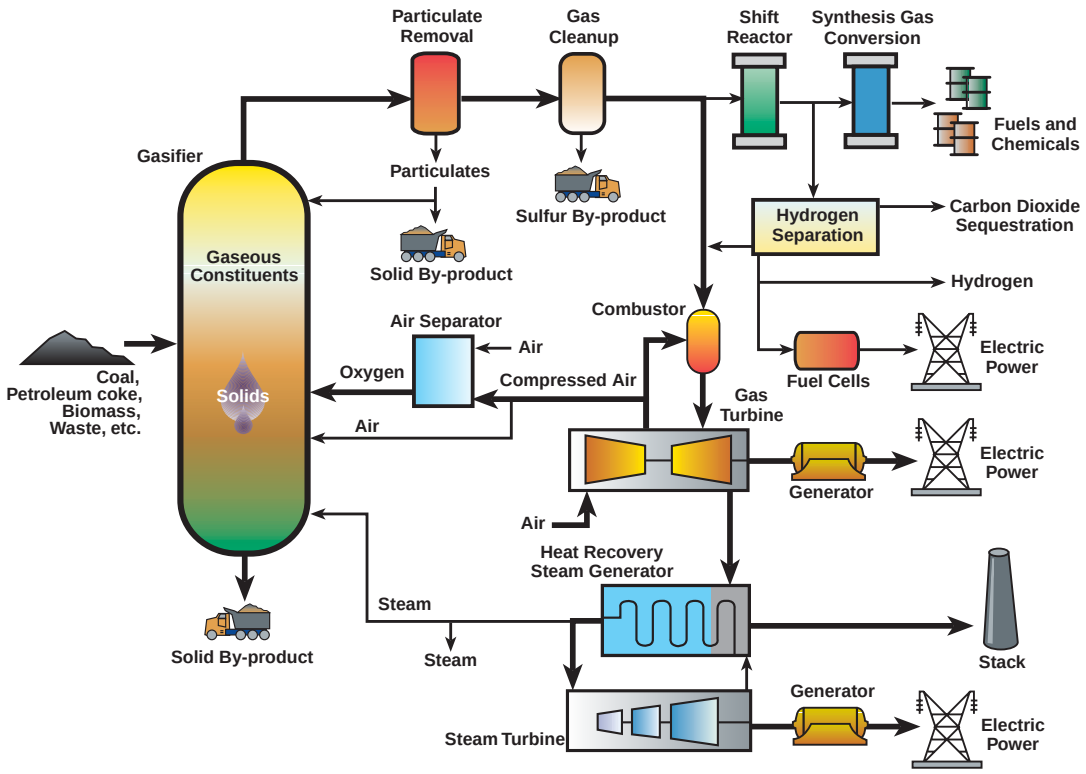

Role of Water Vapor in Oxidative Decomposition of Calcium Sulfide

Shengji Wu, Md.A.Uddin, Shinsuke Nagamine and Eiji Sasaoka

Faculty of Environmental Science and Technology
Okayama University
3-1-1Tsusima-naka Okayam
700-8530 Japan

Introduction

Limestone is very important material as a high-temperature desulfurization sorbent: limestone is used in coal gasifiers for the in-bed removal of H_2S.

In gasifiers of coal, decomposition of limestone into CaO and CO_2 depend on the concentration and /or pressure of CO_2 and the temperature. Therefore, two sulfation reactions have to be considered:

$$CaO + H_2S = CaS + H_2O \quad (1)$$

$$CaCO_3 + H_2S = CaS + H_2O + CO_2 \quad (2)$$

The products CaS has to be converted to $CaSO_4$ before disposal because H_2S is released from the reaction between CaS and Water.[1] The conversion of CaS to $CaSO_4$ is expressed as follows:

$$CaS + (3/2)\ O_2 = CaO + SO_2 \quad (3)$$

$$CaO + SO_2 + (1/2)O_2 = CaSO_4 \quad (4)$$

The molar volume ratio of CaS to $CaSO_4$ in eqs 3 and 4 is ca.1.6/1. This large volume change induces the plugging of the intraparticle pore of CaS if the pore size is not sufficiently large. If a layer of $CaSO_4$ covers the outside of the CaS particle, then CaS is not converted to $CaSO_4$ until the $CaSO_4$ decomposes into CaO , SO_2 and O_2 at a high-temperature.

We have found a method with acetic acid for the preparation for a highly active macroporous lime. The macroporous CaS formed from the macroporous lime was easily converted to $CaSO_4$ and CaO. However, the CaS formed from natural lime to $CaSO_4$ was partially converted to $CaSO_4$ and CaO because only small amount of pore were present in the CaS sample.[2,3]

To find out a method for perfect conversion of CaS formed from a natural lime to $CaSO_4$, the basic characters of the oxidative decomposition of CaS were examined using reagent grade CaS. The decompositions of CaS were examined in the presence of H_2O because hot combustion gas containing moisture is usually used for the decomposition of CaS. The main purpose of this study is to clarify the role of H_2O in the oxidative decomposition of CaS.

Experimental

CaS Samples. Pure CaS powder (average diameter: < 325 micro meter, purity: >99 %) was obtained from Soekawa Chemicals. Cylindrical pellets were formed from the CaS powder by pressing using a cylindrical die. The pellets were crushed and sieved to the two size sample particles (average diameter: 2.0mm and 0.2mm). The pore size distribution of the sample measured by mercury penetration porosimeter showed that the main pore size was around 1micro meter

Apparatus and Procedure. The oxidative decomposition of CaS were carried out using a flow-type thermogravimetric apparatus under atmospheric pressure. About 60mg sample particles (2.0mm dia.) was set in a net sample holder. The reaction temperatures examined were 800, 900 and 1000°C. The reaction commenced when a mixture of (0-10%)O_2, (0-52.8%) H_2O, and N_2 (balance gas) was fed into the reactor at 500cm^{3}STP/min. Weight gain of the sample during the reaction was measured by the balance and also the amount of SO_2 evolved during the reaction was measured by a wet-type absorption method (Arsenazo III). The composition of the oxidized sample was calculated from the weight gain and the amount of the evolved SO_2.

Experiments Using Tracer $H_2{}^{18}O$. To clarify the role of H_2O in the oxidative decomposition of CaS with O_2, $H_2{}^{18}O$ (purity: ca.95%) was used instead of $H_2{}^{16}O$. The experiments using the $H_2{}^{18}O$ were carried out using a micro-reactor system equipped with a small U tube reactor. The concentrations of $S^{16}O_2$, $S^{16}O^{18}O$ and $S^{18}O_2$ in the outlet gas from the sample (0.2mm dia.) were continuously monitored by a quadrupole mass spectrometer.

Results and Discussion

Effect of H_2O on the Rate of the Decomposition of CaS. Figure 1 shows typical weight gains of the samples both in the absence and presence of H_2O at 900°C. **Figure 2** shows the compositions of the samples after the oxidation in Figure 1. it is evident that the presence of H_2O drastically accelerates the decomposition of CaS with O_2. A similar results were obtained in the experiment at 800°C. However, at 1000°C, the acceleration by H_2O was not clearly observed.

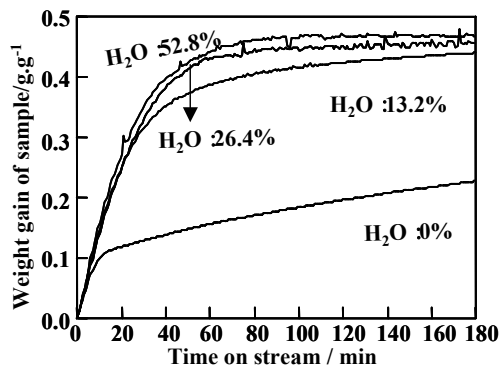

Figure 1. Effects of the concentration of H_2O on the oxidative decomposition of CaS. Temp.900°C; O_2: 1%.

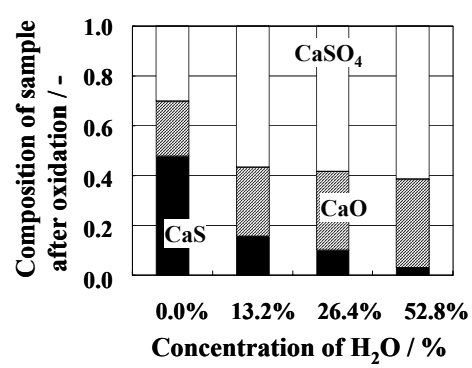

Figure 2. Composition of the samples after the oxidation

Reaction between CaS and H_2O. The reactivity of CaS with H_2O was examined in the temperature range from 800 to 1000°C in the absence of oxygen. From this experiments, it was confirmed that CaS directly reacted with H_2O and formed CaO, SO_2 and H_2 according to the following reaction.

$$CaS + 3H_2O = CaO + SO_2 + 3H_2 \quad (5)$$

In order to know the temperature zone in which the reactions of eq 5 and 3 occur, the temperature programmed reaction (TPR) spectra were measured in 3 systems: system (a): 10%H_2O-He; system (b): 1%O_2-He; system (c): 10%H_2O-1%O_2-He. **Figure 3** shows the evolution of SO_2 during the TPRs. The reaction of eq 5 occurred almost at the same temperature zone. The evolution of SO_2 in the system (c) indicated that there is a synergistic effect of H_2O and O_2 on the oxidative decomposition of CaS.

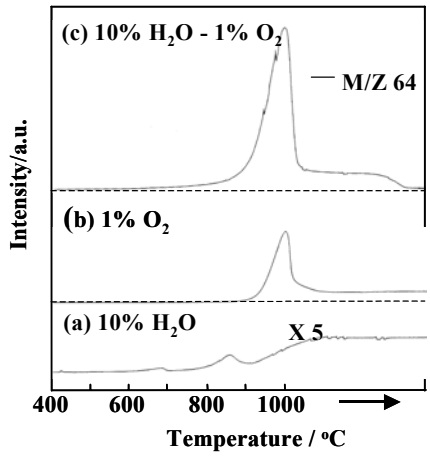

Figure 3. Evolution of sulfur dioxide during the TPR

Role of H_2O in the Oxidative Decomposition of CaS. To clarify the role of H_2O in the oxidative decomposition of CaS with O_2, $H_2{}^{18}O$ was used instead of $H_2{}^{16}O$. **Figure 4** shows the evolution of $S^{18}O_2$, $S^{16}O^{18}O$, and $S^{16}O_2$, during the constant- temperature-decomposition of CaS in the 1000°C in system (c). In this system, $S^{18}O_2$, $S^{18}O^{16}O$, $S^{16}O_2$ evolved from the sample. As the amount of the evolved $S^{18}O_2$ was highest in the three species, it was confirmed that the following reactions mainly occurred.

$$CaS + 3H_2{}^{18}O = Ca^{18}O + S^{18}O_2 + 3H_2 \quad (6)$$
$$CaS + 2\,H_2{}^{18}O + (1/2)^{16}O_2 = Ca^{16}O + S^{18}O^2 + 2H_2 \quad (7)$$

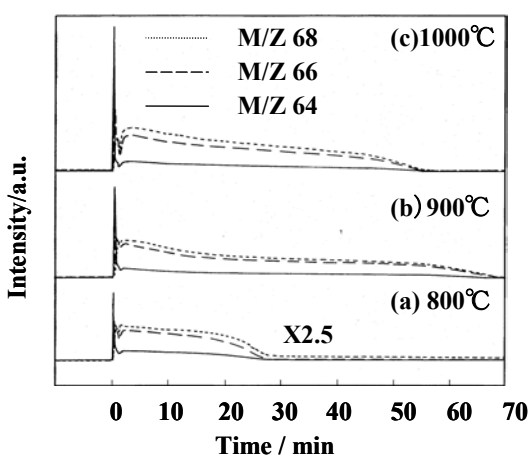

Figure 4. Evolution of sulfur dioxide from CaS in the presence of both $^{16}O_2$ (1%) and $H_2{}^{18}O$(10%).

As these reactions are thermo-dynamically unfavorable, the following reaction followed the reactions of eqs 6 and 7.

$$H_2 + (1/2)^{16}O_2 = H_2{}^{16}O \quad (8)$$

$S^{18}O^{16}O$ might be formed via the following reactions:

$$CaS + 2H_2{}^{18}O + (1/2)^{16}O_2 = Ca^{18}O + S^{16}O^{18}O + 2H_2 \quad (9)$$
$$CaS + 2H_2{}^{18}O + H_2{}^{16}O = Ca^{18}O + S^{16}O^{18}O + 3H_2 \quad (10)$$
$$CaS + {}^{16}O_2 + H_2{}^{18}O = Ca^{16}O + S^{16}O^{18}O + 2H_2 \quad (11)$$

The following reaction was not main reaction in the system (c)

$$CaS + (3/2)^{16}O_2 = Ca^{16}O + S^{16}O_2 \quad (12)$$

Furthermore, reaction of eq 8 might radically occur because the temperature was high enough for the radical reaction in that case OH radical might play an important role in the reactions.

The reaction mechanism seems to be complex. However, the formation of $S^{18}O^{16}O$ clearly indicates that the oxidation of CaS occurs stepwise. Unfortunately, the amount of the evolved S^xO^yO could not be quantitatively analyzed by our mass spectrometer. The ratio of [S^xO^yO] to Total [S^xO^yO] (where S^xO^yO is either $S^{18}O_2$ or $S^{16}O^{18}O$ or $S^{16}O_2$ species and Total [S^xO^yO] = $S^{18}O_2$ + $S^{16}O^{18}O$ + $S^{16}O_2$) was calculated from the data of the S^xO^yO evolution peak areas shown in Figure 4. As shown in **Figure 5**, the three molar ratios of the S^xO^yO were almost constant in the temperature range from 800 to 1000°C. This result suggested that the reaction mechanism did not change in the temperature range in the system (c). When the concentration of O_2 was increased in the presence of 10%H_2O at 1000°C, the ratios changed except the ratio of the $S^{16}O^{18}O$. This result suggests that the direct contribution of $^{16}O_2$ might be high. However, the ratio of the $S^{16}O^{18}O$ to total S^xO^yO was almost constant suggesting that H_2O play an important role even if the O_2 concentration is high.

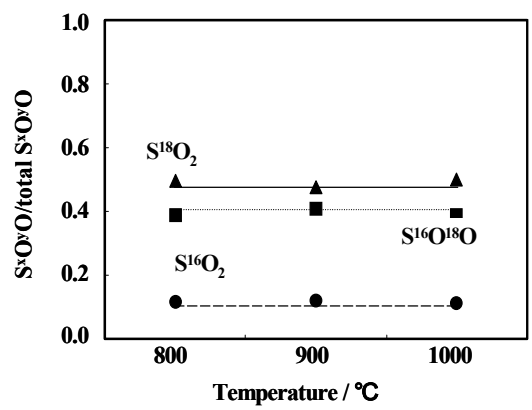

Figure 5. Effect of temperature on S^xO^yO/total S^xO^yO

Acknowledgment. This work was supported by the Ministry of Education, Science, Sport and Culture of Japan through the Grant-in-Aid on Priority-Area Research(Region No.737,Grant No.11218207)

Literature Cited

1. Ninomiya, y.; Sato, A.; Watkinson, A., Int. Conf. Fluidized Bed Combustion, 13th **1995**,1027-33.
2. Sasaoka, E.; Uddin, M, A.; Nojima, S., Ind. Eng. Chem. Res., **1997**, 36, 3639-46.
3. Sasaoka, E.; Sada, N.; Uddin, M, A, Ind. Eng. Chem. Res., **1998**, 37, 3943-49.

Dynamic behavior of sulfur evolved in the gas phase from pyrolysis of seven Chinese coals

Long Xu, Jianli Yang, Yunmei Li, Zhenyu Liu

State Key Laboratory of Coal Conversion,
Institute of Coal Chemistry, Chinese Academy of Sciences,
Taiyuan 030001 P. R. China (zyl@public.ty.sx.cn)

Abatract

Sulfur compounds evolved in the gas phase from pyrolysis of seven Chinese coals are studied using TPD-FPD method in the temperature range of up to 800°C under N_2 and H_2. The effect of H_2 is complex, which promotes certain peak and suppresses other peaks. Interactions between volatile sulfur-containing compounds and the coal matrix are attributed to be the main factor determining the dynamic behavior.

Introduction

More than 70% of the primary energy in China is coal. Sulfur emitted from burning of coal has caused severe environmental pollution. Studies on sulfur emission behavior during thermal processing of coal is very important for development of desulfurization technique prior to combustion, as well as for understanding of sulfur species distributed in coal.

The sulfur compounds in the gases emitted from pyrolysis of coal are generally H_2S, SO_2, COS, CH_3SH and CS_2, with H_2S as the dominant species [1]. The extent of sulfur emission during pyrolysis varies greatly, owing to the variations in coal rank, content of sulfur forms, nature of mineral matters, and the influence of pyrolysis conditions such as reactor design, the temperature, the nature of the atmosphere and the pressure [2].

In this paper, dynamic behavior of the total sulfur emission from pyrolysis of seven Chinese coals, using a TPD-FPD method under both nitrogen and hydrogen atmospheres, is presented. The results are useful in understanding of thermal selectivity in cleavage of C-S and C-C bonds and sulfur emission from different organic matrix.

Experimental

Seven Chinese coals were used. All the samples were ground to less than 0.25mm before use. Ultimate and sulfur-form analyses of the coals are shown in Table 1.

Table 1. Ultimate and Sulfur-form analyses of sample coals

Samples	Ultimate (wt%, daf)					Sulfur-form (wt%, total)		
	C	H	O (diff.)	N	S	pyritic	sulfate	organic
YM	80.18	4.32	12.29	0.86	2.35	77.72	0.00	22.28
PSH	81.32	5.40	11.00	1.57	0.71	76.79	0.00	23.21
YZ	81.35	5.19	8.30	1.21	3.95	65.70	2.03	32.27
DT	82.76	5.07	8.93	0.82	2.42	64.18	2.99	32.83
SHH	78.60	4.95	14.61	1.13	0.71	6.15	0.00	93.85
QJ	62.19	5.67	30.25	1.47	0.42	0.00	5.56	94.44
HLH	76.57	4.59	16.60	1.51	0.73	3.70	0.00	96.30

Temperature programmed decomposition with on line FPD analysis for gaseous sulfur, TPD-FPD, was used. Detailed setup was shown elsewhere [3]. About 5 mg coal sample was heated from 25 to 800°C at a rate of 5°C/min. Hydrogen or nitrogen was used as the carrier gas at a flow rate of 120ml/min to constitute different atmosphere. The FPD was operated at 150°C, and the combustion gases were made up of 60ml/min H_2 and 50ml/min air.

Results and Discussion

According to the sulfur-form distributions in the coal samples listed in Table 1, the coals are categorized into three groups. The first group contains YM and PSH coals, in which the pyritic sulfur contents are dominant (more than 75%) and the sulfate sulfur content is zero. The second group includes YZ and DT coals which contain a less pyritic sulfur than that of the first group (about 65%). The third group, SHH, QJ and HLH coals, has low sulfur content and the sulfur are mainly in organic states (more than 90%).

Figure 1 shows dynamic evolution profiles of total gaseous sulfur from the first group of the coals during pyrolysis in H_2 and N_2. Although YM coal and PSH coal have similar sulfur-form distributions, the sulfur evolution profiles are very different from each other. YM coal (a) shows three evolution peaks at around 410, 510, and 550°C, and H_2 significantly enhances all the three peaks. PSH coal in N_2 (b) shows only one sharp peak at around 520°C, and possibly a weak peak at around 430°C. H_2 significantly suppresses the peak at 520°C, but slightly promotes the peak at 430°C, and possibly generates a flat peak at temperatures greater than 550°C.

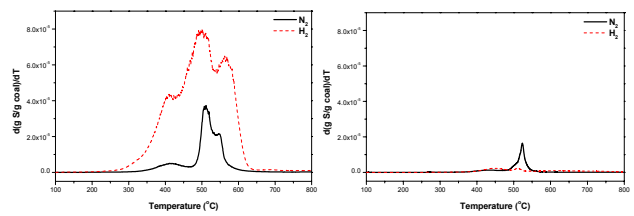

(a) **(b)**

Figure 1. Dynamic gaseous sulfur evolution profiles from the first group of the coals during pyrolysis: (a) YM coal, (b) PSH coal.

The profiles of sulfur evolution from the second group of the coals are shown in Figure 2. YZ coal (a) shows three sulfur evolution peaks at around 400, 530 and 580°C in N_2, and H_2 significantly depresses the sulfur release at above 500°C. DT coal shows one prominent peak at around 505°C in N_2, but only a number of weak peaks in H_2, indicating strong suppression effect on sulfur release at 500°C and promotive effect at around 460°C and at temperatures greater than 600°C by H_2. Overall, H_2 shows negative effect on gaseous sulfur evolution for these two coals.

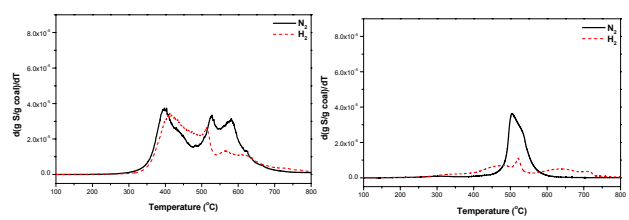

(a) **(b)**

Figure 2. Dynamic gaseous sulfur evolution profiles from the second group of the coals during pyrolysis: (a) YZ coal; (b) DT coal.

Figure 3 shows dynamic evolutions profiles of gaseous sulfur from the third group of the coals in pyrolysis. The peaks in this figure are all small due to small sulfur contents in these coals. SHH coal (a) shows one obvious peak at around 520°C in N_2. H_2 depresses the

520°C peak, but yields small new peaks at lower and higher temperatures, 450°C and 650°C, which is similar to that of DT coal and PSH coal. Both HLH and QJ coals show one main peak in N_2 , at 405°C and 350 °C, respectively, and H_2 promotes these peak and yields new peaks at the high temperature ends, 505 and 570°C for HLH, and 475 and 525°C for QJ. In these cases, H_2 has a little negative effect on gaseous sulfur release on SHH coal and positive effect on HLH and QJ coals.

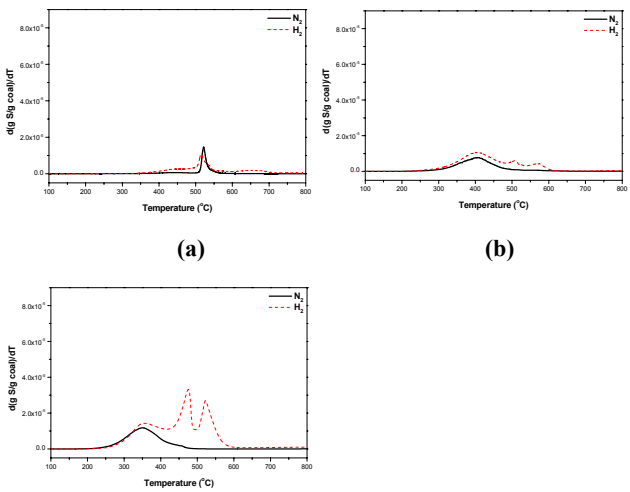

Figure 3. Dynamic gaseous sulfur evolution from the third group of the coals during pyrolysis: (a) SHH coal; (b) HLH coal; (c) QJ coal.

Clearly, H_2 has very different effects on gaseous sulfur evolution in pyrolysis from the coals, promoting certain kinds of sulfur release and suppressing other kinds of sulfur release. This phenominon is different from the general believe that H_2 always promotes sulfur release from the coal compared to N_2. It is very likely that these H_2 effects are related to the physical and chemical states of sulfur in the coals, as well as to the interactions of sulfur with the components of the coals, in their origenal forms or as intermidiate products migrating in the coal matrix during pyrolysis.

It is generally accepted that sulfur in coal stays in organic and inorganic forms, and pyrite is often the dominant form of inorganic sulfur. H_2 accelerates the decomposition of pure pyrite resulting in increased H_2S releas. The decomposition of pyrite in coal are different from and more complex than that of pure pyrite. The pyrite in coal generally begins to decompose at about 500°C during pyrolysis [2]. For the coals in the first and the second groups, more than 64% of the sulfur are pyritic, the peaks between 500-550°C are most probably resulted from decomposition of pyrite, although the contribution of organic sulfur decomposition may be overlapped. The peaks at temperatures below 500°C and higher than 550°C are probably mainly from the decomposition of organic sulfurs. However, H_2 promotes the sulfur release for YM coal, but supresses the sulfur release for PSH, YZ and DT coals, especially at temperatures between 500-550°C. Clearly, these phenomena can not be explained soly by the decomposition of pyrite, and may be related to the interactions of pyritic sulfur or H_2S, generated from decomposation of pyrite, with other components of coal. It was reported [4] that pyrite finely distributed in coals as tiny particles, or entrapped in coal matrix structure, or specially bonded with coal matrix, would result in significant secondary reactions in pyrolysis, which would reduce H_2S release and generate sulfur-containing structures of higher thermal stability[5, 6]. But further increase in temperature may decompose the newly formed sulfur-containing structures and release the sulfur into the gas phase. H_2 may promote the formation of both H_2S and the sulfur-containing structures in pyrolysis. The information presented in Figures 1(b) and 2 seems to suggest that the H_2 promotion on the formation of sulfur-containing structure is much stronger than that on H_2S formation due to supressed sulfur releas from pyrolysis of pyrite, at least in the cases studied. It is important to note, however, that the overall peak areas in H_2 in Figures 1(b) and 2 are much smaller than that in N_2. This may suggest that the newly formed sulfur-containing structures in the secondary reaction are mainly in the form of tar, which leave the reactor as the volatile phase and do not have a chance to experience higher temperatures. This hypothesis needs to be varified by tar and char analysis for sulfur content.

The coals in the third group, SHH, HLH and QJ, all have very high organic sulfur contents, greater than 93%. Therefore, most of the peaks in Figure 3 are resulted from the decomposition of organic sulfur. The promotive effect of H_2 may suggest increased cleavage of S-C bonds in H_2, especially in the high temperature range.

It is well accepted that pyrolysis of coal follows the radical mechanism. The coal undergo thermal cracking at elevated temperatues to generate radicals of different sizes, small and large. The large radicals tend to further crack. All the radicals are reactive and tend to recombine to form relatively stable compounds. The effect of H_2 on the gaseous sulfur evolution may also follow the radical mechanism. Stablizing small sulfur-containing radicals by H_2 may result in increased gaseous sulfur evolution. Stablizing large sulfur-containing radicals by H_2, on the other hand, may result in increased sulfur-containing tars and/or increased sulfur-containing chars. The formed sulfur-containing chars may undergo further pyrolysis at higher temparetures to evolve volatile sulfur-containing compounds.

Conclusions

Dynamic behavior of total gaseous sulfur evolution from pyrolysis of seven Chinese coals show complex H_2 effects, promotion of some peaks, supression of other peaks, generation of new peaks especially at higher temperatures. These behavior can be explained by promotive effect of H_2 on pyrite decomposition, by secondary reactions between the products of pyrite decomposition and the metrix structures of coal, and by the radical mechanism. The negative effect of H_2 on gaseous sulfur release may correspond to increased sulfur in tars. H_2 promotes the formation of gaseous sulfur from organic sulfur in the coals during pyrolysis.

Acknowledgement. The project is subsidised by the Special Founds for Major State Basic Research Project (G19990221), the Chinese Academy of Sciences, and the Natural Science Foundation of China (29725614, 20076050, and 20076049) and the State Key Laboratory of Coal Conversion.

References

(1) Andrzej Czaplicki; Wojciech Smolka. *J. Fuel Processing Technology*, **1998**, 55, 1-11.
(2) Amir Attar. *J. Fuel*, **1978**, 57(4), 201-212.
(3) Xu Long; Li Yunmei; Yang Jianli and Liu Zhenyu. *M. 7th Chinese-Japanese Coal Chemistry and C_1 Chemistry,* Hainan, China, **2001**; pp 259.
(4) Baruah, M. K.; Gogoi, P. C. *J. Fuel*, **1998**, 77(9/10), 979-985.
(5) Chen Hao-kan; Li Bao-qing; Yang Ji-li. *J. Fuel*, **1998**, 77(6), 487-493.
(6) Jose, V. I.; Jose, M. P.; Rafael, M. and Ana, J. B. *J. Fuel*, **1994**, 73(7), 1046-1050.

DESULFURIZATION OF COAL WITH PYROLYSIS IN DIFFERENT ATMOSPHERE

Haoquan Hu, Xiaodan Wu, Shengwei Zhu*

Institute of Coal Chemical Engineering, Dalian University of Technology, 129 street, Dalian116012, P.R. China
*hhu@chem.dlut.edu.cn

Introduction

The release of sulfur during the utilization of coal, especially the pollution caused by coal burning has attracted more and more attention. Therefore, how to remove the sulfur from coal economically and efficiently becomes more and more important and necessary for coal utilization. So far, there have been many physical, chemical and microbial desulfurization methods studied[1], among those coal pyrolysis desulfurization is one of relatively simple and effective one, especially hydropyrolysis[2] which has made a high sulfur removal. However, since many complicated second reactions would occur during coal pyrolysis, especially the formation of some steady thiophenic sulfur[4] such as the reaction of pyrite and hydrocarbon compound, the organic matters in coal and hydrogen sulfide which produced during pyrolysis, and the sulfur retained by mineral in coal etc.; all those would lead to an undesirable sulfur removal and constitute a main problem in coal pyrolysis desulfurization as a result.

A new and effective way is to add some trapping materials which can react with hydrogen sulfide to form metastable sulfur compound and consequently avoid its reacting back with coal. Attar[5] has found that ethylene can react with hydrogen sulfide at 370–430°C, and achieved a better desulfurization result by using pure ethylene as reactive gas for Illinois No.6 bituminous high sulfur coal in pressurized pyrolysis at low temperature. Liu et.al also used ethanol as additives in coal pyrolysis desulfurization[3]. In this paper, coal pyrolysis both in isothermal and non-isothermal manner was carried out by using nitrogen and a mixed gas of nitrogen and ethylene (MG) at atmospheric pressure to investigate the effect of ethylene on sulfur removal during pyrolysis.

Experimental

Huoligele lignite with a particle size -100 mesh was used in this study. The analysis results were listed in **Table 1.** The sulfur in the coal exists in 48% pyrite and 52% organic sulfur.

Table 1 Analysis of Huoligele lignite

Approximate analysis (wt%)			Ultimate analysis (wt%daf)				
M_{ad}	A_d	V_{daf}	C	H	N	O*	S
19.37	24.41	47.33	75.84	5.73	1.28	16.43	0.72

* by difference

Pyrolysis was performed in thermogravimetric analyzer (TGA/SDTA 851^e) at atmospheric pressure. The sample weight is about 20 to 25mg. In non-isothermal experiment, coal was pyrolyzed from room temperature upto end temperature of 400°C, 450°C, 500°C, 550°C, 600°C, 650°C and 700°C, respectively, at heating rate of 5°C /min, then retained at that temperature for 20 min. while in isothermal experiment, the sample was heated from room temperature upto the required end temperature in about 1 to 2 minutes. The gas flow rate is 30ml/min when pure nitrogen was used, and 30ml/min nitrogen and 6ml/min ethylene when MG was used.

The sulfur removal (r_s) was calculated from the expression:

$$r_s(\%) = (S_{char} - S_{coal})/ S_{coal}$$

where S_{coal}: sulfur content in coal; S_{char}: sulfur content in char

Results and Discussion

Comparison of sulfur removal **Figure 1** shows the sulfur removal at different temperature with two gases in isothermal pyrolysis. It can be seen that the desulfurization result under MG is better than that under pure nitrogen at 400°C, while at the other temperatures there is nearly no difference under both atmosphere. The better sulfur removal at 400°C can be attributed to the reaction between ethylene and hydrogen sulfide released during the coal pyrolysis[2], which can compete with the reactions between hydrogen sulfide and coal to hinder hydrogen sulfide from reacting back with coal and consequently gave rise to the removal of sulfur under MG. Since the reaction can only occur at 370-430°C, the trapping effect of ethylene for hydrogen sulfide can't work with the desulfurization at other temperatures.

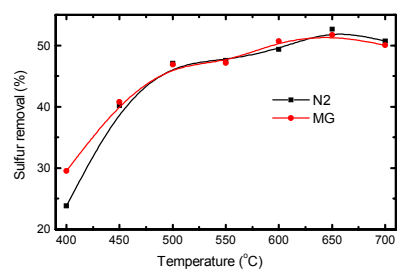

Figure 1 Sulfur removal in isothermal pyrolysis of coal

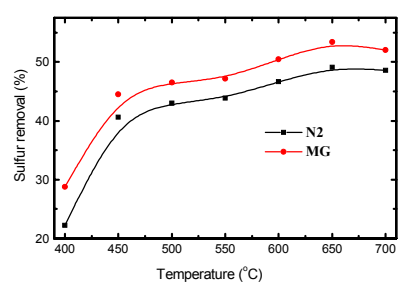

Figure 2 Sulfur removal in nonisothermal pyrolysis

The sulfur removal in nonisothermal pyrolysis was shown in **Figure 2.** Compared with the pure nitrogen pyrolysis, the sulfur removal under

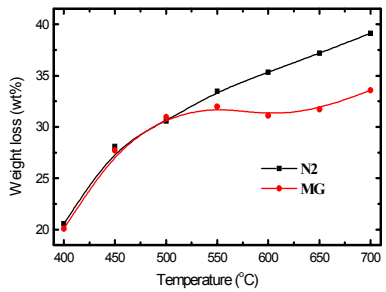

Figure 3 Final weight loss at different end temperature in isothermal pyrolysis

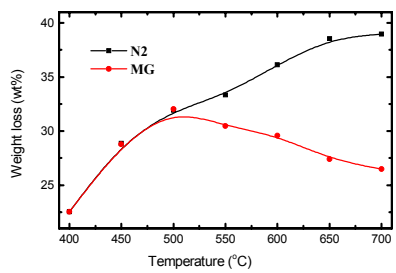

Figure 4 Final weight loss at different end temperature in non-isothermal pyrolysis

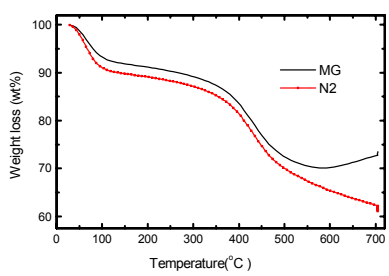

Figure 5 TG curve of Huolingele lignite pyrolysis in nitrogen and MG
(25°C to 700°C at 5°C /min and with a 20min residence time at 700°C)

MG increased in the whole temperature range by 6.55% at 400°C and 4.00% or so at other temperatures. It may be explained that the nonisothermal pyrolysis at each final temperature can provide enough time for ethylene to trap hydrogen sulfide at proper temperature range (370-430°C) since the heating rate (5°C/min) is slow, and the additional 20 min residence time at proper temperature range (about 400°C) lead to the best sulfur removal in pyrolysis.

Comparison of weight loss **Figure 3** and **Figure 4** show the final weight loss of coal pyrolysis at different end temperature. It can be seen that before roughly 500°C the weight loss under two said gases is similar in both isothermal and nonisothermal pyrolysis**,** and after 500°C, MG made a lower weight loss than pure nitrogen. Combining with the TG curve shown in **Figure 5,** where the coal weight increased under MG instead of decreased under nitrogen with increase of temperature after about 500°C. This means that at high temperature ethylene may react with coal and/or pyrolysis to deposit heavy pyrolysis products on coal. The TGA of quartzite with MG under the same condition as that in **Figure 5** suggested that there is no increment in weight after 500°C at all, which means there was no deposition of ethylene pyrolysis products on quartzite. According to the property of the double bond of ethylene, it is possible that an extra reaction between ethylene and coal would occur, and this reaction made no effect on sulfur removal according to the results of **Figure 1** and **Figure 2**.

Correspondingly, the greater difference of weight loss between pure nitrogen and MG in nonisothermal pyrolysis (**Figure 4**) compared with the isothermal pyrolysis (**Figure 3)** may be attributed to the longer pyrolysis time which provide a longer reaction time between ethylene and coal.

Conclusion

A better sulfur removal in Huolingele lignite pyrolysis can be achieved by adding ethylene to nitrogen flow at low temperature (400°C or so). Ethylene can avoid the sulfur retained in coal pyrolysis at low temperature. The lower weight loss of coal pyrolysis under MG at high temperature compared to that under nitrogen may be attributed to the reaction of ethylene with coal.

Acknowledgment. The work was supported by fund of the National Key Fundamental Research and Development Project of China (G1999022101)

Reference

[1] Liu, Shengyu; Zhao, Yulan; Xue, Yongqiang; Wang, Jian; Wu, Guoqing, Coal Conversion, 1997, *20*(2), 20-22.

[2] Wang, Na, Li, Wen; Li, Baoqing; Journal of Fuel Chemistry and Technology, 2001, *29*(1), 29-32

[3] Yu, Long; Yang, Jianli; Li, Yunmei, ACS Fuel chemistry division preprints, 2002, *47*(1), 200

[4] Attar, A., Chemistry, Thermodynamics and Kinetics of Reactions of Sulphur in Coal-Gas Reactions: A Review. Fuel, 1978, 57(4): 201-212

[5] Attar, A., USP 4,465,493. August 14, 1984

DESULFURIZATION OF COAL THROUGH PYROLSIS IN A FLUIDIZED-BED REACTOR

Yongqin Qi, Wen Li, Haokan Chen and Baoqing Li

State Key Lab of Coal Conversion, Institute of Coal Chemistry, Chinese Academy of Sciences, Taiyuan, Shanxi, 030001, China

Introduction

Sulfur in coal has greatly limited its utilization and much attention has been paid to the air pollution caused by combustion of coal in recent years. Sulfur removal is one of the most important problems in coal utilization. So far many methods have been developed to either remove sulfur from the coal, or from the flue gas. Among these methods, pyrolysis, an intermediate stage in various conversion processes such as liquefaction, gasification and combustion, is an important method of sulfur removal from coal prior to combustion because its cost is relatively low and can remove both inorganic and organic sulfur. The sulfur removal from coal through pyrolysis depends on many factors, such as coal rank, the quantity of sulfur and the sulfur forms distribution in the coal, the quantity and kind of mineral matter, the conditions in which the process is conducted. In this aspect, many important conclusions have been obtained, which are mainly based on studies in a fixed-bed reactor [1-4]. In the present study, Yima (YM) and Datong(DT) coal were pyrolyzed in a fluidized-bed reactor in inert atmosphere to examine the sulfur removal efficiency.

Experimental

Coal samples

Raw coal with 0.15-0.25mm was washed by HCl / HF to remove minerals. Demineralized coals were further washed by $CrCl_2$ in order to remove pyrite. Table 1 and Table 2 show proximate, ultimate and sulfur form analysis of the samples.

Table 1 Proximate and ultimate analysis of samples w/%

Samples	M_{ad}	A_d	V_{daf}	C_{daf}	H_{daf}	N_{daf}	S_{daf}
YM	8.82	17.3	40.1	78.1	3.90	0.86	0.60
YM-ash	3.31	2.86	37.7	74.7	5.29	0.85	0.51
YM-p	2.38	1.45	37.6	73.6	5.18	0.81	0.61
DT	3.56	7.93	36.5	82.8	4.88	1.02	0.40
DT-ash	2.16	0.91	28.6	83.3	4.55	0.58	0.37
DT-p	2.51	0.65	28.4	83.4	4.59	0.69	0.38

Table 2 Analysis results of sulfur forms in samples w / %

Samples	$S_{t,ad}$	$S_{s,ad}$	$S_{p,ad}$	$S_{o,ad}$
YM	1.95	1.42	0.08	0.45
YM-ash	2.08	1.60	0.0	0.48
YM-p	0.59	0.0	0.0	0.59
DT	1.04	0.06	0.62	0.36
DT-ash	1.08	0.01	0.71	0.36
DT-p	0.37	0.0	0.0	0.37

YM-ash, DT-ash: demineralized coal
YM-p, DT-p: demineralized and de-pyrite coal

Pyrolysis

Pyrolysis was conducted in a quartz tube reactor (i.d 50mm) in nitrogen. There is a sintered quartz disk in the middle of tube to support coal, which can also be used as gas distributor. Pyrolytic temperature ranged from 500°C to 900°C and residence time was 30 minutes. The flow of fluidized-gas was from 0.15 to 0.21 m^3/h. 20g of coal was fed into the reactor at 5g/min after the desired temperature was reached. The char was collected and weighed after temperature naturally dropped to ambient temperature. Sulfur removal (SR) was calculated according to the following equation:

$$SR\% = \frac{St,coal - St,char \times Yield}{St,coal} \times 100$$

Results and discussion

1.Effect of coal type on sulfur removal

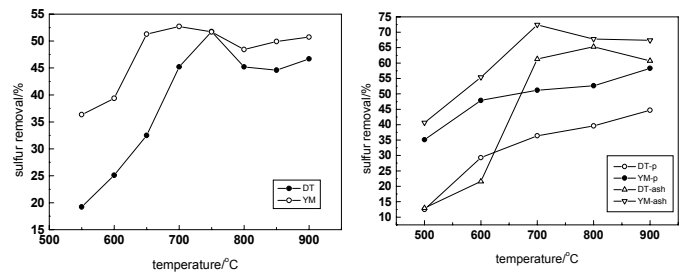

(a) (b)

Figure 1 Sulfur removal as a function of temperature

Figure 1(a) shows the change of sulfur removal with temperature. YM is a lower rank coal compared with DT, hence YM is more active during pyrolysis than DT coal due to its low aromaticity. YM coal has a higher desulfurization than DT coal which reaches maximum desulfurization yield at relatively higher temperature. From demineralized and de-pyrite coal **(Figure 1(b))**, we can get the same conclusion. This proves that coal rank has effect on sulfur removal. At the earlier stage of pyrolysis, desulfurization has remarkable increase because decomposition of pyrite and thermally labile organic sulfur play an important role. The desulfurization decreases starting from 700ºC for YM coal and 750ºC for DT coal. According to a previous study[5], sulfur fixation by alkaline-earth mineral begins at 700ºC, which leads to increase of sulfur in char. On the other hand, high temperature leads to collapse of the pore structure, which inhibits further release of sulfur[6]. Moreover, the desulfurization tends to be constant between 800ºC and 900ºC because stable organic sulfur is difficult to be removed and sulfide sulfur can not further decompose. Hence there is an optimal temperature for maximum desulfurization and varies with coal rank.

2. Effect of mineral on sulfur removal

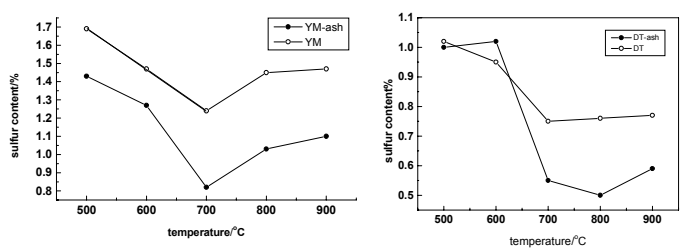

Figure 2 Sulfur content in char of demineralized coal vs temperature

Figure 2 indicates that sulfur content in char of demineralized coal first decreases to lowest value at 700ºC, and then increases slightly for DT and evidently for YM. There is 10.42% and 1.69% CaO in the ash of YM and DT. The sulfur retention by CaO is contributed to the sulfur increase for raw coal. The transformation of inorganic sulfur to organic sulfur is responsible for the sulfur increase in the demineralized coal, mainly the transformation of pyrite to stable organic sulfur due to the influence of indigenous hydrogen and oxygen[7]. The Sulfation product by CaO will turn into sulphate during combustion and will not cause pollution.

3. Organic sulfur removal through pyrolysis

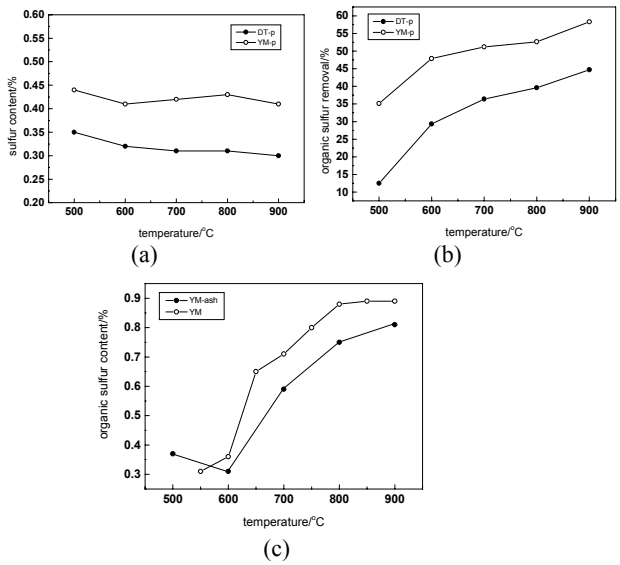

Figure 3 Organic sulfur removal vs temperature

Organic sulfur content in char has no apparent variation according to **Figure 3(a)**. However, yield of char decreases with increasing temperature, hence in fact part of organic sulfur is removed through pyrolysis as shown in **Figure3(b)**. According to our AP-TPR study, there is more aliphatic sulfur in YM and more thiophenes in DT, which results in the high organic sulfur removal for YM. **Figure 3(c)** shows organic sulfur content in char through pyrolysis of YM raw and demineralized coal. It shows that organic sulfur tends to accumulate in char with increasing temperature. Attar[8] believes that pyrolysis of sulfur compounds is the decomposition of C-S bond to free radicals R'• and RS•. In pyrolysis, other hydrocarbon molecules supply the hydrogen to stabilize the radicals, but at high temperature there is no enough hydrogen and the radicals may transform into stable organic sulfur. In addition, lack of indigenous hydrogen may also leads to the transformation of pyritic sulfur into organic sulfur[7]. Cernic-Simic believes that sulfide contributes to increase of organic sulfur[9]. Therefore, alkaline-earth mineral leads to organic sulfur increase to some extent in raw YM. Organic sulfur in the char of YM-ash still accumulates with increasing temperature, clearly sulfide is not the main reason here. Contrasting **Figure 3(c)** with **(a)**, we deduce that the interaction of pyrite with the organic matrix of coal plays an important role in organic sulfur accumulation in char.

4. Effect of residence time on sulfur removal

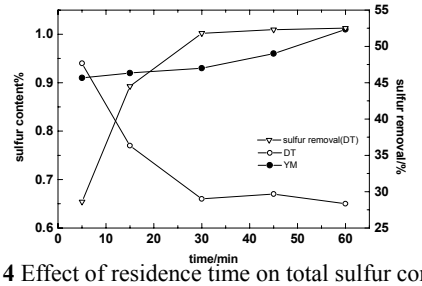

Figure 4 Effect of residence time on total sulfur content of char

The effect of residence time on desulfurization is examined at the temperature for maximum desulfurization. For YM coal the sulfur content in char varies little with time and yield of char is almost not changed at the same temperature. Hence longer residence time has no enhancement effect on sulfur removal for YM coal. However, sulfur content in char of DT coal decreases with increasing time during the first 30 minutes, which leads to increase of sulfur removal. This indicates that DT coal is less active than YM coal to some extent. Therefore, sulfur is difficult to release rapidly in DT coal. However, when most of labile sulfur has released after a period of time, stable sulfur can not decompose and sulfur content in char has little change. Hence for different coal, there is also optimal residence time for maximum desulfurization.

Conclusions

1 There is optimal temperature and residence time for maximum desulfurization, varying with type of coal.

2 The alkaline-earth mineral in the raw coal plays an important role for the fixation of sulfur and makes desulfurization decrease.

3 The interaction of pyrite with the organic matrix of coal is the main reason that leads to organic sulfur accumulation in char.

Acknowledgment

Financial support for this work by the Special Funds for Major State Basic Research Projects (Contact NO. G1999022102) is gratefully acknowledged.

References

1 Sugawara, K., Tozuko, Y., Sugawara, T., Nishiyama, Y., Fuel Processing Technology. 1994, **37**, p. 73-85.
2 Ibarra, J., Bonet, A., Moliner, R., Fuel. 1994, **73** (6), p. 933-939.
3 Gryglewicz, G., Fuel Processing Technology. 1996, **46**, p. 216-226.
4 Gryglewicz, G., Fuel. 1995, **74** (3), p. 356-361.
5 Gryglewicz, G., Jasienko, S., Fuel. 1992, **71** (11), p. 1225-1229.
6 Lin, L., Khang, S. R., Keener, T. C., Fuel Processing Technology. 1997, **53**, p. 15-29.
7 Chen, H. K., Li, B. Q., Zhang, B. J., Fuel. 2000, **79**(13), p. 1627-1631.
8 Attar, A., Fuel. 1978, **57** (4), p. 201-213.
9 Cernic-Simic S., Fuel. 1962, **41** (2), p. 141-151.

ZINC FERRITE AND RELATED SORBENTS FOR HOT GAS DESULFURIZATION PROCESS

Michihiro Ishimori, Takashi Inaba,** and Masafumi Katsuta***

*Advanced Research Institute for Science and Engineering
Waseda University
**Department of Mechanical Engineering
Waseda University
3-4-1 Okubo, Shinjuku-ku , Tokyo
169-8555 Japan

Introduction

Recently global environment issues have been raised worldwide. In relation with CO_2 emission which may lead to climate change, development of the highly efficient coal thermal technology is considered to be increasingly of importance. Integrated Coal Gasification Combined Cycle (IGCC) has been recognized as the most promising coal gasification power generation technology and large scale power plants are currently operated in the United States and in Europe, although thermal efficiencies are not yet so high. In Japan a national project of the 200t/d IGCC pilot plant was carried out at Nakoso from 1986 to 1996. The targets of this project were developments of the air-blown pressurized entrained-flow gasifier, hot-gas cleanup systems, and a gas turbine for low Btu coal gas, where 3 types of hot-gas desulfurization systems were tested by using iron oxide (Fe_2O_3/ Fe_3O_4) sorbents.[1,2]

In order to realize the highly effective coal gasification power plants, development of hot-gas cleanup system, especially highly efficient desulfurization technology for hot coal gas is required. We have studied zinc ferrite and related compounds as sorbents for hot reductive gas produced by an entrained-flow gasifier, with consideration of the results of desulfurization operations at Nakoso pilot plant. The characteristics of zinc ferrite and related systems were investigated in terms of sorbents for hot-gas desulfurization process using simple reductive gas involving reductive sulfur substance represented by H_2S, as described hereafter.

Experimental

Sorbents. Zinc ferrite and related sorbents were prepared as follows. A mixed solution of zinc nitrate (1.5 mol/l, 50 ml) and iron nitrate (III) (1.5 mol/l, 100 ml) was stirred in a flask in the presence of colloidal silica. Then ammonia aqueous solution was added to this solution. The precipitates obtained from the solution (pH 7-8) were washed with water after filtration, dried at 120 °C and calcined at 800°C for 5h. $ZnFe_2O_4$-SiO_2 sorbent thus obtained was confirmed by XRD analysis. $ZnFe_2O_4$-SiO_2-ZrO_2 or $ZnFe_2O_4$-SiO_2-TiO_2 sorbent was prepared by mixing $ZnFe_2O_4$-SiO_2 sorbent with ZrO_2 or with TiO_2 (anatase), and calcined at 500 °C for 1h. The composition of the sorbents was determined by the atomic ratio of component oxides using XRF (X-ray fluorescence system) and ICP (Inductively coupled plasma) methods.

Desulfurization. Sorbent performance test for desulfurization-regeneration (cycle of sulfidation and oxidation of sorbent) was carried out in a down flow fixed-bed reactor made of quartz under atmospheric pressure. The reductive gas for H_2S absorption test is composed of 20% of H_2, 1000 ppmv of H_2S, and N_2 (balance). The sorbent such as $ZnFe_2O_4$-SiO_2-ZrO_2 (or TiO_2) system was prepared by composition of 200 mg of $ZnFe_2O_4$-SiO_2 sorbent and 400 mg of ZrO_2 (or TiO_2). Analyses of the inlet gas and outlet gas from the reactor were carried out by gas chromatography using a thermal conductivity detector (TCD) and a flame photometric detector (FPD). The total gas flow rate was 100 ml/min (20°C, standard) by using mass flow controllers. Concentration of H_2S at the outlet of the desulfurization reactor was determined by gas chromatography equipped with a flame photometric detector (FPD) with a sensitivity of 1 ppmv, where the outlet gas auto-sampling instrument was used. Regeneration of the sulfided sorbent was conducted by oxidation using 2% of oxygen and N_2 (balance) at 450°C.

The breakthrough curves were recorded with a closed measurement system, composed of a reactor equipped with Shimaden model DSM temperature control unit, Yanaco model GSH-263A gas auto-sampling instrument, Yanaco model G2800FPD gas chromatograph, and Simadzu model C-R8A Integrator.

Results and Discussion

$ZnFe_2O_4$-SiO_2-ZrO_2 sorbent. The following three sorbents systems of zinc ferrite and related mixed oxides were prepared: $ZnFe_2O_4$, $ZnFe_2O_4$-SiO_2, and $ZnFe_2O_4$-SiO_2-ZrO_2 sorbents.[3] The desulfurization tests for the reductive gas by the above three sorbent systems were carried out at 450°C under atmospheric pressure, using a fixed-bed type reactor. The reductive gas for H_2S absorption test is a simplified simulation gas of the coal gas in composition assuming an air-blown entrained-flow gasification.

It was found that, as the results of desulfurization test of $ZnFe_2O_4$-SiO_2-ZrO_2 sorbent, concentration of H_2S involved in the reductive gas was decreased from 1000 ppmv to less than 1 ppmv. The activity of the sorbent was observed to be completely regenerated by oxidation, after sulfidation. Breakthrough curves of H_2S for $ZnFe_2O_4$-SiO_2-ZrO_2 system are shown in **Figure 1**. The feature of H_2S breakthrough curves is that all breakthrough profiles are almost identical, suggesting that deactivation of the sorbent during the absorption-regeneration cycles is negligible.

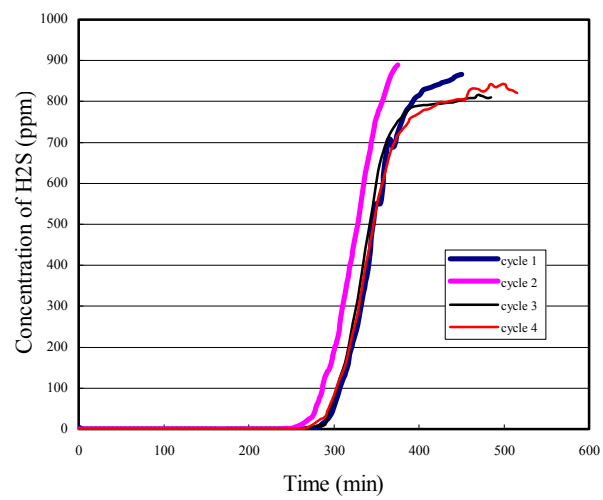

Figure 1. Breakthrough Curves of H_2S for $ZnFe_2O_4$-SiO_2-ZrO_2 system. (Concentration of H_2S: data at the outlet of the reactor).

On the other hand, desulfurization performance with $ZnFe_2O_4$ sorbent itself was found to be unfavorable; time length of high desulfurization (H_2S concentration of less than 1ppm) is very short, compared with $ZnFe_2O_4$-SiO_2-ZrO_2 sorbent. Another sorbent of $ZnFe_2O_4$-SiO_2 system showed high desulfurization performance similarly to $ZnFe_2O_4$-SiO_2-ZrO_2 sorbent at the first desulfurization test. However, performance of the regenerated sorbent obtained after the first desulfurization run, was extremely lowered. It might be thus indicated for the excellent performance of $ZnFe_2O_4$-SiO_2-ZrO_2 sorbent system that activity of $ZnFe_2O_4$ is promoted by SiO_2 and that activity of $ZnFe_2O_4$-SiO_2 species formed is structurally supported by

ZrO_2. In the course of studies, excess Fe_2O_3 present in the $ZnFe_2O_4$-SiO_2-ZrO_2 sorbent was not found to be unfavorable in desulfurization, whereas excess ZnO was observed to show deactivation effect on the sorbent performance.

$ZnFe_2O_4$-SiO_2-TiO_2 sorbent. Desulfurization tests for $ZnFe_2O_4$-SiO_2-TiO_2 system were carried out under similar reaction conditions described above. It was found that $ZnFe_2O_4$-SiO_2-TiO_2 sorbent is more favorable in comparison with $ZnFe_2O_4$-SiO_2-ZrO_2 sorbent from the aspect of time length of high desulfurization performance. Breakthrough curves of H_2S for $ZnFe_2O_4$-SiO_2-TiO_2 system are shown in **Figure 2**.

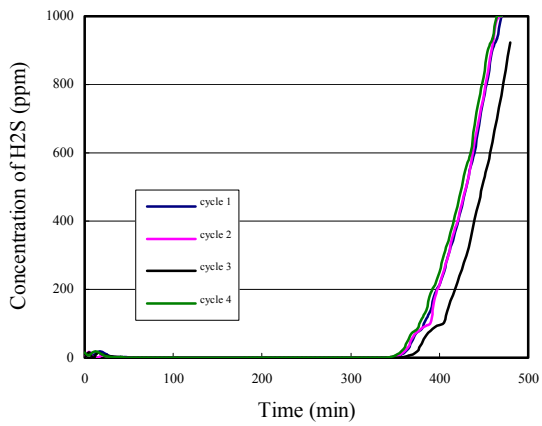

Figure 2. Breakthrough Curves of H_2S for $ZnFe_2O_4$-SiO_2-TiO_2 system. (Concentration of H_2S: data at the outlet of the reactor).

Amount of H_2S reacted with $ZnFe_2O_4$-SiO_2-TiO_2 sorbent was studied. The actual amount of reacted H_2S was experimentally determined by the integration using breakthrough curves of H_2S for $ZnFe_2O_4$-SiO_2-TiO_2 sorbent shown in **Figure 2**. Theoretical amount of H_2S reacted was calculated by the composition and quantity of sorbent used, assuming the equation (A); excess Fe_2O_3 (1 mol) was assumed to become FeS (2 mol) by reaction with H_2S.

$$ZnFe_2O_4+3H_2S+H_2 \rightarrow ZnS+2FeS+4H_2O \quad (A)$$

$$ZnFe_2O_4+4H_2S \rightarrow ZnS+FeS+FeS_2+4H_2O \quad (B)$$

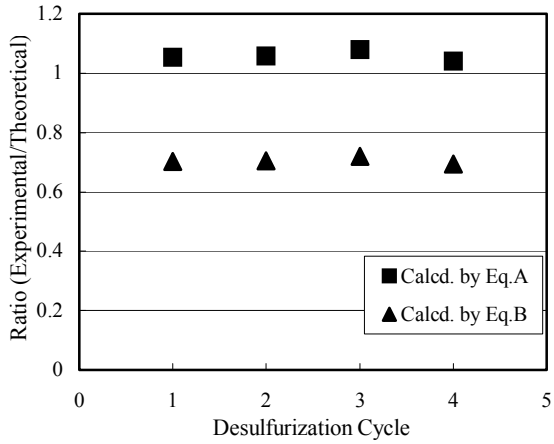

Figure 3. Temperature Effect on Breakthrough Curves of H_2S for $ZnFe_2O_4$-SiO_2-TiO_2 system.

The ratios of amount of H_2S reacted "Experimental/Theoretical" are shown in **Figure 3**. The desulfurization reaction is usually considered to proceed by equation (A). However, experimental value is higher than theoretical value, that is Experimental/Theoretical > 1. The results indicate that another type of reaction such as equation (B) also takes place; formation of $Fe_{1-x}S$ and/or FeS_2 were confirmed by XRD analyses of sulfided sorbents, although quantitative data could not be obtained by this analytical method.

Desulfurization tests for $ZnFe_2O_4$-SiO_2-TiO_2 system were carried out at various temperatures. It was confirmed that highly effective desulfurization was observed in a broad range of temperatures at 600°C~250°C, as shown in **Figure 4**. The fact indicates the above system to be favorable sorbent for hot coal gas from gasifier, since temperature of such gas is variable with time due to deposition of coal ash on gas cooler (heat exchanger).

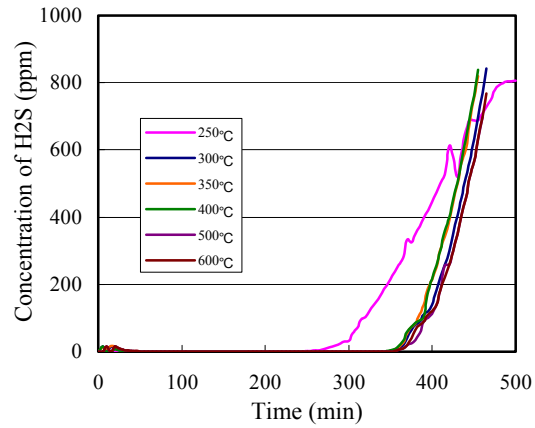

Figure 4. Temperature Effect on Breakthrough Curves of H_2S for $ZnFe_2O_4$-SiO_2-TiO_2 system. (Desulfurization: 250°C ~ 600°C).

Conclusion

The sorbents of $ZnFe_2O_4$-SiO_2-ZrO_2 and $ZnFe_2O_4$-SiO_2-TiO_2 systems prepared in this study were found to show excellent desulfurization performance; the sorbents are considered to be satisfactorily used for hot gas desulfurization process of advanced IGCC plant equipped with high temperature gas turbine, on the basis of the operation data of desulfurization processes of the hot gas cleanup system at Nakoso pilot plant. The sorbents will also be able to be adopted for the Integrated Coal Gasification Fuel Cell Combined Cycle (IGFC) having high temperature fuel cell technologies such as molten carbonate fuel cell (MCFC) to be developed in near future, where concentration of sulfur compounds of the fuel gas is required to be less than 1ppm.

Acknowledgment. This work was partially supported by the Ministry of education, Science, Japan, under contract of a grant-in-aid for priority areas.

References

1. Ishimori, M., Senshu, S., *Eighth Annual Conference on Coal Gasification*, Sponsored by EPRI (Electric Power Research Institute, U. S. A.), San Francisco, **1988**; *EPRI Proceedings GS-6485*, 15-1, **1989**.
2. Ishimori, M., *J. Japan Institute of Energy*, **1995**, *74*, 673.
3. Ishimori, M., Katsuta, M., *The 18th Annual International Pittsburgh Coal Conference, Proceedings, Session33*, 39-03, Newcastle, Australia, **2001**

EXPERIMENTAL STUDY ON SO_2 REMOVAL IN O_2/CO_2 COAL COMBUSTION

Xiaoping ZHANG, Jianrong QIU, Xuewen DONG, Hong WANG, Hao Liu

National Laboratory of Coal Combustion
Huazhong University of Science and Technology
Wuhan, Hubei 430074, P.R.China

Introduction

Coal combustion is the most main sources of CO_2, SOx and NOx emission. About 85% of CO_2, 90% of SO2, 70% of NOx in total pollutants are from coal combustion in China. SO_2 emission increased about 3 times over the past two decades in China. CO2 and NOx emission have also been increasing. Limestone desulfurization efficiency is very low although it is of low cost. O_2/CO_2 recycling combustion is a new coal combustion style developed in recent years [1-2]. This combustion style is expected to be one of promising systems on CO_2-recovery without the process of concentration from pulverized coal-fired power plants. In the system, pulverized coal is fired in a CO_2-based atmosphere. The combustion style use oxygen/recycled flue gas, CO_2 is used to institute the N_2 in combustion air. This style Increases the CO2 concentration in the flue gas by eliminating N2 in air. Up to 95% CO_2 in dry flue gas may be attained, therefore, nearly pure CO_2 for reuse or disposal. Meanwhile, a higher plant efficiency resulted from reducing of volume throughput (60-80%). Most importantly, this combustion style is possible to control CO_2, NOx and SO_2 emission simultaneously[3-4]. However, the mechanism of SO_2 removal is not understood thus far.

The objective of this work is to demonstrate the feasibility of removal of SO_2 and NOx in O_2/CO_2 coal combustion, to compare the emissions of SO_2 and NOx under O_2/CO_2 and conventional combustion conditions with and without limestone injection, to explore the mechanism of SO_2 and NOx removal under O_2/CO_2 conditions and finally find the relationship between the optimal SO_2 and NOx removal efficiency and CO_2 concentration and temperature.

Experimental

Experimental Device. The experiments have been performed on a horizontal electric heating reactor and a drop tube furnace[4].

Coal Samples. In this experiment, two kinds of coal referred to as Hs and Sps with varying volatile matter and sulfur content were provided respectively. Proximate analysis was performed with a LECO MAC-500 by the standard procedure. Carbon, hydrogen and nitrogen were determined with a LECO CHN600 analyzer, and sulfur with a LECO SC-132 sulfur analyzer by the standard procedure. The fusion temperature at reducing atmosphere was measured by ash fusion temperature auto-analyzer (AF600) according to the GB219-74 standard. Chemical method was used to analyze the ash chemical composition. The analyses are shown in Table 1 and Table 2.

Table 1 Coal analysis data

Proximate analysis (%)					Ultimate analysis (%)			
Sample	W^f	V^f	A^f	C^f	C	H	N	S
Sps	2.5	10.60	18.0	68.8	72.0	2.12	0.90	2.56
Hs	4.8	18.23	41.7	35.2	36.6	2.22	0.76	5.51

Results and Discussions

The Effect of CO_2 on SO_2 Emission

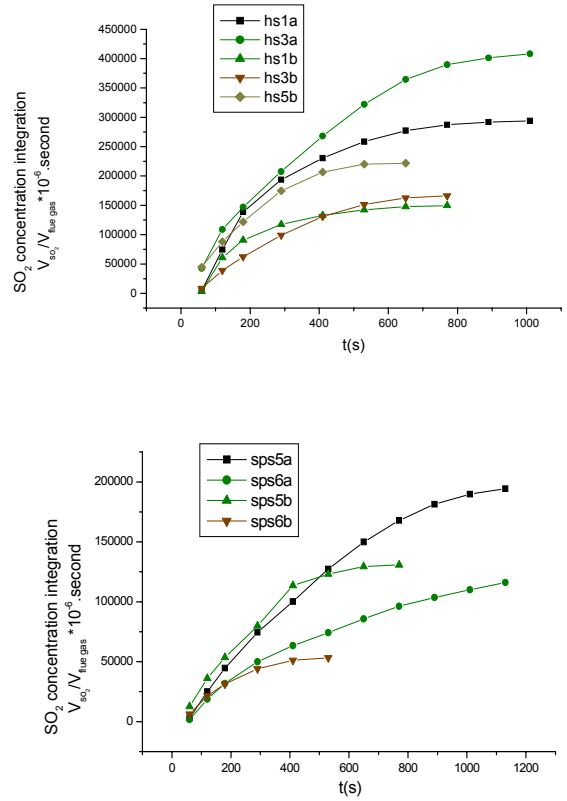

a: air; b: 21%O2/79%CO2

1: 700℃, 3:900℃, 5: 1000℃

Figure 1. Total SO_2 emission as a function of time under different conditions

Figure 1 plots the SO_2 emission under air and O2/CO2 environment respectively at different temperature. Comparing with conventional air condition, the high CO_2 concentration significantly changed the SO_2 emission during coal combustion. For HS coal, the SO_2 emission in the exhausted gas in O_2/CO_2 condition is about 50% of that in O_2/N_2 condition at the temperature of 700℃ (hs1b compares with hs1a). As temperature increase, SO_2 emission increase, but the amplitude in O_2/CO_2 combustion style is lower than that in O_2/N_2 atmosphere. The SO_2 reduction is more notable in O_2/CO_2 combustion style at high temperature.

For SPS coal, the SO_2 emission in O_2/CO_2 condition is about 70% of that in O_2/N_2 condition at the temperature of 1000℃. At the temperature of about 700~1100℃, the SO_2 emission of all investigated coals under O_2/CO_2 are less than that under conventional air combustion.

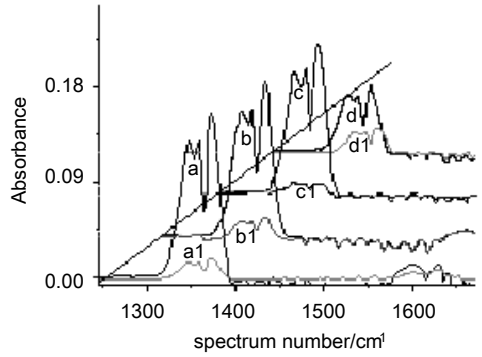

(a) 800℃

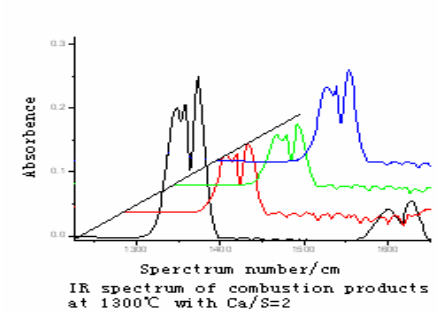

(b) 1300℃

a: air; b: 20%O_2+15%CO_2+65%Ar;
c: 20%O_2+40%CO_2+40%Ar; d: 20%O_2+80%CO_2
1: Ca/s=2

Fig.2. FTIR spectrum of exhaust gas under different atmosphere

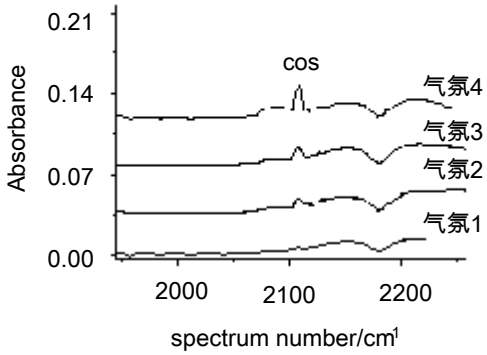

Fig.3 FTIR spectrum of COS in the flue gas under different atmospheres at 800℃

SO2 emission spectrum under different atmosphere from 800--1300℃ are shown in Figure 2. At low temperature, only high CO2 concentration (curve d) can remove SO2 emission effectively. However, at high temperature, the SO2 emission has a remarkable reduction under CO2 conditions.

T The main reasons of SO2 removal under high CO2 condition are as follows: O2/CO2 environment lowers the overall combustion rate of coal char because thermal properties for gas mixtures of O2/CO2 and O2/N2 are different, which resulting in decrease of sulfur evolution. CO2–C reaction which causing a reducing atmosphere and CO formation, which has a comparative contribution to decrease of SO2 emission because of the part formation of H2S and COS. Sulfur retention by coal ash is higher in O2/CO2 than in air environment because the presence of CO2 changes the surface structure and increases the reactivity of alkaline matter. Furthermore, Presented CO2 mitigates the sintering of CaO at high temperature and subsequent produce more reactive surface. The high limestone desulfurization efficiency is consequently resulted by high reactivity CaO reaction with SO2 under CO2 environment. Meanwhile, CO2 inhibits the decomposition of CaSO4 and improves the conversion ratio and consequently improved SO2 removal efficiency.

Acknowledgment

This work is supported by the National Key Project for Fundamental Research, the Ministry of Science and Technology of China (G1999022204-07), and supported by the Teaching and Research Award Program of High Education Institution of China.

References

1. Wolsky A.M., A new method of CO_2 recovery. 79th Annual Meeting of the Air Pollution Control Association, Minneapolis, Minnesota, 1986, June 22-27,1986.
2. Kimura N., Omata K., Kiga T., Takano S. and Shikisima S. The characteristics of pulverized coal combustion in O_2/CO_2 mixtures for CO_2 recovery. Energy Convers.Mgmt 1995, Vol.36, No.6, pp.805-808.
3. Yamada T, Kiga T., Okawa M., Omata K., Characteristics of Pulverized-Coal Combustion in CO_2-Recovery Power Plant Applied O_2/CO_2 Combustion, ICOPE-97, 1997, Vol.2, pp.285-290.
4. Jianrong Qiu, Bo Feng. SOx Reduction Mechanism during O_2/CO_2 Recycling Combustion. Proceeding of the 2nd Korea-China Joint Workshop on Coal & Clean Energy Utilization Technology, 1998, pp. 71-82

PREPARATION OF ZINC FERRITE IN THE PRESENCE OF CARBON MATERIAL AND ITS APPLICATION TO HOT-GAS CLEANING

Toshimitsu Suzuki, Na-oki Ikenaga, Hiro-aki Matsushima, and Yousuke Ohgaito

Department of Chemical Engineering, Kansai University
3-3-35 Yamate-cho, Suita, Osaka 564-8680, Japan

Introduction

Increasing attention is being paid to integrated gasification combined cycle (IGCC) process and gasification-molten carbonate fuel cell (MCFC) technology as one of the most promising technology to reduce CO_2 emission. For these technologies, several thousands ppm of hydrogen sulfide containing in an effluent gas from gasifier must be efficiently removed to several ppm for IGCC and <1 ppm for MCFC at a high temperature. Zinc ferrite ($ZnFe_2O_4$) is known to be one of the candidates for hydrogen sulfide removal[1,2]. In addition to zinc ferrite, various sorbents, such as manganese oxides[3] and zinc titanate[4], have been investigated. We have recently found that activated carbon-supported $ZnFe_2O_4$ could be prepared at much lower calcination temperature required for dry process for ferrite synthesis and that its absorption capacity was much higher than that of dry process ferrite[5].

In the present work, activated carbon-, activated carbon fiber-, and coal-supported zinc ferrite were prepared at a low temperature in order to obtain an effective absorbent for H_2S at a high temperature. Performance of absorption behavior of the prepared absorbent was evaluated using a fixed-bed flow type reactor. Regeneration of the used sorbent was investigated.

Experimental

Preparation of sorbent.

Homogeneous precipitation method. Into a mixed solution of $Fe(NO_3)_3$ and $Zn(NO_3)_2$ (150 mmol/L, 80 mL),0.04 mmol of urea and 0.3 g of activated carbon (AC, Wako Pure Chemical Industries, Ltd., 100-mesh pass, 993 m^2/g), activated carbon fiber (ACF, AD'ALL, Co., Ltd., 2000 m^2/g), or Yallourn coal (YL, C 66.3; H 4.70; N 0.48; S 0.26 daf%; Ash 2.0 d%, 100-mesh pass) was added. The mixture was allowed to keep 90 ^oC for 2h. During this stage, $Zn(OH)_2$ and $Fe(OH)_3$ were precipitated on AC, ACF, or YL coal. The mixture was was dried at 70 ^oC in vacuo, and then it was calcined at 400 or 500 ^oC in air for 2h.

Coprecipitation method. A 0.3 g of AC or YL coal was added into a mixed solution of $Fe(NO_3)_3$ (20 mmol/L, 100 mL) and $Zn(NO_3)_2$ (10 mmol/L, 100 mL), and then into this suspension aqueous ammonia was added until pH of the suspendant solution reaches 10. The combined precipitates were separated and dried in vacuo. The mixture was calcined at 300 or 500 ^oC in air for 2h.

Impregnation method. Zinc ferrite was prepared on AC or YL by the impregnation method described in the previous literature[5].

Characterization of sorbents. The ferrite prepared here and the metal species obtained after the absorption of hydrogen sulfide were analyzed by powder X-ray diffraction using an X-ray diffractometer (Shimadzu XRD-6000) with monochromated CuKα radiation. The surface areas of activated carbon-loaded and unloaded ferrite were measured using a Micromeritics Gemini 2375, applying adsorption isotherms of nitrogen at -196 ^oC to the BET equation.

Breakthrough behavior of sorbents measured by a fixed-bed reactor. The breakthrough curves were obtained by using a fixed-bed flow type reactor according to the procedure that was described in the previous paper[5].

Results and Discussion

Preparation and characterization of sorbents. Table 1 summarizes results of surface area and the content of oxides of various absorbents loaded on activated carbon, activated carbon fiber, and Yallourn coal char prepared by various methods. In the cases of ferrites loaded on organic support, oxide content in the total absorbent was evaluated based on the weight decreases of the samples, by burning the organic part by using a thermogravimetric balance in a flowing air. The surface areas of zinc ferrites prepared in the presence of ACF and AC (Samples D, F, and G) were higher than those zinc ferrites (Samples A, B, and C), which were prepared without carbon materials. The surface area of $ZnFe_2O_4$/ACF reached 1190 m^2/g due to a large amount of remained high surface area ACF. Surface areas decreased to 50 m^2/g with a decrease in the amount of carbon remaining (1-14 %). XRD analyses exhibited only diffraction peaks ascribed to ferrite phase after the calcinations in air at above 500 ^oC, with the exception of some cases. Samples E, F, and H showed very weak diffraction peaks ascribed to ZnO and Fe_2O_3, in addition to those of zinc ferrite.

Table 1 Surafce area and oxide content of various sorbents

Sample	Sorbent	Method	Calcination temp. ^oC	Phase determined by XRD	S.A. m^2/g	Oxide content wt%	Absorption capacity [a] %
A	$ZnFe_2O_4$	Dry process	1000	$ZnFe_2O_4$	17	-	49
B	Fe_2O_3	PPT	500	Fe_2O_3	40	-	94
C	$ZnFe_2O_4$	CoPPT	500	$ZnFe_2O_4$	41	-	48
D	$ZnFe_2O_4$	CoPPT	300	Amorphous	134	-	116
E	$ZnFe_2O_4$/ACF	HomoPPT	400	$ZnFe_2O_4$, ZnO, Fe_2O_3	1190	10.7	145
F	$ZnFe_2O_4$/AC	HomoPPT	500	$ZnFe_2O_4$, ZnO, Fe_2O_3	317	66.2	113
G	$ZnFe_2O_4$/AC	CoPPT	500	$ZnFe_2O_4$	463	56.9	84
H	$ZnFe_2O_4$/AC	IMP	500	$ZnFe_2O_4$, ZnO, Fe_2O_3	50	96.8	100
I	Fe_2O_3/AC	IMP	500	Fe_2O_3	67	99.0	113
J	$ZnFe_2O_4$/YL	HomoPPT	500	$ZnFe_2O_4$	51	93.1	98
K	$ZnFe_2O_4$/YL	CoPPT	500	$ZnFe_2O_4$	58	95.5	97
L	$ZnFe_2O_4$/YL	IMP	500	$ZnFe_2O_4$	50	86.0	90

a) Carried out using a fixed-bed reactor (N_2+H_2S(0.96 vol%) 5 mL/min, H_2 2mL/min, Absorption temperature 500 ^oC)
PPT: Precipitation method, CoPPT: Coprecipitation method, HomoPPT: Homogeneous precipitation method, IMP: Impregnation method

Absorption behavior of hydrogen sulfide. Figure 1 shows examples of breakthrough behavior of H_2S using various sorbents measured at 500 °C. The horizontal axis of Figure 1 designates the absorption capacity, which was calculated assuming that all zinc and iron in the ferrite would be transformed into ZnS and FeS. The absorption capacity exceeded 100% because a part of the iron was transformed into FeS_2. The absorption capacity of each sorbent is shown in the last column of Table 1. The absorption capacities of hydrogen sulfide (48-49%) with unloaded zinc ferrite (Samples A and C) were lower than those (>85%) of loaded zinc ferrites. When Fe_2O_3 (Samples B and I) and $ZnFe_2O_4$ prepared by dry method (Sample A) were used for H_2S absorption, high concentrations of H_2S (<20 ppm) were observed until the breakthrough point. On the other hand, the absorption capacities of H_2S increased to nearly 100% or more with $ZnFe_2O_4$ prepared on AC, ACF, and YL coal (Samples E-L). These absorbents showed no H_2S leakage in the effluent gas (less than 1 ppm). Although the surface areas of Samples F and G were higher than those of Samples E and H-L, the absorption capacities did not change. This fact indicates that the surface area seems not to be an important factor for the high absorption capacity of H_2S.

To examine the effect of the absorption temperature on the absorption capacity of the sorbent, the absorption of H_2S was carried out with $ZnFe_2O_4$/YL at 400-700 °C. When hydrogen sulfide was absorbed at 400 °C and 450 °C, the absorption capacities were 116% and 120%, respectively, and then that slightly decreased to 103% with increasing the absorption temperature to 500 °C and 600 °C. An elevated absorption temperature (700 °C) decreased the absorption capacity to 63%, indicating that optimal temperature of H_2S removal with $ZnFe_2O_4$/YL is 400-600 °C.

In order to elucidate the effect of the calcination temperature of the sorbent on the absorption behavior of H_2S, the breakthrough curves of the YL coal-supported zinc ferrites were calcined at 500-800 °C were measured at absorption temperature of 500 °C. The absorption capacity of $ZnFe_2O_4$/YL gradually decreased with increasing the calcination temperature to 800 °C, indicating that crystallite size of $ZnFe_2O_4$ determined by XRD analyses increased. This result clearly indicates that a crystallite size of $ZnFe_2O_4$ seems to be important for the high absorption capacity of H_2S.

Regeneration and repeated use of sorbent. Regeneration and repeated use of sorbent for H_2S removal is crucial to practical use. In order to ascertain the possibility of regeneration of sorbent after the absorption reaction of H_2S, the temperature programmed oxidation of the H_2S absorbed $ZnFe_2O_4$/YL (ZnS, FeS_2, $Fe_{1-x}S$) was carried out using a mixed gas of Ar and O_2 (50vol%). The releases of SO^+ and SO_2^+ were confirmed with a mass spectroscopy from 350 to 530 °C. Regeneration of H_2S absorbed $ZnFe_2O_4$/YL was carried out at 450 °C for 30 min using the fixed-bed reactor in oxygen-argon gases (O_2: 50vol%, Ar: 50vol%). According to the XRD analyses of $ZnFe_2O_4$/YL before the H_2S absorption and after four sulfurization-regeneration cycles, $ZnFe_2O_4$/YL exhibited diffraction peaks ascribed to $ZnFe_2O_4$ and very weak diffraction peaks of ZnO and Fe_2O_3. YL coal or AC loaded ferrites could successfully be regenerated at 450 °C. YL coal was burned out during the regeneration at 450 °C in a flowing air and the amount of carbon material decreased to nearly nil. Figure 2 illustrates the breakthrough curves that were measured at 500 °C using regenerated zinc ferrite, after second (R-2), third (R-3), and fourth (R-4) regeneration cycles. The absorption capacity of hydrogen sulfide with the fresh sorbent was 90%, and repeated use of the sorbent slightly decreased the absorption capacity to 75%. However, H_2S concentration in the tail gas was kept very low values.

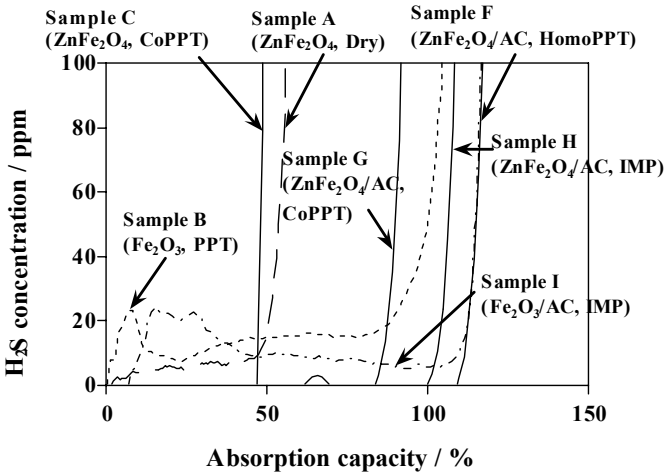

Figure 1 Breakthrough curves of H_2S absorption using various sorbents obtained at 500 °C. (Conditions: Ar 5 mL/min, N_2+H_2S 5 mL/min, H_2 2 mL/min)

Conclusion

Zinc ferrites could be prepared on activated carbon, activated carbon fiber, and Yallourn coal. Performance of the zinc ferrite for H_2S absorption was evaluated using a fixed-bed flow type reactor. These absorbents efficiently remove H_2S at an absorption temperature of 500 °C. Coal-loaded zinc ferrite could be regenerated by air oxidation at 450 °C. The regenerated zinc ferrite can be used for repeated absorption of H_2S with a slight decrease in the absorption capacity.

Acknowledgment. This work was financially supported by a grant-in-aid for priority area (11218212) from the Ministry of Education, Science, Japan.

References

1. Pineda, M.; Palacios, J.M.; Alonso, L.; Garcia, E.; Moliner, R., *Fuel*, **2000**, *79*, 885.
2. Alonso, L.; Palacios, J.M.; Garcia, E.; Moliner, R., *Fuel Process. Tech.* **2000**, *62*, 31.
3. Slimane, R.B.; Abbasian, J., *Adv. Environ. Res*., **2000**, *4*, 147.
4. Ozdemir, S.; Bardakci, T., *Sep. Purif. Technol*., **1999**, *16*, 225.
5. Ikenaga, N.; Chiyoda, N.; Matsushima, H.; Suzuki, T., *Fuel*, **2002**, ***81***, 1569.

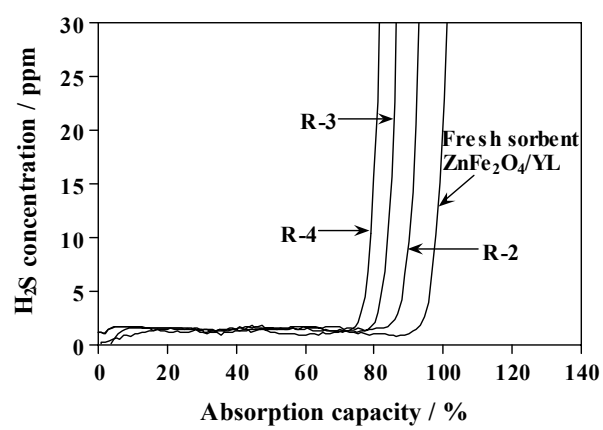

Figure 2 Breakthrough curves of H_2S absorption using $ZnFe_2O_4$/YL and regenerated

Reactor Designed for Continuous Removal of SO_2 in Flue Gas over Pitch Based Activated Carbon Fibers

Kei Tada [1], Takashi Enjoji[1],Seoung-Ho Yoon[1],Yozo Korai[1], Isao Mochida[1], AkinoriYasutake[2], and Masaki Yoshikawa[3]*

1) Institute of Advanced Material Study Kyushu University, 6-1 Kasuga-koen,Fukuoka 816-8580 JAPAN
*E-mail:mochida@cm.kyushu-u.ac.jp
2) Mitsubishi Heavy Industry Corporation
5-717-1Fukahori-cho, Nagasaki 851-0392 JAPAN
E-mail:yasutake@ngsrdc.mhi.co.jp
3) Osaka Gas Company
Technology Coordination Office Research & Development Department
6-19-9 Torishima, Konoha－Ku, OSAKA 554-0051 JAPAN
E-mail:yoshikaw@osakagas.co.jp

Introduction

The present authors have proposed SO_2 removal over pitch based activated carbon fibers (ACFs) by recovering aq.H_2SO_4 at ambient temperatures according to the scheme[1-3] illustrated in **Figure 1** with humidity of 5～10%. Heat-treatment of ACF at 1,100 °C was found to enhance by its activity markedly by introducing more active sites. High concentration of H_2O and O_2 in the feed gas is favorable for SOx fixation while NO inhibits the SO_2 removal.

$$SO_2+Sv \rightarrow SO_{2ads}\text{-}Sv$$
$$SO_{2ads}\text{-}Sv+1/2O_2 \rightarrow SO_{3ads}\text{-}Ss$$
$$SO_{3ads}\text{-}Ss+H_2O \rightarrow H_2SO_{4ads}\text{-}Ss$$
$$H_2SO_{4ads}\text{-}Ss+H_2O \rightarrow aq.H_2SO_4+Sv$$

Figure 1. DeSOx Scheme over ACF

In the present study, reactor for ACF packing was designed to enhance its activity by the same amount of the same ACF in order to reduce the reactor volume, ACF amount, H_2O and O_2 concentration necessary for the complete SO_2 removal at high temperature. The key concept for the reactor design is to recognize that the produced H_2SO_4 occupies the active site to reduce the activity of the ACF. Hence several types of reactors were designed to accelerate the elution of H_2SO_4 with its least contact to the ACF.
The reactors examined were

1. Reactor shape to change width vs length of ACF bed
2. Staged reactors for separation of produced H_2SO_4 at the stages

Experimental

An OG series active carbon fiber (OG-20A) was supplied by Osaka Gas Company. It was heat-treated in Ar gas at 1100℃ for 1hr. OG20A-H1100 carried high surface area of 1500m^2/g. SO_2 removal was carried out at 60℃. ACF was packed densely in the reactor tube. The flow rate was fixed at 100ml/min. Produced H_2SO_4 was trapped at the bottom of the reactor. Therefore, the concentrations of SO_2 in the inlet and outlet gases were analyzed continuously by a flame photometric detector (R268Y-Hamamatsu Photonics).
In **Figure 3** reactors were reference one (diameter 14mm) and wide one (diameter 16mm), respectively. Two reference reactors were arranged in parallel. The parallel reactor corresponded to the broaden one. H_2SO_4 produced in the first reactor was recovered before the second reactor located in sequence. Another type was staged reactors. Staged reactors had separated ACF bed and reduced the inhibition of H_2SO_4 by intermediate trap in **Figure 4**.

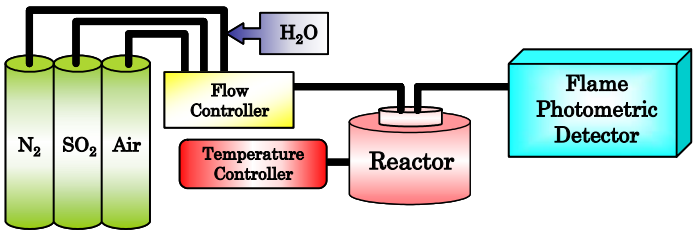

Figure 2. Experimental apparatus for oxidative fixation of SO_2

Results

Bold type reactor was certainly superior to the reference reactor as in **Figure 5**. The reactors of larger diameter showed better performance, confirming the influence of diameter/length ratio of ACF bed in the single reactor.

In figure 6, the performances of various reactor type were compared by using the same amount of ACF and same flow rate of gas feed. The heights of ACF were 50mm in the single reactor and 25mm in the parallel reactor respectively. The parallel reactor showed longer breakthrough time, suggesting the more efficient desulfurization with broad ACF bed. Staged type had better performances too, but not so good compared to parallel type. **Figure 7** compares the performances of the reference, parallel staged reactors against 750ppm SO_2. This result was the staged type. Staged Reactor completely removed SO_2 about 60hr. Parallel was same breakthrough time to reference but better removal ratio. **Figure 8** shows the activity of more amount of ACF (1.0g) achieved complete SO_2 removal by the parallel reactors and staged reactors whereas the reference reactor allowed still breakthrough by 34hr.

Discussion

The present study revealed that the reactor design was very influential on the performance for SO_2 removal of the ACF of the same amount. The up-flow is certainly better than the down flow. Broader reactor is better than thinner one. The intermediate reactors equipped with the respective device for H_2SO_4 recovery at every stages are certainly better than the single reactor at the same ACF amount. All these results indicate that the shorter path for aq.H_2SO_4 elution from the produced to the recovered locations allowed, better performance. Occupation of the active site by produced H_2SO_4 is minimized by the designed reactors to achieve lower SO_2 elution amount.

The reason why the intermediate recovery reactor is inferior to the parallel reactor is smaller supply of water to the upper reactor of the intermediate reactors, since most of water is trapped at H_2SO_4 trap located at the lower reactors. Small amount of water supply at the top of upper reactor solver the problems.

Staged type was the best in **Figure 7**, while parallel type was excellent in the others conditions. This different performance could be due to the different concentration of SO_2 feed gas and removal efficiency of formed H_2SO_4. the amount of H_2SO_4 was mainly related to H_2O and elution speed is the most important parameter.

References

1. I. Mochida, K. Kuroda, S. Kawano, Y. Matsumura, and M. Yoshikawa, *Fuel*, **76**, 533(1997).
2. I. Mochida, K. Kuroda, S. Kawano, Y. Matsumura, M. Yoshikawa, E. Grulke, and R. Andrews, *Fuel*, **76**, 537(1997).
3. I. Mochida, Y. Korai, M. Shirahama, S. Kawano, T. Hada, Y. Seo, M. Yoshikawa, and A. Yasutake, *Carbon*, **38**, 227(2000).

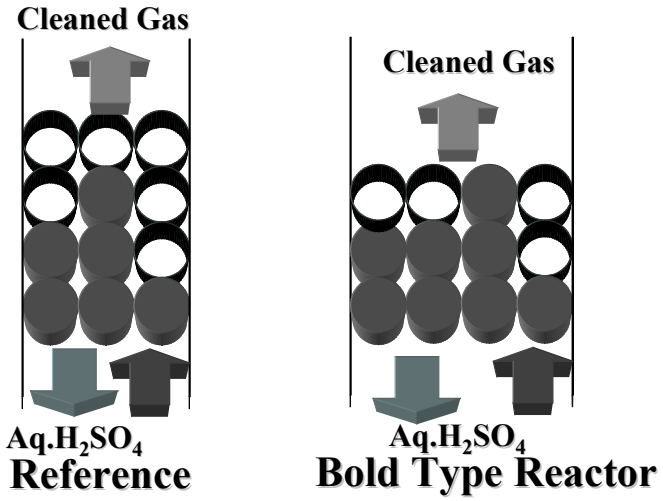

Figure 3.Concept of Designed Reactors (1)

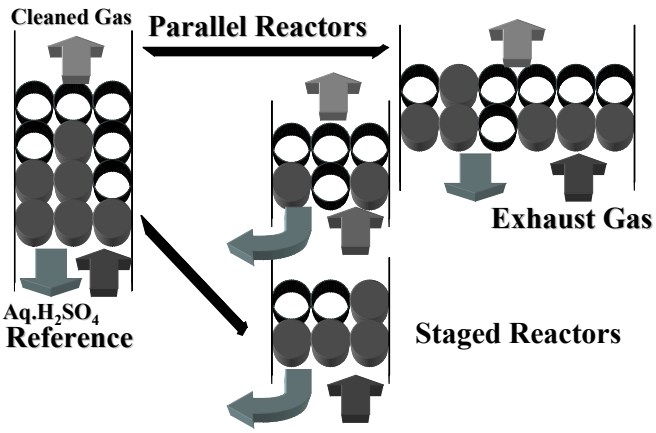

Figure 4.Concept of Designed Reactors (2)

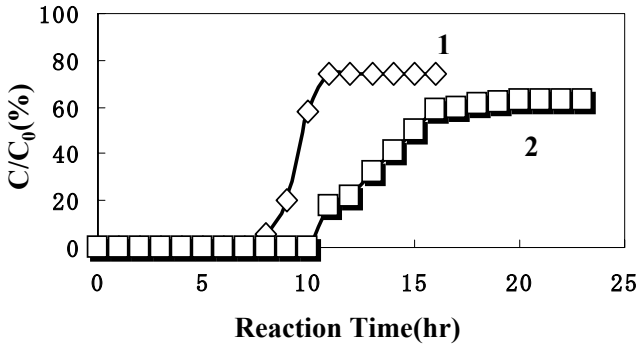

Figure 5. Breakthrough profiles of SO_2 in a reference and Bold Reactor
SO_2=1000ppm, O_2=5vol.% H_2O = 10 vol.%, N_2 balance
W/F = 5.0×10^{-3}g·min·ml-1Reaction temperature 60^0C
1: Reactor Diameter(14mm)
2: Reactor Diameter(16mm)

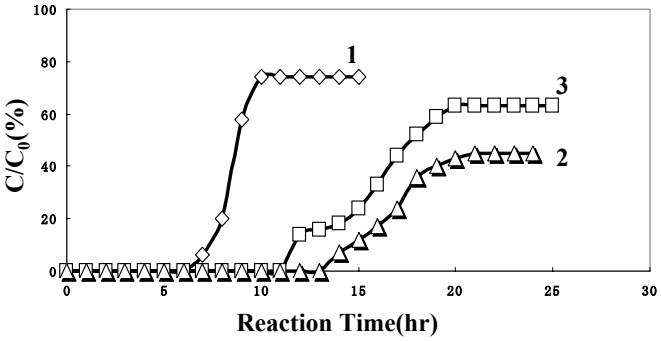

Figure 6. Breakthrough profiles of SO_2 in a reference, Parallel and Staged Reactors
SO_2=1000ppm, O_2=5vol.%H_2O = 10 vol.%, N_2 balance
W/F = 5.0×10^{-3}g·min·ml-1 Reaction temperature 60^0C
1: Reference Reactor
2: Parallel Reactors
3: Staged Reactors

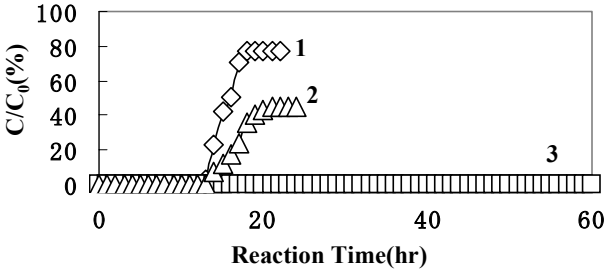

Figure7. Breakthrough profiles of SO_2 in a reference, Parallel and Staged Reactors
SO_2 =750ppm, O_2=5vol.% H_2O = 10 vol.%, N_2 balance
W/F = 5.0×10^{-3}g·min·ml^{-1} Reaction temperature 60^0C
1: Reference Reactor
2: Parallel Reactors
3: Staged Reactors

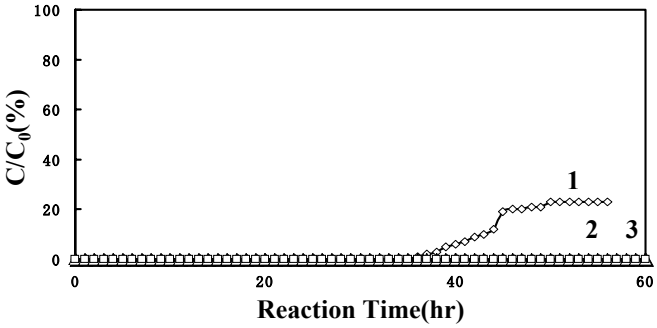

Figure 8. Breakthrough profiles of SO_2 in a reference, Parallel and Staged Reactors
SO_2=1000ppm, O_2=5vol.% H_2O = 10 vol.%, N_2 balance
W/F = 1.0×10^{-2}g·min·ml^{-1} Reaction temperature 60^0C
1: Reference Reactor
2: Parallel Reactors
3: Staged Reactors

CATALYST DEVELOPMENT FOR THE REFORMING OF LIQUID HYDROCARBONS

Christina R. Manns, Bret H. Howard, and Charles E. Taylor

U.S. Department of Energy
National Energy Technology Laboratory
P.O. Box 10940
Pittsburgh, PA 15236-0940

Introduction

Fuel cells are rapidly being recognized as an alternative source of electricity to power automobiles, light-duty trucks and in small stationary applications. Fuel cells, powered by hydrogen, have the potential to be the cleanest and most efficient source of electricity for use by the automotive industry. The goal of this project is to develop a process that utilizes a liquid hydrocarbon fuel as the hydrogen source for an on-board fuel cell. One of the major problems in current reforming processes is the byproduct carbon monoxide (CO). CO is a poison to the proton exchange membrane (PEM) fuel cell catalyst which is platinum based [1,2].

The objective of this research is to reduce the quantity of CO produced during hydrocarbon reforming to near-zero levels under mild reforming conditions. To accomplish this, two major topics must be examined: the composition of the catalyst and the type of liquid hydrocarbon that is being reformed. Currently, methanol is favored as the chemical carrier for hydrogen for fuel cell applications. Methanol can be produced from a variety of fossil fuels and has a high energy density. Since it is a liquid, methanol is more easily adaptable to the existing fuel infrastructure, requiring similar transportation and storage facilities as those already in use.

Ideally, a reforming catalyst would have hydrocarbon feed flexibility or the ability to effectively reform a variety of hydrocarbon feeds. However, this is not easily accomplished at the moderate temperatures (330-400°C) at which the catalyst must operate. The desired products would be hydrogen and carbon dioxide, with no production of CO. Most conventional reforming processes operate at higher temperatures, producing a significant quantity of CO. Also, higher operating temperatures are not cost effective due to increased energy consumption and more stringent materials requirements.

Copper-based catalysts are known to have potential for reforming applications, and were selected for this study. Previous studies have indicated that these catalysts are active for steam reforming at temperatures that are low enough to minimize the production of CO and that these catalysts are stable under the target operating conditions [3,4]. Steam reforming employs the water-gas shift (WGS) reaction maximizing production of H_2 with negligible production of CO.

The purpose of this study is to develop stable, copper-based catalysts capable of reforming methanol at moderate temperatures to produce H_2 and CO_2 with little or no CO or other byproduct yield. This study examined neat methanol feeds as well as methanol/water feeds (1:1 volume) as the reactants in the reforming process. Results are compared to studies reported in the literature that used either water and methanol or water and ethanol as reactants at molar ratios of 1.0 or 1.3.

Experimental

Several techniques were employed in the catalyst preparations. These techniques included sequential precipitation, co-precipitation with sequential precipitation, and incipient wetness impregnation. Generally, nitrate salts of the metals were used to prepare catalyst precursors at carefully controlled pH. Precursors were washed, dried at 120°C overnight followed by calcination in air at 350°C for 6 hours.

For both the freshly prepared and used catalysts, the following were determined: the surface area was determined by the Brunauer, Emmett, and Teller (BET) method, the composition was examined by Inductively Coupled Plasma-Atomic Emission Spectroscopy (ICP-AES), and the morphology was determined by scanning-electron microscopy (SEM).

All reforming reactions were conducted in a 0.5-inch O.D. x 0.375-inch I.D. (1.27 cm O.D. x 0.95 cm I.D.) x 10-inch (25.4 cm) 304 stainless steel reactor. The inside wall of the reactor was coated with Silcosteel® (Restek) coating. The catalyst was supported in the reactor between quartz-wool plugs and the reactor was operated in an up-flow configuration. A gold-plated thermocouple in the center of the catalyst bed was used to monitor the temperature of reaction to ±0.5°C. Proportional ratio mass-flow controllers (Brooks) were used to feed the gases to the reactor. A high-pressure syringe pump (Isco) controlled feeds of liquids to the reactor. The feeds were preheated to approximately 130°C prior to entering the reactor and the products of reaction were held at approximately 150°C between the exit of the reactor and the cold trap, which was maintained at –4°C.

Reaction conditions were as follows: 1 gram (±0.001) of catalyst was placed in the reactor supported between deactivated-quartz wool plugs. A gold-plated thermocouple was placed in the middle of the catalyst bed. The reactor was purged with helium at 5 mL/min for at least 2 hours. The temperature of the reactor was increased to either 150°C or 255°C. Methanol flow was started at a weight hourly space velocity of 1 hr^{-1} after the catalyst had reached the target temperature.

Products of reaction were directly sampled and analyzed by an online dual-column gas chromatograph (GC). The GC (Hewlett-Packard 5890 Series II) was equipped with a 6 ft x 0.125 O.D. 80/100 Porapak Q and a 20 ft x 0.125 O.D. 60/80 Molecular Sieve 5Å (both obtained from Supelco). The GC was operated at a constant temperature of 100°C during elution. Argon was used as the carrier gas having an average linear velocity at 30°C of 30 mL/min for the Molecular Sieve column and 50 mL/min for the Porapak Q column. The Molecular sieve column was used to separate the light gaseous products while the Porapak Q column was used to identify unreacted liquid hydrocarbons. Both columns were equipped with back-flushing capability. Dual thermal conductivity detectors (TCDs) were employed to detect the separated components.

Results and Discussion

Reforming of methanol was done using methanol only and also using methanol and water with a 1:1 volume basis. Reforming of methanol only was run at various reaction temperatures. **Table I** lists the data from a series of methanol-reforming reactions.

TABLE I. Results of Methanol Reforming Reactions

Catalyst	Temp. (°C)	CH_3OH Conversion (%)	H_2 (%)	CO_2 (%)	CO (%)
Cu/Zn/Zr/Al/Y*	150	21.2	8.9	91.1	0.0
Cu/Zn/Zr/Al/Y*	255	72.2	91.1	8.9	0.0
Cu/Zn/Zr/Al/Y**	255	49.1	77.6	16.6	5.8
Cu/Zn/Ce/on γ-Al_2O_3	255	85.1	47.2	22.5	29.3
Cu/Zr/ on γ-Al_2O_3	255	80.9	53.5	40.6	5.9
Cu/Zn/Zr/ on γ-Al_2O_3	255	90.5	45.5	35.2	19.3

* 69/17/10/2/2 mole percent ** 8/2/64/13/13 mole percent

Table I shows that methanol conversion increases with reaction temperature. For the Cu/Zn/Zr/Al/Y (69/17/10/2/2 mole %) catalyst at 150°C, methanol conversion was approximately 21%. The

majority of product detected by the GC was carbon dioxide. When the reaction temperature was increased to 255°C, conversion of methanol increased initially to 80%. The product selectivity also increased, with hydrogen comprising 91% of the product stream.

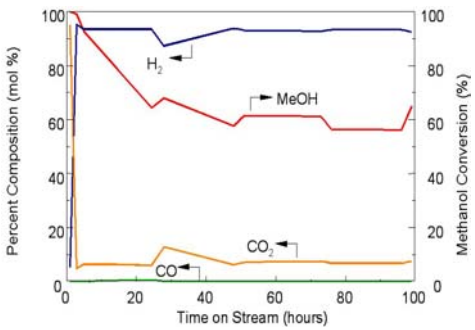

Figure 1. Results of methanol conversion over Cu/Zn/Zr/Al/Y catalyst as a function of time.

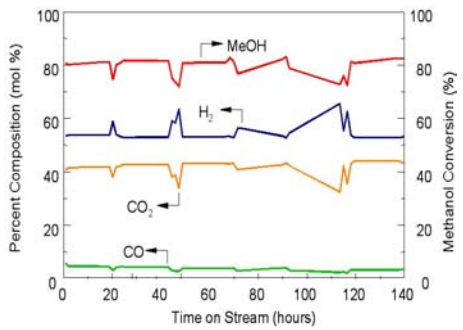

Figure 2. Results of methanol conversion over Cu/Zr on γ-Al_2O_3 catalyst as a function of time.

Figure 1 shows an extended conversion run for the Cu/Zn/Zr/Al/Y (69/17/10/2/2 mole percent) catalyst. Methanol conversion decreased with time on stream at 255°C. This decrease is due to coke formation during the reaction. The results for this catalyst were similar to those reported in the literature [3]. Conversion of methanol was low at 150°C and increased with increasing temperature. Conversions of methanol at 250°C were greater than 50% in both cases. Differences arise when the product slate is examined. This catalyst produced larger quantities of carbon dioxide than reported for the literature catalyst. Of importance is that carbon monoxide was not detected at either reaction temperature in our investigation or in the literature [3] with the Cu/Zn/Zr/Al/Y catalyst.

Figure 2 shows an extended conversion run for the Cu/Zr on γ-Al_2O_3 (7/3/90 mole %) catalyst. As is shown in **Figure 2**, conversion of methanol at 255°C is relatively stable with time on stream as are the products produced. This catalyst did exhibit CO production at 255°C, however coking was much less than that observed with the Cu/Zn/Zr/Al/Y catalyst.

The same group of catalysts was run using a 1:1 volume methanol/water feed and a reaction temperature of 250°C. The results of the reactions of methanol and water are listed in Table II. As shown in **Table II**, conversion of methanol for all the catalysts, except for the Cu/Zn/Zr/Al/Y, which had a very low surface area, were greater than 99%. Experiments using co-fed water with methanol exhibited lower carbon monoxide product levels than experiments run with methanol alone, as would be expected. Table two also shows that when using methanol and water as a co-feed at 250°C, methanol conversions increased by an additional 50%.

TABLE II. Results of Methanol/Water Reforming Reactions

Catalyst	Temp. (°C)	CH_3OH Conversion (%)	H_2 (%)	CO_2 (%)	CO (%)
Cu/Zn/Zr/Al/Y*	250	100	59.0	35.8	4.3
Cu/Zn/Zr/Al/Y**	250	21.2	7.9	4.8	0.0
Cu/Zn/Ce/on γ-Al_2O_3	250	99.0	57.6	38.5	3.7
Cu/Zr/ on γ-Al_2O_3	250	99.4	43.2	30.4	1.1
Cu/Zn/Zr/ on γ-Al_2O_3	250	99.7	60.9	38.0	0.98

* 69/17/10/2/2 mole percent ** 8/2/64/13/13 mole percent

Figure 3 shows an extended conversion run for a 1:1 methanol:water reaction over the Cu/Zn/Zr/ on γ-Al_2O_3 (12/2.5/2.5/83 mole %) catalyst. As shown in **Figure 3**, conversion of methanol at 255°C remains constant with time on stream. It should be noted that carbon monoxide was negligible at either reaction temperature in this investigation with the Cu/Zn/Zr/ on γ-Al_2O_3 catalyst.

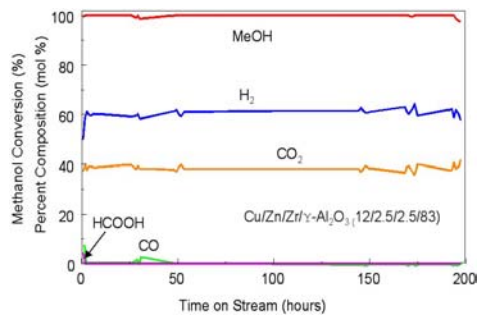

Figure 3. Results of methanol/water conversion over Cu/Zn/Zr on γ-Al_2O_3 catalyst as a function of time.

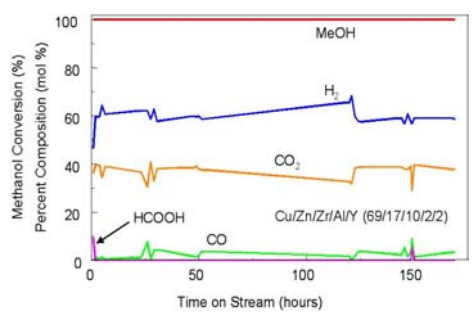

Figure 4. Results of methanol/water conversion over Cu/Zn/Zr/Al/Y catalyst as a function of time.

Figure 4 shows an extended conversion run for a 1:1 methanol/water reaction over the Cu/Zn/Zr/Al/Y (69/17/10/2/2 mole %) catalyst. As shown in **Figure 4**, conversion of methanol at 255°C is relatively stable with time on stream as are the reaction products. This catalyst did exhibit CO production at 255°C; however, coking was not observed.

Table III. Catalyst Surface Area

Catalyst Composition (mole %)	Surface Area (as prepared) (m^2/g)	Surface Area (after reaction) (m^2/g)	Surface Area (after reaction with H_2O) (m^2/g)
Cu/Zn/Zr/Al/Y 69/17/10/2/2	92	55	57
Cu/Zn/Zr/Al/Y 8/2/64/13/13	21	16	54
Cu/Zr on γ-Al_2O_3 12/5/83	200	188	193
Cu/Zn/Zr on γ-Al_2O_3 12/2.5/2.5/83	198	187	186
Cu/Zn/Ce on γ-Al_2O_3 12/2.5/2.5/83	194	195	194

Table III shows the surface area of the catalyst as prepared, after 150 hours of reaction with methanol reforming and after 150 hours of methanol/water reforming. Both catalyst preparations of Cu/Zn/Zr/Al/Y exhibit a loss of surface area after reaction probably due to coking. The three catalysts supported on γ-Al_2O_3 retain more than 90% of the prepared surface area. These catalysts were also the most stable of all the catalysts tested.

In summary, reforming results with neat methanol show higher methanol conversions than those reported in the literature, also using neat methanol, over an extended period of time. Yields of H_2, CO_2, and CO for reforming of neat methanol are comparable to those reported in the literature for reforming of water: methanol mixtures at similar molar ratios [3].

Using methanol with water (1:1 volume) as a feed resulted in higher methanol conversions and slightly higher hydrogen yields than experiments using neat methanol. The methanol:water feed also produced higher hydrogen yields when compared to methanol:water reforming yields reported in the literature [3]. After reviewing the results, a Cu/Zn/Zr catalyst on γ-Al_2O_3 was selected for further testing using other liquid hydrocarbons. This catalyst was selected because it produced the lowest amount of CO during extended methanol:water reforming runs while maintaining high conversion and product yields. Preliminary experimental runs using this catalyst with neat ethanol and ethanol with water (1:1 volume) have been completed. The results show that the production of CO is slightly less with neat ethanol than the methanol:water, while CO production is reduced another 50% in the ethanol:water reforming reaction over neat ethanol only. Preliminary results show that direct reforming of coal derived liquid hydrocarbons with a pre-determined amount of water may remain a low-cost option for on-board production of hydrogen.

Conclusions

Several catalysts have been synthesized that are capable of reforming methanol at moderate temperatures. The main products of reaction using water with either methanol or ethanol are hydrogen and carbon dioxide. A higher selectivity for H_2 was observed for the catalysts prepared for this study although some coking was observed under certain reactor conditions. However, when the WGS reaction was employed, a decrease in CO production resulted. A direct correlation between the catalyst's surface area, methanol and ethanol conversion, and catalyst stability is observed.

Acknowledgement

The authors would like to acknowledge the technical assistance of Richard R. Anderson, Heather A. Elsen, Edward P. Ladner, and Dirk D. Link.

Disclaimer

Reference in this report to any specific commercial product, process, or service is to facilitate understanding and does not necessarily imply its endorsement or favoring by the United States Department of Energy.

References

1. Borroni-Bird, C.E. *Journal of Power Sources* **1996**, *61*, 33-48.
2. National Renewable Energy Laboratory report, DOE/GO-10095-088, DE94011827, February 1995.
3. Breen, J.P. and Ross, J.R.H. *Catalysis Today* **1999**, *51,* 521.
4. S. Velu, K. Suzuki, M.P. Kapoor, T. Osaki, And F. Ohashi *Journal of Catalysis* **2000**, *194*, 373-384.
5. Taylor, C.E. and Manns, C.R. *Preprints of the Fuels Division* 2001, 46(2), 652.

IN-SITU IR STUDIES ON THE OXIDATIVE CARBONYLATION OF METHANOL TO DIMETHYL CARBONATE

Xinbin Ma, Zhenhua Li, Baowei Wang, Genhui Xu

State Key Laboratory of C_1 Chemistry and Technology,
School of Chemical Engineering and Technology, Tianjin University,
Tianjin 30072, China

Introduction

Dimethyl carbonate (DMC) has been used as gasoline extender, an octane number improver and an organic solvent. Dimethyl carbonate is much less toxic than phosgene and dimethyl sulfate. Also, the by-product, when DMC was used to substitute for highly toxic compounds such as phosgene and dimethyl sulfate in many reactions, is methanol or carbon dioxide, which is easily separated from the product and leads to less pollution. So, the synthesis of DMC through an environmentally benign process attracts worldwide attention.

The traditional methods for DMC production are the phosgene-methanol and ester-exchange method[1]. In these two methods, some raw materials are highly toxic and result in pollution, which limits its further application. The oxidative carbonylation of methanol to DMC as shown in reaction (1) is an environmentally benign process[2]. It absorbed many researchers' attention in the past years.

$$CO + 2CH_3OH + 1/2O_2 \rightarrow CO(OCH_3)_2 + H_2O \qquad (1)$$

Many researchers have studied this reaction but their work mainly focused on the catalytic activities of the catalysts, however, little has been reported on the mechanism of the reaction. In this work, the in-situ IR technique was used to study the reaction mechanism of oxidative carbonylation of methanol to dimethyl carbonate over supported Cu catalysts.

Experimental

The catalyst of Cu supported on Al_2O_3 with a Cu content 9 wt% was prepared by incipient wetness impregnated with an ethanol solution of $CuCl_2$. The impregnated sample was dried under a flow of nitrogen gas at 373 K for 3 h. The dried sample was cooled to room temperature and was further treated by incipient wetness impregnation with NaOH solution. Then the sample was subjected to a thermal treatment under a flow of nitrogen gas at 573 K for 3 h. The molar ratio of OH/Cu is 1, calculated from the moles of impregnated $CuCl_2$ and the moles of NaOH.

The activity of catalyst was measured with a micro catalytic reaction system comprising a stainless steel fixed bed reactor of 5 mm inner-diameter[3], with a molar ratio of carbon monoxide to methanol of 1.3, a molar ratio of oxygen to methanol of 0.3. The conversion of methanol was 15.62%, and the selectivity to DMC was 62.43% at reaction temperature of 403 K and pressure of 0.7 MPa.

The IR spectra were obtained using a PE System FT-IR spectrometer. An in-situ infrared reactor cell, equipped with NaCl windows and capable of operating in the range 298 K to 773 K and 0.1 MPa to 2.0 MPa, was used for in-situ IR studies.

The powdered catalysts were pressed into a flake with diameter 12 mm and height 0.1 mm, placed in the reactor cell and purged the air from the reactor cell by nitrogen at flow rate of 5 SCCM. The temperature of the reactor cell was heated to 473 K at a rate of 5 K min^{-1} in the nitrogen in order to clean the surface of the catalyst flake, after 10 minutes the reactor cell was controlled at 403 K and at a pressure of 0.7 MPa. IR data were collected at 4 cm^{-1} resolution and 50 scans.

Results and Discussion

The oxygen, carbon monoxide and methanol was separately introduced the reactor cell in the reaction condition. Fig. 1 displays the in-situ IR spectra of adsorbed oxygen. The intensity of the band at 1292 cm^{-1} increases with the increase of the absorbed time, but the intensity of the band at 1186 cm^{-1} doesn't change. When the oxygen is adsorbed on the supporter Al_2O_3 at the same condition, there is only band at 1186 cm^{-1}, the band at 1292 cm^{-1} don't appear. So the band at 1292 cm^{-1} and 1186 cm^{-1} is attributed to the O_2 adsorbed on the catalyst and the supporter Al_2O_3, respectively. O_2 adsorbed on the catalyst is decomposed further.

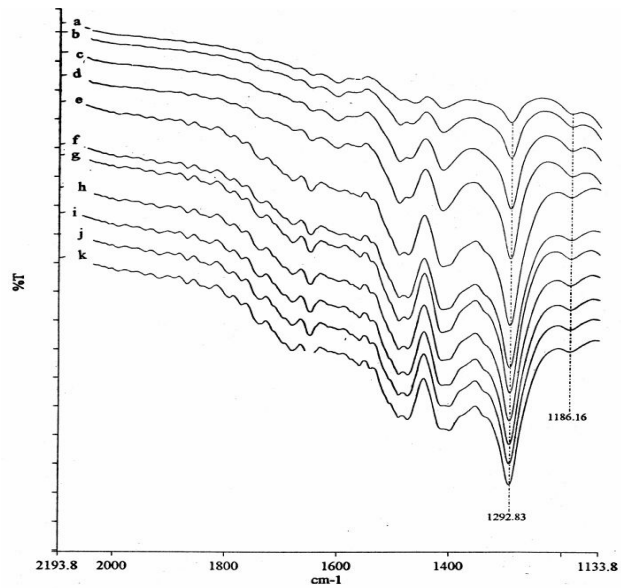

Figure 1. IR spectra for adsorption of O_2 on Cu/Al_2O_3 catalyst a: 1'30", b: 3'30", c: 4'30", d: 7'50", e: 11', f: 13'30", g: 20', h: 25', i: 30', j: 35', k: 40'

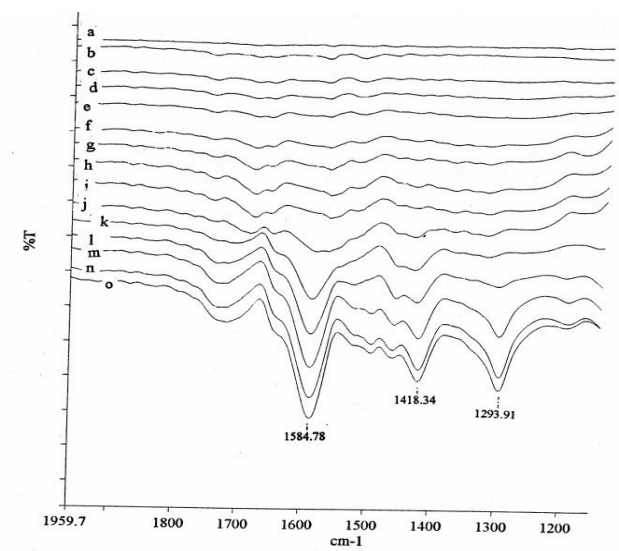

Figure 2. IR spectra for co-adsorption of O_2 and CO on catalyst a: CO was introduced (0'), b: 2'40", c: 4'50", d: 6'50", e: 9'30", f: 20', g: 30', h:50'; i: O2 was introduced (51'), j: 54'15", k: 56', l: 60', m: 64'30", n: 68'30", o: 75'35"

Carbon monoxide was introduced into the reactor cell, no any peaks were observed as shown in Fig. 2. This indicated that carbon monoxide was adsorbed weakly on the surface of the catalyst. When the oxygen and carbon monoxide were introduced the reactor cell together, not only the band at 1292 cm^{-1}, which is oxygen adsorbed on the catalyst, was observed, but also the band at 1585 cm^{-1} and 1418 cm^{-1} appear. This indicated that the oxygen and carbon monoxide are co-adsorbed on the catalyst.

IR spectra for adsorption of methanol on catalyst Cu/Al_2O_3 is shown in Fig. 3. The intensity of the band at 1111 cm^{-1} increased with the increase of the adsorbed time. The band at 1111 cm^{-1} is assigned to the methoxy group[4], which indicated that methanol was absorbed on the catalyst surface. When the pressure of the reactor cell was degraded to the 0.1 MPa and the nitrogen was introduced, the band of the methoxy group disappeared, only the band at 1056 cm^{-1} and 1032 cm^{-1} existed, which is attributed to the vapor methanol. The results indicated that the high pressure was favorable for the methanol absorbed on the catalyst Cu/Al_2O_3 to produce methoxy group.

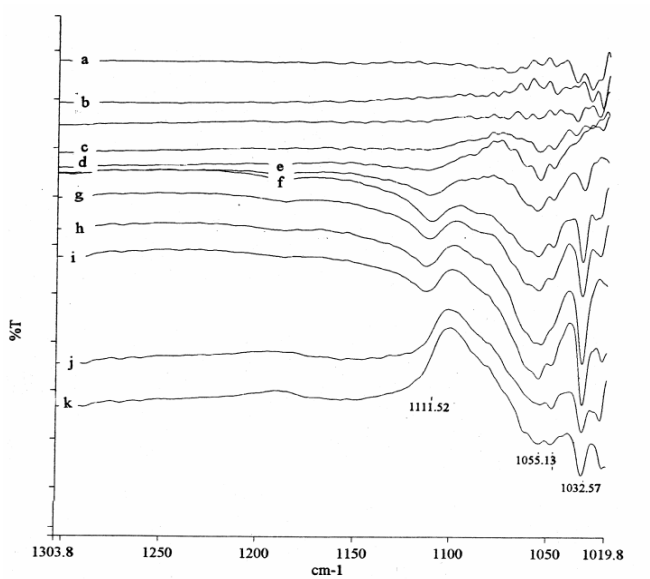

Figure 3. IR spectra for adsorption of methanol on catalyst
a: methanol was introduced (0'), b: 2'5", c: 6'37", d: 12', e: 16'10", f: 21', g: 30', h:40', i: 50', j: nitrogen was introduced (90'), k: 120'

IR spectra for in-situ oxidative carbonylation of methanol to DMC over Cu/Al_2O_3 catalyst are shown in Fig. 4. The oxygen, carbon monoxide and methanol were together introduced into the reactor cell, the band at 1171 cm^{-1}, which is assigned to the dimethyl carbonate, was observed[5]. According to the IR spectra of the in-situ reaction, the reaction mechanism may the insertion reaction of weakly adsorbed carbon monoxide into the adsorbed methoxy groups as shown in reaction (2).

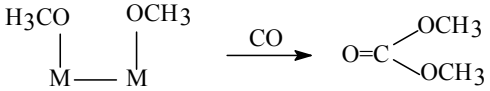

(2)

The molecular oxygen was adsorbed on the supported Cu catalyst and further decomposed. The methoxy groups might react with decomposed oxygen to produce carbon dioxide and water as shown in the reaction (3). So the concentration of oxygen should be controlled reasonably to avoid the oxidation of methanol to produce carbon dioxide.

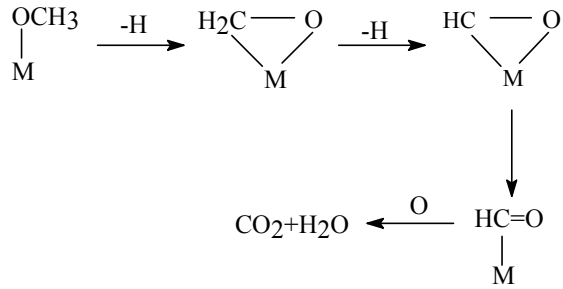

(3)

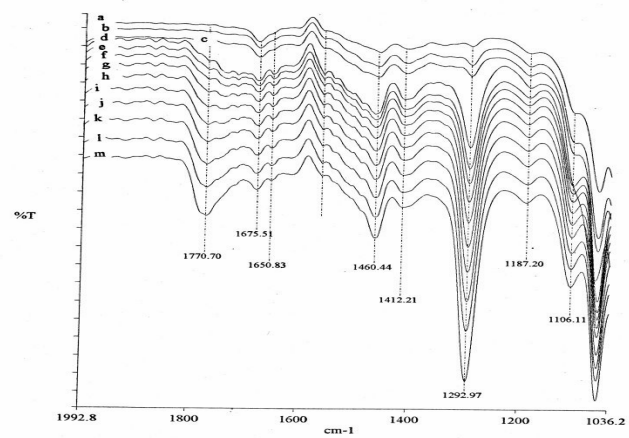

Figure 4. IR spectra for in-situ reaction on Cu/Al_2O_3 catalyst
a: 2', b: 6'15", c: 10'30", d: 12'50", e: 14'30", f: 16',g: 18', h: 20', i: 25', j: 30', k: 35', l: 40', m: 45'

Conclusions

The in-situ IR technique was used to study the reaction mechanism of oxidative carbonylation of methanol to dimethyl carbonate over supported Cu catalysts. The results indicated that oxygen was adsorbed on the supported Cu catalyst and further decomposed. carbon monoxide was adsorbed weakly on the surface of the catalyst. The methoxy groups were found when methanol was introduced to the catalyst and higher pressure was favorable for the formation of methoxy groups. The reaction mechanism is the insertion reaction of weakly adsorbed carbon monoxide into the adsorbed methoxy groups. It was also found that methoxy groups might react with decomposed oxygen to produce carbon dioxide and water. So the concentration of oxygen should be controlled reasonably.

Acknowledgement. This work is supported by Natural Science Foundation of Tianjin in China. (973701711)

References

1. Gilpin, J. A. and Emmons, A. H. US Pat., 803201
2. David; S. G. and Staines, S. M. EP 134668
3. Ma, X. B.; Zhao, R. Z.; Xu, G. H.; He, F.; and Chen, H. F. *Catal Today.* **1996**, 30, 201.
4. Clarke, D. B.and Bell, A. T. *J. Catal.*. **1995**, 154(2), 314.
5. Schild, C.; Wokaun, A. and Baiker, A. *J. Mol. Catal.*. **1990**, 63(2), 223.

DIESEL FUEL FORMULATION EFFECTS ON INJECTION TIMING AND EMISSIONS

James Szybist, David Morris and André L. Boehman

The Energy Institute
The Pennsylvania State University
405 Academic Activities Building
University Park, PA 16802

Etop Esen

ConocoPhillips
600 N. Dairy Ashford
Houston, TX 77252

Introduction

Addition of biomass-derived fuels and synthetic fuels to diesel fuel basestocks is a means of producing a cleaner burning diesel fuel. Blending with oxygenated or zero sulfur fuels can lead to particulate emissions reductions by interfering with the soot formation process and by decreasing the formation of sulfates. However, in the case of biodiesel fueling (e.g., "B20", a blend of 20vol.% methyl soyate in diesel fuel) there is a well documented increase of 2-4% in NOx emissions [1]. As shown by Van Gerpen and co-workers, the NOx increase with biodiesel fueling is attributable to an inadvertent advance of fuel injection timing. The advance in injection timing is due to the higher bulk modulus of compressibility, or speed of sound, in the fuel blend, which leads to a more rapid transferal of the pressure wave from the fuel pump to the injector needle and an earlier needle lift [2,3].

In this paper, we examine this interaction between the bulk modulus of compressibility of various fuel samples and their effect on fuel injection timing. The fuels considered range from methyl soyate (the methyl ester of soybean oil), unrefined soybean oil, and paraffinic solvents to ultra low sulfur and conventional diesel fuels. Both the impact on injection timing and the variation in the bulk modulus of compressibility are measured so that correlation between fuel composition, fuel properties and injection timing can be observed and quantified.

Experimental

Two different experimental systems were used in the work described here: a high pressure viscometer, capable of measuring the bulk modulus of compressibility with the use of a pycnometer; and a highly instrumented, single-cylinder direct injection (DI) diesel engine, with an accompanying spray visualization chamber. The bulk modulus of various fuels was measured, and corresponding measurements were made of the impact of the fuel on the injection timing in the DI diesel engine.

High Pressure Viscometer. This instrument was developed for studies of the viscosity and bulk modulus of hydraulic fluids that contained dissolved gases [3]. The principle of operation for this device is that when a fluid is exposed to higher pressures, it will have a reduction in volume. The governing equation for the calculation of bulk modulus is:

$$B = (P-Po)*Vo/(Vo-V) \quad (1)$$

where B is the bulk modulus in psi, P is the measured pressure in psi, Po is atmospheric pressure, Vo is the volume of the sample at atmospheric pressure and V is the volume at the new pressure.

The measurement equipment consists of a modified 21-R-30 Stainless Jerguson gage capable of handling pressures up to 4000 psi. Two panels with viewing windows allow for viewing of the sample. Each window glass has two gaskets, one on either side, to ensure a tight seal on the chamber. For pressures in the range of 0-1000 psi, a direct connection to a helium gas cylinder provides the necessary pressure. For pressures above 2000 psi, a 4.5-liter Aminco hydrogenation bomb is filled with helium and oil is pumped into the bomb to achieve pressures up to 16000 psi. A constant temperature bath kept the pressure cell at a temperature of 100 degrees F. Bulk modulus is measured via a change in height within the pycnometer tube, as the pressure in the cell is varied. Water was used as a calibration standard.

DI Diesel Engine and Spray Chamber. A Yanmar L40 AE D air cooled 4-stroke DI diesel engine was coupled to an electric motor and motored at speed and fuel consumption conditions that simulated the G2 test modes from the ISO 8178-4.2 [4]. Only results from a load setting of 25% at 3600 RPM are presented here. The experimental system is shown schematically in Figure 1. The fuel consumption was measured by a gravimetric method using an Ohaus Explorer balance, accurate to 0.1g. The fuel injector was removed from the cylinder head and placed into a spray chamber with visual access to the fuel spray. The chamber was positioned so that the original high pressure fuel line could be used without modification of length, although it was necessary to bend the fuel line. Images of the spray were captured using an AVL 513 D Videoscope, an integrated triggering and digital imaging system. The triggering system operated with an AVL 364 shaft encoder mounted on the engine crank shaft, enabling 0.1 CA degree resolution.

The spray timing was also monitored with a light attenuation method. A Uniphase 0.95 mW Helium-Neon laser was positioned so that the laser beam intersected the fuel spray at the injector orifice. During the spray event the laser was attenuated, changing the output voltage and enabling a clear transition at both the beginning and end of the spray.

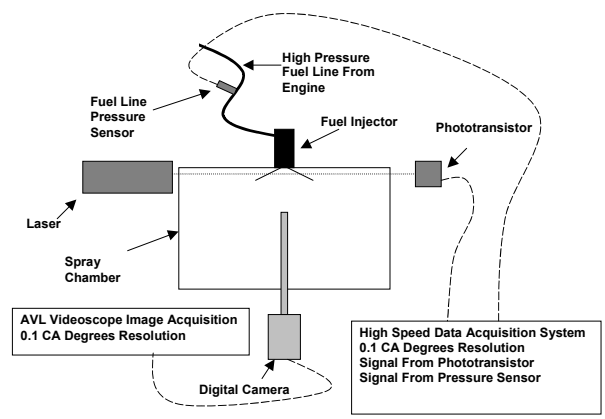

Figure 1. Schematic diagram of the spray visualization chamber connected to the DI diesel engine with access for digital imaging and laser attenuation measurements of fuel injection timing.

Fuel Samples. Fuel samples were selected to examine two separate issues with regard to fuel formulation and engine emissions. The first is verification of the observations of Van Gerpen and co-workers [2,3] regarding the difference in bulk modulus between biodiesel fuels and diesel fuel and the resulting effect on fuel injection timing. The second is examination of the potential impact of the use of paraffinic fuels, such as Fischer-Tropsch diesel fuels, on injection timing. To meet these objectives, the fuel samples tested were a biodiesel fuel (methyl soyate from World Energy), an unrefined soybean oil (from Agricultural Commodities, Inc., New Oxford, PA), Norpar-13 (a normal paraffin mixture from $C_{11} - C_{15}$

from ExxonMobil), paraffinic distillate fuel, a 325 ppm conventional diesel fuel (from BP), and a 15 ppm sulfur diesel fuel (from BP).

Results and Discussion

Figures 2 and 3 show results from the measurements of injection timing and the bulk modulus of compressibility for diesel and biofuel blends. If one takes the indication of 0.4 relative spray intensity as an indication of the start of fuel injection, Figure 2 indicates that there is a 0.2 to 0.3 CA advance of fuel injection timing for the diesel-biodiesel (B20) and diesel – soy oil blends, while there is an advance of 1.0 CA with pure biodiesel (B100). Figures 3 and 4 show that the effect of the purely paraffinic fuels is to retard the fuel injection timing. The largest retardation is 0.5 CA., observed for Norpar, which also has the lowest bulk modulus. The paraffinic distillate yielded a 0.4 CA retardation of injection timing and has a bulk modulus that is lower than diesel fuel, but higher than Norpar.

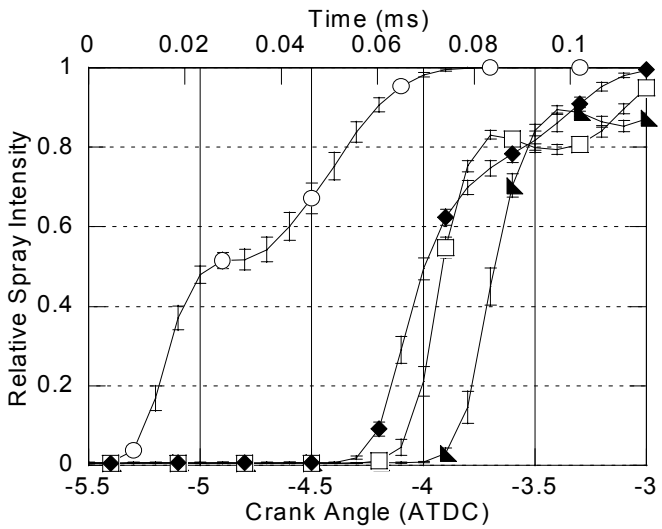

Figure 2. Measured fuel injection timing for biodiesel blends in conventional diesel fuel shown as relative spray intensity as a function of crank angle position relative to TDC. (◣) Baseline diesel fuel, (□) B20, (O) B100, (◆) 16vol.% Soy oil in diesel fuel.

Conclusions

The present work confirms previous observations on the impact of biodiesel fuels on fuel injection timing, that the higher bulk modulus of compressibility of vegetable oils and their methyl esters leads to advanced injection timing. This has been shown in the literature to contribute to the well-documented NOx emissions increase with the use of biodiesel fuel. An opposite trend is observed with paraffinic fuels, which lead to a retarding of injection timing because they have a lower bulk modulus of compressibility than conventional diesel fuels and which supports the observation that paraffinic fuels such as Fischer-Tropsch diesel fuels yield lower NOx emissions.

Acknowledgement. The authors wish to thank Dan Sharrer of Ag Com, Inc. for providing the soybean oil used in this study. This work was supported in part by the West Penn Power Sustainable Energy Fund.

This paper was written with support of the U.S. Department of Energy under Cooperative Agreement No. DE-FC26-01NT41098. The Government reserves for itself and others acting on its behalf a royalty-free, nonexclusive, irrevocable, worldwide license for Governmental purposes to publish, distribute, translate, duplicate, exhibit, and perform this copyrighted paper.

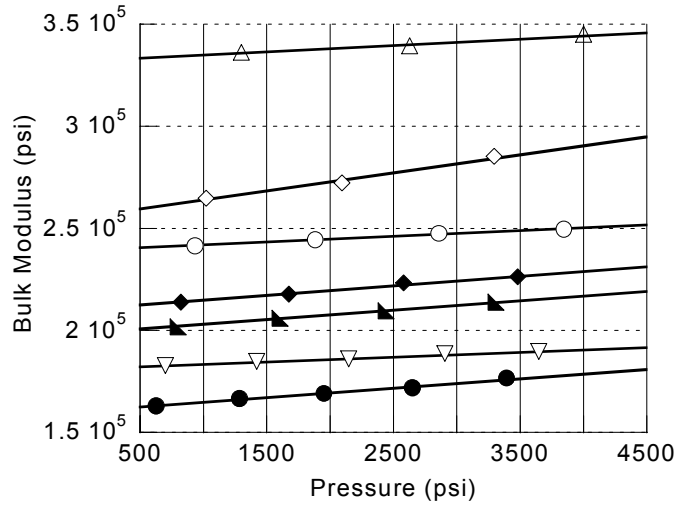

Figure 3. Measured bulk modulus of (△) Water, conventional and ultra low sulfur fuels, (◇) Soy oil, (○) Biodiesel, B100, (◆) 20% Soy oil blend in conventional diesel fuel, (◣) diesel fuel and (▽) paraffinic distillate and (●) Norpar-13 as a function of pressure.

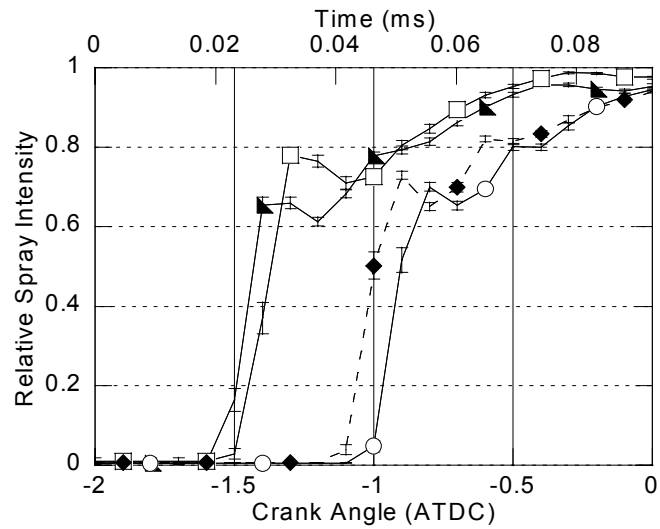

Figure 4. Measured fuel injection timing for paraffinic fuels versus conventional diesel fuel shown as relative spray intensity as a function of crank angle position relative to TDC. (◣) 15 ppm sulfur diesel fuel (BP15), (□) 325 ppm sulfur diesel fuel, (O) Norpar-13, (◆) paraffinic distillate.

References

(1) Graboski, M.S. and R.L. McCormick, "Combustion of fat and vegetable oil derived fuels in diesel engines." *Progress in Energy and Combustion Science*, 1998, **24**(2): p. 125-164.

(2) Monyem, A., J.H. Van Gerpen, and M. Canakci, "The effect of timing and oxidation on emissions from biodiesel- fueled engines". *Transactions of the ASAE*, 2001, **44**(1): p. 35-42.

(3) Tat, M.E., et al., "The speed of sound and isentropic bulk modulus of biodiesel at 21 degrees C from atmospheric pressure to 35 MPa." *Journal of the American Oil Chemists Society*, 2000, **77**(3): p. 285-289.

(4) O'Brien, J.A. "Precise Measurement of Liquid Bulk Modulus." M.S. Thesis, Penn State University,1963.

(5) *ISO 8178: Reciprocating internal combustion engines - Exhaust emissions measurement - Part 4. Test Cycles for different engine applications*. 1995, International Organization for Standardization.

ARTIFICIAL NEURAL NETWORK INVESTIGATION OF THE STRUCTURAL GROUP CONTRIBUTION METHOD FOR PREDICTING PURE COMPONENTS AUTO IGNITION TEMPERATURE

Tareq A. Albahri and Reena S. George*

Chemical Engineering Department, Kuwait University
P.O.Box 5969, Safat 13060, Kuwait
*Tel: (+965) 481-7662 (7459); Fax: (+965) 481-1772
E-mail: albahri@kuc01.kuniv.edu.kw
Web site: http://www.albahri.info

Introduction

In recent years, the term environmental impact has extended its traditional meaning to include other extensive concepts in view of the possibility of industrial accidents which, because of their magnitude, are capable of causing significant damage to people and the environment. This concern, which in the past was principally associated with the nuclear industry, now includes the chemical industry and their safety. Among these concerns are incidents of fire disasters caused by a leak of materials at or above their autoignition temperature in chemical and petrochemical plants.

Autoignition temperature is one of the most important safety specifications used to characterize the hazard potential of a chemical substance. As determined by ASTM standard test method E659-78[1], auto ignition temperature (AIT) is the lowest temperature at which the substance will produce hot-flame ignition in air at atmospheric pressure without the aid of an external energy source such as spark or flame. In the vernacular, autoignition temperature is the temperature at which a material will spontaneously bust into flames when exposed to the atmosphere. At the autoignition temperature, the rate of heat evolved by exothermic oxidation reaction overbalances the rate at which heat is lost to the surroundings and cause ignition. Autoignition temperature is dependent on the chemical and physical properties of the substance and the method and apparatus employed for its determination such as the volume and material of the vessel used, test pressure, and oxygen concentration[1]. In the ASTM test method, autoignition temperature is determined by inserting a small test sample into a heated flask containing air at a predetermined temperature then observing in a dark room for a sudden appearance of a flame and a sharp rise in the temperature of the gas mixture. The test procedure is repeated for a series of prescribed sample volumes and the lowest predetermined internal flask temperature leading to said flame and temperature rise is taken to be the autoignition temperature. Autoignition temperature is also referred to as autogenous ignition temperature, spontaneous ignition temperature, or self-ignition temperature (SIT).

Since the quality of a fuel depends upon its composition, one could theoretically calculate the autoignition temperature from a comprehensive analysis of the individual components in a fuel and their contribution to the overall autoignition quality. Aside from the fact that a theory describing and quantifying the relationship between composition and autoignition has not yet been fully developed, the major obstacles to this approach is in the lack of a method to obtain the compositional data and in the scarcity of autoignition data for pure components. The former impediment is partially solved by the introduction of new analytical (gas and liquid chromatography) and theoretical techniques[2] while the latter which still awaits the introduction of new techniques for estimation, is solved in this work.

Technical Development

A careful examination of the autoignition temperature of hundreds of pure components reveals its complex dependency on the molecular structure. In this work we investigate this structural dependency of autoignition temperature using a structural group contribution approach which has been widely used in the past to predict many other physical and chemical properties[3]. For that purpose an artificial neural network was constructed using MATLAB code to test several structural group methods available in literature[3] and assess their capacity to predict the autoignition temperature of pure components. The network structure is shown in Figure 1 and consists of three layers: input, output, and hidden. The input layer has a number of neurons which is equal to the number of structural groups being investigated. The hidden layer is a single layer with six neurons, and the output layer consists of one neuron.

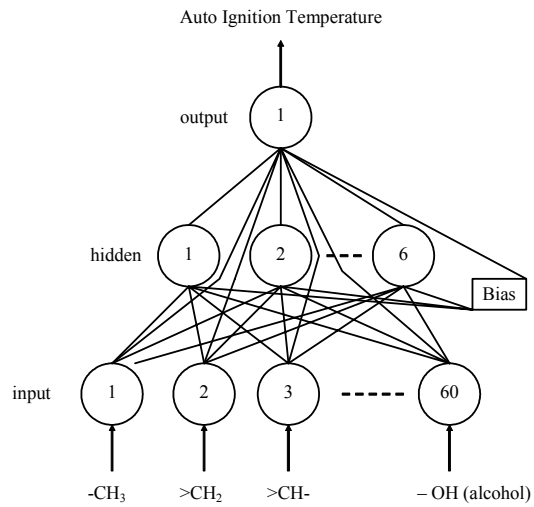

Figure 1. Architecture of artificial neural network for predicting the auto ignition temperature of pure components from their structural groups.

Results

Using the data on the autoignition temperature of 491 pure compounds from the AIChE-DIPPER[4] database, several structural groups derived from the Joback group contribution approach[3] were tested and modified for the location of the functional groups in the molecules. It was finally arrived at the set of groups that can best represent the experimental data with a correlation coefficient of 0.98 consisting of 60 structural groups shown in Table 1. A parity plot showing the accuracy of models predictions is presented in Figure 2. The average deviation in the predicted autoignition temperatures for all types of pure compounds ranging in AIT from 303 to 1283 K was 2.8%. The percentage errors for all 491 compounds are shown in Figure 3.

In conclusion, an estimation technique of the autoignition temperature of pure components, though essential, is inexistent. The group contribution approach presented here is the first and proves to be a powerful tool for predicting the autoignition temperature of pure components if coupled with a proper estimation technique such as neural networks. The clear advantage of the method is its ability to estimate accurately enough the AIT if the chemical structure only is known. This method is useful for the automatic generation and reliable estimation of AIT of pure components, for which no data

exists, with the objective of estimating AIT of petroleum fuels and others. At present the authors are diligently working on modifying the structural groups to improve the model predictions beyond the current results which further include determining the contribution values of these groups using optimization.

Table 1. Structural Groups Used to Estimate Pure Components Auto Ignition Temperature.

Serial no.	Group	Serial no.	Group
1	– CH_3	31	– O – (ring)
2	> CH_2	32	> C = O (ring)
3	> CH –	33	> NH (ring)
4	> C <	34	– N = (ring)
5	= CH_2	35	– SiH
6	= CH –	36	> N – (ring)
7	= C <	37	– H
8	= C =	38	> Si<
9	≡ CH	39	– SiO
10	>CH_2 (ring)	40	BH_3
11	> CH – (ring)	41	– SiH_2
12	> C < (ring)	42	– SO_4
13	= CH – (ring)	43	> S
14	= C < (ring)	44	> SO
15	– F	45	– SH
16	– Cl	46	– SiH_3
17	– Br	47	PH3
18	– OH (alcohol)	48	P
19	– O – (nonring)	49	P=S
20	O = CH – (aldehyde)	50	– CO-O-OC– (anhydride)
21	C = O (nonring)	51	Pb
22	– COOH (acid)	52	Na
23	– COO – (ester)	53	S
24	= O	54	– PO_4
25	– NH_2	55	= S
26	> NH (nonring)	56	≡ O
27	> N – (nonring)	57	– Cl (att. to CH3)
28	– CN	58	– Cl (att. to >CH2)
29	– NO_2	59	– Cl (att. to >CH –)
30	– OH (phenol)	60	– Cl (att. to >C<)

Note: Groups 57 through 60 are for chlorine atoms in paraffinic compounds only.

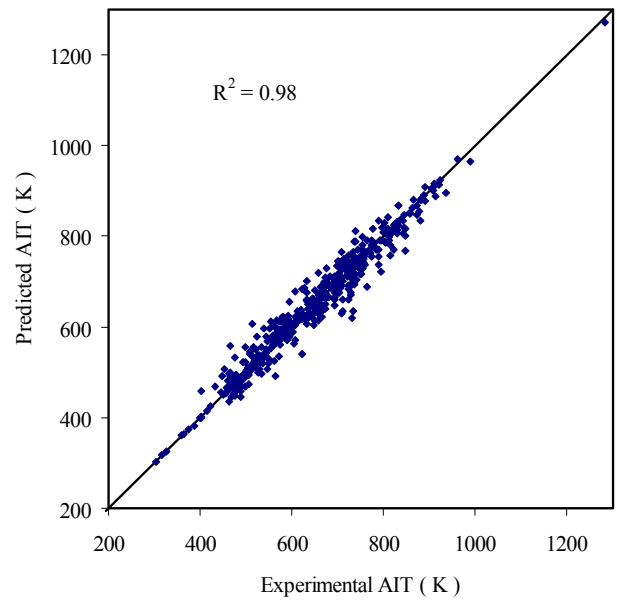

Figure 2. Parity plot for the Auto Ignition Temperature (AIT) of 491 pure components using the structural group contributions method and artificial neural networks.

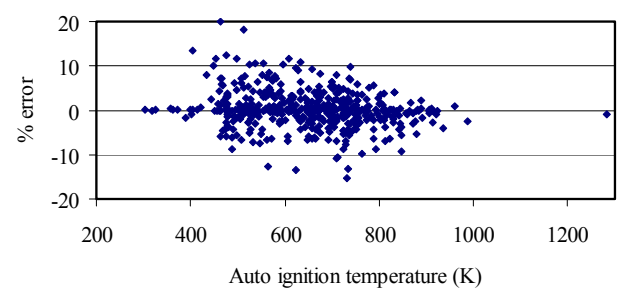

Figure 3. Percentage error range for the auto ignition temperature of 491 pure components using the structural group contributions method and artificial neural networks; 82% of data is below the 5% error range, 15% of data is between 5-10% error range, and only 3% of data is between 10-20% error range.

Acknowledgment

This work was supported by Kuwait University, Research Grant No. EC04/01.

References

(1) ASTM International, *American Standards for Testing and Materials*, Designation: E659-78 (reapproved **2000**).
(2) Neurock, M; Nigam, A.; Trauth, D.; Klein, M.T, *Chemical Engineering Science*, **1994**, 49(24A), 4153-4177.
(3) Reid, R.C.; Prausnitz, J.M.; Polling B.E.; *The properties of gases and liquids*, Hill: N.Y., **1987**.
(4) American Institute of Chemical Engineers, *DIPPER Project 801Pure Component Data in DIPPRO, public version*, January 31, **1996**.

KINETICS OF CO_2-GASIFICATION OF SHENMU MACERAL CHARS

Qinglei Sun, Wen Li, Haokan Chen, Baoqing Li

(State Key Lab of Coal Conversion, Institute of Coal Chemistry, Chinese Academy of Sciences, Taiyuan, 030001, China)

Abstract:
The gasification reactivity of Shenmu vitrinite and inertinite chars was investigated using TG-151 thermal balance. The gasification kinetics was analyzed using integral method, differential method and DAEM. The results showed that with increasing gasification temperature, the gasification reactivity of vitrinite and inertinite chars greatly increased. At the same gasification temperature, vitrinite char had higher gasification reactivity than inertinite char. The value of activation energy calculated using the three methods had the same order, inertinite char always had higher activation energy than vitrinite char, suggesting vitrinite char had higher gasification reactivity. The difference of the three methods was also compared. The integral and differential method can only supply the average of activation energy, while DAEM can supply the variation trends of activation energy during the whole gasification process. Therefore, DAEM was a better kinetics method comparing with the integral and differential method for description of the gasification process.

Keywords: maceral chars, CO_2 gasification, kinetics, integral and differential method, DAEM

Perspectives on Membrane Technology for Advanced Gas Separations

Richard D. Noble

University of Colorado
Chemical Engineering Dept.
P.O. Box 424
Boulder, CO 80309

The use of polymer membranes for gas separations is a well-established separation technology. Membrane-based gas separation technology has developed during last 20 years to an annual business of $150 million. The major current separations are N_2 from air, H_2 separation and recovery, and CO_2 or H_2O removal from natural gas. The evolution of membrane technology to expand the temperature range of operation as well as provide the capability for additional separations will require new materials and/or processes. This talk will provide a brief historical focus and discuss the new materials and processes that can address the current limitations of commercial membrane technology.

The first large-scale industrial application was hydrogen separation started in 1980 by Permea. This was rapidly followed by the introduction of the first N_2 from air membrane separation system in 1982. In the late 1980's, cellulose acetate membranes for CO_2/CH_4 separation as well as new membrane materials for O_2/N_2, H_2/N_2 and H_2/CH_4. At this time, vapor separation membranes also made their first appearance as a commercial product. The mid-90's were the time frame for the introduction of polyimide hollow-fiber membranes for CO_2/CH_4 separation and membrane systems for C_3H_6/N_2 separations.

The use of new materials as membranes also requires support structures that can withstand the same operating conditions and provide the mechanical support. The evolution of sintered stainless steel and alumina membranes for filtration applications provided the support materials for high temperature and/or chemically challenging environments. Zeolite membranes are nanoporous inorganic crystalline structures that can provide highly selective separations up to 500ºC. Recent developments to synthesize thin zeolite films on metal or alumina supports should provide the high flux combined with selectivity needed to move this technology toward commercial development.

Additional new materials being evaluated as membrane materials are lyotropic liquid crystals and ionic liquids. Lyotropic liquid crystals form structured phases that have uniform pore structures down to 1.5 nm. The ability to polymerize these structures and "lock" them in place provides a means to fabricate a nanoporous polymer film. Ionic liquids are salts that are liquid at or near room temperature. Since they are non-volatile, this material could be used as a liquid membrane platform.

The addition of chemical selectivity into the membrane has long been attempted to overcome the "line of death" on a Robeson plot that represents the upper bound for gas selectivity versus permeability for polymers. One recent approach that has shown promise is the incorporation of zeolites or molecular sieves into polymer films (mixed matrix membranes). Another approach that has been evaluated for a long time is facilitated transport. Recent studies on the incorporation of Ag^+, Cu^+ and Co^{2+} complexes into polymer structures could lead to stable membranes for various applications such as olefin/paraffin and O_2/N_2 separations.

SELECTIVE CO OXIDATION IN A HYDROGEN RICH STREAM OVER Au/MnO_x AND Au/FeO_x CATALYSTS

Dao T., Luengnaruemitchai A.*, Osuwan S.*, and Gulari E.***

*The Petroleum and Petrochemical College, Chulalongkorn University, Bangkok, Thailand
**Department of Chemical Engineering, University of Michigan, Ann Arbor, Michigan, USA

Introduction

Having a lot of good characteristics fuel cells have been becoming one of the most considerations in many applications especially in transportation. H_2 is the most suitable fuel for the fuel cell technology. However, because of the H_2 explosion risk and the limitation of H_2 onboard storage tank it requires integrating H_2 production unit with fuel cell unit. Steam reforming is an efficient, economical and widely-used process for H_2-production. Coming out with H_2 is a small amount of CO which poisons the Pt anodes reducing the overall fuel cell performance. Thus, in order to obtain the maximum performance, removal of CO from the reformed gas has been done.

There are several ways to remove CO from H_2-rich gas but selective oxidation of CO is the best choice. It has been found that supported-Au catalyst is one of the best candidates for selective CO oxidation. In comparison with Pt group metal catalysts, it is substantially more active for CO oxidation than H_2 oxidation resulting in the higher selectivity.[1] This paper focused on gold/manganese-oxide catalyst (Au/MnO_x) and gold/ferrous-oxide catalyst (Au/FeO_x).

Experimental

Preparation of Catalysts. Co-precipitation was used for catalyst preparation. An aqueous solution of 1 M Na_2CO_3 was added dropwise into an aqueous mixture of 0.1 M $Mn(NO_3)_2$ or 0.1 M $Fe(NO_3)_3$ and 0.1 M $HAuCl_4$ (Au/Mn or Au/Fe = 1/30 atomic ratio) under vigorous stirring condition at 80°C. The mixture was kept at a pH of 8 for 1 h. The precipitate was separated out from solution by centrifuge at 2,000 rpm for 5 min. Excess ions were eliminated by washing with warm deionized water. Deionized precipitate was dried at 110°C overnight and calcined at 300°C in case of Au/MnO_x and 400°C in case of Au/Fe_2O_3 for 2 h.

Activity Measurement. The catalytic activity measurements were carried out in the fixed bed reactor packed with 100 mg catalyst at 80-120 mesh in size. The feed gas contained 1% CO, 2% CO_2, 1% O_2, 2.6% H_2O and 40% H_2 balanced in He passing through the catalyst bed at the total flow rate of 50 ml/min (SV=30,000 $mlg^{-1}h^{-1}$) at atmospheric pressure. Prior to all experiments, He and O_2 pretreatments[2,3] at 200°C for 2 h were needed for Au/MnO_x and Au/FeO_x, respectively. The effluent gas was detected by online gas chromatograph. For the water vapor effect, reactant gases were passed through a water bubbler.

Catalyst Characterization. The determination of surface area was done using the Autosorb-1 Gas Sorption System and analyzed by Autosorb Anygas Software Version 2.1. Crystallite structure of support and average particle diameter of gold were analyzed by the Rigaku X-Ray Diffractometer system with Cu tube for generating CuK_α radiation (1.5406 Å) and nickel filter. RINT-2200 was used to obtain XRD pattern at 40 kV and 30 mA. Scan speed of 5°/min with scan step of 0.02 was used for a continuous run in 5 to 90° range. Atomic Absorption Spectroscopy (AAS), VARIAN model 300/400 was utilized to determine the actual percent Au loading on the supports. Transmission Electron Microscope (TEM) was carried out using a JEM 2010 operating at 200 kV in bright and dark field modes. Crystallinity and crystal structure of the sample were evaluated from selected area electron diffraction pattern.

Results and Discussion

Catalyst Characterization. Surface area, crystallite size and actual percent Au loading of two types of catalyst are shown in **Table 1**. High surface area of Au/FeO_x due to a well dispersed Au metal on support which is quite cleared by the crystallite size smaller than 3 nm in XRD results is shown in **Figure 1**. The percent Au loadings on both catalysts are about 5-6% which are relatively higher than Pt loading on conventional Pt supported catalyst.[2]

Table 1. Surface Area, Crystallite Size and Actual Percent Au Loading of Catalysts

Type of catalyst	Surface area (m^2/g)	Crystallite size (nm)	Au loading (%)
Au/MnO_x	118.90	14	5.70
Au/FeO_x	94.87	<3	5.38

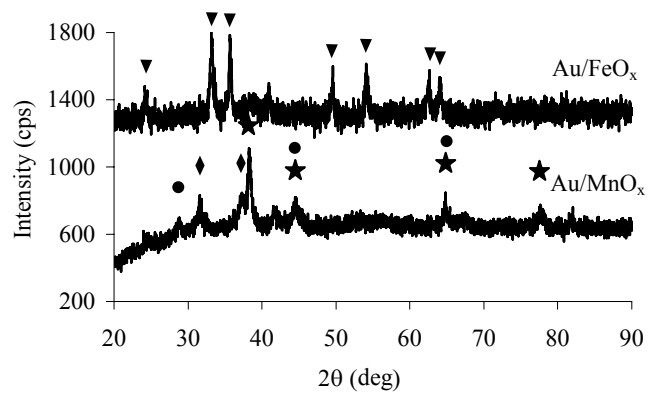

Figure 1. XRD patterns of prepared catalysts. ★, Au; ♦, $MnCO_3$; ●, Mn_3O_4; ▼, Fe_2O_3.

No XRD peak of Au (2θ = 38.2° , 44.4°, 64.1°, and 78.0°) was observed in XRD pattern of Au/FeO_x indicating that Au crystallite size was smaller than 3 nm.

Figure 2 shows TEM images of both catalysts. MnO_x support seems like semi-crystal while FeO_x is highly crystallized. Au crystal structure was also investigated to be hemispherical in shape and that attached to the support by their flat planes.[4] Average Au particle sizes were identical to the results from XRD.

Catalyst Activity. Figure 3 and 4 show the conversion and selectivity of both catalysts as a function of temperature with the reactant gas mixture of 1%CO, 1%O_2, 2%CO_2, 2.6%H_2O, and 40% H_2 balanced in He. The selectivity of both catalysts were maximum at low temperature and then slightly decreased with increasing temperature reflecting a higher apparent activation energy for H_2 oxidation than for CO oxidation. Maximum conversion of Au/MnO_x was approximate 95% with 60% selectivity at the relatively low temperature of 130°C. For Au/FeO_x, the activity was readily reached 100% at 50°C and then slightly decreased to 90% at 90°C. The selectivity was around 50% at this temperature.

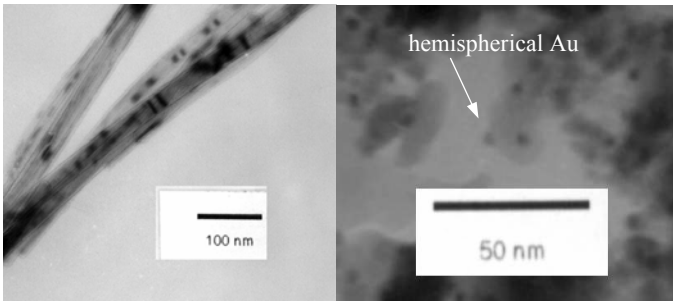

Figure 2. TEM images of Au/MnO_x and Au/FeO_x.

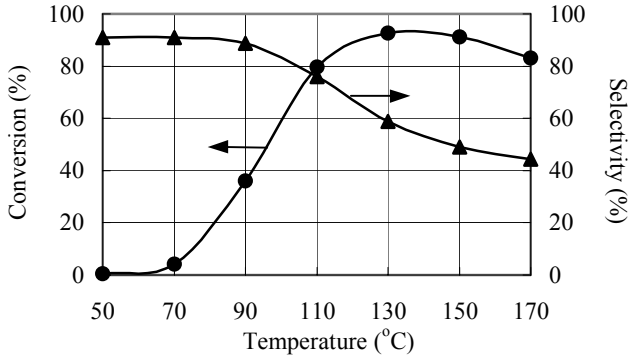

Figure 3. Activity of Au/MnO_x versus temperature.

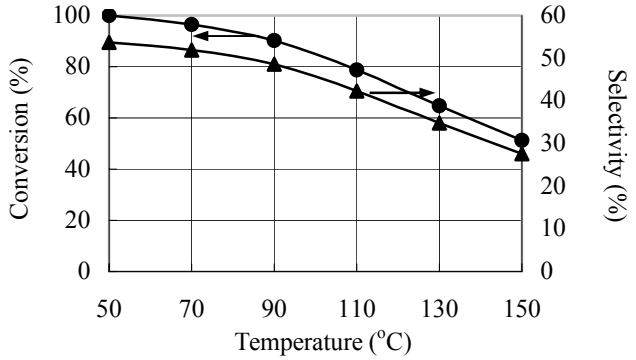

Figure 4. Activity of Au/FeO_x versus temperature.

In comparison with $Pt/\gamma\text{-}Al_2O_3$, a commonly used catalyst requires relatively high operating temperature of 200°C, Au/MnO_x and Au/FeO_x were superior not only in term of their appropriate working temperature but also by high activities. Although the amount of Au needed for these kinds of catalyst were higher than $Pt//\gamma\text{-}Al_2O_3$, it is still preferred because of the shortage of Pt when it is utilized as electrodes for fuel cells.

Effect of CO_2. The effect of the presence of CO_2 in the feed stream on the catalytic behavior of both catalysts is shown in **Figure 5**. Increasing from 2 to 6%, CO_2 lowered the maximum conversion of Au/MnO_x and Au/FeO_x about 4 and 3%, respectively. It seems that CO_2 caused the detrimental effect on the catalyst activity because of the CO_2 retention on the catalyst surface.[3] However, this effect became slightly small at the operating temperature.

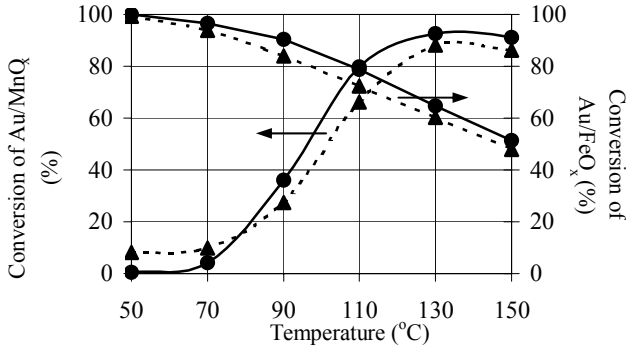

Figure 5. Effect of CO_2 on the activity of both catalysts. Solid lines, 2%CO_2; dotted lines, 6%CO_2.

Effect of Water. Generally, the catalytic activity of catalyst is depressed in the presence of water. **Figure 6** shows the effect of water vapor in the reaction gas mixture on the conversion of catalysts. Under the unhumidified condition, the catalyst activities were less active. Water seemed to be favorable to the catalyst activity[2,5] since it provided hydroxyl group which is necessary for reaction to take place.

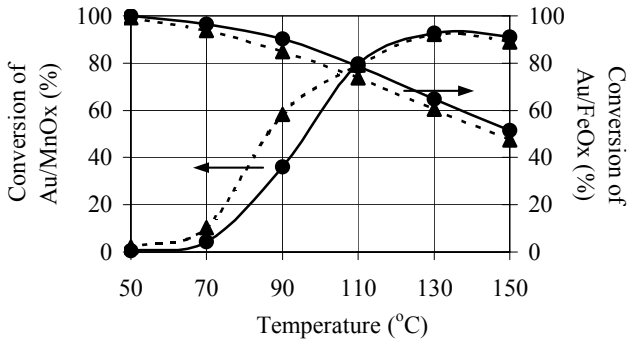

Figure 6. Effect of H_2O on the activity of both catalysts. Solid lines, 2.6%H_2O; dotted lines, 0%H_2O.

Conclusions

The activity of two kinds of catalyst has been studied for selective CO oxidation. It was found that Au/MnO_x gave 95% conversion and 60% selectivity at 130°C while Au/FeO_x gave >90% conversion and >50% selectivity at the temperature ranging from 50-90°C.

The composition of the reactant gas had a definite effect on the catalyst activity. Negative effect had been found for CO_2 and reverse for water.

Acknowledgement. This work was supported by the Petroleum and Petrochemical College, Chulalongkorn University, Bangkok, Thailand and partially supported by The Thailand Research Fund (TRF).

References

(1) Sanchez, R. M. T.; Ueda, A.; Tanaka, K.; and Haruta, M. *J. Cat.*, **1997**, *168* , 125-127.
(2) Kahlich, M. J.; Gasteiger, H. A.; Behm, R. J. *J. Cat*. **1999**, *182*, 430-440.
(3) Hoflund, G. B.; Gardner, S. D. *Langmuir* **1995**, *11*, 3431-3434.
(4) Haruta, M..; Tsubota, S.; Kobayashi, T.; Kageyama, H.; Genet, M.J.; Delmon, B. *J. Cat.* **1993**, *144*, 175-192.
(5) Haruta, M. *Cat. Today* **1997**, *36*, 153-166.

INVESTIGATION OF POLYCYCLIC AROMATIC HYDROCARBON COMPOUNDS (PAHs) ON FLUE GAS DESULFURIZATION (FGD) BY-PRODUCT

Ping Sun and Linda K. Weavers

Department of Civil and Environmental Engineering
and Geodetic Science, The Ohio State University
470 Hitchcock Hall
2070 Neil Avenue
Columbus, OH, 43210

Introduction

Flue Gas Desulfurization (FGD) technology has been widely used throughout the world in an effort to reduce acid rain from sulfur oxide (SOx) emissions in coal combustion. Although this technology reduces SOx emissions efficiently and cost effectively, the application of this technique leads to over 20 million metric tons of FGD by-product generated in the United States annually[1]. Rather than dispose of FGD by-product as waste in landfills, efforts are underway to identify opportunities to reuse it[2,3]. Prior to reuse, FGD by-product must be characterized for potential environmental hazards. Compared with inorganic components such as heavy metals on FGD by-product, organic components are expected to be present in lower amounts and consequently are often neglected. However, they may also have an important impact on the environment when FGD by-product is disposed or reused. Accordingly, research concerning concentration, fate (i.e., potential to leach into the environment), and minimization of organic components on FGD by-product is necessary.

Polycyclic aromatic hydrocarbons (PAHs) are regarded as recalcitrant compounds in the environment because PAHs show very slow release from solid phases such as soil and sediment. They are found worldwide, even in pristine areas such as the poles[4]. In addition, many PAHs are carcinogenic and/or mutagenic; therefore, they are of both environmental and health concern. A major source of PAHs in the environment is from fossil fuel combustion processes (i.e., coal burning)[5,6]. Therefore, PAHs may exist on FGD by-product by deposition from flue gas or by mixing of fly ash carryover with FGD by-product.

The purpose of this study was to investigate the organic compounds, particularly PAHs, on FGD by–products. The correlations of PAHs on FGD by-products with other factors such as unburned carbon were also investigated.

Experimental

In this study, FGD by-product was sampled at boiler #8 at the McCracken Power Plant on The Ohio State University campus. A lime slurry mist is injected into the scrubber to react with sulfur oxides from flue gas leaving the boiler. The by-product, along with fly ash, is collected by filter bags in a pulse jet baghouse.

FGD By-product Sampling. Multiple grab samples were collected to fulfill a clean 950 mL brown glass bottle (cleaned by EPA procedures). Samples were subsequently stored in an environmental room (4 to 12^{0}C) until the appropriate chemical measurement procedures were preformed.

Organic Chemical Analysis. For each sample, 10 g of FGD by-product was extracted in a Tecator Soxtec (Model 1043) extractor with CH_2Cl_2 for 5 hours. The solution from the extraction process was subsequently condensed to 1 mL prior to GC/MS analysis. EPA method 8270C provided the basis for measurement of polycyclic aromatic hydrocarbons (PAHs) and other semivolatile organic compounds. A Thermo-Finnigan GC/PolarisQ ion trap was used for GC/MS analysis. Aliquots of 2 μL were injected into a Varian CP-5 fused silica capillary column (60m×0.25mm×0.25μm) by splitless injection mode. Helium served as the carrier gas. The mass spectrometer was operated in full scan mode for both standards and extracts. The PAHs and other semi-volatile compounds were identified by matching mass spectra to a NIST spectra database. Sixteen EPA-specified PAHs were confirmed using the retention times and quantified using calibration curves from the standard PAH compounds. The detection limits for these 16 PAHs are 0.1~1 ng/g, depending on the boiling point of the individual PAH.

Organic Carbon Content Measurement. Organic carbon content was measured by the STAR Laboratory of the Ohio Agricultural Research and Development Center (OARDC), OSU. Samples were "burned" under pure O_2 at 900°C on Elementar Americas, VarioMax Carbon/Nitrogen Analyzer to measure total carbon (TC). Total inorganic carbon (TIC) was determined by coulometry on an instrument manufactured by UIC Inc. Upon introduction of sample into the sample flask, the system was purged with a CO_2-free carrier gas to eliminate atmospheric carbon dioxide. Then, 2N $HClO_4$ was added, heated and inorganic carbon was oxidized to gaseous CO_2 that was measured by a CO_2-sensitive detector. The difference between TC and TIC is the organic carbon content.

Results and Discussion

In a preliminary study, a series of 10 FGD by-product samples doped with 100 ng surrogate (naphthalene-d_8) were extracted to measure the recovery rate of the extraction process. An average recovery rate of 85% was achieved. In addition, a mixture standard (16 different PAHs) containing 100 ng each PAH was added to four 10 g FGD by-product samples before extraction to measure the matrix recovery rate. **Fig 1** shows the average recovery rates ranged from 0~75% for the 16 different PAHs. The results indicate a low recovery rate and a decreasing recovery rate with an increase in molecular weight of the PAH. For PAHs larger than benzo(a)pyrene, they could not be extracted effectively.

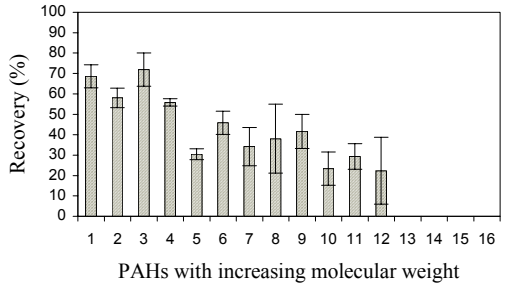

Figure 1. Recovery rate for 16 PAHs spiked onto FGD by-products.

Generally, several factors influence analyte recovery including matrix type, spike level, and total extraction time[7]. Compared with other studies and EPA standard methods on extraction of PAHs, the spike level in our experiments (10 ng/g) is much lower. For example, Chen *et al*. achieved recovery rates of deuterated PAHs ranging from 62% to 102% on coal tar contaminated soil with a matrix spike level of 20 μg/g[8]. However, since EPA standard method 3500B also recommends that the spike level should be 1 to 5 times higher than the concentration of the analyte in the real sample[9], this unusually low matrix spike level was chosen to mimic concentrations expected for PAHs on FGD by-product. In addition, the FGD by-product is a complicated mixture of fly ash, lime, unburned carbon and other

materials. Because the organic matter content in the matrix plays an important role on adsorption of organic compounds[10], the existence of unburned carbon in FGD by-product may also be one reason for the low recovery rate. The increasing of hydrophobicity of the PAHs with an increase in molecular weight may explain the decreasing recovery rate with increasing molecular weight. Currently, other extraction methods such as ultrasonic extraction are being developed to improve the recovery rate.

The identified PAHs on the collected FGD by-product samples were mainly 2-ring and 3-ring PAHs, such as naphthalene, acenaphthene, acenaphthylene, and phenanthrene; no large ring PAHs were found. The quantification data of detected PAHs (based on 4 experiments) on FGD-by product collected on different dates are shown in **Table 1**. The concentrations of these PAHs are low, usually less than a few ng/g. Other organic compounds were also found in the FGD by-product, for example, biphenyl and a series of n-alkanes. However, standards are needed to conclusively verify their existence.

Table 1. Concentration (ng/g) of Detected PAHs on FGD

Sample No.	Naphth-alene	Acenaph-thene	Acenaph-thylene	Phenan-threne
1	2.53±0.24	N/D	N/D	0.37±0.27
2	1.51±0.06	N/D	N/D	N/D
3	2.94±0.20	N/D	0.58±0.02	0.36±0.25
4	5.92±0.22	N/D	N/D	0.67±0.46
5	2.12±0.12	0.98±0.03	0.83±0.03	0.33±0.19
6	2.44±0.14	0.66±0.02	0.46±0.02	0.40±0.27

N/D: not detected

Boiler operation parameters such as combustion temperature and excess air ratio during combustion have been shown to affect PAH formation[11]. At the McCracken Power Plant, coal is burned at 1200^0C and an air pump is used to provide excess air for combustion. The high combustion temperature will produce more energy to break the bonds of macromolecular PAHs in raw coal to form smaller size fragments. With the excess air, these fragments will further undergo oxidation reactions and produce more carbon dioxide and water in the flue gas. Therefore, the high combustion temperature and excess air may be the reason why small ring PAHs are the major compounds identified on FGD by-product[12]. Another reason that large ring PAHs were not detected may be due to their low recovery rate. Since the large ring PAHs have higher affinities with the solid phase, they may strongly adsorb on FGD by-product and may not be easily extracted. Thus, the existence of large ring PAHs on FGD is still possible.

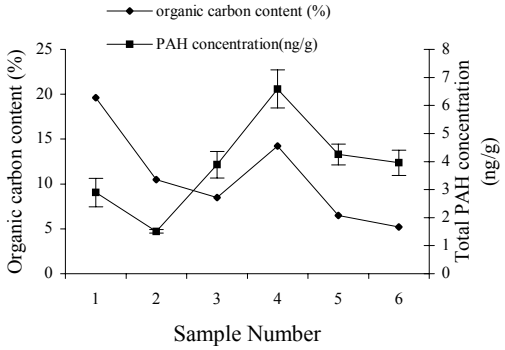

Figure 2. Measured total detected PAH concentration and organic carbon content of FGD by-products.

The organic carbon content on a weight percent basis and measured total PAH concentrations of 6 FGD by-product samples are shown in **Figure 2**. The results suggest a possible correlation between higher PAH concentrations and the organic carbon content in FGD by-product. Since unburned carbon is the major source of organic carbon in FGD by-product, unburned carbon is currently being separated from FGD by-product by initial sieving and following density separation using lithium heteropolytungstate (LST) solution. Measurement of PAH concentrations in separated unburned carbon parts will be performed to test the hypothesis.

Conclusions

This study has shown low recovery rates of PAHs in automatic Soxhlet extraction procedures. Several small ring (2 ~ 4-ring) PAH compounds were identified in FGD by-product, including naphthalene, acenaphthene, acenaphthylene, and phenanthrene. The concentrations of detected PAHs are usually less than a few ng/g. No large ring PAHs were detected, which may be attributed to low recovery rates. Initial indications suggest that concentrations of detected PAHs correlate with the organic carbon content in FGD by-product. Unburned carbon will be separated with initial sieving and density separation,. PAH analysis of each size fraction will be carried out to verify the hypothesis that concentrations of detected PAHs correlate with the presence of unburned carbon in FGD by-product.

Acknowledgement The authors would like to thank the Ohio Coal Development Office (OCDO) and The Ohio State University for funding. Dr. Danold. W. Golightly's help with sampling and Mr. Kevin Jewell's help with organic carbon content measurement are gratefully acknowledged.

References

1. Stewart, B.R.; Kalyoncu, R.S.; *Proc. Int. Ash Utilization Symp.,* Lexington, KY, Oct., 1999.
2. Santhanam, C.J.; *Flue Gas Cleaning Wastes Disposal and Utilization*, Noyes Data Corporation: Park Ridge, New Jersey, 1981.
3. Lamminen, M.; Wood, J.; Walker, H. W.; Chin, Y-P.; He, Y.; Traina, S.; *J. Env. Quality*, **2001**, 30, 1371.
4. Henner, M.; Schiavon, M.; Morel, J.L.; Lichtfouse, E.; *Analusis,* **1997**, 25(9~10), M56.
5. Mastral, A.M.; Callen, M.S.; *Environ.Sci.Technol*, **2000**, 34(15), 3051.
6. Pisupati, S.V.; Wasco, R.S.; Scaroni, A.W.; *Journal of Hazardous Materials*, **2000**, 74(1), 91.
7. Dean, J.R.; *Extraction methods for environmental analysis,* John Wiley, Chichester: New York, 1998.
8. Chen, C.S.; Rao, P.S.; Lee, L.S.; *Chemosphere*, **1996**, 32(6), 1123.
9. U.S. Environmental Protection Agency, Method 3500B, Organic Extraction and Sample Preparation, 1996, U.S. Environmental Protection Agency
10. Watts, R.J.; *Hazardous Wastes: Sources, Pathways, Receptors,* John Wiley & Sons Inc: New York, 1997
11. Mastral, A.M.; Callen, M.S.; Mayoral, C.; Galban, J.; *Fuel*, **1995**, 74(12), 1762.
12. Liu, K.L.; Xie, W.; Zhao, Z.B.; Pan, W.P.; Rilly, J.T.; *Environ.Sci.Technol.,* **2000**, 34(15), 3177.

HIGHLY SELECTIVE MFI-ZEOLITE MEMBRANES FOR HYDROCARBON SEPARATIONS

Christophe CHAU, Mickaël SICARD, Philippe TERRASSE, Ronan Le DRED°*

*Institut Français du Pétrole, Catalysis and Separation Division, 1&4, avenue de Bois-Préau, 92852 Rueil-Malmaison - France, christophe.chau@ifp.fr

°ENSCMu-CNRS, Laboratoire des Matériaux Minéraux, 3, rue Alfred Werner, 68093 Mulhouse - France

Introduction

Zeolite membranes are emerging and promising membrane materials with high potential for gas separation, due to their chemical and thermal resistances, surface polarity and zeolite topology. To date, limitations to industrial and commercial development of zeolite membranes still exist and have to be overcome for successful implementation at industrial scale for gas separations *e.g.* in the field of gas treatment, refining and petrochemistry.

In order to highlight membrane textural integrity, appropriate characterization techniques and gas probe molecules have to be established. Characterization of zeolite membranes is of great importance and among various techniques, gas permeation is a non destructive characterization techniques that allows to evaluate the textural integrity of the zeolitic layer, the separation capability and the molecular transport phenomena involved through the zeolitic channels.

Using hydrocarbon mixtures for the characterization stage can provide particularly valuable data in the screening/selection of membrane materials provided that the experimental conditions are appropriate. The purpose of our study consisted in highlighting the separation performances of high quality MFI-zeolite membranes through a standard reliable and reproducible characterization procedure using hydrocarbonaceous mixtures at high temperatures.

Experimental

MFI-type zeolite membranes. Supported MFI zeolite membranes were prepared by hydrothermal treatment of a silica source using an organic compound as structure directing agent and porous alumina tubes. The synthesis procedure was optimized according to relevant modifications developed by IFP, Institut Français du Pétrole, France and ENSCMu-CNRS.

Gas permeation. These membranes were characterized by gas permeation at high temperatures using butanes (linear and branched isomers) as probe molecules and a gas permeation equipment developed within the Institut Français du Pétrole, with on-line gas-chromatographic analysis. Butanes were chosen to highlight the textural integrity of the synthesized membrane materials in severe conditions (pore apertures of the MFI-type zeolite around 0.55 nm, kinetic diameters: n-butane 0.43nm, isobutane 0.49nm).

Pure gas permeation. This characterization method allows to distinguish between defect-free MFI-type microporous membranes and non selective materials with macro or mesopores, or residual interparticles voids (Fig. 1).

N-butane permeation profile is in good accordance with microporous adsorption-diffusion mechanisms with a maximum of performance at about 180°C, where molecular loading and diffusion coefficients are high. At lower temperatures diffusivity is low, at higher temperatures the higher diffusivities do not compensate the lower molecular loadings.

First generation membranes (before optimisation of the synthesis procedure) revealed good permeances (2-8.10^{-7} mol/m^2.s.Pa). Isobutane permeance remains very low and below detection threshold for all samples, prepared by the first generation and the new synthesis procedure. As a result of our optimization, permselectivity appears to be infinite for n-butane with a very high permeance around 20.10^{-7} mol/m^2.s.Pa, which is about 10 times higher than any published results. In other words, besides a drastic increase of membranes permeability, gas separation capability and separation factors are not affected by material improvement. At this stage mixture gas separation is a prerequisite for highlighting membrane potential for hydrocarbon separations at high temperatures, in a domain where organic membranes can not compete with, *e.g.* by using linear and branched paraffins.

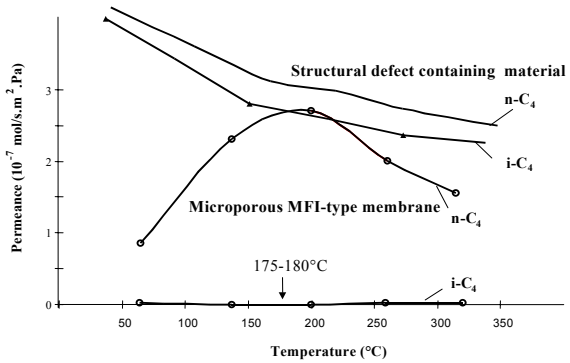

Figure 1. Single gas permeation for MFI zeolite membrane characterization (depicted here for the first generation's membrane IFP-23)

Mixture gas permeation. Characterization with mixture feedstocks (*e.g.* n-butane and isobutane, Fig. 2) at high temperatures revealed more representative of the separation performances of membrane materials as well as appropriate to highlight potential use in industrial applications.

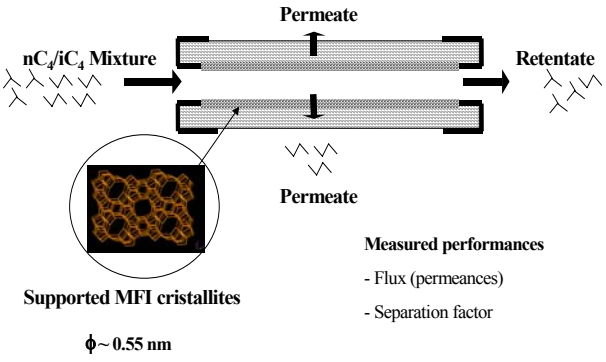

Figure 2. Characterization of MFI-type membranes by n-butane/i-butane mixture permation

On the other hand competitive adsorption, pore mouth blocking effet and/or single file diffusion may govern the molecular transport phenomena through zeolitic channels. More particularly, due to pore

size restrictions (ten membered-rings of MFI-type topology) and steric hindrance of hydrocarbons, molecular and pore wall interactions strongly affect hydrocarbons diffusion and adsorption in mixtures.

Experimental campaigns were carried out on high quality MFI-membranes with varying *e.g.* feed composition, sweep-gas flowrate and temperature, in order to determine the most adequate conditions for the characterization of the membrane separative properties.

Results and Discussion

The influence of isobutane content in n-butane/isobutane mixtures on molecular flux is studied with and without sweep gas at 175°C, where n-butane permeation is the highest (Fig. 3). The higher the isobutane concentration in the feed, the lower the transmembrane fluxes. The influence of isobutane content in n-butane/isobutane mixtures on molecular flux was studied with and without sweep gas.

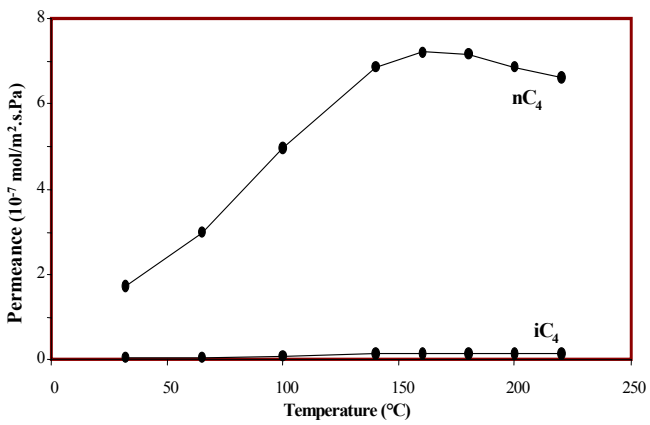

Figure 3. Butane mixture permeation for MFI zeolite membrane characterization

The effect of sweep gas flowrate is investigated and separation factors remain high by using a sweep gas, even at relatively high isobutane concentration (Fig. 4).

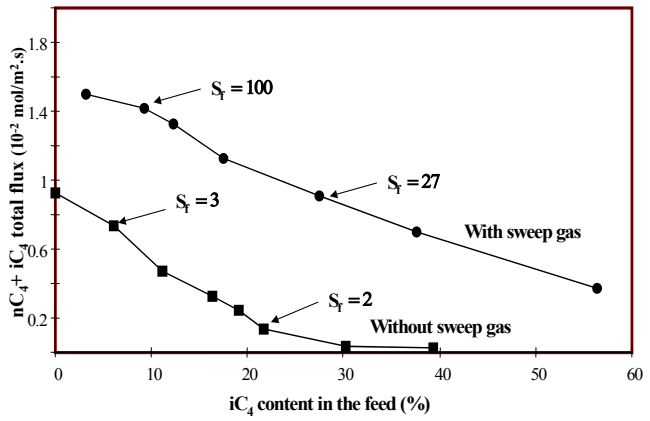

Figure 4. Effect of sweep gas on total flux and separation factor for varying butane mixtures

A comparison of separation performances is carried out among a series of very high quality membranes, taking into account more realistic and conditions (hydrocarbonaceous mixtures, high temperature) with a faster, reliable and reproducible procedure. Moreover the complex phenomena and interactions occurring in zeolitic channels and the influence of the intrinsic material properties may affect a direct correlation between pure gas and mixture permeation.

As a result a typical procedure is adopted and applied with hydrocarbonaceous mixtures to a great number of membrane materials with very high separation performances. A comparison of separation performances is carried out among a series of very high quality membranes with properties varying in a wide range. The behaviour comparison in gas mixture permeation helps select membrane samples, taking into account more realistic conditions (hydrocarbonaceous mixtures, high temperature) with a faster, reliable and reproducible procedure.

Conclusions

Characterization is a key stage of membrane science and effective separation measurements are of great interest to improve the understanding of *e.g.* hydrocarbon transport through high quality and highly permeable zeolite membrane materials. Competitive adsorption, pore mouth blocking effect and/or single file diffusion may govern the molecular transport phenomena through zeolitic channels. Mixture gas permeation, instead of pure gas permeation, appears therefore particularly adapted to highlight membrane effective performances at high temperature for applied purposes, especially in the field of refining, petrochemistry and gas treatment.

References

1. Chau, C.; Terrasse, P.; Sicard, M.; Le Dred, R.; *International Workshop on Zeolite Membrane Materials, July 1-4,* **2001**, Purmerend, the Netherlands

ZEOLITE MEMBRANES FOR FUEL ETHANOL PRODUCTION

Hidetoshi Kita,[1] Ken-ichi Okamoto,[1] Tadahumi Yamamura,[2] and Jun Abe,[2]

[1]Department of Advanced Materials Science and Engineering, Yamaguchi University, Tokiwadai , Ube 755-8611, Japan
[2]Department of Industrial Machinery Design, Mitsui Engineering and Shipbuilding Co. Ltd., Tamano 706-8651, Japan

Introduction

Dehydration of solvents using hydrophilic polymer pervaporation membranes is a well-established technology.[1] However, these polymeric membranes have been limited to applying dehydration of solvents due to insufficiency of their thermal, mechanical and chemical stability. The recent development of hydrophilic zeolite membranes has made it possible to overcome the above limitations of hydrophilic polymeric membranes.[2, 3] The performance of these zeolite membranes is the most favorable one for pervaporation and vapor permeation membranes that have been published so far and is very high enough to put these membranes into practical use. In this work, we report the tubular type pervaporation and vapor permeation module with zeolite membranes for the fuel ethanol production. This can provide more energy efficient concentration of the ethanol to fuel-grade ethanol.

Experimental

NaA type zeolite membrane was grown hydrothemally on the surface of a porous cylindrical mullite support. The hydrothermal synthesis of NaA zeolite membrane was performed as follows. An aluminate solution was prepared by dissolving sodium hydroxide and aluminium hydroxide in distilled water. A silicate solution was prepared by dissolving sodium silicate in distilled water. The aluminate solution was added to the silicate solution and the resulting mixture was stirred vigorously, producing a homogeneous gel. The molar composition of the resulting gel was SiO_2/Al_2O_3=2.0, Na_2O/SiO_2=1.0 and H_2O/Na_2O=60. The porous support coated by the seed crystals of NaA zeolite was placed in the gel. After hydrothermal treatment at 100°C for 4 hours, the support was taken out, washed by water and dried in reduced pressure.

T-type zeolite membrane was also grown hydrothemally on the mullite support. The aluminosilicate gel used in the synthesis was prepared by mixing a colloidal silica solution and an alkaline aluminate solution. The molar compositions of the starting gel were SiO_2/Al_2O_3=54, (Na+K)/SiO_2=0.77, Na/(Na+K)=0.76, H_2O/(Na+K)= 20.75. After aging, the porous support coated by the seed crystals of T-type zeolite was placed in the gel. After hydrothermal treatment at 100℃ for 24 hours, the support was taken out, washed by water and dried.

Pervaporation and vapor permeation experiments were carried out using the apparatus described elsewhere.[4]

The zeolite membranes were characterized by X-ray diffraction. The Si/Al ratio of the zeolite was determined by ICP analysis. The surface morphology of zeolite membranes was examined by scanning electron microscopy.

Results and Discussion

Table 1 shows the flux and the separation factor of pervaporation and vapor permeation for water/alcohol mixtures through the A-type and T-type zeolite membranes. The membranes were selective for permeating water preferentially with the high permeation flux. Although the separation factor of the T-type zeolite membrane was slightly smaller than that of NaA zeolite membrane, T-type zeolite membrane was stable in acidic solution as reported previously.[5]

Table 1. Comparison of Pervaporation (50 and 75ºC) and Vapor permeation (105ºC) performance of A- and T-type zeolite membranes

Membrane	System (10 / 90 wt%)	Temp [ºC]	Flux [kg/m^{2}h]	Separation factor
A Zeolite	H_2O / MeOH	50	0.57	2100
		105	3.50	5700
	H_2O / EtOH	75	2.15	10000
		105	4.53	30000
	H_2O / *i*-PrOH	75	1.76	10000
T Zeolite	H_2O / MeOH	50	0.37	27
		105	1.74	45
	H_2O / EtOH	75	1.25	2200
		105	2.48	3900
	H_2O / *i*-PrOH	75	1.77	10000

Figure 1. Tubular type module with zeolite membrane for dehydration of ethanol.

Figure 1 shows tubular type module with NaA zeolite membrane. This plant is equipped with16 modules, each of which consists of 125 pieces of zeolite membranes and produces 99.8 wt% ethanol from 600 l/h, 90 wt% ethanol feed at module inlet temperature of 120ºC.

References

1. Huang, R. Y. M., Ed., *Pervaporation Membrane Separation Processes*, Elsevier, Amsterdam, 1991.
2. Kita, H.; Horii, K.; Ohtoshi, Y.; Tanaka, K.; Okamoto, K., *J. Mater. Sci. Lett*. **1995**, *14*, 206.
3. Morigami, Y.; Kondo, M.; Abe, J.; Kita, H.; Okamoto, K., *Separation Purification Tech*. **2001**, *25*, 251.
4. Kita, H.; Asamura, H.; Tanaka, K.; Okamoto, K. *Am. Chem. Soc. Symp. Ser*. **2000**, *744*, 330.
5. Tanaka, K.;Yoshikawa, R.; Ying, C.; Kita, H.; Okamoto, K., *Chem. Eng. Sci*. **2002**, *57*, 1577.

ZEOLITE FILM PACKING: APPLICATION TO SYNTHESIS OF ETBE IN A CATALYTIC DISTILLATION COLUMN

Yonghong Li [a], Xigang Yuan [b], Shaomin Wu [b],

[a] National Key Laboratory of C1 Chemical Technology, School of Chemical Engineering, Tianjin University, Tianjin 300072, People's Republic of China
[b] National Key Laboratory of Chemical Engineering, School of Chemical Engineering, Tianjin University, Tianjin 300072, People's Republic of China

Introduction

ETBE (ethyl tert-butyl ether) may become a better option for automotive fuel octane booster since it could be produced from bio-ethanol that can be obtained from renewable resources. In addition, ETBE has superior qualities since its low blending Reid vapor pressure, less than 55kPa, is required in some place during summer. This makes ETBE an interesting alternative to MTBE.

Acidic zeolites have been identified as good catalysts for the reaction of etherification because of their good activity, perfect selectivity, thermo-stability and reproducible response [1]. Nowadays, zeolites are commonly used in the configuration of extrudates or beads. Due to the size of the catalysts, there are some problems for them to be used in a catalytic distillation column such as difficulty in removing products out of the reaction zone promptly and higher pressure drop in the catalytic distillation column than that in conventional distillation column so as to increase energy consumption. Therefore, an operation configuration involving thin active zeolite film on a structured packing, with a large contact surface between reactants and the catalyst, combined with the short diffusion length, in the reaction zone of the catalytic distillation column is expected to ensure good mass transfer and heat transfer. A few kinds of methods for preparation of supported zeolite film or zeolite film packing have been developed so far [2−5], but the performance of the zeolite film packing applied to synthesis of ETBE in a catalytic distillation column has not been addressed.

The aim of the present study is to develop a novel type of zeolite film packing for synthesis of ETBE and exploit its unique advantages in a catalytic distillation column.

Experimental

Preparation of the zeolite film packing. The zeolite film packing was prepared using secondary hydrothermal growth on a precursor seed layer of BEA crystals over a pretreated Si-Al ceramic support with pyramids all over the surfaces. Chemical composition of the precursor solution of Al_2O_3: $30SiO_2$: 6TEABr: 10.5NaOH: $240H_2O$ (in molar ratio) was employed for the formation of the zeolite film at temperature of 145℃ for 40 hours (autogenous pressure) in a 150 cm^3 Teflon lined autoclave. After hydrothermal treatment twice, the sample was calcined at 450℃ for 4 hours in elevation of 1℃/min, modified by ion-exchanging with solution of 0.5M NH_4Cl aqueous and steamed at 350℃ for 3 hours in elevation of 1℃/min to form the acidic zeolite film packing.

Catalytic distillation. The catalytic distillation experiments were carried out in a laboratory-scale stainless steel column (Diameter of 30mm). The column consists of a total condenser with circulating alcohol at a temperature of 273 K as a coolant, a reboiler with a mantle heater, and a column body composed of the three sections: (1) a rectifying section of 200 mm height below the condenser, (2) a stripping section of 400mm height above the reboiler, (both sections were packed with triangle stainless steel gauze packings), and (3) a reaction-separation section of 1200 mm height packed with the acidic zeolite film catalytic packings located at the middle of the column. There were 15 theoretical plates per meter of the stainless steel gauze packing and 12 theoretical plates per meter of the zeolite film packings, as determined by total reflux distillation with benzene and tetrachloromethane.

When the catalytic distillation was carried out, ethanol and C_4-cut olefin were introduced, with positive displacement pumps, into the column body at the higher part and the lower part of the reaction-separation section after being preheated, respectively. The reflux ratio was controlled with a solenoid valve with a timer. Liquid level in the reboiler was maintained by adjusting the valve of the withdrawing pipe connected to a tank. The pressure was controlled with compressed nitrogen at top of the column. After the experiment had been conducted for 4 hours, the liquid streams were sampled from the top of the column and from the reboiler, simultaneously, every half an hour. The compositions of the samples were analyzed with SQ-206 gas chromatography. The experiment would not be finished until the compositions of the samples did not vary with time any more.

Results and discussion

Characterization of the zeolite film catalytic packing. The zeolite film packing was characterized by XRD, SEM, and pyridine-IR. The XRD shows that zeolite BEA film, with relative crystallinity of 99%, has formed. Fig.1 shows the external surface of the zeolite film packing. The sizes of crystals are about 500nm. The film is essentially continuous and free of cracks with a thickness of about 3 μm. The IR spectra show that there are both a lot of stronger Bronsted acidic centers and stronger Lewis acidic centers over the zeolite film.

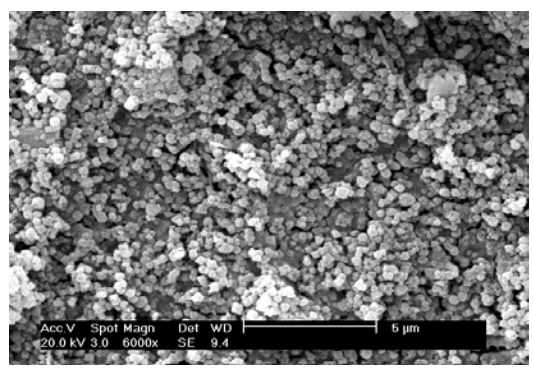

Figure 1. SEM image of the external surface of the zeolite film packing

Synthesis of ETBE in the catalytic distillation using the acidic zeolite film catalytic packings. Synthesis of ETBE from ethanol and isobutene is an exothermic reaction and the temperature highly influences the reaction rate. In the reaction-separation section, the exotherm causes some of liquid to be vaporized so that the compositions of the liquid phase and the vapor phase in this section are influenced by both the reaction and the amount of exotherm. In addition, the effect of pressure on boiling point temperature of the liquid in the column can result in a variation in the temperature of the reaction-separation section. Consequently, operating pressure influences the reaction rate. According to previous work [1], the right temperature for synthesis of ETBE over the zeolite BEA catalyst should be 85℃ that can be obtained in the reaction-separation section

of the column at pressure of about 500 kPa. Therefore, the investigations for the catalytic distillation were conducted at 500 kPa.

It is necessary to optimal the period when reactants flow through the reaction-separation section in order to ensure the sufficient contact between liquid reactants and the catalytic film. There are three factors that can influence on it. They are reflux ratio, reboil rate and space velocity. In this work, the effects of reflux ratio and reboil rate on the conversion of isobutene were investigated at the fixed space velocity of 1 h^{-1}. Also, influence of feed ratio of ethanol/isobutene on conversion of isobutene was concerned. The experiments were conducted by varying one of those operating conditions at the fixed the others.

First of all, ranges of feed molar ratio of ethanol/isobutene (F) corresponding to different conversion of isobutene (X) were investigated and were shown in Fig.2. Higher conversions of isobutene were obtained at the range of feed molar ratio from 1 to 2 where the conversion increases with increasing the feed ratio. It is noticeable that conversion of isobutene increases considerably with feed molar ratio of 1 to 1.1. On the other hand, lower conversions of isobutene were obtained at the range of feed molar ratio from 2.5 to 3 where the conversion decreases with increase of the feed ratio. This result indicates that increase of the feed ratio, in catalytic distillation, does not always advantage the conversion of isobutene, which is different from the situation in a reactor.

There is a distillation boundary in the system of ethanol/C_4–cut/ETBE because of the non-ideal mixture behavior. In non-reaction distillation, the compositions of distillate and the liquid in the reboiler are limited within some regions. According to the results of this experiment, there is an upper limited value in feed ratio of ethanol/isobutene for ETBE synthesis in a catalytic distillation process. As long as the value of feed molar ratio is less than 2, an ordinary distillation boundary can be removed by conducting the reaction and separation simultaneously and a higher conversion of isobutene can be obtained.

In addition, composition of the liquid in the reboiler should be taken into account. Since most extra ethanol may run down into the reboiler, there is a demand for a feed ratio of ethanol/isobutene as lower as possible. Therefore, the optimal value of the feed molar ratio, considering both conversion of isobutene and purity of the product in the reboiler, should be 1.1.

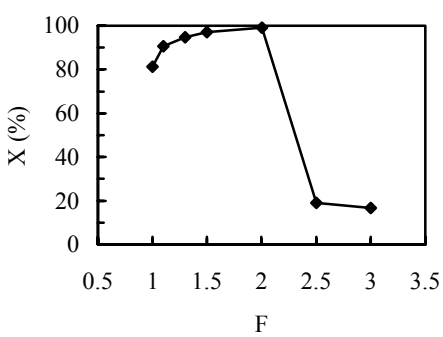

Figure 2. Conversion of isobutene as a function of feed molar ratio of ethanol / isobutene, pressure=500kPa, R=7, B=0.11m^3/h

Next, the effects of reflux ratio (R) on conversion of isobutene were shown in Fig.3. As increase of reflux ratio both can prolong the time for the contact between reactants and the catalysts and can improve the separation of the product from the reactants, there is always an increase in conversion of isobutene with increase of reflux ratio. Fig.3 also shows that the conversion does not vary so much by changing reflux ratio from 6 to 7. To minimize the consumption of energy, the optimal reflux ratio should be 6.

Finally, the variation of conversion of isobutene with respect to reboiler heat duty (B) was shown in Fig.4. The conversions are more than 90% at the range of reboil rate from 0.105 m^3/h to 0.125 m^3/h. The maximum conversion of isobutene appears at a reboil rate of 0.115 m^3/h. Further increase of reboil rate can cause some of the product in the reboiler to be vaporized and to run up into the reaction zone, which is disadvantageous to conversion of isobutene. Therefore, the optimal value of reboil rate can be 0.115 m^3/h.

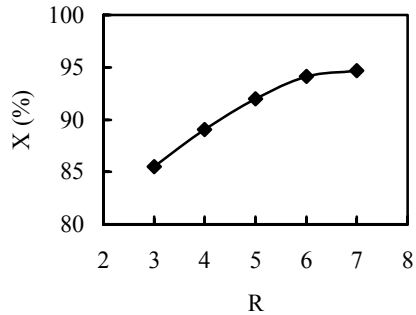

Figure 3. Conversion of isobutene as a function of reflux ratio, pressure=500kPa, F=1.3, B=0.11m^3/h

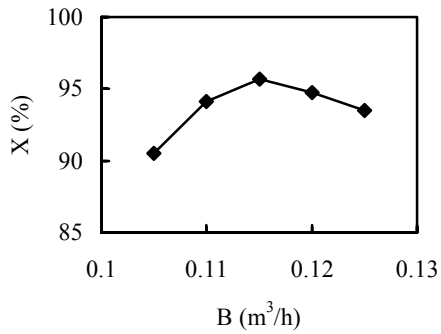

Figure 4. Conversion of isobutene as a function of reboil rate, pressure=500kPa, F =1.3, R = 6

Acknowledgment

The financial supports of the China Petroleum & Chemical Corporation and the fond of the National Key Laboratory of Chemical Engineering at Tianjin University are gratefully acknowledged.

References

[1] Li, Y., Yu, S., Chang, X., Wang, Y., Song, Y., *Acta Petrolei Sinica (Petroleum Processing Section)* in Chinese **2001**, 17(sup), 86.
[2] Oudshoorn, O. L., Janissen, M., Van Kooten, W. E. J., Jansen, J.C., Van den Bleek, C. M., Calis, H.P.A., *Chem. Eng. Sci.* **1999**, 54, 1413.
[3] Aoki, K., Kusakabe, K., Morooka, S., *AIChE J.* **2000**, 46(1), 221.
[4] Alfaro, S., Arruebo, M., Coronas, J., Menendez, M., Santamaria, J., *Micro. & Meso. Mater.* **2001**, 50(2-3), 195.
[5] Coutinbo, D., Balkus, J., Kenneth, J., *Micro. & Meso. Mater.* **2002**, 52(2), 79.

POLYIMIDES FOR BATTERY AND FUEL CELL MEMBRANES

Jennifer A. Irvin[1]*, Daniel Stasko,*[2] *Stephen Fallis*[1]*, Andrew J. Guenthner*[1]*, Cynthia Webber*[1]*, and John Blackwell*[3]

(1) Chemistry and Materials Division, Naval Air Warfare Center Weapons Division, Code 4T4220D, 1 Administration Circle, China Lake, CA 93555, Fax: 760-939-1617, irvinja@navair.navy.mil, (2) Department of Chemistry, University of Toledo, (3) Macromolecular Science and Engineering, Case Western Reserve University

Introduction

Although polymer electrolytes are crucial components of both lithium ion batteries (LIBs) and fuel cells (PEMFCs), the properties of existing polymer materials limit the performance of these devices. For example, the PEO-based polymers typically used in LIB membranes provide sufficient ion conductivity only above room temperature, which prevents their use at high altitude and in outer space. PEMFCs are conversely limited to low operating temperatures due to inadequate membrane thermal stability, which leads to increased catalyst poisoning and lower transport rates. [1] Thus, new polymer materials are needed to improve the performance of these devices.

The low conductivity of LIB membranes at low temperatures results from the mechanism of Li^+ transport, which involves highly temperature-dependent polymer chain segmental motions. If the Li^+ transport mechanism involves electric field-driven motion through open channels, however, high rates of transport over a large temperature range are possible.[2] The combination of molecular geometry and Li^+ affinity makes some crown ethers ideal candidates for these channels, provided they can be incorporated into a polymer matrix and aligned properly.

We have investigated crown ethers as components in high temperature fuel cell membranes, for which polybenzimidazoles, poly (ether ether ketone)s, polysulfones, and polyimides are considered candidates. Although most polyimides contain five-membered imide rings, polyimides in fuel cell membranes require six-membered imide rings[3] in order to exhibit sufficient hydrolitic stability under acidic conditions.[4] However, these six-membered ring polyimides are typically poorly soluble; solubility in polyimides can often be improved by incorporation of hexafluoroisopropylidene (HFIP) groups without detracting from polymer stability. [5]

Experimental

Synthesis. Crown ether-containing diamines were prepared as reported previously.[6] Copolyimides were synthesized by heating equivalent amounts of diamine and dianhydride in m-cresol at 200ºC for 15-24h. Terpolymers were prepared similarly, but the two diamines or two dianhydrides were dissolved together in m-cresol prior to addition of the other monomer. Polyimides were sulfonated according to a literature preparation.[7]

Characterization. Structural verification was accomplished using Bruker 400MHz ^{1}H and ^{13}C NMR and a Nikolet 710 FTIR. Elemental analysis (C, H, N) was performed by Galbraith Laboratories. Degree of sulfonation was determined by titration. (ref) Differential scanning calorimetry (DSC) was performed using a TA Instruments Model 2910 in nitrogen with a 10ºC/minute ramp from –40 to +300ºC. Thermogravimetric analysis (TGA) was performed using a TA Instruments Hi-Res TGA 2950 in nitrogen with a 5ºC/minute ramp to 500ºC. Proton conductivity was determined using electrochemical impedance spectroscopy (EIS) measurements with an EG&G Model 273A potentiostat/galvanostat equipped with a Princeton Applied Research 5210 lock-in amplifier and PowerSine software.

Results and Discussion

A variety of polyimides were prepared as delineated in Table 1. Initially, 1,4,5,8-naphthalenetetracarboxylic dianhydride (NTDA) and/or 4,4'-(hexafluoroisopropylidene)diphthalic anhydride (6FDA) were reacted with diamines to form polyamic acids, which were thermally converted to the polyimides. Diamines used were 2,2-bis(4-aminophenyl)hexafluoropropane (Bis-A-AF), anti-4,4'-diamino-dibenzo-18-crown-6 (C18), 4,4'-diaminodibenzo-24-crown-8 (C24), and/or 2,5-diaminobenzenesulfonic acid (DABS). A general scheme for the synthesis and subsequent sulfonation is shown in Figure 1. The crown ether-containing polyimides (1 and 2 in Table 1) were very poorly soluble, dissolving significantly only in m-cresol. To improve solubility, commercially-available HFIP-containing monomers, either 6FDA or Bis-A-AF, were incorporated into the polyimides. The resulting polyimides (5 and 9 in Table 1) are soluble in chloroform, DMF, NMP, and m-cresol; polymers 5 and 9 have been previously reported[8] but have not been investigated for use as electrolyte membranes. We have also prepared four terpolymers (3, 6s, 7, and 8); the terpolymers exhibit satisfactory solubility, processability, and film-forming properties.

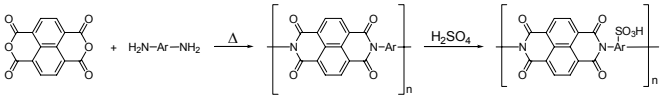

Figure 1. General synthesis and sulfonation of polyimides

Table 1. Summary of Polymer Formulations

	Monomers					
Polymers*	NTDA	6FDA	Bis-A-AF	C18	C24	DABS
1/1s	x			x		
2/2s	x				x	
3	x		x		x	
4s	x					x
5	x		x			
6s	x			x		x
7	x	x			x	
8	x	x		x		
9		x			x	

*Sulfonated polymers are denoted by an s following the polymer number

Incorporation of sulfonic acid groups was accomplished using two strategies, direct sulfonation of polymer materials using reactive reagents or incorporation of sulfonated monomer. The first case, post-polymerization sulfonation, was accomplished using concentrated sulfuric acid according to a literature preparation.[7] The resulting polymers (1s and 2s) were found to be somewhat soluble in hot methanol and in aqueous base. Verification of the extent of sulfonation using standard spectroscopic techniques proved difficult, though changes in solution properties suggested substantial substitution. Ion exchange capacity, and thereby the degree of sulfonation, was determined titrametrically. A significant degree of sulfonation was apparent in some cases with up to three sulfonate groups introduced per repeat unit. Polyimides 4s and 6s were prepared using a presulfonated diamine that allowed for a controlled degree of sulfonic acid incorporation into the polymer. As an internal check, the ion exchange capacity for these polymers was also measured and corresponded to one sulfonate group per repeat unit as expected (Table 2). While introduction of sulfonic acid groups in

this manner is more reliable and reproducible, the overall degree of sulfonation is much lower and more limited.

Proton conductivity (σ, S/cm) of the sulfonated polymers was accomplished using EIS. As expected, water content was found to be critical in the overall conductivity of the pressed samples (see Table 2). Dry conductivity values were very low at room temperature, ~10^{-7} S/cm. Conductivity was improved in moist samples with values reaching 10^{-2} S/cm at room temperature in fully hydrated samples.

Table 2: Proton Conductivity Measurements of Polymer Systems

Polymer	Wt % SO_3H	Approx. # SO_3H per repeat	σ of dry films*	σ at 10% water*	σ saturated w/ water*
6s	6 %	1	$7x\ 10^{-8}$	-	$2x10^{-5}$
4s	12 %	1	$1x10^{-7}$	$5x10^{-7}$	$1x10^{-4}$
1s	32 %	3	$1x10^{-6}$	-	$1x10^{-2}$

*All conductivity measurements performed at room temperature and presented in units of S/cm

These polymers have been found to be thermally stable, with 10% weight loss in air at approximately 400ºC (via TGA). This stability range will more than satisfy the high temperature requirement for fuel cell membranes.

Two different forms of order in the crown ether-containing polyimides have been detected via cryogenic differential scanning calorimetry (DSC; Figure 2) and X-ray diffraction (XRD) of powder samples (Figure 3). XRD indicates that both samples are semi-crystalline, and DSC indicates that the crystals melt at a temperature near to or above the thermal degradation point (320°C) of these polymers. The polyimide with the smaller, *anti*-18-crown-6 repeat unit is more crystalline with better crystalline order than the polyimide with the 24-crown-8 repeat unit, suggesting that the crystallinity is controlled by the tendency of the planar naphthylimide sheets to stack and pack into a crystalline array. This is more readily accomplished with smaller crowns that interfere less with the ordering process. Molecular models based on the X-ray data suggest structures in which the chain axes are in the plane of the film, and the crown ethers are stacked perpendicular to the surface. This type of structure should facilitate Li^+ transport.

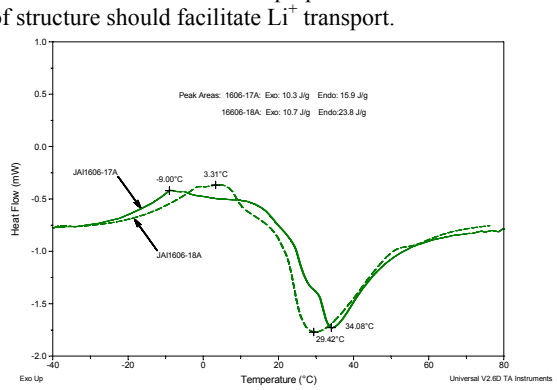

Figure 2. DSC thermograms of polymers 1 (solid line) and 2 (dashed line).

The second form of ordering appears to be present only at or below room temperature and is thus most easily detected via cryogenic DSC. A first-order transition (akin to crystallization) with a modest enthalpy change occurs in both polyimides at approximately 30°C (peak endotherm). Like crystallization, this ordering appears to require activation energy, leading to a maximum in the rate of ordering at -10 to 0°C. DSC scans show that the enthalpy of ordering is larger for the 24-crown-8 containing polyimide than for the *anti*-18-crown-6 polyimide. The most likely interpretation of this ordering phenomenon involves a conformational change in the crown ether repeat units. Whether such changes are sufficient to induce crystal-crystal transformations in these polyimides is presently unknown.

Conclusions

Several polyimides have been prepared; incorporation of HFIP groups improves solubility without detracting from thermal stability. Sulfonation of several of these polymers yielded materials with room temperature proton conductivities reaching 0.01 S/cm. Some evidence of crown ether channel formation has been seen; some of these polymers may be useful as LIB electrolytes.

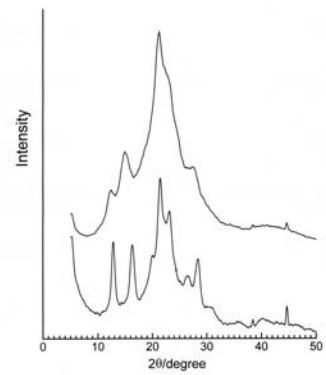

Figure 3. X-ray diffraction patterns for the polymers 1 (bottom) and 2 (top).

Acknowledgements. This work was supported by the Office of Naval Research's ILIR program and by NASA Glen Research Center.

References

1. Rikukawa, M.; Sanui, K., *Prog. Polym. Sci.* **2000**, *25*, 1463-1502.
2. Scanlon, L. G., Jr.; Krawiec, W. T.; Giannelis, E. P., *US Pat. No.* 6,010,805, **2000**.
3. a)Vallejo, E.; Pourcelly, G.; Gavach, C.; Mercier, R.; Pineri, M., *J. Membr. Sci.* **1999**, *160*, 127-137. b) Zhang, Y.; Litt, M.; Savinell, R. F.; Wainright, J. S., *Polym. Prepr. (Am. Chem. Soc., Div. Polym. Chem.*) **1999**, *40 (2)*, 480-481. c) Genies, C.; Mercier, R.; Sillion, B.; Cornet, N.; Gebel, G.; Pineri, M., *Polymer* **2001**, *42*, 359-373. d) Fang, J.; Guo, X.; Harada, S.; Watari, T.; Tanaka, K.; Kita, H.; Okamoto, K., *Macromoecules* **2002**, *35 (24)*, 9022-9028.
4. Genies, C.; Mercier, R.; Sillion, B.; Petiaud, R.; Cornet, N.; Gebel, G.; Pineri M., *Polymer* **2001**, *42*, 5097-5105.
5. P. E. Cassidy, *J. Macromol. Sci.-Rev. Macromol. Chem. Phys.,* **1994,** C34, 1.
6. Zarras, P.; Lindsay, G. A.; Chafin, A. P.; Miles, M. H.; Merwin, L. H.; Fallis, S.; Webber, C.; Yee, R. Y.; Irvin, J. A., Polymer News, 2001, 26 (10), 335-340.
7. Zaidi, S. M. J.; Mikhailenko, S. D.; Robertson, G. P.; Guiver, M. D.; Kaliaguine, S., J. Membr. Sci., 2000, 173, 17-34.
8. a) Togano, T.; Takiguchi, T.; Takao, H.; Hanyu, Y.; Asaoka, M.; Iwaki, T., *Eur. Pat. Appl.* EP499,159, August 19, 1992. b) Russanov, A. L.; Bulycheva, E. G.; Elshina, L. B.; Askadskiy, A. A.; Vlasov, U. M.; Rogozhnikova, O. Yu., *Polym. Prepr. (Am. Chem. Soc., Div. Polym. Chem.)* **1998**, *39 (2)*, 853-854. c) Pethrick, R. A.; Wilson, M. J.; Affrossman, S.; Holmes, D.; Lee, W. M., *Polymer* **2000**, *41*, 7111-7121.

APPLICATION OF SANS IN ANALYSIS OF FUEL CELL CATHODE ION EXCHANGE MEMBRANES

Riza Kizilel[1], Nasrin Khalili[2], Giselle Sandi[3], and Robert J. Selman[1]

[1]Department of Chemical and Environmental Engineering, and
[2]Environmental Management Program, Illinois Institute of Technology, Chicago, Illinois 60616;
[3]Chemistry Division, Argonne National Laboratory, 9700 South Cass Ave, Argonne, IL 60439

Introduction

One of the fundamental components of a fuel cell is the membrane electrode assembly. The electrode is coated on one side with a thin platinum catalyst layer and the electrode, catalyst, and membrane together form the membrane electrode assembly (MEA). Since it is the heart of the fuel cell, more studies are concentrated on synthesis of MEAs.

High or low catalyst loaded cathode material (MEA) prepared by different techniques can be obtained commercially. In most cases high loading helps the system works better but the higher the amount of platinum the more costly is the process. The characterization of new and used MEAs using advanced analytical methods is a key element to determine the problems associated with operations and operating conditions.

In this work, a fuel cell is being used for slightly different purpose from its usual usage. Metal contaminants in acidic solution are removed by electrochemical process which has a cathode fuel cell (**Figure 1**). The contact with the acidic solution was shown to affect negatively the structure and the performance of the MEA. Since the focus of our work was the determination of the effect of Pt loading on the cell performance and ionic flux, a series of experiments were carried out to analyze the impact of process performance on the MEA structure. In each of them overloading (a continuous slow rise in the voltage necessary to maintain a constant current) appeared to be a major problem (**Figure 2**). To solve the problems associated with the cost and the need for a high Pt loading, it was decided to prepare and fully characterize a range of MEAs in our laboratory. Therefore, the structural characterization focused on Small Angle Neutron Scattering (SANS). The results obtained in these studies will help to lower the cost of operation and to find the optimum structure needed for the process to reach its maximum efficiency.

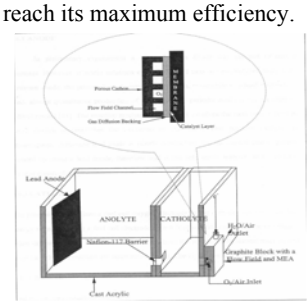

Figure 1: Experimental Setup for regeneration of chromic acid and removal of metal contaminants

Experimental

MEA Preparation. MEAs are prepared by following the procedure described in reference (1).

Characterization Methods.

Powders used in SANS are prepared by first scratching the electrodes from the MEA and then grinding them into fine particles. Four different types of powders were used during the characterization. Specifically, they are Pt-C mixture (Electro-Chem), MEA before used in electrochemical cell (EC), MEA after used in EC without impurities, and MEA after used in EC with impurities.

The SANS measurements were performed at the SAND time-of-flight SANS instruments at the Intense Pulsed Neutron Source, Argonne National Laboratory. Cylindrical Suprasil sample containers with a neutron optical path length of 1 mm were used. SAND provides data in a Q range of 0.001 to 1 $Å^{-1}$ in a single measurement. All samples were studied as dry powders. Additionally, a contrast-variation SANS study was performed on each sample by preparing the powdered sample as slurries in mixtures of normal and deuterated toluene with deuterated toluene proportions of 0, 25, 50, 75 and 100 %. In preparing the slurries, the powder was slowly evacuated to avoid air bubble formation prior to adding the solvent. The scattering from an empty cell was used for background correction in these measurements (2).

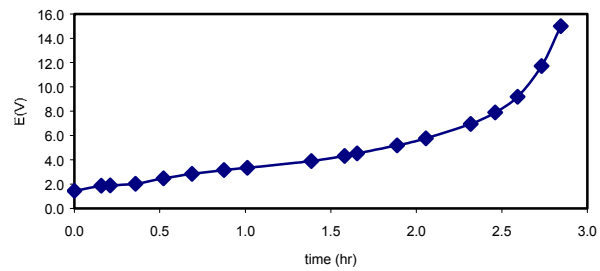

Figure 2: The impact of low platinum loading on potential (E(V))

Results and Discussion

Previous results have shown that a new membrane process can be used to remove the contaminants from hard chromium plating baths. Although energy required to operate the cell was decreased theoretically, experimental results showed that energy consumption during the experiment is still too high. Fortunately, the process removal rate for metal contaminants was observed to be same level of removal rate in porous pot process.

SANS data helps to draw a clear picture of the morhphology of MEAs electrodes. The plot of I (intensity) vs q (scattering vector) is the key element to determine the diameter of agglomerate, and pore size (**Figure 3**).

To analyze the results, SANS data can be fit into an equation derived by Beaucage, B., (2).

$$I(q) = G\exp\left(\frac{-q^2 R_g^{\,2}}{3}\right) + \left(L_i q_i^{\,*}\right)^P$$

where

G: Guinier prefactor
Rg Particulate radius of gyration
Li: characteristic length scale
I: Scattering Intensity
qi* : function of q scaled to cut of power law scattering
q = $4\pi\mathrm{Sin}(\theta/2)/\lambda$ where θ is the scattering angle and λ is the wavelength

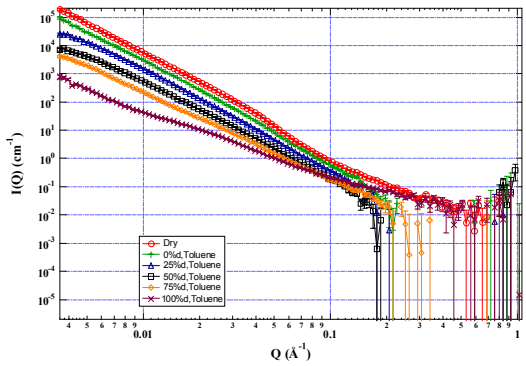

Figure 3: Contrast Variation SANS Data

The fitting shows that dry Pt-C powder has an agglomerate of two layers. The intensity at high values, unfortunately, does not help to define the first layer. But the second layer shows a gyration radius of ~60Å and power law exponent of 3.3. The latter value also indicates a disordered structure in this mixture.

Addition of Nafion to the MEA decreases the gyration radius to 48Å, whereas the power law decreases to 3.19. These two parameters show that the addition of nafion and the application of high pressure help to attach smaller particles to each other in the second layer. Although the disorder level is decreasing, it is still at the high levels.

MEAs were tested in two different cells. One of them is the 2.5 M chromic acid solution without metallic impurities. This electrochemical process increases the potential of the cell in less than two hours. Two layers were observed in the SANS results fitting, however, and the radius of gyration, increases to 100 Å. The disorder level (power law) remains fairly constant at 3.25.

When metallic impurities (Cu,Fe,Ni) are added to chromic acid, another layer is formed because of the impurities. The results show that the impurities diffuse through the second layer first and then form the third one. Radius of gyration in the second layer reaches up to 182.4 Å which means a 277% increase. The disorder level of this layer is at the highest level which is 3.37. Third layer clearly indicates a clogged surface formed during the process. This last layer has a gyration radius of 36.7 Å and a power law of 2.1, indicated a more ordered structure. **Table 1** shows the fitting results for each experiment.

Contrast analysis helps to characterize the porous structure of the materials. The Modified Guinier plot (**Figure 4**) at low Q levels determines the porosity of the materials. **Table 2** shows that there are still available pores inside the agglomerates but they are inaccessible because of the clogged outer region.

Table 1: Relevant parameters obtained from SANS data

		Pt-C	New MEA	Used MEA w/o impurities	Used MEA with impurities
1st Layer	length scale	6.876	7.6109	9.1572	5.6916
	exponent	3.267	3.1539	3.3404	3.0762
2nd Layer	guiner i(0)	183.21	26.323	219.57	6414.1
	guiner rg	60.024	48.422	100.41	182.42
	length scale	10.652	12.131	12.526	8.3657
	exponent	3.3293	3.1938	3.2504	3.3703
3rd Layer	guiner i(0)	-	-	-	5.9373
	guiner rg	-	-	-	36.695
	length scale	-	-	-	12.829
	exponent	-	-	-	2.1476
	reduced chi squared	5.296	11.193	7.3866	1.9676

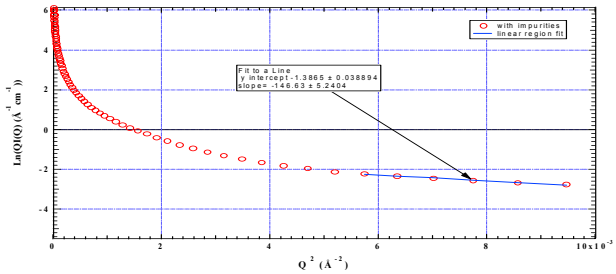

Figure 4: Modified Guinier Plot

Table 2: Morphology of the pores

	Pt-C	Pt-C/Nafion (new)	Used w/o impurities	Used with impurities
Porous Radius (Aº)	27.1	26.8	22.8	24.2

Acknowledgment

Work at Argonne was performed under the auspices of the U.S. Department of Energy, Office of Basic Energy Sciences, Division of Chemical Sciences, Geosciences, and Biosciences under contract number W-31-109-ENG-38. The help from the IPNS personnel is greally appreciated.

References

1. Wilson, M.S., Valerio, J.A. and Gottesfeld, S., *Electrochim. Acta*, 40(3), 355, (1995).
2. Littrell, K., Khalili, N., Campbell, M., Sandi, G. and Thiyagarajan, P. , *Chemistry of Materials* 14 (1), 327-333 (2002).
3-Beaucage, *G,. Journal of Applied Crystallography* 1996, 29, 134.

Novel PEEK Membranes for Fuel Cell Applications

Maria Gil [1], *Xiangling Ji*[1], *Xianfeng Li*[2], *Hui Na*[2], *J. Eric Hampsey*[1] *and Yunfeng Lu*[1]

(1) Chemical Engineering Department, Tulane University, 300 Lindy Boggs Center, Tulane University, New Orleans, LA 70118, ylu@tulane.edu, (2) Department of Chemistry, Jilin University, huina@jlu.edu.cn

Introduction

Proton exchange membrane fuel cells (PEMFC) are promising power sources for vehicles and portable devices [1,2]. Membranes currently used in PEMFC are perfluorinated polymers such as Dupont Nafion®. Even though such membranes have demonstrated good performances and long-term stability, their high cost and methanol crossover makes them unpractical for large-scale production. Among the desired characteristics of a cation-exchange membrane for PEM fuel cells applications are: high ionic conductivity, minimal water/methanol transport, high resistance to dehydration, low gas permeability, low swelling, high mechanical strength, high resistance to oxidation, reduction and hydrolysis and low cost. Sulfonated aromatic polyether ether ketones (S-PEEK) based membranes have been studied due to their good mechanical properties, thermal stability and conductivity [3, 4]. In the present study, poly(aryl ether ether ketone) (PEEK) polymeric membranes fabricated from sulfonated monomer have been evaluated for possible fuel cell applications. The sulfonated PEEK membranes were characterized by measuring the ion exchange capacity, water swelling, proton conductivity, methanol diffusivity and thermal stability.

Experimental

Membrane Preparation. 1.0 g sulfonated PEEK was dissolved into 30ml DMF. The solution was cast into thin films of 30 µm – 60 µm thickness on a 10 cm x 10 cm glass slide, which was placed into an oven at 50°C and dried for 3 days. A dry membrane was peeled off from the substrate with deionized water, and was submerged into 1.5M H_2SO_4 solution overnight. Finally, the membranes were rinsed with deionized water and dried under vacuum for one day.

Membrane Characterization

Swelling Degree. Membrane samples were equilibrated in water at 25°C for 24 h. They were then removed from the water, quickly dry-wiped and immediately weighed. Subsequently, they were dried at 100°C and again weighed. The swelling degree was calculated as follows:

$$SD = m_{wet}/m_{dry} - 1 \qquad (1)$$

Ion-Exchange Capacity (IEC). The IEC was determined through titration. The membranes in H^+ form were immersed in 1M NaCl solution for 24 h to liberate the H^+ ions (the H^+ ions in the membrane were replaced by Na^+ ions). The H^+ ions now in solution were then titrated with 0.01M NaOH.

Proton Conductivity. The proton conductivity of the fully hydrated polymer membrane samples was determined by AC impedance spectroscopy over a frequency range of $1x10^3$ Hz to $1x10^6$ Hz using a Solartron 1260 gain phase analyzer.

Methanol Diffusion Coefficient. Diffusion coefficients were determined using an H-cell arrangement. 1M Methanol was placed on one side of the H-cell and water was placed on the other side. Magnetic stirrers were used on each compartment to ensure uniformity. Methanol analyses were done using a Hewlett Packard GC chromatograph. Peak areas were converted to methanol concentration using a calibration curve.

Thermal Stability. The thermal stability of the membranes was analyzed using a TA instrument SDT 2960 simultaneous DTA-TGA. The sample (~10mg) was heated from 25°C to 900°C at a rate of 10°C/min under a nitrogen atmosphere.

Results and Discussion.

Methanol Diffusion. S-PEEK polymeric membranes prepared from the sulfonated monomer exhibited methanol diffusion coefficients of $3x10^{-7}$ to $5x10^{-8}$ cm^2/s depending on the degree of sulfonation of the starting monomer. These values are significantly lower than that of Nafion® membranes ($2x10^{-6}$ cm^2/s). Such results are expected for S-PEEK membranes and can be attributed to less pronounced hydrophilic and hydrophobic domains within the membrane and to a smaller flexibility of the polymer backbone. These characteristics reduce the hydrodynamic solvent transport (water and methanol), which may help reduce the problems associated with water and methanol crossover for direct methanol fuel cells [4].

Conductivity. Proton conductivities at 25°C of the S-PEEK membranes (shown on Figure 1) are about 13-42 % that of Nafion 117 determined in [5]. The conductivity values are acceptable to obtain good fuel cell performances.

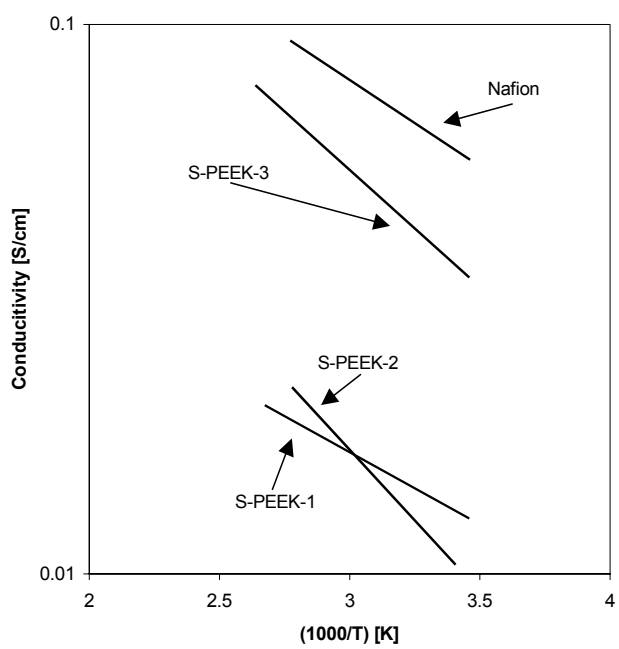

Figure 1. Proton conductivity of fully hydrated Nafion [4] and S-PEEK polymeric membranes prepared from sulfonated monomer.

Thermal stability. The thermal degradation of the S-PEEK membranes starts in the range of 250-270°C and these values are similar to the ones obtained for cross linked polyaryl blend membranes [6]. Three weight loss steps are observed in Figure 2. The first weight loss step corresponds to water loss. The second weight loss step is attributed to the splitting-off of sulfonic acid groups in the PEEK membrane [7]. The third weight loss step corresponds to sulfonic acid decomposition. According to the thermal analysis, the S-PEEK membranes are thermally stable within the temperature range for PEMFC applications.

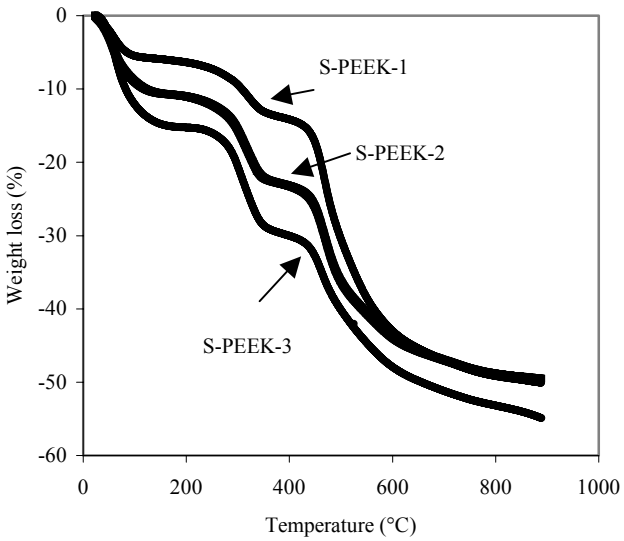

Figure 2. TGA curves of S-PEEK membranes

Comparison with Nafion® membranes.

S-PEEK polymeric membranes prepared from the sulfonated monomer show some similarities with Nafion membranes in IEC and water swelling properties depending on the degree of sulfonation of the PEEK, see Table 1. The main differences between S-PEEK ad Nafion® membranes are ionic conductivity and MeOH diffusion coefficient. Even though the ionic conductivities are lower than that of Nafion®, they are still suitable for PEMFC applications and the lower MeOH diffusion coefficients should reduce methanol crossover in direct methanol fuel cells.

Table 1. Comparison of Nafion and S-PEEK membranes

	S-PEEK 1	S-PEEK 2	S-PEEK 3	Nafion®
Ion Exchange Capacity (IEC)	0.712	1.511	1.465	0.91
Water Swelling (%)	13	37	54	38
Conductivity at 25°C (S/cm)	0.011	0.013	0.035	0.083
MeOH diffusion coefficient at 25°C (cm^2/s)	$5x10^{-8}$	$3x10^{-7}$	$3x10^{-7}$	$2x10^{-6}$

Conclusions

S-PEEK membranes with 0.7-1.5 mmol/g ion exchange capacity exhibited a high proton conductivity (> 0.01 S/cm at room temperature), good thermal stability and methanol diffusion coefficients significantly lower than that of Nafion® (PEM of choice for hydrogen/air fuel cells), making S-PEEK membranes a good alternative to reduce problems associated with high methanol crossover in direct methanol fuel cells.

References

1. Appleby, A.J., *Recent developments and applications of the polymer fuel cell.* Philosophical Transactions of the Royal Society of London, Series A: Mathematical, Physical and Engineering Sciences, 1996. **354**(1712): p. 1681-1693.
2. Shoesmith, J.P., *et al.*, *Status of solid polymer fuel cell system development.* Journal of Power Sources, 1994. **49**(1-3): p. 129-42.
3. Kreuer, K.D., *On the development of proton conducting materials for technological applications.* Solid State Ionics, 1997. **97**(1-4): p. 1-15.
4. Kreuer, K.D., *On the development of proton conducting polymer membranes for hydrogen and methanol fuel cells.* Journal of Membrane Science, 2001. **185**(1): p. 29-39.
5. Zawodzinski, T.A., Jr., *et al.*, *Determination of water diffusion coefficients in perfluorosulfonate ionomeric membranes.* Journal of Physical Chemistry, 1991. **95**(15): p. 6040-4.
6. Kerres, J., *et al.*, *Application of different types of polyaryl-blend-membranes in DMFC.* Journal of New Materials for Electrochemical Systems, 2002. **5**(2): p. 97-107.
7. Zaidi, S.M.J., *et al.*, *Proton conducting composite membranes from polyether ether ketone and heteropolyacids for fuel cell applications.* Journal of Membrane Science, 2000. **173**(1): p. 17-34.

Synthesis and Characterization of Pyridine-Based Polybenzimidazoles as Novel Fuel Cell Membrane Materials

*Lixiang Xiao, Haifeng Zhang, Eui-Won Choe, Eugene Scanlon, L. S. Ramanathan and Brian C. Benicewicz**

NYS Center for Polymer Synthesis,
Department of Chemistry, Rensselaer Polytechnic Institute, Troy, NY 12180

Introduction

Fuel cells based on solid polymer electrolytes have attracted much attention recently due to their promise as high energy density power sources for both mobile and stationary applications. In particular, high temperature polymer electrolyte membranes operational above 120°C without humidification offer many advantages including fast electrode kinetics and high tolerance to fuel impurities.[1] However, the current widely used sulfonated perfluoropolymer membranes such as Nafion® rely on the presence of water to solvate and transport the protons and therefore operate in a limited temperature range and encounter water-management problems.

Acid doped polybenzimidazole (PBI) has emerged as a promising candidate for a low-cost and high performance fuel cell membrane material. It has been shown that this polymer electrolyte membrane exhibits high ionic conductivity at temperatures up to 200°C, low gas permeability, excellent oxidative and thermal stability,[2] and nearly zero water drag coefficient.[3] However, additional progress is still needed for the large-scale application of PBI in fuel cells. Furthermore, the conventional method to prepare acid doped PBI membranes involves a multi-step process while the mechanical properties of the resulting membranes are largely limited by the low molecular weight of PBI used in previous studies.

In this paper, we report the synthesis of a series of high molecular weight (as indicated by the inherent viscosity, I.V.) polybenzimidazoles (PBIs) with additional main chain pyridine groups, using polyphosphoric acid (PPA) as both solvent and polycondensation reagent. A novel process, termed as PPA process,[4] has been developed to prepare pyridine-based PBI (PPBI) membranes loaded with high levels of phosphoric acid by direct-casting of the PPA polymerization solution without isolation or re-dissolution of the polymers, followed by a sol-gel transition induced by the hydrolysis of PPA into phosphoric acid. In addition, we studied the effect of the incorporation of pyridine groups on the properties and film formation process.

Experimental

Materials. Pyridine dicarboxylic acids (2,4-, 2,5-, 2,6- and 3,5- PDAs) were purchased from Acros and purified by recrystallization from dilute hydrochloric acid before use. 3,3′,4,4′-Tetraaminobiphenyl (TAB) was donated by Celanese Ventures, GmbH and used as received. Polyphosphoric acid (115%) was used as supplied from Aldrich Chemical Co.

Polymerization. The general procedure for the synthesis of pyridine-PBIs (PPBIs) is described as follows: Purified pyridine dicarboxylic acid (12.534g, 0.075mol) and TAB (16.074g, 0.075mol) were added to a three-neck resin reaction flask in a nitrogen atmosphere glove box, followed by 220 grams of polyphosphoric acid. The reaction mixture was stirred using a mechanical overhead stirrer under nitrogen and the reaction temperature was ramped to 190°C and maintained for 18hrs at 190°C. The reaction mixture became more viscous and developed a dark brown color. A small amount of the reaction mixture was poured into water to isolate a brown mass. The mass was pulverized, neutralized with ammonia hydroxide, washed thoroughly with water, and dried in a vacuum oven for 24 hours at 100°C to obtain the pyridine PBIs for further characterization.

Film Formation. The polymer films were prepared by casting the polymerization solution directly onto glass plates using a Gardner film applicator. The polyphosphoric acid solvent was hydrolyzed to phosphoric acid by exposing the films for 24h at 25°C and relative humidity 40±5% to obtain polymer electrolyte membranes for film properties and fuel cell testing.

Characterization. I.V. was measured at a concentration of 0.2 g/dL in concentrated sulfuric acid at 30°C. The acid doping level was determined by titrating a piece of membrane sample with standardized sodium hydroxide solution. The sample was then washed with water, dried in a vacuum oven to obtain the dry weight of polymer for calculation. The membrane mechanical property was tested utilizing a United Tensile Tester (SSTM-1-PC) following the ASTM standard D882-97 (Type V specimens). Ionic conductivity was measured by a four-point ac impedance method using a Zahner IM6e spectrometer over the frequency range from 1Hz to 100KHz. Fuel cell testing was conducted using a single cell test station (Fuel Cell Technologies) equipped with mass flow controllers.

Results and Discussion

We investigated the synthesis of pyridine-based PBI starting from 2,4-, 2,6-, 2,5- and 3,5-pyridine dicarboxylic acids in polyphosphoric acid as shown in scheme 1.

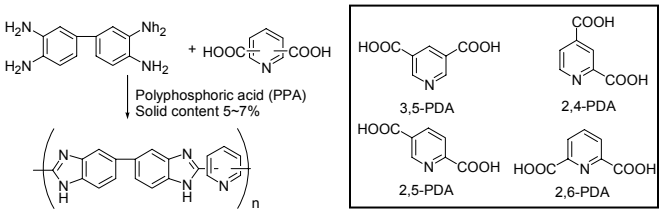

Scheme 1. Synthesis of pyridine-based polybenzimidazoles.

Table 1 summarizes the I.V. and solubility data. After appropriate purification of monomers, three of the four monomers polymerized to give high I.V. PPBIs with properties influenced by the substitution pattern on the pyridine ring as discussed later. The 2,6-PDA monomers did not undergo polycondensation to yield a high polymer, probably due to its limited thermal stability as suggested from the GC-MS spectrum and DSC curves.[5]

Table 1. Inherent Viscosity and Solubility Data of the PPBIs

Polymer	Monomer purity	$\eta_{inh.}$ (dL/g)	Solubility	
			DMAc[a]	Phosphoric acid[b]
2,5-PPBI	As received	0.8		
	Recrystallized	2.5-3.1	S	S (≤ 1%)
3,5-PPBI	As received	0.6		
	Recrystallized	1.3-1.9	S	S (≤ 5%)
2,4-PPBI	As received	0.3		
	Recrystallized	1.0	S	S
2,6-PPBI	As received	0.2		
	Recrystallized	0.6	S	S

[a] Determined by refluxing in dimethylacetamide (DMAc) for 3h.
[b] S: Soluble up to a certain weight percentage.

The solubility of the polymers in dimethylacetamide (DMAc) and phosphoric acid were assessed as shown in Table 1. Overall, the incorporation of the pyridine-group into the polymer backbone increased their solubility relative to the non-pyridine containing PBI. In particular, the meta-oriented 3,5-PPBI showed remarkably high solubility in phosphoric acid of up to 5%, most likely attributable to the strong interaction between the phosphoric acid and the polymer.

When cast from the polymerization mixture, thin films of 2,5-PPBI absorbed moisture from the atmosphere. A sol-gel transition then occurred via the hydrolysis of PPA to phosphoric acid. The subsequent drain-off of the excess phosphoric acid and water increased the solid content and gave rise to strong polymer electrolyte membranes. The acid doping levels of the resulting 2,5-PPBI membranes were approximately 15-25 moles of phosphoric acid per repeat unit of PPBI. The tensile strength and the elongation at break of such 2,5-PPBI membranes varied from 1.0 to 2.5Mpa and from 250% to 300%, respectively, depending upon the different acid doping levels.

In contrast, the 3,5-PPBI showed very different behavior when cast from the PPA polymerization mixture (solid content 5~7%). The 3,5-PPBI polymer retained all the phosphoric acid generated during the PPA hydrolysis process, and liquid drain-off was not observed.

A key feature of a fuel cell membrane is its proton conductivity. As depicted in Figure 1, 2,5-PPBI membranes prepared from the novel PPA process exhibited very high conductivities of around 0.2 S/cm at 160-180°C as a result of the high acid doping level. It also suggests that the incorporation of pyridine groups as an additional nitrogen containing heterocycle increased the basicity of polymer backbone and enhanced the interaction of phosphoric acid and the polymer.

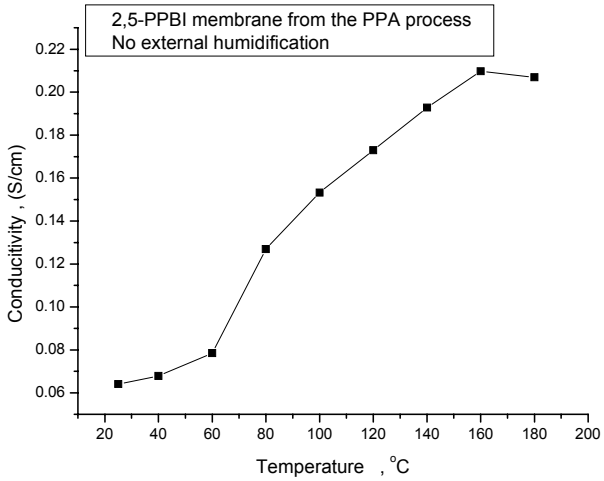

Figure 1. The conductivity of 2,5-PPBI membrane as a function of temperature without external humidification.

Preliminary fuel cell tests illustrated in Figure 2 demonstrate that these membranes prepared from the novel PPA process can be used successfully in high temperature fuel cells operational without any external humidification. As seen from the Figure 2, higher operational temperatures provided better cell performance. The optimization of film composition and the membrane electrode assembly (MEA) fabrication technique is in progress.

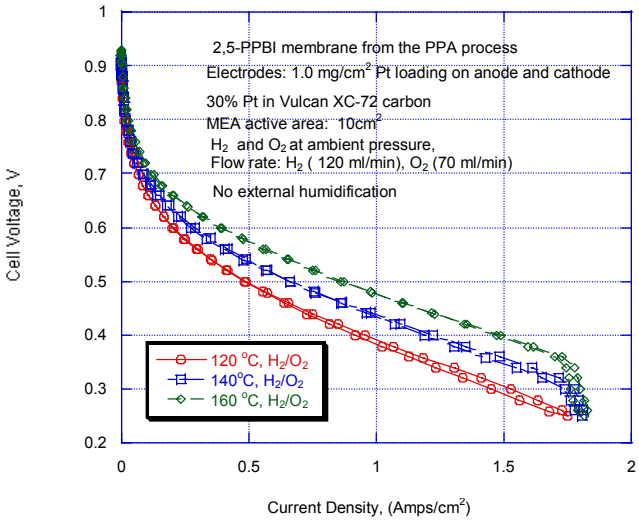

Figure 2. Cell voltage vs. current density curves for a fuel cell based on the 2,5-PPBI membrane from the PPA process.

Conclusion

A series of polybenzimidazoles (PBIs) with additional main chain pyridine groups have been synthesized using polyphosphoric acid (PPA) as both solvent and polycondensation reagent. After appropriate purification of starting materials and optimization of polymerization conditions, three of the four monomers (3,5-, 2,5-, 2,4-pyridine dicarboxylic acids) polymerized to yield high I.V. pyridine-based polybenzimidazoles with properties influenced by the substitution pattern on the pyridine ring. The incorporation of the pyridine group as an additional nitrogen-containing aromatic heterocycle increased the basicity of the polymer and improved the solubility of the polymer in acid while retaining the inherently high thermo-oxidative stability of the polybenzimidazoles.

The PPA process offers a revolutionary method to prepare pyridine-based polybenzimidazole membranes with high acid doping levels, which contribute to their unprecedented high proton conductivities of 0.2 S/cm at 160°C-180°C.

Preliminary fuel cell tests have demonstrated the feasibility of the novel PPBI membranes from the PPA process for operating a fuel cell at temperatures in excess of 120°C without any external humidification or pressure requirements.

Acknowlegements. The authors thank Celanese Ventures, GmbH for financial and technical support. NYSTAR is gratefully acknowledged for partial support in establishing The Fuel Cell Test Laboratory at Rensselaer.

References

[1] Yang C., Costamagna P., Srinivasan, Bemziger J. and Bocarsly A. B., *J. Power Source*, **2001**, 109, 1
[2] Wang J. T., Savinell R. F., Wainright J., Litt M. and Yu H., *Electrochim. Acta*, **1996**, 41(2), 193
[3] Weng D., Wainright J. S., Landau U. and Savinell R. F., *J. Electrochem. Soc.*, **1996**, 143, 1260
[4] Krishnamurthy B., Zhang H., Ramanathan L. S., Xiao L., Scanlon E., Choe E. W. and Benicewicz B. C., 202nd ECS meeting abstract, Salt Lake City, Oct 2002
[5] Xiao L., manuscript in preparation.

Ash Rejection Behavior on Continuous Column Flotation Process

Yasushi SEKINE, Daisuke YAMAGUCHI, Kiyohiro ISHIKAWA, Eiichi KIKUCHI, Masahiko MATSUKATA

Department of Applied Chemistry
Faculty of Science and Engineering
WASEDA University
3-4-1 Ohkubo, Shinjyuku,
Tokyo, Japan 169-8555

Introduction

Column flotation is one of the promising processes for the low-cost next generation coal cleaning technologies. As for the column flotation system, many efforts have focused on optimization of apparatus and/or improvement of flotation results so far. However there have been few studies which tried to estimate the relation of flotation results and characteristics properties of coal. Then we investigated the characterization of demineralization in the column flotation system to estimate the flotation behavior by measuring the contents of inorganic elements in the cleaned coal and the tail refuse. Furthermore we investigated the distribution of coal minerals and their average particle size.

Experimental

Continuous Column Flotation. We employed the continuous column flotation system for the simple coal cleaning process. Samples which used in this study were; Adaro, Wallarah, Ermelo, Datong, Taiheiyo, and they were crushed into particles and sieved under 150 μm. The proximate analysis value and ultimate analysis value of these coal was shown in **Table 1** and the schematic diagram of experimental apparatus was shown in **Fig. 1**. At first, coal and ion-exchanged water were mixed for 30 min in slurry tank after adding Kerosene 1 mg / g-coal. Simultaneously column whose height was 2 m was filled with ion-exchanged water, and 4-methyl-2-pentanol(MIBC) 150 μL / L-water was added to it. Then coal-water mixture was supplied into the column continuously at the rate of 1 L / min from the upper of the column by using a static pump. MIBC was supplied into column continuously from the bottom of column by using a micro feeder. During the experiment, wash-water was supplied into the upper of the column. In upper and bottom of the column, coal-water mixture was obtained and dried. We regarded the upper part; cleaned coal, and the bottom part; ash rejection. Then average particle size of their particles was measured by laser particle size distribution measurement equipment. Inorganic elements of dissolved coal were measured by using ICP-AES after a microwave treatment.

Mineral analysis by CCSEM. The analysis of mineral part was conducted by CCSEM(Computer Controlled Scanning Electric Microscope). For the sample preparation, coal powder was mixed with Carnauba wax and cross-sectional polish of a sample was performed after heat-molding using the automatic grinder. Then, in order to enhance the conductivity of the sample section, carbon evaporation under vacuum condition was performed. The fixed quantity and the quality of the inorganic element contained in the particle on a section were measured. And the classification and the existence form of ash contents (included or excluded) were distinguished according to the mineral-form by using original conversion software.

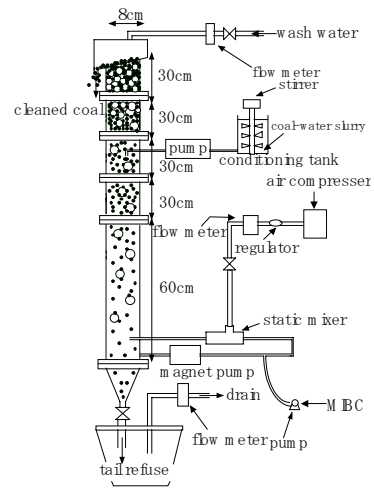

Fig. 1 Schematic diagram of experiment apparatus.

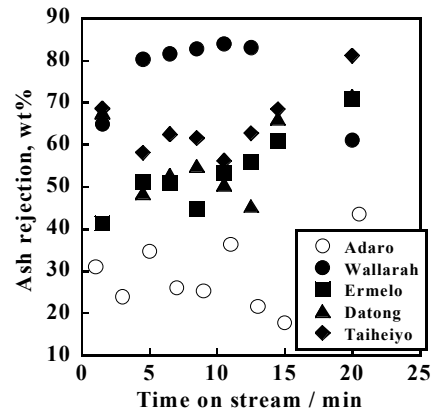

Fig. 2 Time on course of ash rejection.

Table 1 Proximate and ultimate analysis of coal employed in this study

Coal		Adaro	Wallarah	Ermelo	Datong	Taiheiyo
Proximate Analysis value [a.d %]	Water Content	12.58	3.00	3.50	5.21	5.55
	Ash	1.58	13.7	12.90	10.24	11.35
	Volatiles	40.65	29.40	30.90	27.66	43.36
	Fixed carbon	45.19	53.90	52.70	56.89	39.74
Ultimate Analysis Value [db %]	Carbon	71.73	71.90	71.10	71.90	67.33
	Hydrogen	5.02	4.20	4.23	4.40	5.59
	Nitrogen	1.06	1.39	1.76	0.90	1.09
	Sulfur	0.00	0.30	0.65	0.61	0.08
	Oxygen	20.38	8.05	8.89	11.39	13.89
Ash Composition [db %]	SiO_2	21.34	58.30	48.00	57.10	46.26
	Al_2O_3	9.18	28.97	29.39	19.19	24.37
	Fe_2O_3	10.53	4.24	5.00	11.88	8.27
	CaO	20.63	1.99	7.13	3.72	8.79
	MgO	6.84	0.92	2.60	0.82	2.65
	Na_2O	5.84	0.54	0.29	0.45	1.73
	K_2O	0.76	1.62	0.83	1.47	0.96
	SO_3	23.08	0.56	3.74	3.87	3.67
	P_2O_5	0.07	0.05	0.14	0.40	1.07
	TiO_2	0.48	1.29	1.26	0.69	1.27
	V_2O_5	0.04	0.03	0.04	0.03	0.06
	MnO	1.09	0.06	0.09	0.20	0.08

Results and Discussion

Continuous column flotation. Time on course of ash rejection was shown in **Fig. 2**. Ash rejection came to be steady state in 5～14 minutes, and that of Wallarah coal showed highest rejection level. So Wallarah coal was employed for subsequent experiments because of its high separation ability.

The average particle distribution of raw coal, cleaned coal and tail of Wallarah coal were shown in **Fig. 3**. In the raw coal, the distribution of particle size was high around the particle diameter about 100 μm, and the shoulder peak was observed near 10 μm. Although the particles in the tail rejection had the same distribution, the fraction around 100 μm became large. On the other hand in the cleaned coal, the particles near 100 μm were not contained, but the distribution has the peak around 80 μm and 10 μm. From these phenomena, we considered that many of mineral matter were contained in the particle near particle diameter 100 μm, and their particles were removed by the column flotation as the bottom rejection.

Distribution of inorganic elements. Inorganic elements distribution of the cleaned coal and the tail rejection that were obtained during steady state, was shown in **Fig. 4**. As a result, most of contained inorganic elements eluted into the column, or obtained as the tail rejection. In particular, most of Na, Al, and Mn were removed as the tail rejection.

Mineral analysis by CCSEM. The demineralization efficiency of each mineral in Wallarah coal was calculated and shown in **Fig. 5**. Demineralization efficiency means "the ratio of the actual amount of each mineral" by "the theoretical value". The theoretical value is the amount of minerals at the time of separating into cleaned coal and tail, without demineralization. Most of minerals in Walllarah coal were efficiently removed to tail. And Aluminosilicate and Si-Rich minerals were removed in particular.

Conclusion

Most of contained inorganic elements in Wallarah coal were eluted into the column, or obtained as the tail rejection. In particular, most of Na, Al, and Mn were removed as the tail rejection. Most of minerals in Walllarah coal were efficiently removed by the continuous column floatation process. And Aluminosilicate and Si-Rich minerals were removed in particular.

Acknowledgement

This work was partly supported by the fund of National Department of Science and Technology Japan (its group leader; Prof. K.Miura from Kyoto Univ.).

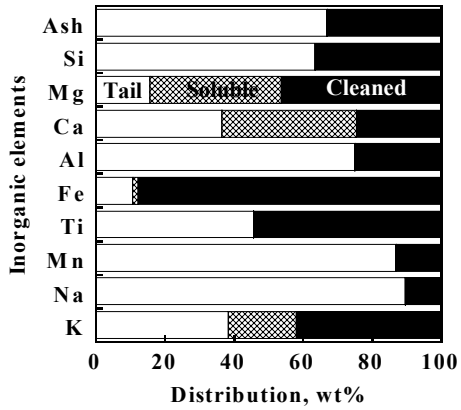

Fig. 3 Distribution of average particle (raw coal, cleaned coal, tail).

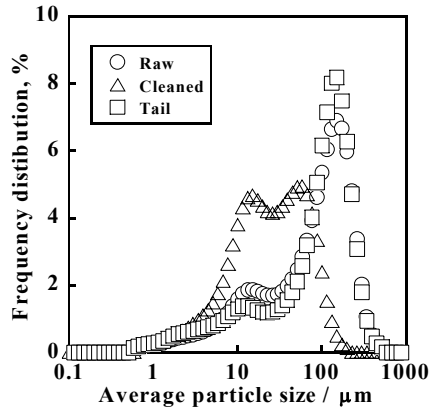

Fig. 4 Distribution of inorganic elements.

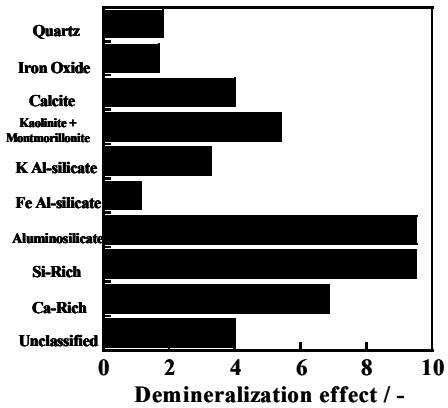

Fig. 5 Comparison of demineralization effect.

A novel coal cleaning with pretreatment in methanol

Takayuki Takarada, Kenji Goto, Megumi Ookawa, Jie Wang[1] and Kayoko Morishita

Department of Biological and Chemical Engineering,
Gunma University,
1-5-1 Tenjin-cho, Kiryu 376-8515 JAPAN
[*1] Institute of Multidisciplinary Research for Advanced Materials,
Tohoku University

Introduction

Coal demineralization prior to use has received much attention because mineral matter in coal causes problems in many aspects of conventional and advanced coal utilization. Physical benification has long been used to reject discrete mineral inclusions from coal. For efficient physical separation of mineral matter, it is necessary to liberate mineral-rich grains by the breakage of coal particles through coal grinding. In order to improve the liberation of mineral inclusions and the efficiency of grinding energy utilization, pretreatment of coal by swelling agents has been explored. In this paper, we use the relatively cheap and available methanol as a swelling agent to study its effect on the breakage of coal particles.

Experimental

Coal Sample. Eleven coals were used in this study. Their proximate analysis and carbon content are shown in Table 1. The coal particle was screened to 1~2 mm before pretreatment.

Table1 Analysis of coal samples

	Carbon [wt%d.a.f]	Mois.	V.M.	F.C.	Ash
			[wt%]		
Pasil	72.0	2.1	47.4	48.5	2.0
Taiheiyo	78.7	3.8	43.9	40.2	12.1
Kitasyuku	78.7		36.4	50.8	12.8
Yangsong	80.5	3.3	40.3	48.3	8.1
Ebenezer	81.2	2.2	38.1	45.2	14.5
Hong-Yie	81.7	0.8	47.3	22.3	29.6
San-Zu-Pa	82.6	1.0	14.3	50.3	34.4
Datong	82.7	3.2	28.7	58.4	9.7
Miike	82.8	1.9	39.9	45.0	13.2
Newlands	85.9	2.5	26.3	56.2	15.0
I-Tem-Pou	86.9	0.8	15.0	64.8	19.4
Burton-st	89.8	1.5	16.6	70.6	11.3

Methanol Treatment. A 100 g sample of coal was treated with 200 mL methanol at room temperature for the desired time. After treatment, the sample was filtered and then dried at 107 °C for 2 h.

Compressive strength. The compressive strength of sample was measured with Kiya strength meter.

Grindability test. It was conducted in a cylindrical ball mill made of stainless steel (i.d., 85 mm; height, 90 mm) with 30 stainless balls. In each test, a 20 g sample of coal was ground at 110 rpm for the predetermined time.

SEM Analysis. SEM was utilized to observe the morphology of coal sample upon the methanol treatment. CCSEM was used to measure quantitatively the mineral inclusion distribution for the fine coal sample with or without methanol treatment, it was accomplished on a TOPCON, ABT-60 scanning electron microscope equipped with an energy dispersive x-ray analyzer (EDAXPV9750) and a computer controlled program.

Results and Discussion

Compressive strength. The compressive strength of samples with and without the methanol pretreatment were shown in **Fig. 1**. The strength of the treated coal particles was reduced to about a half of that of parent coal.

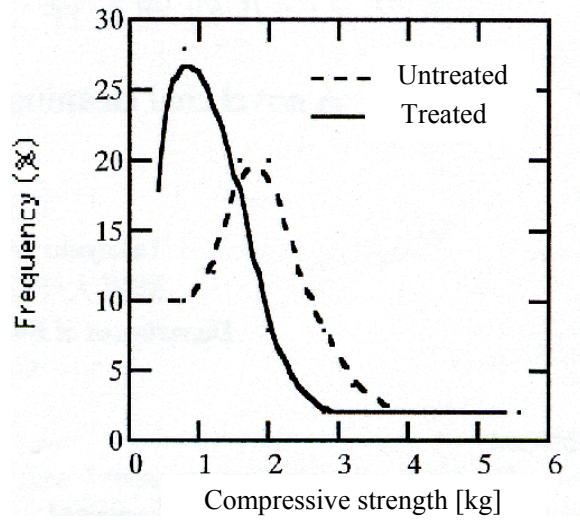

Fig.1 Compressive strength

Grindability. Fig.2 shows the particle size distributions by grinding Yangsong raw coal and the treated coal. The data are the weight percent of the size-graded particles. The grindability of the treated coal was quite higher than that of raw coal. **Fig.2** shows the effect of treatment time on the grindability. Prolonged swelling from 2 to 120 h increased the cumulative weight percent of the particles under 150 μm from 41.8 to 58%.

Similar experiments were conducted for eleven coals. After methanol treatment, all the coals tended to be easily ground. However, the effectiveness of the methanol pretreatment on the grindability depended on coal type. The effectiveness of the pretreatment evaluated as the ratio of the cumulative weight percent

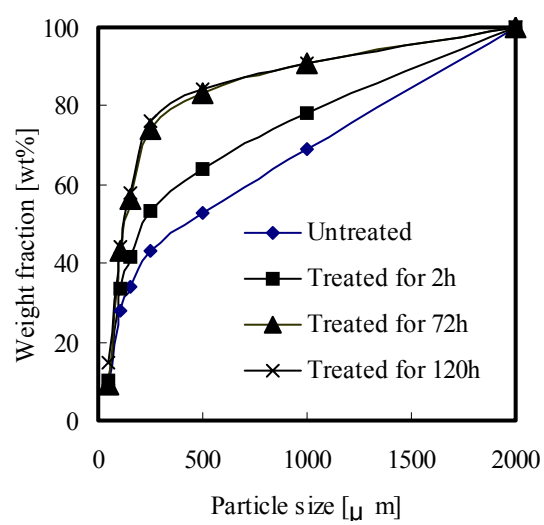

Fig.2 Grindability of Yangsong coal

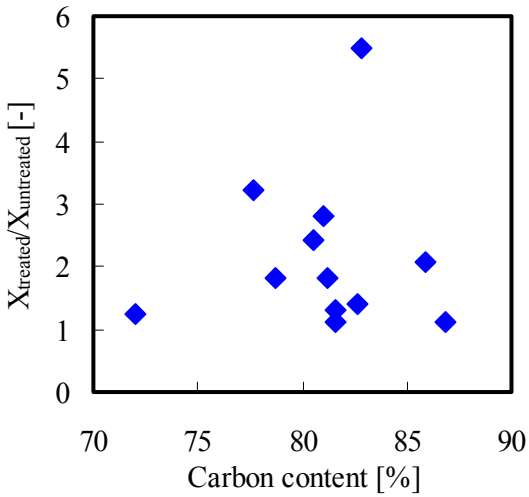

Fig.3 Effectiveness of treatment for various coals

of the particles under 150 μm for raw coal to that for the treated coal is shown in **Fig.3**. It appears that the effectiveness of the treatment has no correlation with coal rank. The effectiveness for coal with carbon content of around 82 wt% was quite large.

SEM Observation. Fig.4 displays the SEM images for the Yangsong raw coal and treated coal samples. There were many fractures formed after methanol treatment. Wang et al.[1)] found the preferential crack along the boundaries between mineral and coal matrix using some mixed agents. Tamai et al.[2)] observed the crack along the boundaries between macerals by the pretreatment with liquid ammonia. The crack formed in the treated coal is one of the reasons for high grindability of treated coal.

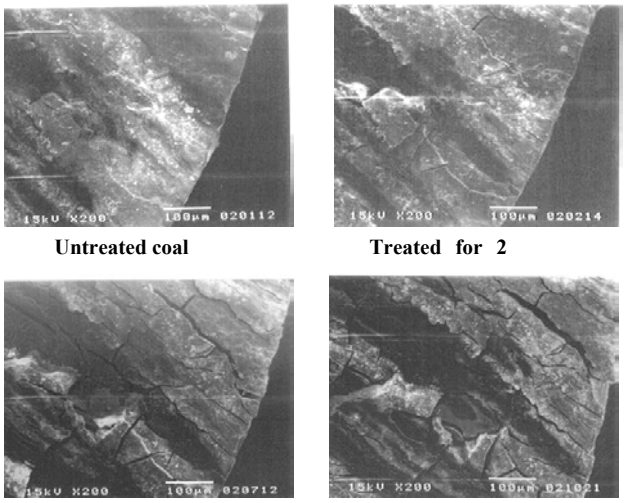

Fig.4 SEM images for Yangsong coal

CCSEM Analysis. To observe the liberation of mineral inclusions from coal matrix, we used CCSEM to quantitatively analyze two Yangsong coal samples with or without methanol treatment, which were subject to the same milling and then were both screened to the particles under 150 μm prior to analysis. **Figs.5 and 6** show the particle number ratio of the particles having different mineral contents. The counted particle numbers were 2168 and 2412, respectively, for the raw coal sample and the treated sample. The mineral content is evaluated from cross sectional area of mineral in coal particle analyzed with CCSEM. Through treatment, the number of the mineral-rich particle containing 90-100% mineral was increased and that of particle containing 50-80% mineral was decreased. From the results obtained, the selective mineral reduction may be achieved by using methanol pretreatment. Some iron-containing minerals appeared to decrease in the number. XRD showed that Yangsong coal mainly contained pyrite, kaolinite, gypsum, ferrous sulfate, and quartz (not shown). Gypsum and ferrous sulfate were significantly dissolved out upon the methanol treatment.

Conclusions

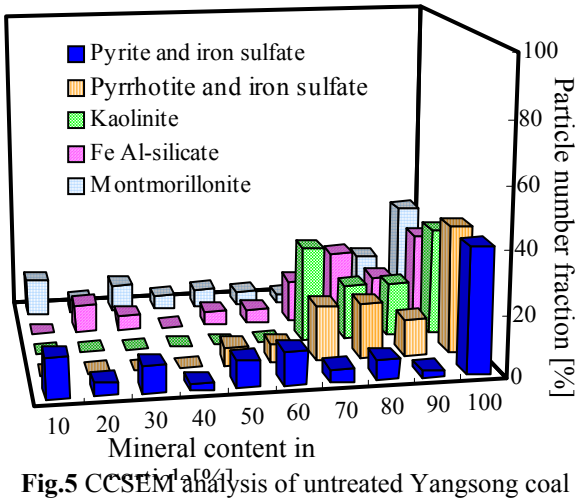

Fig.5 CCSEM analysis of untreated Yangsong coal

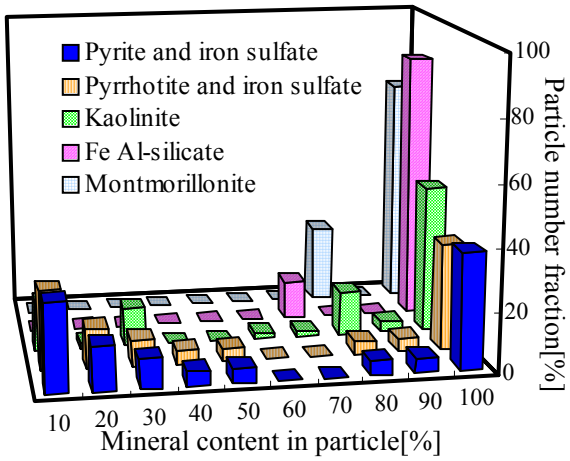

Fig.6 CCSEM analysis of treated Yangsong coal

The compressive strength of the treated coal particles was reduced to about a half of that of parent coal and the grindability of the treated coal was higher than that of raw coal. Many cracks were formed in coal particle by the treatment. CCSEM analysis revealed the possibility of selective mineral reduction by the benification with pretreatment in methanol.

Acknowledgement. This work is under a Scientific Research of Priority Areas---"Development of Clean Coal Technology for Mitigating Global Warming".

References

(1) Wang, X. H. et al. *Coal Prep.* **1996**, *17 (3-4), 185-198*
(2) Tamai, T.;Tomita. A.;Takarada. T. *J. Chem. Soc. Jpn,* **1980**, *951-958*

PRODUCTION OF CLEAN FUELS BY SOLVENT SKIMMING OF COAL AT AROUND 350 °C

Kouichi Miura, Hiroyuki Nakagawa, Ryuichi Ashida, and Takayuki Ihara

Department of Chemical Engineering, Kyoto University, Kyoto 606-8501, Japan

Introduction

The authors have recently presented a new coal extraction method by which various kinds of coals ranging from brown coals to bituminous coals could be extracted up to 80 % in a flowing stream of tetralin or a coal derived oil, carbol oil, under 10 MPa at 350 °C[1,2,3]. However, it doesn't seem cost-effective to use pure solvents from the viewpoint of practical application of the extraction method. In this study the effect of solvent recycling on the extraction behavior was investigated to make the method practically applicable.

It was also found in the previous papers that the extract was almost free from mineral matters[1,2,3]. To examine the result in more detail, the distributions of inorganic elements through the extraction were measured and discussed.

Experimental Section

Coal Samples. The analyses of four coal samples used are given in **Table 1**.

Table 1. Ultimate Analyses of Coal Samples Used

Coal (Abbreviation)	Ultimate analysis [wt%, d.a.f.] C	H	N	O+S (diff.)	Ash [wt%, d.b.]
South Banko (SB)	68.8	5.2	1.4	24.7	4.2
Prima (PR)	76.3	5.5	1.4	16.8	5.4
Miike (Mi)	80.8	6.2	1.3	11.7	19.8
Pittsburgh #8 (PITT)	83.2	5.3	1.6	9.9	9.3

Solvents Used. Tetralin was used as a model solvent, and a coal tar derived oil, so-called carbol oil, was used as a candidate solvent for practical application of the proposed extraction method. The carbol oil is a coal tar distillate whose boiling point ranges from 180 to 220 °C. Main components of the oil are phenolic derivatives.

Experimental Procedure for Extraction. Figure 1 shows a schematic diagram of the apparatus used for extraction. 100 to 1000 mg of coal samples were placed on a filter (11.2 mm OD and 0.5 µm opening) in a reactor made of Swagelok. The solvent was supplied continuously using a high-pressure pump at the flow rate of 1 to 5 ml/min. The pressure was regulated using a pressure-regulating valve (TESCOM) at 10 MPa. The reactor was heated at the rate of 10 K/min to 350 °C where it was kept for 90 min, and then it was cooled immediately by immersing into a sufficient amount of water. The coal fractions extracted at the reactor temperature, which are solublilized in the solvent, came out from the reactor with the flowing solvent, but a part of the solubilized components precipitated as solid when the solvent flow was cooled to room temperature. The solid thus precipitated, called deposit in this paper, was collected by 3 filters (20, 10, and 2 µm openings) placed in series just before the pressure-regulating valve. The deposit that passed these filters was collected in a separation trap with the soluble components at room temperature. The soluble components are called "soluble" here. Product gas was collected in a gasbag, and analyzed using a gas chromatograph for the components smaller than C6 hydrocarbons in molecular weight. The weights of the residue and the deposit were directly measured after drying them in vacuo at 150 °C for 5 hours. The weight of gaseous components was calculated from the analysis using the gas chromatograph. The rest of the product was regarded as the soluble.

Experiments recycling the solvent containing soluble fraction were also performed using tetralin as the solvent. For this purpose, 150 ml of tetralin was used and it was supplied to the extractor at the rate of 5 ml/min. The tetralin, recovered in the separation trap with the soluble fraction, was recycled to the extractor. The recycling solvent passed the coal layer 5 to 6 times during 90 min of experiment. The solvent recovered after the experiment was used again to the extraction of a fresh coal. This extraction cycle was repeated 10 times by using the fresh coal for each cycle.

Analyses of the products. The contents of main inorganic elements in the soluble and the deposit, Na, Mg, Al, Si, Ca, and Fe, were analyzed by the inductive coupled plasma spectrometry (Shimadzu, ICPS7500). The contents of trace elements, Co, Cr, Cu, Mn, Ni, Pb and Zn, in the deposit and the residue were also measured by ICP-AES and Hg, Se, As were analyzed by CVAAS, HGAAS, and GFAAS, respectively[4].

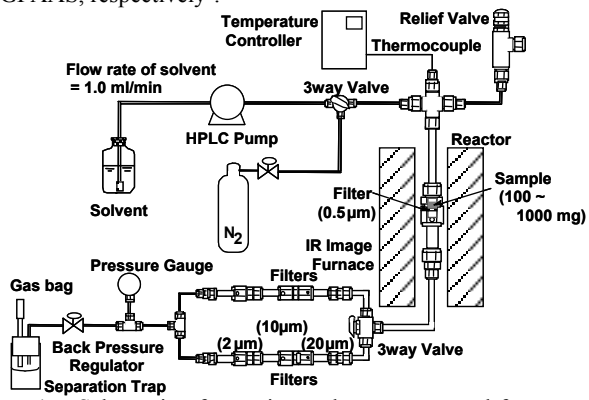

Figure 1. Schematic of experimental apparatus used for extraction in flowing solvent.

Results and Discussion

Effect of Solvent Recycling on the Extraction Behavior. Experiments recycling the solvent were performed using PITT. **Figure 2** shows the relationship between the yield of each component and the number of cycle. The yield of deposit increased with the number of cycle, while the yield of soluble stayed almost constant. The yield of deposit reached 41 % at a maximum, which was twice as large as that in the first extraction. The extraction yield of 80 % was achieved at its maximum. The soluble concentration in the recycling tetralin increased from 0.001 kg/kg-solvent of the 1st cycle to 0.012 kg/kg-solvent of the 10th cycle. These results suggest that the increase of the solubility of the coal with increasing extraction cycle was realized by the increase in the concentration of soluble in the tetralin. It could be concluded that solvent recycling was

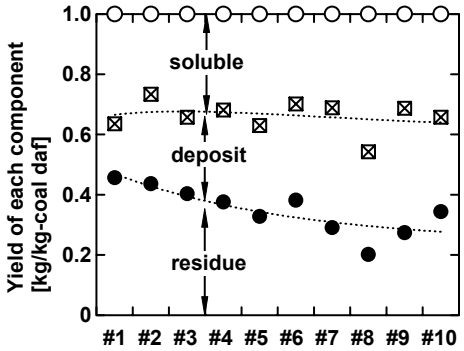

Figure 2. Relationship between the yield of each component and the number of cycle for PITT through the extraction in recycling tetralin at 350 °C.

effective to enhance the extraction yield, suggesting a possibility of the solvent recycling as a cost effective method.

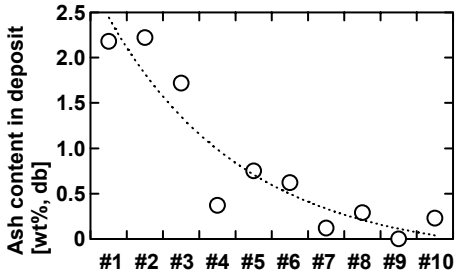

Figure 3. Relationship between the ash content in the deposit and the number of cycle for PITT through the extraction in recycling tetralin at 350 °C.

Figure 3 shows the relationship between the ash content in the deposit and the number of cycle. As presented in the previous papers, the deposit obtained by the extraction using one pass tetralin contained little mineral matters[1,2,3]. The solvent recycling still further reduced the mineral matter content in the deposit. The content decreased dramatically from 2.2 % to 0.2 % with the number of cycle. Thus, it was found that the solvent recycling was effective not only to enhance the extraction yield but also to remove the mineral matters from coals.

Mineral Matters in the Extract. **Figure 4** shows the contents of main inorganic elements in the soluble and the deposit fractions for extractions using tetralin and those in the soluble fractions for extractions using the carbol oil. The figures in the brackets represent the contents of elements in the parent coals. The yields of these fractions through the extractions were also given in Figure 4. Only a small amount of Na and Si were detected in the soluble fractions obtained by the tetralin extraction, indicating that the soluble is very clean. On the other hand, the amounts of the elements in the deposit fractions obtained by the tetralin extraction and the soluble fractions obtained by the carbol oil extraction were relatively larger than those in the soluble fractions obtained by the tetralin extraction, especially for Fe. However, the contents of most elements in the extracts were less than several percents of those in the parent coals.

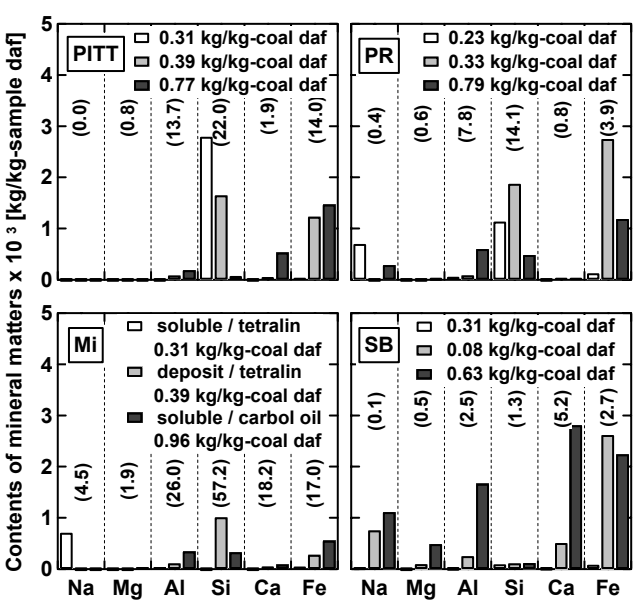

Figure 4. Contents of main inorganic elements in the extracts.

The contents of trace elements including hazardous heavy metals were analyzed as well[4]. **Figure 5** shows the contents of trace elements in the deposit fractions obtained by the first and fifth cycle of extractions of PR in recycling tetralin. The yields of deposits for the extraction cycles are also listed in Figure 5. The contents of Cr, Cu, Ni and Pb in the deposit fractions obtained by the first cycle were larger than those in the parent coal. The Ni content in the deposit fraction obtained by the fifth cycle was still larger than that in the parent coal. The contents of the other elements, Mn, Zn, As, Co, Hg and Se, in the deposit fractions, however, were much less than those in the parent coal, indicating that the proposed method is effective to remove some of the hazardous elements from coals. Furthermore, the contents of almost all the trace elements in the deposit fraction decreased with the number of cycle, which agreed with the results shown in Figure 3. The five cycles of extractions reduced the contents of Mn, Zn and Co in the deposit to 29 %, 19 % and 30 % of those in the parent coal, respectively. These results suggest that the solvent recycling enhances the degree of removal of hazardous trace elements.

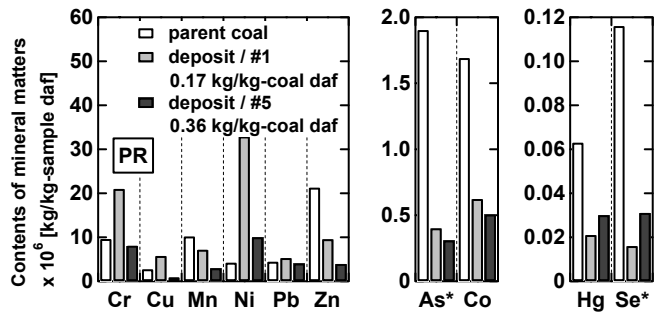

Figure 5. Contents of trace elements in the deposit and parent coal (* calculated from the contents in the parent coal and the residue).

Conclusion

The effect of solvent recycling on the extraction behavior was examined from the viewpoint of practical application of the proposed extraction method. It was found that the solvent recycling was effective not only to enhance the extraction yield but also to remove the mineral matters from coals, suggesting a possibility of the solvent recycling as a cost effective method.

To examine how mineral matters are removed by the extraction, the distributions of inorganic elements, including hazardous trace elements, through the extractions were investigated. It was clarified that the proposed method is effective to remove most of the inorganic elements from coals, although it depends on the kind of element.

Acknowledgement. This work was supported by the Ministry of Education and Science of Japan through the Scientific Research of Priority Area (B) "Development of Clean Coal Technology for Mitigating Global Warming"(Grant NO. 737). The authors express their sincere thanks to Prof. A. Ohki for measuring the contents of trace elements.

References

(1) Miura, K.; Shimada, M.; Mae, K. *15th Pitt. Coal Conf.*, **1998**, Paper No.30-1.
(2) Miura, K.; Shimada, M.; Mae K.; Huan, Y. *Fuel*, **2001**, *80*, 1573.
(3) Miura, K.; Mae, K.; Shindo, H.; Ashida, R.; Ihara, T. *18th Pitt. Coal Conf.*, **2001**, Paper No.2.6-6.
(4) Xu, Y.; Nakajima, T.; Ohki, A. *Toxicol. Environ. Chem.*, **2001**, *81*, 55.

EFFECT OF ACID TREATMENT ON THERMAL EXTRACTION FOR "HYPERCOAL" PRODUCTION

Chunqi Li[1], Toshimasa Takanohashi[1], Takahiro Yoshida[1], Ikuo Saito[1], Hideki Aoki[2], and Kiyoshi Mashimo[2]

[1] Institute for Energy Utilization,
National Institute of Advanced Industrial Science and Technology
[2] College of Science and Technology, Nihon University

Introduction

Thermal extraction using an organic solvent was carried out to produce ashless coal (HyperCoal).[1,2] HyperCoal is expected to be fired directly in a gas turbine to achieve higher net power output and minimize CO_2 emission. The required extraction yield is higher than 60%, and ash content in the HyperCoal is less than 200 ppm, in addition to less than 0.5 ppm sodium and potassium. In our previous work,[1-3] the extraction yields of higher than 60% were obtained for several bituminous coals using a flow-type extractor at 360°C, with nonpolar solvents of 1-methylnaphthalene (1-MN) and Light Cycle Oil (LCO). While, in the case of polar solvents *N*-methyl-2-pyrrolidinone (NMP) and Crude Methylnaphthalene Oil (CMNO) the extraction yields of higher than 80% were attained.The high extraction yields were considered to be mainly due to the heat-induced relaxation of coal aggregates in the case of 1-MN, while in NMP, not only due to the heat-induced relaxation but also solvent-induced one.[3] However, what kinds of coal aggregations were released during the thermal extraction was not clear yet. In addition, these solvents give relatively low extraction yields for some low-rank coals. In the present work, different ranks of coals were acid-treated in organic acids. Effects of acid treatment on the thermal extraction yields and the changes of coal structure were investigated. Furthermore, mechanisms for thermal extraction and acid treatment are discussed.

Experimental

Table 1. Ultimate Analysis and Ash Content of the Coals Used

coal sample	ultimate analysis (wt%, daf) C	H	N	S	O[a]	ash (wt%, db)
Pocahontas No.3(POC)	89.7	4.5	1.1	0.7	4.0	4.8
POC acid-treated [b]	90.0	4.3	1.2	0.6	3.9	3.3
Upper Freeport(UF)	86.2	5.1	1.9	2.2	4.6	13.1
UF acid-treated [b]	86.7	5.0	1.7	2.3	4.3	12.2
Illinois No.6(IL)	76.9	5.5	1.9	5.6	10.1	15.1
IL acid-treated [b]	76.5	5.3	2.0	5.8	10.4	12.0
Wyodak(WY)	75.0	5.4	1.1	0.5	18.0	8.8
WY acid-treated [b]	74.5	5.6	1.2	0.6	18.1	3.9
Ardaro (AR)	73.0	5.1	1.1	0.0	20.8	1.8
AR acid-treated [b]	72.9	5.2	1.1	0.0	20.8	0.7
Pasir(PA)	73.5	5.3	1.9	0.2	19.1	4.9
PA acid-treated [b]	74.4	5.3	1.7	0.2	18.4	3.5
Beulah-Zap(BZ)	71.6	4.8	1.0	0.9	21.7	9.6
BZ acid-treated [b]	72.0	5.0	1.1	0.8	21.1	3.0
Banko 97(BA)	70.0	5.3	1.3	0.3	23.1	2.4
BA acid-treated [b]	70.4	5.4	1.2	0.4	22.6	0.8

[a] By difference [b] 1.0 M methoxyethoxy acetic acid

Coal samples. Six Argonne Premium coals; Pocahontas No.3, Upper Freeport, Pittsburgh No.8, Illinois No.6, Wyodak, Beulah-Zap(<150 μm), and three Indonesia coals; Adaro, Pasir (<150 μm), Banko 97 coal(<74 μm) were used. All coal samples were dried in vacuo at 80 °C for 12h. The ultimate analysis and ash content are shown in Table 1.

Acid treatment. Acid treatment of coal was carried out using aqueous methoxyethoxy acetic acid (MEAA) or acetic acid, which were reported to be effective agents to liberate cation-bridging cross-links through oxygen functional groups in low-rank coals.[4,5] Approximately 4.0g dried coal sample was treated in 150 mL aqueous acid with 10% ethanol under nitrogen atmosphere at room temperature for 24 h. Then, the acid-treated coal was washed with deionized water until the pH of deionized water became near 6.0. Finally, the acid-treated coal was dried in vacuo at 80 °C for 12 h. The ultimate analysis and ash content for acid-treated coals are also listed in Table 1.

Thermal extraction. 1-MN and NMP were used as the thermal extraction solvent without further purification. Thermal extractions of coals were carried out using a flow-type extractor as described before.[1] The coal sample (0.2-0.5 g) was charged into a stainless cell (ca. 4cm^3) that was fitted with stainless filters (0.5μm) on both sides and then set in an oven. The thermal extraction was carried out by supplying fresh solvent (flow rate: 0.1mL/min) under N_2 atmosphere (1Mpa) at extraction temperatures (200, 300, 360 °C) for 60 min. After the extraction, the extract was precipitated by adding *n*-hexane to the extract solution when 1-MN was used as the extraction solvent, or the solvent was evaporated from the extract solution and then the extract obtained was washed with water when NMP was used as the extraction solvent. The extraction yield was calculated on dry ash-free basis from the weight of residue.[3]

FT-IR measurement. FT-IR spectrum was recorded by a diffuse reflectance method using a spectrometer (Nicolet MAGNA-IR) at resolution of 4 cm^{-1}.

Results and Discussion

Effect of the acid treatment on the extraction yield. Figure 1 shows that the extraction yield in 1-MN for the acid-treated (1.0 M MEAA) WY coal did not change significantly. While, the yield in NMP for the acid-treated coal greatly increased to 82.9% from 58.4% for the raw coal.The acid treatment also increased the extraction yield in NMP for a subbituminous AR coal, and a lignite BZ coals. In contrast, for a subbituminous PA, and a lignite BA coal, the acid treatment gave a small effect on the extraction yields. The acid treatment also gave little effect on the extraction yields for high-rank IL, UF and POC coals.

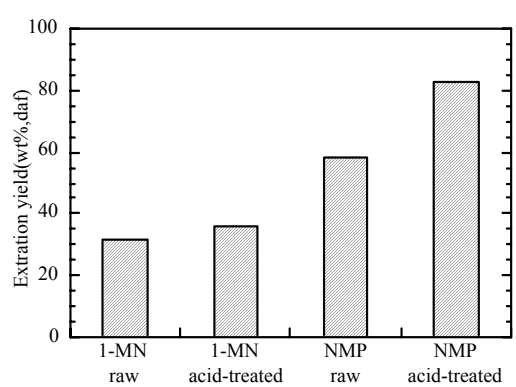

Figure 1. Extraction yields of acid-treated Wyodak coal extracted in 1-MN and NMP at 360°Cfor 1h.

Figure 2 shows the extraction yields for the acid-treated (1.0 M MEAA) and raw WY coals extracted in NMP at different temperatures. Similar as that of the raw coal, the extraction yields for acid-treated coal were increased with increasing the extraction temperature from 200 °C to 360°C, especially, a high extraction yield (81.3%) was obtained at 300 °C, similar to that at 360 °C.

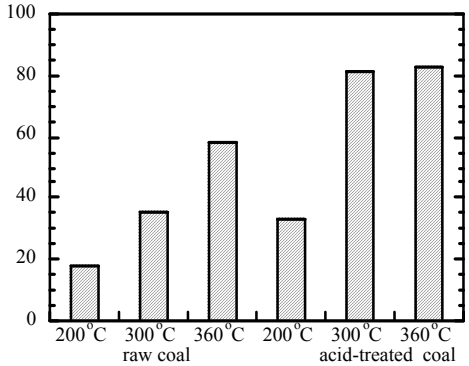

Figure 2. Extraction yields of the acid-treated Wyodak coal extracted in NMP at different temperatures, together with those of the raw coal.

Effect of acid treatment on coal structural changes. Figure 3 shows FT-IR spectra of WY coal acid-treated in 1.0 M MEAA (a), the raw coal (b), and the difference spectrum:(c), (a)-(b). Figure 3 (c) shows that the bands near 1,550 and 1,400 cm^{-1} decreased and the band near 1,720 cm^{-1} increased. The bands near 1,550 and 1,400 cm^{-1} are assigned to carboxylate groups, and that at 1,720 cm^{-1} is assigned to carboxylic acid group.[6] The carboxylate groups were converted to the carboxylic acid groups by the acid treatment,[6, 7] as a result, the cation-bridging cross-links formed through the carboxylate groups in the raw coal might be released, and hydrogen bonds form among the carboxylic acid groups.[4] While, as shown in Figure 4, after the acid treatment for BA coal, there were no clear changes near 1,555 and 1,400 cm^{-1}, and near 1,720 cm^{-1}. Although the acid treatment for BA coal decreased the ash content from 2.4% to 0.8%, as shown in Table 1, there was a small effect on the extraction yield, as described above. BA coal has a high concentration of carboxyl groups,[8] however, as shown in Figure 4, no peak corresponding to carboxylate groups was observed in the raw coal, therefore, most of these functional groups may be in carboxylic acid form.

The removal of cation-bridging cross-links in WY coal maybe allow more NMP to diffuse the inside of coal, and newly formed hydrogen bonds might be more easily broken by NMP, resulting in the higher extraction yield for the acid-treated WY coal. The high yield for BA raw coal with NMP can be also due to releasing weaker noncovalent bonds, such as hydrogen bonds in the coal.

Therefore, releasing some noncovalent bonds, such as hydrogen bonds for low-rank coals can be one reason of heat/solvent-induced relaxation of coal aggregates in NMP.[3] While, for high-rank coals, the structure can be different from that for low-rank coals.The mechanism on the heat/solvent-induced relaxation of coal aggregates during the thermal extraction needs further investigations.

Conclusions

The acid-treatment greatly increased the thermal extraction yields for some low-rank coals, due to conversion of carboxylate groups to carboxylic acid groups. Releasing some noncovalent bonds, such as hydrogen bonds, can be one reason for the relaxation of coal aggregates during the thermal extraction with NMP.

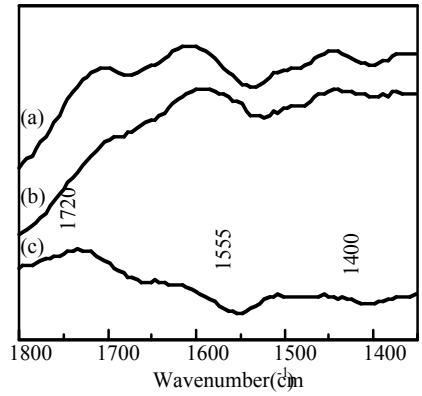

Figure 3. FT-IR spectra of acid-treated Wyodak (a), the raw coal (b), and the difference spectrum :(c), (a)-(b).

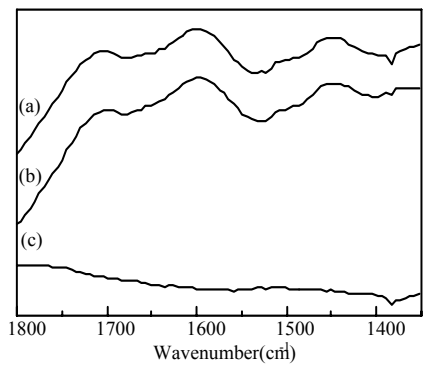

Figure 4. FT-IR spectra of acid-treated Banko 97 (a), the raw coal (b), and the difference spectrum: (c), (a)-(b).

Acknowledgement. This work was financially supported by the New Energy and Industrial Technology Development Organization (NEDO).

References

(1) Yoshida,T.; Takanohashi, T.; Sakanishi, K.; Saito, I.; Fujita, M. and Mashimo, K. *Energy Fuels*, **2002**, 16, 1006.
(2) Yoshida,T.; Li, C.; Takanohashi, T.; Matsumura, A.; Sato, S. and Saito, I. *APCChE/CHEMECA 2002,* submitted.
(3) Li, C.; Yoshida,T.; Takanohashi, T.; Saito, I; Iino, M. *Proceeding of the Japan Institute of Energy Conference,* **2002**, 42.
(4) Shimohara, T.; Mochida, I. *J Fuel Soc Jpn* **1987**, 66, 134.
(5) Sakanishi, K.; Watanabe, I.; Nonaka, T.; Kishino, M. and Mochida, I. *Fuel* **2001**, 80, 273.
(6) Opaprakasit, P.; Scaroni, A. W. and Painter, P. C. *Energy Fuels* **2002**, 16, 543.
(7) Aida, T., Yoshinaga, T., Yamanishi, I.; Tsutsumi, Y., *Proc. Int. Conf. Coal Sci.* 1997, vol. 1, 179.
(8) Murata, S.; Hosokawa, M.; Kidena, K.; Nomura, M. *Fuel Processing Technology*, **2000**, 67, 231.

ELUTION BEHAVIORS OF METAL COMPONENTS FROM COAL DURING PRETREATMENT AND SOLVENT EXTRACTION

Kinya Sakanishi[1)], *Eiko Akashi*[2)], *Hiroyuki Kawashima*[1)], *Ikuo Saito*[1)], *and Takayuki Takarada*[2)]

1) National Institute of Advanced Industrial Science and Technology (AIST), Tsukuba, Ibaraki 305-8569, Japan
2) Gunma University, Kiryu, Gunma 376-8515, Japan

Introduction

Pretreatments for removal of mineral matters and modification of coal have been reported. Recently, UCC (Ultra Clean Coal) project in Australia and HyperCoal(HPC) project in Japan have been demonstrated for the development of efficient demineralization process of coal by alkali solution and organic solvent extraction, respectively. In the former process, the product obtained still contains 0.3-0.7 % of ash, which can damage gas turbine, while the latter process can produce the extract(HPC) at high yields of ca. 60 % with much less ash content as low as 200 ppm under relatively mild conditions without any hydrogen consumption.[1] HPC is expected for the direct introduction to gas turbine power generation system for the higher efficiency and reduction of CO_2 emission.

Coal pretreatment with methanol has been reported for the improvement of selective grindability of organic substance and mineral matters in coal.[2] Coal pretreatments with dilute acid solutions have been also reported for the enhancement of coal depolymerization, liquefaction, and pyrolysis reactions.[3]

In the present study, the effects of pretreatments with methanol and dilute acid solutions on the production of HPC are investigated. Elution behaviors of metals and mineral matters during such pretreatments are also examined based on the characterization of the original coal and its derived HPC.

Experimental

Samples. A Chinese Enshu(EN) coal and an Australian Stratford(STF) coal, and their solvent-extracted coals(Hyper coal: HPC) were used in this study. Their ultimate and proximate analyses are summarized in Table 1.

Coal Pretreatments. Sequential treatment of coal with H_2O, 1 M CH_3COOH and 1N HCl/10%ethanol solution at room temperature was performed as follows;

i) H_2O washing : about 4 g of coal was washed with 150 ml H_2O at room temperature for 24 h under N_2 flow, and filtered and dried in vacuo for 5 h at 60 ^oC.
ii) Acetic acid washing: Residue from H_2O washing was mixed with 150 ml acetic acid solution at room temperature for 24 h under N_2 flow, and filtered and dried in vacuo for 5 h at 60^oC.
iii) HCl washing : Residue from acetic acid washing was mixed with 150 ml HCl at room temperature for 24 h under N_2 flow, and filtered and dried in vacuo for 5 h at 60 ^oC.

Analytical procedure . The filtrates after the pretreatment of coal were analyzed by ICP-AES(Shimadzu, ICPS7000) and cation chromatography(Nihon Dionex, IonPac CS15) for the measurement of eluted metals by the pretreatments. The residues obtained by pre-treatments were also analyzed by X-ray fluorescence(XRF) and ICP-AES after the microwave irradiation acidic digestion treatment by a Maultiwave3000(Perkin-Elmer).

Solid-state ^{29}Si- and ^{23}Na-NMR spectra of the coals before and after acid treatments and solvent extraction were measured by a Chemagnetics CMX-300 spectrometer with SPE-MAS method(Single-pulse excitation-magic angle spining; pulse delay: 20 sec for ^{29}Si, 2 sec for ^{23}Na, MAS: 3-4 kHz for ^{29}Si, 15 kHz for ^{23}Na).

Results and Discussion

Properties of Coals and Their HPC

Enshu(EN) and Stratford(STF) coals contain 12.6 and 10.3 wt% of ash on dry basis, respectively. Although their coal rank and elemental composition were similar, the higher H and S contents and the lower ash in EN coal are noted. The extraction yields with 1-methylnathphalene(1-MN) at 360 ^oC was above 60 % for both of the coals, the ash contents being as low as 200 ppm of the aimed levels as shown in Table 1.

Elution of Metals by Pretreatments.

Table 2 summarizes the eluted metals by the sequential treatment of the coals with H_2O, 1 M CH_3COOH and 1N HCl/10%ethanol solution. It is noted that some portions of Ca and Mg from the coals were eluted into water. Na and K were also detected in the water by cation chromatography. Elements associated with the organic part as ion-exchangeable cations present were easily removed from coal by CH_3COOH washing. Carbonates and oxides minerals were also removed by HCl washing according to the reference.[1] The minerals remaining in the coal after acid washing are indicated to principally consist of aluminosilicate and quartz identified by solid-state ^{29}Si-NMR and XRF measurements.

Table 1 Proximate and elemental analyses of coals and their HPC

Samples	Proximate analysis (wt %, dry)		Elemental analysis (wt %, daf)				
	Ash	VM	C	H	N	S	O [a]
Enshu(EN) coal	12.6	39.3	78.9	5.4	1.3	4.2	10.2
EN-HPC	0.02	51.8	83.4	5.6	1.4	1.8	7.7
Stratford(STF) coal	10.3	28.8	87.0	5.5	2.3	0.7	4.5
STF-HPC	0.02	38.8	87.7	5.3	2.1	0.7	4.2

[a] by difference

Table 2
ICP analyses of metals removed from EN coal by sequential treatment with H2O, CH3COOH, and HCl aqueous solution

Coal-Treatment	Removed metals (wt% based on coal)				
	Ca	Fe	Mg	Si	Al
EN-H2O	0.080	0.001	0.009	0.000	0.000
EN-CH3COOH	0.152	0.034	0.035	0.000	0.018
EN-HCl	0.390	0.412	0.027	0.075	0.069
(Total sum:	0.622	0.447	0.071	0.075	0.087)
STF-H2O	0.009	0.000	0.006	0.000	0.000
STF-CH3COOH	0.062	0.003	0.023	0.000	0.015
STF-HCl	0.195	0.020	0.054	0.098	0.077
(Total sum:	0.266	0.023	0.083	0.098	0.0 92)

According to analyses of the pretreated filtrate with MeOH under the ultrasonic irradiation for 1 h by the cation chromatography, small

amounts of Na, Ca, Mg, and K were eluted during the pretreatment with MeOH or MeOH/H_2O solution. A small amount of Fe was also detected in the filtrate by ICP-AES. Although the accurate amounts of the metals eluted by the pretreatments were not determined due to their low concentration, such a simple impregnation pretreatment with MeOH/H_2O can be expected to remove some amounts of metals prior to solvent extraction as well as to modify the organic part in coal. In addition, since the pretreatment with MeOH has been reported to enhance the coal grindability and separation of organic substances from mineral matters,[2] a more practical coal preparation scheme can be designed by the combination of such pretreatment with coal grinding procedure. It was also reported that organically associated Ca and aluminosilicate species elute into HPC during solvent extraction at high temperature,[1] hence the pretreatment with dilute acidic solution is expected to remove such organically associated species beforehand, since dilute organic acids such as acetic acid have been recognized to reduce not only ion-exchangeable cations of alkali and alkali-earth metals,[3] but also organically associated aluminosilicate species.[1]

Na species in the coals and their HPC were detected by ^{23}Na-NMR to the levels of ppm, although the quantitative analysis of Na is very difficult because of the broadening of the peaks due to the quadrupole interactions of ^{23}Na.[4] A preliminary result with ^{23}Na-NMR revealed that ion-exchangeable Na species may relatively remain in the solvent extracted fraction(HPC).[5] Further detailed investigation is required for the more quantitative analyses.

By the combination with microwave acidic digestion with FI(flow injection)-ICP-AES, alkali metals in the coals before and after the pretreatments were quantified to a satisfactory level.[6]

Figure 1 shows the removal percent of metals by the pretreatments with MeOH, MeOH/H_2O(1:1), and 10% CH3COOH aq. About 20% of alkali metals with 30-40 % of alikali-earth metals were removed even by MeOH and MeOH/H2O. 10% CH3COOH solution removed more amounts of alkali and alkali-earth metals, especially 90% of Ca was removed from EN coal. It is also noted that some of aluminum compounds were removed by such mild treatments, indicating that such Al species may be bonded to or associated with organic parts in the coal through oxygen functional groups.

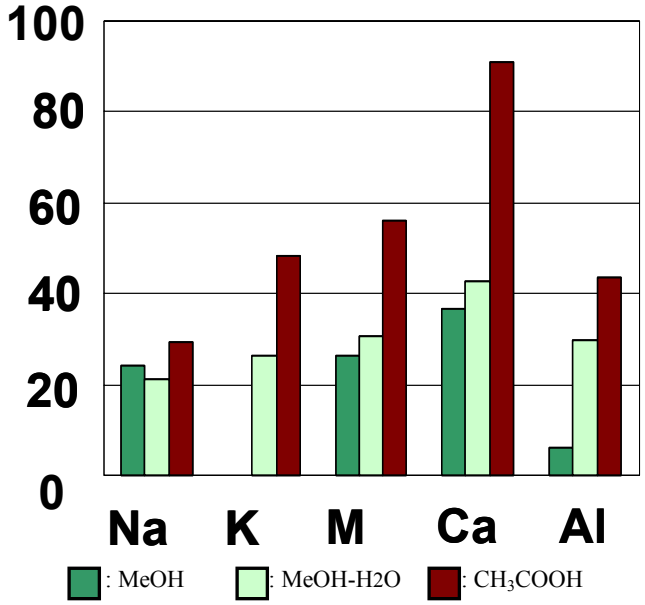

Figure 1 Removal percent of metals by pretreatments

Figure 2 illustrates the HPC yields from the pretreated coal(particle size: 32-60 mesh) under various conditions. The pretreatments with MeOH and MeOH/H2O for 48 h gave a little higher extraction yield of 53.4 and 53.7 %, respectively, while the yield was 51.3 % from non-treated coal. The acid treatment with 1% HCl or CH3COOH slightly increased the HPC yield to 52%.

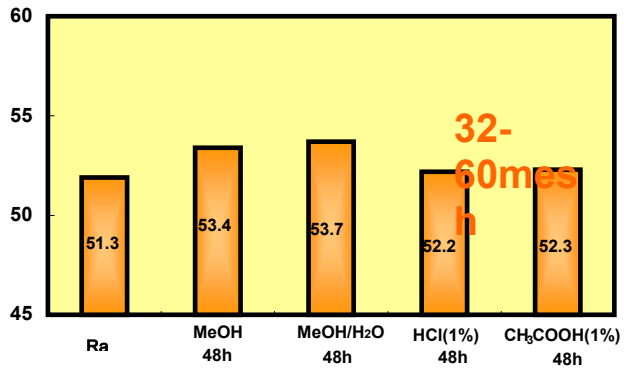

Figure 2 Effect of coal pretreatments on extraction yield(%)

Conclusions

Based on the present study, it is revealed that a mild pretreatment with MeOH, MeOH/H_2O, or dilute acetic acid solution can modify the organic parts of the coals to be more easily solvated with extraction solvent as well as remove some portions of alkali, alkali-earth, and other eluted metals prior to the solvent extraction procedure. A combination of such a mild pretreatment at room temperature with high temperature solvent extraction is expected to be one of the promising ways for the efficient production of HPC, because HPC is required to reduce its content of alkali and alkali-earth metals to the extremely low levels (Na+K < 0.5 ppm; Ca < 2 ppm) for the direct introduction to gas turbine power generation system. More extensive optimized procedures for the production of HPC should be designed in terms of its required strict quality and cost/performance.

Acknowledgment. The authors are grateful to Kobe Steel, Ltd. for providing the samples and useful discussion on the experiments. This work was supported by the New Energy and Industrial Technology Development Organization (NEDO) and Center for Coal Utilization Japan (CCUJ).

References

1. Sakanishi, K., Saito, I., Ishom, F., Watanabe, I., Mochida, I., Okuyama, N., Deguchi, T., Shimazaki, K., *Fuel*, **2002**, 81, 1471.
2. Takarada, T., Ohkawa, M., Wang, J., Goto, K., *Proc. 7th China-Japan Symp. Coal & C1 Chem.*, **2001**, p.359.
3. Sakanishi, K., Watanabe, I., Nonaka, T., Kishino, M., Mochida, I., *Fuel*, **2001**, 80, 273.
4. Soma, M., Tanaka, A., Seyama, S., Hayashi, K., Hayamizu, K., Clay Science, **1990**, 8, 1.
5. Sakanishi, K., Kawashima, H., Akashi, E.,Saito, I., Takarada, T., Proc. Japan Coal Science Meeting, **2002**, No.57, p.131.
6. Akashi, E.,Sakanishi, K., Nakazato, T., Tao, H., Saito, I., Takarada, T., Proc. Japan Coal Science Meeting, **2002**, No.37, p.91.

CLEAN COAL CONVERSION OPTIONS USING FISCHER-TROPSCH TECHNOLOGY

André P Steynberg and Herman G Nel

Research & Development Division
Sasol Technology
1 Klasie Havenga
Sasolburg
1947
South Africa

Introduction

Any meaningful utilization of the vast coal resources in places like China, India, Australia, South Africa and the USA will involve conversion into some other form of energy. Coal, as a solid, has a high energy density and is therefore reasonably convenient as a heating fuel. The problem is that the associated pollutants negate any advantages compared to other cleaner burning fuels. Coal is rather converted into other cleaner forms of energy such as liquid hydrocarbons, synthetic natural gas (SNG) and electric power. Initially these conversion plants simply concentrated the pollutants in one large scale conversion site while enabling the end user of energy to experience a cleaner fuel. With time, more and more success has been achieved in cleaning up the emissions from large scale coal conversion facilities.

One fact that cannot be avoided is that every ton of carbon in mined coal will sooner or later end up as 3.67 tons of carbon dioxide in the atmosphere. Although some attention has been paid to the possibility of carbon dioxide sequestration this is not currently, and may never be a viable option. Certainly the cost of sequestration seems likely to favour the use of other fossil fuel alternatives such as crude oil and natural gas while these are still readily available.

The increased production of carbon dioxide per unit of useful energy for coal relative to other fuels is inevitable. Assuming this is acceptable, it becomes important to ensure that, when coal is used, it is used as efficiently as possible.

Combined production of hydrocarbon liquid and electrical power

The coal fired power stations in South Africa and elsewhere produce some of the world's lowest cost electrical power but this large scale coal combustion has an environmental penalty. An alternative approach is to gasify the coal in order to produce a low heating value synthesis gas which may be cleaned prior to combustion in a combined cycle power plant using both steam and gas turbines. There are alternative uses for this synthesis gas that may offer opportunities that are both economically more attractive and result in more efficient use of the coal. Where a region's economy is dependant on coal utilization, there is a strong case to be made to switch to more efficient and less polluting coal conversion technologies as these become available.

Synthesis gas can also be made from natural gas and the following comparison has been published previously by Shell[1]:

	Syngas Manufacture	Fischer-Tropsch	Thermal* Efficiency	Relative Capital Cost
Coal:				
	$2(-CH-)+O_2 \rightarrow 2CO + H_2 \rightarrow (-CH_2-) + CO_2$		60%	200
Natural Gas:				
	$CH_4 + \frac{1}{2}O_2 \rightarrow CO + 2H_2 \rightarrow (-CH2-) + H_2O$		80%	100

* Theoretical Maximum

This appears to paint a bleak picture for coal utilization but it ignores two factors. Firstly the high energy density of coal allows the feed to be delivered to the conversion plant at a lower cost. Secondly the lower energy efficiency ignores the opportunity to convert the byproduct heat into electrical power.

Another potential use for some of the byproduct heat is to generate steam for the use in the water gas shift reaction to modify the above coal conversion reaction as follows:

$$H_2O + 2CO + H_2 \rightarrow CO + 2H_2 + CO_2 \rightarrow (-CH_2-) + H_2O$$
$$\downarrow$$
$$\text{Removed}$$

This then becomes equivalent to the natural gas route for the synthesis gas conversion step but twice as much oxygen has been used to prepare the synthesis gas and the cost of generating steam and removing carbon dioxide provides a further cost penalty.

The above equations also ignore the reality that coal is gasified with both steam and oxygen together. This leads to a lower oxygen consumption for gasification than is indicated by the above equations. For the coal conversion options considerd, the oxygen consumption per unit of synthesis gas is actually not double that for the partial oxidation of natural gas.

The cost penalty is somewhat negated by the fact that steam generation is required anyway to remove the heat generated by the Fischer-Tropsch reaction and to cool the hot synthesis gas exiting the gasifier. Synthesis gas cleanup to remove acid gases is also required anyway for use is gas turbines.

The concept of producing Fischer-Tropsch liquid hydrocarbons and electrical power from coal derived synthesis gas has been around for quite a long time. A 1978 patent from Chevron pointed out the advantages of using this concept to cope effectively with power demand variations[2]. The US Department of Energy (DOE) supported by contracted studies by MITRE Corporation[3,4] and companies such as Texaco[5], Air Products[6,7] and Rentech[8,9] showed that LTFT reactor technology can be used together with coal or petroleum coke gasifiers for the co-production of hydrocarbon liquids and electrical power. Fluor Daniel[10] have proposed the use of HTFT for this purpose.

It is possible that the combined production of hydrocarbon liquids and electricity can compete with natural gas conversion to only the hydrocarbon liquids. This option has been studied for two

Fischer-Tropsch conversion options i.e. Low Temperature Fischer-Tropsch (LTFT) and High Temperature Fischer-Tropsch (HTFT) both using Iron based catalysts.

Cases Studied

For both cases the use of a Texaco Gasifier was assumed to make a synthesis gas with the following composition (mol%):

H2	37.36
CO	29.26
CO2	13.30
CH4	0.16
H2O	19.43
Inert	0.49

For the LTFT case this gas is fed to a two stage reactor system to form liquid hydrocarbon products. The tailgas is sent to a gas turbine to produce power. Other sources of power are the steam generated in the process of cooling the synthesis gas from the gasifier and in removing the heat generated in the Fischer-Tropsch reactors.

For the HTFT case, a similar quantity of hydrocarbon product can be produced with a single stage reactor. For this case the synthesis gas is subjected to a sour gas shift prior to acid gas removal in order to increase the hydrogen to carbon monoxide ratio in the synthesis gas. This was also found to significantly increase the utility requirements for the acid gas removal step.

The mass and energy balances for the two cases are shown below. These are not necessarily fully optimized but are considered realistic to provide a fair basis for comparison.

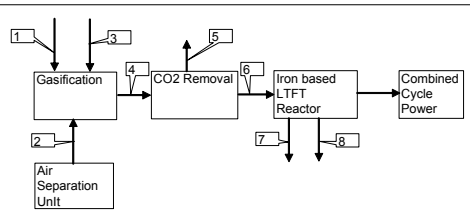

Solid Stream Summary

Stream Number	Stream Name	Flowrate kg/h	LHV kJ/kg	LHV MW
1	Coal	928063	30506	7864
2	Oxygen	951597	0	0
3	Water	654404	0	0

Gas Stream Summary

Stream Number	Stream Name	Flowrate k nm3/h	LHV kj/nm3	LHV MW
4	Raw Gas	2243	9843	6133
5	CO2	364	0	0
6	Syngas	1879	11781	6148
7	Tailgas	695	7831	1513

Liquid Stream Summary

Stream Number	Stream Name	Flowrate bbl/day	LHV MJ/bbl	LHV MW	ton/day	MJ/kg
8	Condensate	18248	4635	979	2090	40.5
9	Wax	35844	5809	2410	4740	43.9
	Total	**54092**		**3389**		

Thermal Efficiency

Stream	LHV MW	%
Coal	7864	100.0
Condensate	979	12.4
Wax	2410	30.6
Power	566	7.2
Overall	**3955**	**50.3**

Figure 1. LTFT Based.

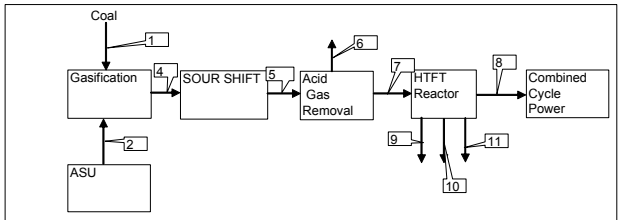

Solid Stream Summary

Stream Number	Stream Name	Flowrate kg/h	LHV kJ/kg	LHV MW
1	Coal	928063	30506	7864
2	Oxygen	951597	0	0
3	Water	654404	0	0

Gas Stream Summary

Stream Number	Stream Name	Flowrate k nm3/h	LHV kj/nm3	LHV MW
4	Raw Gas	2243	9843	6133
5	Shift Gas	2680	7923	5898
6	CO2	799	0	0
7	Syngas	1881	11341	5925
8	Tailgas	360	14553	1453

Liquid Stream Summary

Stream Number	Stream Name	bbl/day	LHV MJ/bbl	LHV MW	ton/day	MJ/kg
9	Decant Oil	1799	6099	127	249	44.1
10	Stabilised Light Oil	34070	4859	1916	3899	42.5
11	Condensate	25002	4112	1190	2334	44.1
		60871		**3233**		

Thermal Efficiency

Stream	LHV MW	%
Coal to Gasifier	7864	100.0
Liquid Products	3233	41.1
Power Export	393	5.0
Overall	**3626**	**46.1**

Figure 2. HTFT Based

Discussion of the results

Natural gas conversion processes can be expexted to have thermal efficiencies in the range of 60 to 66%. For the current state of the technology, cost effective facilities will have thermal efficiencies closer to 60%. Coal conversion is clearly less efficient. It seems 50% efficieny is achievable. The cost of feedstock per unit of energy must therefore be less in order to compensate for this efficiency defecit. However, this is not unrealistic. Existing coal conversion plants operating with thermal efficiencies closer to 40% are cash positive.

Compared to natural gas conversion, the capital cost based on similar quantities of energy product are higher for a number of reasons. Firstly there is the need for acid gas removal from the synthesis gas. This step is not required for a sweet natural gas feed. The capital cost of synthesis gas generation is also significantly higher mainly due to the higher oxygen requirement (by a factor of nearly 1.7). The Fischer-Tropsch conversion step is marginally more expensive for the HTFT technology and nearly double the cost for the LTFT route when compared to natural gas conversion. This is the result of the coal derived synthesis gas being unsuitable for use with modern supported cobalt Fischer-Tropsch catalysts. Another factor that negatively impacts the coal conversion plant is that it is more utility intensive than a natural gas conversion plant. This is an inevitable consequence of the lower thermal efficiency.

Considering the comparison between the HTFT and LTFT options, it is clear that the LTFT route is more efficient. The main reason for the lower efficiency of the HTFT option is that the acid gas removal step becomes more utility intensive. As mentioned previously though, the capital cost for the Fischer-Tropsch section is higher. Only a detailed study beyond the scope of this paper will be able to determine whether the higher efficiency of the LTFT route

can compensate for the higher capital cost. The preferred solution may be different for different potential application sites and may be influenced by whether gasoline or diesel is the desired primary product.

The economic success of the coal conversion plant will inevitably depend on the price received for the products. It seems unlikely that the price for liquid hydrocarbons will be sufficient to provide a suitable return on the capital invested while the energy resources of crude oil and natural gas are still readily available. However, if some assistance is provided for the initial capital costs, coal conversion to liquid hydrocarbons together with electrical power is an efficient option relative to other coal conversion options. It may be important to reduce dependence on imported energy for countries with abundant coal resources. The coal conversion efficiencies are higher when liquid hydrocarbons are produced than for facilities producing only electricity.

Production of liquid hydrocarbons from coal as described above has two further advantages. Firstly the market is huge and the facilities can take advantage of economics of scale for very large facilities producing hydrocarbon fuels steam together with electricity. However, the huge capital investment involved is another reason why state assistance will probably be necessary to fund such a coal conversion facility. The other benefit is that the final liquid hydrocarbon fuels will be ultra clean and will not contain sulfur or nitrogen. This will lead to local environmental benefits where these fuels are used.

Conclusions

Certainly coal conversion to hydrocarbon liquids and electricity is economically attractive from an income/ cash cost viewpoint. However large capital investments are require to reap the benefits from economics of scale and the return on capital invested is not particularly attractive. It is therefore expected that these coal conversion plants will only become a reality if there is some form of state assistance with the initial capital investment, such as low interest loans. This would be motivated by the independence from imported energy and the more efficient and cleaner utilization of the local energy resource. The Chinese government has accepted this approach and China is likely to be the pioneer for this technology option. Places that have abundant coal are likely to use this resource. It is the duty of technology providers to ensure that technology is made available to allow the coal to be used as efficiently as possible.

References

(1) Van den Burgt, M., Van Klinken, J. and Sie, S.T. 'The Shell Middle Distillate Synthesis Process', paper presented at the 5th Synfuels Worldwide Symposium, Washington, D.C., USA, November 11-13,1985.

(2) Egan, C.J., U.S. Pat., No. 4,092,8265, **1978**

(3) Gray, D., and Thomlinson, G.C., Contractor Report DE91-004668, **1990**.

(4) Gray, D. and Thomlinson, G.C.; In *Natural Gas Conversion IV, Studies in Surface Science and Catalysis Vol 107*; de Pontes, M., Espinoza, R.L., Nicolaides, C.P., Sholtz, J.H. and Scurrell, Ed.; Elsevier: Amstedam, 1997; pp. 145-150.

(5) Schrader, C and Shah L, "Gasification Technologies 1: Applications, Texaco Gasification and Fischer-Tropsch Process", (September 2000)

(6) Sorrensen et al, U.S. Pat., No. 5,865,023, **1999**.

(7) Sorrensen et al, U.S. Pat., No. 5,666,800, **1997**.

(8) Botha, MS and Benham, CB, "Coal-to-Liquids via Fischer-Tropsch Synthesis", 244 International Technical Conference on Coal Utilisation and Fuel Systems, (March 1999)

(9) Bohn et al, U.S. Pat., 6,306,917, **2001**.

(10) Stupin, W.; Ruvikumar, R.; and Hook, B.; "Liquid products from Petroleum Coke via Gasification and Fischer-Tropsch Synthesis", NPRA 2000 Annual Meeting, San Antonio, Texas, AM-0010 (March 2000).

Conversion of Coal to Hydrogen by Integrating the Exothermic and Endothermic, Gas Production and Separation Reactions in Gasifier

Shiying LIN, Michiaki HARADA, Yoshizo SUZUKI* and Hiroyuki HATANO*

Center for Coal Utilization, Japan
24, Daikyocho, Shinjuku-ku, Tokyo 160-0014

*National Institute of Advanced Industrial Science and Technology
E-mail: sy-lin@aist.go.jp

Abstract:

Addition CaO in gasifier can absorb CO_2 and release heat during coal gasification. This method was used for producing high concentration hydrogen from one reactor (HyPr-RING method). Previous experimental studies[1-5] have confirmed that high concentration H_2 (above 80%) with a few CH_4 can be made, and no carbon oxides are detected in the product gas phase. In this study, we will discuss the general problems with using calcium base sorbents in high temperature absorption, and our solutions in HyPr-RING method for H_2 production. A H_2 production process was designed in consideration of these solutions, and higher as 75% H_2 production efficiency was expected.

Introduction:

It is necessary to solve the problem between the utilization of fossil fuel and the protection of environment. One of solution is to transform the fossil fuel energy to hydrogen, which is a most clean energy, generates only water without any pollutants.

In previous study [1-5], we proposed to use a solid sorbent ($CaO/Ca(OH)_2$) to remove CO_2 at comparative high temperature which the coal gasification can occur with suitable rate. Namely, absorbing CO_2 in gasifier and releasing the heat of CO_2 absorption to the endothermic coal gasification simultaneously (**Fig.1**). For keeping CaO reactivity, it is better to like CaO first reacts with H_2O in the gasifier to form $Ca(OH)_2$, and then $Ca(OH)_2$ absorbs CO_2 to form $CaCO_3$. The flowing four reactions should be integrated in gasifier.

$$CaO + H_2O \rightarrow Ca(OH)_2 \quad (1)$$

$$C + H_2O \rightarrow CO + H_2 \quad (2)$$

$$CO + H_2O \rightarrow CO_2 + H_2 \quad (3)$$

$$Ca(OH)_2 + CO_2 \rightarrow CaCO_3 + H_2O \quad (4)$$

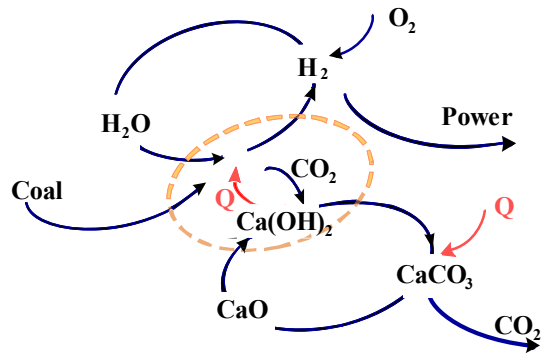

Fig. 1 Concept of HyPr-RING process

In this study, we will discuss in detail in the problems and their solutions in the CaO using process.

Discussion:

Fig. 2 shows problems and solutions in HyPr-RING method. CaO losing reactivity during sorbent recycle is an original problem for using Ca base sorbents. We considered recovering CaO reactivity by calcium hydration in gasifier. Theoretical and experimental results have confirmed that, at high temperature as 873-973 K, CaO can react with steam under higher pressure as 0.3-1.3 Mpa.

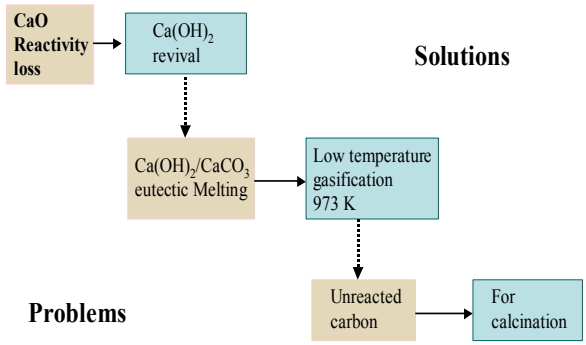

Fig.2 Problems for using CaO and their solution.

The next problem is $Ca(OH)_2/CaCO_3$ eutectic melting. Lower operation temperature must be chosen for the gasifier, such as our confirmations in experiment [5]. We are considering using the unreacted carbon after gasification to be an energy source for $CaCO_3$ calcination (sorbent regeneration).

Fig.3 shows mass flow comparison of HyPr-RING with a conventional H_2 production.

Fig. 4 show an analysis of HyPr-RING process in consideration of above solutions. Since most of calcination energy become chemical energy of CaO, and can be released in the gasifier, higher as 75 % hydrogen production efficiency was expected.

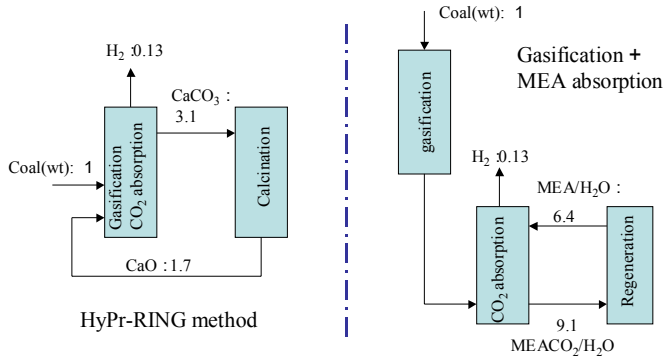

Fig. 3 Mass flow comparison of HyPr-RING with conventional processes.

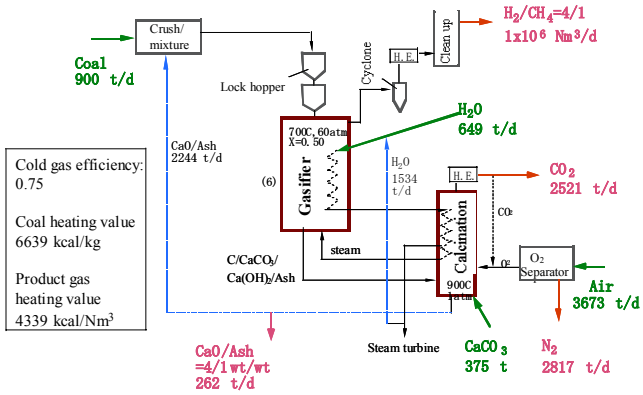

Fig. 4 An anlysis of HyPr-RING process

Reference:

(1) Lin et al., Kagaku Kogaku Ronbunshu 25(3), 498-500 (1999)
(2) Lin et al., Energy & Fuel, 15(2), 339-343 (2001)
(3) Lin et al., Journal of the South African Institute of Mining and Metallurgy, 101, 53-60 (2001)
(4) Lin et al., J. of Energy Conversion & Management, 43, 1283-1290 (2002)
(5) Lin et al., Fuel, 81, 2079-2085 , 2002

ACTIVATION OF THERMAL PLASMA FOR COAL CONVERSION

Tian Yajun[1] *Wang Baojun*[1] *Zhang Yueling*[2] *Zhang Yügui*[3] *Xie Kechang*[1]

1. State Key Lab of C1 Chemistry and Technology, Taiyuan University of Technology, Taiyuan, 030024, P. R. China
2. Department of Applied Chemistry, Nanjing University of Chemical Technology, Nanjing, 210009, P.R. China
3. Jiaozuo Institute of Technology, Jiaozuo 454100,P.R.China

Introduction

Investigations[1-3] of coal conversion by arc plasma has been carried out for long time. Baumann et al.[4] proposed that the release of volatile from coal was the first and an essential step as coal was injected into plasma jet. The generation of acetylene was contributed by the interaction of active species with the releasing volatile matter, after which the reactions stopped. Many publications reported that the active species such as energized ions and atoms had the capacity to convert coal directly even in low temperature [5, 6]. A plasma jet is a hot gas flow containing great deal of active species, so coal conversion in arc plasma jet is very complex. There still is not an agreement for the coal conversion under this condition.

Experimental

The experimental equipment is consisted of arc plasmatron, injector, reactor and quenching unit. The mixture of argon and hydrogen was the working gas of arc generator, their flow rate were 2.2 $m^3 \cdot h^{-1}$ and 5.2 $m^3 \cdot h^{-1}$. The effective power of plasmatron was 25.2 kW. The feedstock was injected into reactor through a tube with diameter of 5mm, the diameter of reactor tube is 20mm,and length is 350mm. Coal powder was carried into jet by argon with the flow rate of 1.7 $m^3 \cdot h^{-1}$, and the coal feed rate ranged from 0.5~4.0$g \cdot s^{-1}$ was controlled by the motor of feeder. The quenching unit was installed downstream position of reactor. A sampling position was sited between quenching unit and separator where the gas phase and the mixture of water and slag were separated. The gaseous products were vented from the outlet sited on the upper part of separator, and the condensed phase was discharged form the outlet sited at the bottom of separator to the filter unit where the slag were trapped. The structure scheme of equipment is shown in **Figure 1**.

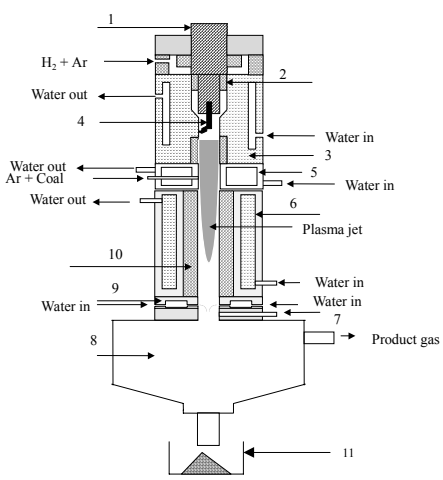

1-Cathode 2-Insulation 3-Anode 4-Arc 5-Injector 6-Reactor 7-Sampling tube 8-Separator 9-Spry 10-Reactor wall 11-Filter

Figure 1 Diagram of experimental equipment.

The compositions of the product gases were measured by a special gas chromatography with two channels and three detectors (two FIDs and one TCD). Argon was used as tracer to calculate the amount of component in the product gas, and then coal conversion was determined. The chemical analysis data of Baode coal is shown in **Table 1**.

Table 1 Chemical analysis data of Baode coal

Proximate (wt%)			Ultimate (wt%)				
M_{ad}	A_d	V_{ad}	C_{daf}	H_{daf}	N_{daf}	S_{daf}	O_{daf}
4.43	3.29	40.35	75.82	5.36	1.86	0.74	16.22

Results

Effect of coal feed rate (CFR) on coal conversion

In our experiment, the coal feed rate (CFR) was controlled form 0.5 to 4.0 g/s. The power input and other conditions kept constant. **Figure 2** shows coal conversions as a function of CFR. It's found that as the increase of coal feed rate, the coal conversion increases. According to the Chinese Test Standard, the volatile content is 40.35% on the basis of air dry. The experiment results showed that the maximum coal conversion reached up to 55.58% on the same basis. The fact indicates that the maximum coal conversion could beyond coal volatile content, which implies not only pyrolysis but also some other factors have the contribution to the coal conversion.

Coal pyrolysis is an easy producer as coal was heated. It's believed that pyrolysis was the first conversion step under the condition of plasma jet with initial temperature of about 3700K. For the producer of devolatilization (pyrolysis), temperature is one of the key factors. As the increase of CFR, more energy was exhausted by the more reactions taking place under this condition, and more energy was consumed by the heat capacity of coal too. The average reaction temperature increased with the decrease of CFR. High temperature is in favor of conversion, so coal conversion increased as the decrease of CFR.

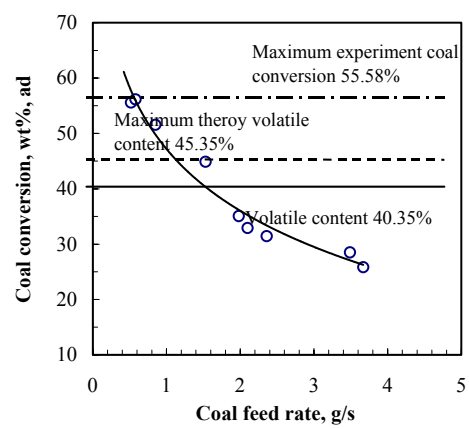

Figure 2 Coal conversion as a function of CFR

Effect of CFR on yield

Experimental results showed yields of CO and C_2H_2 decreased as the increase of CFR, as shown in **Figure 3**, while that of CH_4, C_2H_4+C_2H_6 increased somewhat. Volatile matter released from coal was the precursor of product gas such as C_2H_2 and CO. When CFR is decreased, coal specific energy (CSE) increased and coal conversion increased too, therefore, the yields of C_2H_2 and CO increased. As the increased of temperature the Gibbs free energy of C_2H_2 decreased and that of other hydrocarbons increased, that is C_2H_2 was more stable than other hydrocarbons. This is the reason that the yields of

other hydrocarbons such as CH_4 and $C2H_4$+C_2H_6 decreased as the decrease of CFR shows in **Figure 3**.

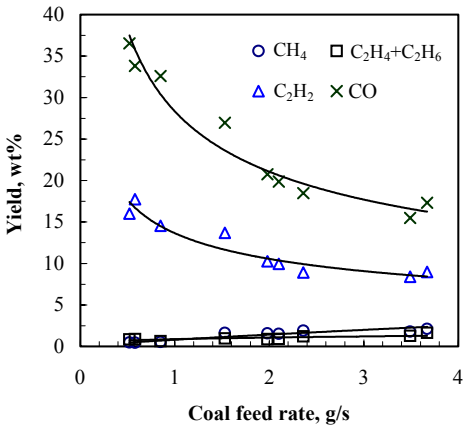

Figure 3 Effect of coal feed rate on the yield of the components in product gas

Effect of CFR on concentration

Although the yield of C_2H_2 decreased as the increase of CFR, it's found in **Figure 4** that its concentration increased as a function of CFR. Since great amount of hydrogen and argon were feed into as working gas of plasmatron, the maximum of C_2H_2 was only about 7% at larger CFR. As a desired product, high concentration means high output and hence the energy requirement for producing the acetylene decreased as the increase of CFR. Other components presented the similar regular as acetylene. Above all, raising CFR lead to the decrease of coal conversion, but increase of output of products.

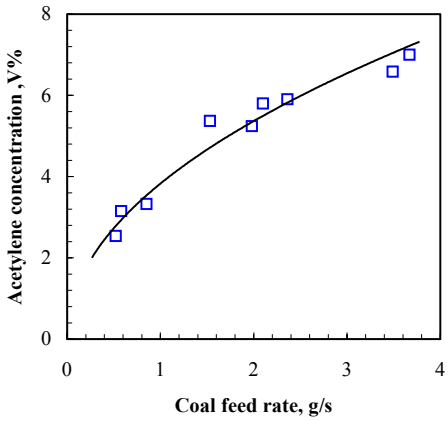

Figure 4 Acetylene concentration in product gas as a function of coal feed rate

Coal is the initial source of the product gas, a litter coal was fed a litter product was produced. So the concentration of product gas increased with CFR is reasonable, which has been discussed in literature[7], although the yields of some products decreased as CFR. Since the improvement of concentration of one component, the output of it increased too. If the C_2H_2 was taken as a desired product, increasing the CFR is helpful for improving its produce cost.

Discussion

As far as pyrolysis is concerned the rapid pyrolysis can enhance coal conversion in some degree[8]. Azhakesan[9] experiments indicated that rapid pyrolysis increased coal conversion about 5% of parent coal in their experiment. Calculating according to their conclusion on the basis of air dry, the maximal theoretical conversion of Baode coal is about 45.35% that is far smaller than the maximum experiment result of 55.58% shown in **Figure 2**. As mentioned above, great deal of active species that can convert coal directly was contained in plasma jet, it is inferred active species played an important role for the coal conversion under this condition.

In experimental section a method of determining coal conversion was introduced, that is regarding the summary of the yields of components in product as total conversion (x_P). In so hot thermal jet, coal particles were heated rapidly; its maximum conversion should be 45.35% if only the pyrolysis producer happened. Assuming only the volatile matter were converted, taking the maximum theory volatile content (45.35%) as the volatile content of parent coal, then the conversion (x_V) can be determined by the expression

$$x_{V,ad} = V_{1,ad} - V_{2,ad}(1 - V_{1,ad}/100)$$

Where, $V_{1,ad}$ is the maximum theoretical volatile content, and the $V_{2,ad}$ is the volatile content of the residual after reaction. **Table 2** is the conversion calculated according to the two methods. By comparing it's found they agree very well when the CFR is larger than 1.98 $g{\cdot}s^{-1}$. That means the CFR of 1.98 $g{\cdot}s^{-1}$ is a critical point. So it's inferred that when CFR was less than 2.0$g{\cdot}s^{-1}$ both the pyrolysis and active species has the contribution to coal conversion, on the contrary, the coal conversion was governed mainly by the pyrolysis. This conclusion is first presented in this paper.

Table 2 Coal conversion calculated according to various methods

	Coal feed rate, $g{\cdot}s^{-1}$					
	0.52	0.58	0.85	1.98	3.49	3.67
$x_{V,ad}$	38.77	38.56	38.24	34.64	26.63	25.86
$x_{P,ad}$	55.58	56.13	51.55	35.08	28.52	25.83

Simulation based on CPD model was carried out.[10] Three different coal feed rate of 0.58, 1.98 and 3.49 $g{\cdot}s^{-1}$, the comparison of calculation and experiment result is showed in **Figure 5**.

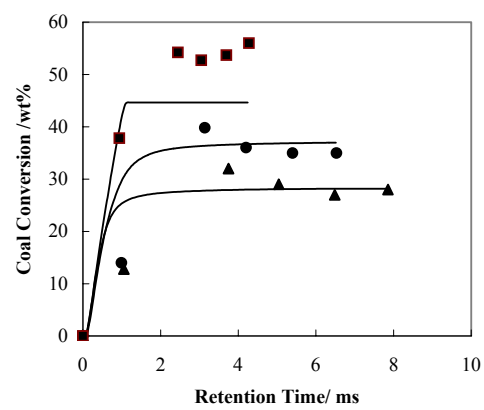

Figure 5 Coal conversion as a function of time at different coal feed rate. (■) 0.58 $g{\cdot}s^{-1}$ (●) 1.98 $g{\cdot}s^{-1}$ (▲) 3.49 $g{\cdot}s^{-1}$

For the case of 0.58$g{\cdot}s^{-1}$, after the conversion predicted reached the value of 45%, it kept a constant without change. That is the maximal prediction did not match the maximal experiment value of 55.58%, but agreed with the maximal theoretical conversion. It also found that the CPD calculation has better agreement with the experiments with feed rates of 1.98 and 3.49$g{\cdot}s^{-1}$, which was consistent with results shown in **Table 2**. In the CPD model, the

degree of conversion is mainly limited by the parameter of total bridge (p0) and char bridge (c0)[11]. The labile bridges (p0-c0) were the main factor for conversion. The difference of the calculation from experiment implied that not only the liable bridges but also the char bridges and the bonds in cluster could be broken in this condition and hence the experiment had larger conversion than the CPD prediction. It was known that the interaction of active species could improve the coal conversion, but the thermal pyrolysis also played an important role in the coal conversion. In the case of low feed rate, both of them have large influence on the coal conversion. As the feed rate increases, the average impact of active species become weaker for its short life, and the conversion is mainly controlled by the thermolysis. It could be noticed that there was still larger difference in the first sampling position, which may be caused by the diffusion of heat and mass.

Conclusions

When coal was injected into plasma jet, the primary volatile was the product as coal was converted. It's found coal conversion decreased as the increase of CFR. Then the volatile matter was converted into gas products. The yields of CO and C_2H_2 decreased as the increase of CFR, and that of CH_4, $C2H_4$+C_2H_6 increased somewhat. The concentration and output of components increased as the increase of CFR. Both coal conversion calculation and CPD simulation indicated that pyrolysis and the active species containing in plasma jet were the two main conversion routines. When CFR is less $2.0 g \cdot s^{-1}$ both the pyrolysis and active species has the contribution to coal conversion, on the contrary, the coal conversion is governed mainly by the pyrolysis.

Acknowledgement

This work was financially supported by National Natural Science Foundation of China (No. 19935010); Natural Science Foundation of Henan Province of China.

References

(1) Bond L R, Ladner W R and Mcconnel, G I T, Fuel, **1966**, 45, 381–395.
(2) Chakravartty S C, Dutta D and Lahiri A, Fuel, **1976**, 55, 43–46.
(3) Baumann H, Bittner D, Beiers H G, et al., Fuel, **1988**, 67, 1120–3.
(4) Beier H G, Baumann H, Bittner D, et al, Fuel, **1988**, 67, 1012–1016.
(5) Gill, P S, Toomy, R E, Moser, H C. Carbon, **1967**, 5: 43.
(6) Sanada, Y, Berkowitz, N. Fuel, **1969**, 48: 375–379.
(7) Xie K C, Tian Y J, et al., J. Chem. Ind. & Eng. **2001**, 52: 516–521.
(8) Desypris, J, Murdoch, P, Williams, A. **Fuel**, 1982, 61: 807–816.
(9) Azhakesan M., Bartle K. D. Murdoch P. L., etal., Fuel, **1991**, 70(3): 322.
(10) Tian Y J, Xie K C, Zhu S Y, Energy &Fuels, **2001**, 15(6): 1354 – 1358.
(11) Fletcher, T. H.; Kerstein, A. R. Energy & Fuels. **1992**, 6, 414–431.

A NEW PHYSICAL CONSTANT AND ITS APPLICATION TO CHEMICAL ENERGY PRODUCTION

By Andrew Anthony Angus, andrewangus@yahoo.com

1435 Olympic Drive, Milpitas, CA 95035

Keywords: Angus' constant, Angus photon, photochemical effect

Introduction

What is a physical constant? The author's own definition of physical constant is as follows: A **physical constant** is a numerical value that reveals a constant relationship between or among measurable characteristics of an object or event.

The Planck's constant is one important physical constant in physics. The pi is a numerical constant so essential in mathematics.

What is the significance of a physical constant?

Physical constants are constant numerical values that are important to physical sciences for many reasons:

a. Physical constants simplify the understanding of a puzzling phenomenon.

b. Physical constants integrate or relate different measurable characteristics of an object or phenomenon observed, which at first, may seem unrelated at all.

c. Physical constants can be used in solving simple or complex equations that describe a simple or complex physical phenomenon.

d. Physical constants can be used to discover new or more complex phenomenon which can never be discovered if the physical constant is not discovered in the first place.

In this paper, the author reveals a new physical constant which he simply calls the "Angus' constant". This new physical constant is equal to 1.98 x 10^-25 J-m. The author uses the Greek letter lambda in upper case (/\) to represent this new physical constant.

Finally, in this paper, the author reveals the application of this new physical constant to chemical energy production.

Review Of Related Literature

Max Planck discovered a constant numerical relationship between energy and frequency. This constant numerical relationship between energy and frequency is now called the Planck's constant (h).

h = 6.626 * 10^-34 J-s (eq. 1)

Furthermore, Max Planck proposed in 1900 that energy can be absorbed or emitted in packet form or in "quantum" form by matter to explain the emission spectrum of thermal radiation. (Krane p.65) For many years, the scientific community did not accept Planck's radical idea that light can be absorbed or emitted by matter in packet form called "quantum" of energy. Planck suggested that energy is in the form of "quantum" and represented by the equation 2 (Halliday and Resnick p.1097):

$$E = nhv \quad n = 1, 2, 3\ldots\ldots \qquad \text{(eq.2)}$$

Legend: E is energy, n is the quantum number, h is the Planck constant, v is the oscillation frequency.

Meanwhile, in 1905 Albert Einstein suggested that light energy behave as localized bundles later called "photon". (Krane p.67 and Hallliday and Resnick p. 1103) The photon's energy has the equation:

$$E = hv \qquad \text{(eq. 3)}$$

Planck's quantum of energy equation (eq.2) and Einstein's photon energy equation (eq. 3) are related.

For many years, Albert Einstein and Robert Millikan helped Planck's radical idea of a quantum of energy to be accepted in the skeptical scientific community.

Einstein applied Planck's radical idea to explain a strange physical phenomenon whereby the electrons are emitted from a surface metal. Einstein called the phenomenon "photoelectric effect". In equation form:

$$\text{Net K.E. (electron)} = hv \text{ -- } W \qquad \text{(eq.4)}$$

Legend: h is the Planck constant, v is the frequency, W is the work function.

When Einstein's equation was proven to be valid by the experiment of Robert Millikan, Planck's radical idea that radiation can be absorbed or emitted by matter in pocket or "quantum" form became acceptable to the physics community.

Max Planck was awarded the Nobel Prize in Physics in 1918 for his discovery of Planck's constant (h) and the quantum nature of radiation. Albert Einstein was awarded the Nobel Prize in Physics in 1921 for applying Planck's quantum of energy to explain the photoelectric effect. Robert Millikan was awarded the Nobel Prize in 1923 for verifying by experiment Einstein's Law of photoelectric effect. (www.nobel.se)

Discussion

A. Derivation of the Angus' constant

The author derived the Angus' constant by studying the data gathered by previous scientists. The author observed the following values in the Lyman series which he made into a three-column table as in Table 1.

The values of photon energy (1st column) and photon wavelength (2nd column) were taken from a physics textbook *Modern Physics* by Kenneth Krane in p. 167. The third column was made by the author by multiplying the 1st column and 2nd column.

Table 1: The Lyman Series

Photon Energy (ev)	Photon Wavelength (nm)	Product (ev-nm)
10.20	121.5	1239.300
12.09	102.5	1239.225
12.76	97.2	1240.272
13.06	94.9	1239.394
13.23	93.7	1239.651
13.60	91.1	1238.960

How did the author derive the Angus' constant? There are two methods to derive the Angus' constant.

1. First Method

Step 1. The author multiplied the values of the photon energy with the photon wavelength of the Lyman series and obtained a product placed in the third column.

Step 2. The author observed that the photon emissions in the Lyman series have a constant product of around 1239 ev-nm as can be seen in the third column. The average value of the third column is 1239.467 ev-nm which I round off to 1239 ev-nm.

Step 3. The author converted the product of 1239 ev-nm into S.I. units (i.e. International System of Units or System Internationale units) using J-m.

Given the following conversions:

1 m = 1x 10 ^9 nm (eq 5)
1 nm = 1x 10^-9 m (eq.6)
1 ev = 1.602 x 10^-19 J (eq.7)

Legend: m is meter, nm is nanometer, ev is electron volt, J is Joules.

Let us convert the constant 1239 ev-nm in terms of S.I. units in J-m as follows:

1239 ev-nm x (1x10^-9 m/1nm) x (1.602 x 10^-19 J/ev) =
1.98488 x 10^-25 J-m (eq.8)

Step 4. We derive a new physical constant after assigning the constant value with the Greek letter lambda in upper case /\ and label it as the Angus constant.

Angus' constant = /\ = 1.98488 x 10^-25 J-m (eq. 9).

2. Second Method

An alternative method of deriving the Angus' constant is as follows:

Step 1. The author observed that energy (E) is inversely proportional to wavelength (w) as seen in Table 1. As energy (E) of photon increases, the wavelength (w) of the photon decreases. As energy (E) of photon decreases, the wavelength (w) of the photon increases. In equation form:

E → 1/w (eq.10)

Step 2. We multiply both sides by w and we get:

E x w = 1 or unit constant (eq. 11)

Step 3. Let us assign this unit constant as the Greek letter lambda in upper case.

E x w = /\ (eq.12)

Step 4. By filling the values for E and w, we can get the product value of /\ in terms of ev-nm in the third column of Table 1.

E = 10.2 ev, w = 121.5 nm, (eq.13)
E x w = 10.2 ev x 121.5 nm (eq.14)
E x w = 1239.3 nm (eq.15)
Round off = 1239 nm (eq.16)

Step 5. Let us covert this product value 1239 ev-nm unit to S.I. units, that is, J-m unit as in equation 8.

1239 ev-nm x (1x10 ^-9 m/nm) x (1.602 x 10^-19 J/ev) =
1.98488 x 10^-25 J-m (as in eq.8)

Step 6. Let us assign this product value as the unit constant or the Greek letter lambda and label it as the Angus' constant.

Angus' constant = /\ = 1.98 x 10^-25 J-m (as in eq.9)

So far, I have revealed two (2) ways on how to derive the new physical constant which I simply call the Angus' constant.

Let us now define the Angus' constant. The **Angus' constant** is a constant numerical value that relates the inverse relationship of energy and the wavelength of the photon.

B. Significance of the Angus' constant

What is the significance of the Angus' constant to the physical sciences?

1. The Angus' photon

Max Planck discovered the 'frequency' characteristic of the energy in quantum form in 1900. On the other hand, Albert Einstein proposed light can be emitted in particle form called "photon" in 1905. Both Planck and Einstein used the frequency (v) in their equation as follows:

Planck's quantum of energy: E = nhv (similar to eq. 2)
Einstein's photon energy: E = hv (similar to eq. 3)

Equation 2 is what I call "Planck's quantum energy equation". Equation 3 is what I call "Einstein's photon energy equation".

On the other hand, the author discovered the 'wavelength' characteristic of the photon's energy. Let the Greek letter in upper case /\ be the Angus' constant and the letter w be the wavelength. The slash symbol (/) is a division operation sign.

Angus' photon energy: E = /\ /w (eq. 17)

Equation 17 is called "Angus' photon energy equation". Equation 17 was derived from Equation 12.

The **Einstein photon** is the photon represented mathematically in terms of frequency and the Planck constant. The Einstein photon: hf

The **Angus photon** is the photon represented mathematically in terms of wavelength and the Angus constant. The Angus photon: /\ /w.

The "Einstein photon" and the "Angus photon" are two ways of representing the Plank's "quantum" of energy radiation and absorption.

The author would like to emphasize that there is only one kind of quantum of light called photon which can be represented mathematically in two ways: a. in terms of its frequency characteristic as revealed by Albert Einstein, b. in terms of its wavelength characteristic as revealed by the author.

2. Dual Nature of Light

The debate on the nature of light has raged the physics community for hundreds of years starting in the 17th century between Isaac Newton and Christian Huygens.

Some physicists like the Dutch physicist-astronomer, Christian Huygens (1629-1695) believed that light has only one nature: wave nature. I call these group of physicists supporting the wave theory of light as "wave theorists". Huygens was the chief advocate of the wave theory of light.

Some physicists like the English physicist, Isaac Newton (1642-1727) believed that light has only one nature: particle nature. I call these group of physicists supporting the particle nature of light as "particle theorists". Newton was the chief advocate of the particle nature of light.

The "particle theorists" gained the upper hand when Max Planck discovered the discrete or "quantum" nature of radiation in 1900. Furthemore, Albert Einstein proposed that light energy travels in particles called "photons" in 1905.

If the Dutch physicist-astronomer Christian Huygens were alive today, he will surely be happy to find out that his wave theory of light is still valid because the author discovered the wavelength characteristic of the photon.

3. Dual Nature of Photon

The photon is supposed to be a discrete "particle" of light.

Question: Does the photon have wave characteristics? Answer: Yes. The author believes the photon has wave characteristics. The equation of the Angus' photon (/\ /w) reveals the wave characteristic of the photon.

The "Angus constant" is significant to physical sciences because the new physical constant leads to the concept of the "Angus' photon", which in turn, helps to affirm the dual nature of the photon i.e. photon has two major characteristics: wavelength (w) and frequency (f) .

The dual nature of the photon is affirmed because Einstein revealed in equation form the frequency characteristic of the photon while the author revealed in equation form the wavelength characteristic of the photon.

The photon although it is a particle can behave like a wave by virtue of its wavelength characteristic. Hence, the photon has a dual nature. A photon is a particle with a wave characteristic at the same time.

C. Applications of the Angus' constant

The applications of the Angus constant are as follows:

1. Law of Photoelectric Effect

We can also use the Angus' constant to give an alternative explanation to Einstein's Law of Photoelectric Effect. The mathematical equation of the emission of electron from a metal surface is known as the "Einstein's Law of Photoelectric Effect".

Net KE of electron = hv -- W (same as eq.4)

We can transform the well-known "Einstein equation" (eq. 4) into an "Angus equation" by substituting Einstein's photonic energy (hv) with Angus' photonic energy (/\ / w). The resulting equation is as follows:

Net KE of electron = /\ / w – W (eq. 18)

What is the meaning of the equation 18?

Equation 18 shows that the energy of the photon (/\ / w) is absorbed by the electron. Then, an energy is needed to overcome the work function (W) which prevents the electron from escaping the atom. The difference between the energy (/\ /w) and the work function (W) is the net kinetic energy (KE) of the electron. A critical wavelength (w) is necessary to induce the emission of electron from the surface of the metal.

A series of electron emissions from the metal surface would be a source of useful energy because these electron emissions possess a net kinetic energy in the form of photonic energy (/\ /w).

This is one application of the Angus' constant (/\) to energy production as revealed in equation 18.

Equation 18 is what the author simply calls the "Angus's Law of Photoelectric Effect". The **Angus' Law of Photoelectric Effect** can be stated formally as follows:

An element or metal that is exposed to radiation will emit electrons: (a.) if the radiation that is absorbed in the form of an Angus' photon (/\ / w) has the critical wavelength (w) and (b.) if the electron overcomes the potential energy (W) of its orbital. Otherwise, the electron will remain bound to the atom.

2. Chemical Reaction Equations

We can demonstrate the "photoelectric effect" phenomenon in chemical reaction equations as follows:

x(Boron) + x(/\ / w) → x(Boron ^+3) + x(3e-) + x(W) + x(net K.E.) (eq. 19)

x(Nickel) + x(/\ / w) → x(Nickel ^+1) + x(1e-) + x (W) + x (net K.E.) (eq. 20)

The chemical reaction equations 19 and 20 show that a useful energy can be produced due to the emissions of electrons which carry the net kinetic energy (net K.E.). The letter W is the amount of energy to overcome the energy barrier or work potential that prevents the escape of electron. The letter x is a coefficient that stands for the number of atoms absorbing the Angus' photon (/\ / w).

The total useful energy that can be produced depends on the number of atoms (x) absorbing the Angus photon (/\ /w) and the critical wavelength (w) of the radiation.

3. Chemical Bond Breaking

The Angus photon is also useful in explaining the net energy that results when chemical bonds are broken.

The chemical bonds of 1 mole of chlorine gas needs a input energy of 242 KJ/ mol to break up. (Masterton p.280)

A chemical bond can be broken if the energy absorbed by the chlorine molecule is greater than the bond energy (K) that keeps the chemical bond intact. Let the energy barrier of a chemical bond be K. In the case of chlorine gas, bond energy K = 242 KJ / mol. The initial photon energy absorbed by the chemical bond is /\ / w. If the initial photon energy that is absorbed by the chemical bond is greater than the "chemical bond energy barrier" K, the chemical bond will break. In equation form:

Net KE = (/\ / w) – K (eq. 21)

Eq. 21 is called the "Angus' Law of Photochemical Effect". The **Law of Photochemical Effect** can be formally stated as follows: A chemical bond of a molecule will break if the chemical bond absorbs a photonic energy (/\ /w) which is greater than the chemical bond energy barrier (K) that holds the chemical bond intact.

4. Chemical Energy Production

Sample Problem: How much net kinetic energy (net KE) can be produced when 1 mole of chlorine gas absorbs a radiation with a wavelength of 335 nanometers ? The solution is as follows.

The chemical bond of a chlorine gas Cl2 can be broken if it absorbs energy of 242 KJ/mol. (Masterton p. 280)

Radiation of wavelength 335 nm corresponds to how much energy E ?

E = /\ / w (Angus photon energy equation) (same as eq.17)
w = 335 nm x (1 m/ 1x 10^9 nm) = 3.35 x10^-7 m (eq. 22)
E = (1.98 x 10^-25 J-m)/ 3.35 x 10^-7 m (eq. 23)
E = 5.9 x 10^-19 J
(This is absorbed by 1 molecule of chlorine gas.) (eq. 24)
Energy per molecule = E/molecule = 5.9 x 10^-19 J/ molecule of chlorine gas (eq. 25)

This amount of "energy per molecule" of chlorine gas is equivalent to how much "energy per one mole" of chlorine gas molecule?

6.022 x 10 ^23 molecules = 1 mole (Avogadro's Number) (eq. 26)
Energy per mole = E/mol = J/molecule x Avogadro's Number (eq. 27)
E/mol = (5.9 x 10^-19 Joules / molecule) x (6.022 x 10^23 molecules/ mole) (eq. 28)
E/mol = 355,927.16 Joules/ mole (eq. 29)
In terms of KJ/mol: 355,927.16 Joules/mole x 1KJ/ 1000 J = 355.9 or 356 KJ/ mol (eq. 30)

Let us now answer the question of the sample problem: How much is the net kinetic energy produced when 1 mole of chlorine gas absorbs a radiation with a wavelength of 335 nanometers ?

Net K.E.. = /\ / w – K (Angus Law of Photochemical Effect) (same as eq.21)
Net K.E. = 356 KJ - 242 KJ = 114 KJ (eq. 31)

The net kinetic energy produced is 114 Kilojoules. This is the net amount of useful chemical energy that is carried by 1 mole of chlorine gas.

The breaking of chemical bonds involving energy absorption in the form of chemical reaction equation is as follows:

1 mole (Cl-2) + (/\ /w) /mol → 1 mole (2 Cl) + K /mol + Net KE/mol (eq. 32)
1 mole (Cl-2) + 356 KJ/mol → 1 mole (2 Cl) + 242 KJ/mol + 114 KJ/mol (eq. 33)

The total photonic energy per mole or [(/\ / w)/ mol] that is absorbed by 1 mole of chlorine gas molecule is 356 KJ/ mol. The total energy per mole needed to break the chemical bond energy barrier (K) of 1 mole of chlorine gas molecule is 242 KJ/ mol. The total net energy per mole carried by one mole of chlorine gas is 114 KJ/mol.

Equation 33 is balanced in terms of mass and energy (i.e the reactant side is equal to the by-product side):

In terms of mass: 1 mole of Cl-2 = 1 mole of 2 Cl (eq.34)
In terms of energy:
356 KJ/ mol = 242 KJ/ mol + 114 KJ/mol (eq.35)

As we can see in the sample problem, the "Angus' Law of Photochemical Effect" is also useful in computing the total energy or the total net kinetic energy that results in the breaking of chemical bonds.

Conclusion

The prevailing notion about photon is that photon has a frequency characteristic but not having a wavelength characteristic. The author reveals in equation form that photon has a wave characteristic in the form of /\ / w.

This paper gives an alternative or new interpretation of the photoelectric effect phenomenon using the Angus' constant. This new interpretation is embodied in equation form called the Angus' Law of Photoelectric Effect.

The "Angus' Law of Photoelectric Effect" and the "Angus' Law of Photochemical Effect" are simply two of the many applications of the Angus'constant to energy production.

Other applications of the Angus' constant or Angus' photon to energy production will be discussed in future papers.

Summary

1. There are two important physical constants related to the photon, namely: the Planck's constant (h) and the Angus' constant (/\)

2. The photon can be mathematically represented in two ways: Einstein's photon (hf) and Angus' photon (/\ /w).

3. The Angus photon is useful in explaining the escape of electrons from atoms with the aid of light (i.e. photoelectric effect) and breaking of chemical bonds with the aid of light (i.e. photochemical effect).

4. The "Angus' Law of Photoelectric Effect" is useful in calculating the net kinetic energy of escaping electrons from atoms.

5. The "Angus' Law of Photochemical Effect" is useful in calculating the net kinetic energy that results after the breaking of chemical bonds.

Equation Summary

1. Planck's Constant:	h = 6.626 x 10 ^-34 J-s	eq. 1
2. Angus' Constant:	/\ = 1.98 x 10 ^-25 J-m	eq. 9
3. Planck's Quantum Energy Equation:		
	E = nhv n = 1, 2, 3…..	eq. 2
4. Einstein's Photon Energy Equation:		
	E = hv.	eq. 3
5. Angus' Photon Energy Equation:		
	E = /\ / w.	eq. 17
6. Einstein's Law of Photoelectric Effect:		
	E = hv – W.	eq. 4
7. Angus' Law of Photoelectric Effect:		
	E = /\ / w – W.	eq. 18
8. Angus' Law of Photochemical Effect:		
	E = /\ / w – K.	eq. 21

Reference

1. Masterton, William, Emil J. Slowinski, and Conrad L. Stanitski. (1981) "Chapter 9: Chemical Bonding" In: *Chemical Principles*. 6th ed. New York and Philadelphia: Saunders College Publishing. pp.258-283

2. Krane, Kenneth. (1983). *Modern Physics*. New York: John Wiley and Sons.

3. Halliday, David and Resnick, Robert.(1986) *Physics Part 2 Extended Version*. 3rd ed. New York: John Wiley and Sons.

4. Kogan, V. I. (2000) "The discovery of the Planck constant" In: *Uspekhi* 43 (12) 1253-1259 (2000).

5. "The Nobel Prize in Physics -- Laureates: 1918 Max Planck". In: *Nobel E-Museum. www.nobel.se*.

6. "The Nobel Prize in Physics -- Laureates: 1921 Albert Einstein". In: *Nobel E-Museum. www.nobel.se*.

7. "The Nobel Prize in Physics -- Laureates: 1923 Robert A. Millikan". In: *Nobel E-Museum*. *www.nobel.se*.

CATALYTIC PYROLYSIS AND KINETICS OF CORN STALK WITH THERMOGRAVIMETRY

Chuncai Song[a], Shengwei Zhu[a], Haoquan Hu[a], Guohua Chen[b]*

[a]Institute of Coal Chemical Engineering, Dalian University of Technology, 129 Street, Dalian 116012, China
[b]Department of Chemical Engineering, The Hong Kong University of Science & Technology, Clear Water Bay, Kowloon, Hong Kong SAR
*hhu@chem.dlut.edu.cn

Introduction

Recently, the global environmental problems, such as global warming and acid rain, have become a serious issue. Biomass, as a renewable and potential resource, its effective utilization has been received considerable attention worldwide. Biomass resources are abundant in China, but they are not been used efficiently, particularly in handling agricultural biomass that is often burned on site, causing not only environmental pollution but also waste of resource. Therefore, in China, it is of great significance to develop new technology to make rational and efficient use of biomass as an alternative energy for fossil fuels or to obtain chemicals.

Thermoanalytical techniques (TG and DTG) have been widely used to study the kinetics of various solid-state fossil fuels decomposition reactions. Researchers have proposed different models to study the characteristics of biomass pyrolysis in the past few years [1-3]. Distributed Activation Energy Model (DAEM), as a new and simple method, which is presented by Miura [4,5], has been used both in the cases where single reactions are occurring and analyzing complex reaction systems, such as pyrolysis of fossil fuels, thermal regeneration reactions of activated carbon and so on. Recently, Liu et. al. [6] gave the explicit analytic expression of activation energy during weight loss process based on the new theoretical analysis of DAEM. However, the application of DAEM to biomass pyrolysis has not been reported yet. It is especially necessary to understand the kinetics of pyrolysis in order to design a suitable pyrolysis reactor and obtain a better insight of effective catalyst or study the mechanisms of liquefaction or pyrolysis of biomass. In this paper, the pyrolysis of corn stalk with sodium carbonate or potassium carbonate as catalyst was carried out with thermal gravimetric analysis, and the activation energy distribution at different weight loss of biomass was determined with DAEM.

Experimental

Raw material Crushed and sieved air-dried biomass of corn stalk obtained from Dalian suburb, northeast of China, and the main components of biomass, including cellulose microcrystalline from Alfa Aesar, lignin with low sulfonate from Aldrich, hemicellulose, replaced with Poly(beta-D-xylopyranose) (xylan) from Sigma were used as the test samples in this study. A certain amounts of catalysts were dissolved in distilled water and impregnated test samples for two hours and then dried.

Equipment and method The pyrolysis of biomass was performed in a thermogravinetric analyzer (Mettler-Toledo TGA/SDTA851^e). Approximately 6mg sample was placed in an Al_2O_3 ceramic pan. The furnace was heated from ambient temperature to 923K at a constant heating rate (5,10,20,40K/min). Purified nitrogen at a constant flow rate of 20mL/min was used as the purge gas to provide an inert atmosphere for pyrolysis and to remove any gaseous and condensable products evolved, thus minimizing any secondary vapor-phase interactions. The sample weight was recorded as a function of time or temperature.

Results and Discussion

Pyrolysis of corn stalk **Figure.1** shows the TG and DTG curves of sodium carbonate and potassium carbonate at the heating rate of 10K/min during the pyrolysis. It can be seen that except about 2 to 3% weight loss of moisture before 420K there is no obviously weight loss with temperature further increased. Therefore, catalysts don't decompose in the range of temperature investigated in this work and the effect on the calculation of thermal gravity analysis in the following experiments can be eliminated by subtracting the quantities of catalyst according to the amount added in the sample.

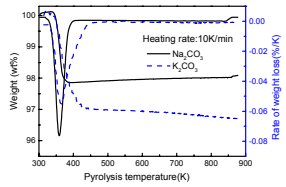

Figure 1. TG and DTG curves of sodium and potassium carbonate

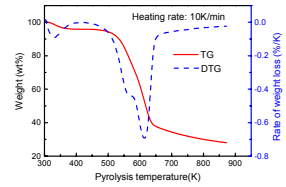

Figure 2. TG and DTG curves of corn stalk

Figure 2 shows TG and DTG curves of corn stalk without any catalyst. It can be observed that the main pyrolysis region of corn stalk is between about 500K and 650K. There are two peaks at 572K and 614K in the DTG curve correspondingly and a long tail at high temperatures. Compared to the TG and DTG curves of hemicellulose, cellulose and lignin shown in **Figure 3**, the first peak on DTG curve of corn stalk is mainly contributed by hemicellulose, the second one by cellulose and the long tail corresponds to the thermal decomposition of lignin.

Figure 4 and **Figure 5** show the catalytic effect on the TG and DTG curves with Na_2CO_3 and K_2CO_3 (0.5, 1.0, 3.0 and 10wt%) addition, respectively. Compared with the result without catalyst addition, catalyst has an effect on pyrolysis of biomass at temperature after about 470K, especially in the range of 550K to 650K. Catalyst can increase the final weight loss of corn stalk. Without catalyst the weight loss is 62.4wt%, while 69.9wt% with addition of 1wt% Na_2CO_3 and 73.1wt% with 1wt% K_2CO_3. But when K_2CO_3 addition is more than 3.0wt%, the final weight loss decreased by about 4wt%, see Fig.5 (A). For the case of Na_2CO_3, more catalyst added, the lower temperature at the maximum weight loss rate results in, from 620K with 0.5wt% to 565K with 10wt% Na_2CO_3. Generally speaking, when catalyst addition is more than 1.0wt%, the shape of the curve of DTG is greatly changed, from two peaks to only one peak meaning that catalyst has more effect on hemicellulose than that on the other main fractions of biomass.

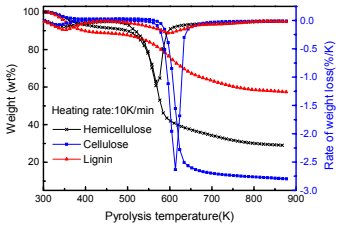

Figure 3. TG and DTG curves of hemicellulose, cellulose and lignin

Figure 6 shows the DTG curves for corn stalk with 3.0wt% Na_2CO_3 or K_2CO_3 and without addition of catalysts at heating rate of 20K/min. Both catalysts can increase the maximum weight loss rate and have obvious effect on pyrolysis results. Under this condition, the temperature at the maximum weight loss rate is 604K with K_2CO_3 and 607K with Na_2CO_3.

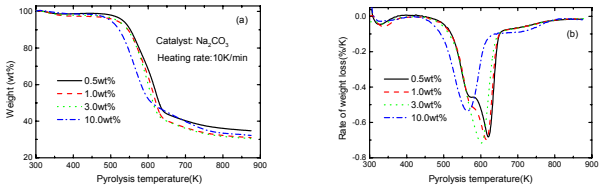

Figure 4. TG and DTG curves of corn stalk with different amounts of sodium carbonate addition (A) TG; (B) DTG

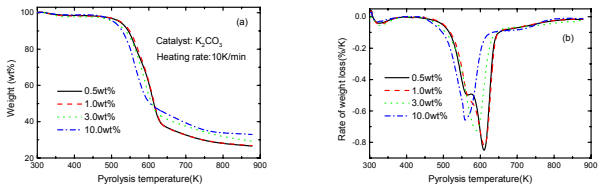

Figure 5. TG and DTG curves of corn stalk with different amounts of potassium carbonate addition (A) TG; (B) DTG

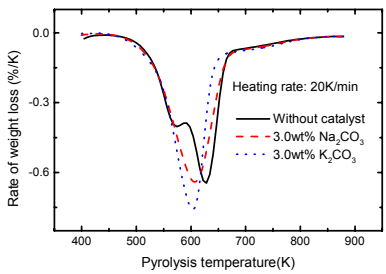

Figure 6. Comparison of DTG curves with different catalyst

Determination of activation energy with DAEM DAEM is based on the following assumptions: 1) complex reactions are consisted of a series of irreversible first-order reactions that have different activation energies and a constant frequency factor. That is, all the reactions are parallel; 2) All the activation energies present continuous distribution functional forms. When applied to pyrolysis, DAEM is expressed as:

$$\frac{\omega}{\omega_0} = 1 - \int_0^{\infty} \Phi(E,T) f(E) dE \qquad (1)$$

where ω is the total volatile matter evolved by time t, ω_0 is the effective volatile matter content of the raw material, $f(E)$ is the distribution function of activation energy to represent the differences in the activation energies of many first-order irreversible reactions.

The $\Phi(E,T)$ function is equal to

$$\Phi(E,T) = \exp(-\frac{k_0 R T^2}{hE} e^{-E/RT}) \qquad (2)$$

and k_0 is the frequency factor corresponding to E value, h is heating rate; R is 8.314(J/mol K). Eq (1) is the function of temperature T and heating rate h. Therefore, at a constant heating rate h, ω/ω_0 satisfies:

$$d(\omega/\omega_0) = \frac{\partial(\omega/\omega_0)}{\partial T} dT + \frac{\partial(\partial(\omega/\omega_0)}{\partial h} dh = 0 \qquad (3)$$

from eq(1) to eq(3), following equation can be deduced[6].

$$\frac{E}{R} = -\frac{d \ln h}{d(1/T)} - 2T \qquad (4)$$

Using eq (4), $f(E)$ and k_0 can be estimated from TG data obtained at different heating rates[6].

Since at temperature below 423K mainly weight loss is due to dehydration, we set the weight loss of samples as 0wt% at the temperature 423K, while 100wt% at the final pyrolysis temperature. That is: $\alpha=1-\omega/\omega_0$, where α is weight loss fraction; ω and ω_0 are the same nomenclatures as above.

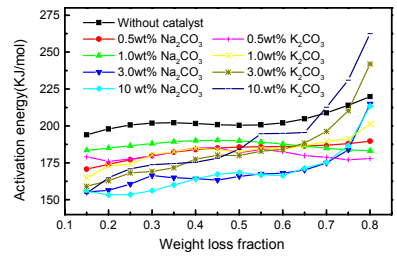

Figure 7. Activation energy *vs* weight loss obtained by DAEM

Figure 7 gives the activation energy obtained by DAEM based on eq (4) for different samples. It can be seen that activation energy of corn stalk is between 194 and 220kJ/mol in the weight loss range of 15% to 80%. And it is interesting that activation energy value, varying continuously with the increasing of temperature, indicated that the thermal pyrolysis of corn stalk is not a single reaction, but a complex reaction containing a series of cracking of chemical bonds with different activation energies. Generally activated energy can be reduced by about 20~40 KJ/mol owing to the addition of catalyst. Sodium carbonate and potassium carbonate are both effective and potential catalyst for biomass conversions.

Conclusions

The results indicated that the catalyst has an effect about upon 470K, especially in the range of 550K~650K. When catalyst addition is more than 1.0wt%, DTG curve is altered greatly, from two peaks to one, for catalyst affecting more on hemicellulose than on cellulose and lignin. In the case of Na_2CO_3, the more added, the lower the temperature at maximum weight loss rate, from 620K with 0.5wt% to 565K with 10wt%.

The DAEM analysis shows that the activation energy is between 194 and 220kJ/mol in the weight loss range of 15% to 80%, which indicated that corn stalk pyrolysis is a complex reaction containing a series of cracking of chemical bonds with different activation energies. Catalyst can reduce activation energies by about 20 to 40 KJ/mol depending on the added amounts.

Acknowledgment

The authors are grateful for financial support by the Special Research Foundation for Doctoral Education of China (No. 2000014115).

References

[1] Demirbas, A. *Bioresource Technology,*1998, *66*, 247.
[2] Kim, S.; Park, J. K. *Thermochinica Acta,* 1995, *264*, 137.
[3] Guo, J.; Lua, A.C. *Biomass and Bioenergy,* 2001, *20*, 223.
[4] Miura, K. *Energy & Fuels,* 1995, *9*, 302.
[5] Miura, K.; Maki, T. *Energy & Fuels,* 1998, *12*, 864.
[6] Liu, X.G.; Li, B.Q.; Miura, K. *Fuel Processing Technology,* 2001, *69*,1.

TREATMENT OF WASTEWATERS FROM DEWATERING PROCESS OF BROWN COAL BY USE OF A NOVEL Ni-SUPPORTED CARBON CATALYST

Hiroyuki NAKAGAWA, Akio NANBA, Marc Boehlmann, and Kouichi MIURA

Department of Chemical Engineering
Kyoto University, Kyoto 606-8501, JAPAN

Introduction

Brown coals are important energy resources in the near future because of their abundant deposits. But dewatering (drying) process is necessary prior to use for power generation because their waters content are very large, and reach as high as 60% by weight for some coals. Current technology for power generation from low rank coals removes most of water by evaporative drying, resulting in a direct loss of the heat of evaporation (~2.3MJ/kg). Therefore, development of an efficient dewatering process is desired for more utilization of brown coals.

Non-evaporating drying process is preferable for this purpose, since the water is separated in liquid form. Fleissner process[1)] has been applied commercially to brown coal since 1920's, and several processes utilizing non-evaporative dewatering have been proposed[2)]. In these processes, brown coals are treated under hydrothermal conditions at 200 ~ 300 °C, where upgrading as well as dewatering of brown coals are realized through the decomposition of oxygen functional groups. Simultaneously, a large amount of wastewater containing organic compounds derived from brown coal is discharged from the dewatering process. Wastewater treatment is a serious concern from the viewpoint of environmental preservation.

Recently the authors have developed a novel Ni-supported carbon catalyst[3)] and showed that the catalyst is effective to gasify small molecular weight organic compounds to convert them to CH_4 and H_2[4)]. In this paper a brown coal was treated under the hydrothermal conditions for dewatering and the catalyst was applied to gasify the wastewater emitted during the dewatering. Organic compounds such as phenol were also gasified for comparison purpose.

Experimental

Catalyst preparation A metacrylic acid type resin (Mitsubishi Chemical, WK-11) was used as a starting material. The resin was treated in an ammonium complex ion aqueous solution of $Ni(SO_4)_2$ at room temperature. It was then heated at the rate of 10 K/min to 500 °C in a nitrogen stream to prepare the Ni-supported carbon catalyst. BET surface are of this catalyst was 170 m^2/g. The amount of Ni supported surprisingly reached as high as 47wt% andl Ni was found to be highly dispersed in the porous carbon from X-ray diffraction pattern. This catalyst was subjected to the experiment without any further treatments such as reduction by hydrogen.

Sample preparation A Victorian brown coal, Morwell, was used in this study. Water content of the coal was 1.31 kg/kg-dry coal. Hydrothermal treatment was conducted in a 20 ml autoclave. About 6 g of coal water mixture (1:1 on weight) was loaded in a reactor. The reactor was purged by 1 MPa of nitrogen several times to remove oxygen in the reactor before heating. The autoclave was heated to 300 °C at which the temperature was maintained for 60 min. The wastewater was obtained by filtering the coal/water mixture after the treatment. The total organic carbon in the wastewater was ca. 2000 ppm. Another type of wastewater derived from the mechanical/thermal dewatering process (MTE) [5)] was also used.

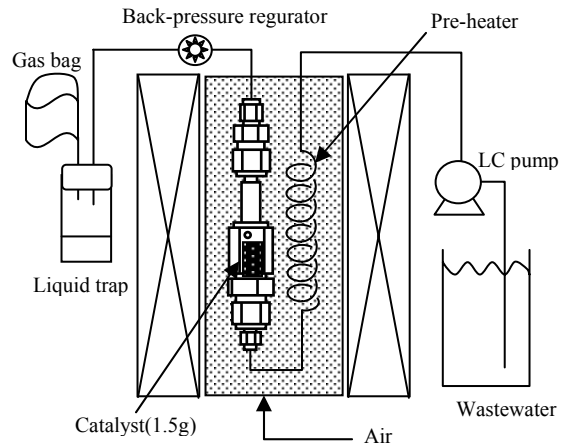

Fig.1 Apparatus for catalytic hydrothermal gasification.

Apparatus and procedure Figure 1 shows the experimental setup for the catalytic hydrothermal gasification. 1.5 g of catalyst was embedded in a reactor made of Swagelok. The wastewater or aqueous solution of containing one of organic compounds (2000 ppm) was supplied to the reactor at the rate of 0.2 to 1 ml/min under the pressure of 20 MPa to maintain liquid phase at the reaction temperature. The LHSV was changed from 10 to 50 h^{-1}. The reactor was heated in a fluidized sand bath where the temperature was maintained at 200 ~ 350 °C. The product gas and treated water was analyzed by gas chromatographs (GC) and a total organic carbon analyzer (TOC), respectively.

Results and Discussions

Catalytic hydrothermal treatment of wastewater Figure 2 shows the carbon conversion and the product gas yields when the wastewater was gasified at 200 ~ 350 °C. The LHSV was 50 h^{-1}. The product yields were all represented on the basis of 1 mol of carbon in the wastewater. The carbon conversion increased with the increase of reaction temperature and reached eventually at 350 °C.

The gaseous products detected were only CH_4, CO_2, and H_2.

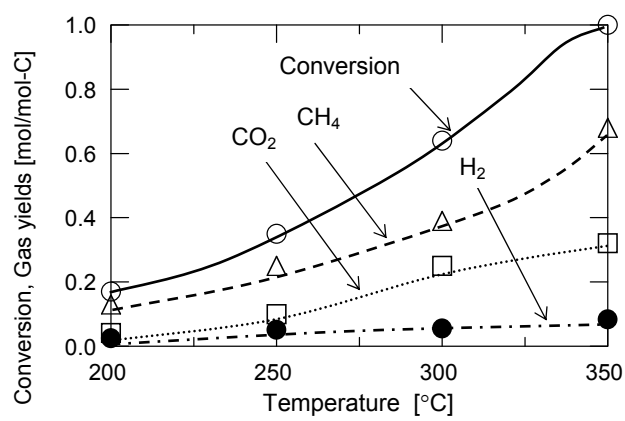

Fig.2 Catlytic hydrothermal gasification of wastewater at 20 MPa (LHSV = 50 h^{-1}).

CO was little produced under these conditions. The total yield of CH_4 and CO_2 was almost the same with the carbon conversion

estimated from the concentration of organic carbon in the wastewater before and after treatments. The gas yields all increased with the increase of reaction temperature. The yield of CH_4 was 0.68 at 350°C. On the other hand, the yield of H_2 was much smaller than the yields of other gases and less than 0.1 even at 350 °C, indicating that CH_4 rich gas could be obtained through the catalytic hydrothermal treatment of wastewater. Above results clearly show that the hydrothermal gasification process using new catalyst is effective not only to treat the wastewater but to recover gaseous energy resources from the wastewater.

Molecular weight distributions of organics in wastewater before and after treatments To examine which components are gasified easily, molecular weight distributions of organics in the wastewater before and after treatments were analyzed by GPC. Figure 3 shows the elution curves of the organics in the wastewater before and after treatment. Corresponding molecular weight, which was calibrated using polyethyleneglycol (PEG), is shown above the figure. The wastewater before treatment contains a fairly large amount of small molecular weight components less than 200 g/mol. About a half of these components were gasified at 200 °C where the carbon conversion was 0.17. This result clearly indicates that the small molecular weight components are more reactive for hydrothermal gasification than high molecular weight components. However, even high molecular weight components more than 100,000 g/mol were completely gasified when the reaction temperature was raised up to 350 °C.

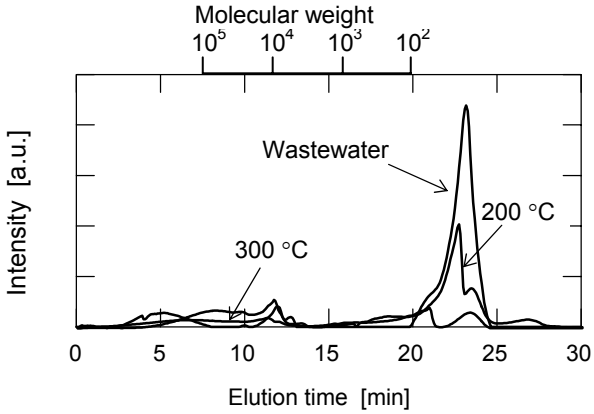

Fig.3 Elution curves of organics in the wastewater before and after treatment.

Treatment of various water-soluble compounds A water-soluble lignin, phenol, *m*-cresol, the wastewater of the MTE process were also gasified at 350 °C with the TOC of 2000 ppm. Figure 4 shows the product gas yields. The sum of the yields of CO_2 and CH_4 corresponds to the carbon conversion, because the formation of other gases containing carbon was negligible. The carbon conversions of lignin, phenol, and *m*-cresol were 0.52, 0.68, and 0.87, respectively when LHSV was 50 h^{-1}. These results indicate that these compounds are less reactive than the wastewater. As for product gas yields, the yields of CH_4 and CO_2 were almost the same for the phenol and cresol. The yields of hydrogen for lignin, phenol, and *m*-cresol were clearly larger than the H_2 yield for wastewater. When the LHSV was lowered to 10 h^{-1}, phenol, cresol, and the wastewater of the MTE process were almost completely gasified at 350 °C. The carbon conversion of lignin was also increased up to 0.77. The product gas composition was, however, not affected by the value of LHSV.

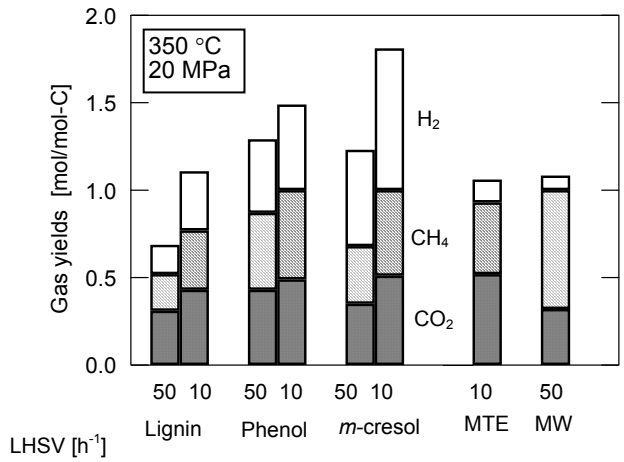

Fig.4 Product gas yields from the catalytic hydrothermal gasification of lignin, phenol, m-cresol, and wastewaters from dewatering. (350 °C, 20 MPa)

Conclusions

Wastewaters from the dewatering process of brown coals were gasified under hydrothermal conditions by use of a novel Ni/carbon catalyst developed by us. Organics in the wastewater were completely gasified under the hydrothermal conditions of 350 °C and 20 MPa, producing H_2, CH_4, and CO_2. This result indicates that this catalytic hydrothermal gasification can recover energy resources from organics in wastewater effectively. It was also found that small molecular weight components were more reactive for the catalytic hydrothermal gasification than large molecular weight components in the wastewater.

A water-soluble lignin, phenol, and *m*-cresol in water were also gasified under the same conditions. They were all less reactive than the organics in the wastewater coming from the brown coal dewatering process. It was found that the carbon conversion increased with the decreace of LHSV value whereas the product gas composition was not affected by the LHSV value.

Acknowledgement. This work was financially supported by Special Coordination Funds of the Ministry of Education, Culture, Sports, Science and Technology, Japan. (Grant No. 11218206)

References

(1) Fleissner H., *Sonderdruck Spartwirtschaft Nos. 10 and 11*, 1927.
(2) Allardice D.J. In *The Science of Victorian Brown Coal: Structure, Properties and Consequences for Utilization*; Durie R.A. Ed.; Butterworth-Heinemann: Oxford, 1991; pp. 104-150.
(3) Miura K., Nakagawa H., Kitaura R., Satoh T., *Chem. Eng. Sci*. **2001**, *56*, 1623.
(4) Miura K., Nakagawa H., Miwa M., Tamura T., *Int. Sym. on Chem. Reaction Eng.,* 2002, No. 169(Hong Kong).
(5) Bergins C., Berger S., Strauss K., *Chem. Eng, Tech*. **1999**, 22, 923

CO-PRODUCTION OF SYNGAS AND LIME BY COMBINED THERMO-NEUTRAL CALCINATION OF LIMESTONE WITH CO_2-REFORMING/PARTIAL OXIDATION OF METHANE OR CARBON

M. Halmann,[a] * and A. Steinfeld [b]

[a] Weizmann Institute of Science, Department of Environmental Sciences and Energy Research, Rehovot 76100, Israel.
[b] ETH - Swiss Federal Institute of Technology, Department of Mechanical and Process Engineering, CH-8092 Zurich, Switzerland.
* Corresponding author. E-mail: m.halmann@weizmann.ac.il

Introduction

The calcination of limestone to produce lime and cement, as well as the steam/CO_2 reforming of natural gas, are highly energy-intensive processes, which together contribute more than 6% to the global anthropogenic CO_2 emissions,[1]

$$CaCO_3 = CaO + CO_2 \quad \Delta H^0_{298K} = 178 kJ/mol \qquad (1)$$
$$CH_4 + H_2O = CO + 3H_2 \quad \Delta H^0_{298K} = 206 kJ/mol \qquad (2)$$
$$CH_4 + CO_2 = 2CO + 2H_2 \quad \Delta H^0_{298K} = 247 kJ/mol \qquad (3)$$

By combining these endothermic processes with the exothermal partial oxidation of methane,

$$CH_4 + 1/2O_2 = CO + 2H_2 \quad \Delta H^0_{298K} = -38 kJ/mol \qquad (4)$$

it is possible to design overall thermo-neutral processes for the co-production of lime and the valuable syngas. In such a combination of the CO_2-emitting calcination with the CO_2-consuming reforming, most of the CO_2 release would be avoided. Also, the endothermicity of these processes would be compensated by the exothermicity of the CH_4 partial oxidation, resulting in fuel saving. The thermodynamic constraints for such combined processes were determined at 1200 and 1400 K. An analogous thermo-neutral co-production of metals and syngas has recently been developed.[2] Such combined processes, which both release CO_2 and utilize it, could be an attractive option for greenhouse gas mitigation.[3]

Results

The calculated equilibrium composition as a function of temperature from 800 to 1450 K for an initial reaction mixture of $CaCO_3 – CH_4 – O_2 – H_2O$ is presented in Figure 1. As shown in the Figure, above 1100 K, CaO, H_2, and CO are stable reaction products. Equilibrium compositions for thermo-neutral reactions of $CaCO_3$ with O_2 and either CH_4 or carbon, in the absence and presence of added H_2O, are shown in Table 1. Carbon was taken for these calculations as a proxy of coal, which would be used in actual practice. The purpose of including H_2O in the reactant mixtures is to promote the *in situ* water-gas-shift reaction,

$$H_2O + CO = H_2 + CO_2 \quad \Delta H^0_{298K} = -41 kJ/mol \qquad (5)$$

thus raising the H_2 to CO molar ratio to $H_2/CO = 2$, as required for the synthesis of methanol, which could be one of the useful products from syngas.

This preliminary assessment of the combined calcination of limestone with the partial oxidation of CH_4 or carbon predicts considerably decreased CO_2 emission, as well as competitive economics, justifying further study.

References

1. Steinfeld, A.; Thompson, G., *Energy,* **1994**, 19, 1077-1081.
2. Halmann, M.; Frei, A.; Steinfeld, A. *Energy,* 2002, 27, 1069-1084.
3. Halmann, M. M.; Steinberg, M. *Greenhouse Gas Carbon Dioxide Mitigation: Science and Technology,* Lewis Publ., Boca Raton, **1999**.

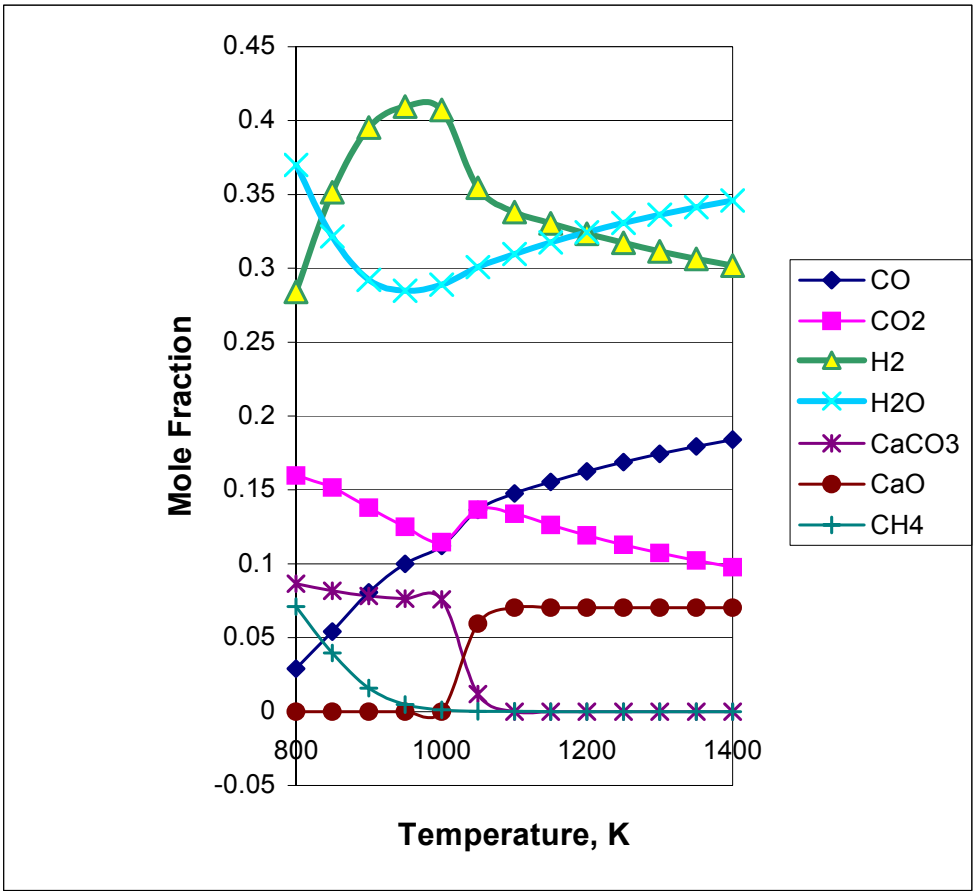

Figure 1. Equilibrium composition vs. temperature for $CaCO_3$ – CH_4 – O_2 – H_2O, initially with molar ratio 1 : 3 : 2.55 : 3.2 at 300 K and 1 bar.

Table 1. Computed equilibrium compositions for thermo-neutral reactions of $CaCO_3$ with O_2 and either CH_4 or carbon in the absence or presence of H_2O at 1200 K and 1 bar. Yields of H_2 are relative to the CH_4 input, while the CO yields are vs. the total carbon input ($CaCO_3$ + CH_4 or Carbon).

Initial mol	Initial mol	Initial O_2 mol	Initial H_2O mol	ΔH kJ/mol	H_2 Yield %	CO Yield %	H_2/CO molar ratio
$CaCO_3$ 1.00	CH_4 2.00	1.80	-	-12.0	59.8	66.9	1.19
$CaCO_3$ 1.00	CH_4 3.00	2.55	3.20	+11.7	76.5	57.7	1.99
$CaCO_3$ 1.00	Carbon 2.00	1.20	-	-1.2	-	53.3	-
$CaCO_3$ 1.00	Carbon 2.00	1.70	8.00	-5.2	5.0*	6.7	1.99

* H_2 yield calculated relative to H_2O input.

PREDICTION OF THE REID VAPOR PRESSURE OF PETROLEUM FUELS

M. R. Riazi, T. A. Albahri and A. H. AlQattan*

Chemical Engineering Department, Kuwait University,
P.O.Box 5969, Safat 13060, Kuwait
*Tel: (+965) 4817662; Fax: (+965) 4811772
*Homepage: http://139.141.199.1/~riazi
riazi@kuc01.kuniv.edu.kw

Introduction

The volatility characteristics of petroleum fuels are very important especially for gasolines. Motor and aviation gasolines are manufactured as liquids but they are consumed in the vapor phase. Consequently, gasoline volatility must be high enough to assure acceptable engine start-up, warm-up, acceleration and throttle-response under normal driving (or flying) conditions. On the other hand, the maximum volatility of a gasoline must be restricted to avoid vapor lock, vaporization losses, air pollution, and unsafe storage and handling. The volatility considerations for other transportation fuels like kerosene and diesel are, to some extent, similar to those for gasoline.

The Reid vapor pressure (RVP) is frequently used as an indication of volatility of liquid hydrocarbons. The RVP is defined as the absolute pressure (i.e., psia or bar) exerted by a mixture, determined at 100 ºF (37.8 ºC) and at a vapor to liquid ratio of 4. This is different than the true vapor pressure which is defined as the pressure of a vapor in equilibrium with its condensed phase at a specific temperature. Although the RVP provides a convenient approximation of the absolute vapor pressure of a partly vaporized sample at 100 °F, it is not equivalent to the true vapor pressure. In general, RVP is lower than the true vapor pressure due to some small sample vaporization and the presence of water vapor and air in the confined space. The apparatus and procedures for determining the RVP are standardized and specified in ASTM method D-323 and IP-402 [1]. The Reid vapor pressure test is widely used as a criterion for blending gasoline and other petroleum products. Once RVP of a fuel is known the methods provided in the API-TDB [2] can be used to estimate true vapor pressure of a fuel or a crude oil at any desired temperature. True vapor pressure is an important thermodynamic property related to volatility and phase equilibrium calculations.

There are a number of methods for estimating the vapor pressure of petroleum fractions but very few for Reid vapor pressure. The method presented in the API-TDB [2] for estimation of RVP is based on rigorous vapor-liquid equilibrium calculations. A number of simple methods have been developed to estimate the Reid vapor pressure of finished petroleum products [3]. In the Bird-Kimball method the gasoline is divided into 28 cuts or boiling ranges characterized by their average boiling point. A blending RVP of each cut is then calculated by the following equation [3]:

$$B_i = \frac{7.641}{\exp(0.03402\, T_{bi} + 0.6048)}$$
$$P_a = \sum_{i=1}^{i=28} B_i x_{v\,i} \qquad (1)$$
$$f = 1.0 + 0.003744\,(VAPB - 93.3)$$
$$RVP = f\, P_a$$

where B_i = RVP blending number for cut i and T_{bi} = normal boiling point of cut i in °C. x_{vi} is the volume fraction of cut i and VABP is the volume average boiling point in °C. RVP is calculated in bars. The constants were obtained from the original constants given in English units. Use of this method requires full distillation curve of the fuel to be known. Another simple method is to use a relation for the true vapor pressure (TVP) of petroleum fractions and to assume that RVP is the same as TVP at 100 ºF (311 K). The vapor pressure relation given by van Nes van Westen [4] can be converted into the SI unit at 311 K as:

$$\log(TVP)_{100} = 3.204 \times \left(1 - 4 \times \frac{T_b - 41}{1393 - T_b}\right) \qquad (2)$$

where T_b is the normal boiling point in K and TVP_{100} is the true vapor pressure at 100 ºF (311 K) in bars. Once TVP is calculated it may be used instead of RVP in case of lack of sufficient data. This method only requires mid-boiling point (or ASTM temperature at 50 volume% vaporized). This give an approximate value for RVP as the difference between RVP and TVP is ignored. The main objective of this work was to develop a simple predictive method for RVP of petroleum fuels from crude oils from around the world which requires minimum laboratory data as input parameters.

Technical Development

A bank of data on RVP and basic characteristics of 52 gasoline and naphtha samples from crude oils around the world was prepared from OGJ Data Book [5]. One simple and relatively accurate equation for correlation of true vapor pressure of hydrocarbons is the Miller equation [6]. We apply this equation at 311 K (100 °F), however, the constants in the equation have been determined from RVP of petroleum fractions and have been related to boiling point (T_b) and specific gravity (SG) of the fraction in the following form:

$$RVP = P_c \exp(Y)$$
$$Y = -X\left(\frac{T_b SG}{T_r}\right)(1 - T_r)^5 \qquad (3)$$
$$X = -276.7445 + 0.06444 T_b + 10.0245 SG - 0.129 T_b SG + \frac{9968.8675}{T_b SG} + 44.6778 \ln T_b + 63.6683 \ln SG$$
$$T_r = 311 / T_c$$

where T_c and P_c are the pseudocritical temperature and pressure of the fraction in degrees Kelvin and bar, respectively. RVP is in bars and T_b mid-boiling point of mixture in degrees Kelvin . This equation is based on data with RVP in the range of 0.0007-1.207 bar (0.01 – 17.5 psia), normal boiling point range of 305 – 494 K and specific gravity range of 0.65-1.08. This method may be used for quick estimation of RVP when only boiling point and specific gravity of a fuel are known. This equation does not give reliable values for RVP of wide boiling range fractions such as the whole crude oil. T_c and P_c needed for use in the above equation may be estimated from the relations given by Riazi and Daubert [7] that are also included in the API-TDB [2] using T_b and SG as input parameters. Therefore, with the minimum knowledge of mid-boiling point and specific gravity one can get estimate of RVP from Equation (3). A summary of evaluation of these three methods is given in Table 1. Equations (1) and (2) nearly give similar result, although Equation (2) is much simpler than Equation (1). However, the average error for Equation (3) is 0.06 bar (0.88 psia) which is nearly half of the other two methods. Predicted versus experimental values of RVP from the

proposed method is also shown in Figure 1. Demonstrated results indicate that when minimum data on a petroleum fuel is available the method proposed in this work can be used to estimate RVP of a fuel.

Table 1. Summary of Results for Prediction of RVP of 52 Fuels

Item	Method	Eqn.	RVP (bar)	
			AAD	MD
1	Proposed model	3	0.06	0.24
2	Nes and Van Westen [4]	2	0.13	0.38
3	Bird and Kimball [3]	1	0.12	0.42

API Gravity range: 51 – 87 ºAPI, T_b Range: 305 – 494 K
RVP Range: 0.0007-1.207 bar,
AAD% = (1/no of data) $\sum|$ (pred. –exp.)/exp. $|\times 100$,
MD%= maximum % deviation

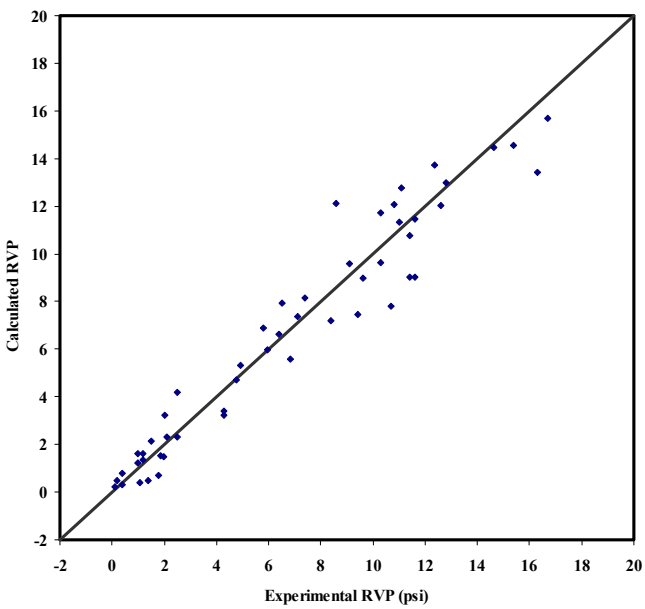

Figure 1. Parity plot for the Reid vapor pressure (RVP) using Equation (3).

References

(1) ASTM, "Annual Book of Standards," American Society for Testing and Materials, Philadelphia, Pennsylvania, 1995.
(2) American Petroleum Institute (API) Technical Data Book – Petroleum Refining. Chapter 5, 6th Edition, American Petroleum Institute., Washington DC, 1997.
(3) Baird, C.T. Crude Oil Yields and Product Properties, Ch. De la Haute Belotte 6, 1222 Vezenaz, Geneva, Switzerland, 1981.
(4) Van Nes, K., and Van Western, H.A., Aspects of the Constitution of Minerals Oils, Elsevier, Amsterdam, 1951.
(5) Oil and Gas Journal Data Book, 2000 Edition, PennWell, Tulsa, Oklahoma, 2000.
(6) Reid, R. C., Pransnitz, J. W., and Poling, B. E. The Properties of Gases and Liquids. 4th Edition., McGraw-Hill, Inc., New York, 1987.
(7) Riazi, M.R., Daubert, T.E., "Characterization Parameters for Petroleum Fractions," Ind. & Eng. Chem. Research, 1987, Vol. 26, pp. 755-759.

POLYPHOSPHAZENE-BASED POLYMER ELECTROLYTE MEMBRANE FUEL CELLS

Serguei. N. Lvov[1], Xiangyang Zhou[1], Elena Chalkova[1], Jamie A. Weston[1], Catherine M. Ambler[2], Andrew E. Maher[2], Richard M. Wood[2] and Harry R. Allcock[2]

[1]The Energy Institute &
Department of Energy and Geo-Environmental Engineering
[2]Department of Chemistry
The Pennsylvania State University
University Park, PA 16802, USA

Introduction

Polymer electrolyte membrane fuel cells (PEMFCs) are efficient electrical power sources. Nafion (DuPont) is the most widely studied polymeric membrane for fuel cell applications due to its good mechanical properties, chemical stability, and high ionic conductivity. However, Nafion is limited to operating temperatures below 100°C due to the tendency of the membrane to dehydrate, resulting in decreased proton conductivity and reduced mechanical stability. The Nafion membranes also suffer from high electro-osmotic drag of water as well as high methanol permeability. To alleviate these problems several approaches have been used to improve Nafion-based MEAs. Polyphosphazene-based proton-conducting membranes are promising materials for use in both H_2/O_2 and direct methanol fuel cells. Polyphosphazenes (POPs) are hybrid inorganic/organic polymers with a –P=N– backbone that is particularly stable to free-radical skeletal cleavage reactions. The chemical and physical properties of polyphosphazenes are highly tunable due to a wide array of side groups, which may be incorporated into these polymers. In this paper we summarize the results of our studies on the newly developed POP-based proton conducting membranes to be used in PEMFCs.

Synthesis

Up to now three kinds of proton conducting poly(aryloxyphosphazenes) have been synthesized and tested in our laboratories. Sulfonated polyphosphazene membranes were fabricated using the methods described by Pintauro and co-authors [1]. Phosphonated polyphosphazene membranes were synthesized as described in detail elsewhere [2]. Synthesis of the sulfonamide functionalized polyphosphazene membranes is described in reference [3]. All cross-linking was achieved through ^{60}Co γ-radiation at the dosage levels up to 40 Mrad. The main characteristics of the polyphosphazene membranes of interest and Nafion 117 (cross-linking radiation dosages, ion exchange capacities (IEC), equilibrium water swelling, and conductivities) are given in Table 1.

Table 1. Polyphosphazene and Nafion membrane properties at ambient conditions (22°C and 1 bar).

Polymer	Radiation (Mrad)	IEC (meq/g^1)	Swelling (%)	Conductivity (S cm^{-1})
Nafion 117	N/A	0.91	30	0.100
Sulfonated POP	20	1.07	38	0.035
Phosphonated POP	40	1.35	14	0.025
Sulfonimide POP	40	0.99	42	0.058

Experimental Systems

Experimental systems for studying the conductivity, methanol permeability, and fuel cell performance of the proton conductive membranes over a wide range of temperatures have been developed in our laboratories.

Proton Conductivity. The proton conductivity of several polymer electrolyte membranes including sulfonated and phosphonated poly[(aryloxy)phosphazenes] was determined at temperatures up to 120°C [4]. Nafion 117 membranes were also tested using the same methods in order to determine the reliability of our approach. The electrical conductivity of protons in water-equilibrated membranes was determined using a four-electrode AC impedance method. The membrane holder was made from Teflon and stainless steel. Two Pt wires are used as reference electrodes for detecting the potential drop along the strip of a membrane. The ends of the membrane strip were pressed against stainless steel sheets that were used as counter electrodes for providing an electrical current along the membrane. The Pt and stainless steel electrical leads were coated with Teflon to ensure good electrical insulation between one another and between electrodes and the body of an autoclave. The entire membrane was immersed in high purity water that was prepared using a Milli-Q gradient system (Millipore Inc.). An electrochemical test station (Gmery Instrument. Inc.) was used to carry out the impedance spectroscopy measurements. It was found that the electrochemical system that we use is close to a pure resistor and the value of the resistance was defined as the average module between 0.01 and 1000 Hz.

Methanol Permeability. Permeability measurements of sulfonated and phosphonated polyphosphazenes membranes at room temperature and pressures were carried out using the method outlined in reference [5]. The measurements at elevated temperatures and pressures were carried out for the same polyphosphazenes using the modified experimental system [4,6], which was specially constructed to be used at high temperatures and pressures. The system consisted of the upper and lower chambers separated by the membrane to be tested. An aqueous methanol solution is pumped into the lower chamber using a high pressure liquid chromatography pump at a particular flow rate to keep the methanol concentration constant. A pressure relief valve was used to keep the pressure constant. It was also found that there was a vigorous convection in the upper chamber because of the temperature gradient and a possible concentration gradient in the bulk of the upper chamber can be minimized. Therefore, the developed design allowed for the pressure on both sides of the membrane to be kept equal and for minimizing the formation of a concentration gradient in the upper chamber.

Methanol passes through a polymer membrane from the lower chamber of the cell to the upper chamber by molecular diffusion. Tests were conducted at temperatures up to 120°C and pressures up to 90 psi. Solution samples were taken by a syringe from the upper chamber once the methanol solution had been pumped through the lower chamber for 3.5 hours. The methanol concentration of the samples was determined by gas chromatography.

Fuel Cell Measurements. A proton conducting sulfonimide polyphosphazene membrane has been used to prepare a membrane electrode assembly (MEA) [7]. The MEA was tested in an H_2/O_2 fuel cell that was obtained from Fuel Cell Technologies, Inc. Hydrogen and oxygen were humidified and pre-heated, if necessary, before entering the fuel cell. Flow rates and pressure of gases were monitored. The voltage-current measurements were carried out using an electronic load (Hewlett Packard Co.) and electrometer (Keithley Instruments, Inc.).

Results of Measurements and Discussion

The results for proton conductivity obtained at elevated temperatures [4] show that the sulfonated and phosphonated polyphosphazenes have significant increases in conductivity with increasing temperature, although these values remained lower than that of Nafion 117 (measured in our laboratory). However, the activation energy values obtained in the present study for the Nafion 117 and the sulfonated and phosphonated polyphosphazene membranes are similar. A difference of only 0.4 kJ/mol was found between the sulfonated derivative and the Nafion 117 sample, while the phosphonated material was about 1.1 kJ/mol less than the Nafion 117 sample. It was found that the conductivity values of the new membranes are not yet ideal, but they are still within a range that holds potential for viable fuel cell applications. Further modifications of these systems are ongoing in order to improve the proton conducting materials and their performance.

The results for the methanol permeability measurements of sulfonated and phosphonated polyphosphazenes at ambient temperatures have shown a significantly lower capacity for methanol cross-over when compared to Nafion 117, leading them to be promising candidates for further DMFC testing [4-6]. At the elevated temperatures explored in this study, it was found that while the gap in methanol cross-over value has been closed significantly for the sulfonated materials, there still remains a large difference between the phosphonated membrane and that of Nafion 117. At 120°C, the sulfonated polyphosphazene membrane exhibits a similar methanol permeability (8.1×10^{-6} cm^2 s^{-1}) to that of Nafion 117 as measured by the present authors, whereas the permeability of the phosphonated polyphosphazene membrane is about nine times lower than that of Nafion 117. This property may permit a more efficient fuel cell operation with the phosphonated polyphosphazene membrane than otherwise expected, because the methanol concentration used in the operating cell can be increased significantly above the level that would be possible in other systems without encountering problems with system poisoning. With respect to the activation energy of the diffusion transport, both the sulfonated and phosphonated polyphosphazene membranes have shown much greater values than that of Nafion 117. The sulfonated derivative was found to have a value of 41.4 kJ/mol and the phosphonated species was 36.8 kJ/mol, whereas Nafion 117 has a value of 22.4 kJ/mol. This difference is thought to indicate that alternative diffusion mechanisms are involved in the transport through the polymeric membranes.

The selectivity of proton conductive membranes was calculated as a ratio of the electrical conductivity and permeability and used to compare the new membranes with Nafion 117. It was found that the sulfonated polyphosphazene is superior (in terms of selectivity) to Nafion 117 at temperatures below 85°C while the phosphonated polyphosphazene is superior to Nafion 117 over a wide temperature range from 22 to 125°C.

Sulfonimide polyphosphazene has been investigated as a proton conducting electrolyte membrane to make an MEA and to test it in a hydrogen/oxygen fuel cell. The membrane of 0.01 cm thickness was cross-linked via gamma radiation of 40 Mrad. The electrodes were prepared by applying an ink, containing Pt on carbon (Vulcan XC-72R), water, and a Nafion solution in a mixture of lower aliphatic alcohols, to ELAT/NC/D5/V2 carbon cloth with 20% wet proofing. The catalyst loading was 0.33 mg/cm^2 for both the anode and the cathode. The sulfonimide polyphosphazene-based MEAs were pressed at elevated temperature and pressure. For the Nafion based MEA, Nafion 117 (E.I. du Pont de Nemours & Co., Inc.) membranes were fabricated using direct ink application to the membrane and the ink composition was the same as for the sulfonimide polyphosphazene based MEAs. The Nafion-based MEAs were pressed at elevated temperature and pressure, too. Uncatalyzed 10% Teflon-bound carbon cloth was used as the gas diffusion backing on both sides of the MEA.

The cell voltage and current density of the fuel cell were measured at temperatures of 22 and 80°C [7]. The voltage-current curve obtained for the Nafion 117 MEA at 80°C was found to be similar to that reported under similar conditions (0.33 mg cm^{-2} catalyst loading for both the anode and cathode; H_2 and O_2 pressures are 3 and 5 bar, respectively; humidification temperature of 95°C for both the anode and cathode) [8]. Results from our Nafion-based MEA tested at 80°C indicate a limiting current density of 1.24 A cm^{-2} and a maximum power density of 0.45 W cm^{-2}. Our data parallels that found in the fuel cell tests conducted by Wilson and Gottesfeld [8] on Nafion 117 MEAs within an H_2/O_2 fuel cell system, which indicated a limiting current density of 1.37 A cm^{-2} and maximum power density of 0.50 W cm^{-2} at 80°C.

The observed limiting current densities of 1.12 A/cm^2 and 1.29 A/cm^2 were found for the sulfonimide polyphosphazene MEA at the ambient and elevated temperatures, respectively. The greatest power for the sulfonimide polyphosphazene MEA at 80°C was 0.47 W cm^{-2} and was achieved when hydrogen and oxygen were humidified at 10°C above the fuel cell temperature, which prevented dehydration of the membrane. On the other hand, the greatest power for the MEA at room temperature was 0.36 W cm^{-2} and was obtained without need of humidification. Thus, the maximum power density for the sulfonimide polyphosphazene-based fuel cell was found to be comparable to our Nafion-based MEA, as well as to the results of Wilson and Gottesfeld [8] for Nafion 117 based fuel cells. However, the tailorability of the sulfonimide polyphosphazene system permits significant flexibility in possible modifications to the side group structure. This should allow for optimization the MEA preparation process and achievement of a higher fuel cell performance.

Acknowledgement. This work was funded by the United States Department of Energy under Contracts DE-PS02-98EE504493 and DE-FC36-01GO11085 and by Los Alamos National Laboratory under Subcontract W7405ENG36.

References

1. Guo, Q.; Pintauro, P. N., Tang, H., O'Connor, S. *J. Membr. Sci.* **1999**, ***154***, 175.
2. Allcock, H. R.; Hofmann, M. A.; Ambler, C. M.; Chalkova, E.; Lvov, S. N.; Zhou, X. Y., Weston, J. A. *J. Membr. Sci* **2002,** *201*, 47.
3. Hofmann, M. A; Ambler, C. M.; Maher, A. E.; Chalkova, E.; Zhou, X. Y. ; Lvov, S. N.; Allcock, H. R *Macromolecules* **2002,** *35*, 6490.
4. Zhou, X. Y.; Weston, J.A.; Chalkova, E., Hofmann, M. A; Ambler, C. M.; Allcock, H. R.; Lvov, S.N. *Electrochmica Acta,* **2002**, in press.
5. Fedkin, M. V.; Zhou, X.Y; Hofmann, M.A.; Chalkova, E.; Weston, J.A.; Allcock, H.R.; Lvov, S.N. *Materials Letters*, **2002**, *52*, 192.
6. Zhou, X. Y.; Hofmann, M. A; Weston, J.A.; Chalkova, E.; Allcock, H. R.; Lvov, S.N. In *Direct Methanol Fuel Cells*; Narayanan, S., Zawodzinski, T. and Gottesfeld, S., Eds.; The Electrochemical Society Proceedings Series: Pennington, NJ, **2002**, pp. 34-41.
7. Chalkova, E.; Zhou, X. Y., Ambler, C. M.; Hofmann, M. A; Weston, J.A.; Allcock, H. R, Lvov, S. N. *Electrochem. and Solid State Lett.* **2002,** *5*, A221-A222.
8. Wilson, M.S.; Gottesfeld, S. *J. Appl. Electrochem.* **1992**, *22*, 1.

APPLYING A MEMBRANE REACTOR TO HYDROGENATE ACETOPHENONE WITH SIMULTANEOUS PRODUCT SEPARATION

Detlev Fritsch and Gisela Bengtson

GKSS Research Centre, Max-Planck-Strasse 1, D-21502 Geesthacht, Germany

Introduction

The stereoselective hydrogenation of acetophenone yields chiral (R)- or (S)- 1-phenylethanol [1], finding application as fragrance or intermediate in pharmaceutical industry. Besides other catalysts, also palladium was used, complexed to the biopolymer chitosan and immobilised to silica [2]. Chitosan is known as a membrane material for de-watering in pervaporation (PV) [3]. For use in a catalytic membrane reactor, however, a more hydrophobic, organophilic membrane material suited to extract acetophenone and the desired product will be required. Related to our work of hydrodechlorination of chloroaromatics [4], we tested membrane-bound Pd-catalysts successfully for this reaction. The possible products are shown in Figure 1.

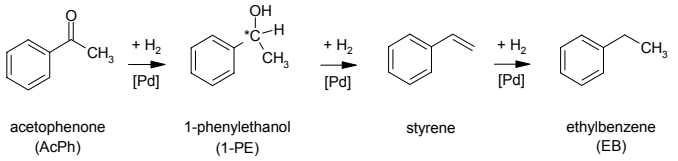

Figure 1. Possible products of the acetophenone hydrogenation

Results and Discussion

We selected the polyether-*b*-amide, PEBA 4033, as an organophilic membrane material. Catalytic active Pd was introduced by a solution-casting-reduction method developed previously [5]. Either direct incorporated Pd nano-clusters of about 10 w% and 3 nm size or newly developed organic/organic/inorganic blend membranes with 2 w% Pd were applied. With these blends of Pebax/polyvinylpyrrolidone/silica the cluster size could be reduced to 1.8 nm and the activity increased notable. At 30°C and 0.1 w% acetophenone in the feed, a conversion of 0.1 mol/g(Pd) * h resulted in the PV mode (see Figure 2, mode B). The membrane material not only serves as catalyst support, but also acts as solid (immobile) extractant able to enrich acetophenone in the membrane by a factor of about 100. Two different process set-ups were tested (see Figure 2). Applying method A, the educts acetophenone and H_2, both dissolved in water, are enriched in the membrane, react at the catalyst, and product leaves the membrane. Method B is the PV mode where educt is extracted into the membrane and product may be detected in the permeate and retentate [4]. Surprisingly, both methods yielded completely different selectivity with the same membrane catalyst. With method A 1-phenylethanol was the main product, besides small amounts of ethylbenzene detected only in the membrane. Method B (PV) generated small amounts of 1-phenylethanol found in the retentate, whereas in the permeate ethylbenzene was detected as the main product. In no case ethylcyclohexane was detected, being the main product of acetophenone hydrogenation by Pd or Pt on carbon catalysts in liquid phase batch processes [6].

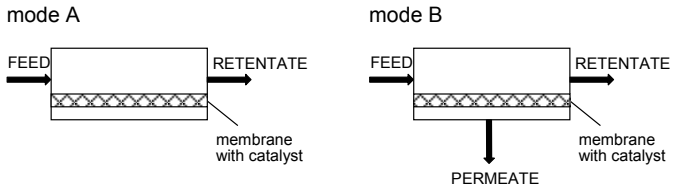

Figure 2. Two modes of membrane catalyst application

Conclusion

In summary, the operation mode of the membrane based Pd-catalyst controls the product selectivity. Also the membrane polarity will contribute to selectivity together with the selected solvent. We will expand our research using stereo-selective, membrane hosted catalysts to generate enantiomeric pure products.

References

[1] S. Wallbaum, J. Martens, Tetrahedron-Asymmetry 3 (1992) 1475-1508.
[2] Mao-Ya Yin, Guo-Li Yuan, Yong-Qiang Wu, Mei-Yu Huang, Ying-Yan Jiang, J. Mol. Catal. A-Chem. 147 (1999) 93-98.
[3] T. Uragami, K. Takigawa, Polymer 31 (1990) 668-672.
[4] G. Bengtson, H. Scheel, J. Theis, D. Fritsch, Chem. Eng. J. 85 (2002) 303-311.
[5] L. Tröger, H. Hünnefeld, S. Nunes, M. Oehring, D. Fritsch, J. Phys. Chem. B 101 (1997) 1279-1291.
[6] P. Tundo, S. Zinovyev, A. Perosa, J. Catal. 196 (2000) 330-338.

CHARACTERIZATION OF POLYMER NANOCOMPOSITES USED IN RECHARGEABLE SYSTEMS

[1]Giselle Sandí, [3]Riza Kizilel, [3]Humberto Joachin, [1]Kathleen A. Carrado, [1]Sönke Seifert, [2]Luis Smith, and [4]Rex E. Gerald

[1]Chemistry, [2]Materials Science, and [3]Chemical Technology Divisions, Argonne National Laboratory, 9700 South Cass Ave., Argonne, IL 60439
[4]Chemical and Environmental Engineering Department, Illinois Institute of Technology, Chicago, IL 60616

Introduction

Nanocomposite materials of poly(ethylene oxide) (PEO) and phyllosilicates were first suggested by Ruiz-Hitzky and Aranda (1) as candidates for polymer electrolytes. Within these materials, the polymer chains are intercalated between the silicate layers. The polymer chains then provide a mobile matrix in which cations are able to move. A considerable amount of interest has been shown in nanocomposites of PEO and montmorillonite, a layered aluminosilicate clay. When this composite contains $LiBF_4$, it displays conductivities up to 2 orders of magnitude larger than those of PEO itself at ambient temperatures (2). However, the addition of lithium salts, which are needed to obtain such conductivity values, is not desirable for two reasons: a more complicated synthetic route and a transference number for lithium that is not unity.

We have prepared a series of nanocomposites containing PEO intercalated in the layers of hectorite clays. These clays, also called phyllosilicates, belong to the family of smectite clay minerals. They are composed of two tetrahedral silicate layers sandwiching a central octahedral layer in a so-called 2:1 arrangement. In hectorite, isomorphous substitutions in the lattice of Li(I) for Mg (II) in the octahedral layers cause an overall negative charge that is compensated by the presence of interlayer, or gallery, cations. A significant amount of interlayer water is also present and the cations are easily exchangeable. A large degree of preferential orientation in films prepared by natural occurring clays tends to occur, however, due to their large platelet size (up to 1 μm). This can lead to non-conducting planes being perpendicular to the current path and thus reduce the conductivity. To avoid this problem, we followed a method developed by Carrado et al. (3) which involves direct hydrothermal synthesis and crystallization of hectorite with smaller platelet size, termed synthetic lithium hectorite (SLH). Organic molecules can be either incorporated directly from the gel or by subsequent intercalation.

Experimental

Clay Preparation. Precursor clay gels are of the composition: 1.32 LiF, 5.3 Mg(OH)2, 8 SiO2, n H2O, to correlate with the ideal hectorite composition of $Li_{0.66}[Li_{0.66}Mg_{5.34}Si_8O_{20}(OH,F)_4]$. A typical reaction begins by suspending the LiF with stirring in water. Separately, $MgCl_{2.6}H_2O$ is dissolved in water and mixed with 2 N NH_4OH to crystallize fresh $Mg(OH)_2$. Prior to use, this brucite source must be washed several times with water to remove excess ions. It is then added wet to the LiF solution. This slurry is stirred for 15-30 min before addition of silica sol (ludox HS-30, Na^+-stabilized, 30%). The total volume is increased to afford a 2 wt% solids suspension, and is stirred and refluxed for 40-48 hours. Solids are isolated by centrifugation, washed, and air-dried.

Film Preparation. Colloidal suspensions of 1 g SLH/100 ml deionized water were stirred for one-half hour. The desired amount of PEO (100,000 average molecular weight, Aldrich) was then added, and the mixture stirred for 24 hours. Mixtures contained 0.6, 0.8, 1.0, and 1.2 g of PEO/g of clay. Films were prepared by casting the slurries onto Teflon-coated glass plates and partially air-drying them. Further drying was carried out at 397 K under an inert atmosphere for 48 hours. The typical thickness of the films was about 40 μm.

Characterization Methods. X-ray powder diffraction (XRD) patterns of SLH and PEO powders were determined using a Rigaku Miniflex, with Cu Kα radiation and a NaI detector at a scan rate of 0.5° 2Θ/min and step size of 0.05.

In situ small angle x-ray scattering (SAXS) was carried out at the Advanced Photon Source, (Basic Energy Sciences Synchrotron Research Center CAT), Argonne National Laboratory. The SAXS intensity of the investigated material I(q) is the function of the angle of scattering (2θ) and the wavelength (λ) of the applied radiation. This relation can be expressed as $q = 4\pi \sin \theta/\lambda$. Monochromatic X-rays (18 keV) are scattered off the sample and collected on a 15 x 15 cm2 CCD camera. The scattered intensity is corrected for absorption and instrument background. The instrument was operated with a sample-to-detector distance of 332 mm to obtain data at $0.1 < q < 3.0$ $Å^{-1}$. For these studies, a specially designed sample holder was used to heat the sample and collect SAXS data at the same time. **Figure 1** shows a diagram of the sample holder. Films of about 1.25 cm in diameter and 40 μm in thickness were placed in the sample holder and held using kapton tape. The furnace temperature program was set to ramp from room temperature to 150 °C at 5 °C/min, and the gas flow of nitrogen was started at room temperature. SAXS data were collected at room temperature, 60, 80, 100, 120, and 150 °C in order to compare the structural results with the conductivity values.

AC impedance measurements as a function of temperature were obtained on films in sealed cells with lithium foil as the counter and working electrode, using a Solartron SI 1256 electrochemical interface and 1254 frequency response analyzer. A Tenney Junior Environmental Test Chamber was used to control the temperature of the cell with a precision of ± 0.5 °C.

Wideline ^7Li NMR experiments were recorded at six temperatures in the range 220-360 K on a Bruker AVANCE 360 MHz spectrometer using a B_1 field that delivered a 90°pulse of 7.7 μs. Magic angle spinning (MAS) ^7Li NMR experiments were recorded at room temperature on a Varian INOVA 300 MHz spectrometer using a 90°pulse of 2.5 μs, and a rotor.

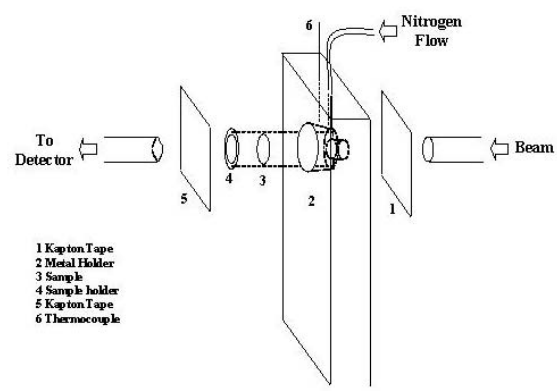

Figure 1. Schematic diagram of the sample holder used for in situ SAXS studies.

Results and Discussion

Understanding the structural changes of the PEO component in the nanocomposite films upon heating is crucial for predicting the conductivity of these materials. *In situ* SAXS is an excellent

technique for deriving such information because of this particular instrument's time-resolving capability and its high flux.

Figure 2 shows SAXS data obtained from a film made of PEO/SLH 1.2:1 mass ratio. The data was collected at room temperature. This figure was chosen because it shows clearly the peaks that correspond to SLH and PEO. The d001 peak is broader than that presented in the XRD plots because it is plotted here as Q in $Å^{-1}$, but the spacing differs only by 0.42 Å. SAXS data was then collected at 60°C and the results are shown in **Figure 3**. It is clear that the structure of the polymer has changed as indicated by the near complete disappearance of the PEO crystalline peaks. It is therefore assumed that the polymer chains have relaxed inside the clay layers. Other evidence of such relaxation is the decrease in d001 spacing, which indicates a more dense polymer phase. Under these circumstances, the polymer matrix is more mobile and the lithium ions associated with the polymer can have higher transference number, leading to a higher conductivity as found by Sandí et al. (4). The samples were also heated at 80, 100, 120, and 150 °C. Except for complete disappearance of the PEO peaks at 80 °C, there are no other polymer structural changes.

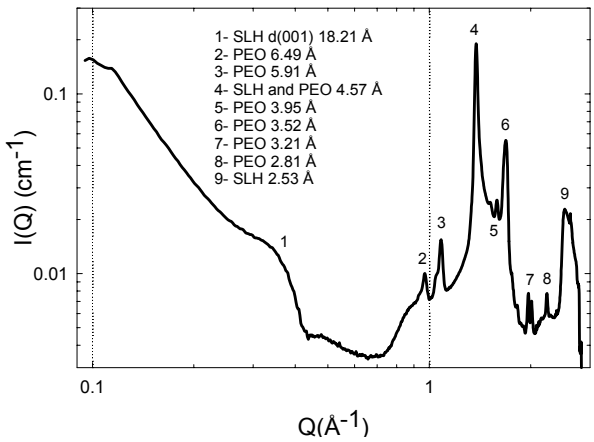

Figure 2. In situ SAXS of a PEO/SLH 1.2:1 mass ratio film taken at room temperature. The inset shows the diffraction peaks attributed to PEO and SLH.

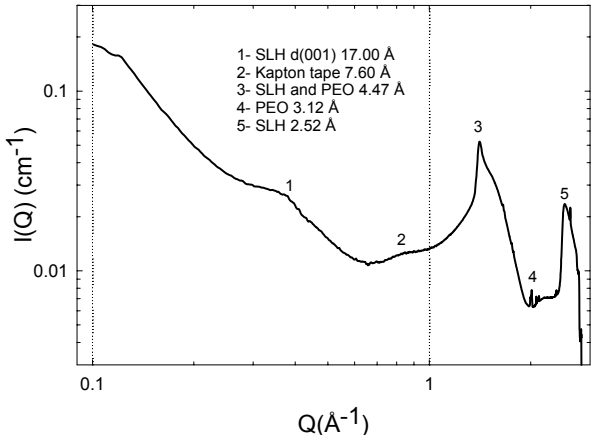

Figure 3. In situ SAXS of a PEO/SLH 1.2:1 mass ratio film taken at 60 °C. The sharp peaks from PEO have broadened, indicating that the PEO has lost its crystallinity. The sample was heated under nitrogen at 5°C/min.

Wideline ^{7}Li NMR spectra of PEO/SLH nanocomposite films revealed a single peak over the temperature range studied. The spectrum at each temperature was decomposed into a sum of two line functions, a narrow Lorentzian and a broad Gaussian. **Figure 4** (top) shows plots of the linewidths of both line functions vs. temperature for three film compositions. **Figure 4** (bottom) maps the integrated Lorentzian component of the spectrum vs. temperature. A ^{7}Li MAS spectrum (**Figure 4**, inset) shows an intense and narrow (<1 kHz) centerline, and a weak, broad manifold of spinning side bands (>80 kHz). These data are consistent with two lithium ion environments in PEO/SLH nanocomposite films. The Lorentzian spectral component is consistent with mobile lithium ions, and become narrower as the temperature of the nanocomposite is increased. In addition, the fraction of the spectral intensity due to the Lorentzian component changed with temperature, increasing to a maximum value of 55-60%, consistent with the stoichiometry of SLH. The Gaussian spectral contribution indicates a large static quadrupolar coupling (>80 kHz), consistent with the static lithium ions locked in the silicate layers.

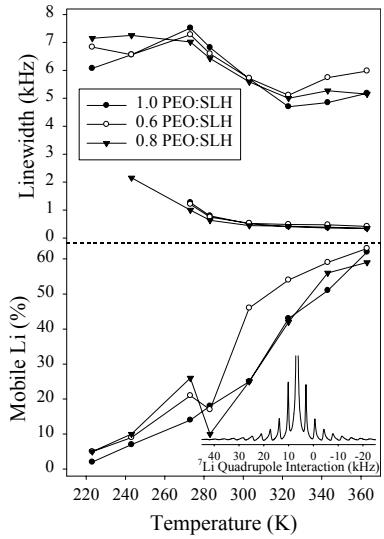

Figure 4. Linewidths of the Lorentzian and Gaussian functions that comprise the ^{7}Li NMR spectrum recorded at different temperatures (top). Percent of spectral intensity from the integrated Lorentzian line function, which is attributed to the fraction of lithium that is mobile (bottom). ^{7}Li MAS spectrum at 273 K (inset).

Based on the NMR results, significant ionic conduction and a high Li transference number can be expected at temperatures above 330 K.

Acknowledgment

This work was performed under the auspices of the U.S. Department of Energy, Office of Basic Energy Sciences, Division of Chemical Sciences, Geosciences, and Biosciences under contract number W-31-109-ENG-38.

References

1. Ruiz-Hitzky, E., Aranda, P. *Adv. Mater*., **1990**, *2*, 545.
2. Wong, S., Vaia, R. A., Giannelis, E. P., Zax, D. B., *Solid State Ionics*, **1996**, *86-88*, 547.
3. (a) Carrado, K. A.; Winans, R. E.; Botto, R. E. US Patent 5,308,808. (b) Carrado, K. A. *Appl. Clay Sci*., **2000**, *17*, 1.
4. Sandí, G.; Carrado, K. A.; Joachin, H.; Lu, W.; Prakash, J. *J. Power Sources*, **2002**. In press

EVALUATION OF FERRITES FOR THE MEMBRANE APPLICATIONS

X.-D. Zhou [1] Zili Chu [2], J. Yang[1], W. B. Yellon[2], W. J. James[1] and H. U. Anderson [1]

1: Materials Research Center, University of Missouri-Rolla, Rolla, MO 65401

2: Department of Physics, University of Missouri-Columbia, Columbia, MO 65211

Introduction

The perovskite-type oxides encompass a large variety of chemical compositions that contribute to their diverse and unique properties. It is the intent of this presentation to study the structural, electric and magnetic properties of ferrites with an emphasis on the compounds of $La_{0.60}Sr_{0.40}FeO_{3-\delta}$, which are particularly interesting in oxygen membrane and the intermediate temperature solid oxide fuel cells. Initial studies on ferrite materials have showed that the structure plays an important role in electrical and catalytic properties and that the electrical, catalytic and magnetic properties have an inter-relationship that is commonly related to the electronic structure and oxygen vacancy concentration. Therefore, it is critical to study the ferrite materials from the atomic structure point of view, for example the hybridization of transitional metal and oxygen orbitals that plays a dominant role in the properties such as the generation of oxygen vacancies, holes, and spin state of the transitional metals. This interrelationship is shown in the (La, Sr)(Fe, Co)$O_{3-\delta}$ system. For 20% Co compound, electrons (holes) move indirectly between Co ions via an O ion rather than directly between Co ions, i.e., the fluctuation of the charges of O ions as well as Co ion causes electrons (holes) to move with a complicated interaction between the generated holes and electrons [1]. The effects of Fe doping in $La_{0.67}Sr_{0.33}CoO_3$ showed that no apparent structure change was introduced by Fe doping up to x=0.3, but the Curie temperature T_c, magnetization M and electrical resistivity are lowered by Fe substitution [2]. A smaller localization length and a more severe disorder in the lattice due to Fe doping were observed. Previous research showed that two transitional metals, Fe and Co, at B site of ABO_3 allowed a better performance compared to only Co or Fe located at B site. For example, cobaltites exhibit a significant weight loss when the annealing temperature is higher 1000ºC (in some case 800ºC) and a higher resistivity and oxygen diffusivity were observed in ferrites.

Experimental

The Pechini method [3, 4] was used to synthesize nanocrystalline particles[2], in this process a polymeric solution was formed due to a chelating reaction between cations and chelants. The polymeric solutions were also used as the thin film sources, which were used to fabricate thin films by spin coating and thermal processing. Electrical conductivity was measured by four-probe method at the temperature from 150 – 1000ºC in a wide range of oxygen activities (10^{-25} to 1). Thermogravimetric analysis was conducted at 1000 and 1200ºC in O_2, air and Ar. Mössbauer spectroscopy and neutron diffraction were performed at room temperature on the sintered and quenched specimens. During the quenching experiments, the specimens were first heated at 1000°C with a flowing gas atmosphere of N_2, air, or CO/CO_2 mixtures for 24 hours, and then quenched to room temperature. For Neutron Diffraction (ND) studies, samples were contained in 3 mm V metal cells and data were collected at 1.4785 Å over a range of 5º-105º (2θ). Rietveld refinement was carried out using the FULLPROF code, in which the magnetic ordering was taken into account because of the sensitivity of neutron diffraction to the magnetic ordering of the Fe atoms.

Results and Discussion

Figure 1 shows powder Neutron Diffraction Patterns of $La_{0.60}Sr_{0.40}FeO_{3-\delta}$ quenched at various gas environments. The powder Neutron Diffraction results showed that all specimens were single phase with an exception of the sample quenched with 90%CO/10%CO_2, in which peak broadening and asymmetry took place that indicated a decomposition of the sample. Four models [5] were used to fit the data for each sample and all results seemed reasonable. However, there did exist different preferred models for the reduced samples than for the air- and N_2- quenched samples and the neutron diffraction patterns for the samples quenched from the reducing atmosphere are significantly different with those quenched from air or N_2. The diffraction peak splitting for the reduced samples is dramatically reduced compared to the N_2- and air- treated samples. The first diffraction peak (~ 19°) is much stronger in the reduced samples than in the air- or N_2- quenched samples. This peak proves to be purely magnetic and the change reflects a large increase in magnetic moment for the reduced samples vis-à-vis the air- and N_2-quenched samples [5].

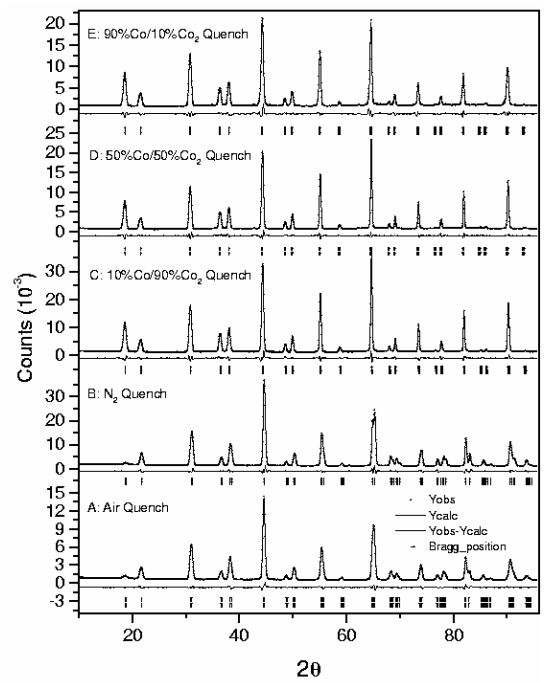

Figure 1. Powder Neutron Diffraction patterns of $La_{0.60}Sr_{0.40}FeO_{3-\delta}$ quenched at various gas environments.

Further study was then performed on the electrical conductivity of $La_{0.60}Sr_{0.40}FeO_3$ at the low pO_2, in which oxygen vacancy concentrations were increased. Figure 3 shows the plot of log(σ) vs. log(pO_2) at 1000ºC with a control over the oxygen activity being made by using a mixture of CO/CO_2, from which the pO_2 can be determined thermodynamically. In figure 3, a transition from p-type to n-type of conductor is obvious at relative low pO_2, at which the majority carriers changed from the holes to electrons because of the valence state decreases in Fe due to the further loss of oxygen. The

oxygen vacancies are generated at high temperature due to loss of oxygen, which results in a higher oxygen vacancy concentration and a lower hole concentration.

In addition to the conductivity, oxygen vacancy concentration also plays a key role in the function of cathodes, in particular in the catalytic properties. Determination of the oxygen vacancy level has been performed by thermogravimetric analysis (TGA) and neutron diffraction. TGA simply measures the weight changes with the variable being time, gas environment and temperatures. Neutron diffraction was performed on the samples which were quenched at 1000ºC from different oxygen activities. A large decrease in 3-δ was observed when the was gas changed from 90%CO to 99%CO. XRD results showed that $La_{0.60}Sr_{0.40}FeO_3$ decomposed in the 99% CO atmosphere. The consistence results between TGA and neutron diffraction confirmed that the quenching experiment could be used to study the ferrites under reducing conditions.

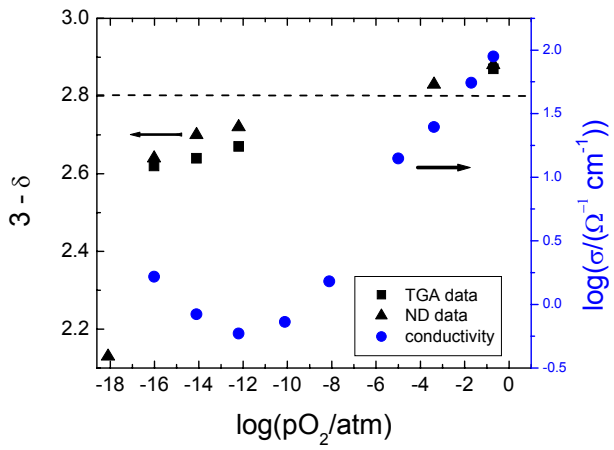

Figure 2. Log(σ) and 3-δ as a function of log(pO_2) for $La_{0.60}Sr_{0.40}FeO_{3-\delta}$.

Figure 3 shows Nèel Temperature and Fe-O-Fe angles as a function of pO_2, at which the specimen was quenched. The bonding angles of Fe-O-Fe were increased with decreasing oxygen partial pressures. Because the bonding lengths were nearly constant, the increasing of the bonding angle increases the overlap between Fe and O atomic states that results in an increase in the superexchange interaction between Fe and Fe. The Fe-Fe super-exchange interaction is highly dependent on the Fe-O-Fe bond angle and the superexchange through the oxygen atoms that is more effective when the Fe-O-Fe paths are close to linear [6]. It is also found that the increase in the superexchange interaction results in an increase in Nèel temperature, as shown in Figure 3. The Fe moments for the three reduced samples refine between 3.72 and 3.82 μ_B while the moments for the other two samples are much smaller (1.4 μ_B and 1.2 μ_B for the air- and N_2- quenched samples, respectively) [5].

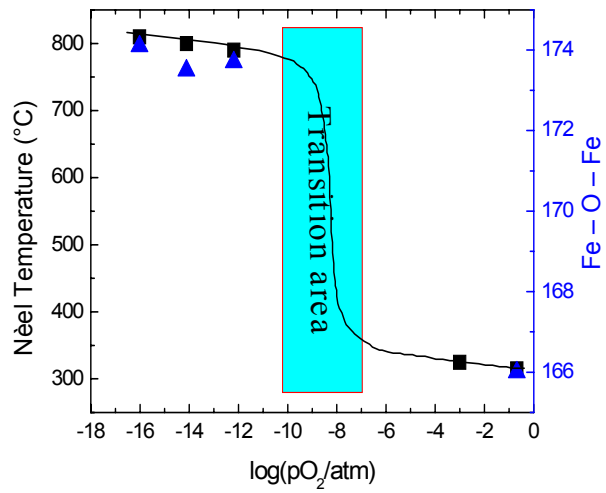

Figure 3. Nèel temperature and Fe – O – Fe angle of the specimens quenched at various oxygen partial pressures (pO_2).

Acknowledgement. The support by DOE under contract UAF99 – 0038 is highly appreciated.

References

(1) Takahashi, H.; Munakata, F.; and Yamanaka, M. *Phys. Rev. B.* **1998**, *57,* 15211.
(2) Sun, Y.; Xu, X.; Zhang, Y. *Phys. Rev. B.* **2000**, *62*, 5289.
(3) Pechini, M., U.S. Pat., No. 3,330,697, **1967**
(4) Anderson, H. U., Chen, C.-C., and Nasrallah, M. N., U.S. Pat., No. 5,494,700, **1996**.
(5) Chu, Zili, University of Missouri-Columbia, Dissertation, **2002.**
(6) J. B. Goodenough, Magnetism and Chemical Bond, Edited by F. A. Cotton (Interscience Publishers, London, 1976) Vol. 1, p. 170

Effect of water adsorption on MFI-type zeolite membrane prepared by *in situ* hydrothermal crystallization

Masahiko Matsukata, Tomoyuki Nara*, Eiichi Kikuchi**
*Sylvain Miachon**, and Jean-Alain Dalmon***

*Department of Applied Chemistry
Waseda University
3-4-1 Okubo
Shinjyuku-ku
Tokyo, 169-8555

**Insititut de Recherches sur la Catalyse
CNRS
2 Avenue Albert Einstein
69626 Villeurbanne Cedex
France

Introduction

Zeolite membranes have recently attracted considerable attention because they allow us to perform difficult liquid and/or gas separations. MFI-type zeolite membrane has extensively been studied. *In situ* crystallization is the most common method for synthesis of supported MFI type zeolite membranes.

In this study, we synthesized MFI zeolite membranes on porous α-alumina support tubes by in situ hydrothermal synthesis. In this method it is likely that alumina was dissolved into a synthesis gel from α-alumina support tubes during crystallization. Hence, the permeation properties of membranes synthesized by this method would be greatly affected by water adsorption. In order to investigate the effect of water adsorption on the permeation properties of MFI-type membranes, permeation tests were carried out using the membranes dried at room temperature after soaking them in deionized water.

Experimental

Membrane preparation. MFI-type zeolite were crystallized on porous α-alumina support tubes by in situ hydrothermal synthesis. The permeation zone was approximately 3 cm long. A gel was prepared with the following molar composition: 1 SiO_2:0.45 TPAOH (tetrapropylammonium hydroxide):22.7 H_2O[1]. After being stirred for 72 h, the gel was centrifuged for the purpose of removing the impurities. The support was put into the gel and crystallization was carried out at 170°C for 72 h. TPA cation contained in the membrane was removed by the calcination in air at 500°C for 5 h.

Characterization. The structure of products was analyzed by X-ray diffraction (XRD) with Cu K_α radiation.

Permeation tests.

The permeation test of mixed gas of H_2/n-C_4H_{10} was carried out in the temperature range of 30-300°C with the membranes which were dried at room temperature after soaking them in ion-exchanged water. The permeances were measured during heating and cooling.

In order to investigate the influence of water adsorption in the zeolite membranes on permeation properties, single gas permeation tests using H_2 were carried out in the temperature range of 30-300°C using a membrane dried at room temperature after soaking it in deionized water. The permeation test was started at 303 K after the water treatment of membrane. The temperature was raised up to 673 K and then fell to 303 K. The permeances were measured after the permeation reached a steady-state at each temperature. Two kinds of gas were used as feed gas: one was H_2 gas containing 500 ppb water stream and another was H_2 gas stream dried with a liquid nitrogen trap.

The permeate through the membrane in the single gas permeation test for H_2 at 100°C was analyzed for water by using Q-mass. The membrane was heated from 30 to 100°C with a rate of 6°C min^{-1} and held at this temperature. To prevent the pump of Q-mass from drawing air from the outlet of the apparatus, He gas was fed into the permeate side.

Results and Discussion

Figure 1 shows the XRD pattern for the MFI membrane synthesized. From the XRD pattern observed, MFI zeolite crystals were nicely grown on the support tube. **Figure 2** shows the gas permeation results of a 50:50 H_2/n-C_4H_{10} mixture. Separation factor

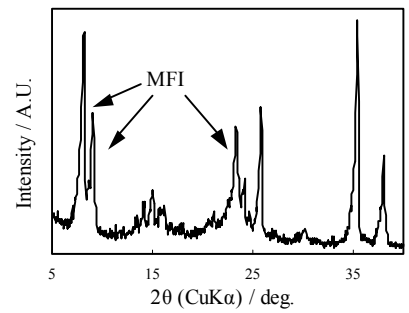

Figure 1. XRD pattern for MFI zeolite membrane.

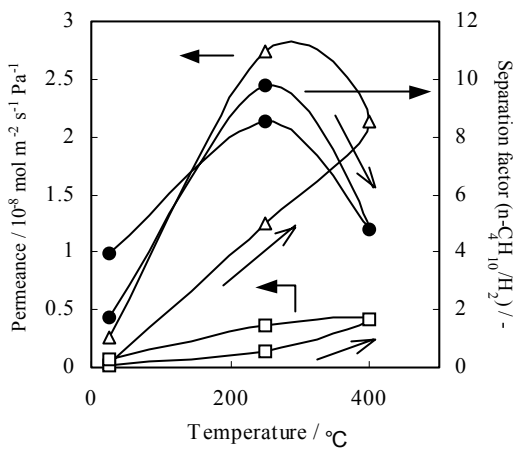

Figure 2. Mixed gas (n-C_4H_{10}/H_2) permeation results using the membrane treated with water. ● :separation factor (n-C_4H_{10}/H_2), △:n-C_4H_{10} permeance, □:H_2 permeance

(n-C_4H_{10}/H_2) was around 10 at 250°C during heating, supporting that the concentration of the defects (or pinholes) in the membrane is low. The separation factor of n-C_4H_{10}/H_2 measured during cooking was less than that observed during cooling. Based on this result, we suppose that the observed difference in the permeances during heating and cooling was due to the desorption of water adsorbed in the membrane.

The results of the single gas permeation of H_2 through the membrane treated with water are shown in **Figure 3.** The solid curve represents the results of single gas permeation tests using a dried H_2 gas stream, and the broken one represents the results of those using H_2 gas containing 500 ppb water stream. It should be noted that the

results of the tests using a dried H_2 gas stream and those using dried H_2 gas stream were different from each other. Even a small amount of water (ca. 500 ppb) influenced the permeation properties of the membrane. In these two cases, the permeances measured during cooling were higher than those during heating. It might be attributed to the removal of water adsorbed in the micropore of zeolite during heating up to 300°C.

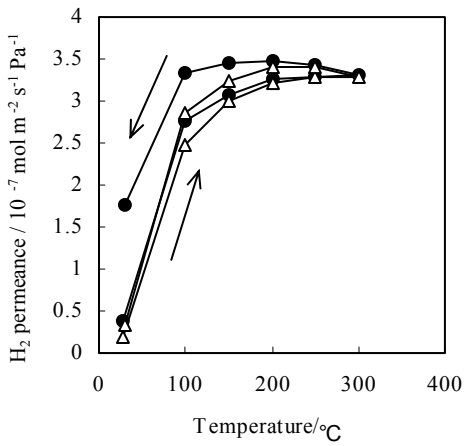

Figure 3. Single gas permeation tests for H_2 using the membrane treated with water. △:H_2 gas containing 500 ppb water stream, ●:Dried H_2 gas stream.

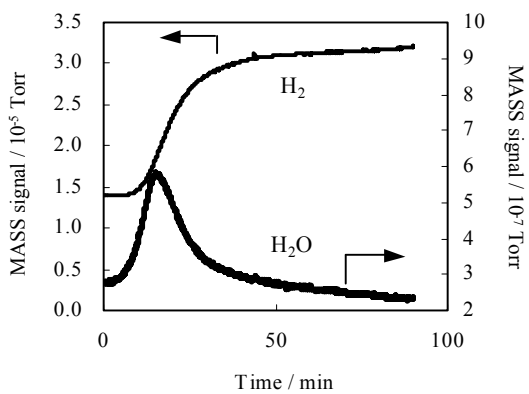

Figure 4. Composition of the permeate in the H_2 permeation test at 100°C. The membrane was heated up to 100°C after the water adsorption.

In order to confirm this assumption, the composition of the permeate side during the H_2 permeation at 100°C was analyzed by Q-mass. **Figure 4** shows the results. The signal intensity of H_2 started to increase at around 15 min while that of H_2O did earlier, at around 7 min. Water was strongly adsorbed in the membrane and blocked the permeation of H_2. Such adsorbed water was partially released to the permeate side, leading to the increase in the permeance of H_2.

From the results obtained in this study, it was suggested that the desorption of water was attributed to the lager permeances measured during cooling as compared with those obtained during heating.

Concluding remarks

The permeation properties of a MFI-type zeolite membrane were influenced by the water adsorbed in the membrane. Even 500 ppb water stream influence the single gas permeation properties of the membrane. These properties of the membranes might be caused by strong hydrophilicity of highly aluminated MFI-type zeolite formed in the *in situ* crystallization method.

References

1. J. Ramsey, A. Giroir-Fendler, A. Julbe, J.-A. Dalmon, French Patent 9,405,562 (1994).

TUBULAR TYPE PERVAPORATION MODULE WITH SILICALITE MEMBRANES FOR DEHYDRATION OF BIOMASS ALCOHOL

Hidetoshi Kita,[1] Xiangshu Chen,[1] Xiao Lin,[1] Ken-ichi Okamoto,[1] Tadahumi Yamamura,[2] and Jun Abe,[2]

[1]Department of Advanced Materials Science and Engineering, Yamaguchi University, Tokiwadai , Ube 755-8611, Japan
[2]Department of Industrial Machinery Design, Mitsui Engineering and Shipbuilding Co. Ltd., Tamano 706-8651, Japan

Introduction

Pervaporation has gained widespread acceptance as an effective process for separation of azeotropic mixtures. [1] It has been applied to the dehydration of organic liquids and many fundamental works have been carried out using polymeric membranes. However, membranes that have both high selectivity and high flux are not commonly available. Furthermore, polymeric membranes have been limited to applying dehydration of solvents due to insufficiency of their thermal, mechanical and chemical stability. The recent development of zeolite membranes has made it possible to overcome the above limitations. Zeolite A membranes have been successfully applied to remove water from aqueous solutions on a large scale.[2] In contrast, silicalite membranes exhibited preferential organic compound permeation from water such as ethanol/water mixtures because silicalite zeolite not only has strong hydrophobic property but also preferentially adsorbs organic compounds.[3] Recently we have reported high-performance silicalite membranes on porous tubular supports could be prepared by a single hydrothermal treatment.[4] Here, the tubular pervaporation module with silicalite membranes is investigated in order to develop more energy efficient concentration of the biomass ethanol.

Experimental

A clear solution for synthesis of silicalite membranes was prepared by mixing and stirring tetraethylorthosilicate (TEOS), tetra-n-propylammonium hydroxide (TPAOH), and water at room temperature for 1 hour. The resultant molar composition is 1:0.17:120 (SiO_2: TPAOH: H_2O). A mullite tubular support with 50 cm in length and a pore size of 1 μm was vertically immersed in the solution. Crystallization was carried out at 185 °C for 40 hours. After crystallization, the sample was taken out, washed carefully with hot distilled water, dried at 100 °C for several hours, and then calcined at 400 °C for 40 hours with heating rate of 1 °C/min.

Pervaporation experiments were carried out using the apparatus described elsewhere.[4] The zeolite membranes were characterized by X-ray diffraction and electron probe microanalysis (EPMA). The surface morphology of zeolite membranes was examined by scanning electron microscopy (SEM).

Results and Discussion

Silicalite membranes were prepared by a single hydrothermal treatment on porous tubular supports. Silicalite crystals slowly grew onto the unseeded supports leading to formation of an incompact crystal layer as shown in Figure 1. On the other hand, the higher crystallization temperature (185ºC), the faster crystal growth rate is the favorable condition for preparation of silicalite membranes with high pervaporation performance for separation of ethanol from aqueous solutions. EPMA characterization indicates the Si content in depth of 1 μm from the top crystal layer was 100 at. % without detection of Al. The Al content in the crystal layer was also negligible levels. The EPMA result confirms that the high siliceous MFI membrane was obtained on the mullite tube.

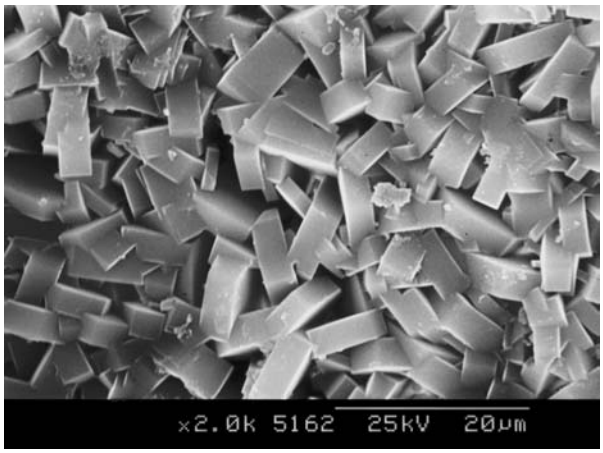

Figure 1. SEM photo of the surface of silicalite membrane prepared at 175ºC for 30h.

The pervaporation results for the silicalite membranes synthesized under typical conditions are listed in Table 1, which clearly shows that our silicalite membranes exhibit high flux and high separation factor. The tubular type module with 50 cm membrane was composed of 7 silicalite membranes. Membranes sealed one end of a support tube is inserted alternatively. Thus, pervaporation using zeolite membranes may have an opportunity for making a significant contribution to more energy efficient production of the ethanol from biomass.

Table 1. Pervaporation Performance of Silicalite Membranes at 60ºC

Synthesis condition		System(A /B)	Flux	$\alpha_{A/B}$
Temp [ºC]	Time [h]	[A 5wt%]	[kg/m^{2}h]	-
175	30	EtOH / H_2O	1.23	46
185	20		1.25	79
185	24		1.24	82
185	40		1.25	96
185	40	Acetone / H_2O	1.43	460
185	40	MEK / H_2O	0.36	1000

Acknowledgement. This research was partly supported by the MAFF project of Bioenergy Conversion in Japan.

References

1. Huang, R. Y. M., Ed., *Pervaporation Membrane Separation Processes*, Elsevier, Amsterdam, 1991.
2. Morigami, Y.; Kondo, M.; Abe, J.; Kita, H.; Okamoto, K., *Separation Purification Tech*. **2001**, *25*, 251.
3. Sano, T.; Yanagishita, H.; Kiyozumi, Y.; Mizukami, F.; Haraya, K. *J. Membr. Sci.* **1994**, *95*, 221.
4. Lin, X.; Kita, H.; Okamoto, K. *Ind. Eng. Chem. Res.* **2001**, *40*, 4069.

Driving Force for Pervaporation through Zeolite Membranes

Travis C. Bowen, Shiguang Li, Richard D. Noble*, and John L. Falconer

Department of Chemical Engineering, University of Colorado, Boulder, CO 80309-0424

Introduction

Zeolites are crystalline structures made mostly of SiO_2 with uniform, molecular-sized pores. Zeolite membranes can separate mixtures by molecular sieving, selective adsorption, and/or diffusion differences. Hydrophobicity or hydrophilicity of the zeolite is important for selective adsorption in organic/water separations. Isomorphous substitution of silicon by other elements in the zeolite framework has been shown to change the relative hydrophobicity/hydrophilicity of the membrane. Germanium substituted ZSM-5 zeolite membranes were more hydrophobic than silicalite-1 membranes prepared by a similar procedure. Although only small changes in the unit cell parameters and lattice vibration frequencies were observed when Ge was substituted for Si in MFI zeolite powders, the adsorption properties could change with substitution due to the changes in the T-O-T bond angle and T-O bond length [1].

Experimental

A Ge-ZSM-5 (Si/Ge = 41) zeolite membrane was synthesized by in-situ crystallization on the inner surface of a porous stainless steel tube. Characterization by XRD and SEM showed that the membrane had an approximately 30-μm thick layer of intergrown crystals with the ZSM-5 structure (~0.53-nm XRD pore size). The membrane had a n-C_4H_{10}/i-C_4H_{10} ideal selectivity of 2.1 at 473 K and a 0.2 g/m^2·h 1,3,5-tri-isopropyl benzene (0.85-nm kinetic diameter) flux at 303 K, indicating that it had few non-zeolite pores larger than 0.85 nm.

Results and Discussion

This membrane removed organics from 5 wt% organic/water mixtures by pervaporation. The organics included acetic acid, propionic acid, methanol, ethanol, 1-propanol, 2-propanol, 1-butanol, acetone, methyl ethyl ketone (MEK), methyl acetate, ethyl acetate, propionaldehyde, and diethyl ether, which were all smaller than the zeolite pore size. These organics exhibited more than a 500-fold range of fugacities and, in general, the organic/water separation factors increased with organic feed fugacity at 303 (Fig. 1), 313, 323, and 333 K. At 303 K, ethanol had an organic/water separation factor of 47, a 0.22 kg/m^2·h total flux, and a 1.30 kPa fugacity. The lowest separation factor was 2.7 for acetic acid, which had a fugacity of 0.12 kPa at 303 K and its total flux was 0.075 kg/m^2·h. The highest separation factor was 1200 for diethyl ether at 333 K. This mixture had a 147 kPa fugacity and its total flux was 1.23 kg/m^2·h. The organic fluxes exhibited a similar dependence on organic fugacity and also decreased with increasing organic heats of adsorption, in general. The water fluxes did not correlate with feed fugacities, but instead generally decreased with increasing organic sizes. Although low organic concentrations were present, water fluxes were significantly lower than the pure water fluxes of 0.22 and 0.66 kg/m^2·h for 303 and 333 K, respectively, indicating that the organics preferentially adsorbed on the zeolite and inhibited water adsorption and transport. Therefore, the separation occurred mainly by selective adsorption.

Fugacity ratios predicted a selectivity inversion for 1-butanol/acetic acid separations from 1-butanol/acetic acid/water mixtures. Three concentrations of equal molar ratios of 1-butanol and acetic acid in water were used. For increasing organic concentration, the 1-butanol/acetic acid separation factor decreased and became less than one. This was the same trend exhibited by the 1-butanol/acetic acid fugacity ratios.

Pervaporation separation factors for the binary and ternary mixtures separations were divided into a membrane contribution (α_{mem}) and an evaporation contribution (α_{evap}):

$$\alpha = \alpha_{evap} \cdot \alpha_{mem} \tag{1}$$

where

$$\alpha_{evap} = \frac{\hat{f}_a / \hat{f}_b}{x_a / x_b} \tag{2}$$

which is an equilibrium separation factor. Membrane quality was investigated and different membranes were compared using this evaluation. As temperatures increased, α_{mem} increased for most of the mixtures and the separation factors were higher than α_{evap} for all of the mixtures at 333 K. This indicates that the membrane selectivity was higher than what could be obtained by ordinary distillation.

Separation factors for hydrophobic and hydrophilic zeolite membranes reported in the literature also correlated with feed fugacities. Separation factors for the hydrophobic membranes increased as the organic/water feed fugacity ratio increased, but separation factors for the hydrophilic membrane increased as the water/organic feed fugacity ratio increased.

The driving force for transport through zeolite membranes is the coverage gradient across the zeolite layer. For pure liquid feeds, the fugacity is usually sufficiently high that the adsorption sites are saturated and intracrystalline flow is not dependent on the feed fugacity [2]. However, in mixtures, molecules compete for adsorption sites and a higher fugacity probably correlates with a higher competitive adsorption coverage at the feed-membrane interface. Using the relationship of selectivity and fugacity, measurements of pervaporation separations for a few mixtures in a given zeolite membrane should allow qualitative prediction of other mixture separations.

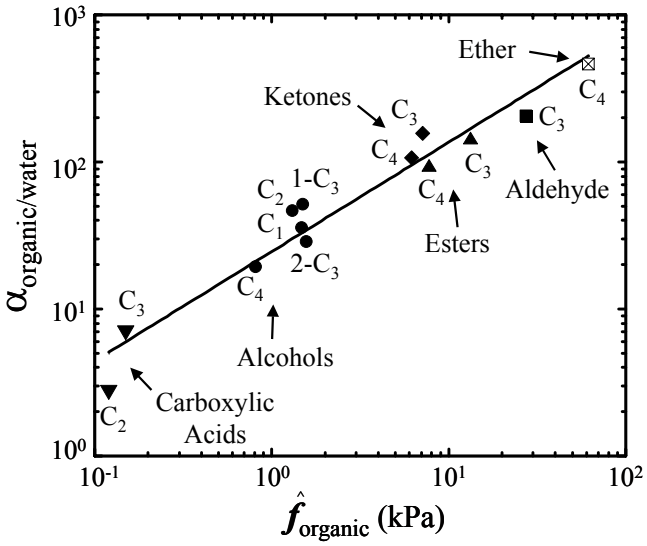

Figure 1: Organic/water separation factor for pervaporation of 5 wt% organic/water mixtures through a Ge-ZSM-5 membrane at 303 K. The line is fit to the data.

Conclusions

Separation factors for pervaporation of organic/water mixtures through zeolite membranes correlate with the fugacities of the feed components, and this correlation allows qualitative predictions of separation performance. Competitive adsorption coverages, and therefore the driving forces for transport, depend on the feed fugacities.

References

[1] H. Kosslick, V. A. Tuan, R. Fricke, C. Peuker, W. Pilz, and W. Storek, J. Phys. Chem., (1993) 97, 5678.

[2] M. Nomura, T. Yamaguchi, and S.-I. Nakao, J. Membr. Sci., (2001)187, 203.

Zeolite Membrane for Dehydration of Biomass Alcohol : Contribution to Mitigation of Global Warming

Shinichi Ichikawa*, Satoru Tanaka, Takashi Nakane, Masanobu Aizawa, Kiminori Sato, Takehito Mizuno, Hiroyuki Chida.
Bio Nanotec Research Institute, Inc., 3-42-3 Nihonbashi Hamacho,Tokyo,Japan. s-ichikawa@BNRI.co.jp

Introduction

The use of biomass alcohol is actively planned worldwide as one of the most viable solution to environmental and energy problems in the 21st century.

Let us consider biomass ethanol and its relation to mitigating global warming. Ethanol is produced through fermentation of biomass created by photosynthesis under the sun with carbon dioxide and water that are available in nature. This is then purified to create sufficiently high concentration of ethanol for use as fuel. The ethanol when it is combusted releases CO_2 into the air, but it is reused in the photosynthesis. Thus the carbon-neutral cycle as depicted in Figure 1 provides energy without increase of CO_2 concentration in the atmosphere.

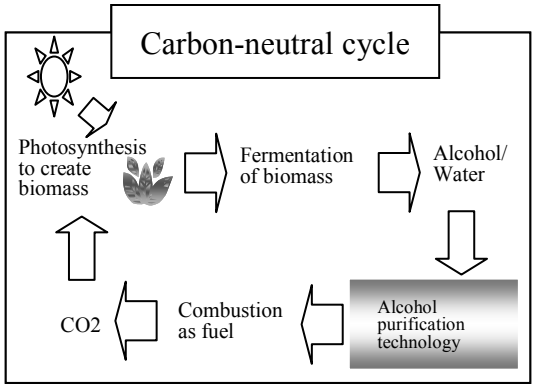

Figure 1. A scheme to mitigate global warming.

Where should we use the ethanol? "Gashol" is one place that has large potential and commercial impact for global contribution where dehydrated ethanol is added to gasoline for automobiles. Suppose half of the 900 million tons of sugarcane produced in the world is applied to biomass ethanol, the effect is extremely large. Implementation of Gashol has already begun in the U.S.A. and in Europe. And the projected increase in ethanol by 2010 is double to triple of the present amount. Meanwhile, Japan needs to decrease CO_2 emission by 6% on average by 2008 to 2012 based on the level of 1990 due to its ratification of the Kyoto protocol. This would be a very difficult goal to meet if not impossible. Introduction of biomass ethanol into the energy source market in Japan would have an immediate effect of 1% reduction in CO_2 emission. This would be the largest contribution by a single approach.

The biomass ethanol produced after fermentation requires purification. This is currently done by a series of distillation which must include azeotropic distillation that is complicated, costly and needs solvents. An alternative approach for the purification process is the zeolite membrane technology.

We have developed a highly efficient zeolite membrane that can provide high purity (more than 99.9 %) ethanol. The membrane system offers simple, safe and less energy-consuming production of ethanol which can be used for automobiles, power plants and elsewhere.

In particular, our zeolite membrane gives much higher flux under pervaporation mode compared to published results on membranes thus far which makes it an universally acceptable technology .

Preparation and Evaluation of Membrane

Zeolites are entering a new era of nanotechnology [1]. The use of zeolites for separation at the molecular level is expected to increase due to their ordered structure in the sub-nanometer range. The zeolite type chosen for the dehydration from ethanol/water mixture is sodium-A which is highly hydrophilic.

The membrane is formed by first introducing seed crystal onto the outer surface of a ceramic tube followed by hydrothermal synthesis. Optimization of every procedure is necessary to create a high performance membrane that is crystalline and continuous without pin holes.

The evaluation of the membrane is done by pervaporation. At the temperature of 75 degree Celsius or lower, the feed mixture (90wt% ethanol / 10wt% water) is introduced to the membrane which preferentially adsorbs and passes water, And the water is pumped by vacuum through the inside opening of the ceramic tube (Figure 2). The weight and components of the liquid permeated are measured and analyzed. The performance of the membrane is expressed as flux Q [Kg/m^2h] and separation factor alpha equal to (Yi/Yj)/(Xi/Xj) where i denotes water and j denotes alcohol, and X denotes feed and Y denotes permeate. Alpha values of 10000 would correspond to about 99.9% purity of ethanol attained.

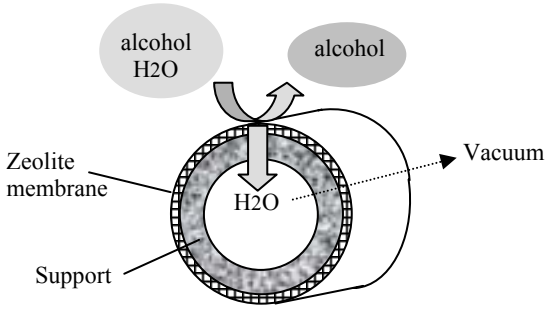

Figure 2. Dehydration of alcohol by pervapration.

Results and Discussion

By the method of pervaporation described above, our newly developed membrane gave redproducible flux of 3.5 [Kg/m^2h]. Also, values as high as 4.0 [Kg/m^2h] could be attained for certain synthesis conditions. The alpha values ranged between 20000 and 40000. These fluxes and separation factors are very high compared to published data on A-zeolite as well as T-,X-, and Y-zeolites which range between roughly 1 to 2 [Kg/m^2h] for the flux and about 10000 maximum for the separation factor [2,3].

Sodium-A type zeolite has a relatively low ratio of Si to Al and the sodium cations are placed in the alpha-cage pores. Therefore the pores are very hydrophilic channel convenient for selective adsorption and transport of water molecules. Also, the alpha-cage is such that it can pass water molecules but not ethanol molecules, thus functioning as a molecular sieve as well.

The X-ray diffraction of the film in its supported form without destruction was measured and only the peaks for A-type zeolite were detected as shown in Figure 3. The crystalline film is so thin that the peak intensities for the support alumina appeared very large.

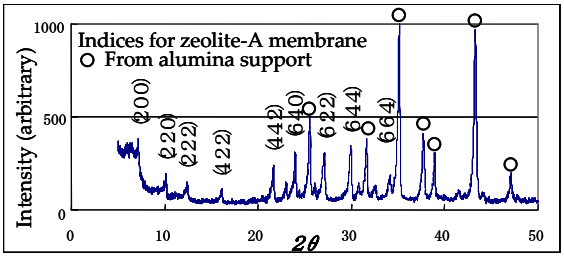

Figure 3. X-ray diffraction pattern.

Analyses of our high-performance membrane by SEM (Scanning Electron Microscopy) from low to high magnification observed perpendicular to the film as well as at its cross section indicated that Na-A zeolite crystal is densely intergrown and forms a continuous thin film.

On the other hand, membranes showing poor performance in terms of flux and separation had problems characterized by existence of amorphous phase, pinholes or cracks in the film or the thickness was too large.

HRTEM (High Resolution Electron Microscopy) showed some interesting features suggesting a kind of ordered interface between crystalline domains in addition to direct observation of the alpha-cage itself. There is no clear indication so far of grain boundary suggesting participation of molecular sieving in that region. Further studies with HRTEM and FIB-STEM (Focused Ion Beam – Scanning Transmission Electron Microscopy) are pursued to understand the relation between the physical structure of the film and its membrane characteristics.

The mechanism of water transport in the pores is difficult to understand while some simple models for gas diffusion have been reported in the past. Suggestions are made for further studies at the molecular level.

Conclusions

We have developed a sodium-A zeolite membrane with high flux and high separation factor for dehydration of ethanol/water mixture. The membrane is a densely intergrown crystalline thin film. The supported membrane elements are integrated into a module to form a total system which takes in biomass ethanol and delivers out purified ethanol. Demonstration and commercial systems are now available for testing and on-site operation.

In addition to biomass alcohol, a wide range of research has started where new types of zeolite membrane are developed for application to liquid and gas separation under mild or extreme operational conditions which use have large impact on improving or completely changing the approach to chemical processes in industry.

Lastly, we would like to thank Dr.Ryu for sample preparation and for taking the bright-field images by HRTEM and also to Professor Terasaki and Professor Ohsuna for their advice, all at Tohoku University.

References

(1) Davis, M. E., Nature, **2002**, 417, 813.
(2) Okamoto, K.; Kita, H.; Horii, K.; Tanaka, K.; Kondo, M. Ind. Eng. Chem. Res., **2001**, 40, 163.
(3) Kita, H. Kagaku Kogyo, **2002**, 53, 704.